AD-A228 652

DTIC
ELECTE
NOV 16 1990
S D
D

R C Hansen

(1)

DTIC FILE COPY

3rd Annual Review of Progress in

APPLIED COMPUTATIONAL ELECTROMAGNETICS

at the
Naval Postgraduate School
Monterey, CA

March 24–26, 1987

Conference Proceedings

DISTRIBUTION STATEMENT A
Approved for public release
Distribution Unlimited

90 11 14 148

ACES NEWSLETTER INFORMATION

Subscriptions. All members of the Applied Computational Electromagnetics Society (ACES) who have paid their subscription fees are entitled to receive the Newsletter (NL), with a minimum of two issues per calendar year. Current annual subscription fees are:

$25 for a practicing professional
$75 for an institution
$15 for a full-time student
FOREIGN MEMBERS (including CANADA) - We now accept ONLY International Money Orders as payment. Check with your financial institution concerning this. The prices above apply to you also.

Back issues, when available, are $15.00 each. Back issues of Conference Proceedings are also sometimes available. Subscriptions to ACES, orders for back issues, and changes of address should be sent to:

Dr. Richard Adler
Secretary, ACES
Naval Postgraduate School
Code 62AB
Monterey, CA 93943 USA

Allow four weeks' advance notice for change of address. Claims for missing issues will not be honored because of insufficient notice of address change or loss in mail unless the Secretary is notified within 90 days for USA and Canadian subscribers or 150 days for subscribers in other countries, from the last day of the month of publication.

Publication Charges. There are no page charges for camera-ready articles of no more than ten printed pages. Excess pages will cost $10.00 each, payable to the Secretary at the time of written acceptance of the article by the Editor(s). Authors are entitled to 20 free reprints of their articles. Additional reprints are available to authors, and reprints are available to nonauthors, according to the following schedule:

$0.20 per page, 1-20 reprints
$0.15 per page, 21-50 reprints
$0.10 per page, 51 or more reprints

Content and Format of Submissions. The NL welcomes original, previously unpublished articles, notes, and correspondence concerning applied computational electromagnetics, which can include associated phenomena (such as elastic wave propagation, charged particle interactions). Articles should treat theoretical and/or experimental aspects of applications, enhancements, limitations, and validation of computer code modeling. Tutorial articles are welcome. Shorter submissions of modelling notes, code descriptions, correspondence, ACES news, special features, and software exchange are suggested by the contents of these sections in the NL.

At present, only camera-ready copies will be accepted for publication, although authors may submit other copies for publication review by the appropriate editor. The recommended format is the Radio Science 2-column format in all respects, as described on the inside back cover of most Radio Science issues. All submissions should be sent in duplicate to the Secretary.

Copyrights and Releases. Each contributor of technical material must sign a copyright form and obtain a release form from his organization vesting the copyright with ACES. Both forms will be provided by ACES and allow both the contributor and his organization to use the copyrighted material freely for their own private purposes. Permission is granted to quote short passages and reproduce figures and tables from a NL issue provided the source is cited. Copies of NL articles may be made in accordance with usage permitted by Sections 107 or 108 of the U.S. Copyright Law. This consent does not extend to other kinds of copying, such as for general distribution, for advertising or promotional purposes, for creating new collective works, or for resale, The reproduction of multiple copies and the use of articles or extracts for commercial purposes require the consent of the author and specific permission from ACES. Institutional members are allowed to copy any NL issue for their internal distribution ONLY.

Software Material. ACES will foster through the NL the sale and exchange of information about software material and the sale and exchange of material itself but will not act as a repository or clearinghouse of such material. Readers wanting more information about such material or the material itself should contact the contributor of the relevant NL information.

Liability. Neither ACES nor the NL editors are responsible for any consequences of misinformation or claims, express or implied, in any published material in a NL issue. Authors of contributions are responsible for information contained in them.

©1987, The Applied Computational Electromagnetics Society

AGENDA

The Third Annual Review of Progress in Applied Computational Electromagnetics
122 Ingersoll Hall
Naval Postgraduate School
March 24-26, 1987

Monday 23 March

1900-2030 Registration

Tuesday 24 March

0730-0930 Registration

0830-0915 ACES General Business Session

0915-1045 Session I - "SCATTERING"

"Solving a Perturbed Problem in a Moment Method Code"
Elizabeth Yip and Brian Tomas — The Boeing Aerospace Company

"Improved Computing Algorithms For Light Scattering By A Spheroid"
Wan-xian Wang and R.T. Wang — University of Florida, Space Astronomy Lab

"Bistatic Scattering Analysis of an Ellipsoid"
Ronald J. Marhefka and J.H. Choi — OSU-ElectroScience Laboratory

"The Use of Method of Moments to Analyze Scattering from Small Metal Gaps"
J.L. Karty and B.L. Harris — McDonnell Douglas Corporation

"Uniform Theory of Diffraction - Moment Method Model Comparison for a Dihedral Corner Reflector"
J.L. Fath, A.J. Terzuoli, E.G. Zelnio — Air Force Institute of Technology

"Quantum-Mechanical Techniques for Electromagnetic Scatter Modeling by Simple, Non-Canonical Shapes"
D.E. Stein — USAF - 6585th Test Group
A.E.S. Green — University of Florida

1045-1100 Break

1100-1130 Session I (cont.)

"Boundary Conditions and Sampling for Method-of-Moment Calculations of Electromagnetic Scattering"
R.J. Balestri, M.V. Hikida & J.W. Williams — Booz, Allen & Hamilton, Inc.

"Prediction of the Scattering from a Cube With GEMACS"
G.R. Salo, D.E. Thomas — The BDM Corporation

1130-1215 Session II - "EM MODELING"

"Recent Updates to the NEC-BSC"
R.J. Marhefka and J.W. Silvestro — OSU - ElectroScience Laboratory

"Transfinite Elements - A High Efficiency Method for Electromagnetic Scattering"
Z.J. Cendes and Jin-Fa Lee — Carnegie-Mellon University

"Adaptive Spectral Response Modeling of Planar MMIC Devices"
Z.J. Cendes and Jin-Fa Lee — Carnegie-Mellon University

1215-1330 Lunch

1330-1430 Session III - "ANTENNAS NEAR GROUND"

"HF Ground and Vegetation Constants"
G.H. Hagn — SRI International

"Comparison of Measured and NEC-Calculated Characteristics of a Vertical Monopole with Buried Ground Radials"
L.O. Hamish, M. Lee and G.H. Hagn — SRI International

"Modeled and Measured Impedance of a Bowtie Antenna Over Imperfect Ground"
Martin L. Perrine — U.S. Department of Defense

"Vertical Monopoles with Elevated Ground Systems"
Al Christman — Ohio U - ECE Dept

1430-1445 Break

1445-1630 NEC USERS PANEL DISCUSSION, Chaired by Jim Breakall
User community suggestions on needed enhancements for NEC
(5 minute limit per participant - Use viewgraphs for maximum efficiency)

1630-1730 PC DEMONSTRATIONS AND CONCURRENT POSTER SESSION, Coordinated by Chuck Vandament
Rooms 368 and 369

Wednesday 25 March

0830-1030 Session IV - "APPLICATIONS OF COMPUTER EM MODELING"

"The Finite Element Radiation Model (FERM) Program"
David A. Shnidman — M.I.T. Lincoln Laboratory

"Finite Element Analysis of Microwave Cavities"
John R. Brauer and Jeffrey J. Ruehl — A.O. Smith Engineering Systems
Anthony B. Bruno — Naval Underwater Systems Center

"Mutual Impedance Computations Using NEC"
D.E. Hudson — Lockheed Aircraft Service Company

"Test of a Coaxial Line Source Model for NEC"
G.J. Burke — Lawrence Livermore National Laboratory

"Accuracy of Wire Grid Model Near Fields"
A.C. Ludwig — General Research Corporation

"A Numerical Method for Solving Maxwell's Equations With a Coarse Grid Bordering a Fine Grid"
Kane S. Yee and John C. Kasher — Lawrence Livermore National Laboratory

"A Reduced Number of Integral Equations for the Numerical Modeling of Two Dimensional Composite Structures"
J.L. Volakis, M.A. Ricoy and T.J. Peters — University of Michigan

"Scattering From Thin Planar Material Plates With Arbitrary Perimeter"
J.L. Volakis and Timothy J. Peters — University of Michigan

"Development of a Modeling Handbook for Use in Computational Electromagnetics"
E.K. Miller — University of Kansas

1030-1045 Break

1045-1200 Session V - "NEC-2 AND PC CODE APPLICATIONS"

"Large Yagi Analysis With MININEC3"
W.B. Seabreeze

"The Quad-Log Periodic Antenna"
C.C. Smith — Kaman Sciences Corporation
M. Baron

"Complex Input Impedance of a Monopole Over a Ground Plane"
Andy McMahon — Kaman Sciences Corporation

"AT/ESP 1 - A PC Version of the OSU Wire-Plate-Patch Code""
R.J. Luebbers — The Pennsylvania State University

"Error Estimates for Large Order Antenna Calculations on a PC"
V.P. Cable — California Microwave, Inc.

1200-1315 Lunch

1315-1430 Session VI - "INPUT - OUTPUT ISSUES"

"Input Impedance Calculations Using the Sperical Wave Expansion Technique"
A.C. Ludwig — General Research Corporation

"I-NAC-3 A User-Friendly Interactive Electromagnetics Code for Workstations, MINIS and Mainframes"
Ruediger Anders — Applied Electromagnetics Engineering

"A Different Approach to User-Friendly and Economical Geometry Data Input for EM Codes"
Ruediger Anders — Applied Electromagnetics Engineering

"Interactive Graphical Display of Scattering Data on the Sphere"
G.D. Kerlick — NASA Ames Research Center

"A Numerical Electromagnetic Engineering Design System"
A.P. Ludwigsen — Lawrence Livermore National Laboratory

1430-1445 Break

1445-1545 COMPUTER GRAPHICS PANEL DISCUSSION, Chaired by Steve Lamont
(Same ground rules as NEC USERS P.D.)

1545-1700 PC DEMONSTRATIONS AND CONCURRENT POSTER SESSION
Rooms 368 and 369

1800-1830 "Early Bird Special" (Dutch Treat) at Cannery Row Restaurant, The Captain's Cove, 643 Cannery Row

Thursday 26 March

0830-0930 ACES Committee Reports and Concluding Business

0930-1045 Session VII - "CODE DEVELOPMENT"

"A New Approach to a Simpler and More Efficient Treatment of Multiple Junctions by Higher Basis Functions"
Ruediger Anders — Applied Electromagnetics Engineering

"An Algorithm for Minimizing Matrix Bandwidth in Method-Of-Moments (MOM) Computer Codes"
R.M. Bevensee — Lawrence Livermore National Laboratory

"Digital Algonthm Specification for the VLSI Implementation of the Electromagnetic Field of an Arbitrary Current Source"
B.A. Hoyt, A.J. Terzuoli, A.V. Lair — Air Force Institute of Technology

"SAC - An Aperature Code With Near Field Excitation"
C.C. Smith — Kaman Sciences Corporation

"PC Workstation - Good News for ACES"
A.J. Lockyer and P. Tulyathan — Northrop Corporation

1045-1100 Break

1100-1215 Session VIII - "ANTENNA MODELING"

"Conformal Wideband Antenna Modeling"
H.A. Karwacki and R.A. Gilbert — Sanders - A Lockheed Company

"NEC-3 Pattern and Impedance Results vs. Analytical and Experimental Results for Two 'Simple' Antennas"
R.M. Marion — Science Applications International Corporation

"Comparison of Pattern Measurements and Calculations for a VHF Dipole on the Empennage of an Aircraft"
S.K. Buchmeyer and C.H. Vandament — Rockwell International

"A Comparison of the Fields of a Medium Wave Directional Antenna as Calculated by the FCC Method and NEC-2"
James B. Hatfield & Paul W. Leonard — Hatfield & Dawson, Inc.

"Numerical Calculation and Experimental Verification of Near Fields from Horns"
Don W. Metzger — Kaman Sciences Corporation

1215-1330 Lunch

1330-1515 Session VIII - (con't)

"Helicopters, HF Antennas: Models, Measurements and All That"
Stanley J. Kubina — Concordia University

"NEC2 Analysis of Archimedean Spiral Antenna"
T.H.B. Cranor — McDonnell Douglas Astronautics Company

"Finite and Infinite Broadside Scan Dipole Arrays"
H.K. Schuman and T.J. Cleary — Atlantic Research Services Corporation

"Problems Encountered While Modeling a Broadband Dipole Using NEC-3"
Lee W. Corrington — US Army - USAISEIC

"A MININEC Model of the Miniloop Antenna"
James C. Logan — Naval Ocean Systems Center

"HF Antenna Handbook"
E.E. Domning and J.K. Breakall — Lawrence Livermore National Laboratory

"GEMACS Update"
Kenneth Siarkiewicz — U.S. Air Force - Rome Development Center

(E)

1515 Break or leave for Monterey Aquarium Tour

OPEN SESSION/LATE PAPERS/FINAL DEMOS

"Relative Communication Efficiency of Short HF Monopole Antennas With Sparse, Abbreviated, Radial-Wire Ground Systems"
Ric Thowless — Naval Ocean Systems Center

"Radiation Hazard Evaluation Using NEC-BSC"
W.J. Koh & R.W. Adler — Naval Postgraduate School

"Two Computer Graphics Simulations of the Electronic Field Radiated by a Dipole Antenna"
Dennis E. Fessenden — Naval Underwater Systems Center
Steven G. Satterfield — U.S. Naval Academy

POSTER PAPERS

"IGUANA - Interactive Graphics Utility for Automated NEC Analysis"
John Strauch — Unisys Defense Systems
J.C. Logan — Naval Ocean Systems Cente.

TENTATIVE PC DEMONSTRATIONS

*NEC2-PC
*IGUANA 4.1
*NAC-3
*AOS/MAGNUM
*MMIC MODELING
*TRANSFINITE ELEMENTS
*NEWS POST-PROCESSOR

DTIC COPY INSPECTED 6

Accesion For
NTIS CRA&I ☑
DTIC TAB ☐
Unannounced ☐
Justification .....
By per AD-A224563
Distribution /
Availability Codes
Dist | Avail and/or Special
A-1

Ground wave (HF, VHF) Ground
Small metal (apps) Scattering
Monopoles
Sparse, limited wires
short monopole codes
predict antennas, (KP)

*Some of the papers contained in these Proceedings are in the form of abstracts and/or viewgraphs. If possible, the full text of the paper will be published in future Newsletters.

SESSION I - "SCATTERING"

Moderator: R. Bevensee

SOLVING A PERTURBED PROBLEM IN A MOMENT METHOD CODE

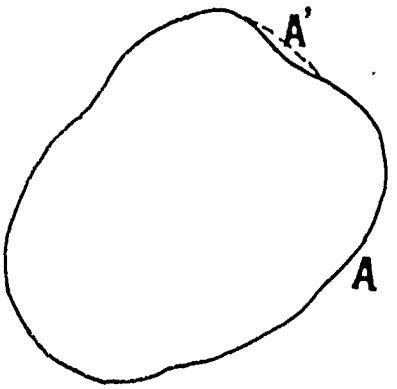
ELIZABETH YIP
BRIAN TOMAS

BOEING AEROSPACE COMPANY
SEATTLE, WA 98124

In this paper, we present an efficient method of computing the solution to scattering problems using a perturbation scheme based on the solution of a related original problem. We show that in practical applications, this method reduces computation times by a factor of 5 or more. Assuming the radar cross section has been computed for a particular scatterer associated with a matrix A using a moment method code, we call the computation of the radar cross section of a slightly perturbed scatterer a perturbed problem of A. If the original problem has n unknowns, and the perturbed problem is formed by changing p cells of the original problem, then our method requires an operation count of $O(n^2p)$ while a direct moment method solution requires an operation count of $O(n^3)$. Our method involves application of the Sherman-Morrison-Woodbury formula for inverses of perturbed matrices. We show that the method can be easily implemented in any moment method code, and the user does not need to learn a new input procedure. Numerical results from huge practical problems demonstrate the efficiency and stability of the new method.

Acknowledgement:
The work of the first author has been funded by Rome Air Development Center/OCTM under contract number F30602-85-C-0225.

PROBLEM:



- HAVE SOLVED Ax=b
- WANT TO SOLVE (A + A')x'=b'

CONTENT:

- COMPUTATION EFFICIENCY ($O(n^2p + p^3)$)

- MATRIX PROBLEM

- THEORY

- COMPUTER IMPLEMENTATION

NUMERICAL EXAMPLES

1. 2D MOM CODE

- IMPEDANCE BOUNDARY CONDITION (RAMZ)
- NO. OF CELLS IN OLD PROBLEM : 312
- NO. OF CELLS APPENDED TO OLD PROBLEM : 22
- NO. OF CELLS IN NEW PROBLEM : 344

FPS164 CP SECONDS ON SOLVER

	RAMZ	SMW-RAMZ
OLD PROBLEM	12.6	
NEW PROBLEM	15.3	3.3

2. 2D MOM CODE - VOLUMETRIC (DMS801)

- NO. OF CELLS IN OLD PROBLEM : 800

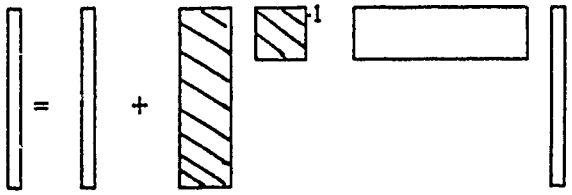
FPS164 CP SECONDS

	NO. OF PERTURBED CELLS	DMS801	SMW-DMS
OLD PROBLEM		434.2	
NEW PROBLEM	3		52.5
	11		62.4
	25		73.3
	32		73.3

THEORY:

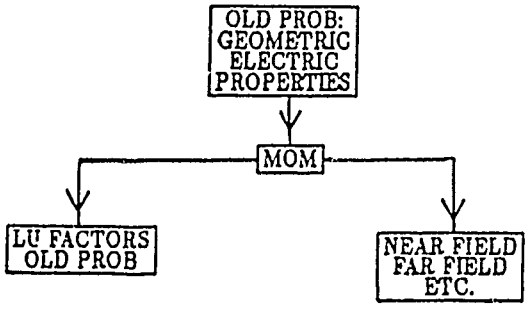
SHERMAN-MORRISON-WOODBURY UPDATING

$$B^{-1}c = A^{-1}c + A^{-1}U(I - V * A^{-1}U)^{-1}V * A^{-1}c$$



COMPUTER IMPLEMENTATION:

1. SOLVE OLD PROBLEM:



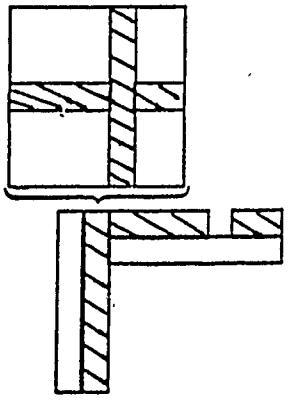
MATRIX PROBLEM:

1. PERTURBING GEOMETRIC AND/OR ELECTRIC PROPERTIES

$Ax = b, x = A^{-1}b$ (SOLVED)

$By = c, y = B^{-1}c$ (TO BE SOLVED)

B = A +

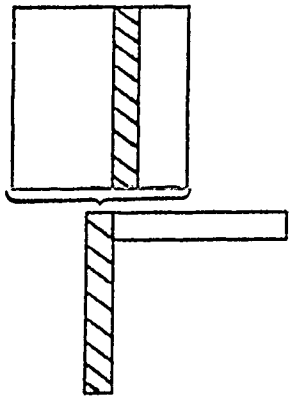


2. PERTURBING ELECTRIC PROPERTIES ONLY

$Ax = b, x = A^{-1}b$ (SOLVED)

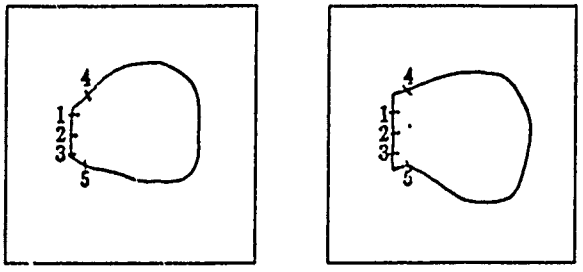
$By = c, y = B^{-1}c$ (TO BE SOLVED)

B = A +



GRAPHIC ILLUSTRATION OF SORTING PROCEDURE

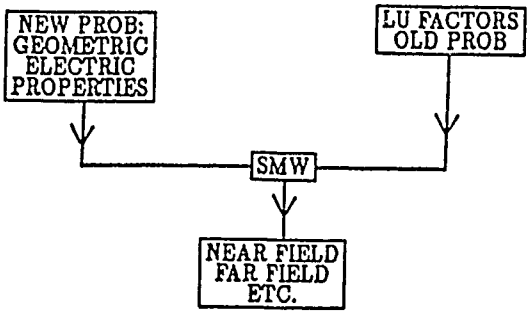
CONSIDER THE X-Y PLANE AS A ONE DIMENSIONAL ARRAY:



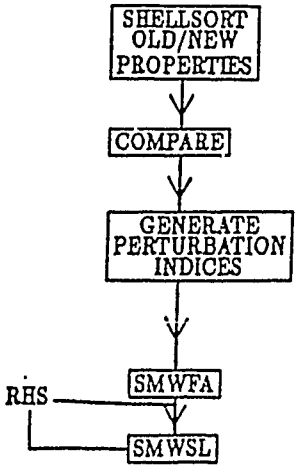
GRAPHIC ILLUSTRATION OF COMPARISON PROCEDURE:

OldGeometry		*NewGeometry*
(1.0, 2.0)		
		(1.5, 2.0)
(2.0, 2.0)	-----	(2.0, 2.0)
⋮		⋮
(1.0, 3.0)	-----	(1.0, 3.0)
(1.0, 3.5)		
(2.0, 3.5)	-----	(2.0, 3.5)

SOLVE NEW PROBLEM:



STRUCTURE OF SMW:



SPECIAL FEATURES OF THIS IMPLEMENTATION:

1. USER FRIENDLINESS :

   - THE USER DOES NOT NEED TO LEARN ANOTHER INPUT PROCEDURE.

2. CONSERVATION OF PROGRAMMING EFFORT:

   - THE CORE SUBROUTINES ARE 'ENVIROMENT' INDEPENDENT:
     WITH FEW CHANGES, THE SORTING, COMPARISON AND INDICES GENERATING SUBROUTINES AS WELL AS SMWFA AND SMWSL CAN BE ADAPTED TO ALMOST ANY MOM CODES.

CONCLUSION :

- AN EFFICIENT METHOD FOR SOLVING A PERTURBED PROBLEM BASED ON MOM CODES.
- VERIFICATION OF STABILITY AND EFFICIENCY OF THE METHOD WITH REAL DATA.
- USER FRIENDLINESS.

Improved Computing Algorithms for Light Scattering by a Spheroid

Wan-xian Wang and R.T. Wang
Space Astronomy Laboratory, University of Florida
Gainesville, FL 32609

ABSTRACT

New computing algorithms for calculating the prolate and oblate spheroidal wave functions are developed and some corrections on published results by other researchers are shown. These algorithms significantly improve the computational accuracy/speed to obtain the scattering coefficients for prolate and oblate spheroids, especially those with high aspect ratio (up to 20:1) and large size parameter (50 to 60). The use of P-Q extinction plots to compare theory and our microwave data shows a good agreement in the particle-orientation dependence of extinction profiles.

I. INTRODUCTION

Asano and Yamamoto[1] had studied the light scattering by a spheroidal particle within a certain range of size parameter α ($=\kappa a$, where κ is wave number, a is semi-major axis). The spheroidal eigenvalues λ_{mn} and the expansion coefficients d_r^{mn} for the angle functions S_{mn} were computed following the Bouwkamp's method,[2] which was also adopted in Flammer's book.[3] However, this method is restricted to smaller size paremeter c ($=\kappa(a^2-b^2)^{\frac{1}{2}}$, where b is semi-minor axis) ($c < 15\sim20$) and large number n, For small number n and/or large values of c, the asymptotic series expansion for eigenvalues, which was given in Meixner's pape.[4] must be employed.

Figure 1 is the convergence diagram for two existing methods — Bouwkamp's and asymptotic. An arrow indicates the direction of faster convergence for the eigenvalues. For large values of c, the asymptotic expansion is only valid for small n, and Bouwkamp's method becomes effective as n goes to large number; some overlap spanning these two methods occurs at the certain numbers n depending upon the size parameter c. Unfortunately,

a notable gap forms in the case of moderate values of c and intermediate n, and one is required to develop these two methods to cover this gap.

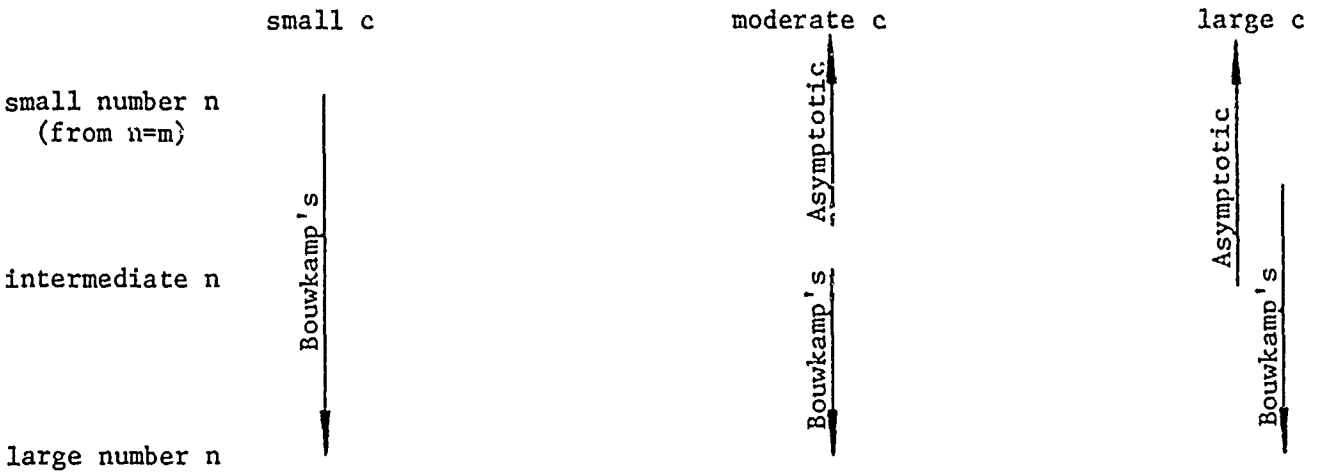


Figure 1. Convergence Diagram for the Bouwkamp's and Asymptotic Methods

II. CORRECTIONS AND DEVELOPMENTS

We have developed Bouwkamp's and asymptotic expansions. For both prolate and oblate, the highest order term in power of c has been expanded from c^{10} in the Bouwkamp's method[3] to c^{16}, and from c^{-5} in the asymptotic expansion to c^{-6}, by Wan-xian Wang.[5]

It is worth pointing out that: the coefficient of c^{10} term in Flammer's book is incorrect because of a sign error in the third term of the second part (the numerator 6n-25 instead of correct 6n+25); also, the asymptotic coefficients for c^{-2} and c^{-5} terms have to be corrected:

uncorrected c^{-2} term:
$$-\left\{5(\ell^4+2\ell^3+7\ell+3)-48m^2(2\ell^2+2\ell+1)\right\}2^{-6}c^{-2} \tag{1-1}$$

where $\ell = n - m$.

corrected:
$$-\left\{5(\ell^4+2\ell^3+\underset{\cdot\cdot\cdot\cdot}{8}\ell^2+7\ell+3)-48m^2(2\ell^2+2\ell+1)\right\}2^{-6}c^{-2} \tag{1-2}$$

where Flammer missed $8\ell^2$ term (see under-dotted).

uncorrected c^{-5} term:
$$\begin{aligned}-\Big\{&527(2\ell+1)^7+61529(2\ell+1)^5+1043961(2\ell+1)^3+2241599(2\ell+1)\\&+2^5m^2\left\{5739(2\ell+1)^5+127550(2\ell+1)^3+298951(2\ell+1)\right\}\\&-2^{11}m^4\left\{355(2\ell+1)^3+1505(2\ell+1)\right\}+2^{16}m^6(2\ell+1)\Big\}2^{-20}c^{-5}\end{aligned} \tag{1-3}$$

corrected:

$$-\Big\{527(2\ell+1)^7+61529(2\ell+1)^5+1043961(2\ell+1)^3+2241599(2\ell+1)$$
$$-2^5m^2\Big(5739(2\ell+1)^5+127550(2\ell+1)^3+298951(2\ell+1)\Big)$$
$$+2^{11}m^4\Big(355(2\ell+1)^3+1505(2\ell+1)\Big)-2^{16}m^6(2\ell+1)\Big\}2^{-20}c^{-5} \qquad (1\text{-}4)$$

where he made several errors in sign (see under-dotted).

One more higher order term is added to the asymptotic expressions for the prolate and oblate eigenvalues, respectively, that is

$$\lambda_{mn} = qc - \frac{1}{2^3}(q^2+5-8m^2) - \frac{q}{2^6c}(q^2+11-32m^2) - \frac{1}{2^{10}c^2}\Big(5(q^4+26q^2+21)-384m^2(q^2+1)\Big)$$

$$- \frac{q}{2^{14}c^3}\Big((33q^4+1594q^2+5621)-128m^2(37q^2+167)+2048m^4\Big)$$

$$- \frac{1}{2^{16}c^4}\Big((63q^6+4940q^4+43327q^2+22470)-128m^2(115q^4+1310q^2+735)+24576m^4(q^2+1)\Big)$$

$$- \frac{q}{2^{20}c^5}\Big((527q^6+61529q^4+1043961q^2+2241599)-32m^2(5739q^4+127550q^2+298951)$$
$$+2048m^4(355q^2+1505)-65536m^6\Big)$$

$$- \frac{1}{2^{25}c^6}\Big((9387q^8+1536556q^6+43711178q^4+230937084q^2+93110115)-1536m^2(2989q^6+112020q^4$$
$$+648461q^2+270690)+196608m^4(175q^4+1814q^2+939)-12582912m^6(q^2+1)\Big)$$

$$+ O(c^{-7}) \qquad \text{for prolate} \qquad (2\text{-}1)$$

where $q = 2(n - m) + 1$.

$$\lambda_{mn} = -c^2 + 2qc - \frac{1}{2}(q^2+1-m^2) - \frac{q}{2^3c}(q^2+1-m^2) - \frac{1}{2^6c^2}\Big((5q^4+10q^2+1)-2m^2(3q^2+1)+m^4\Big)$$

$$- \frac{q}{2^9c^3}\Big((33q^4+114q^2+37)-2m^2(23q^2+25)+13m^4\Big)$$

$$- \frac{1}{2^{10}c^4}\Big((63q^6+340q^4+239q^2+14)-10m^2(10q^4+23q^2+3)+3m^4(13q^2+6)-2m^6\Big)$$

$$- \frac{q}{2^{13}c^5}\Big((527q^6+4139q^4+5221q^2+1009)-m^2(939q^4+3750q^2+1591)+5m^4(93q^2+127)-53m^6\Big)$$

$$- \frac{1}{2^{17}c^6}\Big((9387q^8+101836q^6+205898q^4+86940q^2+3747)-12m^2(1547q^6+9575q^4+8657q^2+701)$$
$$+6m^4(1855q^4+5078q^2+939)-12m^6(167q^2+85)+51m^8\Big)$$

$$+ O(c^{-7}) \qquad \text{for oblate} \tag{2-2}$$

where q = n for (n - m) odd, and q = n + 1 for (n - m) even.

As the aspect ratio becomes higher, the radial coordinate ξ $(=a/(a^2-b^2)^{\frac{1}{2}})$ → 1 for prolate and ξ $(=b/(a^2-b^2)^{\frac{1}{2}})$ → 0 for oblate, we have to use series expansion in powers of (ξ^2-1) for prolate and of (ξ^2+1) for oblate, to replace ordinary expressions for the radial functions of the second kind, $R_{mn}^{(2)}(c,\xi)$ for prolate and $R_{mn}^{(2)}(-ic,i\xi)$ for oblate, respectively.

The prolate radial functions $R_{mn}^{(2)}(c,\xi)$ are found to be

$$R_{mn}^{(2)}(c,\xi) = Q_{mn}(c)R_{mn}^{(1)}(c,\xi)\left\{ \frac{1}{2} \log \frac{\xi+1}{\xi-1} \right\} + g_{mn}(c,\xi) \tag{3}$$

with

$$Q_{mn}(c) = \frac{\left(\kappa_{mn}^{(1)}(c)\right)^2}{c} \sum_{r=0}^{m} a_r^{mn}(c) \frac{(-1)^{m-r+1}(2m-2r+1)!}{r!\left(2^{m-r}(m-r)!\right)^2} \qquad \text{for (n-m) odd} \tag{3-1}$$

$$Q_{mn}(c) = \frac{\left(\kappa_{mn}^{(1)}(c)\right)^2}{c} \sum_{r=0}^{m} a_r^{mn}(c) \frac{(-1)^{m-r+1}(2m-2r)!}{r!\left(2^{m-r}(m-r)!\right)^2} \qquad \text{for (n-m) even} \tag{3-2}$$

where the implications of all the quantities refer to Flammer's book, the summation index r is over from r=0 to r=m, and the coefficients a_r^{mn} are listed up to r=4 in that book. However, the terminated number M (m=0,1,2,...,M) for the spheroid with high aspect ratio, according to the empirical formula given by Asano and Yamamoto,[1] is proportional to the size parameter c, that is, M ≃ c. Thus one must raise the upper limit of the summation index r to evaluate the scattering coefficients. We have developed a_r^{mn} till r=12 in the present work.[6]

In Eq. (3), the functions $g_{mn}(c,\xi)$ are written in the forms:

$$g_{mn}(c,\xi) = (\xi^2 - 1)^{-\frac{1}{2}m} \sum_{r=0}^{\infty} b_r^{mn}(\xi^2 - 1)^r \qquad \text{for (n-m) odd} \tag{4-1}$$

$$g_{mn}(c,\xi) = \xi(\xi^2 - 1)^{-\frac{1}{2}m} \sum_{r=0}^{\infty} b_r^{mn}(\xi^2 - 1)^r \qquad \text{for (n-m) even} \tag{4-2}$$

where the coefficients b_r^{mn} for r≠m and r≠0 can be obtained from the recursion system but

not for r=m, however, the coefficients b_m^{mn} can be determined with the aid of the hypergeometric functions. In Flammer's book, the forms of b_m^{mn} are only valid for $0 \leq m \leq 2$. We have derived the analytical expressions[6] of b_m^{mn} for any number m:

$$b_m^{mn} = -\frac{1}{\kappa_{mn}^{(2)}(c)} \left\{ \sum_{r=0}^{\infty} d_{2r+1}^{mn} \left(\sum_{k=0}^{r} \frac{(2m+4r-4k+1)(2m+2r-2k)!}{2^m m!(2k+1)(m+2r-k+1)(2r-2k)!} - \sum_{\ell=1}^{m} f_1(\ell) \right) \right.$$

$$\left. - \sum_{r=m+1}^{\infty} d_{\rho|2r-1}^{mn} \frac{(2r-2)!}{2^m m!(2r-2m-2)!} \right\} \qquad \text{for } (n-m) \text{ odd} \qquad (4\text{-}3)$$

$$b_m^{mn} = -\frac{1}{\kappa_{mn}^{(2)}(c)} \left\{ \sum_{r=0}^{\infty} d_{2r}^{mn} \left(\sum_{k=0}^{[(2r-1)/2]} \frac{(2m+4r-4k-1)(2m+2r-2k-1)!}{2^m m!(2k+1)(m+2r-k)(2r-2k-1)!} - \sum_{\ell=1}^{m} f_2(\ell) \right) \right.$$

$$\left. - \sum_{r=m+1}^{\infty} d_{\rho|2r}^{mn} \frac{(2r-1)!}{2^m m!(2r-2m-1)!} \right\} \qquad \text{for } (n-m) \text{ even} \qquad (4\text{-}4)$$

with

$$f_1(\ell) = -\frac{m!(2m+2r-\ell+1)!\left(r+\frac{\ell+1}{2}\right)!}{2^{m-2\ell+1}(m-\ell)!(2r+\ell+1)!\left(r+m-\frac{\ell}{2}\right)!} \sum_{k=0}^{\frac{\ell-1}{2}} \frac{\left(r+m-k+\frac{\ell}{2}\right)!}{(m-k)!\left(r+k-\frac{\ell-1}{2}\right)!(\ell-k)(\ell-2k)!k!2^{2k}}$$

$$\text{for } \ell \text{ odd} \qquad (4\text{-}5)$$

$$f_1(\ell) = \frac{m!(2m+2r-\ell+1)!\left(r+\frac{\ell}{2}\right)!}{2^{m-2\ell+1}\ell(m-\ell)!(2r+\ell+1)!\left(r+m-\frac{\ell-1}{2}\right)!} \times$$

$$\left\{ \frac{\left(r+m+\frac{\ell+1}{2}\right)!}{m!\left(r-\frac{\ell}{2}\right)!\ell!} + \sum_{k=0}^{\frac{\ell-2}{2}} \frac{\left(r+m-k+\frac{\ell-1}{2}\right)!\left[4(k+1)(\ell-k-1)+(\ell-2k-1)(\ell-2k-2)\right]}{(m-k-1)!\left(r+k-\frac{\ell-2}{2}\right)!(\ell-k-1)(\ell-2k-1)!(k+1)!2^{2k+2}} \right\}$$

$$\text{for } \ell \text{ even} \qquad (4\text{-}6)$$

$$f_2(\ell) = -\frac{m!(2m+2r-\ell)!\left(r+\frac{\ell-1}{2}\right)!}{2^{m-2\ell+1}(m-\ell)!(2r+\ell)!\left(r+m-\frac{\ell}{2}\right)!} \sum_{k=0}^{\frac{\ell-1}{2}} \frac{\left(r+m-k+\frac{\ell}{2}\right)!}{(m-k)!\left(r+k-\frac{\ell+1}{2}\right)!(\ell-k)(\ell-2k)!k!2^{2k}}$$

$$\text{for } \ell \text{ odd} \qquad (4\text{-}7)$$

$$f_2(\ell) = \frac{m!(2m+2r-\ell)!\left(r+\frac{\ell}{2}\right)!}{2^{m-2r+1}\,\ell(m-\ell)!(2r+\ell)!\left(r+m-\frac{\ell+1}{2}\right)!} - \sum_{k=0}^{\frac{\ell-2}{2}} \frac{\left(r+m-k+\frac{\ell-1}{2}\right)!}{(m-k)!\left(r+k-\frac{\ell}{2}\right)!(\ell-k)(\ell-2k-1)!k!\,2^{2k}}$$

for ℓ even (4-8)

It may be remarked that: Flammer missed the factor product (2k+1) in the denominator of the first part of b_m^{mn} for (n-m) odd case in Eq. (4-3) (see under-dotted); also he made the errors of upper limits for summation index k in the first part in Eqs. (4-3) and (4-4), namely, $\left[(m+2r)/2\right]$ and $\left[(m+2r-1)/2\right]$ instead of the correct limits r and $\left[(2r-1)/2\right]$ for (n-m) odd and even cases, respectively.

Likewise, the oblate radial functions $R_{mn}^{(2)}(-ic,i\xi)$ are found to be

$$R_{mn}^{(2)}(-ic,i\xi) = Q_{mn}^{*}(-ic)R_{mn}^{(1)}(-ic,i\xi)\left[\tan^{-1}\xi - \frac{\pi}{2}\right] + g_{mn}^{*}(-ic,i\xi) \tag{5}$$

with

$$Q_{mn}^{*}(-ic) = -\frac{\left[i^{-m-1}\kappa_{mn}^{(1)}(-ic)\right]^2}{c}\sum_{r=0}^{m}\alpha_r^{mn}(-ic)\,\frac{(2m-2r+1)!}{r!\left[2^{m-r}(m-r)!\right]^2} \qquad \text{for (n-m) odd} \tag{5-1}$$

$$Q_{mn}^{*}(-ic) = \frac{\left[i^{-m}\kappa_{mn}^{(1)}(-ic)\right]^2}{c}\sum_{r=0}^{m}\alpha_r^{mn}(-ic)\,\frac{(2m-2r)!}{r!\left[2^{m-r}(m-r)!\right]^2} \qquad \text{for (n-m) even} \tag{5-2}$$

where the explicit forms of the coefficients α_r^{mn} can be obtained from those of a_r^{mn} by the following relationship

$$\alpha_r^{mn}(-ic) = (-1)^r a_r^{mn}(-ic) \tag{5-3}$$

In Eq. (5), the functions $g_{mn}^{*}(-ic,i\xi)$ are written in the forms:

$$g_{mn}^{*}(-ic,i\xi) = (\xi^2+1)^{-\frac{1}{2}m}\sum_{r=0}^{\infty}\beta_{2r}^{mn}\xi^{2r} \qquad \text{for (n-m) odd} \tag{6-1}$$

$$g_{mn}^{*}(-ic,i\xi) = \xi(\xi^2+1)^{-\frac{1}{2}m}\sum_{r=0}^{\infty}\beta_{2r}^{mn}\xi^{2r} \qquad \text{for (n-m) even} \tag{6-2}$$

where the coefficients β_{2r}^{mn} for $r\neq 0$ can be directly obtained from the corresponding recursion system without any exception for r.

The spheroidal radial functions cited by Asano and Yamamoto[1] need to be corrected for both prolate and oblate cases: the exponential expressions of imaginary number i, which appear in Eqs. (24) and (25) in their paper, should be rather (r+m-n) than (r+n-m), as not reflected in their errata. It is obvious that they also missed the factors $(1-\delta_{0m})$ and $(1+\delta_{0m})$ in the first and the second parts after the coefficient $\top\top^{m}_{nn'}$ in the expression of the scattering cross section for spheroid at oblique incidence. The correct formula is

$$C_{\frac{1}{2},sca} = \frac{\lambda^2(I)}{4\pi} \sum_{m=0} \sum_{n=m} \sum_{n'=m} \top\top^{m}_{nn'} \cdot Re\left[(1-\delta_{0m})\bar{\alpha}_{\frac{1}{2},mn}\bar{\alpha}^{*}_{\frac{1}{2},mn'} + (1+\delta_{0m})\bar{\beta}_{\frac{1}{2},mn}\bar{\beta}^{*}_{\frac{1}{2},mn'}\right] \tag{7}$$

where the subscript 1 stands for TE mode, 2 for TM mode; $\bar{\alpha}_{\frac{1}{2},mn}$ and $\bar{\beta}_{\frac{1}{2},mn}$ are the scattering coefficients, which differ from the coefficients α^{mn}_{r} and β^{mn}_{r} in the oblate radial functions; the delta function is defined as

$$\delta_{0m} = \begin{cases} 1 & (m = 0) \\ 0 & (m \neq 0) \end{cases} \tag{7-1}$$

The following integrals and the property of the angle functions $\sigma_{mn}(\theta)$ are useful to make this correction:

$$\int_0^{2\pi} \sin m\phi \cdot \sin m'\phi \, d\phi = \begin{cases} 0 & (m \neq m') \\ (1-\delta_{0m})\pi & (m = m') \end{cases} \tag{7-2}$$

$$\int_0^{2\pi} \cos m\phi \cdot \cos m'\phi \, d\phi = \begin{cases} 0 & (m \neq m') \\ (1+\delta_{0m})\pi & (m = m') \end{cases} \tag{7-3}$$

$$\sigma_{mn}(\theta) \equiv 0 \qquad \text{for any } \theta \text{ at } m = 0 \tag{7-4}$$

With all the corrections and the developments, we have computed the scattering coefficients for the spheroids with the aspect ratio up to 20:1 and the size parameter c about $50 \sim 60$.

III. COMPARISON WITH EXPERIMENTS

P-Q plot (P and Q are the imaginary and real parts of the extinction efficiency, respectively) for specific orientation is the best way to test the tedious and extremely complicated computing program for spheroid, because the averaged efficiency for random

orientations usually wipes out the hidden, even serious errors in the algorithms; furthermore, any "misorder" of the eigenvalues λ_{mn} will cause the infinite or incredible results on the diagram of P-Q plot but not on that of the averaged efficiency.

In order to arrange the eigenvalues in the increasing order, the choice between Bouwkamp's and asymptotic methods for the calculation of λ_{mn} must be in consideration. Tables 1 and 2 indicate the computational selections of these methods for the spheroids with aspect ratios 2:1, 4:1, and 12:1.

During the computation, the Wronskian is always used for identifying the accuracy of the spheroidal radial functions of the first kind, $R_{mn}^{(1)}$, and of the second kind, $R_{mn}^{(2)}$.

Figures 2 - 5 are the graphs for comparison of the theoretical and experimental results in the forms of P-Q plot. Figure 6 is the theoretical plotting for spheroid with aspect ratio 12:1.

In all figures, x_v $(=\kappa a_v)$ is size parameter of spheroid with a_v being the radius of equal-volume sphere, m is refractive index. Subscripts th and ex denote whether theoretical or experimental. The running number in two curves shows the tilted angle of the particle axis from $\vec{k}$ (propagational) direction as the axis is swept through 90^0 in the incident k-E and k-H planes. Experimental P-Q plots, which depict the particle-orientation dependent extinction cross section, are derived from our microwave measurements.

The computing outcomes on the extinction profiles seem to fit well to the microwave data, if the instrumental drift, due to the temperature gradient upon the microwave equipments, is taken into account. Actually, a little fluctuation of this drift will greatly deform the profile on P-Q plot.

IV. ACKNOWLEDGMENT

This research work is supported by U.S. Army Research Office.

REFERENCES

1. S. Asano and G. Yamamoto, "Light Scattering by a Spherc idal Particle", Appl. Optics, Vol. 14, No. 1, 29 (1975).

2. C.J. Bouwkamp, "on Spheroidal Wave Functions of Order Zero", J. Math. Phys., 26, 79 (1947).

3. C. Flammer, Spheroidal Wave Functions, Stanford University Press (1957)

4. J. Meixner, "Asymptotische Entwicklung der Eigenwerte und Eigenfunktionen der Differentialgleichungen der Sphäroid-Funktionen und Mathieuschen Funktionen", Z. angew. Math. Mech., 28, 304 (1948).

5. Wan-xian Wang, "The Computational Expressions of Spheroidal Eigenvalues", Proc. of the Third Annual Review of Progress in Applied Computational Electromagnetics, Monterey, CA (March 1987).

6. Wan-xian Wang, "The Radial Functions of Spheroidal Wave Functions for High Aspect Ratio", Proc. of the Third Annual Review of Progress in Applied Computational Electromagnetics, Monterey, CA (March 1987).

Table 1
Computational Selection

Method I: Bouwkamp's, Method II: Asymptotic

2:1 and 4:1 Prolate Spheroids (refractive index = 1.61-i0.004)

	$c \leq 7$	$7 < c \leq 10$	$10 < c \leq 12$	$12 < c$
$m = 0$	$n \leq m+3$ II $n > m+3$ I	$n \leq m+5$ II $n > m+5$ I	$n \leq m+7$ II $n > m+7$ I	$n \leq m+8$ II $n > m+8$ I
$2 \geq m \geq 1$	$n \leq m+2$ II $n > m+2$ I	$n \leq m+4$ II $n > m+4$ I	$n \leq m+6$ II $n > m+6$ I	
$m \geq 3$	$n \leq m+1$ II $n > m+1$ I	$n \leq m+3$ II $n > m+3$ I	$n \leq m+5$ II $n > m+5$ I	

Table 2
Computational Selection

12:1 Prolate Spheroid (refractive index = 1.61-i0.004)

	$c \leq 30$		$30 < c$
$m = 0$	$n \leq m+15$ II $n > m+15$ I		$n \leq m+22$ II $n > m+22$ I
$m = 1$	$n \leq m+14$ II $n > m+14$ I		$n \leq m+19$ II
$m = 2$	$n \leq m+13$ II $n > m+13$ I		$n > m+19$ I
$m = 3$	$n \leq m+12$ II $n > m+12$ I		
$m = 4$	$n \leq m+11$ II $n > m+11$ I		$n \leq m+16$ II
$m = 5$	$n \leq m+10$ II $n > m+10$ I		$n > m+16$ I
$m \geq 6$	$c \leq 25$	$25 < c \leq 30$	
	$n \leq m+7$ II $n > m+7$ I	$n \leq m+10$ $n > m+10$	

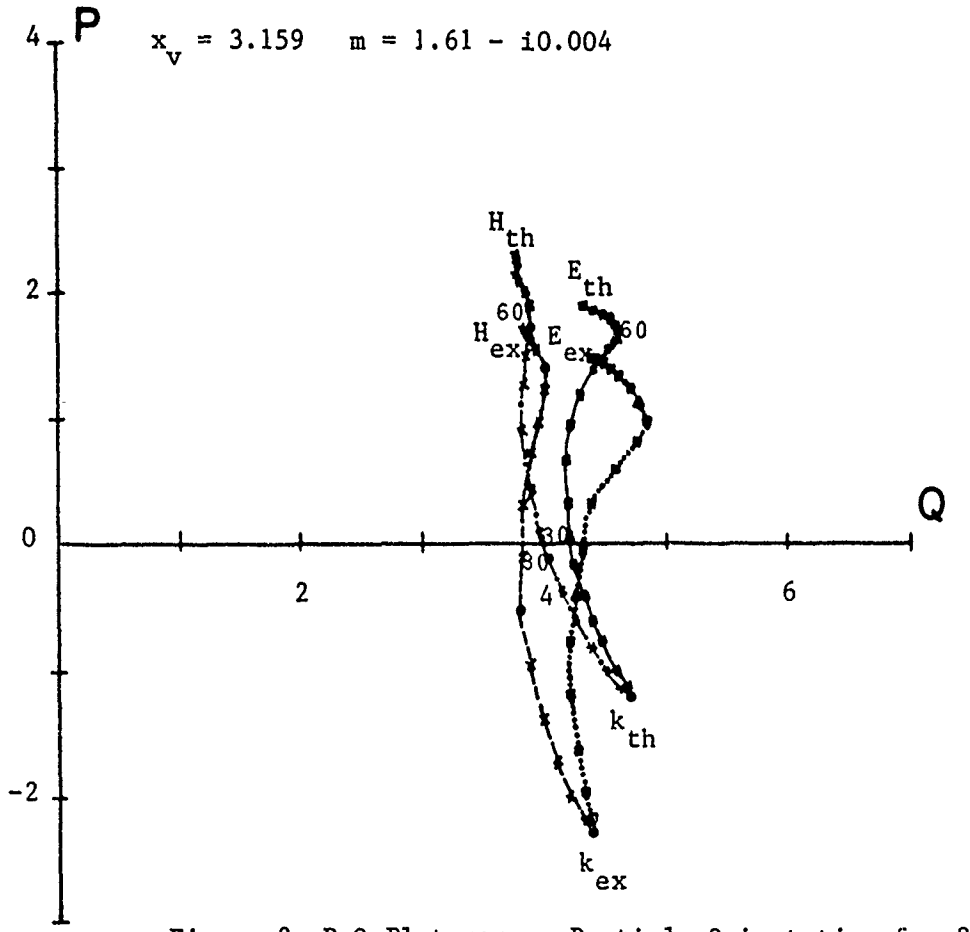


Figure 2. P-Q Plot versus Particle Orientation for 2:1 Prolate Spheroid

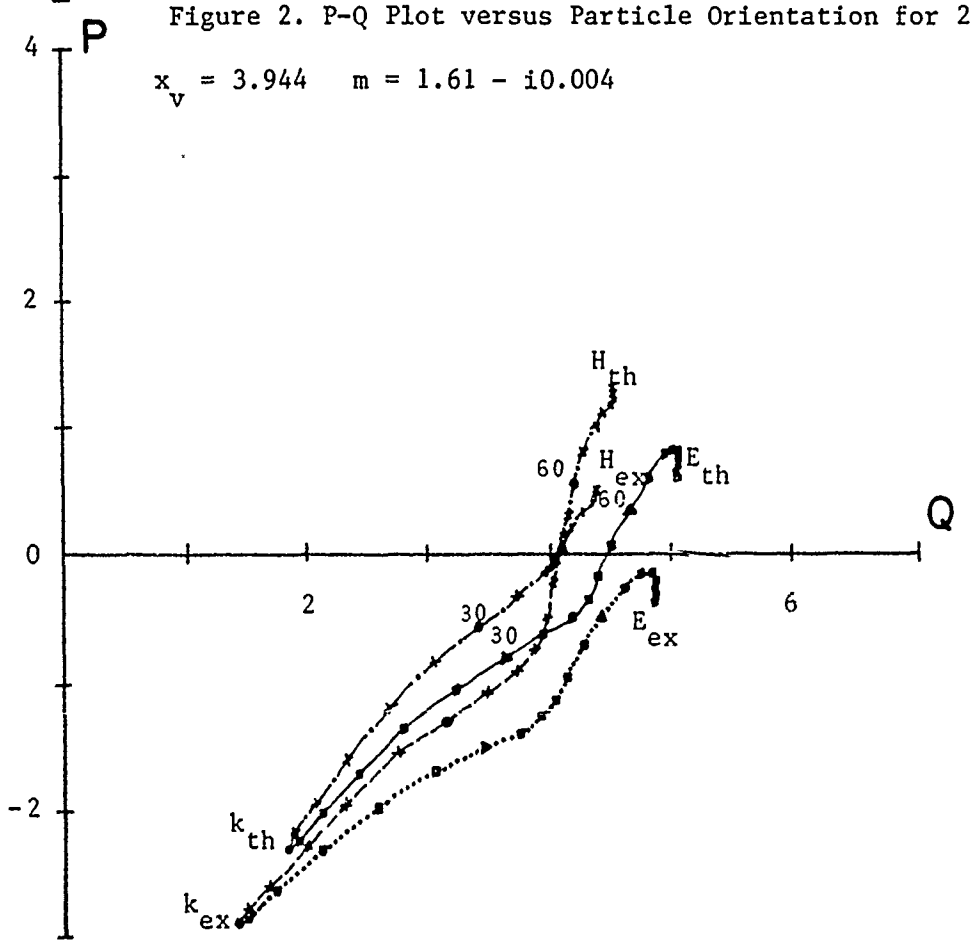


Figure 3. P-Q Plot versus Particle Orientation for 2:1 Prolate Spheroid

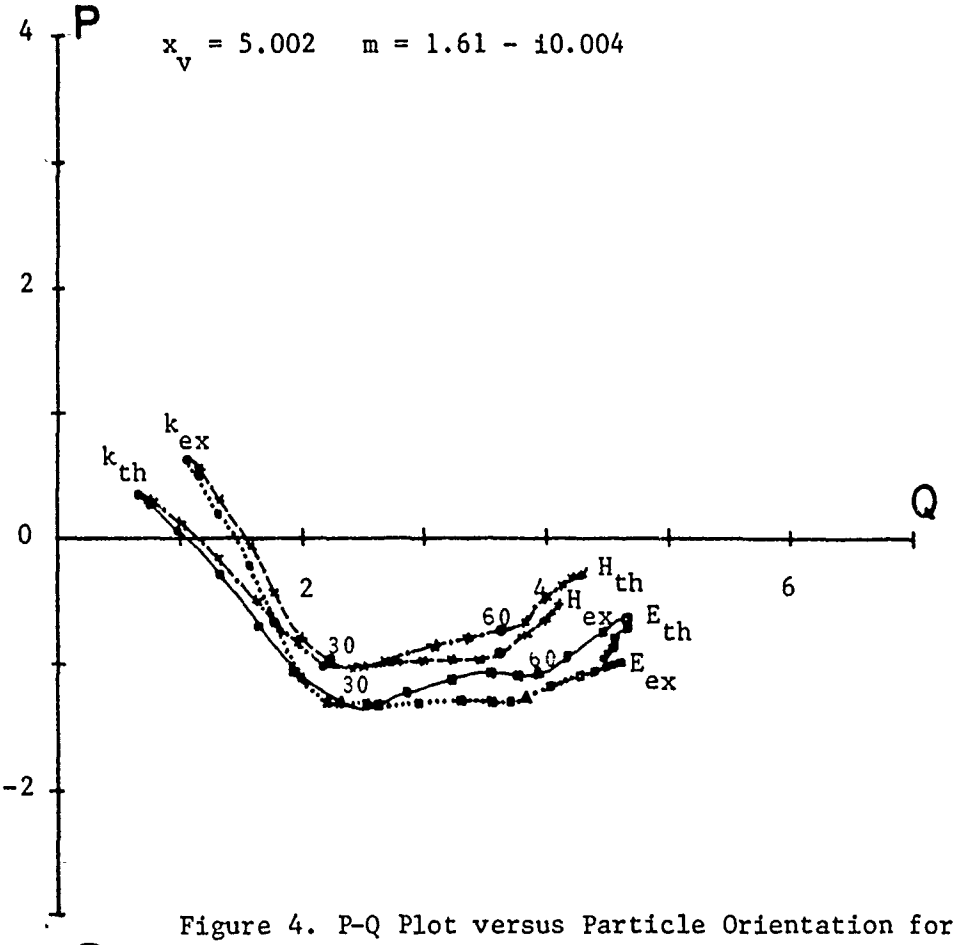


Figure 4. P-Q Plot versus Particle Orientation for 2:1 Prolate Spheroid

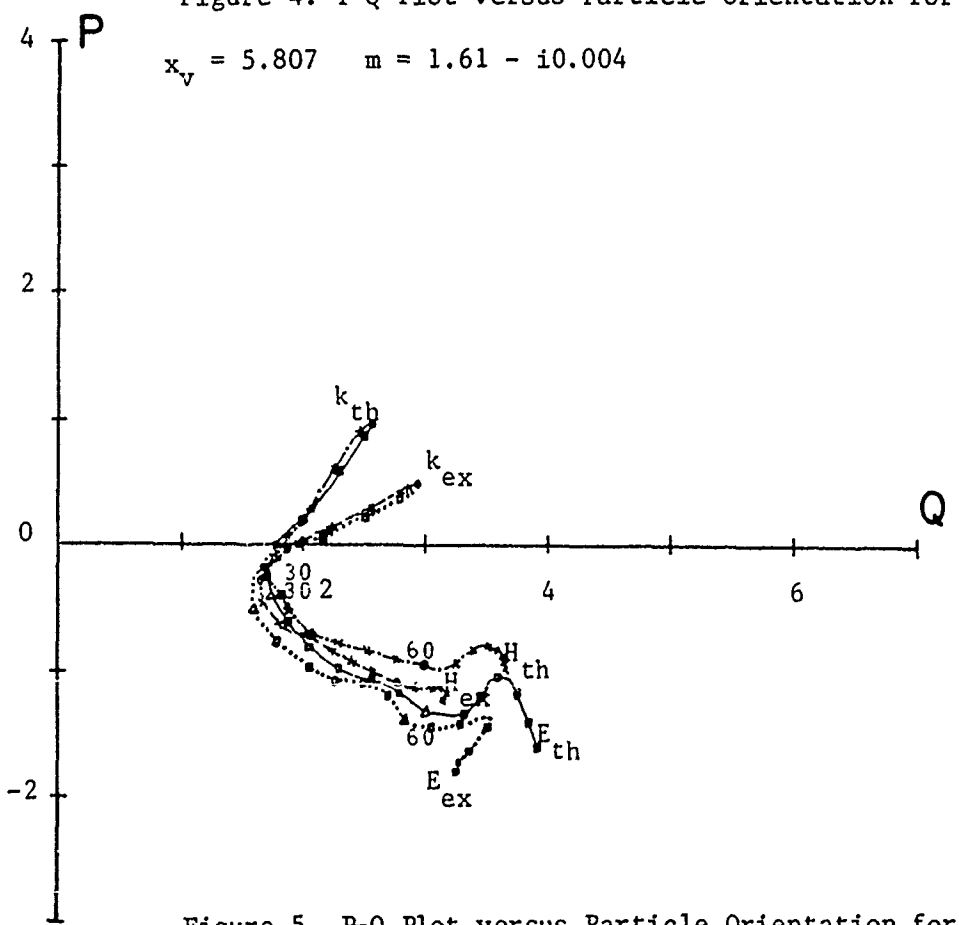


Figure 5. P-Q Plot versus Particle Orientation for 2:1 Prolate Spheroid

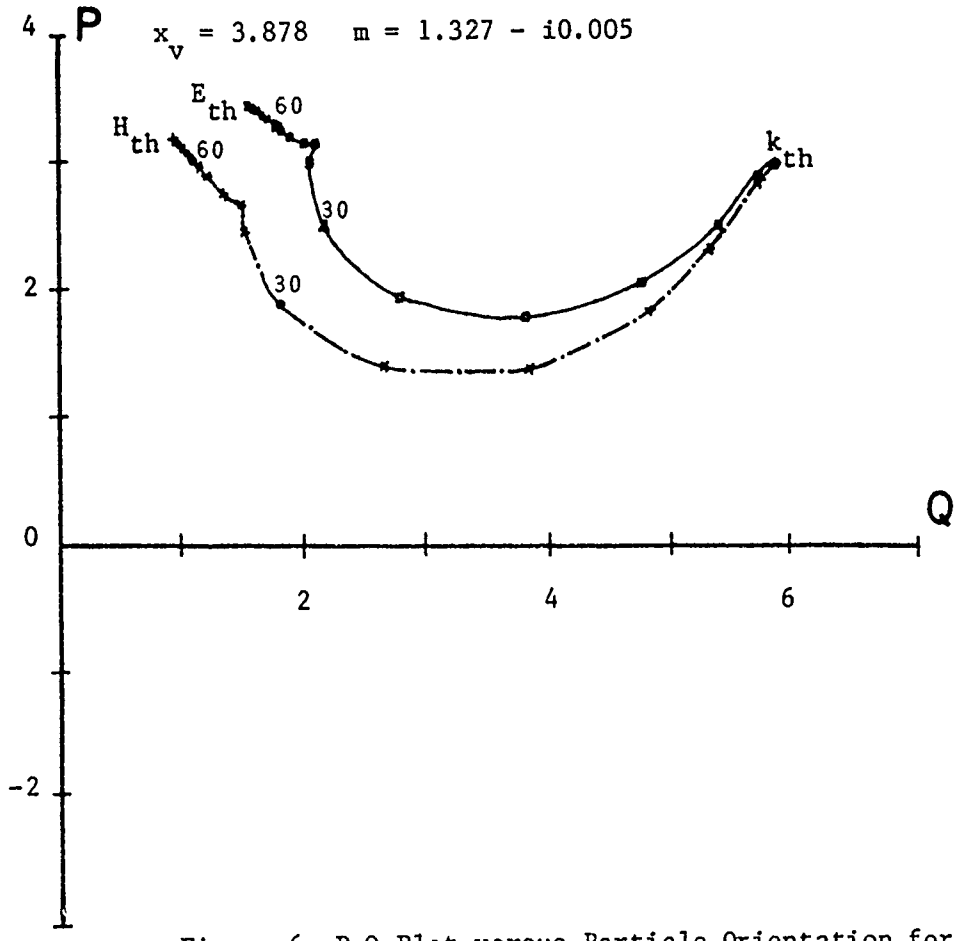


Figure 6. P-Q Plot versus Particle Orientation for 12:1 Prolate Spheroid

BISTATIC SCATTERING ANALYSIS OF AN ELLIPSOID

R. J. Marhefka and J. H. Choi
The Ohio State University
ElectroScience Laboratory
1320 Kinnear Road
Columbus, Ohio 43212

The ability to model complex scattering objects such as aircraft by simpler shapes has been demonstrated in the past to be very useful for a wide range of application. One example is the version 2 of the NEC-BSC which is a user oriented computer code to simulate scattering structures based on multiple flat plates and finite elliptic cylinders. However, in order to better approximate a fuselage of a general aircraft or similar objects, an ellipsoid would provide a much better model than an elliptic cylinder. One advantage of using an ellipsoid over an elliptic cylinder is that one can use the same parametric form of the ellipsoid to represent a sphere, a prolate spheroid, or an elliptic or a circular cylinder as well as an ellipsoid by simply changing a few parameters in the ellipsoid expression.

The near zone bistatic scattering pattern of an ellipsoid by the UTD is studied. In applying the UTD to electromagnetic scattering problems involving curved surfaces, a major task is to find the reflection point, the attaching(grazing) and launching(diffraction) point pairs and corresponding geodesic paths, the energy spreading factor, and the caustic distance at the launching point. Useful and efficient numerical methods to evaluate them are developed and applied to calculate the field patterns of several different shapes of scatterers. The comparison between these numerical results and other methods shows good agreement except for regions near the caustics. Caustic problems can be solved by employing the equivalent current method. This will be studied in the near future. Also the scattering from general doubly curved surfaces, such as a super ellipsoid, a composite ellipsoid, and a truncated ellipsoid, is the next goal of this study along with the interaction between the curved surface and flat plates. These modeling capabilities will be incorporated into future versions of the NEC-BSC.

BISTATIC SCATTERING ANALYSIS OF AN ELLIPSOID

R. J. Marhefka and J. H. Choi
The Ohio State University
ElectroScience Laboratory
1320 Kinnear Road
Columbus, Ohio 43212

1 Introduction

The NEC - Basic Scattering Code version 2 (NEC-BSC2) [1,2] is presently being improved. One of these improvements involve expanding its curved surface modeling capabilities. The present code will handle multiple perfectly conducting finite elliptic cylinders. The elliptic cylinder works well for many modeling situations especially those on shipboard or even for a fuselage away from the nose and tail. In general, however, it is necessary to model the double curvature of a structure. A very useful analytic shape for this purpose is the ellipsoid as illustrated in Figure 1.

An efficient set of algorithms has recently been developed to calculate the near zone Uniform Geometrical Theory of Diffraction (UTD) scattering from from an ellipsoid [3]. This work is being done in anticipation of extending the results into composite finite end-capped ellipsoidal model to be included in future versions NEC-BSC. It will eventually be extended into other types of curved surfaces such as cone frustums, ogives, super ellipsoids, etc. This paper briefly outlines this effort as given below:

- Uniform Geometrical Theory of Diffraction UTD field solutions used.
- Developed a numerically efficient bistatic near zone UTD ray tracing algorithms.
  - Shadowing algorithms
  - Reflection point algorithms.
  - Creeping wave algorithms.

- Validated algorithms with measurements and alternative solutions.

2 UTD Solution

The Uniform Geometrical Theory of Diffraction is used to calculated the field scattered in the near zone of an ellipsoid. The results can also be used in the far zone of an ellipsoid if the far zone range R is defined as being around $R \geq 4D^2/\lambda$ where D is the maximum dimension of the ellipsoid. The UTD solution used is given in Reference [4] and will not be repeated here. It is the same solution that has been used successfully in version 2 of the NEC-BSC code for the finite elliptic cylinders.

This solution goes to the normal geometrical optics reflected field deep in the lit region and goes to the normal creeping wave solution in the deep shadow region. In the transition region the solution provides a continuous result through the shadow boundary. The necessary parameters for the reflected and creeping wave portions of the diffraction coefficients are based on the local geometrical parameters of the surface. This implies that they can be used in wide set of circumstances and not just for so called canonical problems on which they are based.

As in all solutions there are restrictions. For the reflected fields, it is necessary that the radii of curvature be large in terms of a wavelength. In most engineering applications this can be as small as a quarter of a wavelength. For the creeping wave fields, the present solution breaks down for paraxial ray paths, that is, for paths where the transverse radii of curvature is much small than the radii of curvature in the direction of the ray propagation. The solution breaks down gradually. This problem is presently being investigated.

In addition to the above restrictions, there are the possibility of caustics occurring in the solution. The most noticeable caustic effect for the ellipsoid is when a whole ring of creeping wave rays occur in a specular direction. This will be evident in some of the results below. Other caustics can occur when an individual creeping wave field is propagating on the surface and converges in such a way that it focus at the observer. These problems will be studied in the future by the use of equivalent current solutions.

3 Ellipsoid Shadowing Algorithm

Shadowing algorithms are necessary to determine whether a ray from the source to an observation point hits the ellipsoid. This can be used to determine not only if the observer is in the shadow region of the incident field, but also to determine whether the reflected field should be calculated if the observer is in the lit region. An exact shadowing algorithm can be found for the ellipsoid and it is outlined here. The geometry is illustrated in Figure 2.

A vector on the surface of the ellipsoid can be represented as

$$\bar{R}_e = \bar{R} + \bar{R}_s.$$

The point defined by $\bar{R}_e$ represents the possible hit point on the ellipsoid and should satisfy the equation for a ellipsoid, that is,

$$0 = \frac{(R\cos\phi\sin\theta + x_s)^2}{a^2} + \frac{(R\sin\phi\sin\theta + y_s)^2}{b^2} + \frac{(R\cos\theta + z_s)^2}{c^2} - 1.$$

The distance R is unknown in this equation, since we know the direction to the observer, θ and ϕ, but not the distance to the hit point. We can solve for R, however, from the above equations using

$$\alpha R^2 + 2\beta R + \gamma = 0,$$

where

$$\alpha = \frac{\cos^2\phi\sin^2\theta}{a^2} + \frac{\sin^2\phi\sin^2\theta}{b^2} + \frac{\cos^2\theta}{c^2},$$

$$\beta = \frac{x_s\cos\phi\sin\theta}{a^2} + \frac{y_s\sin\phi\sin\theta}{b^2} + \frac{z_s\cos\theta}{c^2},$$

and

$$\gamma = \frac{x_s^2}{a^2} + \frac{y_s^2}{b^2} + \frac{z_s^2}{c^2} - 1.$$

If the value of R is real, then the hit point is on the ellipsoid and therefore the ray from the source to observer is shadowed. Additional tests are needed for the near zone distances to determine whether the actual observer was in front or behind the ellipsoid along the observation ray direction.

4 Reflection Point Algorithm

The reflection point for an ellipsoid can be found by extending the incremental method developed for the elliptic cylinder given in Reference [5]. This technique is based on using a first order Taylor series expansion of the laws of reflection. The laws of reflection can be written as

$$(\vec{n} \times \vec{I})(\vec{n} \cdot \vec{d}) + (\vec{n} \cdot \vec{I})(\vec{n} \times \vec{d}) = 0,$$

where $\vec{n}$ is the unnormalized normal to the surface, $\vec{I}$ is the incident vector, and $\vec{d}$ is the observation direction. The above equation can be rewritten as

$$\begin{aligned} f(u,v,x_s,y_s,z_x,x_o,y_o,z_o)\hat{x} &+ g(u,v,x_s,y_s,z_x,x_o,y_o,z_o)\hat{y} \\ &+ h(u,v,x_s,y_s,z_x,x_o,y_o,z_o)\hat{z} = 0, \end{aligned}$$

where u, v are parametric variables on the ellipsoid surface and x_s, y_s, and z_s are the source location and x_o, y_o, and z_o are the observer location.

A first order Taylor series expansion of these equations can be found such that

$$f_{j+1} = f_j + df_j,$$

$$g_{j+1} = g_j + dg_j,$$

$$h_{j+1} = h_j + dh_j,$$

where the derivatives of the functions actually expand out into partial derivatives of all the variables in the functions. The j subscript represents the fact that the previous known value of the reflected field is used to find the new value. Since the new equations should be equal to zero, the above equations will reduce to a set of three equations and two unknowns, du and dv. A least means square solutions of the matrix can be found using the transpose of the matrix containing the derivatives of the above functions with respect to u and v.

It is interesting to note that this set of equations can be rewritten in the form of two equations and two unknowns with the proper change of variables. This is not as convenient numerically as would first appear, it turns out the transpose operation used here is just as good. In either case the same answer should result.

This type of algorithm needs a know starting point. This is accomplished in this case by using far zone source and observation points along the direction vectors of the actual points as shown in Figure 3. The reflection point for this case can be found simply and exactly. The above approximate algorithm can then be used to increment into the actual location in the near zone. After the field at the next observation point is needed, the previous near zone reflection point can be use as illustrated in Figure 4.

5 Creeping Wave Algorithm

In general, for the near zone there will be four creeping wave paths on an ellipsoid as illustrated in Figure 5. This will be true except near the caustic in possible backscatter and forward scatter directions where a whole ring of rays contribute. The creeping wave algorithms developed will not be given here but only outlined. The details are given in Reference [3].

The way to find the creeping wave path on a curved surface is well known and is given in many differential geometry books. It is usually assumed that the starting location and direction is known and that the next point on the path is to be found. An algorithm developed by Barger [6] is used in this case.

The problem that is needed to be tackled in this case, is how to find the four creeping wave paths that will go from the source to observer located off the ellipsoid. This is accomplished by first finding a set of creeping rays by a brute force search. The geometry is illustrated in Figure 6. The location of the tangent vector from the source to the surface can be found with their corresponding tangent directions. A given starting point's creeping wave path is traced checking the dot product of the tangent direction with a ray from the local creeping wave point to the receiver. If this is converging to one the process proceeds. If it start to diverge the process is stopped and the next starting point along the tangent is chosen and tried. Once four paths are found the search stops and the fields are calculated. The parameters for the field calculations such as the attenuation factor and spread factor are found as the ray paths are computed.

Once a given set of creeping wave paths are known, the next set for a new

observation point is found using a bisectional search instead of the brute force search. This can speed up the solution by a very significant amount. The geometry is illustrated in Figure 7. The method proceeds by looking at a tangent start location on either side of the known path and check the signs of the convergence. Once the direction is known another point is taken on the correct side a small amount over or half way in between paths previous chosen until the right path is found. A given path is normally found in about four tries. This is done for all four paths.

6 Results

The UTD scattering from the ellipsoid developed here is verified by comparing with an exact solution for a sphere and a body of revolution method of moments code [7]. The total UTD solution is found by adding the direct field from the source to observer along with the reflected field and four creeping wave fields. In the results below only the scattered field is shown, which is the total field minus the direct incident field everywhere.

The far zone scattering from a sphere is well known and can be easily computed using the Mie series. Figure 8 compares the UTD solution with the Mie series solution for two different size radii of sphere. The polarization in the plane of incidence is chosen. The forward scatter direction disagrees because the UTD solution is not corrected for the caustic at this time. There is a small discrepancy in the backscatter direction due to a caustic that is not as noticeable because field are much small after having crept around the sphere.

The UTD field scattered from an ellipsoid where $a = 1.5\lambda$, $b = c = 0.7\lambda$ and for a fixed source location is compared with a BOR-MOM result in Figure 9. The actual source and receiver distance is about 40λ. Note again the disagreement at the forward and backscatter caustic directions. Overall the agreement is very good. The caustic regions are small so that in most instances just these regions can be ignored.

The UTD field scattered from an ellipsoid where $a = 2\lambda$, $b = c = 1\lambda$ for a near zone fixed source location and near zone receiver path is shown in Figure 10. Note that the pattern is taken in a slightly skewed direction to the source location. The caustics again occur near the forward directions.

Also note that at $\phi = 0°$ and 125° the creeping wave focusing effect can be seen. Overall the agreement is quite good. As in most cases the caustic errors are either small or at least occur over a small region of the pattern.

7 Conclusion

The bistatic near zone UTD solution for an ellipsoid has been found. Efficient ray tracing algorithms have been developed to find the shadowing, reflection point, and four possible creeping wave paths. The UTD results have been compared with exact or body of revolution method of moments results. In all cases the agreement is good except in small regions where the caustic effects have not been presently handled. This will be accomplished in the future. Presently these algorithms are being included in the NEC-BSC and will show up in later version of this code enabling the user to define composite ellipsoid models of fuselages, etc.

References

[1] R. J. Marhefka and W. D. Burnside, "Numerical Electromagnetic Code - Basic Scattering Code, NEC-BSC(Version 2), Part 1: User's Manual," Technical Report 712242-14, December 1982, The Ohio State University ElectroScience Laboratory, Department of Electrical Engineering; prepared under Contract No. N00123-79-0-1469 for Naval Regional Contracting Office.

[2] R. J. Marhefka, "Numerical Electromagnetic Code - Basic Scattering Code, NEC-BSC(Version 2), Part 2: Code Manual," Technical Report 712242-15, December 1982, The Ohio State University ElectroScience Laboratory, Department of Electrical Engineering; prepared under Contract No. N00123-79-0-1469 for Naval Regional Contracting Office.

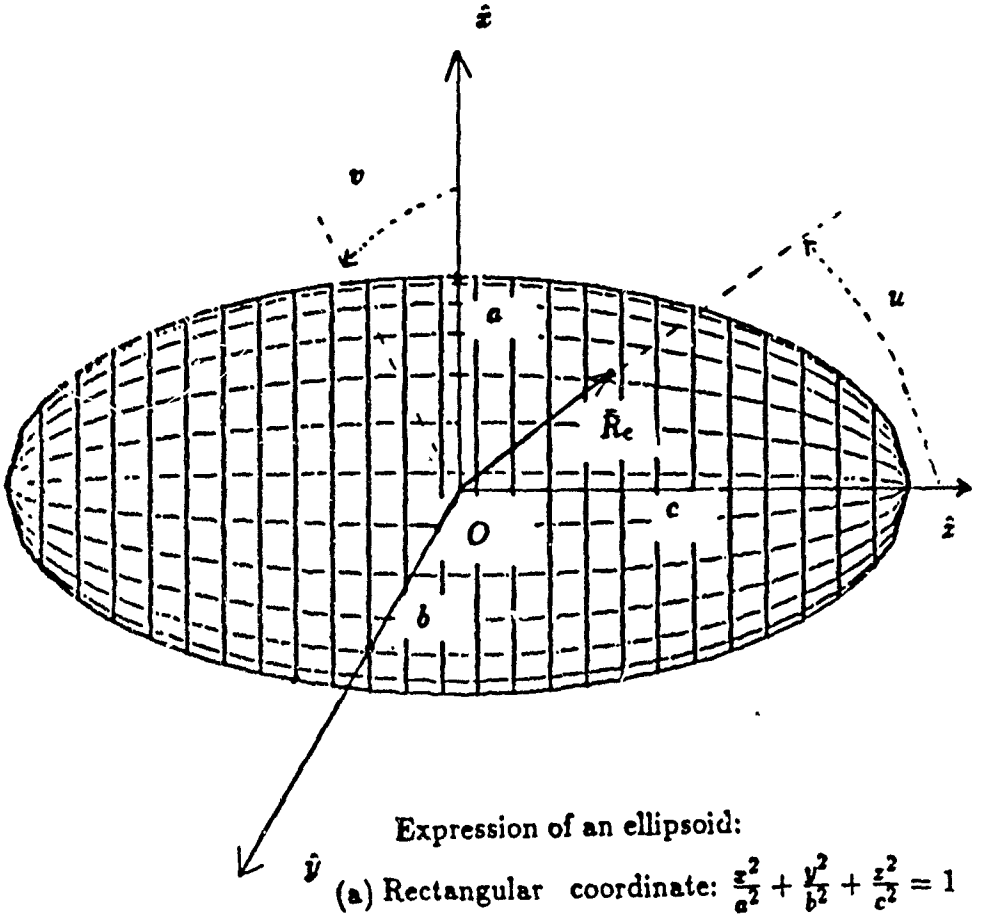
[3] J. H. Choi and R. J. Marhefka, "Bistatic Scattering Analysis of an Ellipsoid," Technical Report 717674-2, November 1986, The Ohio State University ElectroScience Laboratory, Department of Electrical Engineering; prepared under Contract No. N60530-85-C-0249 for Naval Weapons Center.

[4] P. H. Pathak, W. D. Burnside, and R. J. Marhefka, "A Uniform GTD Analysis of the Diffraction of Electromagnetic Waves by a Smooth Convex Surface," IEEE Trans. on Antenna and Propagation, Vol. AP-28, No. 5, pp 631-642, September 1982.

[5] R. J. Marhefka, "Analysis of Aircraft Wing-Mounted Antenna Patterns," Report 2902-25, June 1976, The Ohio State University ElectroScience Laboratory, Department of Electrical Engineering; prepared under Grant No. NGL 36-008-138 for National Aeronautics and Space Administration.

[6] R. L. Barger and M. S. Adams, "Semianalytic Modeling of Aerodynamic Shapes," NASA Technical Paper 2413, 1985, NASA Langley Research Center, Hampton, Virginia.

[7] N. Wang and C. D. Chuang, personal communication at The ElectroScience Laboratory, The Ohio State University, Columbus, Ohio 43212.



Expression of an ellipsoid:

(a) Rectangular coordinate: $\frac{x^2}{a^2} + \frac{y^2}{b^2} + \frac{z^2}{c^2} = 1$

(b) Ellipsoidal parametric form:

$$\bar{R}_e = \hat{x}a \sin u \cos v + \hat{y}b \sin u \sin v + \hat{z}c \cos u$$

Figure 1: Geometrical configuration of an ellipsoid

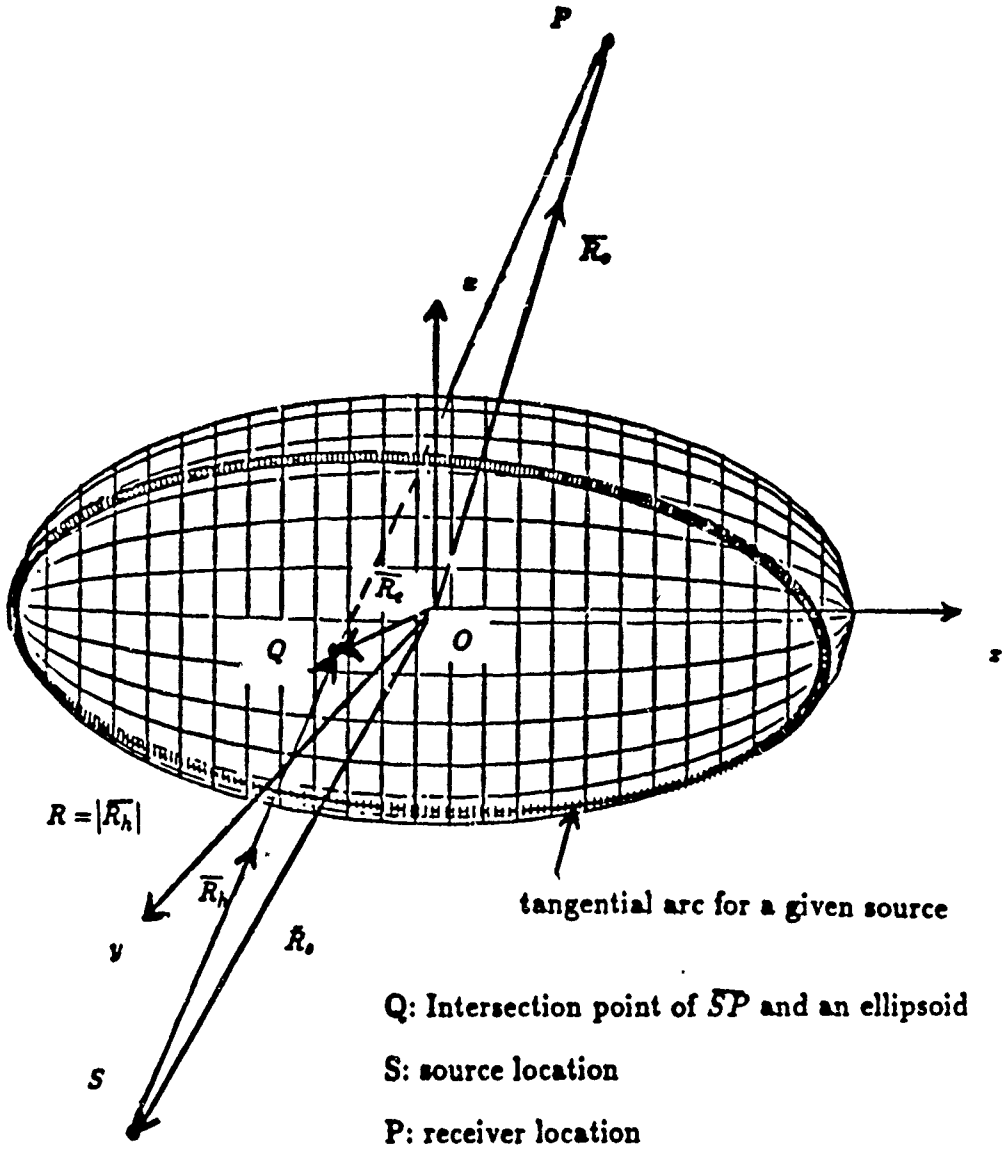


Figure 2 : Shadowing algorithm

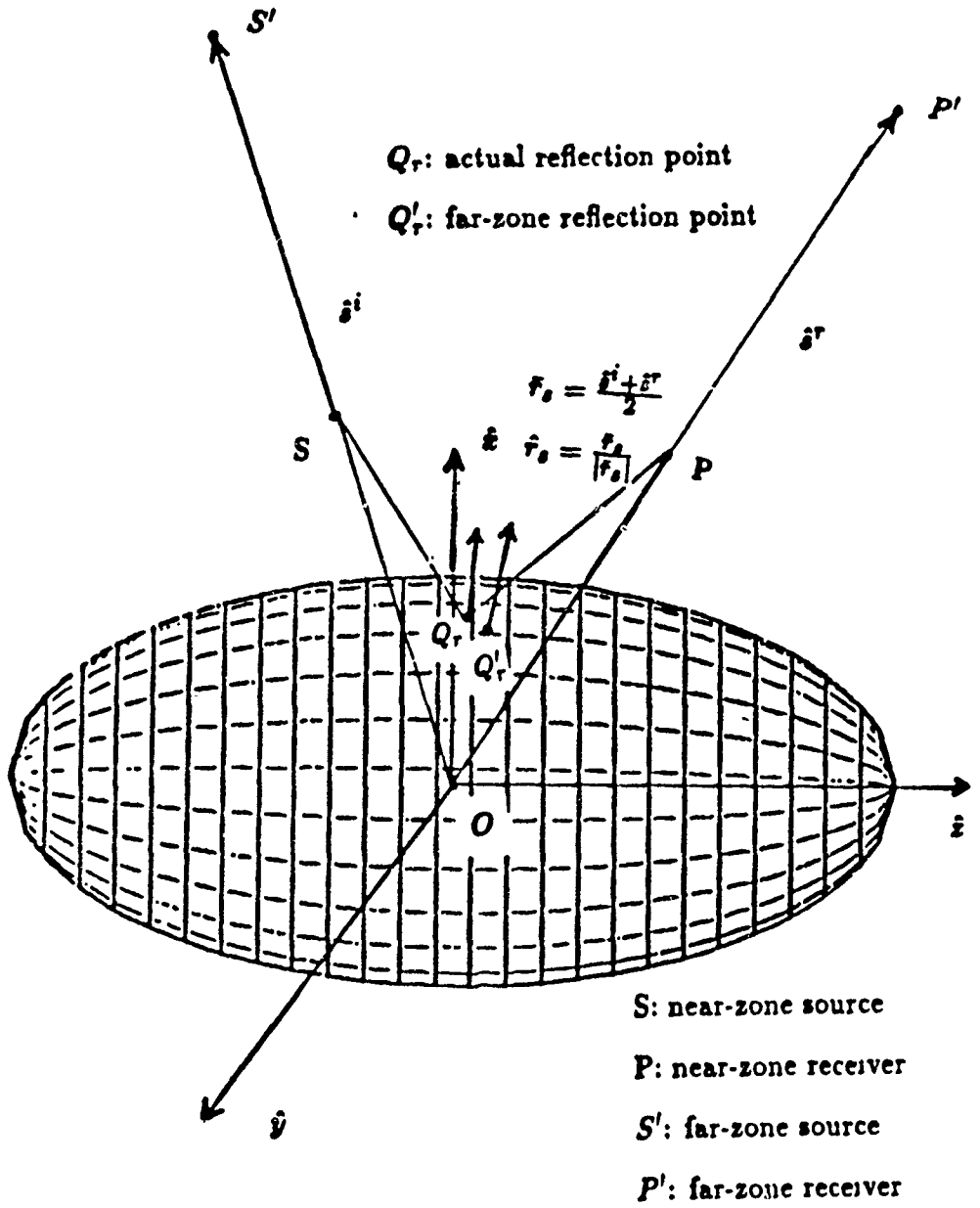


Figure 3: Starting point for actual reflection point calculation

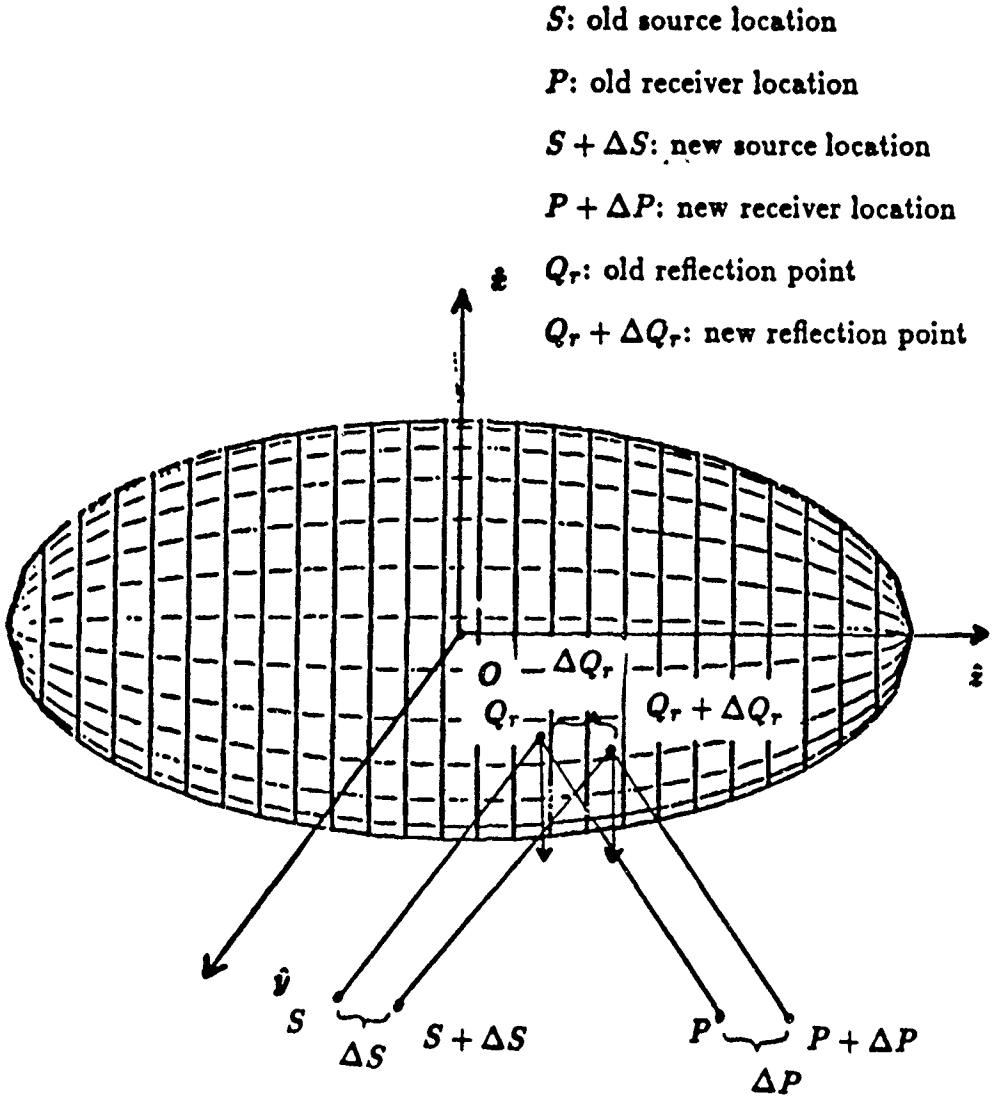


Figure 4: Incremental method to determine reflection point location

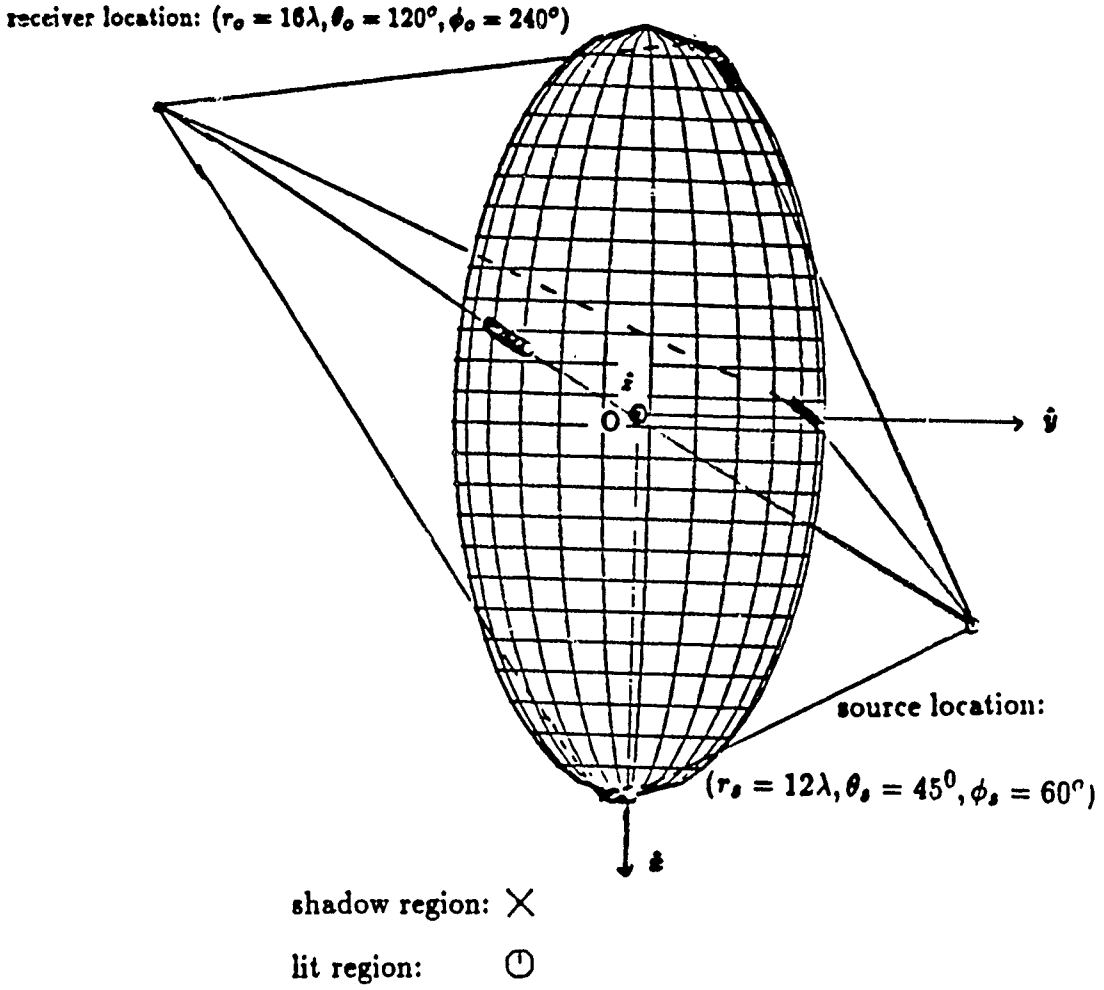


Figure 5 : Four creeping wave paths on a 8 λ × 4 λ × 3 λ ellipsoid

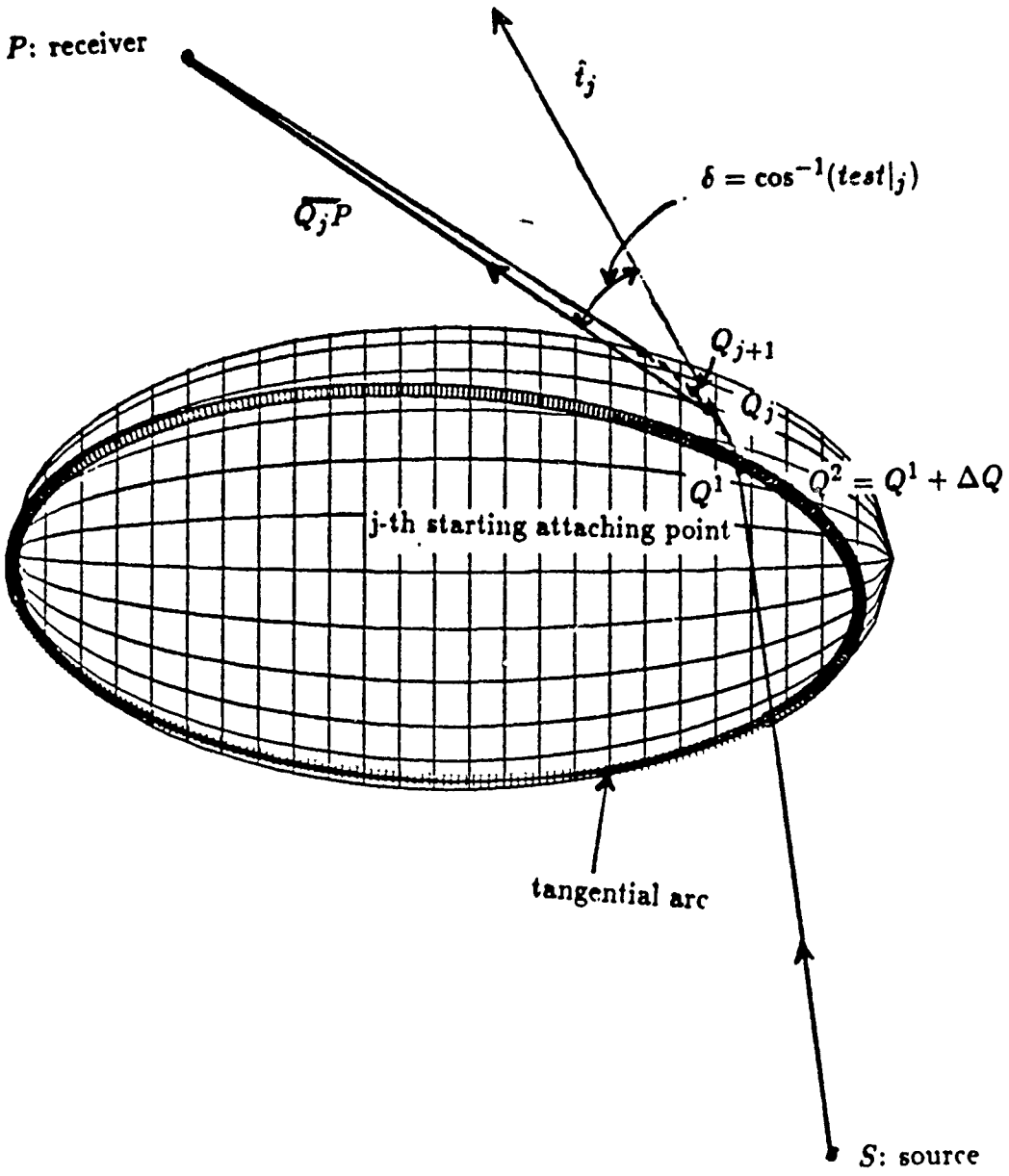


Figure 6 : Initial search method for creeping wave

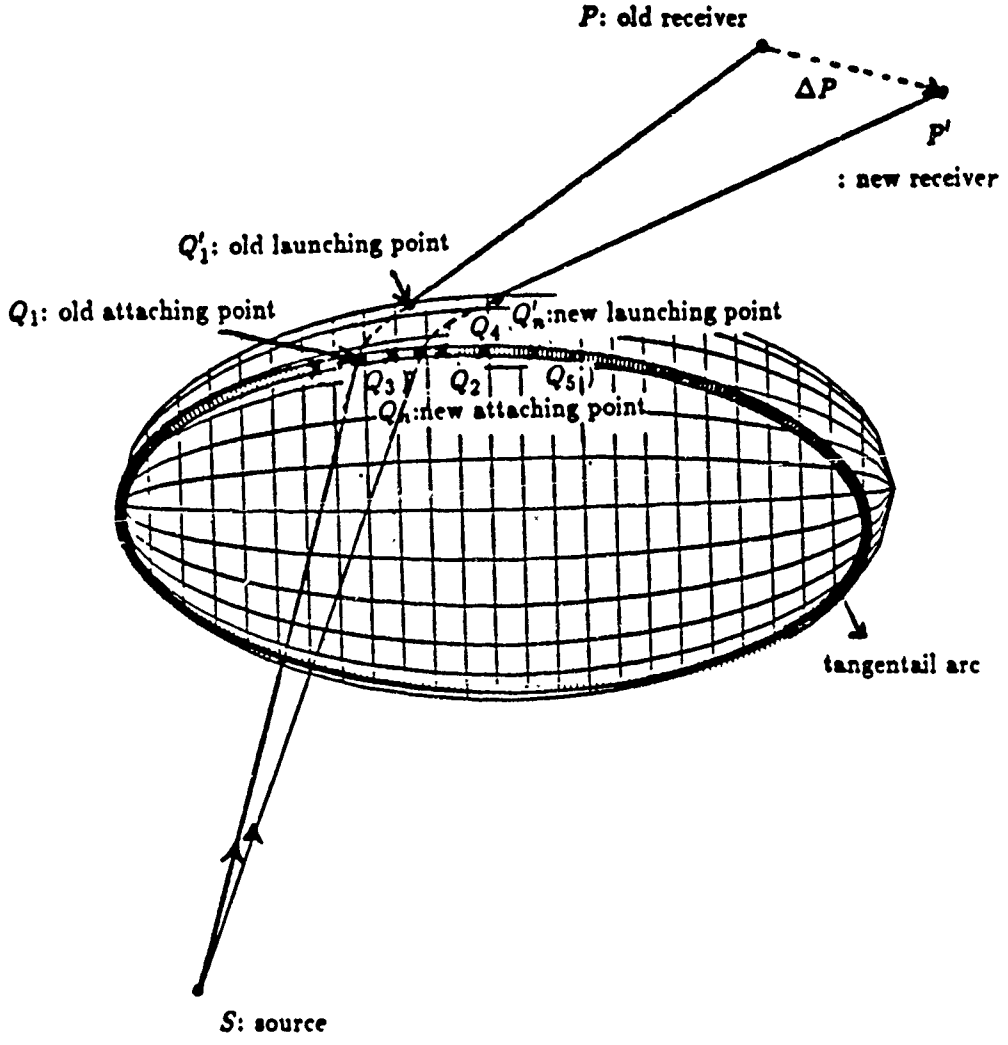
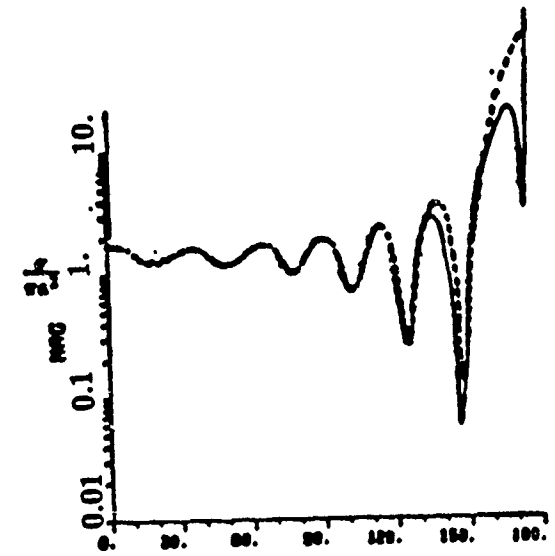
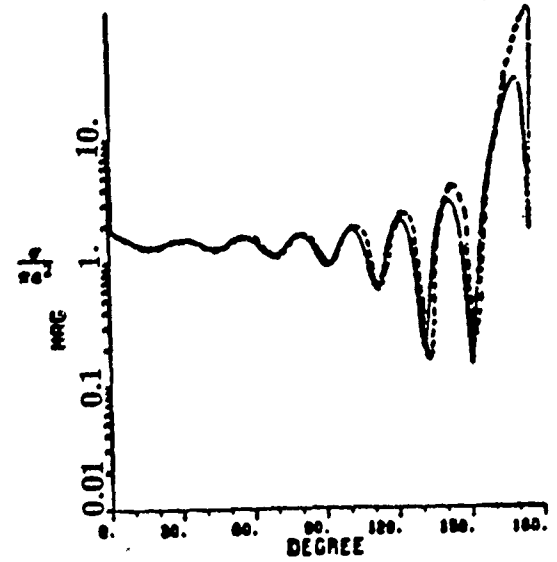


Figure 7 : Bisectional search method



(a): $ka = 8.3$ —— UTD

----- eigenfunction solution



(b): $ka = 9.5$ pattern cut: x-y plane

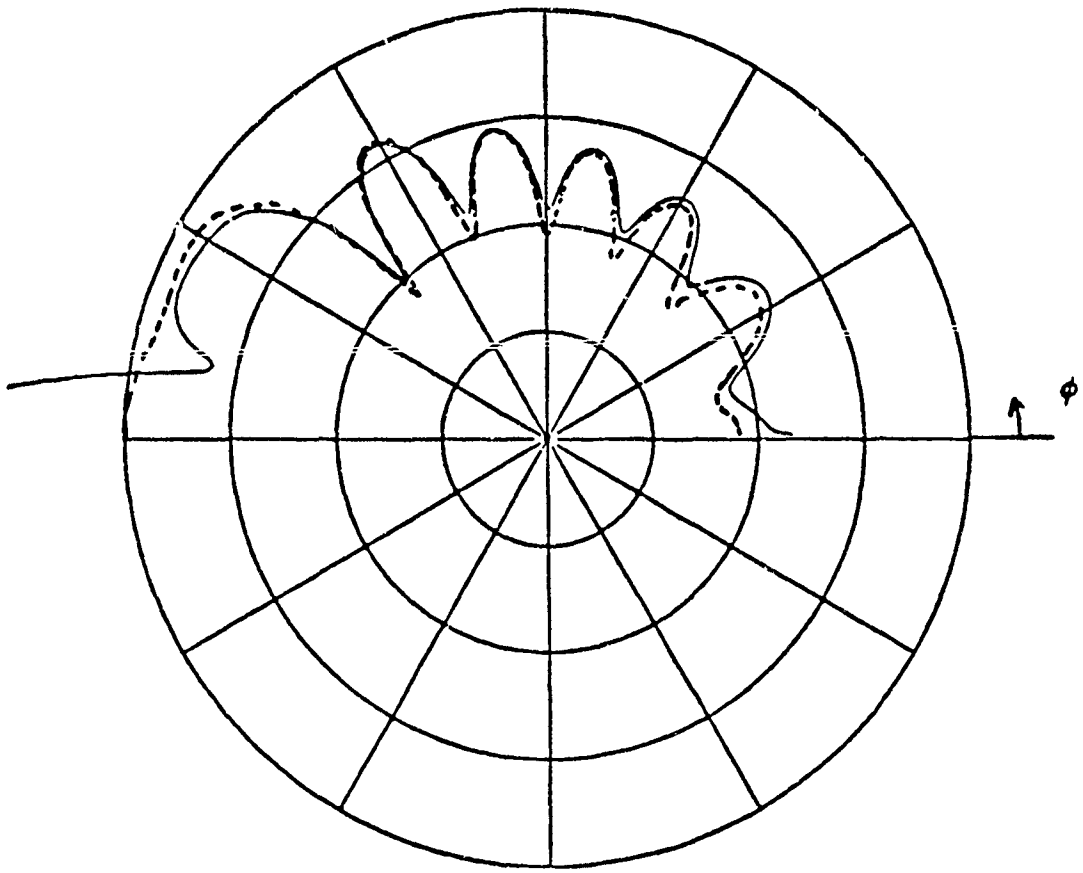
Figure 8 : Principal plane scattered field pattern of spheres $ka = 8.3$ and $ka = 9.5$

source location: $(r_s = \infty, \theta_s = 90^\circ, \phi_s = 0^\circ)$

receiver location: $(r_o = \infty, \theta_o = 90^\circ, \phi_o = \phi)$

source polarization: parallel to the plane of incidence

normalized to 4.2 DB



——— UTD

- - - - method of moments

source location: $(r_s = \infty, \theta_s = 90°, \phi_s = 0°)$

receiver location: $(r_o = \infty, \theta_o = 90°, \phi_o = \phi)$

dimensions of scatterer: $a = 1.5\lambda, b = c = 0.7\lambda$

pattern cut: x-y plane

Figure 9 : Far-zone scattered field pattern of the spheroid $a = 1.5\lambda$, $b = c = 0.7\lambda$

source polarization: parallel to the plane of incidence

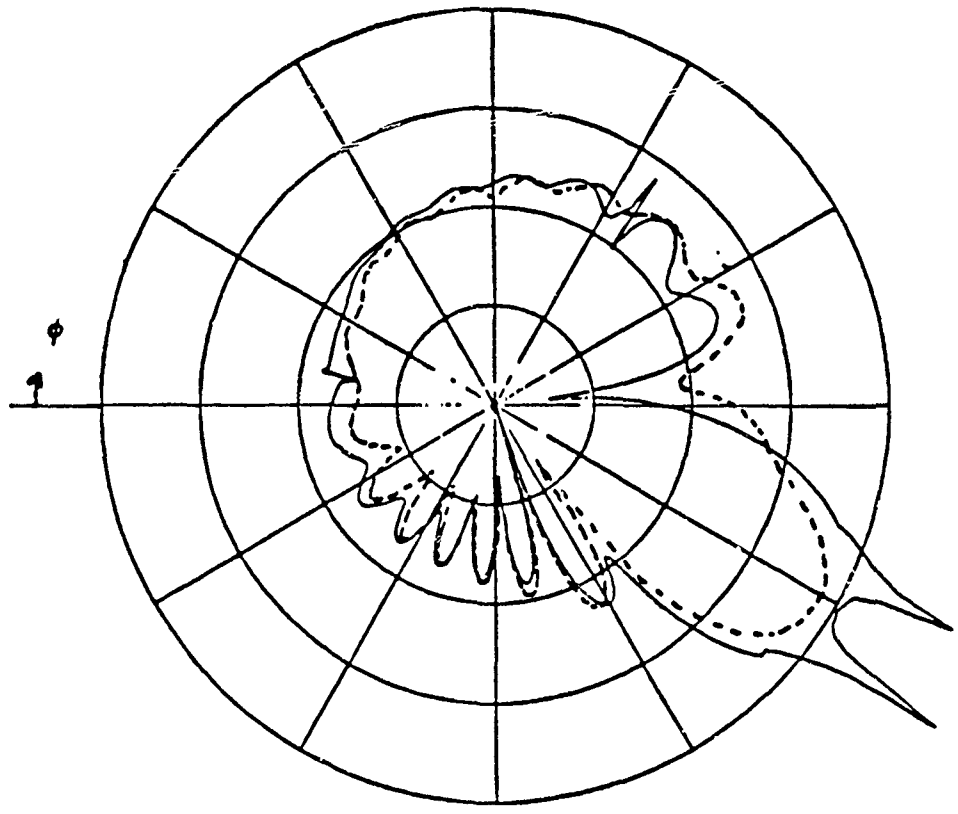


Figure 10: Near-zone scattered field pattern of a $2\lambda \times 1\lambda \times 1\lambda$ spheroid
source polarization: parallel to the plane of incidence

MCDONNELL DOUGLAS ASTRONAUTICS COMPANY—ST. LOUIS

THE USE OF METHOD OF MOMENTS TO ANALYZE SCATTERING FROM SMALL METAL GAPS

ABSTRACT

J. L. Karty and B. L. Harris

McDonnell Douglas Astronautics Company
P.O. Box 516
St. Louis, MO 63166

Plane wave excitation of metal gap imbedded near the center of a strip induces currents which are similar in nature to currents associated with edges. This geometry is a conducting, two-dimensional body of translation. A solution is formulated with the electric field integral equation. Surface currents are obtained using the method of moments with triangle expansion and testing functions. This conducting body of translation code can be modified to handle arbitrary resistive boundary conditions along the width of the strip. Linear resistive tapers installed along the edges of a metal strip eliminate the edges as dominant scatterers for the strip.

Since the technique of method of moments is not typically used to study structures which are very small fractions of a wavelength, the analysis used here has been validated by comparison to narrow band swept frequency High Range Resolution Radar (HRRR) data. This particular comparison is attractive since HRRR can also give information isolating the gap as a single scattering center. Predicted and measured radar cross sections as a function of aspect angle are compared for various small width-depth combinations.

An analytic check for use of method of moments in analyzing small gaps is also possible. This approximate analytic approach considers the gap to be a parallel plate waveguide. In order to simplify the calculations, it is assumed that the magnetic field at the gap interface is negligibly different from the non-gap case. Therefore, results are only valid for small depths. This analytic technique yields a two-dimensional radar cross section as a function of gap width which is in agreement with the numerical solution.

I. INTRODUCTION

To study gaps using planar geometry, the technique of Method of Moments (MOM) was used for various width-depth combinations. It was necessary, however, to investigate this method as a viable and realistic way to analyze small separation gaps in metal bodies. The purpose of this paper is to establish guidelines for the usage of both numerical (i.e., MOM) and analytic approximate methods, such as viewing the gap as a small-depth parallel plate waveguide in an otherwise planar surface. Section II outlines the geometry and presents numerical results for scattering from a metal gap imbedded near the center of a strip. The next two sections provide comparisons of MOM with High Range Resolution Radar (HRRR) data and an analytic check. A summary discussion concerning the use of MOM for separation gaps in metal bodies is also included.

II. METHOD OF MOMENTS PREDICTIONS

In order to solve for induced currents and for far field scattering, a MOM program with triangle expansion and testing functions (from McDonnell Douglas Research Laboratories-MDRL) was modified. Figure 1 shows the applicable strip geometry. From the figure, it can be seen that the gap runs parallel to the strip edges. It would intuitively appear that both the gap and edges would provide similar discontinuities for an incident plane wave. Therefore, scattering characteristics associated with strip edges are expected to also be evident for the two-dimensional gap configuration. The return from edges in the conducting, two-dimensional code handling body of translation geometries was reduced by installing linear resistive tapers.

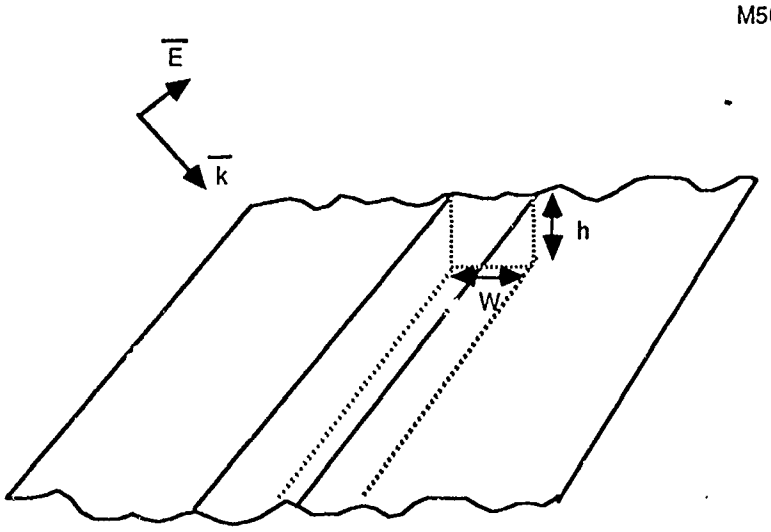


Figure 1. Geometry Used for Method of Moments Calculations

The transverse electric (to the strip axis) polarization is of particular interest here, as seen in Figure 2. Figure 2a shows returns of 10 GHz from an approximately foot wide metal strip in decibels per wavelength. Installing a resistive boundary condition at both edges reduces the signature significantly for both polarizations (Figure 2b). In Figure 2c, a metal gap 0.117 inch deep and wide is imbedded near the center of the strip width. The radar cross section (RCS) is increased substantially above the baseline "no-gap" value for the TE polarization, but the TM polarization is barely changed. The strip is slightly curved so that the underside of the gap does not "show through" the resistive material.

A series of gap width-depth combinations ranging from approximately 0.05 to 0.24 wavelengths was analyzed with the modified MDRL program. These curves were compared to experimental data as described in the next section.

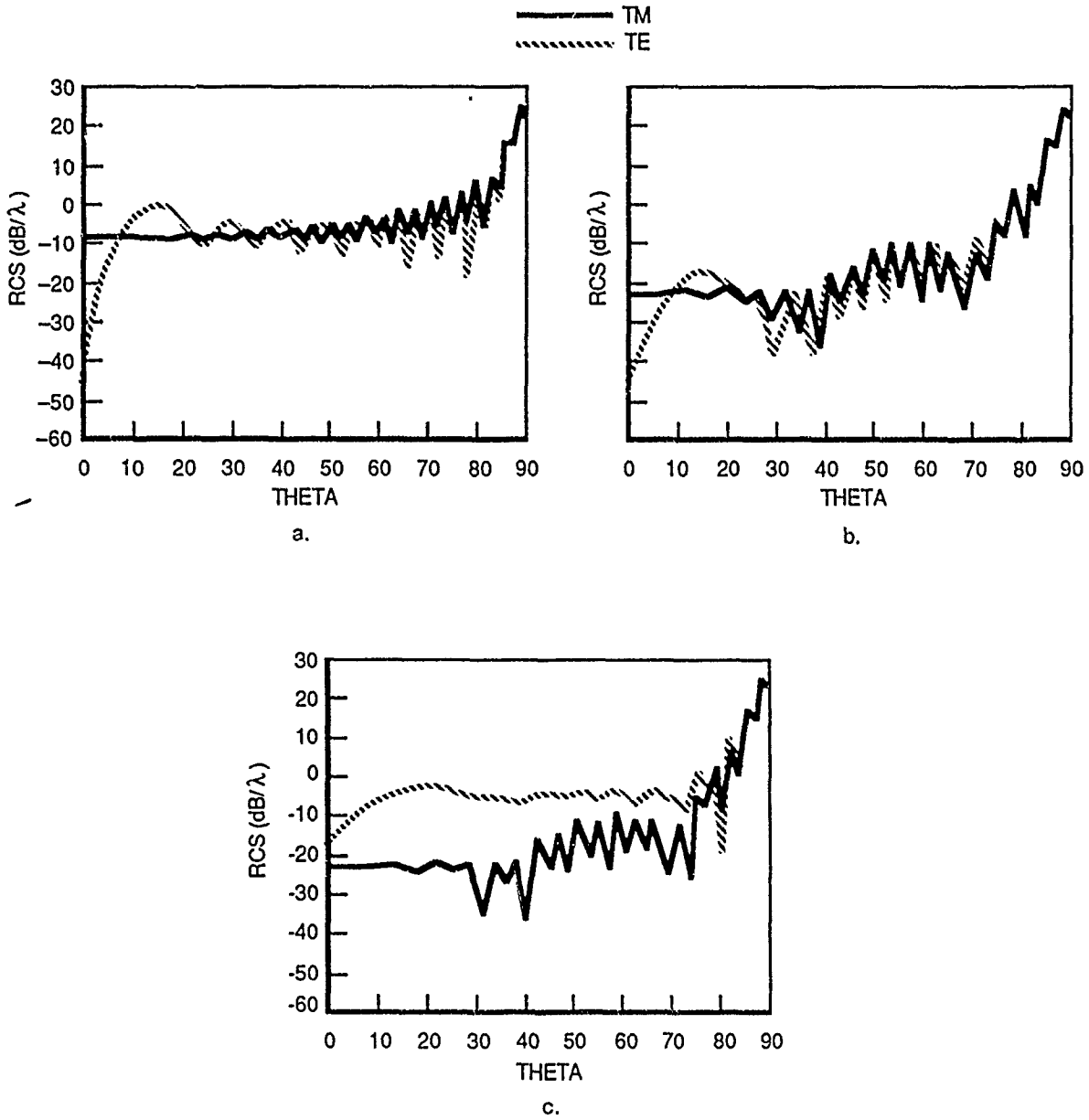


Figure 2. Model for Theory: Effect of Linear Resistive Tapers on Edges to Isolate Gap Return; a. Metal Strip, b. Strip with Resistive Tapers, c. Strip with Resistive Tapers and Gap.

III. EXPERIMENTAL DATA

Figure 3a shows a flat, approximately 30 inch wide double arrowhead split metal plate mounted on beveled 1 inch styrofoam. The width of the gap is obtained by the amount the plates are split. Gap depth is obtained by the metal plate thickness. Plates were stacked for larger depths. Copper tape was mounted atop the styrofoam as well, to provide the imbedded gap effect as in the theory model (see Figure 1). This test fixture was chosen because of flexibility and low cost. Definitions of angles and polarization used are shown in Figure 3b. Physical Optics (PO) return was used for the broadside value because measurements at 90° incidence were saturated.

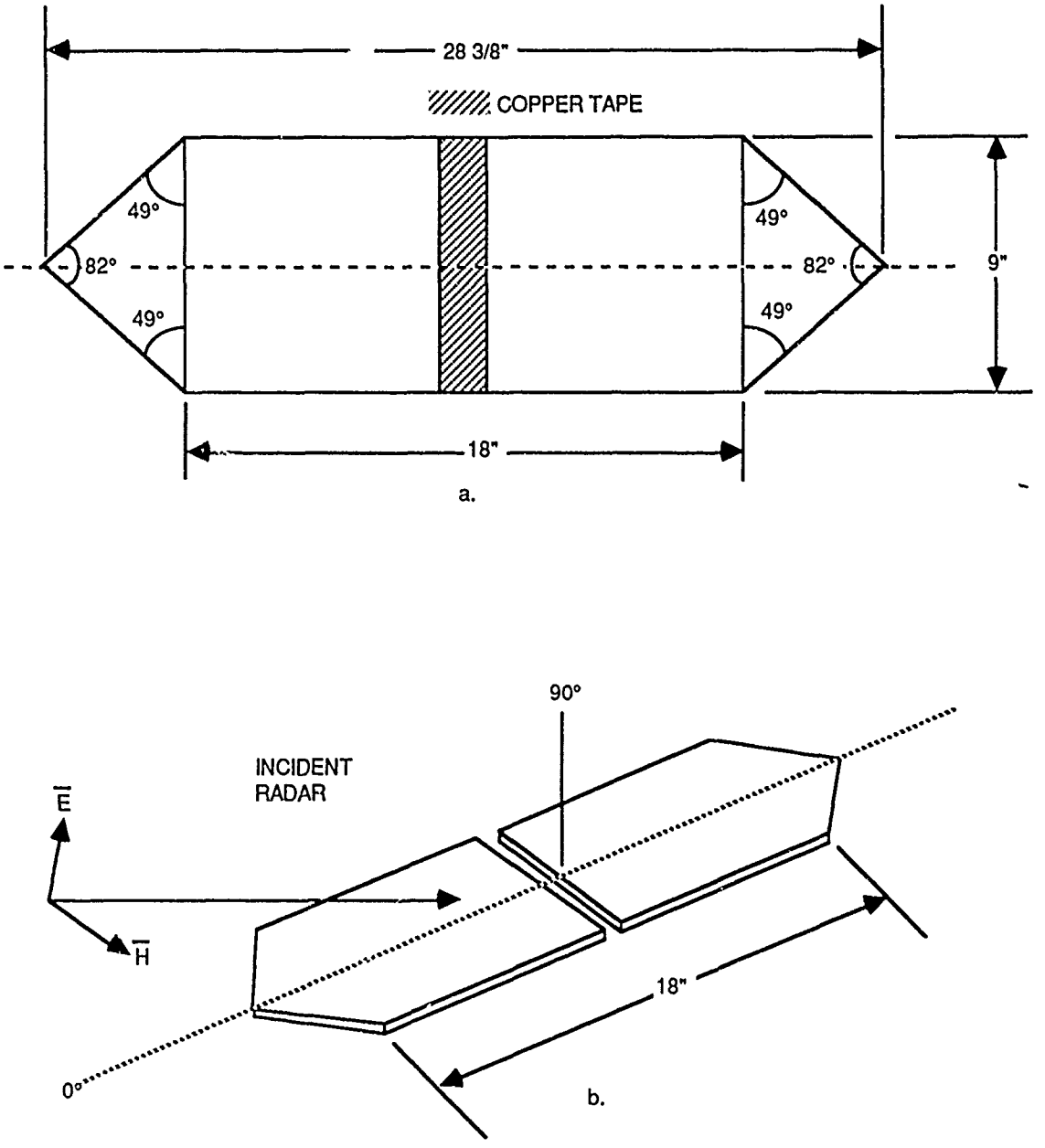


Figure 3. Experimental Test Fixture. a. Split Plates to Simulate Gap, b. Set Up for High Range Resolution Radar Testing

Since predictions were run for an approximately 1 ft wide strip instead of the approximately 30 inch diamond head plate, MOM broadside values were shifted to the PO prediction of a 23 inch width strip. The entire 2-D theory (dB/λ) plot was then vertically adjusted to match the 3-D experimental plot (dBsm) at broadside. After the outlined normalization process, predictions are in agreement with HRRR data in seven of the eleven cases (Figure 4 through 9), are low in two cases and high in two cases. Background level is indicated by the dashed straight lines near the bottom of these plots.

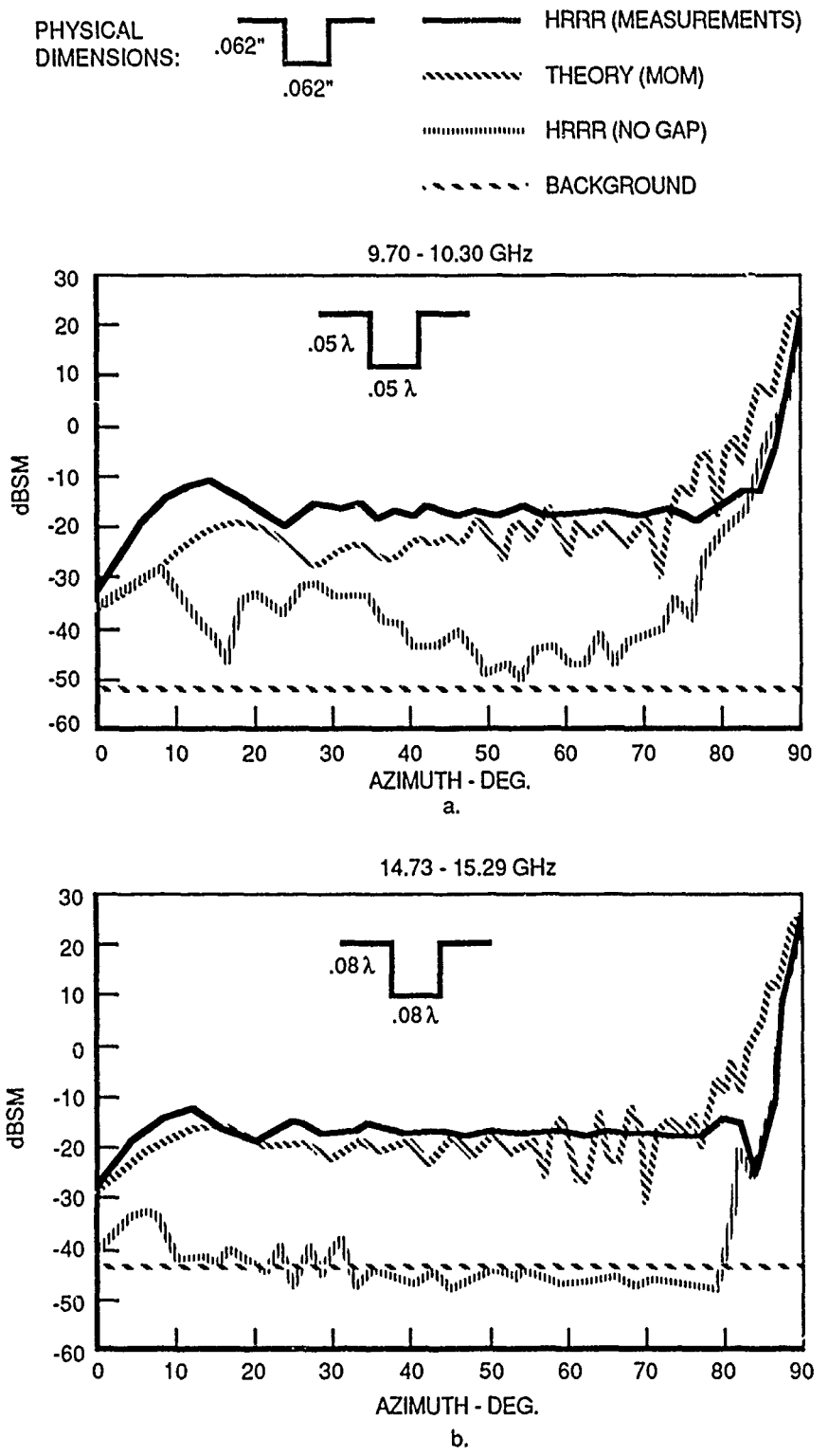
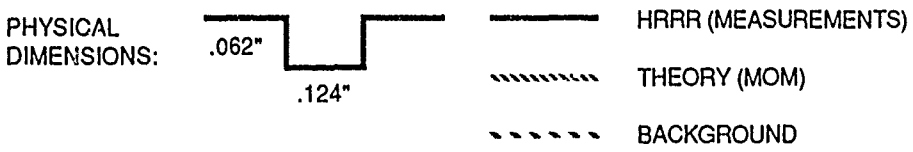
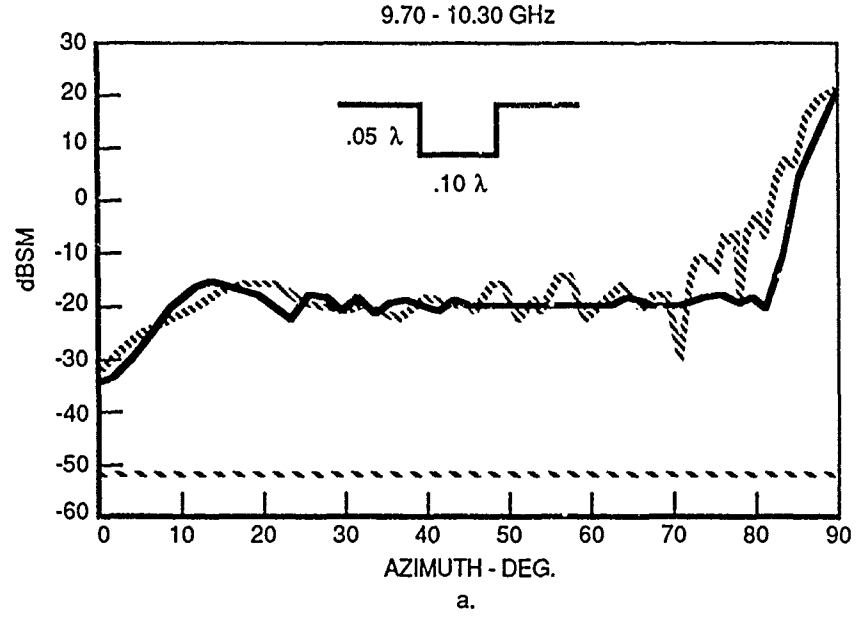


Figure 4. Theory vs. Experiment. Split Plates .062"
a. 10 GHz, b. 15 GHz





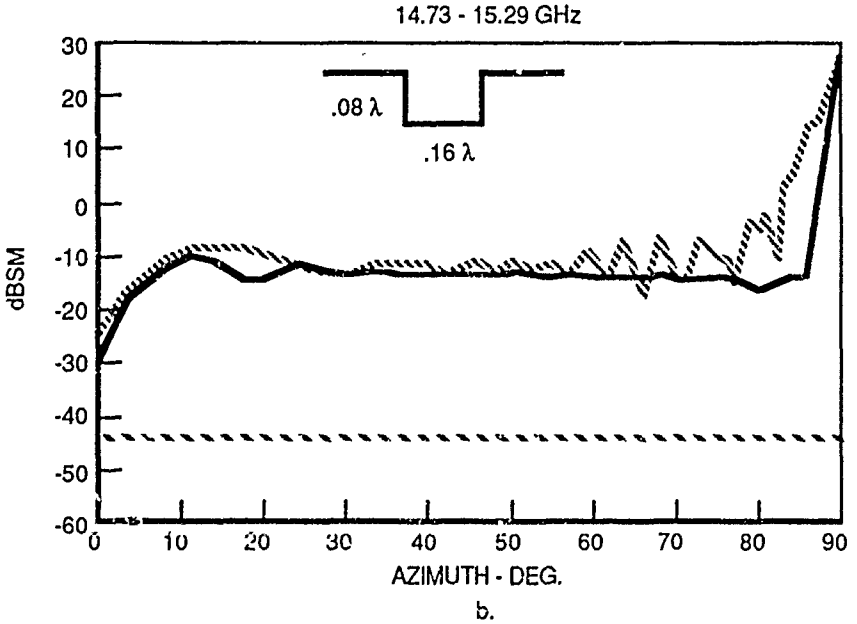


Figure 5. Theory vs. Experiment. Split Plates .124"
a. 10 GHz, b. 15 GHz

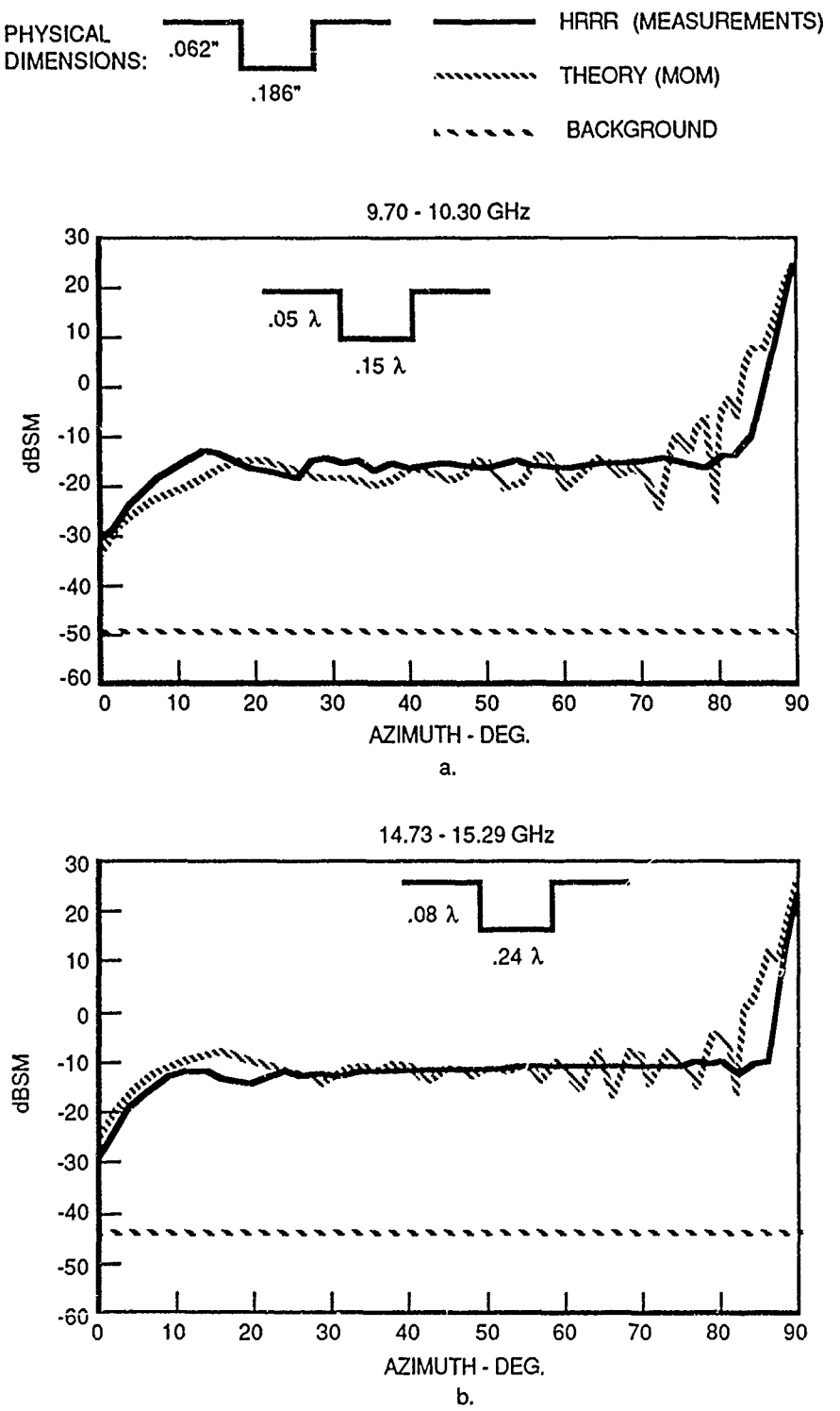


Figure 6. Theory vs. Experiment. Split Plates .186"
a. 10 GHz, b. 15 GHz

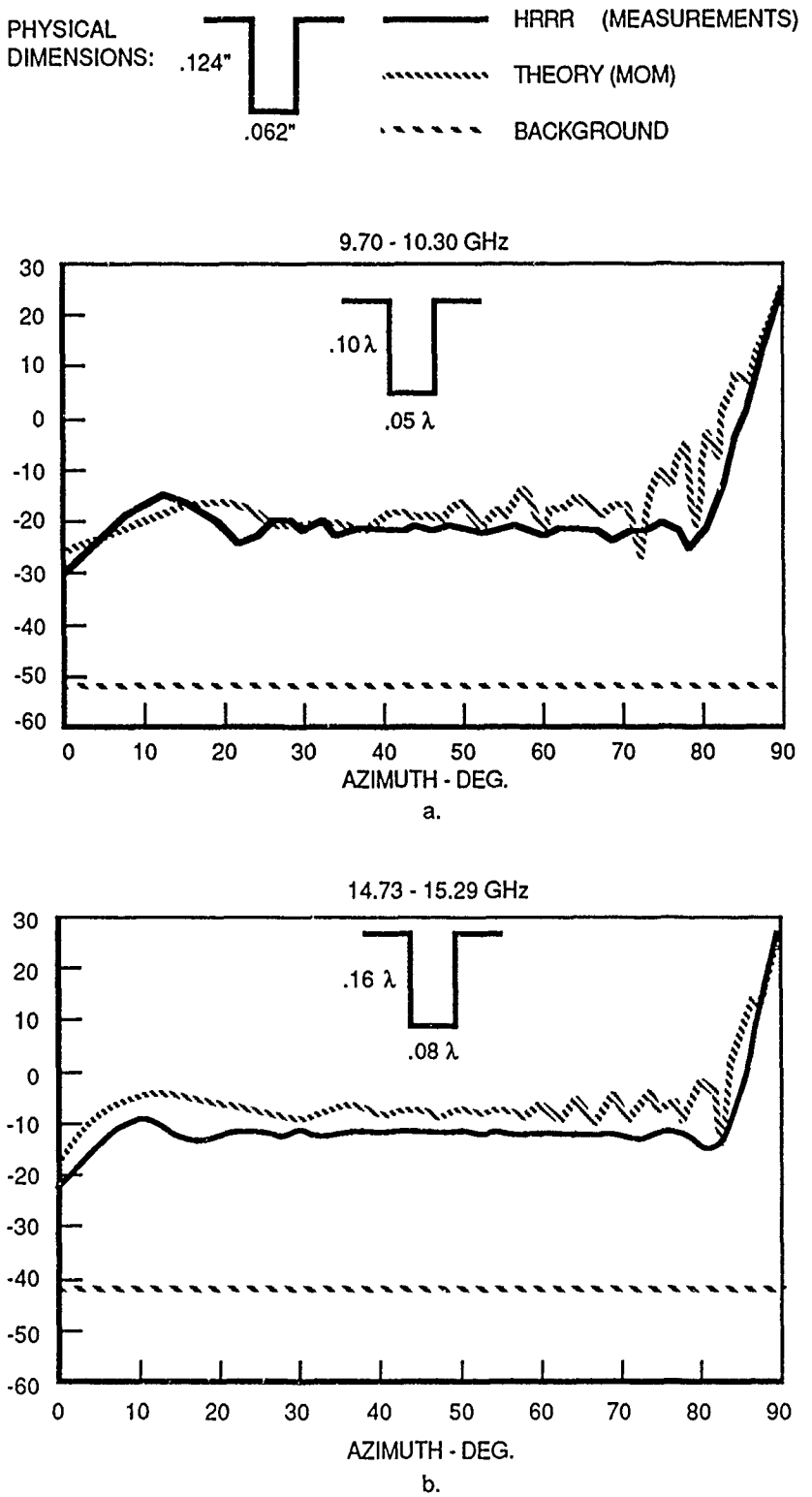


Figure 7. Theory vs. Experiment. Double Thickness, Split Plates .062"
a. 10 GHz, b. 15 GHz

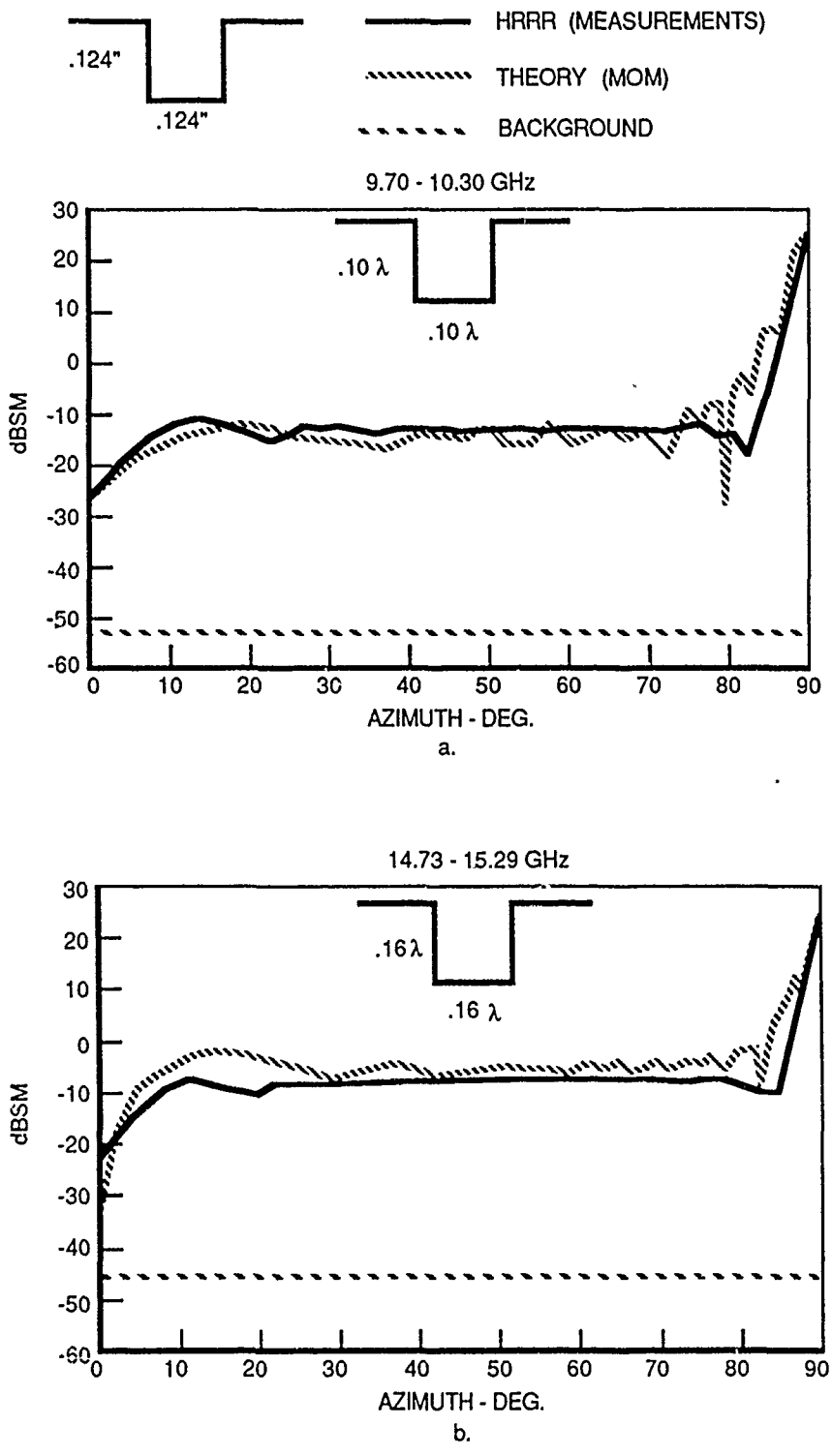


Figure 8. Theory vs. Experiment. Double Thickness, Split Plates .124"
a. 10 GHz, b. 15 GHz

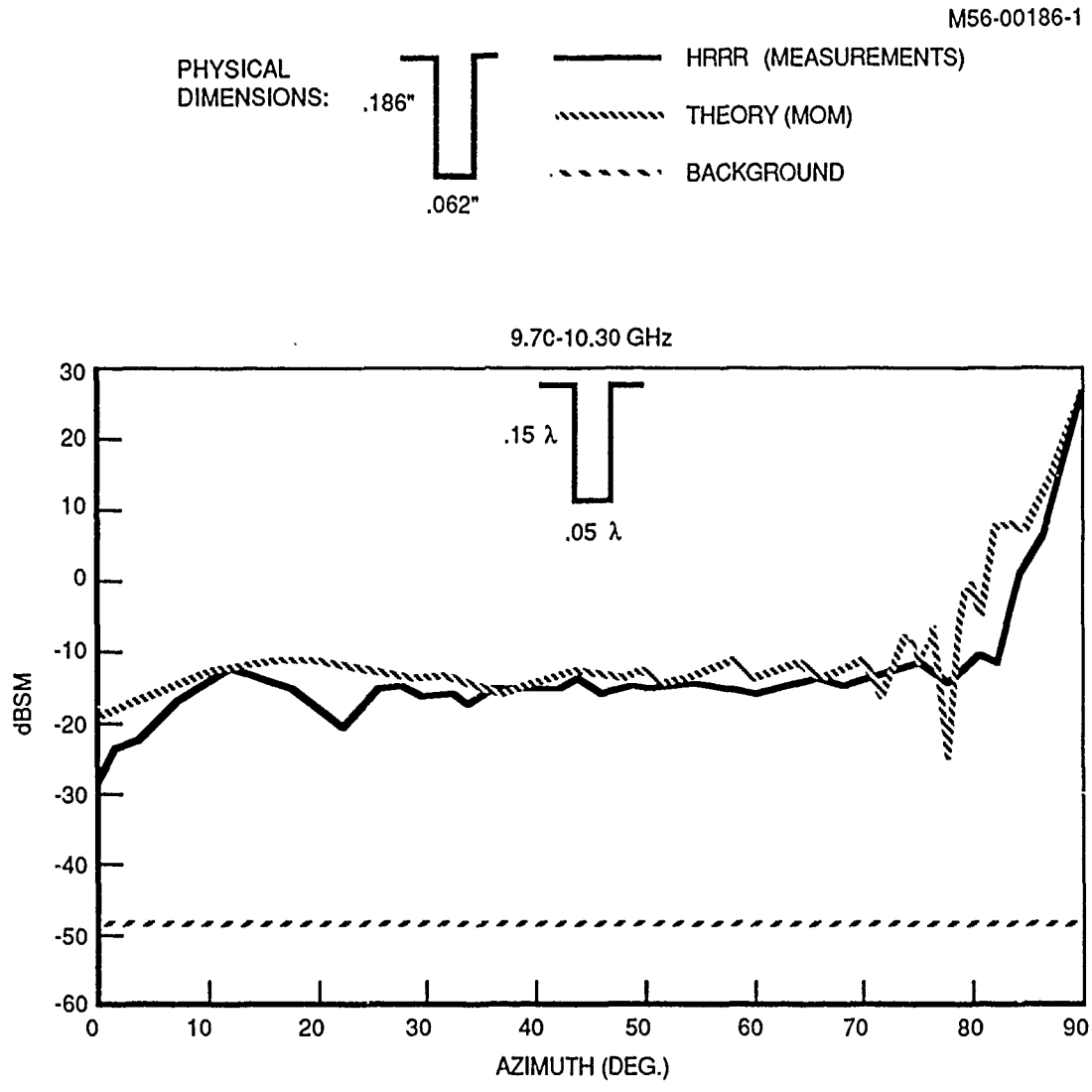


Figure 9. Theory vs. Experiment. Triple Thickness, Split Plates .062", 10 GHz

Some differences in experimental data versus predictions are evident. In these figures, there is less structure to the experimental plots than the theory plots, because there is tip-tip interaction in the test fixture, but straight edge interaction in the theory. Also, since the MOM model is slightly curved, the specular peak near 90 degrees is somewhat broader than in the flat plate case. Furthermore, the "traveling wave peak" tends to be closer to grazing in the experimental curves since tip-tip distance is approximately 30 inches and the strip width was approximately 1 ft. The main features of the analysis, however, concern overall magnitudes and general trends. There is generally very good agreement between theory and experimental curves in Figures 4 through 9.

IV. ANALYTIC CHECK

The gap is viewed as a parallel waveguide in this section. The magnetic field at the interface S shown in Figure 10 is assumed to be negligibly different from the non-gap case. This makes the analysis valid for small depths only. The 2-D RCS of a gap with small depths will be derived.

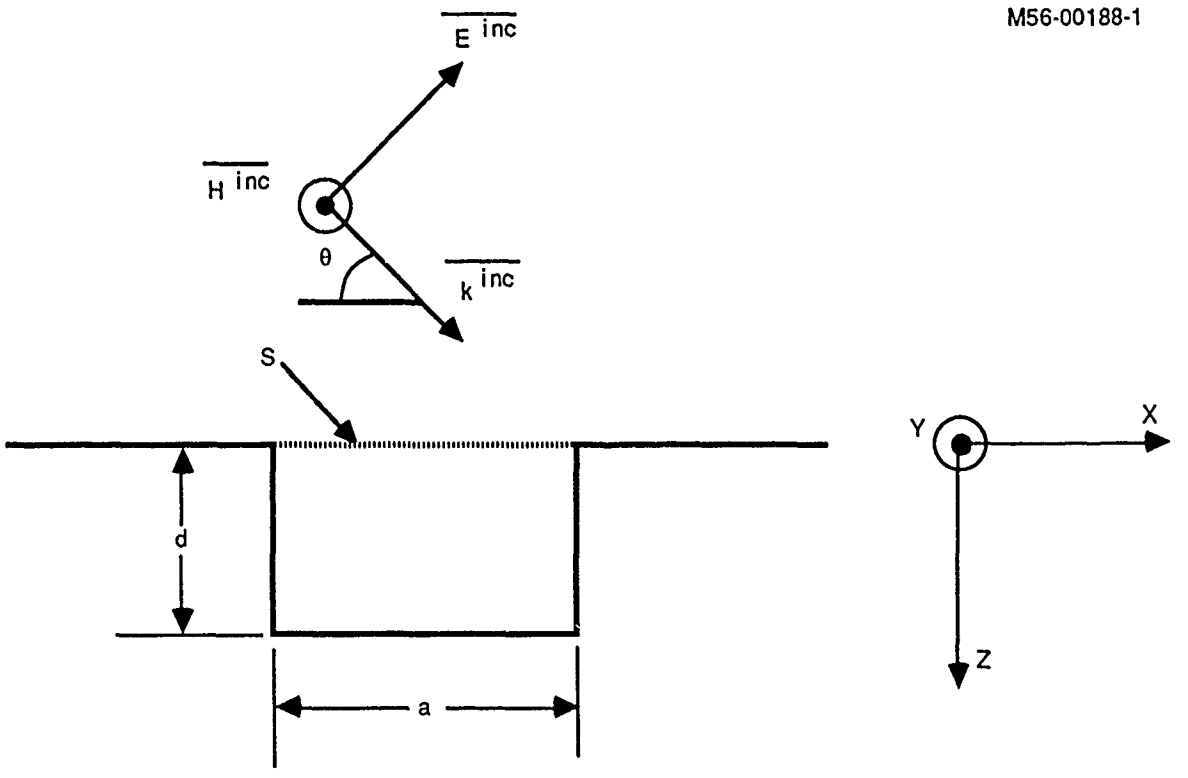


Figure 10. Geometry Used for Analytic Check

This derivation equates the total field inside the gap with the total field outside the gap at the interface S. On S,

$$\left[H^{inc}(x) + H^{scat}(x) \right] \Big|_{z=0^-} = H^{g}(x) \Big|_{z=0^+} \qquad (1)$$

$$\left[E^{inc}(x) \sin\theta + E_x^{scat}(x) \right] \Big|_{z=0^-} = E_x^{g}(x) \Big|_{z=0^+} \qquad (2)$$

where inc, scat and g designate incident, scattered and gap fields respectively. Treating the gap as a parallel plate waveguide, the field inside the gap can be expressed as a linear combination of TM_{no} modes. At $z=0^+$,

$$H^{g}(x) = \frac{1}{\eta_o} \sum_{n=0}^{\infty} h_n^g \cos\frac{n\pi x}{a} \qquad (3)$$

$$E_x^{g}(x) = \sum_{n=0}^{\infty} e_n^g \cos\frac{n\pi x}{a} \qquad (4)$$

where $$e_n^g = -j\frac{\gamma_n}{k}(\tanh \gamma_n d)\ h_n^g , \qquad (4a)$$

$$\eta_o = \sqrt{\frac{\mu_o}{\varepsilon_o}} \text{ , and } \gamma_n^2 = \left(\frac{n\pi}{a}\right)^2 - k^2$$

With the small depth assumption, we can write that the magnetic field is slightly perturbed from the non-gap case:

$$H^{scat}(x) \approx H^{inc}(x) \text{ on surface S} \qquad (5)$$

Combining equations (1) and (5), we have

$$2H^{inc}(x) = H^{g}(x) \qquad (6)$$

$H^g(x)$ is given in equation (3) in terms of coefficients h_n^g.
We express the incident plane wave excitation at $z=0^-$ as

$$H^{inc}(x) = \frac{1}{\eta_o} e^{-jkx\cos\theta} \quad \text{on S.} \qquad (7)$$

By expanding the right hand side of equation (7) as a series in cosines, we can solve for h_n^g as follows. First, note that:

$$e^{-jkx\cos\theta} = 2 \sum_{n=0}^{\infty} \frac{f_n(ka\cos\theta)}{(\delta_{no}+1)} \cos\frac{n\pi x}{a}$$

$$\text{where} \quad f_n(\alpha) = \begin{cases} \dfrac{j\alpha\,[\,1-(-1)^n e^{-j\alpha}\,]}{(n\pi)^2 - \alpha^2}, & \alpha \neq n\pi \\ \dfrac{\delta_{no}+1}{2}, & \alpha = n\pi \end{cases} \qquad (8)$$

Combining equations (6), (7) and (8):

$$H^g(x) = \frac{2}{\eta_o}\left(2\sum_{n=0}^{\infty} \frac{f_n(ka\cos\theta)}{(\delta_{no}+1)} \cos\frac{n\pi x}{a}\right) \qquad (9)$$

Then, comparing equations (3) and (9) term by term gives

$$h_n^g = \frac{4 f_n(ka\cos\theta)}{(\delta_{no}+1)} \qquad (10)$$

The amplitudes h_n^g and e_n^g are related by equation (4a). We now have a solution for $E_x^g(x)$ at $z=0^+$ by using equations (10) and (4a) in equation (4).

Replacing S by a conducting plane, and writing the aperture electric field equivalent to imaged magnetic currents, we have $K_y(x) = 2\,E_x^{scat}(x)$ on surface S. From the magnetic currents, the scattered far electric field and hence 2-D cross section are obtained:

$$\sigma = \frac{\left| ka \sum_{n=0}^{\infty} f_n(ka\cos\theta)\, e_n^g - ka\, f_o(2ka\cos\theta)\sin\theta \right|^2}{k} \qquad (11)$$

Figure 11 shows RCS vs. gap width for a gap of 0.01 wavelengths and $\theta = 0°$. The lowest order RCS is denoted as "1 mode." Using just three more modes (a total of 4) closely resembles the result using 100 modes. However, it is clear that for small widths (w less than or equal to 0.3λ), even the one mode solution is within approximately 4 dB/λ of the 100 mode solution.

M56-00192-1

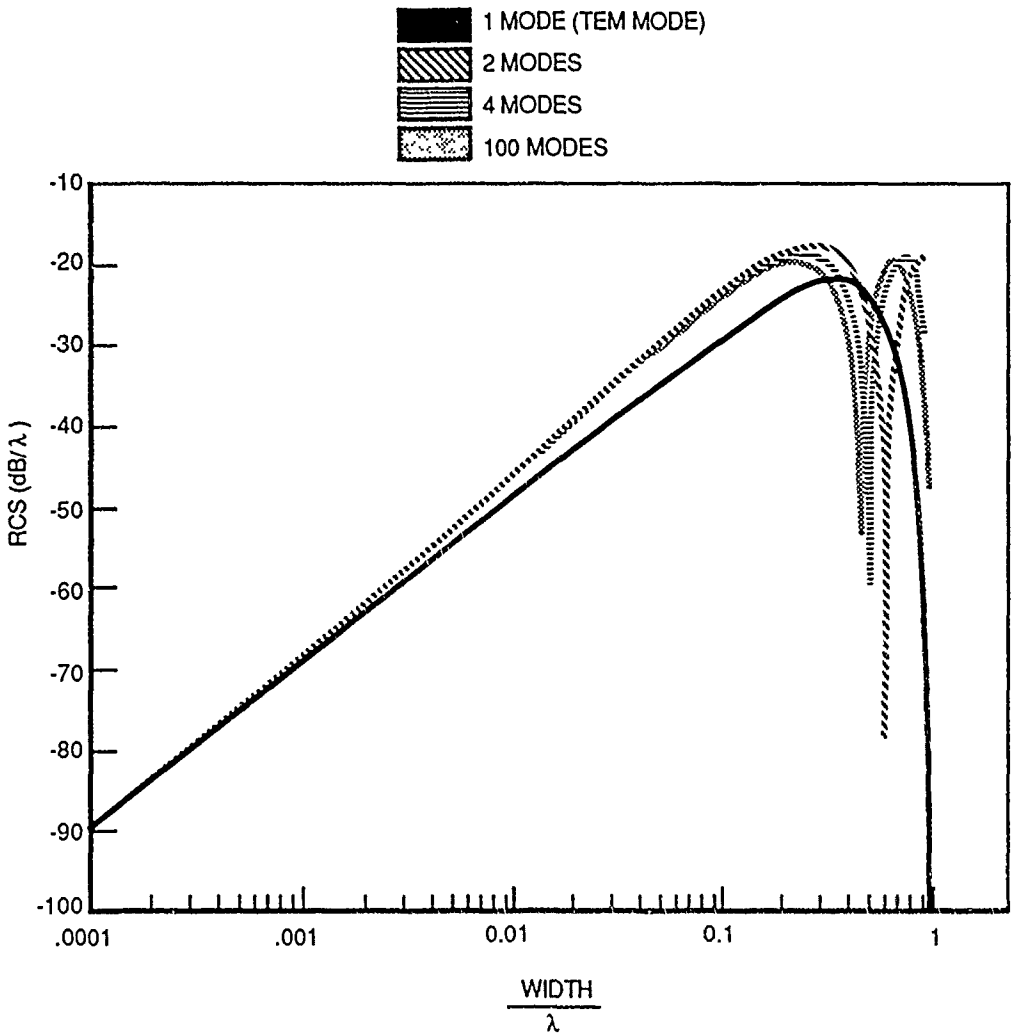


Figure 11. Comparson of Number of Modes Used -RCS vs. Gap Width, for depth = .01 λ and θ = 0°

In Figure 12, 2-D MOM values are from plots such as Figure 2c, with plotted values taken as visual averages after the traveling wave peak, where the RCS becomes fairly constant with angle (except for the broadside flash) in the MOM calculations. In angle scans, such as Figure 2c, the value right at grazing (0°) is due to an edge effect rather than to the gap itself. Figure 12 provides an excellent analytic check for the use of MOM in studying effects of isolated small gaps.

V. SUMMARY DISCUSSION

The overall magnitude and trends found in both predictions from MOM and HRRR data agree extremely well. This establishes the notion that a two-dimensional, conducting body of translation MOM code can be modified with edge resistive tapers to adequately model small separation gaps in metal.

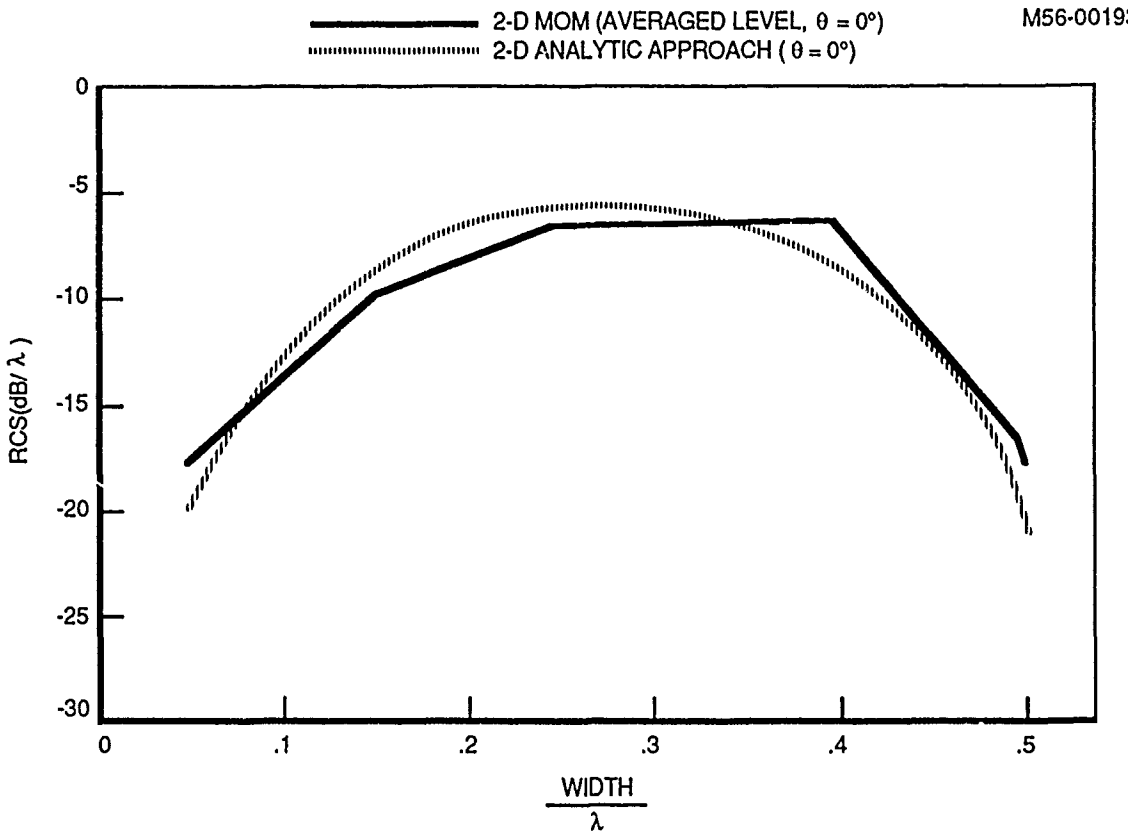


Figure 12. Comparson of Method of Moments to the Analytic Technique. RCS vs. Gap Width, for depth = .05 λ

There were some significant differences between the theoretical 2-D model and the 3-D experimental setup. Most notably, resistive tapers were used in the theory to reduce strip edge effects. Since the radar penetrates the resistive material, the metal part of the strip was slightly curved to hide the underside of the gap. The flat test fixture for HRRR used double arrowhead tips to reduce edge effects.

It is not surprising that there was some disagreement in predictions vs. data (e.g., Figures 4a, 4b, 7b, 8b). Measured values for the smallest gaps studied (widths and depths less than or equal to ~.08λ) are higher than predicted values since the panel double arrowhead tips contribute to the HRRR return for these configurations. (In a wide band diagnostic plot for Figure 4a, the back tip return at 20 degrees illumination is almost as high as the gap return.) For depths greater than ~.08λ, measured values tend to be smaller than MOM predictions (e.g., Figures 7b, 8b) possibly because the panel tips interact with the gap edges less than the straight edges in the model.

A second check was also made to establish the validity of using MOM for measuring the return from small metal gaps. The analytic 2-D model agrees very well with MOM results (see Figure 12). Thus, based upon comparisons to experimental data and an analytic technique, the use of MOM is appropriate for separation gap widths and depths ranging from approximately .05 to .24 wavelengths.

VI. ACKNOWLEDGEMENTS

L. Mitschang and J. Putnam from McDonnell Douglas Research Laboratories have been very generous in providing us with a perfect electrically conducting, two-dimensional body of translation method of moments program for modification.

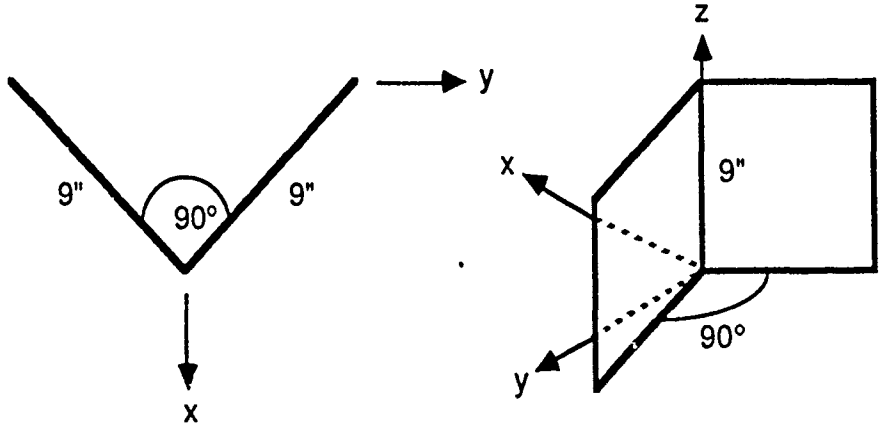
Suggestions from J. Norris and R. Cole (McDonnell Douglas Astronautics Company-MDAC, St. Louis) were very useful for experimental verification. We also thank P. Kohlmeier and C. Raiff (MDAC) for providing us with the HRRR plots presented.

UNIFORM THEORY OF DIFFRACTION - MOMENT METHOD MODEL COMPARISON FOR A DIHEDRAL CORNER REFLECTOR

J.L. Fath, A.J. Terzuoli, E.G. Zelnio
Department of Electrical Engineering
Air Force Institute of Technology
Wright-Patterson Air Force Base, Ohio 45433-6583

This study examined the electromagnetic scattering from a dihedral corner reflector for both monostatic and 90 degree bistatic source-receiver geometries. The dihedral corner reflector was composed of two perfectly conducting 9 inch square flat plates joined along a common edge form an interior angle of 90 degrees. The frequencies of interest included 2, 3, and 10 GHz. The theoretical modeling utilized the Uniform Theory of Diffraction (UTD) and the Method of Moments (MOM). The UTD code implemented was a two dimensional diffraction model developed by K. Aberegg and R. Marhefka of The Ohio State University ElectroScience Laboratory (OSU-ESL). The MOM code implemented was the Electromagnetic Surface Patch Code: Version II - Polygonal Plates and Wires developed by E. Newman also of OSU-ESL. The MOM analysis was performed on a Cray X-MP and a VAX 11/785, and the UTD analysis was performed on a VAX 11/785.

The results from the UTD and MOM models were compared with each other. The interest was in how well could a two dimensional UTD model of an infinite dihedral corner reflector predict the scattering from a three dimensional object like the finite dihedral corner reflector. Also of interest was the implementation of a MOM model on a Cray supercomputer and the computational speed of the Cray versus the VAX.



Dihedral Corner Reflector

UTD-MOM Model Comparison for a Dihedral Corner Reflector

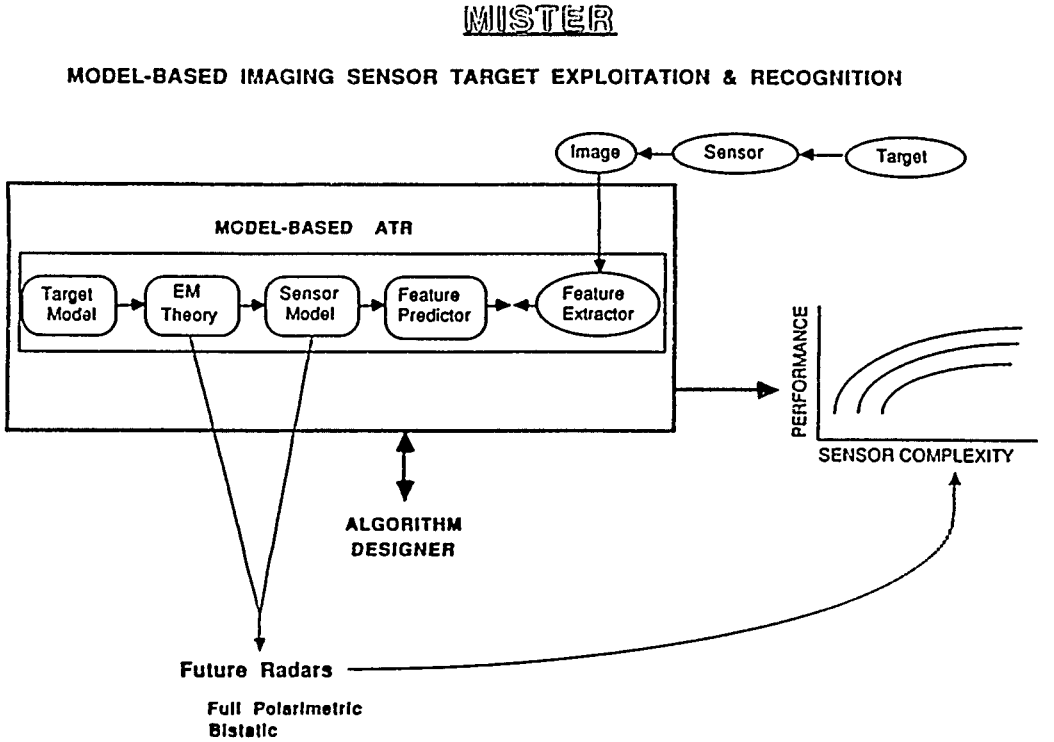
J.L. Fath, A.J. Terzuoli, E.G. Zelnio
Department of Electrical Engineering
Air Force Institute of Technology

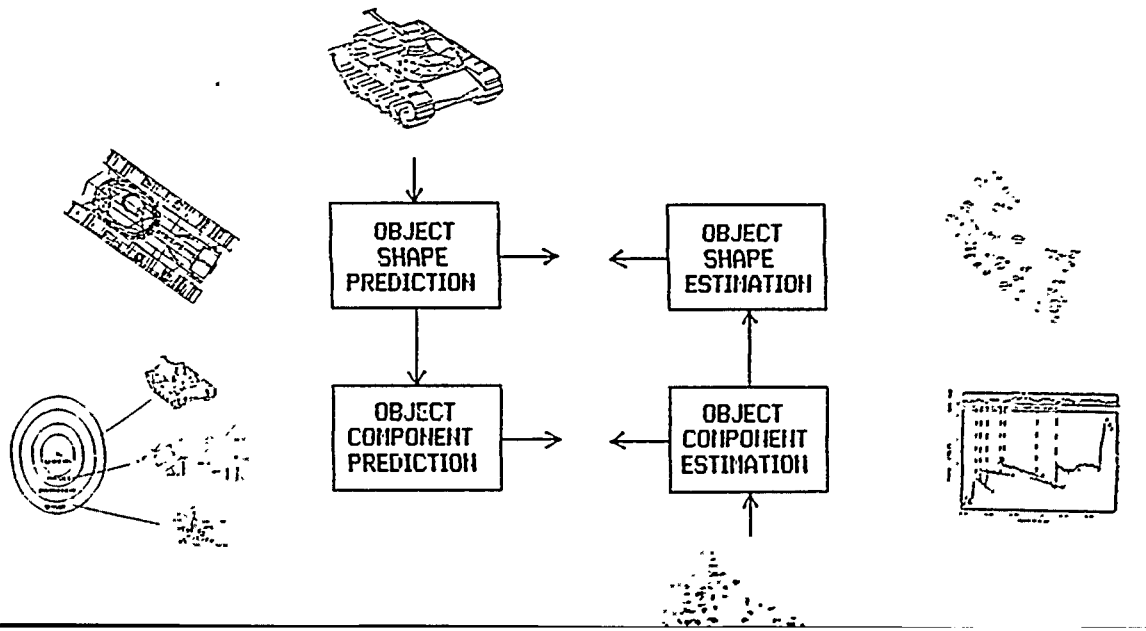
Research Motivation

Object Geometry

EM Codes

Results





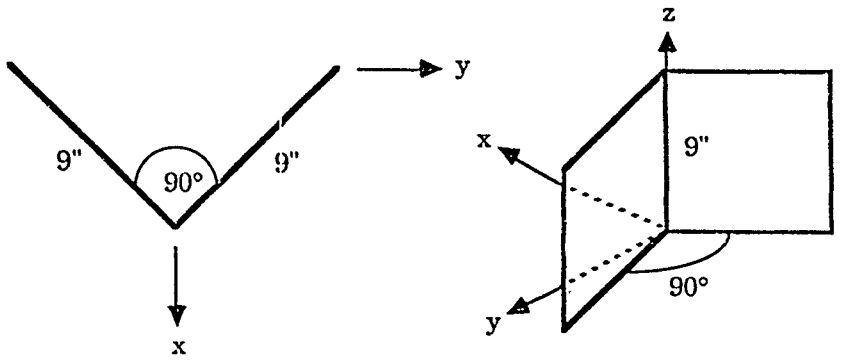


Figure 4.1 Dihedral Corner Reflector

ESP implementation on the Cray

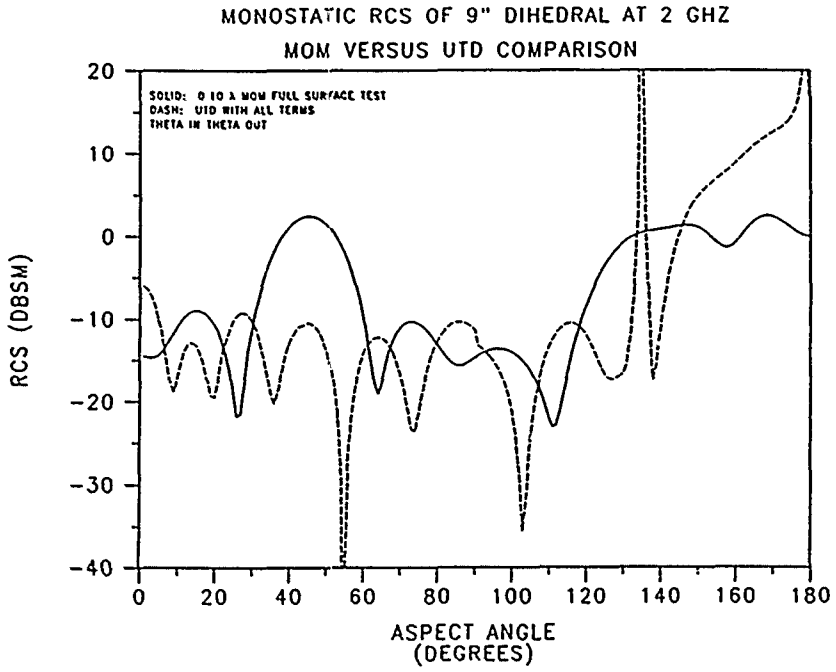
- Fortran compiler ambiguities
- test run
- dihedral run at 3 GHz
  - -- array dimensions increased
  - -- exceeded Cray main memory

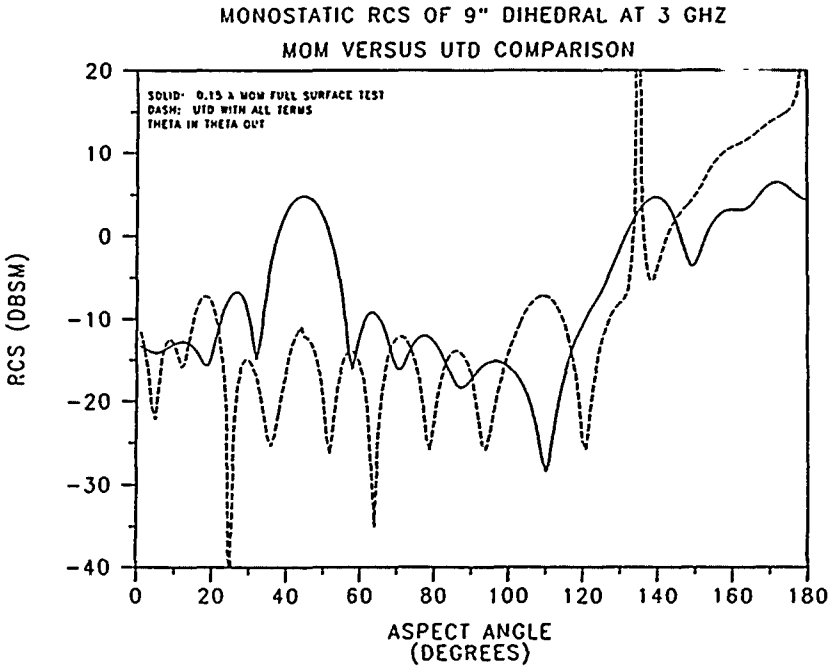
① 2-D UTD Corner Reflector Model Under Development by R. Marhefka, OSU

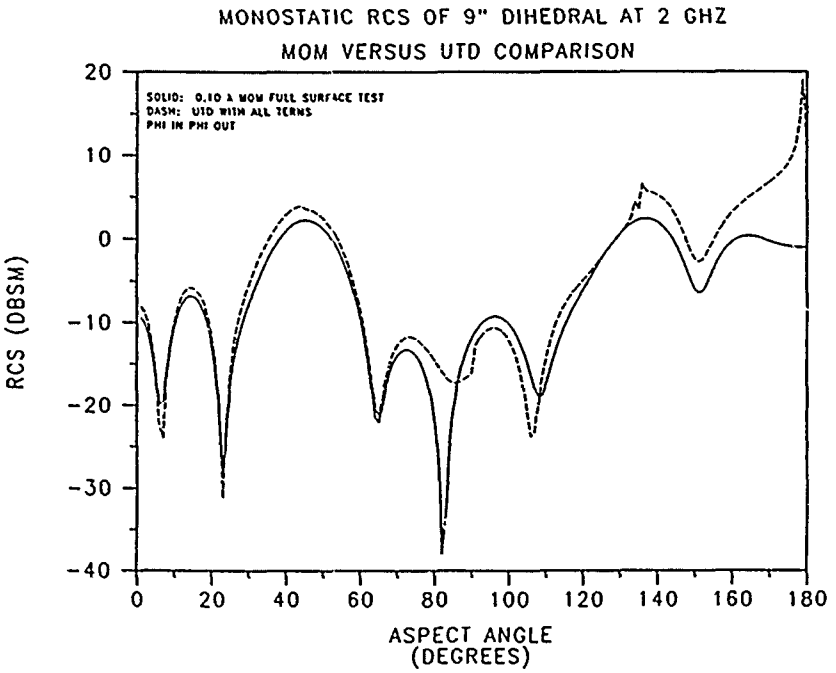
② ESP2 - MOM Code Developed by E. Newman, OSU

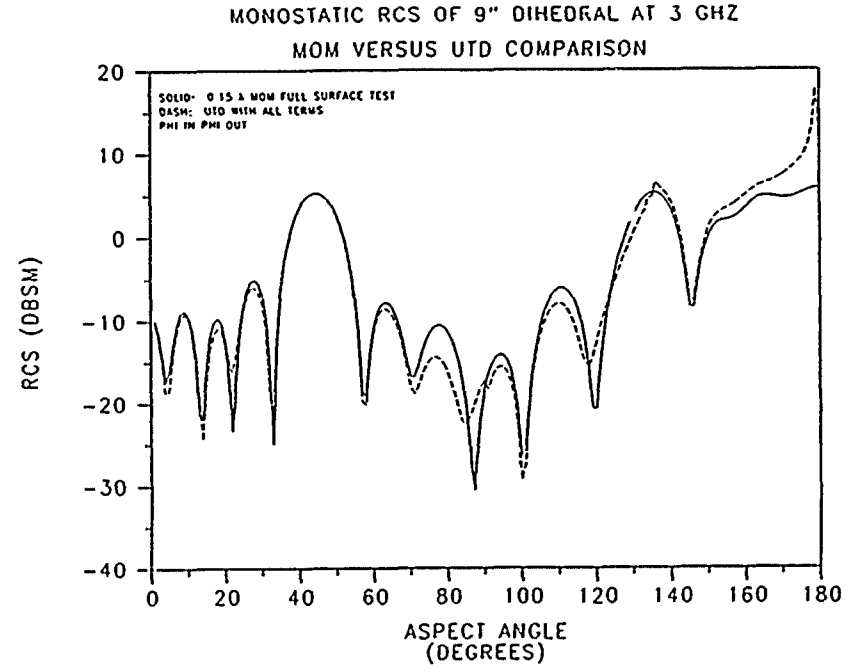
ESP implementation on the VAX

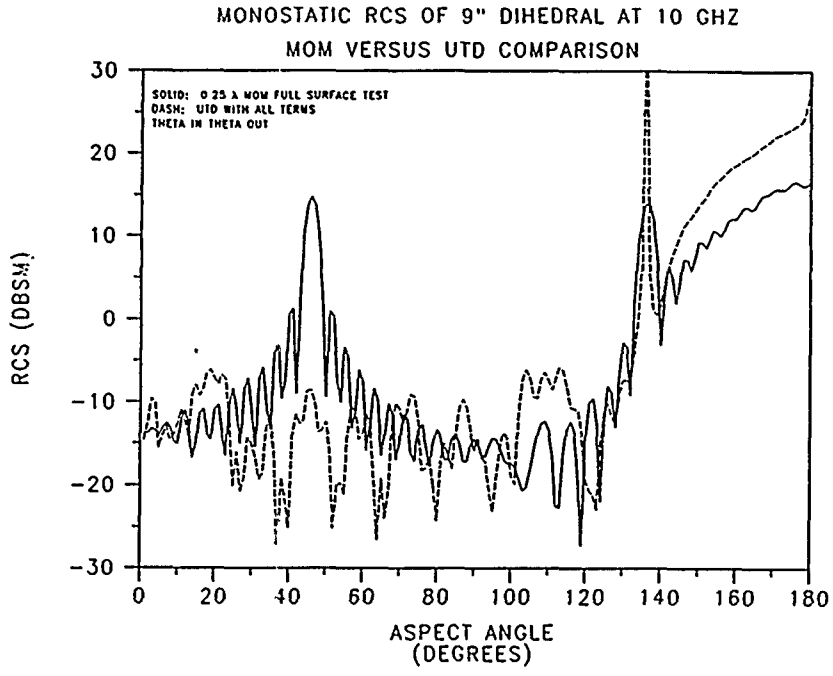
- pagefile and memory problems
- change UAF and SYSGEN parameters
- dihedral run at 3 GHz
- dihedral run at 10 GHz
  - -- increased array dimensions to 4000
  - -- increased UAF and SYSGEN parameters
  - -- pagefile increased
- dihedral run at 2 GHz

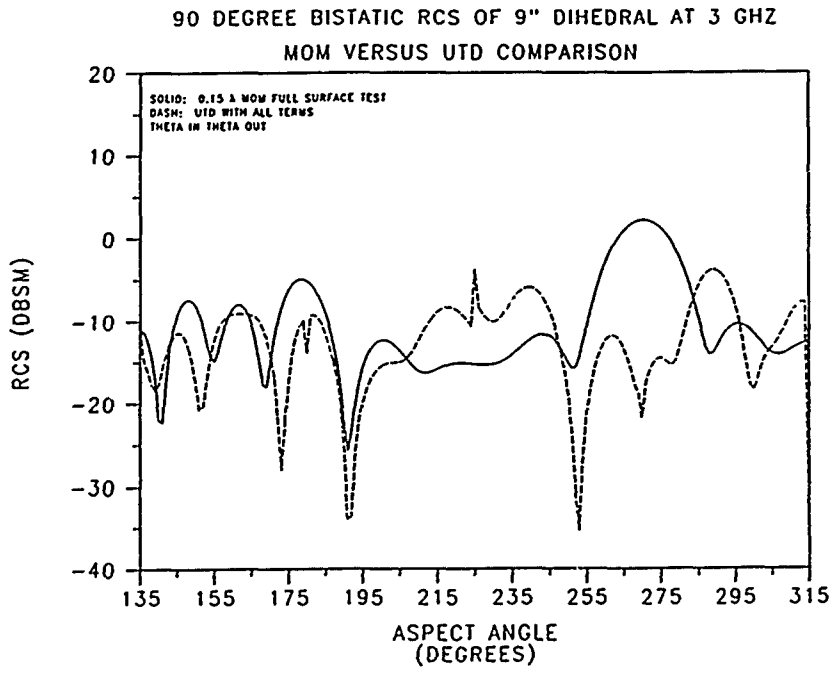

MONOSTATIC RCS OF 9" DIHEDRAL AT 2 GHZ
MOM VERSUS UTD COMPARISON
SOLID: 0.10 λ MOM FULL SURFACE TEST
DASH: UTD WITH ALL TERMS
THETA IN THETA OUT
RCS (DBSM)
ASPECT ANGLE
(DEGREES)

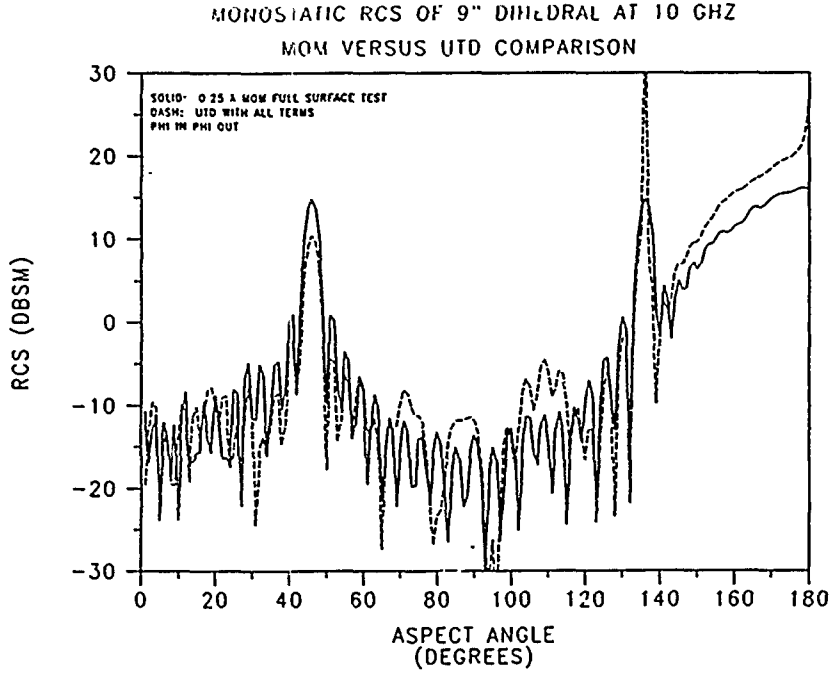

MONOSTATIC RCS OF 9" DIHEDRAL AT 3 GHZ
MOM VERSUS UTD COMPARISON
SOLID: 0.15 λ MOM FULL SURFACE TEST
DASH: UTD WITH ALL TERMS
THETA IN THETA OUT
RCS (DBSM)
ASPECT ANGLE
(DEGREES)

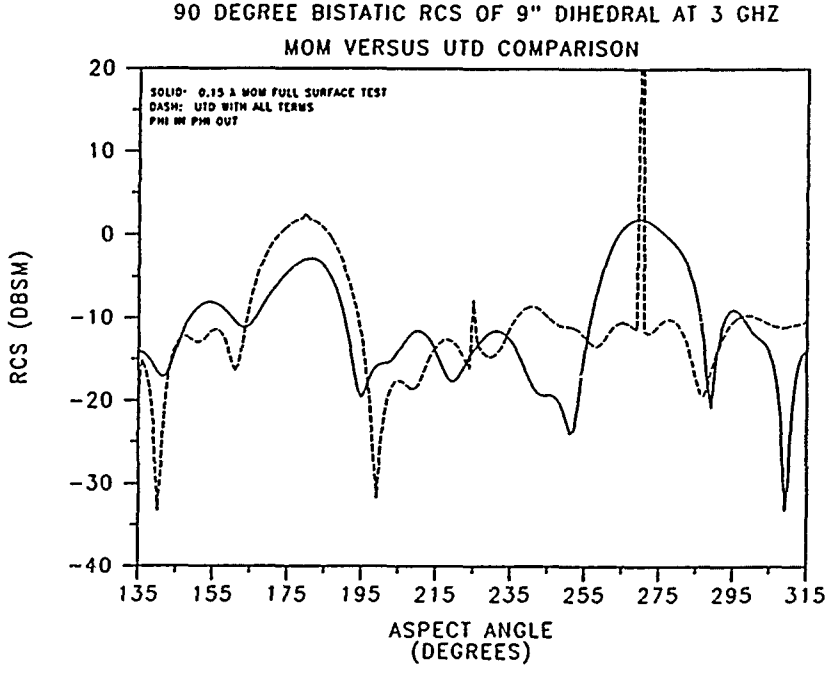

MONOSTATIC RCS OF 9" DIHEDRAL AT 2 GHZ
MOM VERSUS UTD COMPARISON
SOLID: 0.10 λ MOM FULL SURFACE TEST
DASH: UTD WITH ALL TERMS
PHI IN PHI OUT
RCS (DBSM)
ASPECT ANGLE
(DEGREES)

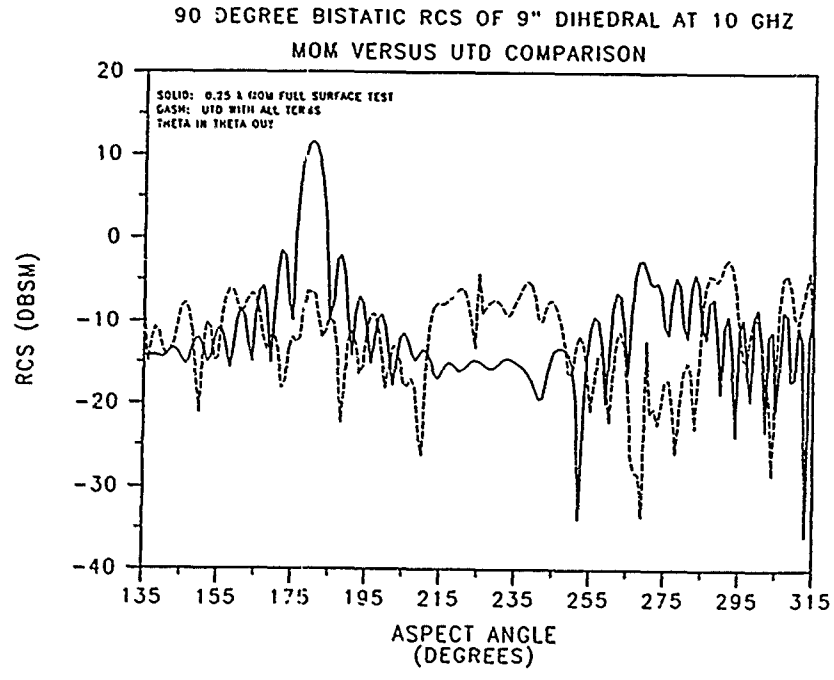

MONOSTATIC RCS OF 9" DIHEDRAL AT 3 GHZ
MOM VERSUS UTD COMPARISON
SOLID: 0.15 λ MOM FULL SURFACE TEST
DASH: UTD WITH ALL TERMS
PHI IN PHI OUT
RCS (DBSM)
ASPECT ANGLE
(DEGREES)

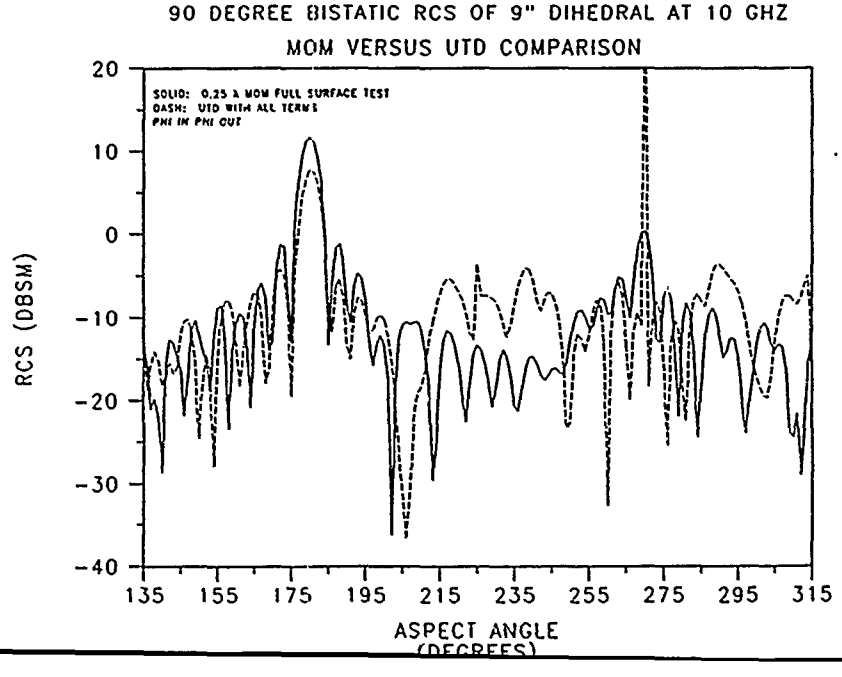

MONOSTATIC RCS OF 9" DIHEDRAL AT 10 GHZ
MOM VERSUS UTD COMPARISON
SOLID: 0.25 λ MOM FULL SURFACE TEST
DASH: UTD WITH ALL TERMS
THETA IN THETA OUT
RCS (DBSM)
ASPECT ANGLE
(DEGREES)


90 DEGREE BISTATIC RCS OF 9" DIHEDRAL AT 3 GHZ
MOM VERSUS UTD COMPARISON
SOLID: 0.15 λ MOM FULL SURFACE TEST
DASH: UTD WITH ALL TERMS
THETA IN THETA OUT
RCS (DBSM)
ASPECT ANGLE
(DEGREES)


MONOSTATIC RCS OF 9" DIHEDRAL AT 10 GHZ
MOM VERSUS UTD COMPARISON
SOLID: 0.25 λ MOM FULL SURFACE TEST
DASH: UTD WITH ALL TERMS
PHI IN PHI OUT
RCS (DBSM)
ASPECT ANGLE
(DEGREES)


90 DEGREE BISTATIC RCS OF 9" DIHEDRAL AT 3 GHZ
MOM VERSUS UTD COMPARISON
SOLID: 0.15 λ MOM FULL SURFACE TEST
DASH: UTD WITH ALL TERMS
PHI IN PHI OUT
RCS (DBSM)
ASPECT ANGLE
(DEGREES)





SUMMARY

Motivation - Future Radar

EM Models - UTD and MoM

Results for a Dihedral Corner Reflector - 2D UTD vs 3D MoM

QUANTUM-MECHANICAL TECHNIQUES FOR ELECTROMAGNETIC SCATTER MODELING BY SIMPLE, NON-CANONICAL SHAPES

D. E. Stein
6585th Test Group
Holloman Air Force Base, NM 88330

A. E. S. Green
Departments of Nuclear and Mechanical Engineering
University of Florida
Gainesville, FL 32611

Many scattering problems involve non-canonical geometries for which separation of coordinates in the wave equation is not possible. In this effort, a multipole-expanded potential is used to model such a geometry, which deviates from sphericity and which is prolate-spheroidal only to first order. While earlier similar efforts (Refs. 1,2) did not conclusively establish the validity of this technique for low energies or frequencies, the validity is now established by the significantly-improved fits with experimental data.

The current focus is on a quantum-mechanical problem, the electron scattering by the nitrogen molecule, for which the multipole-expanded potential enables a solut on to the scalar wave equation. The electrostatic potential which is expanded into multipoles is parametric, and its multipoles are analytic. Furthermore, this potential provides the basis for a parametric exchange potential. The "acid test" of the technique is its capability to model the low-energy resonance peak at 2.3ev.

However, a previous study (Ref. 3), in conjunction with current observations, shows that the electromagnetic scattering by a Mie sphere can be modeled by two quantum mechanical potentials -- both potentials being necessary for a full solution to the vector wave equation. Together, the results of the previous and current studies indicate that multipole-expanded potentials can be used to model the electromagnetic scattering, including low-frequency resonances, by simple but non-canonical shapes. (The multipole-expansion of the potentials rather than the shapes themselves makes semi-analytic phase shifts feasible via modified Born approximations.) The mathematical features of the coupled phase shifts associated with the multipole-expanded potentials are also discussed.

I. QUANTUM-MECHANICAL POTENTIAL MODELING OF MIE SCATTERING

The capability of quantum-mechanical potentials to model Mie scattering suggests that such potentials may also be used to model electromagnetic scattering by other simple shapes. This capability was largely established in a previous study,[3] in which a quantum-mechanical potential was identified for the homogeneous, isotropic, dielectric, nonpermeable, and nonabsorbing sphere of radius a. It was shown that the Mie phase shifts β_n, which correspond to the Mie coefficients b_n, are generated by a (normalized) attractive spherical-square well potential of depth

$$W_\beta = -k^2a^2(m^2-1) = -W \quad , \tag{1}$$

where $k=2\pi/\lambda$ is the wavenumber, λ is the incident wavelength, and m is the refractive index of the sphere relative to the surrounding medium. (In these same normalized units, the incident energy is k^2a^2, and the incident energy relative to the potential well depth is $K^2a^2=m^2k^2a^2$.) From this potential, the Born-approximation phase shifts were obtained for β_n. Inasmuch as the Born approximation is valid only for weak potentials and/or high incident energies (or frequencies), these phase shifts were modified so as to extend their range of validity. The modified phase shifts were found to be

$$\beta_n(W,x) = L_{n\beta}(W,x)\ S_{n\beta}(y) \tag{2a}$$

where

$$S_{n\beta}(y) = 1 - y\ [G_{n\beta}(y) + j_0(y)j_{-1}(y)] \tag{2b}$$

$$G_{n\beta}(y) = 2\ [j_n(y)j_{n-1}(y) + j_{n-1}(y)j_{n-2}(y) + \ldots + j_1(y)j_0(y)] \tag{2c}$$

$$y = mx = (x^2+W)^{1/2} \tag{2d}$$

$$x = ka \quad \text{is the size parameter} \tag{2e}$$

$j_n(y)$ is a spherical Bessel function of order n

$$L_{n\beta}(W,x) = \frac{W}{2}\left[x + \frac{WS_{n\beta}(0)}{2[\Lambda_{n\beta}(W)+1.5x]}\right]^{-1} \tag{2f}$$

$\Lambda_{n\beta}(W) = N_n\pi$ is the phase shift at zero incident energy or frequency, where N_n is an integer (2g)

(By Levinson's theorem,[4-7] N_n is also the number of "bound states" of the potential at zero incident energy, provided that the phase shift at infinite incident energy is taken as zero.) At "critical values" of the potential strength, N_n changes discontinuously by 1. For the Mie sphere, the square roots of these critical values are tabulated in the literature,[8] albeit under different terminology. Now, for intermediate and large size parameters ka (> 6), the phase shifts β_n obtained from this modified Born approximation agreed with the exact phase shifts over a large range of potential strengths W_β. The agreement was not as good for small but nonzero size parameters, because a suitable splining function had not been identified. Inasmuch as such splining functions have been found for other quantum-mechanical problems,[9] this is not believed to be a fundamental limitation. As expected, the incorporation of Levinson's theorem forced agreement for x=0.

In this previous study, ad hoc methods were used to obtain the Mie phase shifts α_n which correspond to the Mie coefficients a_n. Subsequently, however, the potential which generates these phase shifts has been identified.[10,11] In normalized form, it is given by

$$W_\alpha = -W + (3/4\varepsilon^2)(d\varepsilon/dp)^2 - (1/2\varepsilon)(d^2\varepsilon/dp^2) \tag{3}$$

where ε is the dielectric constant (and is equal to m^2 for a nonpermeable sphere), while p=r/a is a normalized radial coordinate. For the Mie sphere, the derivatives become

$$d\varepsilon/dp = (W/x^2)\ \delta(1-p) \tag{4a}$$

$$d^2\varepsilon/dp^2 = (W/x^2)\ \delta'(1-p) \tag{4b}$$

respectively. In a follow-on to the original study,[3] the modified Born phase shifts for α_n were obtained:

$$\alpha_n(W,x) = L_{n\alpha}(W,x)\ [S_{n\beta}(y) + G_{n\alpha}(y)] \tag{5a}$$

where

$$G_{n\alpha}(y) = 2yj_n(y)j_n'(y) \tag{5b}$$

$$L_{n\alpha}(W,x) = \frac{W}{2}\left(x + \frac{W[S_{n\beta}(0)+G_{n\alpha}(0)]}{2[\Lambda_{n\alpha}(W)+1.5x]}\right)^{-1} \tag{5c}$$

As for the phase shifts β_n, the square roots of the critical values for

the phase shifts α_n are tabulated in the literature.[8] Furthermore, the modified Born phase shifts α_n agree with the corresponding true Mie phase shifts for size parameters $x > 6$ (and for $x=0$, as forced).

It is noted that the large-ka limit of Eqs. 2 and 5 provides a simple but powerful approximation:

$$\beta_n \rightarrow (W/2x)\ [1 - (-1)^n y^{-1} \sin y \cos y] \qquad (6a)$$

$$\alpha_n \rightarrow (W/2x)\ [1 + (-1)^n y^{-1} \sin y \cos y]\ . \qquad (6b)$$

The agreement between the true Mie phase shifts and those obtained from Eqs. 2 and 5 (for $ka > 6$) further demonstrates the viability of potential-well analysis for electromagnetic scattering. It is observed, however, that there are a few subtle differences between quantum-mechanical and electromagnetic scattering. First, in Mie theory, it is the refractive index m which remains constant while the potential strength changes with energy or frequency. Secondly, there is no phase shift α_0 or β_0 in Mie theory, and the interpretation of partial waves is less straightforward for Mie theory than for quantum mechanics.[3] Third, the angular functions in Mie theory are $\tau_n(\theta)$ and $\pi_n(\theta)$, while in quantum mechanics (at least for many situations) they are the Legendre polynomials $P_n(\theta)$. Finally, there is a trivial phase difference between the Mie coefficients and those for the spherical square well, as plotted on an Argand or related diagram.[3] None of these subtle differences are limiting factors.

While the electromagnetic scattering by a Mie sphere can be modeled by two quantum-mechanical potentials, little practical benefit would be realized if such modeling were not possible for other shapes. The next section discusses a multipole-expansion technique for modeling a non-spherical potential which does not correspond exactly with any other canonical shape. While the technique is demonstrated for a true quantum-mechanical potential (which arises from electromagnetic forces), preliminary results indicate that the technique may also be applied to the potentials used to model electromagnetic scattering.

II. THE MULTIPOLE-EXPANDED MOLECULAR INDEPENDENT PARTICLE MODEL (IPM) POTENTIAL AND EARLY RESULTS

It now remains to demonstrate that a multipole-expanded potential

can provide a simplistic (preferably, analytic) model for a geometry which deviates from a canonical shape. An example of such a geometry is a homonuclear, diatomic molecule such as N_2, the potential for which is neither spherical nor prolate-spheroidal in the strict sense. An independent particle model (IPM), specifically the Green-Sellin-Zachor potential, provides the basis for such a simplistic model for the scattering of electrons by N_2. The success of the IPM has already been demonstrated for the elastic scattering of electrons by atoms,[12-14] the electron-impact excitations of atoms,[15-18] and the study of bound states of N_2.[19] The techniques are demonstrated for an ensemble of randomly-oriented molecules with multiple scattering effects assumed to be negligible. However, certain orientation-averaging operations can be skipped for the case of the oriented molecule or other particle.

In a previous study,[1] moderate success was realized in applying an energy-independent, phenomenological IPM to N_2 in the fixed-nuclei approximation. The electron-molecule IPM used was

$$V(\vec{r}) = U(r,u) + V_q(r,u) + V_p(r,u) \tag{7}$$

where $u=\cos\theta$, θ is the angle defined by $\vec{r}$ and the symmetry axis of the molecule, r is the radial distance from the molecular center, $U(r,u)$ is the sum of the electron-atom IPM potentials, $V_q(r,u)$ is a quadrupole-interaction potential (which is dominant at large r), and $V_p(r,u)$ is the polarization potential. (It is noted that for scattering of electromagnetic radiation by a dielectric particle, the quadrupole and polarization potentials do not appear. Their presence in the current situation does not invalidate the conclusions.) The quadrupole and polarization potentials used were respectively

$$V_q(r,u) = -(Q/r^3)\, P_2(u)\, \Gamma(r,R_c) \tag{8}$$

$$V_p(r,u) = -(1/2r^4)\, [A_0 + A_2 P_2(u)]\, \Gamma(r,R_c) \tag{9}$$

where

$$\Gamma(r,R_c) = 1 - \exp[-(r/R_c)^6] \tag{10}$$

is a cutoff factor of the form used by Lane and Geltman[20] as well as by Burke and Chandra,[21] while $P_2(u)$ is a Legendre polynomial. The sum of the electron-atom IPM potentials was modeled by

$$U(r,u) = -(2Z)\left[\frac{1-e^{-sr_+}}{r_+}\,\Omega(r_+) + \frac{1-e^{-sr_-}}{r_-}\,\Omega(r_-)\right] \qquad (11)$$

where Z is the atomic charge, 2f is the internuclear equilibrium distance (and f is the semifocal distance in prolate spheroidal coordinates), r_+ and r_- are the radial distances from the two atoms,

$$r_\pm = (f^2+r^2\pm 2fru)^{\frac{1}{2}} \quad , \qquad (12)$$

$\Omega(r_\pm)$ is the Green-Sellin-Zachor (GSZ) screening factor,[12]

$$\Omega(r_\pm) = [H(e^{r/d}-1)+1]^{-1} \quad , \qquad (13)$$

and s is a regulator which removes the singularities in U(r,u) at u=±1, r=f. It is noted that to first order, the diatomic molecular potential is prolate-spheroidal.[19,22] Nonetheless, the calculations were performed in spherical coordinates by expanding the potential $V(\vec{r})$ of Eq. 7 into multipoles:

$$V(\vec{r}) = (\hbar^2/2m_e) \sum_\lambda{}' v_\lambda(r)\, P_\lambda(u) \qquad (14)$$

where m_e is the electron mass and $\hbar$ is Planck's constant reduced by 2π. For homonuclear, diatomic molecules, only the even multipoles contribute, and this is denoted by the primed summation sign. With a proper choice of parameters H and d, the calculated values for both the total cross section σ_t and the differential cross section $d\sigma(\theta_L)/d\Omega$ agreed moderately well with experimental data for energies between 10ev and 500ev. (θ_L is the bistatic scattering angle in laboratory coordinates.) However, agreement was not obtained for energies below 5ev. The minima in $d\sigma(\theta_L)/d\Omega$ were too deep, and for extremely low energies, they occurred at the wrong angles. Moreover, the shape resonance in σ_t at 2.3ev was not reproduced. (The broad peak at 3ev and the secondary peak at 15ev were then believed to be the cumulative effects of several partial waves.) It was believed that a different choice of H and d might have produced better fits at low energies, but if such fits were obtained at the expense of fits at higher energies, then an energy-dependence of the parameters H and d would be suggested.

Such an energy dependence was later attempted and resulted in improved fits.[2] It was also observed that no improvement in fitting data

was obtained by adding an imaginary potential to incorporate inelastic effects. In addition, equivalent results were obtained with a spherical model (f=0) with a somewhat different set of parameters, in this same study. Therefore, the results suggest that shape effects may be less important at low energy. Still, however, the greatest discrepancies occurred at the low energies.

Although success in fitting low-energy scattering data with a multipole-expanded IPM was not realized in these earlier efforts, other theoretical models have been more successful,[23-26] thereby providing the motivation for the current effort.

III. THE MULTIPOLE EXPANSION OF THE ORIGINAL GREEN-SELLIN-ZACHOR MOLECULAR POTENTIAL

The GSZ molecular potential, as given by Eq. 11, is really a quadruple Yukawa potential. To demonstrate this, it is necessary to define

$$\tilde{U}(r_{\pm}) = -(2Z)\frac{1-e^{-sr_{\pm}}}{r_{\pm}}\,\Omega(r_{\pm}) \tag{15}$$

such that $U(r,u) = \tilde{U}(r_+) + \tilde{U}(r_-)$. Now, $\tilde{U}(r_{\pm})$ can be approximated as a double-Yukawa potential.[2] Then, the factor $1-e^{-sr_{\pm}}$ converts each of these two Yukawa potentials into a double-Yukawa potential. Thus,

$$\tilde{U}(r_{\pm}) = -(2Z)\left\{\frac{1}{H}\,\frac{e^{-r_{\pm}/D_1}-e^{-r_{\pm}/D_2}}{r_{\pm}} + \left(1-\frac{1}{H}\right)\frac{e^{-r_{\pm}/D_3}-e^{-r_{\pm}/D_4}}{r_{\pm}}\right\} \tag{16a}$$

where the "range" parameters are

$$D_1 = d \tag{16b}$$

$$D_2 = (s+d^{-1})^{-1} \tag{16c}$$

$$D_3 = d/(H+1) \tag{16d}$$

$$D_4 = [s+d^{-1}(H+1)]^{-1} \tag{16e}$$

The quadruple-Yukawa nature of this potential suggests a partial redundancy between H and s. Some calculations performed in this effort suggest another partial redundancy, between H and d. These calculations further suggest that H can be set equal to one, in which case the screening

about each nucleus becomes pure exponential. (If this is done, then smaller and seemingly-nonphysical values of d are needed to compensate.) Nonetheless, the primary effect of s on the potential strength is near each nucleus, while the primary effect of H is at larger ranges. Retention of all parameters is expedient and provides more degrees of freedom to adjust the radial shape of the two atomic IPM potentials.

It is observed that the original GSZ potential is the sum of four Yukawa potentials, each of the form

$$U_i^A(r,u) = -(2Z)\left(\frac{1}{r_+}e^{-r_+/D_i} + \frac{1}{r_-}e^{-r_-/D_i}\right) \tag{17}$$

Now, let $w_\lambda(r)$ denote that part of $v_\lambda(r)$ which is due to U(r,u). (In other words, $w_\lambda(r)$ excludes the quadrupole and polarization effects as given by Eqs. 8-10. For $\lambda \geq 2$, $v_\lambda(r) = w_\lambda(r)$, since the quadrupole and polarization potentials used herein have no multipoles higher than λ=2.) Then, the multipoles are

$$w_\lambda(r) = H^{-1}\,[M^A_{\lambda 1}(r) - M^A_{\lambda 2}(r)] + (1-H^{-1})\,[M^A_{\lambda 3}(r) - M^A_{\lambda 4}(r)] \tag{18}$$

where

$$M^A_{\lambda i}(r) = 2Z(2\lambda+1)(2D_i^{-1})\; h_\lambda(ip_{>i})\; j_\lambda(ip_{<i}) \quad , \tag{19}$$

$h_\lambda(ip_{>i})$ is a spherical Hankel function, $j_\lambda(ip_{<i})$ is a spherical Bessel function, $p_{>i} = D_i^{-1}\max(r,f)$, and $p_{<i} = D_i^{-1}\min(r,f)$.

It is noted that although the retention of parameter s has been justified herein, s is no longer necessary as a mathematical convenience. This is because $w_\lambda(r)$ is obtained analytically in the current effort. In the original study,[1] the multipoles were obtained numerically, and s was necessary to prevent numerical problems near the nuclei in the integrals $\int_{-1}^{1} U(r,u)\; P_\lambda(u)\cdot du$.

As further discussed in Section V, the effect of the multipoles is to couple adjacent even or odd partial waves. For plausible values of the internuclear separation 2f and of the other parameters, the dominant multipole near r=f is $v_2(r)$, as illustrated in Fig. 1 of the original study.[1] This indicates that the coupling of adjacent even or odd partial

waves is strong, and that multipole $v_2(r)$ represents the first-order effects of distortion from sphericity. For sufficiently large r, the dominant IPM multipole is $w_0(r)$, but the quadrupole and polarization potentials can override this dominance, again giving rise to coupled partial waves.

Section V discusses the calculation of cross sections for multipole-expanded potentials. First, however, the modified GSZ molecular potential -- and its multipoles -- must be examined.

IV. THE MULTIPOLE EXPANSION OF THE MODIFIED GREEN-SELLIN-ZACHOR MOLECULAR POTENTIAL

As attempts were made to improve the cross section fits of the original study,[1] the inclusion of exchange effects became necessary. The original model produced two peaks, at 3ev and at 15ev, in the calculations of σ_t versus incident energy. These calculated peaks were believed to correspond to the peaks in the experimental data, at 2.3ev and at 15ev respectively. It was believed that a better choice of parameters would cause the respective peaks to correspond in height, width, and energy-position. However, in the current effort, it was discovered that the calculated peak at 3ev is due to a p-wave. The 2.3ev peak, on the other hand, is known to be a d-wave resonance.[27]

Furthermore, Gingquan et. al.[28] pointed out that exchange effects would be more significant for lower-energy electrons, which spend more time near the target atom. Morrison-Collins[26] used an exchange potential in their study, and they noted that exchange involves primarily the outermost molecular orbitals and the low-l partial waves. Their study, as well as that by Hara[29] for $e^- - H_2$ scattering at low energies, used exchange potentials based on the free-electron gas (FEG) approximation.

The FEG facilitates the inclusion of exchange effects, which are formidable to model explicitly. The exchange potential, in Rydbergs, is given by

$$V_x(\vec{r}) = -(4/\pi)\, k_F\, F(h) \qquad (20a)$$

where

$$F(h) = \frac{1}{2} + \frac{1-h^2}{4h} \ln \left|\frac{1+h}{1-h}\right| \tag{20b}$$

$$h = k/k_F \tag{20c}$$

$$k_F^3 = 3\pi^2 \rho_{\#}(r) \tag{20d}$$

$$k = (E + I + k_F^2)^{\frac{1}{2}} \quad , \tag{20e}$$

$\rho_{\#}(r)$ is the electron number density, k_F is the Fermi momentum, E is the incident energy, and I is the ionization potential. (Eq. 20e is obtained from the Morrison-Collins study.[26] In some applications, k is the wavenumber corresponding to E only.) The exchange potential varies from $-4k_F/\pi$ in the zero-energy limit to zero in the high-energy limit. If the electron number density $\rho_{\#}(r)$ can be modeled analytically, then an analytic exchange potential $V_x(\vec{r})$ is possible.

Application of Poisson's equation,

$$\rho_{\#}(r) = -(4\pi)^{-1} \nabla^2 U(r,u) \tag{21}$$

yields $\rho_{\#}(r)$ in terms of the IPM potential U(r,u). (The electronic charge factor e^2 is already divided out of the IPM potential. Moreover, U(r,u) represents the total potential, from which the potential due to the two nuclei must be subtracted. However, the nuclear contribution to $\rho_{\#}(r)$ is only a delta-function at each nucleus.)

Inasmuch as U(r,u) is expanded into multipoles, such an expansion of the charge density -- and hence the exchange potential -- would also be expected. It is desirable to use a form of U(r,u) which would provide a near-spherical charge density. Otherwise, as will become apparent, the exchange potential would require the retention of many more multipoles than would the static potential U(r,u) itself. It is noted that the exchange contribution to the Morrison-Collins "static-exchange" potential was insignificant even for the λ=2 multipole.

An IPM potential which provides a nearly-spherical exchange potential is of the Yukawa+exponential form. To each Yukawa term, an exponential term is now added:

$$\frac{e^{-r_\pm/D_i}}{r_\pm} \quad \rightarrow \quad e^{-r_\pm/D_i} \left(\frac{1}{r_\pm} + \frac{1}{2D_i}\right) \tag{22}$$

(This is identical in form with the time-averaged potential of a neutral hydrogen atom as given by Jackson.[30]) No new parameters are introduced when the exponential term is added. Now, in the fashion of Eq. 17, let

$$U_i^B(r,u) = (2D_i)^{-1} [e^{-r_+/D_i} + e^{-r_-/D_i}] \tag{23}$$

Then,

$$\begin{aligned} \rho_{\#}(r) &= -(4\pi)^{-1} \nabla^2 [U_i^A(r,u) + U_i^B(r,u)] \\ &= -(4\pi D_i^2)^{-1} U_i^B(r,u) \end{aligned} \tag{24}$$

Thus, while the static potential U(r,u) is Yukawa+exponential, the charge density is exponential only. The consequences of this become apparent after the potential multipoles $v_\lambda(r)$ are obtained. The multipoles corresponding to the exponential part of the potential are

$$\begin{aligned} M_{\lambda i}^B(r) = & -(1/2) M_{\lambda i}^A(r) \\ & -(2Z)(2\lambda+1) D_i^{-1} [p_{>i} h_\lambda'(ip_{>i}) j_\lambda(ip_{<i}) \\ & + p_{<i} h_\lambda(ip_{>i}) j_\lambda'(ip_{<i})] \quad . \end{aligned} \tag{25}$$

Eq. 18 still gives the multipoles $w_\lambda(r)$ if the substitution

$$M_{\lambda i}^A(r) \rightarrow M_{\lambda i}^A(r) + M_{\lambda i}^B(r) \tag{26}$$

is made. It is observed that the multipoles are analytic.

Figs. 1-3 are typical plots of $w_\lambda(r)$ for $\lambda = 0$, 2, and 4, for various internuclear separations 2f. These plots illustrate certain properties of the potential multipoles. First, in the limit $2f \rightarrow 0$, (the "united-atom approximation"), $w_\lambda(r) \rightarrow 0$ for $\lambda \geq 2$, as expected. Secondly, in the limit $2f \rightarrow \infty$ (the "separated-atom approximation"), the higher multipoles become more significant. Finally, for any nonzero f, $w_\lambda(r)$ has a maximum at r=f for $\lambda \geq 2$. These properties apply for each $M_{\lambda i}^A$ and $M_{\lambda i}^B$ individually.

Fig. 4 is a typical plot of $w_0(r)$, $w_2(r)$, $v_0(r)$, and $v_2(r)$. The small differences between $v_0(r)$ and $w_0(r)$, and between $v_2(r)$ and $w_2(r)$, suggest that the effects of the quadrupole and polarization potentials are negligible, especially for small r. On a semi-logarithmic plot, such as that in Fig. 1 of the original study,[1] however, the differences

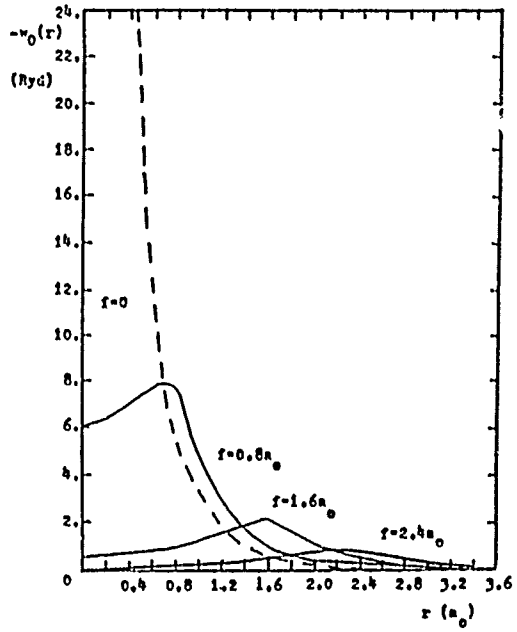


Fig. 1. Typical IPM multipoles $w_0(r)$ versus r for various hypothetical internuclear separations 2f. The three cases $f=0.8a_o$, $1.6a_o$, and $2.4a_o$ are shown. Also shown is the f=0, or spherically-symmetric case (dotted line).

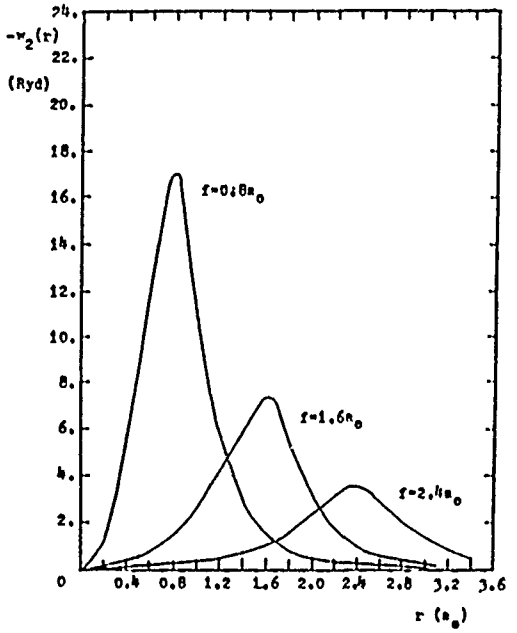


Fig. 2. Typical IPM multipoles $w_2(r)$ versus r for various hypothetical internuclear separations 2f. The three cases $f=0.8a_o$, $1.6a_o$, and $2.4a_o$, corresponding to the cases of Fig. 1, are shown.

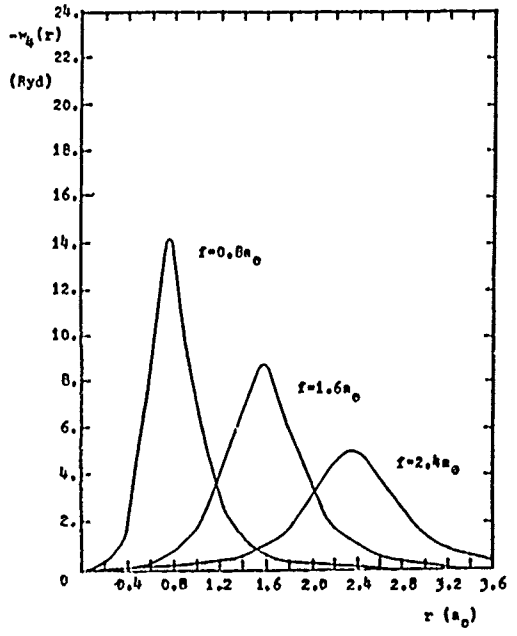


Fig. 3. Typical IPM multipoles $w_4(r)$ versus r for various hypothetical internuclear separations 2f. The three cases $f=0.8a_o$, $1.6a_o$, and $2.4a_o$, corresponding to the cases of Fig. 1 and 2, are shown.

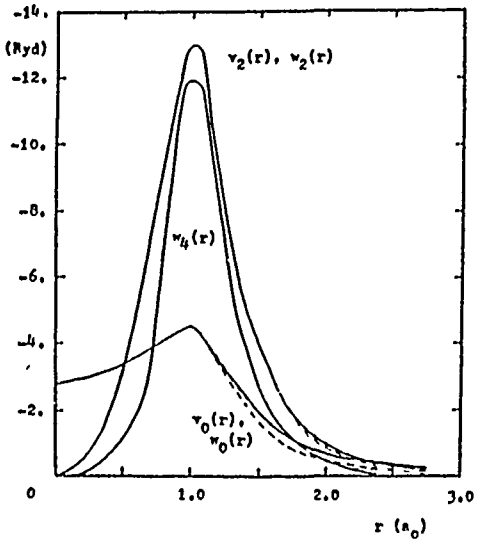


Fig. 4 IPM multipoles $v_0(r)$, $v_2(r)$, and $v_4(r)$ versus r, for the original (Ref. 1) model of [illegible] shown for comparison are $w_0(r)$ and [illegible] r (dotted lines). The potential [illegible] ate Z=7, d=0.5a_o, H=1.139, s=7.0, 2f=[illegible]a_o, Q=-1.13ea_o^3, A_0=11.9a_o^2, A_2=3.13a_o^2, and R_c=2.0a_o.

are more apparent. The primary effect of the quadrupole and polarization potentials is to extend the range of $v_0(r)$ and $v_2(r)$. This extended range would be most significant for low-energy electrons, which spend more time near the target atoms as Gingquan et. al. indicated.[28] Blaha and Davis,[31] in their study of atomic nitrogen and oxygen, found that inclusion of a polarization potential was necessary to achieve accuracy for energies below 10ev. It is observed that the quadrupole potential can cause a sign reversal in $v_2(r)$ at sufficiently large r (in the original study,[1] at around $r=3.6a_o$).

In light of the foregoing discussion, it is not surprising that the second study[2] did not produce substantially better agreement with experimental data at low energies. In that study, the partial wave responsible for the 2.3ev resonance peak had not been identified. Furthermore, the potential strength parameters increased with increasing energy -- in contrast with the behavior characteristic of an exchange potential.

V. CROSS SECTION CALCULATIONS FOR MULTIPOLE-EXPANDED POTENTIALS

The physical quantities of interest, averaged over all orientations, are given by[1]

$$\sigma_t = (4\pi/k^2) \sum_{\ell\ell' m} |C^m_{\ell\ell'}|^2 \tag{27}$$

$$d\sigma(\theta_L)/d\Omega = (4\pi/k^2) \sum_{Lm'} (2L+1)^{-1} |F^{m'}_L(\theta_L)|^2 \tag{28}$$

where $F^{m'}_L(\theta_L)$ is the orientation-averaged scattering amplitude and $C^m_{\ell\ell'}$ are the scattering coefficients. They are given respectively by

$$F^{m'}_L(\theta_L) = \sum_{\ell\ell' m} i^{\ell-\ell'}(2\ell+1)(-1)^m C^m_{\ell\ell'} X^{m'}_{\ell'}(\theta_L) \tag{29}$$
$$\langle \ell,0,\ell',-m' | L,-m' \rangle \langle \ell,m,\ell',-m | L,0 \rangle$$

$$X^{m'}_{\ell'}(\theta_L) = \left[\frac{(2\ell'+1)\ (\ell'-|m'|)!}{4\pi\ \ (\ell'+|m'|)!}\right]^{1/2} P^{|m'|}_{\ell'}(u)\ \varepsilon_{m'} \tag{30}$$

$$\varepsilon_{m'} = \begin{cases} (-1)^{m'} & m' \geq 0 \\ 1 & m' < 0 \end{cases} \tag{31}$$

$$C^m_{\ell\ell'} = -(D^m_{\ell\ell'}+iI)^{-1} \cdot -\{(D^m_{\ell\ell'})^2+I\}^{-1}(D^m_{\ell\ell'}-iI) \quad (32a)$$

$$D^m_{\ell\ell'} = B^m_{\ell\ell'}(A^m_{\ell\ell'})^{-1} \quad (32b)$$

$$A^m_{\ell\ell'} = Y^m_{\ell\ell'}(Kr)\psi'_\ell(kr) - (Y^m_{\ell\ell'}(Kr))'\psi_\ell(kr) \quad (32c)$$

$$B^m_{\ell\ell'} = Y^m_{\ell\ell'}(Kr)\chi'_\ell(kr) - (Y^m_{\ell\ell'}(Kr))'\chi_\ell(kr) \quad (32d)$$

where $\psi_\ell(kr)$ and $\chi_\ell(kr)$ are respectively the Riccati-Bessel and -Neumann functions and I is the identity matrix. The $Y^m_{\ell\ell'}(Kr)$ are the ℓ' linearly-independent solutions of the Schrodinger equation,

$$\{d^2/dr^2 - \ell(\ell+1)/r^2 + K^2 - v_0(r)\}\, u^m_\ell(Kr) \quad (33)$$

$$= \sum_{\ell''} \sum_{\lambda\geq 2}{}' (-1)^{\ell+\ell''} v_\lambda(r)\, u^m_{\ell''}(Kr)$$

$$\langle \ell,0,\lambda,0|\ell'',0\rangle \langle \ell'',m,\lambda,0|\ell,m\rangle \ ,$$

and K=K(r) and k are respectively the internal and external wavenumbers. The quantities of the form $\langle \ell_1,m_1,\ell_2,m_2|\ell_3,m_3\rangle$ are the well-known Clebsch-Gordon coefficients. The $u^m_\ell(Kr)$ are linear combinations of the $Y^m_{\ell\ell'}(Kr)$ which are chosen to satisfy the asymptotic boundary conditions. Eqs. 32 incorporate this boundary-condition matching.

The effect of the multipole terms $v_\lambda(r)$, $\lambda \geq 2$ is to couple all even-ℓ waves together and all odd-ℓ waves together, while simultaneously lifting the degeneracy in m. The scattering coefficients $C^m_{\ell\ell'}$ represent this coupling. Each of these coefficients has an associated phase shift (as discussed in the Appendix), and these are likewise coupled. Mixing in m is avoided by performing the calculations in the body-coordinate system and transforming via rotation matrices into the laboratory coordinate system. For the spherically-symmetric case, the matrices C^m, D^m, A^m, and B^m -- and other associated matrices (discussed in the Appendix) become diagonal. In addition, the summation over m in Eq. 27 reduces to the familiar factor $2\ell+1$ for the spherically-symmetric case.

In the current study, it was observed that

$$\sum_{\ell\ell' m} |C^m_{\ell\ell'}|^2 = \sum_{\ell m} C^m_{I,\ell\ell} \quad (34)$$

where subscripts R and I denote the real and imaginary parts respectively. Then Eq. 27 may be re-expressed

$$\sigma_t = (4\pi/k^2) \sum_{\ell m} C^m_{I,\ell\ell} \tag{35}$$

This "diagonal theorem" is further discussed in the Appendix.

A more comprehensive discussion of the mathematical formalism (Eqs. 27-33) is found in the literature.[32-34]

VI. SHAPE EFFECTS AND MULTIPOLE-SERIES TRUNCATION

The number of multipoles which must be retained in the expansion (Eq. 14) is determined by the shape effects of the potential for the range of energies considered. First, the aforementioned Ganas-Green study[2] indicated that shape effects may be inconsequential at low energies. This may be even more true with the addition of an exchange potential, which is essentially spherical[26] and which therefore strengthens $w_0(r)$ relative to the other multipoles. Secondly, the deBroglie wavelength for the electron is larger at low energies. For the extremely low energies considered herein (0.01 Ryd), this wavelength is large relative to the dimensions of U(r,u), and smaller effects of shape would be expected than for higher energies. For the higher (but still low) energies considered herein (3.0 Ryd), the deBroglie wavelength is much smaller.

Third, the equipotential surfaces should be examined. For extremely large r, the equipotential surfaces for U(r,u) are almost spherical. For somewhat smaller r, they are prolate-spheroidal, to first order. For extremely small r, they become hourglass-shaped and eventually split into two sets of concentric quasi-spheres, one set about each nucleus. Therefore, fewer multipoles should be needed for large r; more should be needed at smaller r. Now, a low-energy electron does not penetrate in as far as a higher-energy electron before it is "reflected" by the centrifugal barrier (for partial waves other than the s-wave). This further suggests that fewer multipoles are needed for low-energy scattering.

Next, analysis of the first, second, and higher-order effects of distortion (from sphericity) indicates that $w_2(r)$ incorporates the first-

order effects, $w_4(r)$ incorporates the second-order effects, and so on. This corroborates the conclusion drawn from the relative magnitudes of the $w_\lambda(r)$ as discussed in Section III. Multipole $w_0(r)$ is also affected by higher-order effects.

It is also observed that the Yukawa-potential singularities at the nuclei (r=f, u=±1) normally require the retention of several multipole terms. Each multipole term $M^A_{\lambda i}$ is finite, and omission of the higher multipoles can lead to errors in the total potential strength near the two nuclei. This error is less if the total IPM potential U(r,u) includes an exponential part in addition to the Yukawa part. An exponential potential is less vulnerable to this type of error.

VII. RESULTS AND CONCLUSIONS

The computer code used in the original study[1] was modified to calculate the Yukawa+exponential and exchange potential multipoles, all analytically rather than numerically. Then, the code was used to obtain the cross sections for energies between 0.01 Ryd and 3.15 Ryd, in approximately even increments on a logarithmic scale. The solution involves a Runge-Kutta integration of Eq. 33, which is actually a set of coupled equations. Parameter adjustment was implemented manually.

The calculated data were compared with the Porter-Jump data prepared for the Goddard Space Flight Center.[35] The Porter-Jump data are actually averages of experimental data from several sources and include only the "gross features" of the σ_t versus energy behavior. These gross features, as plotted in Fig. 5, include the 2.3ev peak (approximately 0.17 Ryd) and the broader secondary peak at approximately 15ev. They do not include the "fine structure" which is known to exist on the 2.3ev peak. This fine structure consists of four extremely narrow peaks superimposed on the already narrow shape resonance peak at 2.3ev.[27] This fine structure is due to pseudovibrations of the $^2\Pi_g$ compound state N_2^-, which is extremely short-lived.[27] Inasmuch as the current IPM potential does not incorporate inelastic effects, it is precisely the gross features of the experimental data which the IPM attempts to reproduce.

The current IPM potential does in fact reproduce the 2.3ev resonance

peak if reasonable values for the potential parameters are selected. Fig. 5 illustrates the results obtained from one such set and with a three-term multipole expansion (λ = 0, 2, and 4). This truncation is justified by the successful reproduction of the peak position (in energy), the sensitivity of the peak position to shape effects (indicated both empirically and by perturbation theory), and the discussion in Section VI. The parameter values are indicated in Fig. 5. The value of d may appear unreasonable, but it compensates for H=1.0. An almost identical curve was obtained with $d=0.400a_o$ and H=1.139. The C-matrix phase shift tabular data were examined to verify that the calculated peak is in fact a d-wave resonance. The sharp peak occurs in the partial cross section $\sigma_{1m}=\sigma_{21}$, and this peak corresponds to the $3d\pi$ state in the united-atom notation.[36] The lack of complete agreement between experimental and calculated data on either side of the peak is believed to be a consequence of non-optimal choices of parameters.

The fact that the calculated peak is too high, on the other hand, is a consequence of non-inclusion of inelastic effects in the current model. These inelastic processes include vibrational excitation, rotational excitation, core excitation, and spin-axis coupling. The current IPM potential was never intended to incorporate these effects.

It is possible that different values of d, s, or H for each Rydberg series would improve the model. In the case of d and H, this was done in a previous study of bound states for homonuclear diatomic molecules.[22]

Another possible improvement would be in the polarization potential, for which alternate forms exist.[25,28,37,38] A common form for the spherically-symmetric case is[28,37]

$$V_p(r) = -\frac{A_0}{2(R_c^2+r^2)^2} \tag{36}$$

These alternate forms differ primarily at smaller r. However, the differences may be inconsequential for sufficiently low energies, at which the primary effects of the polarization potential occur.[28,31]

The present results establish two points. First, a parametric IPM potential of Green-Sellin-Zachor form can model the e^--N_2 scattering

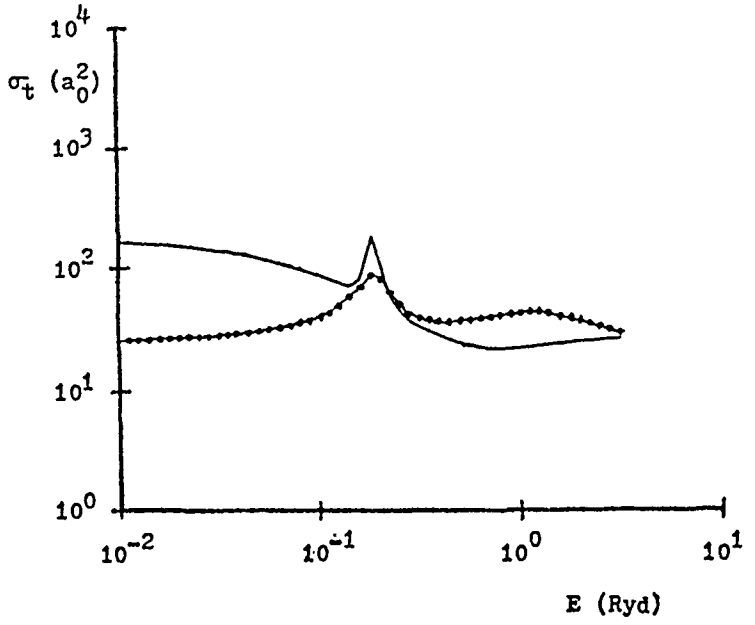


Fig. 5. Matching of the experimentally-determined 2.3ev resonance peak (•-•-•-•) by the modified IPM potential (————). The potential parameters are Z=7, s=7.0, d=0.375a_o, H=1.0, 2f=2.068a_o, R_c=2.3a_o, Q=-1.13ea_o^2, A_0=11.74a_o^3, A_2=3.13a_o^3, and I=1.146Ryd. (Some of these "parameters" are known values, particularly Z, I, and 2f. Setting H=1.0 effectively removes H as a parameter.) The experimental data are the Porter-Jump data,[35] which include only the gross features of the cross-section versus energy behavior.

at lower energies than previously thought possible,[1,2] provided that the IPM potential is modified to include an exponential component, which in turn completes the basis for the exchange potential. (The phenomenological quadrupole and polarization potentials must also be retained.) Secondly, the multipole-expansion technique, as applied to this modified IPM potential, is valid at low energies. Furthermore, for lower energies (and a given internuclear separation), fewer multipoles are necessary in the expansion. Any errors arising from the omission of higher

order multipoles are believed to be errors in the total effective potential strength, especially near the nuclei. If this is the case, then the IPM potential parameters can absorb these errors.

It is anticipated that the multipole expansion technique can also be applied to electromagnetic scattering by dielectric spheroids or similar nonspherical but simple shapes. In electromagnetic scattering, there are no "add-on" potentials (exchange, quadrupole, and polarization) as such, but there are two scalar potentials. For a dielectric but nonpermeable object, one of these potentials has a "well" part and a "boundary" part, while the other potential has a "well" part only. The conclusions regarding shape effects at low energies may be even more valid for electromagnetic scattering than for quantum-mechanical scattering, since as the energy (or frequency) approaches zero (as in the Rayleigh region), the "well" potentials approach zero. Only the "boundary" potential remains. Multipole expansion of the two potentials would be an attractive technique to model low-frequency electromagnetic scattering, if few multipoles were needed.

Nonetheless, there remains a complication. Because of the curl operator in the vector wave equation,[39] the relation between the true phase shifts and those obtained from the two potentials may not be as straightforward as for the Mie sphere. This relation is being examined.

The use of Clebsch-Gordon coefficients for orientation-averaging is also promising. Such orientation-averaging would be useful for modeling the scattering by an ensemble of particles such as aerosols. However, the orientation-averaging is more complicated for electromagnetic scattering, inasmuch as the orientation relative to two directions (propagation and polarization) must be specified. This procedure is also being examined.

It is emphasized that this study does not represent the first use of multipole-expanded potentials in e^{-}-N_2 scatter modeling.[25,26] Nor does it represent the first attempt to solve electromagnetic scattering problems by multipole-expansion of the particle shape.[40,41] From a computational electromagnetics standpoint, however, the feasibility of certain techniques is established: modeling of electromagnetic scattering

by two quantum-mechanical potentials, expansion of these potentials into analytic multipoles, and semi-analytic phase shifts for the two potentials via modified Born approximations. It is believed that these techniques may be used simultaneously to model electromagnetic scattering by simple, non-canonical shapes. In addition, the feasibility of modeling low-energy resonances in e^{-}-N_2 scattering with a (parametric) Green-Sellin-Zachor potential -- together with a parametric exponential potential and with analytic multipoles -- is demonstrated.

APPENDIX. THE MATHEMATICS OF COUPLED PHASE SHIFTS

The phase shifts are best understood in terms of the C-matrix, the reaction matrix (or K-matrix), and the scattering matrix (or S-matrix). These matrices are related as follows:

$$S = I + 2iC = \frac{I + iK}{I - iK} \tag{A1}$$

$$K = \frac{C}{I + iC} = \frac{C_R}{I - C_I} = i\frac{I - S}{I + S} \tag{A2}$$

$$D = -K^{-1} \tag{A3}$$

$$S^m_{\ell\ell'} = e^{2i\delta^m_{\ell\ell'}} \tag{A4}$$

where the C and D matrices are also related by Eq. 32a and the D matrix is given by Eq. 32b. $\delta^m_{\ell\ell'}$ is the phase shift, and the subscripts R and I denote the real and imaginary parts respectively. All of these matrices are diagonal for a spherically symmetric potential.

For the spherically symmetric case, the phase shifts are given by a simplified form of Eq. A2:

$$\tan \delta^m_{\ell\ell} = K^m_{\ell\ell} = C^m_{R,\ell\ell}/(1-C^m_{I,\ell\ell}) \tag{A5}$$

$K^m_{\ell\ell}$ is real. The C-matrix elements and phase shifts are also related by

$$C^m_{I,\ell\ell} = (C^m_{R,\ell\ell})^2 + (C^m_{I,\ell\ell})^2 \tag{A6}$$

$$C^m_{R,\ell\ell} + iC^m_{I,\ell\ell} = -\tfrac{1}{2}i\,(e^{2i\delta^m_{\ell\ell}} - 1) \tag{A7}$$

Fig. A1, a plot of C_I versus C_R, is an Argand-type diagram which illustrates these relationships, and the circle in the complex plane is the locus of the values of $C^m_{\ell\ell}$.

It is noted that if the lines of constant K_R and K_I are plotted on Fig. A1 then a Smith-type chart is obtained, as illustrated in Fig. A2. From this chart, or from Eq. A1 with the identification of $S^m_{\ell\ell}$ as a reflection coefficient, -iK can be identified as an impedance. While the concept of impedance may be more nebulous in quantum mechanics than in electromagnetics, it suggests the possibility that the deBroglie waves consist of two parts, similar to the E- and H-fields of electromagnetism.

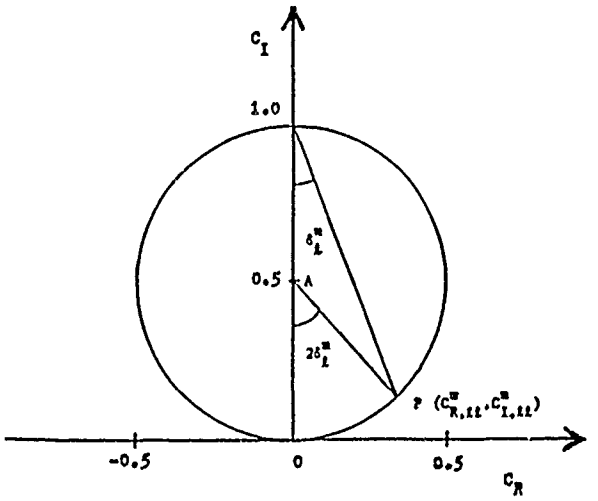


Fig. A1. For a spherically-symmetric, non-absorbing potential, each diagonal C-matrix element is related to the respective phase shift δ_ℓ^m as indicated. The circle of radius 0.5 centered at (0.0, 0.5i) in the complex plane represents the locus of values of $C^m_{\ell\ell}$.

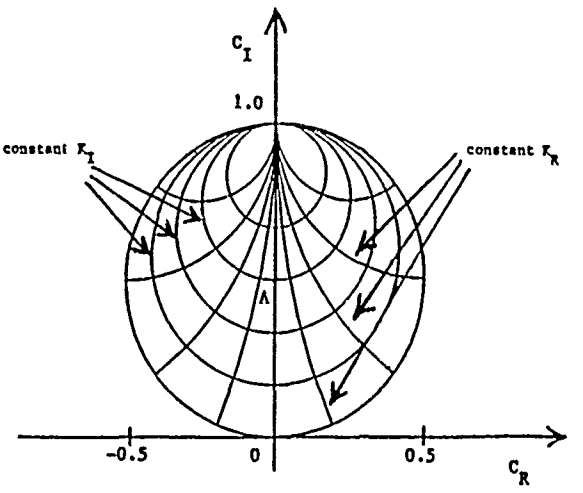


Fig. A2. If lines of constant real K and lines of constant imaginary K are plotted on Fig. A1, the resulting diagram resembles a Smith chart. The "impedance" (for the deBroglie wave) is -iK.

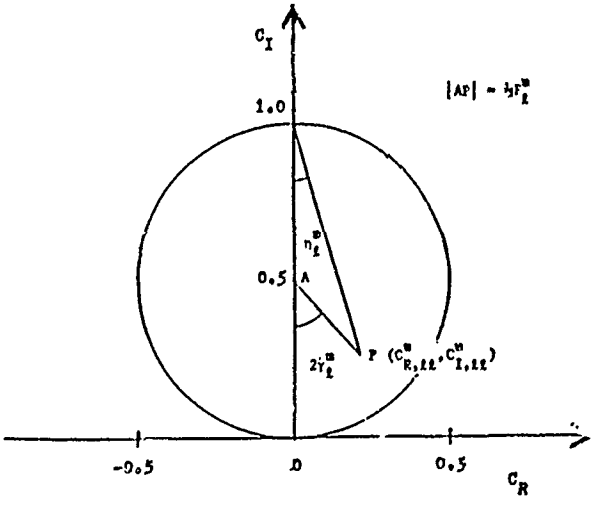


Fig. A3. For a non-spherical potential, the phase shifts for given m are coupled in even ℓ or odd ℓ. The locus of values of $C^m_{\ell\ell}$ now consists of all points on or within the circle, as contrasted with Fig. A1. As the coupling strength F^m_ℓ increases, the point $(C^m_{R,\ell\ell}, C^m_{I,\ell\ell})$ moves closer to the center of the circle. The relation between this point and the angles η^m_ℓ and γ^m_ℓ is as indicated, and γ^m_ℓ is more realistic as a phase shift than is η^m_ℓ. (This diagram also describes scattering by a spherically-symmetric, absorbing potential.)

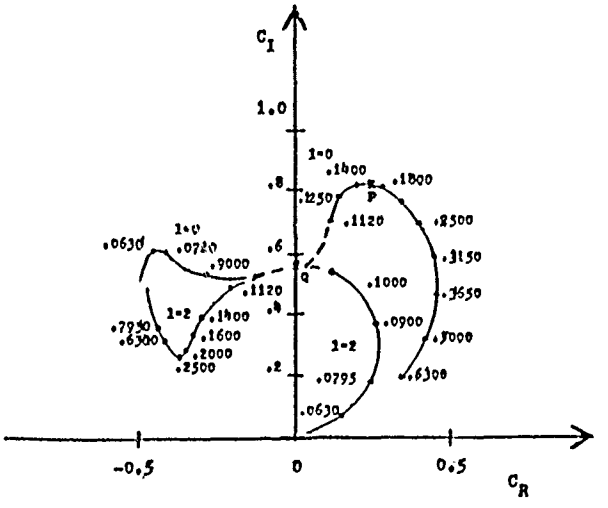


Fig. A4. Loss of physical significance of the phase shifts γ^m_ℓ is illustrated by plotting C^0_{22} and C^0_{00} in the complex plane for a set of typical potential parameters and for various incident energies. The incident energies (Rydberg units) are shown. The two corresponding waves are strongly coupled, especially in the region indicated by dotted lines. The maximum contribution of partial wave (0,0) to σ_t occurs at point P, but neither phase shift is $n\pi/2$ there. (Both phase shifts are multiples of $\pi/2$ at point Q.) Physical significance is restored by diagonalizing the phase shift matrix.

For the non-spherically symmetric case, the phase shifts are coupled in ℓ and are complex, as are the K-matrix elements. Eq. A6 becomes (for the diagonal elements):

$$C^m_{I,\ell\ell} \geq (C^m_{R,\ell\ell})^2 + (C^m_{I,\ell\ell})^2 \tag{A8}$$

and the locus of values for $C^m_{\ell\ell}$ now includes all points on or within the circle, as illustrated in Fig. A3. It is observed that $2\gamma^m_\ell$ no longer equals $2\eta^m_\ell$, in general. Eq. A5 still relates $\tan \eta^m_\ell$ and the scattering coefficient $C^m_{\ell\ell}$, but this "phase shift" is not very useful. This is because the contribution of the (ℓ,m)th partial wave to the cross section is maximized when $C^m_{I,\ell\ell}$ is maximized (see Eq. 35), and for the spherically symmetric case, this occurs when $\tan \eta^m_\ell = \infty$. For the non-spherically symmetric case, the maxima of $C^m_{\ell\ell}$ generally occur when $\tan \eta^m_\ell = 0$.

A more useful phase shift is γ^m_ℓ. Eq. A7 still holds if δ^m_ℓ is allowed to be complex. Then $\delta^m_{R,\ell} = \gamma^m_\ell$, and

$$C^m_{R,\ell\ell} + iC^m_{I,\ell\ell} = -\tfrac{1}{2}i\,(F^m_\ell\, e^{2i\gamma^m_\ell} - 1) \quad , \tag{A9}$$

where $F^m_\ell \equiv \exp(-2\delta^m_{I,\ell})$. It is observed that F^m_ℓ is mathematically equivalent to an absorption parameter, but it is actually a coupling parameter. Furthermore, Eq. A5 may be replaced by

$$\tan 2\gamma^m_\ell = C^m_{R,\ell\ell}/(\tfrac{1}{2}-C^m_{I,\ell\ell}) \tag{A10}$$

It follows that

$$C^m_{I,\ell\ell} = \tfrac{1}{2}\,[1 - F^m_\ell \cos 2\gamma^m_\ell] \tag{A11}$$

$$|C^m_{\ell\ell}|^2 = \tfrac{1}{4}\,[1 + (F^m_\ell)^2 - 2F^m_\ell \cos 2\gamma^m_\ell] \tag{A12}$$

For the spherically symmetric case, no coupling occurs. Then $\delta^m_{I,\ell} = 0$, $F^m_\ell = 1$, and the more familiar expression for the total cross section σ_t,

$$\sigma_t = (4\pi/k^2) \sum_{\ell m} \sin^2 \delta^m_\ell \tag{A13}$$

is recovered. The m-summation may be further reduced to the factor $2\ell+1$.

Some properties of the nondiagonal C-matrix elements may also be obtained from Eqs. A11 and A12, together with the empirical "diagonal theorem," Eq. 34. The relation

$$C^m_{I,\ell\ell} = |C^m_{\ell\ell}|^2 + \sum_{\ell'\neq\ell} |C^m_{\ell\ell'}|^2 \tag{A14}$$

where the prime denotes even-ℓ or odd-ℓ summation, has been rigorously proven for two-wave mixing and is believed to be true when three or more waves are coupled. This relation is the mathematical basis for the diagonal theorem. Moreover, from Eqs. A11, A12, and A14, it follows that

$$\sum_{\ell' \neq \ell}{}' \left| C^m_{\ell\ell'} \right|^2 = \tfrac{1}{4} \left[1-(F^m_\ell)^2\right] \tag{A15}$$

Then, F^m_ℓ is a measure of the coupling of the ℓth partial wave to all other partial waves ℓ' for the same m. The F^m_ℓ's for the same m and various ℓ's are not all independent. In fact, if only two waves (ℓ,m) and (ℓ',m) are coupled, then $F^m_{\ell'} = F^m_\ell$. The effect of F^m_ℓ is to damp out the maxima and minima in $C^m_{I,\ell\ell}$ as the phase angle γ^m_ℓ varies, and this effect is similar to that caused by absorption terms.

Although γ^m_ℓ is preferable to η^m_ℓ, as a phase shift, it also has drawbacks. First, local maxima in $C^m_{I,\ell\ell}$ do not necessarily coincide with "resonances" in γ^m_ℓ, that is, values equal to $(n+\frac{1}{2})\pi$. Some of the physical significance of this "phase shift" is thereby removed. Additionally, when only two waves are coupled, then their "resonances" are coupled. Both effects are illustrated in Fig. A4. These phenomena are consequences of the fact that ℓ is no longer a good quantum number. The cross sections may still be obtained from the C-matrix elements with summations over ℓ and m, but the phase shifts must be diagonalized if the partial waves in resonance are to be identified.

These eigenphase shifts are obtained by diagonalizing the K-matrix. For two-wave $(\ell-\ell')$ mixing, they are given by

$$\tan \varepsilon^m_\nu = \frac{\sin(\gamma^m_\ell+\gamma^m_{\ell'}) \pm \left[1-(F^m_\ell)^2\cos^2(\gamma^m_\ell-\gamma^m_{\ell'})\right]^{\frac{1}{2}}}{\cos(\gamma^m_\ell+\gamma^m_{\ell'}) + F^m_\ell \cos(\gamma^m_\ell-\gamma^m_{\ell'})} \tag{A16}$$

where label $\nu = 1$ or 2. The new C-matrix elements associated with ε^m_1 and ε^m_2 correspond to points on the circle and are designated $(G^m_{R,11}, G^m_{I,11})$ and $(G^m_{R,22}, G^m_{I,22})$ respectively. Fig. A5 illustrates the relationships among the angles γ^m_i, ε^m_ν and the coefficients C^m_{ii}, $G^m_{\nu\nu}$. It is seen that

$$G^m_{R,11} + G^m_{R,22} = C^m_{R,\ell\ell} + C^m_{R,\ell'\ell'} \tag{A17}$$

$$G^m_{I,11} + G^m_{I,22} = C^m_{I,\ell\ell} + C^m_{I,\ell'\ell'} \tag{A18}$$

From Eq. A18, it is seen that the total contribution to σ_t is invariant under diagonalization, as expected. This is not the case for $d\sigma(\theta)/d\Omega$, the expansion for which still includes the (no longer valid) quantum number ℓ in the Legendre polynomials.

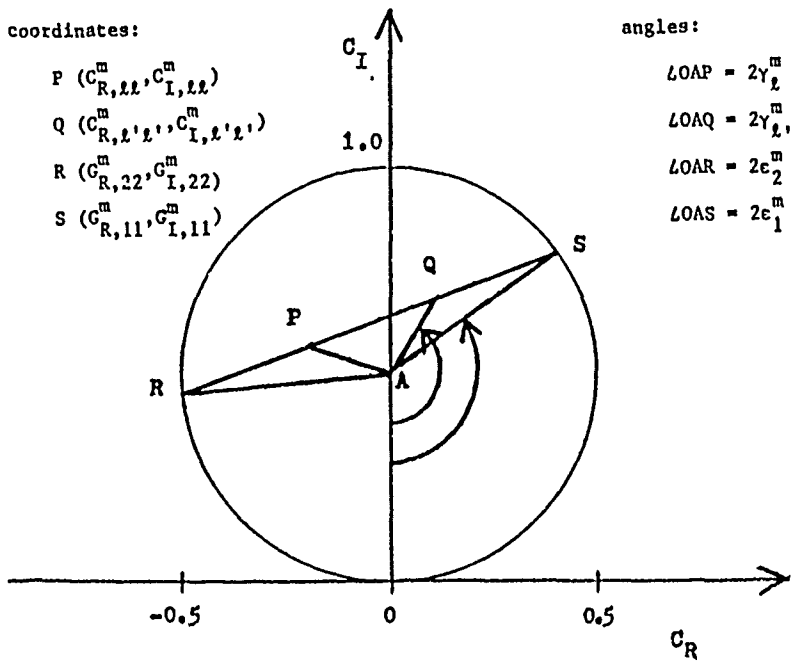


Fig. A5. For two-wave coupling (for example, γ^0_0 and γ^0_2), the eigenphase shifts (or the diagonalized phase shifts) correspond to a set of new (diagonalized) C-matrix elements $G^m_{\nu\nu}$ which now lie on the circle (see Figs. A1 and A3). The four points P, Q, R, and S are co-linear.

REFERENCES

[1] T. Sawada, P.S. Ganas, and A.E.S. Green, Phys. Rev. A 9, 1130 (1974).

[2] P.S. Ganas and A.E.S. Green, J. Chem. Phys. 76, 1819 (1982).

[3] D.E. Stein and A.E.S. Green, Am. J. Phys. 50, 1120 (1982).

[4] N. Levinson, Kgl. Danske Videnskak Silskb. Mat-Fys. Medd. 1949, 25-29 (1949).

[5] N.F. Mott and H.S.W. Massey, Theory of Atomic Collisions, 3rd ed. (Oxford University, London and New York, 1965), p. 340.

[6] M.L. Goldberger and K.M. Watson, Collision Theory (Wiley, New York and London, 1964), p. 289.

[7] F. Calogero, Variable Phase Approach to Potential Scattering (Academic, New York, 1967), p. 176-181.

[8] H.C. van de Hulst, Light Scattering by Small Particles (Wiley, New York, 1957), p. 143.

[9] A.E.S. Green, D.E. Rio, P.F. Schippnick, J.M. Schwartz, and P.S. Ganas, Int. J. Quantum Chem.: Quantum Chemistry Symposium 16 (1982).

[10] D. Arnush, IEEE Trans. Antennas and Propagation AP-12, 86 (1964).

[11] R.S. Marguiles and F.L. Scarf, IEEE Trans. Antennas and Propagation AP-12, 91 (1964).

[12] A.E.S. Green, D.L. Sellin, and A.S. Zachor, Phys. Rev. 184, 1 (1969).

[13] J.E. Purcell, R.A. Berg, and A.E.S. Green, Phys. Rev. A 2, 107 (1970).

[14] R.A. Berg, J.E. Purcell, and A.E.S. Green, Phys. Rev. A 3, 508 (1971).

[15] P.S. Ganas and A.E.S. Green, Phys. Rev. A 4, 182 (1971).

[16] T. Sawada, J.E. Purcell, and A.E.S. Green, Phys. Rev. A 4, 193 (1971).

[17] P.A. Kazaks, P.S. Ganas, and A.E.S. Green, Phys. Rev. A 6, 2169 (1972).

[18] T. Sawada and P.S. Ganas, Phys. Rev. A 7, 617 (1973).

[19] J.E. Whalen and A.E.S. Green, Am. J. Phys. 40, 1484 (1972).

[20] N.F. Lane and S. Geltman, Phys. Rev. 160, 53 (1967).

[21] P.G. Burke and N. Chandra, J. Phys. B 5, 1696 (1972).

[22]K.J. Miller and A.E.S. Green, J. Chem. Phys. 60, 2617 (1974).

[23]J.B. Fisk, Phys. Rev. 49, 167 (1936).

[24]H.C. Stier, Z. Phys. 76, 439 (1932).

[25]N.T. Padial and D.W. Norcross, Phys. Rev. A, in press.

[26]M.A. Morrison and L.A. Collins, Phys. Rev. A 17, 918 (1978).

[27]G.J. Schulz, Rev. Mod. Phys. 45, 378 (1973).

[28]G. Gingquan, P. Shofu, Z. Yougfang, X. Hongshan, and D. Peizhu, Scientia Sinica 24, 1085 (1981).

[29]S. Hara, J. Phys. Soc. Japan 22, 710 (1967).

[30]D. Jackson, Classical Electrodynamics, 2nd ed. (Wiley, New York, 1975), p. 50.

[31]M. Blaha and J. Davis, Phys. Rev. A 12, 2319 (1975).

[32]P.G. Burke and A.-L. SinFaiLam, J. Phys. B 3, 641 (1970).

[33]D.E. Golden, N.F. Lane, A. Temkin, and E. Gerjuoy, Rev. Mod. Phys. 43, 642 (1971).

[34]T. Tamura, Rev. Mod. Phys. 37, 679 (1965).

[35]H.S. Porter and F.W. Jump, Analytic Total and Angular Elastic Electron Impact Cross Sections for Planetary Atmospheres, prepared for Goddard Space Flight Center by Computer Sciences Corporation under contract NAS 5-24350 (1978).

[36]G. Herzberg, Spectra of Diatomic Molecules, 2nd ed. (van Nostrand, Princeton, 1950), p. 329.

[37]P.S. Ganas, S.K. Dutta, and A.E.S. Green, Phys. Rev. A 2, 112 (1970).

[38]K. Onda and A. Temkin, Phys. Rev. A 28, 621 (1983).

[39]S. Asano and G. Yamamoto, Appl. Opt. 14, 29 (1975).

[40]M. Elwenspoek, J. Opt. Soc. Am. 72, 747 (1982).

[41]W. Wiscombe and A. Mugnai, in Light Scattering by Irregularly Shaped Particles, D. Schuerman, ed. (Plenum, New York, 1980), p. 141.

BOUNDARY CONDITIONS AND SAMPLING FOR METHOD-OF-MOMENT CALCULATIONS OF ELECTROMAGNETIC SCATTERING

R. J. Balestri, M. V. Hikida, and J. W. Williams
BOOZ, ALLEN & HAMILTON INC.
2201 Buena Vista Drive, S.E., Suite 400
Albuquerque, New Mexico 87106

Abstract

Applications of the method-of-moment (MM) solution technique to integral equations arising from electromagnetic theory are abundant. In view of the ever expanding improvements in computer technology, the popularity of this technique is not likely to wane. In this paper we present MM calculations of electromagnetic scattering from metal bodies of revolution (BOR) with generating curves having lengths from a few wavelengths to roughly 40 wavelengths. These calculations were performed with two widely used MM models. One is the NEC code developed by Lawrence Livermore Laboratories (Ref. 1). The other is a body of revolution (BOR) code developed by Medegesi-Mitschang and coworkers (Ref.2). Comparisons are presented for the bistatic scattering calculated with the NEC code using wire grid and surface patch models of a conducting sphere. Backscatter from a sphere near an internal resonance is computed with the NEC and BOR codes. Similar comparisons among computer models and boundary conditions are provided for cylindrical and conical scatterers. Although the results at low frequencies are in reasonably good agreement with measured data and diffraction theory, sampling rates required for accuracy and convergence appear to be increasing with the electrical size of the scatterer. This implies that computer resources required for applications for the MM technique may be expanding more rapidly than expected.

Introduction

The purpose of this paper is to present some comparisons of scattered fields obtained with various boundary conditions and sampling rates. Two computer codes were used for the calculations. Wire grid and surface patch models available in the NEC code were used to investigate sampling rates, which are expressed in terms of expansion functions per wavelength (EF/λ), for electric field boundary conditions (EFIE) and magnetic field boundary conditions (MFIE). Results are compared with experimental data and with combined field (CFIE) calculations obtained from the BOR computer codes.

Results and Comparisons

It has long been known that MM solutions in the MFIE and EFIE formulations are unstable and inaccurate at frequencies corresponding to internal resonance for a scatterer. Mautz and Harrington have shown that although the MFIE and EFIE formulations are separately unstable at such frequencies, stability and uniqueness for the solution could be obtained by combining the electric field and magnetic field boundary conditions (Ref. 3). The combined treatment has recently been extended in dielectrically clad metal scatterers (Ref. 2).

For the relatively complex geometries of interest in practical problems, the internal resonance frequencies are not easily obtained. If the scatterer is electrically large, then numerical experimentation can be impractical. Hence, we will begin by examining a simple sphere at frequencies near a known resonance. Figure 1 shows the segmentation scheme included in the NEC documentation as Example 9 (Ref. 1, Vol. 2). We will use this model of the sphere for calculations with of bistatic scattering from a sphere. A corresponding wire grid model was obtained by replacing the patches shown in Figure 1 by wire segments along the perimeter of each patch. In an early investigation of wire grid representations of a surface, it was found that differences between wire grid and surface models were at least partly quantified by (Ref. 4):

$$\Delta L = (\mu_o \ell / 2\pi) \ln (\ell / 2\pi r_o) \qquad (1)$$

where ΔL represents the difference in the inductive part of the impedance matrix for wire grid and closed surface models: $\Delta L = L_{\text{wire grid}} - L_{\text{closed surface}}$

ℓ denotes the grid spacing (wire length), and r_o represents the wire radius. Figure 2 shows the bistatic radar cross section (BRCS) calculated under the constraint

$$r_o = \ell/n\pi \qquad (2)$$

where n = 1,2,4, and 16. Calculations were performed with the NEC computer code using the extended thin wire kernal for the case with n=1 and the thin wire kernal for the remaining cases. For comparison, the BRCS calculated with the corresponding surface patch model is shown in Figure 3. Except near monostatic backscatter at 0^o, the selection n=2 in Equation 2 yielded the overall best results. Common selections for the length-to-radius ratio of the wires in the grid lie in the range from 2π to 4π. It should be noted that although the patch model results are reasonably close to those obtained with the wire grids, the patch model results are not bounded by wire grid results with $r_o = \ell/2\pi$ and $r_o = \ell/4\pi$. We have not yet investigated the magnitude of this disparity between wire grid and patch results with increasing electrical size of the scatterer.

Figure 4 shows the results obtained for a sphere with $2.7 \leq ka \leq 2.8$. This figure was extracted from Reference 3. Original results obtained by Mautz and Harrington are shown as open circles, triangles or squares. Computed values of the normalized RCS obtained with the BOR codes are shown as solid circles, triangles and squares. Calculations with the wire grid model shown in Figure 1 (with n=2 in Equation 2) are indicated with an "x". Note that a sampling rate slightly less than $10EF/\lambda$ was used in the BOR calculations. As indicated in Figure 1, the wire grid model used a sampling rate of roughly $5.5\ EF/\lambda$ for values of ka in the range from 2.7 to 2.8. At first glance at Figure 4, it would appear that the wire grid model is somewhat more susceptible to instabilities near resonance than the surface patch models. However, the lower sampling rate used for the wire grid model most likely accounts for the observed increase.

Calculated values of the monostatic RCS for a conducting cylinder are shown in Figures 5 through 7. Results shown in Figures 5 and 6 were obtained with the BOR codes with combined field ($\alpha = 0.5$) and electric field ($\alpha=1.0$) boundary conditions, respectively. Calculations using GTD extracted from Reference 4 are shown for comparison in Figure 7. The comparison is

reasonably favorable between the CFIE calculation and GTD results. As indicated in Figure 6, the electric field boundary condition yielded relatively poor results although the segmentation was identical to that used in the CFIE calculation. For this scatterer, the generating curve exceeds 40 wavelengths so that numerical experimentation to improve the EFIE results was not practical.

As a final example, we show the backscatter from a metal cone. Numerical estimates of the monostatic RCS were included in a previous paper (Ref. 5). Figure 8 shows a comparison of measured data obtained from the radar range at Sandia National Laboratories and calculations performed with electric field and magnetic field boundary conditions. Calculations with the NEC code were performed by rotation of surface patches along the generating curve about the z-axis. The degree of symmetry, N_S, was chosen to insure that the sampling rate along the generating curve, in the case $8EF/\lambda$, was identical to the sampling rate around the base of the cone. Both boundary conditions yielded reasonably good agreement with test data for the case of vertical-vertical (V-V) polarization. Agreement between the NEC results and measured data was noticeably poorer for horizontal-horizontal (H-H) polarization in which the incident field tends to drive longitudinal rather than circumferential currents. A similar effect is shown in Figure 9 which compares NEC and BOR calculations at a lower frequency.

As a final note, Figure 10 shows the nose-on RCS computed for a metal cone as a function of coupling parameter α at L-band, S-band, and C-band frequencies. Although the target is relatively small in terms of electrical wavelength, the sensitivity of the results to sampling rate appears to be steadily increasing with frequency. Stability obtained with the combined field boundary condition is relatively good for values of the coupling parameter which are not near 0 or 1. However, the trend toward increased sampling rates with increasing frequency is bothersome because the CFIE formulation offers no direct method for selecting optional values of the coupling parameter.

Conclusion

This paper presented some comparisons of calculations performed with electric field, magnetic field and mixed boundary conditions with experimental data and other numerical calculations. It was shown that in general, the agreement between models and test data was reasonably good for electrically small objects. However, as the electrical size of the scatterer increases, sampling rates required for numerical convergence and accuracy appear to be increasing . Results are noticeably dependent upon the boundary condition used in the calculation. This implies that requirements for computer resources in this type of calculation may increase more rapidly than might be expected. The potential dependence of this effect upon the basis and weight function used in the MM formulas was not addressed in this study.

References

1. G. J. Burke and A. J. Poggio, "Numerical Electromagnetics Code - Method of Moments (Vol. 1 and Vol. 2)," Lawrence Livermore Laboratory, NOSC TD116, January 1981.

2. Philip L. Huddleston, Louis N. Medgyesi-Mitschang, and John M. Putnam, "Combined Field Integral Equation Formulation for Scattering by Dielectrically Coated Conducting Bodies," IEEE Trans, Antennas Propogat., AP-34, pp 510-520, April 1986..

3. Joseph R. Mautz and Roger F. Harrington, "H-Field, E-Field, and Combined Field Solutions for Bodies of Revolution," RADC-TR-77-109, March 1977.

4. K. S. H. Lee, Lennart Marin, and J. Phillip Castillo, "Limitations of Wire-Grid Modeling of a Closed Surface," IEEE Trans. Electromag Compat, EMC-18, pp 123-129, August 1976.

5. M. C. Liang and R. C. Rudduck,"Calculated Near Zone Backscattering Data for Finite Cylinders", The Ohio State University ElectroScience Laboratory, 715968-2, January 1985.

6. John W. Williams and Jiunn S. Yu, "Computational Resources and Convergence for MM Calculations with Electrically Large Scatterers," Conference Proceedings, Second Annual Review of Progress in Applied Computational Electromagnetics, March 1986.

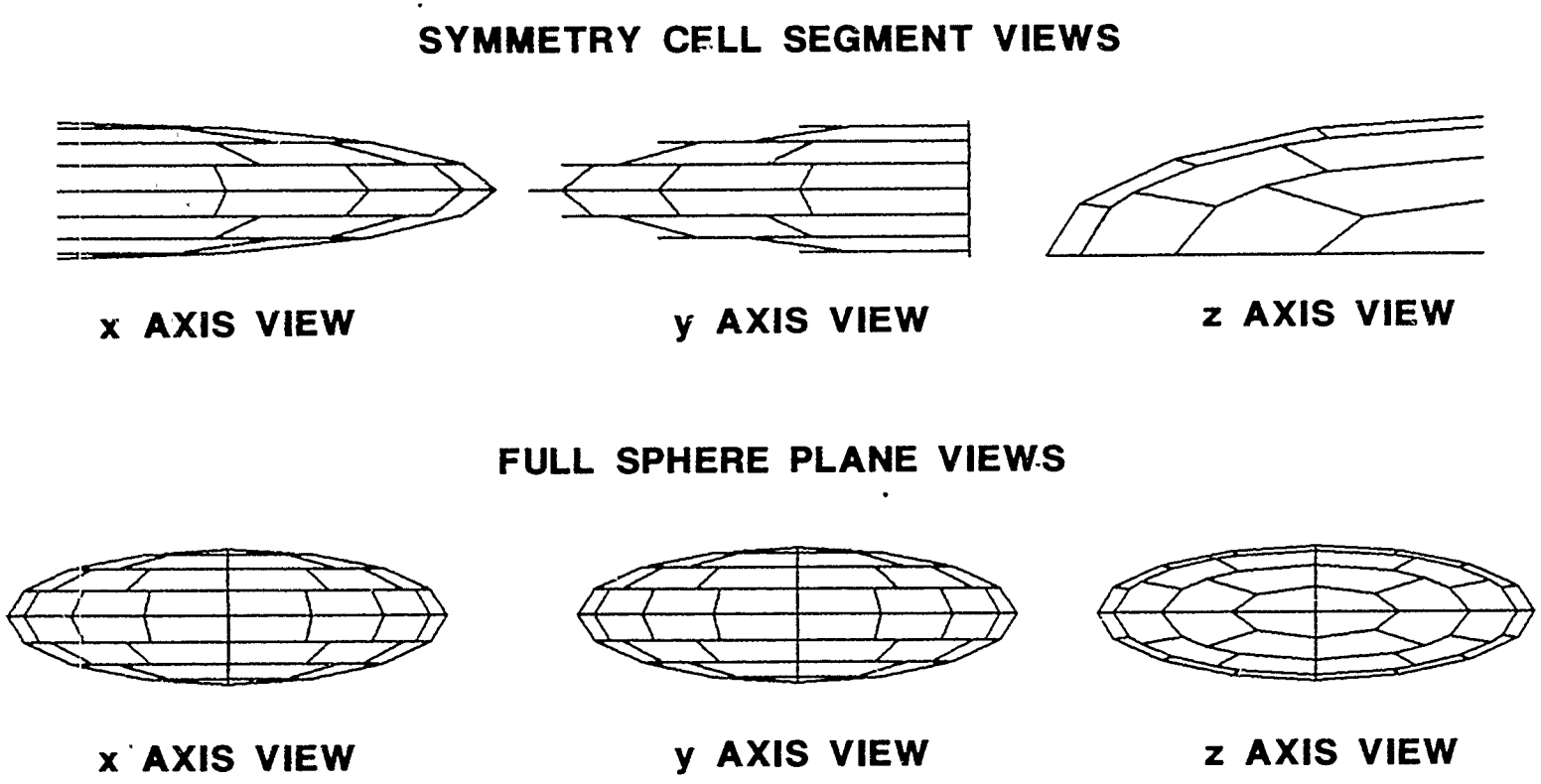


Figure 1. Model of a sphere used for NEC calculations of bistatic scattering with $2.7 \leq ka \leq 2.9$.

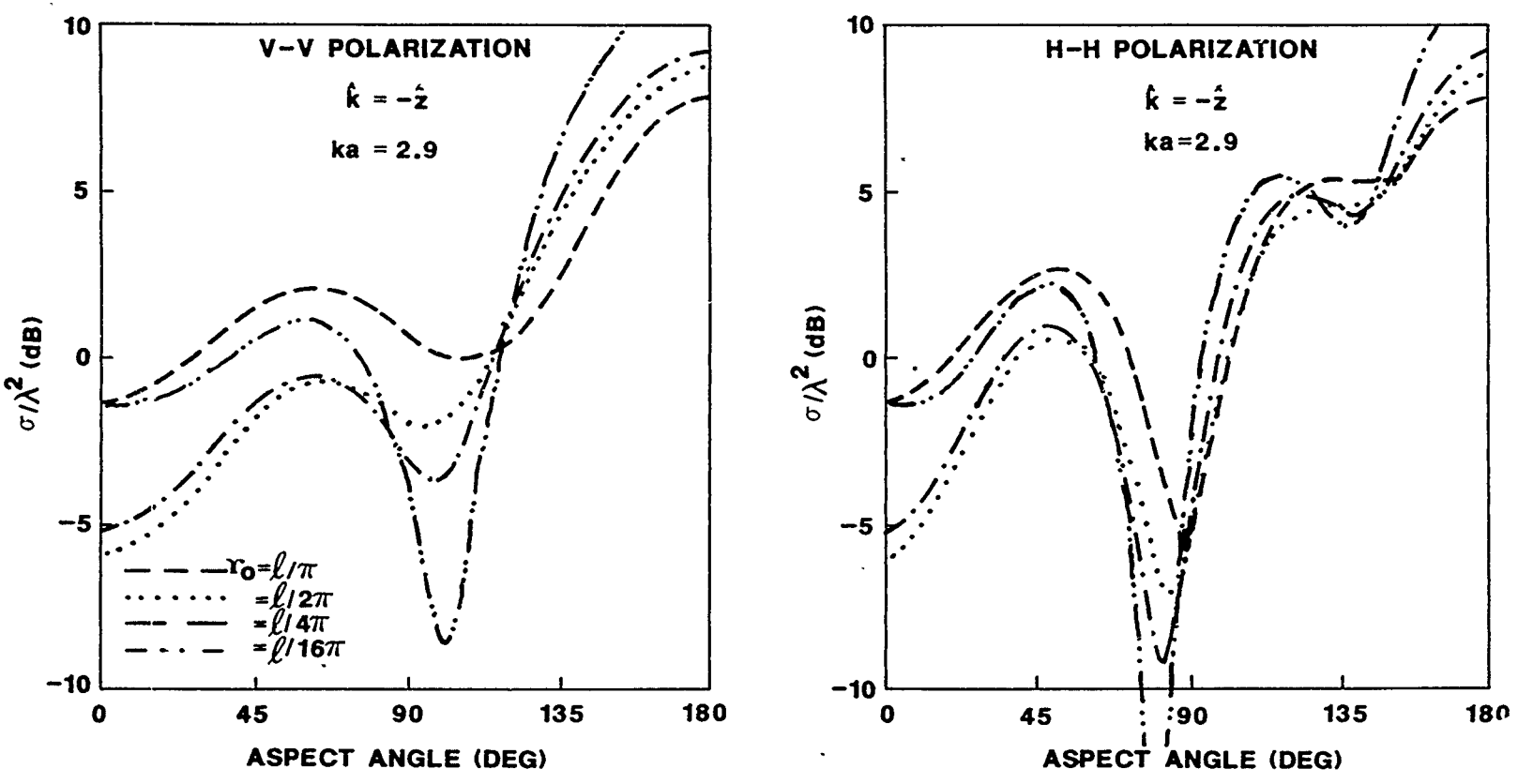


Figure 2. Bistatic RCS computed with a Wire Grid Model of a sphere using the NEC code.

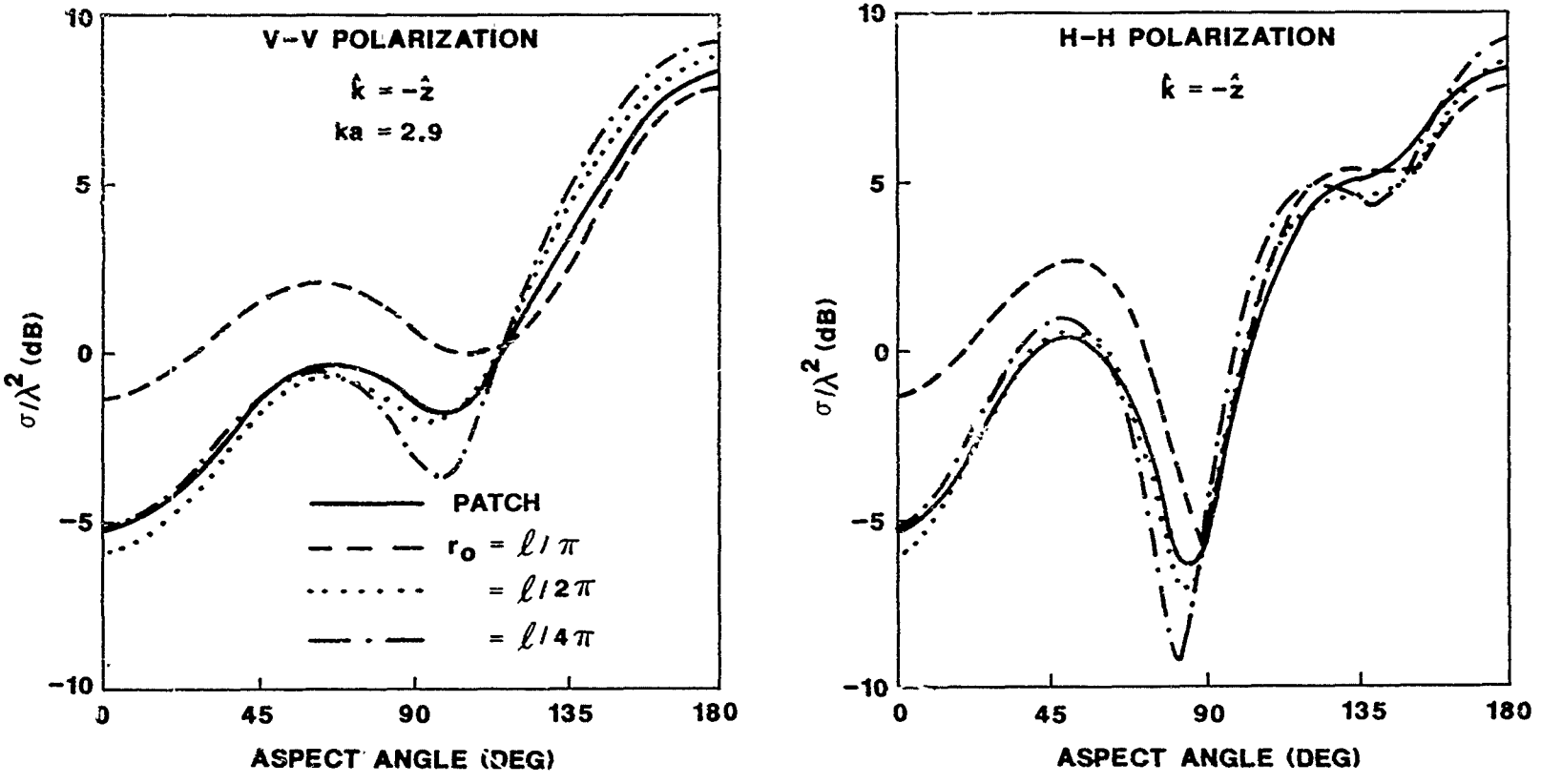


Figure 3. Comparison of Wire Grid and surface patch calculations for a sphere computed with the NEC code.

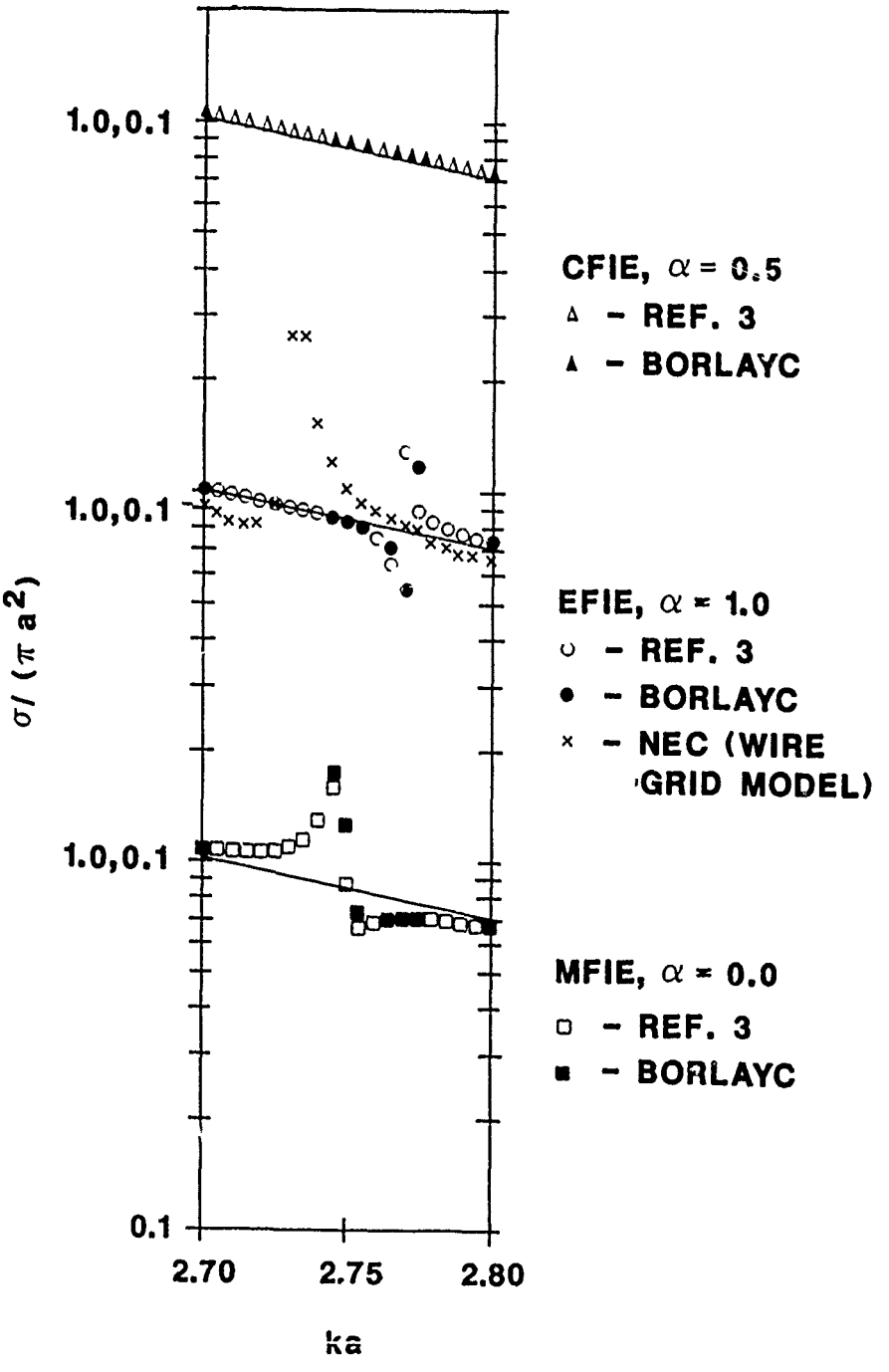


Figure 4. Normalized RCS for a metal sphere near resonance calculated with various models and boundary conditions.

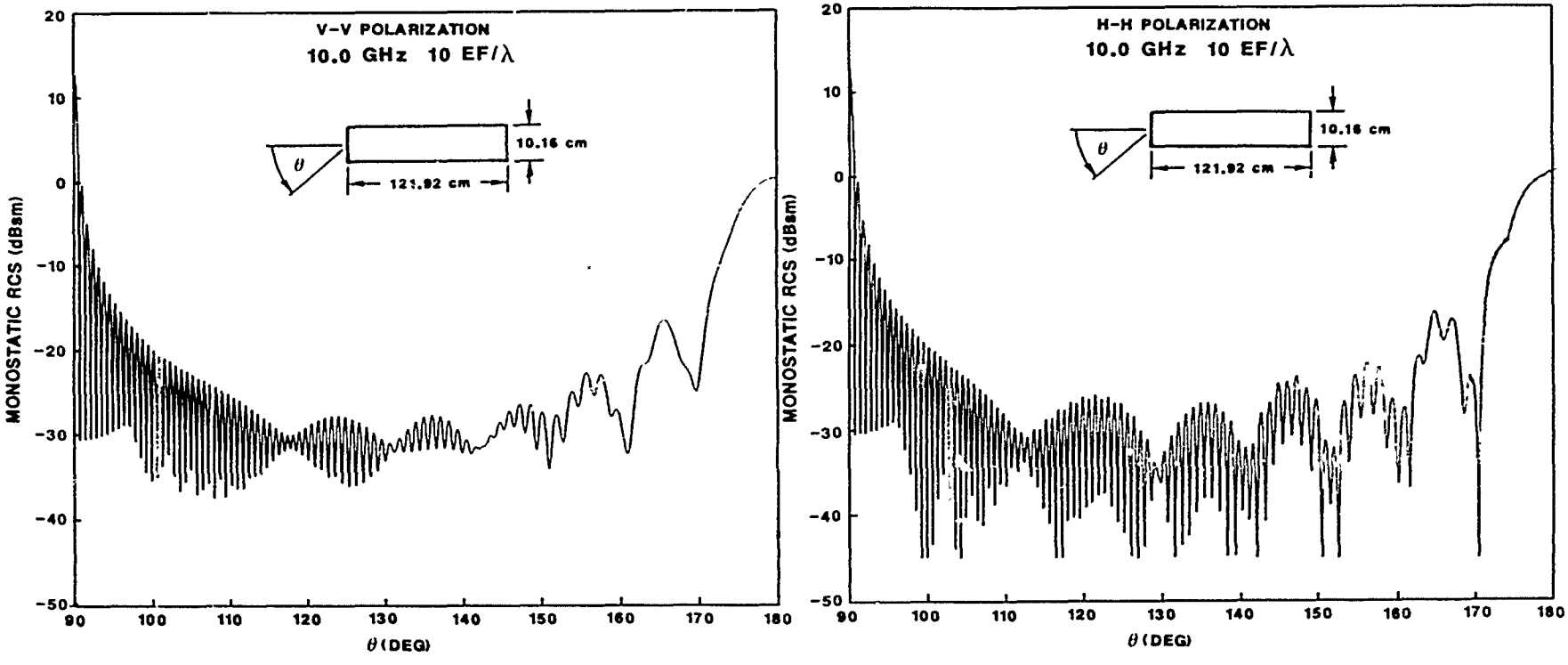


Figure 5. Monostatic RCS for a conducting cylinder computed with $\alpha = 0.5$

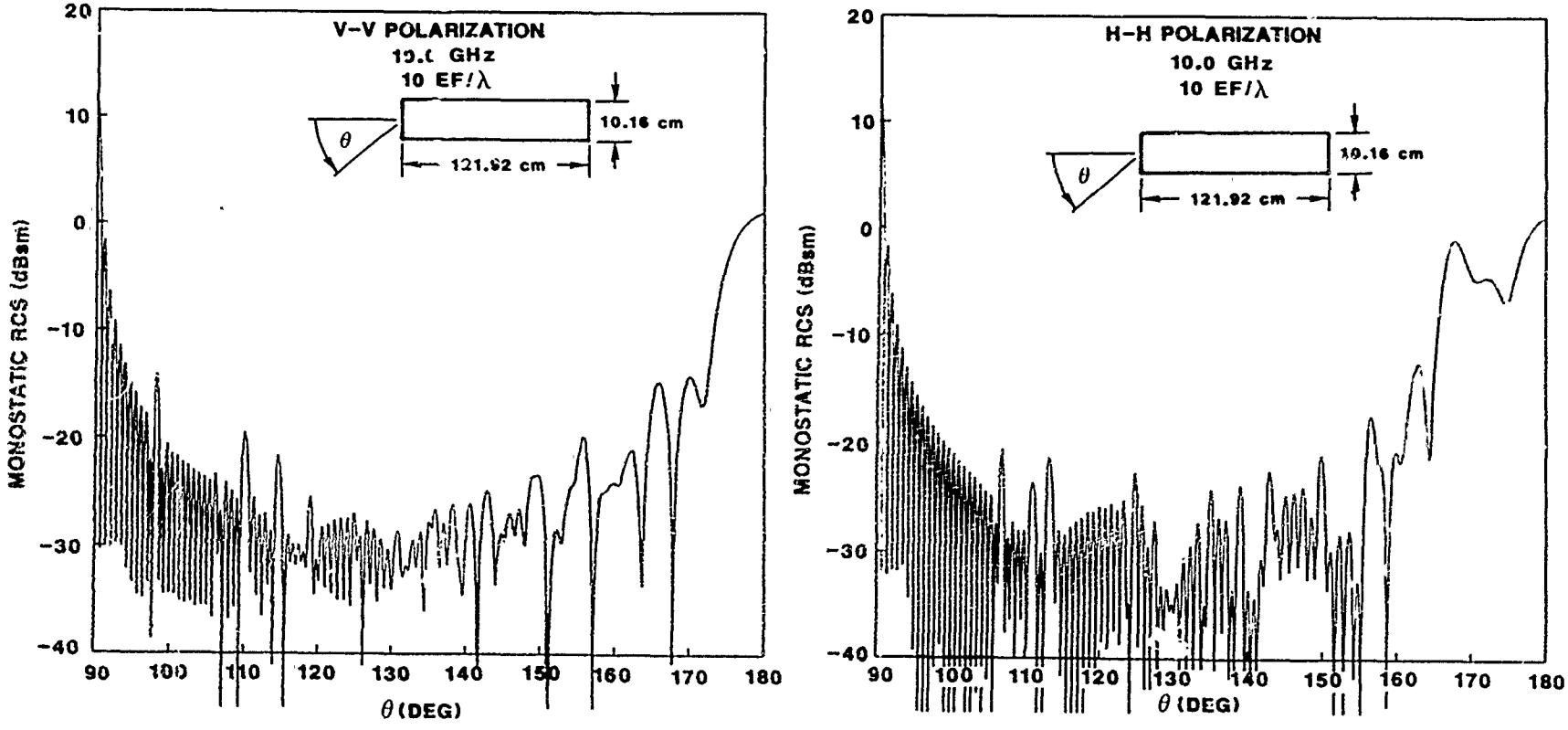
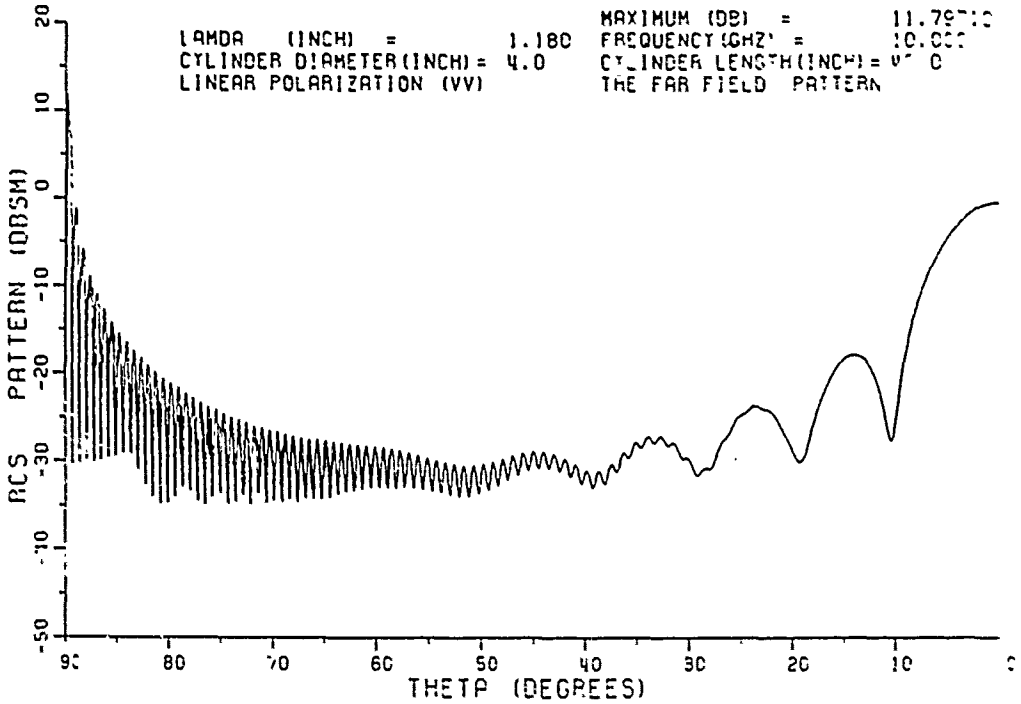


Figure 6. Monostatic RCS for a conducting cylinder computed with $\alpha = 1.0$



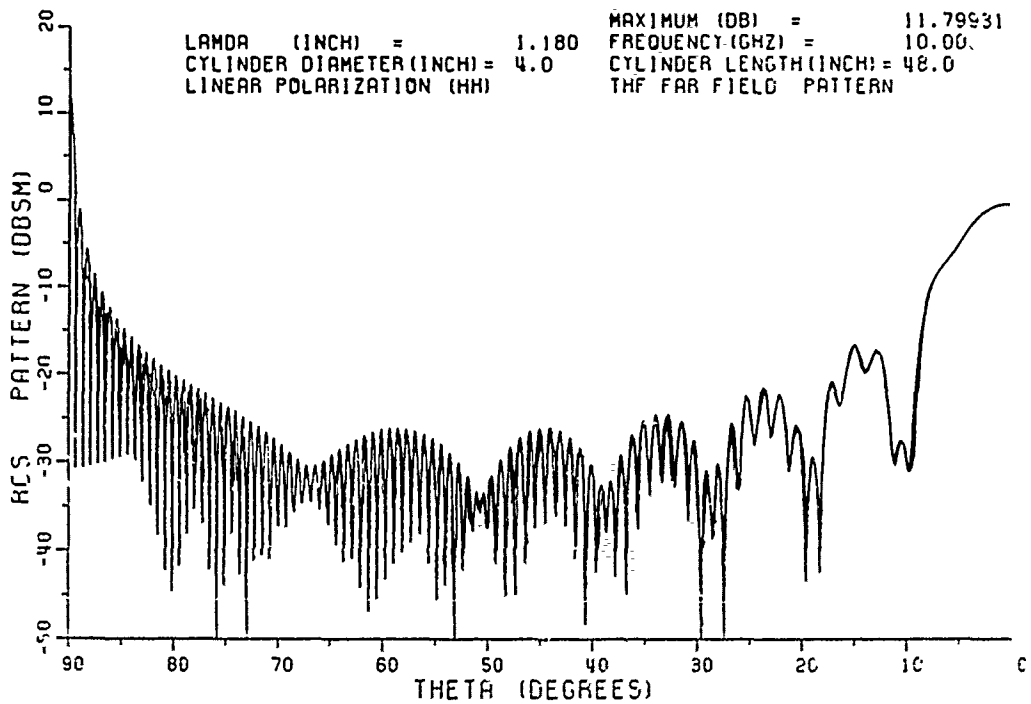


Figure 7. Monostatic RCS computed with GTD by OSU (Ref. 5).

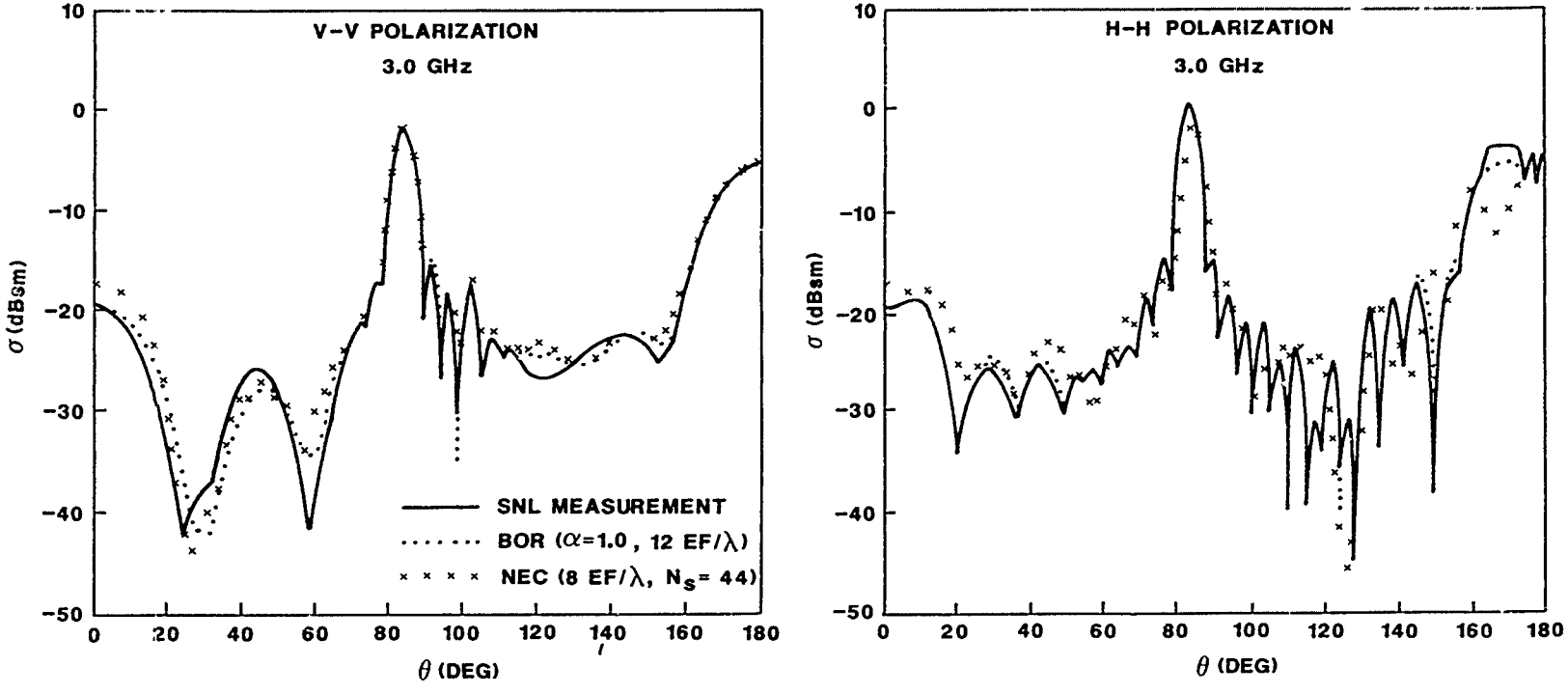


Figure 8. Comparison of measured and calculated RCS for a metal cone at 3.0 GHz.

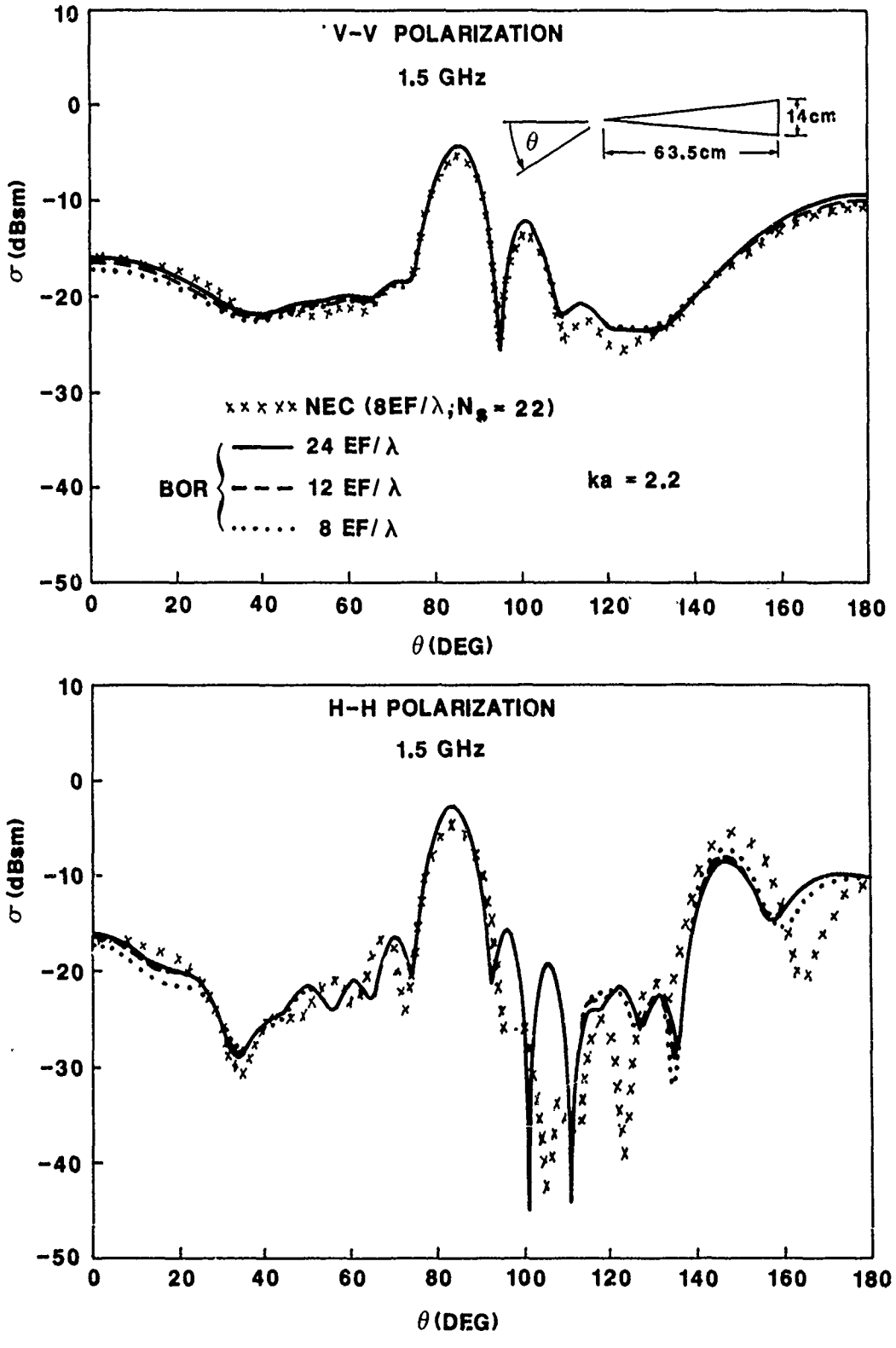


Figure 9. Comparison of NEC and BOR calculations of backscatter from a metal cone at 1.5.GHz.

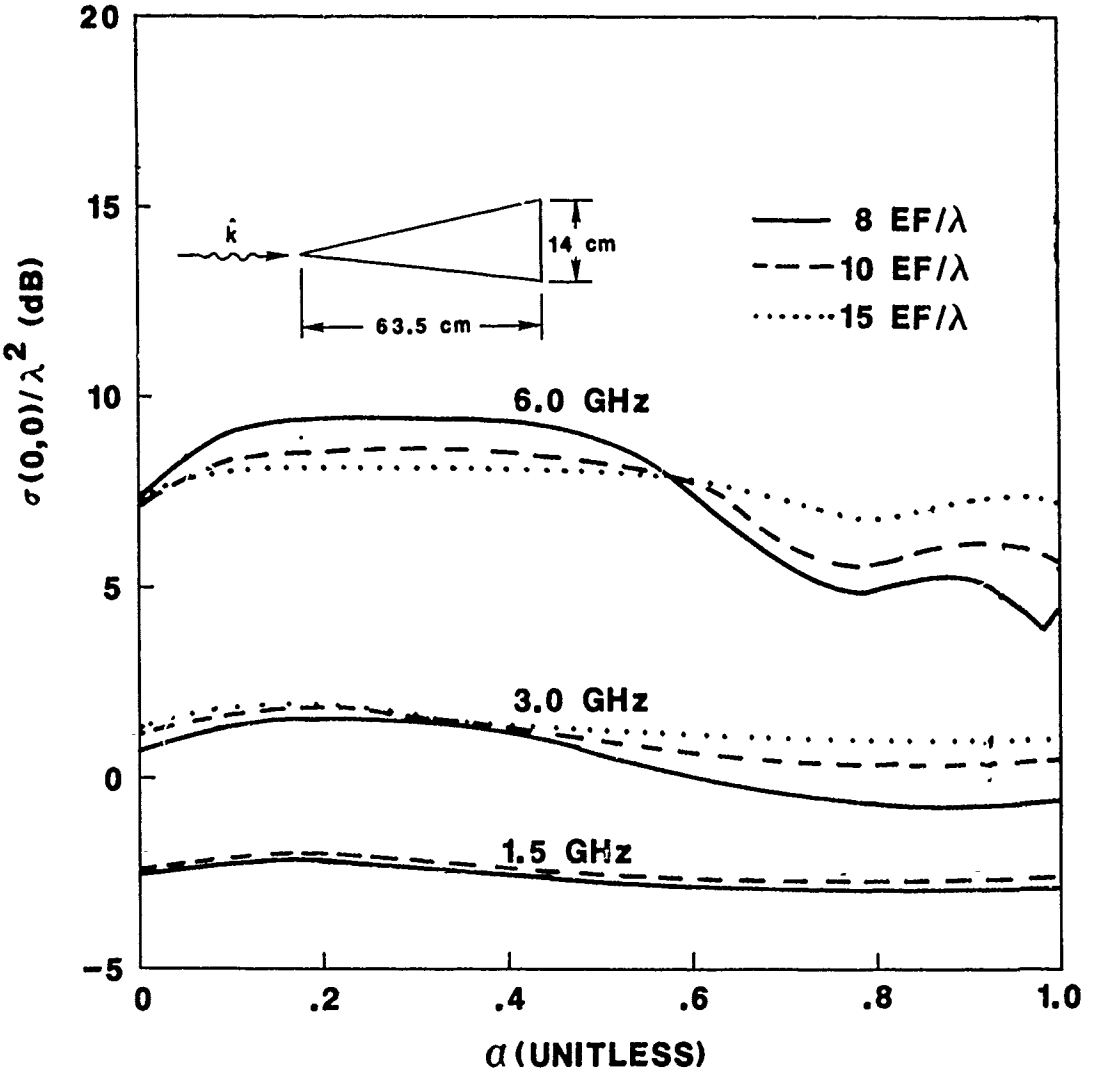


Figure 10. Nose-on RCS calculated for a metal cone with various values of the coupling parameter.

PREDICTION OF THE SCATTERING FROM A CUBE WITH GEMACS

G.R. Salo , D.E. Thomas
The BDM Corporation
1801 Randolph Road , SE
Albuquerque, NM , USA 87106

INTRODUCTION

It is commonly known that it is easier to predict the radiation pattern of an antenna in the presence of scatterers than it is to obtain an accurate prediction of the scattered fields from a complex object. In most cases, an accurate radiation pattern of an antenna in the presence of a scatterer can be obtained by approximating the scatterer with a simple geometric model. However, the accurate prediction of the scattered fields from a complex object requires a very detailed model of the geometry of the scatterer. This is exactly why techniques such as the geometric theory of diffraction (GTD) are good for predicting the radiation pattern of an antenna in the presence of scatterers, and not very good for predicting the scattered fields of a complex object.

On the other hand, the method of moments (MOM) technique is capable of modeling the geometry of a complex scatterer in greater detail. Thus, MOM has the potential to predict the scattering off of complex objects more accurately than GTD. However, the MOM technique is limited in most applications by the number of unknowns (basis functions or wire segments) that can be used in the solution of a given problem. This number is dependent on the cost, time, and potential possibility of round-off error that the user is willing to accept.

A method is sometimes employed to reduce the number of unknowns for problems concerning the radiation patterns of antennas in the presence of a scatterer; this method is based on modelling only the dominant geometrical contributions of the scatterer. These include both sources of direct interactions (specular reflections) and major scattering centers (edges and corners) of the structure. Since this method has been used to obtain reasonable results for antenna radiation patterns for complex structures, it is tempting to apply the same modelling technique to predict the scattered fields from a complex object exposed to a given external field excitation. The user could model all direct interactions and the scattering centers with MOM and expect to get good results. However, this technique is not appropriate for predicting the scattered fields from a complex object since a detailed model of the geometry of the scatterer is, in general, needed. This paper will present several examples in which a complex scatterer was modelled with the major scattering centers only. These examples demonstrate the need to model the entire scattering object, not just scattering centers.

PROCEDURE

A set of calculations was performed which used a perfectly conducting cube as the scattering object. The cube was modeled several different ways with MOM , and the resulting predictions were compared to measured data. Three different models of a cube were generated to predict the monostatic and bistatic radar cross section (RCS) of a cube and then compared to experimental results. The various cube models are shown in Figure 1: the first model represents a complete cube (Figure 1a); the second model represents only the front face of the cube (Figure 1b); and the third model represents the front face and additional major scatteres (i.e., rear edges) of the cube (Figure 1c). The general geometrical configuration for all analyses performed is given in Figure 1d.

The computer code GEMACS (General Electromagnetic Model for the Analysis of Complex Systems) was used in all the cases to generate the MOM results.

RESULTS

The results for the monostatic case appear in Figure 2, for the complete cube model (Figure 2a), the model consisting of a complete front face only (Figure 2b), and the model consisting of the front face and rear edges only (Figure 2c). Results for the bistatic cases are presented in Figures 3 and 4; Figure 3 shows E-plane and H-plane bistatic RCS results for the model consisting of only the front face of the cube, while Figure 4 shows results for the model consisting of the front face and rear edges only.

Model 1 is the proper way to model a cube with MOM. The entire surface of the cube is modeled with wire segments approximately one tenth of a wavelenth long. Comparison between the predicted and measured monostatic results shown in Figure 2a show good agreement between the two. A comparison between predicted and measured results for bistatic RCS was not possible since no bistatic measurements were available for a cube smaller than 4S/lambda=3. This size of cube would have required approximately 850 segments, which was too costly to run on the computer. However, since model 1 was able to accurately predict the null in the monostatic RCS at 4S/lambda=1.5 when the other models were unable to, it is also expected that the bistatic results would be in good agreement with the measured results.

The second model used for the cube was simply a wire grid model of the front face. The front face is the dominant scatterer in this example, and therefore, one would expect to obtain reasonable results with this simple model. For the monostatic case (Figure 2b), this simple model failed to predict

the null in the monostatic RCS, but appears to be converging to the correct solution for larger cubes. This result is consistent with those obtained by others.

However, the bistatic case results for the front-face-only model, shown in Figure 3, are not as good. The H-plane results are roughly the same as the measured results, but the E-plane results fail to predict accurately the null in the pattern. Therefore, it can be concluded that this model is not sufficiently detailed to accurately model the scattered fields.

The third model shown in Figure 1 models the front face of the cube as well as the remaining rear edges. The front face and edges constitute all of the major scattering centers. Comparing the predicted results against the measured results for the monostatic RCS in Figure 2c, it can be seen that there is a slight improvement in the prediction of the backscatter field in model 3 over model 2. This improvement, however, is very small and probably does not warrant the added expense of including the additional scattering edges.

The bistatic results are compared in Figure 4; once again a general improvement is noticed, but the improvement is very unpredictable. In this example, the addition of the scattering edges improved the prediction of the E-plane null, but it also introduced an artifical null in the pattern. In general, this technique is not a valid method to obtain accurate predictions to the field pattern, since it is difficult to determine the angles of validity without having measured data to compare the results against.

CONCLUSION

The examples shown in this paper verify that a complete model of a scattering object is needed to accurately predict the scattered fields. Approximations can be made which may simplify the problem and be valid for certain scattering angles, but it is difficult to know the region of validity without measured data. Therefore, it is recommended that a complete model of the scattering object should be used if the end result is to predict the scattered fields.

Figure 1. Representations of the Various Cube Models Which Were Examined:

Figure 1a : a Complete MOM Cube Model.

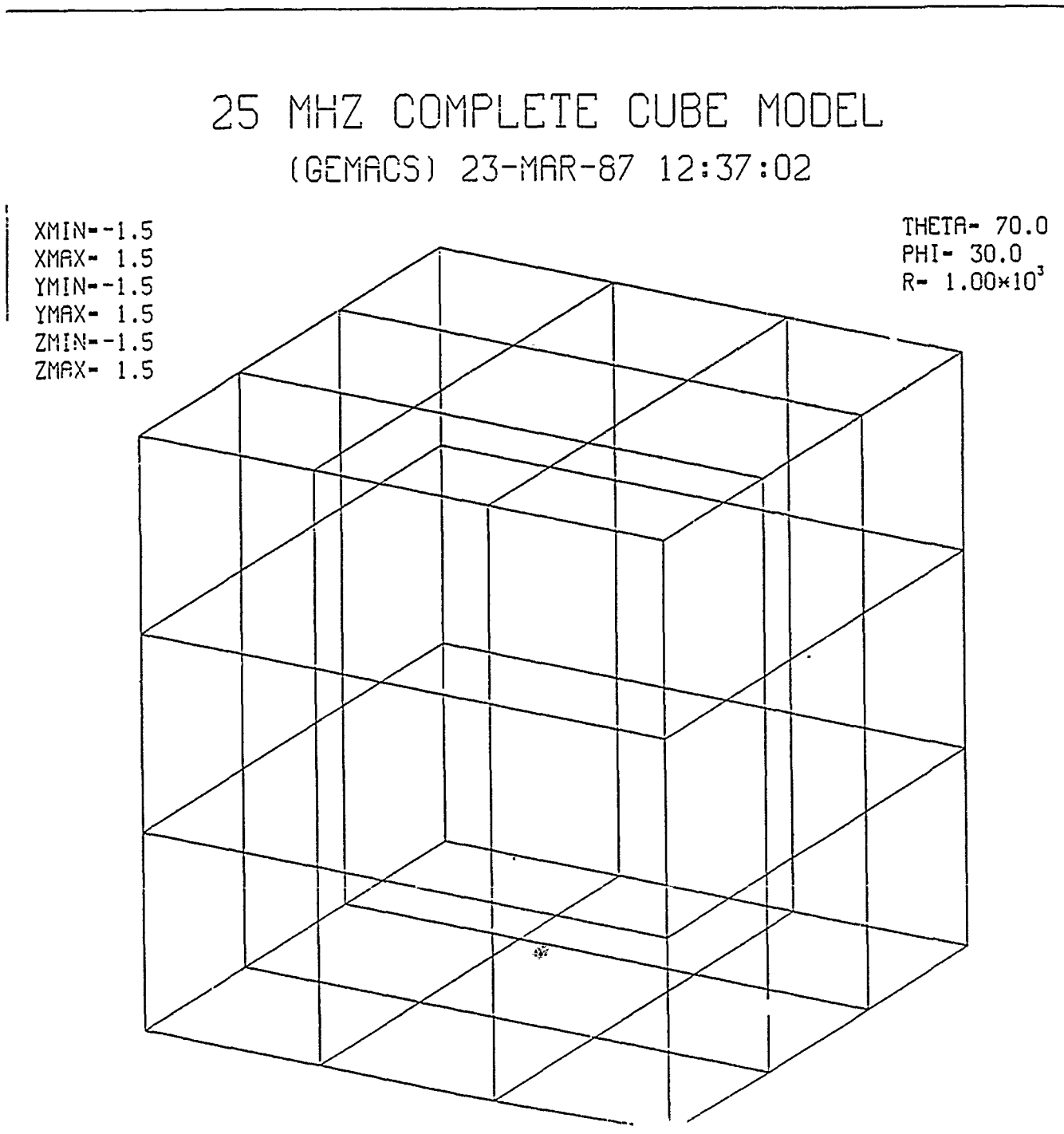


Figure 1b : a Model Consisting of the Front Face of the Cube.

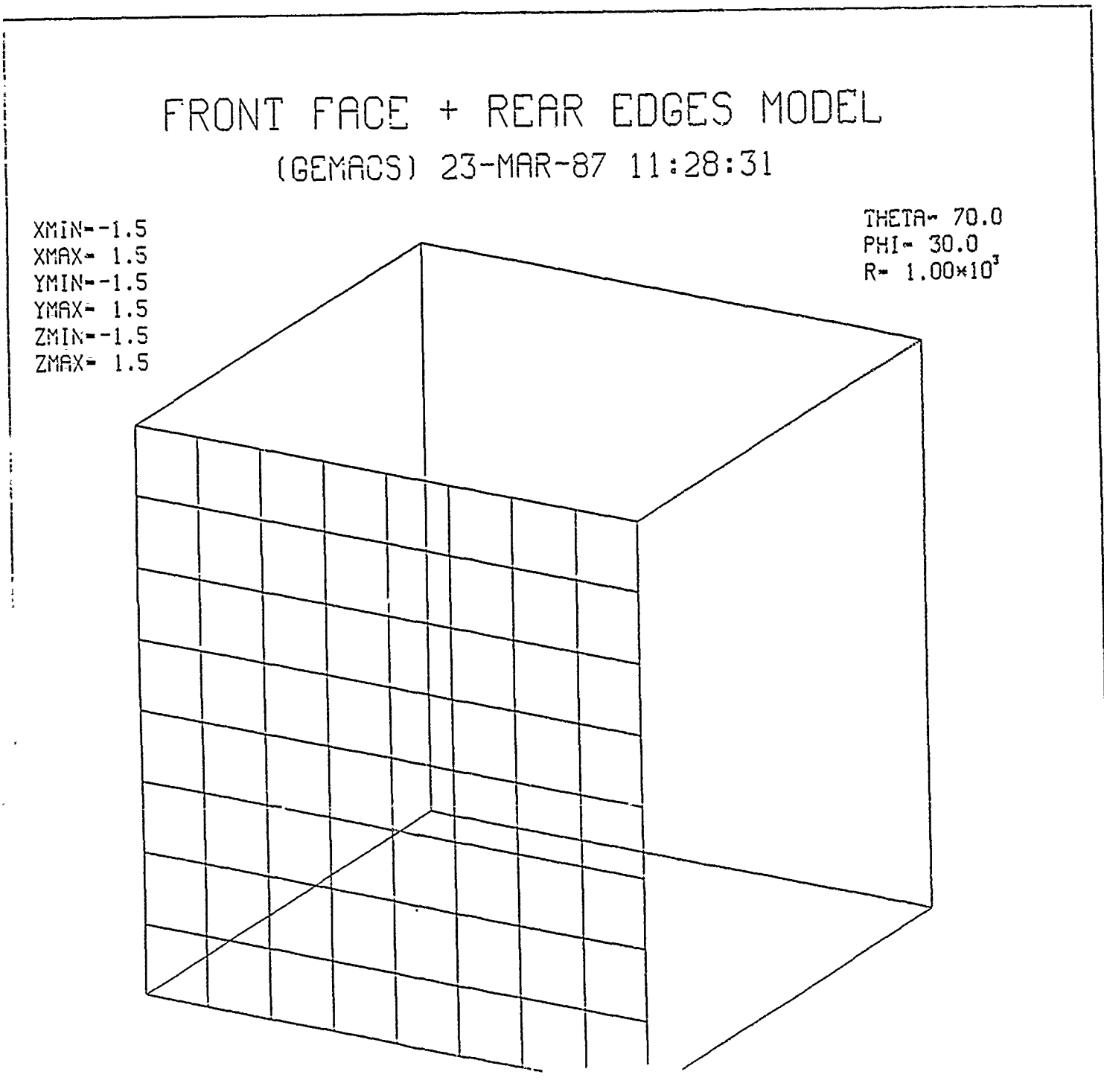
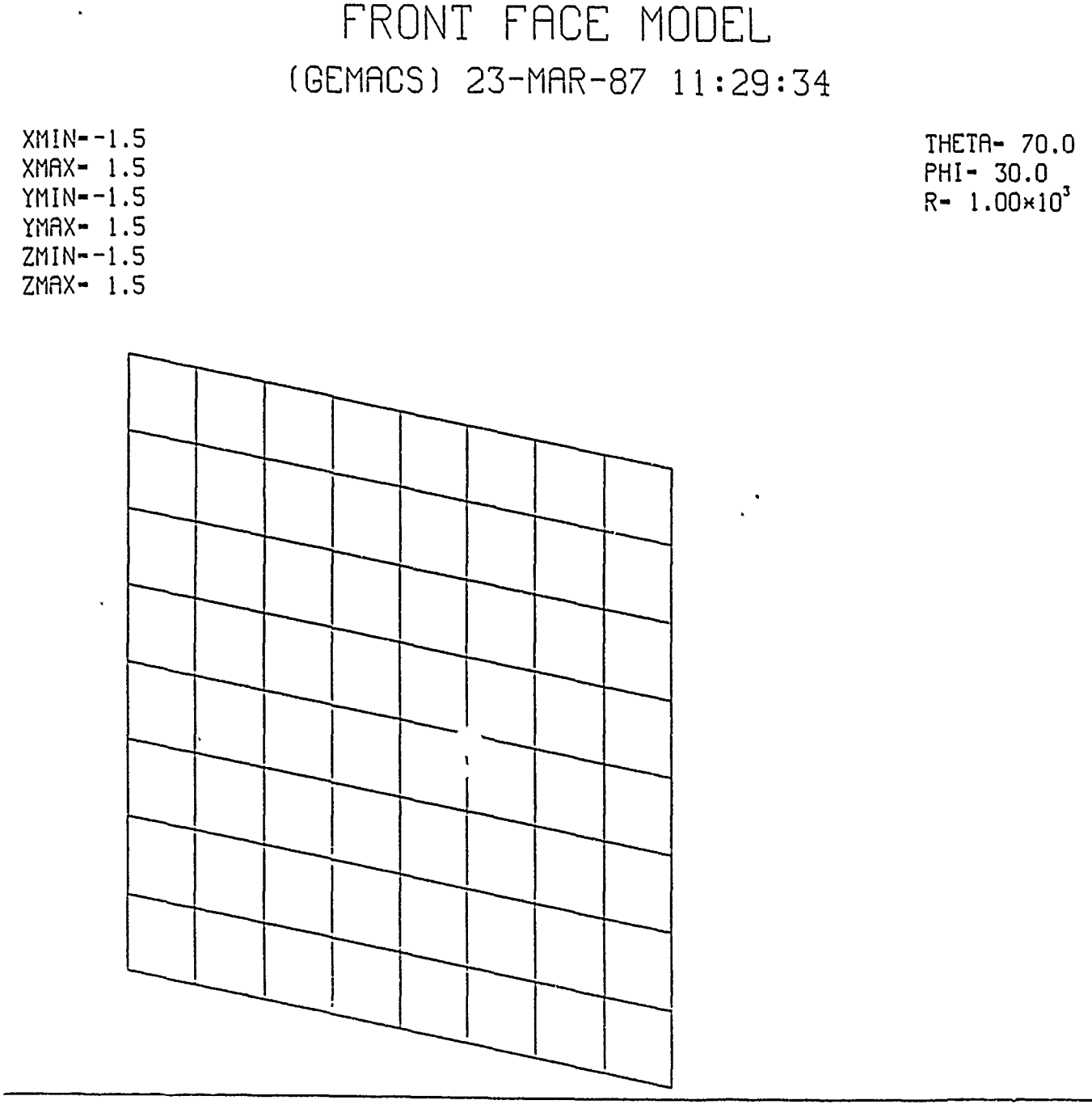


Figure 1c : a Model Consisting of of the Front Face and Rear Edges of the Cube.



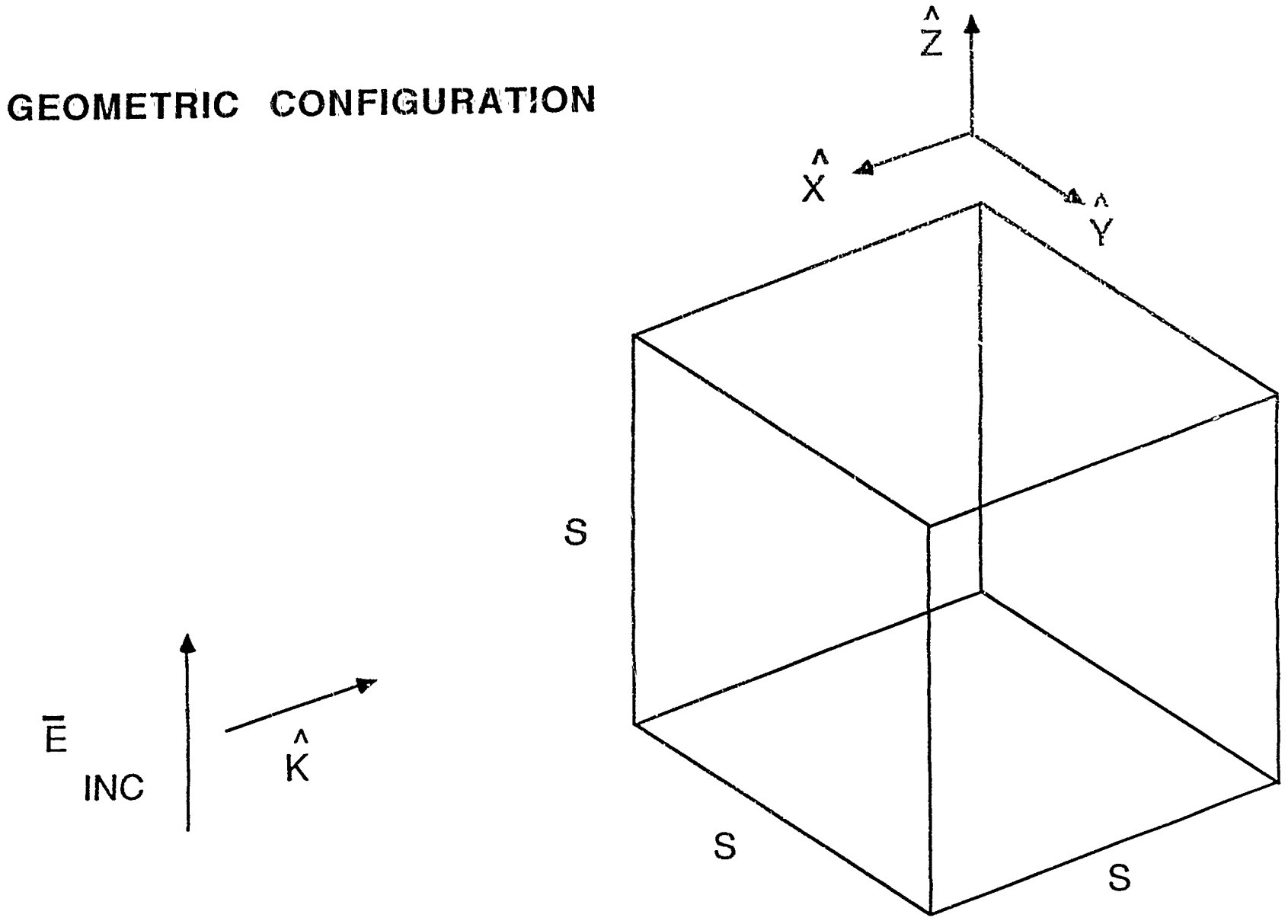


Figure 1d : The General Geometrical Configuration for the Analyses.

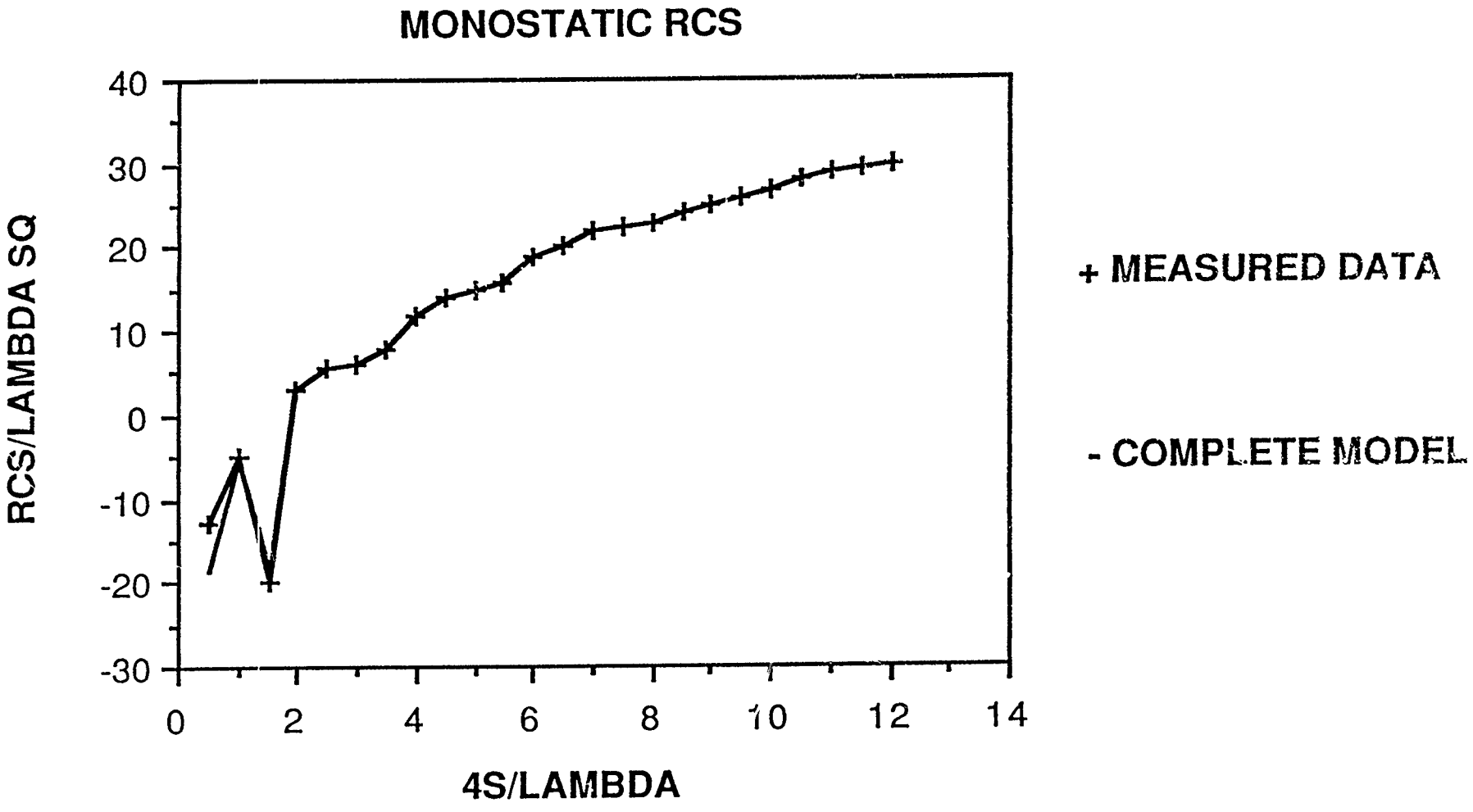


Figure 2. Results for Monostatic RCS as a Function of the Cube Size/Problem Frequency :

Figure 2a : RCS for the Complete Model.

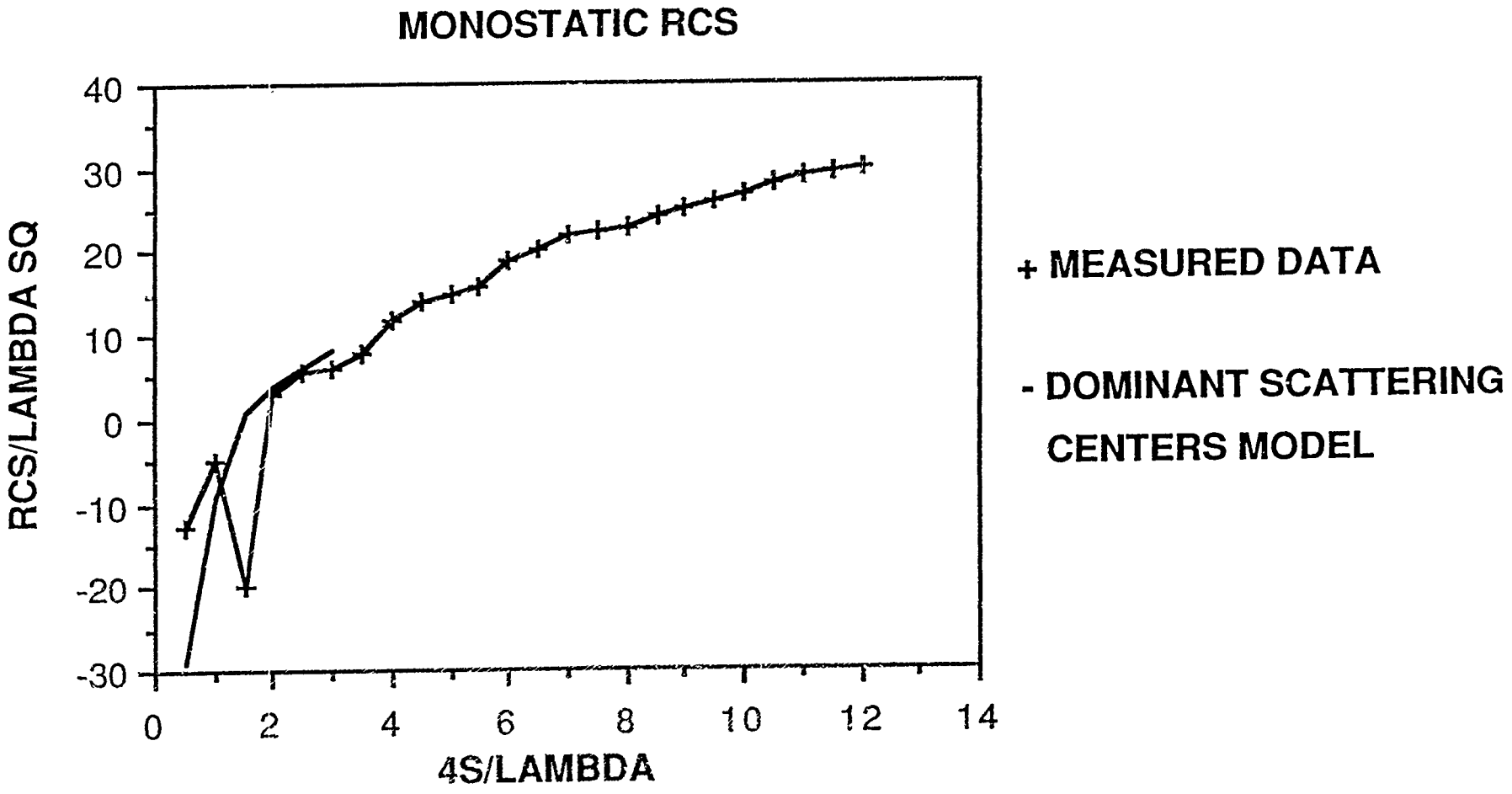


Figure 2b : RCS for the Front-Face-Only Model.

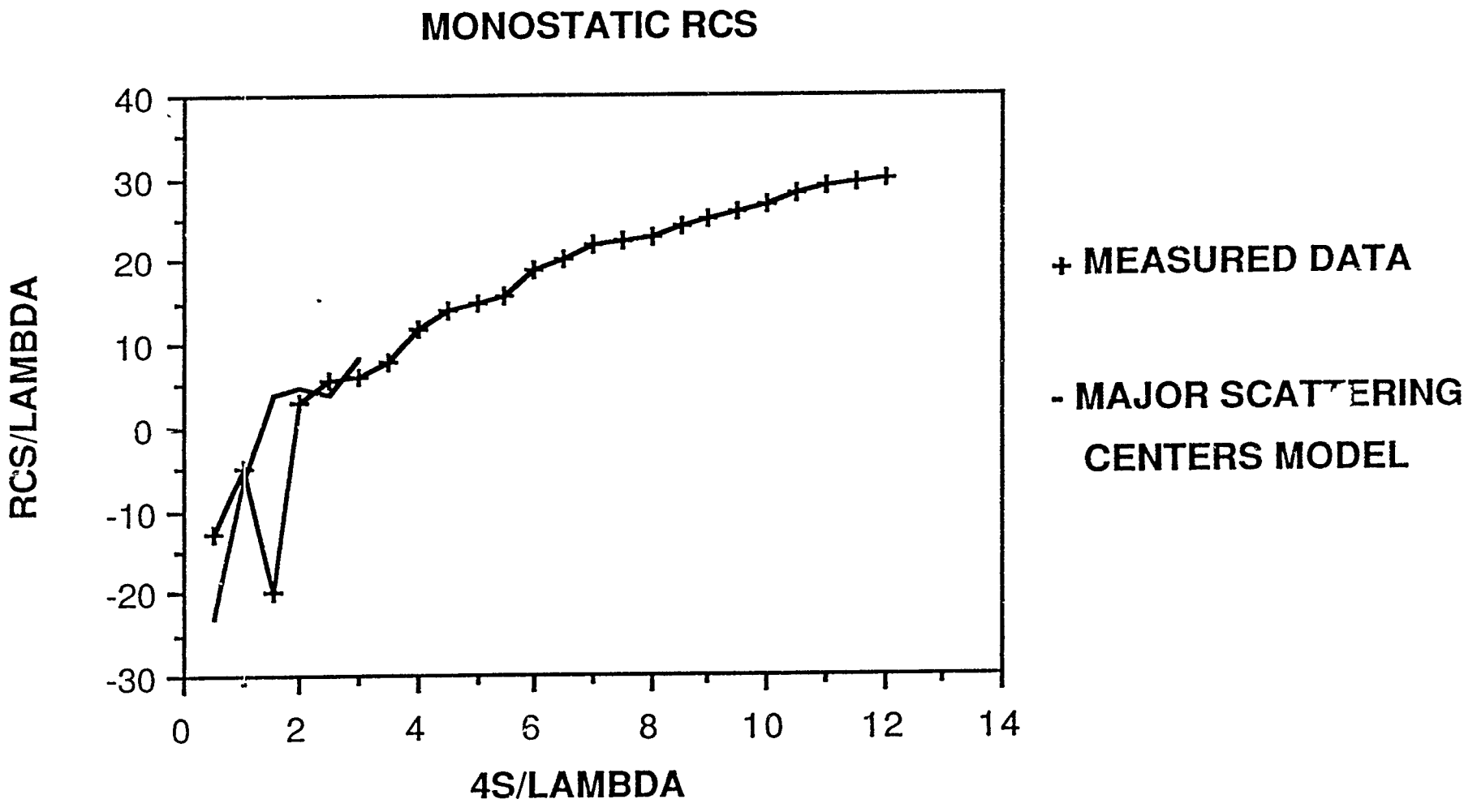


Figure 2c : RCS for the Front-Face-Plus-Rear-Edges Model.

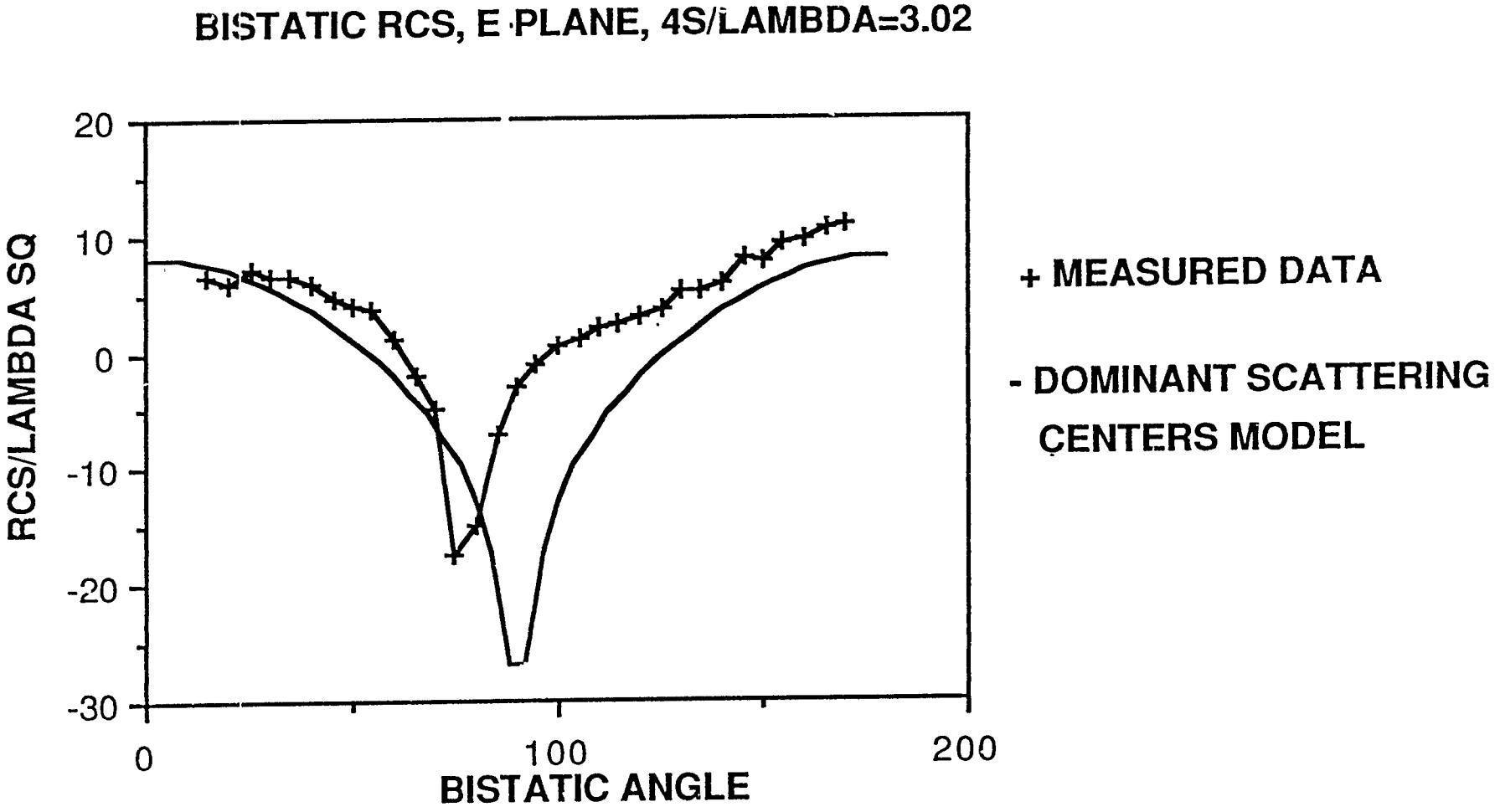


Figure 3. Bistatic RCS for the Front-Face-Only Model :

Figure 3a : E-plane Bistatic RCS.

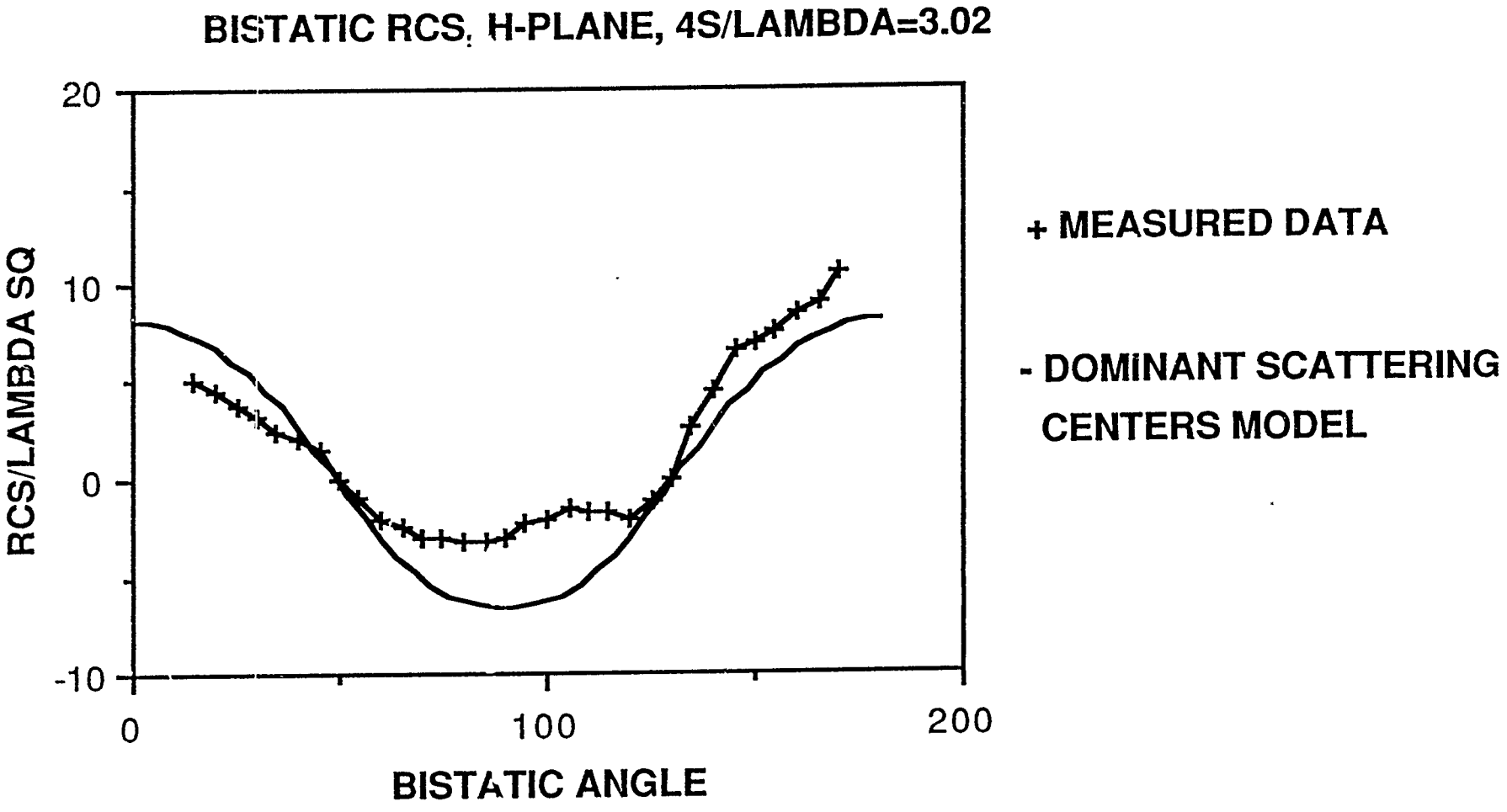


Figure 3b : H-plane Bistatic RCS.

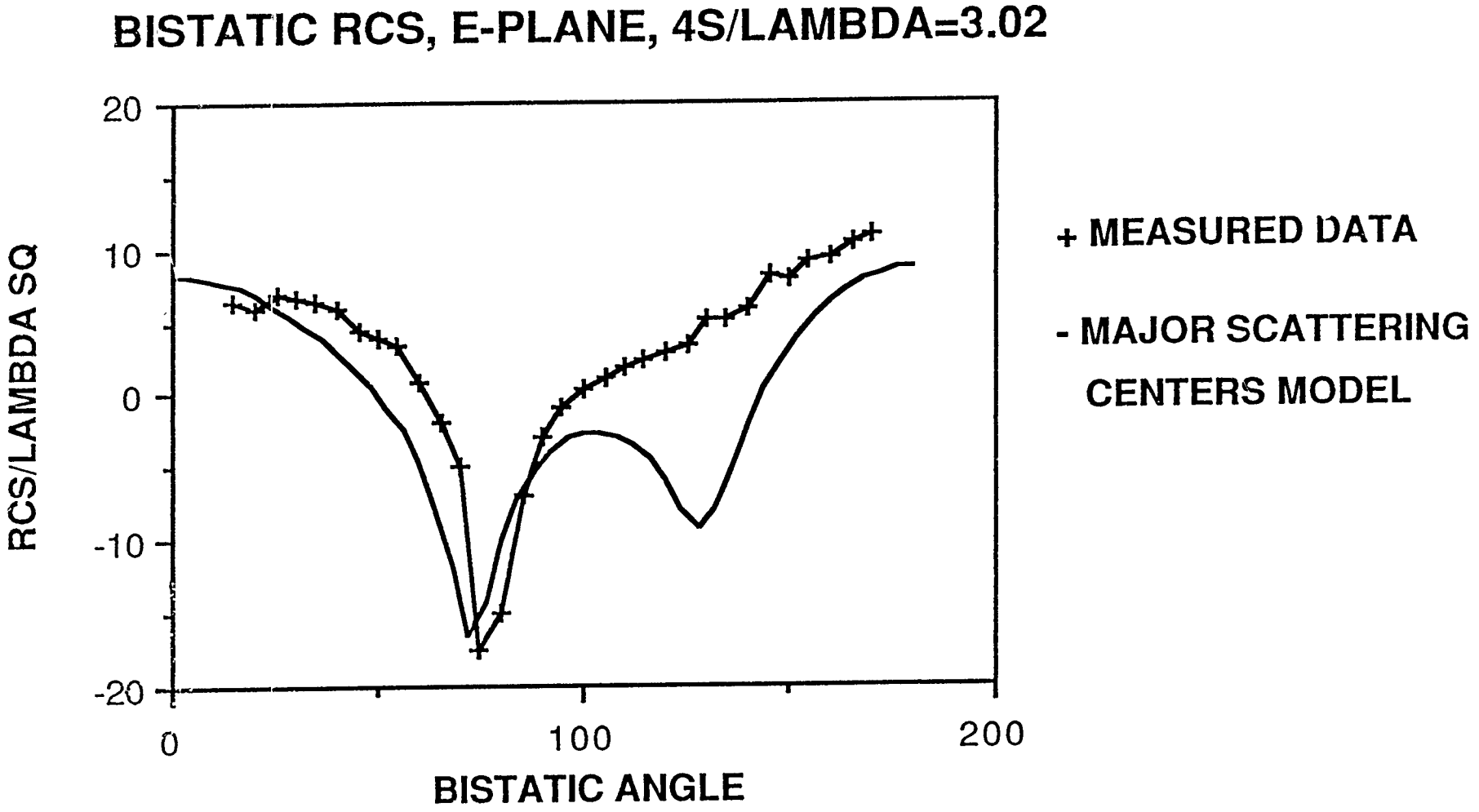


Figure 4. Bistatic RCS for the Front-Face-Plus-Rear-Edges-Only Model

Figure 4a : E-plane Bistatic RCS.

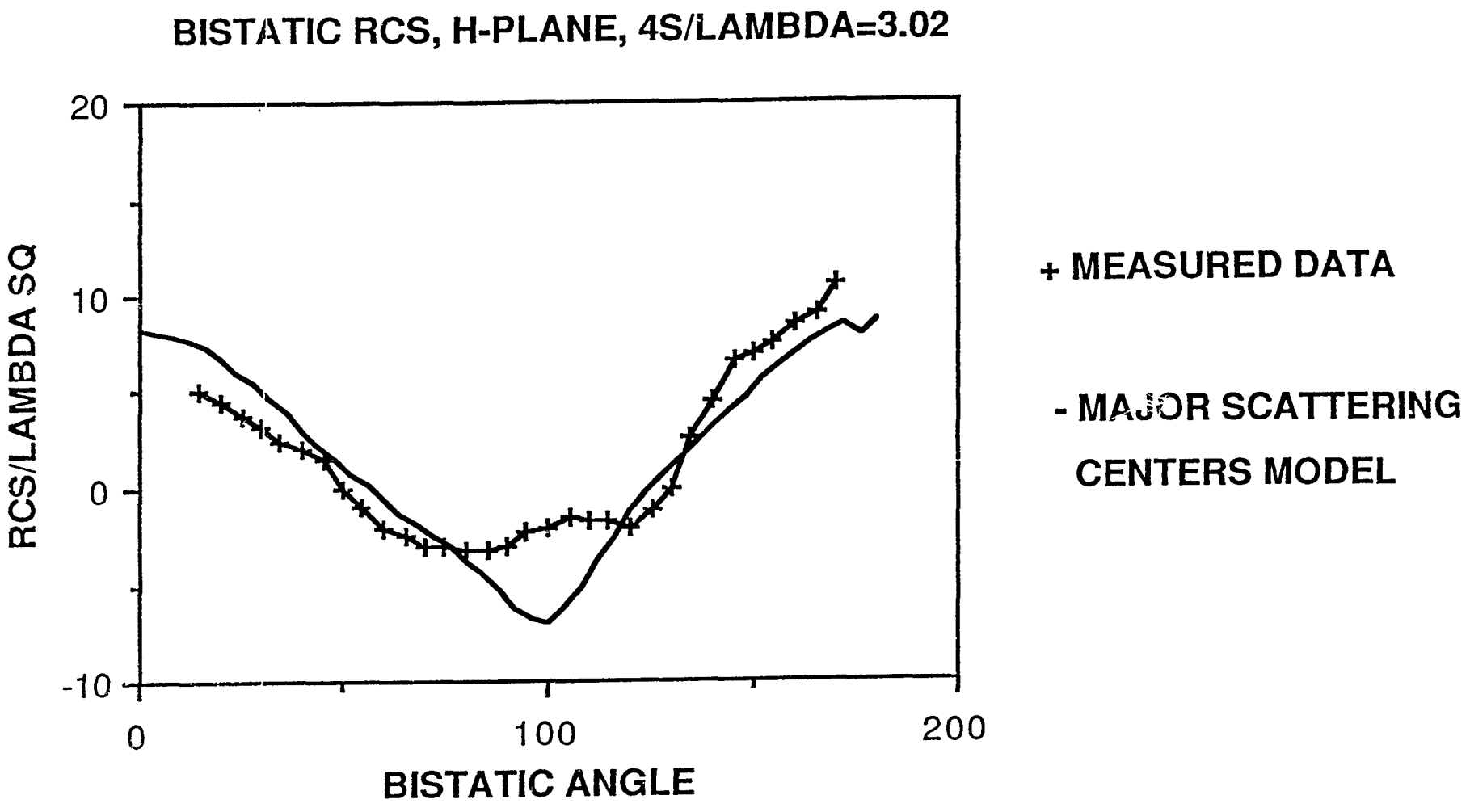


Figure 4b : H-plane Bistatic RCS.

SESSION II - "EM MODELING"

Moderator: R. Marhefka

RECENT UPDATES TO THE NEC-BSC

R. J. Marhefka and J. W. Silvestro
The Ohio State University
ElectroScience Laboratory
1320 Kinnear Road
Columbus, Ohio 43212

Abstract

The NEC-BSC is in the process of being revised and updated. The last major change occured when version 2 came out in 1982. It is being rewritten using FORTRAN 77 capabilities to make the code more adaptable to individual user needs. In restructuring the code several main program operations have been placed in subroutines. By doing so the code can now be easily updated or changed as the situation warrants.

New commands and capabilities have been added in this revision. For example, the new code allows for control of the scattering from individual geometric features (i.e. diffraction from plate 1 edge 2). This can be used to increase physical understanding and/or to greatly decrease run time and to enhance modeling tricks. Pattern control has also been enhanced by including commands that allow non-integer far zone pattern angles, volumetric pattern cuts and individual control of the sources and receivers. The way a moving antenna is defined has been revised to reduce confusion.

The types of antennas that can be input in the source and receiver commands have been updated. A circular current distribution, including a TE_{11} type of distribution, has been added. A new command has been implemented that adds an interpolated antenna. The user inputs a set of measured or calculated data points from several pattern cuts and the code using linear interpolation determines the proper field values over the entire space. Several changes have also been made to the antenna array command in an effort to increase code speed for cases where a complex antenna exists. An extra phase term has been added to the array factor terms for cases where a scatterer is in the far zone of the elements but not in the far zone of the array and the command now allows for each element in the array to have it's own orientation, type and size. This latter change allows for arrays of circularly polarized elements.

A new faster plate shadowing algorithm has also been implemented. Some examples will be given.

The NEC-BSC, a near zone UTD scattering code developed at Ohio State, has been revised. In addition to adding new features the code has been re-

structured in this update. These changes have made the code more powerful and at the same time faster.

The outline presented below shows an overview of the features of the original code. These apply to the new version also.

Overview of NEC-BSC's Features

- Near Zone Scattering Code Utilizing UTD
- User Oriented.
- Multiple Flat Plates.
  - Infinite Ground Plane.
- Multiple Elliptic Cylinders.
- Pattern or Antenna to Antenna Calculations.
- Efficient Representation of Antennas.
- Limited Dielectric Plate Capablity.

The revisions to the code are listed below:

Code Updates

- FORTRAN 77.
- Several Main Program Operations Placed in Subroutines. (command input, initialization and field computation sections)
- Ability to Pick Individual Scattering Centers.
- Enhanced Pattern Commands.
  - Volumetric Pattern Cuts.
  - Moving Sources Independent of Receivers.
- New Antennas.
- Faster Plate Shadowing Algorithm.

The first two items show the restructuring performed on the code. It has been rewritten in FORTRAN 77 and several operations that were performed in the main section of the code are now in subroutines. This last change makes the code more flexible by allowing updates to or replacements for these operations easier to perform later. For example, if someone wanted a new

input set (possibly from a graphics package) the appropriate subroutine could be replaced.

The restructured code allows the user to choose which scattering features are to be included or excluded from the pattern. This can be used to reduce run times by turning off features that are known to have little effect on the overall scattering. It can also be used to isolate the effects of different scattering centers by looking at their scattering individually while still being able to include higher order effects. To illustrate this, example 5 from the orginal users manual was re-run. In this case the diffraction from edge 1 was turned off and then as a another test only the diffraction from edge 2 was used. These are shown in Figure 1.

The next two changes are to the pattern commands. New commands have been added, including ones for volumetric patterns (i.e. patterns where both θ and ϕ vary). These commands are listed below:

New Pattern Commands

VN: volumetric pattern with integer angles

VF: volumetric pattern with non-integer angles

VD: far zone volumetric pattern

GR: range gate (optional range weight)

OB: shadowing only

The ability to move the source and receivers independently is a useful option that can be used to study the coupling between antennas in the presence of scattering objects. This is illustrated in Figure 2 where the coupling between two moving $\lambda/2$ dipoles, with and without a plate between them, is plotted. The dipoles were driven in phase and with unity magnitude.

There have also been many additions to the antenna specification commands. The orginal code allowed for rectangular patches of currents with 3 different tapers. These could be arrayed into a single antenna located at the weighted center with an array factor. This array antenna is quite fast since the shadowing and other ray operations are performed only once for the entire array and not for each element of the array. New features have been added to the array commands, hoping to take advantage of this. Now the elements in the array can have individual orientations and shapes. This would allow the user to have arrays of circularly polarized elements. Another array update is the option to add an extra phase term to the far zone array factor approximation for the cases where the structure is not quite far enough away to be in the far zone. The new array factor is given:

$$FA = \sum_{n=1}^{N} I_n e^{jk(\hat{r}\cdot\vec{x}_n + \frac{1}{2r}((\hat{r}\cdot\vec{x}_n)^2 - r^2))}$$

where $\vec{r} = r\hat{r}$ = observation point and $\vec{x}_n$ = source location.

This must be used with care since the shadowing would not be correct if the structure is too close. An example of the effect of this extra term on an array pattern is shown in Figure 3 where the pattern is measured at $D^2/2\lambda$ for 5 $\lambda/2$ dipoles. These array changes were implemented to allow the user to make use of the speed advantage of the array commands.

In addition to the array updates mentioned above new antennas have been added. Two circular patches of current have been included. The first is a constant current over a circular area and the second is a TE_{11} current distribution. These could be used to model circular waveguides or conical horns. Another command that has been added is for an interpolated antenna. With this command user entered data points for various phi pattern cuts (at various theta angles) are linearly interpolated by the computer. This means that antennas with analytic pattern functions too complicated to be modeled using the existing antennas could be included by inputting calculated field values for variuos pattern points. Also, antennas where only measured data exists could be included by inputting these measured values directly. The accuracy of this antenna is dependent on the number of points entered. This is illustrated in Figure 4 where the pattern of a 5 element array is plotted using the analytic pattern factor and using the interpolated pattern factor for two different sets of input data.

Finally, it was determined using timing studies that for multi-plated structures that the code was spending alot of time in the plate shadowing algorithm. A new algorithm was devised that sped up this operation and thus greatly improved performance. An example of this is given in Figure 5. A model of the corner of a possible space station configuration was run. The model had 26 plates and a single slot antenna. The pattern cut is for θ from 0-90 degrees calculated at every degree. The CPU time with the orginal algorithm was 5.66 minutes, but with the new algorithm this time was reduced to 2.89 minutes. These improvements are of course dependent on the number of plates present.

In conclusion it can be seen that the changes implemented in the code should allow the user to decrease run times for many situations. The new features will also allow the code to be used to analyze more complex problems and to include new antenna models. In closing, the following table shows the ongoing areas of development:

On Going Areas of Development

- More Complex Curved Surfaces (i.e. cones, ellipsoids, etc.).
- Coated Cylinders.
- Higher Order Terms (i.e. plate-cylinder interactions).
- Improved I/O

- Drawing of Input (GKS)
- Drawing of Output (GKS)
- Improved Commands

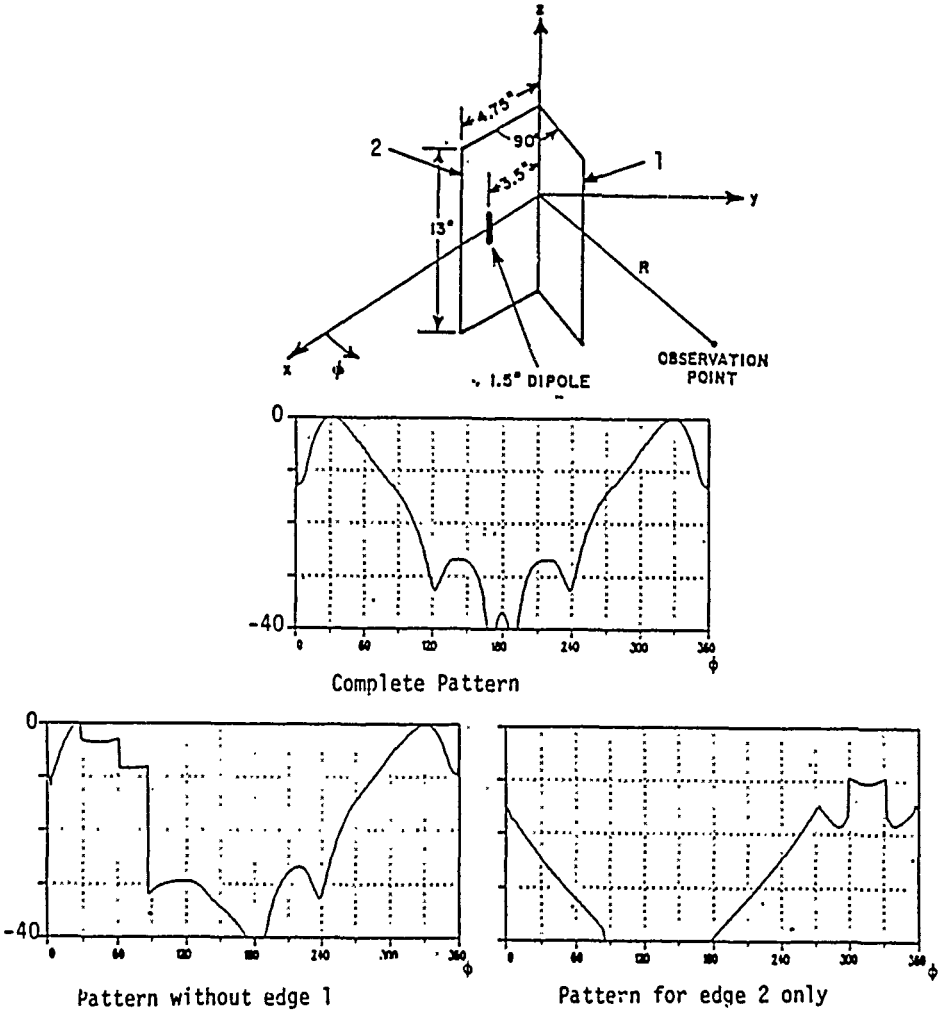


Figure 1: Example of control of individual scattering centers.

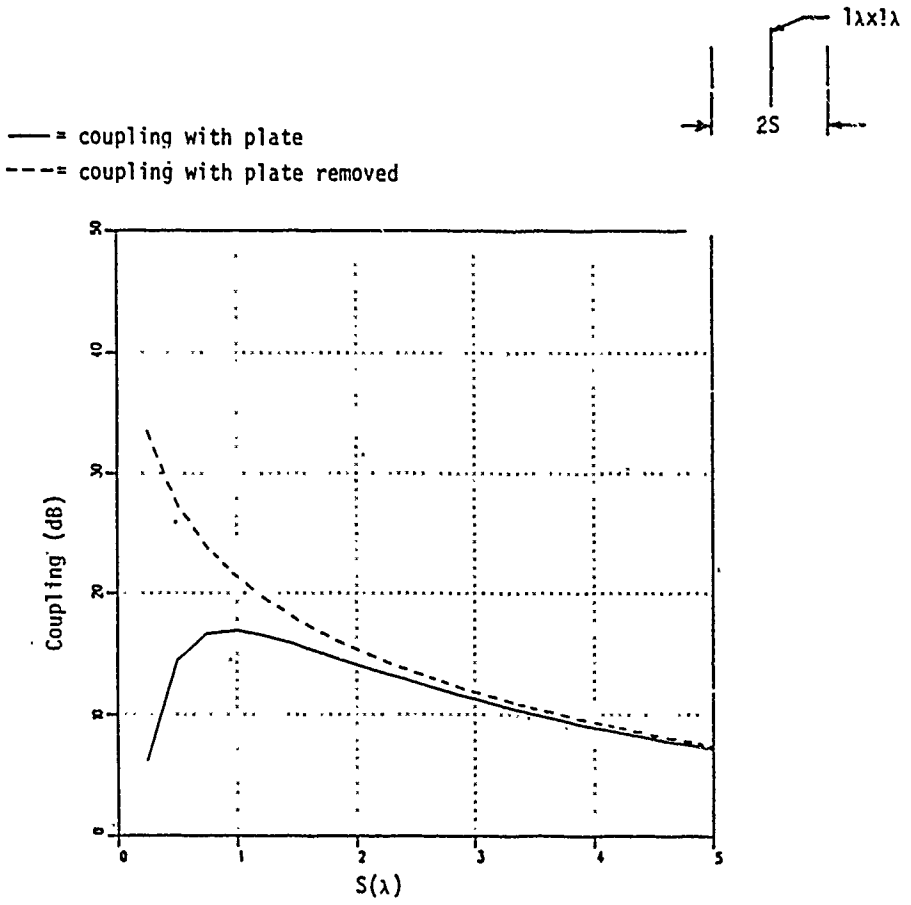


Figure 2: Example of source and receiver moving independently

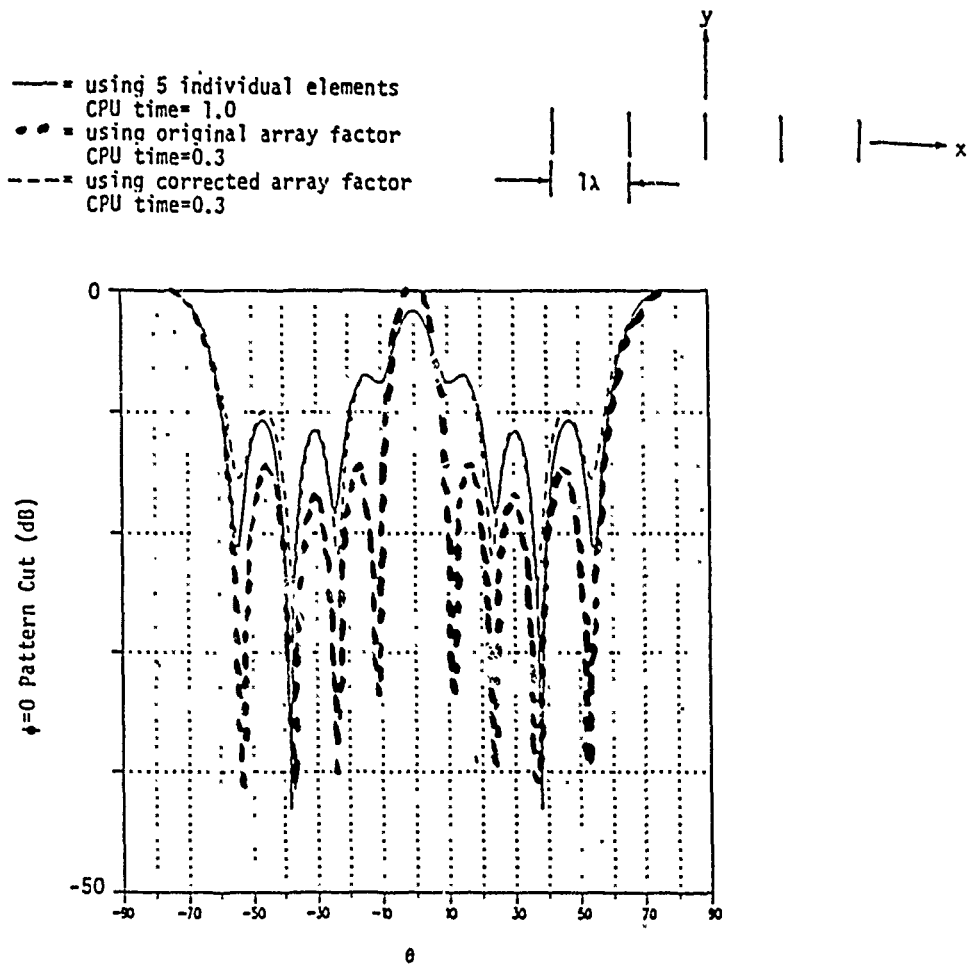


Figure 3: Example of added phase term in array factor. CPU times are normalized.

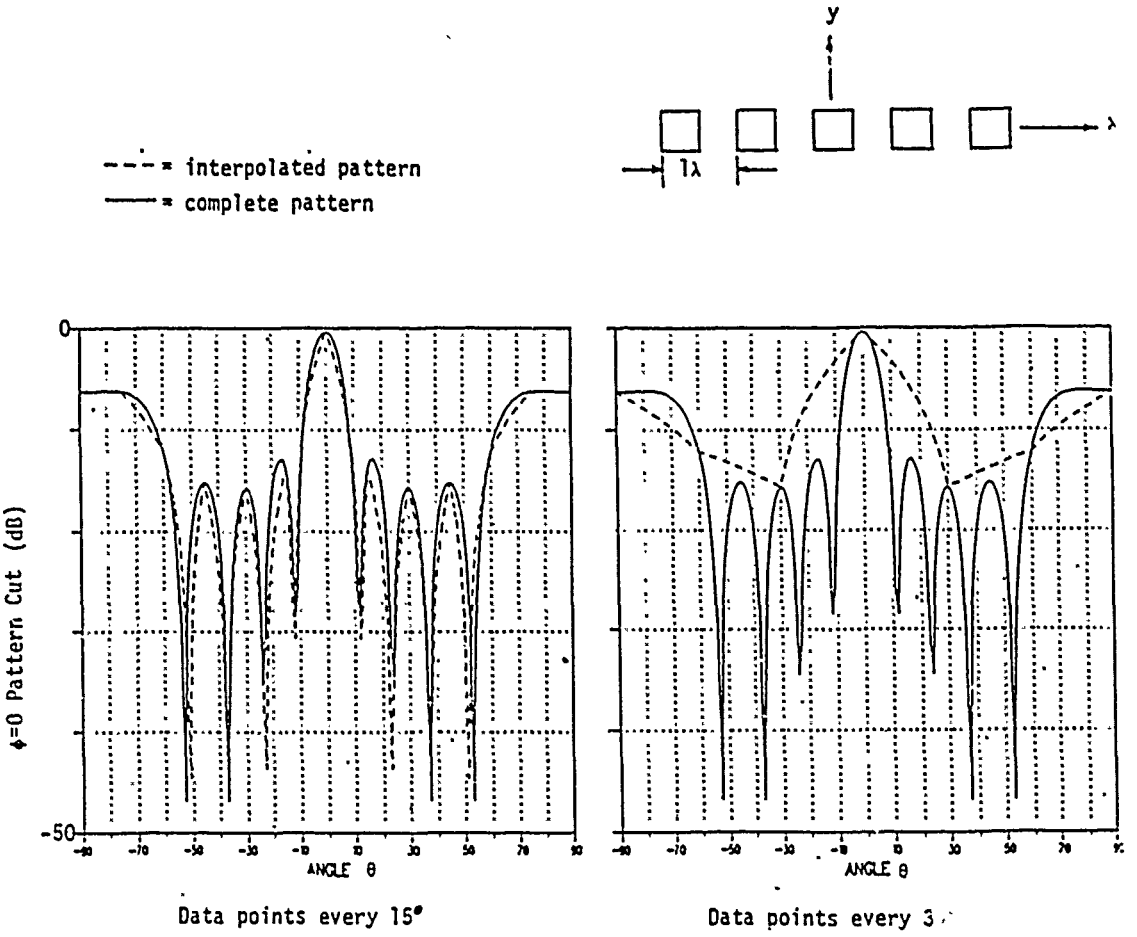


Figure 4: Examples of interpolated antenna command.

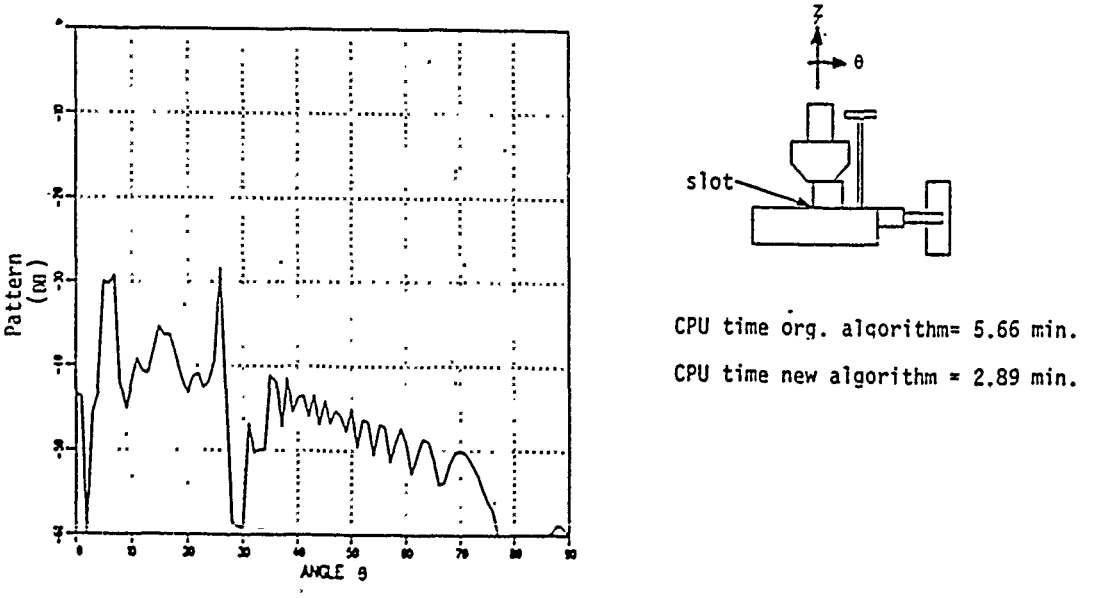


Figure 5: Case run in shadowing algorithm test (times for the code run on a VAX 11/780)

TRANSFINITE ELEMENTS - A HIGH EFFICIENCY METHOD FOR ELECTROMAGNETIC SCATTERING

Z. J. Cendes Jin-Fa Lee
Department of Electrical and Computer Engineering
Carnegie Mellon University
Pittsburgh, PA 15213

The numerical solution of open electromagnetic problems is often performed by using a technique developed by Chang and Mei[1] called the "unimoment method". In this procedure, the finite element method is used to model the fields inside a circular boundary enclosing the scatterer and cylinderical harmonics are used to represent the fields outside. A unique solution is obtained by matching the interior and exterior fields with respect to both function and normal derivative values at the nodal points on the circle. While this procedure works, it has two disadvantages: For n expansion functions in the exterior region, 2n finite element boundary value problems must be solved to determine the interior basis functions, and numerically inaccurate derivatives of the finite element solution must be computed for each mode for each point on the boundary. We show here that a new procedure called the transfinite element method provides a more efficient method for solving electromagnetic scattering problems. In the transfinite element method, a single set of finite element basis functions is used to represent the fields inside the circular boundary and a separation of variables technique used to compute the fields on the outside. In this way, only a single finite element boundary value problem must be solved for each scattering problem and the need to compute derivatives of the finite element solutions is eliminated. Examples of the input and solution of scattering problems such that shown in Figure 1 will be demonstrated live (conditions permitting) on an PC.

1. S.K. Chang and K.K. Mei, "Application of the Unimoment Method to Electromagnetic Scattering of Dielectric Cylinders", IEEE Trans. on AP, pp.35-42, 1976.

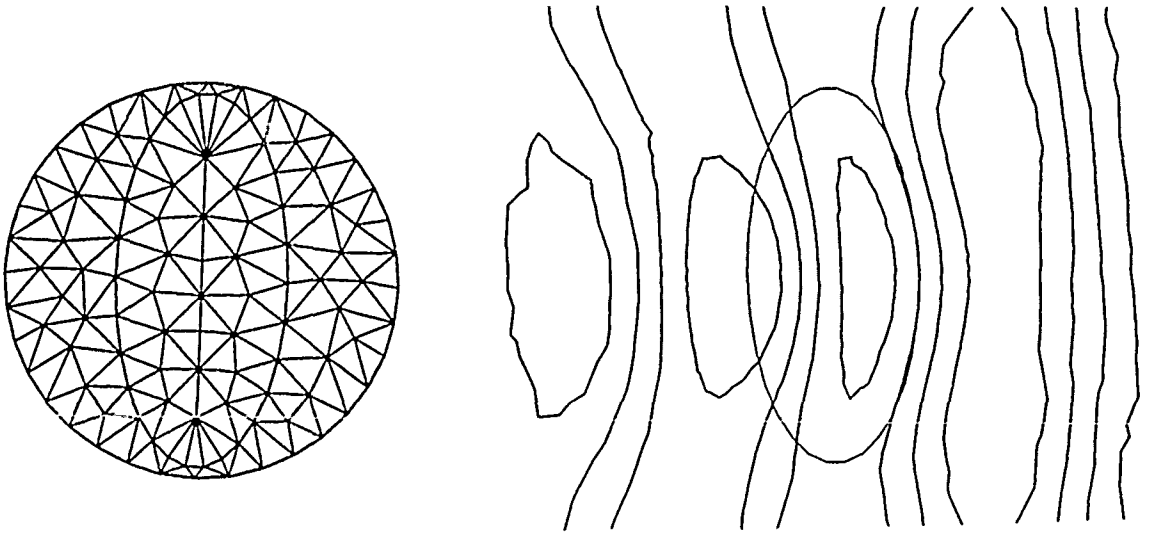


Figure 1. Transfinite element solution of the E field scattered by an elliptical cylinder.

ADAPTIVE SPECTRAL RESPONSE MODELING OF PLANAR MMIC DEVICES

Z. J. Cendes Jin-Fa Lee
Department of Electrical and Computer Engineering
Carnegie Mellon University
Pittsburgh, PA 15213

We introduce a new, highly efficient procedure for modeling MMIC devices. The basis of the procedure is the transfinite element method in which modal basis functions are combined with finite element basis functions to provide solutions for problems involving open boundaries. We show that this procedure results in a symmetric sparse matrix equation that can be solved by using the pre-conditioned conjugate gradient algorithm. Further, we develop a spectral response estimation procedure by which solutions at a few adaptively selected frequencies are used to generate the full solution in the frequency range of interest. With large problems, this approach is orders of magnitude more efficient than the existing alternatives. In particular, with the standard deterministic approach, the frequency response must be computed many times to give sufficient accuracy. In the adaptive approach developed here, the matrix equation approximating the system is solved at only a few selected frequencies and then these solutions are used as basis functions to generate the full spectral response. The operation of the procedure on an PC will be demonstrated live (conditions permitting).

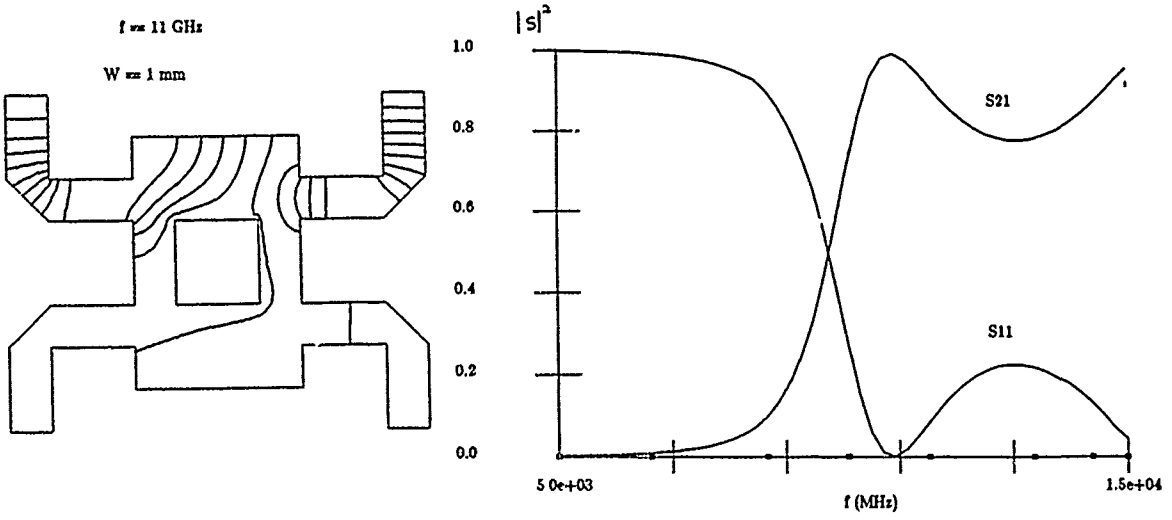


Figure 1. Typical field solution and frequency dependent scattering parameters for a four-port circuit.

SESSION III - "ANTENNAS NEAR GROUND"

Moderator: R. Marhefka

SRI International

HF GROUND AND VEGETATION CONSTANTS

George H. Hagn
Information Sciences and Technology Center
SRI International
1611 North Kent Street
Arlington, Virginia 22209

(703) 524-2053

Presented at the 3rd Annual Meeting of the
Applied Computational Electromagnetics Society (ACES)

Monterey, California

24-26 March 1987

SRI International®

ABSTRACT

Analytical models of propagation and antenna performance such as the Numerical Electromagnetics Code (NEC) require accurate input data in order to produce accurate answers. NEC-3 requires information about the macroscopic electrical properties of the soil, the permittivity (relative dielectric constant) and conductivity, in order to model properly wire antennas in proximity to the earth. Most of the values available in the literature are "constants," and many of them were derived from data taken at MF using AM broadcast stations so they do not necessarily pertain to the HF band. The actual values for most soils exhibit dispersion (i.e., they are a function of frequency) which is a primary function of the moisture content of the soil and a secondary function of other variables (e.g., temperature, compaction, mineralization, etc.). This has been known since the mid-1930s [Smith-Rose, 1934, 1935]. This paper will review selected handbook values for ground constants at HF; present examples of data measured at various sites in CONUS and around the world with the SRI open wire line (OWL) ground constants kit and E(d) method; and present recommended "generic" values for different types of terrain which are useful in the absence of measured data. These "generic" curves of ground constants versus frequency, when used in NEC, should provide some improvement in the predicted results relative to the results which would have been obtained using current handbook values. The "generic" curves are especially useful for sensitivity analyses. In-situ measurements with the SRI OWL kit should provide the best NEC results however, and such measured values should be used for NEC-3 validations, site calibration, etc. The E(d) (or wave tilt) techniques can be used in open areas to supplement the OWL technique.

INTRODUCTION

The macroscopic electrical and magnetic properties of media are the electrical permittivity (dielectric constant), the magnetic permeability, and the conductivity. It is convenient to normalize the permittivity and permeability by their free-space values to obtain the relative dielectric constant and relative permeability. These values are given in Table 1, where the SI units are given. Note that Siemens/m (S/m) has replaced mho/m as the preferred unit for conductivity.

A distinction needs to be made between the complex intrinsic electrical and magnetic properties useful for microscopic analyses of the media required for physical insight and the real effective electrical and magnetic properties required for use in models based on Maxwell's equations to solve antenna and propagation problems such as the Numerical Electro-

TABLE 1

MACROSCOPIC ELECTRICAL PARAMETERS

ε =	Permittivity (Dielectric Constant), F/m
ε_o =	8.8542×10^{-12} F/m
ε_r =	$\varepsilon/\varepsilon_o$ = Relative Dielectric Constant
μ =	Permeability, H/m
μ_o =	4×10^{-7} H/m
μ_r =	μ/μ_o = Relative Permeability
σ =	Conductivity, S/m (mho/m)

magnetics Code (NEC) [Burke and Poggio, 1981; Burke, 1983; Breakall, et al., 1985]. The equations for these intrinsic properties (given the subscript i) and the effective properties (given the subscript e) are summarized in Table 2, which also gives the relationship between the intrinsic and effective properties. The complex intrinsic values also can be used in Maxwell's equations, of course, when the equations are formulated using them properly; however, the NEC formulation assumes the real effective values.

In the general case, it is not possible to distinguish between σ' (the ionic conduction current at DC) and the $\omega\varepsilon_o \varepsilon_r''$ (the polarization effect of the medium). Also, it is not possible to distinguish between ε_r' (the real part of the relative dielectric constant) and $\sigma''/\omega\varepsilon_o$ without an atomic or molecular interpretation of the medium and laboratory measurements of the variation of σ_e and ε_{re} with both frequency and temperature. For example, the ionic conduction is a function of temperature, but (to a first order) the polarization effect is independent of temperature [King, et al., 1981].

Table 2

CONSTITUTIVE RELATIONS FOR HOMOGENEOUS MEDIA

$$\bar{D} = \epsilon_r \epsilon_o \bar{E}$$
$$\bar{B} = \mu_r \mu_o \bar{H}$$

INTRINSIC (i)	EFFECTIVE (e)
COMPLEX	REAL
MICROSCOPIC	MACROSCOPIC
ATOMIC OR MOLECULAR	BULK PROPERTIES
$\epsilon_{ri} = \epsilon_r' - j\epsilon_r''$	$\epsilon_{re} = \epsilon_r' - \sigma''/\epsilon_o\omega$
$\sigma_i = \sigma' - j\sigma''$	$\sigma_e = \sigma' + \omega\epsilon_o\epsilon_r''$
$\mu_{ri} = \mu_r' - j\mu_r''$	$\mu_{re} \cong \mu_r' \cong \mu_o$

$$\sigma' - j\sigma'' + j\omega(\epsilon_o\epsilon_r' - j\epsilon_o\epsilon_r'') = \sigma_e + j\omega\epsilon_o\epsilon_{re} \quad \text{(EFFECTIVE CONDUCTIVITY)}$$

$$\frac{\sigma' + \omega\epsilon_o\epsilon_r''}{\omega\epsilon_o\epsilon_r' - \sigma''} = \frac{\sigma_e}{\omega\epsilon_o\epsilon_{re}} = \delta_e \quad \text{(LOSS TANGENT)}$$

USE FOR PHYSICAL INSIGHTS

USE IN MAXWELL'S EQUATIONS

When considering the macroscopic electrical and magnetic properties of soil for use in modeling antennas and propagation, one usually does not care whether the effective conductivity results from ionic conduction or from the polarization effect. The important consideration is that the proper effective value is used. It should be noted that soil in-situ is a mixture of components including air and water. The dielectric constant of mixtures [Encyclopedia of Physics, 1958] based upon fractional volumes provides bounds on the actual value, but the bounds are too broad to be useful for this application. The asymmetrical shape of the water molecule (H_2O) and the electrical properties of mixtures contribute to a variation of σ_e and ε_{re} with frequency (for any given soil) and moisture content (for the same soil and frequency)[King, et al., 1981]. One result is that ε_{re} for very moist soil can greatly exceed the value for water (approximately 80) at the low end of the HF band. This result has proven surprising to those who are accustomed to using handbook values [Terman, 1943; ITT, 1985; CCIR, 1982] for "ground constants" (see Table 3) under the assumption that these electrical and magnetic properties really are constants for a given type of soil independent of frequency and moisture content.

One method of determining the effective properties of a medium such as soil (also called earth or ground) is to measure the propagation constant $\Gamma = \alpha + j\beta$ in situ or in the laboratory and compute σ_e and ε_{re} from α and β. The values of σ_e and ε_{re} for the bulk medium (e.g., soil) are then used as σ and ε_r in models such as NEC or Norton's smooth earth model [Norton, 1941; as corrected by R.J. King], to solve antenna or propagation problems. Hereafter in this paper we will assume that σ and ε_r refer to the real macroscopic parameters which are used in Maxwell's equation in models such as NEC.

The relative magnetic permeability is unity at HF for most soils except for those containing magnetic minerals such as magnetite, ilmenite, etc. Therefore, we will concentrate in this paper on the effective values of permittivity and conductivity in the HF band (defined here as 2-30 MHz) as used (assuming $e^{j\omega t}$ time variation of $\overline{H}$ and $\overline{E}$):

Table 3

HANDBOOK VALUES OF GROUND CONSTANTS FOR SELECTED TERRAIN CATEGORIES

TERRAIN CATEGORY	SOURCE:	RELATIVE DIELECTRIC CONSTANT, ϵ_r CCIR (HF)	ITT (LF,MF)	TERMAN (MF,HF)	CONDUCTIVITY (S/m) CCIR (HF)	ITT (LF,MF)	TERMAN (MF,HF)
Sea Water		70	80	81	5	5	4.64
Fresh Water (20°)		80	80	80	0.003	0.008	0.001
Wet Ground		30			0.01		
Pastoral, low hills, rich soil (e.g., Dallas, TX; Lincoln, NE)				20			0.03
Rich agri[illegible]l land, low hills			15				0.01
Medium dry ground		15			0.001		
Pastoral, low hills, rich soil (e.g., OH, IL)				14		0.01	
Rocky soil, steep hills (New England)				14			0.002
Pastoral, medium hills, forestation, (e.g., MD, PA, NY.)				13			0.006
Pastoral land, medium hills, forest			13			0.005	
Pastoral, medium hills, forestation, heavy clay (e.g., VA.)				13			0.004
Marshy, forested flat land			12			0.008	
Flat country, marshy, densely wooded (e.g., LA near Mississippi River)				12			0.0075
Rocky land, steep hills			10			0.002	
Sandy, dry flat coastal land			10	10		0.002	0.002
Cities, residential area			5			0.002	
Mountainous, hills up to 3000 Feet			5			0.001	
Cities, industrial areas (average attenuation)				5			0.001
Cities, industrial areas (maximum attenuation)			3	3		0.0001	0.0001
Very dry ground		3			0.0001		
Dry glacier in mountainous area, northern permafrost (MF)					0.00001		
Antarctica (MF)					0.000001		

$$\nabla \times \bar{H} = (\sigma + j\omega \varepsilon_0 \varepsilon_r)\bar{E}$$

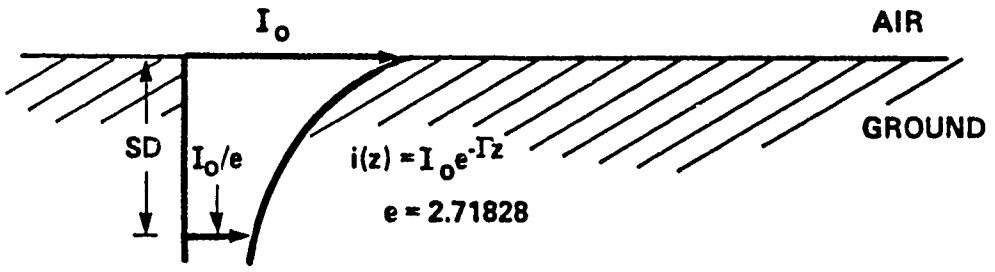
$$\nabla \times \bar{E} = \mu_r \mu_0 \bar{H}$$

Other useful parameters to compute from the effective properties are the dissipation factor and skin depths. The dissipation factor (DF, also called loss tangent) is defined as $\sigma / \omega \varepsilon_0 \varepsilon_r$. When DF >> 1 we have a lossy conductor and when DF << 1 we have a lossy dielectric. The transition when DF $\approx$ 1 (corresponding to a semiconductor) occurs in (or just below) the HF band for many soils.

The skin depth (SD) is that depth into the medium at which the currents have decreased to 1/e of their value at the surface, where e = 2.71828. This concept is illustrated in Figure 1. The equation for skin depth pertinent to a lossy conductor has been given in nomograph form [Wheeler, 1952]. Unfortunately, this nomogram does not apply at HF for most soils, and the more general equation given in Figure 1 must be used.

METHODS OF MEASUREMENT

Many methods of measurement have been developed for obtaining the effective electrical and magnetic properties of soil, and some of these are listed in Table 4. These methods were surveyed by the CCIR [1982a] and by Lytle in 1974 and 1979. The IEEE has recommended practices for measuring ground conductivity and these [IEEE, 1974] are being reviewed and revised by the IEEE Antennas and Propagation Wave Propagation Standards Committee [King, Cavanagh, 1987]. The data and generic curves of relative dielectric constant and conductivity presented in this paper were obtained using the SRI open wire line (OWL) ground constants kit [Goldstein, et al., 1967; Hagn and Gaddie, 1983, 1984] which was developed using techniques originally suggested by Kirkscether in 1960. The SRI OWL kit (see Figure 2) permits sampling in situ in proposed and existing antenna fields. The kit works well in the HF band, but it is not possible to insert the probes down to a skin depth in the drier soils. It is necessary to use a priori knowledge of the homogeneity of soil's electrical and magnetic properties



LOSSY CONDUCTOR $(\sigma \gg \omega \epsilon_r \epsilon_o)$

$$SD = \frac{\sqrt{2}}{\sqrt{\sigma \omega \mu}} \text{ , m}$$

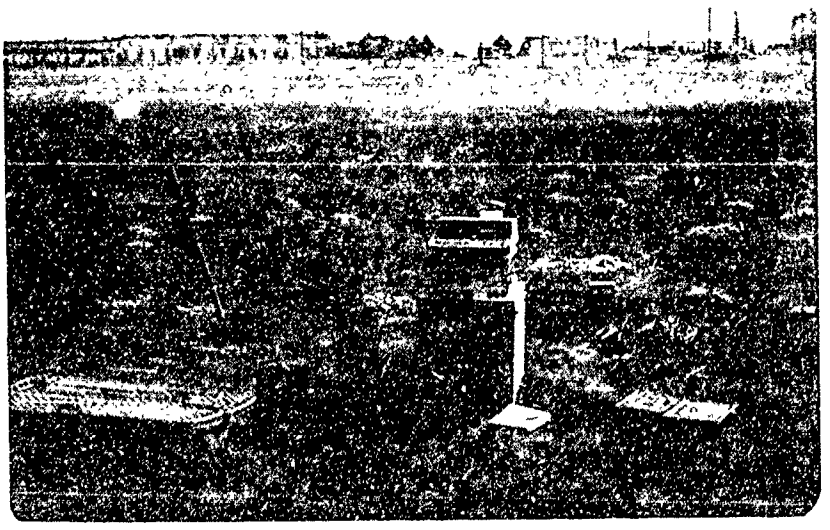
GENERAL CASE $(\sigma \lesssim \omega \epsilon_r \epsilon_o)$

$$SD = \frac{1}{\sqrt{\sqrt{\frac{\omega^4 \mu^2 \epsilon_o^2 \epsilon_r^2}{4} + \frac{\sigma^2 \omega^2 \mu^2}{4}} - \frac{\omega^2 \mu \epsilon_o \epsilon_r}{2}}} \text{ , m}$$

Figure 1 SKIN DEPTH (SD)



a) View toward Gang 1



b) View toward Transmitter Building

Figure 2 SRI OWL KIT IN USE AT LOCATION 10, KAVALA, GREECE

TABLE 4

METHODS OF IN-SITU MEASUREMENT

EARTH	VEGETATION
E (d,f)	E(d,f,h)
OWL	OWL
WAVE TILT	
RESONANT AND SHORT MONOPOLE	
POLARIMETER	
INDUCTION (TWO LOOP)	
REFLECTION COEFFICIENT	
TRANSMISSION COEFFICIENT	
TIME DOMAIN REFLECTOMETER	
RADAR	

with depth to determine if the surface values measured with such probes can be expected to apply down to a skin depth. The depth of water in nearby wells or the use of DC, ELF or VLF geophysical prospecting techniques [Keller and Frischknecht, 1966; Wait, 1971] are useful in making this determination. When dry soils overlay a shallow water table, it frequently is necessary to use a two-layer slab model to describe antenna characteristics and propagation over terrain without vegetation similar to the model used at HF for the forested case (see Figure 3). A modified version of the SRI OWL kit can be used to measure the conductivity and relative dielectric constant of vegetation [Parker and Hagn, 1966; Hagn and Barker, 1970; Hagn, 1974]. The E(d) methods of measuring field strength vs distance do not give unique solutions, but they can be used to check results obtained using other techniques.

TYPES OF GROUND

There are several important variables which should be measured as ground truth data to describe the soil for which the data on electrical and magnetic properties apply (see Table 5). Perhaps the most important variable is volumetric moisture content (often approximated by measurements of

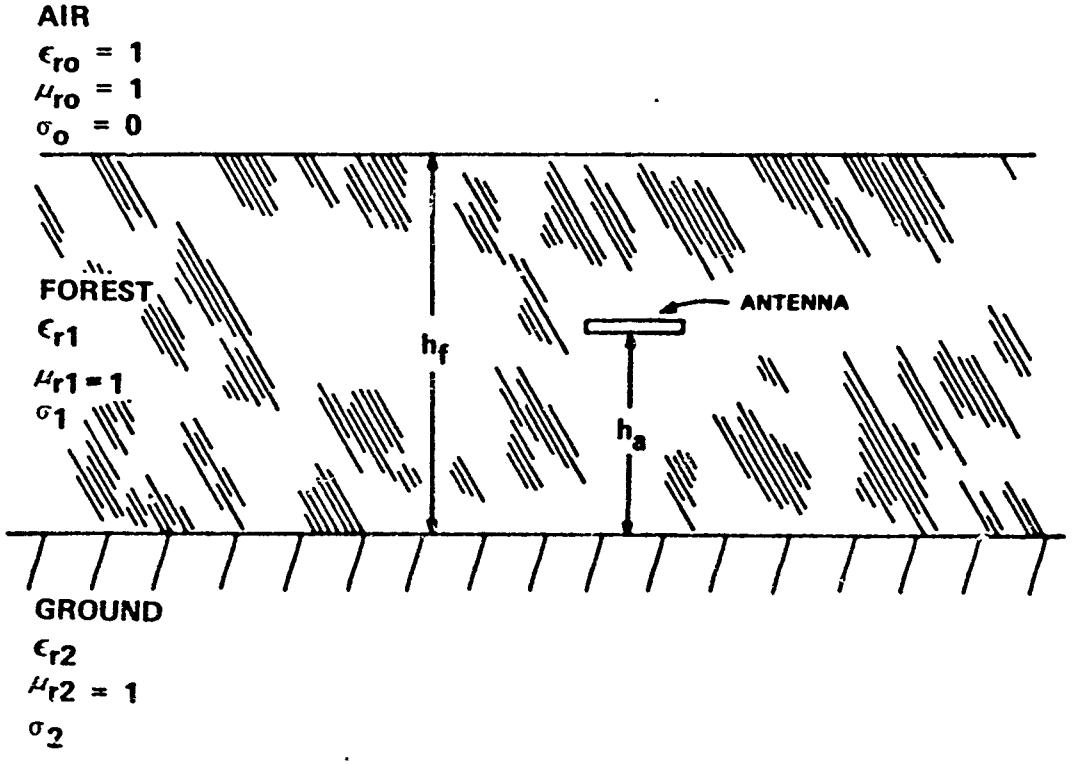


Figure 3 IDEALIZED LOSSY DIELECTRIC SLAB MODEL

the percent moisture content by weight). Longmire and Smith [1975] have developed expressions for permittivity and conductivity (except for the additive DC conductivity) versus frequency which are solely a function of moisture content. The Longmire and Smith predictions show good agreement with measured data for relative dielectric constant and for conductivity when accurate values of the DC conductivity are known. Temperature can be important, especially if a change of state of the ground is involved (i.e., if it is frozen). The soil type and mineralization is important in determining the conductivity (DC conduction), and the compaction of the soil can be important for both conductivty and permittivity. Soil color is important regarding soil homogeneity. Other parameters (e.g., pH) also can be measured to help describe a soil. Handbook authors have given several types of categories to soils, ranging from the magnitude of the conductivity (e.g., good ground, poor ground) to a description of the environmental setting (e.g., pastoral) to the amount of moisture (e.g., dry, moist). We will revisit this issue when discussing generic values for permittivity and conductivity which are more accurate than the constant values given in handbooks (but less accurate than values measured at a site of interest). At frequencies below HF the skin depth is so great that the geology underlying the soil is very important. Geologic maps have been

TABLE 5

IMPORTANT VARIABLES

- PERMITTIVITY
  - MOISTURE CONTENT
  - TEMPERATURE
- CONDUCTIVITY
  - MOISTURE CONTENT
  - TEMPERATURE
  - SOIL TYPE α MINERALIZATION (IONS AVAILABLE)
  - COMPACTION

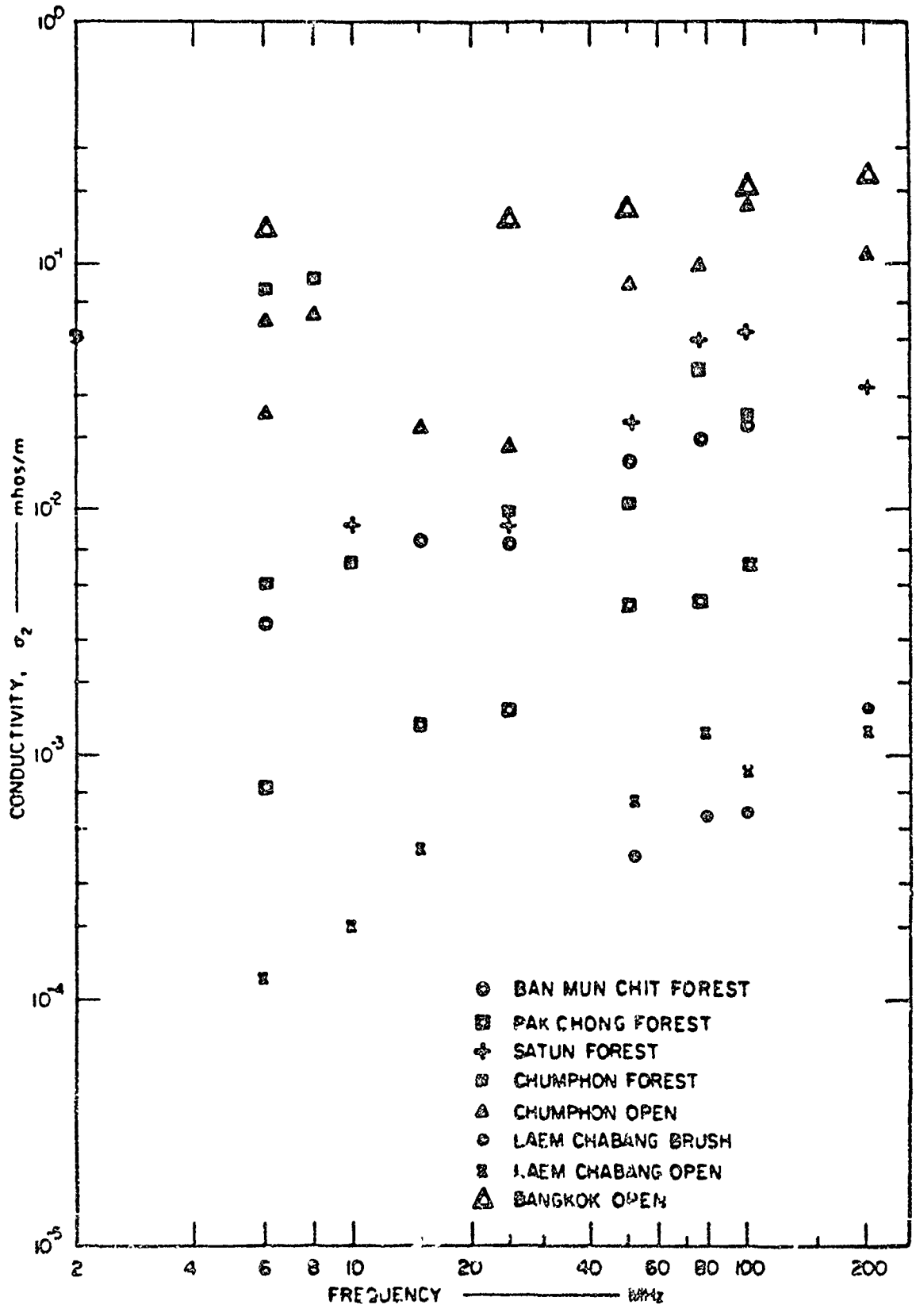
used to develop conductivity maps of the world and of specific countries like the U.S. [Fine, 1954] and Thailand [Kovattana, 1967]. At HF, the soil down to a few meters (or tens of meters in dry soil at 2 MHz) tends to be more important than the underlying geology due to the skin depth.

EXAMPLES OF MEASURED SITE MEDIAN DATA USING OWL KIT

We now will consider some measured values of conductivity and relative dielectric constant measured with the SRI open wire line (OWL) kit. The first use of this kit was in CONUS [Goldstein, et al., 1969] and in Thailand [Parker and Makarabhiromya, 1967] in the 1960s. Data from eight sites in Thailand for conductivity and relative dielectric constant for the band 2-200 MHz are given in Figures 4 and 5, respectively [Parker and Makarabhiromya, 1967; Hagn and Barker, 1970]. Note that there is greater frequency dispersion for lower conductivities (drier soil such as the dry beach sand at Laem Chabang) and for higher relative dielectric constants (moist, but not flooded, rice paddy labeled Bangkok open). The conductivity increases with increasing frequency, and it varies over three orders of magnitude for this set of data. The relative dielectric constant varies over one order of magnitude for the frequencies above 15 MHz and it decreases with increasing frequency for a given soil. The relative dielectric constant values for frequencies below 15 MHz exceed 90 for the rice paddy.

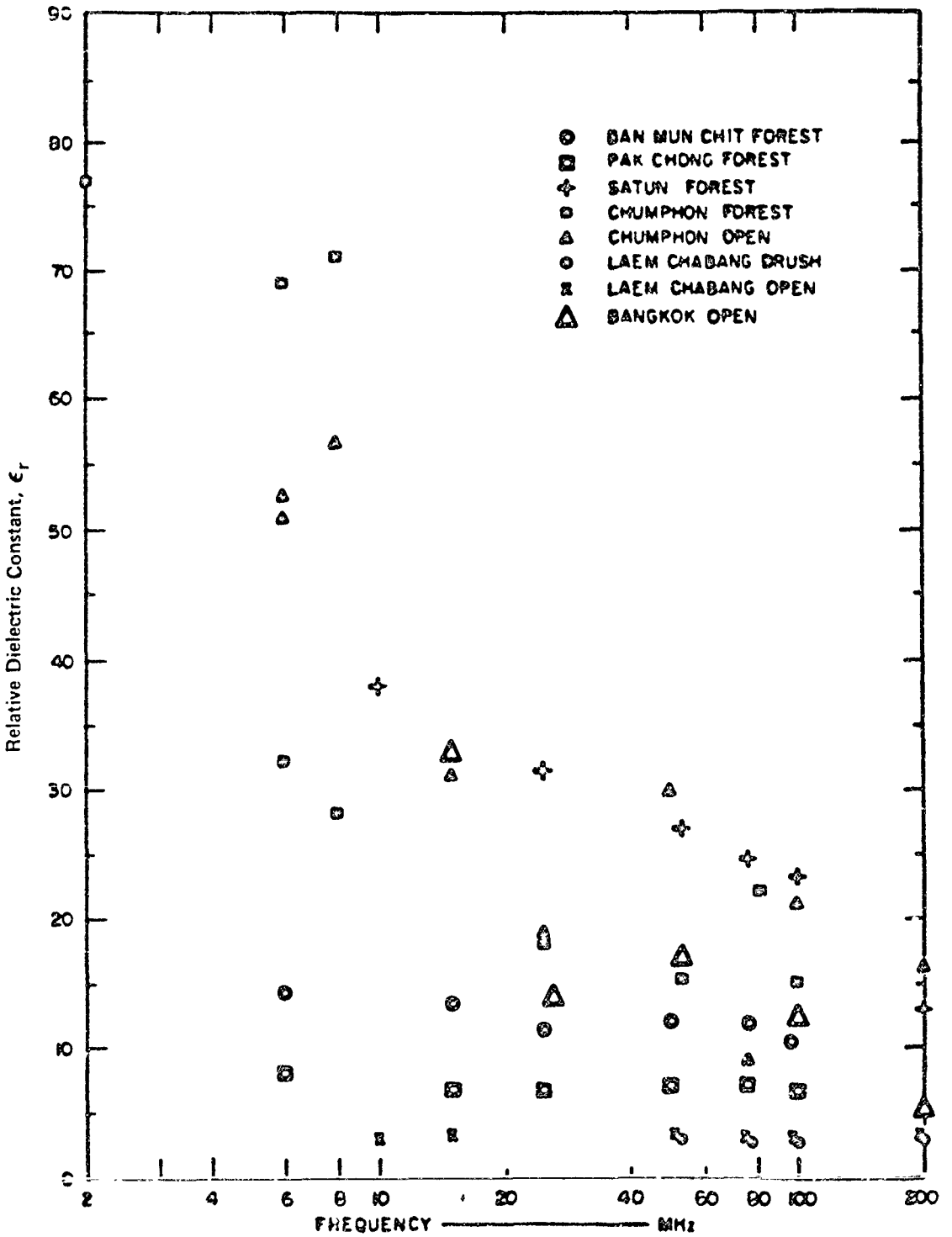
Site median values of conductivity and relative dielectric constant for six U.S. Army bases are shown in Figures 6 and 7 [Hagn and Gaddie, 1984]. The soil at Ft. Lewis, WA was very dry and contained small stones. The values were similar to those obtained in dry beach sand at Laem Chabang. The data from Ft. Leavenworth, KS were taken in moist soil very near the banks of the Missouri River, and they are comparable to the values obtained in the Bangkok rice paddy.

Data were taken recently at several Voice of America (VOA) transmitter sites around the world [Hagn and Sarran, 1985; Hagn and Faulconer, 1985a-f; Sarran, et al., 1985], and the median surface values for these sites are



(Parker and Makarabhiromya, 1967)

Figure 4 MEDIAN SURFACE CONDUCTIVITY OF GROUND AT SELECTED SITES IN THAILAND



(Parker and Makarabhiromya, 1967)

Figure 5 MEDIAN SURFACE GROUND PERMITTIVITY MEASURED AT SELECTED SITES IN THAILAND

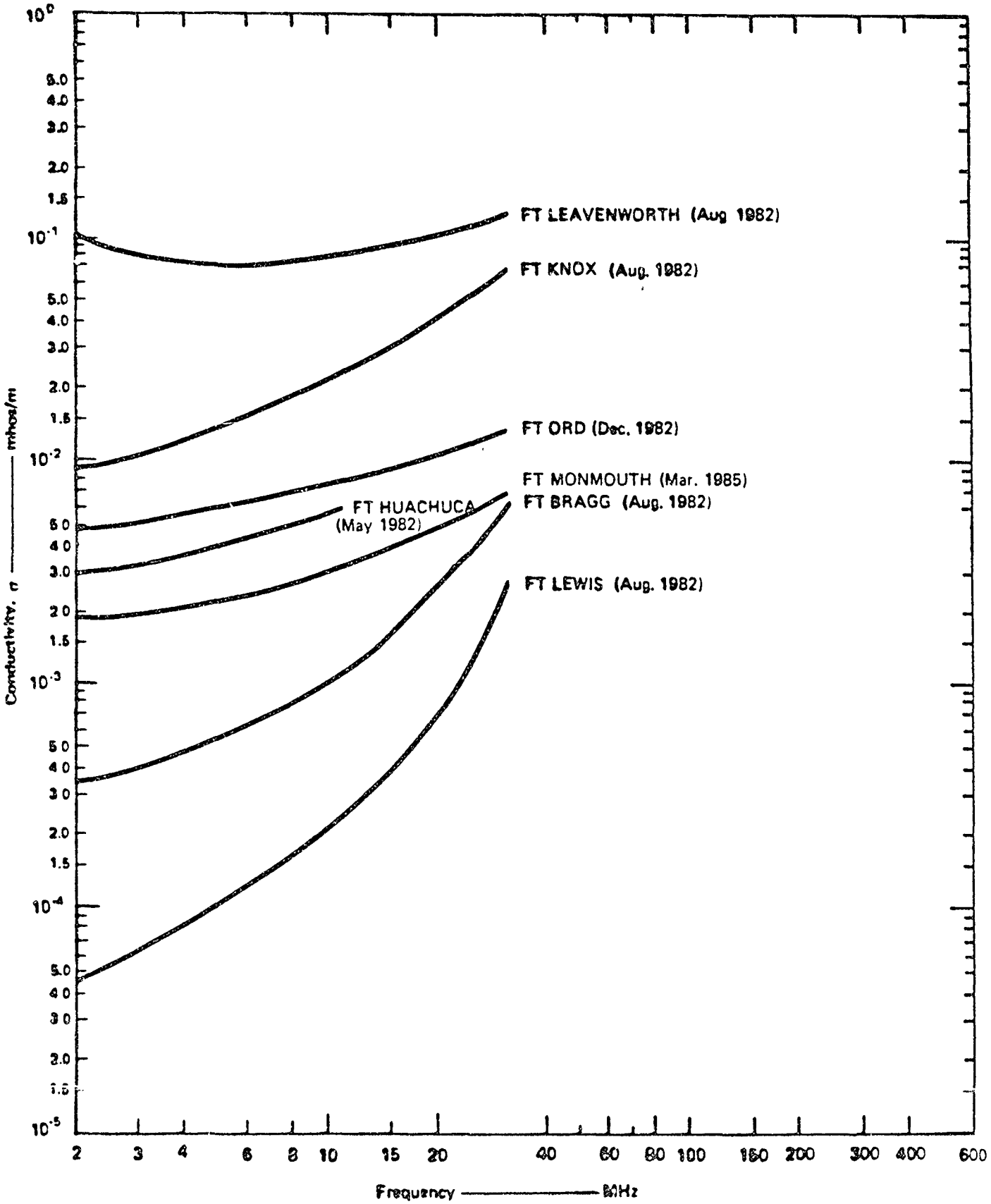


Figure 6 COMPARISON OF MEDIAN CONDUCTIVITIES MEASURED AT SELECTED U.S ARMY BASES

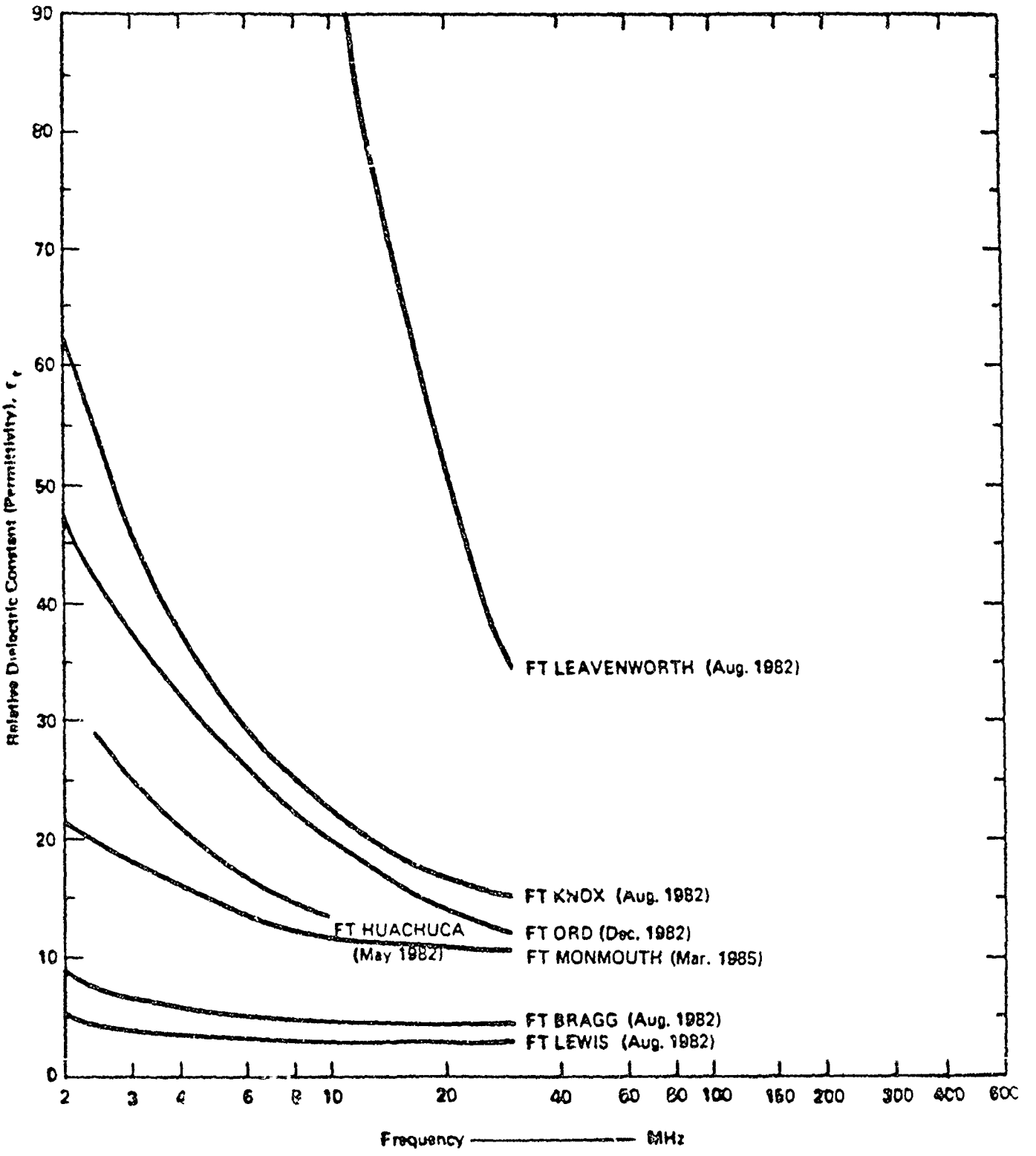


Figure 7 COMPARISON OF MEDIAN RELATIVE DIELECTRIC CONSTANTS MEASURED AT SELECTED U.S. ARMY BASES

given in Figures 8 and 9 for conductivity and relative dielectric constant. The data at Tinang in the Philippines are comparable to the Bangkok rice paddy data, but the Delano, CA data values are even higher. The Delano soil was a highly compacted dry lake bed with mineralization. The data for the dry beach sand at Chilaw, Sri Lanka is comparable to the data for the dry beach sand at Laem Chabang. Except for the high values at Delano and Tinang, the conductivity values follow fairly regular trends. The data sample for Poro in the Philippines was not a true site median. It was not possible to get the OWL probes far enough into the coral rock and only two samples were taken with short probes. At several of the VOA sites the water table was closer to the surface than the skin depth of the overlaying soil, so a two-layer model was required to adequately describe the ground.

VARIABILITY ABOUT SITE MEDIAN VALUES

There can be considerable variability about the site median for both the conductivity and the relative dielectric constant (particularly at the lower frequencies in the HF band). Let us consider as an example the data in Figures 10 and 11 taken at Site 2 with a 12-inch probe at Ft. Ord, CA [Hagn and Gaddie, 1983a]. These data from different sample locations separated by several hundred meters are reasonably closely grouped at a given frequency. Data taken at Site 1, only 150 m away, on a steeper slope of the same hill, showed greater variability. The bounds on the data from both of these sites are shown in Figures 12 and 13. Such bounds are useful when performing sensitivity analyses to determine the robustness of NEC results to changes in the ground constants.

The results obtained at any given site and location depend on the probe length due to a lack of soil homogeneity with depth. This is caused primarily by a gradient of soil moisture content. Figures 14 and 15 give values taken with 6-inch and 9-inch probes in thawed permafrost in Fairbanks silt [Hagn, 1983b]. At this site the soil was more moist nearer the surface. The appropriate probe length at any given site is the length closest to the skin depth at the frequency of interest. For this reason, SRI OWL kit probes of different lengths are required to cover the HF band.

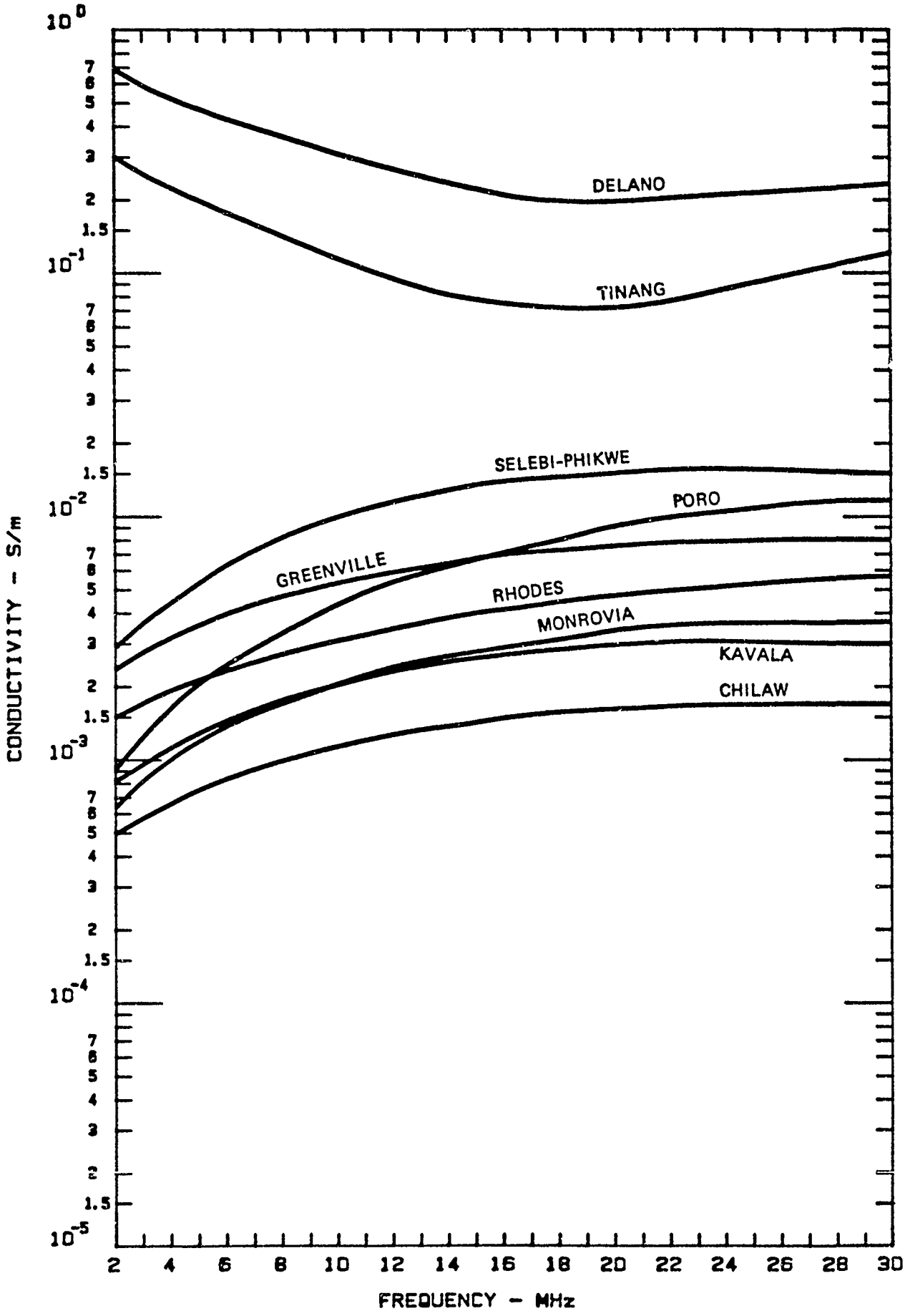


Figure 8 SITE MEDIAN VALUES OF CONDUCTIVITY VS FREQUENCY FOR SELECTED VOA TRANSMITTER SITES

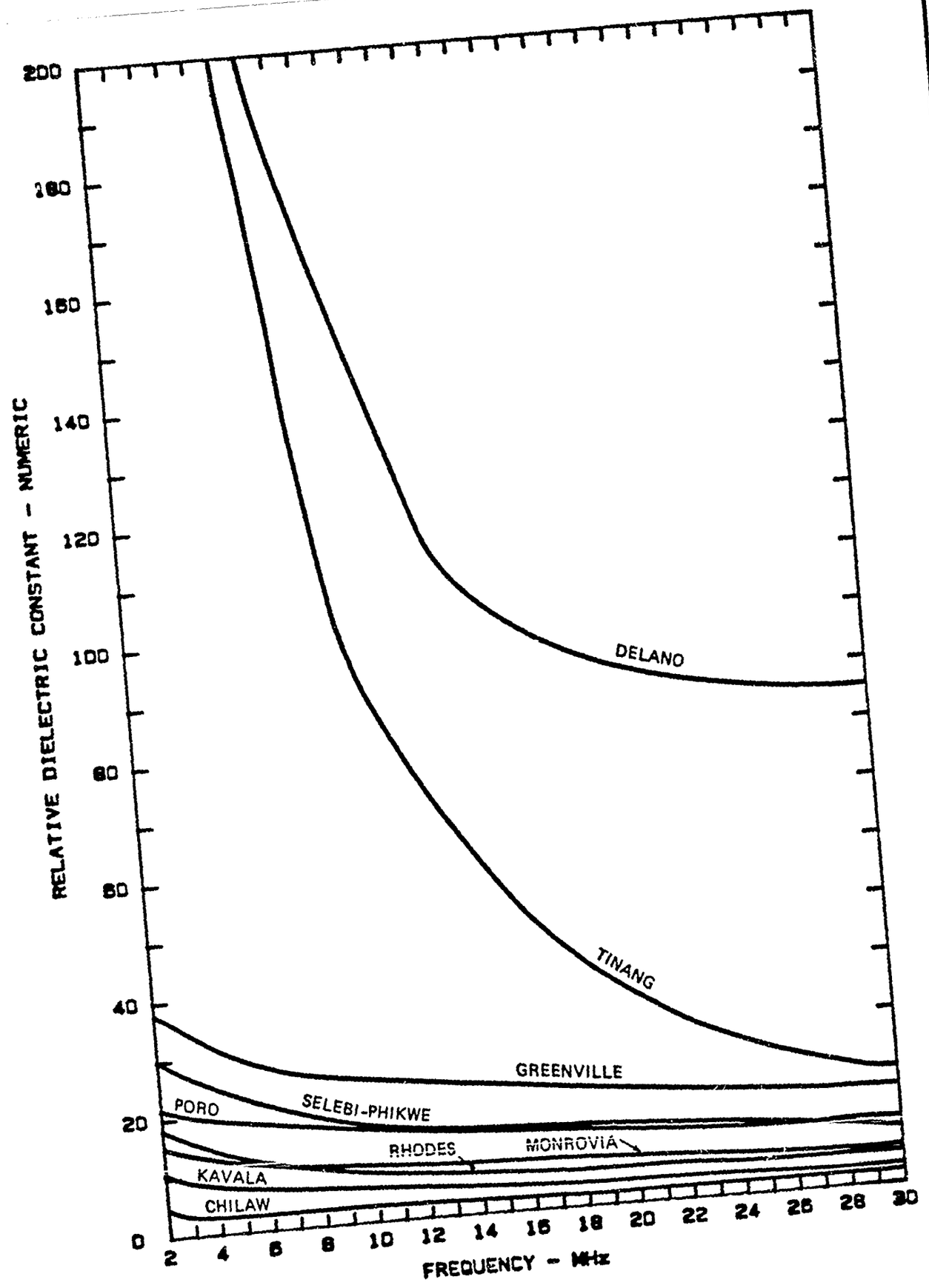
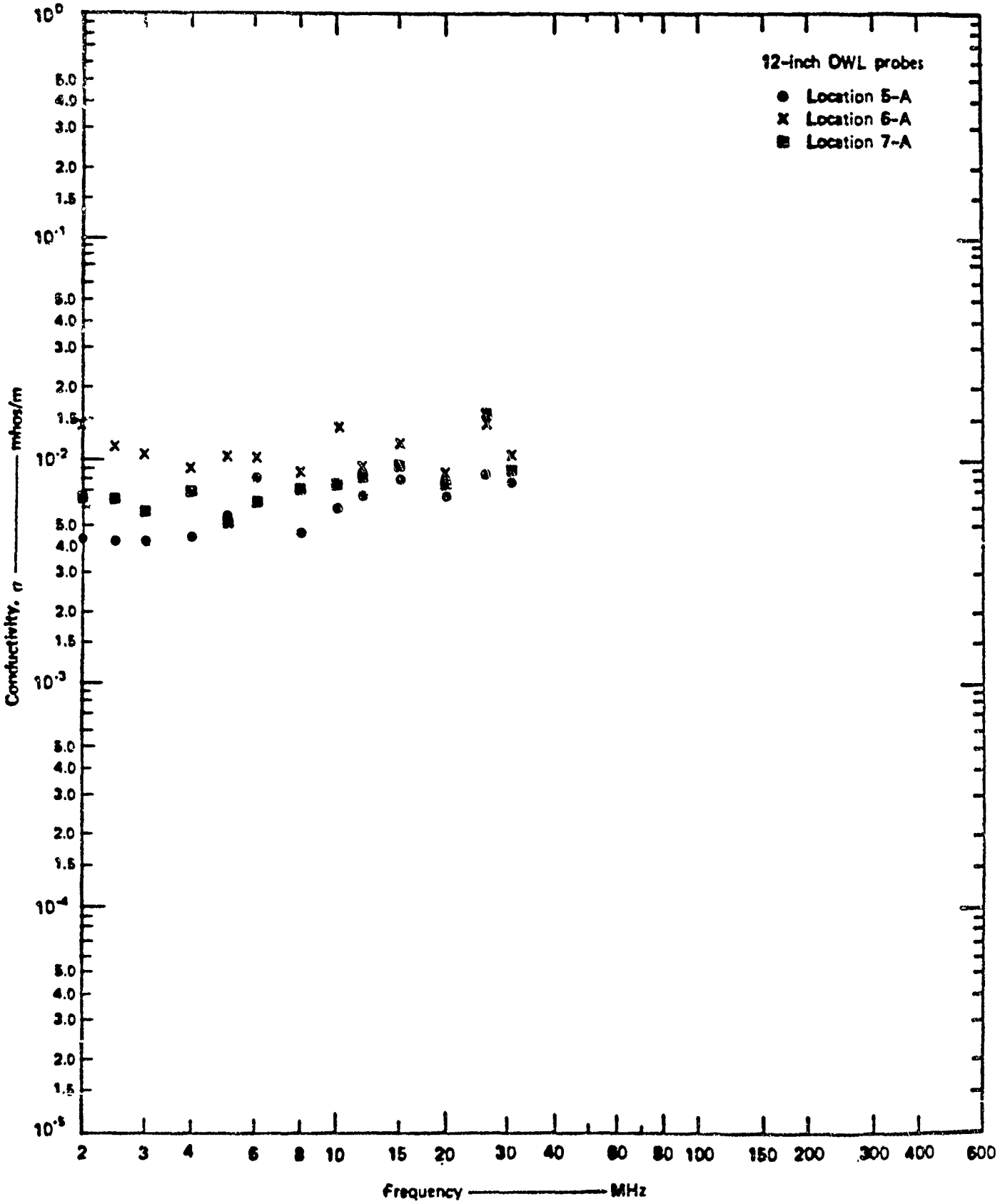
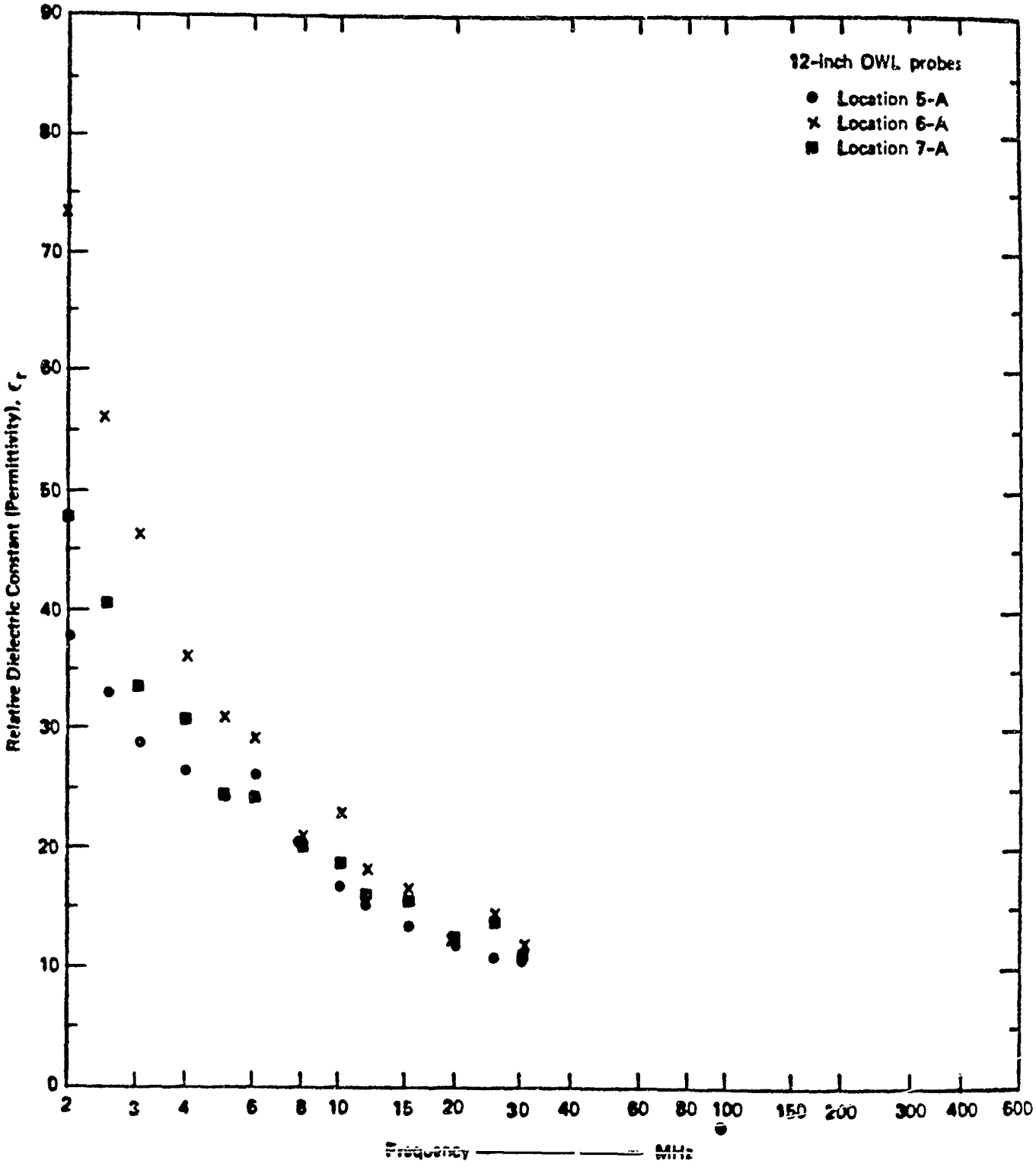


Figure 9 SITE MEDIAN VALUES OF RELATIVE DIELECTRIC CONSTANT VS FREQUENCY FOR SELECTED VOA TRANSMITTER SITES



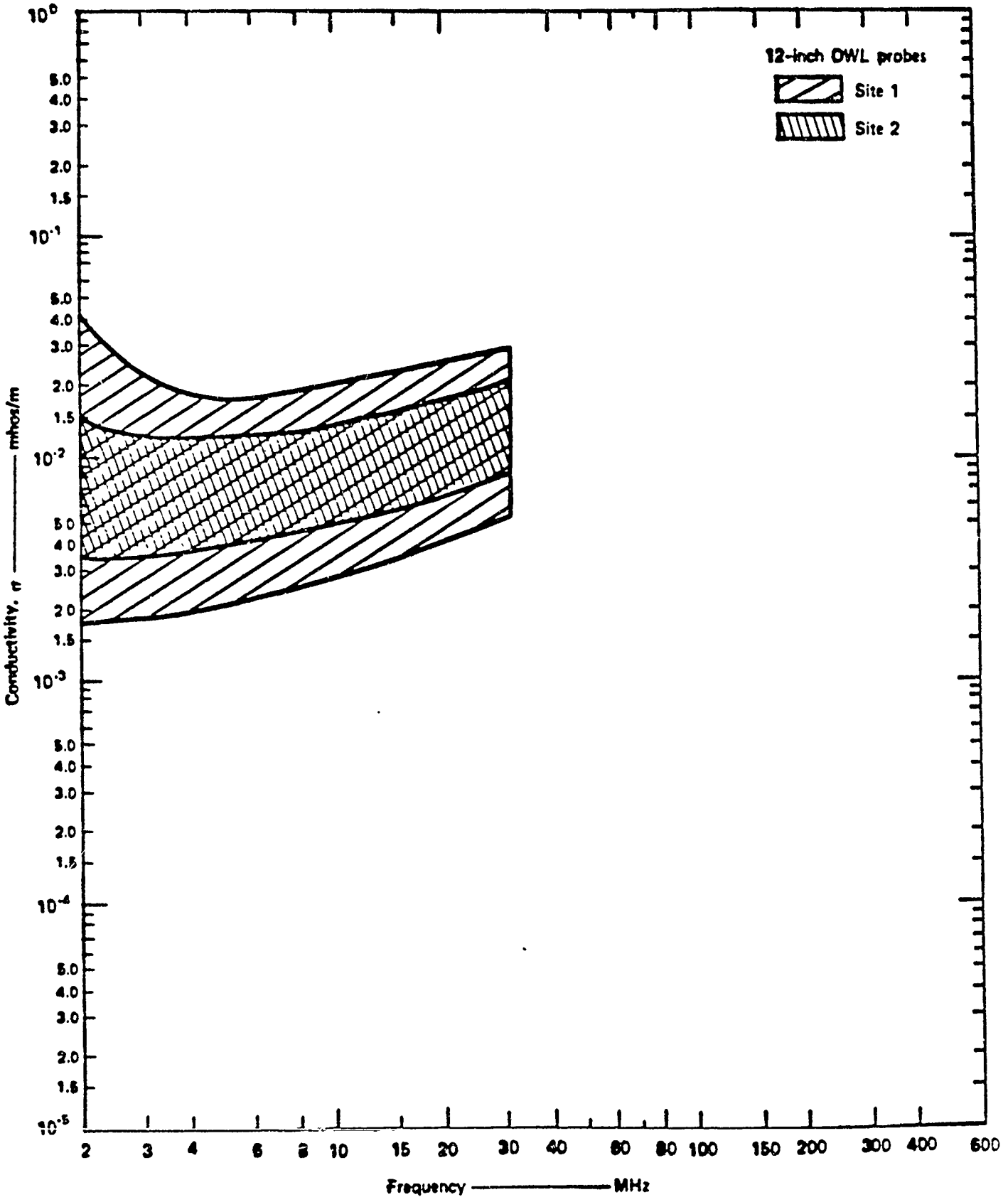
(Hagn and Gaddie, February 1983)

Figure 10 EXAMPLES OF EFFECTIVE GROUND CONDUCTIVITY VS FREQUENCY AT SITE 2 AT FORT ORD



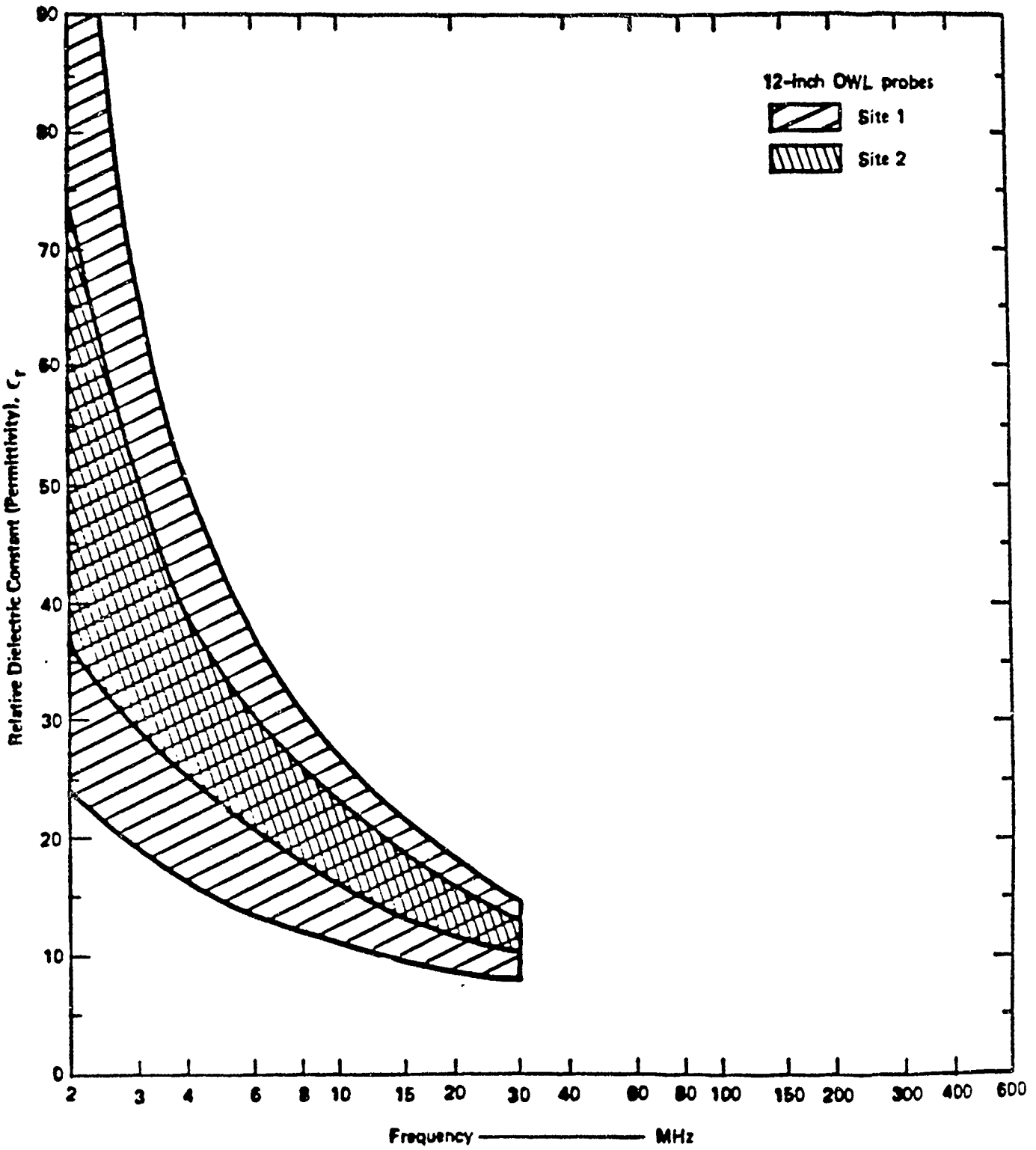
(Hagn and Gaddie, February 1983)

Figure 11 EXAMPLES OF RELATIVE DIELECTRIC CONSTANT VS FREQUENCY AT SITE 2 AT FORT ORD



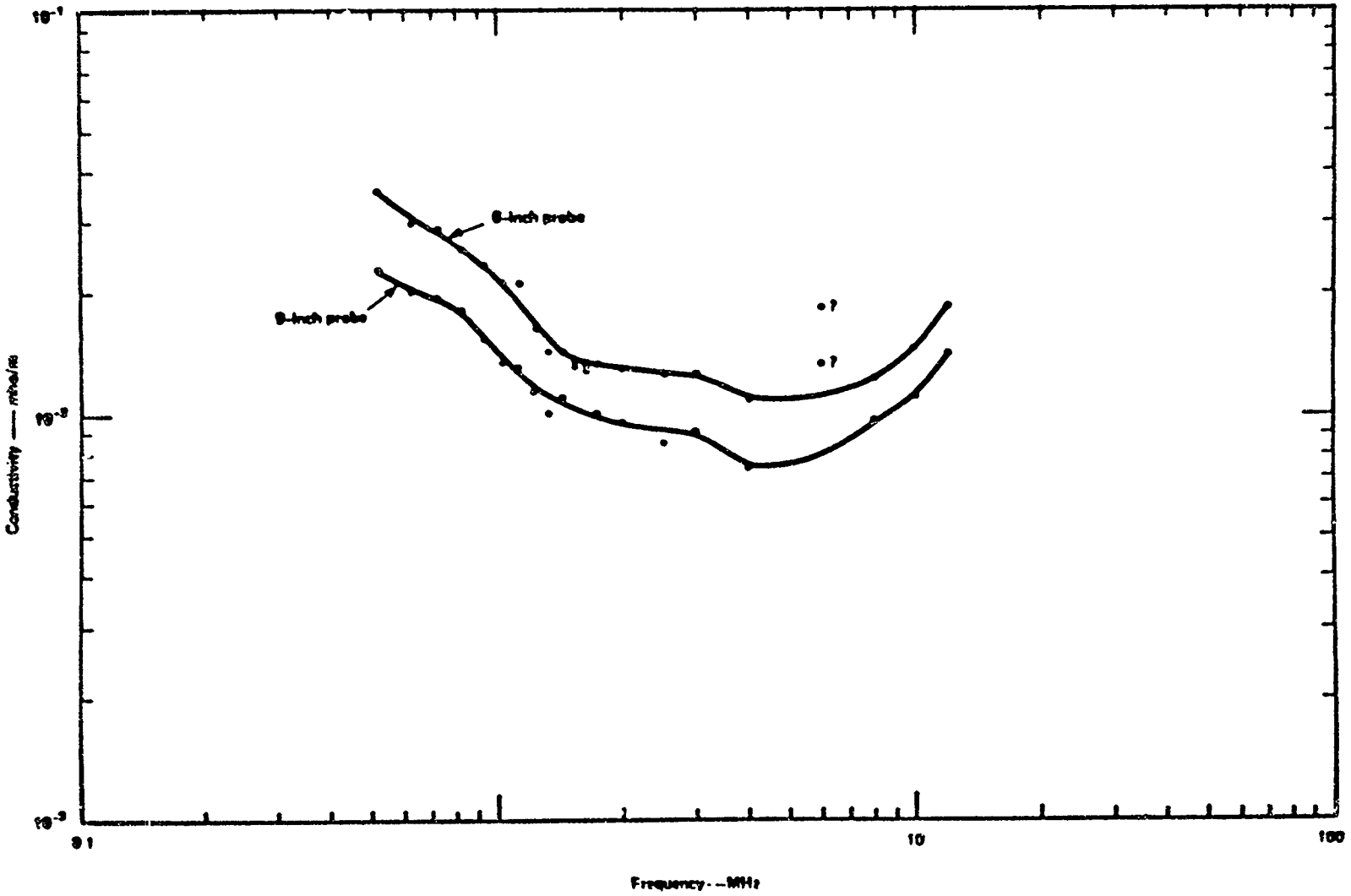
(Hagn and Gaddie, February 1983)

Figure 12 EFFECTIVE GROUND CONDUCTIVITY VS FREQUENCY FROM SRI OWL DATA AT FORT ORD



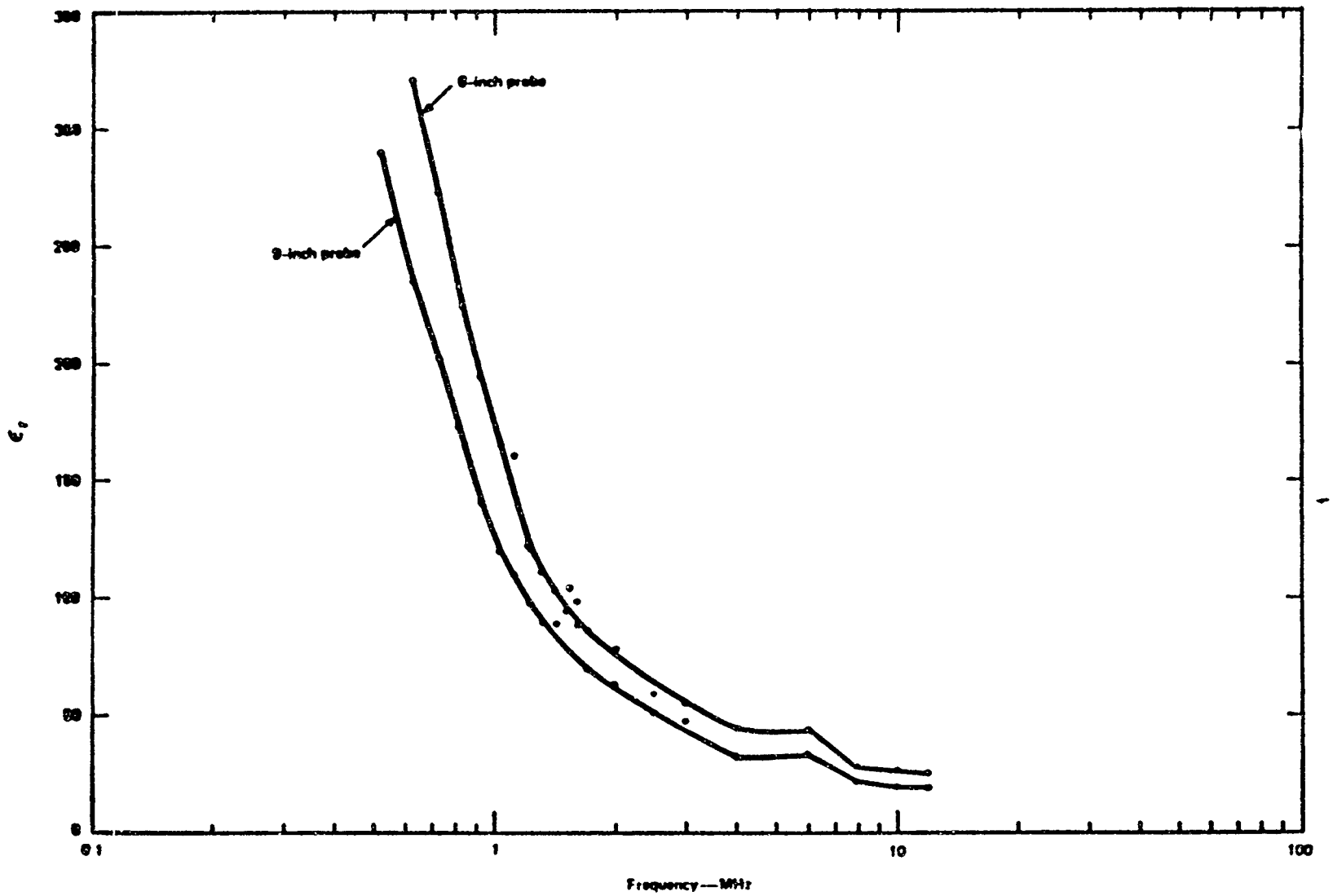
(Hagn and Gaddie, February 1983)

Figure 13 EFFECTIVE GROUND RELATIVE DIELECTRIC CONSTANT VS FREQUENCY FROM SRI OWL DATA AT FORT ORD



(Hagn, April 1983)

Figure 14 CONDUCTIVITY VS FREQUENCY FOR THAWED PERMAFROST AT FAIRBANKS



(Hagn, April 1983)

Figure 15 RELATIVE DIELECTRIC CONSTANT VS FREQUENCY FOR THAWED PERMAFROST AT FAIRBANKS

COMPARISON OF OWL AND E(d) DATA

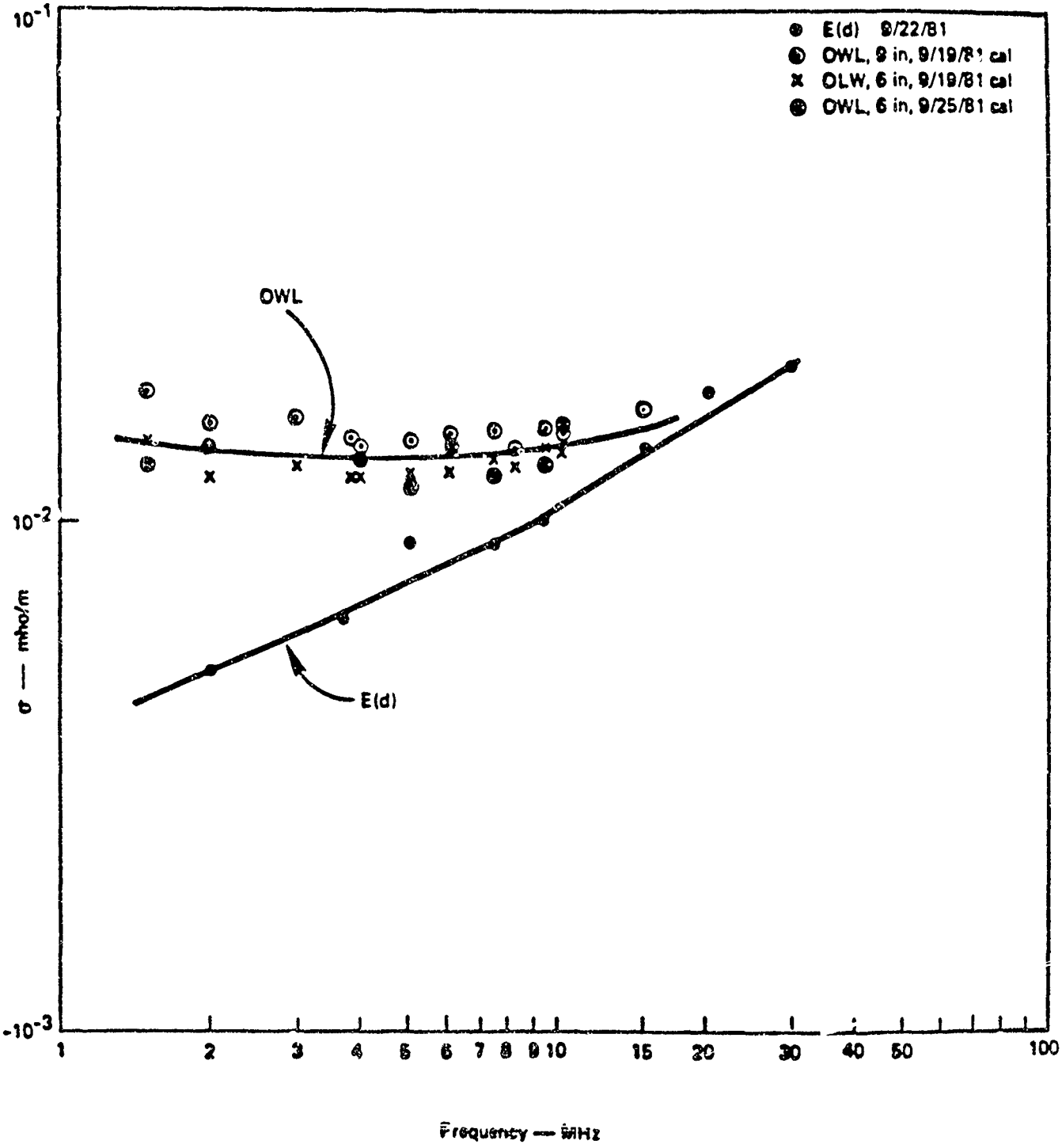
SRI has used the OWL kit and the E(d) method based on Norton's solution to the Sommerfeld integral [Norton, 1941] at several sites. The E(d) data were taken using the SRI XELEDOP [Barker, 1973; Hagn and Harnish, 1986] at 6 ft above ground as the source and measuring the vertically polarized ground wave versus distance out to 1500 feet. The results for a rice paddy are given in Figures 16 and 17 [Hagn, 1982a]. The data for the relative dielectric constant showed good agreement, but the conductivity only agreed at the higher frequencies. The reason for the disagreement of the conductivity data is not totally understood. The E(d) data were obtained down a dry road through the rice paddy; whereas, the OWL data were taken at several locations out in the dry paddy. The rice paddy had considerable "night soil" added to it for fertilizer.

This type of experiment was repeated for the lava fields at the Keflavik, Iceland NATO base [Hagn and Gaddie, 1983b] (see Figures 18 and 19). Here the agreement was reasonable for both the conductivity and relative dielectric constant. There was considerable variability from one sample location to another due to lateral variation of moisture content. The E(d) data tend to smooth out these lateral variations. The site median OWL data provide reasonable agreement with the E(d) data.

Note that the E(d) technique can only give valid estimates for both conductivity and dielectric constant when the DF is reasonably close to unity. When DF >> 1 it is not possible to get good estimates of the relative dielectric constant. For the same reason, however, good values of relative dielectric are not needed for this situation.

GENERIC GROUND CONSTANTS AT HF

Ideally, one could use measured values of ground constants for input values for NEC or other models based upon Maxwell's equations, but this usually is not practical. The alternatives are to use handbook values or data from sites which appeared to be similar. The current handbook values



(Hagn, 1981)

Figure 16 CONDUCTIVITY VS FREQUENCY FOR RICE PADDY

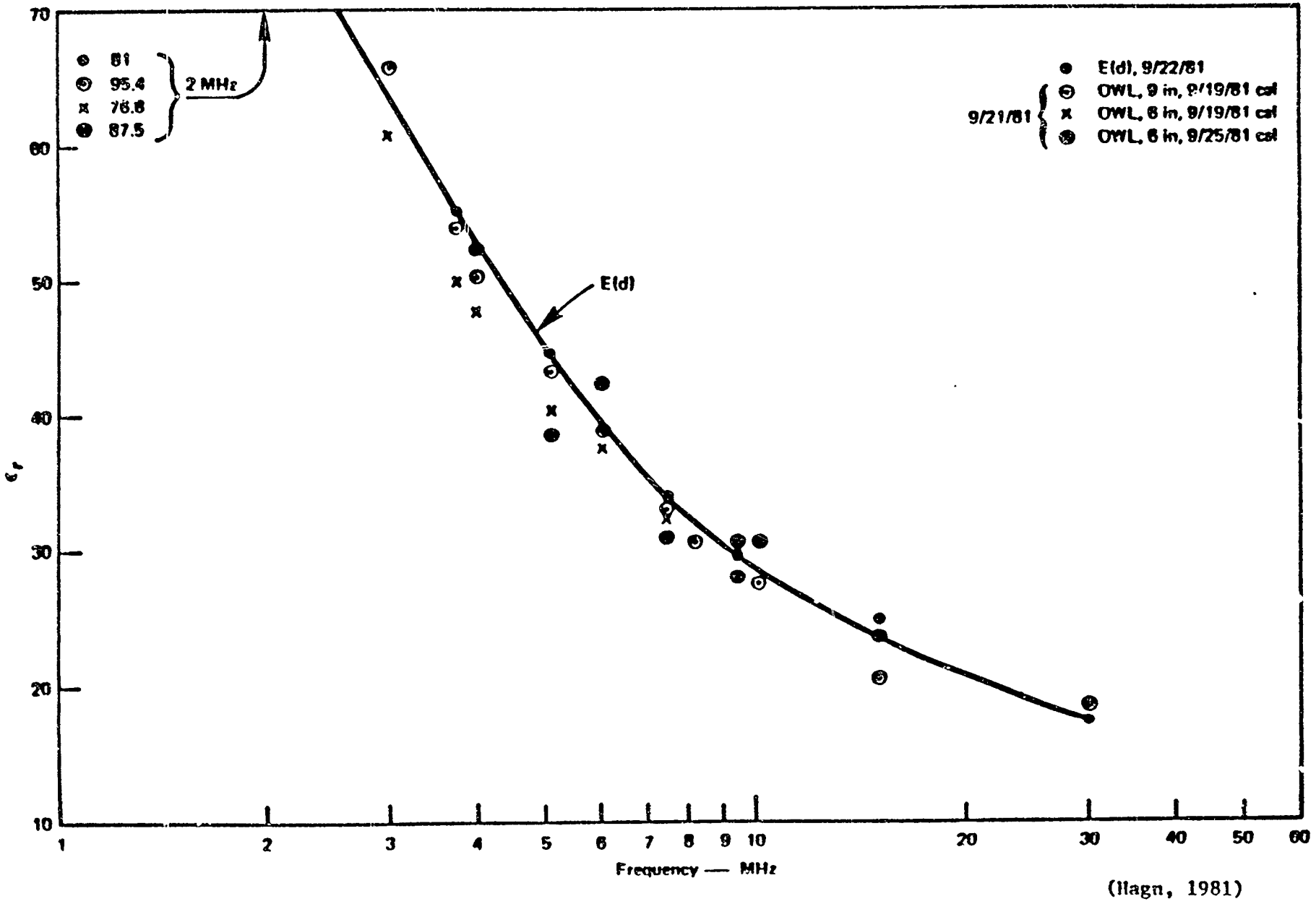
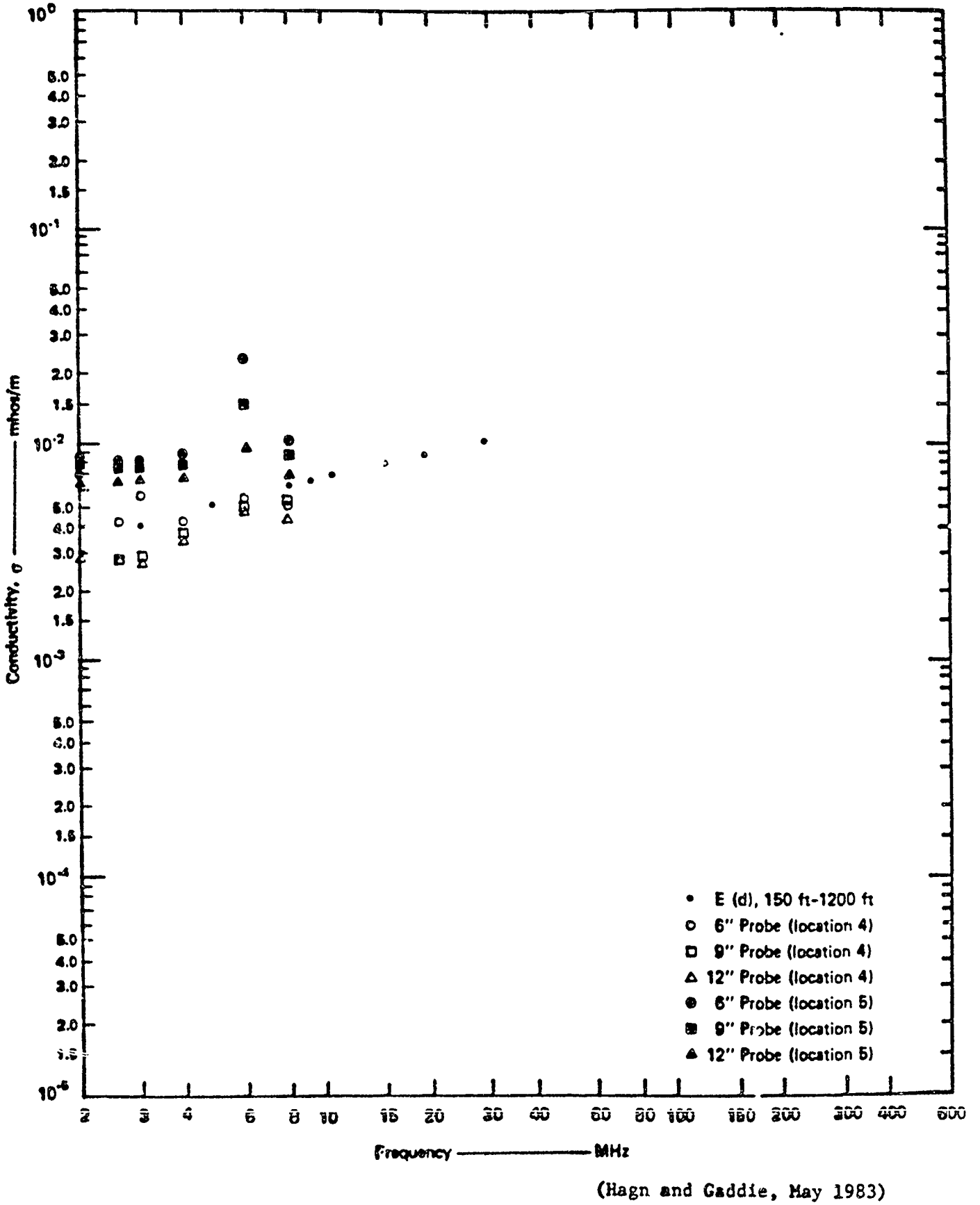
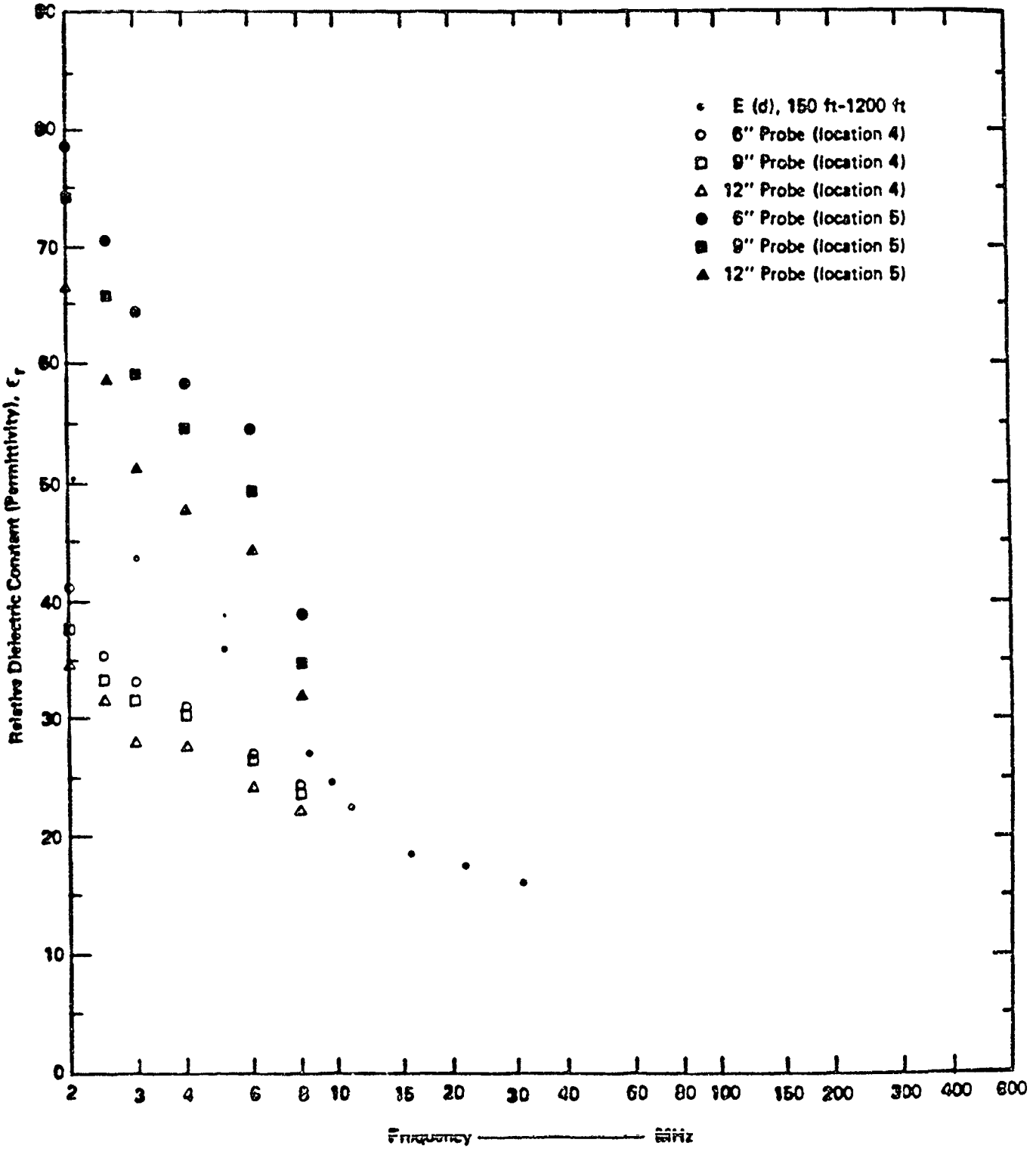


Figure 17 RELATIVE DIELECTRIC CONSTANT VS FREQUENCY FOR RICE PADDY



(Hagn and Gaddie, May 1983)

Figure 18 MEDIAN CONDUCTIVITY OF THE GROUND AT ICELAND LOCATIONS 4 AND 5 VS FREQUENCY MEASURED WITH THE SRI OWL KIT



(Hagn and Gaddie, May 1983)

Figure 19 MEDIAN RELATIVE DIELECTRIC CONSTANT OF THE GROUND AT ICELAND LOCATIONS 4 AND 5 VS FREQUENCY MEASURED WITH THE SRI OWL KIT

are inadequate because they do not allow for variation with frequency acros the HF band. The CCIR has presented generic curves of ground constant with different moisture content vs frequency [CCIR, 1982] which were developed some years ago by Albrecht [1965] and others (see Figure 20). The CCIR also provides curves of penetration depth (skin depth computed using the correct equation) based upon these generic curves (see Figure 21). While the CCIR curves do vary with frequency, they exhibit no dispersion in the HF band. The author developed generic curves [Hagn, et al., 1982a] which were based primarily on the Thailand data and other limited data then available. Handbook-type physical descriptions were applied, and the data were extrapolated from 200 MHz to 600 MHz using the trends below 200 MHz. The purpose was to provide a source of input data for the SRICOM model [Hagn, 1980; Hagn, et al., 1982a]. These generic curves are reproduced here as Figures 22 and 23. Mr. William Moision of the Naval Ocean Systems Center developed equations to describe these curves in the HF band (see Table 6 and [Sailors, et al., 1984]). These equations are depicted for conductivity and relative dielectric constant in Figures 24 and 25, and the corresponding values of DF and SD are given in Figures 26 and 27, respectively.

COMPARISON OF GENERIC CURVES WITH MEASURED DATA

How well do these generic curves work? Figures 28 and 29 show data obtained at the same site in Iceland in 1981 and 1982 inferred from E(d) data [Hagn and Gaddie, 1983b]. The data taken in 1981 from the relatively dry lava agrees well with the generic curve for mountains and rocky, steep hills. The data taken in 1982 after significant rains, exhibited somewhat higher values as expected due to the increase in moisture content. The results followed the shape of the generic curves; but, the conductivity was more closely approximated by pastoral land; whereas, the relative dielectric constant followed the generic curve for rich agricultural land. In other words, the curve pairs did not match up too well.

Other comparisons for site median data taken in CONUS with the SRI OWL kit are given in Figures 30 through 33. The Platteville, CO and Fort

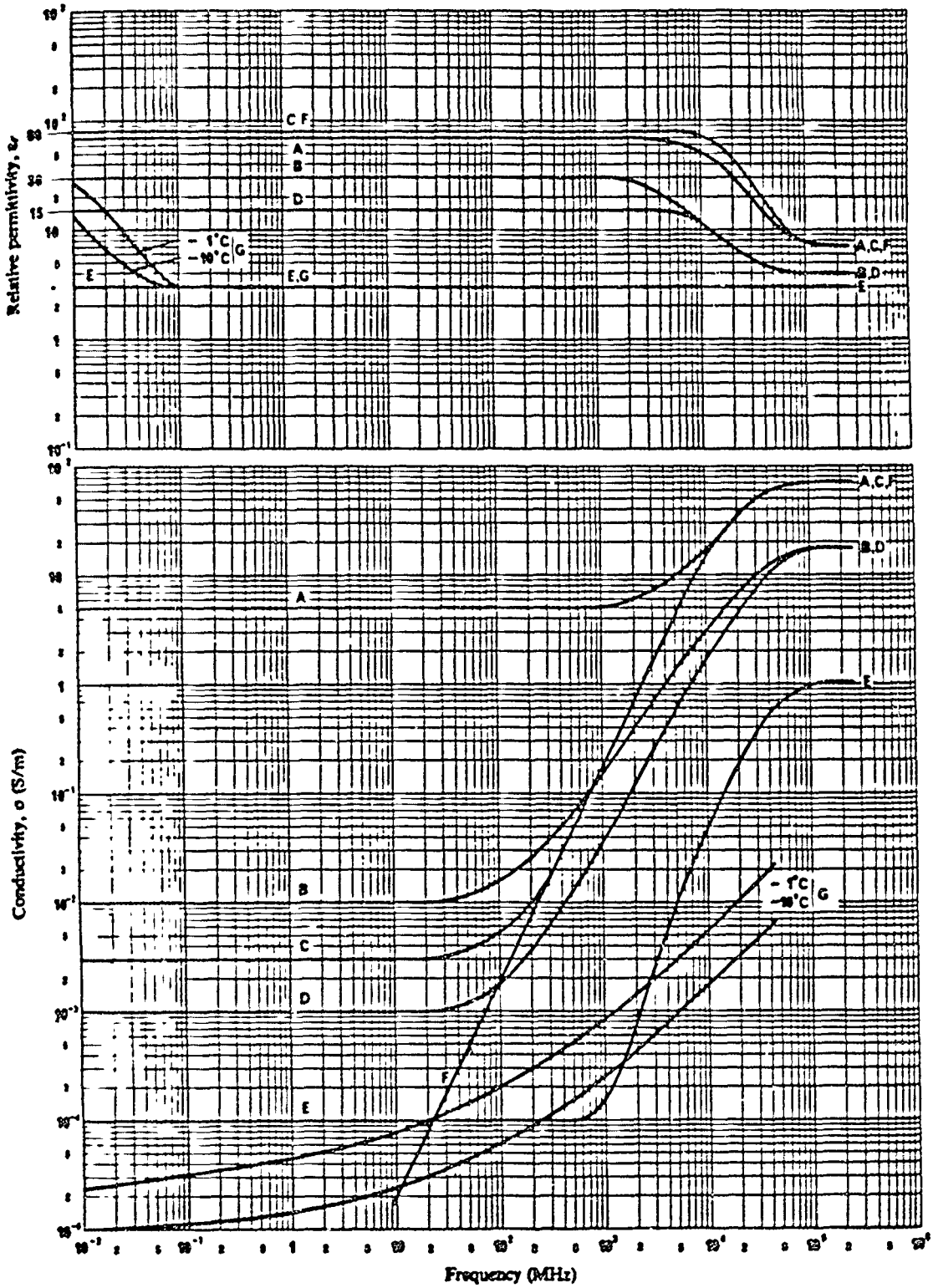
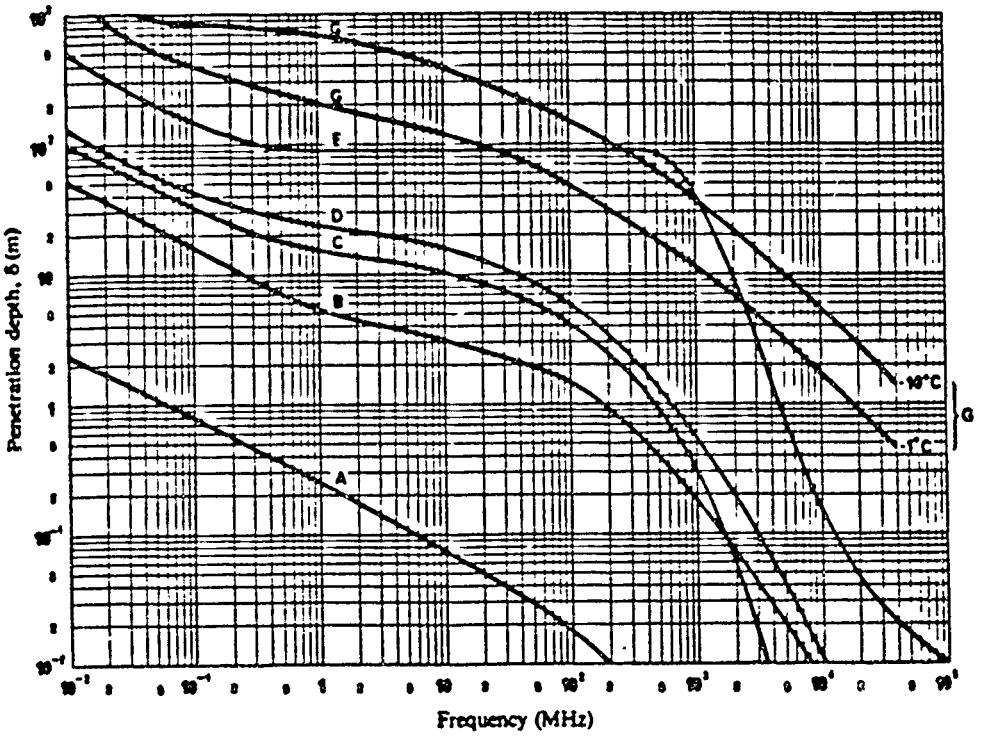


Figure 20 RELATIVE PERMITTIVITY, ϵ_r, AND CONDUCTIVITY, σ, AS A FUNCTION OF FREQUENCY

A: sea water (average salinity), 20° C
B: wet ground
C: fresh water, 20° C
D: medium dry ground
E: very dry ground
F: pure water, 20° C
G: ice (fresh water)

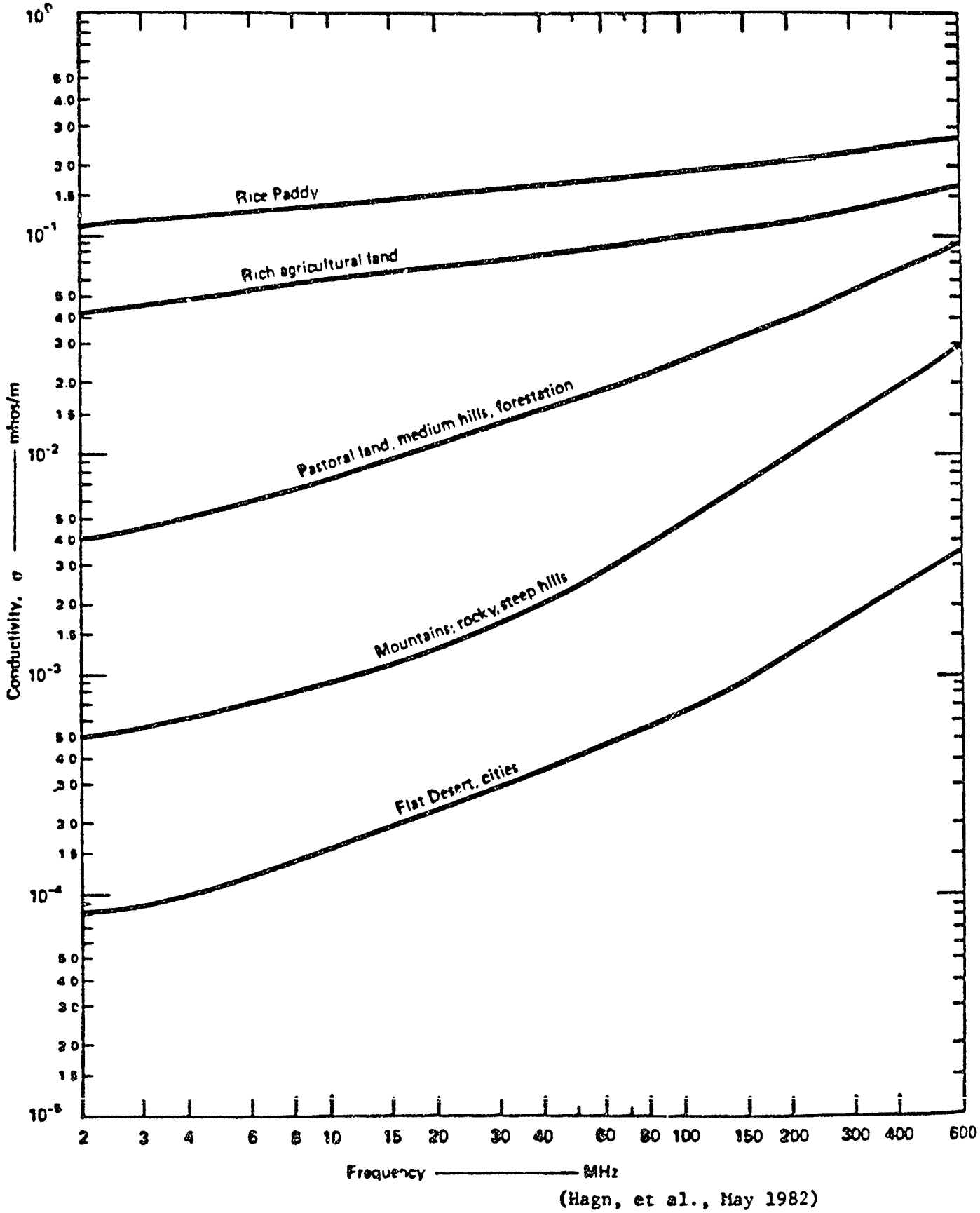
(CCIR, Vol. V,1982)



A: sea water
B: wet ground
C: fresh water
D: medium dry ground
E: very dry ground
G: ice (fresh water)

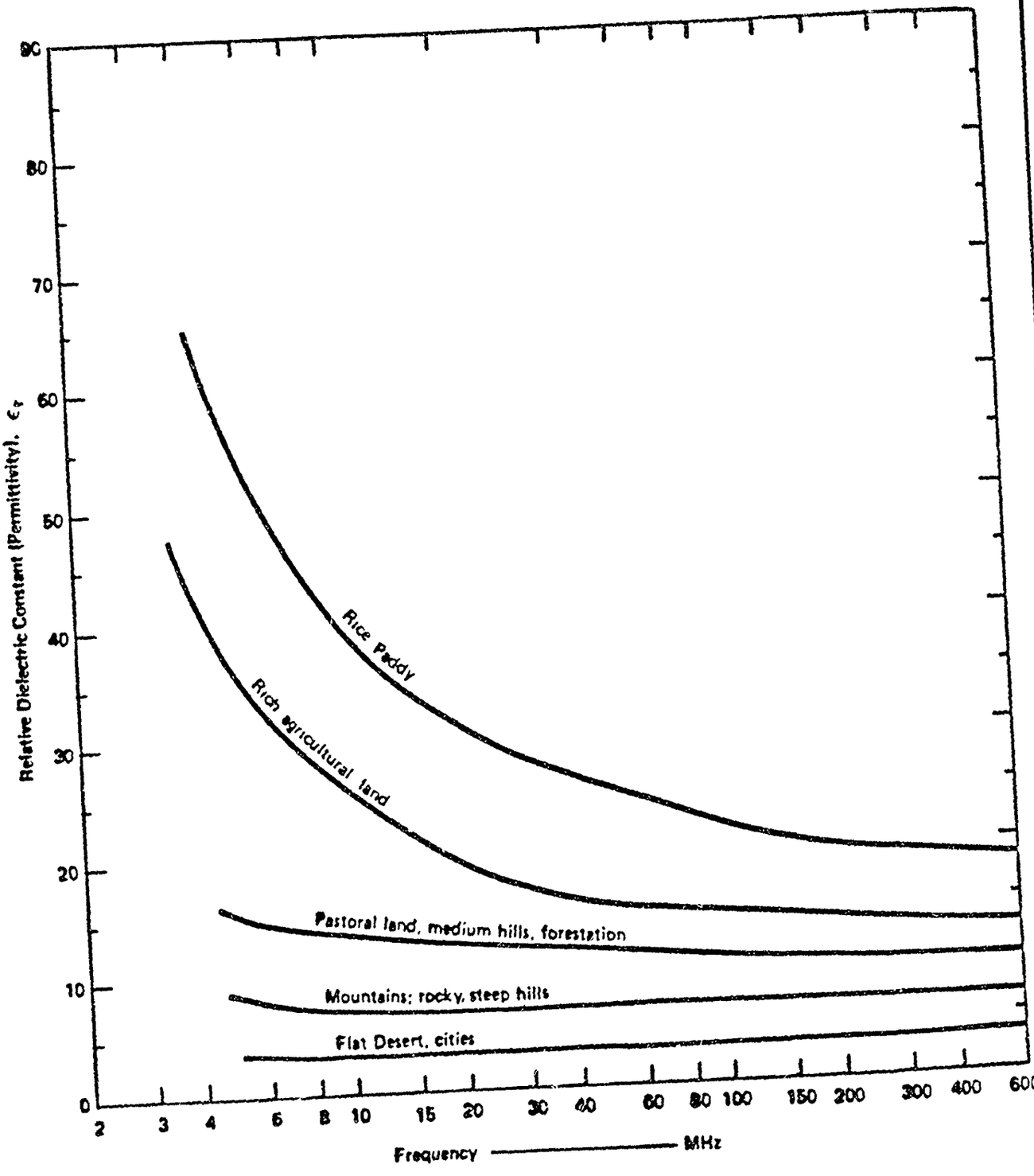
(CCIR, Vol. V, 1982)

Figure 21 PENETRATION DEPTH δ AS A FUNCTION OF FREQUENCY



(Hagn, et al., May 1982)

Figure 22 EFFECTIVE GROUND CONDUCTIVITY VS FREQUENCY FOR SELECTED TERRAIN CATEGORIES



(Hagn, et al., May 1982)

Figure 23 EFFECTIVE GROUND RELATIVE DIELECTRIC CONSTANT VS FREQUENCY FOR SELECTED TERRAIN CATEGORIES

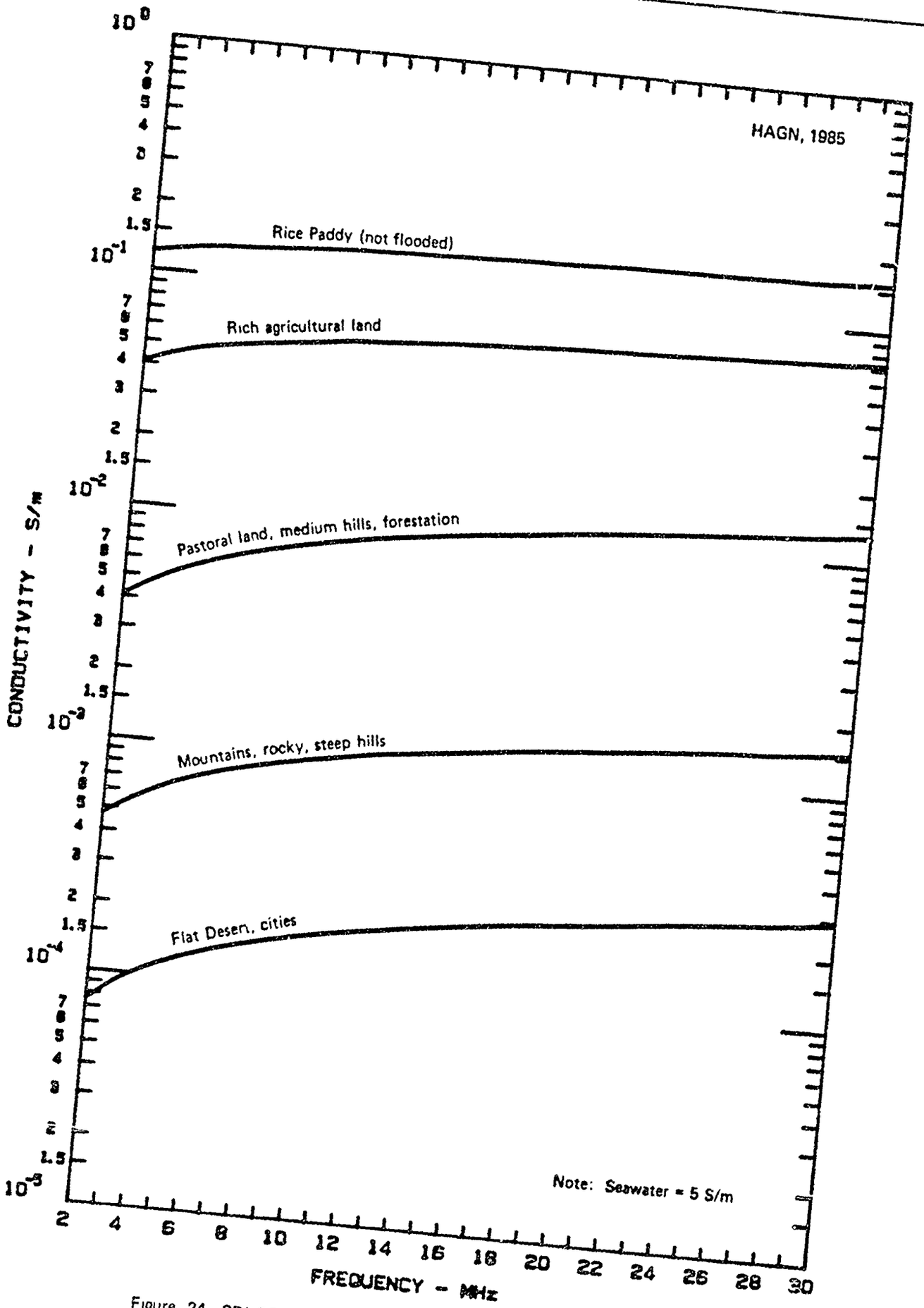


Figure 24 SRI GENERIC CURVES OF EFFECTIVE GROUND CONDUCTIVITY VS FREQUENCY FOR SELECTED TERRAIN CATEGORIES

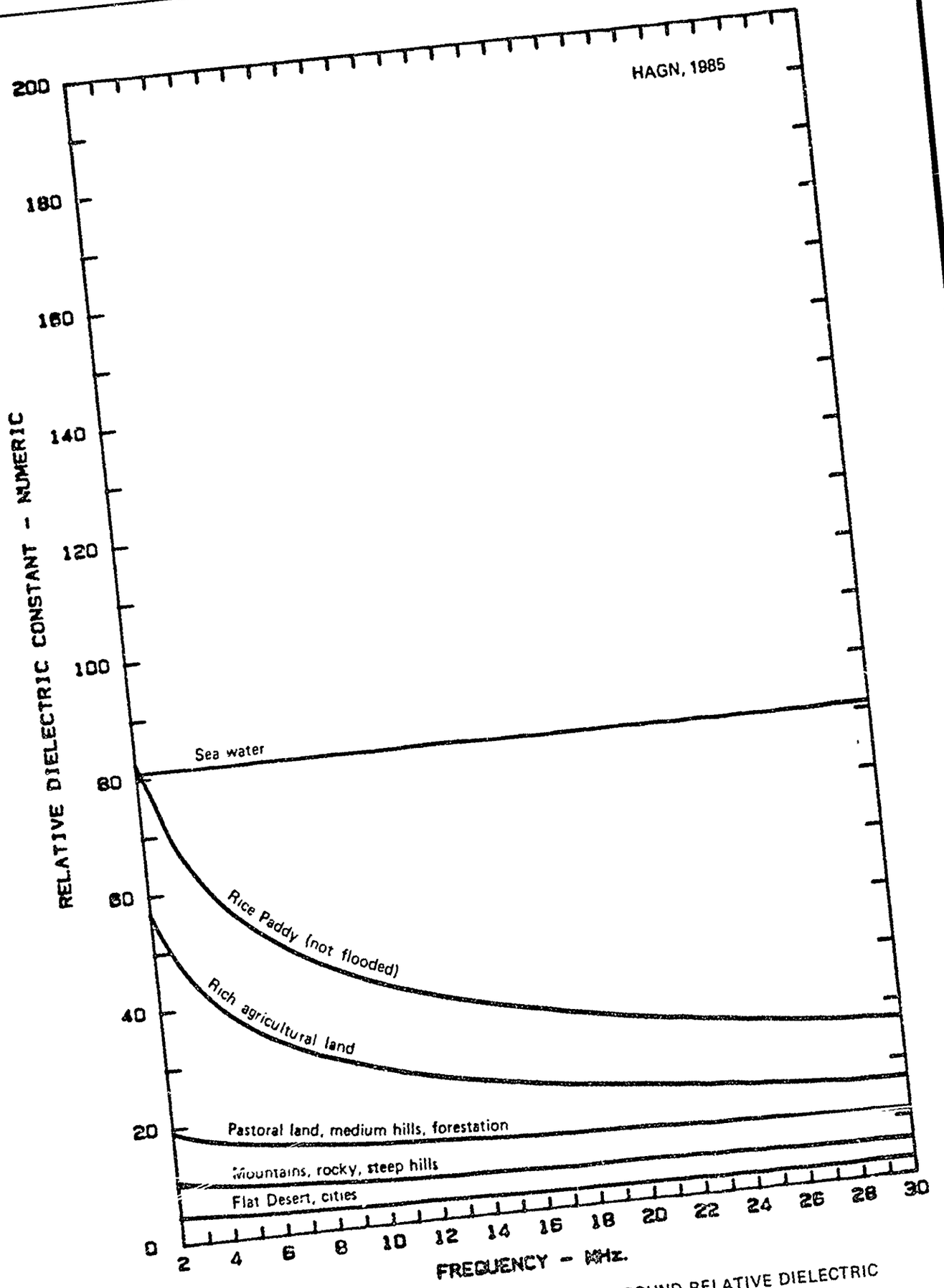


Figure 25 SRI GENERIC CURVES OF EFFECTIVE GROUND RELATIVE DIELECTRIC CONSTANT VS FREQUENCY FOR SELECTED TERRAIN CATEGORIES

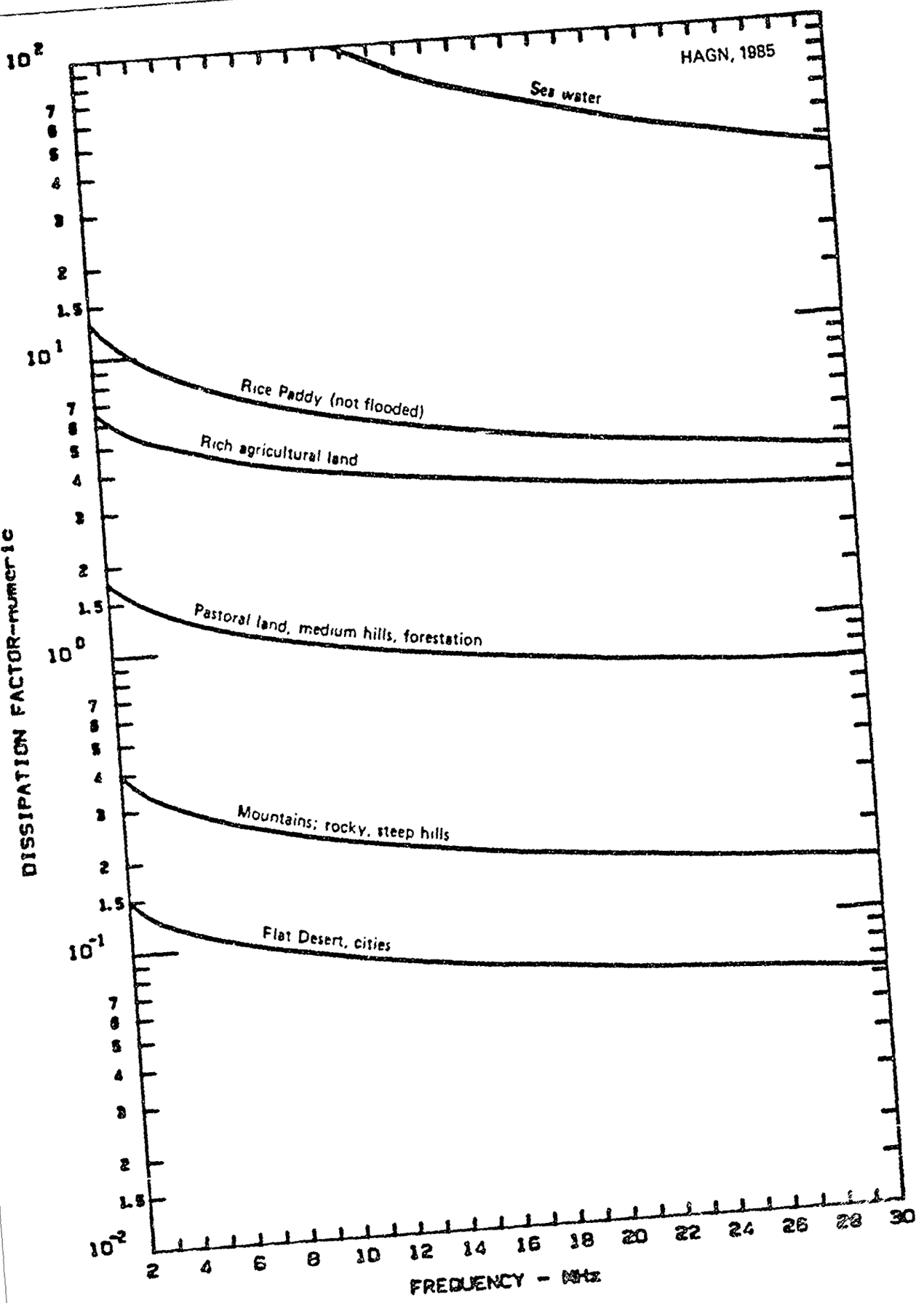


Figure 26 SRI GENERIC CURVES OF EFFECTIVE GROUND DISSIPATION FACTOR VS FREQUENCY FOR SELECTED TERRAIN CATEGORIES

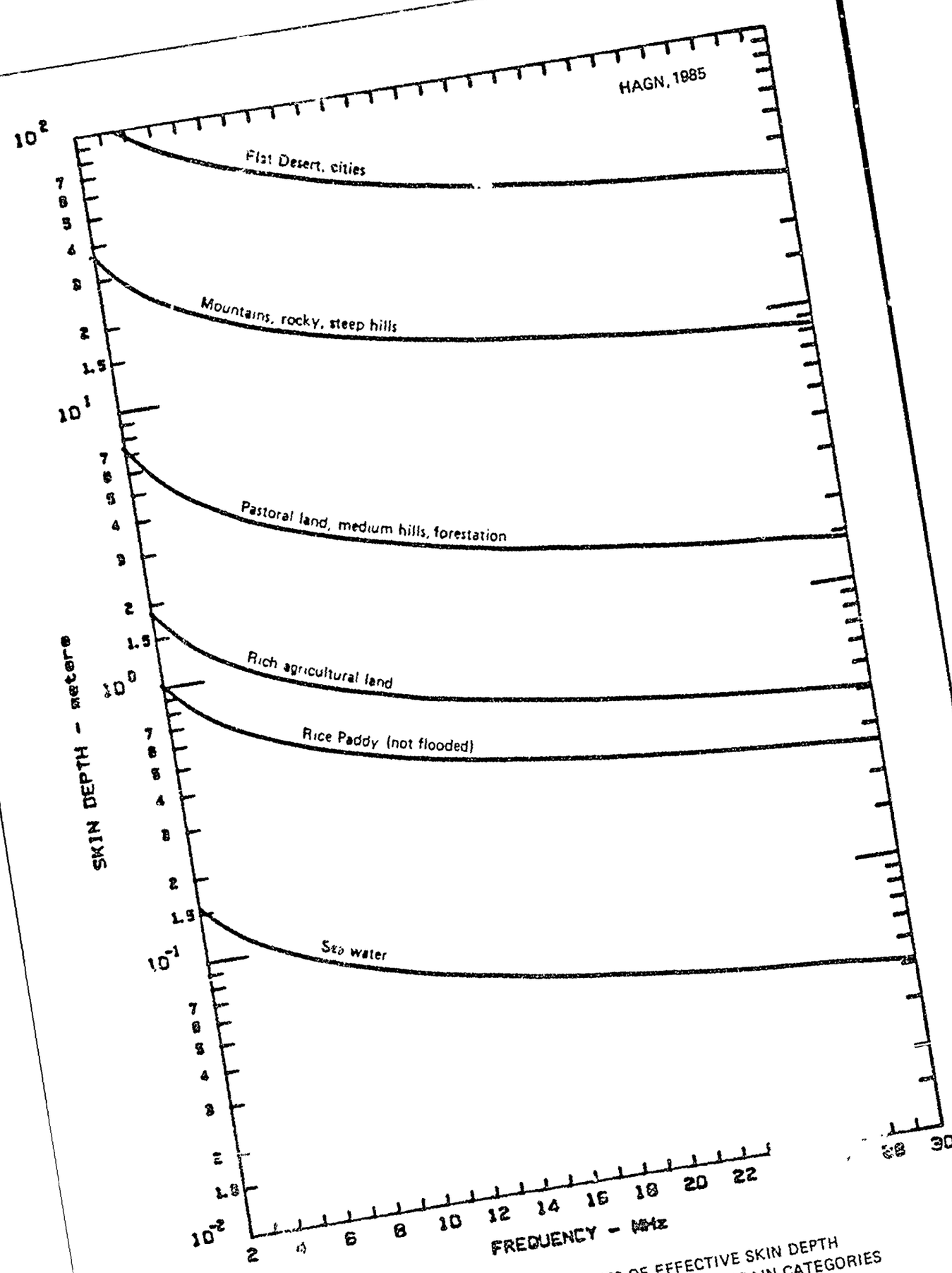
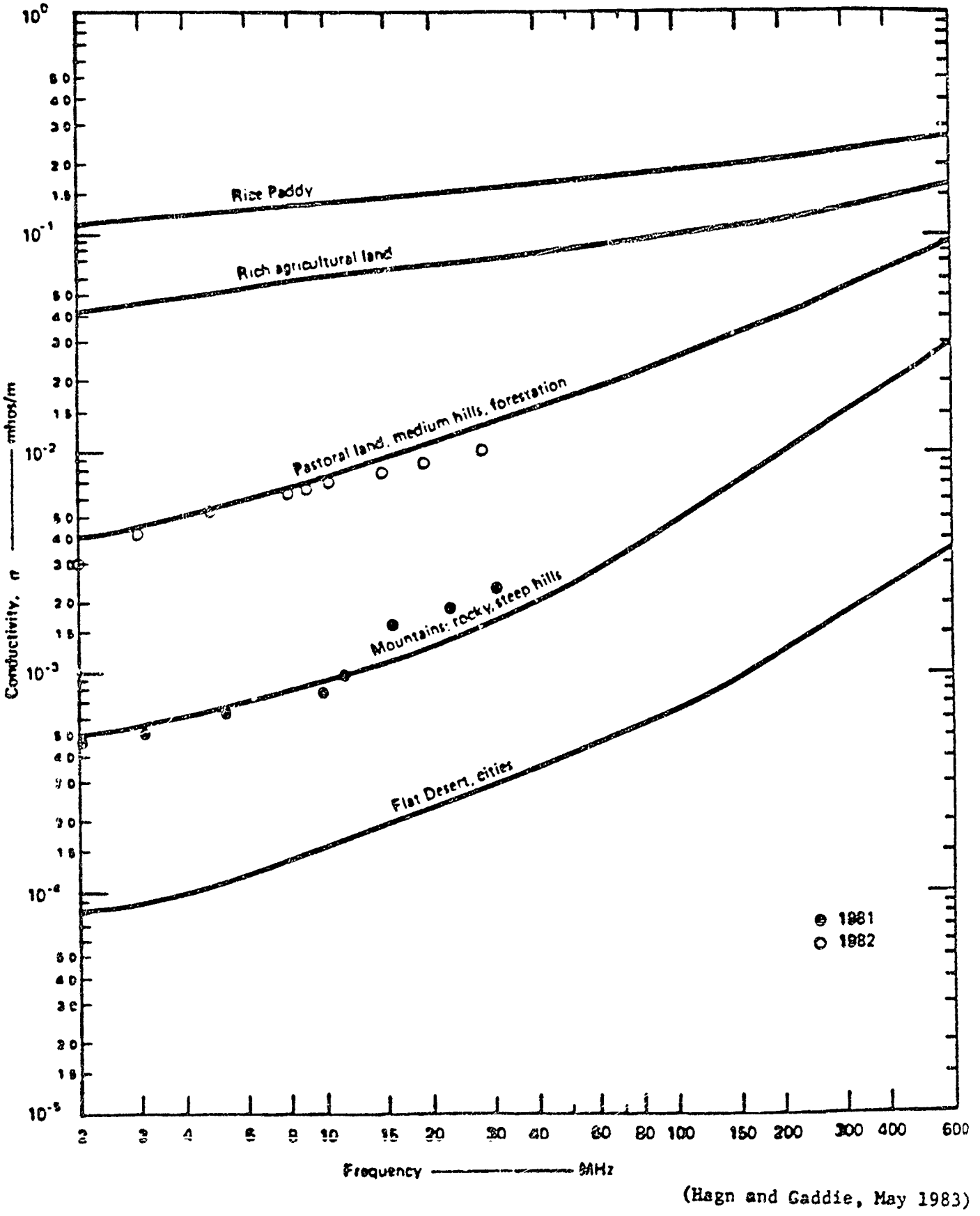
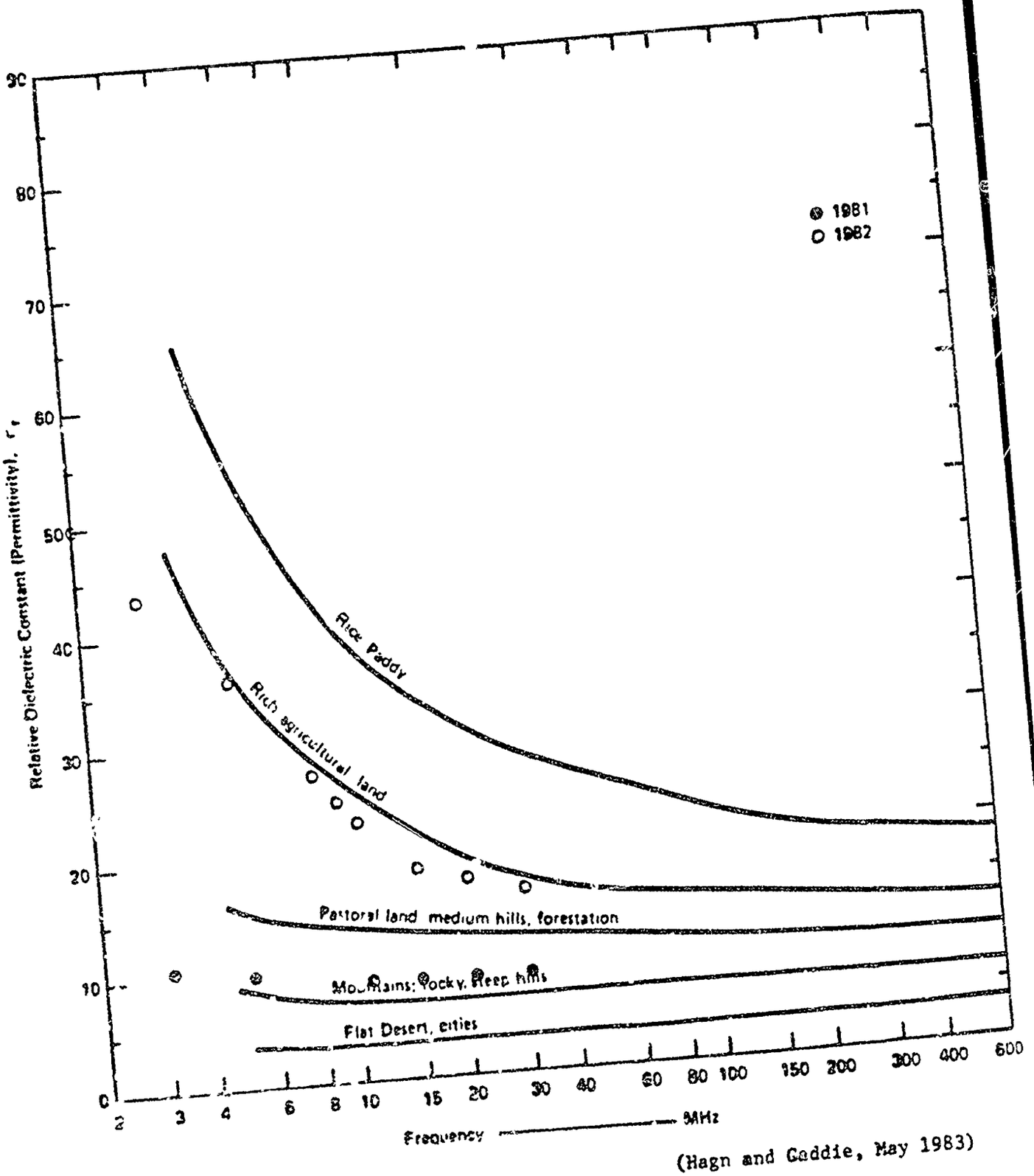


Figure 27 SRI GENERIC CURVES OF EFFECTIVE SKIN DEPTH VS FREQUENCY FOR SELECTED TERRAIN CATEGORIES



(Hagn and Gaddie, May 1983)

Figure 28 EFFECTIVE GROUND CONDUCTIVITY VS FREQUENCY INFERRED FROM E(d) DATA



(Hagn and Caddie, May 1983)

Figure 29 EFFECTIVE GROUND RELATIVE DIELECTRIC CONSTANT VS FREQUENCY INFERRED FROM THE E(d) DATA

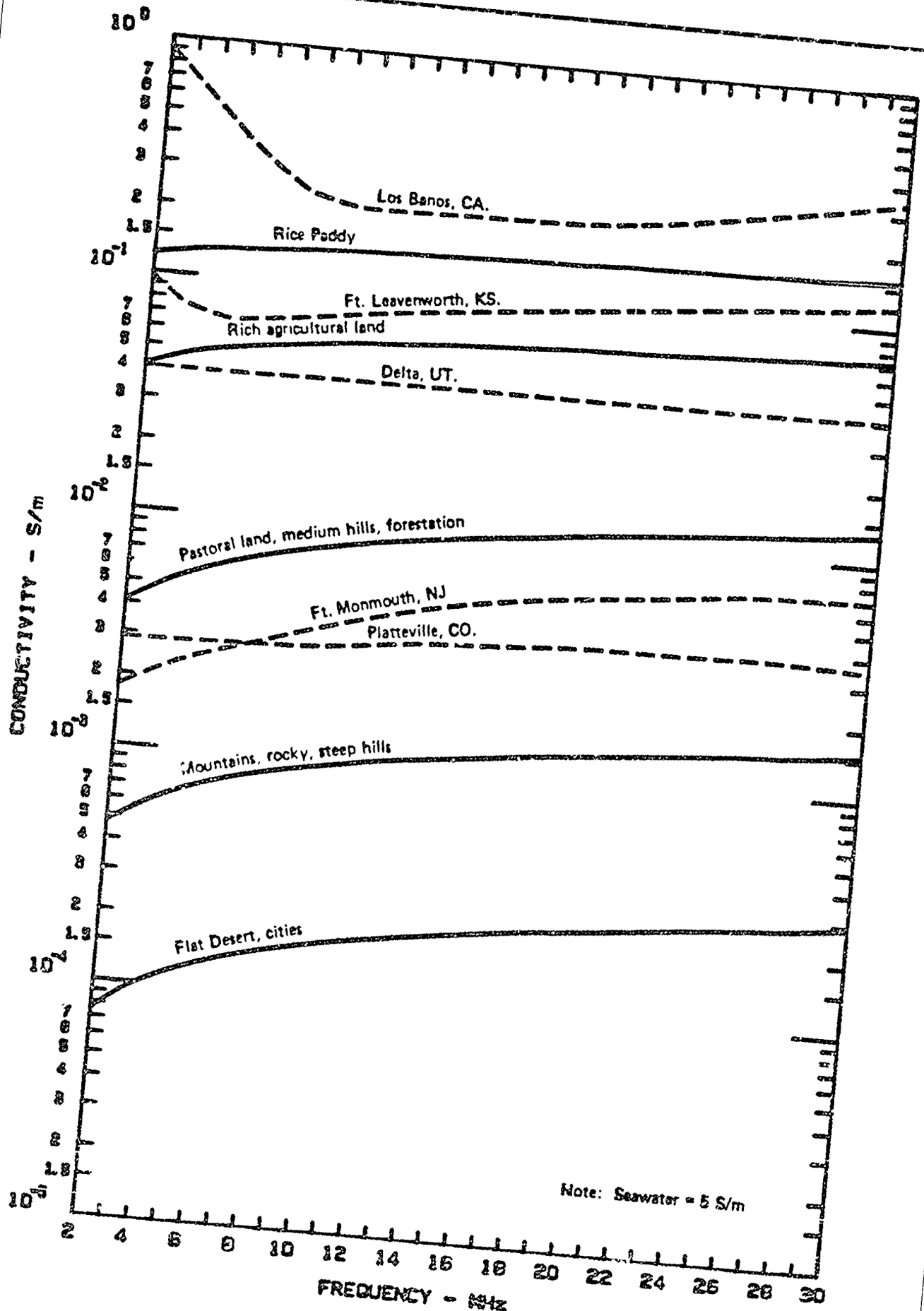


Figure 30 EFFECTIVE GROUND CONDUCTIVITY FOR FIVE ANTENNA TEST FIELD SITES VS SRI GENERIC CURVES FOR SELECTED TERRAIN CATEGORIES

(Harnish, et al., 1985)

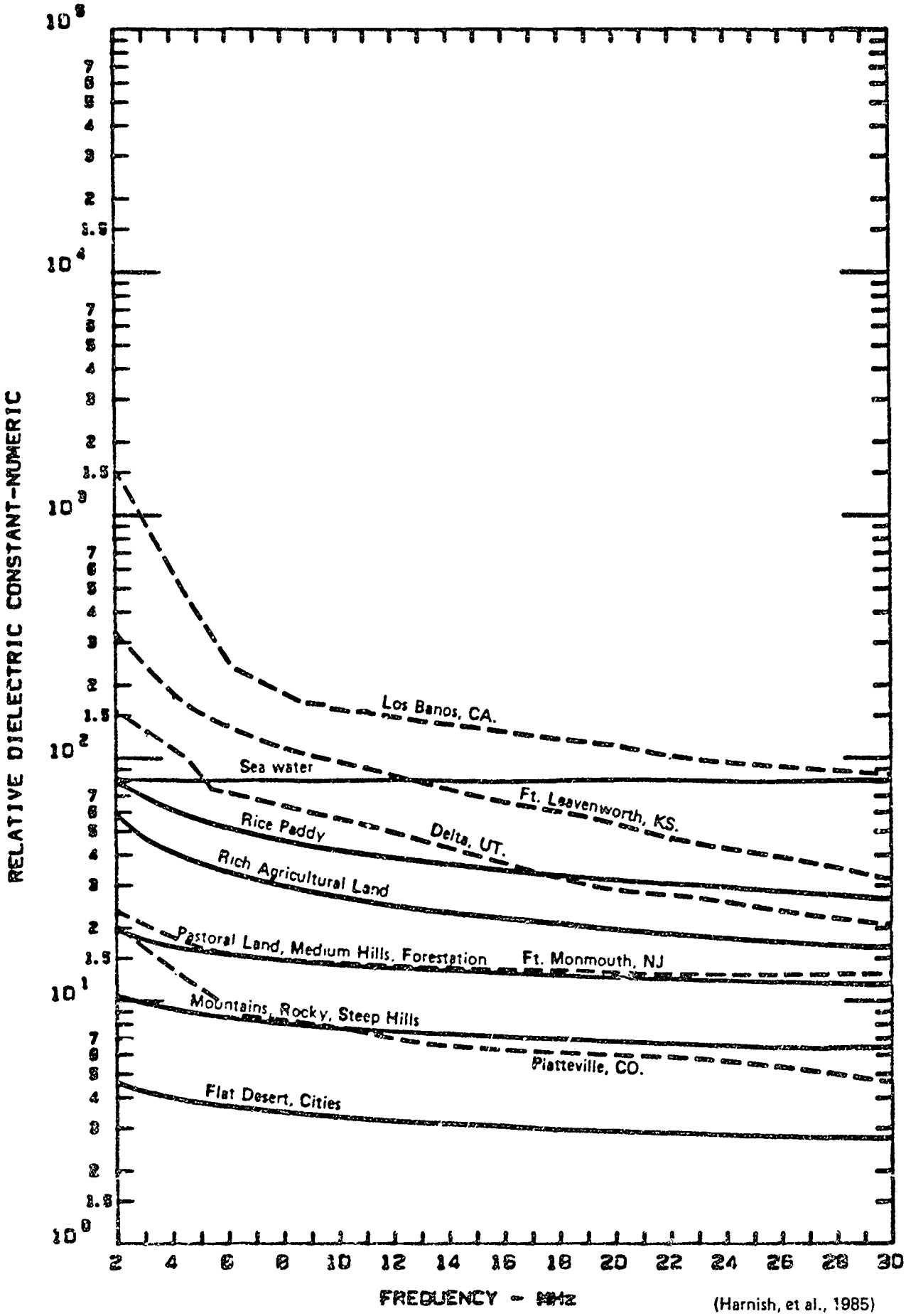


Figure 31 EFFECTIVE RELATIVE DIELECTRIC CONSTANT FOR FIVE ANTENNA TEST FIELD SITES VS SRI GENERIC CURVES FOR SELECTED TERRAIN CATEGORIES

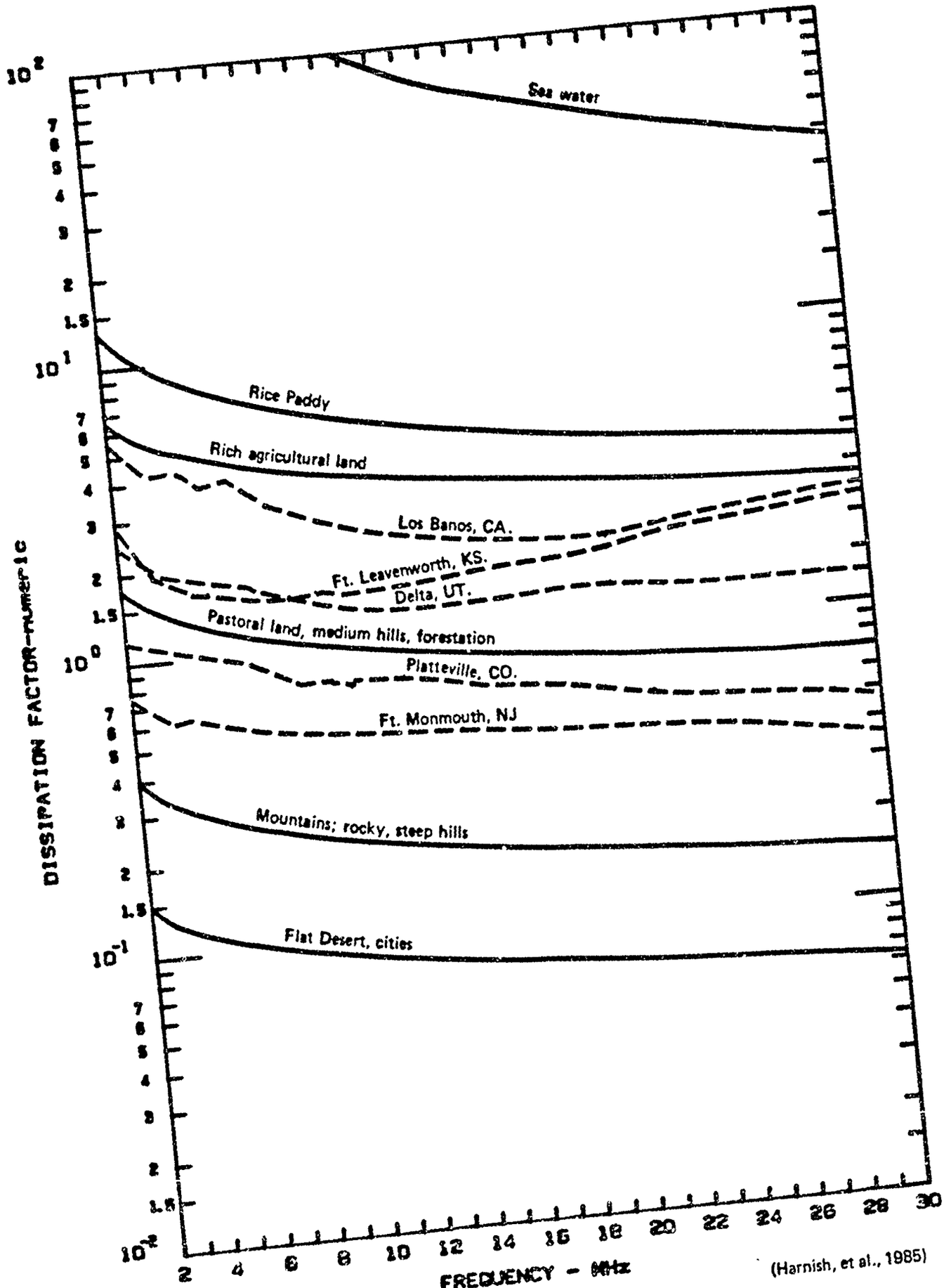


Figure 32 EFFECTIVE GROUND DISSIPATION FACTOR FOR FIVE ANTENNA TEST FIELD SITES VS SRI GENERIC CURVES FOR SELECTED TERRAIN CATEGORIES

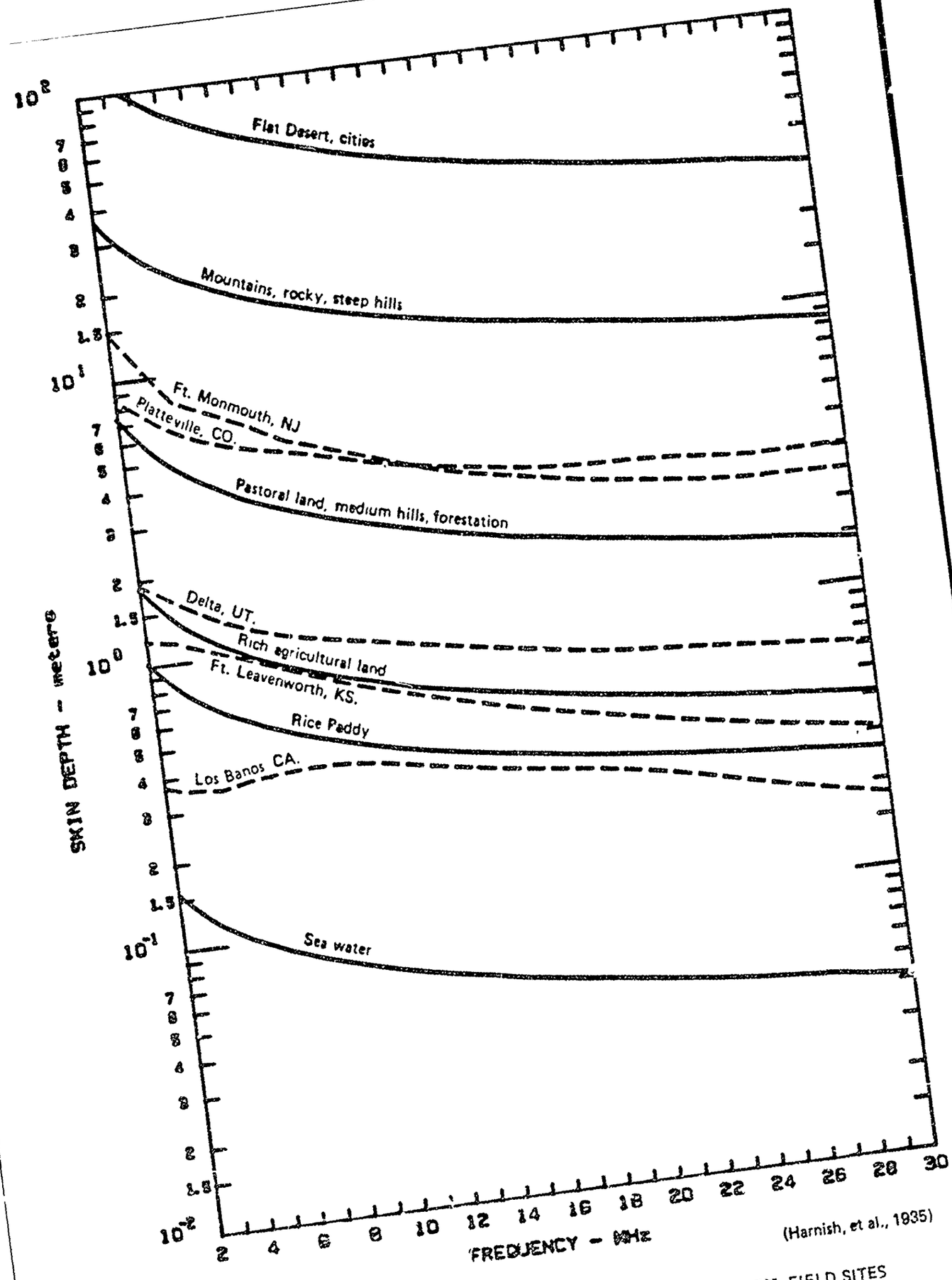


Figure 33 EFFECTIVE SKIN DEPTH FOR FIVE ANTENNA TEST FIELD SITES VS SRI GENERIC CURVES FOR SELECTED TERRAIN CATEGORIES

TABLE 6

Bill Moision's Equation for
Hagn's Generic Effective Ground Relative Dielectric Constant
and Ground Conductivity Versus Frequency (2 to 30 MHz) Model
for Selected Terrain Categories:

$y = BX^M$, where X = Frequency in MHz

TERRAIN TYPE	RELATIVE DIELECTRIC CONSTANT	CONDUCTIVITY
1. Seawater	B = 81.0 M = 0.0	B = 5.0 M = 0.0
2. Marsh (Rice Paddy)	B = 110.295 M = -0.417	B = 0.1115 M = 0.106
3. Rich agricultural land	B = 78.349 M = -0.459	B = $3.547X10^{-2}$ M = 0.214
4. Medium hills, forestation	B = 22.142 M = -0.192	B = $2.754X10^{-3}$ M = 0.459
5. Mountains, rock, steep hills	B = 12.323 M = -0.198	B = $3.419X10^{-4}$ M = 0.447
6. Flat Desert, cities	B = 5.256 M = -0.195	B = $5.300X10^{-5}$ M = 0.495
7. Permafrost - winter	B = 14.417 M = -0.128	B = $5.973X10^{-4}$ M = 0.559
8. Permafrost - summer	B = 110.295 M = -0.417	B = 0.1115 M = 0.106

[Sailors, 1984] (Corrected by Hagn, 1985)

Monmouth, NJ sites were in what could be described as pastoral land. The Delta, UT site was on a good farm and the Ft. Leavenworth, KS site was at the edge of a very fertile corn field, and both could be described as rich agricultural land, which, when wet, could even approximate a rice paddy. The dry mineralized lake bed at Los Banos (and Delano, see Figures 8 and 9) is a special type of soil which was not considered when the original generic curves were developed. The agreement by category is at least fair,

and the agreement between curve pairs is reasonable with the higher conductivity and the higher relative dielectric constant coming from the same site.

CONCLUSIONS

The following conclusions are offered:

- The current handbook values for ground constants are incorrect at HF, and they can cause significant errors in predictions made by models such as NEC.
- The effective permittivity and conductivity of most soils are both important at HF and they are a function of frequency in the HF band (i.e., they are not constant as assumed by the CCIR and others).
- The effective permittivity and conductivity for a specific soil are a strong function of the volumetric moisture content (MC) of the soil and the MC varies with depth at a given time and with time after a rain at a given depth. This variation of moisture content vs type of soil with depth and time has not yet been modeled.
- Despite the variations of moisture content and electrical properties of soil with time, it is useful to develop curves of "ground constants" versus frequency for different types of soils described in environmentally relevant terms.
- The generic curves of ground constants versus frequency given in this paper are the best available values to use in NEC and other antenna or propagation models in the absence of data measured at HF, but they should be revised in light of the data now available.
- These generic curves are useful for parameter sensitivity studies, but measured values of permittivity and conductivity on the frequency of interest are required for validation of NEC and for other applications (e.g., radiation hazard fields) where accurate predictions of antenna or propagation characteristics are required.
- The SRI OWL kit is useful in open fields and in existing antenna fields and in forests; whereas, the E(d) method is restricted to open areas.

- In the absence of measured values for the effective permittivity and conductivity, but when volumetric moisture content is known, the universal curves of Longmire and Smith provide reasonable estimates at HF. Measured or a priori estimates of dc conductivity are required to use the Longmire and Smith curves to estimate conductivity.

RECOMMENDATIONS

It is recommended that:

- The generic curves for relative permittivity and conductivity versus frequency presented in this paper should be used at HF instead of the current handbook values.

- Where measured volumetric moisture content data are available, the universal curves of Longmire and Smith can be used to estimate relative permittivity, and they can be used along with the matching generic curve to estimate conductivity (i.e., to estimate the effect of dc conductivity).

- The generic curves should be used in a parameter sensitivity analysis to determine the accuracy of ground constants needed for a given application.

- When more accurate values than the generic curves are required (e.g., NEC validation, important installations, antenna calibration, etc.) it is necessary to perform in situ measurements from the surface down to the skin depth using the SRI OWL kit in a sampling manner.

- The E(d) technique can be used at open sites in conjunction with the SRI OWL kit.

- If measurements down to the skin depth are not practical (e.g., 2 MHz in dry soil), then it is important to determine soil homogeneity with depth by other means (e.g., geophysical prospecting, a priori knowledge, etc.) for depths beyond the probe depth for HF techniques involving probes inserted into the soil.

- The data now available should be used to revise and improve the generic curves, and equations should be developed to describe these new curves.

- The relacionship between volumetric moisture content and any new generic curves should be developed.
- The accuracy of any new generic curves should be estimated based upon the data used to develop them and upon independent checks.

ACKNOWLEDGMENTS

The author appreciates the support in data acquisition form Mr. A. Sparks and Mr. R. Ball of Contel Federal Systems, Inc. at the VOA sites, and from Messrs. H. Parker, W. Makarabhiromya, J. Gaddie, R. Sarran and L. Harnish of SRI for the remainder of the sites. Mr. Sarran also generated the software used for data reduction and for creation of the generic curves. Any errors of omission or commission are the responsibility of the author.

REFERENCES

Albrecht, H.J., "On the Relationship Between Electrical Ground Parameters," Proc. IEEE, Vol. 53, p. 544, May 1965.

Barker, G.E., "Measurement of the Radiation Patterns of Full-Scale HF and VHF Antennas," IEEE Trans. on Antennas and Propagation, Vol. AP-21, No. 4, pp. 538-544, July 1973.

Breakall, J.K., G.J. Burke and E.K. Miller, "The Numerical Electromagnetics Code (NEC)" Proceedings of the 6th Symposium and Technical Exhibition on Electromagnetic Compatibility, pp. 301-308, Zurich, March 1985.

Burke, G.J., and A.J. Poggio, "Numerical Electromagnetic Code (NEC)--Method of Moments," NOSC Technical Document 116, Vol. I, Contract MIPR-N0095376MP, Lawrence Livermore Laboratory, Livermore, CA, January 1981.

Burke, G.J., "Numerical Electromagnetics Code--User's Guide Supplement for NEC-3 for Modelling Buried Wires," Lawrence Livermore Laboratory, Livermore, CA, October 1983.

CCIR, "Methods for Estimating Effective Electrical Characteristics of the Surface of the Earth," Report 879, Recommendations and Reports of the CCIR, 1982, Vol. V Propagation in Non-Ionized Media, International Radio Consultative Committee, International Telecommunication Union, Geneva, pp. 65-73, 1982a.

CCIR, "Electrical Characteristics of the Surface of the Earth," Recommendation 527-1 and Report 229-4, Recommendations and Reports of the CCIR, 1982, Vol. V, Propagation in Non-Ionized Media, International Radio Consultative Committee, International Telecommunication Union, Geneva, pp. 57-65, 1982.

The Encyclopedia of Physics, Vol. 16, p. 706, Springer-Verlag, Berlin, 1958.

Fine, H., "An Effective Ground Conductivity Map of the Continental United State," Proc. IRE, Vol. 42, No. 9, pp. 1405-1408, September 1954.

Goldstein, N.E., H.W. Parker and G.H. Hagn, "Three Techniques for Measurement for Ground Constants in the Presence of Vegetation," Special Technical Report 30, Contract DA-36-039 AMC-00040(E), SRI Project 4240, Stanford Research Institute, Menlo Park, CA, March 1967. AD 672 496.

Hagn, G.H., and G.E. Barker, "Research-Engineering and Support for Tropical Communications," Final Report, Contract DA-36-039 AMC-00040(E), SRI Project 4240, Stanford Research Institute, Menlo Park, CA, February 1970. AD 889 169.

Hagn, G.H., "Electrical Properties of Forested Media," Presented at Workshop on Radio Systems in Forested and/or Vegetated Environments, Fort Huachuca, AZ, 6 November 1973, pp. I-c-1 to I-c-15, Technical Report ACC-ACO-1-74, February 1974. AD 780 712.

Hagn, G.H., "VHF Radio System Performance Model for Predicting Communications Operational Ranges in Irregular Terrain, IEEE Trans. Com., Vol. Com-28, No. 9, Part I, pp. 1637-1644, September 1980.

Hagn, G.H., Private Communication, February 1982a.

Hagn, G.H., B.M. Sifford and R.A. Shepherd, "The SRICOM Probabilistic Model of Communication System Performance -- A Users Manual for Engineers, Applications Programmers, and Systems Programmers," Final Report, Contract NT-81-RC-16011, SRI Project 3603, SRI International, Arlington, VA, May 1982b.

Hagn, G.H., and J.C. Gaddie, "MF and HF Ground Constants at Fort Ord, California," Final Letter Report, Contract N00014-83-M-0113, SRI Project 5082, SRI International, Arlington, VA, February 1983a.

Hagn, G.H., "Calibration of the University of Alaska 615-Ft End-Fed Longwire Antenna," Final Letter Report, SRI Project 4729, SRI International, Arlington, VA, April 1983b.

Hagn, G.H., and J.C. Gaddie, "A Follow-Up Evaluation of the AN/FRG-13(V) Pusher Antenna at Keflavik, Iceland," Final Report, Contract DAEA-18-81-0062/Order GG01, SRI Project 4701, SRI International, Arlington, VA, May 1983c. FOUO.

Hagn, G.H., and J.C. Gaddie, "Medium and High Frequency (MF and HF) Ground Electrical Parameters Measured During 1982 at Seven Locations in the United States With the SRI OWL Probe Kit," Presented to URSI Com. A, National Radio Science Meeting Abstracts, Boulder, CO, p. 78, 11-14 January 1984.

Hagn, G.H. and R.D. Sarran, "HF Ground Constants at the Voice of America (VOA) Station at Greenville, N.C.," SRI Project 8081-020, SRI International, Arlington, VA, May 1985.

Hagn, G.H. and J.H. Faulconer, "HF Ground Constants at the Voice of America (VOA) Station at Kavala, Greece," Letter Report, Contract IA-21531-23, Subcontract SC-G-48254 SRI Project 8081-020, SRI International, Arlington, VA, June 1985a.

Hagn, G.H. and J.H. Faulconer, "HF Ground Constants at the Voice of America (VOA) Station at Tinang, Philippines," Letter Report, Contract IA-21531-23, Subcontract SC-G-48254, SRI Project 8081-020, SRI International, Arlington, VA, June 1985b.

Hagn, G.H. and J.H. Faulconer, "HF Ground Constants at the Voice of America (VOA) Station at Rhodes, Greece," Letter Report, Contract IA-21531-23, Subcontract SC-G-48254, SRI Project 8081-020, SRI International, Arlington, VA, June 1985c.

Hagn, G.H. and J.H. Faulconer, "HF Ground Constants at the Voice of America (VOA) Station at Monrovia, Liberia," Letter Report, Contract IA-21531-23, Subcontract SC-G-48254, SRI Project 8081-020, SRI International, Arlington, VA, June 1985d.

Hagn, G.H. and J.H. Faulconer, "HF Ground Constants at the Voice of America (VOA) Station at Selebi-Phikwe, Botswana," Letter Report, Contract IA-21531-23, Subcontract SC-G-48254, SRI Project 8081-020, SRI International, Arlington, VA, June 1985e.

Hagn, G.H. and J.H. Faulconer, "HF Ground Constants at the Voice of America (VOA) Station at Delano, California," Letter Report, Contract IA-21531-23, Subcontract SC-G-48254, SRI Project 8081-020, SRI International, Arlington, VA, July 1985f.

Hagn, G.H., and L.O. Harnish, "Measurement Techniques for HF Tactical Antennas," Presented at the DARPA-AFCEA-IEEE Technical Conference on Tactical Communications, The Next Generation, Fort Wayne, Indiana, 22-24 April 1986.

Harnish, L.O., J.H. Faulconer and G.H. Hagn, "Advanced Development Model Tactical HF Antenna Kits and Related Field Tests," Quarterly Technical Status Report: 22 March 1985 - 21 June 1985, Contract DAAB07-84-C-K545, SRI Project 7439, SRI International, Arlington, VA, July 5, 1985.

IEEE, "IEEE Guide for Radio Methods of Measuring Earth Conductivity," IEEE Standard 356-1974, Institute of Electrical and Electronics Engineeers, New York, 1974.

ITT, Reference Data for Radio Engineers, Howard W. Sams and Co., Inc., 7th Edition, New York, 1985.

Keller, G.V., and F.C. Frischknecht, Electrical Methods in Geophysical Prospecting, Pergamon Press, London, 1966.

King, R.J., "Wave Tilt Measurements," IEEE Trans. Ant. and Prop., Vol. AP-74, pp. 115-119, 1976.

King, R.W.P., S. Smith, M. Owens and T.T. Wu, Antennas in Matter, The MIT Press, Cambridge, MA, p. 428, 1981.

King, R. and J. Cavanagh, Private Communication, January 1987.

Kirkscether, E.J., "Ground Constant Measurements Using a Section of Balanced Two-Wire Transmission Line," IEEE Trans. Ant. and Prop., Vol. AP-8, No. 3, pp. 307-312, May 1960.

Kovattana, T., "Electrical Ground Constants of Central, Eastern, and Northeastern Thailand," Special Technical Report 29, February 1967. AD 661 058.

Longmire, C.L., and K.S. Smith, "A Universal Impedance for Soils," Topical Report, Contract DNA 001-75-C-0094, Mission Research Corp., Santa Barbara, CA, October 1975.

Lytle, R.J., "Electrical Characteristics of Earth Medium," in "Workshop on Radio Systems in Forested and/or Vegetated Environments," ed. by J.R. Wait, R.H. Ott and T. Telfer, Technical Report No. ACC-ACO-1-74, pp. I-0-1 to I-0-7, USACC, Fort Huachuca, AZ, February 1974. AD 780 712.

Lytle, R.J., "Measurement of Earth Medium Electrical Characteristics: Techniques, Results and Applications," IEEE Trans. Geosc. Electron., Vol. GE-12, No. 3, pp. 81-101, July 1974.

Lytle, R.J., "Properties of the Ground Inferred from Electromagnetic Measurements," IEEE Trans. on Antennas and Propagation, Vol. AP-27, No. 6, pp. 899-901, November 1979.

Norton, K.A., "The Calculation of Groundwave Field Intensity Over a Finitely Conducting Spherical Earth," Proc. IRE, Vol. 29, p. 623, December 1941.

Parker, H.W., and W. Makarabhiromya, "Electric Constants Measured in Vegetation and in Earth at Five Sites in Thailand," Special Technical Report 43, Contract DA36-039 AMC 00040(E), SRI Project 4240, Stanford Research Institute, Menlo Park, CA, December 1967. AD 674 740.

Sailors, D.B., "Tactical Decision Aids for HF Communication," Technical Document 782, Naval Ocean Systems Center, San Diego, CA, 15 November 1984.

Sarran, R.D., J.H. Faulconer, M. Lee, K.P. Springfield and G.H. Hagn, "HF Ground Constants at the Voice of America (VOA) Station at Chilaw, Sri Lanka," Letter Report, Contract IA-21979-23, Subcontract SC-G-48266, SRI Project 1089, SRI International, Arlington, VA, November 1985.

Smith-Rose, R.L., "Electrical Measurements on Soil with Alternating Currents," Proc. IEE, Vol. 75, pp. 221-237, 1934 (see also Wireless Section, Proc. IEE, Vol. 8, p. 293, 1934).

Smith-Rose, R.L., "The Electrical Properties of Soil at Frequencies up to 100 MHz; With a Note on the Resistivity of Ground in the United Kingdom," Proc. Phys. Soc. London, Vol. 47, p. 923, 1935.

Smith, G.S., and R.W.P. King, "The Resonant Linear Antenna as a Probe for Measuring the In-Situ Properties of Geological Media," J. Geophys. Res., Vol. 79, pp. 2623-2628, 1974.

Terman, F.E., Radio Engineer's Handbook, McGraw Hill Book Co., Inc., New York, p. 709, 1943.

Wait, J.R., editor, Electromagnetic Probing in Geophysics, Golem Press, Boulder, CO, 1971.

Wheeler, H.A., "Universal Skin Effect Chart for Conducting Materials," Electronics, Vol. 25, pp. 152-154, November 1952.

NOTE ADDED IN PROOF:

The measured conductivity data for highly conducting ground exhibit a decreasing trend with increasing frequency in the lower part of the HF band. This is an instrumentation effect, and it was accounted for in making the generic curves.

COMPARISON OF MEASURED AND NEC-CALCULATED CHARACTERISTICS OF A VERTICAL MONOPOLE WITH BURIED GROUND RADIALS

Lawrence O. Harnish
Mary Lee
George H. Hagn

Information Sciences and Technology Center
SRI International
1611 North Kent Street
Arlington, Virginia 22209

Presented at the 3rd Annual Meeting of the
Applied Computational Electromagnetics Society (ACES)

Monterey, California

24-26 March 1987

COMPARISON OF MEASURED AND NEC-CALCULATED CHARACTERISTICS OF A VERTICAL MONOPOLE WITH BURIED GROUND RADIALS

L.O. Harnish, M. Lee and G.H. Hagn
Information Sciences and Technology Center
SRI International
1611 North Kent Street
Arlington, Virginia 22209

A 7.5-ft vertical monopole with 16 symmetrical 40-ft buried ground radials was installed over several types of ground and used as a reference antenna during HF antenna tests. At each test site, the RF ground constants were measured using the SRI open wire line (OWL) kit, and the feedpoint impedance of the 7.5-ft monopole was measured on selected frequencies across the HF band. At one test location, the SRI XELEDOP full-scale pattern measurement system was used to measure the elevation plane directivity pattern and absolute gain of the monopole for vertical polarization from the horizon up to 45 degrees. The Numerical Electromagnetics Code (NEC-3) was used to compute the impedance, directivity, and gain of the monopole for comparison with the measured values. One implementation of NEC-3 was developed for the monopole by Dr. R. W. Adler. A second implementation was made by Ms. M. Lee to evaluate the effectiveness of a more detailed geometric representation on the accuracy of NEC calculations. The results of these comparisons show good correlation between the antenna characteristics predicted by NEC and those measured during the field tests over several types of ground. This paper presents the results of those comparisons, and it also discusses the usefulness of these types of data for future validation of NEC.

INTRODUCTION

A reference antenna with known characteristics is a key component of the instrumentation required to conduct effective antenna measurements [IEEE, 1979]. At HF, the significance of the reference antenna increases due to the many other measurement variables which are generally involved [FitzGerrell, 1967a, b; Hagn and Harnish, 1986]. The reference antenna provides data which can be used to: 1) calibrate the relative gains of test antennas for absolute gain; 2) verify measurement results; and, 3) estimate measurement error. SRI designed and built a 7.5-ft vertical monopole for use as a reference antenna during measurements of vertically-polarized HF antennas [Harnish, et al., 1985a; Harnish, et al., 1985b; Harnish, et al., 1986]. The monopole was installed at several test locations over 16 symmetrical 40-ft wire radials buried 7 inches below the ground surface. The monopole's feedpoint impedance and the RF ground constants were measured at each location to support post-test computer analysis of the antenna. Additionally, when SRI's XELEDOP full-scale airborne antenna pattern measurement system [Barker, 1973; Hagn and Harnish, 1986; Harnish, et al., 1986] was employed, the directivity and gain of the reference antenna also were obtained. The data gathered during these measurements were then compared to similar values calculated using the Numerical

Electromagnetics Code (NEC-3) [Burke and Poggio, 1981; Breakall, et al., 1985; Burke, 1983] to verify the calibration of the measurement system and to estimate the accuracy of the measurements. Through an iterative comparison process between the measured and modelled data, it was possible to refine the model geometry to obtain a high level of confidence in the NEC-3 characterization of the antenna.

During the past two years, the 7.5-ft monopole antenna has been installed over several types of ground throughout CONUS in support of HF antenna tests [Harnish, et al., 1985a; Harnish, et al., 1985b; Harnish, et al., 1986]. The measured impedance data from three of these installations and the measured directivity and gain from a recent test are presented herein to demonstrate the accuracy of the calculations which can be obtained from NEC. A comparison of the measured impedance data with calculations from two NEC models is provided for a geometric representation of the monopole and ground radials produced by Dr. Richard Adler [Adler, 1985], and for a more detailed geometric model created at SRI by Ms. Mary Lee. Also, the measured gain and directivity pattern data are compared to the SRI-developed NEC model.

DESCRIPTION OF THE 7.5-FT MONOPOLE

At each test site, the 7.5-ft monopole was installed over the buried ground radials and used as the primary reference antenna for validating the antenna measurements. The same physical monopole was used at Los Banos, CA and Platteville, CO, but a new structure was built for use at Merrimack, NH. New ground radials were installed at all three sites. Figure 1 shows the monopole installed at Sanders Associates' Merrimack, NH field site. The monopole element was a 7.5-ft length of AWG #10 tinned copper wire mounted inside an 8-ft long, 2-inch diameter PVC pipe. The monopole had no matching device, and it was fed through a BNC connector located 6 inches above ground. The monopole was erected over 16 ground radials which were 40 feet in length and buried 7 inches below the ground. The 10-gauge copper ground wires were brought to the surface and clamped together to form a 12-inch circular tie ring at the monopole's base as shown in Figure 2.

DESCRIPTION OF THE NEC MODELS

Two NEC models were developed for comparison with the measured data. The Adler model consisted of a segmented vertical wire from the ground to the top of the monopole. A single segment (2 segments for frequencies above 20 MHz) was used to penetrate the air-ground interface to a depth of 2 inches. Using the submerged end of this penetration wire as a tie point, sixteen (16) symmetrical sloping radials were created to reach a depth of 7 inches at a distance of 2 feet from the antenna. The radials were then extended to a total length of 40 feet at a constant 7-inch depth. The antenna was fed at the lowest (or bottom) segment of the 7.5-ft wire. Ground constants measured at the three sites using the SRI OWL kit [Goldstein, et al., 1967; Hagn and Gaddie, 1984; Hagn, 1987] were used in the model. Figure 3 shows the geometry employed for the Adler model.

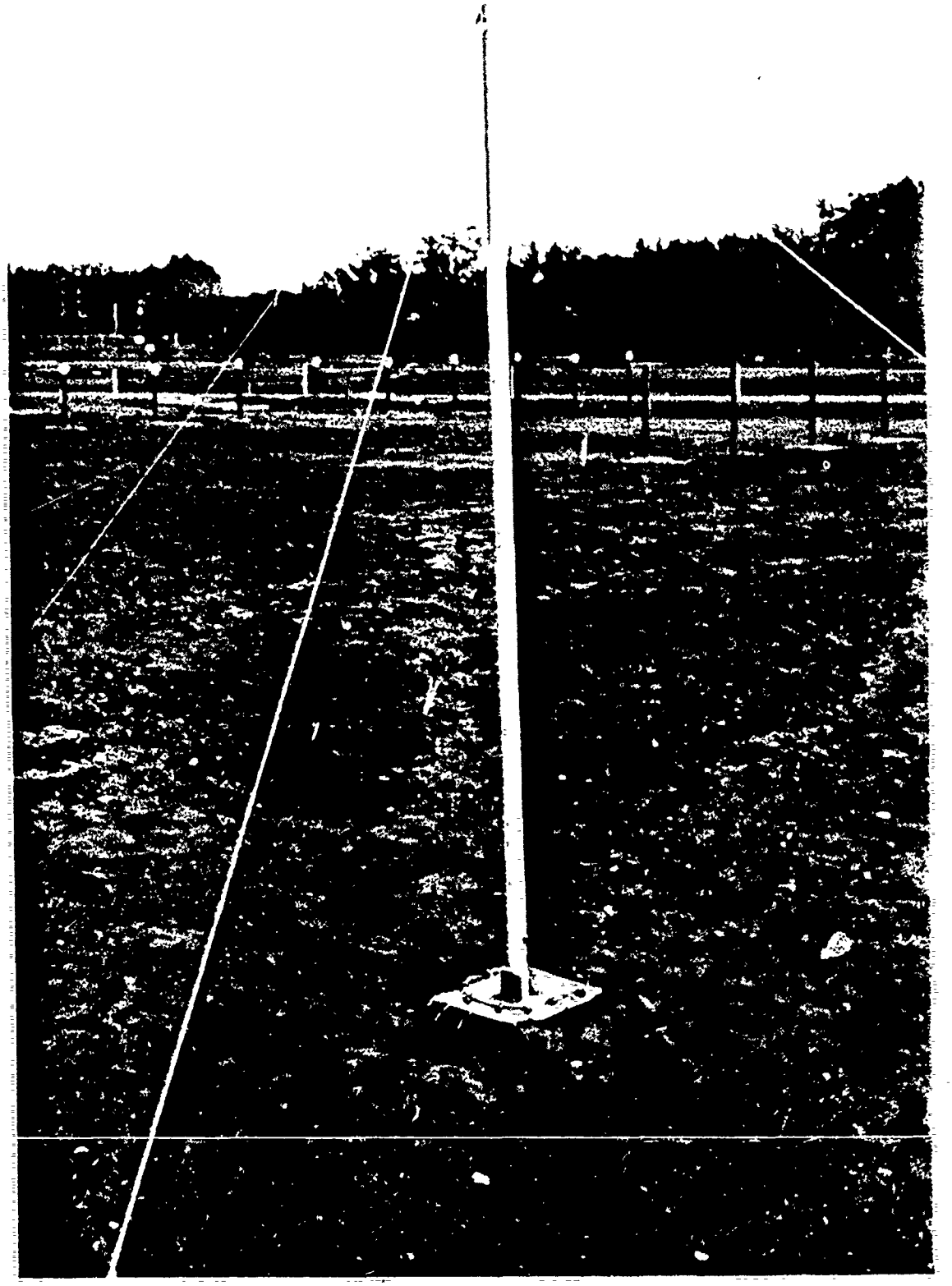


Figure 1 7.5-FT MONOPOLE REFERENCE ANTENNA AT MERRIMACK, NH

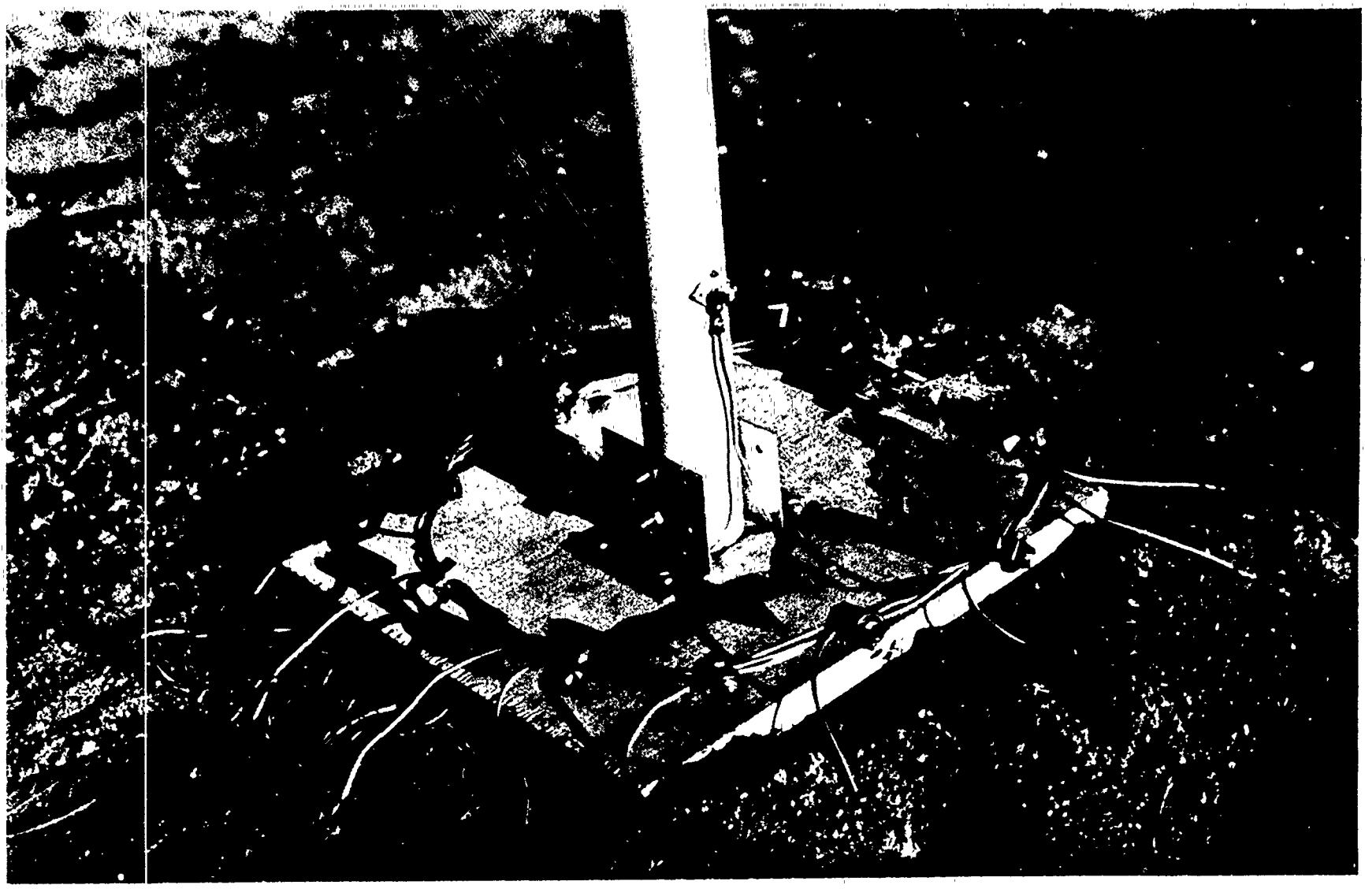


Figure 2 BASEPLATE OF THE 7 5-FT MONOPOLE SHOWING THE FEEDPOINT AND BURIED GROUND RADIAL CONNECTIONS

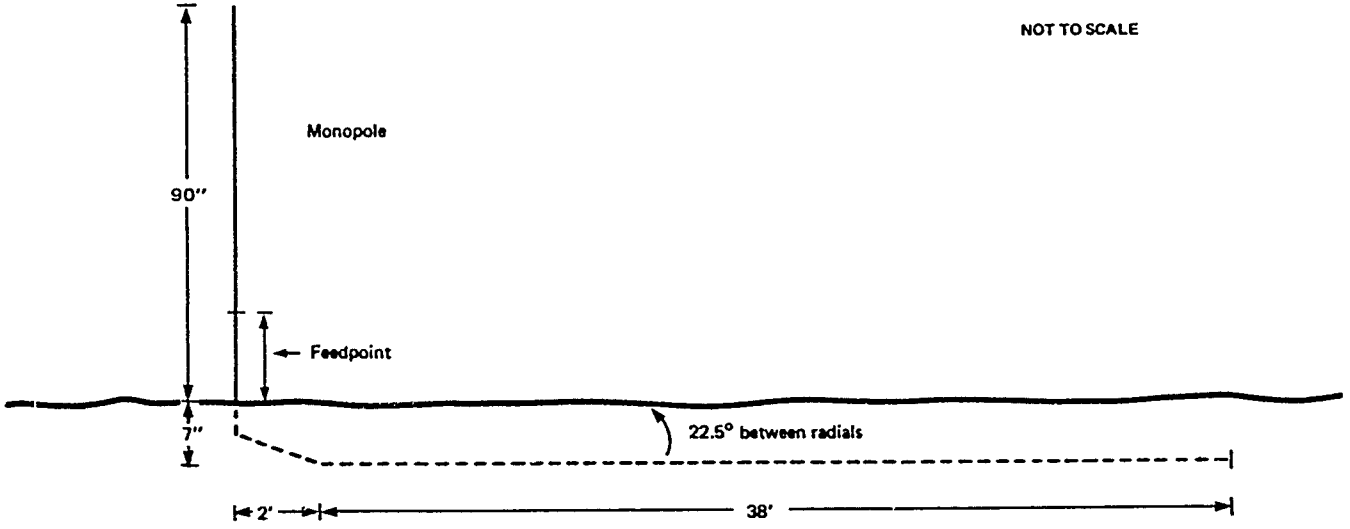


Figure 3 WIRE GEOMETRY USED IN THE ADLER MODEL OF THE 7.5-FT MONOPOLE OVER 16 SYMMETRICAL 40-FT BURIED GROUND RADIALS

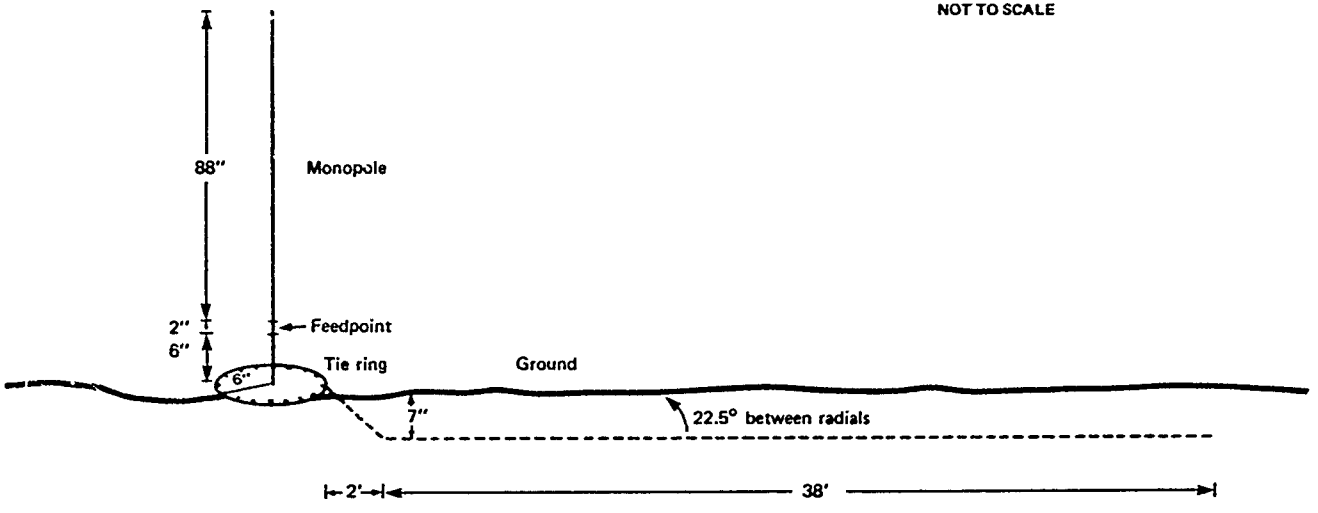


Figure 4 WIRE GEOMETRY USED IN THE LEE MODEL FOR THE 7.5-FT MONOPOLE OVER 16 SYMMETRICAL 40-FT BURIED GROUND RADIALS

A second model was created at SRI to examine the sensitivity of the model to small changes in the structure's geometry. The wire geometry used in this latter model was a more detailed representation of the monopole's feedpoint and ground radial tie ring. The monopole was represented by a multi-segmented wire from the feedpoint (6 inches above the ground) to the top at 8 feet above the ground. A thick wire tie ring was constructed 1-inch above the ground from which the 16 radials sloped into the ground to a depth of 7 inches and then extended out at that depth to a total length of 40 feet. Figure 4 shows the geometry employed for the Lee model.

DESCRIPTION OF THE ANTENNA MEASUREMENTS

The feedpoint impedance of the 7.5-ft monopole was measured on each test frequency using a computer-controlled vector impedance bridge. The measurements, in polar form (magnitude and phase angle), were converted to the rectangular form (R + jX) and used to compute the antenna's VSWR and mismatch loss relative to a 50-ohm impedance level.

The directivity pattern and gain measurements were obtained at the Sanders Associates' field site in Merrimack, NH using the SRI XELEDOP airborne antenna pattern measurement system [Barker, 1973; Hagn and Harnish, 1986; Harnish, et al., 1986]. The XELEDOP transmitter was towed in its vertically polarized configuration to a known distance from the monopole. Slant range from the helicopter to the antenna was measured with an X-band (8.6 GHz) distance measuring system with an accuracy of $\pm$ 10 m. The helicopter towcraft lifted the XELEDOP to a predetermined hover altitude (corresponding to a desired elevation angle) and the maximum received power was measured using the SRI antenna data acquisition system. Multiple data samples were collected on each of six (6) test frequencies before the XELEDOP was lifted to the next hover altitude. These lift-then-hover flight profiles were then repeated at the same and other distances ranging from 3,000 ft to 20,000 ft to obtain the elevation plane directivity pattern and gain data for the 7.5-ft monopole. The accuracy of the XELEDOP position was better than $\pm$ 1 degree in azimuth below 25^{0} and $\pm$ 2 degrees at higher angles. The elevation angle accuracy was better than $\pm$ 1 degree as verified with a transit.

HF GROUND CONSTANTS

The ground constants were measured at each site using the SRI open wire line (OWL) kit [Goldstein, et al., 1967; Hagn and Gaddie, 1984; Hagn, 1987]. Figure 5 shows the kit in operation at the Merrimack, NH site. Values for the macroscopic relative dielectric constant (permittivity, ϵ_r) and conductivity (σ) were measured versus frequency for selected depths at several sampling locations. At a given site, the values for probe depths most closely matching the skin depth were selected. Site median values were computed and used in the NEC models.

The soil at Los Banos, CA consisted of relatively soft clay to a depth of 6 inches, and beneath this was a layer of very hard compacted clay to a depth of 24 inches or more. The surface of this old, dry lake bed was covered with a white alkaline powder. The conductivity and relative

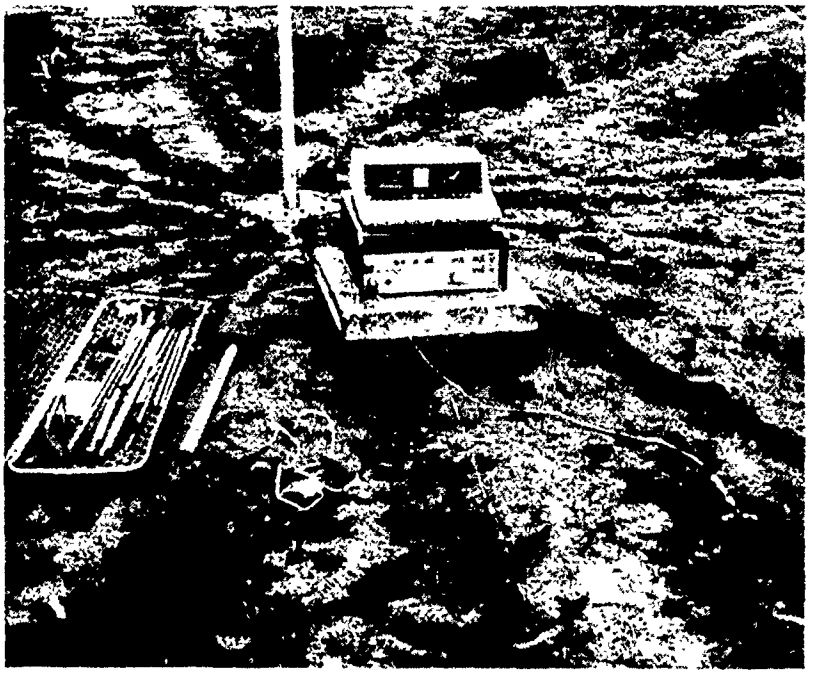


Figure 5 SRI Open-Wire Line (OWL) Ground Constants Measurement Kit at 7.5-ft Monopole Feed at Merrimack, NH

dielectric constant values measured at Los Banos were extremely high with both sets of values exceeding those typical of a "rice paddy." At Platteville, CO and Merrimack, NH, the soil was loose sandy brown loam. At Platteville, the ground was frozen to a depth of 6 inches during the antenna measurements. The RF ground constants at both locations approximated those typical of mountains or pastoral land; however, both the permittivity and conductivity values measured at Platteville were slightly higher than those measured at Merrimack. The foreground terrain in the vicinity of the antenna was relatively flat at all three sites. However, the ground at Merrimack dropped 75 feet at a distance of approximately 1,500 feet in front of the antenna.

ANALYSIS OF IMPEDANCE DATA

The measured feedpoint impedance for the 7.5-ft monopole at each of the three sites described above were compared to NEC-calculated impedance values for the wire geometries used by Adler and Lee. Table 1 shows the measured and modelled impedance for the highly conductive ground at Los Banos. The agreement between the two NEC-3 models was reasonable for frequencies below 25 MHz. Both NEC models predicted a slightly higher input resistance than was observed, although the Adler model provided closer agreement above 20 MHz. The Lee model predicted resonance at slightly above 28 MHz, whereas, the Adler model predicted resonance above 30 MHz. The observed resonant frequency was 29.1 MHz, and the input resistance was 38.4 ohms at resonance.

TABLE 1

Comparison of Measured and Computed Impedance
for the 7.5-ft Monopole at Los Banos, California

Frequency (MHz)	ϵ_r	σ (S/m)	Measured R + jX (ohms)	NEC Adler Model R + jX (ohms)	NEC Lee Model R + jX (ohms)
2.0	1480.0	0.90	5.5 -j3160	0.6 -j5363	0.1 -j4088
5.0	377.3	0.41	2.2 -j1242	2.3 -j2096	1.9 -j1596
7.0	206.8	0.28	7.6 -j 868	4.0 -j1457	3.1 -j1107
9.0	165.9	0.23	3.4 -j 655	6.1 -j1091	4.7 -j 827
12.0	145.2	0.23	5.6 -j 461	7.9 -j 597	7.7 -j 570
14.0	134.6	0.23	7.8 -j 372	10.3 -j 480	10.1 -j 453
16.0	125.7	0.23	9.0 -j 303	13.1 -j 367	12.9 -j 360
18.0	115.0	0.23	12.3 -j 244	16.2 -j 311	16.1 -j 283
20.0	110.0	0.24	15.1 -j 191	19.6 -j 247	19.6 -j 216
24.0	94.0	0.28	25.8 -j 109	27.4 -j 141	28.0 -j 104
28.0	85.8	0.33	33.8 -j 26	37.1 -j 53	39.1 -j 7
30.0	85.0	0.35	42.7 +j 19	42.9 -j 13	46.0 +j 38

Data also were taken down to 2 MHz at Platteville (see Table 2), where the ground was significantly less conductive than at Los Banos. The Adler model provided a better match to the measured input resistance on most frequencies below 25 MHz. The measurements may have experienced some interference at 9.51 MHz, causing an abnormally high input resistance to be recorded. The Lee model provided a better match of the measured input resistance at 27 MHz and 30 MHz, and the agreement with the measured reactance was better at all frequencies. The measurements and the Lee model show resonance near 28 MHz; whereas, the Adler model again shows resonance above 30 MHz.

The Adler model work preceded the measurements at Merrimack, and it was rerun by SRI for that site. The Lee model provided excellent agreement with the measured results for Merrimack (see Table 3). The reactances predicted with the Lee model were higher than observed on frequencies below 24 MHz at all three sites. The Adler model also provided excellent agreement with the measured input resistance at frequencies below 30 MHz. Again, the Adler model predicted a higher resonant frequency than did the Lee model and the measurements. The observed resonant frequency was 27.9 MHz, and the input resistance was 40.3 ohms at resonance.

TABLE 2

Comparison of Measured and Computed Impedance
for the 7.5-ft Monopole at Platteville, Colorado

Frequency (MHz)	ϵ_r	σ (S/m)	Measured R + jX (ohms)	NEC Adler Model R + jX (ohms)	NEC Lee Model R + jX (ohms)
2.01	22.6	0.0030	15.8 -j3020	8.6 -j5342	0.0 -j4066
5.12	10.6	0.0030	6.1 -j1169	8.7 -j2049	2.0 -j1554
6.91	8.9	0.0031	7.4 -j 847	9.4 -j1481	3.4 -j1121
9.51	7.8	0.0032	36.9 -j 586	11.4 -j1023	6.2 -j 770
12.90	6.4	0.0034	9.1 -j 400	13.6 -j 543	10.6 -j 510
17.50	5.8	0.0038	24.6 -j 238	19.0 -j 328	18.2 -j 295
20.43	5.7	0.0038	20.0 -j 165	24.2 -j 231	25.0 -j 196
24.13	5.3	0.0038	32.6 -j 84	32.6 -j 132	35.0 -j 93
27.60	4.8	0.0037	46.9 -j 14	41.7 -j 54	46.7 -j 9
30.10	4.8	0.0037	60.1 +j 33	49.6 -j 2	57.3 +j 48

TABLE 3

Comparison of Measured and Computed Impedance
for the 7.5-ft Monopole at Merrimack, New Hampshire

Frequency (MHz)	ϵ_r	σ (S/m)	Measured R + jX (ohms)	NEC Adler Model R + jX (ohms)	NEC Lee Model R + jX (ohms)
9.5	5.8	0.0008	8.3 -j598	11.6 -j1029	7.3 -j772
15.0	5.5	0.0016	15.2 -j321	15.2 -j 433	14.2 -j398
19.5	5.5	0.0015	22.3 -j185	22.2 -j 260	23.2 -j225
24.7	5.5	0.0010	33.6 -j 71	34.2 -j 119	37.2 -j 79
30.0	5.5	0.0007	56.7 +j 51	49.4 -j 5	57.7 +j 44
35.0	5.5	0.0005	121.0 +j197	69.3 +j 88	84.0 +j155

A second technique was used to assess the accuracy of the NEC-computed impedance. For this analysis, both the measured and modelled impedance data were used to predict the VSWR (V) and mismatch loss (MML) relative to 50 ohms at the feedpoint:

$$MML = 10\log_{10}\left[\frac{(V+1)^2}{4V}\right], \text{ dB}$$

where

V = (1+p)/(1-p), voltage standing wave ratio; and,

p = reflection coefficient (for a 50-ohm cable in this case).

Table 4 compares the predicted and measured values of VSWR and mismatch loss for all three sites.

TABLE 4

Comparison of Measured and Predicted VSWR and Mismatch Loss

Site	Frequency (MHz)	Measured		Adler Model		Lee Model	
		VSWR	MML (dB)	VSWR	MML (dB)	VSWR	MML (dB)
Los Banos, CA	2.0	36313.3	39.6	958697.0	53.8	3050402.0	58.8
	5.0	14044.4	35.5	38172.4	39.8	26842.6	38.3
	7.0	1989.3	27.0	10627.6	34.2	7924.0	33.0
	12.0	768.1	22.8	908.8	23.6	850.5	23.3
	14.0	361.4	19.6	452.4	20.6	411.5	20.1
	16.0	209.8	17.2	232.7	17.7	205.1	17.1
	18.0	101.1	14.1	122.8	14.9	102.9	14.2
	20.0	51.9	11.3	65.2	12.3	50.5	11.2
	24.0	11.6	6.3	16.8	6.7	10.0	4.8
	28.0	2.1	0.6	3.3	1.5	1.3	0.1
	30.0	1.5	0.2	1.4	0.1	2.2	0.6
Platteville, CO	2.0	11545.6	34.6	66181.3	42.2	n.d.**	n.d.
	5.1	4489.1	30.5	9657.7	33.8	24191.1	37.8
	6.9	1945.8	26.9	4672.3	30.7	7406.2	32.7
	9.5*	188.2	16.8	1840.6	26.6	1920.8	26.8
	12.9	357.3	19.5	437.5	20.4	495.7	20.9
	17.5*	48.6	11.0	116.2	14.7	98.7	14.0
	20.4	30.1	9.0	46.6	10.9	33.2	9.4
	24.1	6.4	3.3	12.8	5.7	6.9	3.6
	27.6	1.3	0.1	3.1	1.3	1.2	0.1
	30.1	1.9	0.4	1.0	1.8	2.4	0.8

TABLE 4
(Concluded)

Comparison of Measured and Predicted VSWR and Mismatch Loss

Site	Frequency (MHz)	Measured		Adler Model		Lee Model	
		VSWR	MML (dB)	VSWR	MML (dB)	VSWR	MML (dB)
Merrimack, NH	9.5	867.9	23.4	1830.2	26.6	1640.0	26.1
	15.0	139.2	15.5	250.3	18.0	226.9	17.6
	19.5	33.4	9.5	60.6	12.1	46.2	10.8
	24.7	5.0	2.5	10.3	4.9	5.3	2.7
	30.0	2.5	0.9	1.1	0.0	2.2	0.7
	35.0	9.0	4.5	4.1	2.0	7.9	4.0

* Probable interference
** n.d. = no data.

The computed VSWR and MML values for both models compared favorably with the values measured at Los Banos on frequencies above 7 MHz. Both models show a difference in MML of 1 dB or less on frequencies above 7 MHz, except at 24.0 MHz, where the Lee model differed from the measured value by 1.5 dB (see Table 5). At frequencies below 7 MHz, both models were unable to accurately predict the measured input resistances, resulting in an MML difference of up to 14.2 dB for the Adler model and up to 19.2 dB for the Lee model. At Platteville, the Adler model showed a MML difference of 2.4 dB or less on frequencies above 7 MHz, while the Lee model showed a difference of 1.4 dB or less over the same frequency range. At 9.5 and 17.5 MHz, the difference was 9.8 dB and 10.0 dB for the two models, respectively. These latter differences are probably due to interference on the measurement frequencies. Again, both models were unable to accurately predict the measured input resistances for frequencies below 7 MHz. The Adler model differed from the measured values on all frequencies by 3.2 dB or less, and the Lee model differed by 2.7 dB or less at Merrimack where the lowest test frequency was 9.5 MHz.

In summary, the mismatch loss computed from the NEC calculations of R + jX using both models agree to within 3 dB of the measured values on interference-free frequencies above 7 MHz. The average difference between the measured and modelled MML (for all sites on frequencies above 7 MHz) was 0.7 dB for the Lee model and 1.4 dB for the Adler model. Below 7 MHz, neither model could approximate the measured MML values due to predicting input resistances that were lower than the measured values.

DIRECTIVITY AND GAIN ANALYSIS

SRI used the XELEDOP full-scale antenna measurement system to assess the low elevation angle response of the 7.5-ft monopole installed at

TABLE 5

Difference Between Measured and Modelled Predictions of Mismatch Loss (in dB)

Site	Frequency (MHz)	Adler Model	Lee Model	Frequency (MHz)	Adler Model	Lee Model
Los Banos, CA	2.0	14.2	19.2	16.0	0.5	0.1
	5.0	4.3	2.8	18.0	0.8	0.1
	7.0	7.2	6.0	20.0	1.0	0.1
	9.0	1.0	0.6	24.0	0.4	1.5
	12.0	0.8	0.5	28.0	0.9	0.5
	14.0	1.0	0.5	30.0	0.1	0.4
Platteville, CO	2.0	7.6	n.d.**	17.5*	3.7	3.0
	5.1	3.3	7.8	20.4	1.9	0.4
	6.9	3.8	5.8	24.1	2.4	0.3
	9.5*	9.8	10.0	27.6	1.2	0.0
	12.9	0.9	1.4	30.1	1.4	0.4
Merrimack, NH	9.5	3.2	2.7	24.7	2.4	0.2
	15.0	2.5	2.1	30.0	0.9	0.2
	19.5	2.6	1.3	35.0	2.5	0.5

* Probable interference
** n.d. = no data.

Merrimack, NH [Harnish, et al., 1986]. The data base obtained between 9 and 12 October 1986 contains approximately 5,000 signal strength measurements on the monopole. These samples were taken at various distances from the antennas on six (6) frequencies and at approximately 17 elevation angles from 1 to 45 degrees. Figure 6 shows a block diagram of the overall data reduction and analysis methodology. The first step in the data reduction process was to transfer the tracking data and the P_r data to an IBM-PC/XT where the data analysis software was resident. Following the transfer of all data, the tracking data and P_r data were merged by matching the time tag for each P_r record with the closest time tag from the tracking data. Since the tracking data were obtained at 4-second intervals throughout each flight, the selected tracking data samples were always within $\pm$ 2 seconds of the P_r measurement.

Prior to analyzing data obtained on the 7.5-ft monopole, it was necessary to analyze the calibration data obtained during the horizontal polarization overflights of the half-wave horizontal dipoles in order to compute the maximum effective radiated power [ERP(0°)] of the XELEDOP. The XELEDOP

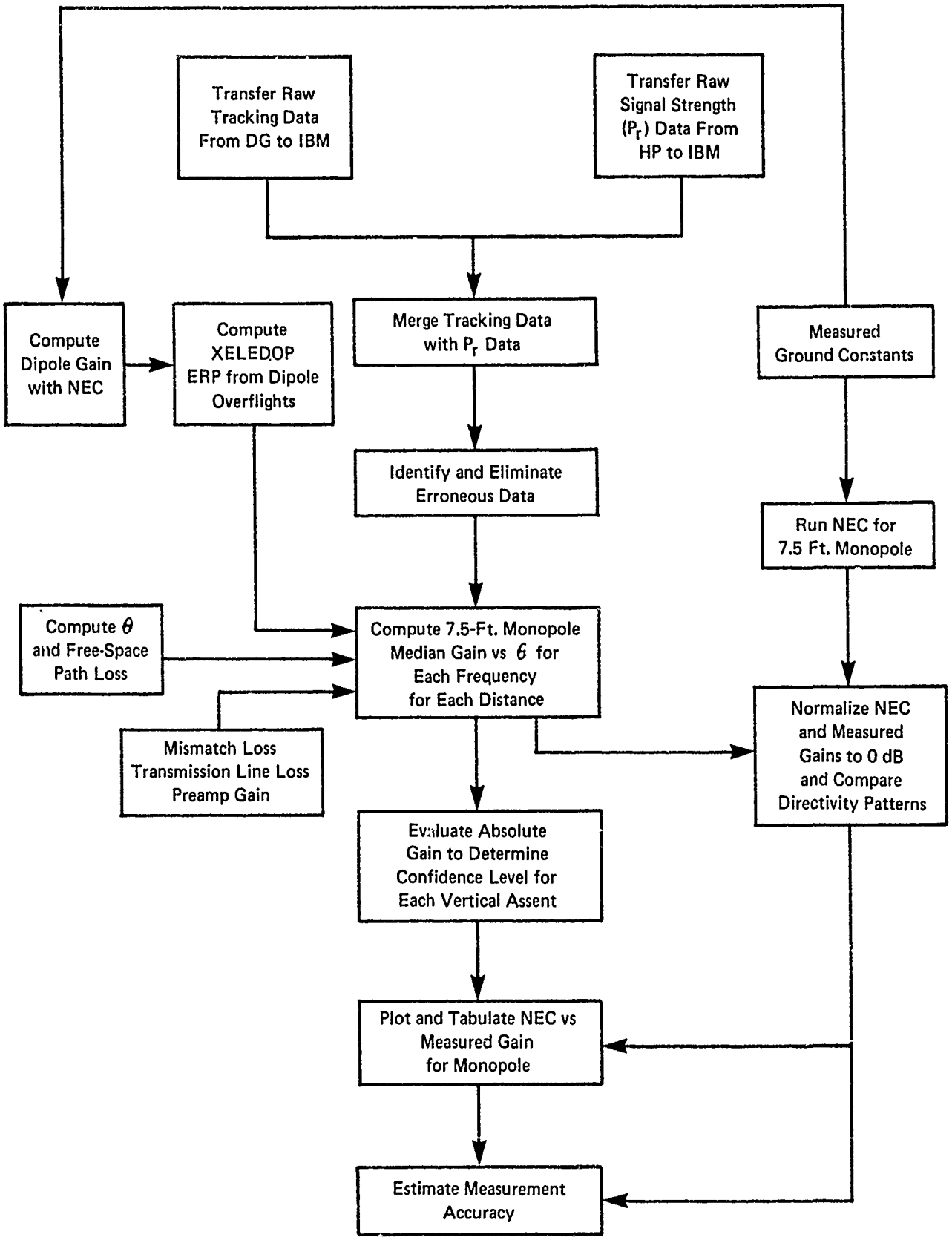


Figure 6 OVERVIEW OF PATTERN AND GAIN DATA REDUCTION AND ANALYSIS PROCESS

ERP values, obtained from the dipole overflights, were used in a detailed analysis of the 7.5-ft monopole reference antenna to estimate the overall accuracy of the measured antenna data. The power received on the dipoles during eight successive overflights using the same frequency was typically repeatable to better than $\pm$ 0.5 dB of the mean value and the standard deviation was less than 0.4 dB except at 30 MHz where the repeatability from the lower powered transmitter was typically within 1 dB and the standard deviation was 0.8 dB [Harnish, et al., 1986].

NEC-3 was used to compute the gain (in dBi) of the 7.5-ft monopole (Lee model) on each of the 6 test frequencies using the RF ground constants measured at the Merrimack field site. The NEC and measured gains were then compared and an RMS difference between the values was computed over all elevation angles for each test frequency as the measure of accuracy for the absolute calibration of the measured data. The absolute gain values measured at each elevation angle and distance from the reference monopole were normalized to reflect 0 dB at the elevation angle corresponding to the peak measured gain (G_{amax}) in order to compare the antenna's directivity patterns versus the NEC-computed patterns. The angle of G_{amax} was limited to elevation angles within $\pm$ 4 degrees of the NEC-computed peak gain angle to permit a better comparison between the measured directivity and the NEC-computed directivity patterns. Standard deviations were computed as a measure of data variability for each frequency/distance/elevation angle combination in order to quantify measurement variability. All data gathered on a single azimuth from the monopole were then combined and the accuracy and variability measures were computed again.

The 7.5-ft monopole measurements of maximum received power were adjusted to obtain absolute gain (G_a, in dBi) versus elevation angle for each test frequency. The gains were computed for each elevation angle (θ) using:

$$G_a(\theta) = P_r(\theta) - ERP(\theta) + K + L_t + L_m - G_p + C, \text{ in dBi}$$

where:

$P_r(\theta)$ = measured maximum received power for each θ, in dBm;

$ERP(\theta)$ = $ERP(0^o) + 20 \log_{10} \cos \theta$, in dBm (XELEDOP effective radiated power);

$$K = 20\log_{10}\left[\frac{4\pi df}{300}\right] \text{, in dB;}$$

f = frequency, in MHz;

d = slant range to XELEDOP, in meters;

L_t = transmission line loss, in dB;

L_m = mismatch loss, in dB;

G_p = preamp gain, in dB; and,

C = correction factor for XELEDOP output power stability, in dB.

The G_a values from all ascents on a given azimuth were sorted and a median value was computed for each elevation angle. The absolute gain at each angle was then compared to the NEC gain at the corresponding angle. The differences for all angles were then used to compute the RMS difference between the measured and modelled data to obtain an estimate of the model (and measurement) accuracy. An RMS difference also was calculated for the range of elevation angles between 10 degrees and 30 degrees, where the measurements tend to be more accurate due to the XELEDOP's Hertzian dipole pattern and the 7.5-ft monopole's patterns at these angles [Tupper, et al., 1974]. Table 6 summarizes the accuracy estimates for the absolute gain calibration over all elevation angles. These data indicate that the absolute gains calculated using the calibration data obtained during the test are accurate over all elevation angles to within ± 2.3 dB for frequencies on or below 25 MHz and to within ± 3.1 dB for test frequencies of 30 and 35 MHz. Over the elevation angle range of 10 to 30 degrees, the accuracy estimates improve to less than 2 dB except for 35 MHz.

TABLE 6

Estimated Accuracy of Absolute Gain Calibration

Frequency (MHz)	RMS Difference in dB	
	1 to 45 degrees	10 to 30 degrees
9.5	1.8 dB	1.7 dB
15.0	2.1 dB	1.9 dB
19.5	1.3 dB	1.0 dB
24.7	2.3 dB	1.8 dB
30.0	3.0 dB	1.8 dB
35.0	3.1 dB	2.4 dB

The median G_a values were normalized to reflect a 0-dB peak of beam and compared to normalized NEC-pattern in order to assess the accuracy of the measured directivity patterns. Figure 7 shows the directivity pattern comparison for each frequency. At frequencies of 9.5, 15, and 19.5 MHz, the directivity patterns agree within ± 2 dB at nearly all elevation angles. However, the lowest angles (between 1 and 3 degrees) agree to within ± 3 dB. At 24.7 MHz there is close agreement (± 1 or 2 dB) at angles less than 20 degrees; whereas, above 20 degrees, the patterns agree

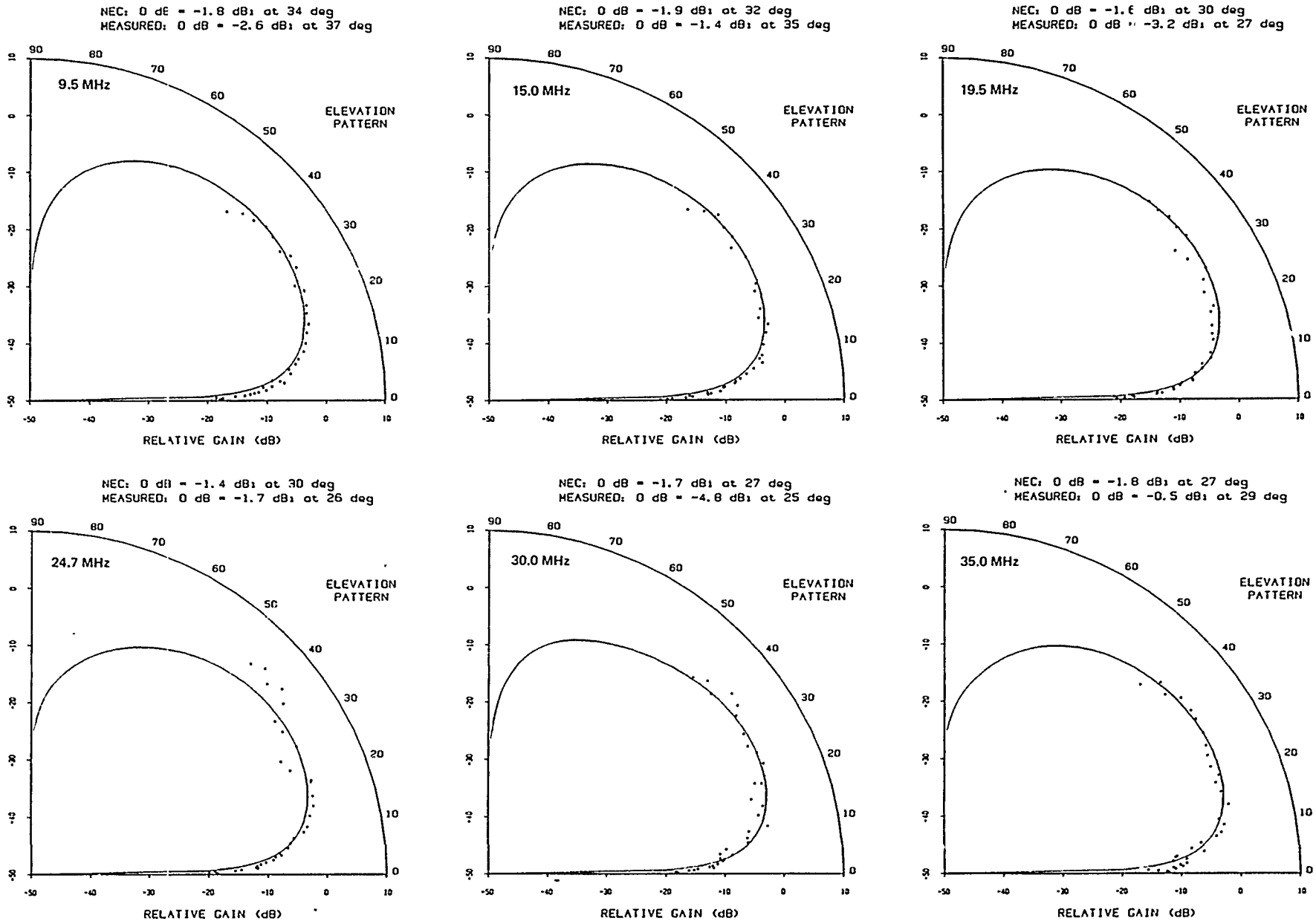


Figure 7 MEASURED VERSUS MODELLED DIRECTIVITY PATTERNS FOR THE 7.5-FT MONOPOLE

to within ± 3.5 dB. At 30 and 35 MHz, the patterns are similar to within ± 2 dB except at very low take-off angles where agreement between the measured pattern and the NEC calculations decreases to ± 4 dB, due to the lower signal-plus-noise-to-noise ratio of the measurements. Measured and modelled maximum gain results for the monopole are summarized in Table 7, which compares both G_{amax} values and the elevation angle for G_{amax}. The predictions and measurements agree to within ± 3.1 dB for all frequencies, and to within ± 1.6 dB, excluding 30 MHz. The predicted angle of maximum gain agree with the measured angle to within ± 3 degrees except at 24.7 MHz where the agreement was ± 4 degrees.

TABLE 7

Comparison of Measured and Modelled Maximum Gain (G_{amax}) for the 7.5-Ft Monopole Reference Antenna

Frequency (MHz)	Measured		Lee Model	
	Max. Gain (dBi)	Max. Angle (degrees)	Max. Gain (dBi)	Max. Angle (degrees)
9.5	-2.6	37	-1.8	34
15.0	-1.4	35	-1.9	32
19.5	-3.2	27	-1.6	30
24.7	-1.7	26	-1.4	30
30.0	-4.8	25	-1.7	27
35.0	-0.5	29	-1.8	27

CONCLUSIONS

The 7.5-ft monopole with buried radials provided a good test of NEC-3 against measured directivity, gain and impedance data obtained at sites with measured ground constants. The NEC-3 computations of directivity of the 7.5-ft monopole over the range of elevation angles from 1 degree up to 45 degrees showed excellent agreement with the values measured with the SRI XELEDOP. The angle of maximum gain was predicted to within ± 3 degrees in most cases, and the maximum absolute gain computations agreed with the measured values to within ± 3.1 dB, and to within ± 1.6 dB excluding 30 MHz. The overall accuracy, computed as an RMS difference using the gains measured at all angles, is estimated to be within ± 3.1 dB. This accuracy was improved to within ± 2.4 dB when the elevation angle range under consideration was reduced from 1-45 degrees to 10-30 degrees. The relatively low RMS differences between computed and measured absolute gain speaks well for the accuracy of both the XELEDOP ERP calibration as well as the NEC-3 model used with ground constants measured with the SRI OWL kit.

A more severe test of the NEC-3 model involves the input impedance. Both NEC-3 models accurately predicted the input resistance at frequencies above 7 MHz. Although neither model yielded accurate results below 7 MHz,

the Adler model tended to predict the input resistance more accurately on those frequencies below approximately 7 MHz. The Lee model predicted the input reactance more accurately than the Adler model over all three types of ground; however, both models tended to predict a higher reactance than was measured. Lee's more detailed model closely predicted the monopole's resonant frequency; whereas, the Adler model tended to predict a higher resonant frequency than was observed. The mismatch loss calculations relative to a 50-ohm reference impedance level were within $\pm$ 3 dB of the measured values at all three sites on frequencies above 7 MHz, with the more detailed Lee model providing the closer comparison with the measured data.

RECOMMENDATIONS

We recommend that further tests of NEC-3 be performed using data available from past measurements, as well as new data from experiments that are designed specifically to check selected aspects of NEC-3 (e.g., input resistance of wires penetrating the air-ground interface versus penetration depth and type of ground). The details of segmentation and formation of functions (e.g., the feed of the 7.5-ft monopole and other antennas like the Sloping V) should also be investigated using a combined approach of modeling and measurements to refine the guidelines for the use of NEC-3 for wire structures which penetrate the air-ground interface.

ACKNOWLEDGMENT

The authors appreciate the assistance and encouragement of Dr. Richard Adler. He suggested the 7.5-ft monopole antenna structure as being especially useful for a reference antenna to be calibrated by NEC-3. Dr. Adler performed the original NEC-3 model work on this monopole as a consultant to SRI under Contract No. DAAB07-84-C-K545. The authors also received encouragement from Mr. Bob Hoverter who monitored that contract at the U.S. Army Communications-Electronics Command. The authors also appreciated the support of the Sanders Associates staff during the monopole installation and XELEDOP tests at their Merrimack, NH site: Mr. Don Strang, Mr. Ron Nelson, Mr. Don LaRochelle, Mr. Tim Royce and Ms. Maria McDonough. Mr. Rick Sarran and Mr. Russ Scofield of SRI also assisted with those measurements. Finally, the authors appreciated the assistance of Mr. Bud Sargent of SRI in the design, construction and installation of the monopole at Los Banos and Platteville.

REFERENCES

Adler, R.D., Private Communication, December 1985.

Barker, G.E., "Measurement of the Radiation Patterns of Full-Scale HF and VHF Antennas," IEEE Trans. on Antennas and Propagation, Vol. AP-21, No. 4, pp. 538-544, July 1973.

Breakall, J.K., G.J. Burke and E.K. Miller, "The Numerical Electromagnetics Code (NEC)," Proceedings of the 6th Symposium and Technical Exhibition on Electromagnetic Compatibility, pp. 301-308, Zurich, March 1985.

Burke, G.J. and A.J. Poggio, "Numerical Electromagnetics Code (NEC) -- Method of Moments," NOSC Technical Document 116, Volume 1, Contract MIPR-N0095376MP, Lawrence Livermore Laboratory, Livermore, CA, January 1981.

Burke, G.J., "Numerical Electromagnetics Code - User's Guide Supplement for NEC-3 for Modelling Buried Wires," Lawrence Livermore Laboratory, Livermore, CA, October 1983.

FitzGerrell, R.G., "Gain Measurements of Vertically Polarized Antennas Over Imperfect Ground," IEEE Transactions on Antennas and Propagation, AP-15, No. 2, March 1967a.

FitzGerrell, R.G., "The Gain of a Horizontal Half-Wave Dipole Over Ground," IEEE Transactions on Antennas and Propagation, AP-15, pp. 569-571, July 1967b.

Goldstein, N.E., H.W. Parker and G.H. Hagn, "Three Techniques for Measurement for Ground Constants in the Presence of Vegetation," Special Technical Report 30, Contract DA-36-039 AMC-00040(E), SRI Project 4240, Stanford Research Institute, Menlo Park, CA, March 1967. AD 672 496.

Hagn, G.H. and J.C. Gaddie, "Medium and High Frequency (MF and HF) Ground Electrical Parameters Measured during 1982 at Seven Locations in the United States with the SRI OWL Probe Kit," Presented to URSI Com. A., National Radio Science Meeting, Boulder, CO, Abstract, p. 78, 11-14 January 1984.

Hagn, G.H. and L.O. Harnish, "Measurement Techniques for HF Tactical Antennas," Proceedings of the DARPA-AFCEA-IEEE Conference on Tactical Communications: The Next Generation, Fort Wayne, Indiana, 22-24 April 1986.

Hagn, G.H., "Ground Constants at High Frequencies (HF)," Proceedings of the 3rd Annual Review of Progress in Applied Computational Electromagnetics, Monterey, CA, March 1987.

Harnish, L.O., G.H. Hagn and J.H. Faulconer, "Advanced Development Model Tactical HF Antenna Kits and Related Field Tests," Quarterly Technical Status Report: 2 December 1984 - 21 March 1985, Contract DAAB07-84-C-K545, SRI Project 7439, SRI International, Arlington, VA, 21 March 1985a.

Harnish, L.O., J.H. Faulconer and G.H. Hagn, "Advanced Development Model Tactical HF Antenna Kits and Related Field Tests," Quarterly Technical Status Report: 22 March - 21 June 1985, Contract DAAB07-84-C-K545, SRI Project 7439, SRI International, Arlington, VA, 5 July 1985b.

Harnish, L.O., G.H. Hagn and M. Lee, "Full-Scale Measurements of the Boresight Elevation-Plane Directivity Pattern and Gain of an HF Beverage Antenna Array," Final Report, Contract P.O. NB2149, SRI Project 2624, SRI International, Arlington, VA, 15 December 1986.

IEEE, IEEE Standard Test Procedures for Antennas, IEEE Std 149-1979, Institute of Electrical and Electronics Engineers, Inc., New York, 1979.

Tupper, B.C., M.E. Muller, V.D. Cone and D.F. Alves, "Measured Radiation Patterns of Full-Scale HF Antennas: Volume 1," Final Report, SRI Project 3417, Contract CSD-C-74-1029, Stanford Research Institute, Menlo Park, CA, December 1974.

Note Added In Proof:
The Lee model predicted 0.04 ohms at 2.01 MHz at the Platteville site. The impedance bridge (polar coordinates) did not accurately measure the monopole input resistance at 7 MHz and lower frequencies. The NEC model computations are believed to be more accurate than the measurements for these lower frequencies, but the measured data cannot be used to assess model accuracy at and below 7 MHz.

MODELED AND MEASURED IMPEDANCE OF A BOWTIE ANTENNA OVER IMPERFECT GROUND

MARTIN L. PERRINE

U.S. Department of Defense
Radio Science Division
9800 Savage Road
Ft. George G. Meade, MD 20755
Tel. (301) 859-6555

ABSTRACT

Comparisons are made of the impedances of a rigid "wire" bowtie antenna 7.7 meters over imperfect ground from field measurements and a moment method model, using the Numerical Electromagnetic Code (NEC version 3). Earlier measurements (Brown and Woodward, RCA REVIEW, December, 1952, p. 425) of a sheet bowtie are also included for general comparison. Good agreement was found between 10 and 50 MHz for a 3.4 meter horizontally polarized antenna. The model also showed that the imperfect ground had minimal affect.

The bowtie antenna is being investigated as a passive receiving element of a VHF adaptive array; wherein it is desired that each element should have uniform electromagnetic characteristics over the frequency band. NEC modeling provided a means to evaluate element design tradeoffs.

INTRODUCTION

Super-resolution adaptive antenna arrays require that either all signal channels of the array are precisely characterized electrically (so that differences can be calibrated out) or that all have identical characteristics. The antenna is one element of the signal channel that is difficult to characterize, therefore attempts are generally made to fabricate the antennas identically and to place them in the array such that coupling to other objects is minimized or made as uniform as possible.

This paper will discuss impedance data collected during the design of a bowtie antenna for a four antenna broadband VHF adaptive array. The bowtie was chosen for its simplicity of fabrication, well characterized design parameters, and fulfillment of other array requirements. From a physical standpoint a wire is preferable to a sheet antenna to reduce weight and wind loading. However it was reported by Jasik (p. 29-12 ref. 1) that broadband performance is degraded when a sheet antenna is reduced to a wire outline.

Comparisons of measured and modeled impedances for a horizontally polarized rigid "wire" bowtie over imperfect ground are reported and show good agreement between 10 and 50 MHz. Results are also shown comparing wire and sheet antennas which include measurements by Brown and Woodward (ref. 2).

FIELD MEASUREMENTS

The rigid "wire" bowtie antenna element fabricated for the adaptive array is shown in fig. 1. The antenna is 3.4 m long and made from one inch square anodized aluminum tubing and supported with fiberglass beams. The antenna is made up of two triangular sections, each made with 4 tubes, that are spaced one quarter inch apart at the center where the feed is located.

The antenna is fed with coaxial cable which is balanced by a balun device. The balun used, fig. 1, is simply a set of ferrite beads creating a high impedance (10 times the coaxial cable impedance is sufficient) on the outside of the feed coaxial cable. This in turn, reduces currents flowing from the antenna down the outside of the cable which would otherwise radiate and interfere with the measurement. This balun is ideal for measurements because it has a unity impedance conversion and a transfer function that simply phase shifts the measured reflection coefficient, discussed below, by twice the electrical length of the balun cable.

The antenna impedance, from 10 to 60 MHz was found by:

1) measuring the reflection coefficient at the input of the balun fed by the antenna with a Hewlett Packard 3577A network analyzer, then
2) calculating the reflection coefficient at the antenna by correcting for the phase shift of the balun, then
3) converting the corrected reflection coefficient into antenna impedance.

The antenna itself was mounted on a wooden pole at a height of 7.7 m and was fed with 100 feet of RG-223 coaxial cable, fig. 2. This measurement was repeated at 2.2 m above ground and repeated again with six radial wires added into the bowtie as shown in fig. 1. The ground had a measured conductivity of .0036 S/m and an estimated dielectric constant of 10.

NEC MODELING

The wiring configuration to model the 20 degree 3.4 m bowtie with NEC-3 is shown in fig. 3a. Segment lengths were kept under .1 wavelength and as uniform in length over the structure as possible. A wire radius of .005 m was used. The antenna feed configuration, as pictured, is three collinear segments joining the two triangles. The center segment was fed

with a voltage source. Environment parameters included: free space, ideal ground, and usage of the measured ground constants. Other apex angles and wire configurations were also modeled throughout the process including dipoles.

To compare sheet and wire antennas, several mesh models with a 30 degree apex angle and a 2.5 m length were made with both transverse and radial wires added to simulate a sheet.

RESULTS

The modeled and measured impedances, magnitude and phase, versus frequency, in MHz, for a 3.4 m long, 20 degree wire bowtie over imperfect ground are plotted in fig. 4. The modeled and measured results compare well between 10 and 50 MHz, where the rms value of the impedance difference is approximately 27 degrees for phase and 24 ohms for magnitude.

Impedance values, calculated from resistance and reactance measurements by Brown and Woodward, of a 20 degree bowtie, are also plotted in fig. 4. These values are not strictly comparable to the other two because their work was with a bowtie sheet in free space which was approximated by a unipole triangular sheet over a conducting ground plane. Their measurements were taken at 500 MHz and the antenna length was altered physically. Their free space electrical antenna length was converted to an equivalent frequency for a 3.4 m antenna for comparison purposes.

Modeling indicated that by adding radial wires to the triangle structure, a sheet antenna, which has flatter impedance curves, is approximated. The impedance versus frequency of three NEC wire models and Brown's equivalent sheet results for a 2.5 m long, 30 degree bowtie are plotted in fig. 5. As can be seen from comparing the "no middle wire" case to that of the "5 wire", adding radial wires reduces the fluctuation of impedance over the frequency range. Brown's results show even more reduction of impedance fluctuation. It was not conclusive from the measurement mentioned earlier of the 20 degree bowtie at a 2.2 m height, that the impedance fluctuation was reduced by adding the six radial wires. Further investigation is warranted.

The effect of transverse wires in the model was found to be minimal. When the transverse wire were removed from the "many wire" case both phase and magnitude curves remained the same.

Modeling also showed that at a height of 7.7 m the ground had little interaction on the impedance. This conclusion is based on close agreement between the free space and 7.7 m above imperfect ground situations for the 3.4 m long 20 degree bowtie.

FUTURE WORK

One possible source of modeling inaccuracy is a boundary condition problem when modeling the excitation of a wire segment near a multiple wire junction. It was suggested (personal communication with Mr. G. J. Burke, Lawrence Livermore Laboratory) that the segment should be replaced by three closely-spaced parallel wires, each having identical excitation, fig. 3b. The wires would not touch but fan out at the junction point. This representation was successfully incorporated into a NEC model of an existing HF "dual-fan" array by D. H. Sinnott (ref. 3).

The NEC thin wire approximation, combined with the wire radius used in the bowtie model, is a second possible source of model inaccuracy. Modeling on simple wire structures has suggested that wire radius does effect impedance and should be further considered.

SUMMARY

The measured input impedance of a "wire" bowtie antenna planned for use with an adaptive array was compared to numerical computations derived from a NEC-3 model. For the 10 to 50 MHz band, good agreement was found. Modeling also indicated that a sheet antenna could be approximated by adding radial wires to the antenna, and that at a height of 7.7 m the ground had minimal effect on impedance.

There are indications that the accuracy of the model may be improved by incorporating an alternate feed configuration and changing wire radius.

ACKNOWLEDGMENT

I would like to thank my colleagues, especially Dr. H. K. Kobayashi, for their assistance in this work.

REFERENCES

1) Jasik, H, and Johnson, R. C., eds., ANTENNA ENGINEERING HANDBOOK second edition, McGraw Hill Book Company, 1984.

2) Brown, G. H., and Woodward, O. M. Jr., "EXPERIMENTAL DETERMINED RADIATION CHARACTERISTICS OF CONICAL AND TRIANGULAR ANTENNAS", RCA REVIEW, December, 1952, p. 425.

3) Sinnott, D. H., "MODELLING BY NEC OF A DUAL-FAN WIDE-BAND HF RECEIVING ANTENNA.", Proceedings of the First Annual Review of Numerical Electromagnetics Code, March 19-21, 1985, LLNL, Livermore, CA.

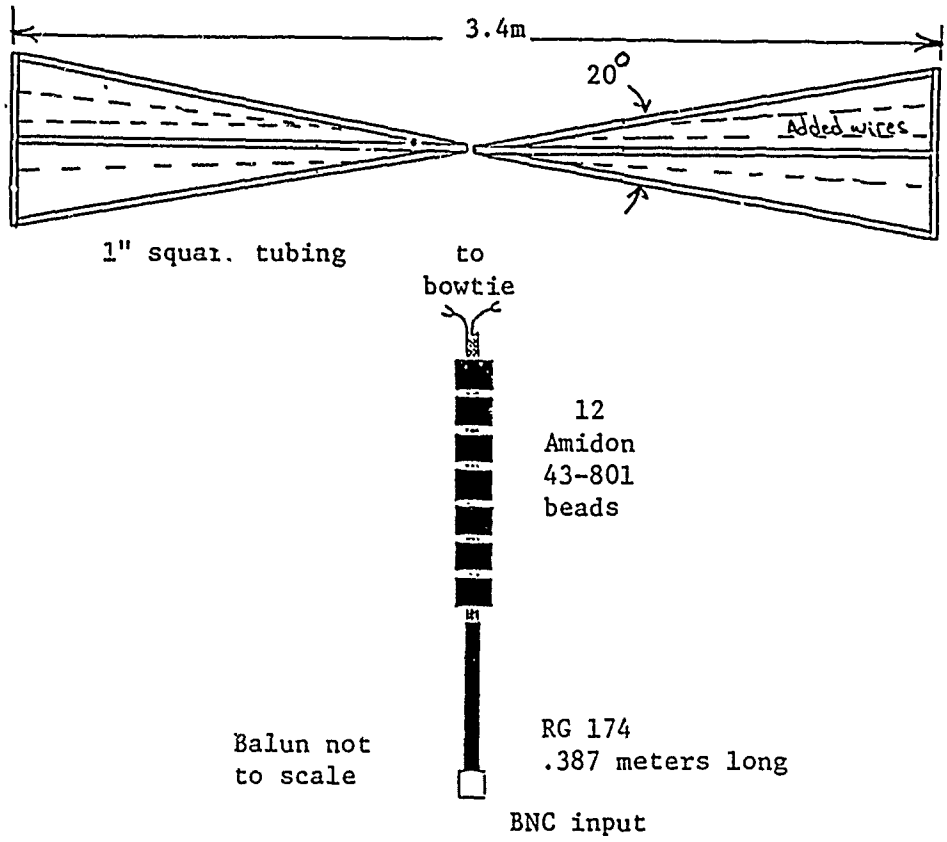


Figure 1 Bowtie Antenna and Ferrite Bead Balun

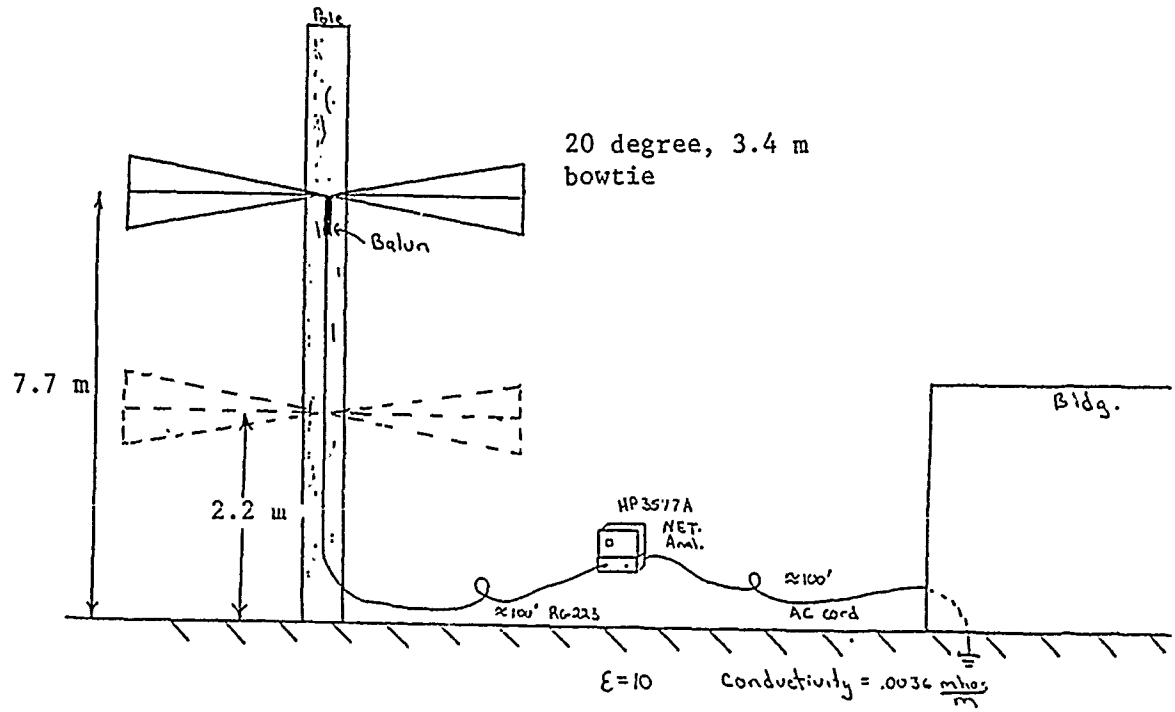


figure 2 Measurement Configuration

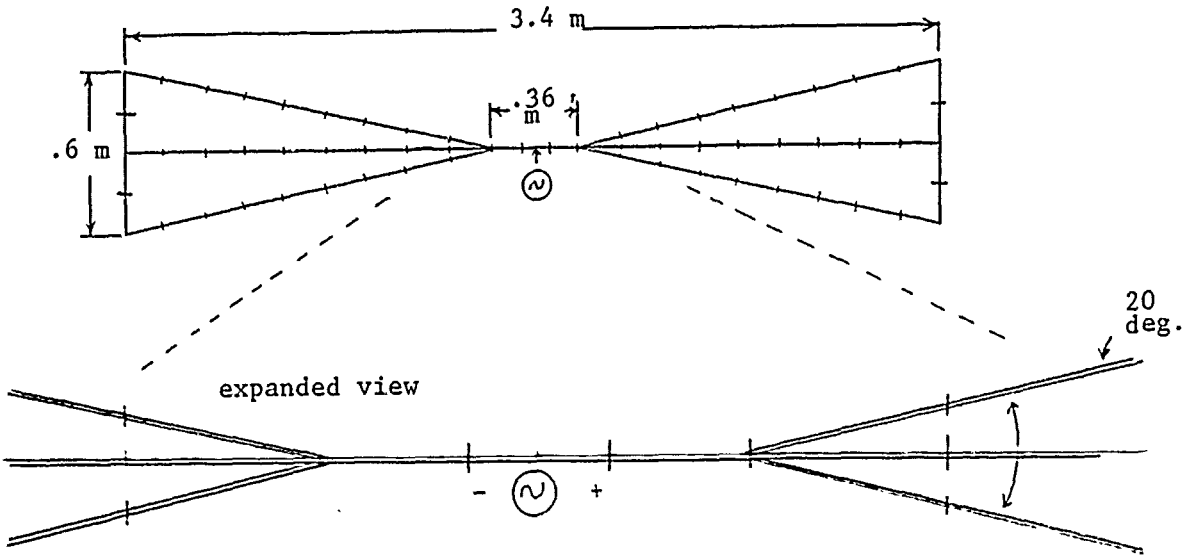


Figure 3a NEC bowtie antenna wire model

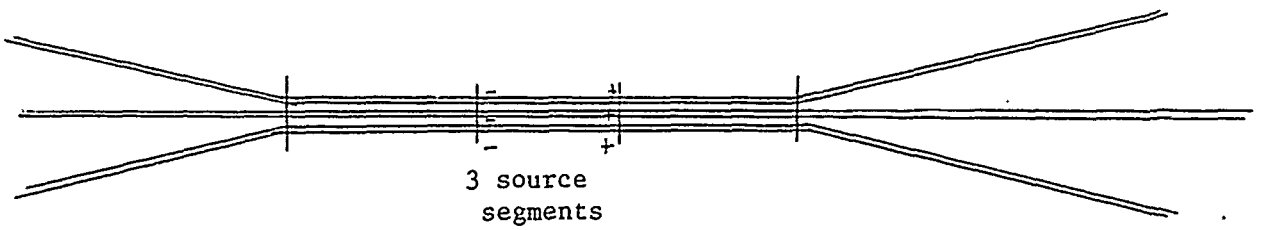


Figure 3b Alternate NEC bowtie feed configuration

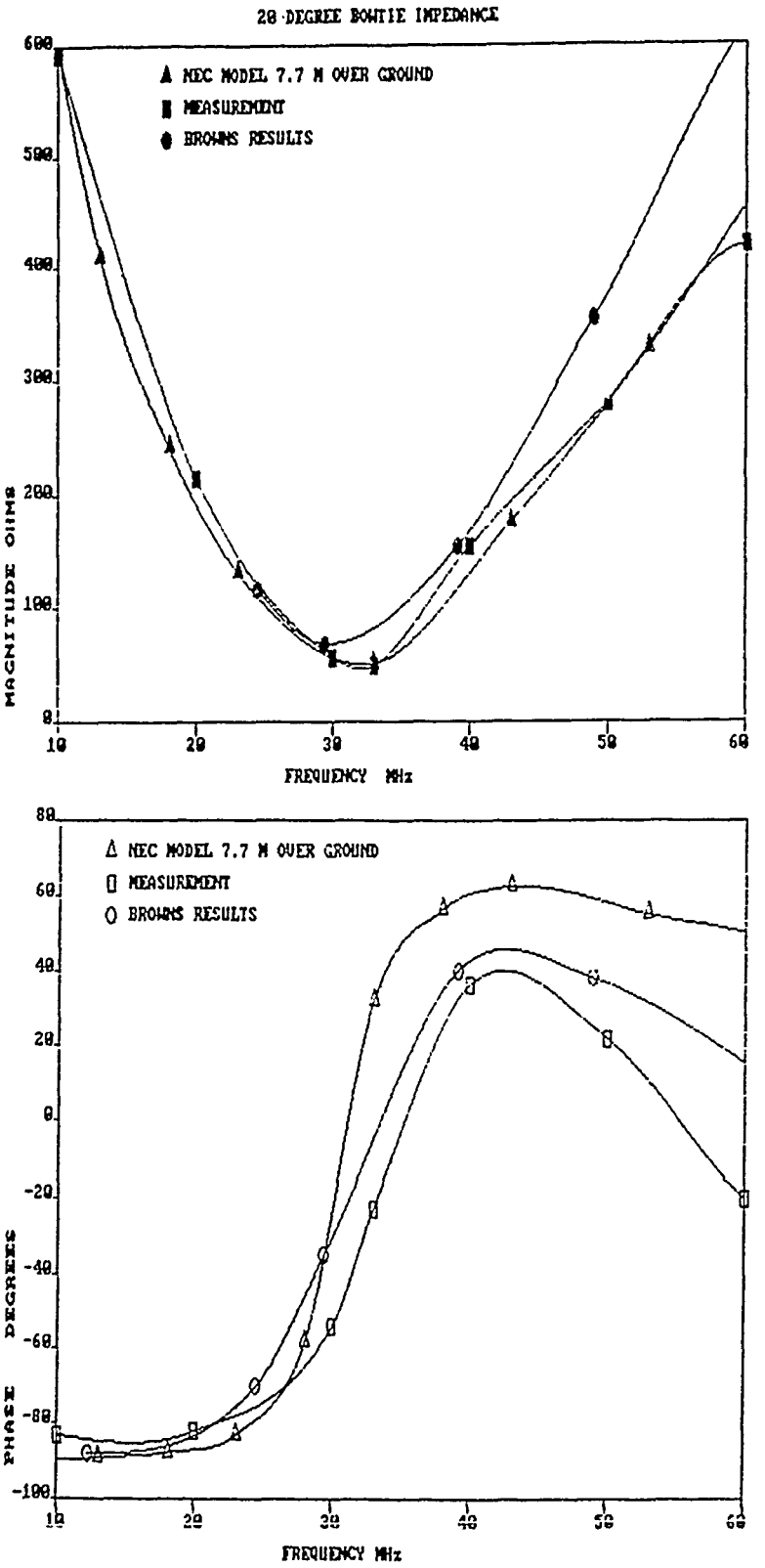


Figure 4 Antenna impedance for a 3.4 m long, 20 degree bowtie

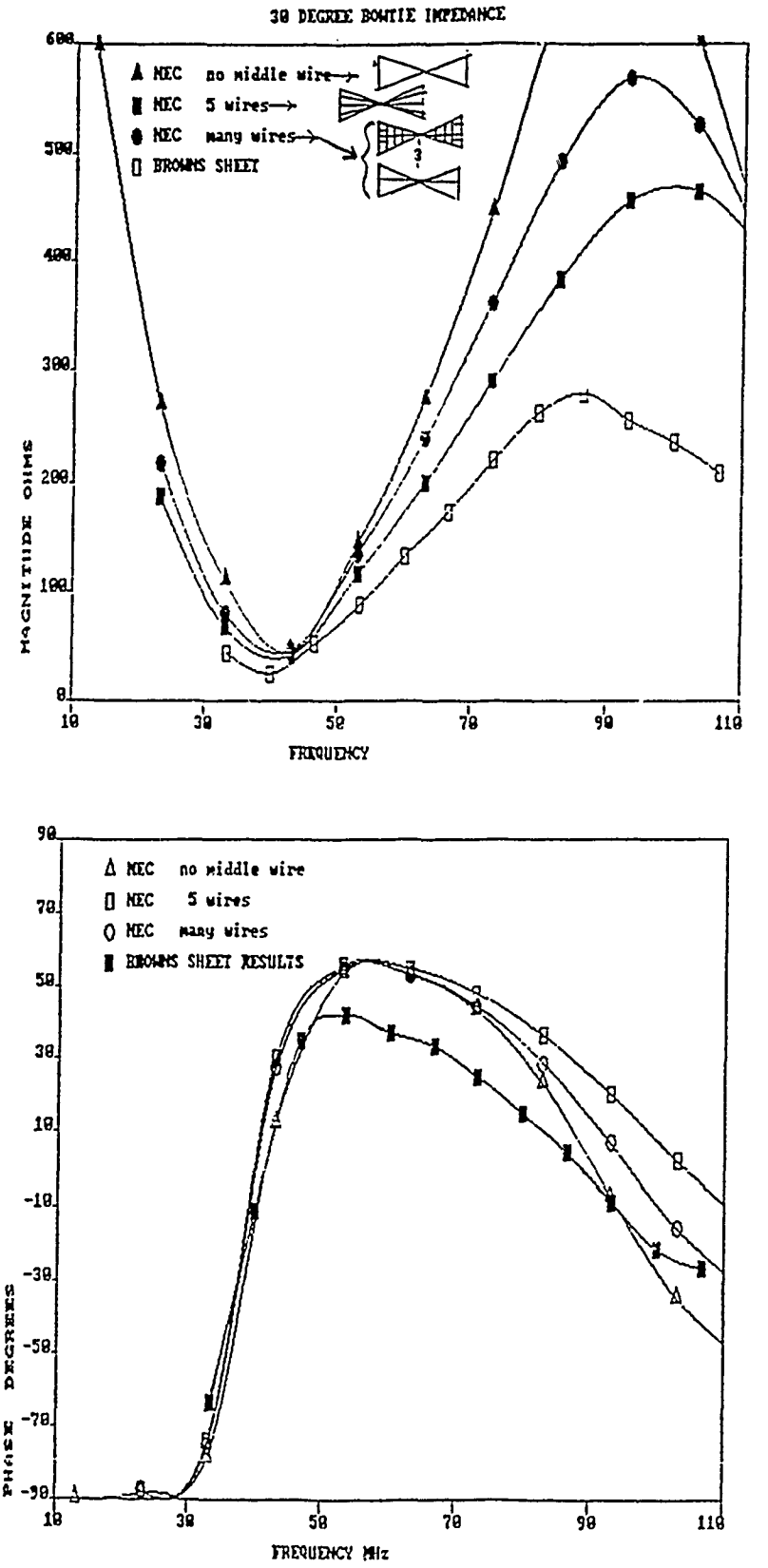


Figure 5 30 Degree Bowtie Antenna Impedance
2.5 meters long

"Vertical Monopoles with Elevated Ground Systems"

by

Al Christman
Department of Electrical and Computer Engineering
Ohio University
Athens, Ohio 45701-2979

Abstract

Computer modeling studies indicate that an elevated vertical monopole with four elevated horizontal radials provides more power gain at low elevation angles than does a conventional ground-mounted monopole with 120 buried radials. For the analysis, the length of the radials and the height of the monopole were set equal to 0.25 wavelength, and the frequency of operation was fixed at 3.8 MHz. Three different sets of ground constants (σ and ϵ) were used, simulating "average", "very good", and "very bad" soil electrical parameters. The computer code used for this work was NEC-GS.

Background

For many years, radio stations in the US "standard broadcast band" have utilized vertical monopoles (towers) as transmit antennas. These monopoles are required by the FCC to have an extensive ground system, usually consisting of 120 or more buried radial wires which are used to simulate a perfectly-conducting image plane beneath the monopole. The length of the radials is usually 0.25 λ (wavelength), although radiators whose height is greater than 0.25 λ often use radials whose length is equal to or greater than the tower height. Electromagnetic energy leaving the radiator travels through space in the form of displacement currents until reaching the earth's surface, where it is transformed into conduction currents which flow through the soil to the radials and hence back to the antenna feed point.

The FCC mandate requiring the use of many buried radials is apparently due to the findings of three RCA engineers: Brown, Lewis, and Epstein. These men performed extensive tests on buried-wire radial ground systems in the mid-1930's, and published their results in a now-classic paper in the Proceedings of the Institute of Radio Engineers (1). In the 1937 paper, a single test was performed where the radials were laid on the surface of the earth rather than buried in the soil. Their conclusion was that "this ground system is about as good as an equal number of buried wires" (2). Their normal procedure was to bury the wires to a depth of "approximately six inches" (3). Although this work was carried out at a frequency of 3 MHz, the results were quickly applied by AM broadcasters to their own part

of the spectrum (540-1600 kHz), and buried radials have been used ever since.

It is the author's belief that the use of elevated radials would provide superior performance, allowing the collection of electromagnetic energy in the form of displacement currents rather than forcing it to flow through lossy earth in the form of conduction currents.

Testing the Hypothesis

If the assumption stated above is correct, then radials which are buried near the earth's surface should produce more gain than radials buried at greater depths. NEC-GS was used to model a 0.25-wavelength vertical monopole with four 0.25-wavelength buried radials. The operating frequency was 3.8 MHz, and "average" ground was used (σ = 0.003, ϵ_r = 13). As the burial depth of the radials was decreased, the power gain of the antenna increased (see Table I.), even at the low elevation angles which are most important for long-range communications.

Next, vertical monopole antenna systems were modeled in which the radiator and its four horizontal radials were raised above the earth's surface. As the height of the radials was increased, the low-angle power gain of the antenna also increased, although high-angle gain was slightly attenuated (see Table II.).

Finally, a vertical monopole study was performed where the radials were shallowly buried (0.003 m) and the number of radials was varied from 4

Table I. Power Gain of a Vertical Monopole Antenna as a Function of Burial Depth of Radials; Number of radials = 4; Length of radials = 0.25λ; Height of monopole = 0.25λ; f = 3.8 MHz; σ = 0.003; ϵ_r = 13; Wire radius = 1 mm

Elevation Angle (degrees)	Power Gain (dBi)		
	burial depth 0.05 m	burial depth 0.005 m	burial depth 0.003 m
0	-∞	-∞	-∞
5	-8.71	-8.61	-8.60
10	-4.97	-4.87	-4.86
20	-2.74	-2.65	-2.63
30	-2.59	-2.50	-2.48
40	-3.41	-3.31	-3.29
50	-4.95	-4.85	-4.83
60	-7.27	-7.16	-7.14
70	-10.72	-10.62	-10.60
80	-16.73	-16.62	-16.60
85	-22.75	-22.64	-22.62
90	-172.66	-175.96	-168.55

Table II. Power Gain of an Elevated Vertical Monopole Antenna as a Function of Height of Radials above ground; Number of radials = 4; Length of radials = 0.25λ; Height of monopole = 0.25λ; f = 3.8 MHz; σ = 0.003; ϵ_r = 13; Wire radius = 1 mm

Elevation Angle (degrees)	Power Gain (dBi)			
	height 0.1 m	height 1 m	height 3 m	height 5 m
0	$-\infty$	$-\infty$	$-\infty$	$-\infty$
5	-6.82	-6.24	-5.82	-5.47
10	-3.09	-2.51	-2.13	-1.81
20	-0.88	-0.36	-0.10	+0.06
30	-0.75	-0.31	-0.26	-0.36
40	-1.59	-1.26	-1.50	-1.94
50	-3.17	-2.96	-3.53	-4.41
60	-5.52	-5.44	-6.36	-7.73
70	-9.00	-9.03	-10.27	-12.09
80	-15.03	-15.13	-16.59	-18.75
85	-21.06	-21.18	-22.70	-24.94
90	-156.48	-158.93	-156.16	-152.26

to 360, in order to determine the improvement in power gain which could be obtained by adding more radials (see Table III.). In this case of a ground-mounted antenna, more radials were always better than less radials.

Figures 1, 2, and 3 show elevation-plane power patterns for a ground-mounted vertical monopole with 120 buried radials versus an elevated monopole with four elevated horizontal radials, for 3 different sets of ground constants. In each case, the elevated antenna produces more power gain at low elevation angles and reduced radiation at high angles. If the burial depth had been greater (in these figures the radials are only 3 mm deep), the performance advantage achieved with elevated radials would have been even more pronounced. The four radials were placed at the cardinal points of the compass (ϕ = 0°, 90°, 180° and 270°) while the elevation-plane power patterns were taken at ϕ = 45°. At this azimuth angle, midway between two of the radials, gain was only slightly below that which was observed at the cardinal points. In fact, an elevated monopole was tested using only 2 radials (ϕ = 0° and 180°) at a height of 3 meters. Performance was inferior to that of a 4-radial monopole at the same height, but better than that of a 4-radial monopole at 1 meter. Azimuthal gain variations amounted to 0.21 dB at an elevation angle of 10°.

All of the studies described above were carried out using NEC-GS. As a check, the antenna systems utilizing elevated radials were also modeled using NEC-2. In every instance, the power gains predicted by the two codes agreed with each other within a few hundredths of a deciBel.

Table III. Power Gain of a Ground-mounted Vertical Monopole as a Function of Number of Buried Radials; Length of radials = 0.25λ; Height of monopole = 0.25λ; f = 3.8 MHz; σ = 0.003; ϵ_r = 13; Wire radius = 1 mm

Elevation Angle (degrees)	Power Gain (dBi)			
	4 radials	30 radials	120 radials	360 radials
0	-∞	-∞	-∞	-∞
5	-8.60	-6.33	-5.87	-5.79
10	-4.86	-2.59	-2.13	-2.05
20	-2.63	-0.37	-0.10	+0.17
30	-2.48	-0.21	+0.25	+0.32
40	-3.29	-1.01	-0.57	-0.50
50	-4.83	-2.54	-2.11	-2.04
60	-7.14	-4.85	-4.42	-4.36
70	-10.60	-8.29	-7.88	-7.82
80	-16.60	-14.29	-13.88	-13.83
85	-22.62	-20.31	-19.90	-19.85
90	-168.55	-146.90	-132.94	-127.95

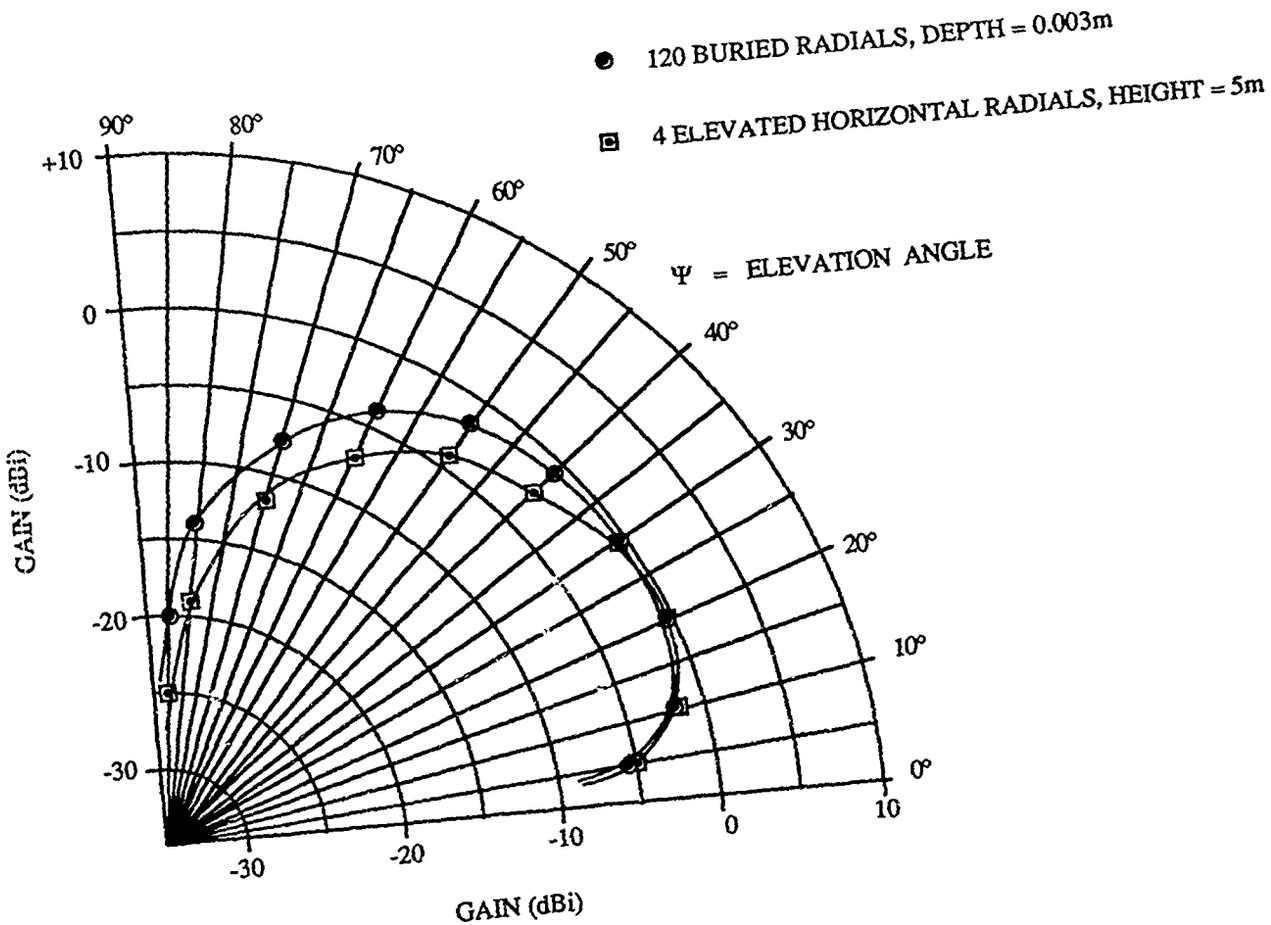


Figure 1. Elevation-plane power patterns for ground-mounted and elevated vertical monopole antennas over "average" ground.
Length of radiator and radials = 0.25λ ; f = 3.8MHz; σ = 0.003; ε_r =13.

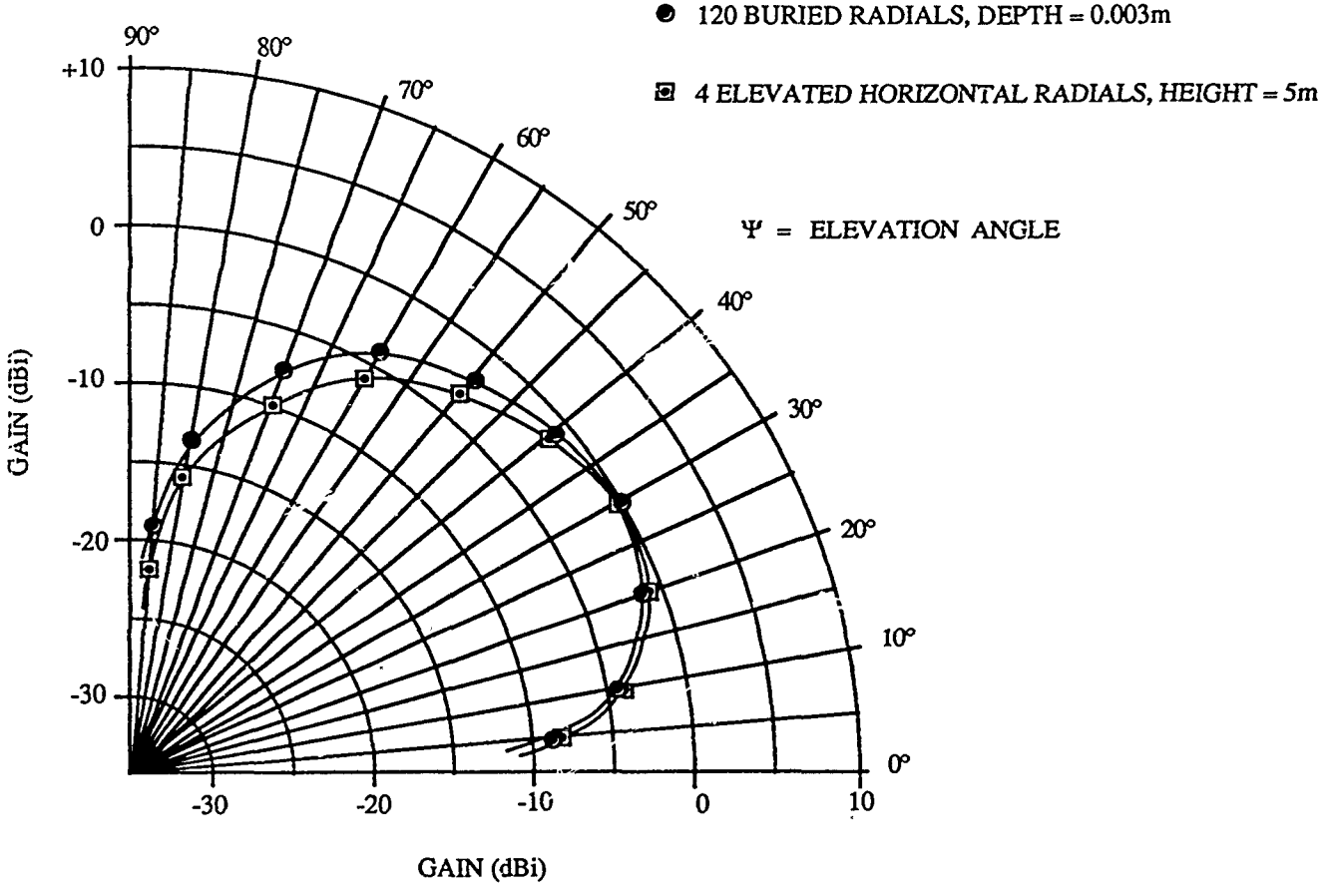


Figure 2. Elevation-plane power patterns for ground-mounted and elevated vertical monopole antennas over "very poor" ground.
Length of radiator and radials = 0.25λ ; f = 3.8MHz; σ = 0.00015; $\varepsilon_r = 4$.

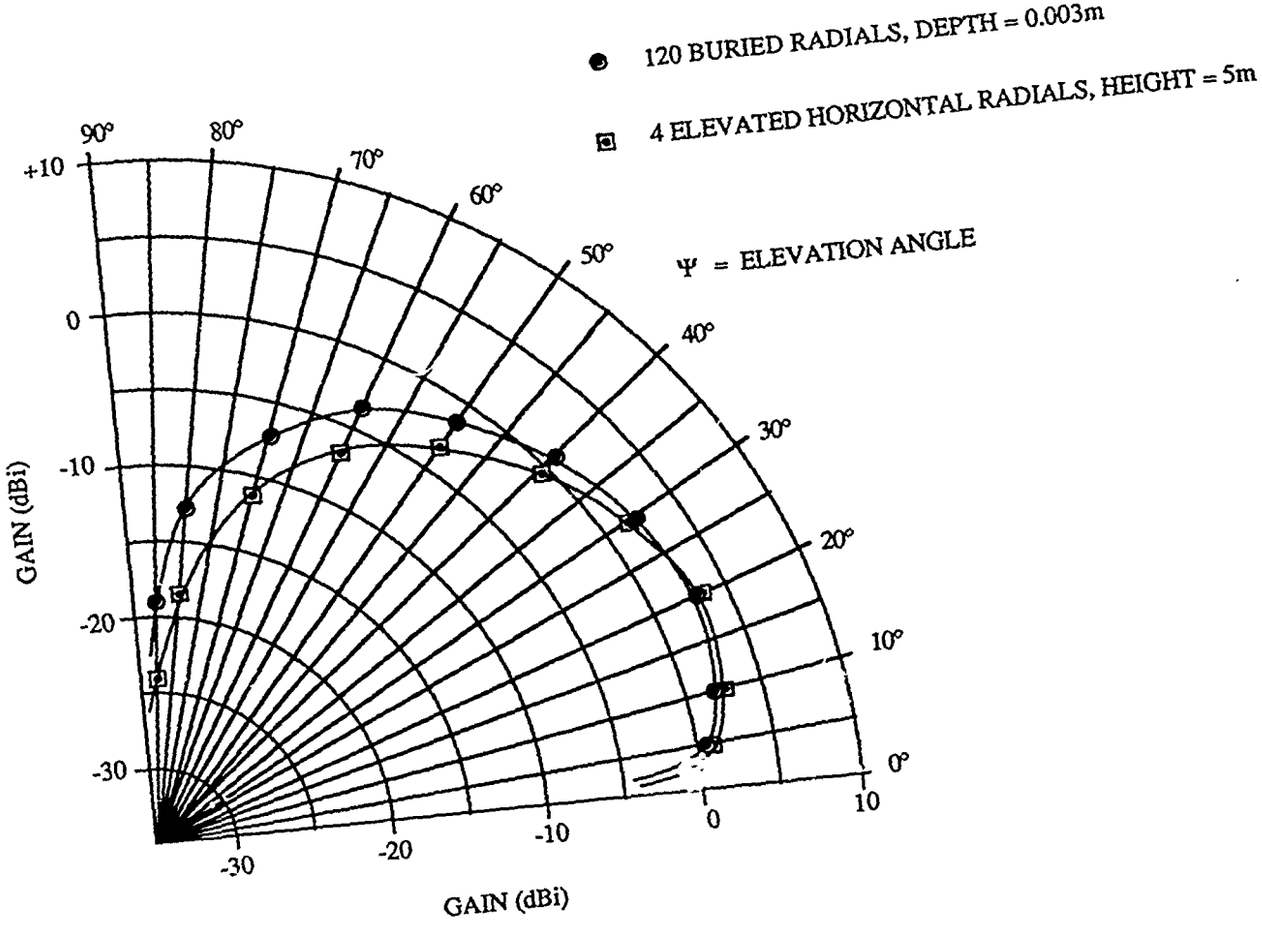


Figure 3. Elevation-plane power patterns for ground-mounted and elevated vertical monopole antennas over "very good" ground.
Length of radiator and radials = 0.25λ ; f = 3.8MHz; σ = 0.05; ε_r = 42.

Conclusion

Studies on vertical monopole antennas, using NEC-GS, indicate that a monopole elevated a few meters above ground and having only 4 elevated horizontal radials can outperform a ground-mounted monopole with 120 buried radials, over any type of ground. Field studies are planned this summer for the purpose of verifying these computer predictions. If the computer output from NEC is correct, then the construction cost and complexity of radial ground screens can be greatly reduced, while installation flexibility and low-angle gain will be increased. Tests by Dick Adler and Jim Breakall show that similar performance improvements can be obtained at frequencies in the AM broadcast band. The elevated-radial technique thus seems applicable at medium frequencies as well as in the lower part of the HF band.

Acknowledgement

The author wishes to express his thanks to Nancy Butcher for her expert typing of the manuscript, and to Annamay McMillan for construction of the figures.

References

1. Brown, G. H., R. F. Lewis, J. Epstein, "Ground Systems as a Factor in Antenna Efficiency," Proceedings of the Institute of Radio Engineers, Vol. 25, No. 6, June 1937, pp. 753-787.

2. Ibid, p. 784.

3. Ibid, p. 769.

EM Users Panel Discussion Summary

J. K. Breakall, Panel Chairman

University of California

Lawrence Livermore National Laboratories, Livermore, CA

The EM Users panel discussion took place on Tuesday, March 24, 1987 from 1430 to 1630 hours at the ACES meeting. The agenda was an informal panel discussion and question and answer session with audience participation and interaction. The panel started by making a brief introduction of each of the panel members. Then each member made a very short presentation (5 to 10 minutes) of a particular experience, problem, enhancement, suggestion for improvement, etc. of a specific EM code. This resulted in a more effective presentation of not just NEC related issues, but of a wide spectrum of various other EM techniques.

The list of panel participants follows with their affiliation and code experiences discussed:

1. Phil Barnard, Lockheed M.S. Div. - GTD, NEC Basic Scat. Code

2. Jerry Burke, LLNL - Author of NEC, Hybrid GTD-NEC, NECGS, NECVLF

3. Stan Kubina, Concordia Univ. - NEC pre and post processing, graphics

4. Pete Ludwigsen, LLNL - Main developer of NEEDS workstation

5. John Peterson, TRW/MED - NEC, EFIE patch code, Body of revolution code

6. Ted Roach, TR Applied Dev. Corp. - MININEC enhancements, software

7. Chuck Vandament, Rockwell Intl. - NEC, GTD, PC development

Questions from the audience concerned all of the various codes and other software and hardware issues. An informal p ,ll was taken and a good representative percentage of people in the audience were using NEC, GTD, GEMACS, MININEC, and other codes.

It was heard and felt that the panel discussion was one of high interest and benefit to all in attendance and should be held again.

SESSION IV - "APPLICATIONS OF COMPUTER EM MODELING"

Moderator: D. Stein

The FINITE ELEMENT RADIATION MODEL (FERM) PROGRAM *

David A. Shnidman and Steven Lee
M.I.T. Lincoln Laboratory, Group 44
244 Wood Street
Lexington, MA 02173-0073

Introduction

Highly accurate numerical solutions of Maxwell's equations applied to metallic surfaces are obtained with the Finite Element Radiation Model (FERM) software package. Although FERM is based on the triangular patch basis functions of Rao, Wilton, and Glisson (RWG)[1], FERM has the following significant improvements over the released RWG listing:

1. Efficient and effective code
2. User modeling interface
3. Modeling graphics
4. Antenna and RCS applications
5. Multiple connection edges
6. Pattern analysis and graphic presentation

These enhancements provide both qualitative and quantitative improvements: users can model, with greater ease and fewer mistakes, more general and more complicated structures, at higher frequencies, to obtain better answers, and present them graphically to provide deeper insight and understanding.

*This work was sponsored by the Department of Defense. The views expressed are those of the authors, and do not reflect the official policy or position of the U.S. Government.

Background

Dramatic cost decreases in computational capabilities and noteworthy improvements in numerical techniques have stimulated efforts to achieve practical solutions to Maxwell's equations. The numerical approach couples either the Electric Field Integral Equations (EFIE) or the Magnetic Field Integral Equations (MFIE)[2] with the method of weighted residuals[3] to transform Maxwell's equations into a linear system of equations. The solution is then expressed as a set of scalar coefficients for a set of vector basis functions. The procedure is not entirely straightforward; the following difficulties were encountered. The use of EFIE with patches to model metal plates initially met with failure because the basis functions chosen produced charge accumulations at boundaries, which corrupted the solution. Finding basis functions which avoided this pitfall was easy for one-dimensional wires, but not so obvious for two-dimensional patches. The use of MFIE instead worked for closed surfaces, yet was impractical for open geometries like a flat metal plate. The first successful approach to the plate problem was the wire grid model[4]. The Numerical Electromagnetic Code (NEC) software[5] incorporated the wire grid model coupled with MFIE as an option for closed surfaces. Later, RWG introduced satisfactory two-dimensional basis functions for the triangular patch. Not only did their basis functions avoid charge accumulation at boundaries, but the triangular shape permited general modeling of complicated contours. Patches are superior to wire grids for modeling surfaces because fewer finite elements (and hence less computation) are needed to obtain the same degree of accuracy. Thus, for the same amount of computation, more finite elements can be used for better performance. The original RWG software contained various deficiencies and limitations. To overcome these, FERM was developed.

FERM Enhancements

Efficient and effective code With improved numerical techniques and code streamlining, FERM runs much faster and makes practical sophisticated applications: up to 3000 unknowns can be solved reasonably on a VAX 11/785. There is also an interrupt feature which circumvents computer crashes (and makes feasible piecemeal runs) by saving partial results. In addition, partial results can be reused, saving even more computation for problems which are variations on a basic configuration. Finally, the techniques and coding for numerical integration were tested for speed and accuracy, and some corrections and improvements were made.

User modeling interface Rather than specifying individual triangles vertex by vertex, users of FERM describe shapes and forms parametrically. This allows for both ease and accuracy in modeling. That ease and accuracy is essential given the increased ability to model larger and more complicated structures.

Modeling graphics FERM includes graphic display of the geometry for visual feedback of the modeled configuration. That feedback allows rapid and reliable checking of the geometry. It also can provide a colorful, insightful visual representation of the current distribution solution.

Antenna and RCS applications FERM includes basis functions for modeling wires as well as surface patches, in order to model wire antenna structures. Voltage excitations can be applied to wires or to thin strips of surfaces. The latter surface excitation allows the modeling of antenna structures electrically connected to larger surface structures. FERM can calculate both monostatic and bistatic scattering for RCS applications.

Multiple connection edges This provides for general interconnection between modeled surface structures. The difficulty with multiply connecting surfaces at a common edge is that basis functions are defined in terms of triangle pairs, so that overlapping triangle pairs meet at a multiple connection edge. As Kong[6] noted, all combinations of triangle pairs cannot be used since that produces linearly dependent vector basis functions (VBFs). Fig. 2 shows three triangle patches meeting at a single edge, with three possible triangle pairs. While three VBFs can be defined, only two can be linearly independent. To maintain linear independence, only one additional VBF can be introduced when a new patch is connected to an interior edge. This new VBF is defined as follows. Assume that n distinct triangular patches are connected at one edge with $n-1$ VBFs satisfactorily defined. Then two of the triangular patches have only one active basis function associated with the common edge. Either of these can be paired with the new patch to define an additional VBF in a way that maintains linear independence. That $n-1$ VBFs can independently span an n-fold multiple connection arises from the initial case that one VBF is defined for a patch pair, and that one additional VBF is necessary and sufficient for each additional patch. FERM automatically generates the proper set of VBFs for multiple connection edges.

Pattern analysis and graphic presentation Because effective presentation is essential to make results worthwhile, extensive software was added to combine, compare, and otherwise flexibly manipulate radiation patterns, and then to graph them in user-customized plots.

Numerical Enhancements

The critical numerical issues were numerically evaluating the integrals and solving the resulting linear equations, since these are the computationally intensive parts of FERM. Attention was focused on maximizing speed with minimum loss of significant accuracy; code streamlining was done throughout. The finite element method is already an approximation. Therefore, additional error from further approximations may not necessarily increase the inherent imprecision. Several such approximations are made in numerically evaluating the integrals, for rapid evaluation is essential. These approximations were tested for their effect on accuracy, and in some cases modified and improved. In both numerical evaluation of integrals and linear equation solving, double precision proved to be almost always superfluous. Symmetric LU/Choelesky decomposition was selected as the fastest way to solve the linear equations. Various methods for minimizing error when solving with ill-conditioned matrices were left out when it was recognized that, for physical reasons, the matrix was guaranteed to be well-behaved.

The realized efficiencies from these enhancements allow for the solving of problems with up to ten times as many parameters as the original RWG listing. CPU times for the two computationally intensive phases of FERM are given in Fig. 1. The EFIE2 program numerically evaluates the integrals for a given configuration to establish the Z-matrix; EFIE3 then decomposes this matrix. All other computational efforts are of secondary significance. We note that EFIE2 dominates the computation effort for cases less than 1600 parameters, while EFIE3 dominates for cases greater than 1600 parameters. Since for EFIE3 large parameter runs can be done piecemeal, they are practical on many computer systems.

The utility of solving EFIE for a large parameter configuration was greatly extended by adding a way to reuse the computation. Consider the example of testing several possible antenna locations near a large scattering object. The ability to reuse that portion of the Z-matrix associated with this large object spares the major computation involved in calculating and decomposing it for each test case. Instead, only the additional portions of the Z-matrix associated with the antenna element are calculated, and the

decomposition is then just finished for the full Z-matrix. The reuse feature thus makes feasible studying variations of large parameter configurations.

Numerical Results, Verifications, and Applications

The triangular patch shape and their corresponding basis functions are flexible enough to follow the form of almost any object to be modeled. If we are willing and able to pay the price in computational effort and running time, we should be able to achieve very accurate results. One caution, however, is that we should avoid very long thin triangles as they stress the accuracy of the numerical integrations. A maximum aspect ratio of 10 to 1 is recommended but far from absolute. In a similar vein, the wire approximations require the cylinder segments not to be too squat; i.e., the length should be much greater than the diameter so that the thinner the wire the finer the allowable segmentation. If suitable for the model, the zero diameter wire model can be employed. The numerical approximations used for the wires are not as good as those for the patches so that their integration values generally have larger errors.

As a general rule, 1/6 to 1/10 of a wavelength segmentation is satisfactory for antenna problems but, for sharp edges, corners, or points, finer segmentation may be called for. If we limit our interest to far field excitations and patterns, as opposed to near field exciations and surface current densities, then the segmentation requirements are far less severe. Therefore, RCS problems generally admit coarser segmentation than antenna problems. For antenna problems, some coarser segmentation (1/4 or even 1/3 of a wavelength) is suitable for surfaces on which, for physical reasons, the currents are expected to be weak. On the other hand, finer segmentation may be needed near antenna elements or feeds or anywhere strong current densities can occur.

One should also be aware of the fact that the surface current solutions obtained represent the combined currents on both sides of the metal plates. It would be preferable if the solution represented these surface currents separately, but this is not possible. With a closed object, which is excited only from the exterior, currents exist only on one side and the solution is that current density. If the model is excited both inside and out or it is not closed, the current solution represents the combination from both sides. The far field patterns are, theoretically, unaffected by this issue but numerical errors sometimes do influence those results. Finally, closed surfaced objects have resonance frequencies so that, if excited at or close to those frequencies,

the resonances can have disastrous results on the solution. If this problem is recognized, it can be averted by judicious placement of additional plates to shift the resonance frequencies.

It should be kept in mind that those parts of the radiation patterns which are more than 15 or 20 dB below the peak are susceptible to numerical errors and model imperfections. By the peak, we mean the global pattern peak which may or may not be evident in any paticular cut. One needs to have some idea of the levels of any particular pattern cut relative to the overall maximum.

We now compare computed and expected results.

Sphere Since theoretical results for a spherical object are well known for both its RCS[7] and the surface current density[8], we consider this model first. A 3.2 meter diameter sphere was divided into 1296 patches. This corresponds to about a quarter wavelength partition at the highest calculated frequency of $2\pi a/\lambda = 10$ (a is the radius) and a much finer one as we go down to lower a/λ. We see in Fig. 3 the excellent match between the calculated and theoretical RCS results. Fig. 4 compares the calculated and theoretical currents and again the result is an excellent match.

Plate Next we consider a simple square plate one wavelength on a side. We compare, for a horizontally polarized plane wave excitation, the surface current densities as determined by FERM, with 98 triangular patches (corresponding to 1/7 wavelength segmentation), to those of Glisson[9] and, once again, note the good agreement in Fig. 5. The A-A cut represents the current flow in the polarized direction and the B-B cut the cross polarized direction.

Cylinder Measurements were made on a pair of dipole antennas mounted on a cylinder. The antennas were ganged together to create a doublet cardiod-like pattern. Numerical results for both FERM and NEC (wire grid)[5] models were generated with approximately 1/10 wavelength segmentation for both and the results compared. Fig. 6 exhibits the results of an elevation cut for the measurement, FERM, and NEC. The measurement data shows clearly the effects of multipath in that obvious symmetries have been distorted. It is not difficult to see that the overall shape of the FERM result agrees well with the measurement and that the differences are due in large part to multipath. By comparison, the NEC result is not symmetric,

only hints at one of the nulls, and is not in close similarity to the other two patterns.

After test range modifications to reduce the relative multipath level to below -35 dB, further measurements were taken and compared to FERM. We note, in Fig. 7, that the amplitude pattern agreement is good to a fraction of a dB over most of the range. The phase is also quite good despite some evidence of multipath effects.

Beechcraft 1900 A Beechcraft 1900 aircraft was modeled, both physically and numerically, in association with a flight test experiment. Its actual dimensions are 57 feet 10 inches, nose to the tip of the tail. The model was about 1/7 scale but we will present data scaled to the true aircraft size. Feed arangements and modeled antenna elements were introduced into the physical model so test range measurements could be made. The elements were paired monopoles, one on the top of the fuselage and one on the bottom, acting in concert to form a single dipole-like element. This arrangement was used since it formed a complete element which is electrically much less dependent on the vagaries of the fuselage than would be a strict monopole element. This resulting element substantailly reduces the effects of wings and other protuberances on the pattern.

A detailed numerical model was developed using a total of over 2000 unknowns. There are eleven element placed on the aircraft with element number 1 placed directly behind the the cockpit and element number 11 nearest the tail. There are three elements fore of the wing, four elements over the wing, and four elements aft of the wing. In order to save computational effort, the elements were separated into three groups: the first three, then four and four. The computational effort for the body alone need be done only once as the result is saved. It is then combined with each of the groups of elements. Fig. 8 illustrates the rear four elements on the aircraft. Note that there is no hidden line removal in the figure so that plates formed on both sides of the fuselage are visible. In Figs. 9 and 10 are plotted the comparison of measured and calculated patterns, amplitude and phase, for element positions 1 and 10. Some measurement error is apparent in the jaggedness of the measured curve, but the overall agreement is quite good.

Impedance Since dipole impedances are so well understood, we use the dipole as the model to test our ability to numerically determine impedances. We can use the triangular patches to model "printed circuit" or strip elements. There is an approximate relationship between the a/h ratio for a

cylindrical wire (a is the radius, h the total height) dipole and the w/h ratio (w ,the width and t the thickness of the strip, $w \gg t$)[10]. We can model a strip dipole and, using this relationship, compare its impedance with Hallén generated curves for wires. The relationship is $w + t = 4a$ or, ignoring t, $w/h = 4\ a/h$. A narrow strip with $w/h = 10^{-4}$ has been subdivided into 200 triangles and compared to the impedance of a wire for which $a/h = 2.5 * 10^{-5}$. Even though the aspect ratio for the triangles is a large 100 to 1, the match (see Fig. 11) is nearly perfect up to $kh/2 = 6.5$ for both resistance and reactance.

Also plotted in Fig. 11 are the impedances for a 20 segment model wire dipole representing a wire of radius $2.5 * 10^{-5}$h. Although these curves have the same general shape, there exists a large disparity between them and the others. This is due to the numerical approximations employed for the evaluations of the integrals. The equations used are not as accurate as the commonly employed sinusoidal basis functions[2] but have the advantage of not being limited to parallel segments. These approximations can be upgraded in the next round of improvements. It is important to note that the inaccuracy is limited to the impedance calculations. In Fig. 12 we see a plot of the FERM calculated wire model currents on the wire compared to those calculated using Hallén's integral equation[10] for a half-wave dipole with $a/\lambda = 0.01$ and note that there is good agreement everywhere except near the feed point. But this point is precicely where the currents determine the impedance. We can conclude that the currents and fields have been accurately represented despite the discrepency in the impedance.

Acknowledgment

The authors gratefully acknowledge their indebtedness to Dr. Irvin G. Stiglitz of Group 44 for his enthusiastic support. Mr. Faustino A. Lichauco, as the major user and verifier of the software, made numerous suggestions which greatly improved FERM's usefulness, and provided most of the test runs for the verification section. Mr. Andrew Vierstra Jr. provided all the measurements cited in the text. All of the above are with M.I.T. Lincoln Laboratory.

References

[1] Rao, Sadasiva M., Wilton, Donald R., Glisson, Allen W., "Electromagnetic Scattering by Surfaces of Arbitrary Shape," *IEEE Transactions on Antennas and Progpagation*, vol. AP-30, No. 3, May 1982, pp. 409-418.

[2] Stutzman, Warren L. and Thiele, Gary A., *Antenna Theory and Design*, John Wiley & Sons, New York, NY, 1981, pp 323-332.

[3] Jain, Mahinder K., *Numerical Solution of Differential Equations*, 2nd ed., Wiley Eastern Halsted Press, New York, NY 1984, chapter 8.

[4] Richmond, Jack H., "A Wire-Grid Model for Scattering by Conducting Bodies," *IEEE Transactions on Antennas and Propagations*, vol. AP-14, no. 6, pp. 782-786.

[5] Burke, Gerald J., and Poggio, Andrew J., "Numerical Electromagnetic Code (NEC) — Method of Moments," Naval Ocean Systems Center, San Diego, CA, Tech. Document 116, July 1977.

[6] Kong, Jin Au (Massachusetts Institute of Technology), private communications.

[7] Skolnik, Merrill I., *Introduction to Radar Systems*, McGraw-Hill, New York, NY, 1962, p41.

[8] Mautz, J. R., and Harrington, R. F., "H-field, E-field , and Combined Field Solutions for Conducting Bodies of Revolution," *AEÜ*, vol. 32, no. 4, pp157-164, Apr. 1978.

[9] Glisson, Allen W., "On the Development of Numerical Techniques for Treating Arbitrary-Shaped Surfaces," Ph.D. dissertation, Univ. Mississippi, 1978.

[10] Elliott, Robert S., *Antenna Theory and Design*, Prentice-Hall, Inc., Englewood Cliffs, New Jersey, 1981.

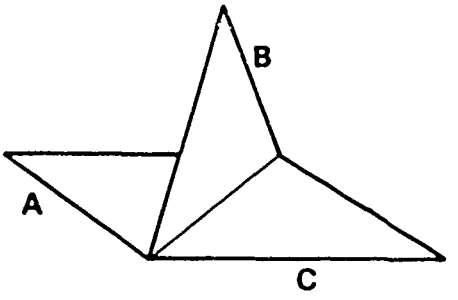


Figure 1. Triple edge connection.

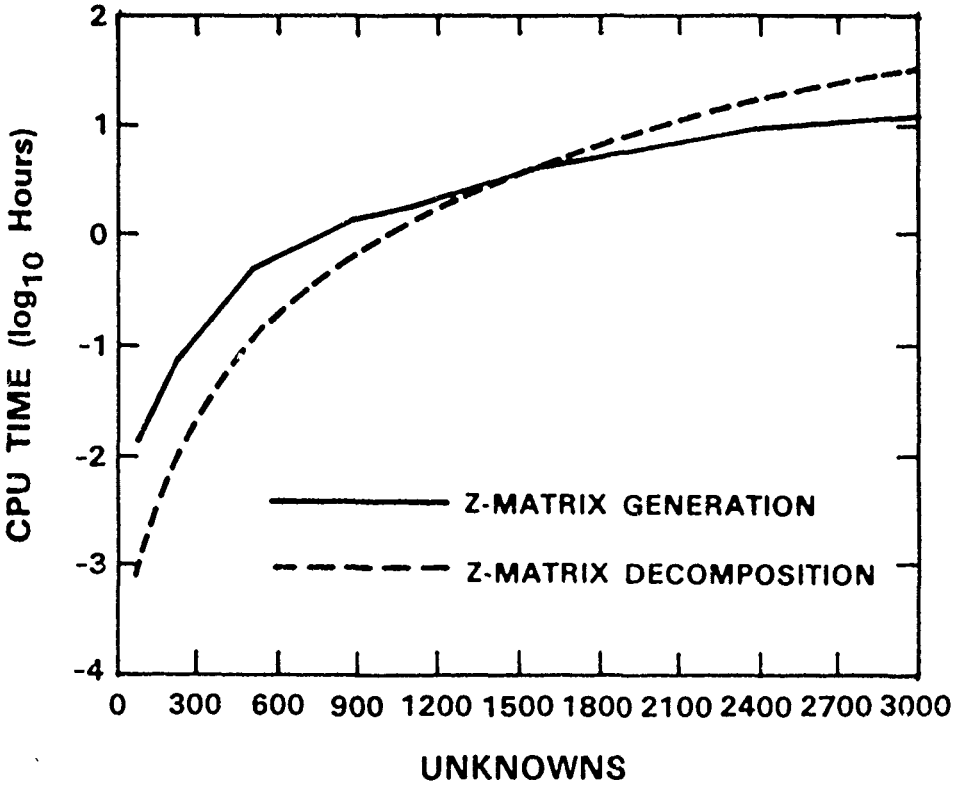


Figure 2. CPU run times for FERM on a VAX 11/785.

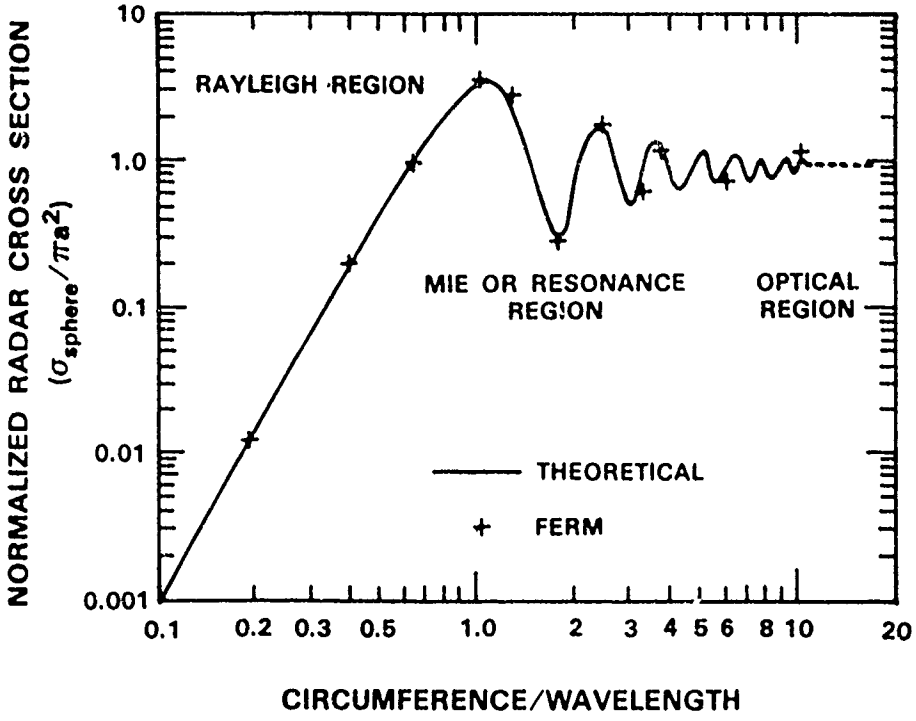


Figure 3. Radar cross section of a sphere.

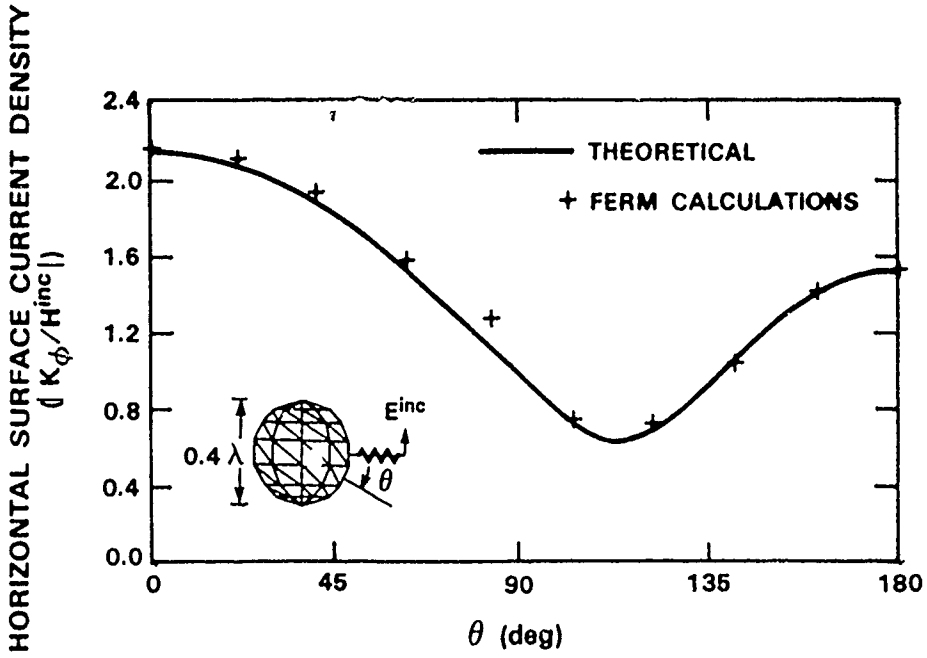


Figure 4. Surface current density of a 0.4 λ diameter Sphere.

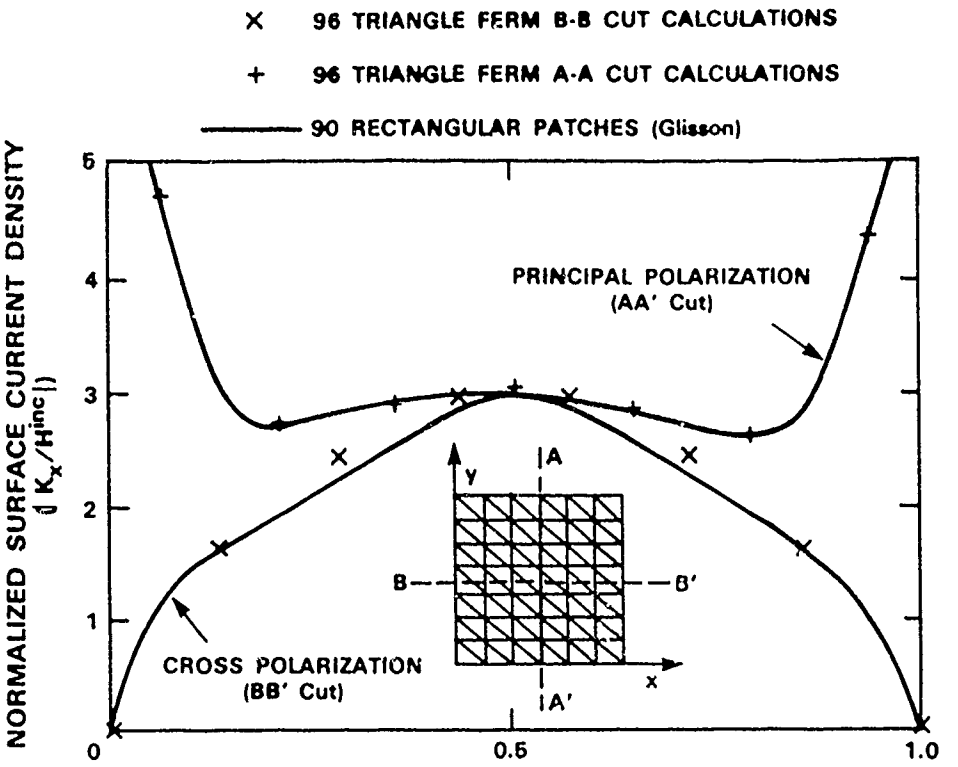


Figure 5. Square plate surface current densities.

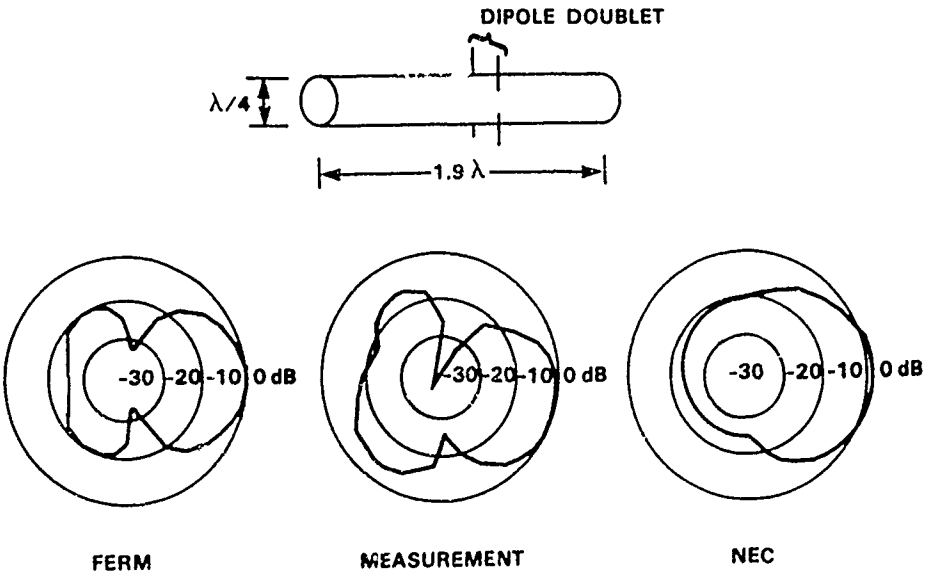


Figure 6. Comparison of elevation cuts for dipole doublet element on a cylinder.

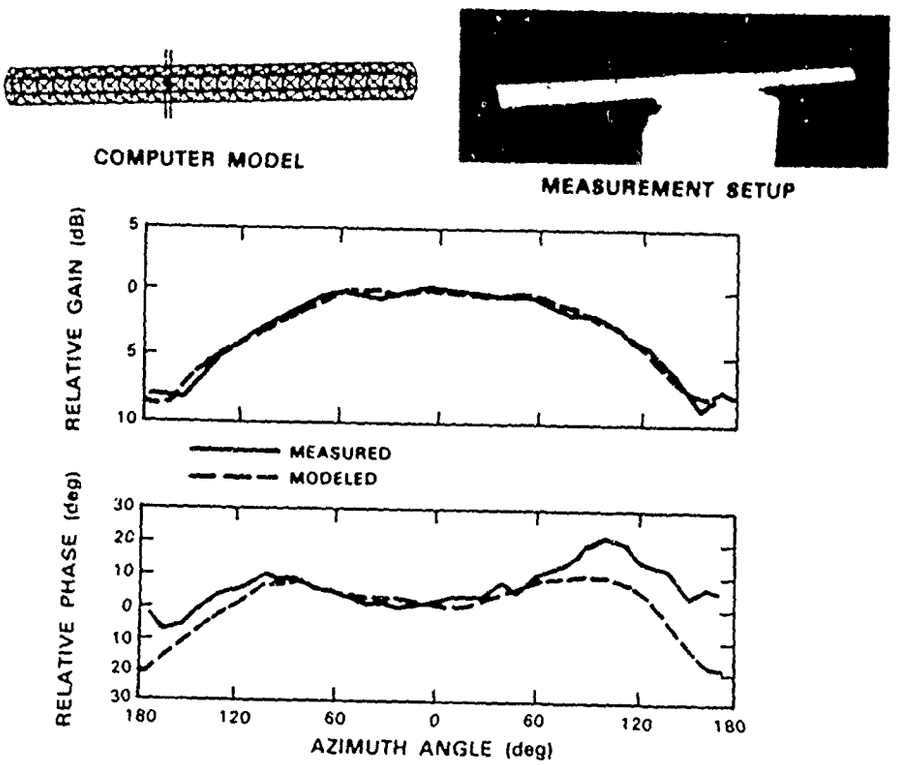


Figure 7. Comparison of azimuth cuts for element on a cylinder.

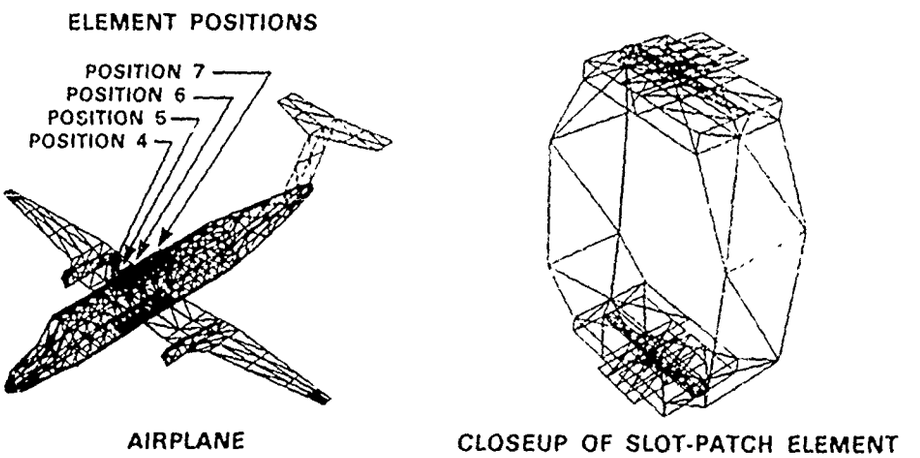


Figure 8. Segmentation of Beechcraft 1900 airplane, 1836 unknowns

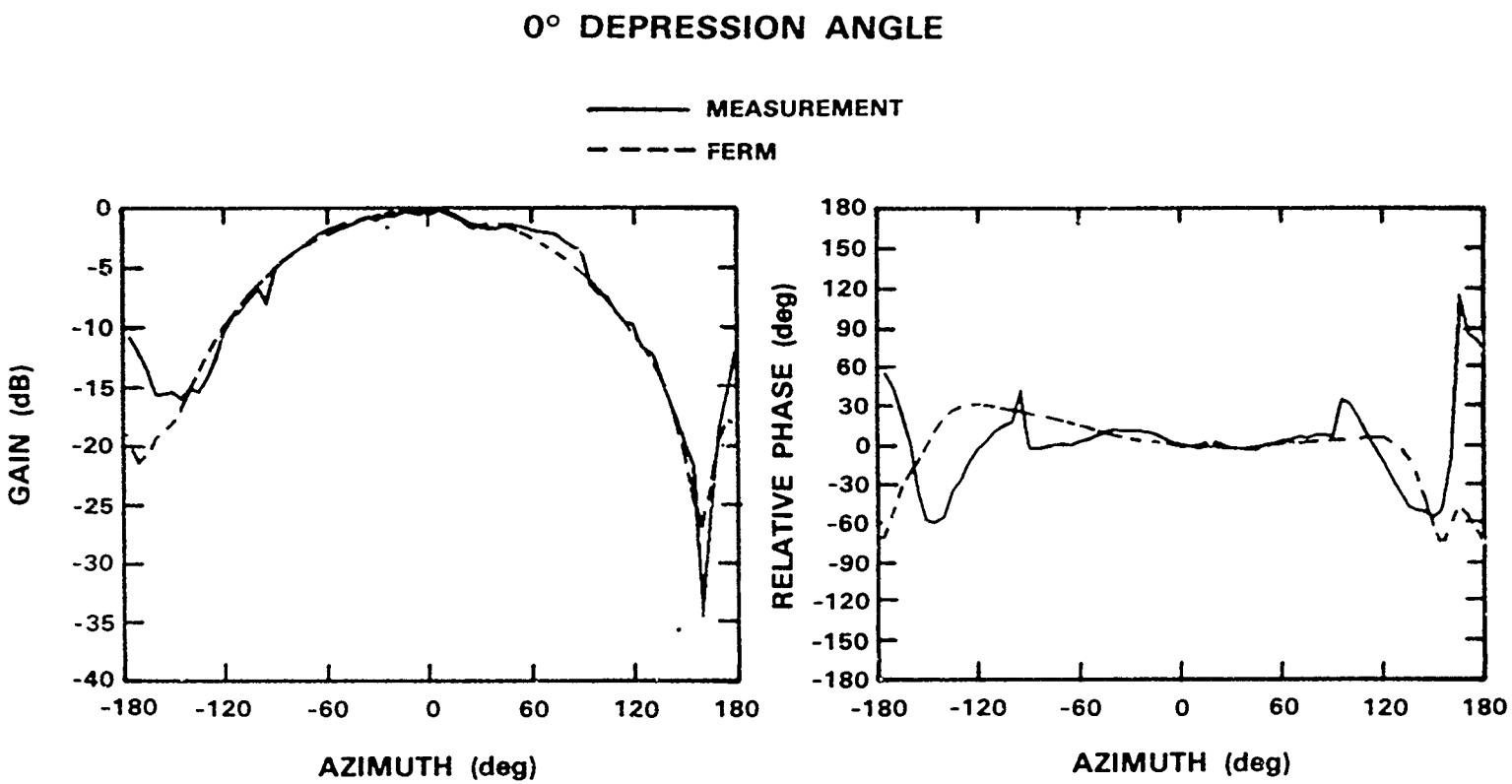


Figure 9. Comparison of element patterns, position 1.

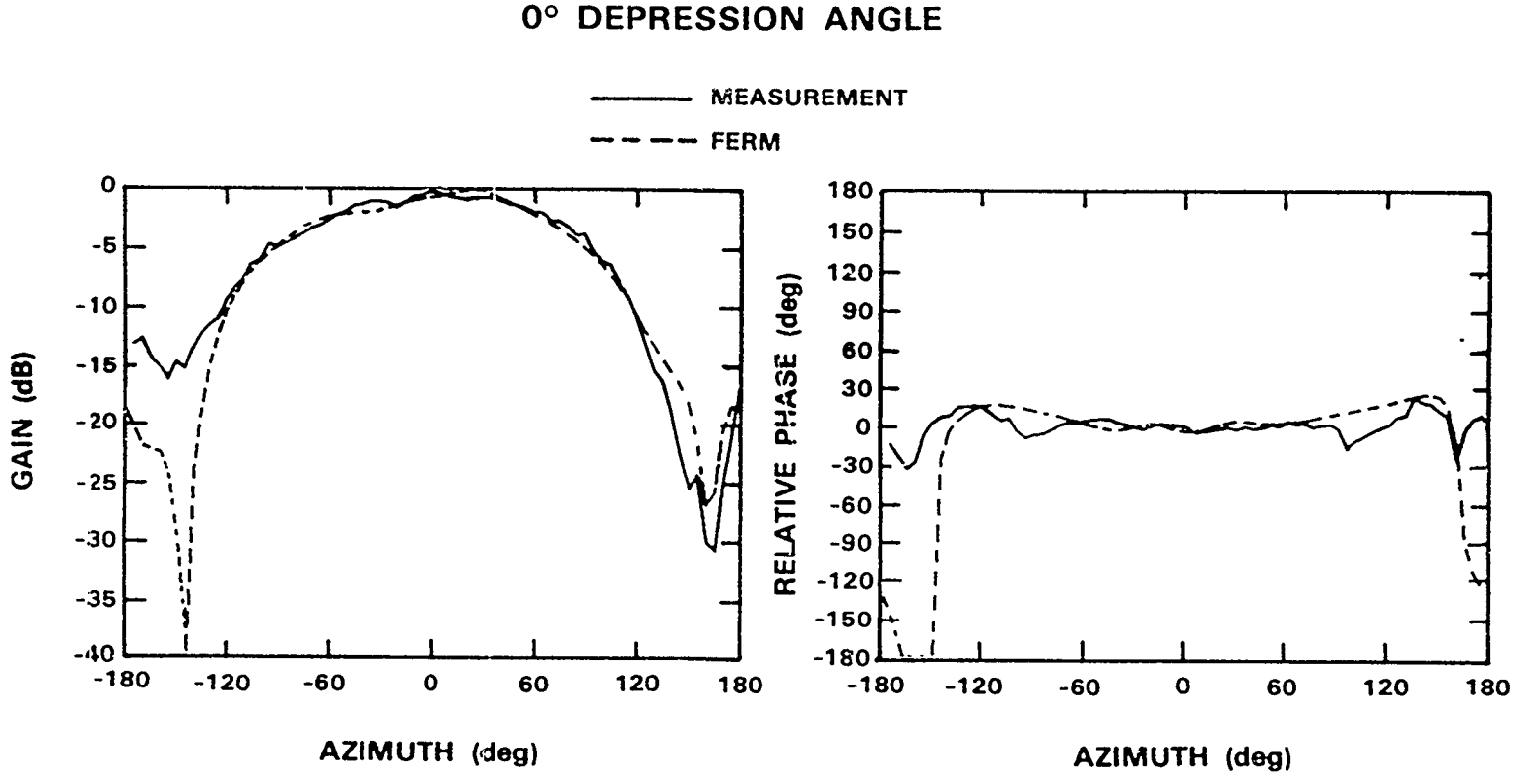
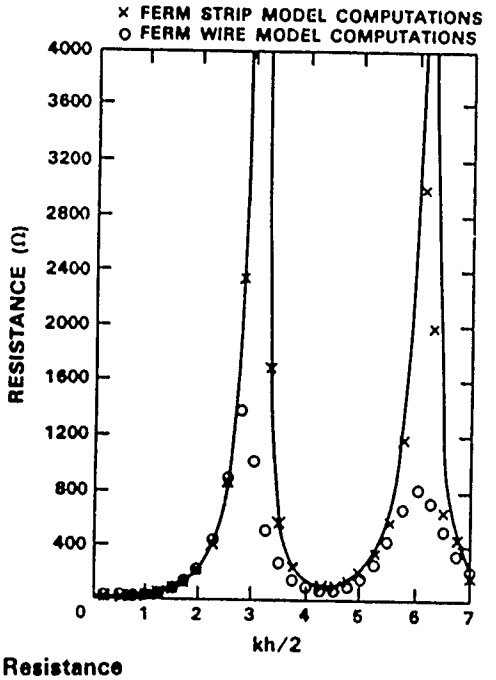
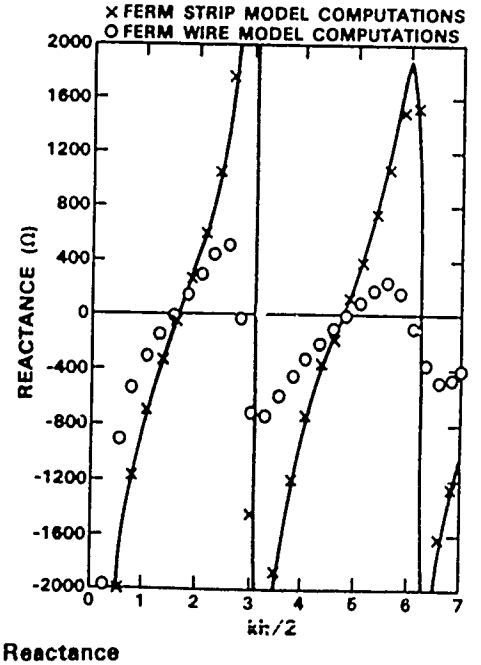


Figure 10. Comparison on element patterns, position 10.



a) Resistance



b) Reactance

Figure 11. Comparison of FERM calculations to Hallén's curves.

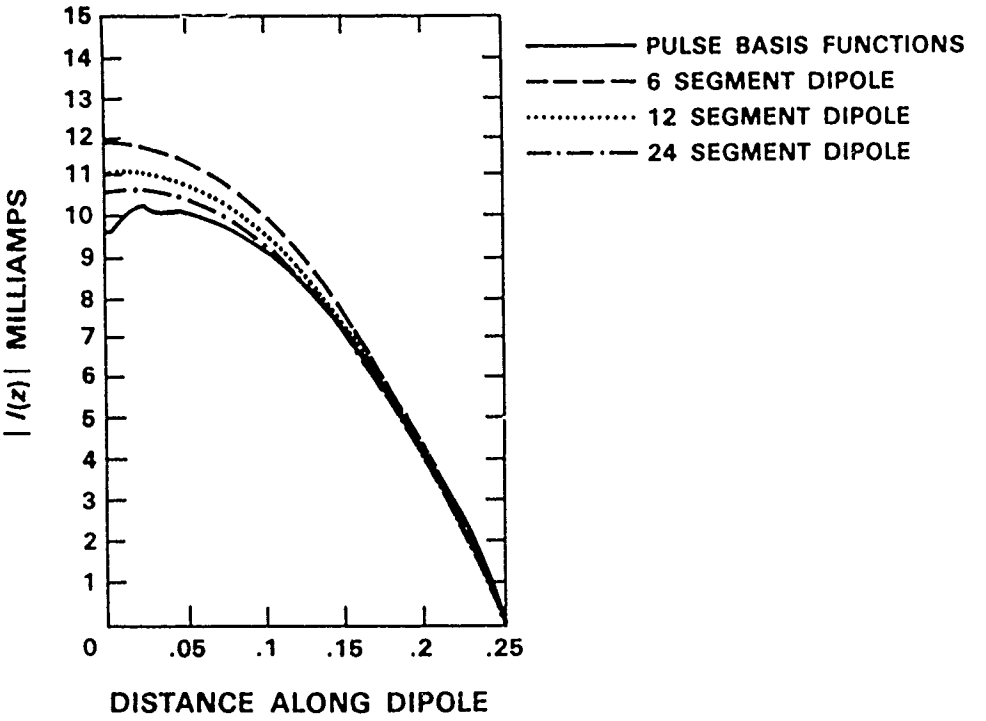


Figure 12. Comparison of wire currents for FERM and pulse basis functions.

FINITE ELEMENT ANALYSIS OF MICROWAVE CAVITIES

John R. Brauer and Jeffrey J. Ruehl
A. O. Smith Engineering Systems
8901 N. Kildeer Court
Milwaukee, WI 53209

Anthony B. Bruno
Naval Underwater Systems Center
Building 43
New London, CT 06320

ABSTRACT

The electromagnetic fields and resonant frequencies of a wide variety of cavities can be calculated by the vector potential finite element method. Examples analyzed here include TE and TM modes and resonant frequencies in rectangular, cylindrical, and beam waveguide cavities. The results of the finite element computer programs are shown to agree closely with classical theory. The programs can analyze cavities of any two- or three-dimensional shape, and they include the effects of lossy materials.

INTRODUCTION

Microwave cavities serve as resonators and filters in sources such as magnetrons. They also can serve as components of narrow-band antennas.

For simple cavity shapes, classical closed form solutions have been derived that appear in textbooks [1]. These solutions usually are for lossless cavities, and cannot easily be extended to arbitrarily-shaped cavities. This paper describes how the magnetic vector potential finite element method, which calculates low frequency or static fields [2], can be extended to calculate the coupled electromagnetic fields of cavity resonators. The cavities analyzed here will have simple shapes to enable comparison with classical solutions. The advantage of the finite element method is that cavities of arbitrary three dimensional shapes and nonuniform lossy materials can be analyzed.

THEORY OF VECTOR POTENTIAL FINITE ELEMENTS

The finite element method solves for fields by minimizing an energy functional [3]. Here the functional is

$$F = \int_V B^{**}2/(2\mu)\ dv + \int_V \epsilon E^{**}2/2\ dv - \int_V \bar{J}\cdot\bar{A}/2\ dv + W_d \qquad (1)$$

where the first term is the stored magnetic energy, the second is the stored electric energy, and the third is the electric energy input through current density $\bar{J}$. The fourth term, W_d, accounts for other energy such as that lost in dissipation. In equation (1) $\bar{A}$ is the magnetic vector potential, defined in terms of the magnetic field $\bar{B}$ by

$$\bar{B} = \nabla \times \bar{A} \qquad (2)$$

The electric field $\bar{E}$ in equation (1) is related to $\bar{A}$ at high frequencies by

$$\bar{E} = -d\bar{A}/dt \qquad (3)$$

Minimizing the functional of equation (1) insures that energy is conserved [3]. The minimum occurs when the derivative is zero. Thus

$$dF/d\bar{A} = 0 \qquad (4)$$

This equation is the basis of the vector potential finite element method for electromagnetics. The region analyzed must first be subdivided into finite elements, which are simple geometric shapes each assumed to have simple variation of $\bar{A}$. The shapes can be large or small within the "finite element model" of the region. Typical shapes are triangles in 2 dimensions and hexahedral "bricks" in 3 dimensions. Assembling all of the finite elements, equations 4 and 1 give the matrix equation

$$[K]\ \{A\} = \{J\} \qquad (5)$$

where in general {A} is the unknown column vector of $\bar{A}$ to be determined and {J} is the known column vector of input current density $\bar{J}$. Both vectors have a number of entries equal to 3 times the number of grid points, which are corners of the finite elements. However, in certain 2 dimensional problems where J is in only 1 direction the number of entries in each column vector is the same as the number of grid points. Determining the square "stiffness" matrix [K] from the materials and geometry of the finite elements, solving (5) for {A} on the computer then gives $\bar{B}$ and $\bar{E}$ from equations (2) and (3). This method is available in the AOS/MAGNETIC^{tm} two dimensional analysis program [4] and in the AOS/MAGNUM^{tm} three dimensional analysis program [5].

3D RECTANGULAR CAVITY TE101 MODE

The first example is a cubic cavity one meter on each side. One quadrant of the cavity is modelled with 12 three-dimensional finite elements. As shown in Figure 1, the finite elements are six-sided bricks called hexahedrons. The remaining three quadrants of xz space in Figure 1 contain the other three quadrants of the cavity, which need not be modelled here due to symmetry. The cavity is assumed to be excited by J = 1 amp per square meter in the y direction of finite element number 1. The cavity interior is given the conductivity of 1.E-4 S/m.

AOS/MAGNUM was used to calculate the complex magnetic vector potential at grid points and the corresponding E and B fields in the finite elements for various source frequencies. Figure 2 graphs the calculated peak E versus frequency, and shows a resonant peak at 223 MHz. In comparison, the equation for the resonant frequency of the TE101 mode of classical theory is [6]

$$f = (c/2)\sqrt{(1/d)^{**}2 + (1/a)^{**}2} \qquad (6)$$

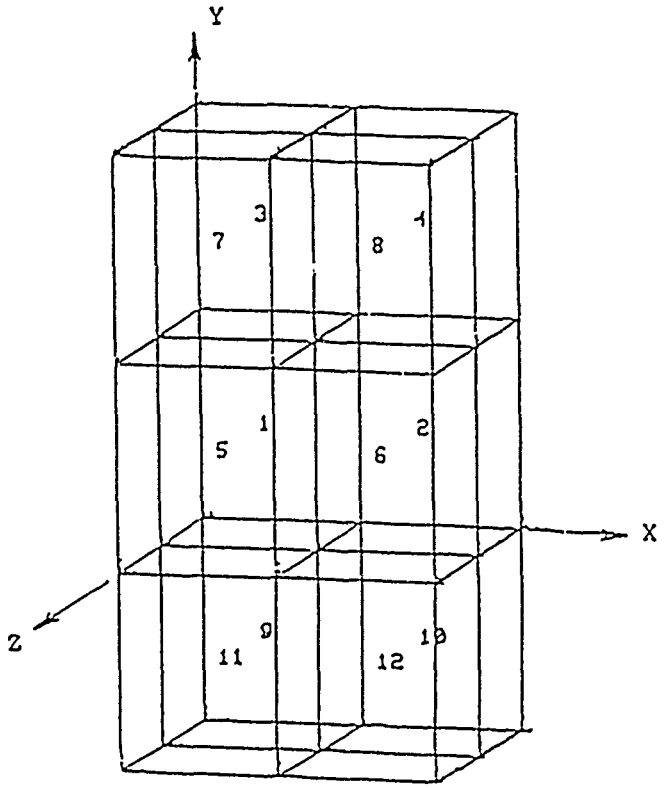


FIGURE 1. 3D finite element model of one quarter of a cubic cavity.

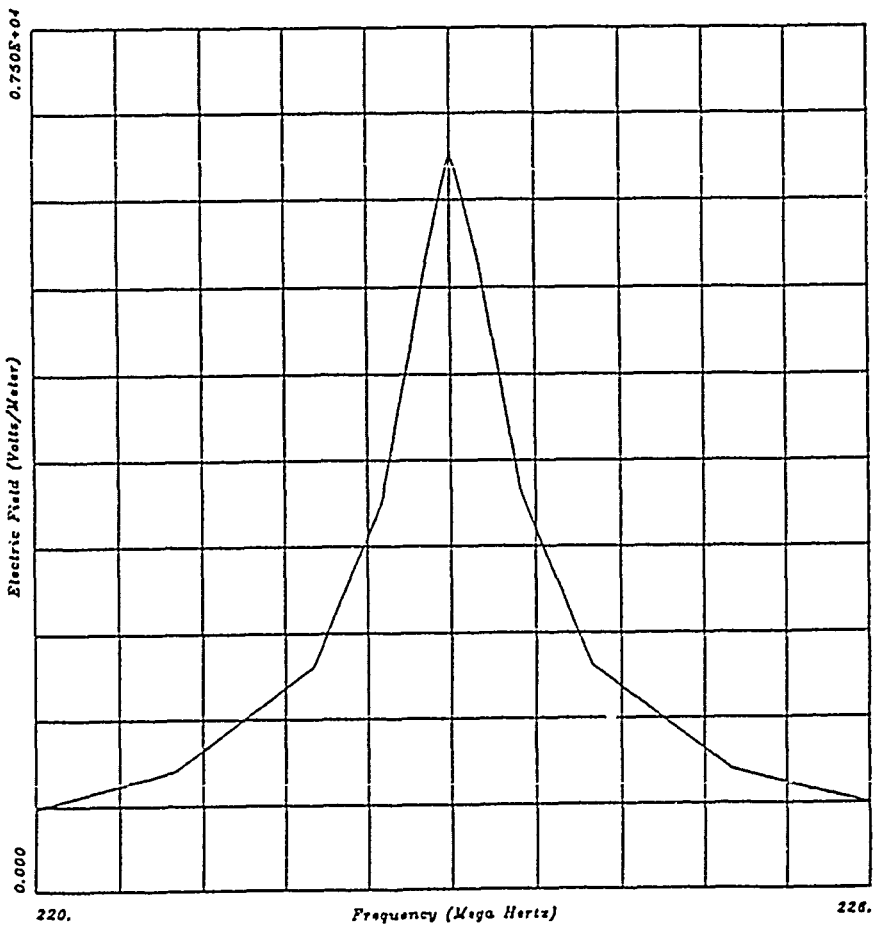


FIGURE 2. Frequency response curve computed for Figure 1.

where c = speed of light and a and d are the cavity dimensions in the x and z directions respectively. Here a=d=1 meter, giving f = 212.13 MHz. Thus the finite element resonant frequency is 5.1% above the classical frequency.

Color postprocessing of the AOS/MAGNUM output at resonance gives displays such as the one shown monochromatically in Figure 3 for the field B_x. Figure 4 graphs the calculated $\bar{B}$ and $\bar{E}$ field distributions at resonance, and shows them to agree closely with the classical sinusoidal mode shapes.

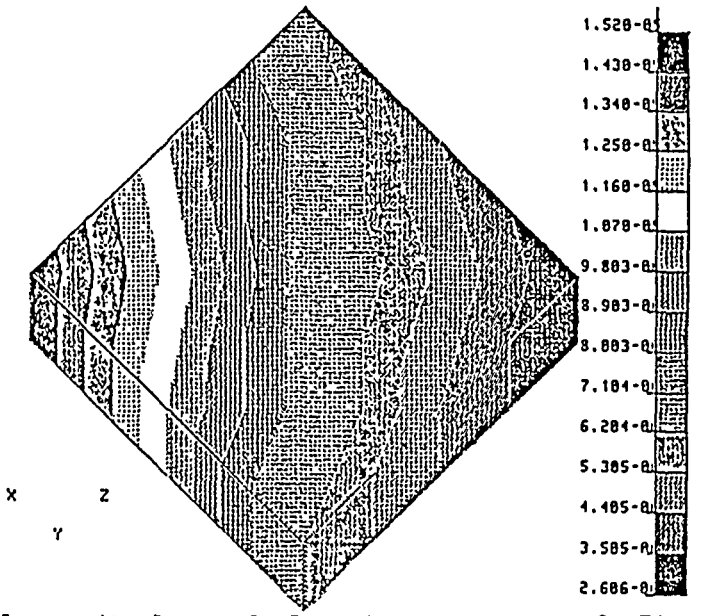


FIGURE 3. Color display of Bx at resonance of Figure 1, shown monochromatically.

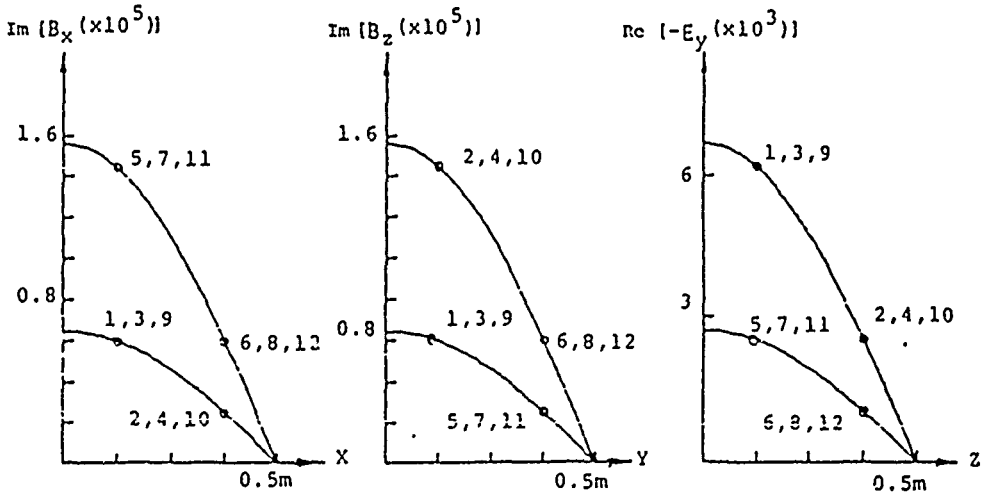


FIGURE 4. Finite element fields (calculated data points) vs. classical curves for cavity of Figure 1.

The ratio of peak E_y to peak B_x is the impedance from classical theory [6]

$$E_{ypk}/B_{xpk} = i\ 2\ f\ d \qquad (7)$$

Using d = 1 and f = 212.13E6 gives i424.26E6 ohms. In comparison the finite element calculation of Figure 4 gives the ratio -6104/i1.44367E-5 = i422.811E6 ohms. Thus the impedance agrees within 0.34%.

The accuracy of the calculations increases with the number of finite elements. For example, if the number of elements in the cubic cavity is increased from 12 to 250 the computed resonant frequency becomes 213.7 MHz, or 0.74% above the classical frequency.

3D CYLINDRICAL CAVITY TM010 MODE

Figure 5 shows the 3D finite element model developed for one quadrant of a cylindrical cavity. The outer radius of Figure 5 is 2.099 cm, and the axial height is 1 cm. Figure 5 contains 6 hexahedrons and 3 pentahedral finite elements. The excitation is $\bar{J}$ in the axial z direction in the 3 pentahedrons. The cavity has perfectly conducting walls surrounding a material of conductivity 1.E-4 S/m.

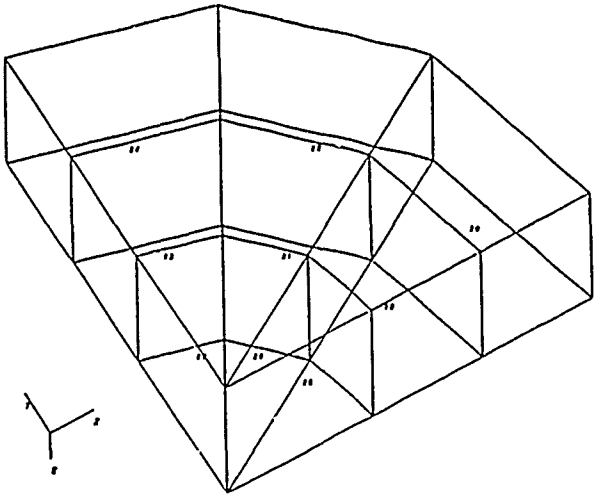


FIGURE 5. 3D finite element model of one quarter of a cylindrical cavity.

The resonant frequency was calculated by varying the frequency in AOS/MAGNUM. The fields were found to peak at 5.67 GHz. In comparison, the resonant frequency of the TM010 mode of classical theory is [1]

$$f = c/(2.61a) \qquad (8)$$

where a is the radius 2.099E-2 meter, giving f = 5.48 GHz. Considering that only 9 finite elements are used, the finite element calculations agree well with theory.

2D RECTANGULAR CAVITY TE101 MODE

The rectangular cavity of Figure 1 can also be analyzed in two dimensions using the AOS/MAGNETIC analysis program, assuming that the dimension in the direction of the exciting current is infinite. According to equation (6) the resonant frequency is independent of that cavity dimension.

Figure 6 shows the two dimensional finite element model developed for one quarter of the 1 meter by 1 meter cavity. The exciting current density $\bar{J}$ is indicated in the center element of the 4 quadrilateral finite elements. $\bar{J}$ is assumed to be directed out of the paper, which is now defined as the z direction. Thus the calculated $\bar{A}$ and $\bar{E}$ values are all of one component only, in the z direction.

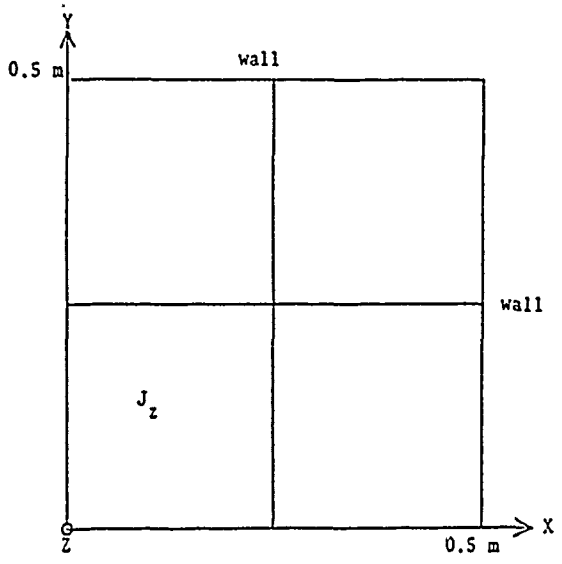


FIGURE 6. 2D finite element model of one quarter of a rectangular cavity.

The model of Figure 6 was input to AOS/MAGNETIC as a two dimensional planar model. The frequency was swept automatically from 220 MHz to 240 MHz, and resonance was found to occur at 228 MHz. From equation (6) the TE101 theoretical frequency remains at 212.13 MHz. Considering that only 4 finite elements are used here, the finite element results are in reasonably good agreement.

2D CYLINDRICAL CAVITY TE011 MODE

AOS/MAGNETIC also analyzes axisymmetric geometries. The model of Figure 6 can be analyzed as a cavity with the y axis as the axis of symmetry. Then the cavity becomes a cylinder of radius 0.5 meter and length 1 meter. Since E is assumed to come out of the page in AOS/MAGNETIC, this 2D program can calculate the TE modes but not the TM modes of the previous 3D cylindrical cavity model.

The swept frequency capability of AOS/MAGNETIC was used for the axisymmetric solution. The calculated frequency of resonance was 435 MHz. In

comparison, the classical resonant frequency formula is [1]

$$f = c\sqrt{1 + [2L/(1.64a)]^{**2}} \;/\; (2L) \qquad (9)$$

where L is the axial length = 1 meter and a is the radius = 0.5 meter. Thus equation (9) gives 395.41 MHz. For the finite element results to be more accurate, more than 4 finite elements would be necessary.

BEAM WAVEGUIDE RESONATOR AND ANTENNA MODES

A cavity resonator of more complicated geometry than the preceding cavities is the beam waveguide resonator. Beam waveguide resonators are suitable for microwave through optical frequencies [1].

Figure 7 shows the cross section of one half of the rectangular beam waveguide resonator for which classical theory and experimental measurements have been published [7]. The other half of this planar resonator is symmetric about the y axis. The dimensions of Figure 7 are such that resonances are expected in the 9 GHz region of the frequency spectrum.

Figure 7 also shows the 2D finite elements which have been used to model this resonator. Because $\bar{E}$ is expected to have one component directed out of

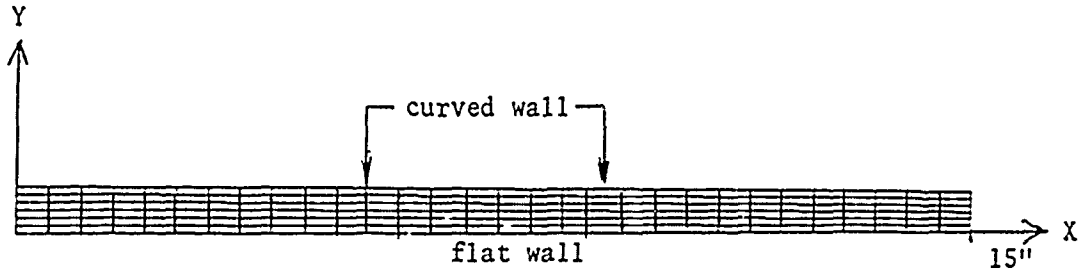


FIGURE 7. 2D finite element model of the right half of a beam waveguide resonator.

the page, AOS/MAGNETIC can be used to solve for the resonant frequencies and mode shapes.

From classical theory [7] the beam waveguide resonator is known to have resonant modes at fairly closely spaced frequencies. The modes are given the designation numbers 0, 1, 2, 3, 4, etc. The shapes of the modes are Hermite polynomials times a Gaussian. Thus E of each mode n obeys

$$E = E_{pk}\, He_n(2ux)\, \exp(-u^{**2}*x^{**2})\, \sin(2\pi y/\lambda) \qquad (10)$$

where He_n is the Hermite polynomial of order n, u is a geometric factor and λ is free space wavelength. The resonant frequencies increase with mode number n. Thus the lowest resonant frequency is for n=0. Even modes (n even) have been excited with a current source such as the center conductor of a coax cable at x = 0. Odd modes have been excited with antisymmetric sources at positive and negative x [7].

To simulate excitation of the even modes J was assumed to exist in the elements of Figure 7 near x=0. The model was input to AOS/MAGNETIC, and the frequency was swept from 9.0 GHz to 9.6 GHz. Figure 8 shows the calculated resonances. Included in Figure 8 are the resonances obtained by antisymmetric excitation and constraints in the model of Figure 7. which are for the odd modes. The computed resonant frequencies agree within 3 percent with those of theory and measurement [7].

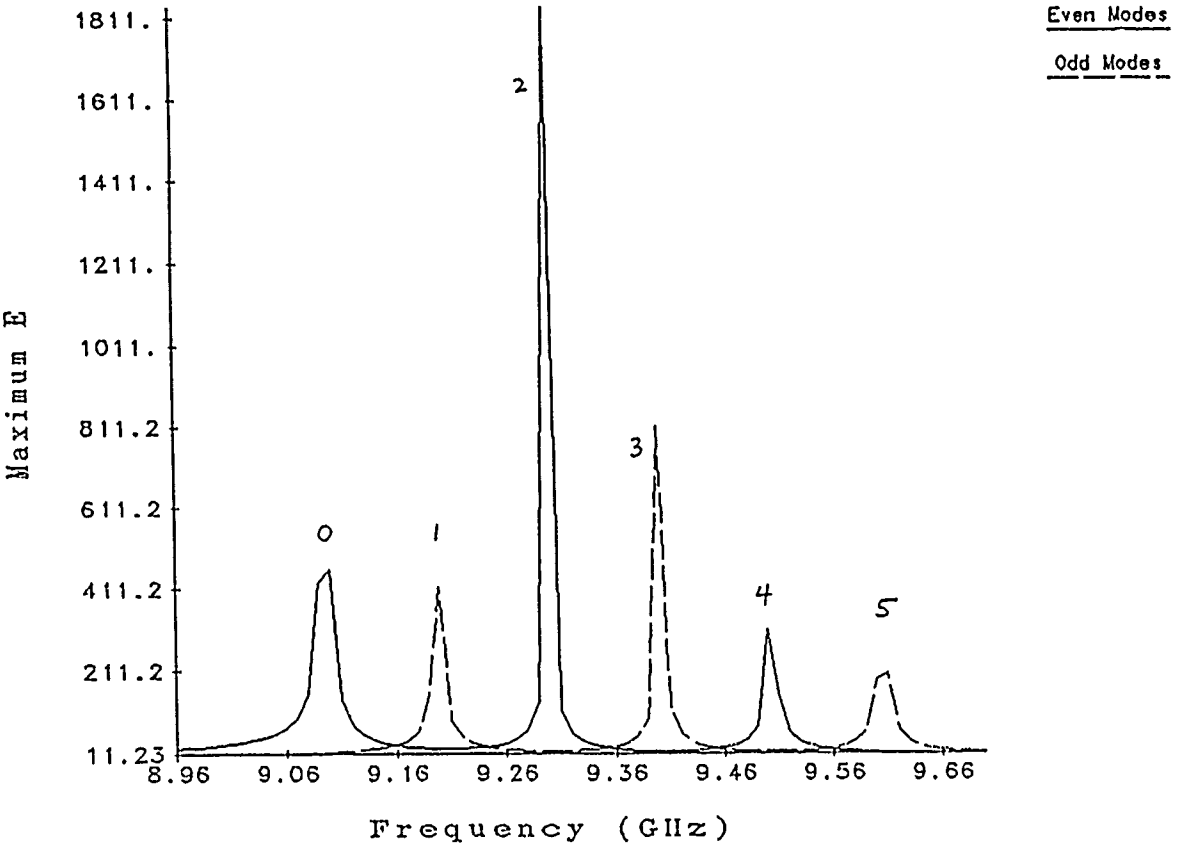


FIGURE 8. Frequency response curve computed for Figure 7.

The mode shapes calculated by AOS/MAGNETIC for the n=0 and n=1 modes are graphed in Figures 9 and 10, respectively. The n=0 field follows a Gaussian distribution, agreeing with equation (10). Also in agreement with theory is the calculated n=1 distribution of Figure 10.

The beam waveguide resonator can also be made into an antenna by introducing holes in the metal wall at y=0. Such holes can also be introduced into the finite element model.

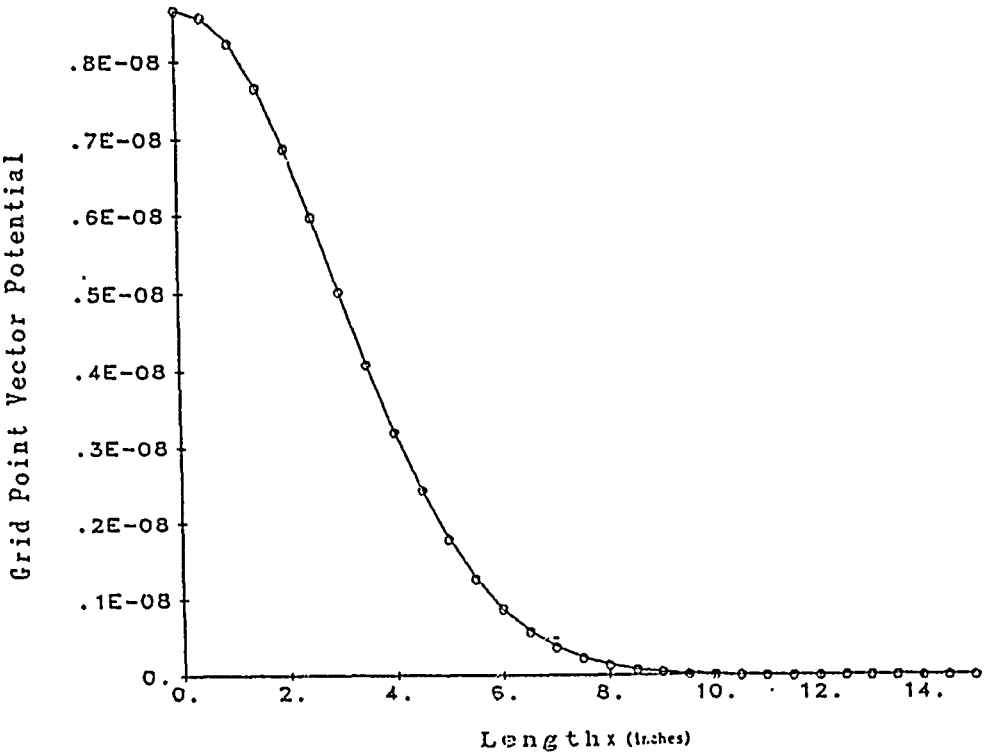


FIGURE 9. Computed field distribution for n=0 mode of Figures 7 and 8.

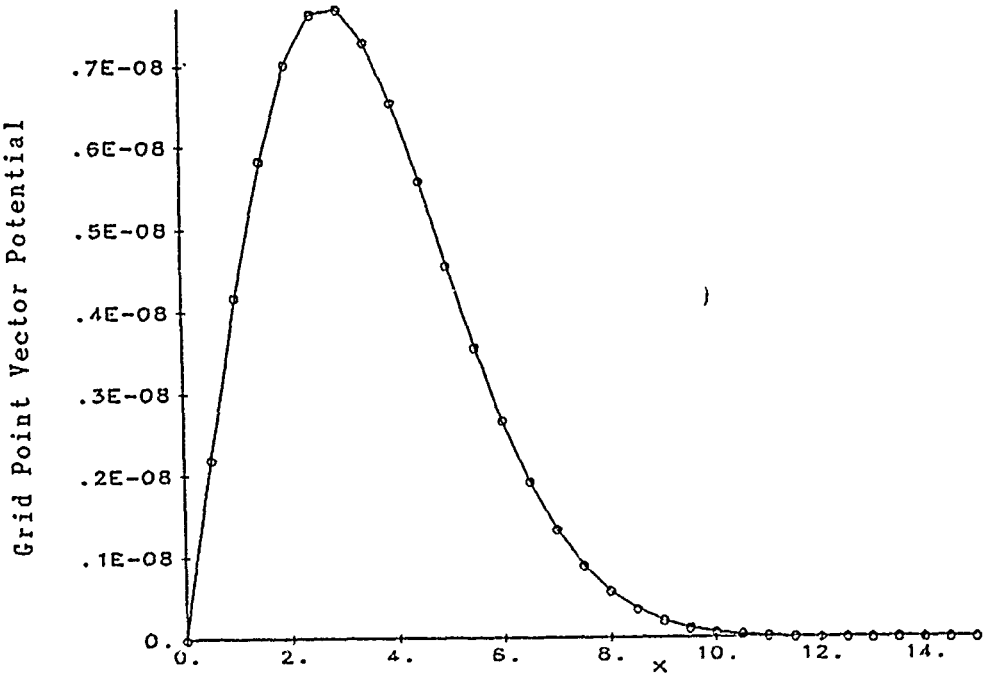


FIGURE 10. Computed field distribution for n=1 mode of Figures 7 and 8.

CONCLUSIONS

The electromagnetic fields and resonant frequencies of several types of cavities have been accurately calculated by the vector potential finite element method. The accuracy increases with the number of finite elements used to model the cavity. The method includes the effects of nonuniform lossy materials and can analyze cavities of a wide variety of two- and three-dimensional shapes.

REFERENCES

[1] S. Ramo, J.R. Whinnery, and T. Van Duzer, Fields and Waves in Communication Electronics, John Wiley & Sons, Inc., New York, 1965.

[2] F.L. Zeisler and J.R. Brauer, IEEE Trans. Magnetics, 21, 2453-2456, 1985.

[3] J.R. Brauer (ed.), What Every Engineer Should Know About Finite Element Analysis, Marcel Dekker, Inc., New York, to appear.

[4] AOS/MAGNETIC is a proprietary product of A.O. Smith Data Systems, Inc., 8901 N. Kildeer Court, Milwaukee, WI 53209.

[5] AOS/MAGNUM is a proprietary product of A.O. Smith Data Systems, Inc., 8901 N. Kildeer Court, Milwaukee, WI 53209.

[6] R. Plonsey and R.E. Collin, Principles and Applications of Electromagnetic Fields, McGraw-Hill Co., New York, 1961.

[7] J.R. Brauer, IEEE Trans. Antennas & Prop., 20, 595-601, 1972.

MUTUAL IMPEDANCE COMPUTATIONS USING NEC

D. E. Hudson
Lockheed Aircraft Service Company
P.O. Box 33, Dept. 1-330
Ontario, CA 91762

When modelling multi-element antenna systems, mutual impedance data is often a necessary output so that each element's driving impedance can be computed. The Numerical Electromagnetic Code (NEC-3) software has a "compute maximum coupling" (CP) card. but this feature yields a "dB coupling" figure, not the mutual impedance values.

This presentation will outline a straightforward method to derive the mutual impedance from multi-element antenna computations using the NEC program. We will present the algorithms necessary to convert NEC software outputs to mutual impedance data and show how computations involving specific coupled antennas can be handled. We will also make validation comparisons of computed data based on NEC to measured mutual impedance values.

Lockheed -Ontario

MUTUAL IMPEDANCE COMPUTATIONS USING NEC

BY

D.E. HUDSON, P.E.
LOCKHEED AIRCRAFT SERVICE CO.
P.O. BOX 33, DEPT. 1-330
ONTARIO, CALIFORNIA 91761

Lockheed -Ontario

EQUATIONS USED TO COMPUTE DRIVING (ACTIVE) IMPEDANCE

$$Z_1' = Z_{11} + \frac{I_2}{I_1} Z_{12} + \quad + \frac{I_n}{I_1} Z_{1n}$$

$$Z_2' = \frac{I_1}{I_2} Z_{21} + Z_{22} + \quad + \frac{I_n}{I_2} Z_{2n}$$

$$Z_n' = \frac{I_1}{I_n} Z_{n_1} + \frac{I_2}{I_n} Z_{n_2} + \quad + Z_{nn}$$

Lockheed -Ontario

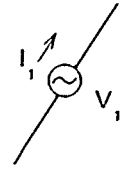
MUTUAL IMPEDANCE: ESSENTIAL FOR DESIGN AND OPERATION OF MULTI-ELEMENT (ARRAY) ANTENNAS

- NECESSARY TO CALCULATE DRIVING (ACTIVE) IMPEDANCE OF EACH ELEMENT
- DESIGN OF ARRAY FEED STRUCTURE FOR POWER DIVISION AND PHASE CONTROL
- EXAMPLES: DIRECTIONAL AM BROADCAST ANTENNAS SHAPED-BEAM TV/ FM ANTENNAS, GENERAL ARRAYS

Lockheed -Ontario

SELF-IMPEDANCE

STARTING WITH A SINGLE, ISOLATED ANTENNA ELEMENT



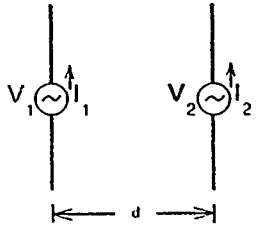
$$Z_1' = Z_{11} = \frac{V_1}{I_1}$$

$Z_{11} \equiv$ SELF-IMPEDANCE OF ELEMENT 1 ALONE

Lockheed -Ontario

COUPLED ANTENNAS

PLACING A SECOND ANTENNA IN PROXIMITY,



$$V_1 = I_1 Z_{11} + I_2 Z_{12}$$

$$V_2 = I_1 Z_{21} + I_2 Z_{22}$$

SOLVING FOR DRIVING (ACTIVE) IMPEDANCE,

$$\frac{V_1}{I_1} = Z_1' = Z_{11} + \frac{I_2}{I_1} Z_{12}$$

$$\frac{V_2}{I_2} = Z_2' = \frac{I_1}{I_2} Z_{21} + Z_{22}$$

Lockheed -Ontario

CIRCUIT RELATIONSHIPS

FROM NETWORK THEORY,



TWO-PORT NETWORK

VOLTAGE-CURRENT RELATIONS

$$V_1 = I_1 Z_{11} + Z_{12} I_2$$

$$V_2 = I_1 Z_{21} + Z_{22} I_2$$

FOR A RECIPROCAL NETWORK, $Z_{12} = Z_{21}$

WHERE

$$Z_{11} = \left.\frac{V_1}{I_1}\right|_{I_2 = 0}$$

$$Z_{21} = \left.\frac{V_2}{I_1}\right|_{I_2 = 0}$$

AND

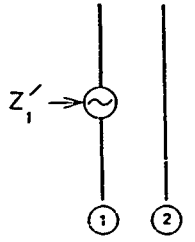
$$Z_{12} = \left.\frac{V_1}{I_2}\right|_{I_1 = 0}$$

Lockheed -Ontario

HOW TO COMPUTE MUTUAL IMPEDANCE BY NEC?

ALTERNATE METHOD:

1. APPLY $Z_{12} = \sqrt{Z_{22}\left(Z_{11} - Z_1'\right)}$
2. COMPUTE Z_{nn}'s (1 or 2 runs)
3. COMPUTE Z_1' BY ADDING COUPLED ANTENNA IN MODEL

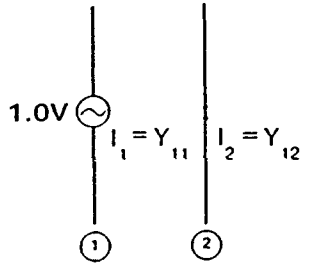


- DUPLICATES MEASUREMENT PROCEDURE
- USER SHOULD BE AWARE OF CAVEATS

Lockheed -Ontario

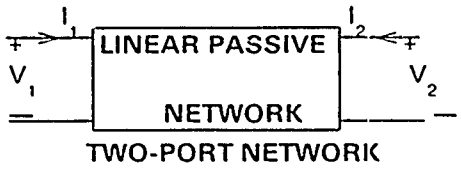
PREFERRED METHOD: COMPUTE ADMITTANCES, CONVERT TO IMPEDANCES

1. MODEL STRUCTURES AS THEY ARE.
2. DRIVE (1) WITH 1.0 VOLT, SHORT TERMINALS OF (2)
3. IF ELEMENTS ARE IDENTICAL, $Y_{11} = Y_{22}$
4. IF ELEMENTS ARE DIFFERENT, INTERCHANGE DRIVE AND SHORT POINTS FOLLOWED BY XQ CARD.
5. USE ADMITTANCE TO IMPEDANCE CONVERSION ALGORITHMS



Lockheed -Ontario

DERIVATION OF SELF — AND MUTUAL ADMITTANCE



TWO-PORT NETWORK

$$I_1 = V_1 Y_{11} + V_2 Y_{12}$$

$$I_2 = V_1 Y_{21} + V_2 Y_{22}$$

$$Y_{11} = \frac{I_1}{V_1}\Big|_{V_2 = 0}$$

$$Y_{21} = \frac{I_2}{V_1}\Big|_{V_2 = 0}$$

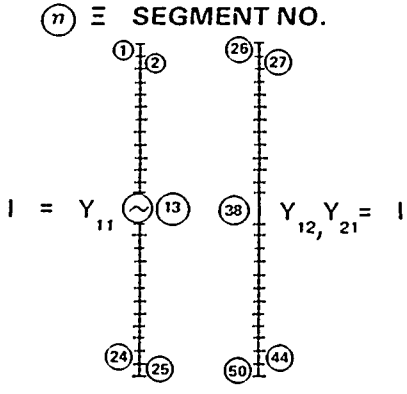
$$Y_{22} = \frac{I_2}{V_2}\Big|_{V_1 = 0}$$

$$Y_{12} = \frac{I_1}{V_2}\Big|_{V_1 = 0}$$

Lockheed -Ontario

COMPUTATION OF MUTUAL IMPEDANCE OF HALF-WAVE DIPOLES

- FREQUENCY = 10 MHz
- LENGTH = 0.4781 λ (TH.ELE AND STUTZMAN, p. 154f
- SPACING: FROM 0.1 λ to 0.9λ



Lockheed -Ontario

ADMITTANCE TO IMPEDANCE CONVERSION

- SET $|Y| = Y_{11} Y_{22} - Y_{12}^2 \left(= \begin{vmatrix} Y_{11} & Y_{12} \\ Y_{21} & Y_{22} \end{vmatrix} \right)$
- COMPUTE: $Z_{11} = \frac{Y_{22}}{|Y|}$

$$Z_{12} = Z_{21} = -\frac{Y_{12}}{|Y|}$$

$$Z_{22} = \frac{Y_{11}}{|Y|}$$

Lockheed -Ontario

NEC OUTPUTS GIVE Y_{11} AND Y_{12}

---CURRENTS AND LOCATION---
DISTANCES IN WAVELENGTHS

SEG NO	TAG NO	COORD X	OF SEG Y	CENTER Z	SEG LENGTH	CURRENT (AMPS) REAL	IMAG	MAG	PHASE
1	1	0 1000	0 0000	0 2295	0 01912	0 2029E 02	0 4233E 03	0 2072E 02	11 788
2	1	0 1000	0 0000	0 2104	0 01912	0 5635E 02	0 1187E 02	0 5758E 02	11 891
3	1	0 1000	0 0000	0 1912	0 01912	0 8959E 02	0 1904E 02	0 9159E 02	12 002
4	1	0 1000	0 0000	0 1721	0 01912	0 1207E 01	0 2591E 02	0 1234E 01	12 117
5	1	0 1000	0 0000	0 1530	0 01912	0 1495E 01	0 3244E 02	0 1530E 01	12 238
6	1	0 100	0 0000	0 1339	0 01912	0 1759E 01	0 3856E 02	0 1801E 01	12 368
7	1	0 1000	0 0000	0 1147	0 01912	0 1994E 01	0 4422E 02	0 2042E 01	12 504
8	1	0 1000	0 0000	0 0956	0 01912	0 2198E 01	0 4935E 02	0 2253E 01	12 653
9	1	0 1000	0 0000	0 0765	0 01912	0 2369E 01	0 5390E 02	0 2430E 01	12 816
10	1	0 1000	0 0000	0 0574	0 01912	0 2504E 01	0 5781E 02	0 2570E 01	12 998
11	1	0 1000	0 0000	0 0382	0 01912	0 2602E 01	0 6105E 02	0 2673E 01	13 203
12	1	0 1000	0 0000	0 0191	0 01912	0 2662E 01	0 6364E 02	0 2737E 01	13 447
13	1	0 1000	0 0000	0 0000	0 01912	0 2662E 01	0 6522E 02	0 2760E 01	13 670
14	1	0 1000	0 0000	0 0191	0 01912	0 2662E 01	0 6384E 02	0 2737E 01	13 447
15	1	0 1000	0 0000	0 0382	0 01912	0 2602E 01	0 6105E 02	0 2673E 01	13 203

Lockheed -Ontario

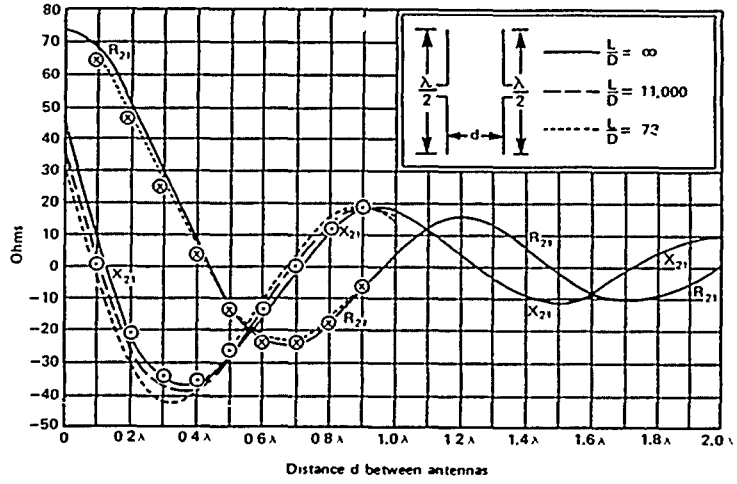
NEC OUTPUTS GIVE Y_{11} AND Y_{12}

---CURRENTS AND LOCATION---
DISTANCES IN WAVELENGTHS

31	2	0 1000	0 0000	0 1339	0 01912	0 1269E 01	0 2277E 02	0 1290E 01	169 830
32	2	0 1000	0 0000	0 1147	0 01912	0 1440E 01	0 2584E 02	0 1463E 01	169 825
33	2	0 1000	0 0000	0 0956	0 01912	0 1588E 01	0 2850E 02	0 1613E 01	169 821
34	2	0 1000	0 0000	0 0765	0 01912	0 1711E 01	0 3074E 02	0 1739E 01	169 818
35	2	0 1000	0 0000	0 0574	0 01912	0 1809E 01	0 3251E 02	0 1838E 01	169 815
36	2	0 1000	0 0000	0 0382	0 01912	0 1880E 01	0 3379E 02	0 1911E 01	169 813
37	2	0 1000	0 0000	0 0191	0 01912	0 1923E 01	0 3457E 02	0 1954E 01	169 812
38	2	0 1000	0 0000	0 0000	0 01912	0 1938E 01	0 3483E 02	0 1969E 01	169 811
39	2	0 1000	0 0000	0 0191	0 01912	0 1923E 01	0 3457E 02	0 1954E 01	169 812
40	2	0 1000	0 0000	0 0382	0 01912	0 1880E 01	0 3379E 02	0 1911E 01	169 813
41	2	0 1000	0 0000	0 0574	0 01912	0 1809E 01	0 3251E 02	0 1838E 01	169 815
42	2	0 1000	0 0000	0 0765	0 01912	0 1711E 01	0 3074E 02	0 1739E 01	169 818
43	2	0 1000	0 0000	0 0956	0 01912	0 1588E 01	0 2850E 02	0 1613E 01	169 821
44	2	0 1000	0 0000	0 1147	0 01912	0 1440E 01	0 2584E 02	0 1463E 01	169 825
45	2	0 1000	0 0000	0 1339	0 01912	0 1269E 01	0 2277E 02	0 1290E 01	169 830
46	2	0 1000	0 0000	0 1530	0 01912	0 1079E 01	0 1934E 02	0 1096E 01	169 836
47	2	0 1000	0 0000	0 1721	0 01912	0 8704E 01	0 1559E 02	0 8842E 01	169 842
48	2	0 1000	0 0000	0 1912	0 01912	0 6457E 01	0 1156E 02	0 6560E 01	169 849
49	2	0 1000	0 0000	0 2104	0 01912	0 4059E 01	0 7263E 02	0 4124E 01	169 856
50	2	0 1000	0 0000	0 2295	0 01912	0 1461E 01	0 2611E 02	0 1484E 01	169 863

Lockheed -Ontario

VALIDATION COMPARISONS WITH KRAUS (1950), p. 266



Lockheed -Ontario

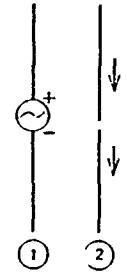
COMPUTED MUTUAL IMPEDANCE VS. SPACING

d/λ	MUTUAL IMPEDANCE	
	R_{21}	jX_{21}
1	64.	+j1.5
.2	47.	-j21.
.3	25.	-j34.
4	3.9	-j35.
.5	-13.	-j27.
.6	-23.	-j14
.7	-23.	+j1.1
75	-21	+j7.4
8	-17	+j12
.9	-6.0	+j18.

Lockheed -Ontario

PRECAUTIONS IN COMPUTING AND MEASURING Z_{nn}, Z_{mn}

- EVEN IF COUPLED ELEMENT IS OPEN, I_2 MAY NOT BE NEGLIGIBLE
- IN GENERAL CASE, BEST TO SHORT CIRCUIT ANTENNA #2



TEST OF A COAXIAL-LINE SOURCE MODEL FOR NEC *

G. J. Burke
Lawrence Livermore National Laboratory
Livermore, CA 94550

1. *Introduction*

Modeling of the voltage source is probably the most critical step in the method-of-moments (MOM) analysis of wire antennas. The requirements for the source model are that it accurately represent the desired source voltage and, as closely as possible, duplicate the physical characteristics of the actual antenna excitation. In addition the model should introduce a minimum of computational overhead. It is also highly desirable that the MOM model be independent of the location of the source so that solutions for several different excitations can be obtained with a single evaluation and inversion of the MOM impedance matrix.

Various models have been used for voltage sources, including finite excitation gaps, delta-function or slice generators and models based on biconical or coaxial transmission lines. The usefulness of these models often is dependent on the form of the MOM solution, particularly whether point matching or a continuously weighted integral of the field is used. The code NEC [1] currently offers two models for a voltage source on a wire: the "gap" or "applied field" source and the "bicone" or "charge discontinuity" source. The gap source yields generally stable results but, particularly at low frequencies, may be much wider than the actual source. The bicone model produces a more localized excitation but, as will be seen, may yield inaccurate results for input admittance.

A coaxial-line source model, employing a magnetic current frill, has been demonstrated by B. D. Popović, M. B. Dragović and A. R. Djordjević [2] in a MOM solution similar to that in NEC. Popović et al. use polynomial current expansion and point matching of the field, while NEC has a spline current expansion of $\sin(ks)$, $\cos(ks)$ and constant terms with point matching. Popović et al. obtain excellent agreement between their computed input admittances and measurements. Their coaxial-line model has been tested in NEC and results for this and the other NEC source models are compared in this paper.

2. *NEC Voltage Source Models*

The simplest, and at the present time most reliable, source model for the point-matched solution in NEC is the gap or applied field source. For a source voltage V on segment i with length Δ_i the field at the match point at the center of segment i is set to $-V/\Delta_i$. The field at all match points without sources remains zero. The current and its derivative are continuous through the source region. If the segments on either side of the source have lengths equal to that of the source segment the resulting current produces an electric field with a roughly rectangular distribution over the source segment and with an

* Work performed under the auspices of the U. S. Department of Energy by the Lawrence Livermore National Laboratory under Contract W-7405-Eng-48.

integral approximately equal to V.

The bicone source [3] was an attempt to obtain a narrower distribution of the source field. The source region is viewed as a biconical transmission line, as shown in Fig. 1, where the voltage can be related to the derivative of current as

$$V(z) = \frac{-jZ_0}{k}\frac{dI(z)}{dz}.$$

Z_0 is the characteristic impedance of the bicone,

$$Z_0 = \frac{\eta}{\pi}\ln(\cot\theta/2).$$

Since the choice of cone angle θ is uncertain for the cylindrical wire, Z_0 was averaged for δ in Fig. 1 varying from zero to the match point at $\Delta/2$ for segment length Δ. A condition was thus derived for a discontinuity in the derivative of current at the source of

$$\left.\frac{dI(z)}{dz}\right|_{z=0+} - \left.\frac{dI(z)}{dz}\right|_{z=0-} = \frac{-j2\pi kV}{\eta[\ln(\Delta/a) - 1]}.$$

The source, assumed to be at $z = 0$ here, must be at the junction between two parallel segments with equal lengths and radii. The discontinuity in derivative of current is introduced by including a modified basis function with discontinuous derivative in addition to the normal spline basis functions. Since this additional basis function has fixed amplitude it does not modify the MOM matrix, but produces an excitation field over all segments that goes on the right hand side of the matrix equation.

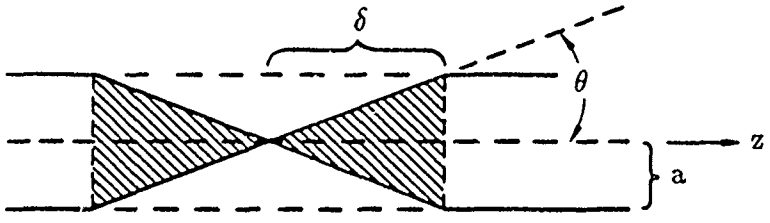


Fig. 1. The biconical transmission line source on a wire.

The coaxial-line source model can closely approximate the common practical case of excitation by a coaxial transmission line through a ground plane. It has been used in a number of wire antenna codes. Thiele [4] uses it with point matching and entire-domain basis functions. The treatment of Popović et al. [2] is more compatible with NEC since they use point matching and a polynomial basis in which a discontinuity can be introduced into the derivative.

As illustrated in Fig. 2, the coaxial line with electric field

$$E_\rho(\rho) = \frac{V}{\rho\ln(b/a)} \qquad \text{for} \qquad a < \rho < b$$

in the opening is replaced by the equivalent case of a frill of magnetic current $J_{m\phi} = -E_\rho$ over the plane. It is assumed here that only the TEM mode is present in the coaxial line opening, a condition that Popović et al. state is accurate for $kb < 0.1$. The magnetic current frill produces an excitation field over the structure. On the axis of the frill the z component of this field is

$$E_z(z) = \frac{V}{2\ln(b/a)}\left(\frac{e^{-jkR_a}}{R_a} - \frac{e^{-jkR_b}}{R_b}\right)$$

where $R_a = (z^2 + a^2)^{1/2}$ and $R_b = (z^2 + b^2)^{1/2}$. Thiele [4] gives the field at an arbitrary location.

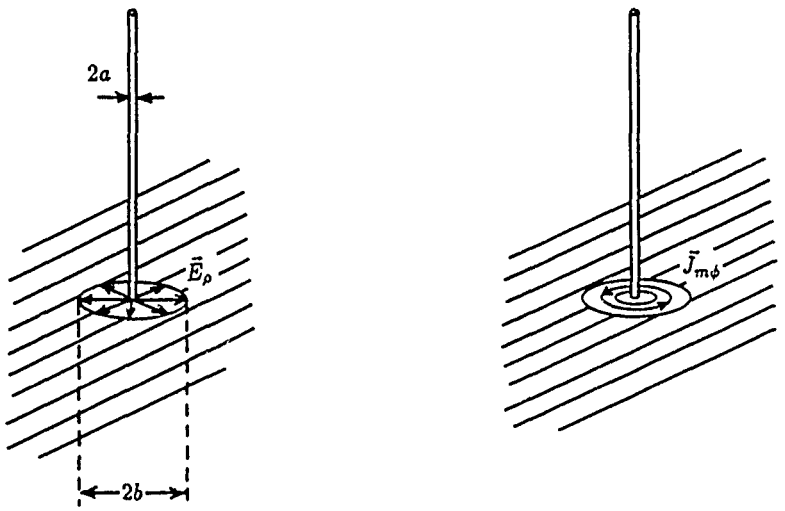


Fig. 2. The coaxial-line source and equivalent magnetic current frill.

At the frill location the discontinuity in $\vec{E}_\rho$ requires a discontinuity in charge density and hence in the derivative of current on the wire of

$$\left.\frac{dI(z)}{dz}\right|_{z=0+} - \left.\frac{dI(z)}{dz}\right|_{z=0-} = \frac{-j2\pi kV}{\eta\ln(b/a)}$$

Building this discontinuity into the current expansion, as Popović et al. have done, should improve the convergence of the solution. In NEC this can be done with a simple modification of the bicone source code along with calculation of the field of the frill.

The bicone source can also be considered to include a magnetic current frill at the apex of the cone. However, it has shrunk to zero dimensions and produces a delta function field that cannot be sampled in the point-matched solution.

3. *Comparison of Results*

Input admittances obtained with these source models in NEC were compared with the second order King-Middleton results [5] for a dipole with $kh = 1.6$ for half length h and for three thicknesses, $\Omega = 8$, 11 and 20. The King-Middleton values are not necessarily "correct" but are a convenient and widely accepted standard. Second order King-Middleton is

the result of two iterations of a solution of Hallén's integral equation with a delta-function source model. All NEC results here are from the double precision code. In single precision severe errors would occur for more than about 50 segments on a $\lambda/2$ dipole. Corrections have been developed for this problem [6] but are not yet in NEC-3. The extended thin wire kernel [7] was used for $\Omega = 8$ and 11 for all source models.

Results from the gap source model are shown in Fig. 3. For $\Omega = 8$, G converges, although ten percent from King-Middleton. B continues to change due, at least in part, to the increasing susceptance of the gap as it becomes narrower. It has been suggested [8] that the gap source model could be improved by subtracting a gap susceptance determined from the capacitance of the gap or empirically. King [9] applied a similar correction to the King-Middleton results using the measured susceptance at a single frequency. For Ω of 11 and 20 the NEC results show increasingly better convergence and agreement with King-Middleton.

The bicone source results, shown in Fig. 4, blow up for $\Omega = 8$ at 20 segments. A similar blow-up occurs for $\Omega = 11$ with 90 segments but is excluded from the plot. The results for $\Omega = 11$ appear useable to about 40 segments. At $\Omega = 20$ the results are acceptable but neither relative convergence nor agreement with King-Middleton is as good as with the gap source. It has been observed previously that the accuracy of the bicone source model degrades with increasing wire radius.

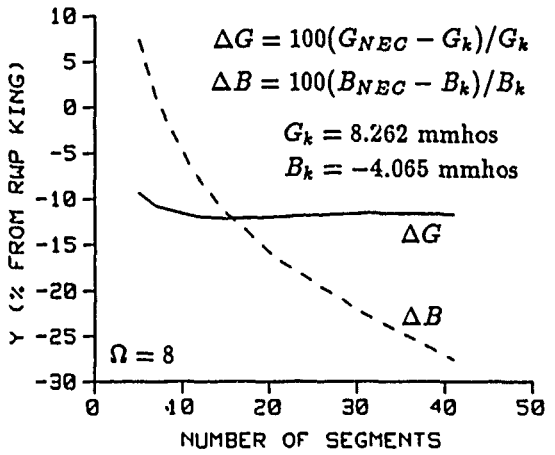
Accuracy of the coaxial-line source model depends on a sufficient sampling of the field of the magnetic current frill which decreases by half in a distance on the order of the wire radius. As shown in Fig. 5, the convergence of the coaxial-line source is best for $\Omega = 8$. Convergence is slow for $\Omega = 11$ and very poor for $\Omega = 20$.

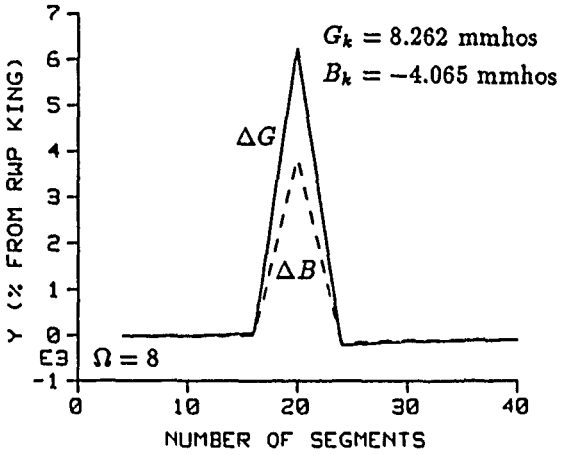
Popović et al. [2] recommend a nonuniform sampling with about four match points within a distance of $3a$ to $10a$ on either side of the source. Results of nonuniform sampling in NEC are shown in Fig. 6. A length L_1 of the dipole on either side of the source was covered with segments of length Δ_1. The remainder of the dipole was modeled with five segment on each side. For $\Omega = 20$ a transition segment with length 0.01λ was included between the short and longer segments. For $\Omega = 11$ good agreement with King-Middleton is obtained with about six segments and $\Delta_1/a = 1$. For $\Omega = 20$ results are converging but are still not good for seventy segments or a total of 152 segments. Continuous tapering of the segment length might yield better results, but was not tried due to lack of time.

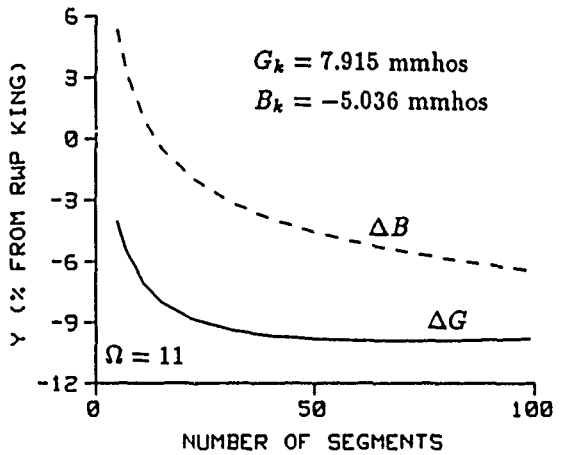
4. *Conclusions*

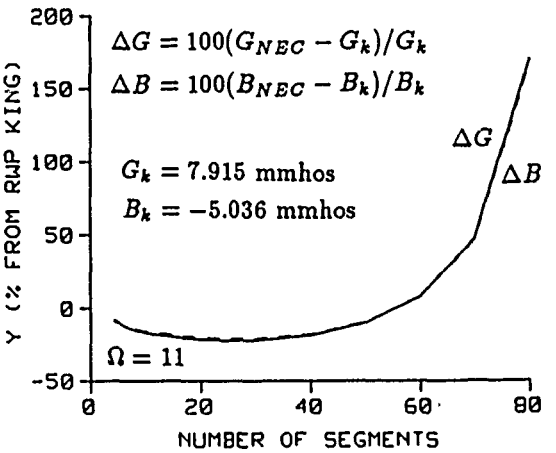
The coaxial-line source model could be useful in NEC for thick wires. For thin wires the difficulty in sampling the frill field appears to limit its usefulness. Experimentation with tapered segment lengths is needed to determine an optimum sampling for thinner wires. This would have the disadvantage of making the model dependent on the source location, however.

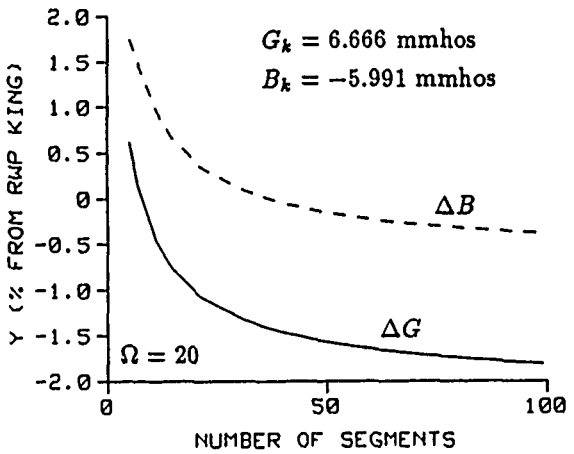
The excellent results shown by Popović et al. [2] are apparently the result of a very careful treatment of the problem. For a thick monopole ($a = 0.01\lambda$, $\Omega = 7.8$) they include











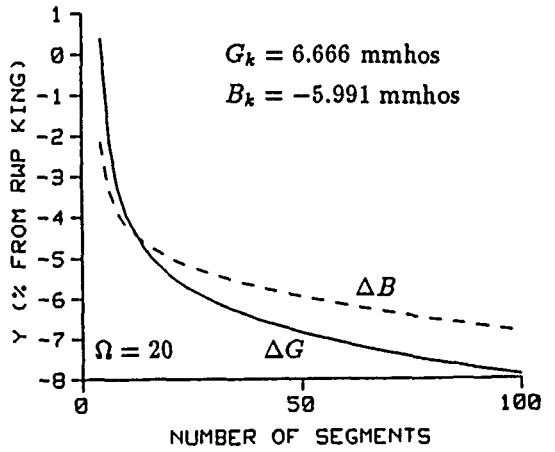


Fig. 3. Convergence of input admittance from the gap source in NEC relative to King-Middleton result $G_k + jB_k$. Dipoles with $\Omega = 2\ln(2h/a)$ of 8, 11 and 20 are shown for length $kh = 1.6$.

Fig. 4. Convergence of input admittance for the bicone source in NEC relative to King-Middleton result $G_k + jB_k$. Dipoles with $\Omega = 2\ln(2h/a)$ of 8, 11 and 20 are shown for length $kh = 1.6$.

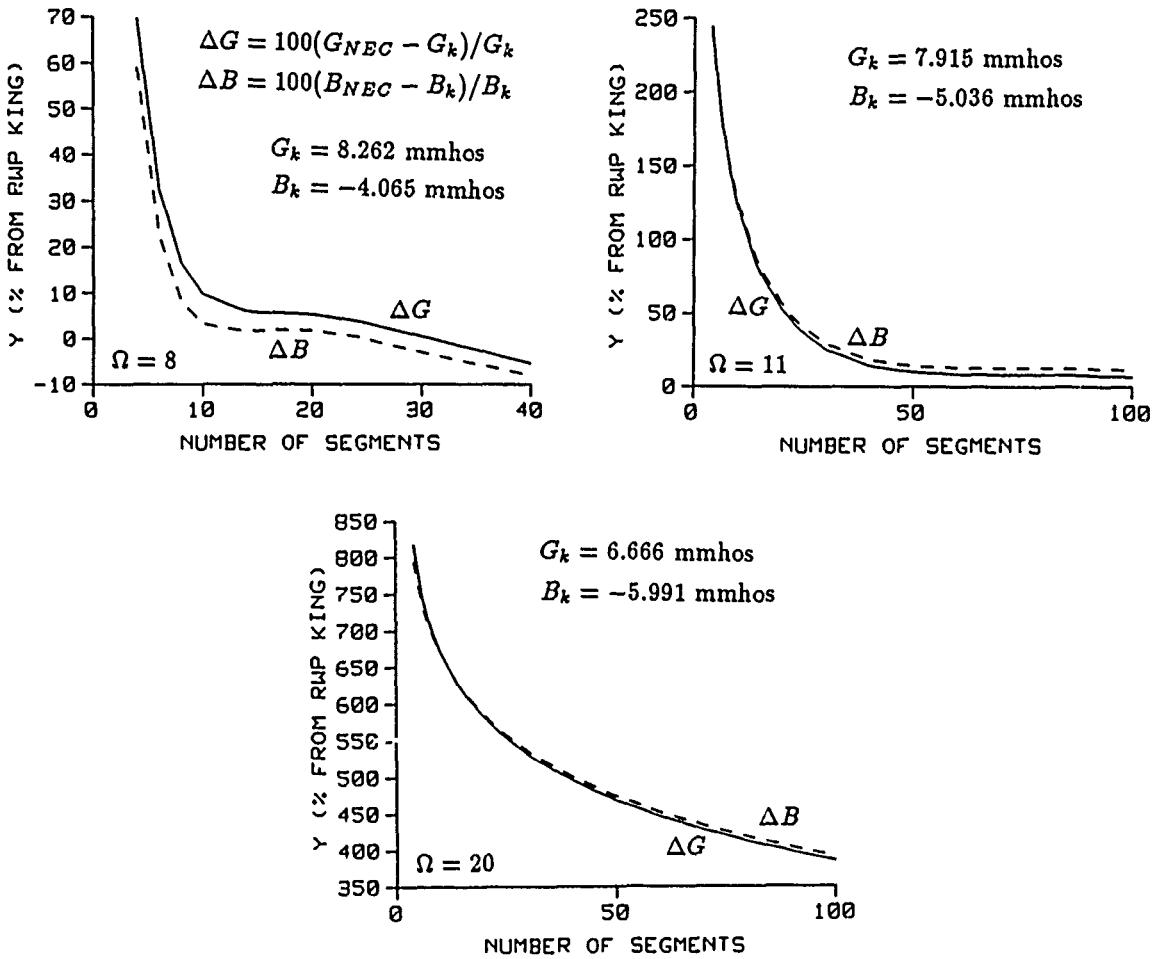


Fig. 5. Convergence of input admittance for the coaxial-line source in NEC relative to King-Middleton result $G_k + jB_k$. Dipoles with $\Omega = 2\ln(2h/a)$ of 8, 11 and 20 are shown for length $kh = 1.6$.

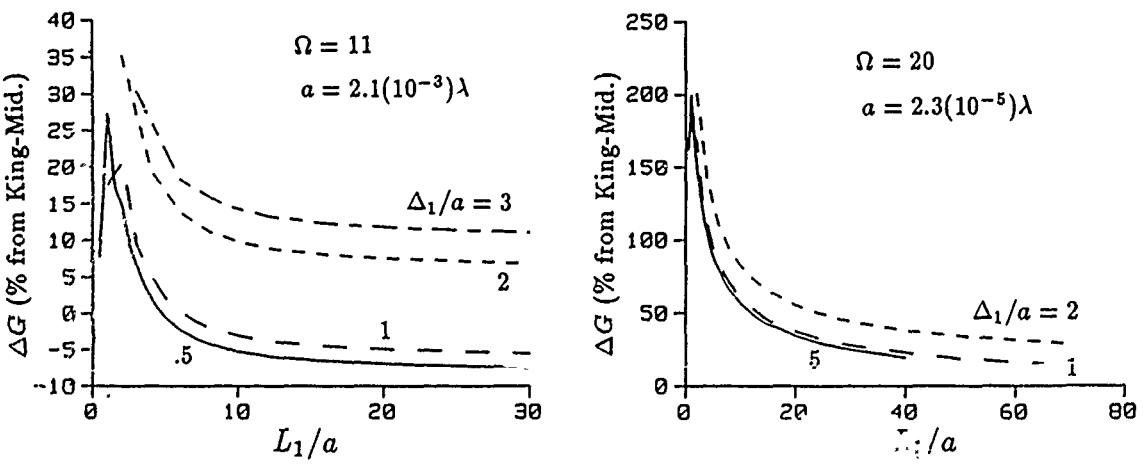


Fig. 6. Convergence of input admittance for the coaxial-line source with n[illegible] segmentation in NEC for a dipole with $kh = 1.6$ and wire radius a. The dipole was modeled with [illegible]ents of length Δ_1 for a distance of L_1 from the source.

a hemispherical end cap on the wire and report using 4 match points in a region of $6a$ of the source, 4 on the central part, 4 on a length $3a$ from the end cap, and 3 match points on the end cap. They use the extended boundary condition with the match points on the wire axis. For thinner wires they report, in addition, needing one or more progressively longer sections going away from the source to accurately approximate the rapidly changing second derivative of current. An end-cap treatment is not presently available in NEC but is one of the items that we would like to add in the future.

This work was supported by the U. S. Army ISEIC (J. McDonald) and CECOM (P. Cunningham), and by the U. S. Navy NOSC (J. Logan and S. T. Li).

REFERENCES

[1] G. J. Burke and A. J. Poggio, *Numerical Electromagnetics Code (NEC) - Method of Moments*, Lawrence Livermore National Laboratory, Rept. UCID-18834, Jan. 1981.

[2] B. D. Popović, M. B. Dragović and A. R. Djordjević, *Analysis and Synthesis of Wire Antennas*, Research Studies Press, New York, 1982.

[3] R. W. Adams, A. J. Poggio and E. K. Miller, *Study of a New Antenna Source Model*, Lawrence Livermore National Laboratory, Rept. UCRL-51693, Oct. 28, 1974.

[4] G. A. Thiele, "Wire Antennas", Chapt. 2 in *Computer Techniques for Electromagnetics*, ed. by R. Mittra, International Series of Monographs in Electrical Engineering, vol. 7, 1973.

[5] R. W. P. King, *Theory of Linear Antennas*, Harvard Univ. Press, Cambridge, MA, 1956.

[6] G. J. Burke, *Enhancements and Limitations of the Code NEC for Modeling Electrically Small Antennas*, Lawrence Livermore National Laboratory, Rept. UCID-20970, Jan. 1987.

[7] A. J. Poggio and R. W. Adams, *Approximations for Terms Related to the Kernel in Thin-Wire Integral Equations*, Lawrence Livermore National Laboratory, Rept. UCRL-51985, Dec. 19, 1975.

[8] E. K. Miller, Univ. of Kansas, Private communication.

[9] R. W. P. King, E. A. Aronson and C. W. Harrison, Jr., "Determination of the Admittance and Effective Length of Cylindrical Antennas", *Radio Science*, Vol. 1, pp. 835-850, 1966.

ACCURACY OF WIRE GRID MODEL NEAR FIELDS

A.C. Ludwig, General Research Corporation, Santa Barbara, CA

Solid bodies may be represented by wire grid models for numerically solving electromagnetic scattering problems. A recent paper has utilized an exact canonical problem to address the question of what grid wire diameter should be used to accurately model far-field radiation [1]. This paper uses the same approach to address the question of the accuracy of the near-field results.

The canonical problem is shown in Fig. 1. The true problem is defined to be a uniform current on the surface of an infinite cylinder of radius a. The wire grid model consists of a uniform current on the surface of n wires of radius b. The wire grid currents are selected such that the E-field at the center of a wire exactly matches the E-field of the true problem at that point. The grid model therefore mimics a numerical solution obtained using a method of moments technique. However, the problem has been defined such that an exact solution is easily obtained for both the true problem and the wire grid model [1]. The two exact solutions may then be compared to determine the inherent accuracy of the wire grid model.

Sample results for the near field are shown in Figs. 2-5, for a cylinder with $ka = 1.2$, where k is the free-space propagation constant. The wire grid model consists of $n = 6$ wires of radius $b = a/6$. This satisfies the "equal surface area" criterion discussed elsewhere [1]. E- and H-fields are shown as a function of radius from the center of the cylinder to twice the cylinder radius. The H-field is multiplied by the free-space impedance Z_o. The results for the real part of the E-field and the imaginary part of the H-field are virtually identical for the true problem and wire grid model. The most interesting results are for the real part of the H-field. At $r = a$, the H-field of the true problem has a discontinuity due to the surface current. The wire grid model has similar discontinuities, but at the surface of the wires rather than the surface of the cylinder. One diameter or so away from the wire the results agree very well. The imaginary part of the E-field has a similar discontinuity in its first derivative.

The conclusion is that the near fields of the wire grid model are remarkably accurate as long as the wire diameter satisfies the same surface area criterion.

---

[1] A.C. Ludwig, "Wire Grid Modeling of Surfaces," to be published.

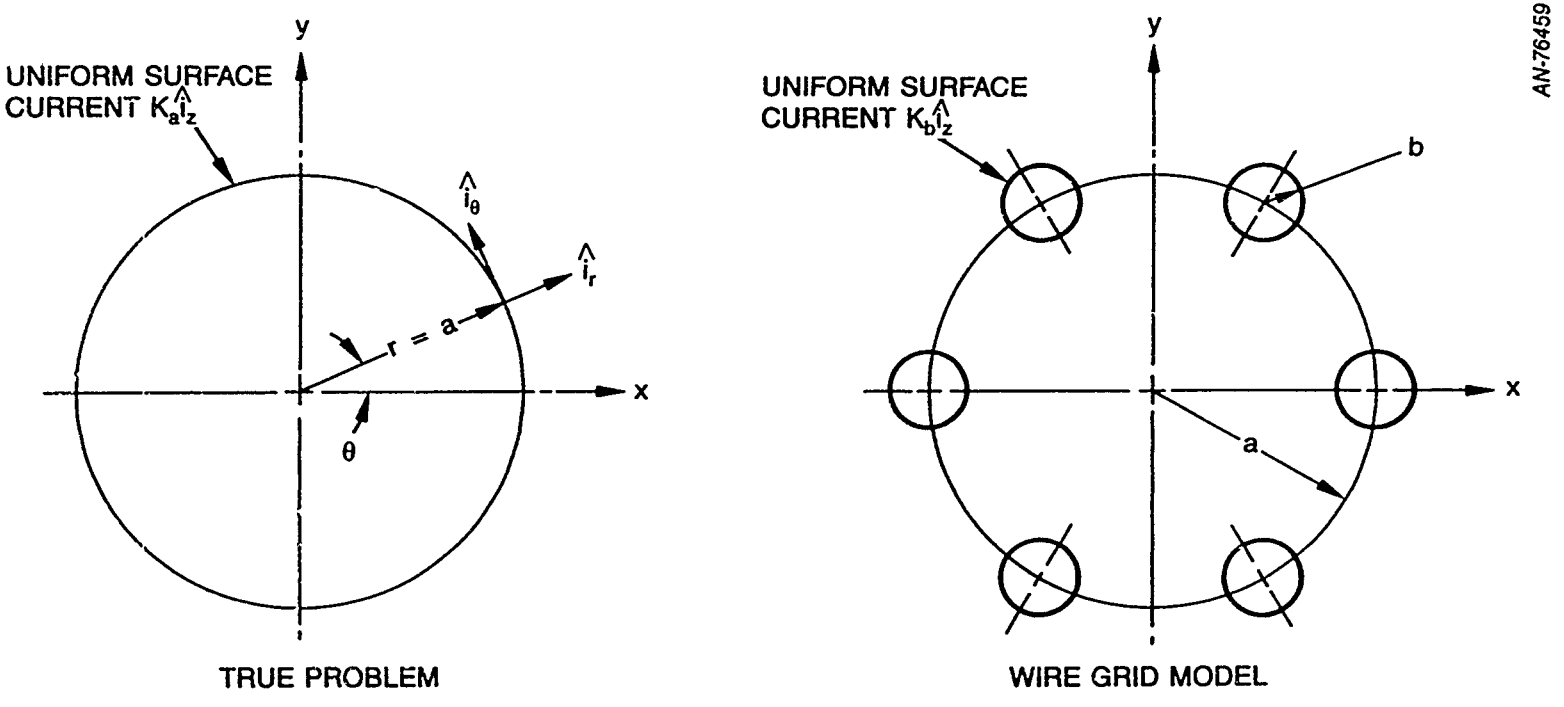


Figure 1. The canonical problem.

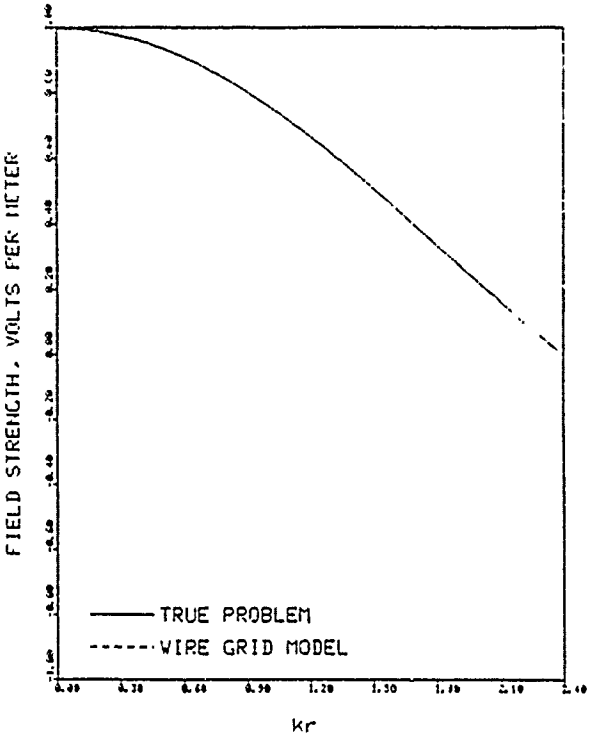


Figure 2. Real part of E-field, ka = 1.20, phi = 0.00.

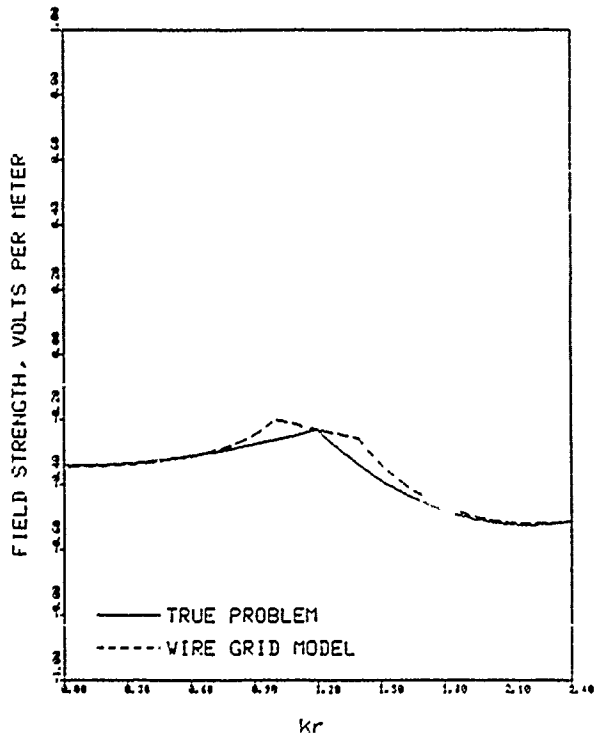


Figure 3. Imaginary part of E-field, ka = 1.20, phi = 0.00.

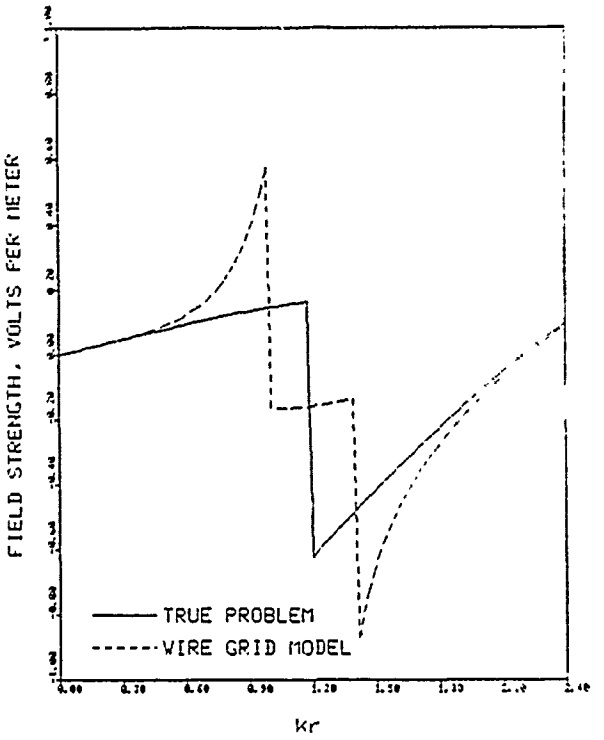


Figure 4. Real part of H-field, ka = 1.20, phi = 0.00.

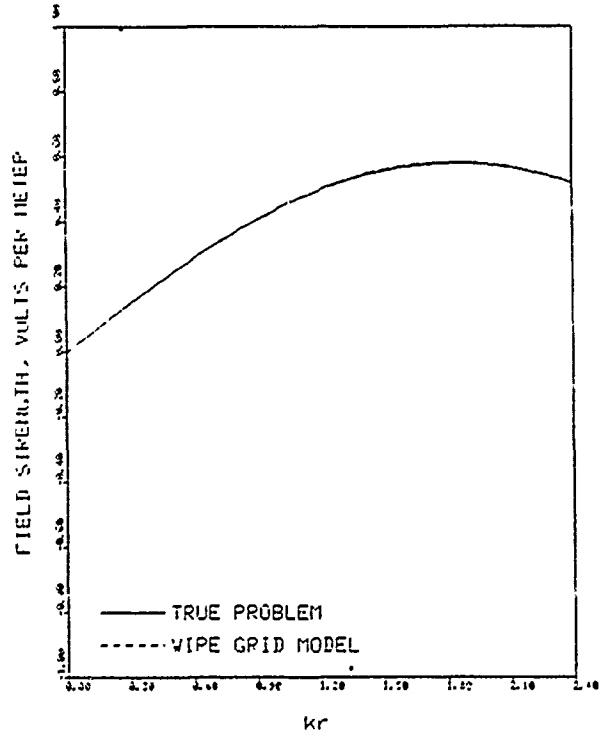


Figure 5. Imaginary part of H-field, ka = 1.20, phi = 0.00.

A NUMERICAL METHOD FOR SOLVING MAXWELL'S EQUATIONS WITH A COARSE GRID BORDERING A FINE GRID*

Kane S. Yee and John C. Kasher
P.O. Box 808, L-84
Lawrence Livermore National Laboratory
Livermore, CA 94550

It is well known that in any numerical computation the variables to be computed should not change significantly over the linear dimensions of the numerical grid. Thus, in the classic finite difference time domain (FDTD) algorithm (K. S. Yee, IEEE Trans. on Antenna and Propagation, Vol. AP-14, No. 3, p. 302-307, 1966) for solving Maxwell's equations, the numerical zones are much smaller than the scattering objects. Occasionally one can use special techniques to model sub-grid size scattering objects. The clever Holland-Simpson thin wire formulation (R. Holland and L. Simpson, IEEE Trans. Electromag. Compat., Vol. EMC-23, May 1981, pp. 88-97) modifies the FDTD in zones containing a thin wire. Recently, thin wire and small slot gaps have been modeled in the FDTD through the integral form of Faraday's law (K. S. Yee, Proc. of 1st Annual Review of Numerical Electromagnetics Code, March 19-21, 1985; A. Taflove, K. R. Umashankar, B. Beker, and K. S. Yee, submitted to IEEE Trans. Antennas Prop.; A. Taflove, K. Umashankar, B. Beker, F. Harfoush, and K. S. Yee, submitted to IEEE Trans. Ant. Prop.) In all these special formulations the local field behavior is inferred from static problems. This means that in one linear dimension the thin wires or thin slots are several zones long. These techniques would be of questionable applicability in some high power microwave (HPM) vulnerability problems where accurate coupling calculations through small irregular holes, grooves, or slots are required. For these cases, subgridding must be introduced. Because of numerical stability, smaller time increments will be required. The problem becomes, at best, intolerably slow if one uses a uniform time increment and, at worst, impossible to run because of the memory requirements due to the very fine zoning.

In this paper we introduce a scheme showing how the calculational volume can be divided into subvolumes, in each of which a spatial grid is introduced. The time increments in different subvolumes will be guided by the CFL criterion. In the transition from a coarse grid to a fine grid, we make use of the integral form of Maxwell's equations and follow the FDTD algorithm. Thus, the efficiency of the FDTD is retained and the modification to the FDTD can be done locally.

---

*Work performed under the auspices of the U.S. Department of Energy by the Lawrence Livermore National Laboratory under Contract W-7405-Eng-48.

A Reduced Number of Integral Equations for the Numerical Modeling of Two Dimensional Composite Structures

by

Mark A. Ricoy and John L. Volakis
Radiation Laboratory
Dept. of Electrical Engineering and Computer Science
The University of Michigan
Ann Arbor, MI 48109-2122

Abstract

A pair of integral equations are presented for simulating two dimensional material structures having arbitrary permittivity, conductivity and permeability. These are equivalent to the traditional three (coupled) integral equations usually required for simulating a material of arbitrary composition. As expected, their numerical implementation involves a substantial reduction in computer memory and CPU cost. Both E and H polarizations are considered.

I. INTRODUCTION

In this paper we propose the simulation of two-dimensional scatterers by stacks of thin layers of material as shown in Fig. 1. Traditionally, each layer can be equivalently replaced by a set of volume equivalent currents satisfying the relations

$$\bar{J} = j\omega\varepsilon_0 (\varepsilon_r - 1)(\bar{E}^s + \bar{E}^i) \tag{1}$$

$$\bar{J}^* = j\omega\varepsilon_0 (\varepsilon_r - 1)(\bar{H}^s + \bar{H}^i) \tag{2}$$

where $\bar{J}$ and $\bar{J}^*$ are the equivalent electric and magnetic currents, respectively ($\bar{E}^s$, $\bar{H}^s$) denote the scattered fields caused by J and J^*, ($\bar{E}^i$, $\bar{H}^i$) are the incident fields, ε_r and μ_r are the relative permittivity and permeability of the layer, respectively, and $k_0 = \omega\sqrt{\mu_0\varepsilon_0}$ is the free space propagation constant. If τ is the thickness of the layer, (1) and (2) can be written as:

$$\bar{E}^s + \bar{E}^i = R\bar{K} \tag{3}$$

$$\bar{H}^s + \bar{H}^i = R^*\bar{K}^* \tag{4}$$

where

$$\bar{J} = \tau\bar{K}, \qquad J^* = \tau\bar{K}^* \tag{5}$$

$$R = \frac{-jZ_0}{(\varepsilon_r - 1)k_0\tau}, \qquad R^* = \frac{-jY_0}{(\mu_r - 1)k_0\tau} \tag{6}$$

and $Z_0 = 1/Y_0$ is the free space impedance. In the subsequent development, we will assume that τ is sufficiently small so that $\bar{K}$ and $\bar{K}^*$ can be assumed constant across the thickness of the layer.

Substituting the integral expressions for the scattered fields ($\bar{E}^s$, $\bar{H}^s$) in (3)-(4) and assuming H_z - incidence, we obtain the integral equations

$$E_s^i = \varepsilon_r R K_s(s) + \frac{Z_0}{4\tau}\iint_{A'} K_{s'}(s')\frac{\partial}{\partial n}\left[(\hat{\rho}\cdot\hat{n}')H_1^{(2)}(k_0\rho)\right]ds'dn'$$

$$\frac{Z_0}{4\tau}\iint_{A'} K_{n'}(s')\frac{\partial}{\partial n}\left[(\hat{\rho}\cdot\hat{s}')H_1^{(2)}(k_0\rho)\right]ds'\,dn' + \frac{jk_0}{4\tau}\iint_{A'} K_z^{*}(s')(\hat{\rho}\cdot\hat{n})H_1^{(2)}(k_0\rho)ds'\,dn'$$

(7)

$$E_n^i = \varepsilon_r R K_n(s) - \frac{Z_0}{4\tau}\iint_{A'} K_{s'}(s')\frac{\partial}{\partial s}\left[(\hat{\rho}\cdot\hat{n}')H_1^{(2)}(k_0\rho)\right]ds'\,dn'$$

$$+\frac{Z_0}{4\tau}\iint_{A'} K_{n'}(s')\frac{\partial}{\partial s}\left[(\hat{\rho}\cdot\hat{s}')H_1^{(2)}(k_0\rho)\right]ds'\,dn' - \frac{jk_0}{4\tau}\iint_{A'} K_z^{*}(s')(\hat{\rho}\cdot\hat{s})H_1^{(2)}(k_0\rho)ds'\,dn'$$

(8)

$$H_z^i = R^{*}K_z^{*} + \frac{jk_0}{4\tau}\iint_{A'} K_{s'}(s')(\hat{\rho}\cdot\hat{n}')H_1^{(2)}(k_0\rho)ds'\,dn'$$

$$-j\frac{k_0}{4\tau}\iint_{A'} K_{n'}(s')(\hat{\rho}\cdot\hat{s}')H_1^{(2)}(k_0\rho)ds'\,dn' + \frac{k_0 Y_0}{4\tau}\iint_{A'} K_z^{*}(s')H_0^{(2)}(k_0\rho)ds'\,dn'$$

(9)

where s is the unit tangent to the surface of the layer, n is the unit normal to the surface of the layer and A' corresponds to the cross sectional area of the scatterer. Thus all current and field components with the subscript n denotes those components along the direction of the layer surface normal and a similar definition holds for the components with subscripts s and z. Furthermore, $H_n^{(2)}(k\rho)$ denotes the Hankel function of order n and

$$\rho = \sqrt{(x-x')^2 + (y-y')^2}\,, \quad \hat{\rho} = \frac{(x-x')\hat{x} + (y-y')\hat{y}}{\rho} \tag{10}$$

where, as usual, (x, y) in the observation point and (x', y') is the integration/source point.

In the case of E_z incidence, the appropriate integral equations are the dual of those given in (7) - (9).

The integral equations (7) - (9) or their dual involve three unknown current components at each location of the layer. However, as will be shown in the next section, these can be reduced to only two unknowns for all layer locations except the endpoints. This translates to a substantial memory and CPU cost reduction in their implementation and is therefore worthwhile to pursue even if the resulting pair of integral equations is more complex.

II. A Reduced Set of Integral Equations

The three integral equations (7) - (9) can be equivalently replaced by only two integral equations. This is achieved by noting that in accordance with Maxwell's equations [1], the layer of dipoles represented by K_n can be equivalently replaced by a magnetic current (sheet)

$$K_z^{**} = \frac{jZ_0}{k_0} \frac{\partial K_n}{\partial s} \tag{11}$$

Mathematically, the above magnetic current is now indistinguishable from K_z^* appearing in (7) - (9), and we can therefore treat them as a single unknown current defined by

$$K_z^* = K_z^* + K_z^{**} = K_z^* + \frac{jZ_0}{k_0} \frac{\partial K_n}{\partial s} . \tag{12}$$

In order to introduce (12) in (7) - (9) we must first apply integration by parts to all integrals in (7) - (9) that contain the current component K_n. In so doing and after utilizing (12), (7) - (9) become:

$$E_s^i = \frac{Z_0}{4\tau}\int\Big[K_{n'}(s_e)\,(\hat{\rho}_e \cdot \hat{n}_e)H_1^{(2)}(k_0\rho_e) - K_{n'}(s_b)(\hat{\rho}_b \cdot \hat{n}_b)H_1^{(2)}(k_0\rho_b)\Big]dn' + \varepsilon_r R K_s(s)$$

$$+\frac{Z_0}{4\tau}\iint_{A'} K_{s'}(s')\,\frac{\partial}{\partial n}\Big[(\hat{\rho}\cdot\hat{n}')H_1^{(2)}(k_0\rho)\Big]ds'\,dn' + \frac{jk_0}{4\tau}\iint_{A'}\tilde{K}_z^*(s')(\hat{\rho}\cdot\hat{n})H_1^{(2)}(k_0\rho)ds'\,dn'$$

(13)

$$E_n^i = \frac{Z_0}{4\tau}\int\Big[K_{n'}(s_e)\,(\hat{\rho}_e \cdot \hat{s}_e)H_1^{(2)}(k_0\rho_e) - K_n(s_b)\,(\hat{\rho}_b \cdot \hat{s}_b)H_1^{(2)}(k_0\rho_b)\Big]dn' + \varepsilon_r R K_n(s)$$

$$-\frac{Z_0}{4\tau}\iint_{A'} K_{s'}(s')\frac{\partial}{\partial s}\Big[(\hat{\rho}_e \cdot \hat{n}')H_1^{(2)}(k_0\rho)\Big]ds'\,dn' - \frac{jk_0}{4\tau}\iint_{A'}\tilde{K}_z^*(s')\,(\hat{\rho}\cdot\hat{s})H_1^{(2)}(k_0\rho)ds'\,dn'$$

(14)

$$H_z^i = \frac{-j}{4\tau}\int\Big[K_{n'}(s_e)\,H_0^{(2)}(k_0\rho_e) - K_{n'}(s_b)\,H_0^{(2)}(k_0\rho_b)\Big]dn' + R\,K_z^*(s)$$

$$+\frac{jk_0}{4\tau}\iint_{A'} K_{s'}(s')\quad\Big[(\hat{\rho}\cdot\hat{n}')\,H_1^{(2)}(k_0\rho)\Big]\,ds'\,dn' + \frac{k_0}{4\tau}\iint_{A'}\tilde{K}_z^*(s')\,H_0^{(2)}(k_0\rho)\,ds'\,dn'$$

(15)

where the subscripts b and e denote the value of the variables at the beginning and end points of each modeled thin material layer or strip.

The integral equations (13) - (15) can now be reduced to only two equations by proceeding as follows. We first differentiate (14) with respect to s to obtain an integral equation for $\partial K_n/\partial s$. This and $K_z^*(s)$, as obtained from (15), are then substituted in (12) to obtain an integral equation for $K_z^*(s)$. When this final integral equation is coupled with (13) we obtain the new reduced system of equations

$$\frac{H_z^i}{R^*} + \frac{jZ_0}{k_0}\frac{\partial}{\partial s}\left(\frac{E_n^i}{\varepsilon_r R}\right) = \tilde{K}_z^*(s) - \int \frac{jK_{n'}(s_e)}{4\tau}\left\{\frac{H_0^{(2)}(k_0\rho_e)}{R^*} + \frac{Z_0^2}{k_0}\frac{\partial}{\partial s}\left[\left(\frac{\hat{\rho}_e\cdot\hat{s}_e}{\varepsilon_r R}\right)H_1^{(2)}(k_0\rho_e)\right]\right\}dn'$$

$$-\int \frac{jK_n(s_b)}{4\tau}\left\{\frac{H_0^{(2)}(k_0\rho_b)}{R^*} + \frac{Z_0^2}{k_0}\frac{\partial}{\partial s}\left[\left(\frac{\hat{\rho}_b\cdot\hat{s}_b}{\varepsilon_r R}\right)H_1^{(2)}(k_0\rho_b)\right]\right\}dn'$$

$$+\frac{jk_0}{4\tau}\int\int_{A'} K_s(s')\left\{\frac{(\hat{\rho}\cdot\hat{n})H_1^{(2)}(k_0\rho)}{R^*} - \frac{Z_0^2}{k_0}\frac{\partial}{\partial s}\left(\frac{1}{\varepsilon_r R}\right)\frac{\partial}{\partial s}\left[(\hat{\rho}\cdot\hat{n}')H_1^{(2)}(k_0\rho)\right]\right\}ds'\,dn'$$

$$+\frac{k_0}{4\tau}\int\int_{A'} \tilde{K}_z^*(s')\left\{\frac{Y_0 H_0^{(2)}(k_0\rho)}{R^*} + \frac{1}{k_0}\frac{\partial}{\partial s}\left[\left(\frac{\hat{\rho}\cdot\hat{s}}{\varepsilon_r R}\right)H_1^{(2)}(k_0\rho)\right]\right\}ds'dn' \qquad (16)$$

$$\frac{E_s^i}{\varepsilon_r R} = K_s(s) + \int \frac{Z_0}{4\varepsilon_r R\tau}\left[K_{n'}(s_e)\left(\hat{\rho}_e\cdot\hat{n}_e\right)H_1^{(2)}\left(k_0\rho_e\right) - K_{n'}(s_b)\left(\hat{\rho}_b\cdot\hat{n}_b\right)H_1^{(2)}\left(k_0\rho_b\right)\right]dn'$$

$$+\frac{Z_0}{4\varepsilon_r R\tau}\int\int_{A'} K_{s'}(s')\frac{\partial}{\partial n}\left[(\hat{\rho}\cdot\hat{n})H_1^{(2)}(k_0\rho)\right]ds'\,dn'$$

$$+\frac{jk_0}{4\varepsilon_r R\tau}\int\int_{A'} \tilde{K}_z^*(s')(\hat{\rho}\cdot\hat{n})H_1^{(2)}(k_0\rho)\,ds'\,dn'. \qquad (17)$$

The above equations involve only two unknown tangential or sheet currents along the length of the strips, namely the electric current K_s and the equivalent magnetic current K_z^*. In addition to these, they also involve the normal current components at the terminations of the strips. The last must be found by enforcing (16) - (17) at the end points of the strips, if they exist. Clearly the numerical solution of (16) - (17) requires the construction of a $(2N \times 2N)^+$ impedance matrix, whereas that of (7) - (9) requires a

(3N x 3N) impedance matrix. This translates to a substantial reduction in memory and CPU cost.

III. Brief Description of the Computer Code.

A moment method computer code using pulse basis functions has been written for implementing equations (16)-(17). This code is referred to as RESTCOMB and is intended to supersede and replace the previous University of Michigan Radiation Laboratory two dimensional codes, including RESTE, RESTH, RAMD and RAMVS. The input format to the code is similar to that of the original codes. More specifically, the geometry is accepted in terms of material layer segments having complex constitutive parameters. Each of the layers can be independently assigned as specific material composition or taper. In this new code we have added several choices in tapers, including linear, Gaussian, cosine and Blackman-Harris tapers. Also, one can choose to taper the computed current distribution for the purpose of isolating individual scattering centers. An example of this application is shown in Figures 3 and 4. The code has not yet been completely checked-out. Thus, so far only a few test results have been obtained via the use of this code. A sample of these are the scattering patterns shown in Figures 5 and 6.

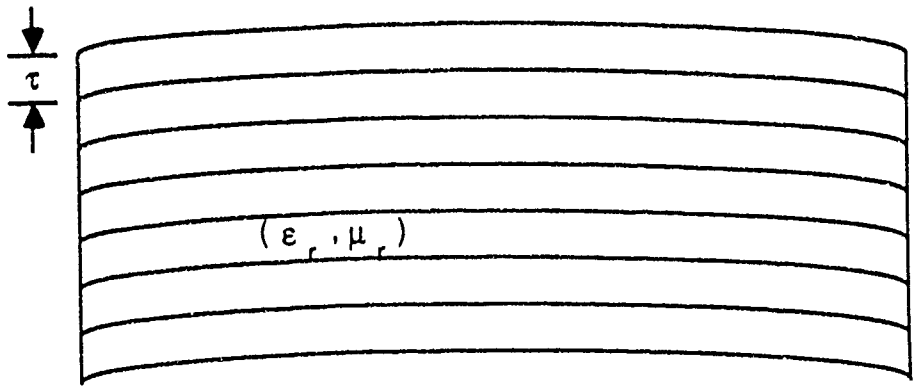


Figure 1. Layer Simulation of a Composite Structure

(x,y) observation point
(x',y') integration point

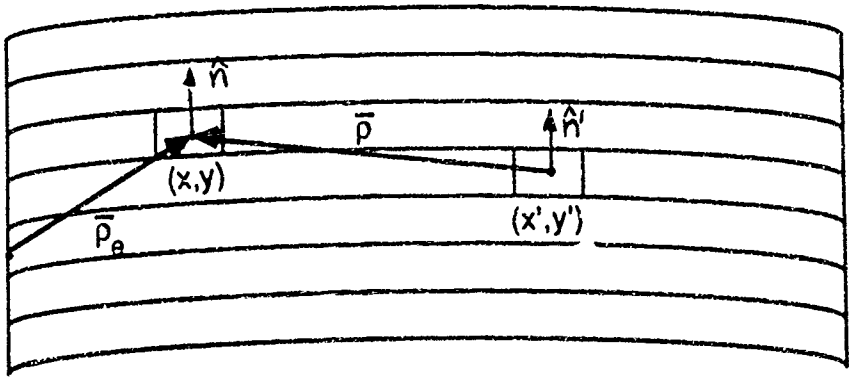


Figure 2. Description of some parameters appearing in the integral equations.

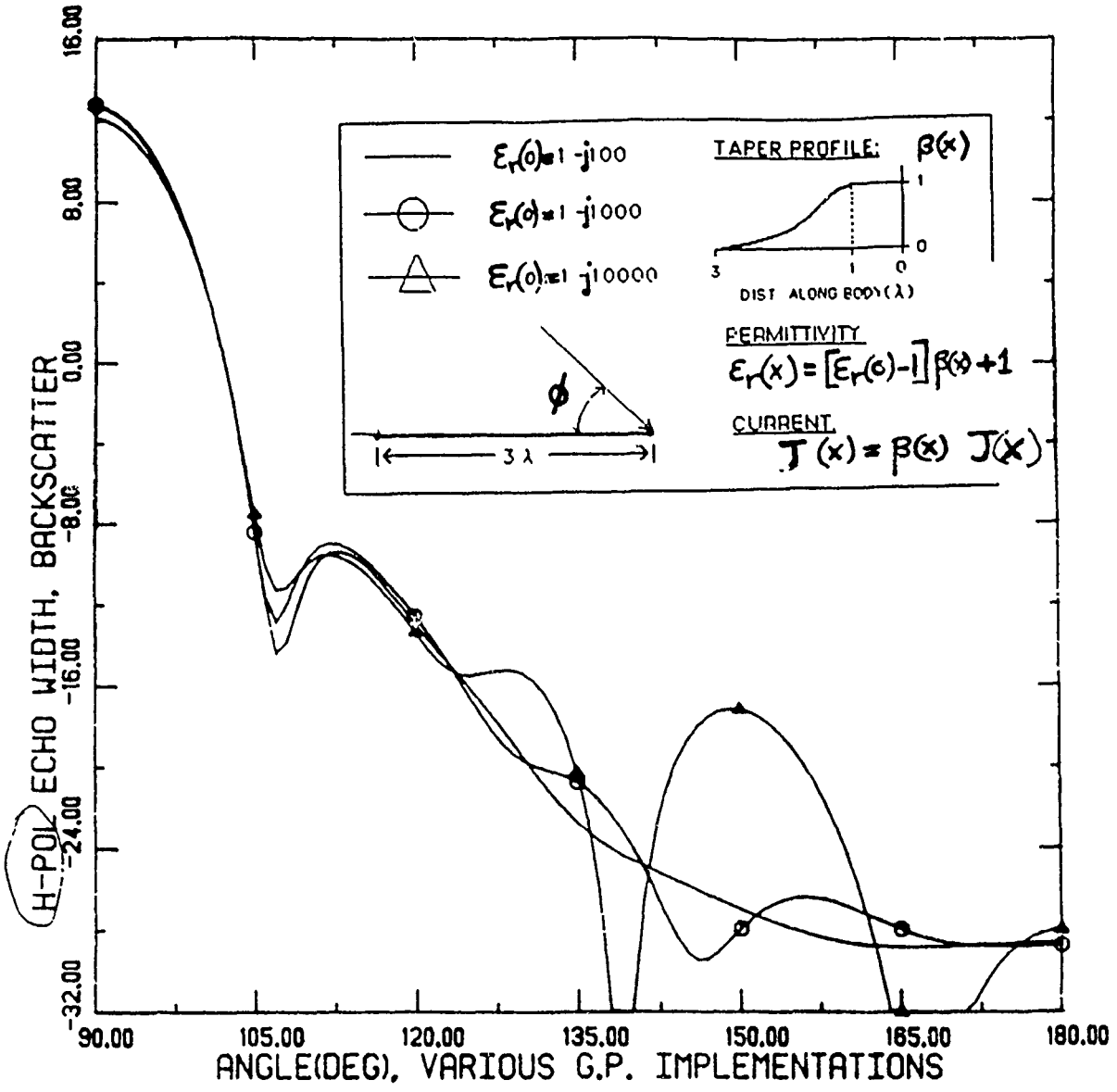


Figure 3. Simulation of a half plane using a Blackman Harris material and current taper profile in association with a 3 wavelength strip.

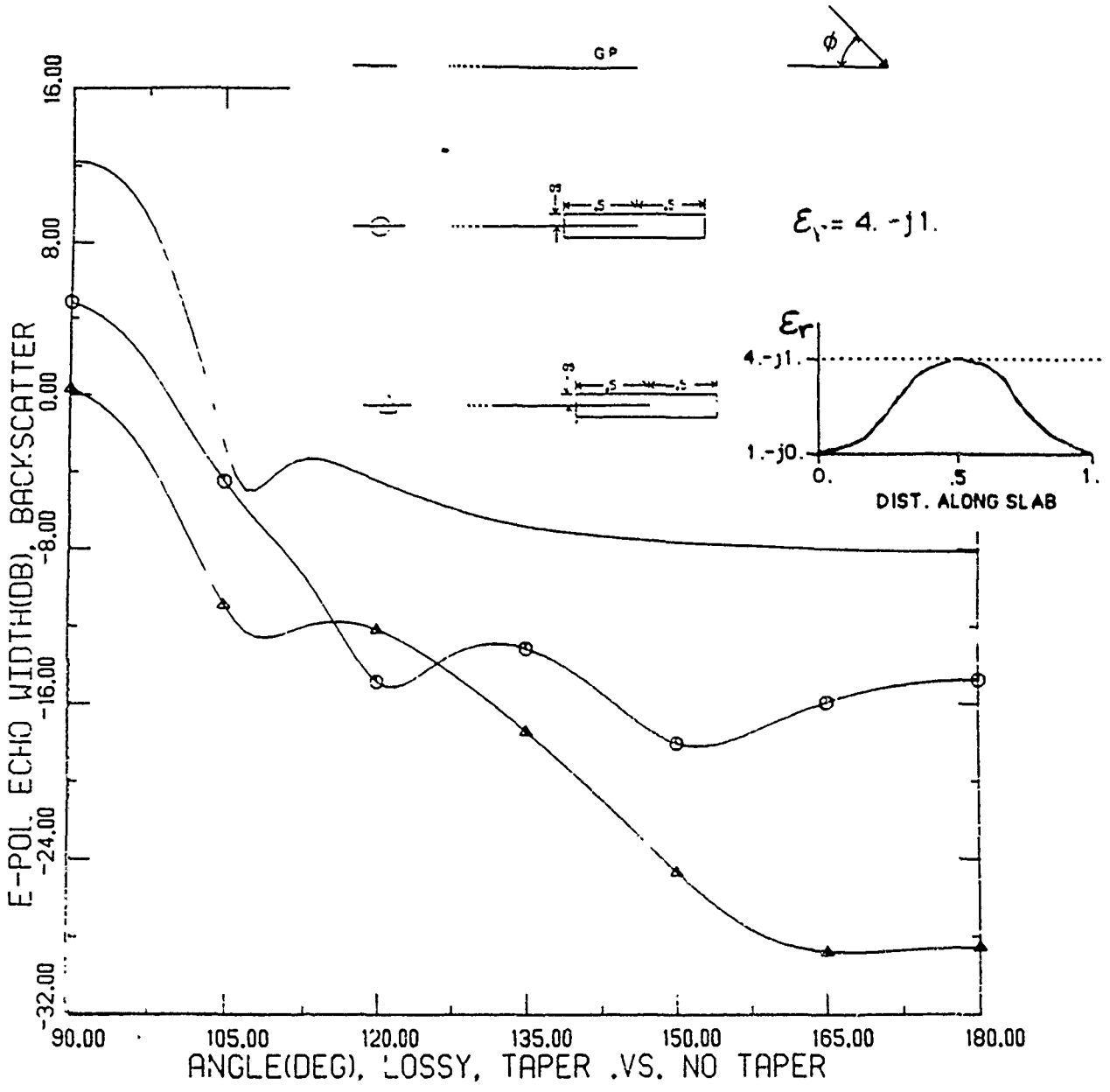
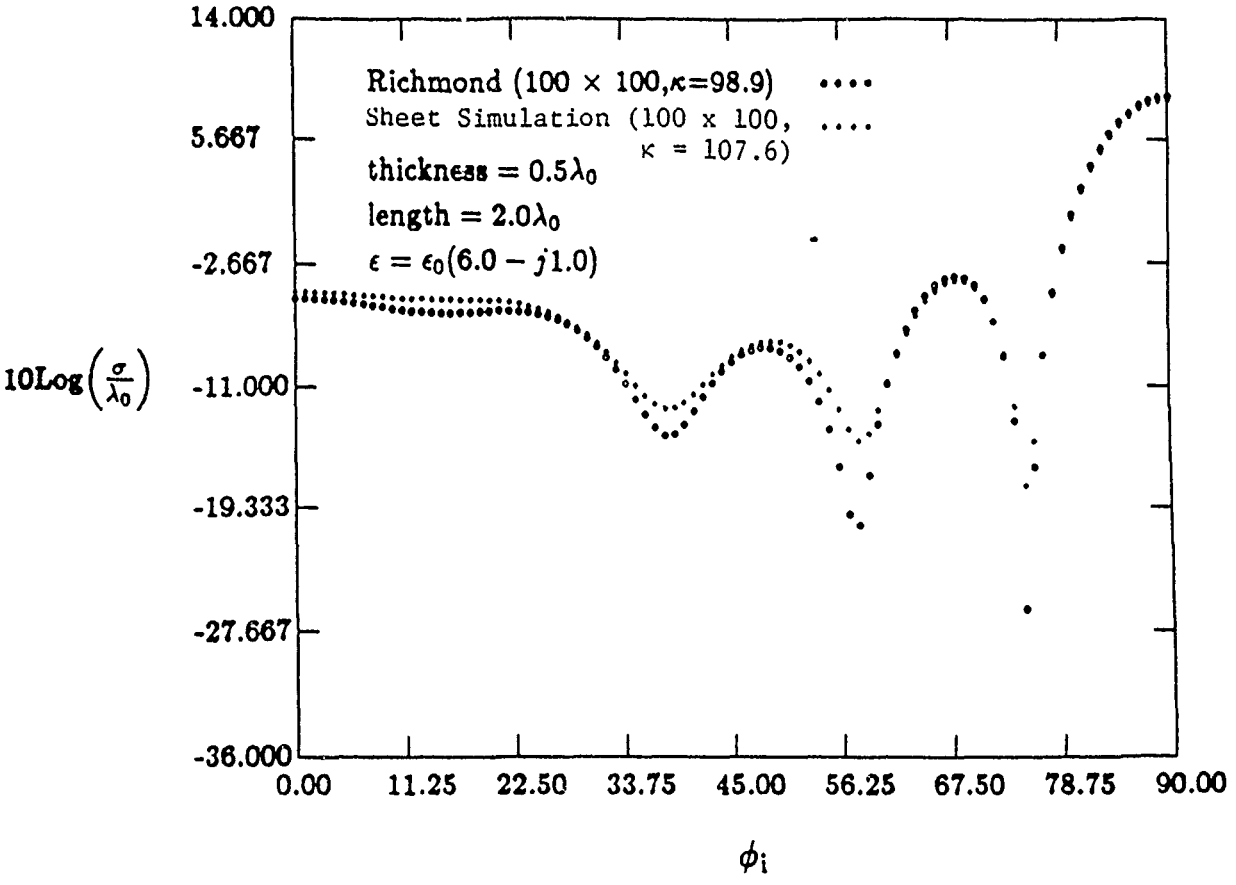


Figure 4. Simulation of a dielectric coated edge with various coating distributions using the RESTCOMB code.



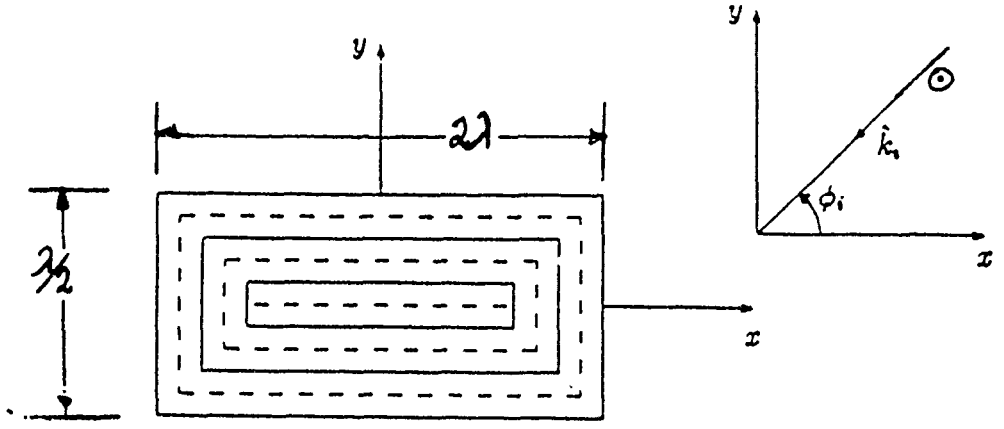
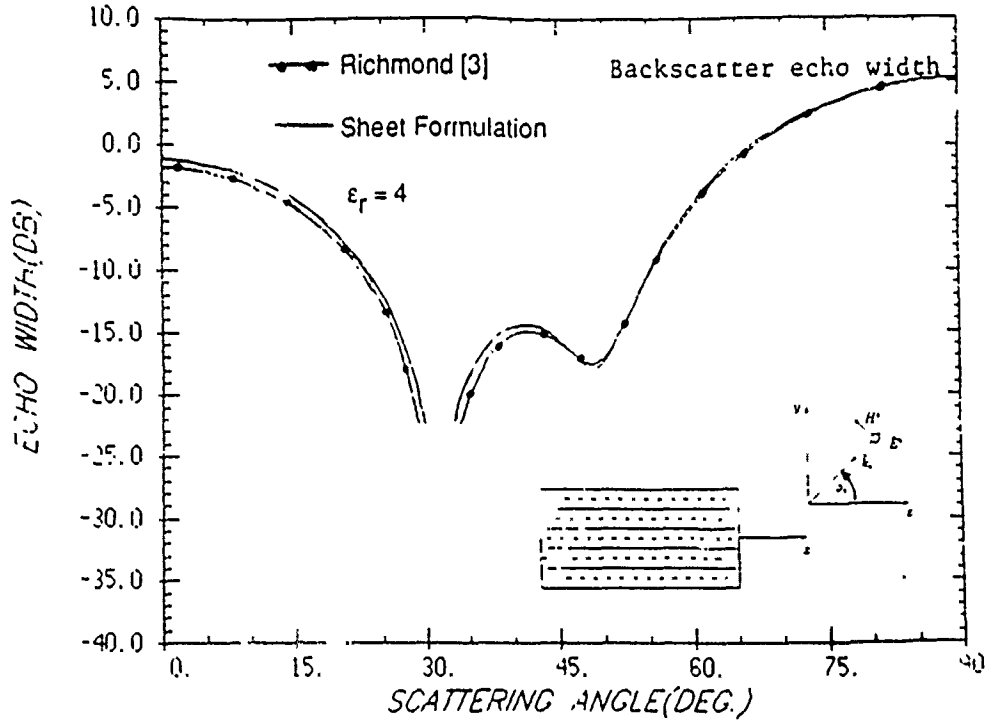


Figure 5. E-polarization echowidth results for a rectangular dielectric cylinder 2λ x 0.5λ.

(a)



(b)

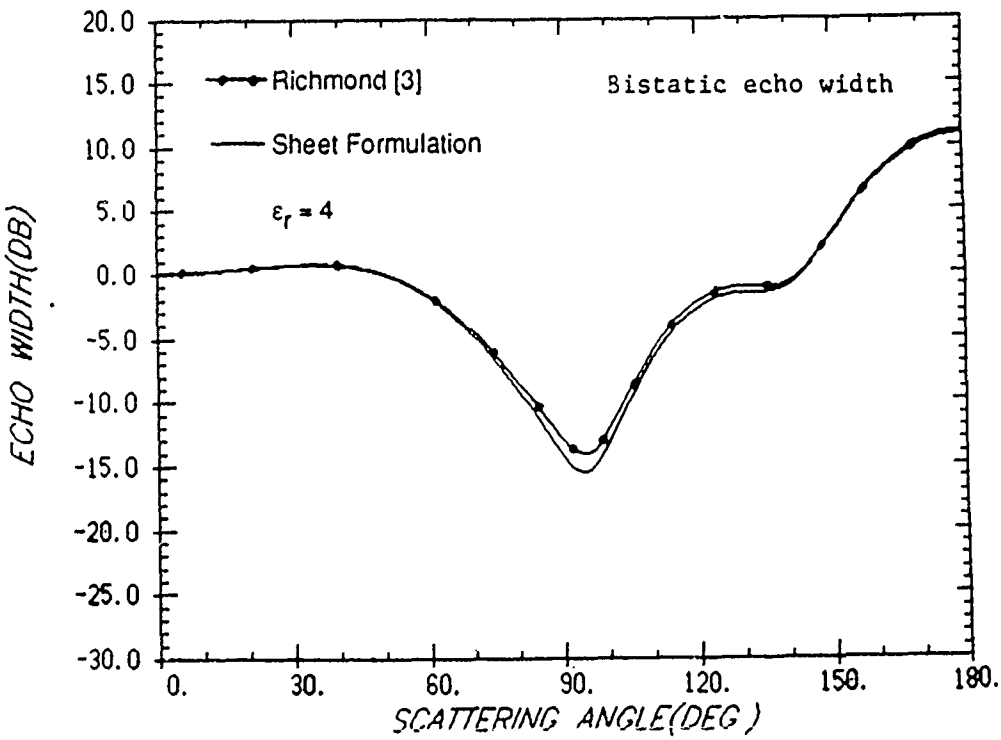


Figure 6. Comparison of echowidth results based on the sheet and volume equivalent currents with H-incidence. (a) Rectangular dielectric cylinder 1λ x 0.4λ. (b) Thin dielectric shell having an inner radius R_{in} = 0.5λ and a outer radius of R_{out} = 0.6λ.

Scattering From Thin Planar Material Plates With Arbitrary Perimeter

Radiation Laboratory
Dept. of EECS
The University of Michigan
Ann Arbor, MI 48109-2122
March 23, 1987

Timothy J. Peters
John L. Volakis

Abstract- The radar cross section is calculated for thin material plates with constitutive parameters ϵ,σ and μ illuminated by a plane wave. The plates are assumed to be planar with an arbitrary perimeter. The integral equations are formed and solved by the CG-FFT method.

I. Introduction

A plate is a basic modeling element for many scattering problems. Plate scattering has been studied for many years, however, because of the lack of canonical solutions there exists no single best method of solution. The purpose of this paper is to present a method which has the potential to solve a wide class of plate scatterers in an efficient manner. At the present time efficiency is still a prime concern in solving scattering from general material bodies. The work of Newman et al [1] and Naor et al [2] treat rectangular material plates. However, the basis functions are inappropriate for curved perimeters and the boundary conditions employed are not valid at edge on incidence [3]. Rigorous numerical solutions for perfectly conducting plates have been implemented by Glisson et al [4] and Rao et al [5] using triangular cells and linear basis functions. This method yields accurate results. However, the size of the matrix $O(N^2)$ becomes restrictive for a body of above resonant dimensions. The above methods solve the operator equation indirectly by first forming a matrix of coefficients and then solving the corresponding system of equations. Sarkar et al [6] and Christodoulou et al [7] combine the method of conjugate gradients [8],[9],[10],[11] with the FFT [12],[13] to solve the operator equation directly using $O(N)$ storage. The following presentation is an application of the combined CG-FFT method to the material plate scattering problem.

II. Geometry

The orientation of the plate to the incident field is shown in Fig. 1. The plate

is assumed to be planar with a perimeter in the x-y plane. The composition is such that the thickness w satisfies the relation w<< λ_p where λ_p is the wavelength inside the plate.

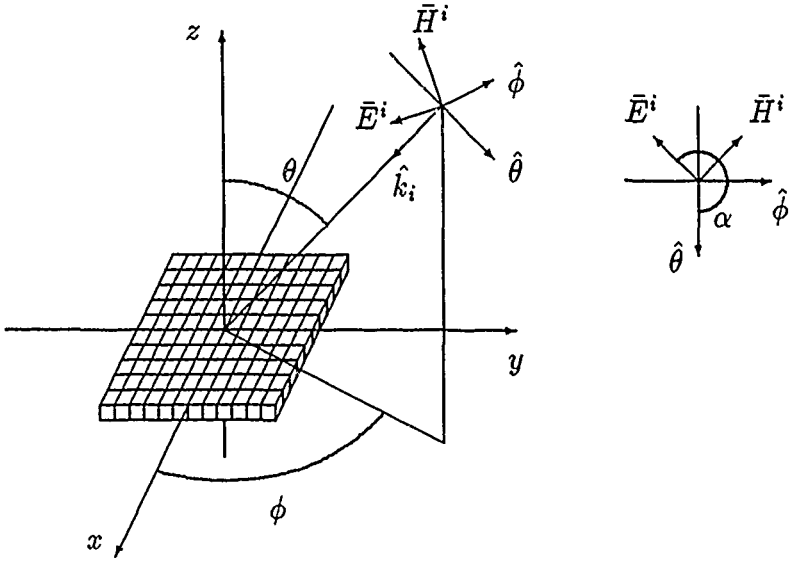


Fig. 1. Plate with plane wave incidence.

The incident electric field has unity amplitude and may be decomposed into the $\hat{\theta}$ and $\hat{\phi}$ components

$$\bar{E}^i = [(\hat{\alpha}\cdot\hat{\theta})\hat{\theta} + (\hat{\alpha}\cdot\hat{\phi})\hat{\phi}]e^{-j\zeta}. \tag{1}$$

Further decomposition yields

$$\begin{aligned} E_x^i &= [\cos(\alpha_i)\cos(\theta_i)\cos(\phi_i) - \sin(\alpha_i)\sin(\phi_i)]e^{-j\zeta} \\ E_y^i &= [\cos(\alpha_i)\cos(\theta_i)\sin(\phi_i) + \sin(\alpha_i)\cos(\phi_i)]e^{-j\zeta} \\ E_z^i &= -\cos(\alpha_i)\sin(\theta_i)e^{-j\zeta} \end{aligned} \tag{2}$$

where

$$\zeta = \bar{k}_i \cdot \bar{R} = -k_0 \sin(\theta_i)\left[\cos(\phi_i)x + \sin(\phi_i)y\right]. \tag{3}$$

and the corresponding magnetic field components are computed from $\bar{H}^i = \frac{1}{Z_0}\hat{k}^i \times \bar{E}^i$. The E-polarization case is defined at $\alpha_i = 90°$ and H-polarization occurs at $\alpha_i = 0°$.

III. Integral Equations

The scattered fields may be written in terms of vector potentials as

$$\bar{E}^s = -\nabla \times \bar{F} - j\frac{Z_0}{k_0}(\nabla \times \nabla \times \bar{A} - \bar{J}^e) \tag{4}$$

$$\bar{H}^s = \nabla \times \bar{A} - j\frac{1}{k_0 Z_0}(\nabla \times \nabla \times \bar{F} - \bar{J}^m) \tag{5}$$

where $\bar{A}$ and $\bar{F}$ satisfy the inhomogeneous vector Helmholtz equations

$$\nabla^2 \bar{A} + k_0^2 \bar{A} = -\bar{J}^e \tag{6}$$

$$\nabla^2 \bar{F} + k_0^2 \bar{F} = -\bar{J}^m \tag{7}$$

which have the solutions in integral form given by

$$\bar{A} = \iiint_{v'} \bar{J}^e(\bar{R}')G(\bar{R}, \bar{R}')dv' \tag{8}$$

$$\bar{F} = \iiint_{v'} \bar{J}^m(\bar{R}')G(\bar{R}, \bar{R}')dv' \tag{9}$$

where

$$G(\bar{R}, \bar{R}') = \frac{e^{-jk_0|\bar{R}-\bar{R}'|}}{4\pi|\bar{R} - \bar{R}'|}. \tag{10}$$

The incident fields induce electric and magnetic polarization currents inside the material body. These currents are the source of the scattered field. The volume

integral equations are formed by relating the internal fields as $\bar{E}^T - \bar{E}^s = \bar{E}^i$ and $\bar{H}^T - \bar{H}^s = \bar{H}^i$. The polarization currents are defined by the expressions $E^T = \beta_e \bar{J}^e$ and $H^T = \beta_m \bar{J}^m$ where

$$\beta_e = \frac{-jZ_0}{(\epsilon_r - 1)k_0} \tag{11}$$

$$\beta_m = \frac{-j}{(\mu_r - 1)k_0 Z_0}. \tag{12}$$

If the plate is electrically thin the field components have no z variation such that $\frac{\partial}{\partial z} = 0$. Although no boundary conditions are explicitly enforced in a polarization model, the fact that the thickness may become small requires that the correct discontinuity in the normal fields be preserved. Thus, the normal components E_z and H_z are found from (4) and (5) directly and the tangential components are found after substituting (6) and (7) into (4) and (5). The six equations reduce to

$$\beta_e J_x^e + j\frac{Z_0}{k_0}\left[\left(k_0^2 + \frac{\partial^2}{\partial x^2}\right)A_x + \frac{\partial^2}{\partial x \partial y}A_y\right] + \frac{\partial}{\partial y}F_z = E_x^i \tag{13}$$

$$\beta_e J_y^e + j\frac{Z_0}{k_0}\left[\frac{\partial^2}{\partial x \partial y}A_x + \left(k_0^2 + \frac{\partial^2}{\partial y^2}\right)A_y\right] - \frac{\partial}{\partial x}F_z = E_y^i \tag{14}$$

$$\epsilon_r \beta_e J_z^e - \frac{\partial}{\partial y}F_x + \frac{\partial}{\partial x}F_y - j\frac{Z_0}{k_0}\left(\frac{\partial^2}{\partial y^2} + \frac{\partial^2}{\partial x^2}\right)A_z = E_z^i \tag{15}$$

$$\beta_m J_x^m + j\frac{1}{k_0 Z_0}\left[\left(k_0^2 + \frac{\partial^2}{\partial x^2}\right)F_x + \frac{\partial^2}{\partial x \partial y}F_y\right] - \frac{\partial}{\partial y}A_z = H_x^i \tag{16}$$

$$\beta_m J_y^m + j\frac{1}{k_0 Z_0}\left[\frac{\partial^2}{\partial x \partial y}F_x + \left(k_0^2 + \frac{\partial^2}{\partial y^2}\right)F_y\right] + \frac{\partial}{\partial x}A_z = H_y^i \tag{17}$$

$$\mu_r \beta_m J_z^m + \frac{\partial}{\partial y}A_x - \frac{\partial}{\partial x}A_y - j\frac{1}{k_0 Z_0}\left(\frac{\partial^2}{\partial y^2} + \frac{\partial^2}{\partial x^2}\right)F_z = H_z^i. \tag{18}$$

The E-pol case will be used to illustrate the numerical solution. This polarization results in three coupled equations for J_x^e,J_y^e and J_z^m and two coupled

equations for J_x^m and J_y^m.

$$\beta_e J_x^e + j\frac{Z_0}{k_0}\left[\left(k_0^2 + \frac{\partial^2}{\partial x^2}\right)A_x + \frac{\partial^2}{\partial x \partial y}A_y\right] + \frac{\partial}{\partial y}F_z = E_x^i \quad (19)$$

$$\beta_e J_y^e + j\frac{Z_0}{k_0}\left[\frac{\partial^2}{\partial x \partial y}A_x + \left(k_0^2 + \frac{\partial^2}{\partial y^2}\right)A_y\right] - \frac{\partial}{\partial x}F_z = E_y^i \quad (20)$$

$$\mu_r \beta_m J_z^m + \frac{\partial}{\partial y}A_x - \frac{\partial}{\partial x}A_y - j\frac{1}{k_0 Z_0}\left(\frac{\partial^2}{\partial x^2} + \frac{\partial^2}{\partial y^2}\right)F_z = H_z^i \quad (21)$$

$$\beta_m J_x^m + j\frac{1}{k_0 Z_0}\left[\left(k_0^2 + \frac{\partial^2}{\partial x^2}\right)F_x + \frac{\partial^2}{\partial x \partial y}F_y\right] = H_x^i \quad (22)$$

$$\beta_m J_y^m + j\frac{1}{k_0 Z_0}\left[\frac{\partial^2}{\partial x \partial y}F_x + \left(k_0^2 + \frac{\partial^2}{\partial y^2}\right)F_y\right] = H_y^i \quad (23)$$

IV. Sampling and Surface Generation

Arbitrary perimeter geometries may be generated by passing a rectangular array of points through a series of constraints. Figures 2-5 are examples of 1, 2, 3 and 4 constraint perimeters. Assume that each square cell has an associated tag which indicates whether it is inside the perimeter. Application of the sampling theorem requires that the spatial sampling frequency be at least twice the maximum spatial frequency of the induced current. Thus once Δx is chosen $f_{max} = \frac{1}{2\Delta x}$ and $\Delta f = \frac{2f_{max}}{n} = \frac{1}{n\Delta x}$ where n is the size of the two dimensional sampling array. The size n must be chosen such that $n\Delta x > 2$d where d is the maximum dimension of the scatterer.

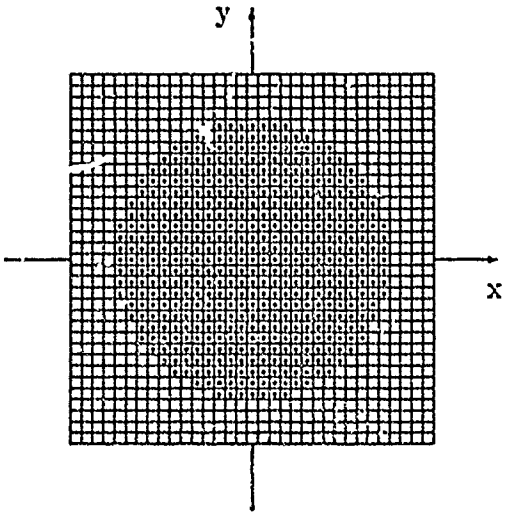


Fig. 2. Circular Plate

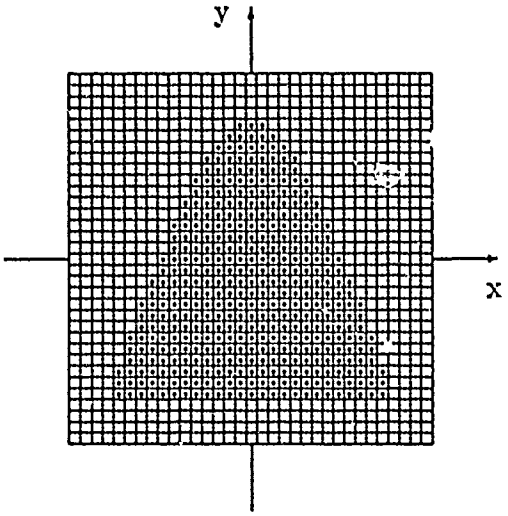


Fig. 3. Parabolic Plate

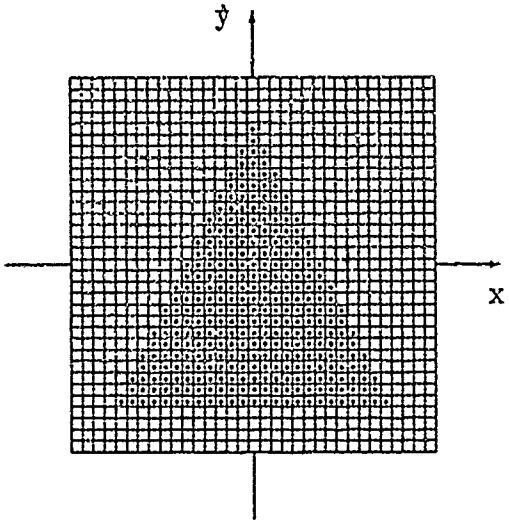


Fig. 4. Triangular Plate

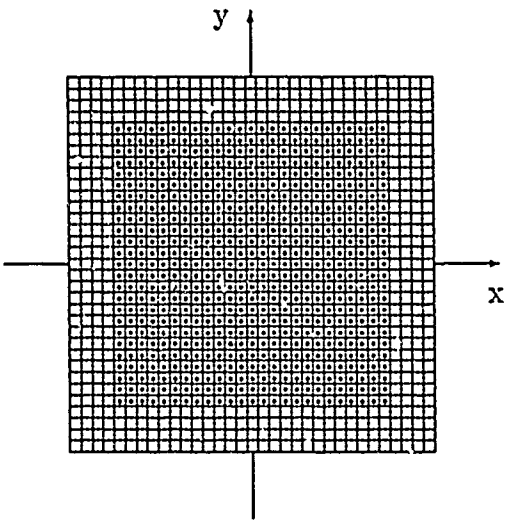


Fig. 5. Square Plate

V. CG-Method

The conjugate gradient method [8] appears to be quite efficient with respect to computation and storage as shown by Sarkar et at [6] and Christodoulou et al [7]. The general procedure is to assume a system $Ax = y$ where A is a linear operator. The adjoint operator A^a is defined by the inner product relation $(Ax, y) = (x, A^a y)$. If A is an $n \times n$ matrix then A^a is the conjugate transpose of A. However if A is a functional then the adjoint must be found for each case. Given the Fredholm equation of the second kind

$$\alpha f(s) + \beta \int_a^b f(s')g(s,s')ds' = y(s) \tag{24}$$

the adjoint operator is

$$A^a f = \alpha^* f(s) + \beta^* \int_a^b f(s')g^*(s',s)ds' \tag{25}$$

where $*$ denotes the complex conjugate. The algorithm is given as

initialize

$$r_1 = y - Ax_1 \tag{26}$$

$$\beta_0 = \frac{1}{|A^a r_1|^2} \tag{27}$$

$$p_1 = \beta_0 A^a r_1 \tag{28}$$

for $k = 1, \ldots, n$

$$\alpha_k = \frac{1}{|Ap_k|^2} \tag{29}$$

$$x_{k+1} = x_k + \alpha_k p_k \tag{30}$$

$$r_{k+1} = r_k - \alpha_k A p_k \tag{31}$$

$$\beta_k = \frac{1}{|A^a r_{k+1}|^2} \tag{32}$$

$$p_{k+1} = p_k + \beta_k A^a r_{k+1} \tag{33}$$

The algorithm is terminated at $k = n$ or when

$$\frac{|r_{k+1}|}{|y|} < \text{tolerance.} \tag{34}$$

For this algorithm the magnitude of the residual r_{k+1} will decrease at each step since it represents the actual function being minimized. Excluding the initialization this algorithm requires two matrix vector products per iteration. The number of multiplications and divisions per iteration is $2n^2 + 5n + 2$.

VI. CG-FFT Method

For convolution integral equations the matrix vector products in the CG method may be replaced by a series of FFT's which reduce the compution significantly. The CG-FFT Method will be illustrated by applying it to E-pol scattering from a material plate with constitutive parameters ϵ,σ and μ. Since the plate is electrically thin the volume integral may be reduced to two dimensions. Making the substitutions $\bar{K}^e = \mathrm{w}\bar{J}^e$, $\bar{K}^m = \mathrm{w}\bar{J}^m$, $\eta_e = \frac{\beta_e}{\mathrm{w}Z_0}$ and $\eta_m = \frac{\beta_m Z_0}{\mathrm{w}}$ (19)-(23) become

$$w_1 K_x^e + \iint_{S'} \left[w_2 \left(\Psi_1 K_x^e + \Psi_2 K_y^e \right) + \Psi_3 K_z^m \right] dS' = E_x^i \tag{35}$$

$$w_1 K_y^e + \iint_{S'} \left[w_2 \left(\Psi_2 K_x^e + \Psi_4 K_y^e \right) - \Psi_5 K_z^m \right] dS' = E_y^i \tag{36}$$

$$w_3 K_z^m + \iint_{S'} \left[\Psi_3 K_x^e - \Psi_5 K_y^e - w_4 \Psi_6 K_z^m \right] dS' = H_z^i \tag{37}$$

$$w_5 K_x^m + w_4 \iint_{S'} \left[\Psi_1 K_x^m + \Psi_2 K_y^m \right] dS' = H_x^i \tag{38}$$

$$w_5 K_y^m + w_4 \iint_{S'} \left[\Psi_2 K_x^m + \Psi_4 K_y^m \right] dS' = H_y^i \tag{39}$$

where

$$\Psi_1 = \left(k_0^2 + \frac{\partial^2}{\partial x^2}\right) G \tag{40}$$

$$\Psi_2 = \frac{\partial^2}{\partial x \partial y} G \tag{41}$$

$$\Psi_3 = \frac{\partial}{\partial y} G \tag{42}$$

$$\Psi_4 = \left(k_0^2 + \frac{\partial^2}{\partial y^2}\right) G \tag{43}$$

$$\Psi_5 = \frac{\partial}{\partial x} G \tag{44}$$

$$\Psi_6 = \left(\frac{\partial^2}{\partial x^2} + \frac{\partial^2}{\partial y^2}\right) G \tag{45}$$

and

$$w_1 = \eta_e Z_0 \tag{46}$$

$$w_2 = j\frac{Z_0}{k_0} \tag{47}$$

$$w_3 = \frac{\mu_r \eta_m}{Z_0} \tag{48}$$

$$w_4 = j\frac{1}{k_0 Z_0} \tag{49}$$

$$w_5 = \frac{\eta_m}{Z_0}. \tag{50}$$

The two dimensional fourier transform and inverse transform are defined as

$$\tilde{g}(k_x, k_y) = \int_{-\infty}^{\infty}\int_{-\infty}^{\infty} g(x,y) e^{-j(k_x x + k_y y)} dx, dy \tag{51}$$

$$g(x,k) = \frac{1}{4\pi^2}\int_{-\infty}^{\infty}\int_{-\infty}^{\infty} \tilde{g}(k_x, k_y) e^{j(k_x x + k_y y)} dk_x, dk_y. \tag{52}$$

The green's function has the fourier transform given by

$$\frac{e^{-jk_0\sqrt{x^2+y^2}}}{4\pi\sqrt{x^2+y^2}} \longleftrightarrow \begin{cases} \frac{1}{d} & k_x^2 + k_y^2 > k_0^2 \\ -j\frac{1}{d} & k_x^2 + k_y^2 < k_0^2 \end{cases} \tag{53}$$

where $d = 2\sqrt{|k_x^2 + k_y^2 - k_0^2|}$. Let $\widetilde{X}$ denote the fourier transform operation and X^* denote conjugation. The fourier transforms of the operators are

$$\tilde{\Psi}_1 = \begin{cases} \frac{k_0^2 - k_x^2}{d} \\ -j\frac{k_0^2 - k_x^2}{d} \end{cases} \tag{54}$$

$$\tilde{\Psi}_2 = \begin{cases} -\frac{k_x k_y}{d} \\ j\frac{k_x k_y}{d} \end{cases} \tag{55}$$

$$\tilde{\Psi}_3 = \begin{cases} j\frac{k_y}{d} \\ \frac{k_y}{d} \end{cases} \tag{56}$$

$$\tilde{\Psi}_4 = \begin{cases} \frac{k_0^2 - k_y^2}{d} \\ -j\frac{k_0^2 - k_y^2}{d} \end{cases} \tag{57}$$

$$\tilde{\Psi}_5 = \begin{cases} j\frac{k_x}{d} \\ \frac{k_x}{d} \end{cases} \tag{58}$$

$$\tilde{\Psi}_6 = \begin{cases} -\frac{k_x^2 + k_y^2}{d} \\ j\frac{k_x^2 + k_y^2}{d} \end{cases} \tag{59}$$

where the adjoint operators are computed from $\tilde{\Psi}_n = \tilde{\Psi}_n^*(-k_x, -k_y)$. Introducing an intermediate storage vector q^k the CG-FFT algorithm for the three coupled equations for K_x^e, K_y^e and K_z^m assumes the following form.

initialize

$$\begin{bmatrix} r_x^1 \\ r_y^1 \\ r_z^1 \end{bmatrix} = \begin{bmatrix} E_x^i - w_1 K_x^{e,1} - \mathcal{F}^{-1}\left[w_2(\tilde{\Psi}_1 \widetilde{K}_x^{e,1} + \tilde{\Psi}_2 \widetilde{K}_y^{e,1}) + \tilde{\Psi}_3 \widetilde{K}_z^{m,1}\right] \\ E_y^i - w_1 K_y^{e,1} - \mathcal{F}^{-1}\left[w_2(\tilde{\Psi}_2 \widetilde{K}_x^{e,1} + \tilde{\Psi}_4 \widetilde{K}_y^{e,1}) - \tilde{\Psi}_5 \widetilde{K}_z^{m,1}\right] \\ H_z^i - w_3 K_z^{m,1} - \mathcal{F}^{-1}\left[\tilde{\Psi}_3 \widetilde{K}_x^{e,1} - \tilde{\Psi}_5 \widetilde{K}_y^{e,1} - w_4 \tilde{\Psi}_6 \widetilde{K}_z^{m,1}\right] \end{bmatrix} \tag{60}$$

$$\begin{bmatrix} q_x^0 \\ q_y^0 \\ q_z^0 \end{bmatrix} = \begin{bmatrix} w_1^* r_x^1 + \mathcal{F}^{-1}\left[w_2^*(\tilde{\Psi}_1^a \tilde{r}_x^1 + \tilde{\Psi}_2^a \tilde{r}_y^1) + \tilde{\Psi}_3^a \tilde{r}_z^1\right] \\ w_1^* r_y^1 + \mathcal{F}^{-1}\left[w_2^*(\tilde{\Psi}_2^a \tilde{r}_x^1 + \tilde{\Psi}_4^a \tilde{r}_y^1) - \tilde{\Psi}_5^a \tilde{r}_z^1\right] \\ w_3^* r_z^1 + \mathcal{F}^{-1}\left[\tilde{\Psi}_3^a \tilde{r}_x^1 - \tilde{\Psi}_5^a \tilde{r}_y^1 - w_4^* \tilde{\Psi}_6^a \tilde{r}_z^1\right] \end{bmatrix} \tag{61}$$

$$\beta_0 = \frac{1}{|q_x^0 \;\; q_y^0 \;\; q_z^0|^2} \tag{62}$$

$$\begin{bmatrix} p_x^1 \\ p_y^1 \\ p_z^1 \end{bmatrix} = \beta_0 \begin{bmatrix} q_x^0 \\ q_y^0 \\ q_z^0 \end{bmatrix} \tag{63}$$

for $k = 1, \ldots$

$$\begin{bmatrix} q_x^k \\ q_y^k \\ q_z^k \end{bmatrix} = \begin{bmatrix} w_1 p_x^k + \mathcal{F}^{-1}\left[w_2(\tilde{\Psi}_1 \tilde{p}_x^k + \tilde{\Psi}_2 \tilde{p}_y^k) + \tilde{\Psi}_3 \tilde{p}_z^k\right] \\ w_1 p_y^k + \mathcal{F}^{-1}\left[w_2(\tilde{\Psi}_2 \tilde{p}_x^k + \tilde{\Psi}_4 \tilde{p}_y^k) - \tilde{\Psi}_5 \tilde{p}_z^k\right] \\ w_3 p_z^k + \mathcal{F}^{-1}\left[\tilde{\Psi}_3 \tilde{p}_x^k - \tilde{\Psi}_5 \tilde{p}_y^k - w_4 \tilde{\Psi}_6 \tilde{p}_z^k\right] \end{bmatrix} \tag{64}$$

$$\alpha_k = \frac{1}{|q_x^k \;\; q_y^k \;\; q_z^k|^2} \tag{65}$$

$$\begin{bmatrix} K_x^{e,k+1} \\ K_y^{e,k+1} \\ K_z^{m,k+1} \end{bmatrix} = \begin{bmatrix} K_x^{e,k} \\ K_y^{e,k} \\ K_z^{m,k} \end{bmatrix} + \alpha_k \begin{bmatrix} p_x^k \\ p_y^k \\ p_z^k \end{bmatrix} \tag{66}$$

$$\begin{bmatrix} r_x^{k+1} \\ r_y^{k+1} \\ r_z^{k+1} \end{bmatrix} = \begin{bmatrix} r_x^k \\ r_y^k \\ r_z^k \end{bmatrix} - \alpha_k \begin{bmatrix} q_x^k \\ q_y^k \\ q_z^k \end{bmatrix} \tag{67}$$

$$\begin{bmatrix} q_x^{k+1} \\ q_y^{k+1} \\ q_z^{k+1} \end{bmatrix} = \begin{bmatrix} w_1^* r_x^{k+1} + \mathcal{F}^{-1}\left[w_2^*(\tilde{\Psi}_1^a \tilde{r}_x^{k+1} + \tilde{\Psi}_2^a \tilde{r}_y^{k+1}) + \tilde{\Psi}_3^a \tilde{r}_z^{k+1}\right] \\ w_1^* r_y^{k+1} + \mathcal{F}^{-1}\left[w_2^*(\tilde{\Psi}_2^a \tilde{r}_x^{k+1} + \tilde{\Psi}_4^a \tilde{r}_y^{k+1}) - \tilde{\Psi}_5^a \tilde{r}_z^{k+1}\right] \\ w_3^* r_z^{k+1} + \mathcal{F}^{-1}\left[\tilde{\Psi}_3^a \tilde{r}_x^{k+1} - \tilde{\Psi}_5^a \tilde{r}_y^{k+1} - w_4^* \tilde{\Psi}_6^a \tilde{r}_z^{k+1}\right] \end{bmatrix} \tag{68}$$

$$\beta_k = \frac{1}{|q_x^{k+1} \;\; q_y^{k+1} \;\; q_z^{k+1}|^2} \tag{69}$$

$$\begin{bmatrix} p_x^{k+1} \\ p_y^{k+1} \\ p_z^{k+1} \end{bmatrix} = \begin{bmatrix} p_x^k \\ p_y^k \\ p_z^k \end{bmatrix} + \beta_k \begin{bmatrix} q_x^{k+1} \\ q_y^{k+1} \\ q_z^{k+1} \end{bmatrix} \tag{70}$$

The two coupled equations for K_x^m and K_y^m are solved in an anogolous manner.

initialize

$$\begin{bmatrix} r_x^1 \\ r_y^1 \end{bmatrix} = \begin{bmatrix} H_x^i - w_5 K_x^{m,1} - w_4 \mathcal{F}^{-1}\left[(\tilde{\Psi}_1 \widetilde{K}_x^{m,1} + \tilde{\Psi}_2 \widetilde{K}_y^{m,1})\right] \\ H_y^i - w_5 K_y^{m,1} - w_4 \mathcal{F}^{-1}\left[(\tilde{\Psi}_2 \widetilde{K}_x^{m,1} + \tilde{\Psi}_4 \widetilde{K}_y^{m,1})\right] \end{bmatrix} \tag{71}$$

$$\begin{bmatrix} q_x^0 \\ q_y^0 \end{bmatrix} = \begin{bmatrix} w_5^* r_x^1 + w_4^* \mathcal{F}^{-1}\left[(\tilde{\Psi}_1^a \tilde{r}_x^1 + \tilde{\Psi}_2^a \tilde{r}_y^1)\right] \\ w_5^* r_y^1 + w_4^* \mathcal{F}^{-1}\left[(\tilde{\Psi}_2^a \tilde{r}_x^1 + \tilde{\Psi}_4^a \tilde{r}_y^1)\right] \end{bmatrix} \tag{72}$$

$$\beta_0 = \frac{1}{|q_x^0 \;\; q_y^0|^2} \tag{73}$$

$$\begin{bmatrix} p_x^1 \\ p_y^1 \end{bmatrix} = \beta_0 \begin{bmatrix} q_x^0 \\ q_y^0 \end{bmatrix} \tag{74}$$

for $k = 1, \ldots$

$$\begin{bmatrix} q_x^k \\ q_y^k \end{bmatrix} = \begin{bmatrix} w_5 p_x^k + w_4 \mathcal{F}^{-1}\left[(\tilde{\Psi}_1 \tilde{p}_x^k + \tilde{\Psi}_2 \tilde{p}_y^k)\right] \\ w_5 p_y^k + w_4 \mathcal{F}^{-1}\left[(\tilde{\Psi}_2 \tilde{p}_x^k + \tilde{\Psi}_4 \tilde{p}_y^k)\right] \end{bmatrix} \tag{75}$$

$$\alpha_k = \frac{1}{|q_x^k \;\; q_y^k|^2} \tag{76}$$

$$\begin{bmatrix} K_x^{m,k+1} \\ K_y^{m,k+1} \end{bmatrix} = \begin{bmatrix} K_x^{m,k} \\ K_y^{m,k} \end{bmatrix} + \alpha_k \begin{bmatrix} p_x^k \\ p_y^k \end{bmatrix} \tag{77}$$

$$\begin{bmatrix} r_x^{k+1} \\ r_y^{k+1} \end{bmatrix} = \begin{bmatrix} r_x^k \\ r_y^k \end{bmatrix} - \alpha_k \begin{bmatrix} q_x^k \\ q_y^k \end{bmatrix} \tag{78}$$

$$\begin{bmatrix} q_x^{k+1} \\ q_y^{k+1} \end{bmatrix} = \begin{bmatrix} w_5^* r_x^{k+1} + w_4^* \mathcal{F}^{-1}\left[(\tilde{\Psi}_1^a \tilde{r}_x^{k+1} + \tilde{\Psi}_2^a \tilde{r}_y^{k+1})\right] \\ w_5^* r_y^{k+1} + w_4^* \mathcal{F}^{-1}\left[(\tilde{\Psi}_2^a \tilde{r}_x^{k+1} + \tilde{\Psi}_4^a \tilde{r}_y^{k+1})\right] \end{bmatrix} \tag{79}$$

$$\beta_k = \frac{1}{|q_x^{k+1} \quad q_y^{k+1}|^2} \tag{80}$$

$$\begin{bmatrix} p_x^{k+1} \\ p_y^{k+1} \end{bmatrix} = \begin{bmatrix} p_x^k \\ p_y^k \end{bmatrix} + \beta_k \begin{bmatrix} q_x^{k+1} \\ q_y^{k+1} \end{bmatrix} \tag{81}$$

For backscattering calculations the current for the (n-1)th angle is used as the first guess for the nth angle. This significantly reduces the number of iterations per angle.

V. Numerical Considerations

Although application of the FFT may greatly enhance the solution technique some difficulties may be encountered. The sampling interval and the pad size are chosen based on the assumed spectrum of the current. However, observation of the algorithm shows that Ap^k and $A^a r^k$ are both calculated with the same FFT but have very different spectrums. The search vectors p^k are linearly related to the currents however the residuals r^k consist of the difference between two pure phase functions. For the case of a large rectangular plate $\tilde{r}^k$ represents a narrow sinc function which has its peak shifted with the phase of the incident field. It may be shown that at edge on incidence the peak of this function occurs at the singularity of the transform of G. Thus, the pad size must be increased toward edge on incidence to avoid loss of the incident field phase information. Also the singular edge currents produce a continuous spectrum which dominates at edge

on incidence and must be addressed by an increase in pad size. This effect occurs most distinctly for perfectly conducting plates.

VI. Calculation of Radar Cross Section

The far zone electric field is given by

$$\bar{E}(R) = jk_0 G(R)[\hat{R} \times \bar{N}_t^m(\theta,\phi) - Z_0 \bar{N}_t^e(\theta,\phi)] \tag{82}$$

where $\bar{N}_t^{e,m}(\theta,\phi)$ has the θ and ϕ components

$$\begin{aligned} N_\theta^{e,m} &= \cos(\theta)[\cos(\phi)S_x^{e,m}(\theta,\phi) + \sin(\phi)S_y^{e,m}(\theta,\phi)] - \sin(\theta)S_z^{e,m}(\theta,\phi) \\ N_\phi^{e,m} &= -\sin(\phi)S_x^{e,m}(\theta,\phi) + \cos(\phi)S_y^{e,m}(\theta,\phi) \end{aligned} \tag{83}$$

and

$$\bar{S}^{e,m}(\theta,\phi) = \iint_{S'} \bar{K}^{e,m}(\bar{R}')e^{jk_0(\bar{R}'\cdot\hat{R})}dS'. \tag{84}$$

If the current is constant over the square cell

$$\bar{S}^{e,m}(\theta,\phi) = F(\theta,\phi)\sum_{p=1}^{N}\sum_{q=1}^{N}\bar{K}^{e,m}(p,q)e^{jk_0\sin(\theta)[\cos(\phi)x(p,q)+\sin(\phi)y(p,q)]} \tag{85}$$

where

$$F(\theta,\phi) = \frac{4}{k_0^2}\frac{\sin\left[k_0\frac{\Delta}{2}\sin(\theta)\cos(\phi)\right]}{\sin(\theta)\cos(\phi)}\frac{\sin\left[k_0\frac{\Delta}{2}\sin(\theta)\sin(\phi)\right]}{\sin(\theta)\sin(\phi)}. \tag{86}$$

The backscattering cross section is given by

$$\begin{aligned} \sigma &= \lim_{R\to\infty} 4\pi R^2 \frac{|\bar{E}^s|^2}{|\bar{E}^i|^2} \\ &= \frac{k_0^2}{4\pi}\left[|N_\phi^m + Z_0 N_\theta^e|^2 + |N_\theta^m - Z_0 N_\phi^e|^2\right]. \end{aligned} \tag{87}$$

VII. Test Results

The method was tested for several geometries and compositions. Results for the square plate backscatter pattern were compared to measured data obtained at the University of Michigan using an HP8510-based system. The results for the circular plate were compared calculations based on the Chu-Weil-Willis formulation [14].

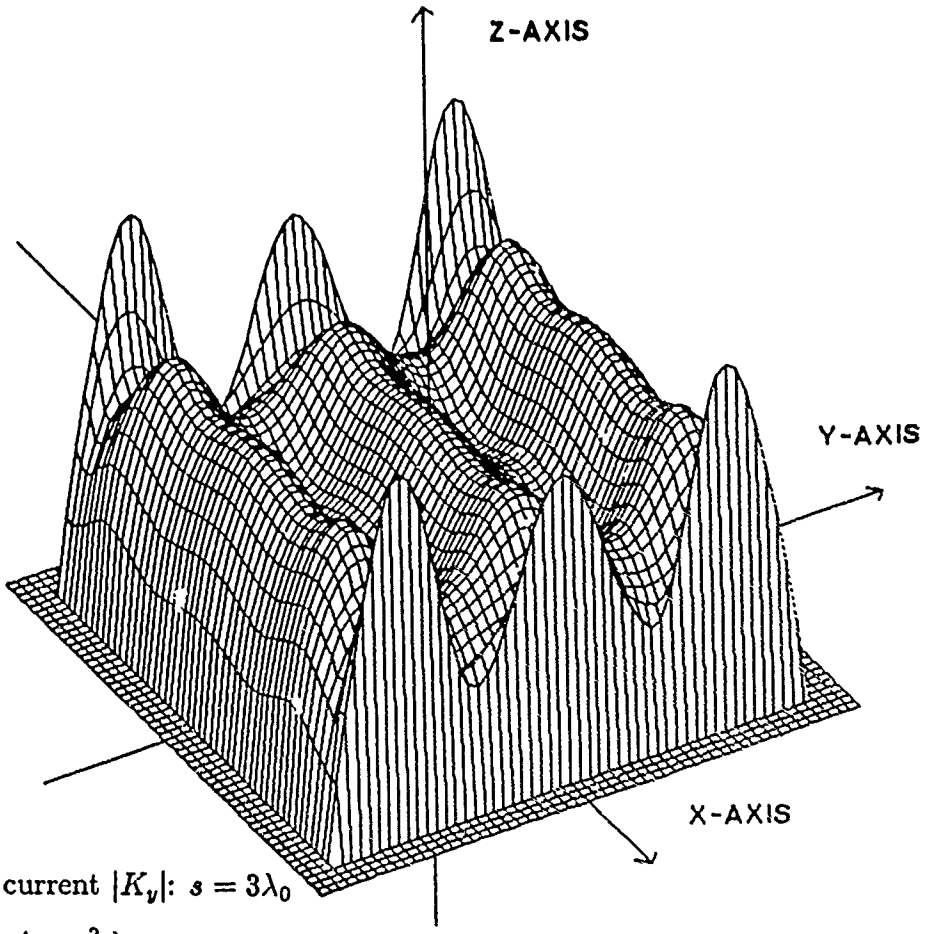


Fig. 6. . Surface current $|K_y|$: $s = 3\lambda_0$
tol=.05, $\Delta = \frac{2}{39}\lambda_0, \sigma = \infty$
$\theta = 0°, \phi = 0°$

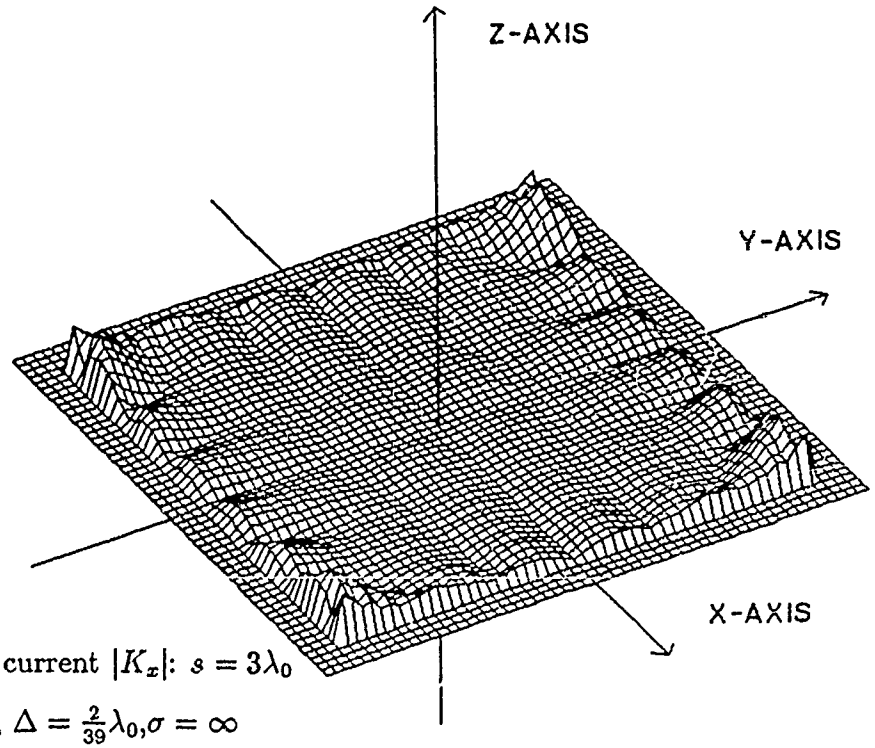


Fig. 7. Surface current $|K_x|$: $s = 3\lambda_0$
tol=.05, $\Delta = \frac{2}{39}\lambda_0, \sigma = \infty$
$\theta = 0°, \phi = 0°$

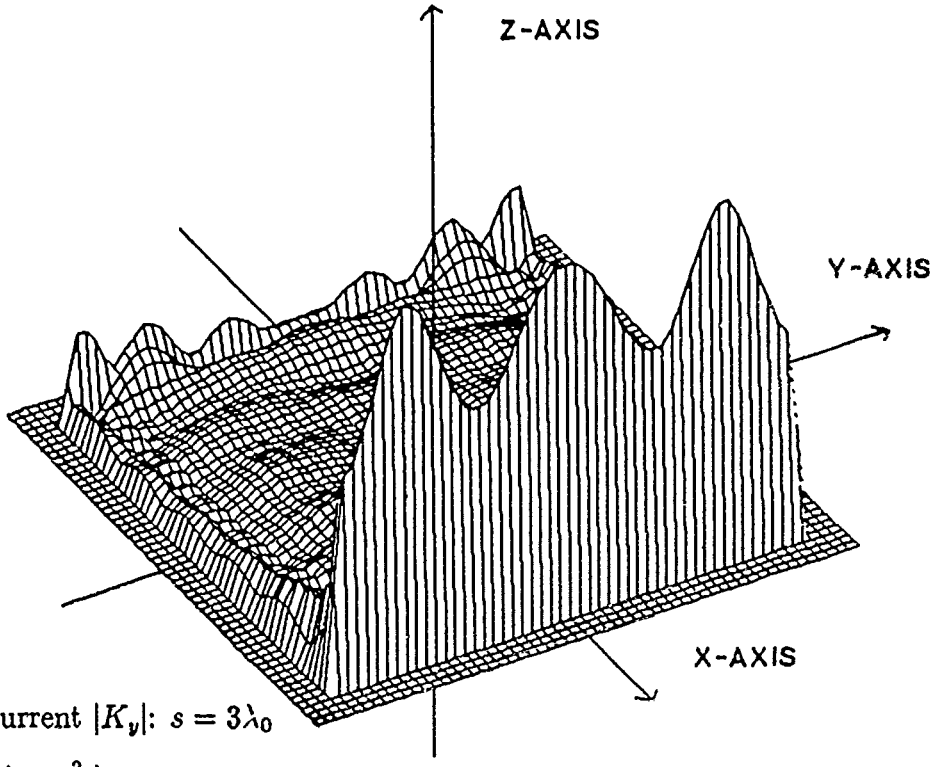


Fig. 8. Surface current $|K_y|$: $s = 3\lambda_0$
tol=.05, $\Delta = \frac{2}{39}\lambda_0, \sigma = \infty$
$\theta = 90°, \phi = 0°$

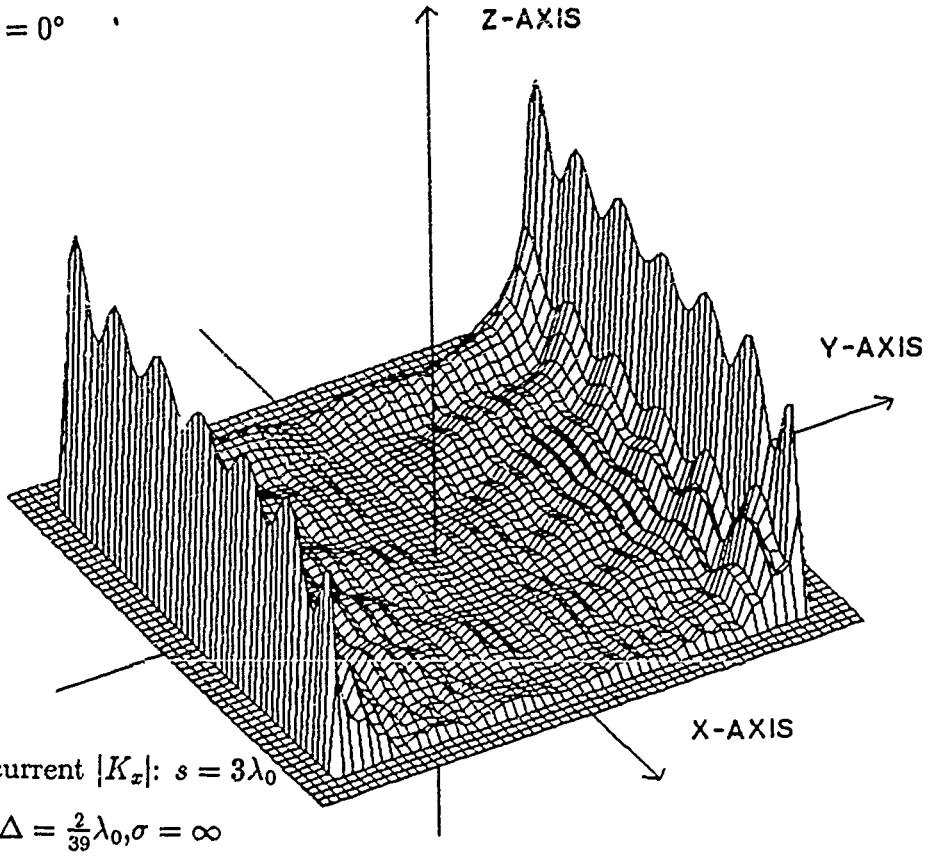


Fig. 9. Surface current $|K_x|$: $s = 3\lambda_0$
tol=.05, $\Delta = \frac{2}{39}\lambda_0, \sigma = \infty$
$\theta = 90°, \phi = 0°$

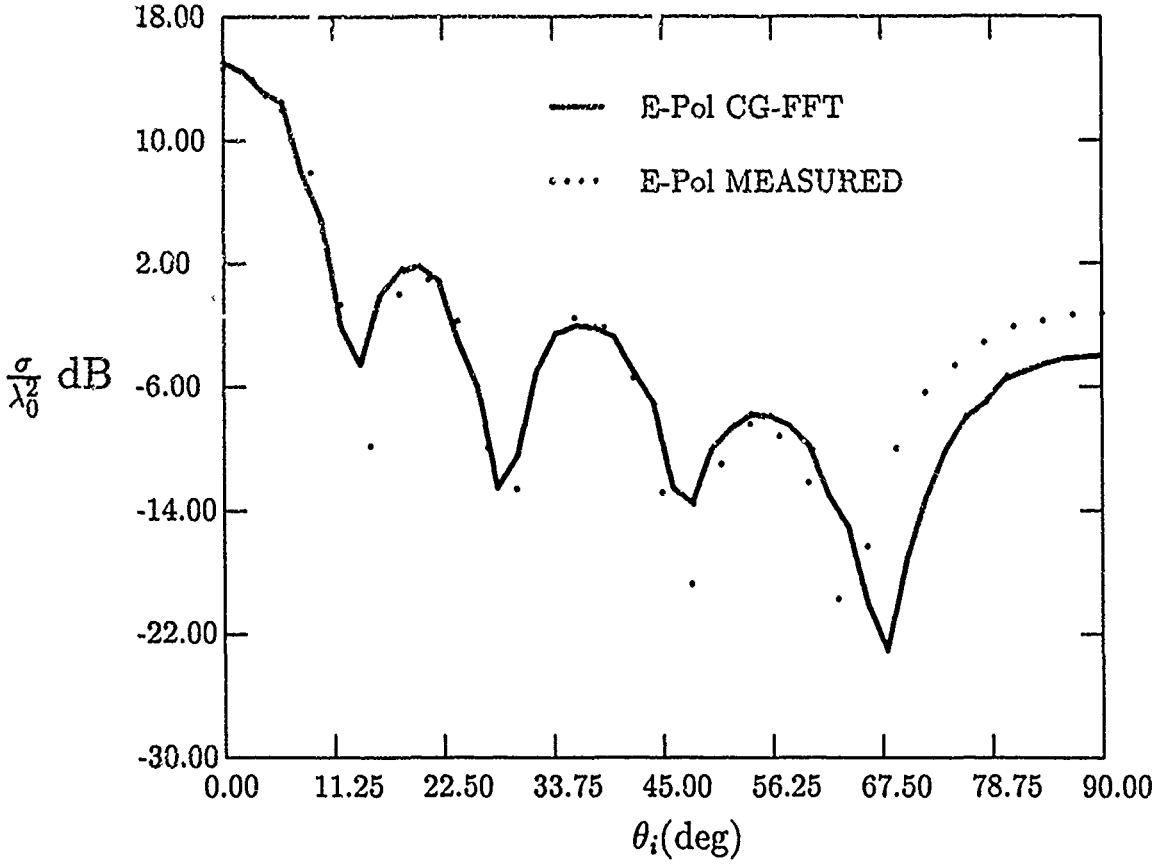


Fig. 10. Square Plate: $s = 2\lambda_0$,w=.0254λ_0,$\epsilon_r = 7.4 - j1.11$, $\mu_r = 1.4 - j0.672$,tol=.05,$\Delta = \frac{2}{39}\lambda_0$,N=128

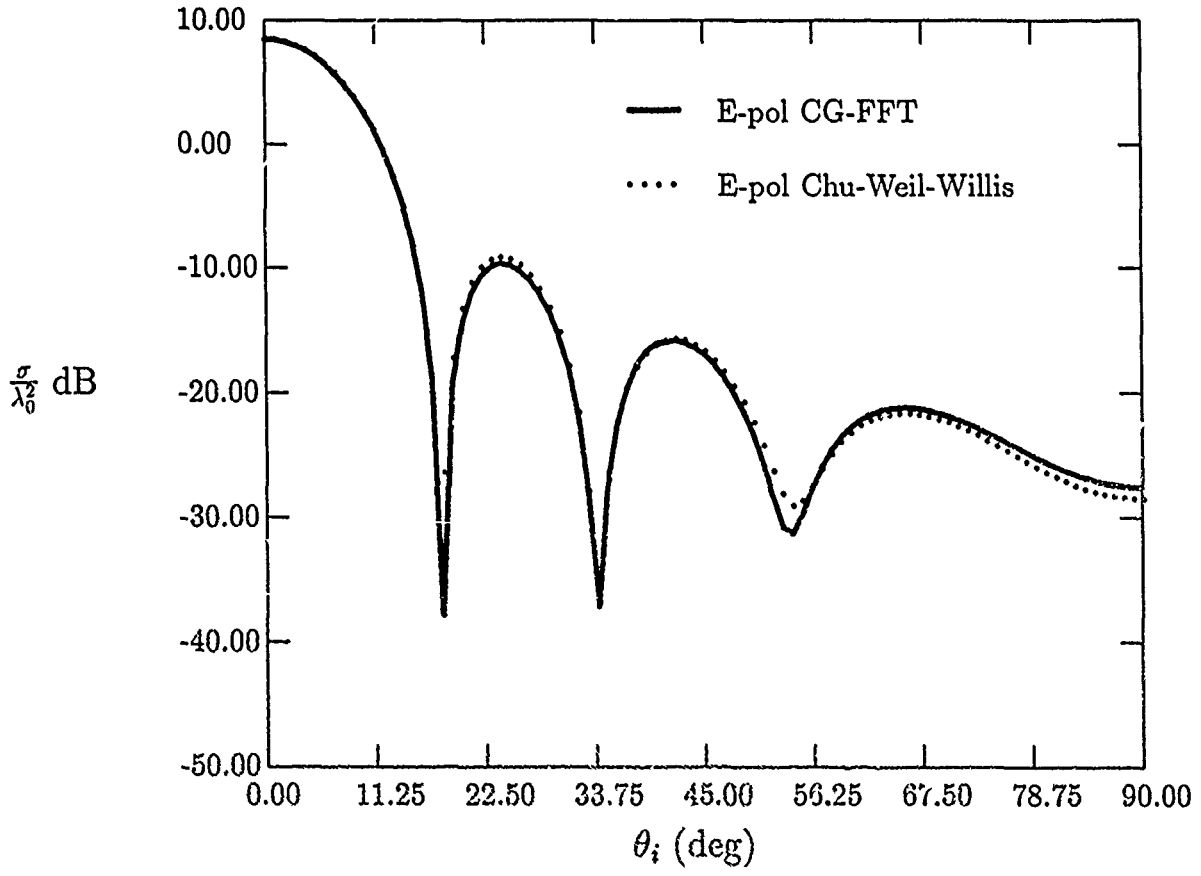


Fig. 11. Circular Plate: $r_0 = \lambda_0$,w=.01λ_0,$\epsilon_r = 2 - j10$, tol=.02,$\Delta = \frac{2}{39}\lambda_0$,N=128

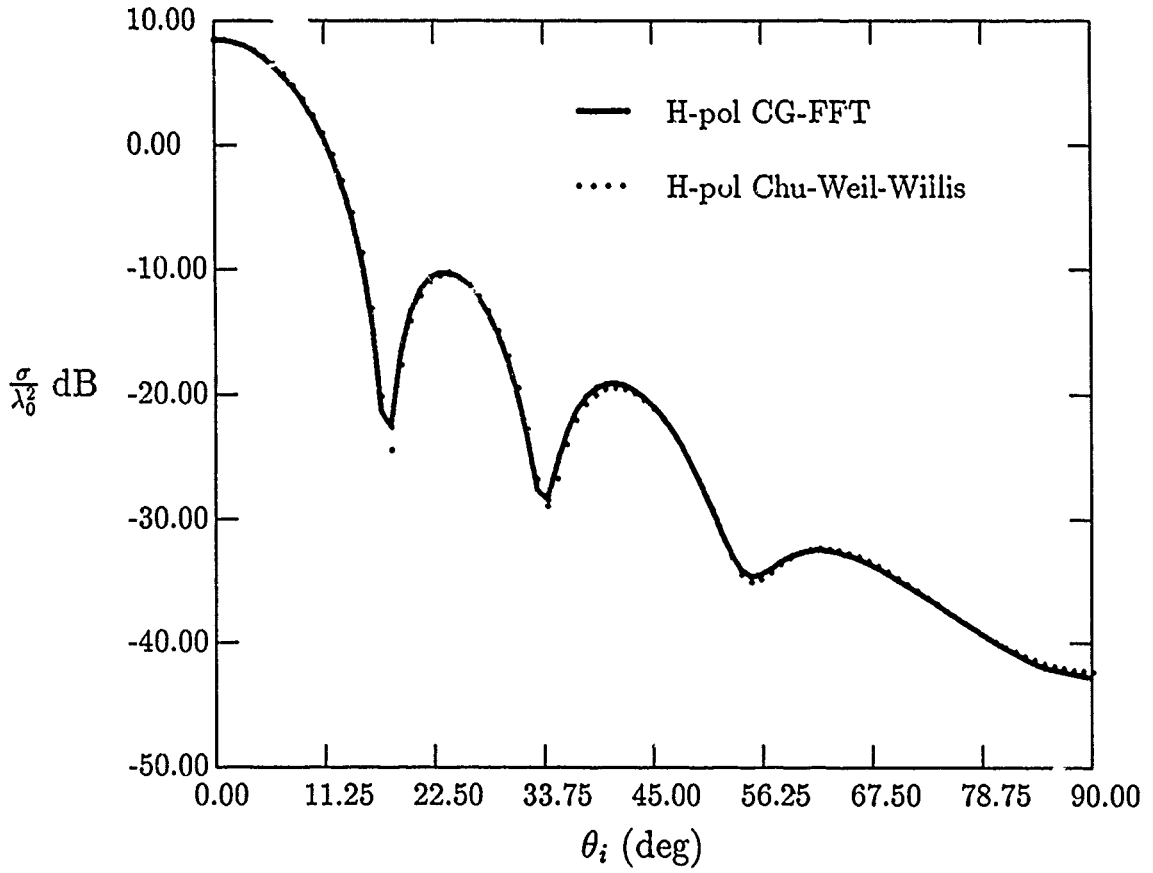


Fig. 12. Circular Plate: $r_0 = \lambda_0$,w=.01λ_0,$\epsilon_r = 2 - j10$, tol=.02,$\Delta = \frac{2}{39}\lambda_0$,N=128

VIII. Conclusion

The combined CG-FFT method can be used effectively to solve plate scattering problems. The flexibility of the formulation allows solution of a wide variety of perimeter shapes and composition with minimal change of inputs. The computational difficulties discussed are being investigated by the authors at the present

time with the hope of eliminating them altogether.

Aknowledgment

The authors wish to thank Mr. Kamal Sarabandi and Mr. Earnest Rho for collecting the measured data presented in this paper.

References

[1] E. H. Newman and M. R. Schrote, "An open integral formulation for electromagnetic scattering by material plates",IEEE Trans. Antennas Propagat., vol. AP-32,No. 7 ,July, 1984, pp. 672-678.

[2] M. Naor and T. B. A. Senior, "Scattering by resistive plates",Technical report no. 1, Radiation Lab., The University of Michigan, Sept., 1981.

[3] R. F. Harrington and J. R. Mautz, "An impedance approximation for thin dielectric shells", IEEE Trans. Antennas Propagat., vol. AP-23,No.4,July, 1975, pp. 531-534.

[4] A. W. Glisson and D. R. Wilton, "Simple and efficient numerical methods for problems of electromagnetic radiation and scattering from surfaces",IEEE Trans. Antennas Propagat., vol. AP-28,No. 5 ,Sept, 1980, pp. 593-603.

[5] S. M. Rao, D. M. Wilton,and A. W. Glisson, "Electromagnetic scattering by surfaces of arbitrary shape",IEEE Trans. Antennas Propagat., vol. AP-30,No. 3 ,May, 1982, pp. 409-418.

[6] T. K. Sarkar,E. Arvas and S. M. Rao, "Application of FFT and the conjugate gradient method for the solution of electromagnetic radiation from electrically large and small conducting bodies",IEEE Trans. Antennas Propagat., vol. AP-34,pp. 635-640,May. 1986.

[7] C. G. Christodoulou and J. F. Kauffman, "On the electromagnetic scattering from infinite rectangular grids with finite conductivity ",IEEE Trans. Antennas Propagat., vol. AP-34,pp. 635-640,May. 1986.

[8] M. R. Hestenes and E. Steifel, "Method of conjugate gradients for solving linear systems", J. Res. Nat. Bur. Standard., vol. 49,no. 152, pp.409-436.

[9] M. R. Hestenes, "Conjugate direction methods in optimization", New York, Springer-Verlag,1980.

[10] J. W. Daniel, "The conjugate gradient method for linear and nonlinear operator equations",Siam J. Numer. Anal., vol. 4, no. 1,1967,pp. 10-26.

[11] J. W. Golub,and C. F. VanLoan "Matrix computions",John Hopkins University Press, Baltimore, MD, 1983, pp. 363-379.

[12] IEEE, "Special issue on the fast fourier transform and its application to digital filtering and spectral analysis",IEEE Trans.on Audio and Electroacoustics,vol. AU-15,no.2,June 1967.

[13] A. Rosenfeld and A. C. Kak, "Digital picture processing",2nd ed.,vol 1,New York, Academic Press, 1976. pp. 20-27.

[14] C. M. Chu and H. Weil, "Integral equation method for scattering and absorption of electromagnetic radiation by thin lossy dielectric discs",J. Comp. Phys.,vol.22,pp. 111-124,1976.

[15] D. M. Le Vine, A.Schneider,R. H. Lang and H. G. Carter, "Scattering from thin dielectric disks", IEEE Trans. Antennas Propagat., vol. AP-33,No.12,Dec., 1985, pp. 1410-1413.

[16] H. L. Thal and J. F. Finger, "Scattering by dielectric containers", IEEE Trans. Antennas Propagat., vol. AP-18,pp. 709-711,Sept. 1970.

[17] J. S. Hey, and T. B. A. Senior, "Electromagnetic scattering by thin conductiong plates at glancing incidence",Proc. Phys.Soc.(London),vol.72,pp. 981-995,1956.

[18] T. B. A. Senior, "Disk scattering at edge-on incidence", IEEE Trans. Antennas Propagat., vol. AP-17,No. 6,Nov., 1969, pp. 751-756.

[19] R. A. Ross, "Radar cross section of rectangular flat plates as a function of aspect angle", IEEE Trans. Antennas Propagat., vol. AP-14,No. 3 ,May, 1966, pp. 329-335.

[20] F. A. Sikta, "UTD analysis of electromagnetic Scattering by flat plate structures", Dissertation,The Ohio State University, 1981.

DEVELOPMENT OF A MODELING HANDBOOK FOR USE IN COMPUTATIONAL ELECTROMAGNETICS

E. K. Miller
University of Kansas
Lawrence, KS 66045

ABSTRACT

As computer modeling in electromagnetics becomes more routinely used in design applications, there is a accumulating volume of practical experience being developed. If this experience could be collected into a "user-experience" data base, many practical benefits could be realized. We suggest that the ACES Newsletter offers an opportunity for developing this data base into a modeling handbook for CEM, and briefly consider how this might be done and how such a handbook might be used.

I. INTRODUCTION

The continuing development and application of numerical solution techniques to problems in electromagnetic radiation, propagation and scattering is leading to a diversity of modeling approaches. On the one hand, this diversity is beneficial because of the increasing variety of choices it provides to the prospective modeler. On the other hand however, the proliferation of modeling tools and the problems to which they might be applied can be a source of confusion and uncertainty over which tool to select and how it might most appropriately be used for the problem of interest. In this presentation, we suggest that one of the primary activities and contributions of the Applied Computational Electromagnetics Society should be the ongoing development of a modeling handbook designed in such a way as to promote the efficiency and reliability of the modeling process.

The basic idea of the modeling handbook is to collect, collate, and report in the ACES Newsletter the experiences of those using modeling codes for solving problems of practical interest. This should be done in a uniform, consistent fashion employing a standard format like that suggested in the November 1986 ACES Newsletter (and included below) for at least two reasons. Firstly, by employing a simple "fill-in-the-blanks" form, the effort required to submit a modeling note to the ACES Newsletter should be appropriately minimized so as to encourage the participation of those who might not otherwise write technical articles. Secondly, the material provided in these short modeling notes then will be more likely to include the information most helpful to others who encounter similar modeling problems to thereby save them expenditure of unnecessary time and effort. Other features appropriate for such a modeling handbook might include modeling guidelines, code summaries, and recommendations for future modeling developments and extensions. Various aspects of initiating a modeling handbook under ACES auspices are further discussed below.

II. EVOLUTION OF COMPUTATIONAL ELECTROMAGNETICS

Since the 1960s, growing computer utilization in electromagnetics has produced several transitions in the expanding role of computer modeling. Most of the work in the 1960s focussed on the research involved in formulating, developing, and demonstrating the

feasibility of computer modeling. The 1970s saw the onset of a more development-oriented environment where computer models were being used increasingly for solving problems of practical interest. Into the 1980s, the trend towards applications has continued as computer models are being used more routinely in design applications as indicated graphically in Figure 1. This trend towards increasing applications is mirrored by development of modeling tools like NEC (Numerical Electromagnetics Code), and is analagous to the shift towards an increasing software-development effort and away from hardware design in computer systems.

The increasing ubiquity of computer applications in electromagnetics has produced a proliferation of modeling approaches and modeling tools. Among the problems that this tool proliferation produces are the decisions required of a modeler with respect to selecting the one best suited for a particular application, and possibly the need to be acquainted with the input requirements and limitations of two or more modeling codes. In addition, because more and larger problems are being modeled, there is proliferation of modeling results being produced, further increasing the difficulty of discovering those that might be relevant to one's own application, even when they are openly documented. Finally, there are a growing variety of computer resources available, ranging from mainframes to personal computers, adding another information dimension that needs tracking. It seems clear that the individual experience acquired by each modeler represents an increasingly valuable commodity in the aggregate if this information could somehow be collected and organized as a user-experience data base.

Such a user-experience data base will provide many benefits. Perhaps most important, it could provide examples of what modeling approaches do work for given applications, as well as what doesn't work. It could also be used to build a catalog of solved problems and provide validation data. Information could be exchanged on "tricks of the trade", to document those special techniques that are not often widely discussed because they are regarded to be well known or otherwise not worth talking about. Finally, needed modeling enhancements and refinements could be identified and collected to provide guidance for future research.

We stress that the information included in this "user-experience" data base or handbook would be different from the usual journal articles found in professional-society publications. Those articles deal primarily with research issues. The emphasis of the handbook instead would be on how to use computer models for real-world design applications. But to ensure that the appropriate information is collected, a standard format is advisable as discussed next.

III. DATA-BASE FORMAT

In order to expedite the process of user "feedback", we suggest use of the short-note format which follows, having two goals in mind. One is to encourage members of ACES to submit material to the Newsletter by providing a form that is easy to complete and less laborsome to prepare than might be the case of a typical full-blown journal article. The other is to ensure some standards of consistency, accuracy and uniformity for these short notes so that they will be most likely to contain the key information needed by someone else who is embarking upon a similar modeling problem and for whom the note(s) will provide knowledge of what has worked before.

We emphasize that the ACES Newsletter is intended to include not only short notes, but longer articles, tutorials and regular columns. It is our expectation however, that the short notes could and should develop into the most valuable part of the Newsletter in that they will become an accumulation of modeling know how and experience that will guide the subsequent work of other modelers as well as to identify needed modeling developments and research.

We therefore suggest the format below for short-note (1-3 pages) submittals to the Newsletter.

SHORT-NOTE FORMAT FOR ACES NEWSLETTER
VERSION 1.0

AUTHOR

Name_____
Affiliation_____
Address_____
_____
_____
Telephone_____

APPLICATION--

Radiation_____Propagation_____Scattering_____
Congifuration (Whip antenna on tank; aircraft; . . .)
Excitation (Plane wave, voltage source, GTD field,. . .)
Purpose (Basic physics, design, validation, etc.)

PROBLEM DESCRIPTION--This could be a brief narrative or a fill-in-the-blank exercise to include information such as:

Object Geometry (Dipole, LP, Vehicle, Ship)
Object Size (Major dimensions in feet or meters)
Frequency Range (in MHz and wavelengths)
Environment (Free space, Perfect Ground, Lossy Ground)
Other Details (Elaborate in written description as needed)

COMPUTER CODE USED--

Name of Code (NEC, MININEC, TWTD, etc.)
Version (Name and/or date of release)
Originator (Name, Organization, Address)
Computer on which run (CRAY2, VAX 750, Macintosh, etc.)
Formulation (Integral equation and type, differential equation, GTD)
Domain (time, frequency)
Numerical treatment (bases and weight functions)
Special Features_____
Other Details (Elaborate in written description as needed))

MODEL DESCRIPTION--

Number of unknowns_____
Type of unknowns (linear, surface, volumetric)
Physical approximations (wire mesh for surface, open gap for insulator, etc.)
Problem features omitted (_____)

Other Details (Elaborate in written description as needed))

RESULTS OBTAINED-- Current distribution_____
Input impedance_____
Near-field_____
Far-field_____
Other_____

HOW VALIDATED-- Numerical_____Analytical_____Experimental_____
Estimated accuracy_____
Other Details (Elaborate in written description as needed)

COMMENTS-- What went right_____
What could be improved_____
Overall value of the modeling exercise_____
Recommendations_____

By adhering to a standard note to promote data-base utility, we should realize other benefits as well. User input will be encouraged by reducing the time and effort needed to prepare a note, and we would hope to alleviate company proprietary concerns. The standard format will also expedite newsletter preparation by requiring less editing and revision and producing shorter, more succinct inputs. Finally, the eventual utility of the notes will be enhanced by increasing their archieval value and making their organization into an evolving handbook easier and more logical.

IV. HANDBOOK FEATURES AND ORGANIZATION

As mentioned above, the handbook will contain information other than short notes alone. Among its other features we expect to include a code directory, modeling tutorials, check cases, and future research recommendations. Each of these features is briefly summarized below.

Code Directory--Modeling codes are what CEM is all about, and we intend to develop a catalog of codes to provide information concerning their formulation, availability, machines on which they run, areas of applicability, and other relevant information. The ACES software form exemplifies a succinct, but informative, code description that will be used in the handbook.

Tutorials--Information concerning how to use computer models is often not easily obtained. Although all integral-equation computer models, for example, incorporate the same basic ingredients, aside from some of the most basic modeling guidelines such as sampling densities in wavele. ,ths, other commonly encountered but more subtle aspects of modeling are not as often articulated. We hope to develop a series of tutorials to provide guidance concerning the practical realities of applying computer models to real-world problems.

Check Cases--Validation is probably the most effort-consuming part of CEM. While modeling new problems will always require extra validation effort, the overall difficulty of determining solution validity can be greatly reduced if a set of check cases were to be developed for this purpose including anlaytical, numerical, and experimental

results. It is essential that a set of problems be developed, observables selected, and data formats designed for use in comparative validation of existing and new models.

Solved Problems--The existing literature, the IEEE Antennas and Propagation Society Transactions for example, contains a vast quantity of information relevant to computer modeling. However, these sources are developed chronologically with the result that tinformation relevant to a given problem can be scattered throughout many issues and years of the publication. A particularly useful feature of the ACES Newsletter and Handbook will be the topical storage of the applications notes. By using a loose-leaf format, notes accumulating over time that are related to the same modeling application can be kept together so that they can be more easily referred to. To aid this procedure, we propose to use a set of icons as well as key words for this purpose.

V. HANDBOOK USEAGE

The basic idea of the handbook is to collect together information useful for purposes of computer modeling in electromagnetics, primarily in radiation and scattering, but also to include other applications as appropriate. Although this sounds like a worthwhile idea in the abstract, it is useful to consider how such a handbook might be used in practice. We briefly list here some of the purposes to which the ACES Handbook could be put.

Surveying Modeling Codes--Since computer codes are the tools of CEM, they provide a focus for all modeling activities. By providing a catalog of modeling codes, the handbook will be a logical starting point for someone unfamiliar with the codes availalbe or who needs to compare the applicability of the codes that might be useful for a given problem. In order to make such comparisons more relevant, it will be important to provide not only the codes' modeling capabilities but their resource requirements.

Reviewing Solved Problems--The handbook will include a growing set of solved problems that should be helfpul to both new and experienced modelers. When a problem new to the modeler is encountered, the set of applications' notes will provide a useful reference to find whether the same or similar problem may have already been modeled. If it has, the previous work should represent a useful starting point. If not on the other hand, completion of the problem will represent a useful new addition to the handbook.

Developing the Model--Beyond the guidance that the applications notes contain, generic modeling guidelines will also be available from tutorial articles in the Newsletter as well as through modeling checklists. This means that the handbook will be a valuable reference for model development, especially when specific past experience is not available.

Checking Results--Confidence in the results obtained from a new modeling code, or when using a validated code for a new problem, can be greatly increased by finding that it agrees with a set of well validated test problems. By providing a library of check cases, the validity of code modifications, their implementation on new computers, and their application to different problems could be greatly facilitated.

VI. CONCLUDING REMARKS

As the collection of computer codes useful in electromagentics continues to increase, the benefits of collecting the applications' experience of those using such codes becomes increasingly valuable. The ACES Newsletter is being designed to encourage input of user experience and to organize this information in such a way as to make subsequent reference easier.

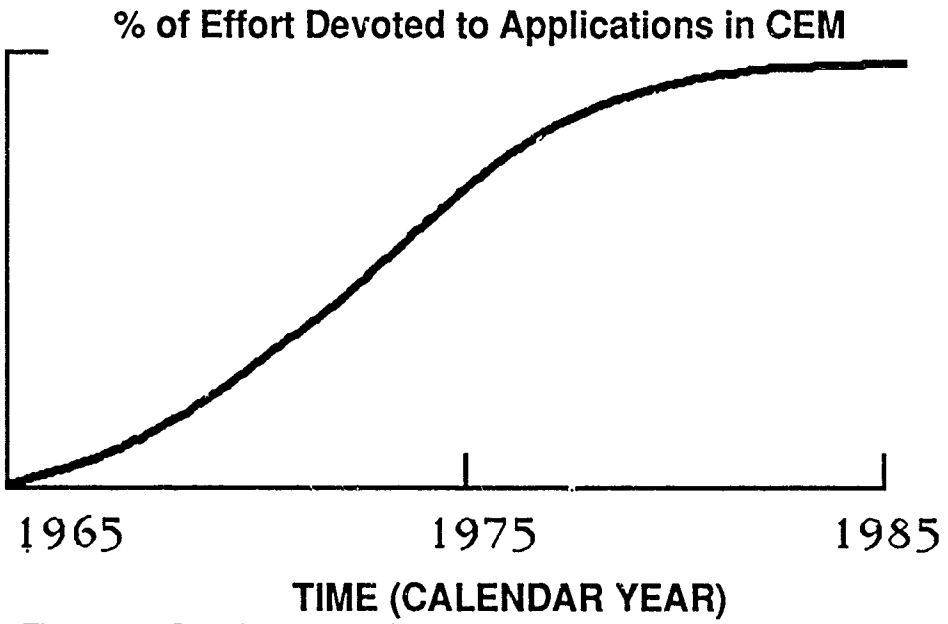


Figure 1. Growing proportion of computational electromagnetics activities over time is being devoted to applications, making exchange of user experience increasingly important.

SESSION V - "NEC-2 AND PC CODE APPLICATIONS"

Moderator: J. McDonald

Large Yagi Analysis with MININEC3

W. B. Seabreeze
202 Fletcher Road
Sterling, Virginia 22170

Large Yagi Analysis with MININEC3

After many unsuccessful attempts to find a method of adapting MININEC for large antenna problems on a PC compatible, a solution seems to have been found. Using QuickBASIC 2.0 with the 64 kByte array size capability, it is possible to expand the capability of MININEC3 to 225 current pulses. Previous attempts using other BASIC compilers did not yield the desired performance in either speed or array sizes. Enhanced speed was obtained using a commercially available 8087 library package for the QuickBASIC compiler. Antennas modeled as 217 current pulses are analyzed in 4 hours, 38 minutes using a turbo PC compatible (7.16 MHz clock). This article describes some thoughts and methods used to achieve this capability.

Limited financial resources and programming expertise prevented me from exploring as many different compilers as I would have liked for MININEC expansion. The popular IBM BASCOM compiler (version 1.0 with required patches which were found in public domain disks) provided impressive speed enhancements, especially after linking with 8087 libraries available for this compiler. The maximum number of segments is, however, small with this setup which prevent working with anything but short yagis. BASCOM allows a maximum of 64 Kbytes for program and another 64 Kbytes for data. While this is a lot of memory for many applications, antenna analysis using MININEC can benefit greatly by more RAM.

Other workers pursuing high performance yagi designs have suggested that use of 8 segments per element is desirable if reasonable antenna pattern accuracy is desired. This fact dictates the need for expansion beyond the 50 segment horizon provided by the original code if long high-performance yagi are sought. While most professionals scoff at such narrowband designs, it is significant that so much electromagnetic aperture is possible with so little weight and wind cross section when yagis antennas are employed. Stacking of smaller yagis has been popular in the past, but in many applications the cost, complexity, and reliability may dictate use of fewer higher performance yagis. Many

professionals are also surprised to learn that so many enhancements to the original yagi designs described in the AP Proceedings and elsewhere have arisen. Indeed amateur radio experimenters have done some noteworthy work in this area (1,2).

Investigation into using Turbo Pascal offers significant promise, except that conversion of the program can be an overbearing task for many. A friend of mine who is proficient at Pascal programming spent two complete days at this task before giving up. He wasn't particularly excited about the prospect of designing 31 element yagis anyhow, but we both were convinced that this much tedious labor is not to be taken casually in ones spare time. Apparently a Turbo Pascal version of modified MININEC was developed at Virginia Tech. (3) I would love to experiment with this program since Turbo Pascal seems to be a high-performance language. Turbo with 8087 support, however, uses double precision math only, which could make it significantly slower, although more accurate than compiled BASIC. In the past, experts have agreed that MININEC does not require use of double precision math, although this is probably a function of the particular problem being analyzed. Turbo without 8087 support uses six-byte precision, which is two bytes more than the BASIC default of four bytes per floating point numeric.

Other computer languages for the PC also offer excellent 8087 support, but a program the size and complexity of MININEC3 is not a good way to get one's feet wet in a new computer language. Like many others working in the RF area, I find that the vast majority of existing RF software is available in BASIC. Maybe someday I'll become more computer literate and write some 'C' or Modula-2 myself, but for now it seems there's lots of fun and challenge to be had in good ole BASIC.

I had done some previous experimenting with expanding the array sizes in MININEC using Professional Basic. This set up got me up to 20 wires at 5 segments per wire, which was a big improvement over where I started (the Artech House book version of MININEC) (4). I could then perform analysis of my new

18 element yagi which had already been successfully built and used on the 220 MHz amateur band. The calculated gain was just where it was supposed to be, and my confidence in MININEC grew. Professional Basic is not, however a true compiler as it compiles to "P-code" rather than directly to 8086 assembly language. It is faster and more accurate than the BASIC interpreters, but I was disappointed at having to wait more than 8 hours for the answer (even with 7.16 MHz clock and an 8087). The strength of this package does not lie in its speed, but rather in its mathematical accuracy and debugging features. I have heard from others that Better Basic is similar in performance (slow). The IBM Business BASIC compiler (version 2.0) sounded good since it is supposed to handle expanded memory (640 Kbytes), but I couldn't find any 8087 support for it, and it was quite expensive. Reviews in the magazines didn't sound particularly favorable either. Quickbasic 2.0 was finally tried due to its good reviews, its ability to address the full PC compatible memory, and best of all the price. At least 2 sources offer 8087 support for this package as well, which is important to those of us who enjoy slapping 225 x 225 matrices onto the PC (and watching it sweat). Announcements were just spotted in the literature for a new Borland product called Turbo Basic. This sounds like a red hot compiler, but I don't think it's available to the general public as yet. It offers potential for a significant improvement over QuickBASIC as real numbers are stored in IEEE format as opposed to IBM or Microsoft format. This allows the 8087 to directly access numeric data without the need for format conversion such as is required by QuickBASIC 2.0 (and all other Microsoft BASIC products). The result should be faster number-crunching performance.

After some initial experimenting, and discovering that the original MININEC3 worked OK with QuickBASIC (unmodified), I finally got out the book and pursued expanding the array sizes. Using single precision, each element of a numeric array takes up 4 bytes of memory in Microsoft BASIC. Quickbasic limits any single array to a maximum of 64 Kbytes which means that the biggest array possible is 128 by 128. Even this is a big improvement over the interpreter which wont

allow more than 64 Kbytes for the program plus the data (everything must be in same segment). Such large arrays must be declared as dynamic using a "metacommand", which is straightforward to implement. Large dynamic arrays do slow down the program somewhat compared to smaller static arrays, however, due to increased assembly language overhead. Just like in the RF world, nothing comes for free in the software world either.

In MININEC3 the arrays which need the significant expansion are ZI and ZR. Many other arrays also are expanded, but none come close in size to these two. So now with ZI and ZR both up to 64 Kbytes it is possible to tackle antennas up to 18 elements using 8 segments (7 pulses) each. Not bad, but still not sucking up all the rest of that "spare" memory. I really wanted something more meaningful to do with those RAM chips besides impressing myself with ramdisks. The solution chosen was based totally on the BFI (brute force and ignorance) principle. Any suggestions for improvements are highly welcome.

By making ZI and ZR into four arrays each, and carefully deciding which quadrant was needed throughout the program, a pair of 225 by 225 arrays were hatched. This probably sounds trivial, but it took me a pretty long damn time to find all of the typos and stupid errors. Fortunately, QuickBASIC does not require line numbers, but works merrily along if you want to leave the original ones in and just "wing-in" the new number-less lines. This means that you don't have to go crazy renumbering lines and squeezing in changes. There are 12 references to ZI and ZR in MININEC3 that required insertion of new code to compare the array subscripts to determine which of the four quadrants of the new big array (virtual) is accessed. It was not possible to use full 64 kbyte arrays everywhere to yield a 256 by 256 array. Nasty messages such as "CRITICAL MEMORY ERROR" began to appear after long compile and link operations. This means you're in BIG trouble and need to reduce the memory requirements in the code before starting the operation over again. You can really shoot up a weekend debugging these big programs since compiling and linking take a long time using floppies. By the way, it is

not possible to use the compile in memory feature of QuickBASIC for this program since the memory resident screen editor code steals too much memory. Compiling to memory is fast (like Turbo Pascal) but wont cut it for this application. It is necessary to do the whole operation to and from disk files with the /O compiler switch. A Winchester disk really shows its value here.

By trial and error I found that four arrays of 125 x 125 (ZI and ZR), 125 x 100 (ZZR, ZZI), 100 x 125 (ZRR, ZII), and 100 x 100 (ZZII, ZZRR) worked nicely to yield the 225 x 225 virtual array. These maximum array sizes may be machine dependent, and will certainly not work if you try to use other memory resident stuff like Sidekick or ramdisks. I don't think newer versions of DOS should take up much more memory than the DOS 2.11 that I use, but it is certainly possible that your PC with a different DOS version might not like these array sizes, or it may beckon to you to go for more pulses and make the arrays bigger. Be aware that doubling the number of pulses for an antenna problem quadruples (or worse) the execution time. A small price to pay for the ability to do such large antennas on the measly PC! A 31 element yagi analysis using 8 segments per element takes 4 hours and 38 minutes on a system using an 8087-2 at 7.16 MHz. The results agree reasonably well with those obtained by actual measurement. There are some areas of concern, however, which will be discussed subsequently.

When the program with the modifications was first tested, significant difficulties were evident, it was not possible to get a pattern at all like that obtained by measurement. This was probably good, as I may not have found several typing errors even yet if the lousy results hadn't forced me to check for bugs and serpents about 10 times. It's difficult to check and recheck a program which you typed yourself and especially one which is as redundant as the quadrant detection-comparison routine for four subscript variables (16 combinations which all look alike after a while). The > and < symbols all look alike after a while.

The antenna used as a bench mark is a 31 element yagi for the amateur 432 MHz band. It was designed by Steve Powlishen (K1FO) and

Joe Reisert (W1JR), and was published in Ham Radio magazine (reference 5). The boom length is 24 feet long, which significantly exceeds anything commercially available in both size and performance. The design is based on the work of a German amateur, Gunter Hoch (DL6WU). His technique for using a logarithmic taper for the director lengths has proven highly effective and is the antenna-to-beat in the long yagi circles today.(2) Previous experimenters had falsely concluded that there was a point of diminishing returns for boom length beyond which little or no improvement in gain was possible. This can be the case, if one restricts himself to equal director lengths which many of the predominant yagi experimenters have done. There are, in fact, infinite numbers of combinations of structure geometry which will yield a prescribed phase velocity per unit length. It is much easier to work with one parameter fixed and vary the other, if one is to minimize the effort required to develop a valid yagi synthesis procedure as Mr. Hoch has done. His slow wave structure uses a fixed director spacing for distant directors, but those closer to the driven element are non-uniform. This approach, using closer director spacings near the driven element, has been used in many previous designs to achieve an acceptable wave launching region. Previous workers were apparently unwilling to add another dimension to the problem to the extent that Mr Hoch has done, using variable director lengths and spacings over the length of the structure.

After desperately trying to convince myself that the modified program had no further bugs, I was still getting suspect patterns which had the first side lobes sort of folded in toward the main lobe (Figure 1). The gain appeared to be in error as well (20.7 vs 19.4 dBi). The patterns obtained by others looked much cleaner in addition to exhibiting more realistic boresight gain. I finally called the designer on the phone to discuss the possibility that some errors crept into the magazine article. After being assured that the dimensions had been triple checked, the problem, at least partly, came to light. The dimensions in the article had been length corrected for the element mounting method used. Different means of attaching the elements can have a profound

effect on performance, and has convinced many that yagis don't work (or are black magic).

Using MININEC3 the only practical way to perform yagi analysis is to place all elements in free space, ignoring boom effects. Then, after a successful design is reached, a conversion to new element lengths is made using empirical data (maybe someone has some analysis techniques for this problem ?). In this case, using insulated elements, the correction factor was determined to be .25 times the boom diameter through many hours of experimentation by Mr. Powlishen. By the way, the push to use insulated elements arises from contact deterioration in the environment when non-insulated elements are used. This can cause a high performance yagi to slowly go south over the years. NBS tech note 688 (8) describes an accurate means of correcting for non-insulated elements. I began reducing the lengths from the Ham Radio article by constant amounts until I arrived at performance similar to that reported in reference 5. I was finally convinced that the modified version of MININEC3 was working, although with some minor problems.

It is always necessary to lengthen the elements to tune out the effect of the boom, unless the elements are insulated and are several boom radii away. The mounting technique used in the article uses plastic shoulder washers to insulate the element from the boom while allowing passage through it. Stainless steel retaining rings hold the elements firmly in place on each side, flush against the plastic washers. It was once thought that this mounting method didn't require a correction factor, but this is not the case. The boom effect is greater if the elements are in direct contact, but the shunt capacitances of the insulated structure are not negligible.

I had to subtract nearly 0.75 inches from each length to get the same results as reported. This is where the results obtained by the modified MININEC3 appear to diverge from reality by a significant, but not prohibitive amount. The author of the article assured me that his dimensions were correct and that the effect of the 1 inch diameter boom was significant, especially at a wavelength of 70 CM where the elements are

not so very long. Some research into the effect of the element mounting method by Steve Powlishen has determined that a correction of about 0.25 inches should have to be applied to the free space dimensions to yield the performance stated in reference 5. The conclusion from this finding is that the modified
program appears to exhibit a frequency shift of about 4 percent. That is, the frequency used for the analysis using MININEC3 should be about 4 percent higher than the actual frequency of interest. Breakall reported a similar phenomenon in reference 6.

A second problem which is evident from the use of this version of MININEC3 is that the calculated gain is approximately 1.3 dB high. The measured results indicate 19.4 dBi for the antenna, and reference 7 indicates 20 dB as an upper limit for this array length. The designer of this yagi agrees that an answer of 20.7 dBi is quite optimistic. Perhaps the use of so many current pulses for the yagi model cause the calculated field to be in error by a larger amount than if fewer pulses were used. This could be explained if the single precision currents were always off in the same direction due to round-off or some other error source.

Antenna pattern calculations fo the 31 element yagi are shown in Figures 1,2,and 3. The correction factors which were applied to the original director lengths are shown just below the title. The pattern of Figure 3 looks enough like that of the pattern from reference 5 to satisfy my concerns about the modified version of MININEC3 operating correctly. The effect of using single precision math, as done in this version of the software may be significant. Double precision would, of course, cut in half the number of segments to be used for the model since we are memory limited to 640 kbytes in the PCs. Hopefully some of the readers will have access to larger machines and can verify the effects of double vs single precision math on the results of a large yagi analysis with 200 plus current pulses. Further experiments are needed to better characterize these problems. Time did not permit comparison of double precision versus single precision results.

Further antenna pattern calculations were made using the NBS 4.2 wavelength yagi as a reference. These results are sh Figures 4,5,and 6. It is evident that difference in peak gain is negligible w 6,8,or 10 segments per element are used. suspected that the nulls between sidelobes would get deeper when more segments were used, but just the opposite was found. Even though the characteristic deep nulls were not produced, all three calculations agree surprisingly well with the measured data in reference 8. The gain calculated by MININEC3 (mod) was only 0.2 dB different from that measured by Viezbickie which lends much to the credibility to MININEC3. From my experience, antenna range measurements are usually more suspect than the computer analysis, but it gives one a good feeling to see both agree this nicely (even with a low cost PC). It is worth noting that the measurements of reference 8 were taken fairly close to ground (within a few wavelengths) which may account for some gain differences. Perhaps the ground modeling of MININEC3 can account for the difference. This is left as an exercise for the student (!).

In summary, a version of MININEC3 is offered which appears to bridge the gap between small antenna problems and large ones. The ability to model large yagis as well as other antennas with more segments can improve the accuracy of pattern calculation and permit the PC to handle problems which previously required a minicomputer. Today expanded memory is cheap, and coupled with the phenomenal price/performance ratio of an 8087 numeric processor new horizons are achieved for those of us who don't have lots of free CPU time on large machines. The version of MININEC3 described shows a few minor problem areas in the frequency offset and in the calculated peak gain. These problems may be partially attributable to the use of single precision by the IBM PC compatible type computer used with QuickBASIC 2.0. Further research is needed into this area, to determine where the computer analysis limitations lie.

A few comments about the modified version of MININEC3 will now be made. If possible, the program will be made available

through the ACES software library. The are a few obstacles remaining here, however. File handling capability was added which allows one to save an antenna file after entering, and to later recall this information from disk. Using a word processor in the non-document mode it is possible to edit the antenna geometry (change element lengths) and subsequently recall the new antenna for analysis saving lots of error-prone typing (at least in my case). Retyping the dimensions of a 31 element yagi can become very error prone after a few runs. A printer must be connected as the program prints out the start time of execution followed by the end time. This is useful when the console (C) output option is selected if you want to go back and marvel at how long a particular problem took to solve.

I am extremely interested in hearing from anyone with ideas for speeding up execution of MININEC3. I am pursuing the use of 8087 matrix handling subrcutines which are commercially available 9, as well as using assembly language to replace pieces of the compiled BASIC code. It appears rather challenging especially since all those arrays were butchered and spread all over memory. It also worthy of note that QuickBASIC does not support the generation of assembly language list files as did the older BASIC compiler. It is, therefore, more difficult to see what can be done to the executable file to enhance its speed. Any suggestions for additional reading and/or methods of 8087 coding, floating point assembly language routines, in-line patches to compiled BASIC, or other means of speeding up compiled BASIC are very much desired. Maybe the Fortran or "C" compilers are far better...comments please?

1 Stanley Jaffin, "Applied Yagi Antenna Design Part 5", Ham Radio Magazine, September, 1984, p 93. pp 75-80.

2 Gunter Hoch, "Extremely Long Yagi Antennas", VHF Communications, Volume No. 14, Autumn 3/1982, pp 130-138.

3 Edmund Miller, "PCs for AP", Antennas and Propagation Society Newsletter, October, 1986, p 30.

4 Li, Rockaway, Logan, Tam, "Microcomputer Tools for Communications Engineering", Chap 4, MININEC, pp 21-52.

5 Joe Reisert, "VHF/UHF World", Ham Radio Magazine, December, 1986, pp 75-80.

6 J. Breakall, ACES Newsletter 2.

7 H.Jasik, Antenna Engineering Handbook, First Edition. p 16-14.

8 P. Viezbickie, "Yagi Antenna Design," NBS Technical Note 688, December, 1976 (available from Superintendent of Documents, U.S. Government Printing Office, Washington DC 20420).

9 87 Software Pak, Hauppauge Computer Works, (8087 Libraries and Linkable Routines for IBM PCs and compatibles; similar software available from MicroWay).

FIGURE 1.

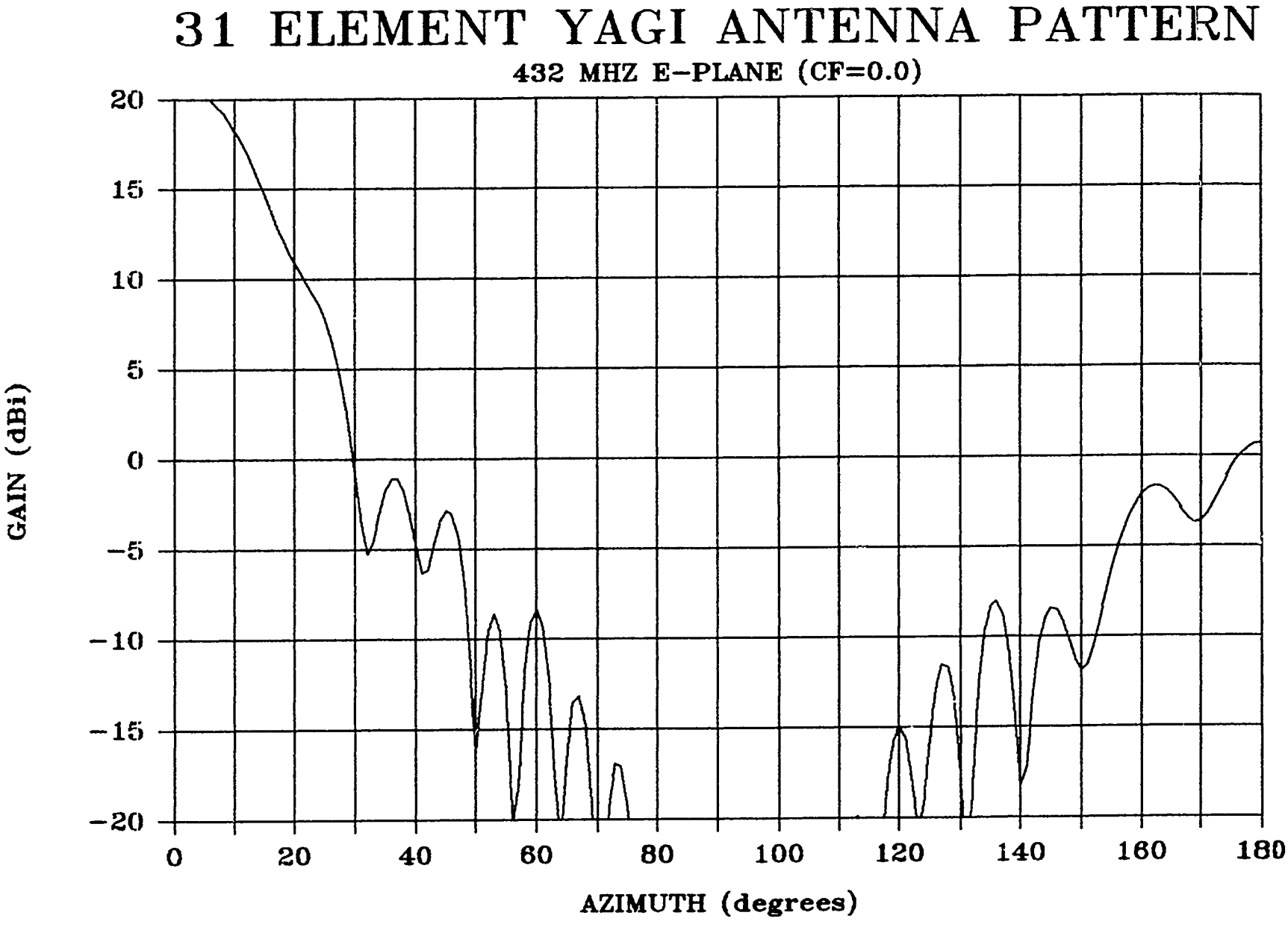

31 ELEMENT YAGI ANTENNA PATTERN
432 MHZ E-PLANE (CF=0.0)
GAIN (dBi)
20
15
10
5
0
-5
-10
-15
-20
0
20
40
60
80
100
120
140
160
180
AZIMUTH (degrees)

FIGURE 2.

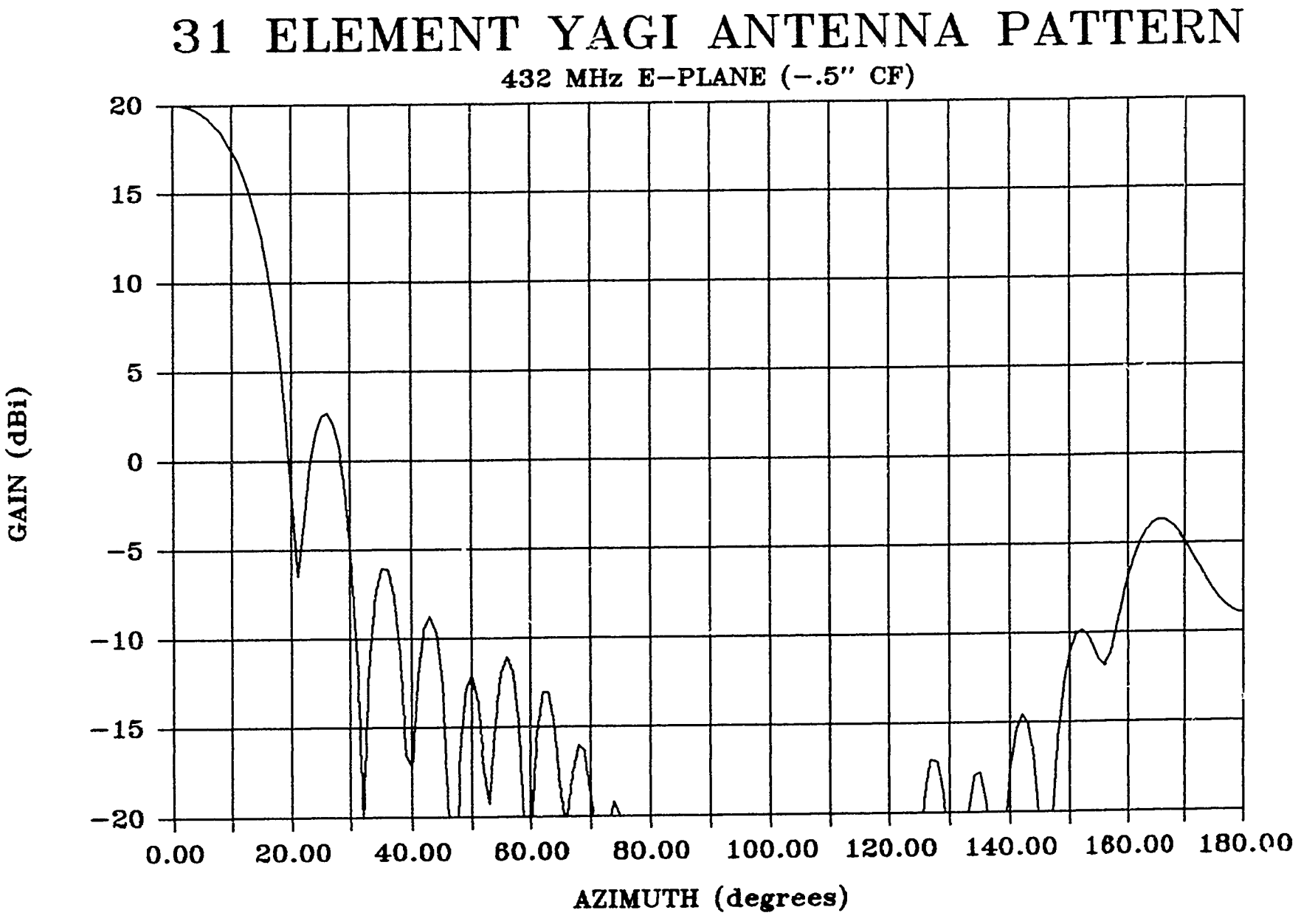

31 ELEMENT YAGI ANTENNA PATTERN
432 MHz E-PLANE (-.5" CF)
GAIN (dBi)
20
15
10
5
0
-5
-10
-15
-20
0.00
20.00
40.00
60.00
80.00
100.00
120.00
140.00
160.00
180.00
AZIMUTH (degrees)

FIGURE 3.

31 ELEMENT YAGI ANTENNA PATTERN

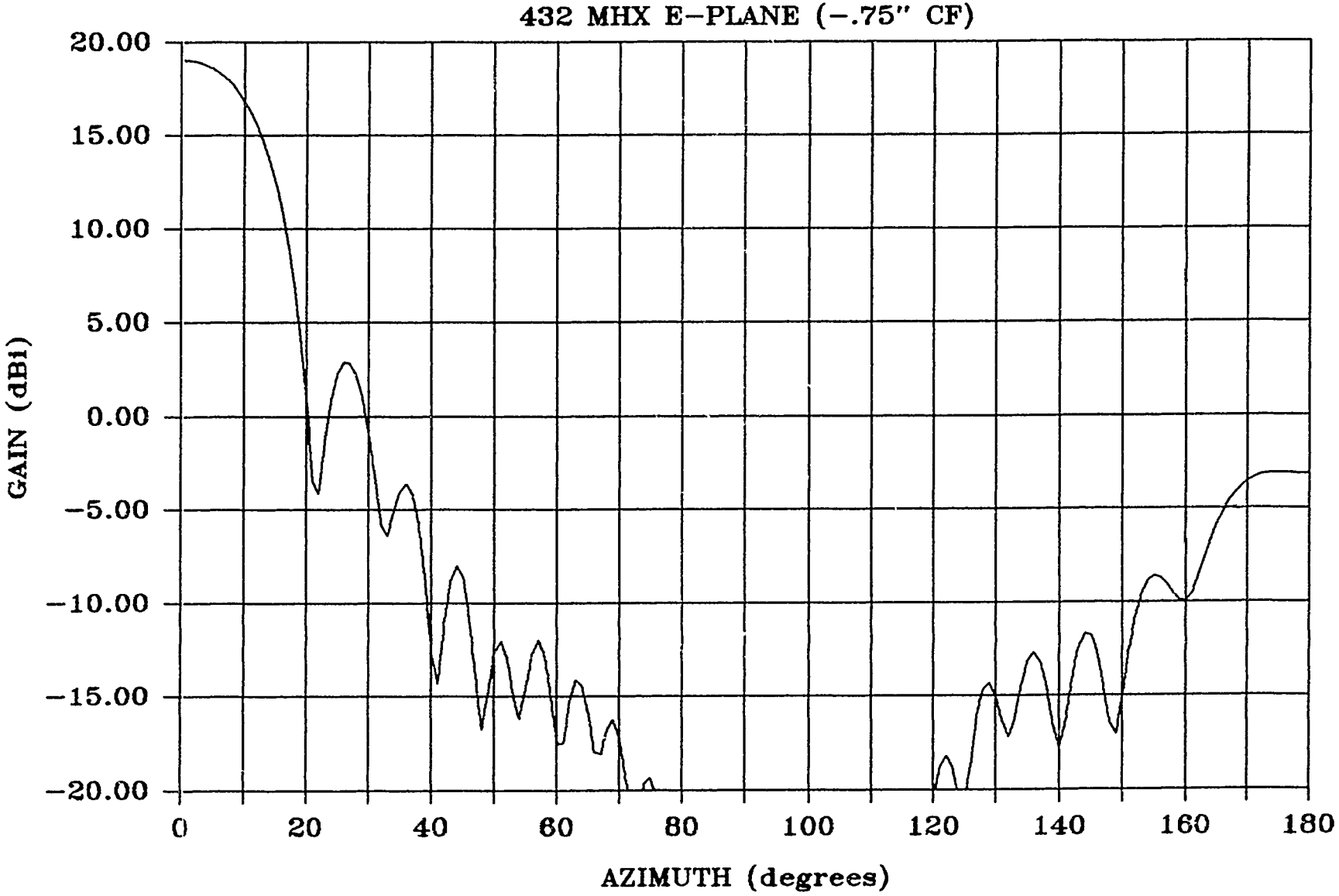


FIGURE 4.

NBS YAGI ANTENNA PATTERN (4.2 lambda)

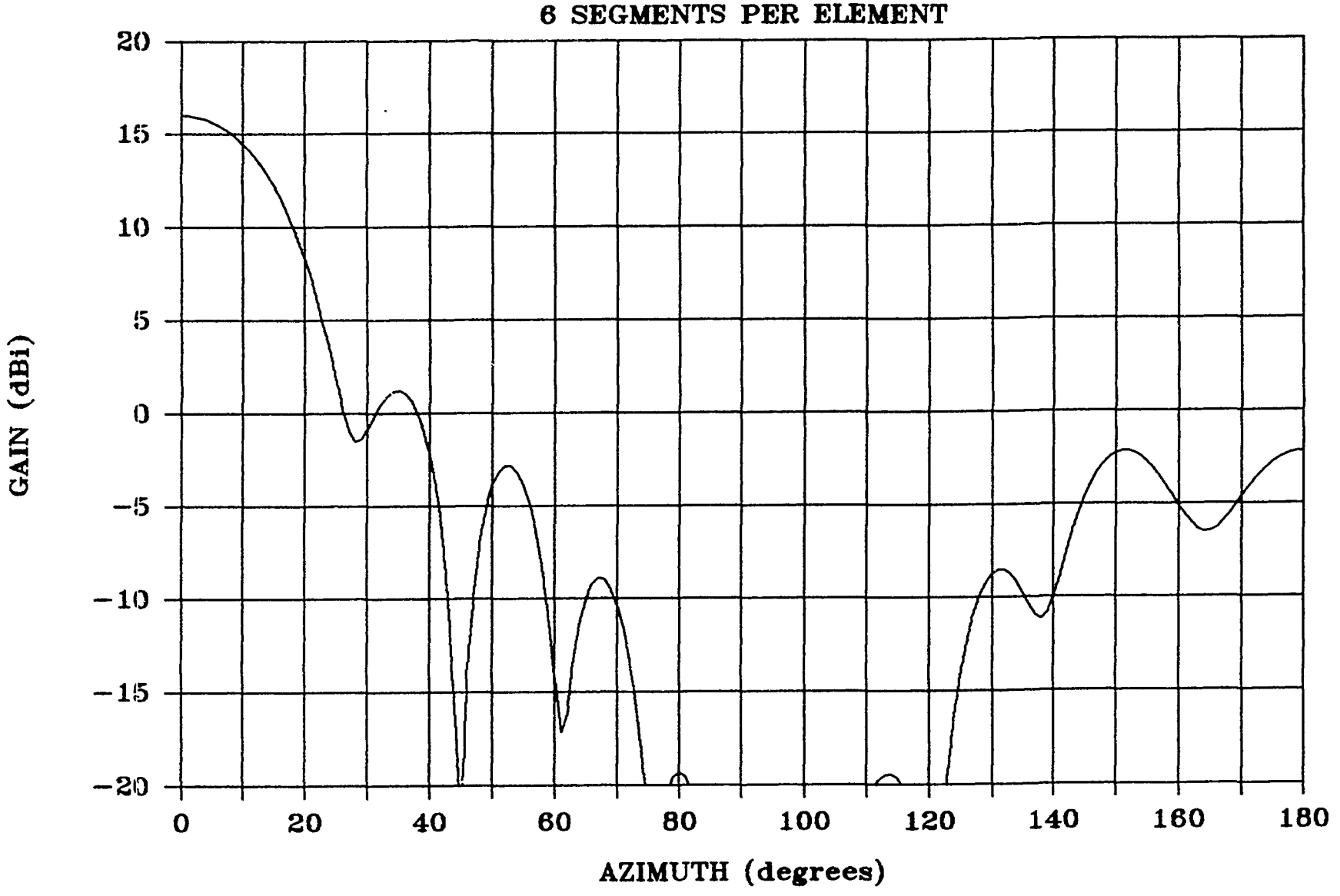


FIGURE 5.

NBS YAGI ANTENNA PATTERNS (4.2 LAMBDA)

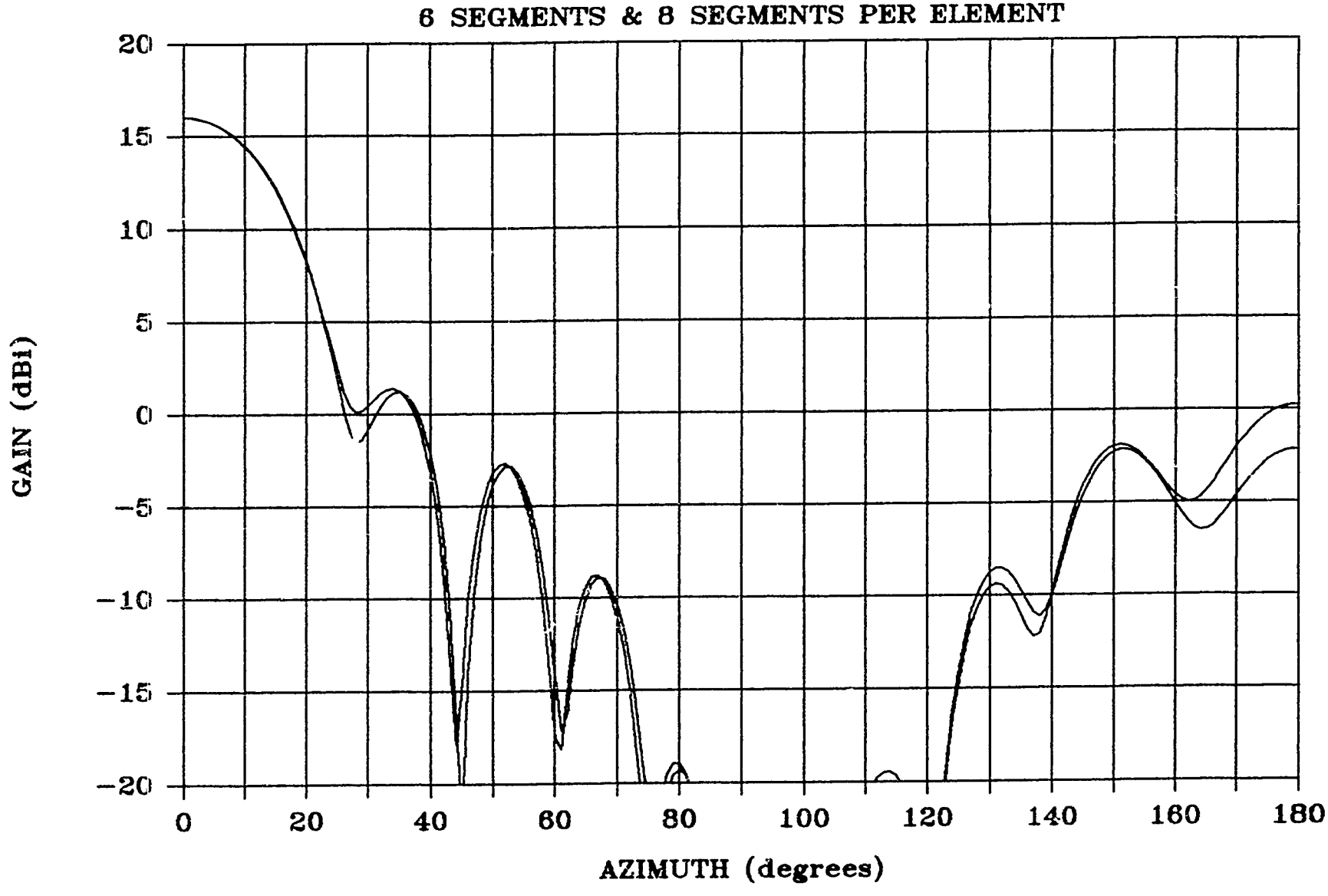
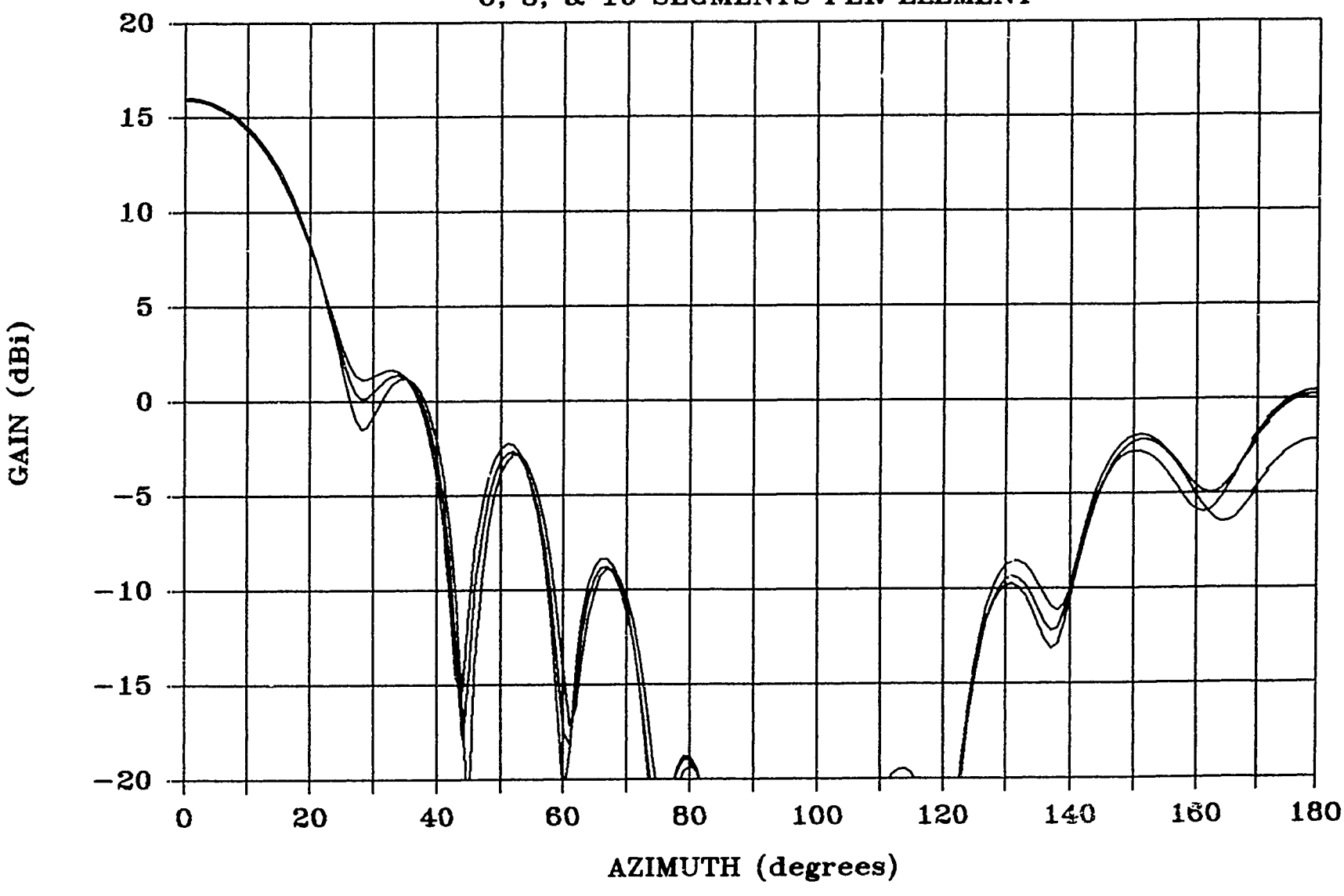


FIGURE 6.

NBS YAGI ANTENNA PATTERNS (4.2 lambda)



THE QUAD LOG-PERIODIC ANTENNA

C. C. Smith
Kaman Sciences Corporation
P. O. Box 7463
Colorado Springs, CO 80933

M. Baron
Technology for Communications International
34175 Ardenwood Blvd.
Fremont, CA 94536

ABSTRACT

A log-periodic sequence of one-wavelength loops may be driven to form a log-periodic array. A study was undertaken using NEC2 to analyze a number of such designs in order to make a set of design curves. An actual example of a practical design was analyzed using method of moments codes. Higher gain and less interaction of broadside arrays of QLPs for a given spacing make such antennas attractive for certain applications. Several ideas for future investigation are mentioned.

INTRODUCTION

The original quad, consisting of a one wavelength loop and a slightly smaller director in a Yagi-type array, was developed by an amateur, Moore, W9LZX [1]. The quad log-periodic (QLP) described in this paper is a log-periodic sequence of one wavelength square loops. The conventional method of connecting the elements through a single transposed transmission line has been reported as having deficiencies leading to VSWR excursions [2].

These deficiencies are reportedly solved by feeding the quad loops with two transmission lines situated on opposite sides of the loop and ties in parallel at the drive point. This method results in two log periodic dipole arrays being driven in parallel, joined at the ends of the dipoles. This approach is patented by Collins Radio Company (U. S. Patent 3,279,159 [3]).

A systematic appr ach was undertaken to determine if the reported deficiencies were inherent to the quad log-periodic design or the result of improper design parameters. Analysis of a large number of designs was undertaken using NEC2. An initial study of this type most often points out the desirability of choosing some other set of parameters for study - but hindsight is clearer than foresight. This study is no exception and further work remains to be done.

DESCRIPTION OF THE QUAD LOG-PERIODIC ANTENNA

Figure 1 illustrates the basic quad log-periodic antenna. A scaling parameter, tau, is the ratio of the size of an element to the next smallest element. This is similar to the definition for

conventional LPDA antennas. The geometric sequence of element sizes converges to a point in space called the virtual apex. As is conventional in studies of log-periodic antennas, the virtual apex is placed at the origin of the coordinates. Thus if one element is situated at a distance x from the origin, the next nearest will be at tau times x.

LPDA antennas are further defined by an angle (alpha) that the line of the tips of the dipoles makes with the X-axis. In like fashion, the QLP antennas may be described by an angle, denoted C, which has been arbitrarily chosen as the angle that the line of corners makes with the X-axis. Tau and C, then, describe the logarithmic sequence of the antenna. To completely describe a particular QLP antenna, the dimension of the largest and smallest elements must be given. For this study, the dimensions were chosen so that the largest element was a full wavelength at 13Ø MHz. The smallest element was chosen to be the size just larger than a full wavelength at 26Ø MHz as permitted by the log periodic sequence. The antennas are in free space.

DESCRIPTION OF THE IMPROVED FEED QLP ANTENNA

Figure 2 shows an improved method of feeding the QLP antenna. Each element is fed on one side and the feed to the next element is taken from the opposite side. All elements are fed on the same side (the "bottom") and the transmission line is not transposed. All descriptive parameters are as defined for the basic QLP antenna, though the particular 2:1 range of frequencies happened to differ and an optimized choice of tau and C was chosen.

This method of feed was investigated by one author, Baron, who found that it provides more uniform gain and better VSWR properties than the basic QLP antenna.

DESCRIPTION OF ANALYSIS

The investigation of the basic QLP antenna was a systematic variation of tau, C, and the characteristic impedance of the transmission line "feeder" connecting the elements. It should be noted that the reference impedance for the VSWR calculation may differ from that of the transmission line connecting the elements.

The values of tau studied were Ø.8Ø, Ø.85, Ø.9Ø, and Ø.95. The angle C was 5, 1Ø, 2Ø and 3Ø degrees. The feeder ZØ values were 75, 15Ø and 3ØØ ohms. NEC2 input was generated by a FORTRAN program written for this purpose. This not only simplified the process of generating an input deck for NEC2 but was not subject the errors that manual data generation would produce.

DESCRIPTION OF RESULTS

The results for the calculations, performed in single precision, are shown in Figures 4 through 15. The gain versus frequency is shown for each combination studied. A VSWR plot versus frequency

is also shown. The choice of reference impedance for a VSWR plot is not obvious. The best solution would have been a Smith chart plot of the input impedance, since any natural grouping of impedances would have been obvious. However, a suitable graphics routine was unavailable at the time Figures 4 - 15 were prepared. Rather, the VSWR for each combination of tau, C and ZØ was computed referred to a series of impedances. They were chosen to be easy to attain in practice: 5Ø, 75, 1ØØ, 15Ø, 2ØØ, 4ØØ and 6ØØ ohms. The plot to be shown was then chosen from that which gave the lowest sum of the VSWRs over the frequency range. This is a rather arbitrary choice; other methods may be better suited.

CONCLUSIONS

An examination of the figures certainly verifies that a random choice of parameters is likely to give poor results. Yet certain combinations of parameters produce reasonable results. For example, a tau of Ø.9Ø or Ø.95 with a C of 5 degrees and feeder of 3ØØ ohms works reasonably well. This is a region of parameter space that bears further investigation. Other areas appear promising as well. For a tau of Ø.85, a C of 3Ø degrees and an impedance of 15Ø ohms is also a reasonable choice.

Figure 3 shows the results of the improved feed. The gain is reasonable at about 8 dBi (free space) and the VSWR is excellent at less than 2.Ø:1 throughout the frequency range. Clearly this is a technique that needs further investigation. It is hoped that model may be constructed for verification of the computer results.

A late result that is not shown graphically is an investigation of the geometry of the improved feed antenna but with conventional feed. The VSWR degraded to about 2.5:1 and the reference impedance shifted from 2ØØ ohms to 3ØØ ohms. However, the gain improved by about 2 dBi.

This study has shown that the quad log-periodic antenna may yet prove to provide high gain and a broad bandwidth. The geometry is such that the width of a QLP antenna is half that of the LPDA with the same low frequency. This permits closer spacing, or alternativly, less coupling for a given center-to-center spacing. Further research is certainly justified by the results obtained to date.

ACKNOWLEDGMENTS

The authors wish to thank Technology for Communications International, the Naval Surface Weapons Center, and Kaman Sciences Corporation for their support in making the presentation of this study possible.

REFERENCES

1) The ARRL Antenna Book; thirteenth edition; The American Radio Relay League; 1974; p 158

2) Fisher, Jim; The ARRL Antenna Compendium; The American Radio Relay League; 1985; p 51

3) Fisher, Jim; *op. cit.*

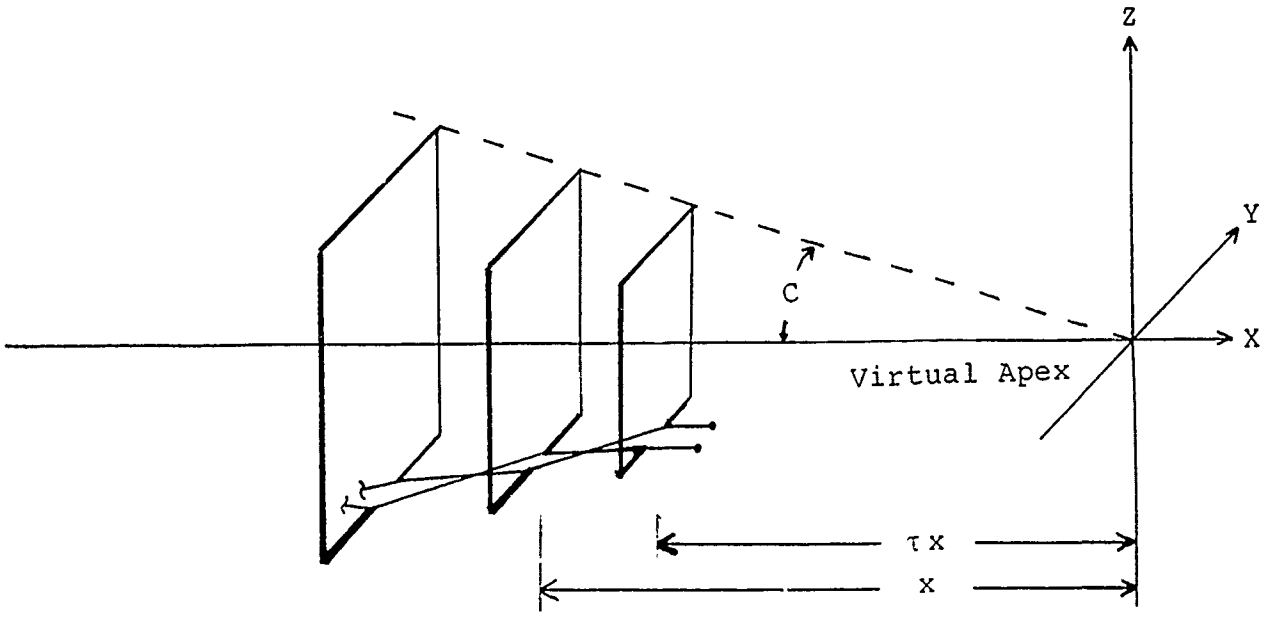


Figure 1. Quad Log-Periodic Antenna

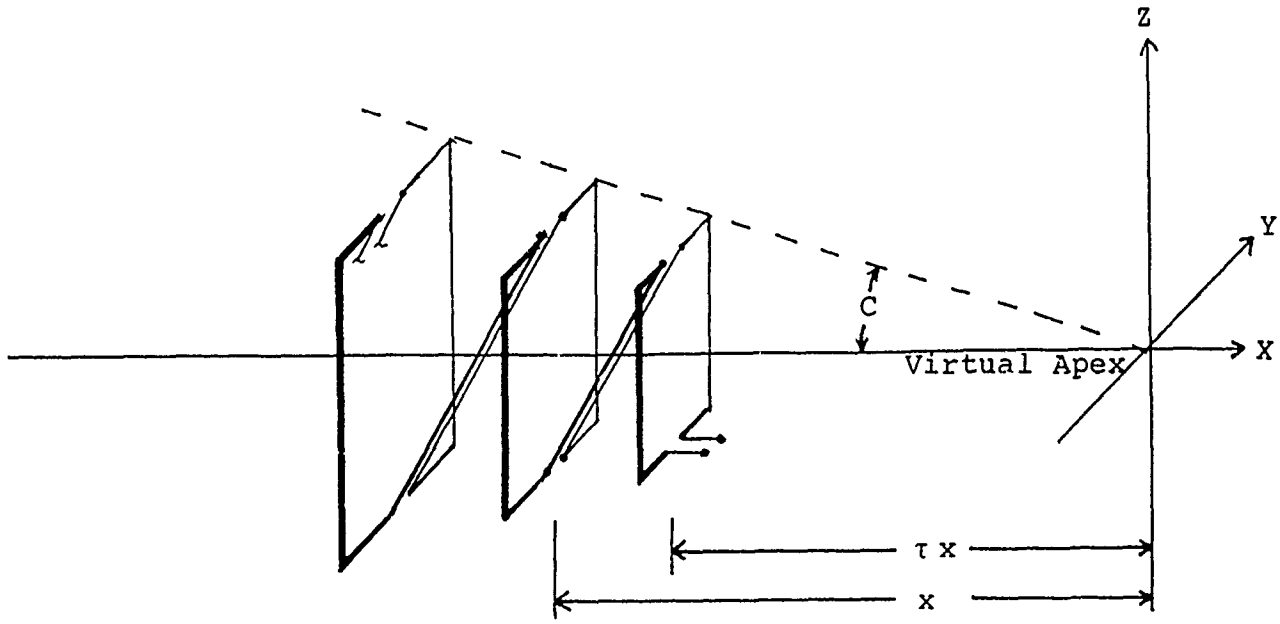
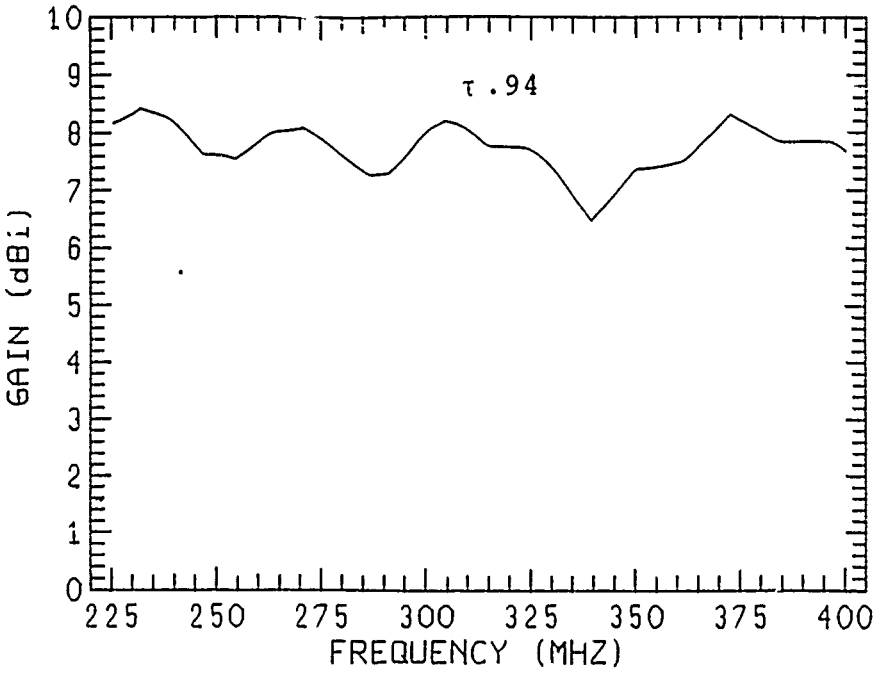


Figure 2. Quad Log-Periodic Antenna with Improved Feed



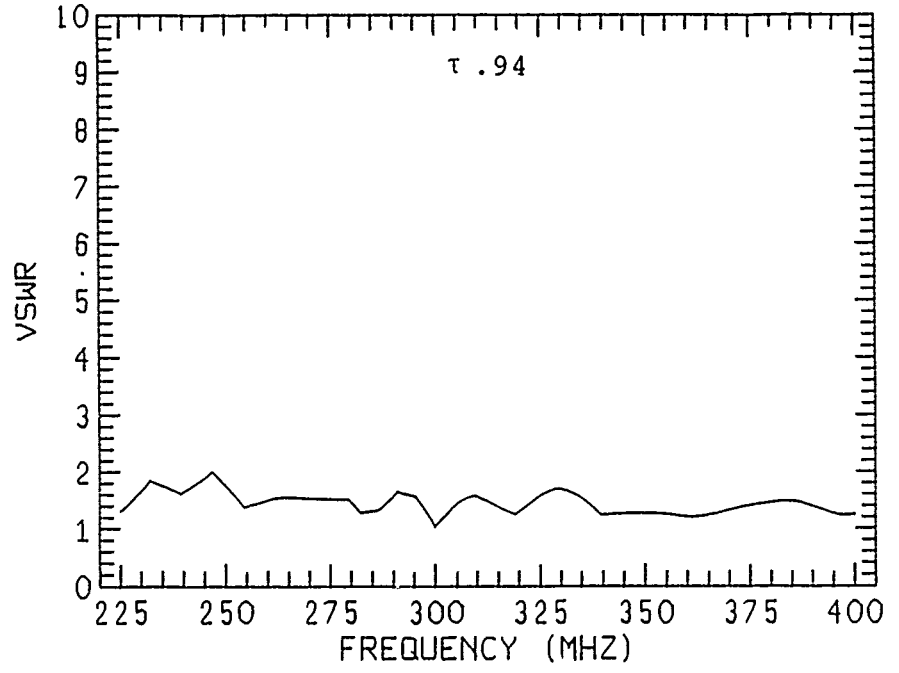
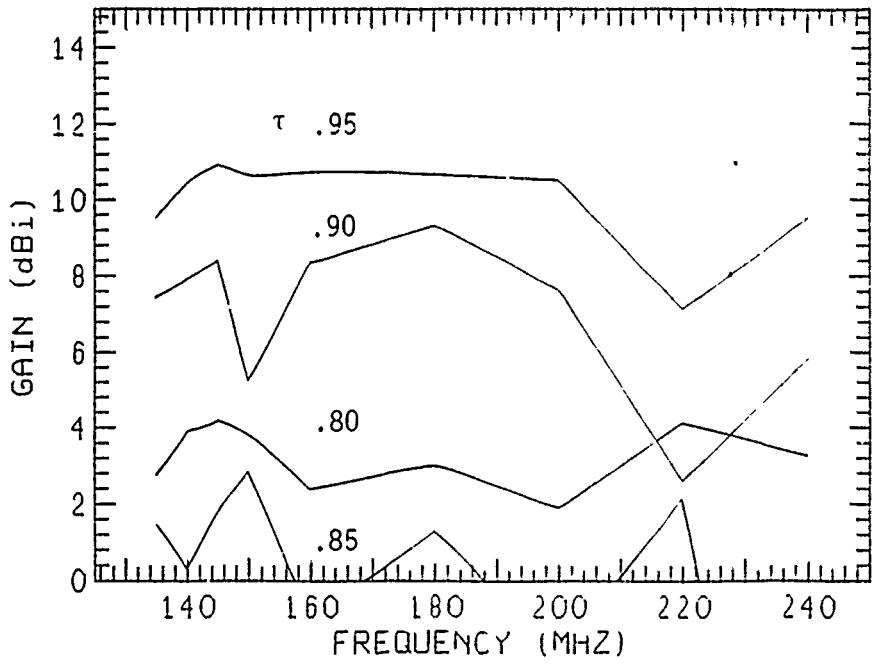


Figure 3. Gain and VSWR, C=3.4°, Z0=500 ohms.



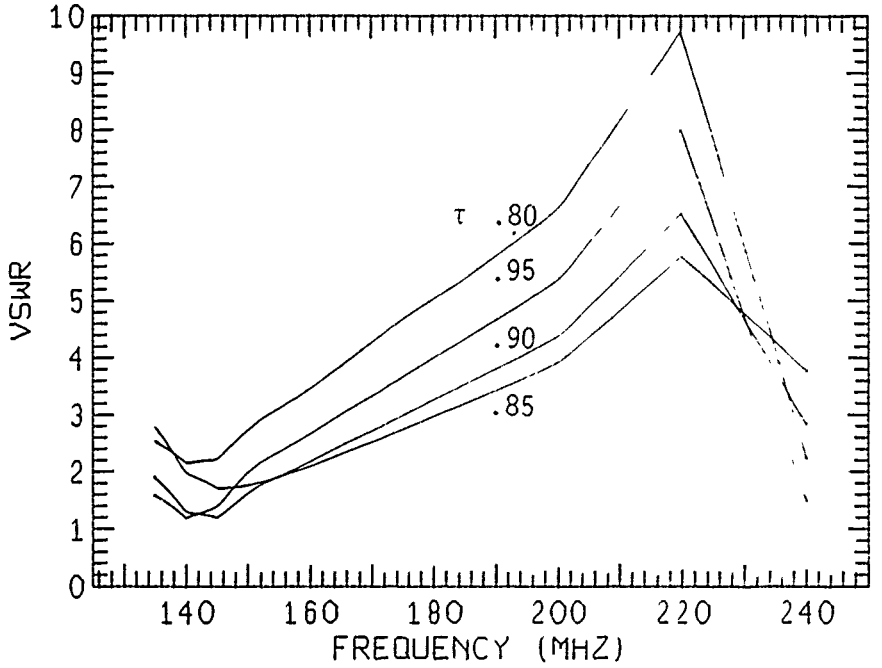
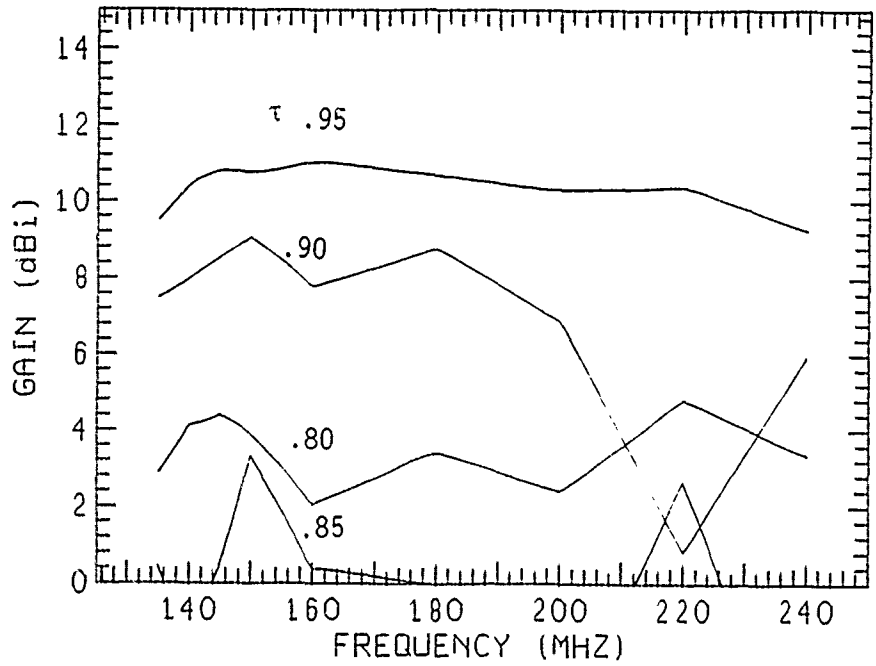


Figure 4. Gain and VSWR, C = 5°, Z0 = 75 ohms.



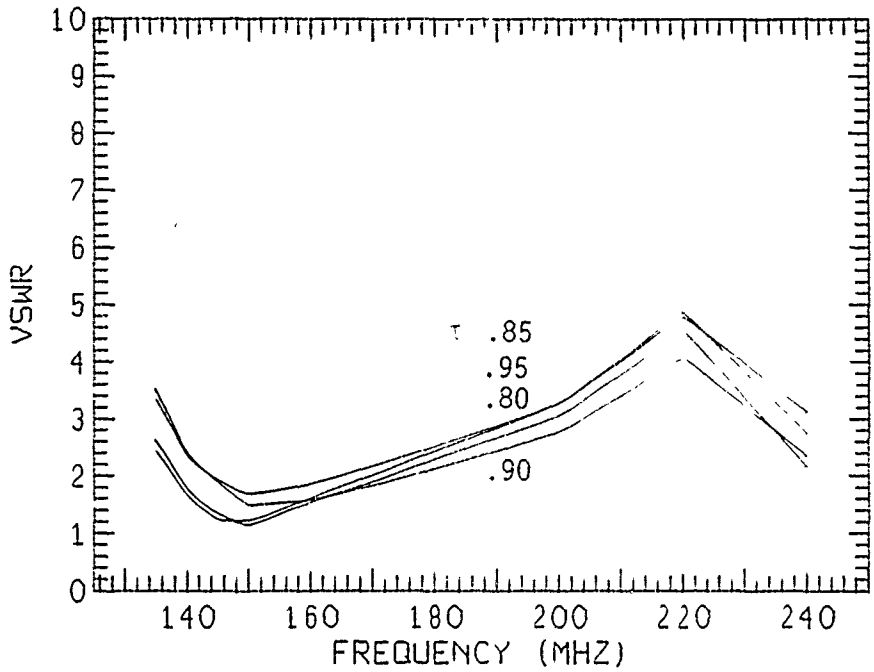
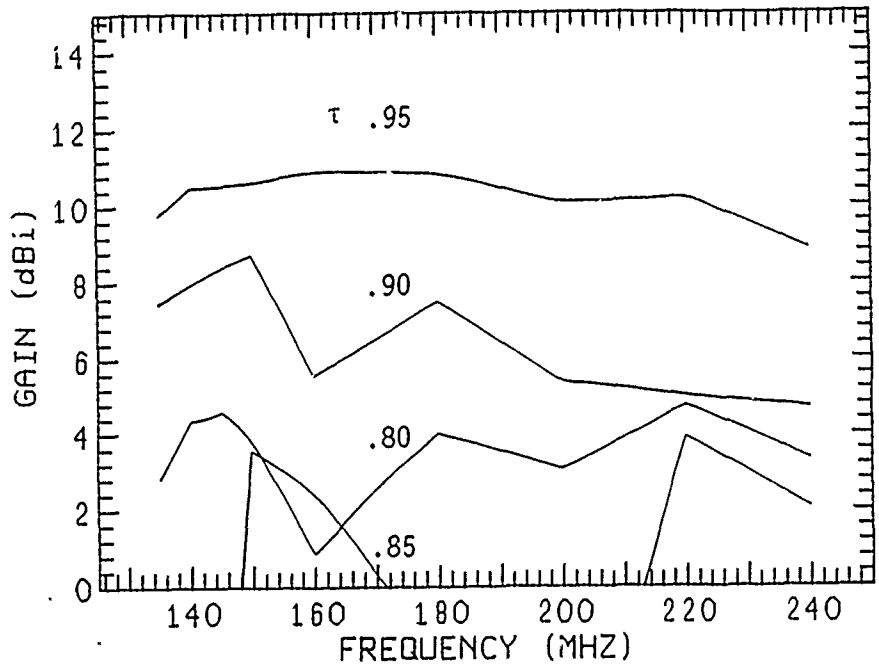


Figure 5. Gain and VSWR, C = 5°, Z0 = 150 ohms.



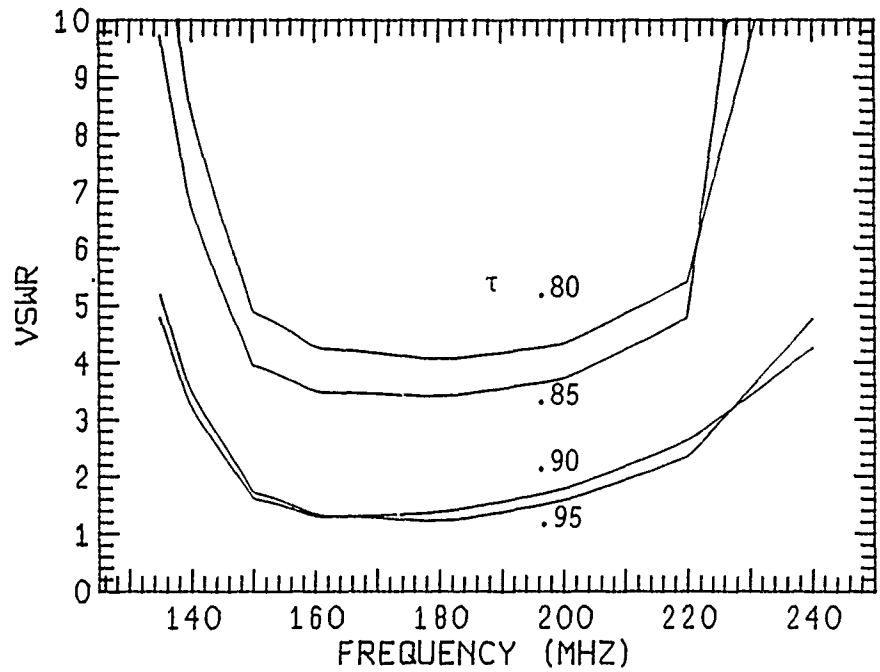
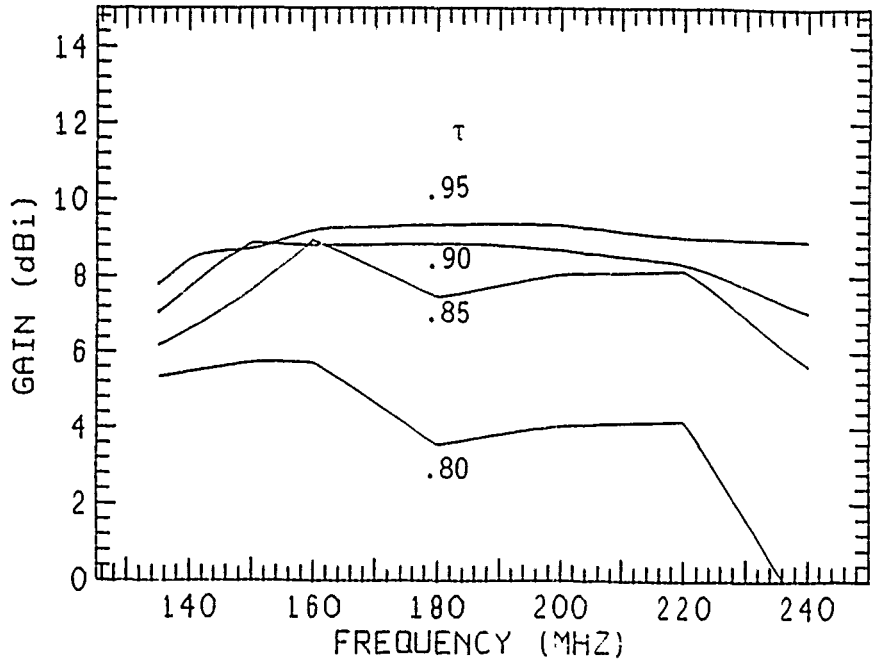


Figure 6. Gain and VSWR, C = 5°, Z0 = 300 ohms.



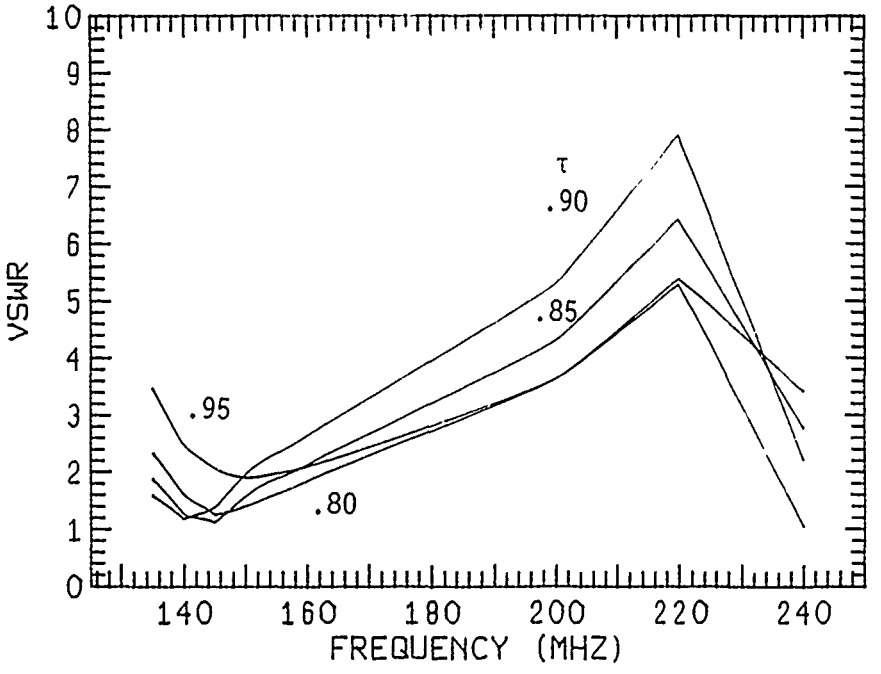
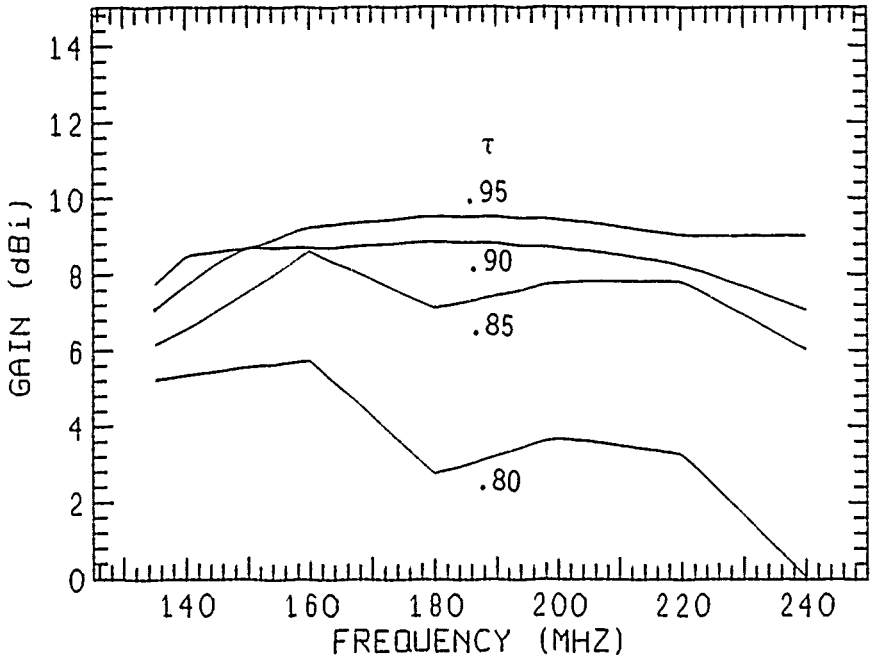


Figure 7. Gain and VSWR, C = 10°, Z0 = 75 ohms.



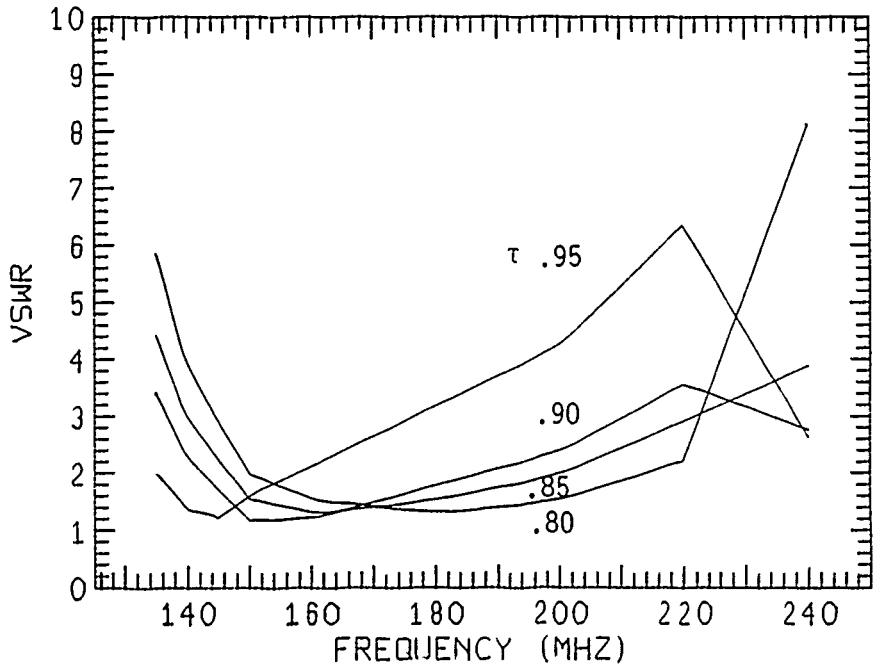
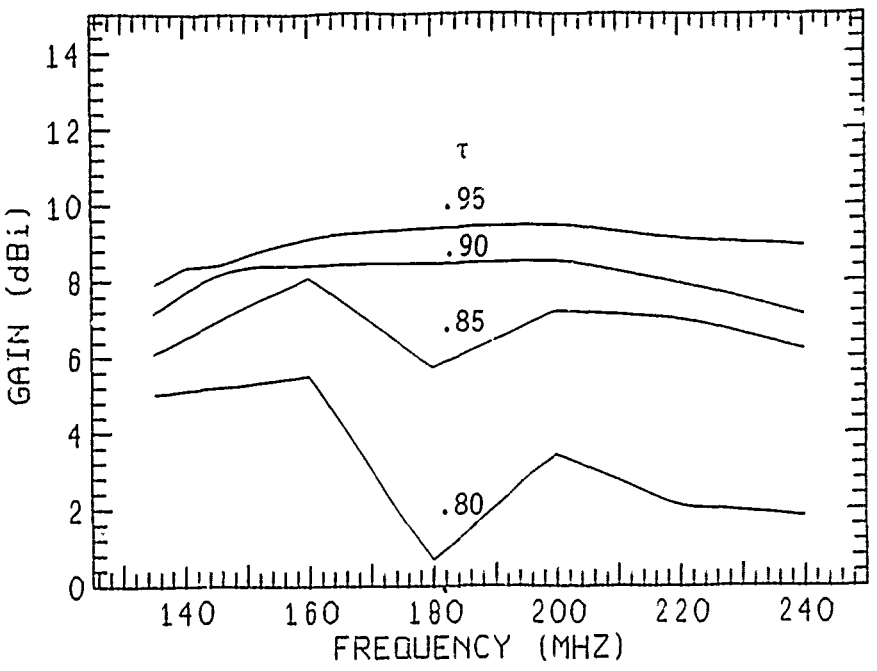


Figure 8. Gain and VSWR, C = 10°, Z0 = 150 ohms.



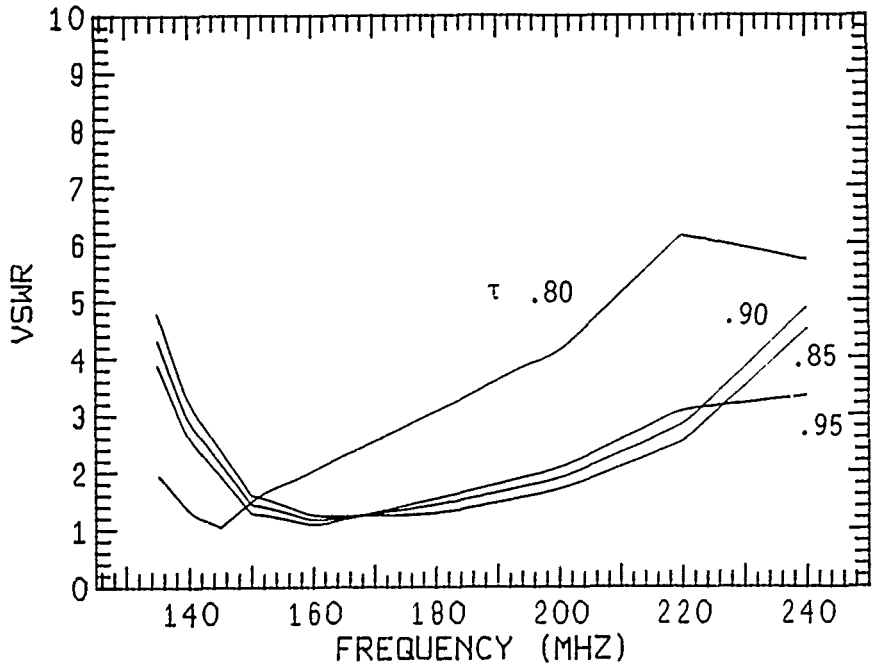


Figure 9. Gain and VSWR, C = 10°, Z0 = 300 ohms.

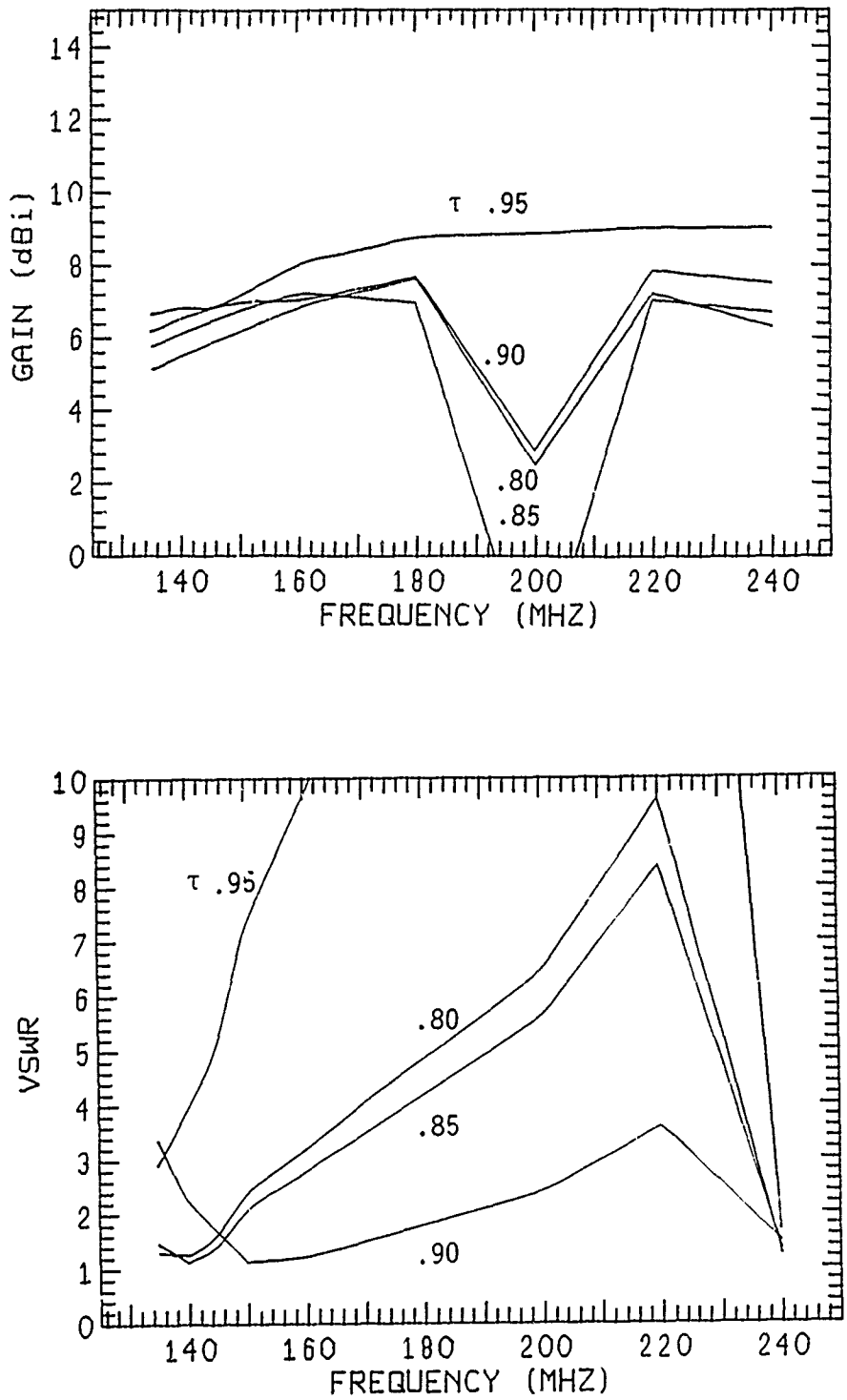
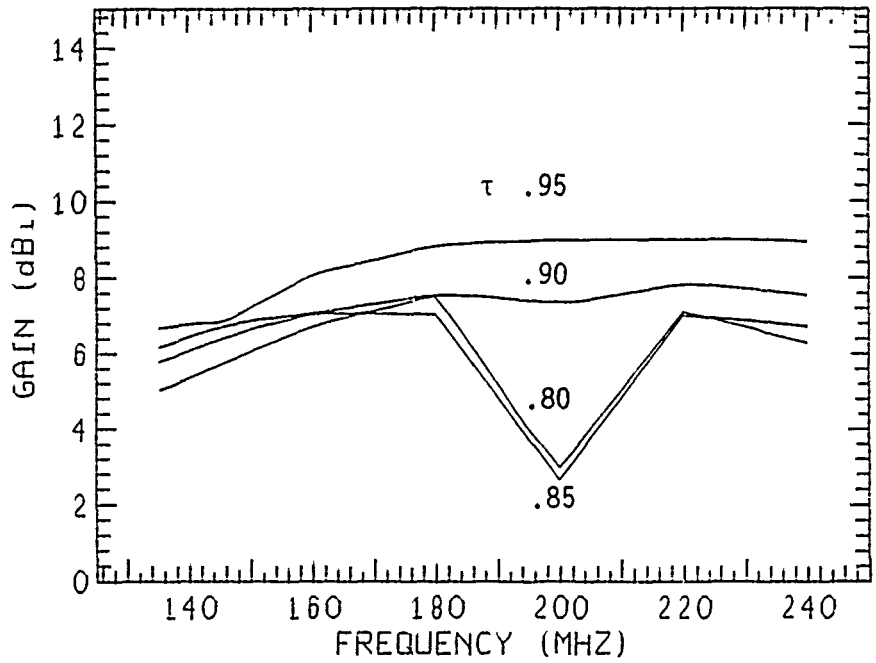


Figure 10. Gain and VSWR, C = 20°, ZO = 75 ohms.



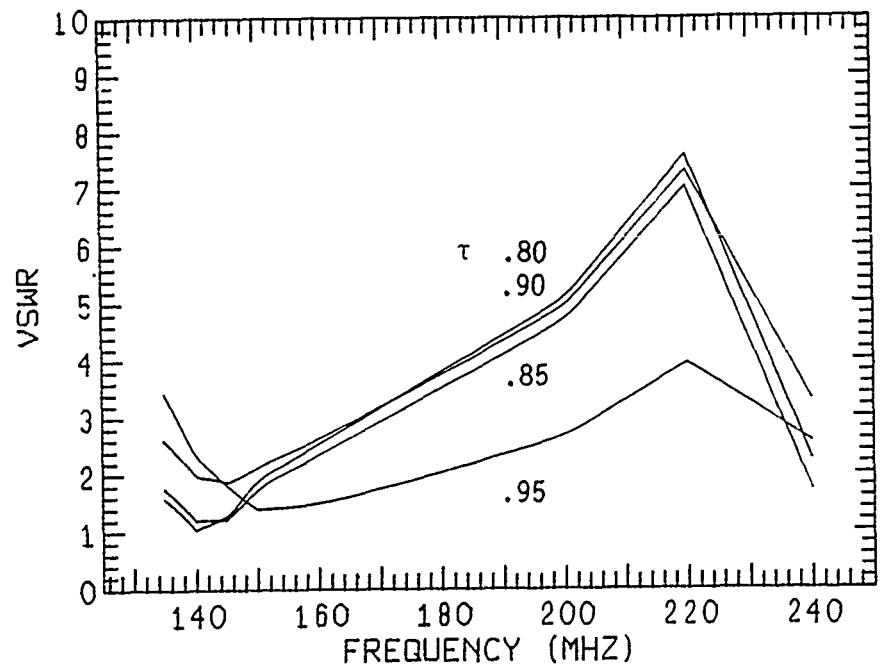


Figure 11. Gain and VSWR, C = 20°, Z0 = 150 ohms.

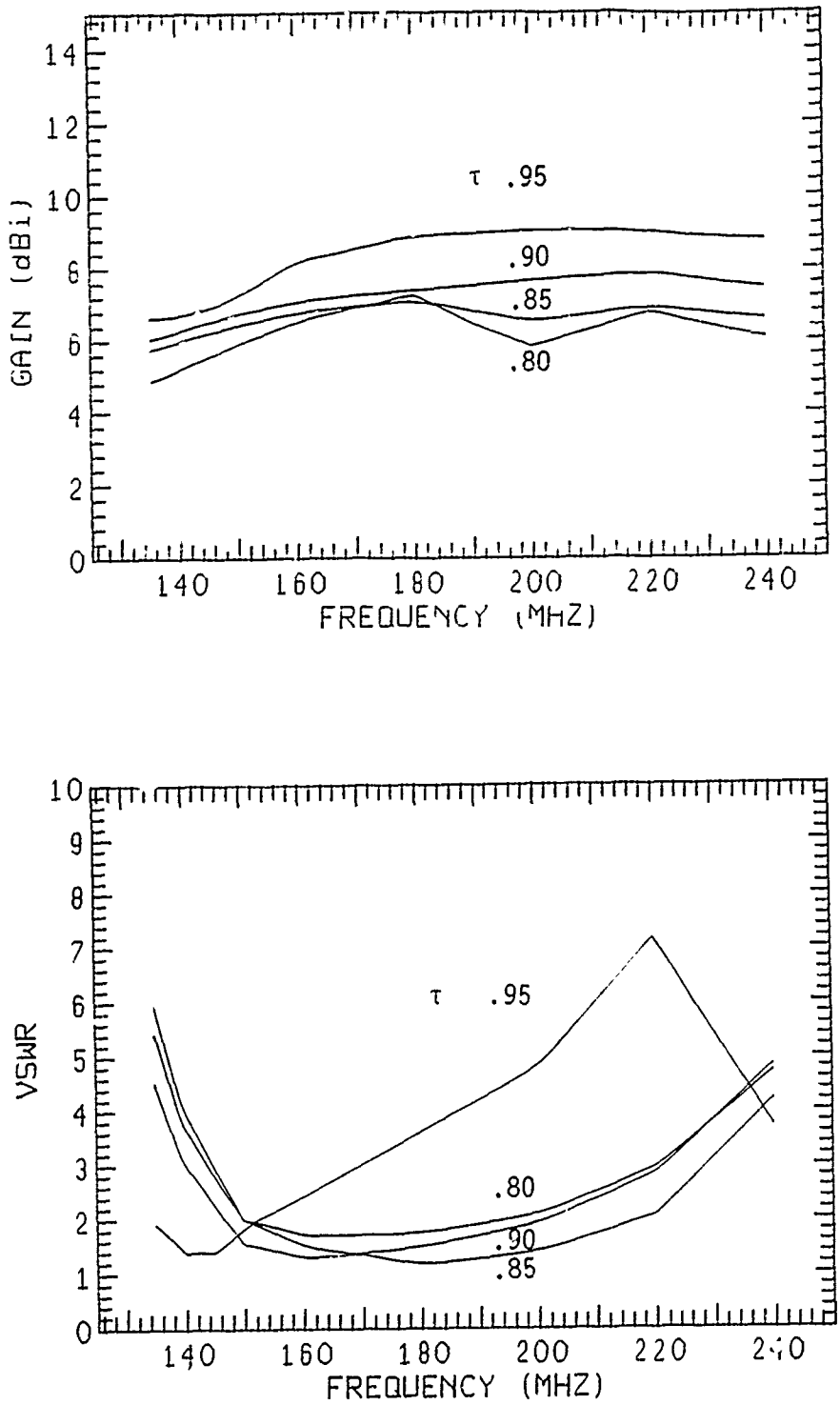
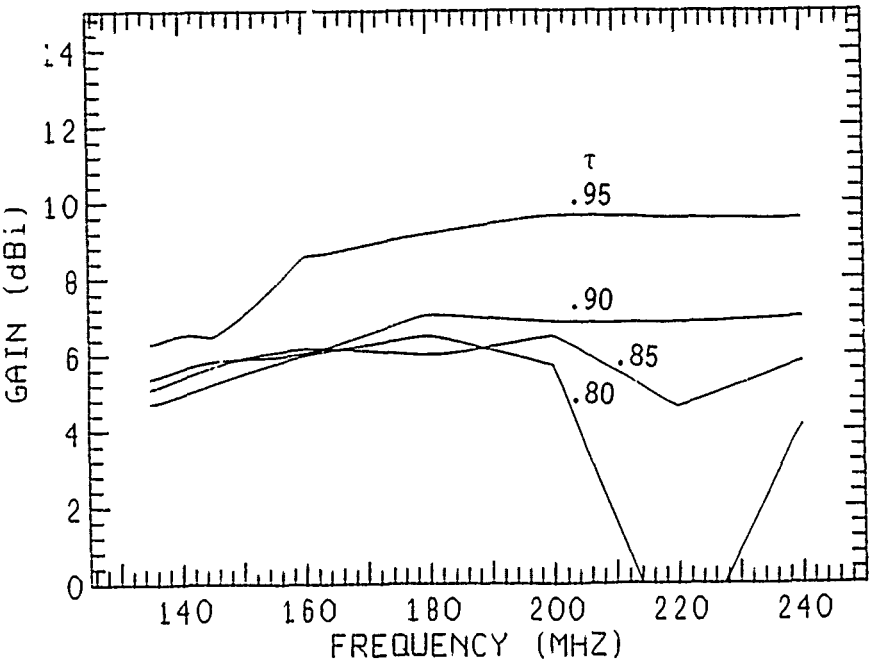


Figure 12. Gain and VSWR, C = 20°, Z0 = 300 ohms.



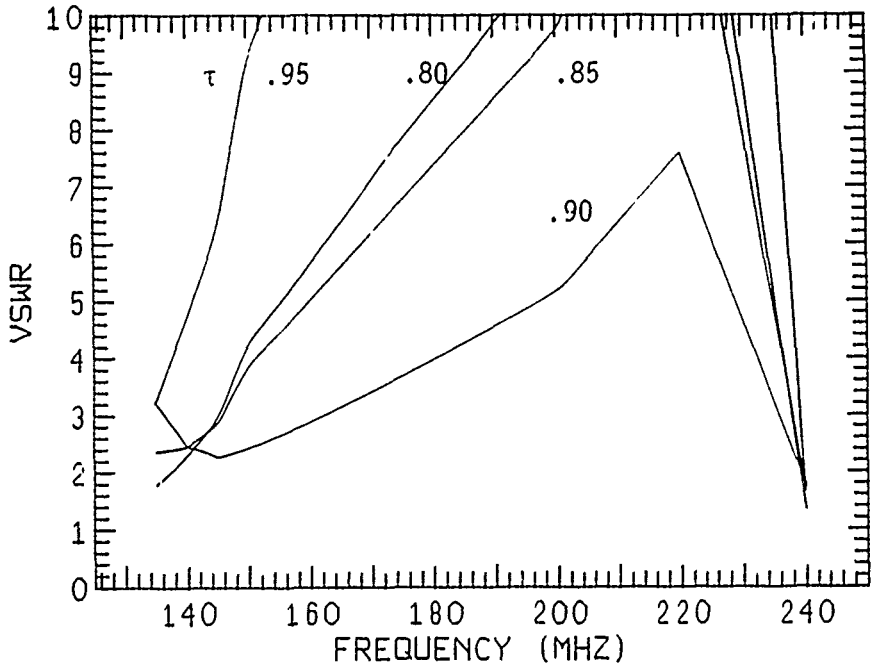
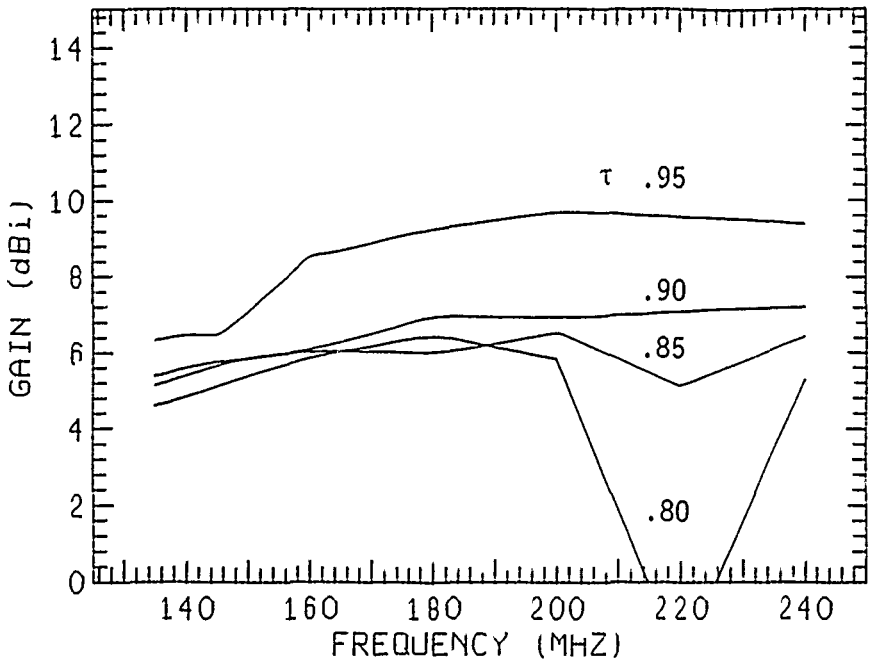


Figure 13. Gain and VSWR, C = 30°, Z0 = 75 ohms.



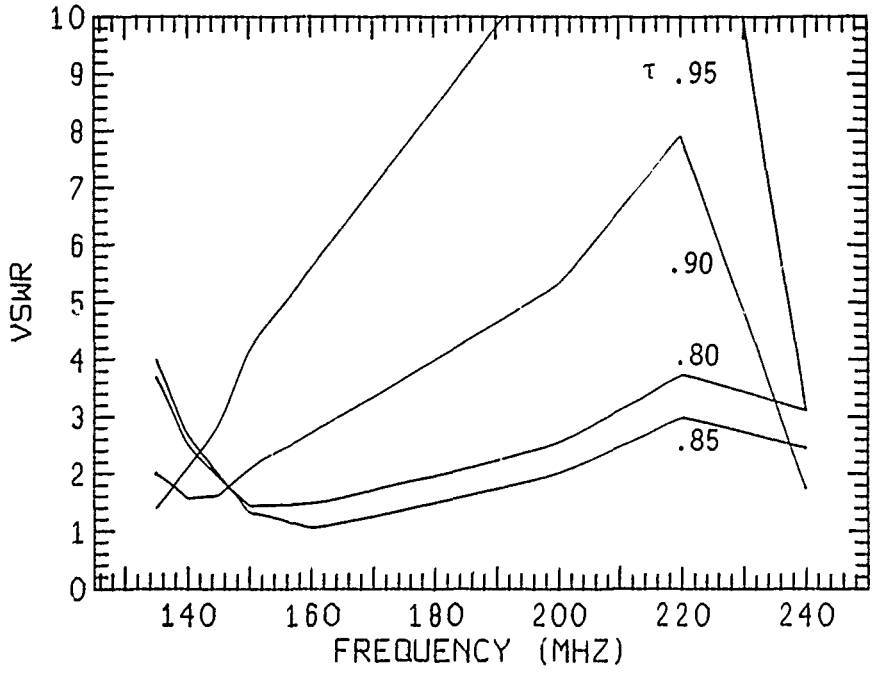
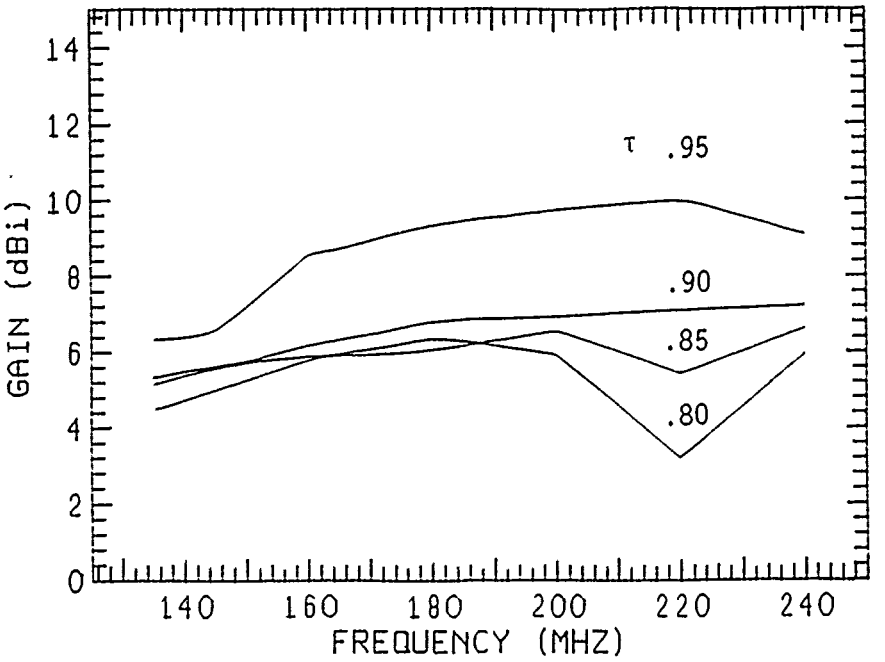


Figure 14. Gain and VSWR, C = 30°, Z0 = 150 ohms.



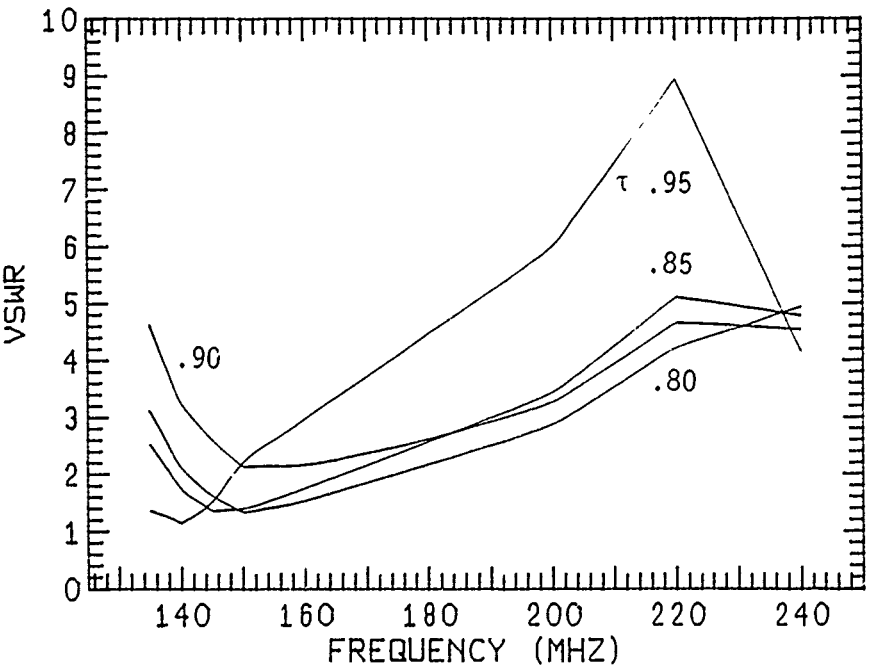


Figure 15. Gain and VSWR, C = 30°, Z0 = 300 ohms.

COMPLEX INPUT IMPEDANCE OF A MONOPOLE OVER A GROUND PLANE

Andy McMahon
Kaman Sciences Corporation
P.O. Box 7463
Colorado Springs, CO 80933

ABSTRACT

Using a vector network analyzer, the complex input impedance of a 2 cm, 4 cm, and 8 cm monopole over a ground plane was measured from 500 MHz to 25.5 GHz in 500 MHz increments. Several different test configurations were used. For each configuration, the measured data is compared with data calculated using NEC. Although not normally used for modeling antennas at microwave frequencies, NEC shows excellent agreement with the measured data.

INTRODUCTION

This paper describes work done at Kaman Sciences Corporation to measure the complex input impedance of monopoles at microwave frequencies. In order to validate our various test configurations, we also examined impedance data calculated using NEC (Numerical Electromagnetic Code). Because of the small wavelengths (60 cm to 1.176 cm) in the frequency band examined, actual measurements are very demanding. NEC proved to be an invaluable tool used for gradually improving the accuracy of our measurement configurations.

NEC ASSUMPTIONS

The antenna parameters used in NEC were developed to model, as closely as possible, the actual monopoles used in the measurements. Three different monopoles (2 cm, 4 cm, and 8 cm) were modeled, each with a radius of 0.39 mm. Each NEC monopole was subdivided into 1 mm segments, and excited with an applied E-Field source on the segment closest to the ground plane. Because each segment's length to radius ratio was only 2.56, the extended thin-wire kernel option was used. The complex input impedance of the monopole was then calculated from 500 MHz to 25.5 GHz in 500 MHz

increments on a DEC VAX 11/750. These calculated impedances were used as a measure of the accuracy of the various test configurations.

MEASURED DATA

A general description of the test configuration is shown in Figure 1. A Hewlett Packard HP 8510 vector network analyzer, configured in the S11 single port mode, was used to measure the real and imaginary values of input impedance. An HP 8340A synthesized sweeper provided an RF source from 500 MHz to 25.5 GHz in 500 MHz increments. The monopole under test was connected to the network analyzer via an HP 8515 S-parameter test set and Wiltron 40 GHz semi-rigid coaxial cable.

An expanded view of Device Under Test (DUT) is shown in Figure 2. The radius of the monopole was chosen so as to fit into the female end of an SMA-compatible connector attached to the end of semi-rigid coaxial cable. The connector was then threaded into the outer housing of a Wiltron flange launcher which in turn was attached to a 1 m x 1 m copper ground plane with nylon bolts. It should be noted that the reference plane for the network analyzer is the plane at which the system is calibrated. In this particular configuration, that plane is the connector/monopole interface, which lies 10.7 mm below the upper surface of the ground plane.

Figure 3 shows a comparison of the measured input impedance of a 2 cm monopole and that predicted by NEC. The data shows little correlation because the reference plane of the network analyzer is not coincident with the surface of the ground plane. To correct this error, we introduced an electrical delay (or reference plane extension) into the network analyzer that compensates for the additional 10.7 mm. The amount of the delay, 81.25 ps, was determined by using simulated Time Domain Reflectometry (TDR) in which the network analyzer performs an inverse Discrete Fourier Transform (DFT) and then shifts the location of the VSWR peak (associated with the surface of the ground plane) to the actual reference plane. After the time domain shift another DFT displays the compensated frequency domain data. This new impedance data is shown in Figure 4. Even though the

correlation is not very good, this figure does demonstrate the importance of compensating data whenever the desired measurement plane is not coincident with the network analyzer's reference plane.

The electrical delay used to generate the data in Figure 4 is assumed by the network analyzer to have been created by a 50-ohm air line. However, the flange launcher housing is not 50 ohms. To compensate for this, the dimensions of the housing are used with standard transmission line equations to more accurately calculate the change in input impedance caused by the reference plane/ground plane separation.

If we assume a lossless line, then the characteristic impedance (Z_o) of any section of the housing is:

$$Z_o = \frac{1}{2\pi} \sqrt{\frac{\mu}{\epsilon}} \ln\left(\frac{b}{a}\right)$$

where μ = permeability
ϵ = permittivity
b = housing radius
a = monopole radius.

The impedance at an arbitrary point B (Z_B) can be calculated from a known impedance at point A (Z_A) by:

$$Z_B = Z_o \frac{Z_A/Z_o - j\tan(k\ell)}{1 - j\, Z_A/Z_o \tan(k\ell)}$$

where $k = \frac{2\pi}{\lambda}$
λ = wavelength
ℓ = length from point A to point B.

Using these equations, the measured input impedance is cascaded through the three distinct regions of the flange launcher housing and the ground plane. The final results of this compensation are shown in Figure 5. As expected, the data compares favorably with that calculated using NEC. Most of the errors associated with this particular configuration can be attributed to the multiple-impedance mismatches in the housing.

In order to further improve the accuracy of our measurements, the first test configuration was modified so the SMA-compatible connector at the end of the semi-rigid coaxial cable attached directly to the ground plane. This located the network analyzer's reference plane flush with the upper surface of the ground plane, so no electrical delay or transmission line compensation was required. The results of this measurement configuration are shown in Figures 6, 7, and 8 for the 2 cm, 4 cm, and 8 cm monopoles respectively. The agreement is very good.

CONCLUSIONS

When making antenna measurements, NEC is an excellent tool for cross-checking the accuracy of measured data as well as the validity of a particular test method. Given the proper modeling constraints on antenna size, NEC can be useful for analyzing antenna measurements at microwave frequencies.

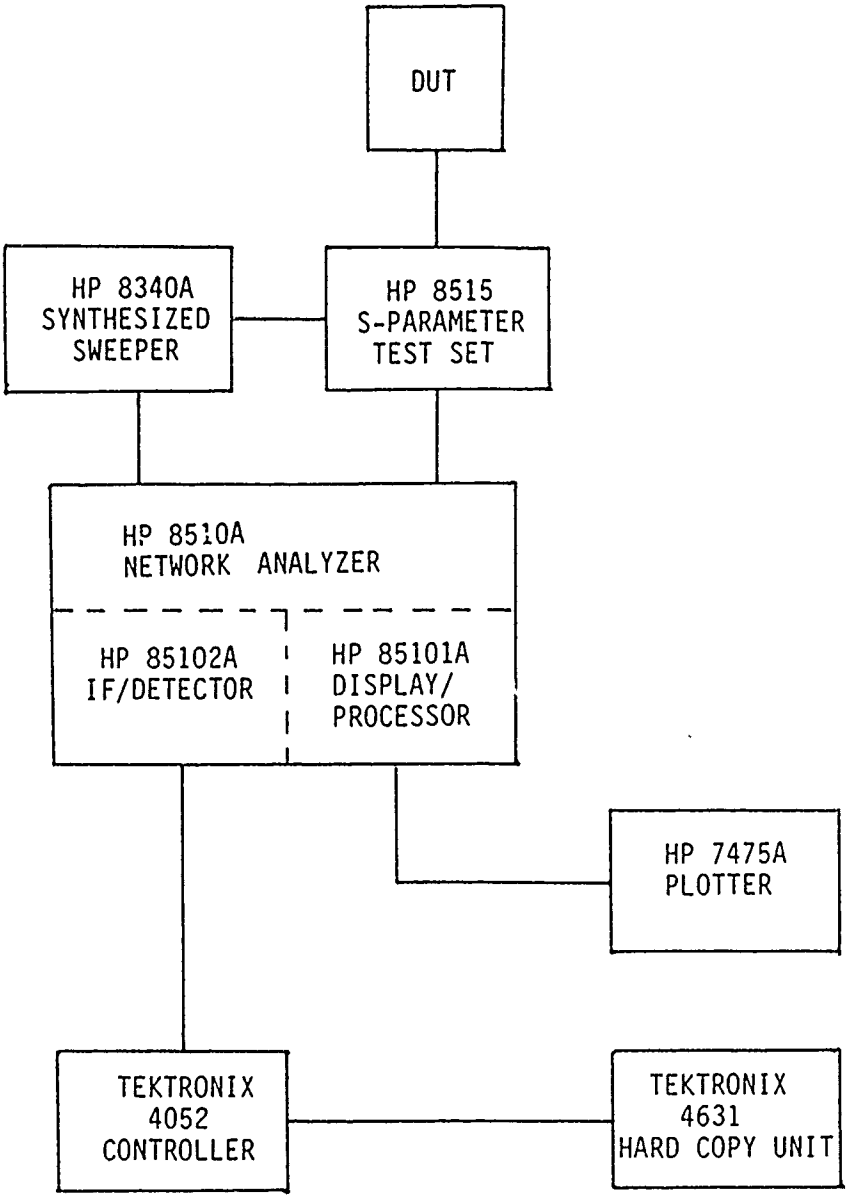


Figure 1. General test configuration.

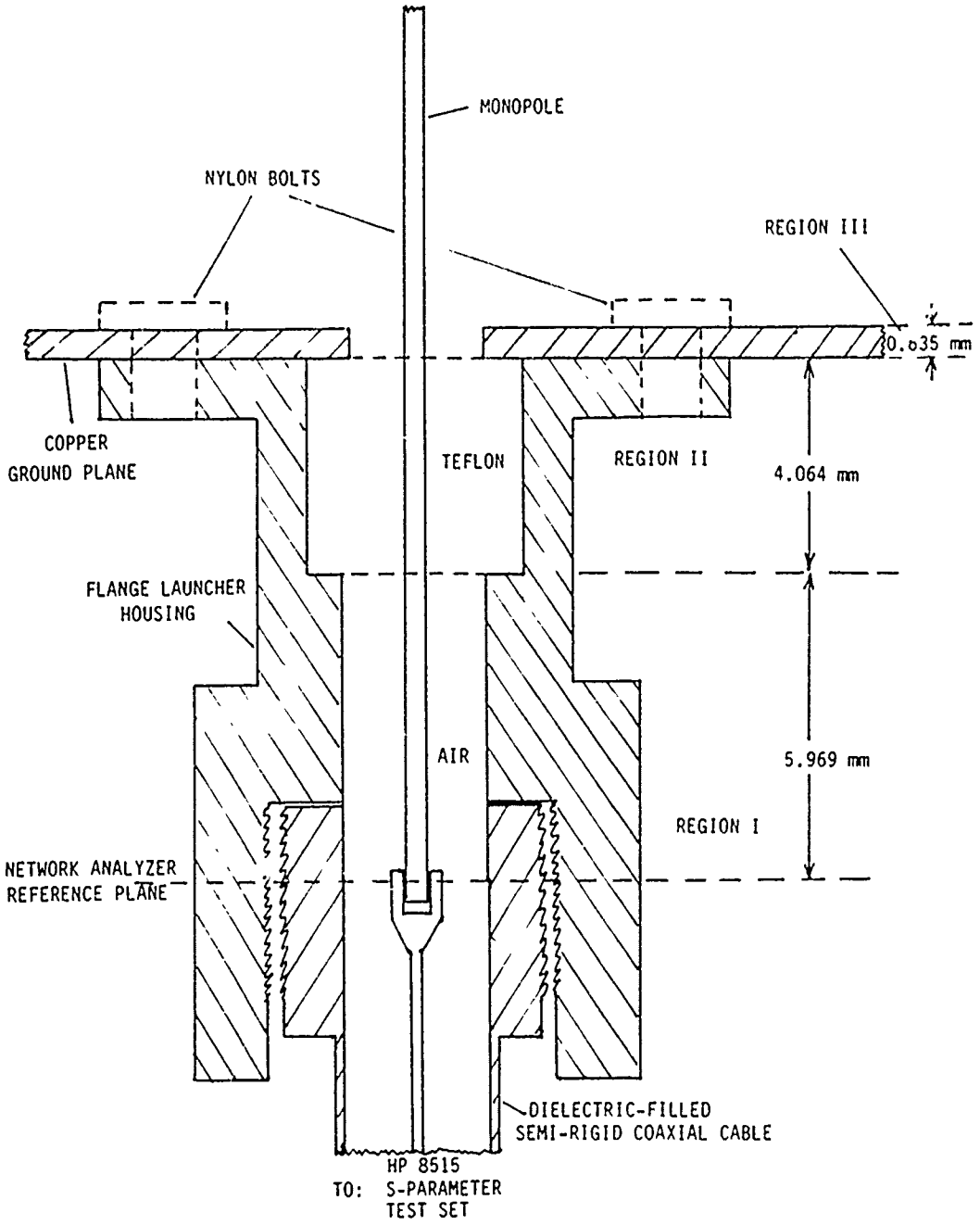


Figure 2. Device under test - monopole/connector interface.

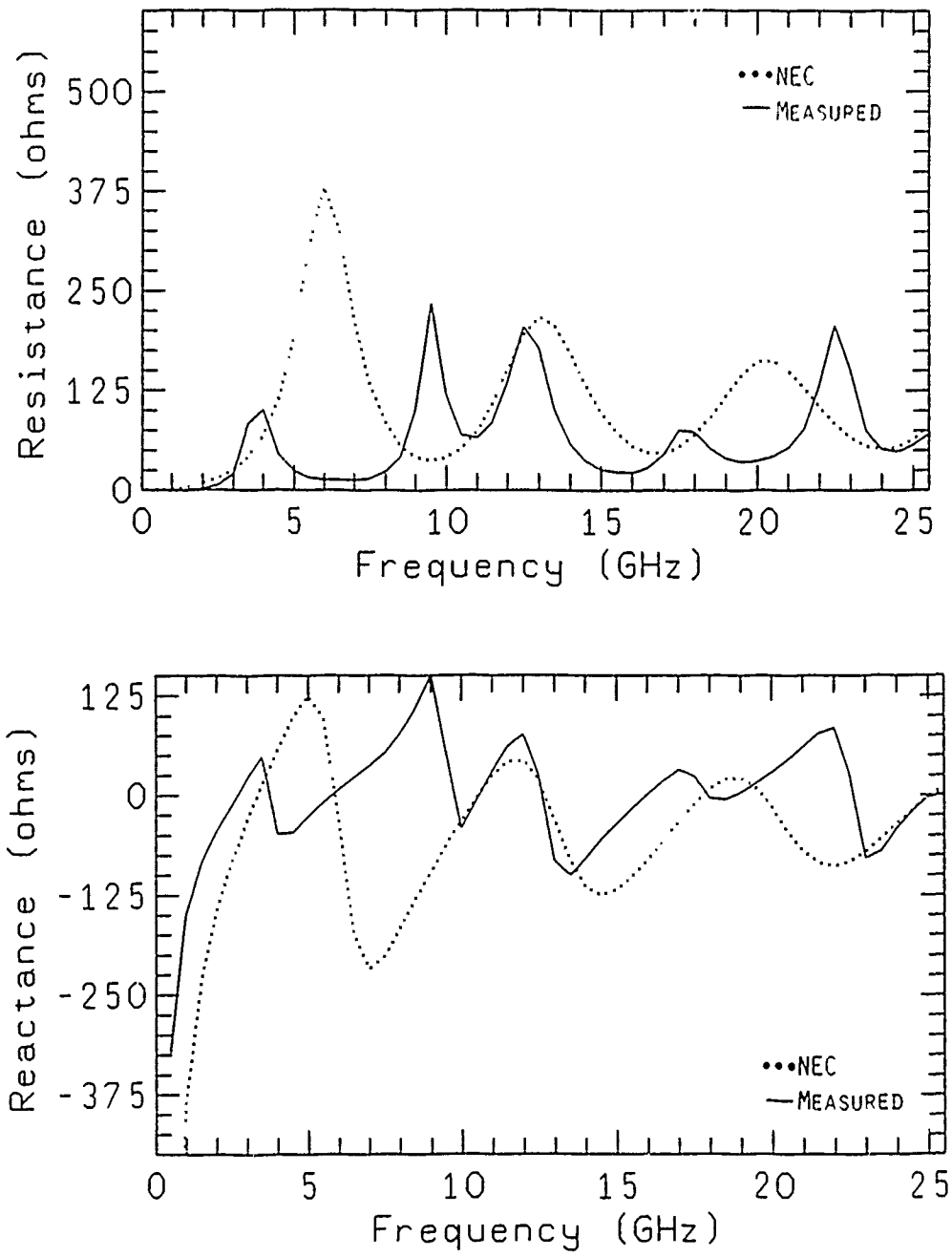


Figure 3. Input impedance of 2 cm monopole over ground plane - no compensation.

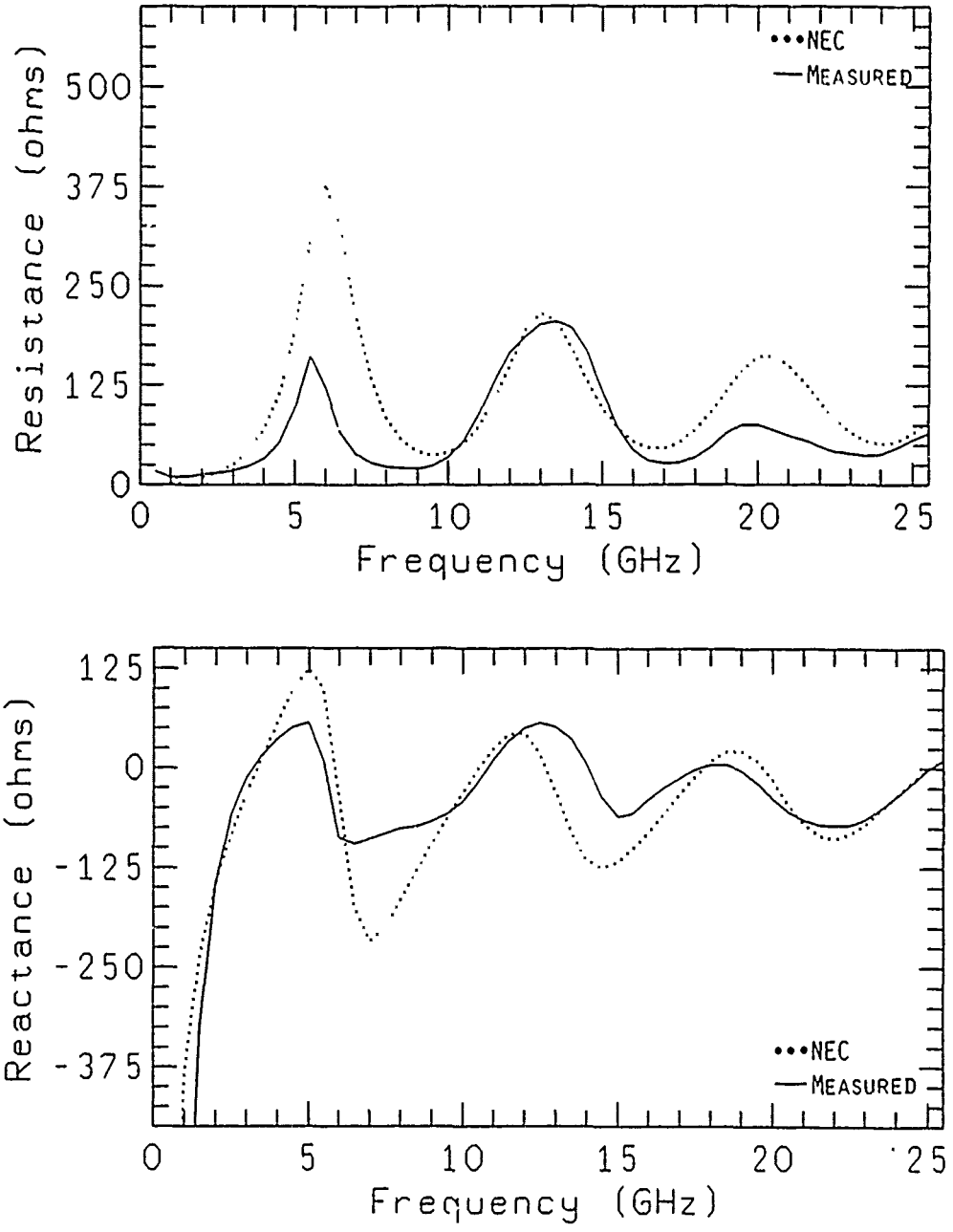


Figure 4. Input impedance of 2 cm monopole over ground plane - 81.25 ps delay.

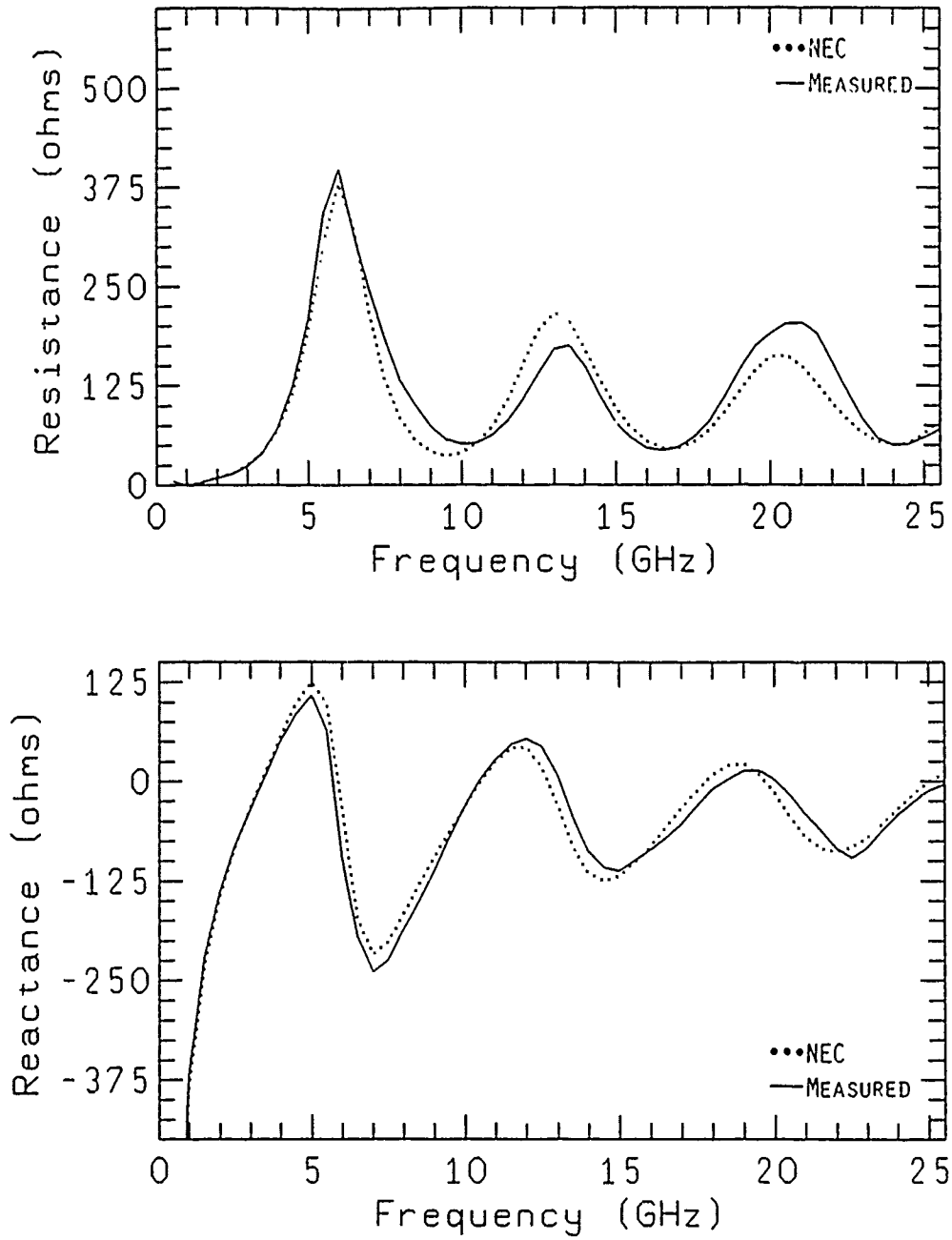


Figure 5. Input impedance of 2 cm m[illegible]le over ground plane - transmission line compen.

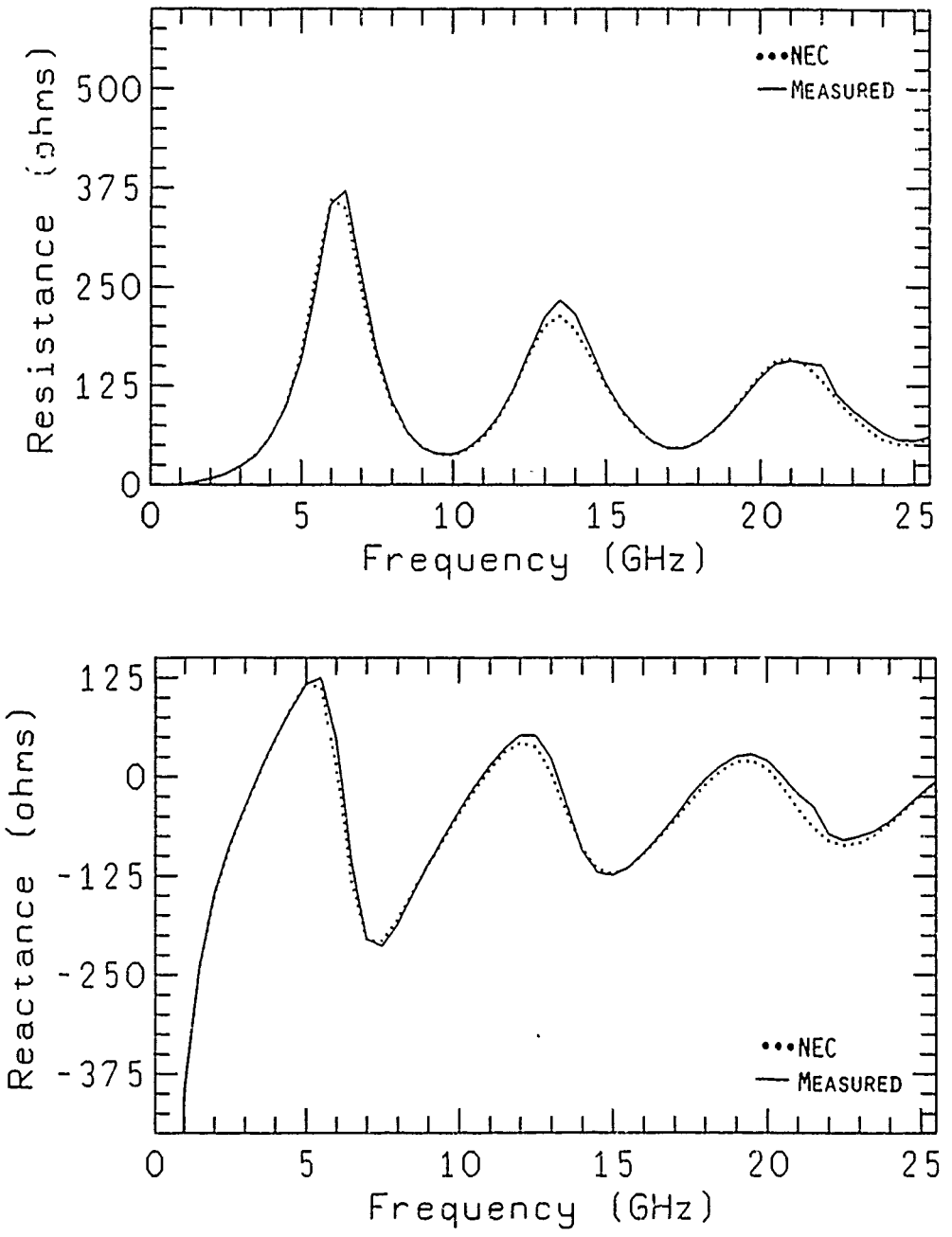


Figure 6. Input impedance of 2 cm monopole over ground plane.

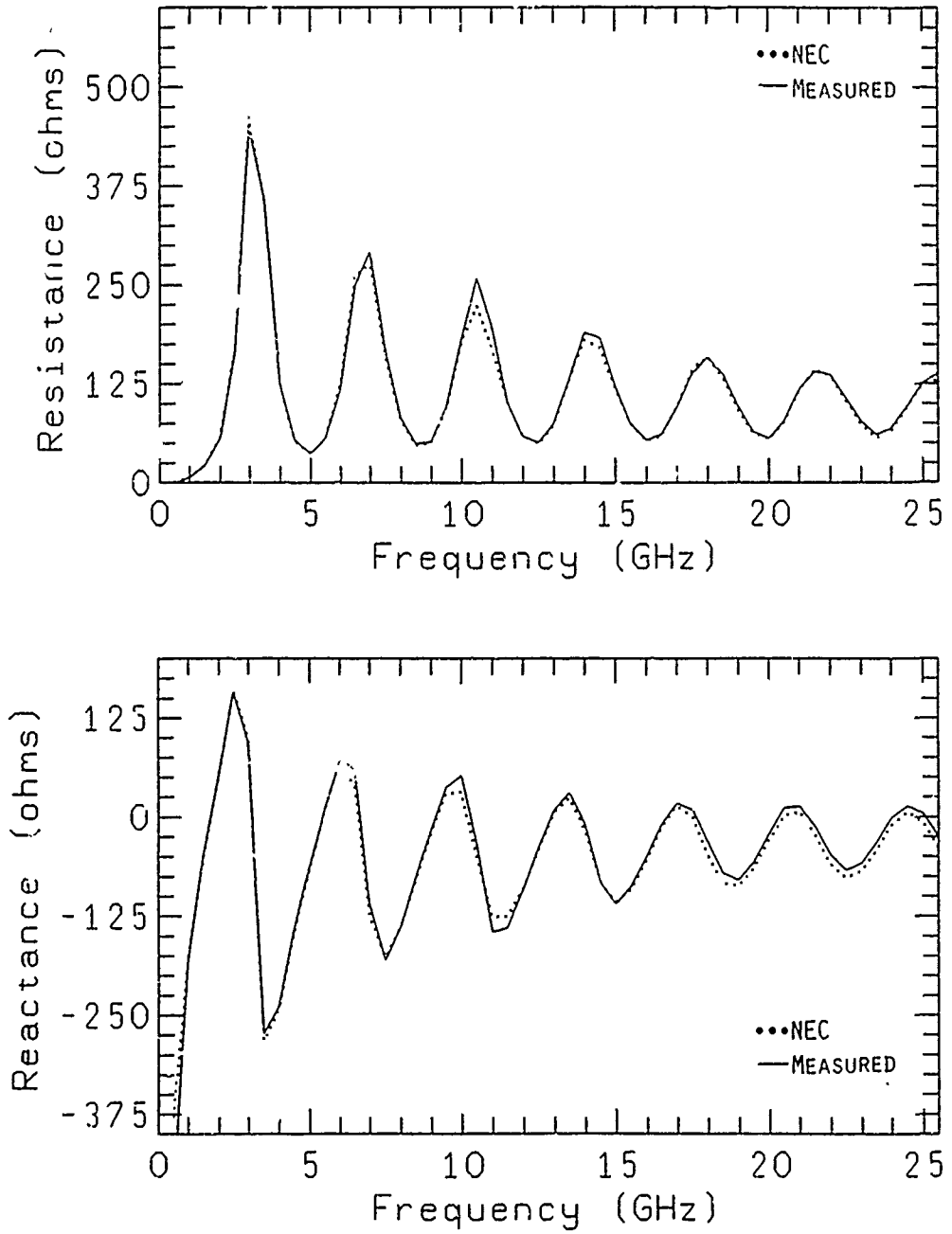


Figure 7. Input impedance of 4 cm monopole over ground plane.

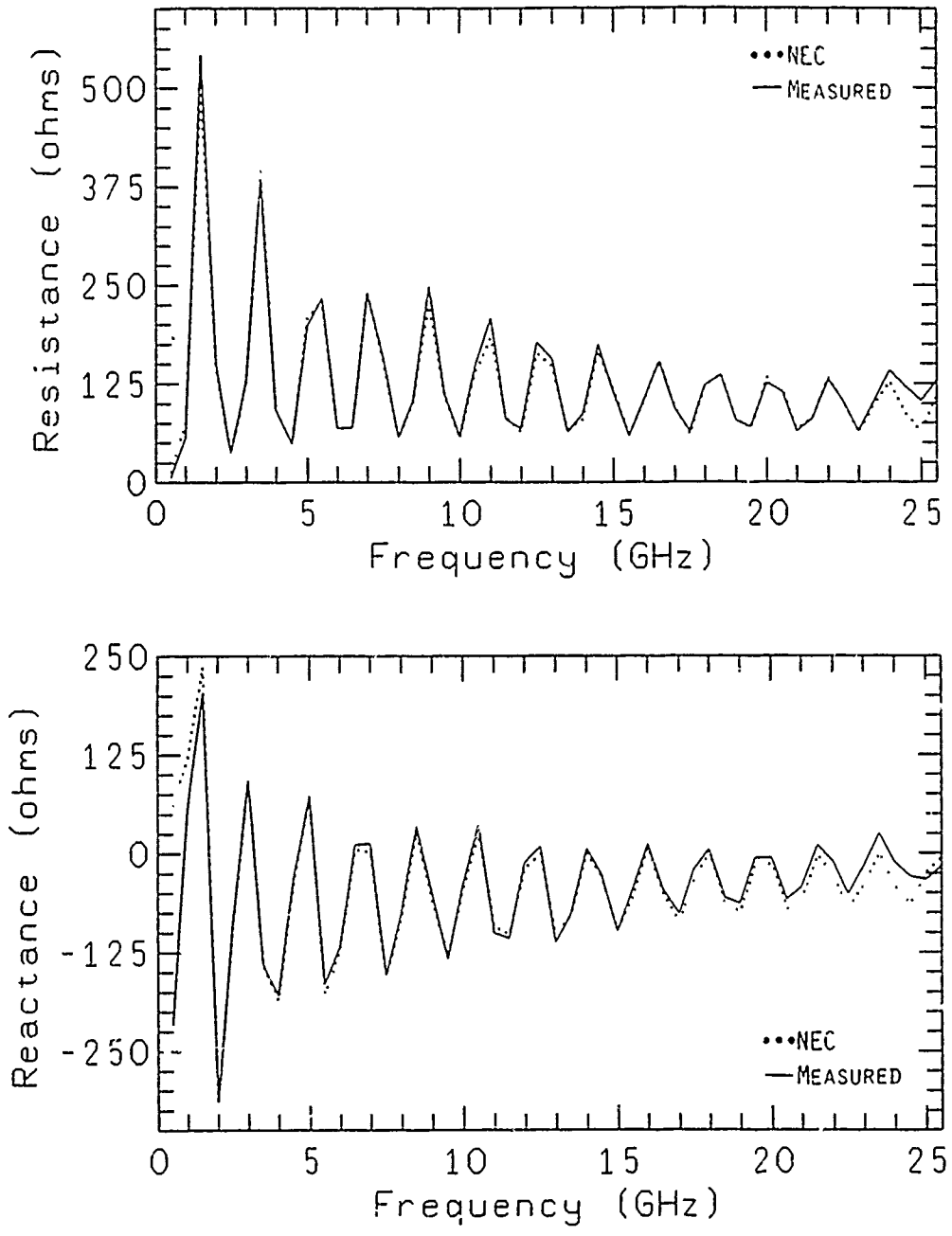


Figure 8. Input impedance of 8 cm monopole over ground plane.

AT/ESP--A PC VERSION OF THE ORIGINAL OSU WIRE-PLATE-PATCH CODE

R. J. Luebbers
Communications and Space Sciences Laboratory
Department of Electrical Engineering
The Pennsylvania State University
University Park, PA 16802
(814) 865-6337

INTRODUCTION

Numerical methods are widely applied to electromagnetics problems, often using general purpose codes which are widely disseminated. The majority of these codes are written and used on mainframe computers. When using such codes on machines other than the one for which they were developed there are usually program modifications which must be made in order to adapt the code to a new compiler, new plotting system, etc.

Such adaptations are reduced or minimized for programs written to run in the IBM PC or compatible environment which utilize standard graphics output. Some codes, such as MININEC for example, have been written especially for operation on a PC. But as PCs become more powerful it becomes desirable to convert mainframe programs to operate using a PC, gaining their increased computational power and versatility. A by-product of this is improved portability of the resulting codes.

The primary limitations are memory, which in the current version of MS/DOS is limited to 640K, and running time. The latter is usually not a serious limitation, since the machine can be set to run overnight for larger jobs once they are setup. The memory limitation may be removed to going to a UNIX-type operating system, or waiting for the rumored release of a new MS/DOS version without the 640 K

limitation. Alternatives are mini-mainframes such as the MICROVAX or IBM AT-370, which are capable of running mainframe programs without modification. However, their usefulness is limited to situations where a mainframe computer is available from which to download necessary software. For many situations a PC version of a code is desirable primarily because no mainframe is available.

Thus in the current computational environment there is a niche for mainframe-derived electromagnetic analysis codes which can operate on a PC within the 640 K limitation, especially if the graphics output is readily portable. This paper discusses the conversion of a popular electromagnetic analysis moment method code, the Ohio State Electromagnetic Surface Patch Code (ESP) [1-3], to operation on an IBM PC/AT or compatible. This conversion includes graphical output utilizing Virtual Device Interface (VDI) Drivers for portability, with output drivers for most CRT displays, graphics printers, and pen plotters being available. This makes the resulting code highly portable while maintaining the full capabilities of the mainframe version subject only to constraints of available memory and running time.

The ESP is a moment method code which is capable of modeling wires, plates, and wire-plate attachments. Piecewise-sinusoidal basis functions are used, which reduces the memory storage requirements. Approximately 5 modes per wavelength are required for wires, 24 modes per square wavelength for plates. Wires may be finitely conducting, but the plates must be perfectly conducting. Plates must be rectangular, and may be attached at edges to form more complicated structures. Overlap modes between attached plates are automatically

inserted as needed. The code will perform both scattering and antenna analysis. Since the code is based on the Electric Field Integral Equation open surfaces may be modeled, which is an advantage for some problem geometries.

CONVERSION PROCESS

Starting with the mainframe version of ESP [1-3], and working primarily on an IBM mainframe, several steps were involved in the conversion process. First, the plotting portion of the code was separated from the computational portion and modified to stand alone. Next a standard FORTRAN 77 compiler (WATFOR77) was used on the mainframe to convert "VAX" fortran to FORTRAN 77. In the process the code was cleaned up with undefined variables, jumps into DO loops, etc., being removed using the mainframe compiler. It should be emphasized that when available a mainframe should be utilized as much as possible in the conversion process due to the relatively slow operation of the PC compiler.

With the code cleaned up as much as possible, it was downloaded to the PC-AT, compiled and further debugged using IBM Professional Fortran. This process was greatly complicated due to the presence of a "bug" in the CMPLX function in the compiler. All of the timer calls in the mainframe version which documented running time were incorporated, as well as the provision to read and write the impedance matrix to and from a file. Memory requirements were reduced by eliminating one large redundant matrix storage array.

To adapt the graphics output to the PC, software was written using the IBM Graphics Development Toolkit to convert the original

"CALCOMP" plotting calls to output via VDI drivers. Drivers are available for most output devices from either IBM or Graphic Software Systems [4]. The drivers are resident in memory and require from 30 to 60K depending on the output device(s) being supported.

PC VERSION CHARACTERISTICS

An executable which will allow a maximum of 50 wire mode modes, 65 plate modes, and 2 attachment modes produces a .EXE file of 350K, and is capable of running all of the examples in the ESP manual [3]. An executable for 100 wire modes, 100 plate modes, and 8 attachment modes is 496K. More modes can be accommodated using overlay linking [5].

Example 1 in the ESP manual (2 wire modes, 24 plate modes, 1 attachment mode) took 117 seconds on a VAX 11780 with floating point accelerator. On a PC-AT with an 8 MHz clock this example takes 855 seconds using Ryan-McFarland fortran to compile the code, a time factor of approximately 7. Example 5 in the manual (1 wire mode, 64 plate modes, 1 attachment mode, 2 geometries) writes and reads back the impedance matrix during the run and took 506 seconds on the VAX machine, 4658 seconds on the PC-AT, for a time factor of about 9. This difference is probably due to the slower disk access time of the PC-AT while writing and reading the impedance matrix.

The figures illustrate the graphical output which is produced via the VDI drivers on different devices. The IBM Proprinter does not have a driver written specifically for it, so the driver for the IBM graphics printer was used. The interface software was written primarily to produce a clean output on the pen plotter, with the CRT

display and printer outputs as shown produced by utilizing the appropriate driver without changing the plotting programs. The obvious difference is the discrete steps in letter sizes on the printers, while the pen plotter can draw letters of any size.

SUMMARY

The Ohio State Electromagnetic Surface Patch (ESP) moment method analysis code has been converted to operate on an IBM PC-AT or compatible. The full capabilities of the code have been retained, subject to memory and time constraints on the PC. The graphical output produced by the mainframe version has been converted to produce output on PC displays, graphics printers, and pen plotters utilizing Virtual Device Interface (VDI) drivers which are available for most CRT displays, printers, and plotters, and which allow general portability of the code. The resulting code has been used to analyze problems requiring up to 200 modes.

ACKNOWLEDGEMENTS

The author would like to acknowledge the important contributions to this conversion made by Mr. Warren Weis of Lockheed Palo Alto Research Laboratories, Dr. Edward Newman of The Ohio State University, Mr. Robert Divany of The Pennsylvania State University and Dr. Vaughn Cable of California Microwave.

REFERENCES

1) E. H. Newman and D. M. Pozar, "Electromagnetic modeling of composite wire and surface geometries," IEEE AP-S, Vol AP-26, pp 784-789, Nov. 1978.

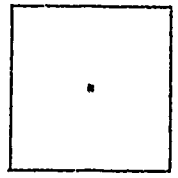
2) E. H. Newman and D. M. Pozar, "Consideration for efficient wire/surface modeling," IEEE AP-S, Vol AP-28, pp 121-125, Jan. 1980.

3) E. H. Newman, "A User's Manual For: Electromagnetic Surface Patch Code (ESP)," Ohio State University Electro Science Laboratory, Technical Report Number 713402-1, July 1981.

4) S. Armbrust and T. Forgeron, "Forward-Looking VDI," PC Tech Journal, September 1985.

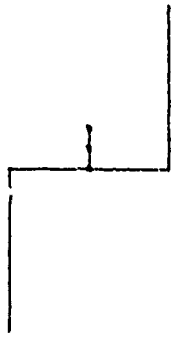
5) V. P. Cable, private communication.

IBM 7371 PEN PLOTTER

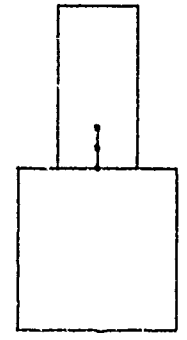


Z AXIS VIEW

1 WIRE MODES
64 PLATE MODES
1 ATTACH. MODES
66 TOTAL MODES
SCALE = 0.79WVL

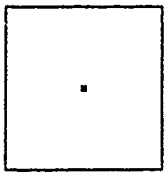


X AXIS VIEW



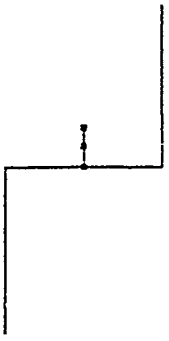
Y AXIS VIEW

IBM COLOR PRINTER

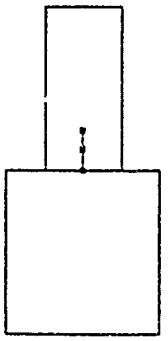


Z AXIS VIEW

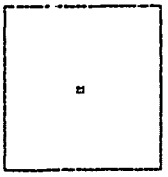
1 WIRE MODES
64 PLATE MODES
1 ATTACH. MODES
66 TOTAL MODES
SCALE = 0.79 WVL



X AXIS VIEW

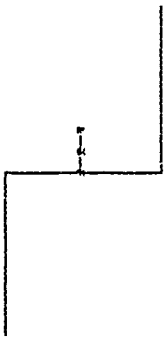


Y AXIS VIEW

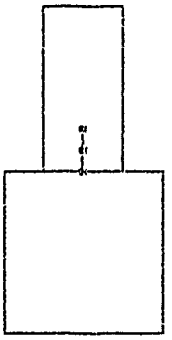


1 WIRE MODES
64 PLATE MODES
1 ATTACH. MODES
66 TOTAL MODES
SCALE = 0.79WL

Z AXIS VIEW



X AXIS VIEW

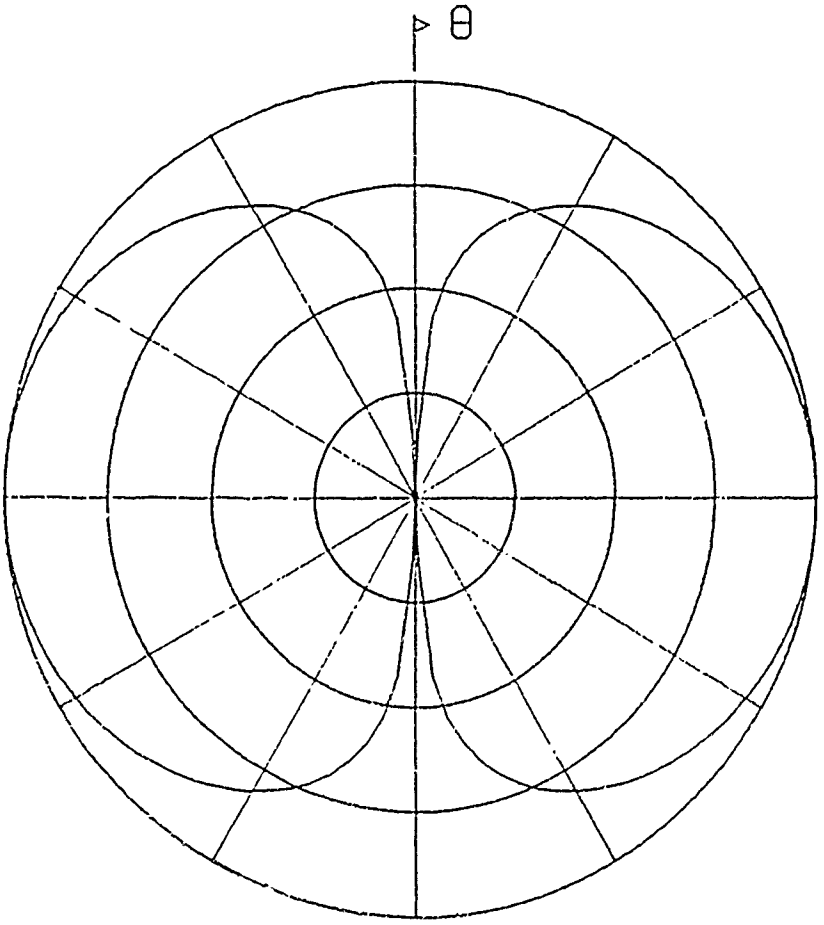


Y AXIS VIEW

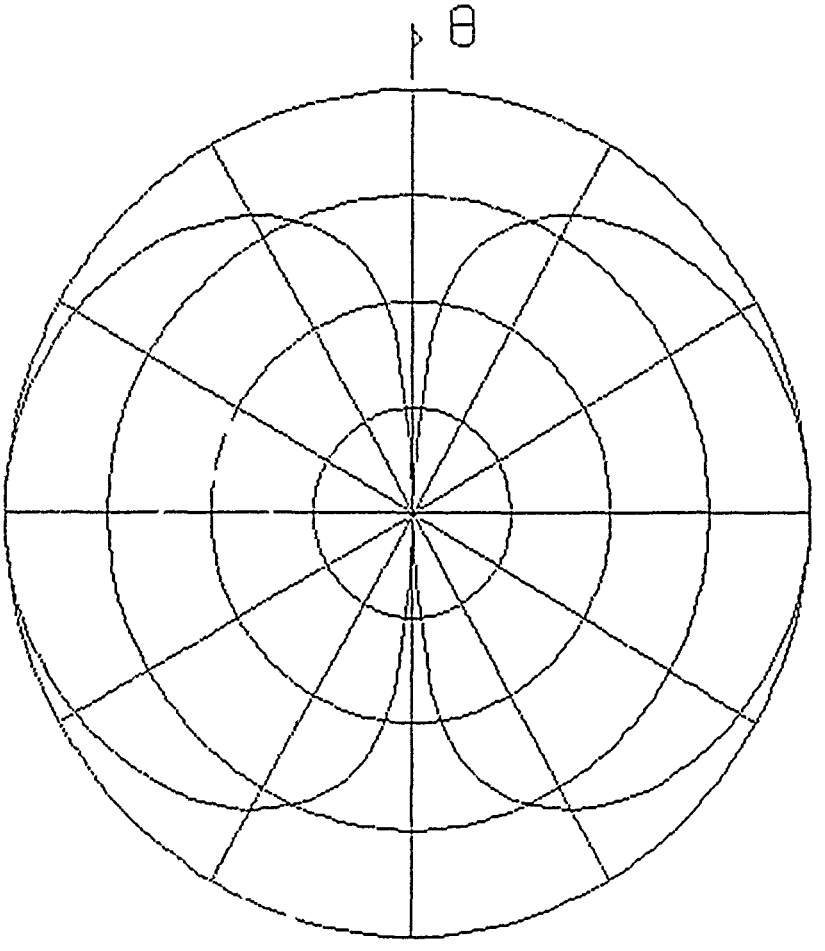
IBM PROPRINTER USING DRIVER
FOR IBM GRAPHICS PRINTER

IBM 7371 PEN PLOTTER

DB PLOT 10 DB/DIV
NORMALIZED TO 2.166 DB
Φ=0.00 DEG.
GTHETA



DB PLOT 10 DB/DIV
NORMALIZED TO 2.166 DB
Φ=0.00 DEG.
GTHETA



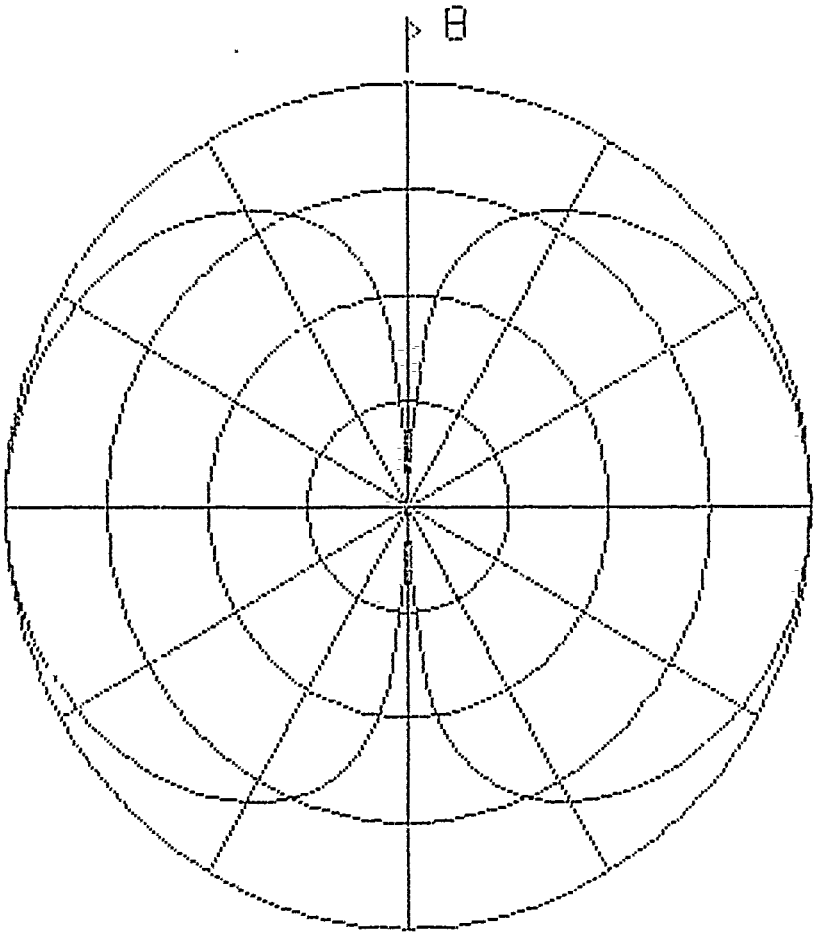
IBM COLOR PRINTER

DB PLOT 10 DB/DIV

NORMALIZED TO 2.166 DB

Φ=0.00 DEG.

GTHETA



IBM PROPRINTER USING DRIVER

FOR IBM GRAPHICS PRINTER

ERROR ESTIMATES FOR LARGE ORDER ANTENNA CALCULATIONS ON A PC

by

V. P. Cable

California Microwave, Inc.
P. O. Box 2800
Woodland Hills, CA 91365

ABSTRACT

The gain and impedance of a single cavity backed dipole were computed over a 10:1 frequency range on a PC. The EM analysis behind this study was originally developed and coded as ESP by Newman in VAX/VMS/FORTRAN. However, for these results, the version converted by Luebbers to run in a DOS/FORTRAN environment was used.

Over this 10:1 frequency range, the size of the matrix resulting from the Method of Moments exceeded 200 unknowns at the high frequency end. Cholesky's method was used to solve this system for the surface current distribution and gain and impedance calculations followed from this current. An effort was made not to take these solutions for granted and, to do this, an available error bound for this numerical solution method was also computed for each case. Results are presented which track this error bound over the 10:1 frequency range.

I. INTRODUCTION

This paper reports on results of performing calculations of the electromagnetic (EM) characteristics of a common cavity backed dipole antenna on a PC. The study was done for > 10:1 frequency range which resulted in a numerically large problem at the high end of this range. Antenna gain, radiation pattern and driving point impedance were computed in standard Fortran 77 single precision. Relative error bounds on these solutions were also computed. The PC environment included a 10 MHz 80286 CPU /8 MHz 80287 NDP running under DOS with a full 640K bytes of core memory installed.

The analysis technique used was based on the Method of Moments (MM) [Harrington, 1968]. The computational code used was a recent derivative of the original EM Surface Patch (ESP) code developed by Newman [Newman, 1981]. While the original ESP code was written in Fortran for the DEC VAX, the version used here has been made available in ANSI Fortran 77 for the PC environment by Luebbers [Luebbers, 1987]. This version treats arbitrary configurations of thin rectangular plates and bent wire with some

minor restrictions on wire-plate attachment geometries.

The maximum order (N) of the system of equations resulting from the MM can become large, especially at the high end of a 10:1 frequency range. The compiled code used here was dimensioned to cover up to 250 unknowns. For single precision calculations, this pushes the matrix problem to the limits of a DOS environment. Some array size relief is possible if the system of equations is symmetric and Cholesky's square root reduction [Richmond, 1973, p. 40] can be used; this is exactly the case in ESP. However, this usually leads to considering larger geometries or a wider frequency range and the limits of the computing environment are again reached.

Even for the largest of matrix problems inferred above, many direct solution techniques exist (including Cholesky's) which, under certain conditions (e.g., positive-definite coefficient matrix), are guaranteed to yield a solution in a fixed number of steps [Householder, 1964, p. 129]. However, even though solutions to positive-definite systems tend to behave ideally, all implementations of direct methods are inexact due to rounding. Since matrices derived by standard EM-MM techniques are non-Hermitian and positive-definiteness (-semidefiniteness) is not defined for such matrices [Householder, 1964, p. 12], this adds another dimension to the question of accuracy of these solutions.

So, how does one check a solution for accuracy? The answer is not obvious. The circumstances are aggravated when the computing system is already pushed to the size limit; e.g., if single precision no longer suffices, double precision is excluded by the same matrix size limitation. A technique known as iterative improvement can help under certain conditions [Ralston and Wilf, 1960, Vol.2, p. 73], however, this approach is of little use if storage of the original unprocessed matrix is required.

The following sections present background and results on computed solutions of EM performance and the relative errors associated with these solutions.

II. BACKGROUND

The EM problem considered is the characterization of the cavity backed dipole antenna illustrated in Figure 1. The cavity geometry was modeled by thin rectangular flat plates and the dipole and feed regions by finite diameter wires. The balanced feed region is considered part of the radiating structure and a push-pull transmission line mode was fed from ports 1 and 2 at the back of the cavity (see Fig. 1).

The wire/plate code used here assumes plates to be perfect electrical conductors (PEC), but wires are not held to be PEC; wires were input as 2 millimeter diameter copper with conductivity 58 Mmho/meter. This code is based on a Reaction

Integral Equation approach [Richmond, 1969] which yields an integral equation for the antenna currents. The MM solution then proceeds by expanding the unknown antenna currents into a finite dimensional vector of piecewise sinusoidal overlapping modes. The unique relationship between these modes, and the source(s) driving the structure is expressed by the following matrix equation,

$$Z\ I = V \quad . \tag{1}$$

Precise definitions of these terms can be reviewed in the work of Pozar, et al. [Pozar, 1981, p. 488]. This application of the MM requires the current modes to be subsectional on the wire segments and plate patches. These piecewise sinusoidal modes require segment length and patch dimensions < 1/4 wavelength and the minimum mode count for these calculations ranged from N = 40 at .50 GHz to N = 218 at 7.0 GHz.

A RELATIVE ERROR BOUND

A relative error bound for the direct solution algorithm known as the Doolittle method was presented previously [Cable, 1986]. This "pessimistic" bound is reviewed here and refinements to this bound are then discussed which lead to a more realistic form.

The relative error bound (REB) on the LU factorization technique known as the Doolittle method was previously given by

$$REB \leq \frac{1.01\ K\ g\ P(N)\ Cond\{Z\}}{1 - 1.01\ K\ g\ P(N)\ Cond\{Z\}} \tag{2}$$

with the restriction that $[1.01\ K\ g\ P(N)\ Cond\{Z\}] < 1$

where

$$K = \max_{ijk} |z_{ij}^{(k)}| / \|Z\| \tag{3}$$

$$g = .5\ t^{1-d} \tag{4}$$

and

$$P(N) = 1.003N^3 + 2.006N^2 + .0026N. \tag{5}$$

The variables t and d in Eq. 4 are, respectively, machine base (modulo) and mantissa size. The Cond{Z} term in Eq. 2 refers to the condition number of Z (Eq. 1) and is defined in terms of consistent matrix norms [Stewart, 1973, p. 173] as

$$Cond\{Z\} = \|Z^{-1}\|\ \|Z\| \quad . \tag{6}$$

Here, the matrix norm of choice is the row sum norm given by

$$\|Z\| = \max_{i} \sum_{j=1}^{N} |z_{ij}| \ , \ i=1,2,\ldots,N \quad . \tag{7}$$

Assumptions made in arriving at Eq. 2 include neglecting truncation errors in the elements of Z and V. Only rounding errors due to precision in the solution algorithm are considered. This bound is is too consevative to be useful on a regular basis. The following discussion describes a bound which gives a less pessimistic estimate. Such a bound might serve as a practical check.

A PRACTICAL RELATIVE ERROR BOUND

The matrix representation for the solution of Eq. 1 is given by

$$I = Z^{-1} V \qquad (8)$$

where the inverse Z^{-1} is not actually computed. Instead, LU decomposition is used followed by forward and backward substitution to yield the final solution vector I.

A more realistic bound is achieved by taking into account the following effects:

1. The inherent randomness of rounding errors can be modeled as "probable error" [Ralston, 1965, p. 8]. In this case, the error process is assumed to take on a normal distribution and the bound is said to depend on $N^{.5}$ instead of N.

2. Application of Cholesky's method to positive definite matrices guarantees no growth in the sequence of matrices leading to the reduced L matrix [Stewart, 1973, p. 153]. For the diagonal predominant Z matrix, this still appears to hold in all cases considered here, even without the definition of positive-definiteness. As a result, the factor defined by Eq. 3 can be set to unity.

3. High accuracy is generally obtained in solving triangular systems of equations. In this case, the final solution of triangular systems L and U is assumed to add negligible roundoff. Hence, the factor defined by Eq. 5 can be set to unity.

The final relative error bound for the solution represented by Eq. 8 is given by

$$REB \leq \frac{g\, N^{.5} Cond(Z)}{1 - g\, N^{.5} Cond(Z)} , \qquad (9)$$

subject to the condition $[g\, N^{.5}\, Cond(Z)] < 1$. The same definitions previously given in Eqs. 4, 6 and 7 remain valid.

III. RESULTS

Calculations of antenna gain, pattern and impedance are presented in Figures 2, 3 and 4 respectively. The impedance has been normalized to 50 ohms. The indicated impedance is that seen at one balanced feed port with the other port fed in opposition. Convergence of the MM was also checked; these increases in the number of modes generally had little effect on these results.

Relative error bound (REB) and Cond{Z} are plotted in Figure 5 verses minimum N at a given frequency. Values are shown only for frequencies above 1 GHz ($N \geq 40$). At frequencies below approximately 2 GHz, the same minimum ($N = 40$) was used for all frequencies. These results are shown separately as a function of frequency in Figure 6.

As an indication of the average diagonal predominance (ADP) of the Z matrix, the following definition was made:

$$ADP \triangleq N^{-1} \sum_{i=1}^{N} |z_{ii}|^{-1} \sum_{\substack{j=1 \\ j \neq i}}^{N} |z_{ij}| \quad . \qquad (10)$$

Results from this expression are plotted in Figure 7.

IV. DISCUSSION OF RESULTS

The computed antenna characteristics of Figs. 2, 3 and 4 are generally as expected for the wide frequency range considered (> 10:1). Measured gains, patterns and mismatches for similar antenna structures follow these general characteristics. Useful modeling of rather sophisticated antenna geometries is clearly possible using this "mini-mainframe" code on a PC.

Most of the calculated estimates of roundoff effects also had expected results. For example, in Fig. 5 the REB in the region of the 1st dipole resonance (near 2 GHz) rose significantly. This is expected in terms of Cond{Z} for frequencies near cavity type resonances and have near singular conditions for Z. Another expected result, not shown but mentioned, was MM convergence as indicated by increased N at a given frequency. The general result was a 10 X increase in Cond{Z} for every doubling of N.

An unexpected result in Cond{Z} (and REB) was noted in Fig. 6, at the lower frequencies (.5 - 1.5 GHz), where the order of the system was relatively small ($N = 40$). Here, Cond{Z} and hence, REB, increased dramatically (nearly 100 X) from 1.5 GHz down to did not show a supporting trend. In fact, the ADP decreased monotonically with decreasing frequency over the entire .5 - 7 GHz range. The apparent ill-conditioning in Fig. 7 is not indicated by the ADP.

The above background and results have been presented with the primary goal of gaining a better understanding of solution accuracy. Some initial steps toward developing a meaningful check on relative solution error have also been taken.

References

Cable, V. P., "Error Bounds on Direct and Indirect Solution of EM Scattering Problems," Second Annual Review of Progress in ACE, Monterey, CA, 1986.

Harrington, R. F., Field Computation by Moment Methods, Krieger Publishing, Malabar, FL, 1968.

Householder, A. S., The Theory of Matrices in Numerical Analysis, Dover, N.Y., 1964.

Luebbers, R. J., "AT/ESP 1 - A PC Version of the OSU Wire-Plate-Patch Code," Third Annual Review of Progress in ACE, Monterey, CA, 1987.

Newman, E. H., "A User's Manual for: Electromagnetic Surface Patch Code (ESP)," OSU-ESL TR 713402-1, Columbus, OH, 1981.

Pozar, D. M. and E. H. Newman, "Analysis of a Monopole Mounted near or at the Edge of a Half-Plane," IEEE Trans. AP-S, May 1981.

Ralston, A., A first Course in Numerical Analysis, McGraw-Hill, N.Y., 1965.

Ralston, R. and H. S. Wilf, Mathematical Methods for Digital Computers, Volume 2, Wiley, N.Y., 1967.

Richmond, J. H., "Computer Analysis of Three Dimensional Wire Antennas," OSU-ESL TR 2708-4, Columbus, OH, 1969.

Richmond, J. H., "Computer Program for Thin-Wire Structures in a Homogeneous Conducting Medium," OSU-ESL TR 2902-12, Columbus, OH, 1973.

Stewart, G. W., Introduction to Matrix Computations, Academic Press, N.Y., 1973.

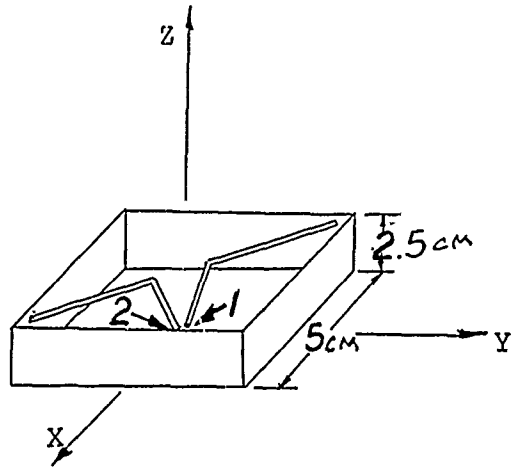


Figure 1. Cavity backed dipole.

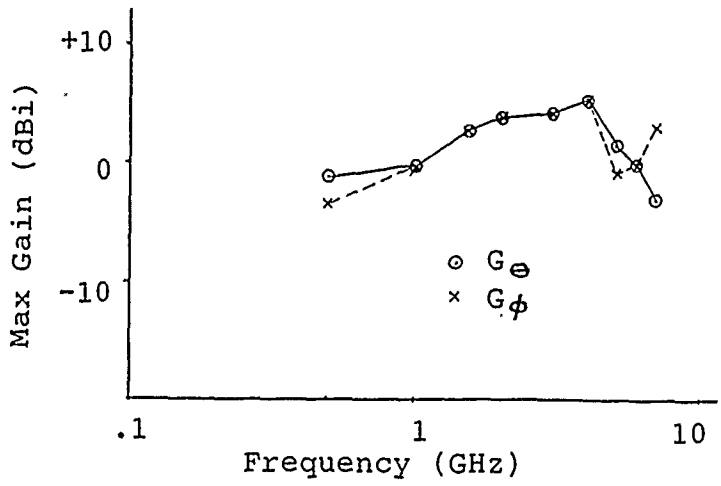


Figure 2. Maximum antenna gain (dBi)

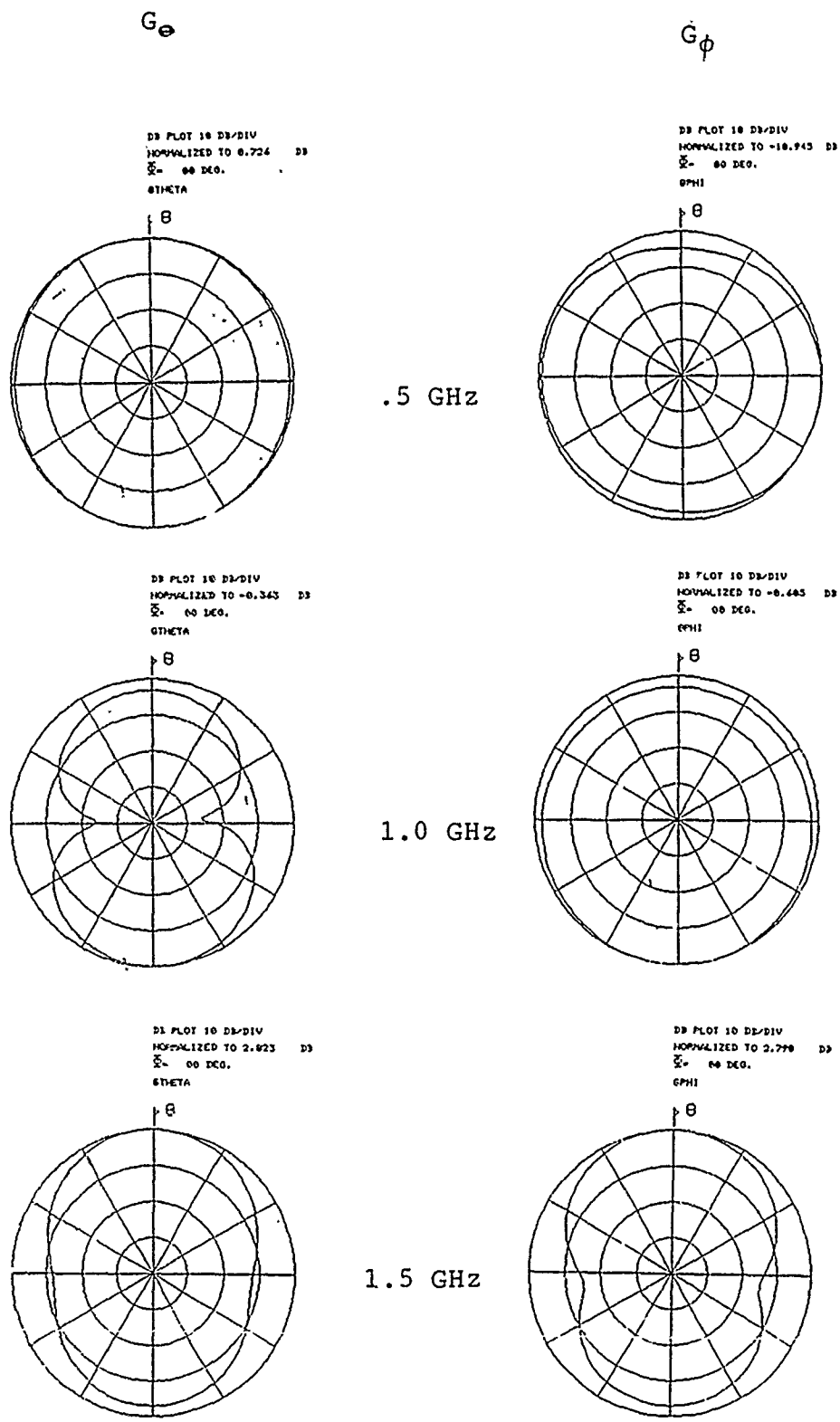


Figure 3. Antenna radiation patterns.

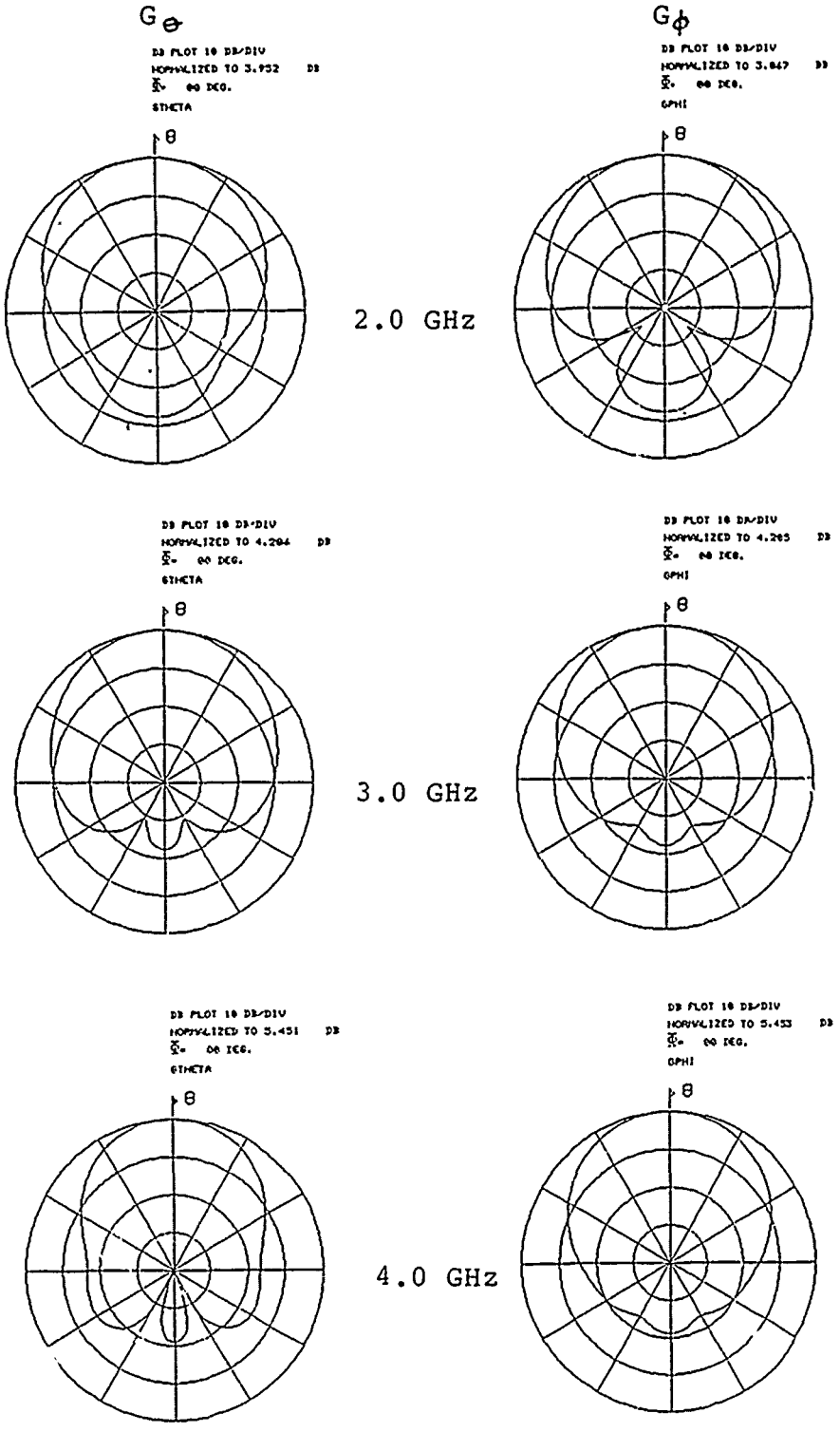


Figure 3 (cont). Antenna radiation patterns.

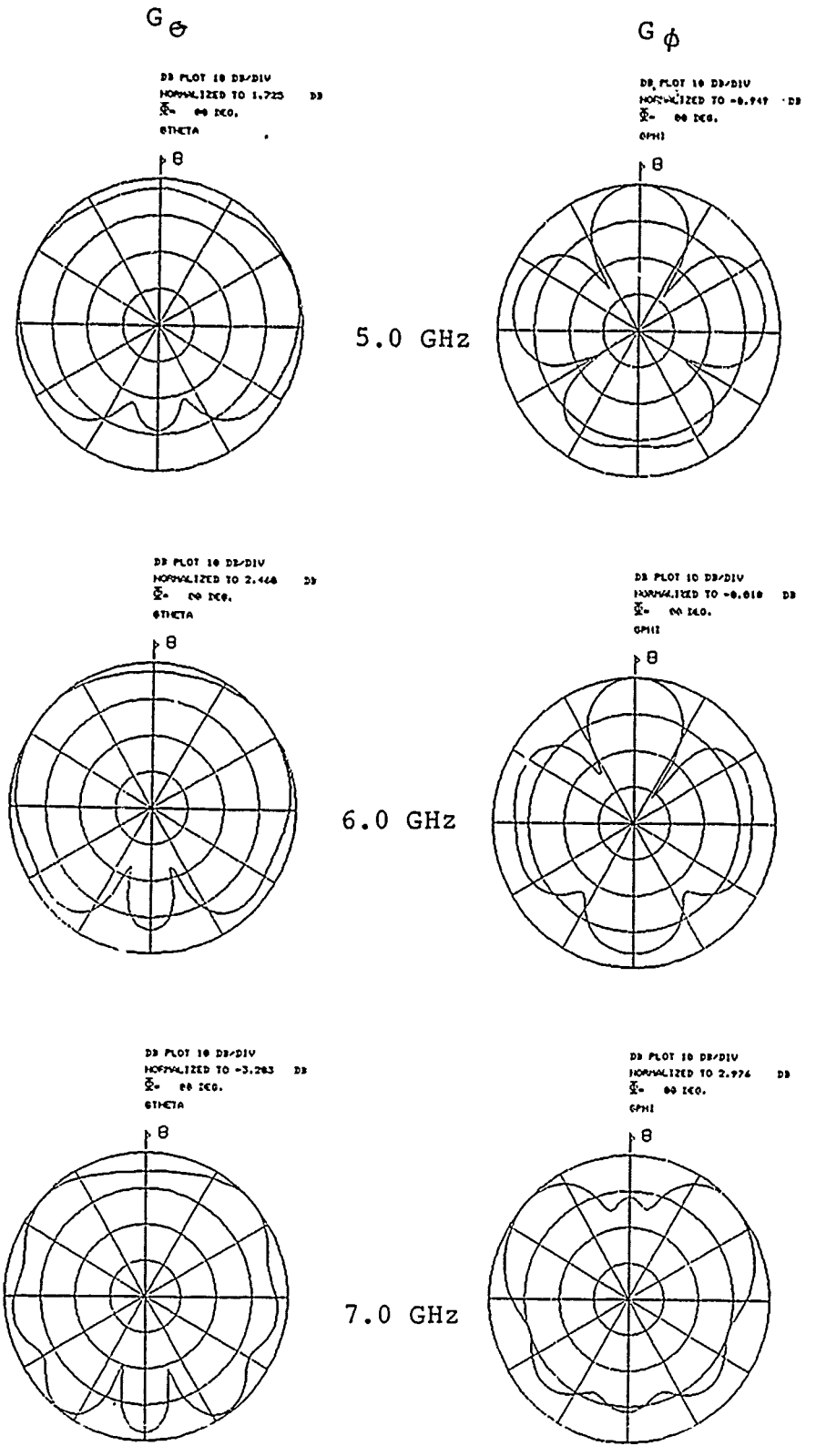


Figure 3 (cont). Antenna radiation patterns.

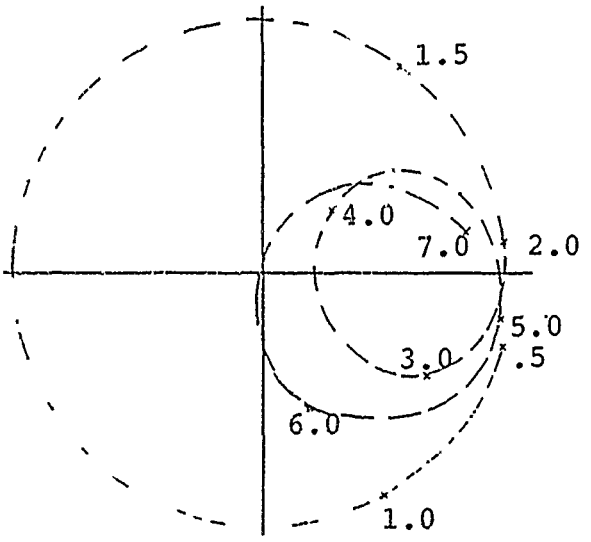


Figure 4. Normalized impedance verses frequency (GHz).

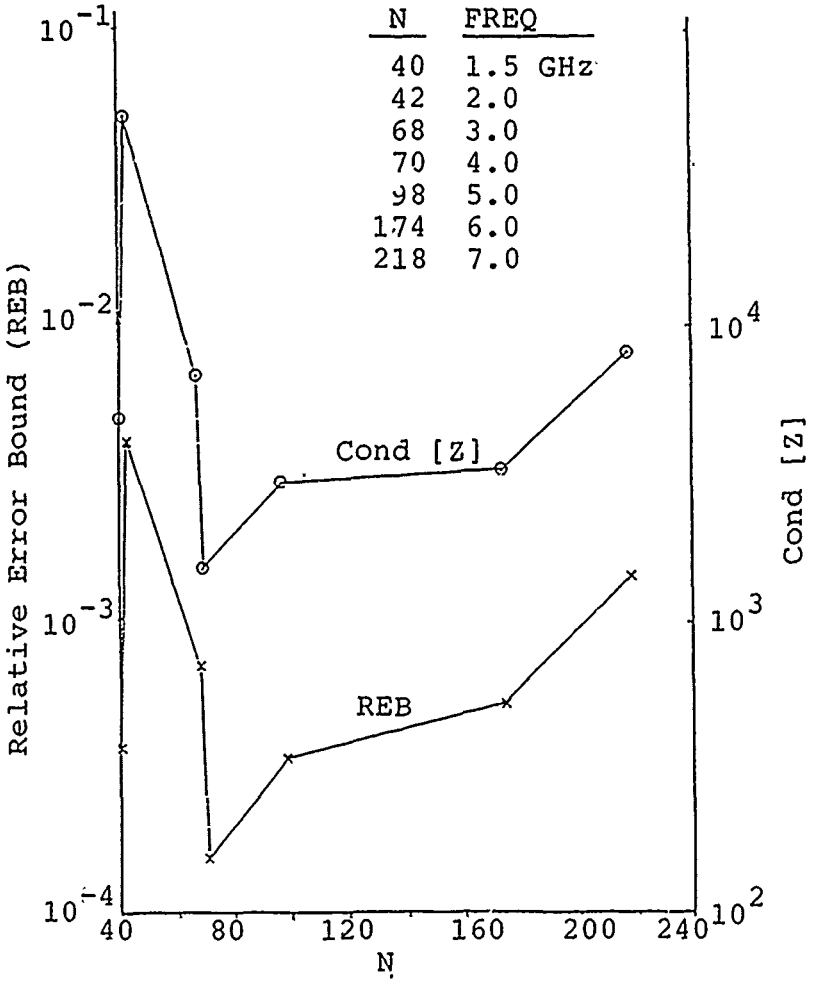


Figure 5. Relative error bound (REB) and Cond [Z] verses N for 1.5-7.0 GHz.

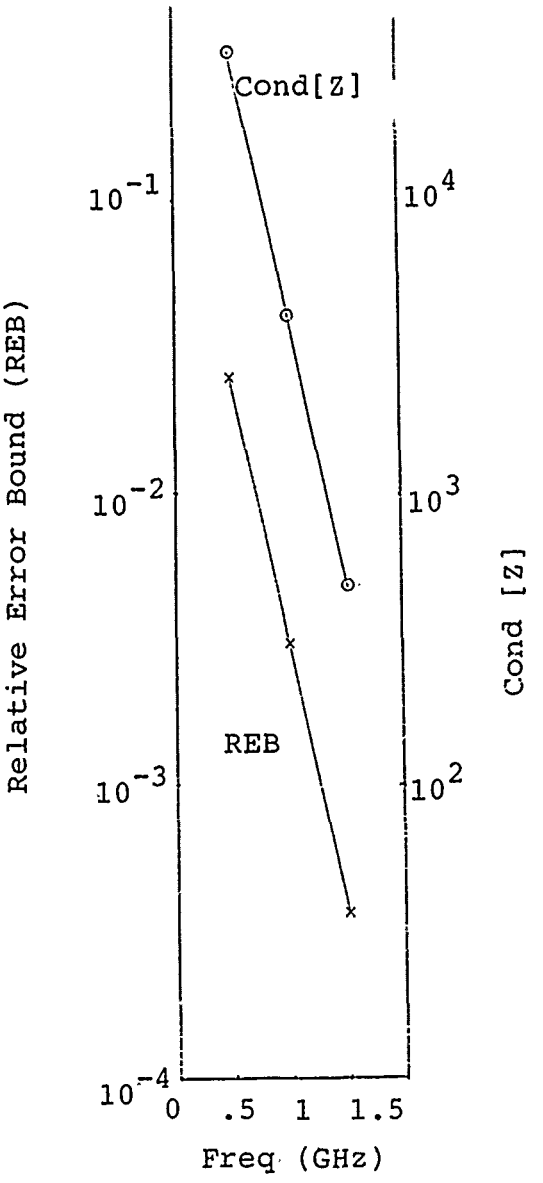


Figure 6. Relative error bound (REB) and Cond[Z] verses frequency for N = 40.

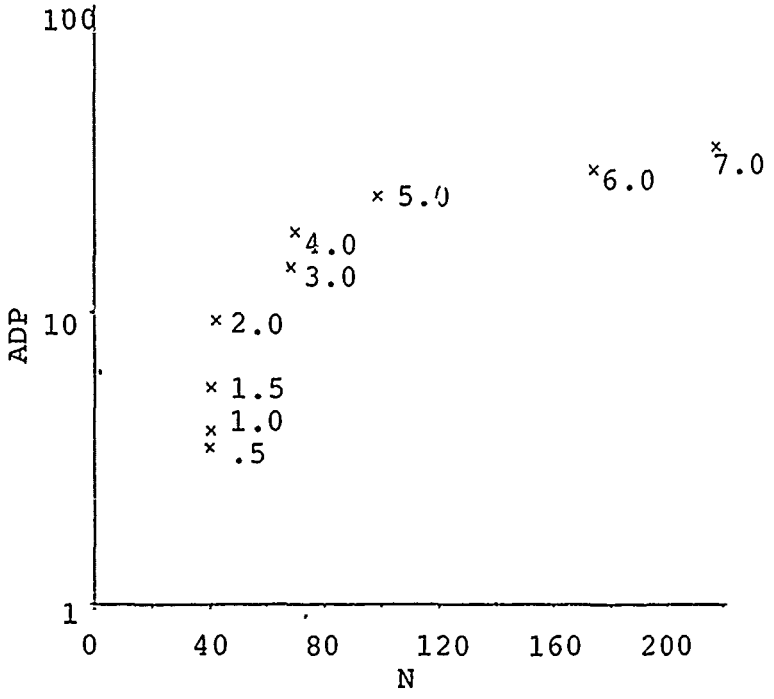


Figure 7. Average diagonal predominance (ADP) verses N for frequencies in GHz.

SESSION VI - "INPUT - OUTPUT ISSUES"

Moderator: R. Bevensee

INPUT IMPEDANCE CALCULATIONS USING THE SPHERICAL WAVE EXPANSION TECHNIQUE

A.C. Ludwig, General Research Corporation, Santa Barbara, CA

The spherical wave expansion (SPEX) technique has been described previously, where it was applied to the case of scattering from a smooth perfectly conducting body [1]. Recently, the technique has been extended to apply to a dipole excited by a voltage across a gap in the center, as illustrated in Fig. 1.

The fields in the exterior region are represented by multiple spherical wave expansions exactly like the scattering case [1]. The two differences for the present application are:

1. The tangential E-field on the surface of the dipole is zero everywhere except across the gap, where $E_z = 1 \text{ volt} \cdot m^{-1}$

2. The field inside the dipole is zero everywhere except in the gap region $|z| \leq g/2$ and $r \leq a$ where

$$\overline{E}_{in} = \frac{J_o(kr)}{J_o(ka)} \hat{i}_z$$

$$\overline{H}_{in} = -\frac{j}{Z_o} \frac{J_o'(kr)}{J_o(ka)} \hat{i}_\phi$$

where $\hat{i}_z$ and $\hat{i}_\phi$ are unit vectors in the z and φ directions, respectively, $k = 2\pi/\lambda$, λ being the free-space wavelength, and J_o is the zero-order Bessel function.

The exterior fields $\overline{E}_{out}$ and $\overline{H}_{out}$ are found by matching the boundary condition on the surface, exactly like the scattering calculation. The gap current is found from

$$\overline{J}_g = \hat{n} \times (\overline{H}_{out} - \overline{H}_{in})$$

elsewhere on the surface

$$\overline{J} = \hat{n} \times \overline{H}_{out}$$

---

[1] A.C. Ludwig, "A Comparison of Spherical Wave Boundary Value Matching Versus Integral Equation Scattering Solutions for a Perfectly Conducting Body," IEEE Trans., AP-34, No. 7, July 1986.

The resulting currents and fields are shown in Figs. 2 and 3 for the case $\ell = 0.417\lambda$, $a = g = 0.0208\lambda$. The normalized arc length is the distance along the surface of the dipole normalized such that the extreme left and right points are -1 and 1, respectively.

It is seen from Fig. 3 that the gap field deviates somewhat from the desired 1 volt/m value, but is generally quite close; similarly, the field on the remainder of the surface deviates slightly from zero, but is again quite close to zero. The average value of the field across the gap is 0.974 v/m with a phase angle of 0.03 degrees. The average gap current is 0.002809 amps/m with a phase angle of 31.26 degrees. The voltage across the gap V_g is of course E_z multiplied by the gap width g , and the total gap current I_g is J_z multiplied by the dipole circumference. We may then calculate the dipole impedance

$$Z_g = \frac{V_g}{I_g} = 47.2 - j28.6 \text{ ohms}$$

A value obtained using the Livermore Numerical Electromagnetics Code (NEC) [2] for the same dipole is 49.9 - j30.5 ohms . The SPEX and NEC results agree to within 7% which is very good for impedance calculations, which are notoriously tricky. One of the advantages of SPEX is that the result is a rigorous solution of Maxwell's equations. The only error is due to imperfections in the boundary condition match, which can be inspected in great detail, as shown in Fig. 3. The good quality of the match over the entire surface--rather than a set of match points--provides a basis for high confidence in the results.

---

[2] G. Burke and A. Poggio, Numerical Electromagnetics Code (NEC)--Method of Moments, NOSC Tech. Doc. 116, Naval Ocean Syst. Center, San Diego, CA, January 1981.

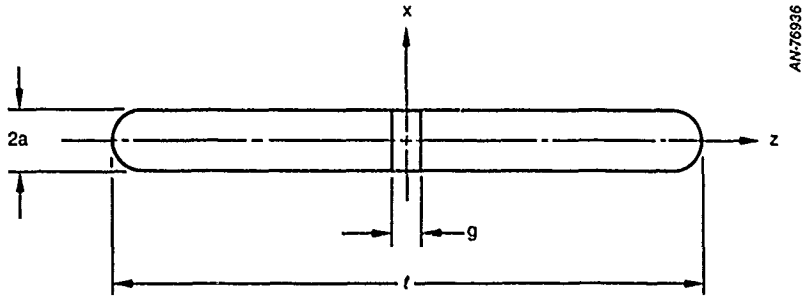


Figure 1. Dipole with gap excitation.

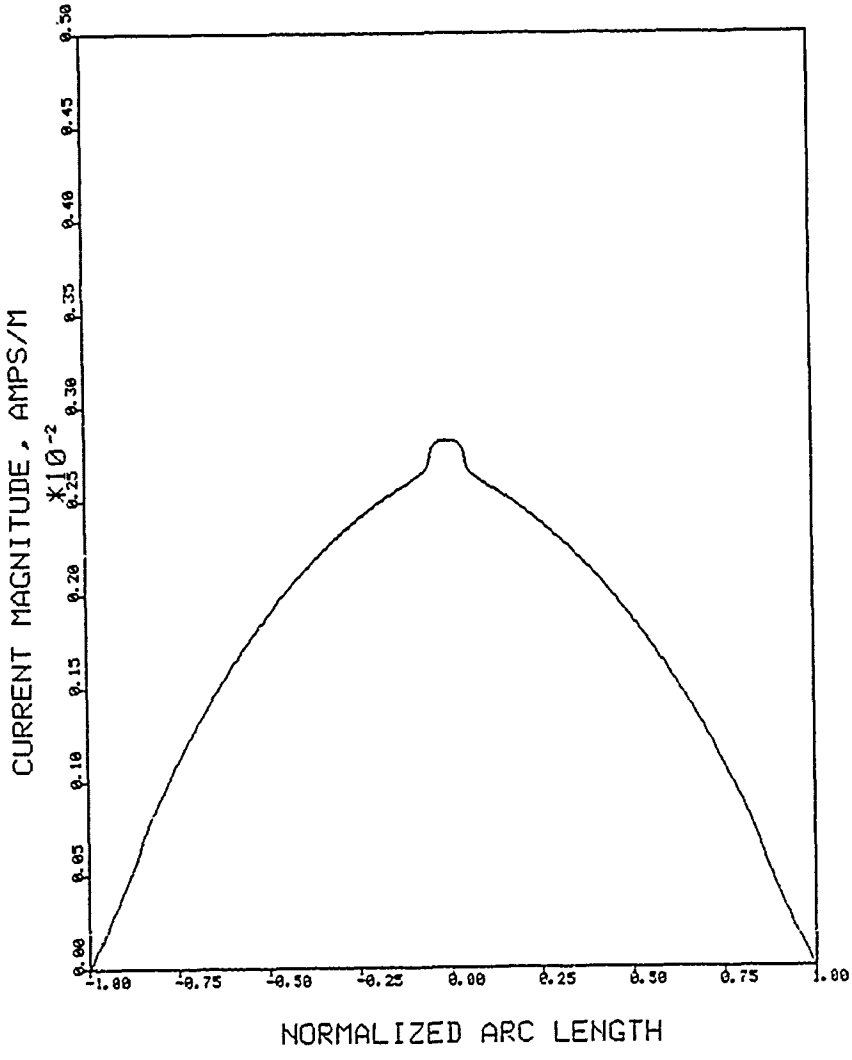


Figure 2. Surface currents J_z.

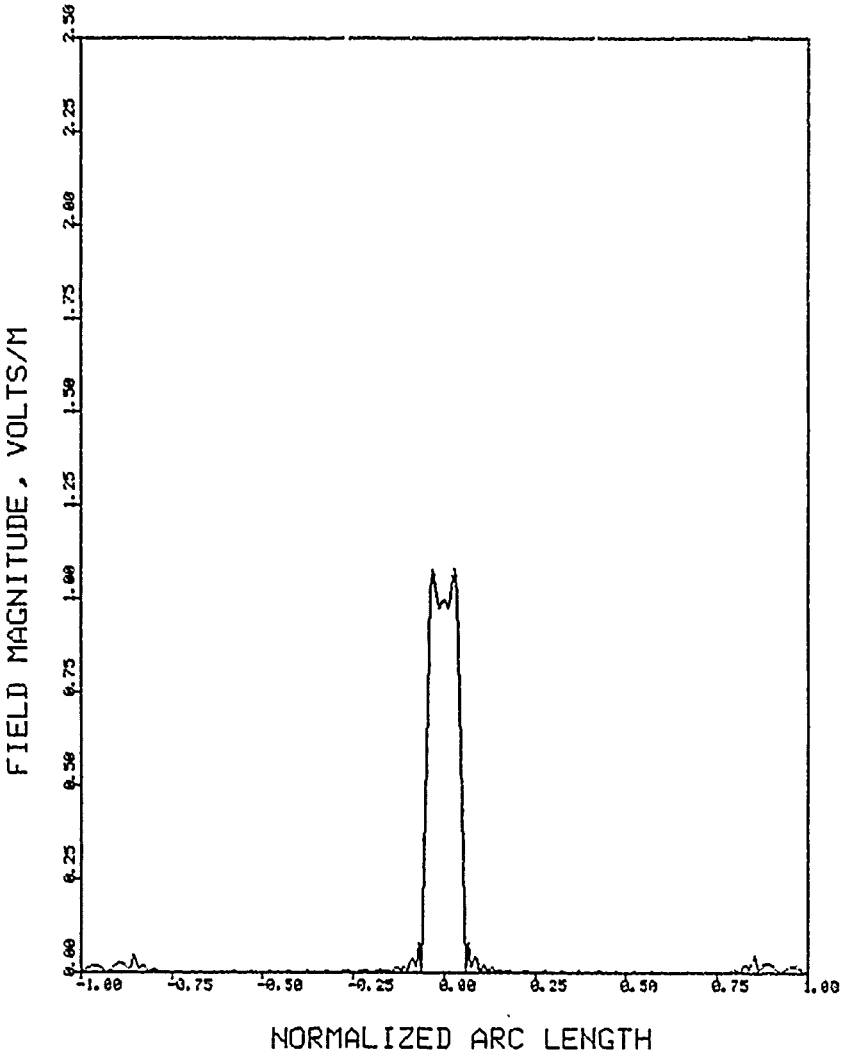


Figure 3. Surface field E_z.

I-NAC-3 A USER-FRIENDLY INTERACTIVE ELECTROMAGNETICS CODE FOR WORKSTATIONS MINIS AND MAINFRAMES

RUEDIGER ANDERS
Applied Electromagnetics Engineering
Vorder Halden 11, D - 7777 Salem 1
West Germany

A user friendly interactive version of the computer program NAC-3 called I-NAC-3 is presented for frequency domain analysis of TW antennas and scatterers of arbitrary geometry in isotropic but arbitrary lossy propagation media.

The MoM code is based on a point matching collocation technique and utilizes 3-term hyperbolic basis functions of complex arguments for enhanced convergence.

NAC-3 is highly modular and basically comprised of independent pre- and post-processors and an optional single or double precision core module that may be resident on host mainframes or minis for extensive number crunching if the I-NAC-3 is operatin on a PC.

The algorithms and methods used with NAC-3 have been optimized for efficiency, numerical stability and accuracy particularly at VLF. As the Data input is based on the storage minimizing 'node approach' antenna structures comprised of up to 800 segments and leading to matrix sizes up to 200x200 can be analysed on a fully equipped IBM AT personal computer.

Data input is tested for input syntax errors and immediately depicted graphically to detect possible input errors. Geometry input is made easy thru special geometry generating modules and extensive symmetry handling with automatic removal of redundant segments.

The post-processor provides all antenna features of interest in printed and graphical diagram form and offers disk file saving of geometry, current and impedance as well as far fields. The presentation may be followed by a demonstration if an IBM AT is on hand.

A DIFFERENT APPROACH TO USER-FRIENDLY AND ECONOMICAL GEOMETRY DATA INPUT FOR EM CODES

RUEDIGER ANDERS
Applied Electromagnetics Engineering
Vorder Halden 11, D - 7777 Salem 1
West Germany

One of the major problems in running EM codes is to enter the geometry data which specifies the real life object to the code. As there are as many philosophies as code developments, attempts are being made to establish a standard on a universal geometry description and data input that will free the user of the variing guidelines associated with each code.

An approach (used in NAC-3) that is different from the widely used input philisophy of NEC and MININEC is presented as contribution to the discussion of an EM code input standard.

The NAC-3 data input is macro controlled for improved readability, where each macro addresses data specific to the logic of the problem set up, such as geometry, symmetry,transformation, excitation or loads and operation environment.

Simila. to network analysis or finite element methods the geometry is set up nodewise. As all nodes are specified in consecutive order of the topolical graph, segments spanned by these nodes are defined automatically. Remaining segments will be specified merely by their associated node indices which eliminates the input of redundant coordinates and reduces input errors.

Among other advantages of the node approach there is mini-minimized storage allocation and very fast handling of multiple junctions and symmetries which is highly appreciated during interactive operation. As multiple junctions are determined merely by their integer node indices there will be no miss of a junction due to insufficient coordinate accuracy.

The node approach allows for segments to be located in symmetry planes or on symmetry axes thru automatic removal of redundant segments generated by symmetry imaging and is particularly suited for easy and fast generartion of 3-D geometries with help of a library of geometry modules.

INTERACTIVE GRAPHICAL DISPLAY OF SCATTERING DATA ON THE SPHERE

G. DAVID KERLICK

Sterling Software Corp.
Mail Stop 258-1
NASA Ames Research Center
Moffett Field, California 94035

ABSTRACT

Two families of computer programs have been developed for the interactive editing and display of complex-valued functions of spherical coordinates, such as the far-field radiation from acoustical or electromagnetic sources. The first family, called CSPUD, plots data which can be represented as two-dimensional arrays in spherical coordinates. A second family of codes, called AZSCAT, developed at Arizona State University, interpolates and interactively displays irregularly spaced data on the sphere. These programs take advantage of the three-dimensional interactive capabilities of advanced graphics workstations for manipulation of the graphical image of the data.

INTRODUCTION

With the advent of supercomputers, it has now become easier to simulate the near- and far-field behavior of complicated radiating systems for a large number of view angles. Such data often vary rapidly with spherical angle. In common practice, this data has been represented in a series of polar plots which represent conical "cuts" through the sphere at infinity, as illustrated in Figure 1. This representation is adequate for some purposes, but it does not provide a clear overall look at the behavior of the spherical functions. The present paper outlines two families of computer programs which use advanced graphical devices to present this information in a readily understandable form. This is accomplished by representing the data as colored, shaded polygons on a sphere in three dimensions.

Advanced Graphics Hardware.

Graphics workstations[1], such as the Silicon Graphics IRIS, have the capability of performing fast (hardware) manipulation of geometric entities and therefore permit interactive viewing of vector and polygon data in three dimensional space. For example, the latest version of the IRIS displays 1024 pixels horizontally and 768 pixels vertically in 24 color planes. It will perform 80,000 4×4 coordinate transformations per second, and will draw lines at the rate of 3 million pixels (40,000 linear inches) per second or fill polygons at the rate of 44 million pixels (7000 square inches) per second.

The first section of the paper describes the CSPUD programs for representing complex data on rectangular patches of spherical coordinates. The output of the program is a device-independent graphical image file which can be displayed on a workstation screen for interactive viewing, animation, and the generation of photographs, video recordings, or motion pictures.

The second section describes a related effort, in which the interpolation and display of irregularly spaced, real-valued data on the sphere has been investigated. The AZSCAT family of programs was developed as a result. These programs can be used when the scattering data is at an arbitrary collection of spherical angles.

The final sections describe the availability of software and devices supported and offers some conclusions and future directions for work. The input format for the CSPUD program, and contact addresses for obtaining the software are included as Appendices.

REGULARLY SPACED COMPLEX DATA

The CSPUD programs.

A set of FORTRAN programs called CSPUD (for Complex Spherical Update of Datasets) has been developed at NASA Ames Research Center. In this set of programs, datasets defined as complex-valued functions over two-dimensional arrays of spherical coordinates are plotted as colored four-sided polygons in space. The data, represented in a standard file format, can be summed coherently or incoherently, medianized, compared, and edited by use of programs in this family. A flow diagram of these programs is shown in Figure 2.

Data Format.

The input (*.CSP*)format for the CSPUD code is presented in Appendix 1. Data from a single co-latitude angle θ forms a "conical cut" of directions which intersect the sphere at infinity, as illustrated in Figure 1. The value of the scattered field for each cut is then a function of the longitude angle ϕ. This is usually represented as a separate polar plot in ϕ for each value of θ. The CSPUD code takes each of these cuts and represents it as a band of colored polygons on a sphere in three dimensions. The value of the scattered field (intensity, phase, etc.) is encoded as the color of the polygon. Thus a hundred or more polar plots can be represented in a single image.

The spherical angles are entered as two one-dimensional arrays

$$\theta = \theta_L, \qquad L = 1, N_\theta, \qquad 0 < \theta < 180$$
$$\phi = \phi_M, \qquad M = 1, N_\phi, \qquad 0 < \phi < 360$$

where N_θ and N_ϕ are the numbers of grid lines in the $\theta-$ and $\phi-$ directions. The values of θ and ϕ need not be evenly spaced or have integer values. Thus, the data corresponds in general to a large spherical rectangle which may be closed to form a band around the sphere, or to cover it completely.

A parameter called ISLICE in the input format relates the orientation of the spherical data set in Cartesian rectangular coordinates. At present, the choice ISLICE=1 is supported, with the pole of the sphere in the positive $z-$direction.

These arrays define a set of polygons on the sphere, as shown in Figure 3. These polygons are planar trapezoids with corners A, B, C, D defined as follows:

$$A = \left(r, \frac{1}{2}(\theta_{L-1} + \theta_L), \frac{1}{2}(\phi_{M-1} + \phi_M)\right)$$

$$B = \left(r, \frac{1}{2}(\theta_{L-1} + \theta_L), \frac{1}{2}(\phi_M + \phi_{M+1})\right)$$

$$C = \left(r, \frac{1}{2}(\theta_L + \theta_{L+1}), \frac{1}{2}(\phi_{M-1} + \phi_M)\right)$$

$$D = \left(r, \frac{1}{2}(\theta_L + \theta_{L+1}), \frac{1}{2}(\phi_M + \phi_{M+1})\right)$$

The value of the radius r of the sphere is arbitrary, and is chosen for convenience in programming.

The complex field data is entered as a two-dimensional array array of complex data values $F_{LM} = F_{real} + jF_{imag}, j = \sqrt{-1}$ at each spherical angle (θ, ϕ)

$$F(L, M) = (F_{real}(\theta_L, \phi_M), F_{imag}(\theta_L, \phi_M)), \qquad L = 1, N_\theta, \qquad M = 1, N_\phi,$$

Data Editing.

We now assume that data has been obtained for a range of spherical angles either from a simulation or an experiment and has been put into the standard *.CSP* format. Several utility programs have been written to manipulate the *.CSP* data files. The program CSPEDT allows the user to modify the data file by taking proper subsets of the data set, or by normalizing with respect to wavelength or a specified maximum value, or by changing the units of measurement. It is also possible to produce comparison plots of two different datasets, each plot occupying half of the sphere. The program CSPDIF permits the data from two different data sets over the same angles to be coherently or incoherently summed or differenced. The phase information is lost in incoherent summation, of course. This is very useful in evaluating the scattering behavior of multi-component configurations. A separate calculation can be made for each component, and the results can be superimposed. The program CSPMED allows the medianization of the data, that is, a sliding average based on a specified rectangular window in θ and ϕ angles. At present, this program only accepts data over uniformly spaced arrays of angles. Another program CSPINT will produce integrals of the data (e.g. radiated power) over user-specified sectors of the sphere.

Operation.

CSPUD reads in the data from the *.CSP* file, and queries the user as to which of six available functions of the complex data are requested. The choices supported are

(1) REAL PART
(2) IMAGINARY PART

(3) FIELD AMPLITUDE
(4) FIELD INTENSITY
(5) dB FIELD INTENSITY
(6) PHASE in degrees

The most useful functions are dB intensity and phase. After this request is made, the program computes a real scalar array to be color coded and plotted. This array F_{LM} is evaluated for every value of θ_L and ϕ_M and the minimum and maximum values are returned to the user. The user is then asked for two values FBOT and FTOP which define the color scale.

The color scale in common use at Ames consists of a smooth ramp from black to white through the color spectrum in the order

$$black \rightarrow blue \rightarrow cyan \rightarrow green \rightarrow yellow \rightarrow red \rightarrow white$$

Accordingly, polygons corresponding to values of the data less than FBOT are colored black, and all values greater than FTOP are colored white, and values in between are assigned a color on the scale. Regions of the sphere on which no data is given are colored gray.

Next, the user is asked which views of the dataset are desired. The views supported are

(1) FRONT (-x)
(2) REAR (+x)
(3) TOP (+z)
(4) BOTTOM (-z)
(5) LEFT (+y)
(6) RIGHT (-y)
(7) USER-SPECIFIED VIEWPOINT
(8) ENTIRE SPHERE (Z-buffer)

There can also be an optional additional light source for shading. Shading is accomplished by computing the dot product of the unit normal vector **N** of the panel with the unit normal **L** in the direction of the light source, as illustrated in Figure 4. The value of this product is also used to eliminate polygons on the dark side of the sphere opposite the light sources, and to order the polygons for drawing. In the last choice, all polygons are produced, and the hardware Z-buffer feature may be used in conjunction with animation software to produce a motion picture of a turning sphere.

Output to ARCGraph Files.

With this information in hand, CSPUD now produces a plot with shaded polygons, latitude and longitude lines, and a default set of titles. The data is written

to a device-independent graphical image file, which can then be displayed on a workstation.

CSPUD generates the image file using the NASA Ames standard device-independent subroutine library ARCGraph[2]. The ARCGraph system takes advantage of the three-dimensional interactive capabilities of the IRIS workstation. Graphical entities reside in a two- or three-dimensional "world space." The ARCGraph file specification consists of vector, polygon, and raster objects which reside in this space. The program produces all three types of graphical data: (1) a legend and titles file in the 2-dimensional vector *.PLO* file format which contains titles and a color bar and key, (2) a three-dimensional shaded polygon image (*.POL*) file of color-coded polygons on the sphere, and (3) a three-dimensional vector (*.VEC*) file which contains a wire frame image of the latitude and longitude lines of the sphere.

The ARCGraph file can be displayed interactively on an IRIS workstation using GAS (Graphics Animation System) software developed at NASA Ames. GAS reads the ARCGraph image file into the IRIS display memory where it can be accessed quickly and manipulated in 3D on the IRIS monitor via mouse control. This allows for viewing the image from any angle and scaling to any size, which is helpful when one is concentrating on small regions of the sphere.

Hardcopy Devices.

The images created by CSPUD can be saved via GAS to a number of hardcopy devices. Still pictures can be created using a Dunn Instruments Model 635 camera. This device creates a high resolution, full color Polaroid picture (or slide or viewgraph) of the image on the IRIS graphics monitor. Video tape sequences can be generated using the Lyon Lamb VAS IV animation controller system. This system, when used with the IRIS and GAS, does single frame animation of a pre-defined sequence of motions of an image in a totally automated fashion. 16mm motion picture sequences can be generated using the Dunn Instruments Model 632 camera. This device also does single frame animation in a manner similar to the Lyon Lamb controller.

Examples.

Some colored viewgraphs, here reproduced in black and white, are presented as illustrations of the graphical images produced by CSPUD. The first set of examples are of the far field generated by an ensemble of point monopoles arrayed in a $3 \times 3 \times 3$ cube, illustrated in Figure 5. There is a monopole of strength -10 dB at the body center of the cube, sources of strength -20 dB at the eight vertices, sources of strength -30 dB at the six face centers, and sources of strength -40 dB at the twelve edge centers. In the first case studied, the sources are regularly spaced a wavelength apart.

Figure 6 shows the CSPUD plots of the regular cube. Two views of the dB intensity of the far field are shown, on a color scale ranging from -42 to 0 dB. The actual values of the data varied between -115.7 db and 5.89 dB. Values of the far field were computed at intervals of 1.25 deg in θ and 2 deg in ϕ. Due to the symmetry of the sources, The rear and top views of the data are identical; the only difference in the images is due to the resolution of the coordinate grid.

Figure 7 shows a phase portrait of the same ensemble of monopoles. There is an equiphase surface at infinity with discontinuities that correspond with the intensity minima.

In the second example, shown in Figures 8 and 9, a random perturbation of up to a quarter of a wavelength is applied to each source. The configuration is no longer symmetric, and subtle differences can be noted in the the dB intensity and phase plots.

The NEWAIR antenna code[3] from Ohio State University, based on the Geometrical Theory of Diffraction, was adapted for the CRAY computer and modifications were made to produce output in the *.CSP* format. The result shown here, Example 1 from the NEWAIR user's manual is the pattern of a monopole antenna mounted over a composite ellipsoid, as illustrated in Figure 10. A viewgraph of the radiation pattern from this antenna is shown as a dB intensity plot in Figure 11. Here, at a resolution of 1 degree in both θ and ϕ, the image contains over 30,000 polygons, as much data as 180 polar plots.

This method of representation could also be used with the eightrm NEC basic scattering code[4], or with antenna or scattering simulations based on Physical Optics or the Physical Theory of Diffraction, with trivial modifications to the output subroutines. Experimental data could be also be plotted this way, provided that the range of spherical angles measured is consistent with the input format.

Irregularly Spaced Real Data

In a related effort, conducted at at Arizona State University[5], the problem of interpolating and representing data irregularly spaced over the sphere was investigated. That is, for a countable number of points $V_i, i = 1, n$ on the surface of a sphere, A function $F(V)$ is constructed so that $F(V_i) = f_i$ where f_i is the data value at the ith point. Such data can arise naturally from geometric optics or ray-tracing programs or in the calculation of extended Gaussian images[6] of surfaces approximated by polygonal facets.

The principal result of this work was the generalization to the sphere of the planar concept of a minimum norm network of triangles. The sphere is triangulated using the points V_i as vertices, an approximating function and first derivatives are constructed, and the construction is extended to cover the entire sphere. A minimum-norm triangulation of the sphere is shown in Figure 12.

Several ways of providing graphical output of the function were investigated, including colored contour lines, shown in Figure 13, colored shaded surfaces (Figure 14), and raised surface plots (Figure 15). The raised surface is a plot of a function which has been scaled so that $r = 1$ corresponds to the minimum value of F and $r = 2$ corresponds to the maximum value. The smoothing is done via Gouraud shading of the polygons, which can be done in hardware on the IRIS 2000 and 3000 series workstations.

Availability of Software

All codes are written in FORTRAN-77, except for AZSCAT, which is written in

Pascal.

The CSPUD code is available in versions for the VAX and CRAY X-MP computers.

The ARCGraph library is presently supported on these computers and operating systems: VAX/VMS, CRAY X-MP/COS, and IRIS 2000 Series Workstations. It is also being developed for the VAX, AMDAHL, and CRAY-2 computers running UNIX. It is supported on the Tektronix 4010 series of terminals, as well as the IRIS, and conversion programs exist to the DICOMED photographic system and QMS and Versatek printers.

The GAS program resides on the IRIS 2000 and 3000 series workstations.

The AZSCAT codes run on the IRIS 1000 series workstations.

Contact addresses for the software are given in Appendix 2.

SUMMARY

Computer graphics techniques have been found to be of substantial value in displaying the results of radiation and scattering calculations. In particular, 3D graphics allows about an order of magnitude of compression in the data that can be presented in a single image. As such, it makes a useful adjunct to present and future programs for the numerical simulation of acoustic and electromagnetic scattering. As workstations continue to increase in computational power, we may look forward to the day when the scattering simulation can be integrated with graphical output to allow instant feedback in the interactive design of radiating and scattering sources.

ACKNOWLEDGEMENTS

The graphics subroutines of the CSPUD code and the GAS graphics animation system were written by Fergus J. Merritt and Gordon V. Bancroft, of Sterling Software. The ARCGraph programs were written by George Makatura of Sterling Software and Eric Hibbard of the Computer Graphics Research Group at NASA Ames. The AZSCAT code was written by Ramamani Ramaraj and Gregory Nielson of Arizona State University.

REFERENCES

1. V. Watson, P. Buning, et. al., *Use of Computer Graphics for Visualization of Flow Fields*, AIAA Aerospace Engineering Conference and Show (February 1987), Los Angeles, CA.
2. G. Makatura and E. Hibbard, "ARCGraph System User Manual", Computer Systems Division, Computer Graphics Research Group, NASA Ames Research Center. Moffett Field, CA 94035, April 1986.
3. H.-H. Chung and W. D. Burnside, "General 3D Airborne Antenna Radiation Pattern Code User's Manual", Technical Report 711679-10, Ohio State University ElectroScience Laboratory, July 1982.
4. R. J. Marhefka, "Numerical Electromagnetic Code - Basic Scattering Code (Version 2) Part II: Code Manual", Naval Ocean Systems Center, San Diego, CA, July 1983.
5. R. Ramaraj, "Interpolation and Display of Scattered Data over a Sphere", M. S. Thesis, Arizona State University, Tempe AZ., August 1986.
6. B. K. P. Horn, *Extended Gaussian Images*, Proc IEEE **72 No. 12** (December 1984).

APPENDIX 1

File Format for Complex Spherical Data (.CSP) Files

Record 1: *Array dimensions and Orientation*

```
READ(LUN) ITHETA, IPHI,ISLICE
```

Record 2: *Elevation Angles*

```
READ(LUN) (ATHETA(L),L=1,ITHETA)
```

Record 3: *Azimuth Angles*

```
READ(LUN) (APHI(M),M=1,IPHI)
```

Section 4: *Field Values*

```
DO 100 L=1,ITHETA
READ(LUN) (FR(L,M),FI(L,M),M=1,IPHI)
100 CONTINUE
```

APPENDIX 2

Contact Addresses for Software

CSPUD and GAS

Dr. Val Watson
Mail Stop 258-2
NASA Ames Research Center
Moffett Field CA 94035

ARCGraph

Mr. Eric Hibbard
Mail Stop 233-14
NASA Ames Research Center
Moffett Field CA 94035

AZSCAT

Prof. Gregory Nielson
Dept. Computer Science
Arizona State University
Tempe, AZ 85287

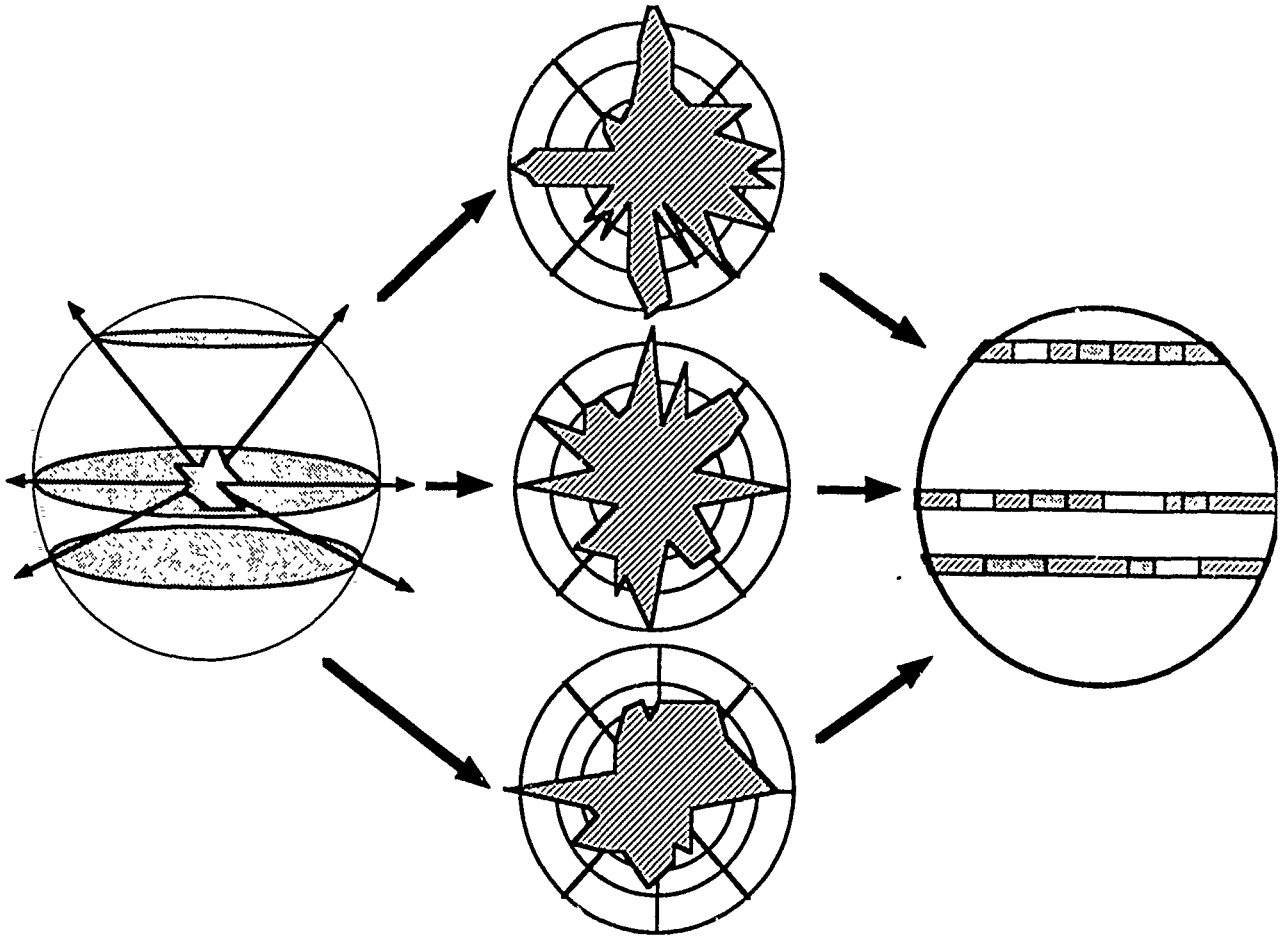


Fig. 1. Scattering geometry, conical cuts, polar plots, and spherical polygon representation of radiation fields.

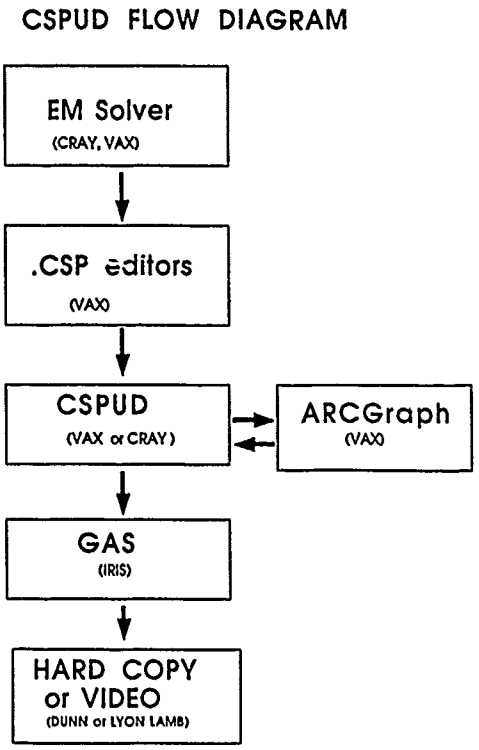


Fig. 2. Flow diagram of the CSPUD code.

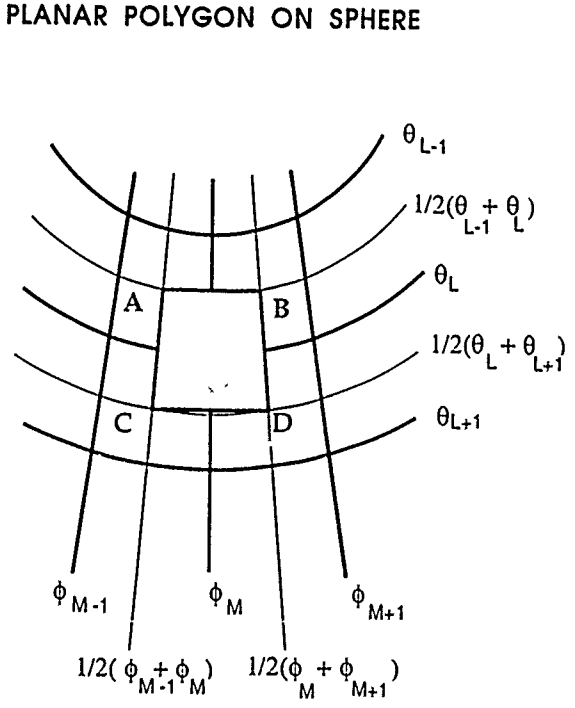


Fig. 3. Planar polygon formed by on the unit sphere by intersection of constant-θ and constant-ϕ curves.

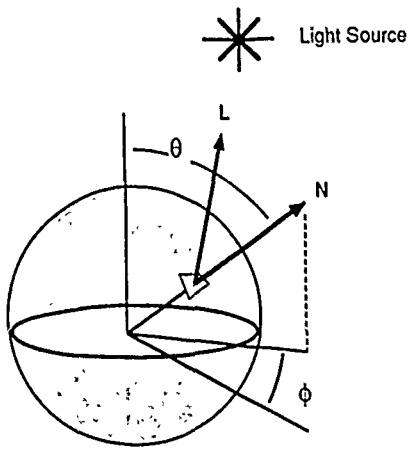


Fig. 4. Shading of polygons on the sphere.

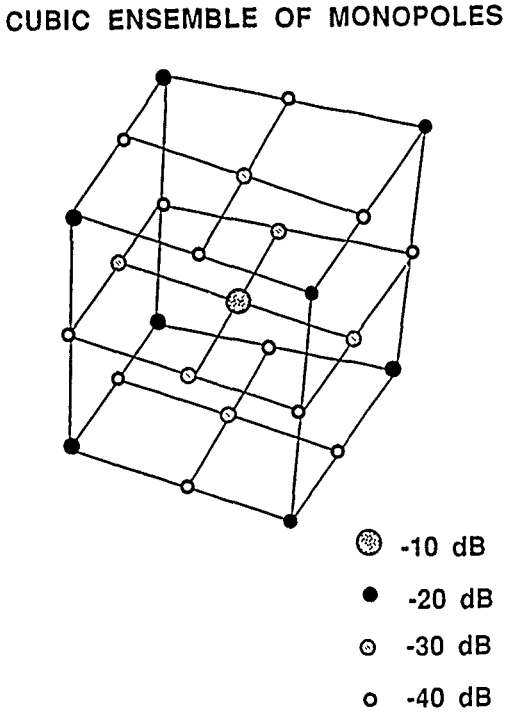


Fig. 5. Schematic drawing of ensemble of monopole radiators

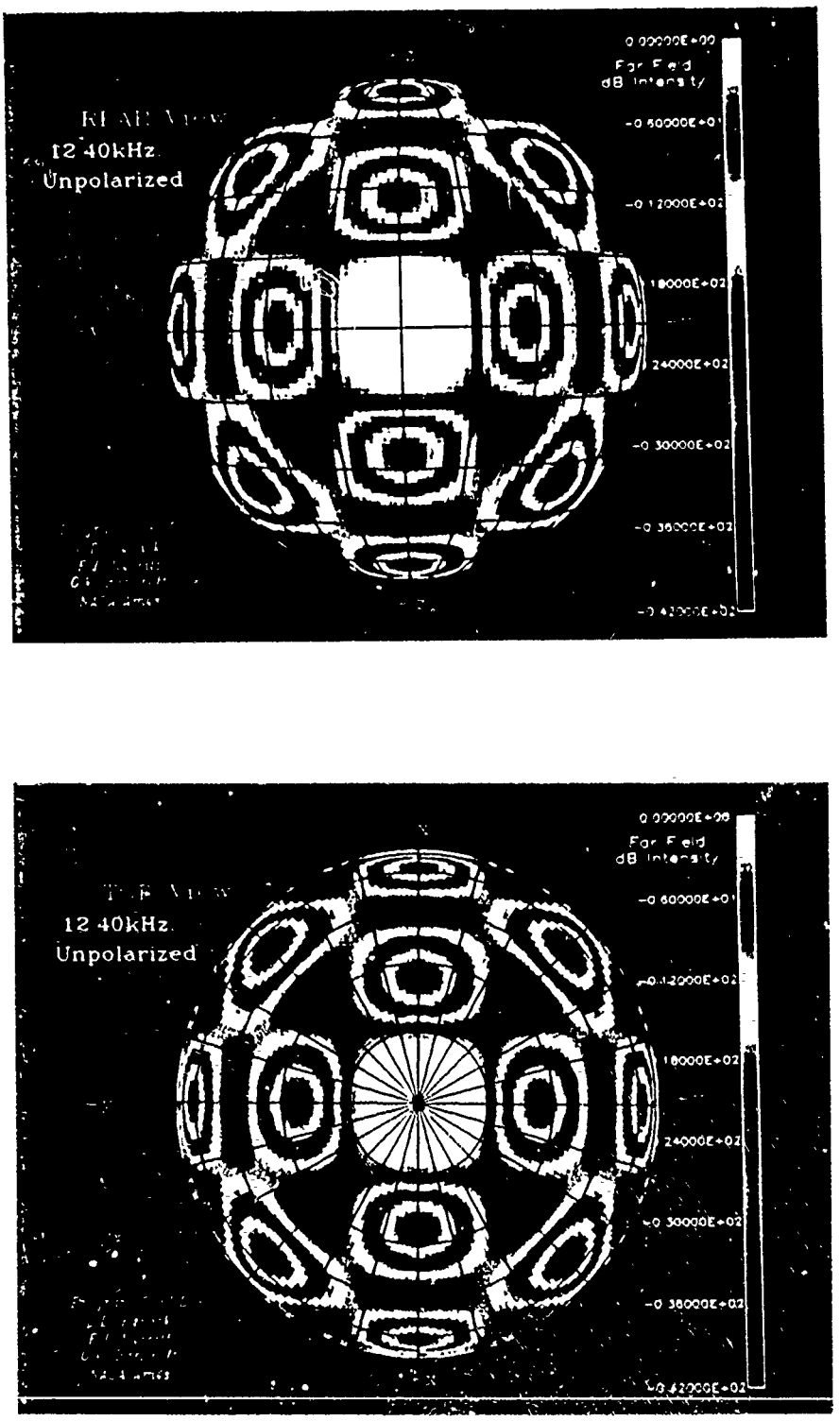


Fig. 6. a) dB intensity of radiated field of a cube of monopoles, Rear view. b) Top view.

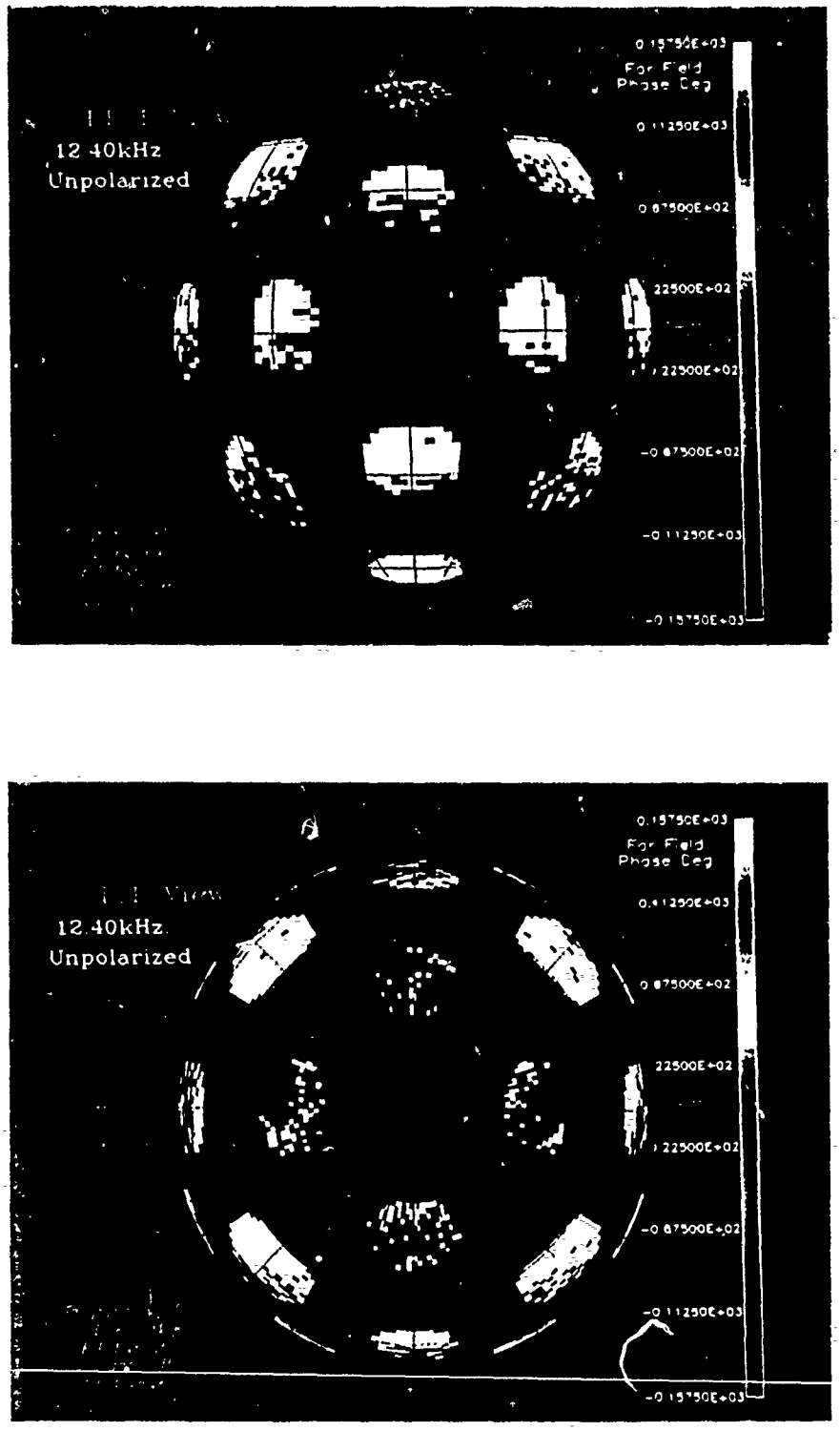


Fig 7. a) Phase plot of cubic ensemble of monopoles, rear view. b) Phase plot, top view.

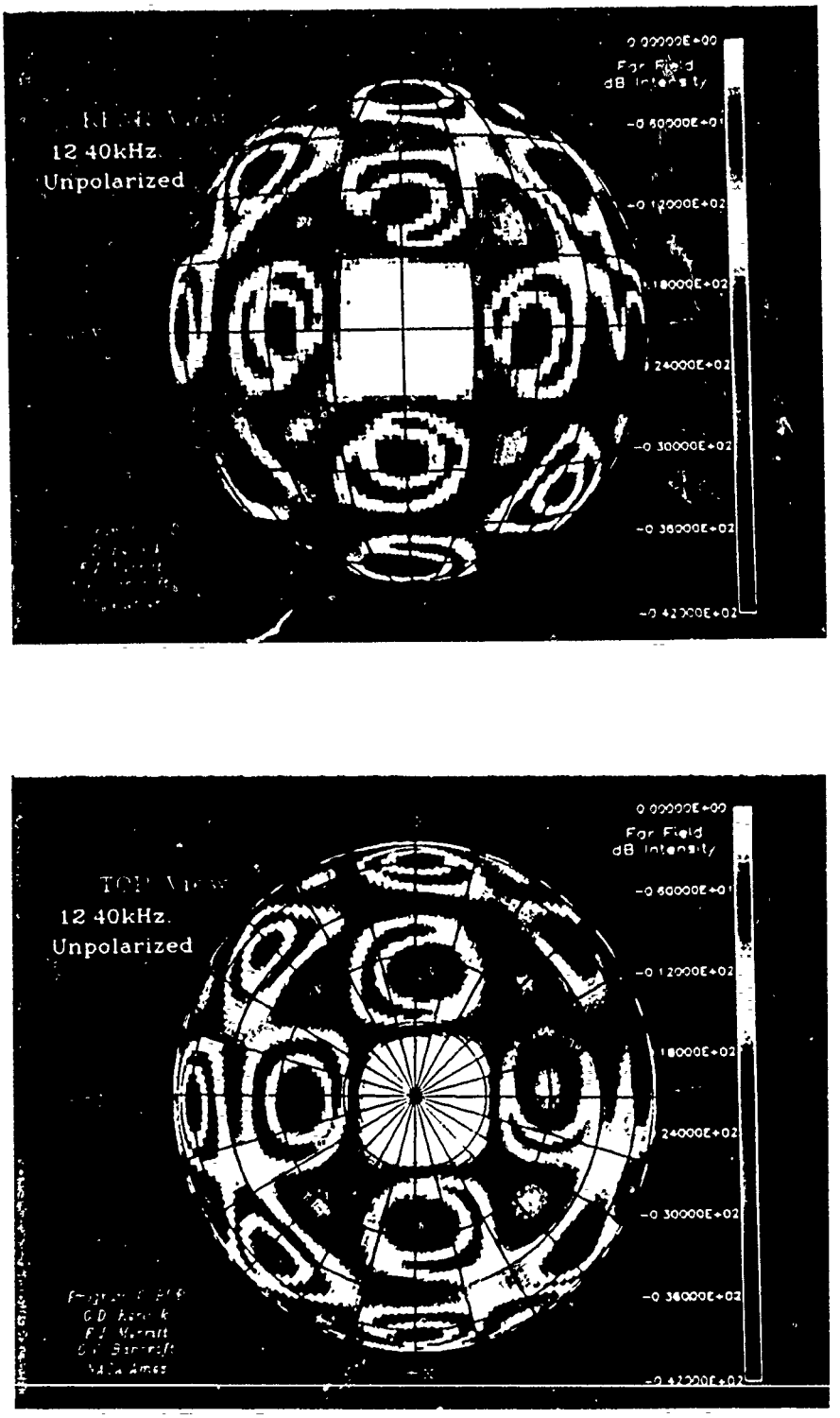


Fig. 8. a) dB intensity of radiated field of a randomly perturbed cube of monopoles, Rear view. b) Top view.

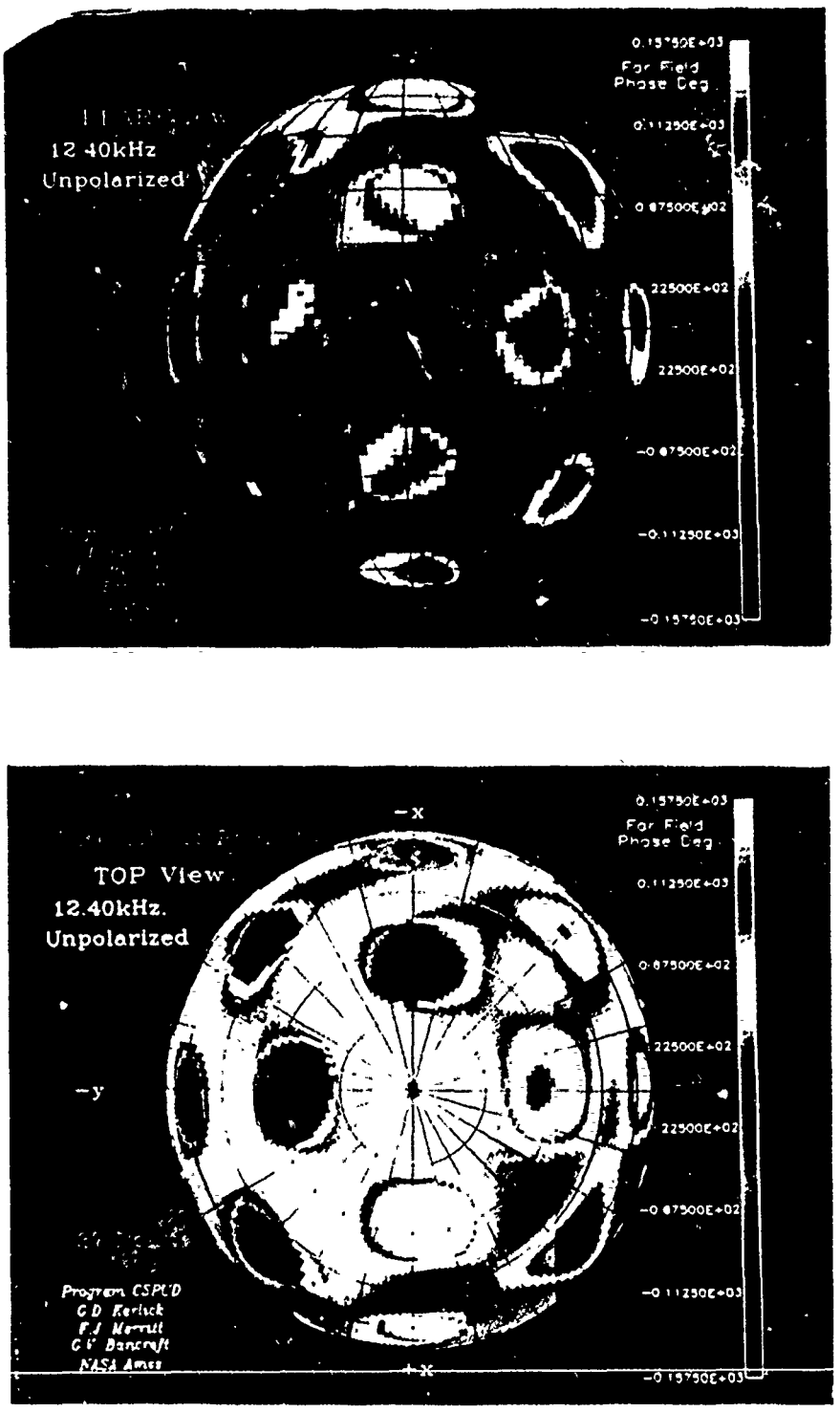
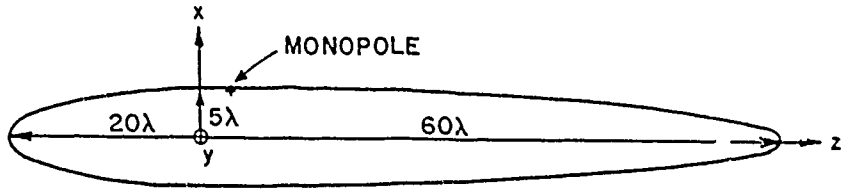
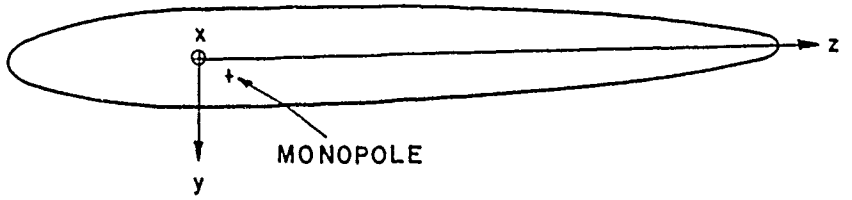


Fig. 9. a) Phase plot of perturbed cube, rear view. b) Phase plot, top view.



(a) SIDE VIEW



(b) TOP VIEW

Fig. 10. A monopole mounted on a composite prolate spheroid (from Ref. 3, Ex. 1).

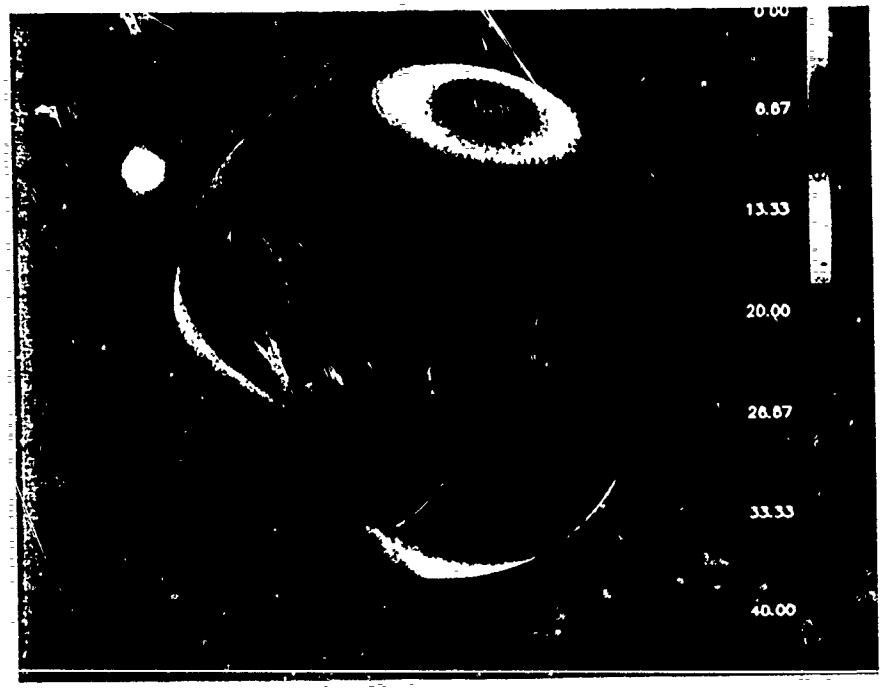


Fig. 11. CSPUD plot of the field of the monopole and spheroid of Fig. 10 in the θ-polarization.

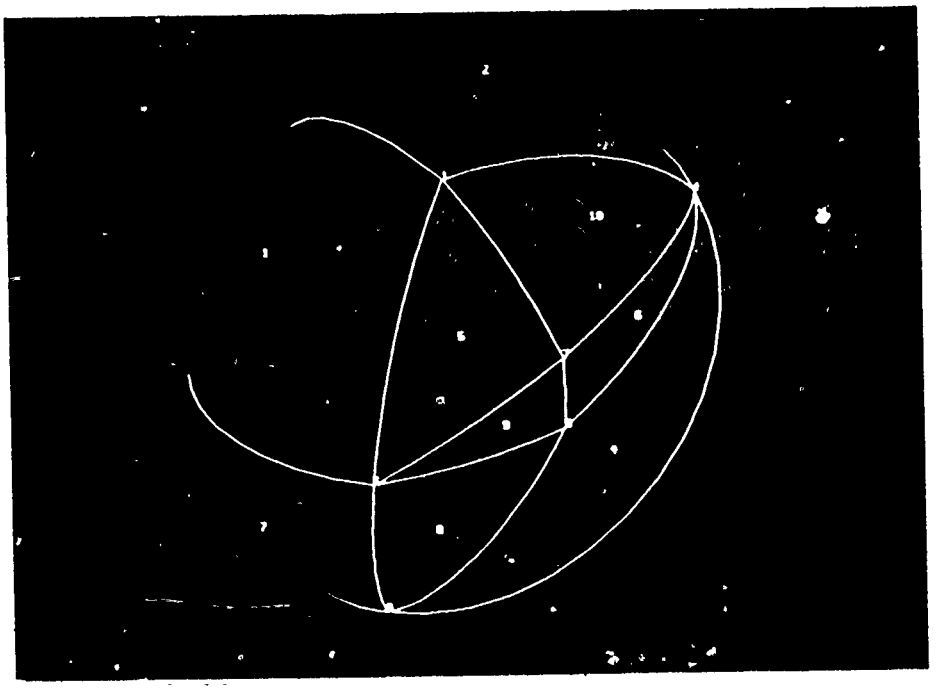


Fig. 12. Minimum norm network triangulation of scattered data on the sphere (from Ref .5).

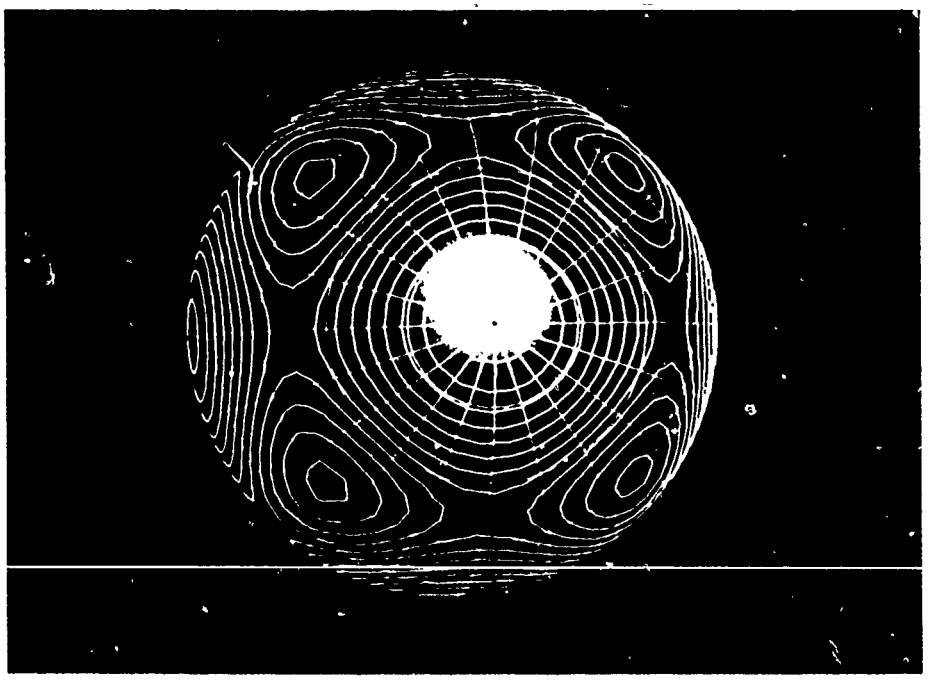


Fig. 13. Contour line plot on sphere of the function $cos(x^2-y^2)cos(y^2-z^2)cos(z^2-x^2)$ (from Ref. 5).

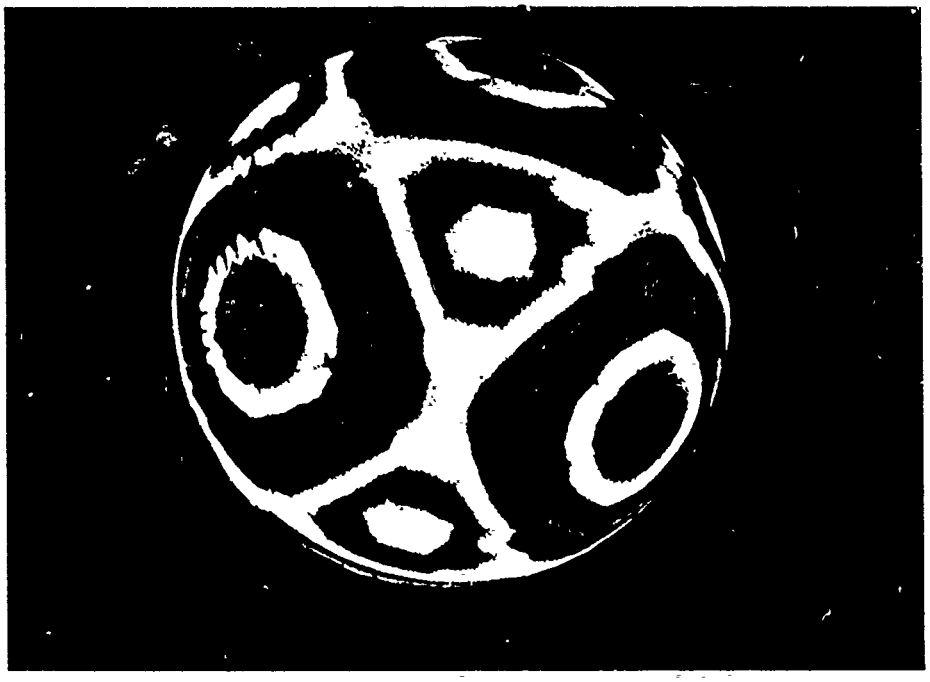


Fig. 14. Colored shaded plot on the sphere of the function $cos(x^2 - y^2)cos(y^2 - z^2)cos(z^2 - x^2)$ (from Ref. 5).



Fig. 15. Shaded plot of a function surface on the sphere.

A NUMERICAL ELECTROMAGNETIC ENGINEERING DESIGN SYSTEM*

A. P. Ludwigsen
University of California
Lawrence Livermore National Laboratory, Livermore, CA

Introduction

The Numerical Electromagnetic Engineering Design System (NEEDS) is a computer aided electromagnetic design and modeling system being developed at Lawrence Livermore National Laboratory. It is being developed to assist the design engineer in using the various modeling codes available by simplifying the model development and output examination. This paper examines some of the features and the development of the system.

Background

Present electromagnetic modeling programs are useful but lack the convenience necessary for efficient design practices. They are difficult to learn and for many codes, the documentation is poor. Additionally, there is no unifying standard with which the user can define the model being studied or examine the results. It is difficult to analyze large problems due to the quantity of data produced by the codes and there are no general purpose graphics programs to examine the geometrical model, impedance behavior, radiation patterns, etc.

Implementation

NEEDS provides an alternative to the present system for electromagnetic engineering design. It presently supports the Numerical Electromagnetics Code (NEC) (G. J. Burke and A. J. Poggio, "Numerical Electromagnetics Code - Method of Moments", NOSC TD 116, Naval Ocean Systems Center, San Diego, CA, Jan. 81) and the Ohio State Basic Scattering Code (R. J. Marhefka and W. D. Burnside, "Nu-

* Work performed under the auspices of the U. S. Department of Energy by the Lawrence National Laboratory under Contract W-7405-Eng-48.

merical Electromagnetic Code - Basic Scattering Code", Technical Report 712242-14, Ohio State University ElectroScience Laboratory, Dec. 82). It is an easy to use system, being equipped with an on-line help package. It is a series of pull-down menus and forms, based on developments by the *EAGLES* team at Livermore (B. S. Lawver, D. W. O'Brien, and M. E. Poggio, "Code Development with the EAGLES Engineering Problem-Solving Environment", UCID-20666, Lawrence Livermore National Laboratory, Feb. 86), which prompts the user for the proper input. A sample shown in Figure 1.

There are several packaged graphic displays presently available, a model geometry previewer, wire segment current display, Smith chart, and polar radiation pattern plots. The Smith chart uses a parametric spline to approximate the impedance curve between data points. Future plans call for expanded capabilities for the existing packages, a near-field contour plot, rectangular pattern plots and current displays, and other graphics as deemed necessary. The model previewer is useful in that it allows the model to be examined for errors before a costly computer run is made and is demonstrated in the examples below.

Examples

Figure 1 shows a sample menu and form display in which the wire geometry data is entered. The values entered must fit into pre-defined limits established by the modeling code or the form will not accept them. An error message is displayed in this case and the user is returned to the invalid entry. Figure 2 shows a wire model with connected segments (small dots). This simple demonstration shows how the model previewer can help by allowing the user to check a complicated model before submitting it to the modeling code.

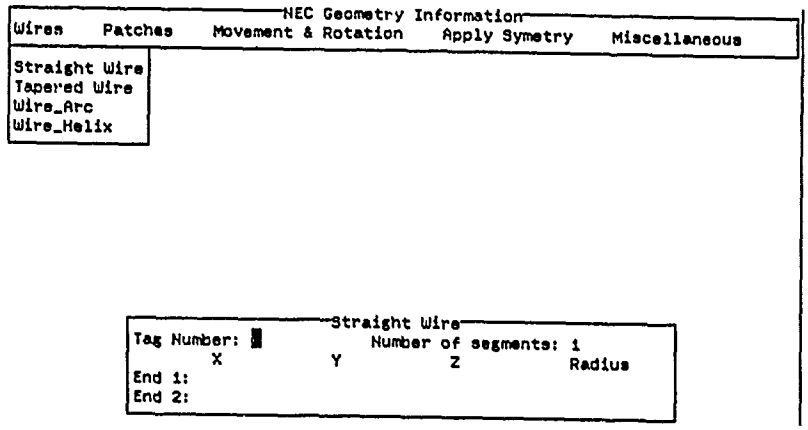


Figure 1. Sample Menu and Form Display

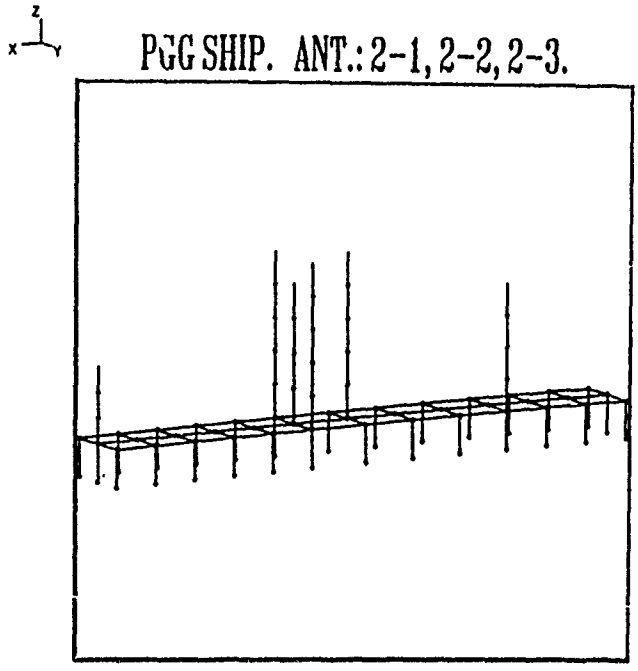


Figure 2. Wire Model showing connections

EXAMPLE 2. CENTER FED LINEAR ANTENNA.

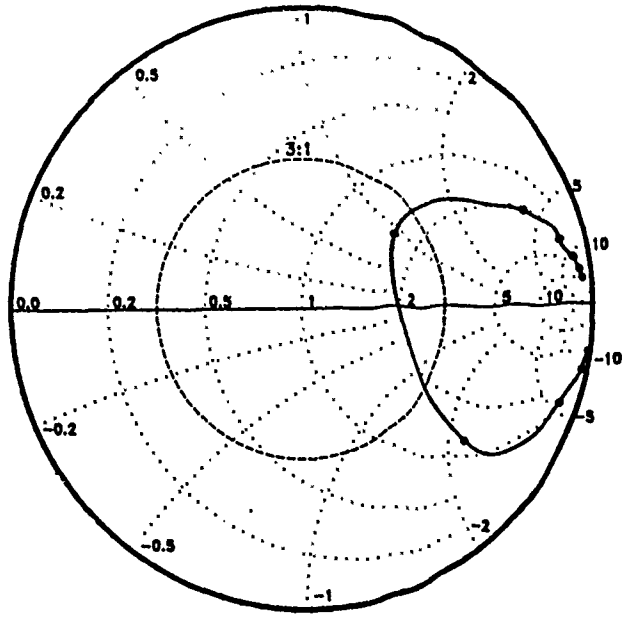


Figure 3. Sample smith chart

Conclusions

The development of an engineering workstation for electromagnetic design can ease the difficulties found in designing and examining electromagnetic systems. It allows the design process to be more interactive and can thereby reduce the amount of time necessary to reach a final solution.

GRAPHICS PANEL

CHAIR
Steve Lamont
SAN DIEGO SUPERCOMPUTER CENTER
SAND DIEGO, CA

PANELISTS

PETER LUDWIGSEN
Lawrence Livermore National Laboratory
Livermore, CA

EDMUND K. MILLER
Kansas State University
Lawrence, KS

JOHN STRAUCH
Unisys Corporation
San Diego, CA

The discussion ranged widely, from the applicability of graphics standards to computational electromagnetics software to the place of graphics in EM education to the need for new paradigms for visualization.

Brief presentations were given by each panelist. Pete Ludwigsen reviewed the graphics aspects of the NEEDS project in progress at LLNL and proposed a library of graphics programs and subroutines for use in EM research and engineering. John Strauch discussed IGUANA graphics. Ed Miller spoke about aspects of animation, the place of computer graphics and animation in the field of computational electromagnetics. Steve Lamont covered the need for standards in graphics and discussed some of the current and future standards.

The open discussion covered a broad range of topics. The discussion centered on the place of graphics and animation in education. What are the motivating factors in choosing a career in electromagnetics engineering or research? Are they flashy graphics? Will "sexy" tools like animation really attract more students into the field of EM or will EM go the way of power engineering and attract fewer and fewer students?

There was also some discussion of the place of color graphics. Is color graphics just a way to embellish data for presentation to a, possibly, non-technical representation of a funding agency to attract more funding or is color graphics a vital and useful tool in the process of research and engineering? Where does this leave those practitioners who don't have the large budgets for fancy graphics workstations?

What place do workstations play in EM and graphics? Certainly, the PC revolution over the past decade has brought remarkable advances in computing power and made them readily available to the average engineer or scientist. Certainly IGUANA and the Northrop "NEWS" system shown at ACES III, as well as the LLNL "NEEDS" project in progress, will provide a powerful user interface in the model generation and output interpretation processes. But have we progressed beyond the "batch mode" paradigm, simply replacing punched card input with more sophisticated graphic and text editors?

This writer believes that while the large mainframe computer will certainly never be replaced in computer modeling -- the size of the problems we study will certainly grow to meet and exceed the capacities of our computing resources -- the workstation can be exploited in a number of ways that have not as yet been fully explored. The workstation should not just be considered a front end tool for editing input and post-processing output, but treated as a synergistic entity, symbiotically interacting with the larger mainframe system in a way that enables the whole (system) to exceed the sum of its individual component parts. Cooperative or distributed network computing is becoming a reality and those of us involved in software, and particularly graphics software, should be ready to exploit its capabilities.

As the reader can readily see, this report consists largely of questions rather than answers. This writer feels that these questions remain open and will be the subject of discussion and research into the forseeable future.

*The Minutes of the ACES Committee Reports and Concluding Business will be contained in the May 1987 Newsletter.

SESSION VII - "CODE DEVELOPMENT"

Moderators: H. Schuman & R. Bevensee

A NEW APPROACH TO A SIMPLER AND MORE EFFICIENT TREATMENT OF MULTIPLE JUNCTIONS BY HIGHER BASIS FUNCTIONS

RUEDIGER ANDERS
Applied Electromagnetics Engineering
Vorder Halden 11, D - 7777 Salem 1
West Germany

Higher order basis functions require considerably more effort to handle multiple junctions than do simple pulse basis functions. This disadvantage is usually far offset by higher convergence rates but can in some instances lead to undesirable loss of accuracy and code limitations, particularly at VLF.

If for example 3-term basis functions are employed by means of B-splines, each B-spline will span over n+m+1 subsections, where n and m are the number of branches connected to the center section. But as the current distribution on each subsection is comprised of 3 overlapping splines, there will be as many as $n+m+1+\sum_{n} i+\sum_{m} j$ segments involved in calculating the coefficient terms.

A new approach (based on S-splines and used with NAC-3) is presented, where 3-term (or higher order) basis functions span over only 2 adjacent segments and still keep the same degree of continuity.

Even though the current interpolation on a segment is still made up by 3 overlapping functions, only n+m+1 segments are involved. This does not only result in faster execution since less connecting branches need to be considered, but also reduces the error propagation considerably, in particular with multiple junctions in wiregrid modeling.

As opposed to B-splines the S-splines offer a simpler way of enforcing continuity on the current or charge distribution, or end conditions on current and dicontinutity conditions on charge. If applied for instance to bare/insulated wire junctions or wires penetrating an interface no extra spline function and additional match point will be neccesary.

AN ALGORITHM FOR MINIMIZING MATRIX BANDWIDTH IN METHOD-OF-MOMENT COMPUTER CODES*

R. M. Bevensee
Lawrence Livermore National Laboratory Livermore, California 94550

INTRODUCTION.

The Method-of-Moments technique in electromagnetics reduces an integral equation for the response vector of an object to matrix form: V=ZI, where V is the column matrix of amplitudes of the excitation functions, Z is the N x N square interaction matrix, and I is the column matrix of amplitudes of the response functions. It is expedient to solve some large-N problems by banded matrix iteration [1] rather than the conventional LU-decomposition followed by forward and backward substitution (an N-cubed operation). Banded matrix iteration requires all the large- $|z_{ij}|$ elements above a selected reference level $|z_r|$ to lie within a band of width B on either side of the diagonal. The remaining z_{ij} may fall anywhere in Z. Usually the initial element numbering specifies a B which can be reduced by renumbering to a minimum determined by $|z_r|$.

We describe an algorithm for iteratively exchanging pairs of elements (i.e., interchanging row and corresponding column pairs in a reduced form of Z) until the minimum or near-minimum B is attained. The final element renumbering scheme yields the banded full-matrix Z_B to employ in a banded-matrix iteration scheme.

Other algorithms for reducing bandwidth of sparse matrices include the popular reverse Cuthill-McKee algorithm and the Gibbs-Poole-Stockmeyer algorithm [2]. Both are based on graph theory. Neither guarantees the minimum possible bandwidth for a given matrix after reduction.

FORMULATION OF THE PROBLEM.

Since each z_{ij} is declared either large or small commpared to the selected reference it may be replaced by 1 or 0 to yield a reduced matrix Z_r. Z_r is symmetric in a reciprocal system with $z_{ij} = z_{ji}$. Then the problem becomes that of iteratively interchanging pairs of columns, and their corresponding row pairs, consisting of 1's and 0's, until all the 1's lie within a minimum bandwidth about the diagonal. An index continually records the original position of each column so that the element renumbering is evident at all times.

DEFINITION OF COLUMN PARAMETERS.

The six distinct types of columns which may appear in Z_r or any subsequent reduced form Z_B of it, are illustrated in Fig. 1. Each column (except (3)) is identified by a vertical line of e's on which lie 1's and 0's in any order, but bounded by an x which denotes the highest and lowest 1 in the column. The upper (lower) bandwidth BU (BL) of a column is zero if the highest (lowest) 1 corresponds with the diagonal 1 (also denoted by x). The columns (1) and (2) have BU>0, BL(<BU)>0 or =0, respectively. Column (3) has only the diagonal 1 and BU=BL=0 for a physical element labelled i weakly coupled to the others in the sense that $|z_{ij}| < |z_{rr}|$ for all $j \neq i$. Column (4) has BU>0, BL<0. Columns (5) and (6) have BU=0 or <0, respectively, and BL(<BU)<0.

A column bandwidth BW is max ($|BU|$, $|BL|$).

We define a column as left- or right-moving if, by moving it to the left or right, we can reduce its bandwidth. Its range R is defined as the largest number of columns it can move to restore its starting bandwidth. If a left-(right-)moving column moves right (left) or moves left (right) beyond its range its bandwidth increases. With this definition, R=BU+BL, and is >0 for a left-moving column and <0 for a right-moving one. A column of R=0 cannot be moved without increasing its bandwidth BW. However,

*Work performed under the auspices of the U.S. Department of Energy by the Lawrence Livermore National Laboratory under Contract W-7405-ENG-48.

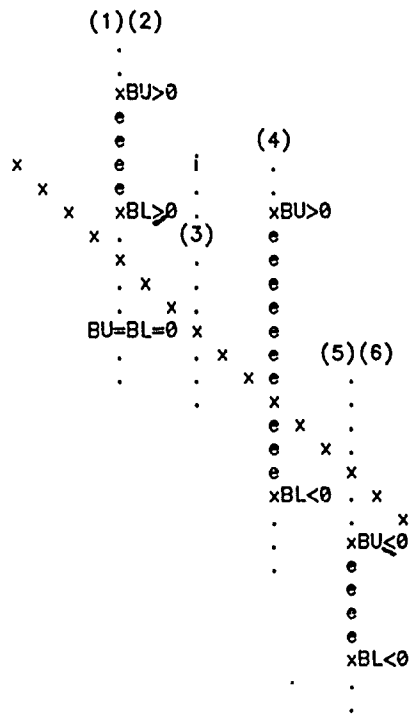


Fig. 1. The six types of columns and their defined upper and lower bandwidths BU and BL. Each column is identified by a series of e's denoting 0's and 1's, bounded by an x which denotes the highest or lowest 1 on the column (excluding the diagonal element if possible). Column i of case (3) with just the diagonal element, BU(i)=BL(i)=0 represents a physical element uncoupled to the others: $|z_{ij}| < |z_r|$ for all $j \neq i$.

it might be interchanged with another column if the larger bandwidth of the two after the interchange were less than the larger bandwidth before the interchange!

RULES FOR INTERCHANGING TWO COLUMNS j and k.

Let Z_e be the current form of reduced matrix after a number of pairs of column interchanges in the initial Z_r. To reduce the bandwidth we consider interchanging columns j and k in order to have the larger bandwidth of the two less after the exchange than before. Let $e_{\alpha\beta}$ denote either a 0 or 1 in row α, column β. Two rules govern the interchange of elements on row i in the two columns:

Rule 1. For $i \neq j$ or k, $e_{ij} \Longleftrightarrow e_{ik}$
Rule 2. For i=j or k, e_{ij} and e_{ik} do not interchange.

Table 1 gives the formulas for the new upper and lower bandwidths BU(k)' and BL(k)' for the new column k which results when column j replaces it. BU(j), BL(j), and $Z_e(j,k)$ are the parameters of column j and the current matrix Z_e before it is exchanged with column k.

The element numberings are updated for the two-column exchange as follows. The initial numbering is stored as NSCOL(j)=j for all elements j. At any stage of the iterative column exchange process NSCOL(j)=α means element α is now renumbered j. When column j is moved to column k according to the two rules and the formulas of Table 1 the element α which was renumbered j is now renumbered k. This is represented by changing NSCOL(k) to NSCOL(k)'= NSCOL(j). Of course we also re-store NSCOL(j)'=NSCOL(k).

TABLE 1. Transformation formulas for column k when it is exchanged with column j. BU(k)' andl BL(k)' are the new upper and lower bandwidths of the new column k. BU(j), BL(j) and $Z_e(j,k)$ are the parameters before the interchange. ISH=(j-k) is qualified where necessary. Columns (1)-(6) are delineated in Fig. 1.

Col.	BU(j)	BL(j)	$Z_e(j,k)$	BU(k)'	BL(k)'
(1)	>0	>0	0	BU(j)-ISH	BL(j)-ISH
	>0	>0	1	BU(j)-ISH	-ISH
(2)	>0 (>ISH)	0	0	BU(j)-ISH	0
	>0 (=ISH)	0	0	0	0
	>0 (<ISH)	0	0	0	BU(j)-ISH
	>0	0	1	BU(j)-ISH	-ISH
(3)	0	0	0	0	0
	0	0	1 (ISH>0)	0	-ISH
	0	0	1 (ISH<0)	-ISH	0
(4)	>0	<0	0 or 1	BU(j)-ISH	BL(j)-ISH
(5)	0	<0 (<ISH)	0	0	BL(j)-ISH
	0	<0 (=ISH)	0	0	0
	0	<0 (>ISH)	0	BL(j)-ISH	0
	0	<0	1	-ISH	BL(j)-ISH
(6)	<0	<0	0	BU(j)-ISH	BL(j)-ISH
	<0	<0	1	-ISH	BL(j)-ISH

DESCRIPTION OF THE ALGORITHM MATBAND.FOR (DATED 4/1/87).

The code operates on the reduced symmetric matrix Z_r = ZMAT consisting of 0's and 1's. In the first stage of computation it stores the initial parameters NSCOL(J)=J and BU(J),BL(J), and BW(J) for all columns J via subroutine BCOL.

In the second stage it searches on each row IROW for a "bisected" column. This is one for which the row intersects the column with either the same number of rows up to BU as down to BL or else one or two more, depending on whether (BU-BL) is odd or even, respectively. The code finds and stores the number NCOL and BW of only the first maximum-BW bisected column (if there are several with this BW). It then calls subroutine EXCHB to evaluate, according to Table 1, the new bandwidths BU(IROW)' and BL(IROW)' of the "diagonal" column and BU(NCOL)' and BL(NCOL)' which would result if the two columns were exchanged. If their new maximum bandwidth would be less after the exchange than before the code makes the exchange: stores the new NSCOL-, BU-, BL-, and BW-indices for these two columns, and calls subroutine EXCHZ to exchange the two columns and rows IROW and NCOL in Z_e. Since this row exchange affects the bandwidth parameters of the columns other than IROW and NCOL the code calls BCOL to recompute the new BU, BL, and BW of all these other columns (IROW and NCOL were already recomouted).

After exchanging the "diagonal" column with a bisected column of the last row for which the exchange will reduce the maximum bandwidth of the two the code begins stage three. Now the code iterates a cycle of computations. In a given cycle it finds the first column NCOL1 of current maximum bandwidth BW1 and the number IND of columns with this same maximum. It computes the range R1 of column NCOL1 and searches through the range calling EXCHB to locate that column NCOL2 which—if NCOL2 and NMCOL1 were interchanged—would minimize the new maximum bandwidth, BW2, of the two. If BW2<BW1 it effects the exchange, stores the new NSCOL, BU, BL, and BW of the two new columns, calls EXCHZ to exchange the columns and the rows NCOL1 and NCOL2 in Z_e, and finally calls BCOL to recompute the BU, BL, and BW of the columns other than NCOL1 and NCOL2 which were affected by the row exchange. Then the code begins the next cycle of computations.

If, in the cycle just described, BW2≥BW1 for a particular NCOL1 and there are more such columns of the same BW1 (IND currently >0) the code locates the next such column, labels it NCOL1, computes its range R1, and repeats the procedure of the last paragraph to try to exchange this column with another column NCOL2 so as to reduce the new maximum bandwidth of the two below BW1. If successful, it effects the exchange and begins the next cycle of computations.

After iterating through a number of cycles which effect a monotonic decrease of maximum BW in Z_A the code encounters a cycle in which there is no column of current maximum bandwidth BW1 which can be exchanged with another one in its range to achieve a reduction of their new maximum bandwidth, BW2, below BW1. The code then writes the number NCOLMAT of the last column which exhibits the minimum matrix bandwidth, BWMAT, and writes BWMAT, the NSCOL-array of renumbered elements, the BU- and BL-arrays, and the final banded matrix Z_B = ZMAT.

The user may then renumber the object elements according to the prescription NSCOL(J)=K, where K is the original element number and J is the final number, and proceed to solve the full matrix equation V= Z·I for I by banded matrix iteration. Note that V and I now refer to the renumbered elements. The mutual impedances $Z_B(I,J)$ of the renumbered elements are related to those of the elements in the original matrix Z as

$$Z_B(I,J) = Z_r(NSCOL(I),NSCOL(J))$$

A TRIAL CASE: WIRE MESH ON A CUBICAL SURFACE.

Each edge of the cube is bisected by a node and each face has four segments from the four bisection nodes on the edges to the central face node. The entire mesh consisted of 48 segments. Each corner node connected three segment ends, while the other nodes each connected four segments. The reference level $|z_r|$ was arbitrarily specified by taking the coupling between any two connected segments as $> |z_r|$, while any two segments not connected had $< |z_r|$ interaction.

Casual numbering of the segments yielded an initial Z_r consisting of 0's and 1's with a bandwidth of 40. The code renumbered the segments to yield a final bandwidth of 17 in Z_B. It made 9 iterations in the second stage and 56 in the third stage of computation. However, by renumbering the segments clockwise, starting with the four intersecting in the top face and ending with the four in the bottom face we achieve a bandwidth of 16, which seems to be the minimum.

Hence the code will not always realize the minimum matrix bandwidth possible. Perhaps we can be forgiven for this by the fact that the Cuthill-McKee and Gibbs-Poole-Stockmeyer algorithms usually do not yield the same "minimum" bandwidth for the same problems [2]. For several cases quoted of $N \lesssim 100$ their "minima" differed by 1 or 2. We reduced the N=24 Z_r matrix, Eq. (5.1) of [2], with our algorithm and obtained a "minimum" matrix bandwidth of 6. However, the true minimum was 5, as shown in the reduced matrix of Eq. (5.11).

It appears that our code will achieve nearly the minimum matrix bandwidth for a specified $|z_r|$ in a general problem with little or no physical symmetry.

TEST CASE INPUT AND OUTPUT.

To validate the user operation of the code we quote the MAT.IN file of N=20, which includes all six types of columns in Fig. 1. The code made ten column exchanges in stage 2 and five more in stage 3. The final output of MAT.OUT below shows that the minimum matrix bandwidth of 2 was achieved.

MAT.IN

```
  20
10000010000000000000
01000000000000000000
00100000000000000000
00010100100100000000
00001000000000000000
00010100000000000000
10000010000000100000
00000001000000000000
00010000100100000001
00000000010000000000
00000000001000000000
00100000100100000000
00000000000010000000
00000000000001000000
00000010000000100100
00000000000000010000
00000000000000001000
00000000000000100100
00000000000000000010
00000000100000000001
```

MAT.OUT

NCOLMAT= 11 BWMAT= 2

NSCOL ARRAY:

5	2	3	13	8	10	11	6	4	12	9	20	16	14	1	7	15	18	19	17
0	0	0	0	0	0	0	0	1	1	2	1	0	0	0	1	1	1	0	0
0	0	0	0	0	0	0	-1	-2	-1	-1	0	0	0	-1	-1	-1	0	0	0

```
10000000000000000000
01000000000000000000
00100000000000000000
00010000000000000000
00001000000000000000
00000100000000000000
00000010000000000000
00000001100000000000
00000001111000000000
00000000111100000000
00000000011100000000
00000000001100000000
00000000000100000000
00000000000010000000
00000000000001000000
00000000000000110000
00000000000000111000
00000000000000011100
00000000000000001100
00000000000000000010
00000000000000000001
```

REFERENCES.

[1] T. R. Ferguson, T. H. Lehman, R. J. Balestri, "Efficient Solution of Large Momer[illegible] Problems: Theory and Small Problem Results", IEEE Trans. Ant. Prop., AP-24, March, 1976. pp 230-235.

[2] N. E. Gibbs, W. G. Poole, P. K. Stockmeyer, "An Algorithm for Reducing the Bandwidth and Profile of a Sparse Matrix", Siam J. Num. Anal., 13, April, 1976. pp 236-250.

DIGITAL ALGORITHM SPECIFICATION FOR THE VLSI IMPLEMENTATION OF THE ELECTROMAGNETIC FIELD OF AN ARBITRARY CURRENT SOURCE

B. A. Hoyt, A. J. Terzuoli, A. V. Lair
Air Force Institute of Technology
School of Engineering
Wright-Patterson AFB, OH 45433

Abstract

A digital algorithm specification has been developed for the VLSI implementation of the electromagnetic fields of an arbitrary current source. The algorithm solves for the magnetic (**H**) and electric (**E**) fields of a finite length dipole with arbitrary current sources. A mid-point summation technique is employed for the numerical solution for **H** and **E**. MACSYMA, an algebraic manipulation program, was utilized to separate the **H** and **E** field equations into real and imaginary parts with rectangular vector components.

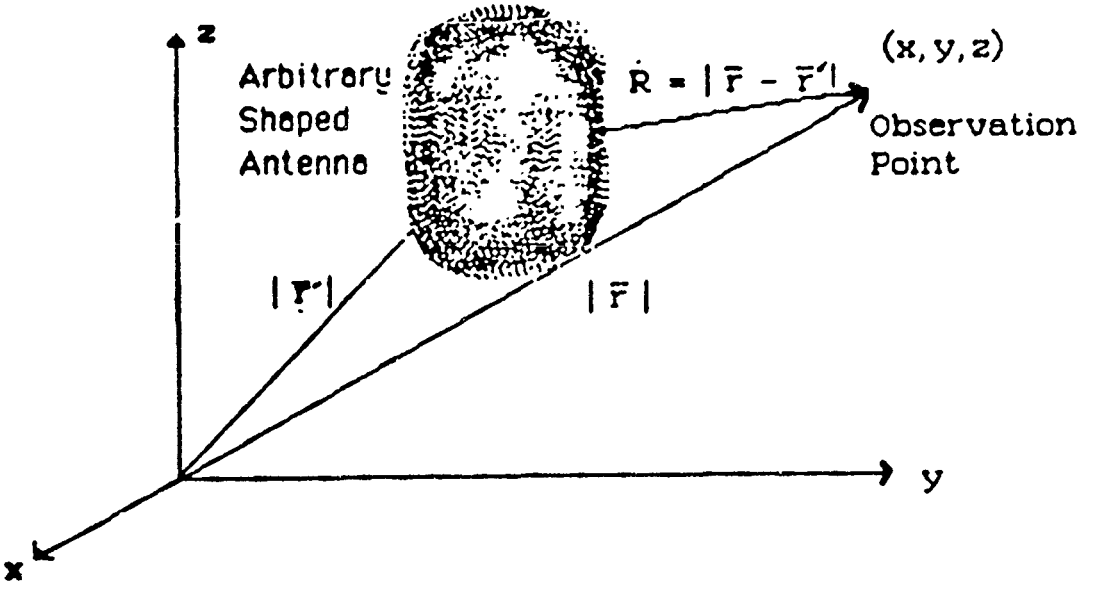
A digital simulation was accomplished with a single z-directed dipole, 10 λ long, for the test antenna. Numerical solutions utilizing uniform and triangular envelope current distributions were compared with the far-field solution for the test antenna at ranges of 250 and 500 λ. The number of sub-elements in the mid-point summation were 50, 100, and 500. The numerical solution compared reasonably well with the far-field solution when the test antenna was segmented into 50 sub-elements. The percent difference between the numerical and far-field solutions decreased to less than 1 percent difference for 95 percent of the observation points when the test antenna was segmented into 500 sub-elements. The greatest differences between the numerical and far-field solutions occurred in the null regions of the radiation pattern.

PROBLEM STATEMENT

- THE SPECIFIC PROBLEM TO BE SOLVED IS THE DEVELOPMENT OF EQUATIONS FOR H AND E WHICH CAN BE IMPLEMENTED WITH A DEDICATED COMPUTER PROCESSOR CHIP

RADIATION INTEGRAL

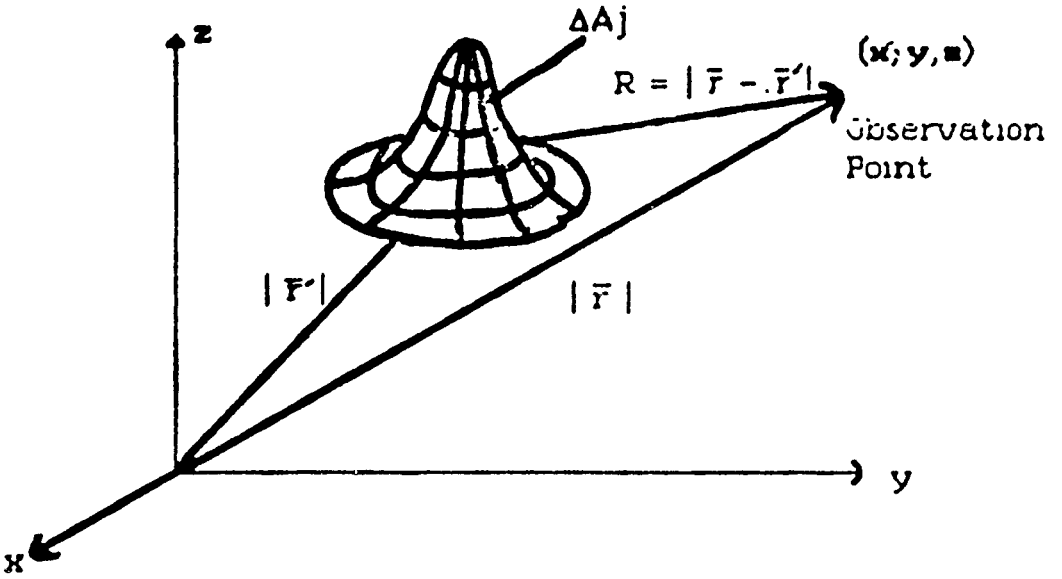
- THE EVALUATION OF THE COMPLEX INTEGRAL IS NECESSARY TO ANALYZE EVEN THE SIMPLEST ANTENNA



$$A(\bar{r}) = \iiint_{|\bar{r}'|} \frac{J(\bar{r}')\, e^{-jk|\bar{r}-\bar{r}'|}}{4\pi|\bar{r}-\bar{r}'|} d|\bar{r}'|$$

NUMERICAL EVALUATION OF RADIATION INTEGRAL

- PREVIOUS WORK DEFINED A NUMERICAL ALGORITHM FOR VECTOR POTENTIAL (A)
  - UTILIZED A MID-POINT SUMMATION TECHNIQUE
  - 2 DECIMAL PLACE ACCURACY WITH 500 SUB-ELEMENTS
- HOWEVER, A NUMERICAL SOLUTION FOR $\underline{A}$ DOES NOT YIELD MEANINGFUL RESULTS FOR H OR E.
- THE CURL OPERATIONS FOR H AND E MUST BE PERFORMED PRIOR TO ANY NUMERICAL SUMMATION.



SECTIONED GENERAL SHAPED ANTENNA

$$\iiint_{|\bar{r}'|} \frac{J(\bar{r}')\, e^{-jk|\bar{r}-\bar{r}'|}}{4\pi|\bar{r}-\bar{r}'|} d|\bar{r}'| \approx \sum_{i=1}^{m} \frac{\Delta A_i\, J_i(\bar{r}_i')\, e^{-jk|\bar{r}-\bar{r}_i'|}}{4\pi|\bar{r}-\bar{r}_i'|}$$

ΔA_i = surface area of the i^{th} element

$J_i(\bar{r}_i')$ = current on the i^{th} surface element

$\bar{r}_i'$ = distance from origin to the i^{th} surface element

APPROACH

- EMPLOY MID-POINT SUMMATION
- OBTAIN EQUATIONS FOR H AND E FROM RADIATION INTEGRAL
- UTILIZE MACSYMA TO SEPARATE THE COMPLEX EXPRESSIONS FOR H AND E INTO THEIR REAL AND IMAGINARY PARTS
- TEST ALGORITHM
  - SIMPLIFY GEOMETRY
    - Z-DIRECTED DIPOLE
    - Y-Z PLANE OF OBSERVATION
  - WITH UNIFORM AND TRIANGULAR CURRENT DENSITIES
  - 50, 100, AND 500 SUB-ELEMENTS

SOLVING FOR H AND E

- **THE ELECTRIC FIELD HAS THREE COMPONENTS**

$$\mathbf{E} = \hat{x}\, Ex + \hat{y}\, Ey + \hat{z}\, Ez$$

WHERE

$$Ex = \exp(-j\,k\,R)\,((Jxri + j\,Jxii)\,(k^2\,R^2 - 3\,j\,k\,R - 1)\,((z - zi)^2 + (y - yi)^2) + (-k^2\,R^2 + 3\,j\,k\,R + 3)\,((Jzri + j\,Jzii)\,(x - xi)\,(z - zi) + (Jyri + j\,Jyii)\,(x - xi)\,(y - yi)))/(4\,\pi\,R^5)$$

$$Ey = \exp(-j\,k\,R)\,((Jyri + j\,Jyii)\,(k^2\,R^2 - 3\,j\,k\,R - 1)\,((z - zi)^2 + (x - xi)^2) + (-k^2\,R^2 + 3\,j\,k\,R + 3)\,((Jzri + j\,Jzii)\,(y - yi)\,(z - zi) + (Jxri + j\,Jxii)\,(x - xi)\,(y - yi)))/(4\,\pi\,R^5)$$

$$Ez = \exp(-j\,k\,R)\,((-k\,R + 3\,j\,k\,R + 3)\,((Jyri + j\,Jyii)\,(y - yi)\,(z - zi) + (Jxri + j\,Jxii)\,(x - xi)\,(z - zi)) + (Jzri + j\,Jzii)\,(k^2\,R^2 - 3\,j\,k\,R - 1)\,((y - yi)^2 + (x - xi)^2))/(4\,\pi\,R^5)$$

SOLVING FOR H AND E

- **THE MAGNETIC FIELD HAS THREE COMPONENTS GIVE AS:**

$$\mathbf{H} = \hat{x}\, Hx + \hat{y}\, Hy + \hat{z}\, Hz$$

- **UTILIZING MACSYMA TO SIMPLIFY THE H FIELD COMPONENTS WITH THE XTHRU(EXP) COMMAND**

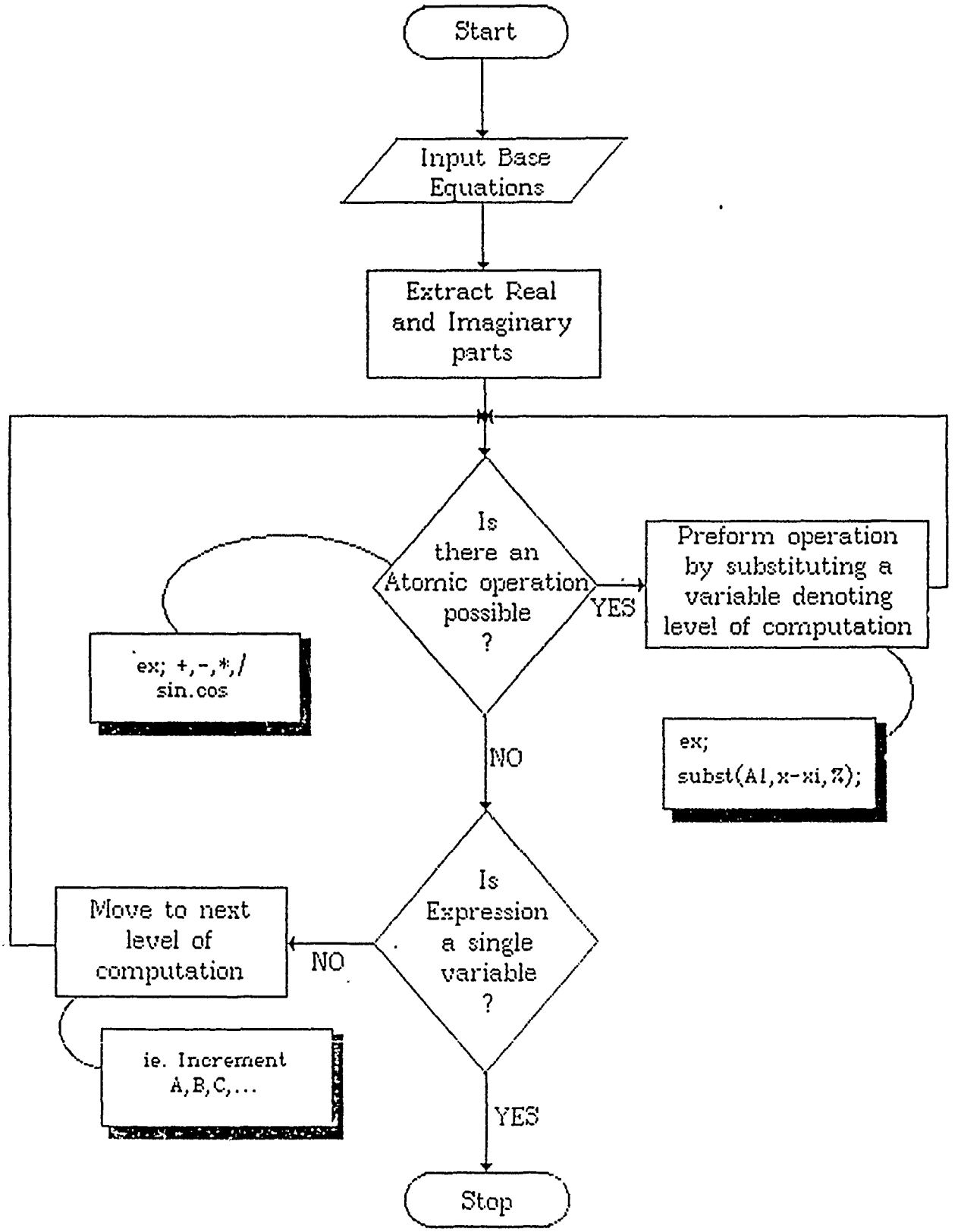
$$Hx = (j\,k\,R + 1)\,\exp^{-JkR}\,((Jyri + j\,Jyii)\,(z - zi) - (Jzri + j\,Jzii)\,(y - yi))/(4\,\pi\,R^3)$$

$$Hy = (j\,k\,R + 1)\,\exp(-j\,k\,R)\,((Jzri + j\,Jzii)\,(x - xi) - (Jxri + j\,Jxii)\,(z - zi))/(4\,\pi\,R^3)$$

$$Hz = (j\,k\,R + 1)\,\exp(-j\,k\,R)\,((Jxri + j\,Jxii)\,(y - yi) - (Jyri + j\,Jyii)\,(x - xi))/(4\,\pi\,R^3)$$

$$R = [\,(x - xi)^2 + (y - yi)^2 + (z - zi)^2\,]^{1/2}$$

STRAUSS	VWE Thesis Briefing	2 Mar 87



STRAUSS	VWE Thesis Briefing	2 Mar 87

Data-Flow Graph Development

realpart(ex) The real part is extracted with MACSYMA.

```
(c10) exr;
                                2  1    3 b jxri            2        2
(d10) (sin(b r) ((jxii (b  - --) - --------) ((z - zi)  + (y - yi) )
                                2     r
                               r

      3 b (jzri (x
+ ---------------

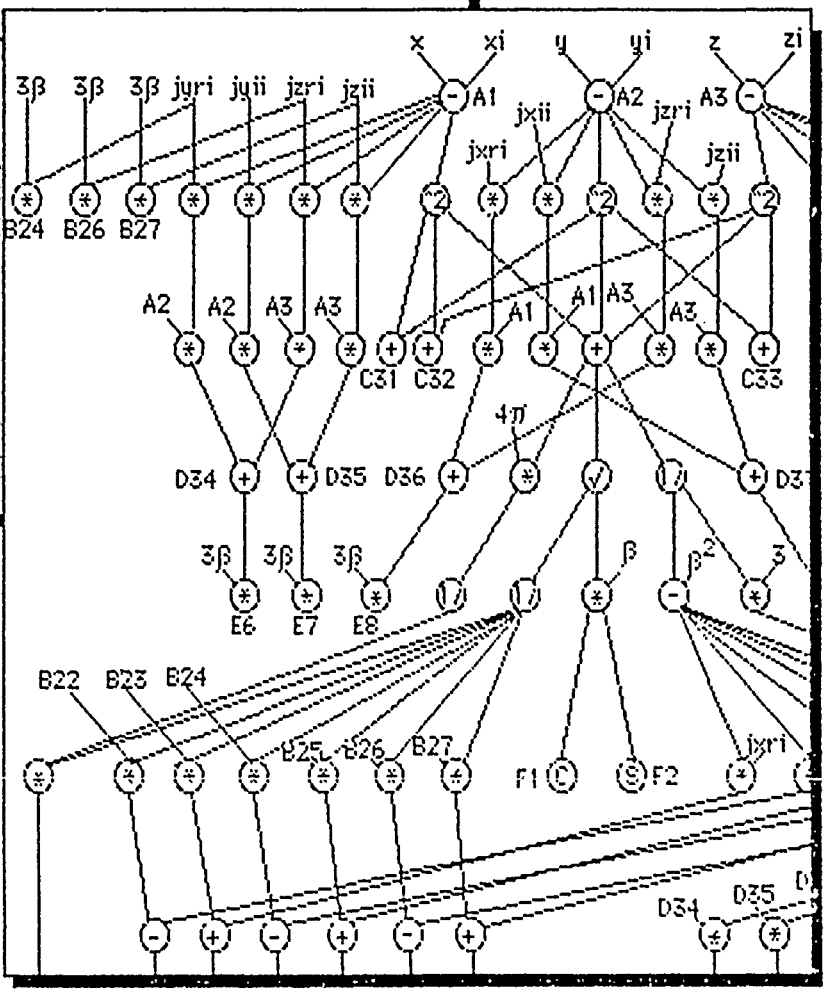
   3   2
+ (-- - b ) (jzii (:
   2
  r
                3 b
+ cos(b r) ((-----
                r

   3   2
+ (-- - b ) (jzri (
   2
  r
      3 b (jxii (
```

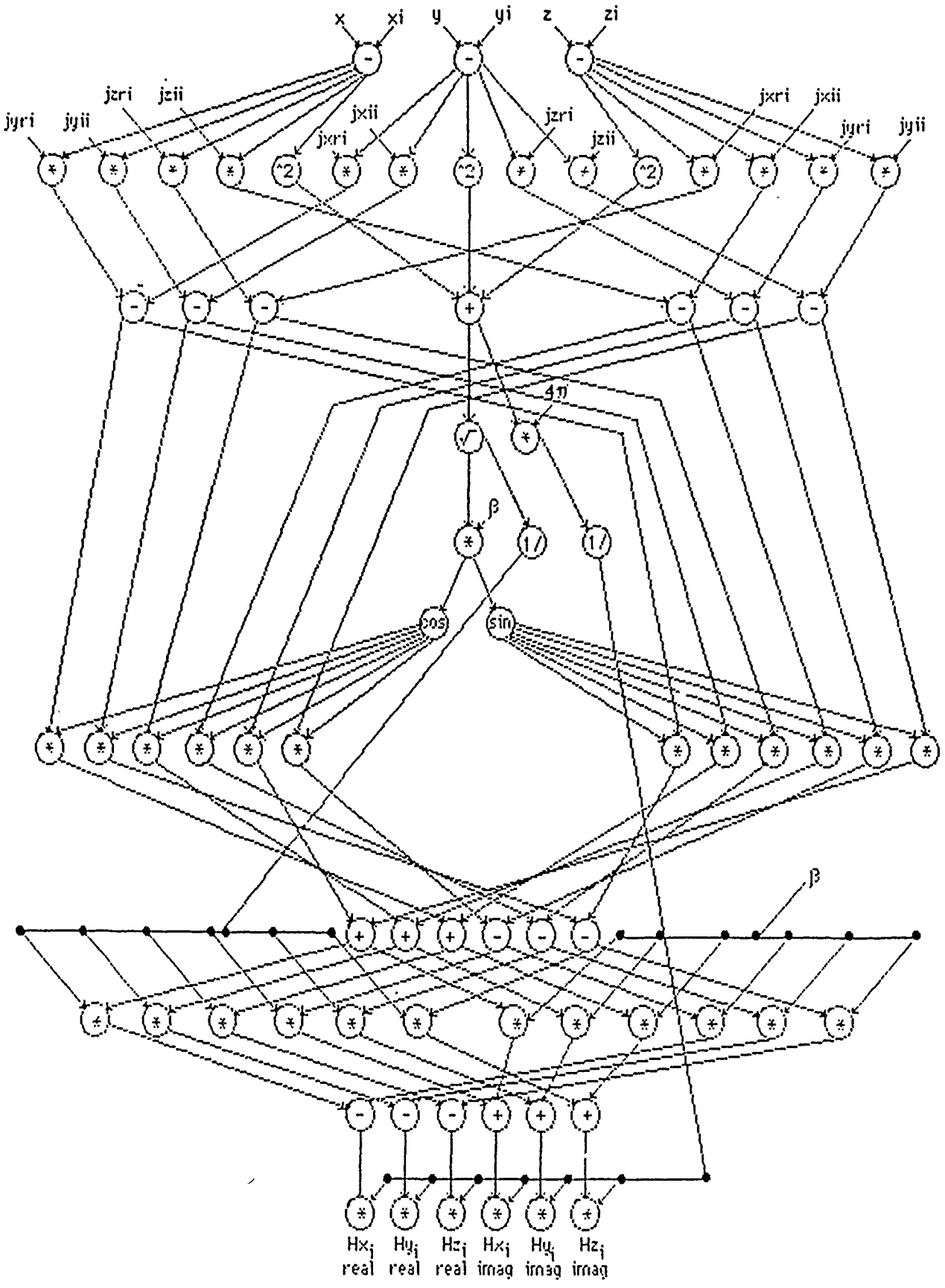
```
subst("F5","E2"*"B22",%)$
subst("F6","E2"*"B23",%)$
subst("F7","E4"*jxri,%)$
subst("F8","E4"*jxii,%)$
subst(1,"E2",%)$
subst(1,"E3",%)$
subst(%*"F3",%,%);

subst("F9",
subst("F10"
subst("F11"
subst("F12"
subst(1,"E2
subst(1,"E3
subst(%*"F

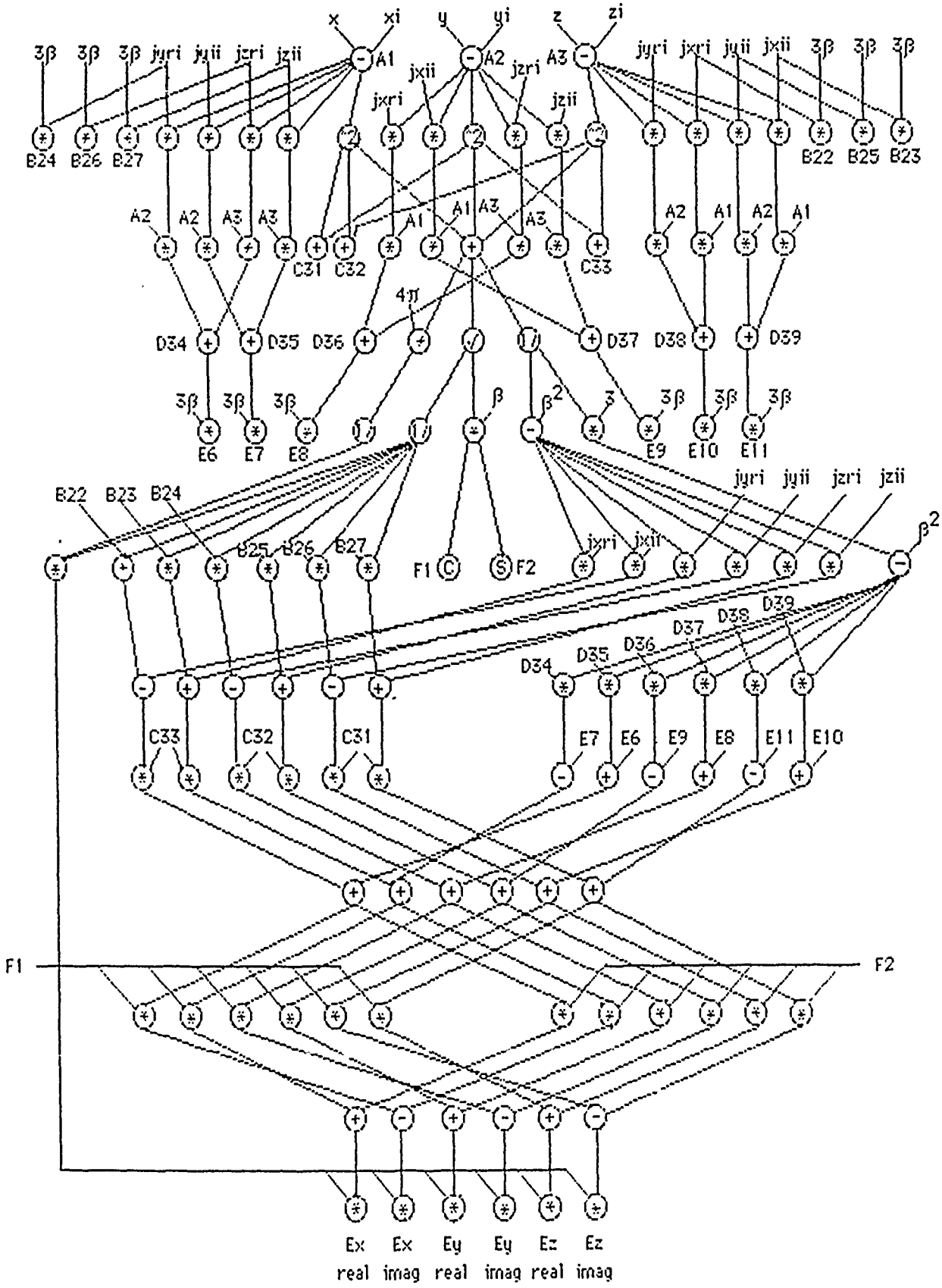
subst("F13"
subst("F14"
subst("F15"
subst("F16"
subst(1,"E2
subst(1,"E3
```



STRAUSS	VWE Thesis Briefing	2 Mar 87



STRAUSS	VWE Thesis Briefing	2 Mar 87

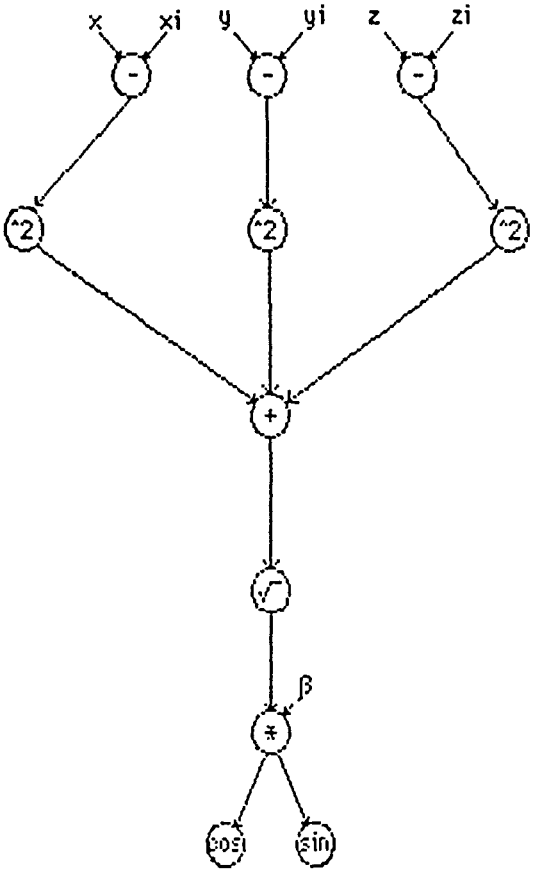


STRAUSS	VWE Thesis Briefing	2 Mar 87

THE ALGORITHMIC CORE

THE EXPRESSION COMMON TO

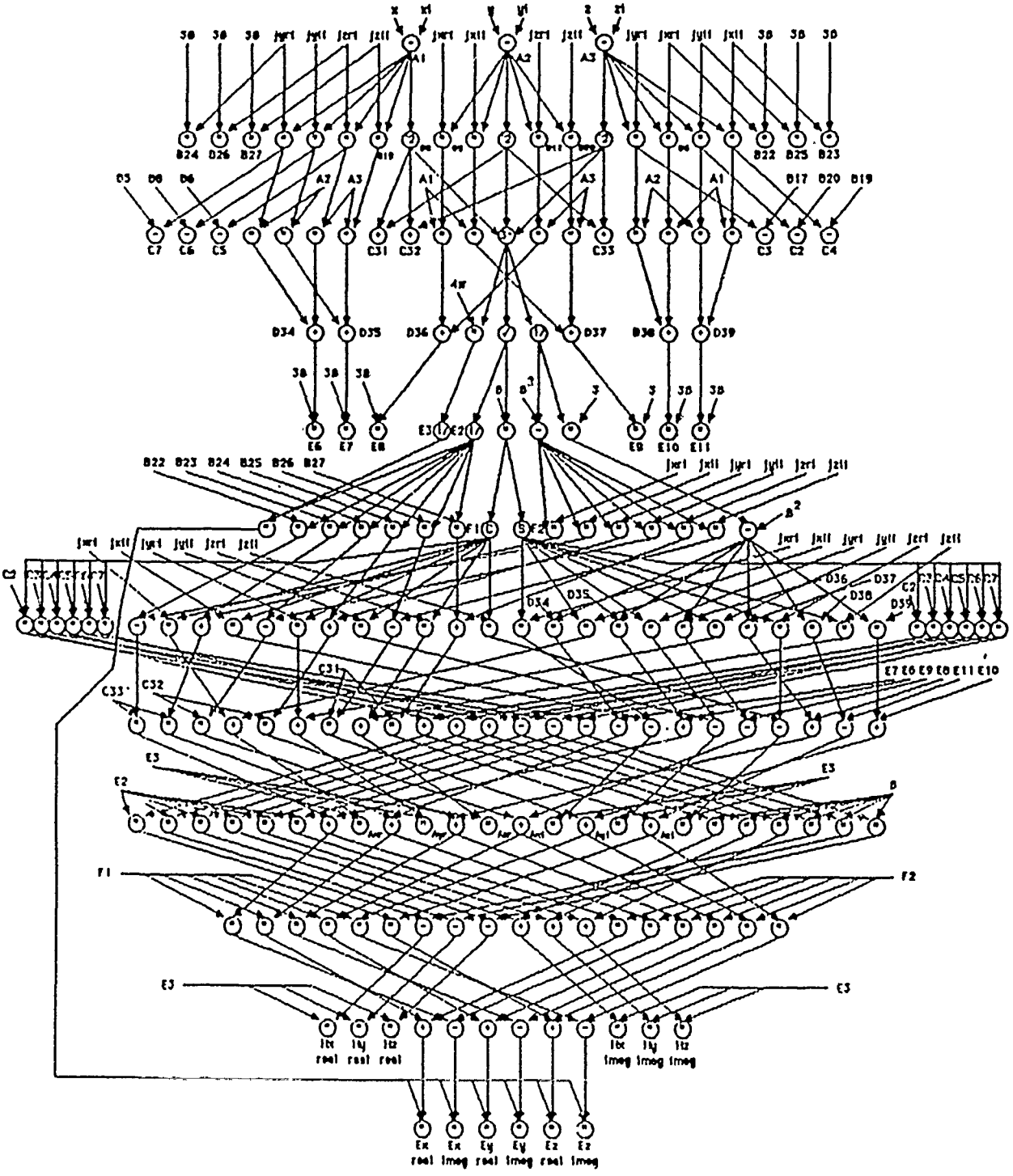
ALL THREE VECTOR QUANTITIES



$$\cos\left[\beta \,\mathrm{SQRT}\left((X-X_i)^2+(Y-Y_i)^2+(Z-Z_i)^2\right)\right]$$

$$\sin\left[\beta \,\mathrm{SQRT}\left((X-X_i)^2+(Y-Y_i)^2+(Z-Z_i)^2\right)\right]$$

STRAUSS	VWE Thesis Briefing	2 Mar 87



Fully Overlayed Vector Quantities

STRAUSS	VWE Thesis Briefing	2 Mar 87

Computational Requirements for i^{th} Vector Calculation. Summation over "m" Dipole Elements

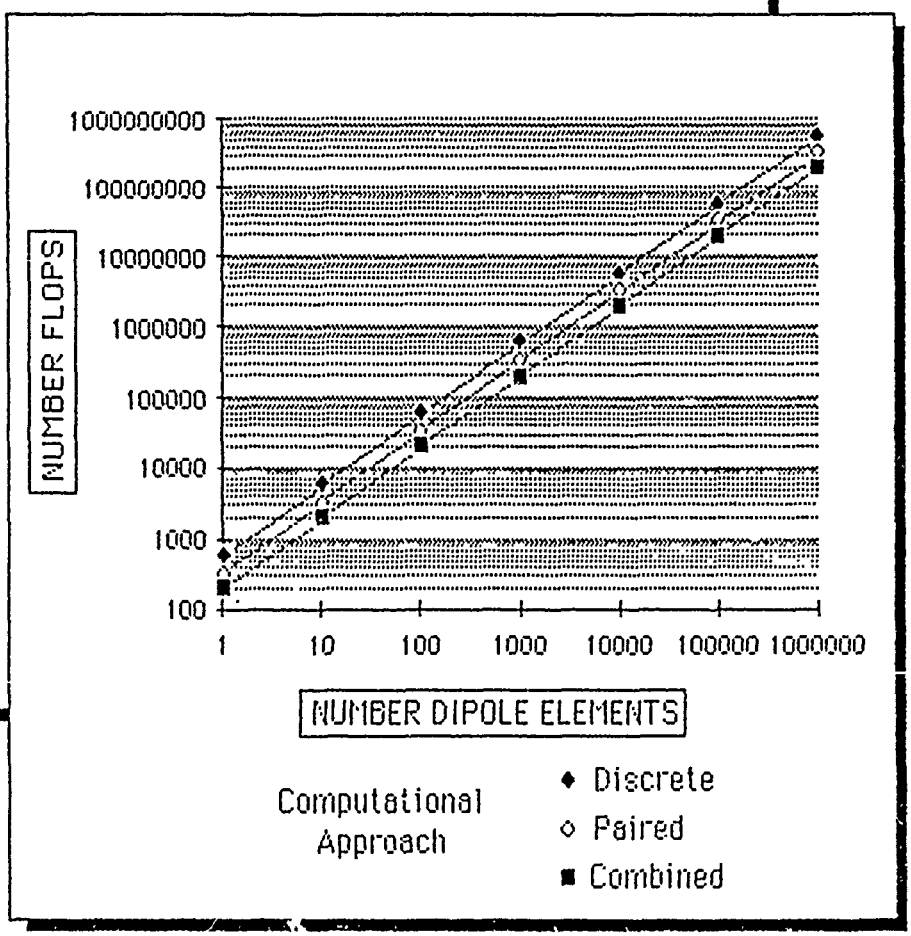
Chart is in FLOPs required

	Discrete (Hxr, Hxi, ..., Hzi)	Paired (H_x, H_y, H_z)	Combined ($\hat{H}, \hat{E}$)
Vector Potential	17/102	21/63	37
H FIELD	30/180	34/102	74
E FIELD	52/312	56/168	130
E & H FIELDS	——	——	178
E & H FIELDS & Vector Potential	——	——	202

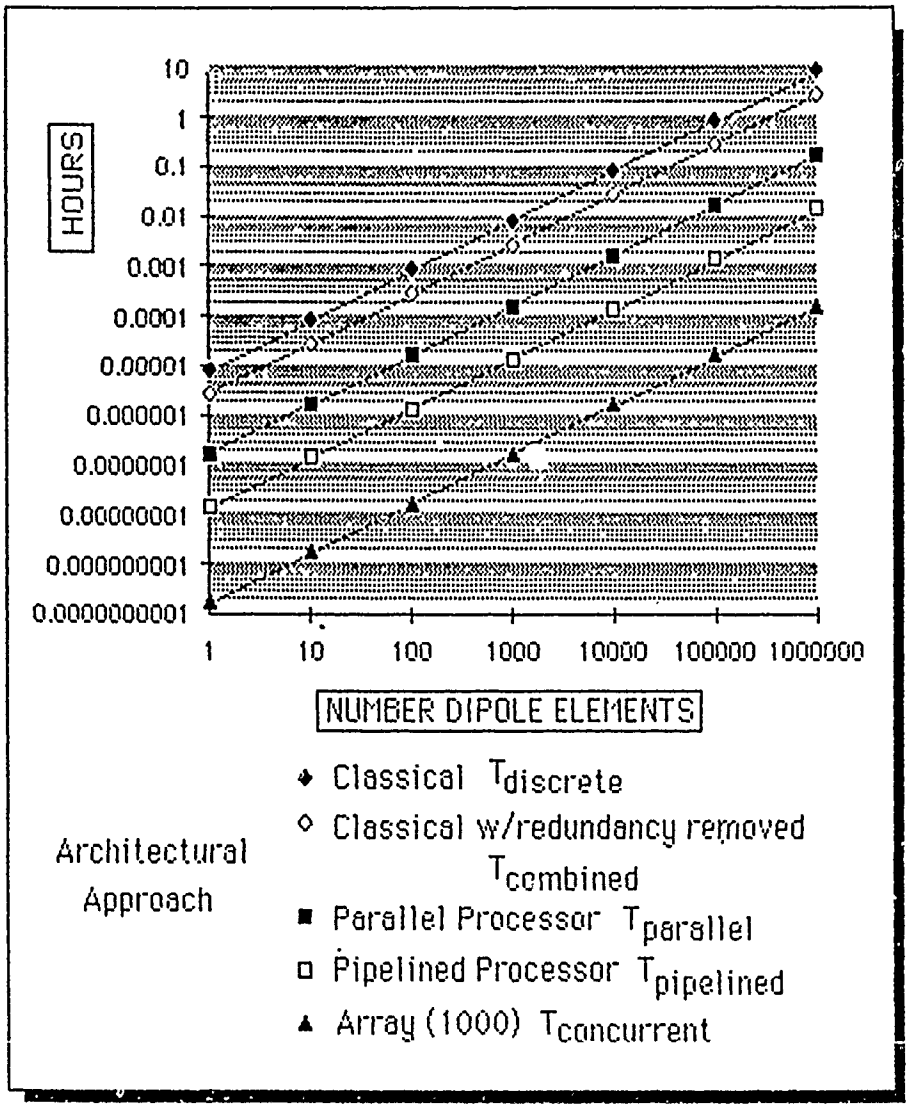
FLOPs; Floating Point Operations

Impact of Computational Approach

	Discrete (Hxr, Hxi, ..., Hzi)	Paired (H_x, H_y, H_z)	Combined ($\tilde{H}, \tilde{E}$)
Vector Potential	17/102	21/63	37
H FIELD	30/180	34/102	74
E FIELD	5		
E & H FIELDS			
E & H FIELDS & Vector Potential			



Summary of Architectural Considerations



STRAUSS	VWE Thesis Briefing	2 Mar 87

Summary of Research

- Algorithmic Specification at various levels of Parallelism
- Architectural Specification at Functional Element level
- Analytic Error Model, concept proven

Conclusion

- AS/VHSIC-Class Multiprocessor Array can support an interactive environment.
- It can be done!

SAC - AN APERTURE CODE WITH NEAR-FIELD EXCITATION

Christopher C. Smith
Don Metzger
Kaman Sciences Corporation
P. O. Box 7463
Colorado Springs, CO 80933

Introduction

The testing for vulnerability to high power microwaves is usually performed in the near-field of a microwave source in order to maximize incident power densities. If an actual threat pulse is likely to be a plane wave, a question arises regarding the suitability to testing with near-field sources. This paper addresses the computer predicted differences between near-field and plane wave coupling in a multiple-aperture infinite extent plane structure.

Method of Moments Computer Code

Sarkar, Costa, I, and Harrington described a code for the calculation of transmission through an aperture in a conducting screen [1]. This computer code was used as the basis of a code which also addresses near-field coupling through apertures in infinite planes. The unknowns to be determined are magnetic currents in the location of the aperture. Once found, these currents can be used to calculate the scattered power from the aperture and to generate radiation patterns. The method is shown schematically in Figure 1.

The original computer code had to be modified to allow input from the near-field calculations, to model near-field exitation. The code requires each aperture to be divided into triangular patches. The incident H-field is needed at the centroid of each triangular patch in order to form the excitation vector. The proximity of the source and aperture require that the position vector from the source coordinate system origin to each centoid be calculated in order to evaluate the incident field. Coordinate translation followed by coordinate rotation using an Euler matrix provides an efficient method for calculating the many vectors.

The source employed for this study is a TE10 standard gain horn at 7.5 GHz. The method used to calculate the near-field of this horn is described by Metzger [2].

Near-Field Calculations

The geometry of the horn is show in figure 2. The frequency used is 7.5 GHz. The E plane of the horn is the y-z plane and the H plane is the x-z plane. The far-field limit is given by R=(2D**2)/lambda where D is the largest separation of points in the horn mouth (the slant distance from corner to corner) and lambda is the wavelength. For the horn used in this study the far-field limit is 8.Ø feet.

Coupling to Apertures Results

The MOM code calculates the power incident on the aperture, the power scattered from the aperture and the scattered far-field pattern. The ratio of the forward scattered power to the incident power, termed the transmission coefficient, gives a measure of the efficiency with which the aperture captures and re-radiates energy into the region beyond.

Coupling to a Single Slit

The aperture chosen for study was a rectangular aperture with a length of lambda/2 and a width of lambda/2ØØ as shown in figure 3. The aperture lies in a plane perpendicular to the direction of propagation with its long dimension along x. The exitation applied to the aperture in the MOM code is the tangential magnetic field value. With the aperture so oriented, the dominant coupling is from the Hx component of the magnetic field.

Slit Polarization

The first test was to place the aperture on boresight, oriented as described above. The aperture was then illuminated by a plane wave and a far-field distribution from the horn. Both types of illumination predicted a transmission coefficient of 52.3.

When the slit is turned so that the length of the slit is in the y direction, the transmission coefficient for the plane wave case is dramatically lower having a value of 3.Ø X 1Ø**-7. Since the TE1Ø distribution produces no significant Hy field component, the plane wave, far-field and near-field results agree quite closely on transmission coefficient for this configuration.

Summarizing the previous results, for a TE1Ø distribution the coupling will be maximum when the slit aperture has its length in the x direction; no significant coupling will occur for slits oriented in the y direction.

Coupling to a Seam

The case of greatest interest involves a coupling structure which has a large extent in the near-field pattern. It is this type of structure which is expected to be most significantly varied from plane wave response when placed in the near field. The object chosen for this part of the study was a seam constructed from ten of the slits previously studied. The half wavelength slits were placed end-to-end with a half wavelength spacing between the end of one aperture and the end of its neighbor, as illustrated in figure 4. Thus, the seam had a 50% fill factor consisting of half aperture, half solid conductor. Placed in this fashion, the mutual coupling of each slit to its neighbors seam was assumed to be insignificant. In order to reduce the computation time, the response of each slit was calculated independently of the others. This could be done efficiently, because once the admittance matrix for the subdivided aperture was filled and inverted, the solution for each aperture in the seam could be found by calculating the position-dependant excitation vector followed by matrix multiplication. Once the response of each slit was determined, the scattered field pattern from the seam was determined by pattern addition.

Seam on Boresight

Figure 5 shows the results obtained when the seam was placed symmetrically across the beam. The horizontal scale is the angle at which power is scattered from the seam, while the vertical axis is the ppower scattered at that angle normalized to the sum total power incident on all slits of the seam. The plane wave results agree with what is expected from a ten element array, that is, its pattern is symmetric in angular distribution and the maximum gain is approximately a factor of ten. The near-field results show a gain of about three at maximum. This indicates that three elements of the seam are dominating the pattern. Considering the decrease of both field strength and transmission cofficient for the parts of the seam not on boresight, this is as expected, i.e. the central few elements of the seam determine the far-field radiation pattern. Quantitatively, the gain for the plane wave case is 9.3 dB at 90 degrees, while the near-field has a gain of scattering is about 4.8 dB.

A more meaningful way of presenting the previous results is to normalize the power scattered in a direction to the incident power density at the center of the central slits of the seam. Since, in general, the power density at the center of the object under test is measured and used as the reference field strength, this normalization provides a method for comparing near-field and plane wave coupling when the central power densities are the same. This is illustrated in figure 6. The vertical scale is the power scattered normalized to the power density at the center of the

seam. At the peak coupling direction of 9Ø degrees there is about an order of magnitude difference between the plane wave and near-field results. Therfore, given equal power densitie' at the center of the seam, the near-field distribution will couple about 1Ø% as efficiently in the principal direction as will the plane wave.

Figure 7 shows the result of illuminating the seam with the horn aimed at the center at an angle of 45 degrees. The boresight is in the plane of the seam and surface normal. Once again the near-field excitation produces peaks about 1Ø dB below the plane wave response, and the angular position of the peaks is displaced. The plane wave response shows deep nulls that are filled in when the source is the near-field of the horn.

Seam off Boresight

Next, the seam was placed so that one end was on boresight and the rest of the seam extended off axis in the x direction. Thus, this arangement extened farther off boresight than the seam symmetric with respect to boresight. The results for this case are shown in figure 7. The plane wave pattern is the same, as expected, since the angle of interaction with the seam has been preserved. However, the near-field results show a shift from the symmetric case. The peak gain is about a factor of two indicating that two slits are dominating the pattern. Quantitatively, the shift in peak gain is 5.9 dB with an angular shift of that peak value of about 6 degrees.

Conclusions

For a single aperture on boresight, there is little difference between near-field and plane wave coupling except in the extreme near-field region (less than 5% of the fff). When an aperture is moved off boresight the phase incoherence across the aperture degrades its coupling ability. This degradation, along with the limited beam width, tend to limit the spot size for comparable power coupling with respect to plane waves.

Seams constructed of slits show variations between near-field and plane wave results. These variations are on the order of 1Ø dB for the models chosen. If a seam longer than the one used for this analysis were illuminated, the plane wave results would show a higher peak gain, but the near-field results would remain essentially the same.

Acknowledgement

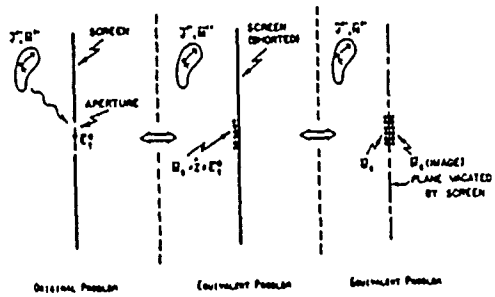
The authors wish to thank the Defense Nuclear Agency for funding this work.

References

1) Sarkar, Tapan K., et al; Electromagnetic Transmissision Through Mesh Covered Apertures and Arrays of Apertures in a Conducting Screen; IEEE Transactions on Antennas and Propagation, Vol. AP-32, No. 9 September 1984

2) Metzger, Donald W.; Numerical Calculation and Experimental Verification of Near Fields From Horns; Conference Proceedings, 3rd Annual Review of Progress in Applied Computational Electromagnetics; March 24-26, 1987

MFIE MOM SOLUTION OF APERTURE COUPLING



$$H = -j\omega F - \nabla\Phi$$

F IS ELECTRICAL VECTOR POTENTIAL

Φ IS MAGNETIC SCALAR POTENTIAL

$$F = \frac{\epsilon}{4\pi}\int\int_A M\ G\ ds'$$

$$\Phi = \frac{-1}{4\pi\mu}\int\int_A \nabla\cdot M\ G\ ds'$$

M IS MAGNETIC CURRENT

G IS GREEN'S FUNCTION

KAMAN

Figure 1. Method of Moments for Apertures.

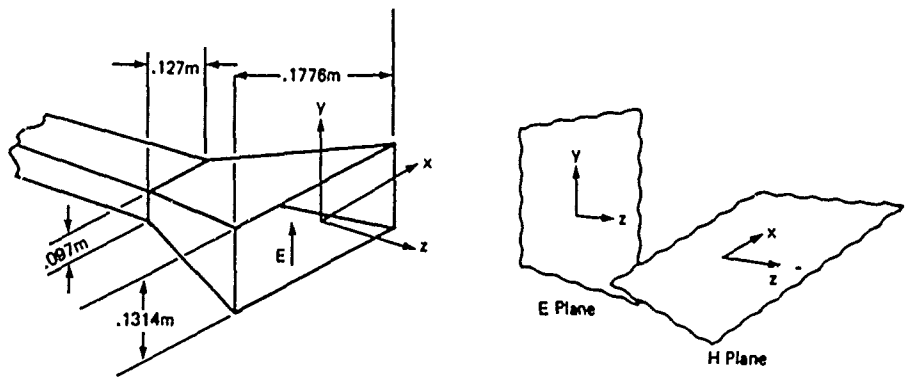


Figure 2. Horn Geometry, Frequency = 7.5 GHz.

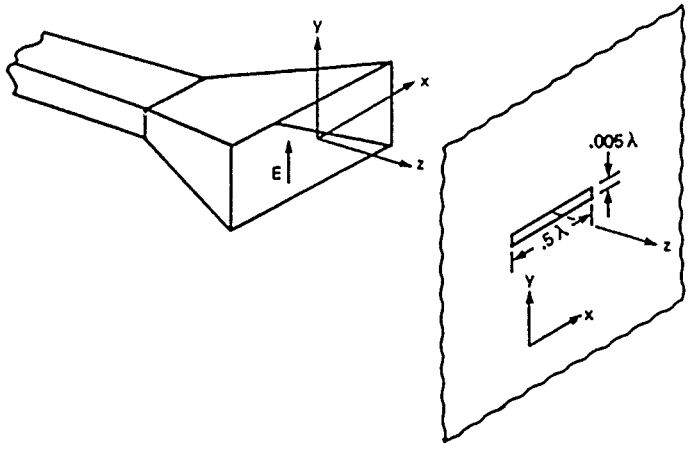


Figure 3. Single Slit Geometry.

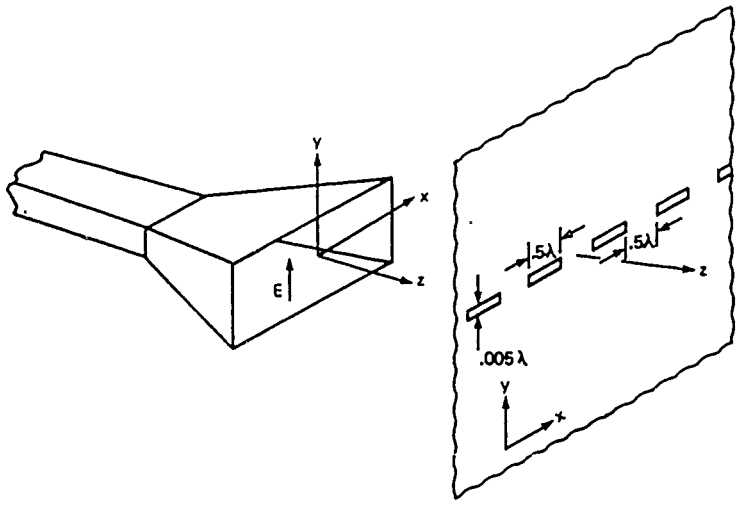


Figure 4. Seam Geometry.

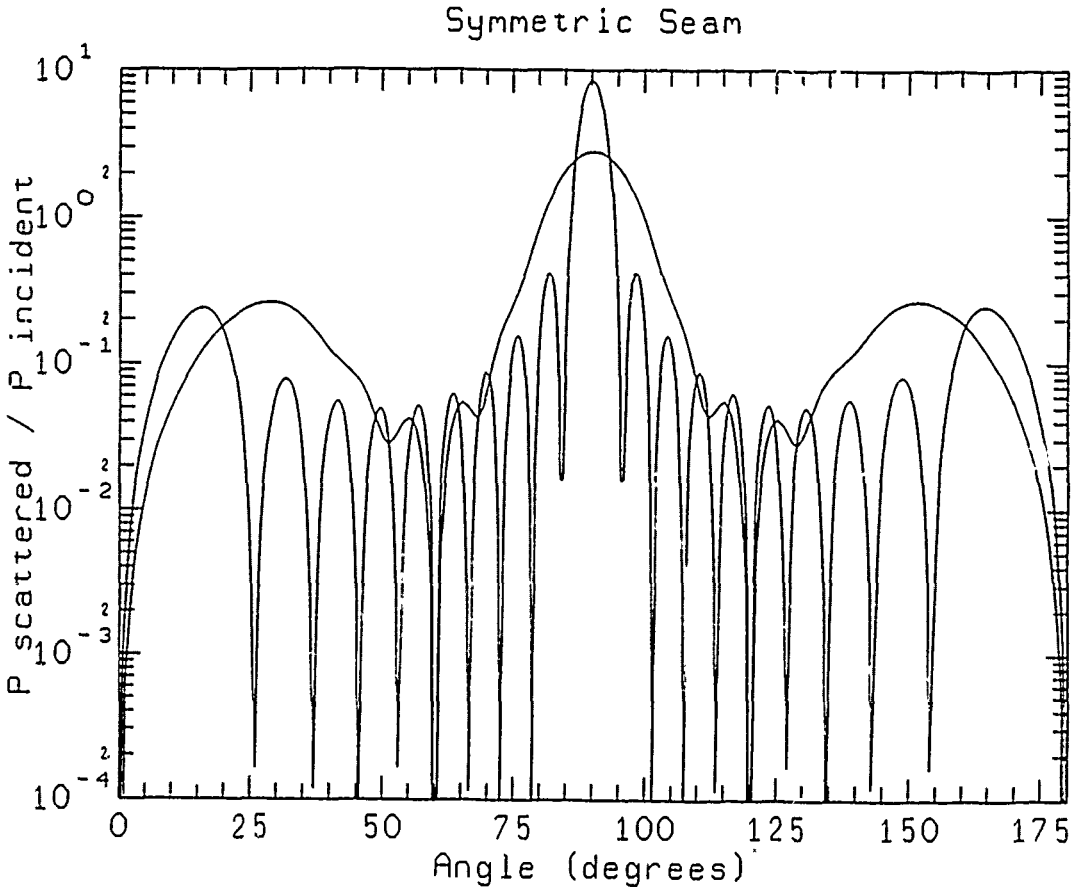


Figure 5. Scattered Field Patterns for a Seam on Boresight.

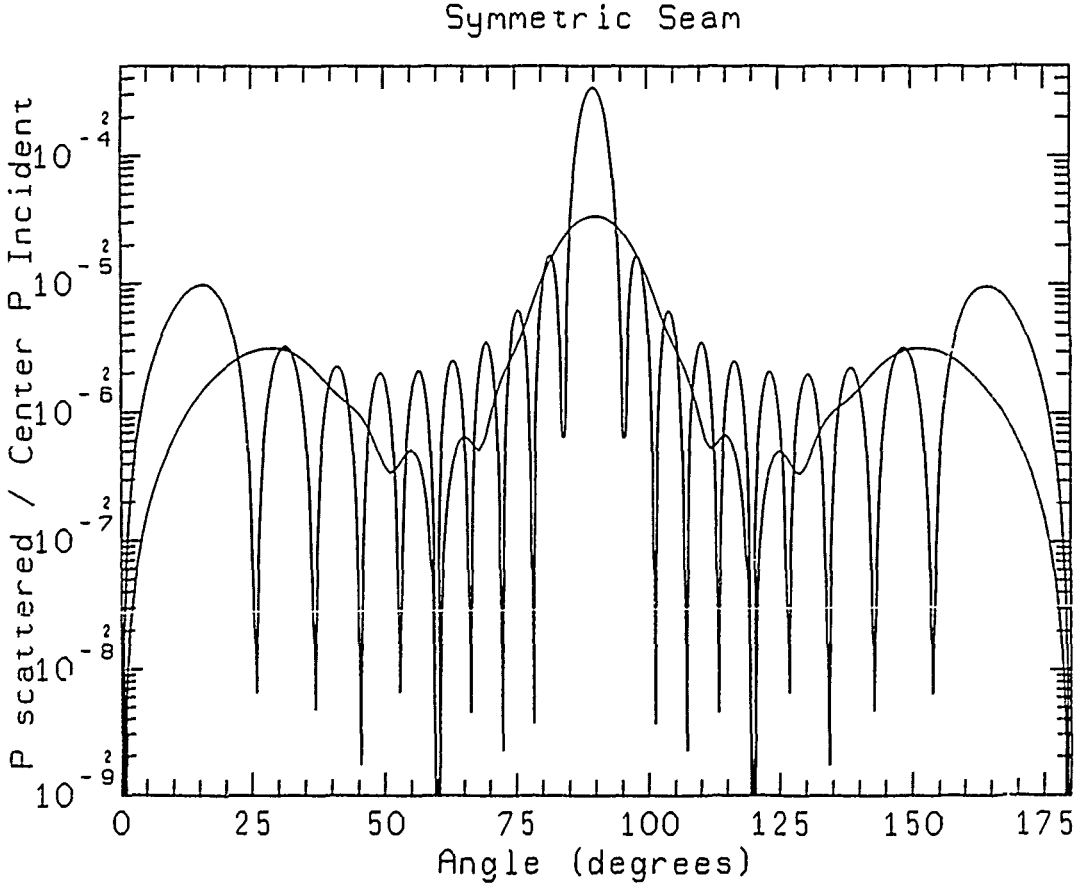


Figure 6. Normalized Field Patterns for a Seam on Boresight.

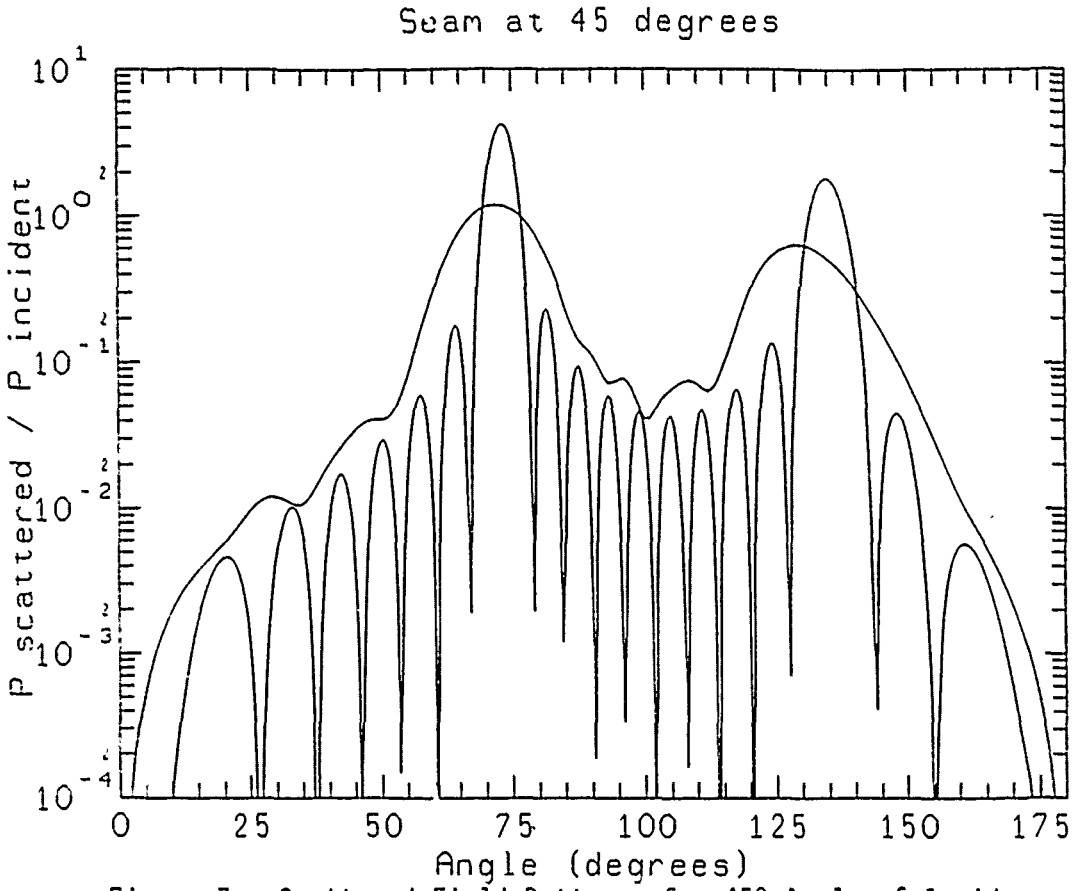


Figure 7. Scattered Field Patterns for 45° Angle of Incidence.

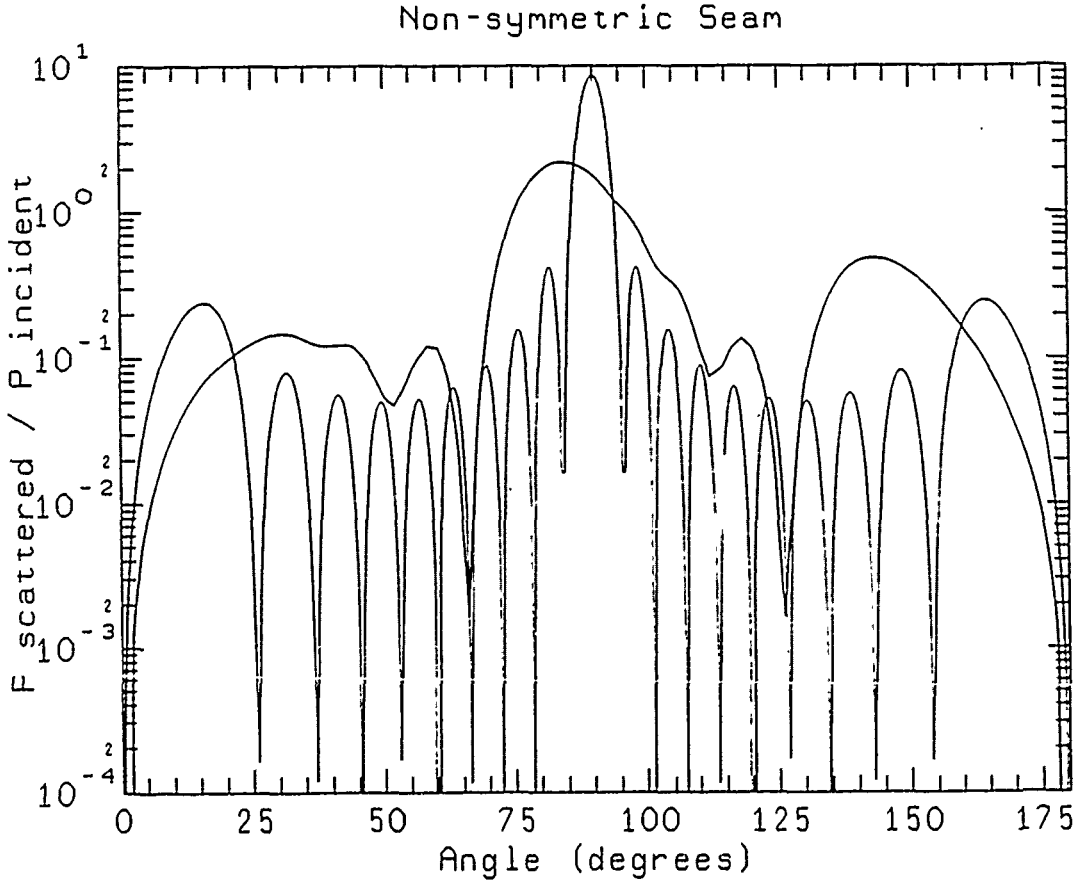
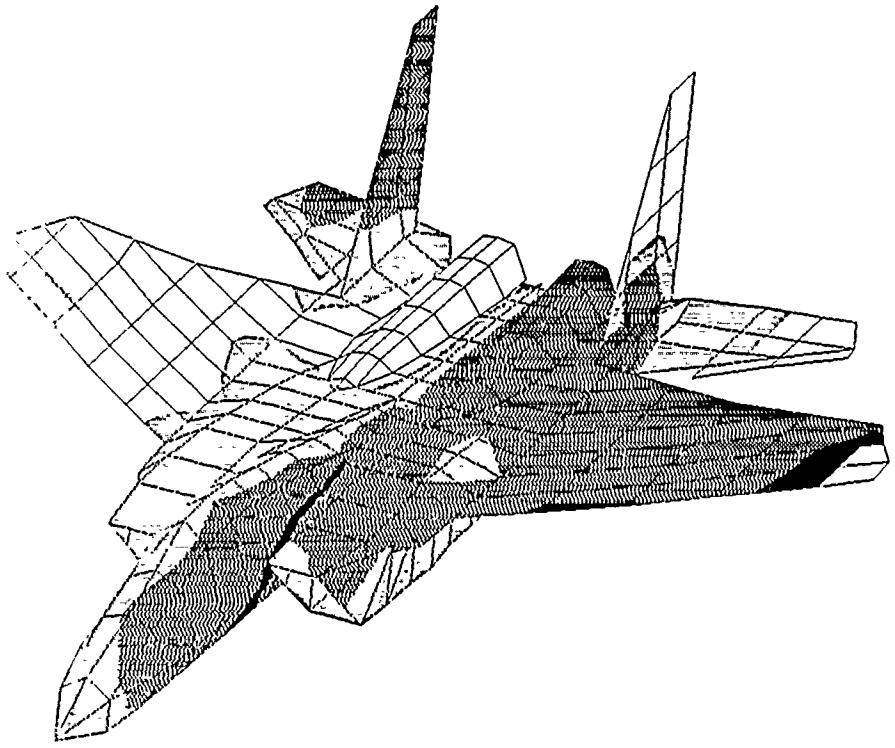


Figure 8. Scattered Field Patterns for Seam off-Boresight.

PC Electromagnetic Workstation Good NEWS For ACES' NEEDS

Allen Lockyer and Pravit Tulyathan
Aircraft Division
Northrop Corporation
Hawthorne, California



Third Annual Review of Progress In
Applied Computational E[illegible]magnetics
Naval Postgraduate School
Monterey, California — 24-26 May, [illegible]

PC ELECTROMAGNETIC WORKSTATION - GOOD NEWS FOR ACES' NEEDS

Allen Lockyer and Pravit Tulyathan

Aircraft Division, Dept. 3564/83
Northrop Corporation
Hawthorne, California 90250

ABSTRACT

The Northrop Electromagnetic Workstation (NEWS) provides electromagnetic (EM) analysis codes a graphic interface free from mainframe dependence. NEWS, based on the IBM PC microcomputer, simplifies data entry, checks model integrity and displays computed observables for a host of electromagnetic codes and techniques.

The NEWS graphic interface includes user-friendly pre- and post-processors based on pop down windows. These processors feature 3-D rotations, translations, scaling, zoom, hidden surfaces, line- or color-filled contouring, color-coding options, skeletons, animation and show/no show options, tailored to the EM community requirements. In addition, a unique wire-to-surface conversion algorithm allows a wire-grid model of a solid object to be converted to a surface patch representation.

INTRODUCTION

The Northrop Electromagnetic Workstation (NEWS) was conceived to provide electromagnetic codes a user-friendly, cost-effective graphic interface. Many public domain computer codes, such as NEC, GEMACS, THREDE, WIRANT, and IEMCAP, although comprehensive in their ability to solve a wide range of electromagnetic problems, do not have an adequate graphic input/output interface. This deficiency can demand considerable effort from an electromagnetic analyst, both to model a problem and to interpret results. This is particularly true for the Method of Moment (MOM) gridding of complex structures with many segments. Without graphics, how can the integrity of the MOM modeling be readily checked before one runs a CPU intensive analysis, and how can the results be meaningfully displayed? This is of great importance since one small error in input data entry can waste hours of CPU time.

Similar questions arise for electrically large objects treated by the Geometrical Theory of Diffraction (GTD) formalism. For GTD, a structure is more simply modeled with cylinders and flat plates, but it is often difficult to visualize how these objects should be constructed to model a complex engineering problem. As in the MOM case, error checking for model integrity is still necessary, and it is important for a user to be able to display, rotate, zoom, and change the model view, with hidden lines removed.

How are these problems currently being handled by the EM user community? In a host of different ways. In the majority of cases, a user will modify one of the many "canned" commercial graphics packages, sometimes at great expense (e.g., DISSPLA), to suit his particular EM code application. Or he may write his own customized software, using assembly code for the basic plotting routines. In any event, a proliferation of graphic interface designs have been spawned with varying levels of sophistication. Some may offer slick pop down menus, rich in graphic features such as fonts, electronic cut and paste, color-coded contouring, Smith Chart, and antenna patterns, while others offer only the crudest plotting graphics capability that has to be touched up for document quality reports.

The Numerical Electromagnetic Engineering Design Station (NEEDS), developed at Lawrence Livermore National Laboratory, is a system that addresses these problems. A panel discussion is also scheduled during this symposium to discuss the merits of standardizing EM portable graphics. This paper presents a pre- and post-processor design for EM modeling based on the IBM PC.

NEWS INTERFACE PHILOSOPHY

The philosophy of the NEWS interface is to standardize the general needs of the EM user community into one common graphic interface for electromagnetic codes. EM program output physical observable quantities, such as antenna patterns, current densities, field quantities, input impedances, and RCS, are the same for many codes. Similarly, many codes share a need for program input data, like thin wire and surface patch coordinates, elliptical cylinder and flat plate coordinates. The problem is to design a graphic pre-processor and post-processor that will have widespread EM community appeal, employ inexpensive hardware, provide attractive, but not too sophisticated interface features, including pop down menus, zoom, and rotate capabilities, and above all, modular construction for interfacing new codes, techniques or data bases. This kind of graphic interface should be freely available to the user community and not dependent on commercial software packages or company proprietary restrictions.

The Northrop approach to designing the NEWS pre- and post-processors is structured around the user community, its needs, and level of technical

sophistication. The typical NEWS user is an engineer with foundational electromagnetic knowledge that relates to his particular area of specialization, but without in-depth theoretical or analysis expertise. Hence, the interface design must place minimal demands on the EM user. For example, data entry must be quick, efficient and directly related to terms already familiar to the NEWS user. The checking for modeling errors by the pre-processor must be as automatic as possible, such as flagging on the display error message annotations and modeling elements which require attention. Post-processor displays of items like currents and fields must be semi-automatic, while still giving the user control of parameters important to him, including dynamic range, plot type, and textual annotation.

The NEWS interface design, while embracing the issues discussed above, focuses on four important factors: (1) Hardware, (2) Language, (3) Modularity, and (4) Menu Execution.

Hardware

The design of the post-processor is based on the IBM PC for the following reasons:

1. Freedom from mainframe hardware dependence (such as expensive refresh tube graphics, e.g., IBM 3250)

2. More universal availability due to prevalence throughout the user community. Nearly every government organization, school, and office has access to an IBM PC or clone

3. The IBM PC will prove to be an enduring standard and will have more computing power as technology grows.

The minimum configuration for NEWS is an IBM PC with a floppy disk drive, 512K of memory, and a Color Graphics Adapter (CGA). The recommended configuration is an IBM AT with a hard disk, one Megabyte of RAM, an 80287 numerical coprocessor, and either an Enhanced Graphics Adapter (EGA) or Hercules graphics card.

Language Choice

The post-processor package is programmed in the C language for the following reasons:

1. Efficiency – C uses low level operators which are close to machine code. This leads to compact efficient code running graphics applications at higher speeds.

2. Flexibility – C supports low level functions, such as bit operations and dynamic allocation of memory, and also high level features, such as flexible data types and structures, and a rich set of program control statements.

3. Portability – C interacts with the "outside world" entirely through library calls, making applications very portable. An application written in C can be ported to a variety of other machines, since a large user base of C systems currently exists, from micros to mainframes.

The C language also comes with a powerful set of library functions, which can perform very general disk reads and string manipulations. Choosing C enables the NEWS graphics interface to be coded quickly, and provides a sophisticated user interface based on pop down windows.

Modular System Design

Figure 1 shows a satellite approach to the system design. The NEWS pre- and post-processors communicate with other mainframe or PC analysis programs via an ASCII neutral file format and translator. The translator converts the analysis program output to the standard NEWS data base format, if necessary. This isolates the post- and pre-processors from problems caused by accommodating a large variety of file formats passed down from the mainframe analysis programs. Binary files are particularly troublesome in this respect. In this approach, a modular system is conceived in which each analysis program – NEC, GEMACS, IEMCAP, WIRANT, THREDE, and others – is entirely independent. New applications can be added and written in the preferred language, such as FORTRAN, PASCAL, ALGOL, and C. This feature also allows growth for hook-up to very sophisticated company 3-D Packages, such as Northrop Computer-Aided Design (NCAD) or CADAM.

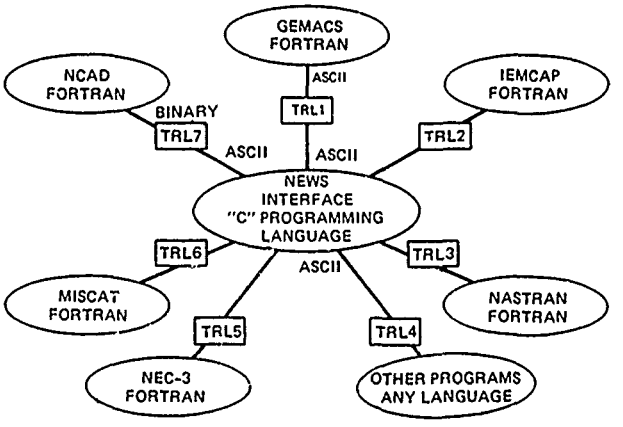


FIGURE 1. NEWS SATELLITE MODULAR DESIGN.

An important feature of Northrop's approach has been to give maximum freedom to software design in developing the interface primitives, including pop down menus, key presses, user program interaction, hidden surfaces, contours, zoom and pan, 3-D rotations, scaling, shrink, renumber, animation, show/no show, hardcopy and color options. However, it is now important to determine the minimum sophistication necessary and develop one package that will satisfy most EM users. There is still room for growth to incorporate new codes into the interface scheme and for tailoring to new EM specific requirements.

Menu Execution

There are three basic approaches to communicating with an interactive computer program: (1) keyboard commands (e.g., DOS), (2) text menus, and (3) keystroke macro commands (e.g., WordStar, PC-Write, and most PC-based CAD programs). The text menu approach, where text fills

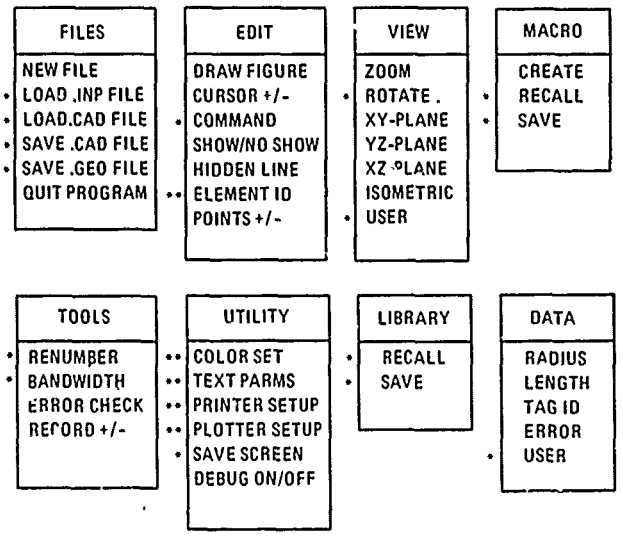
the entire screen and is logically connected based upon the function to be performed, was disregarded. Such menus destroy the entire geometry of the figure being created. The pop down menu approach is preferred, allowing a figure to be only partially destroyed and instantaneously redrawn when the window is closed. Advantages of the pop down menus are:

1. Reduces redraw time. This is significant since PCs take longer to redraw graphics than mainframe machines.

2. Easy to modify menus in pop down windows as design evolves.

3. Menus can be chained together logically and visually by having a subordinate menu pop down over its parent. This prevents the user from performing an ill-defined operation and becoming lost in the menu tree.

Figures 2 and 3 illustrate pop down menu trees for the NEWS pre- and post-processor.



* MENU ITEMS HAVE USER PROMPT BOXES
** MENU ITEMS HAVE SUB-MENUS

FIGURE 2. NEWS PRE-PROCESSOR MENU TREE.

NEWS PRE-PROCESSOR DESIGN

The NEWS pre-processor illustrated in Figure 4 has been designed to create geometry data for any of the individual EM analysis codes included in the NEWS interface. By auxiliary file manipulation, the geometry data may also be supplied from a company's own CAD/CAM package and used for subsequent analysis program runs. If the external analysis program has a modular construction, for instance GEMACS, the pre-processor may interact with a prior step of program execution. In this instance, the geometry is first created by the analysis program itself, fed to the pre-processor for model integrity checking or geometry manipulation, and relayed back to the donor analysis program for problem solution processing.

Important considerations in the NEWS pre-processor desig include the menu driven software, the ability to create, manipulate and store 3-D geometry in a system model library, and the ability to store macro command procedures.

Geometry Element Generation

All NEWS geometry elements are based on the location of points, as shown in Figure 5. The functions concerned with the manipulation of geometry data are best performed with keystroke action rather than menus. Cycling through menus can be tedious when performing simple geometry modeling tasks. The geometry is built-up from basic elements as shown below in Table 1.

TABLE 1. TYPICAL GEOMETRY ELEMENT GENERATION.

NEWS GEOMETRY	NEWS POINT-BASED DEFINITION	POINT LOCI FOR PRE-PROCESSOR
SEGMENT/WIRE	SEGMENT ENDPOINTS	ENDPOINT #1 ENDPOINT #2
PATCH (OPT 1)	CENTER POINT NORMAL DIRECTION	CENTER POINT NORMAL POINT
PATCH (OPT 2)	CENTER POINT 3 PTS DEFINING PLANE	CENTER POINT 3 PLANE PTS
PLATE	PLATE CORNER POINTS	PLATE CORNERS
CYLINDER	CENTER RADII (2) LENGTH	CENTER RADII (2) LENGTH
END CAP	NORMAL DIRECTION	END CAP EXTREMA

The pre-processor also allows an element to be entered with an arbitrary orientation or position. A number of rotation and translation commands have been designed for easy 3-D data entry.

These commands enable a figure to be located in any arbitrary coordinate system and facilitate 2-D projection of figures onto a screen for display purposes. An example of this follows:

Entry of a cylinder into an arbitrary coordinate system.

1. Rotate/translate into coordinate system centered at one end of the cylinder.

2. Enter the following points (by moving the cursor):

   a. Cylinder center point
   b. Cylinder system x-axis radius
   c. Cylinder system y-axis radius.

3. Enter the keystroke command for cylinder (CY).

4. Pre-processor prompts user for length, which can be entered into a box appearing on the screen.

The method of "point and shoot" was adopted to free the user of the burden of manually specifying all point coordinates, thereby allowing him to concentrate on geometry design.

Macro-models

Macro-models are each a collection of NEWS geometry elements which can be stored in a macro-model library, recalled by the user and added to his existing model. A geometry, or portion thereof, that has been entered into the pre-processor from an external file, may also be

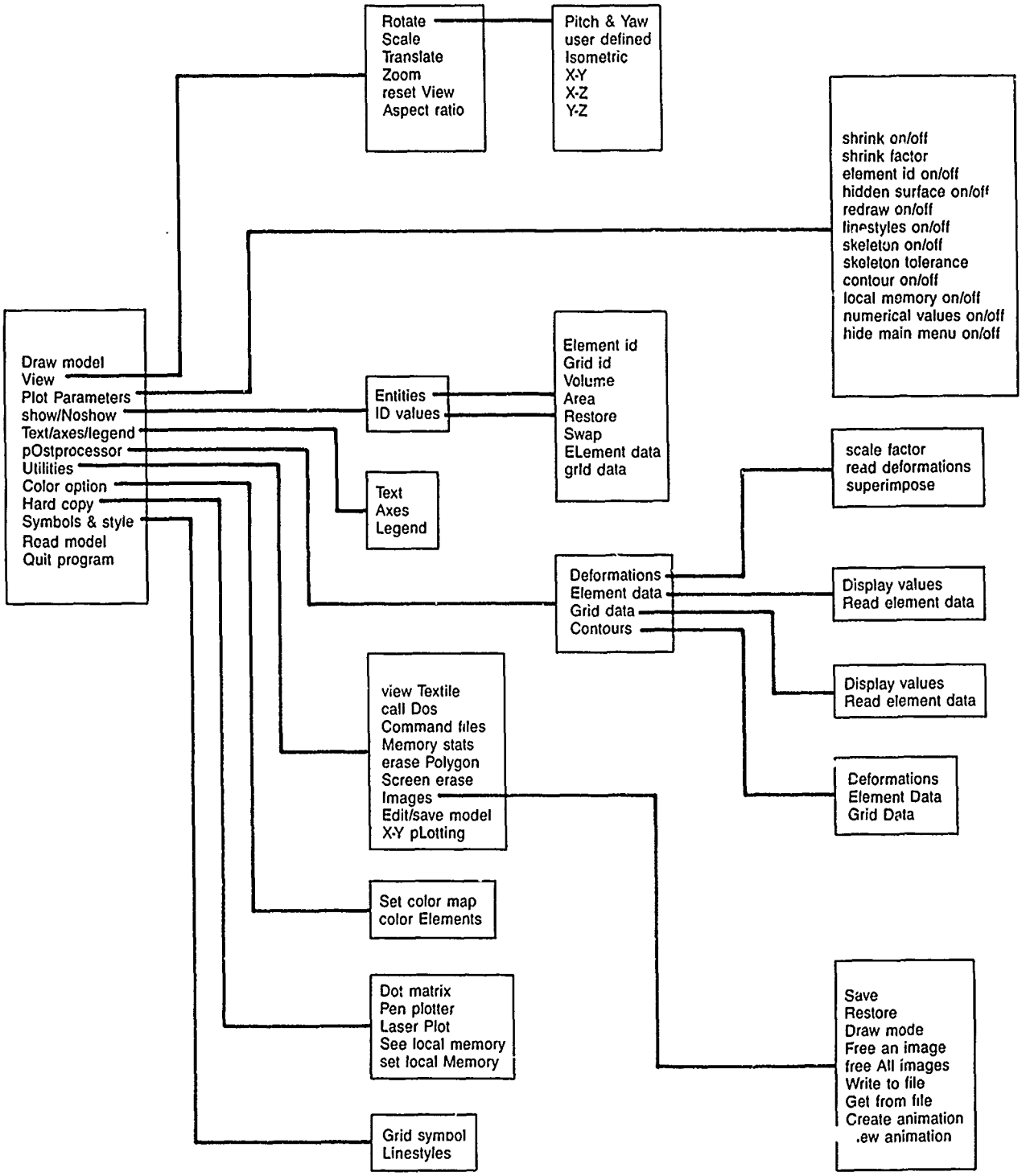


FIGURE 3. NEWS POST-PROCESSOR MENU TREE.

stored in the macro-modeling library. Hence, the user may create and edit his own macro-models. In addition to this basic macro-modeling capability, the NEWS pre-processor uses three special types of macro-models: (1) Macros with user-replaceable parameters, (2) Generalized Body of Revolution (BOR) "pseudo-geometry" elements, and (3) Generalized Body of Translation (BOT) "pseudo-geometry" elements.

Auto-Renumber

The GEMACS code, for example, employs the Banded Matrix Iteration (BMI) solution techniques to facilitate the solution of large matrices like those encountered in MOM techniques. This requires wire segments to be numbered so that the difference between a wire segment number and that of its nearest neighbor is kept to a minimum. In

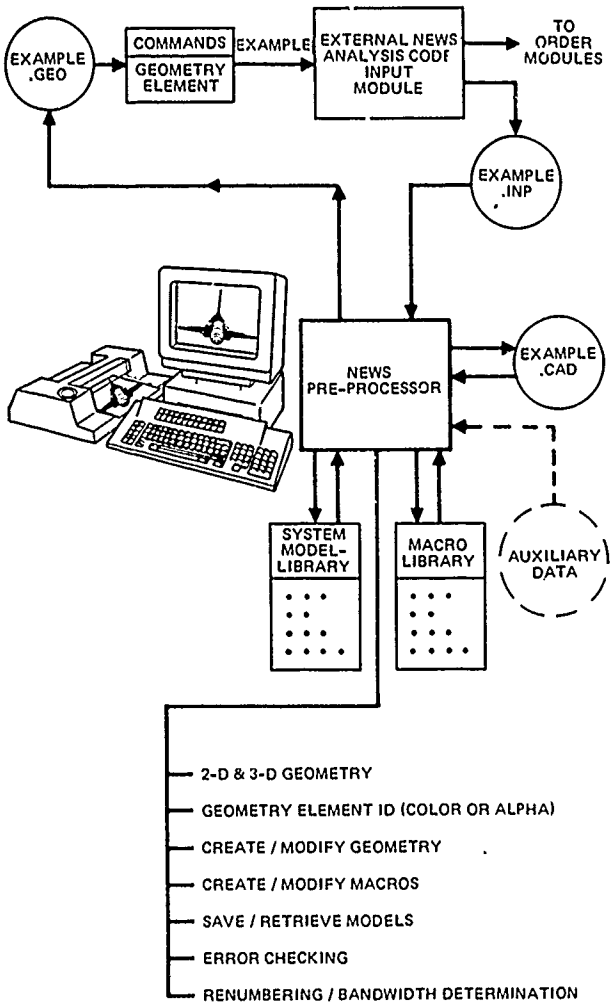


FIGURE 4. NEWS PRE-PROCESSOR DESIGN.

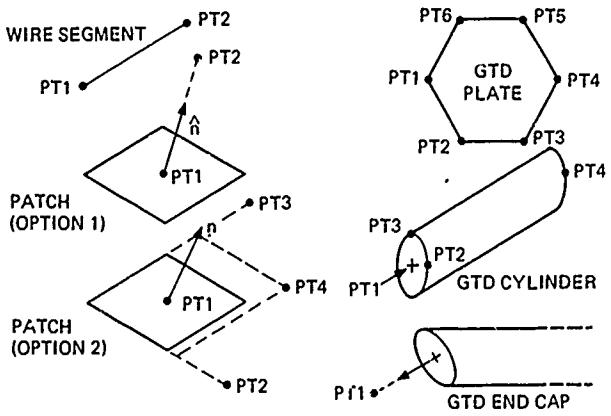


FIGURE 5. POINT BASED DESCRIPTION OF MOM AND GTD OBJECTS.

the pre-processor, the elements in a model can be renumbered in ascending order, with distance from a base point specified by the user. A 923 segment F-15 model was computed on an IBM 3090 mainframe (35 MIPS), first with the full matrix decomposition, and repeated with the BMI solution. The BMI solution technique reduced the solution time from 95 to 38 minutes of CPU, a saving of 2.5:1.

Auto-grid

The pre-processor auto-grid uses pseudo-geometry macro elements. First, the user calls the macro, positions it appropriately in the figure, and then calls the autogridding command for each pseudo-geometry element. A pseudo-geometry element is selected for autogridding by first pointing to the element with the cursor, and then pulling down the auto-grid window. The auto-grid command prompts the user for grid sizes in the two surface tangent directions. Gridding is performed along the surface of an element in two dimensions (u,v), as illustrated in Figure 6. This shows the automatic gridding of an ogival section.

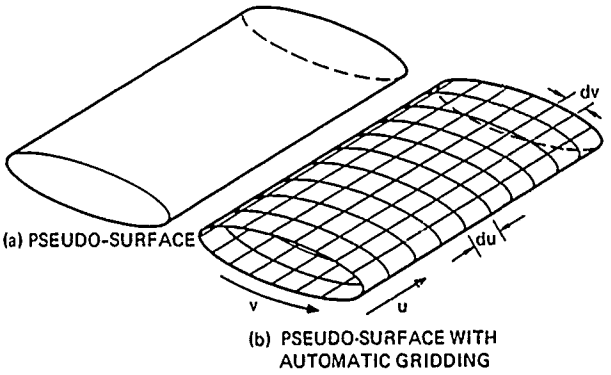


FIGURE 6. AUTO GRID FOR PSEUDO GEOMETRY MACRO-MODEL.

Wire-to-Surface Conversion

In the MOM thin-wire modeling, the wire-frame may actually represent a solid object. An algorithm was written to take a wire-frame model and use the connectivity information to create three and four sided patches. This algorithm will not add any new edges or change the original model in any way except by creating an equivalent surface patch representation. Without doing a hidden line or shrink plot, the user would not be able to tell the difference between the original model and the new model. Hidden line and shrink features of the new surface model make graphic examination of large models easier.

The wire-to-surface conversion algorithm can also be used by the pre-processor to convert a thin-wire model into a surface patch model.

Figure 7 illustrates a portion of the wire-grid model of the F-20 fuselage and the same portion of the resultant model after executing the wire-grid to surface algorithm. Shrink plot and hidden line, with the surface patches, were used to make the distinction clearer.

NEWS POST-PROCESSOR

The post-processor design is illustrated in Figure 8. The initial design goal hinged on concept exploration. What interface primitives or building blocks should a post-processor have? The resulting features accomplished are: 3-D rotations, translations, scaling, zoom, hidden surfaces, either 'line' or 'color-filled' contouring, color-coding options, skeletons, animation, show/no show options, and, like the pre-processor, a user-friendly interface based on pop down menu. Most of the menu items of the interface primitives are shown in Figure 3.

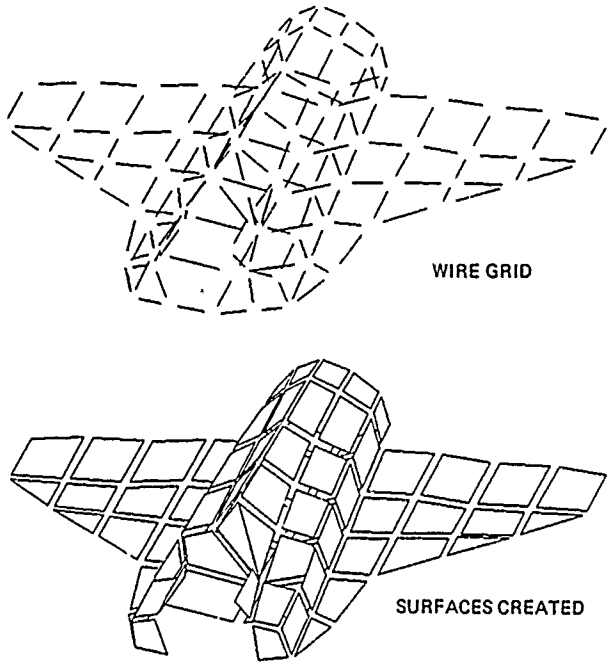


FIGURE 7. WIRE-FRAME TO SURFACE PATCH CONVERSION.

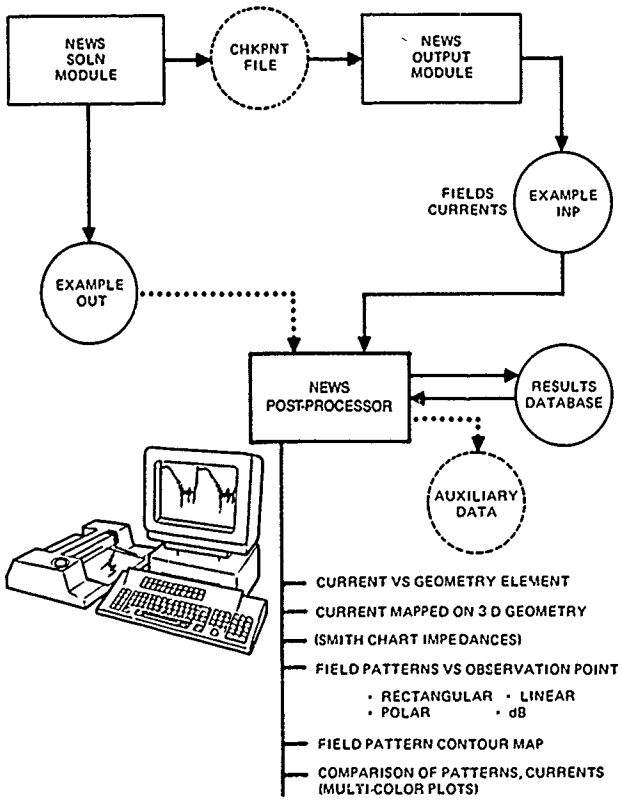


FIGURE 8. NEWS POST-PROCESSOR DESIGN.

The post-processor is currently being tailored to the needs of the EM community, allowing electromagnetic and geometric data from various NEWS external analysis programs, like GEMACS, NEC, and IEMCAP, to be manipulated by the user. These needs fall into the following categories: (1) currents, (2) impedances, and (3) fields.

1. Currents

Surface current density is the primary unknown solved by several EM techniques such as MOM. The pre-processor should include: color mapped currents on a structure geometry model; rectangular plots of current magnitude and/or phase versus segment patch number; currents versus a user-selected independent variable such as frequency; overlays of two or more currents and other currents on the same plot for purposes of comparison; generation of ASCII file of currents and other parameters for use by other EM codes; and ability to read current data generated by other programs in a standard file format.

2. Impedances

Impedance is an important parameter for an antenna design engineer. A post-processor should include the following features: impedance magnitude and/or phase versus frequency; efficiency, power input, or power absorbed versus frequency; Smith Chart of impedance versus frequency; overlays of two or more impedances on the same plot for purposes of comparison; ability to read impedance data generated by other programs; and generation of an ASCII file of impedance, efficiency, etc. for use by other EM programs.

3. Fields

Field quantities are primarily observables for antenna and scattering problems. A post-processor should include: polar and Cartesian plots of field strength (V/m, W/m^2, or dB) for any valid NEWS coordinate system; separation of field strength by polarization component or combining all components to obtain total fields; generation of other important polarization, for instance RH and LH circular polarization components, and axial ratio, from NEWS data; conversion of field data to related quantities including radar cross section in m^2 or dBsm; 2-D contour plots of field strength, overlays of two or more field data sets on the same plot for the purposes of comparison; ability to use symmetry when the field pattern is symmetric; ability to offset pattern angles and magnitudes; generation of ASCII file of field parameters for use by other EM programs; and ability to read field data generated by other EM codes in the ASCII format.

Example plots illustrating the above features are shown in Figure 9.

NEWS GRAPHICS FEATURES AND DISPLAY

The graphic aspect of NEWS will be described in this section. Unless otherwise stated, the discussion is for the post-processor, since it is more developed. Most of the basic graphics utilities are

based on the MetaWINDOW graphics toolkit from METAGRAPHICS Software Corporation, 4575 Scotts Valley Drive, Scotts Valley, CA 95066. MetaWINDOW provides a powerful set of graphic drawing functions, plus an expanded set of advanced utilities for developing multi-window desktop applications. This deviation from the design philosophy (avoiding commercial software) reduces graphics development time. In addition, MetaWINDOW package is relatively inexpensive.

Data Base Structure

The geometry representation of the present NEWS post-processor is composed of grid points and elements. A grid is a collection of x,y,z points in space together with an ID number for identification. An element is a polygonal surface defined by listing, in order, the grid ID of points along its boundary. A wire element is specified by two grid IDs. A NEWS post-processor handles 3500 grid points and 2600 elements. The file format listing is shown below:

GEOMETRY				
NGRID				
ID (1)	X (1)	Y (1)	Z (1)	
.	.	.	.	
.	.	.	.	
.	.	.	.	
ID (N)	X (N)	Y(N)	Z (N)	
NELEM				
IDELM (1)	ITYPE (1)	ID (IEL1)	.	ID (IELQ)
.	.	.	.	.
.	.	.	.	.
.	.	.	.	.
IDELM (M)	ITYPE (M)	ID (IELR)	.	ID (IDELS)

KEY WORDS IN THE ABOVE LISTING ARE AS FOLLOWS:

GEOMETRY	=	KEY WORD
NGRID	=	NUMBER OF GRID POINTS
ID (I)	=	ARRAY OF GRID IDs
X (I), Y (I), Z (I)	=	ARRAYS OF X,Y,Z COORDINATES
NELEM	=	NUMBER OF ELEMENTS
ITYPE (I)	=	ARRAY OF ELEMENT TYPE IDs

The current view of a model can be controlled by the following submenu options:

1. Rotate

   The view angle can be specified by using the view planes, i.e., isometric, x-y, y-z, or x-z, angles with respect to xyz axis, or the pitch/yaw angle. The pitch/yaw angle is interactively changed by the arrow keys. The global axes and real time rotation of the axes are shown in the screen. Figure 10 shows different viewing angles for a model plotted with the associated coordinate axis. The electronics cut-and-paste capability of NEWS allows several models to be displayed on one figure.

2. Scale

   The size of the object shown on the screen can be varied by the scale parameter. A scale of 1.0 makes the model fit exactly in the viewing window. Larger scales make the model larger, thus clipping some of the model.

3. Translate

   The object can be shifted away from the center of the screen by specifying two points. The points are chosen interactively by using the arrow keys and the object is shifted from point one to point two. Another option redraws the model each time an arrow key is pressed.

4. Zoom

   A detailed screen plot of a small area of a shown model can be accomplished with the zoom/pan capability. The region within a model for the zoom area can be specified by a rectangular box with the same aspect ratio as that of the plot screen, as shown in Figure 11. Any portion of a model can be expanded or contracted by this function without limitation. More than one zoom/pan function may be executed during the editing of a structure. A "zoom upon zoom" merely multiplies the scale factors together. The rectangular zoom-box can be interactively positioned with the arrow keys and sized with the PgUp and PgDn keys.

5. Default

   This option resets a number of different flags to the preprogrammed defaults. Thus, a model that has been shifted and zoomed can be restored to the original screen image by using this option.

6. Aspect Ratio

   An aspect ratio is needed to compensate for the fact that most display screens do not have square pixels. This option can be used to make a square model look square on the screen. The height of the screen is multiplied by the aspect ratio, so the larger the aspect ratio, the wider the viewing window.

Plot Parameters

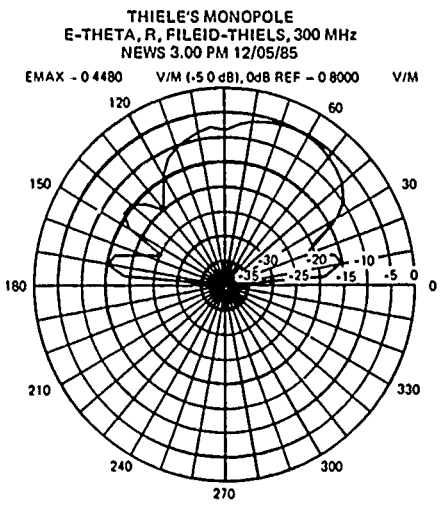
A number of different parameters controlling the plotting will be described in the following submenu. Once these options are set, they will remain active until the user turns them off. The initial state of the plot parameter is read from a file. A user may customize the initial state of the plot parameter by modifying this file. Several of the options described below can be toggled On/Off:

1. Shrink

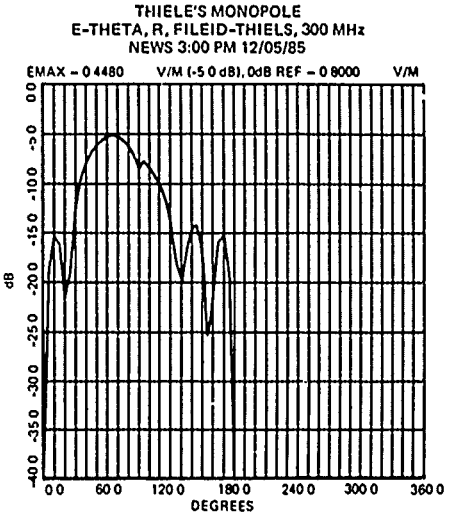
   When on, each element is plotted with its edges "shrunk" in towards the center. Figure 12 illustrates a zoomed view of the F-15 model with shrink, hidden line removal and element IDs.

2. Shrink Ratio

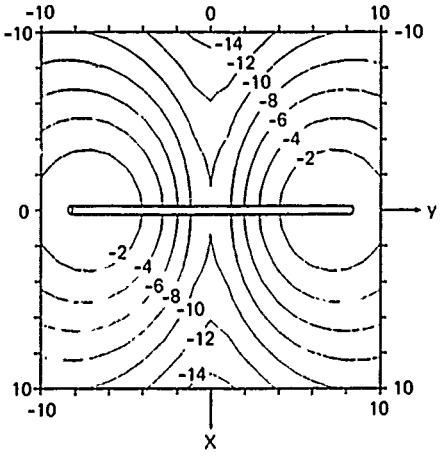
   This controls the amount of shrinkage. The value of 0.0 will cause no shrinkage



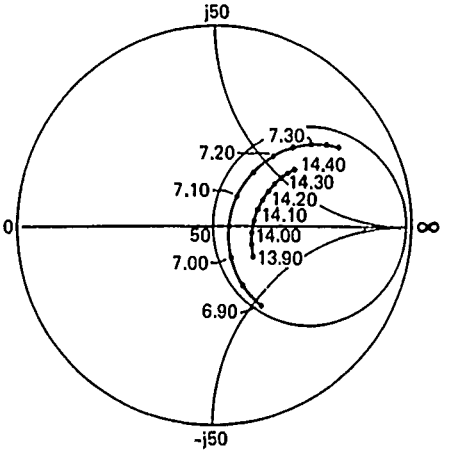
(a) POLAR PLOT OF THIELE'S MONOPOLE



(b) RECTANGULAR PLOT OF THIELE'S MONOPOLE



(c) CONTOUR FIELD PLOT



(d) SMITH CHART

FIGURE 9. EXAMPLE PLOTS FROM THE POST-PROCESSOR.

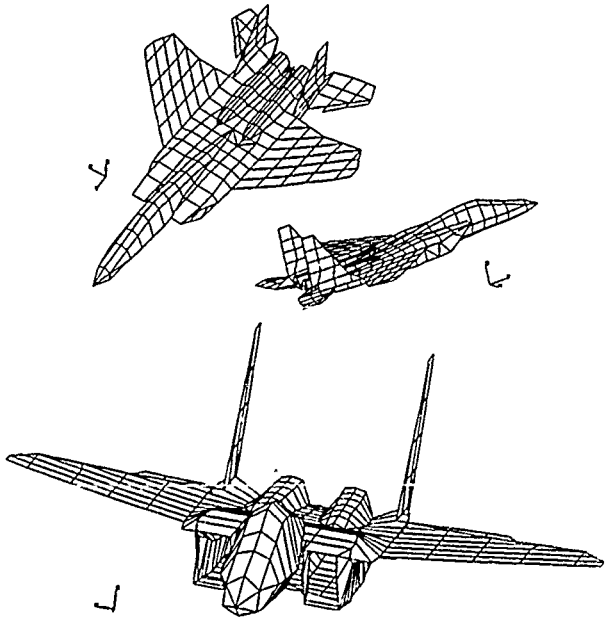


FIGURE 10. DIFFERENT ANGLES, VIEWS AND ELECTRONIC CUT-AND-PASTE OF A F-15 SURFACE PATCH MODEL.

while a value of 1.0 will shrink each element to a point.

3. Element ID

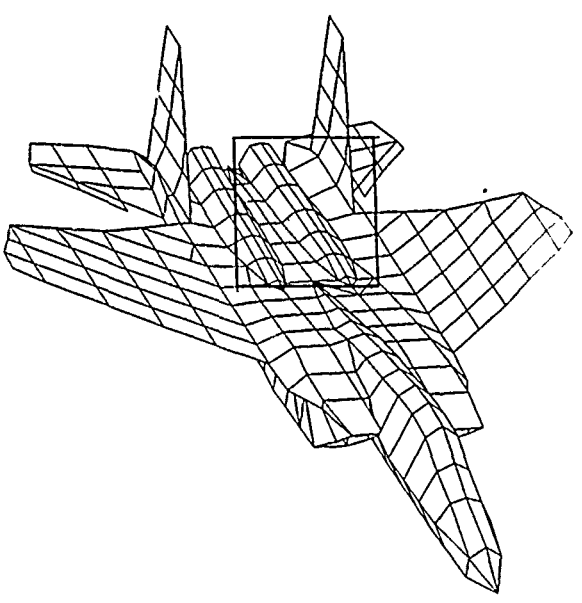
ID values can be displayed at each element's center.

4. Grid ID

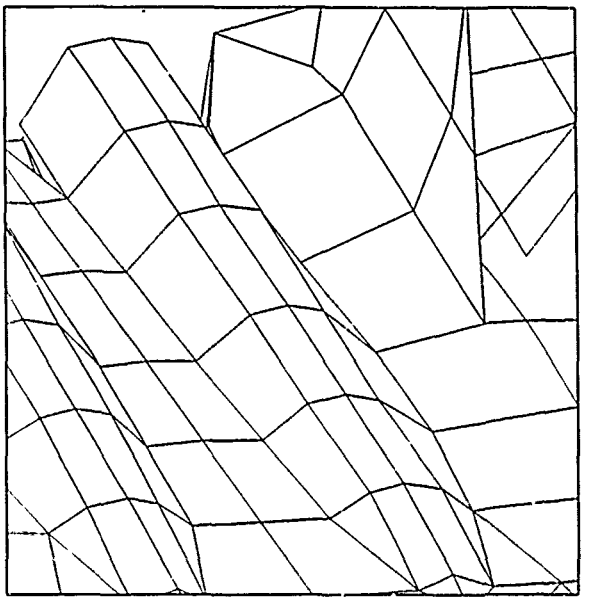
Grid ID values can be displayed at each grid point.

5. Hidden Surface

When on, the model is plotted without the hidden surface (line). The elements are sorted by depth and drawn in order, using the painter's algorithm. This algorithm is employed, since a raster device allows overpainting of the elements and color-filling can be performed progressively from background to foreground. The screen image can be dumped to the dotmatrix printer for draft quality hardcopy, as seen in Figure 13. It can also be written to the local memory at a higher resolution and output to the laser printer for a high quality monochrome hardcopy, as shown in Figure 14.



(a) ZOOM WINDOW OF F-15 TAIL SECTION



(b) ZOOM WINDOW ON F-15 TAIL SECTION FILLS ENTIRE SCREEN

FIGURE 11. ZOOM OF F-15 TAIL SECTION.

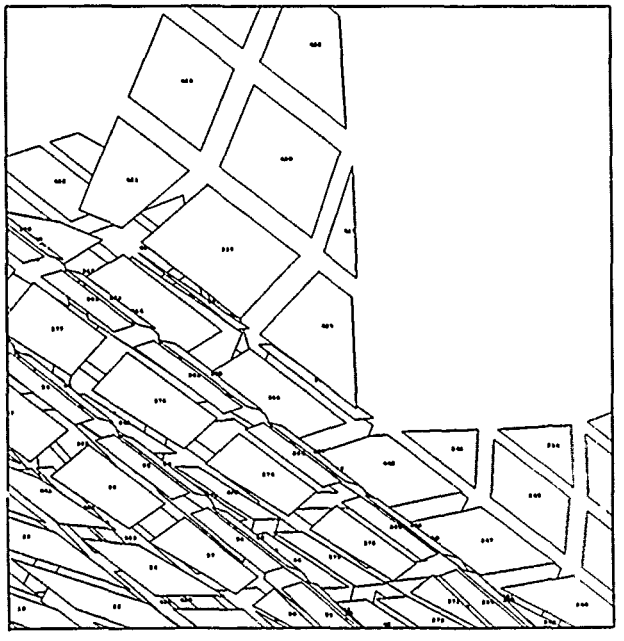


FIGURE 12. SURFACE PATCH, SHRINK, ZOOM AND ELEMENT ID OF THE F-15 MODEL.

However, the above technique of hidden line removal is not suitable for pen plotters. An alternate approach is to compare each of the polygonal faces to the remaining faces in order to eliminate faces or portions of faces that are not visible. This method has to be used since no screen overpainting can be performed with a pen plotter. The difficulty with using a true hidden line algorithm at the PC level is that the process is very CPU intensive. In the worst case, each element must be compared to every other element. Also, many intersection points may have to be computed.

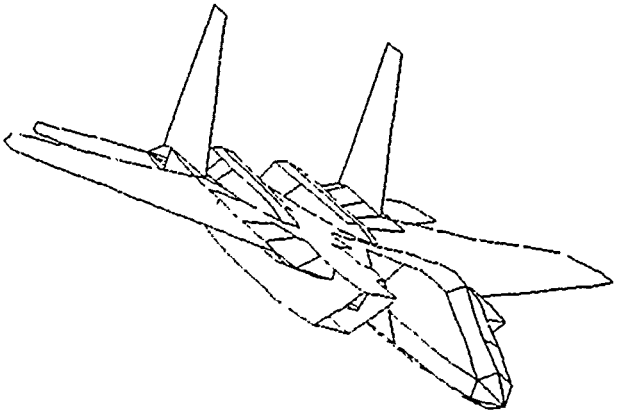


FIGURE 13. DRAFT QUALITY PRINT SHOWING SKELETON PROFILE OF F-15.

6. Skeleton

When on, the edges of all the elements are compared and only edges where the elements meet at a large enough angle will be drawn.

7. Skeleton tolerance

This controls the angle used in the skeleton plot algorithm. An angle of 0 will wash out all edges, while an angle of 180 will keep all edges.

8. Contour

When on, contour lines, based on element or grid data read from an external file, will be drawn. If no contour values have been defined, this option has no effect. Either contour lines and color-filled contours, as shown in Figures 15 and 16, are available.

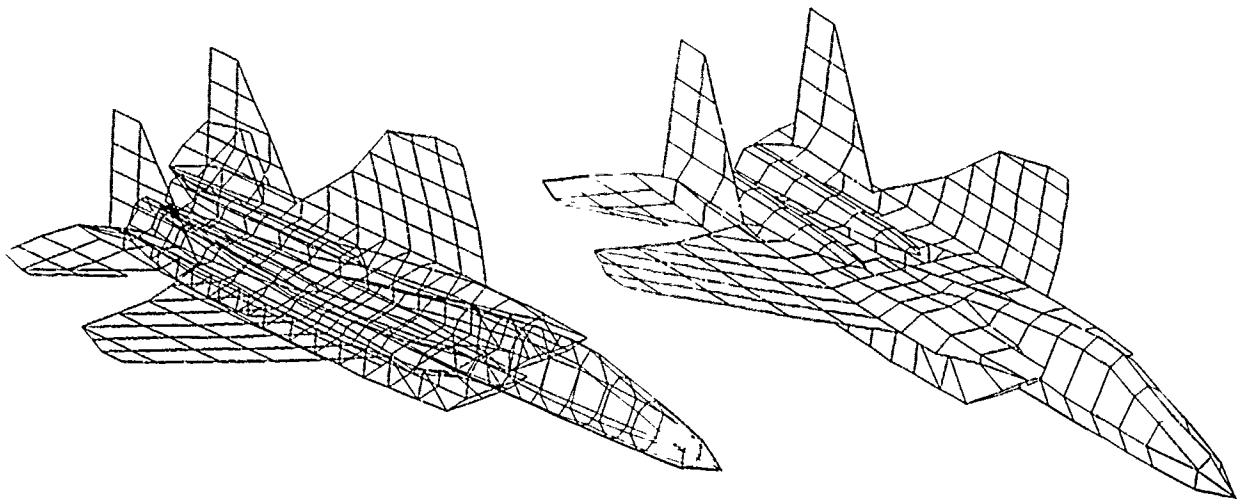


FIGURE 14. F-15 SURFACE PATCH MODEL DRAWN WITH AND WITHOUT HIDDEN LINE REMOVAL.

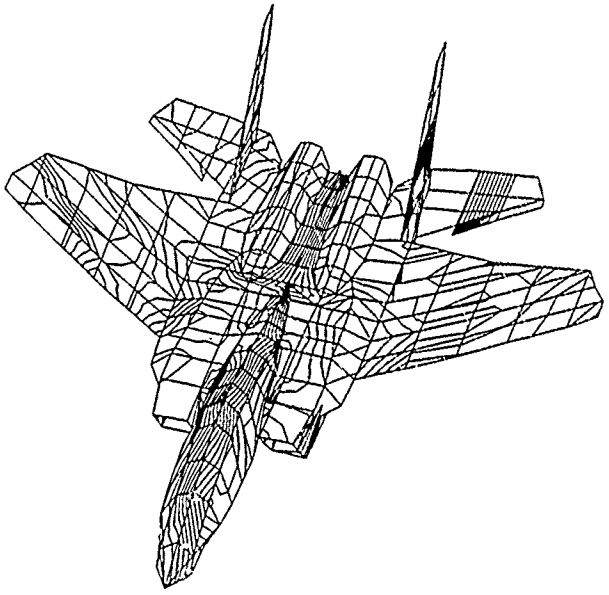


FIGURE 15. SURFACE CURRENT CONTOUR LINES.

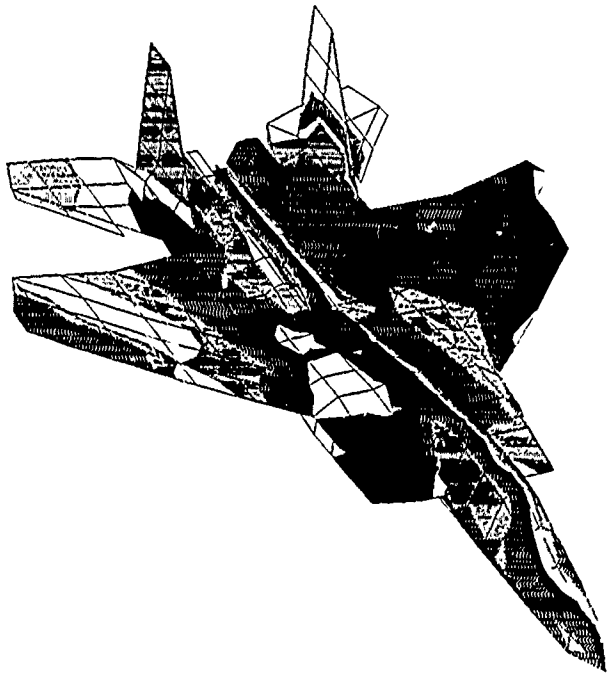


FIGURE 16. SURFACE CURRENT CONTOUR FILL.

Post-Processing

The nongeometric data which can be viewed is controlled by this module. Supplemental data files are necessary.

1. Element Data

   This data file contains a list of element IDs and one real number for each element. This real number may represent observable quantities, such as current density.

2. Grid Data

   This is a data file containing a list of grid IDs and one real number for each grid.

3. Contours

   This submenu can be used to draw contour lines which can be generated by using either the element or grid data. When the values are generated, the menu displays the minimum and maximum values, and a default number of increments. The number of lines drawn is determined by the increment value, starting at the minimum and ending at the maximum. The minimum, maximum, and increment values can all be changed by the user.

Utilities

Two of the most important post-processor utilities are as follows:

1. Command Files

   A command file is a recording of the keys pressed during a session. A command file can be opened and records the key presses. The NEWS post-processor can read a command file and play back the previously recorded keypresses.

2. Rectangular and Polar Plots

The post-processor can output field quantities in a colored polar or rectangular format. Figure 9-a shows a field plot for monopole on a circular ground plane in rectangular coordinates. Figure 9-b shows the same antenna pattern in polar coordinates. The text annotation at the top of the figures helps identify the plot with the title, date, and other important parameters. These include frequency and pattern cut information. Figure 9-c and Figure 9-d show a contour field plot and Smith Chart plot, respectively.

Current Mapping

The post-processor has several ways of representing current density, since this is one of the most useful observable quantities in any EM analysis. Figure 15 shows how the surface current density may be mapped onto the modeled structure by contour lines. The current density is highest where the contour lines are more closely spaced. Figure 17 illustrates contours plotted on a wing. For an uncluttered image, the line contouring should be combined with the hidden line feature as described earlier. An alternative method of contouring can be achieved with contour fill. For this monochrome paper, Figure 16 shows the surface current density displayed, using contour fill with gray scale shading. The shading can be replaced by user defined color; up to 16 colors with the Extended Graphic Adapter Card are possible. Similarly, Figure 18 shows a surface patch representation of the F-15, where the average value of the current density is plotted with each patch element. Figure 19 shows a zoomed view where the magnitude of the patch current is displayed numerically. A useful NEWS interface output currently under development is the capability to plot current versus selected MOM segment numbers. This will allow the user to visualize current distribution on a portion of the structure with a classic Cartesian plot.

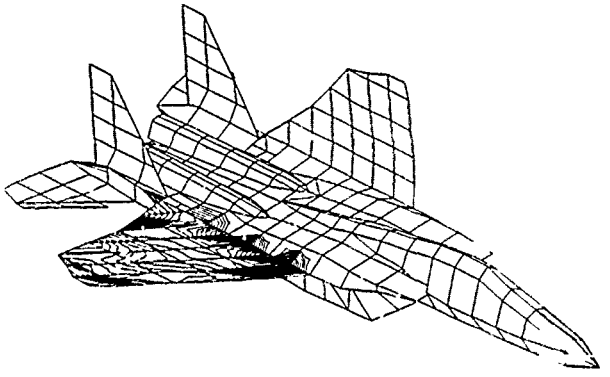


FIGURE 17. CURRENT CONTOURS PLOTTED ON WING.

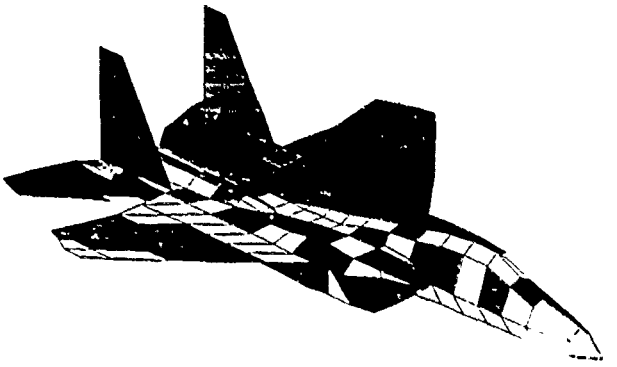


FIGURE 18. SURFACE ELEMENT SHOWING CURRENT BY COLOR (SHOWN WITH GRAY SCALE SHADINGS FOR BLACK AND WHITE REPRODUCTION).

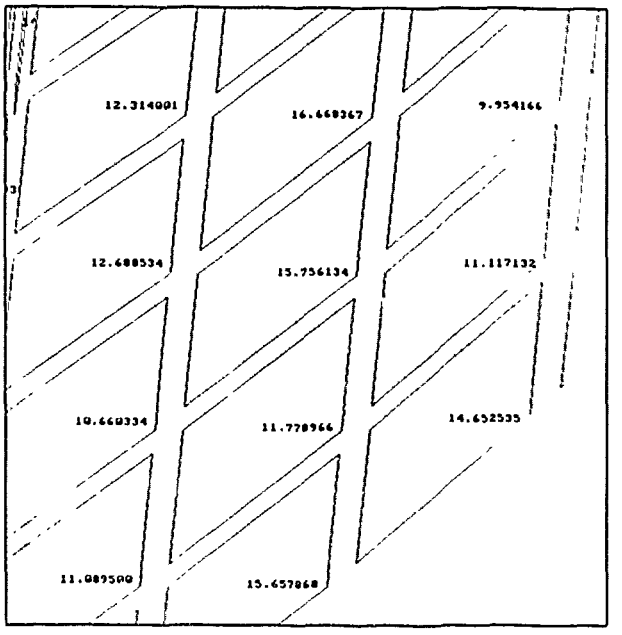


FIGURE 19. CURRENT MAGNITUDE ON SURFACE ELEMENT (WHICH MAY BE CONVERTED FROM A WIRE-GRID STRUCTURE).

CONCLUSIONS

There is need among the EM community to develop a common standard for portable graphics and tools to be used in the EM modeling process. The Northrop Electromagnetic Workstation, still in the experimental stage, offers an approach towards satisfying this requirement. The NEWS design features portability and inexpensive hardware based on the IBM PC. The workstation described also includes powerful graphics, independence from mainframe hardware, modular design, and user-friendly interface primitives based on the C programming language.

ACKNOWLEDGEMENTS

The authors greatly acknowledge the extensive design and software support for the NEWS concept provided by Mr. W. Hartman and Mr. G. Upshaw of Northrop Corporation, Aircraft Division.

SESSION VIII - "ANTENNA MODELING"

Moderator: R. Anders

CONFORMAL WIDEBAND ANTENNA MODELLING

H. A. Karwacki and R. A. Gilbert
Sanders - A Lockheed Company
95 Canal Street
Nashua, N.H. 03061-2004

ABSTRACT

A wideband conformal aperture antenna composed of a notch element feeding a triangular dielectric lens and flat plate reflector mounted in a finite conducting ground plane was modelled using a hybrid of geometrical optics, physical optics and Geometric Theory of Diffraction (GTD).

Two dimensional ray tracing techniques were applied to determine the aperture field distribution in the ground plane resulting from the notch excitation of the lens. The summed aperture distribution was numerically integrated and combined with a GTD solution for the scattered field from the ground plane edges to predict the far field radiation pattern. Computed patterns are compared with measured results.

This model is an application of simple techniques to predict the general pattern characteristics of a complicated antenna structure and allow for design parameter variation and optimization prior to fabrication.

I. INTRODUCTION

Conformal wideband antennas are preferable for applications requiring low profile, light weight, compactness, simplicity, and ease of installation. Conventional antennas, such as spirals and planar log-periodic antennas, are commonly prescribed for these applications. A new antenna design which fulfills the above requirements in addition to directing the main beam away from broadside to the aperture is described herein. The notch-fed aperture antenna consists of a wideband notch antenna element placed in a cavity to feed a rectangular aperture via a reflector and dielectric lens combination. Various parameters such as the notch and reflector plane orientations and the dielectric constant of the lens have direct influence on the radiation pattern of the antenna. The complex interaction of these major parameters and numerous other parameters prohibit designing the antenna by empirical methods alone. A simple two-dimensional ray tracing approach coupled with physical optics in conjunction with a corrective GTD technique were effectively used to model the antenna.

A model antenna (Figure 3) was fabricated and tested to verify the computer model. The flexibility of

page flipped

perpendicular to the aperture, is illuminated by the near field of the source. The third face is backed by the conducting reflector plate. Conducting walls enclose the parallel faces of the wedge along with the small cavity containing the source.

The notch element [1] is comprised of a shielded stripline package with a narrow slit in each of the two ground conductors flared out at one end and excited by an open circuited stub line perpendicular to the slits (Figure 2). This type of element was chosen for its broadband impedance and pattern characteristics and compactness. The stripline notch element source would ideally have been modelled by measured near field pattern data. Since that data was not available, the source was modelled using an analytical formulation of a cosine raised to a power over the angular sector of interest.

III. THEORY AND COMPUTATIONAL MODEL

The antenna consisting of a stripline notch element, dielectric lens and flat plate reflector as shown in Figure 1 was modelled for computational analysis with a combination of geometrical optics ray tracing, aperture field integration, and GTD (geometric theory of diffraction) techniques.

perpendicular to the aperture, is illuminated by the near field of the source. The third face is backed by the conducting reflector plate. Conducting walls enclose the parallel faces of the wedge along with the small cavity containing the source.

The notch element [1] is comprised of a shielded stripline package with a narrow slit in each of the two ground conductors flared out at one end and excited by an open circuited stub line perpendicular to the slits (Figure 2). This type of element was chosen for its broadband impedance and pattern characteristics and compactness. The stripline notch element source would ideally have been modelled by measured near field pattern data. Since that data was not available, the source was modelled using an analytical formulation of a cosine raised to a power over the angular sector of interest.

III. THEORY AND COMPUTATIONAL MODEL

The antenna consisting of a stripline notch element, dielectric lens and flat plate reflector as shown in Figure 1 was modelled for computational analysis with a combination of geometrical optics ray tracing, aperture field integration, and GTD (geometric theory of diffraction) techniques.

The rectangular radiating aperture of the antenna was assumed to be on an infinite ground plane and the far field radiation was computed by performing a numerical integration of the free space Green's function over the distributed sources across the aperture [2,3].

The initial step in obtaining the aperture distribution involved tracing rays from the source point, which was assumed to be at the phase center of notch element, to the lens interface at S1 including the amplitude and phase variation due to the ray paths. The source rays were included over the range of angles which intercept the first dielectric interface (S1) in one degree increments. This divides the lens input face into small increments in terms of wavelength for the particular frequency range and geometry modelled. The transmitted rays whose amplitudes are determined by applying Snell's Law at the air/dielectric interface, propagate through the dielectric medium to the aperture (S2) either directly or indirectly by reflection from the conducting plate (S3).

The incident rays at the aperture must pass through interface S2 from a higher dielectric constant medium to air. If the angles of the incident rays are greater than the critical angle the rays are reflected from the S2 interface back into the dielectric medium. Those rays which pass through S2 are summed at cells which

subdivide the aperture and form an imaginary aperture directly above the surface S2.

The ray tracing model was at first restricted to these simple refracted and reflected rays. The patterns calculated for the lens reflector system without considering multiply reflected rays did not exhibit the pattern steering which was measured. This prompted the extension of the ray tracing to include one internal reflection for each ray that reached the aperture air/dielectric interface. This improved the match between predicted and measured pattern characteristics. Typical ray paths for a relative dielectric of 2.54 are presented in Figures 4a to 4d. The solid lines represent the rays which are refracted at S1, reflected at S3 and travel to S2. The dashed lines represent rays which are refracted at S1, internally reflected at S2 and reflected at S3 back to S2. The chain-dot lines represent the rays which are subject to two reflections at S3 before emerging at S2. It is obvious that a significant group of rays would be ignored if internal reflection were not included. It is probable that inclusion of higher order multiply reflected rays would further improve the predicted to measured pattern

correlation, but time was not available to study the relative improvement versus the increased complexity.

The radiating aperture was divided into incremental "cells" to permit a numerical integration of the aperture field. The aperture field distribution is the vector sum of the fields associated with each ray which intercepts a particular aperture "cell". The total field is assumed to be at the center of each cell. Figures 5a and 5b show typical aperture amplitude and phase distributions at midband with the solid line representing the E-field and the dashed line the H-field. The aperture fields are then replaced with equivalent electric and magnetic currents and numerically integrated to obtain the far field contribution of the aperture [2,3].

The total far field pattern of the test antenna includes the contributions of both the radiating aperture and the diffracted field components from the edges of the finite sized ground plane. The diffraction components for the plate edges are found by assuming that the incident field on the edges is the far field value obtained from the aperture at grazing. The diffraction coefficients calculated were for an infinitely thin wedge [4]. The addition of the edge

diffraction field to the aperture field improved the predicted pattern match.

IV. VERIFICATION OF COMPUTED RESULTS

The computational model was used to select the geometry for the initial test antenna. The antenna far field patterns were measured at several frequencies in the H-plane for the geometry shown in Figure 1. The resulting predicted patterns are plotted next to the measured patterns for comparison.

The calculated patterns were all normalized to the maximum radiated power. It can be seen in Figures 6 to 12 that the calculated patterns compare quite well with measured patterns especially at the higher frequencies, considering the simplicity of the computational model and given the complexity of the problem. The prediction accuracy could be improved if several sources of error were eliminated or reduced. These are 1) the lack of near field source data, 2) accurate source phase center location versus frequency, 3) an accurate formulation for the aperture edge diffraction components, and 4) the effects of higher order internally reflected rays.

The unknown near field amplitude of the notch element is felt to be a minor error contributor since changing the analytical function used to represent it in

the model produced very little change in the predicted pattern. The location of the phase center of the notch element would be a source of error in the computed pattern since it directly affects the aperture phase distribution.

The diffraction due to the aperture edges is also an important factor since the presence of additional scattering sources near the aperture is known to produce a significant effect on the overall antenna pattern. This aperture edge diffraction was not included in the model since a self consistent formulation for the multiple media boundary involved is not yet available. The impact of including higher order multiply reflected rays in the model is hard to assess since data has not been obtained on the relative amplitude of these rays. It does seem obvious that these multiply reflected rays would have a significant effect on the pattern prediction.

V. CONCLUSION

A notch fed aperture antenna was fabricated and its measured radiation pattern compared closely with the computed pattern obtained from a simple computational design model. A ray tracing technique was used to determine the aperture field distribution of the antenna. Rays emanating from a notch element illuminated the aperture through a dielectric

lens/reflector. Multiple reflections at the interfaces were considered. The far field of the antenna was obtained by taking the Fourier transform of its aperture distribution. The edge diffraction of the truncated ground plane was also included.

The comparison of the measured and calculated radiation characteristics demonstrates the applicability of geometrical optics even when the dimensions of the surfaces involved are on the order of a few wavelengths.

REFERENCES

[1] L. R. Lewis and J. Pozgay, "Broadband Antenna Study", Final Report # AFCRL-TR-75-0178, March 1975.

[2] S. Silver, Microwave Antenna Theory and Design, McGraw-Hill, pp. 334-347, New York, 1949.

[3] C. A. Balanis, Antenna Theory, Harper & Row, pp. 446-477, New York, 1982.

[4] R. G. Kouyoumjian and P. H. Pathak, "A Uniform Geometrical Theory of Diffraction for an Edge in a Perfectly Conducting Surface", Proc. IEEE, vol. 62, pp. 1448-1461, Nov. 1974.

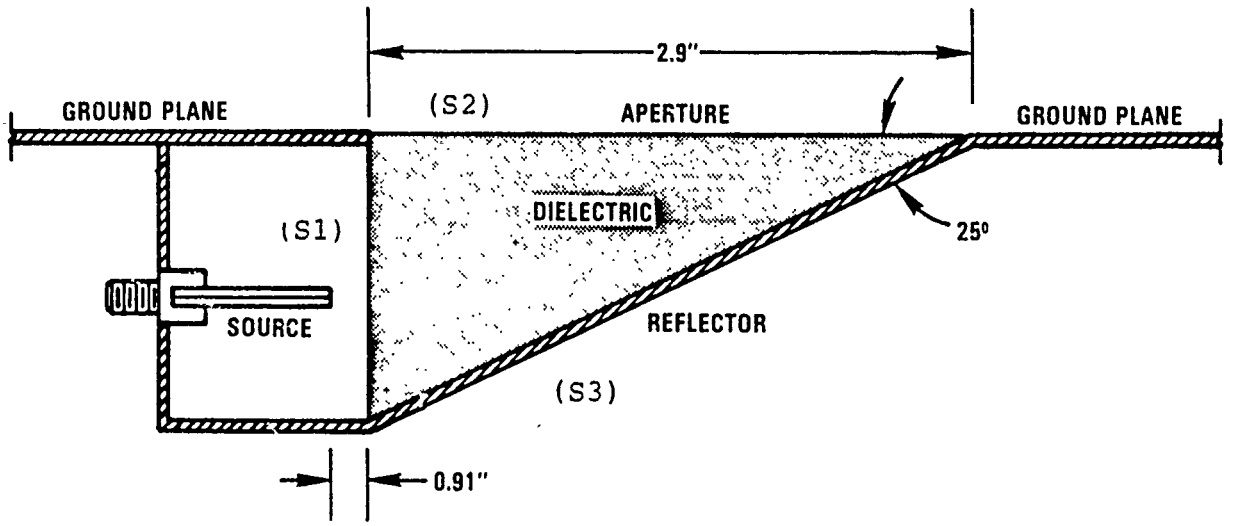


FIGURE 1. ANTENNA GEOMETRY

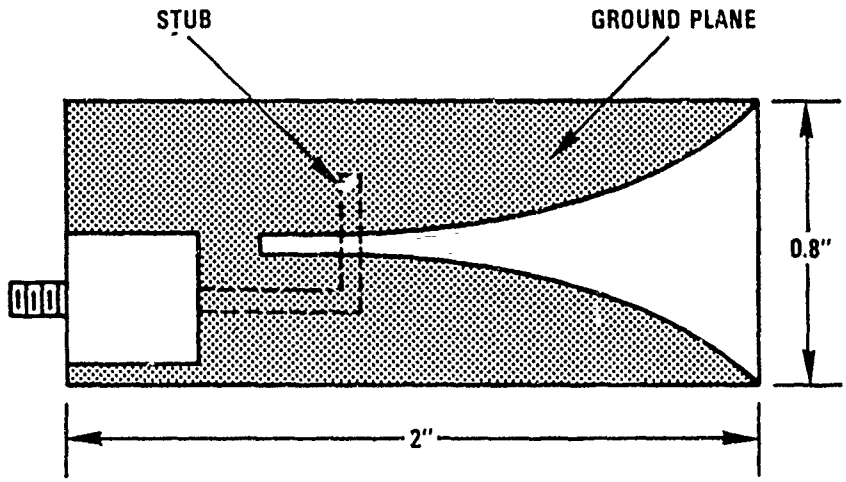


FIGURE 2. NOTCH ELEMENT

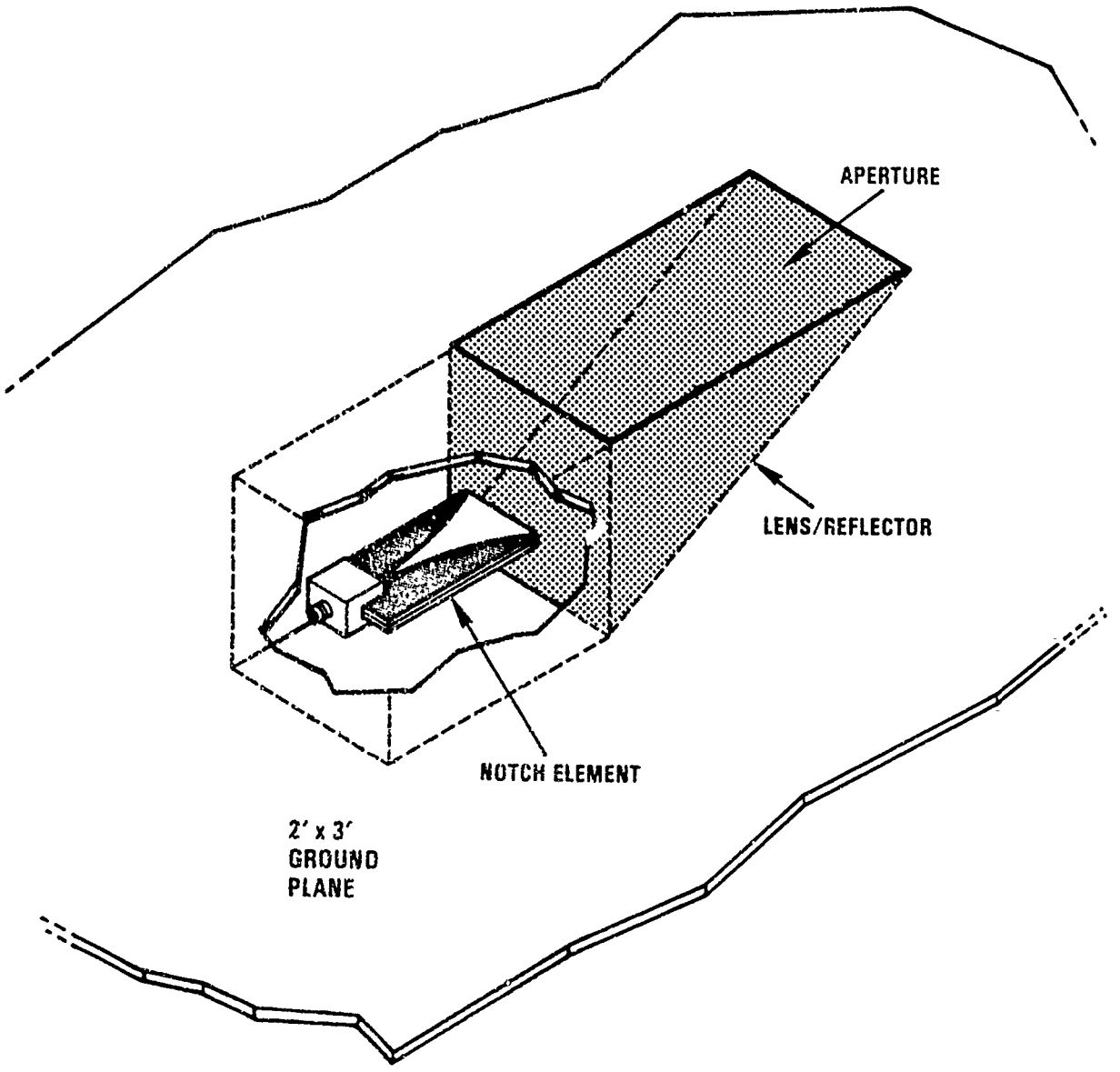
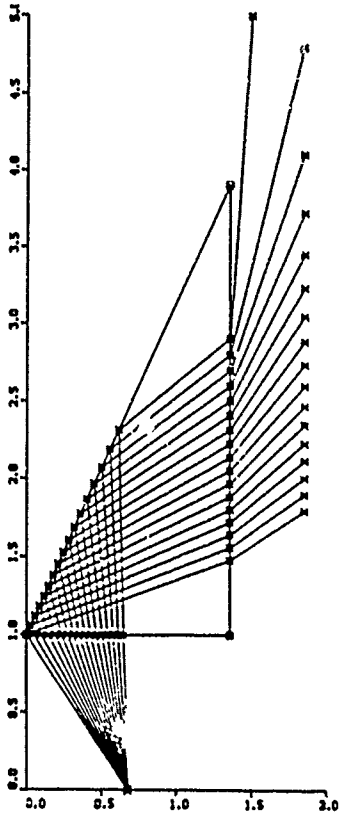
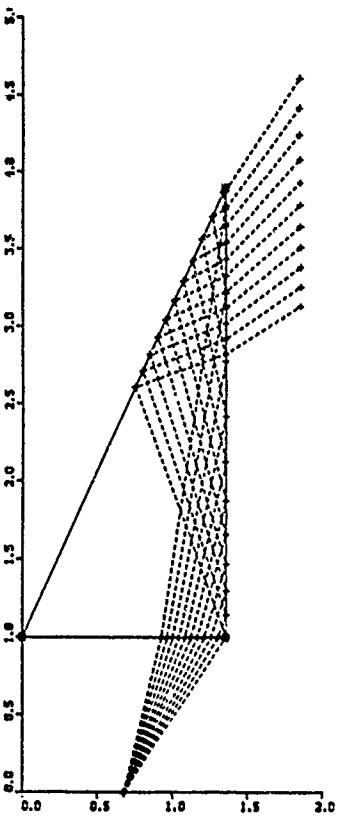


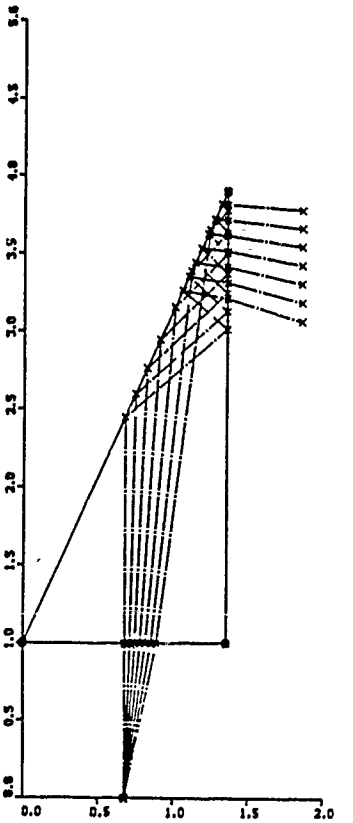
FIGURE 3. GROUND PLANE ANTENNA INSTALLATION



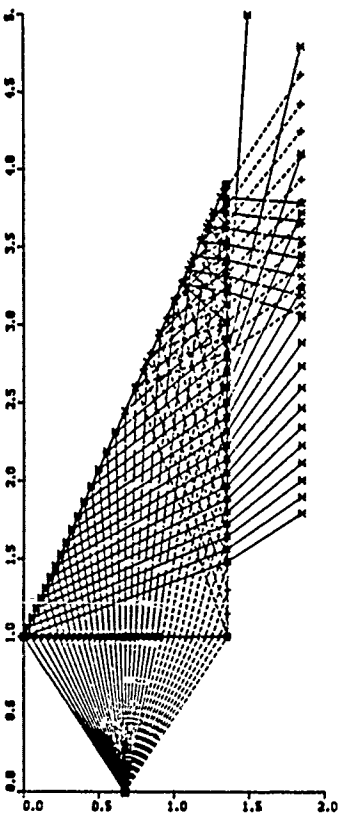
4A



4B



4C



4D

FIGURE 4. RAY DIAGRAMS

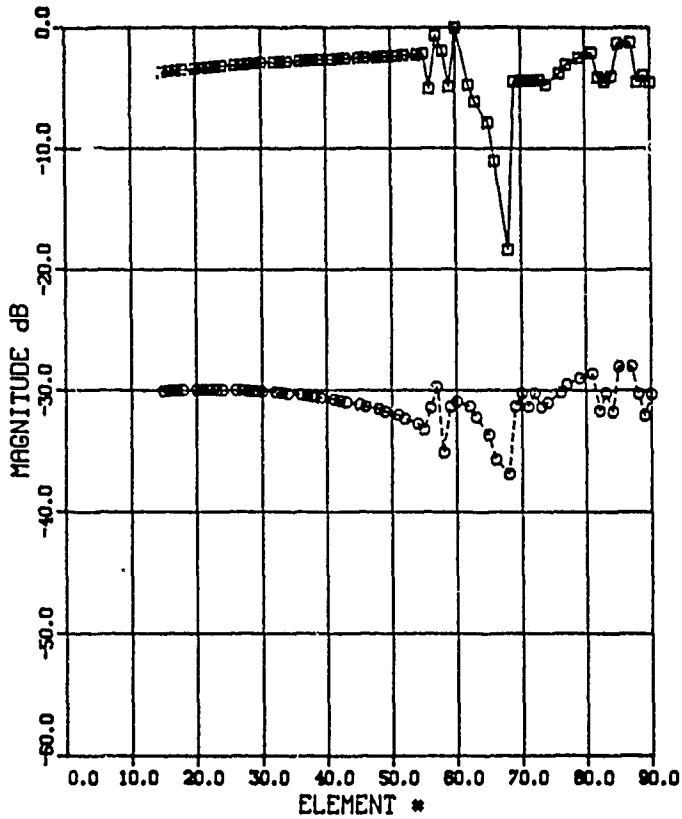


FIGURE 5A

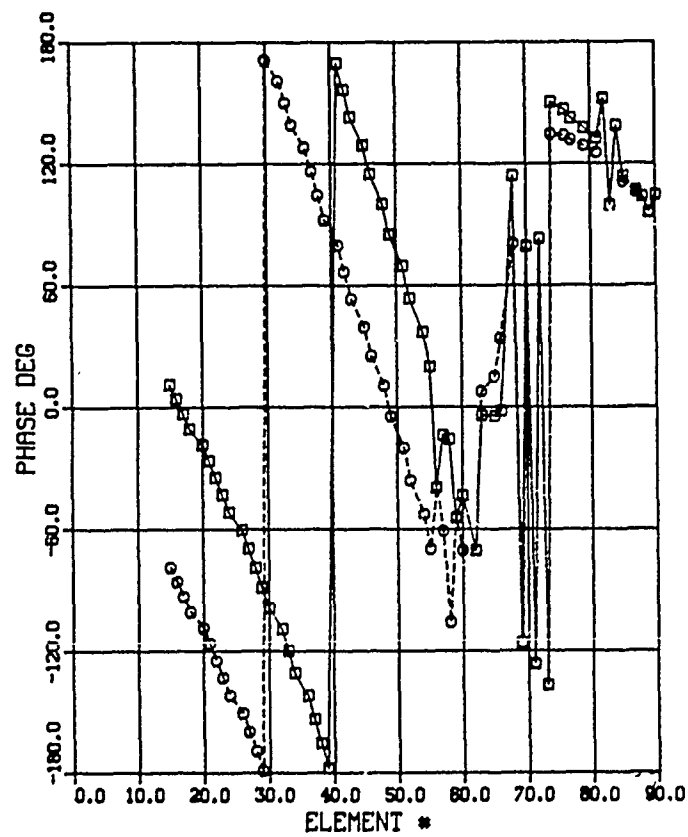


FIGURE 5B

FREQUENCY (GHZ)- 6.0
EPSILON - 2.54
REFLECTOR ANGLE (DEG)- 25.0
FEED TILT ANGLE (DEG)- 0.0
SOURCE LOCATION (IN)- 1.03

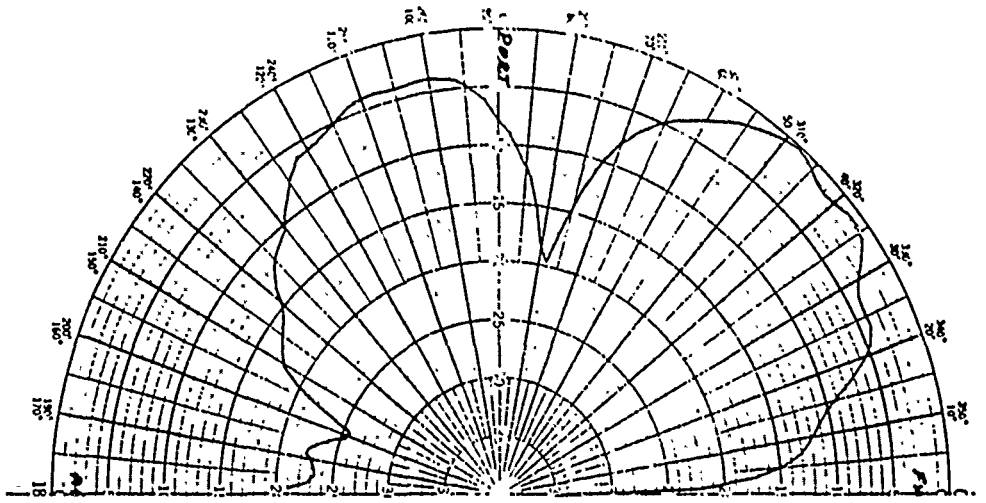


FIGURE 6A

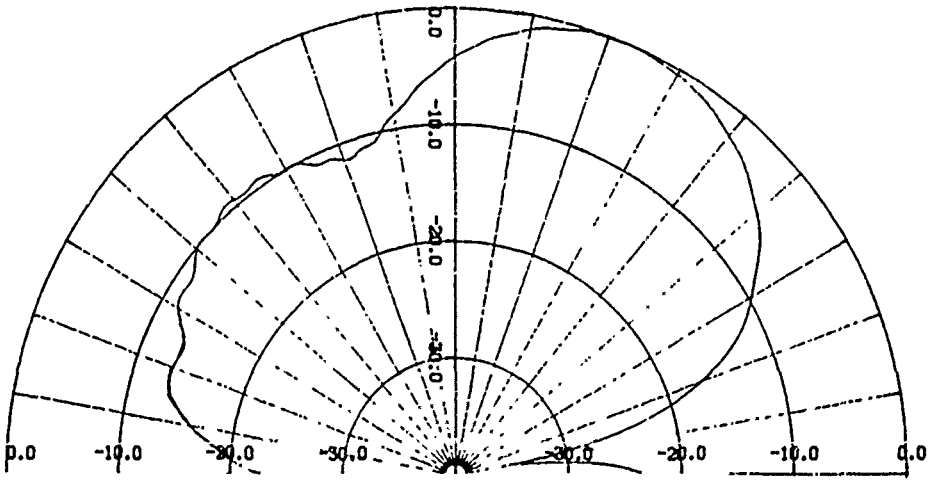


FIGURE 6B

FREQUENCY (GHZ)= 7.0
EPSILON = 2.54
REFLECTOR ANGLE (DEG)= 25.0
FEED TILT ANGLE (DEG)= 0.0
SOURCE LOCATION (IN)= 1.01

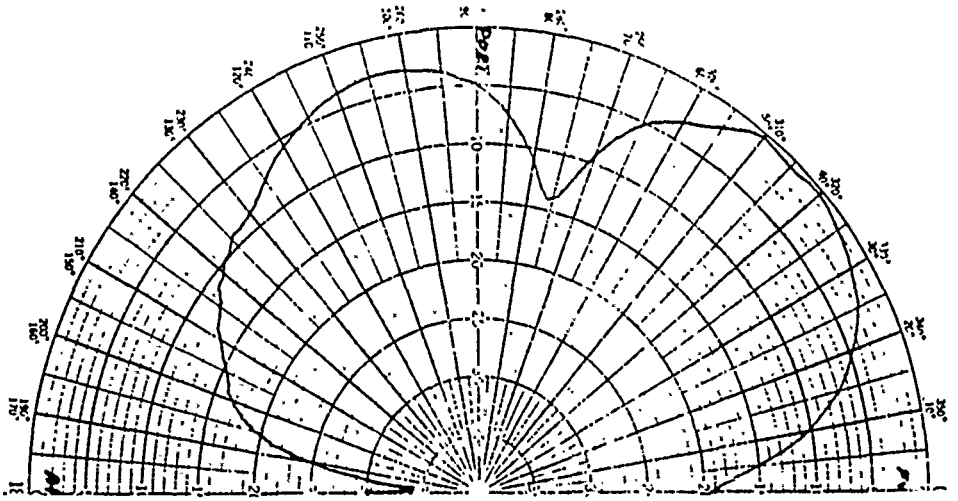


FIGURE 7A

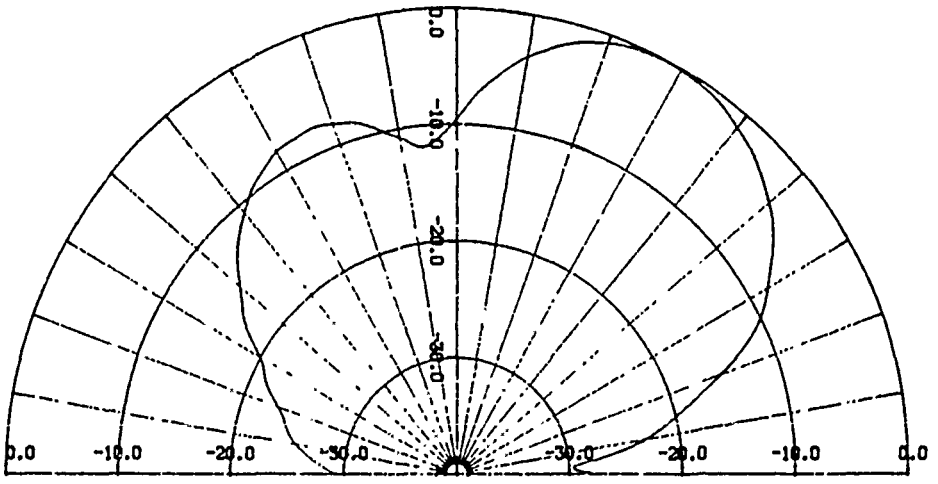


FIGURE 7B

FREQUENCY (GHZ)- 9.0
EPSILON - 2.54
REFLECTOR ANGLE (DEG)- 25.0
FEED TILT ANGLE (DEG)- 0.0
SOURCE LOCATION (IN)- 0.97

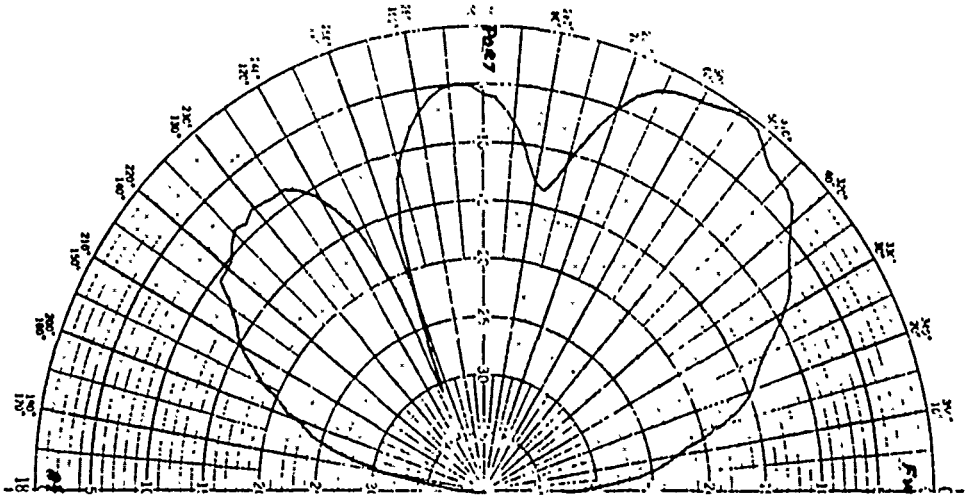


FIGURE 8A

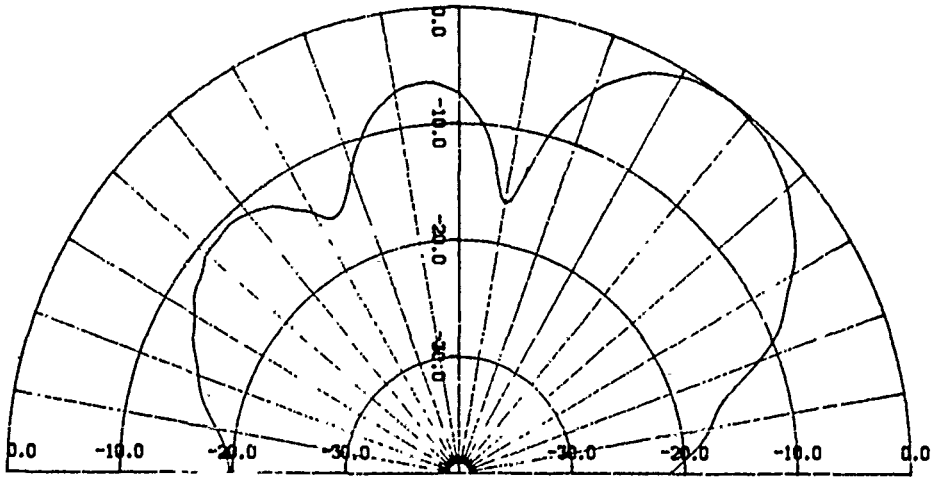


FIGURE 8B

FREQUENCY (GHZ)= 12.0
EPSILON = 2.54
REFLECTOR ANGLE (DEG)= 25.0
FEED TILT ANGLE (DEG)= 0.0
SOURCE LOCATION (IN)= 0.91

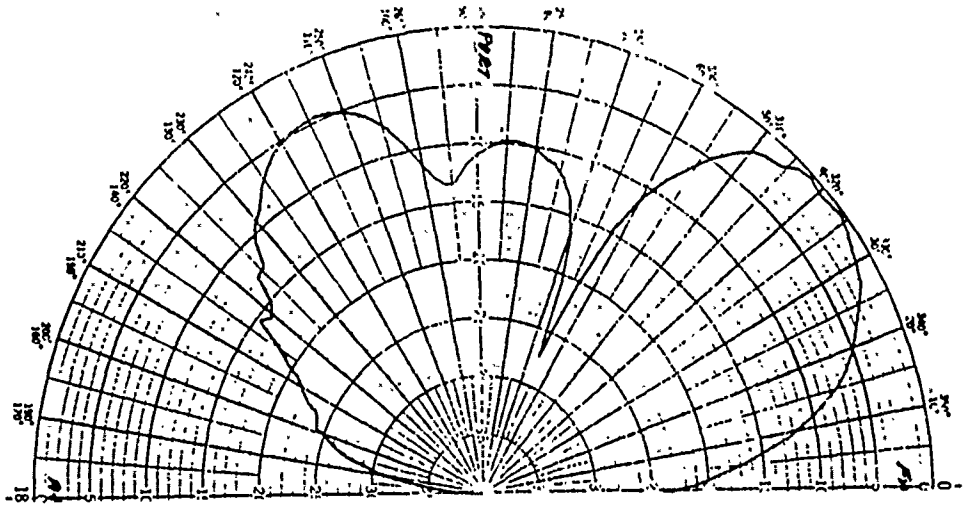


FIGURE 9A

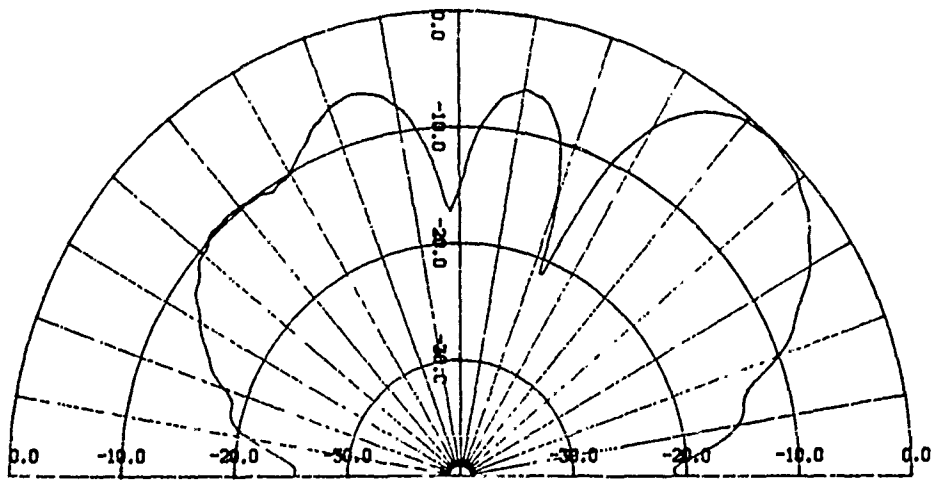


FIGURE 9B

FREQUENCY (GHZ)- 14.0
EPSILON - 2.54
REFLECTOR ANGLE (DEG)- 25.0
FEED TILT ANGLE (DEG)- 0.0
SOURCE LOCATION (IN)- 0.87

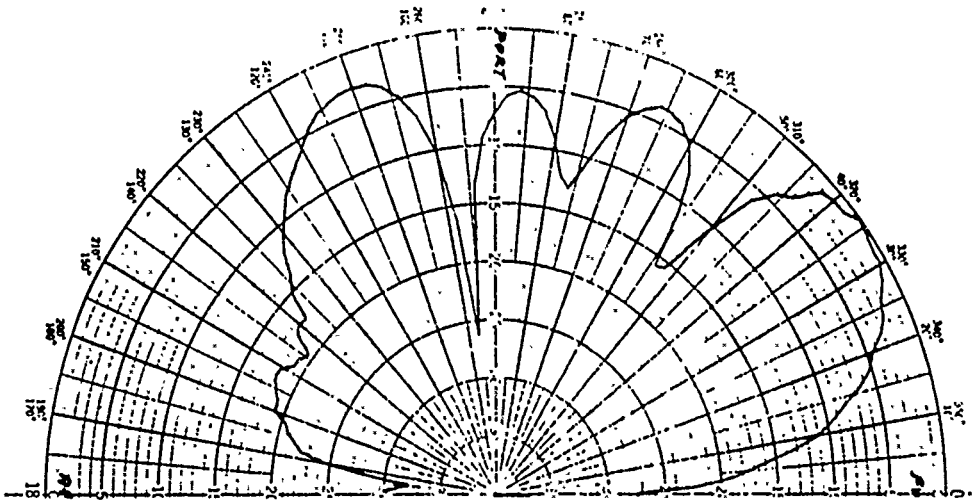


FIGURE 10A

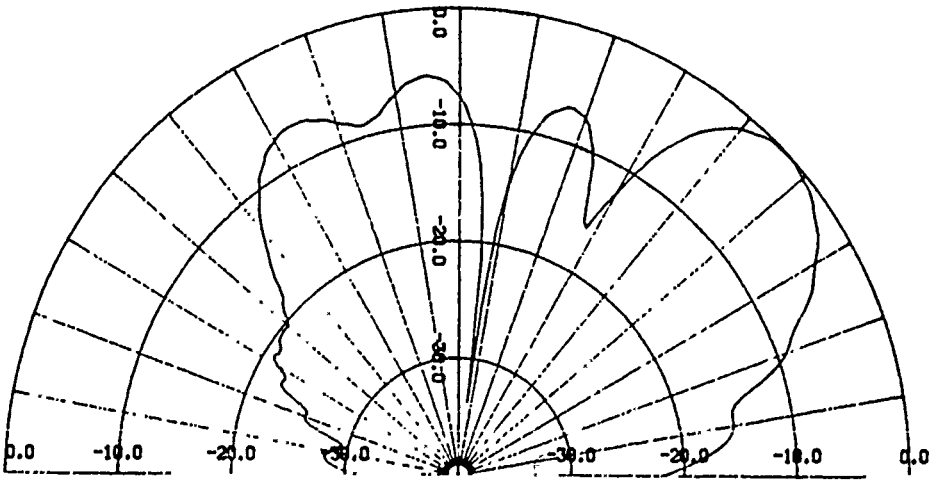


FIGURE 10B

FREQUENCY (GHZ)= 16.5
EPSILON = 2.54
REFLECTOR ANGLE (DEG)= 25.0
FEED TILT ANGLE (DEG)= 0.0
SOURCE LOCATION (IN)= 0.81

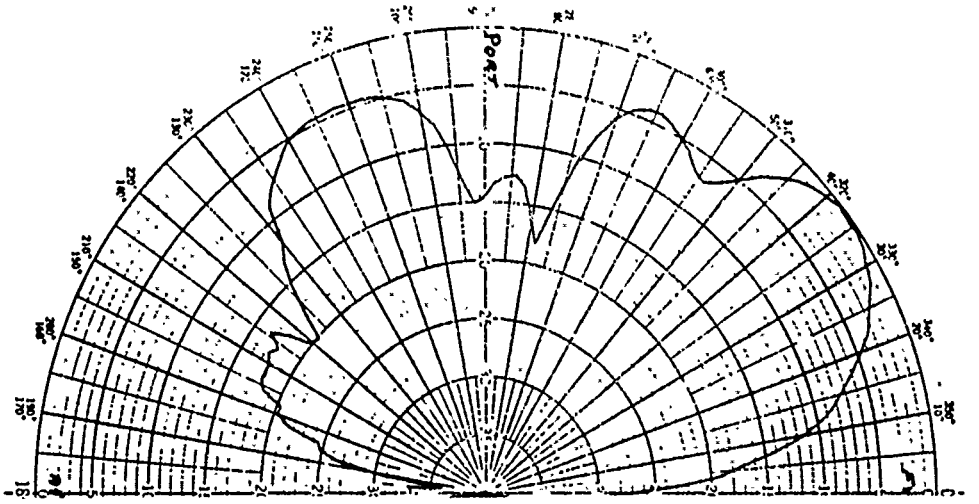


FIGURE 11A

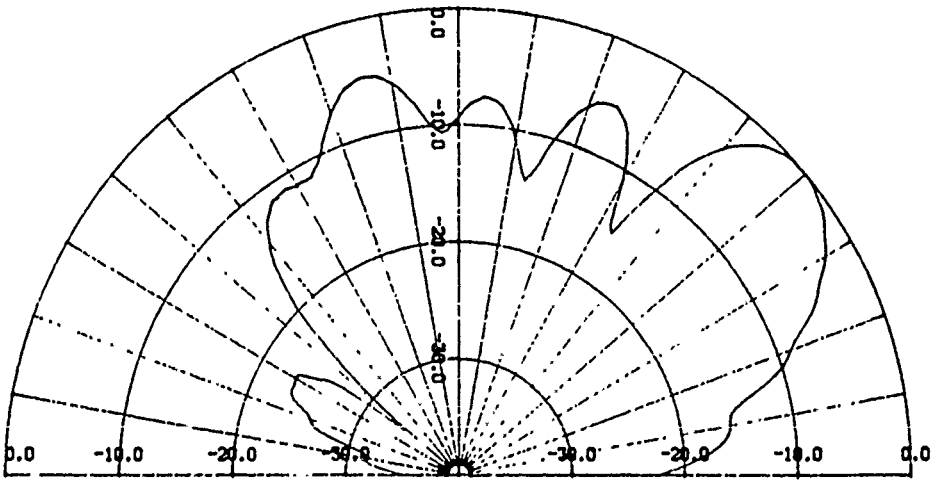


FIGURE 11B

FREQUENCY (GHZ)= 17.5
EPSILON = 2.54
REFLECTOR ANGLE (DEG)= 25.0
FEED TILT ANGLE (DEG)= 0.0
SOURCE LOCATION (IN)= 0.79

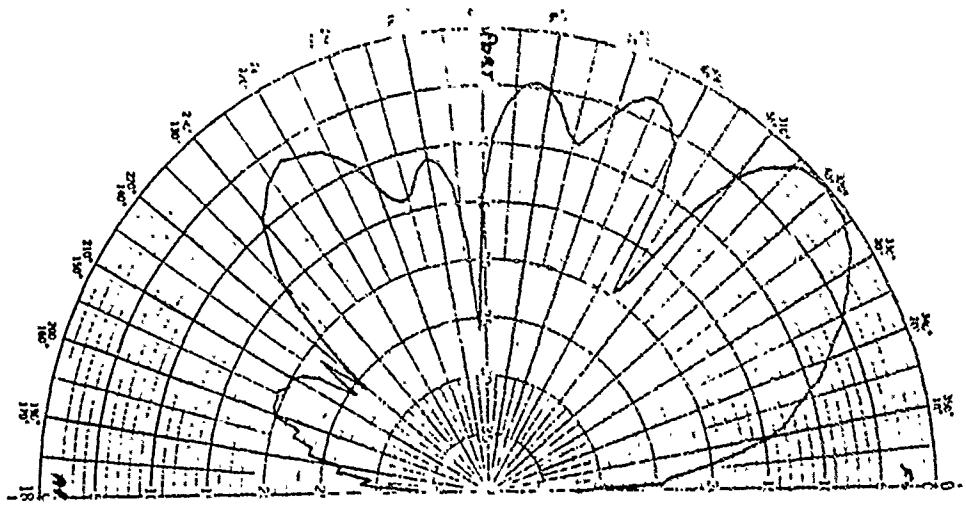


FIGURE 12A

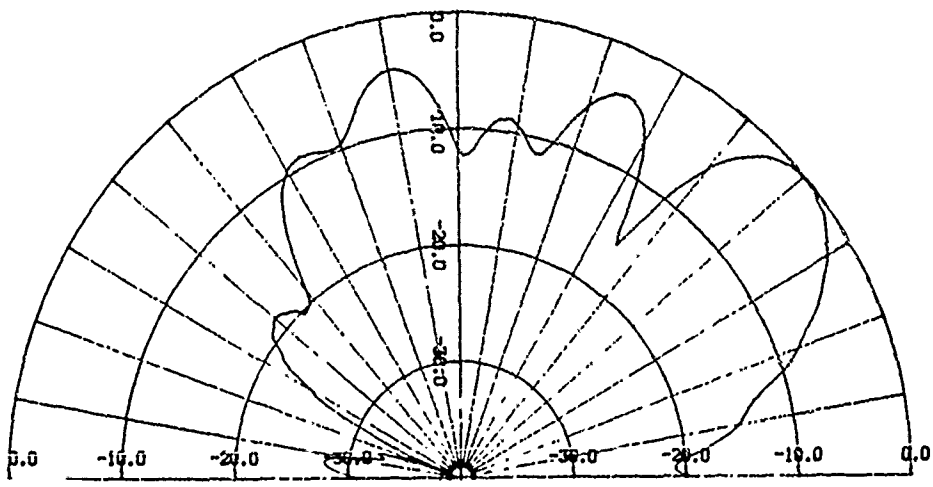


FIGURE 12B

ANALYTICAL CORRELATION OF NEC-3 IMPEDANCE AND PATTERN RESULTS FOR TWO "SIMPLE" ANTENNAS

R.M. Marion
Science Applications International Corporation
P.O. Box 371
Stow, MA 01775

Introduction

In order to determine the utility of NEC-3 in performing pattern analysis and impedance calculations for complicated structures, a series of verification runs were made. Simple structures were chosen for which theoretical treatments were readily available.

A quarter-wave monopole on a circular ground was the first model selected. Both radial wire and surface patch ground planes were used. The computed radiation patterns were compared to those predicted by the geometric theory of diffraction (GTD).

As a second test, a circular loop dipole was modeled in free space and next to a planar reflector. The Fourier expansion of the current distribution was used to test NEC-computed impedance and directive gain values.

All structure dimensions are given in units of the wavelength unless otherwise noted.

Monopole on a circular ground plane

The antenna was modeled in NEC-3 as a 1/4 wave vertical wire along the z-axis. The ground screen had 6 equally spaced radial wires with a segmentation density of 10 per wavelength. As a surface patch model for the ground plane, a box-like structure was used, one wavelength on a side and 1/8 wavelength thick.

An effort was made to model the same antenna as was being evaluated in theory, the only discrepancy evident is the manner of the antenna excitation: NEC-3 excitations are the usual voltage excitations; in the theoretical result, excitation is a point source at the base of the antenna.

When this antenna was first modeled, the radius (R) of the ground screen was varied from 0.5 up to 1.0. It was at this point that a seemingly anomalous situation presented itself. When the radius of the ground screen was less than about 0.8, the pattern produced was very close the that which was expected. There was a single lobe in the pattern with a single null directly over the antenna. Above this ground screen radius, however, a second null was observed in the pattern at

roughly 35 degrees from the vertical. This result is shown in figures 1 and 2a.

A theoretical result was presented by Tai[1] using the geometric theory of diffraction (GTD). When this theory is evaluated, the off-vertical null evident in the NEC pattern does not appear at the 1.0 radius (figure 2b). However, when the radius in the theory is increased to 1.5 (figure 3), an off-vertical null in the pattern is observed, almost precisely where NEC-3 predicts.

NEC-3 does not, however, predict the degree of asymmetry shown by the theory. The GTD shows a very pronounced diffraction pattern when the ground screen radius is roughly 2 (figure 4), NEC-3 does not begin to show this effect until the radius reaches around 3 (Figure 5).

When the NEC-3 surface patch model is used (figure 6), no diffractive effects are observed. The field magnitudes are comparable to those obtained for the radial wire ground screen, but the pattern exhibits none of the structure found in the radial wire NEC-3 model or in the theory.

Circular Loop Dipole

The loop thickness parameter:

$$\Omega = 2\ln(2\pi b/a)$$

where b is the loop radius and a is the wire radius, for all cases studied was equal to 10. Drive point impedance was studied as a function of the ratio of loop circumference to the wavelength:

$$\beta b = 2\pi b/\lambda \ .$$

In the NEC-3 model, this product was varied by sweeping the frequency from 10 to 130 MHz, keeping the loop radius constant.

The theoretical analysis referred to was summarized by Smith[2]. A more viggrous treatment of the subject may be found in King and Harrison[3]. The method used was a Fourier expansion of the current around the loop, from which drive point impedances and directivities were calculated.

The theoretical and NEC-3 results of the free space loop are given in figures 7 and 8. It can be seen that an excellent correspondence exists between the two methods. Even the magnitudes of the reactance and resistance values are nearly equal for the entire range of frequencies studied.

Finally, a reflective structure was added to the free space loop. In the theoretical case, an infinite reflector was used. The NEC-3 model used a finite square wire grid reflector with an edge dimension of 1.

Figures 9-11 contain plots of the data obtained from NEC-3 and theory. One finds that with the addition of the reflector, the quantitative agreement found in the free space model is no longer present. There is, however, an excellent qualitative correlation between the two sets of data.

Conclusions

For the case of the monopole on a circular ground screen the field patterns predicted by NEC-3 give an excellent representation of those obtained through the theoretical calculation. Quantitative discrepancies between the two may be attributed to any number of sources. The theoretical structure uses a solid circular disc as a ground plane whereas NEC-3 uses the radial wire approximation. The difference in the magnitude of the diffraction effects (particularly for $R < 2$), could be due to the fact that theory predicts diffraction from a continuous edge. Furthermore, the theoretical approach used as a reference is in itself an approximation.

Any comparison of the square surface patch model ground screen with the result for a circular ground is arguably a tenuous one. However, one would expect qualitatively similar behavior if the model were a valid one. This failure to correlate with the other methods could point to the surface patch model's inability to handle edge effects.

A most remarkable correlation is found for the free space loop, but the method used necessitates a relatively long computer run. As the structure becomes more complicated, the computational overhead grows quickly. It seems that obtaining impedance trend data except over narrow frequencies could, depending on the computer used, be very time consuming and expensive.

The utility of multiple runs to obtain impedance values is also called into doubt by the results obtained when the reflector is added. However, the NEC-3 calculation does give a good idea as to trends in the data. The time for each computation was decreased greatly by using the numerical Green's function, since here only one frequency was examined. With the Green's function, NEC appears to be quite useful for examining impedance changes with variations in an antenna structure or surroundings.

Overall, this work seems to point to the fact that while NEC appears to be excellent for showing gross features of field patterns or impedances, it should be used with caution (as should any approximate method) when system absolutes are in question.

References

1 C.T. Tai, "Dipoles and Monopoles," *Antenna Engineering Handbook*, R.C. Johnson and H. Jasik ed., McGraw-Hill, New York, 1984, ch4, pp26-32

2 G.S. Smith, "Loop Antennas," *Antenna Engineering Handbook*, R.C. Johnson and H. Jasik ed., McGraw-Hill, New York, 1984, ch5, pp9-16

3 R.W.P. King and C.W. Harrison Jr., *Antennas and Waves: A Modern Approach*, The M.I.T. Press, Cambridge, MA, 1969, ch. 9

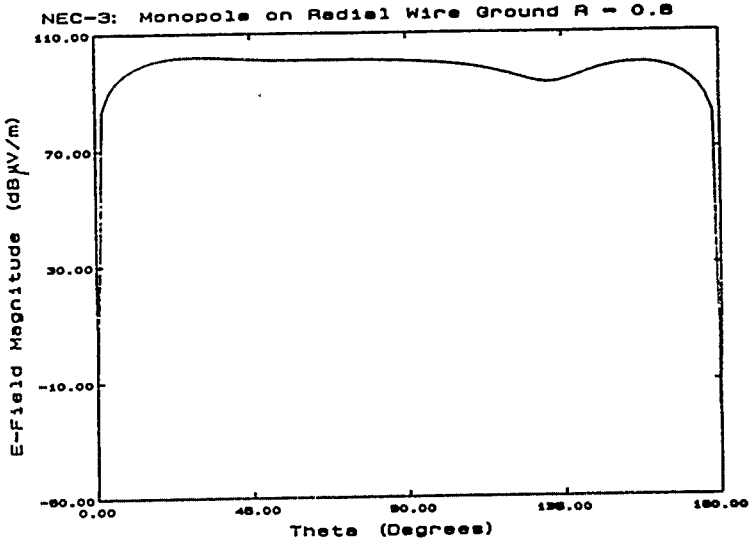
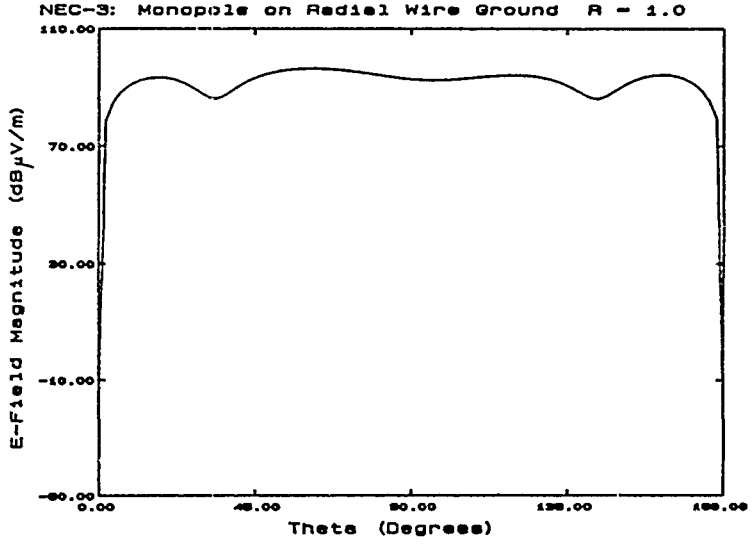
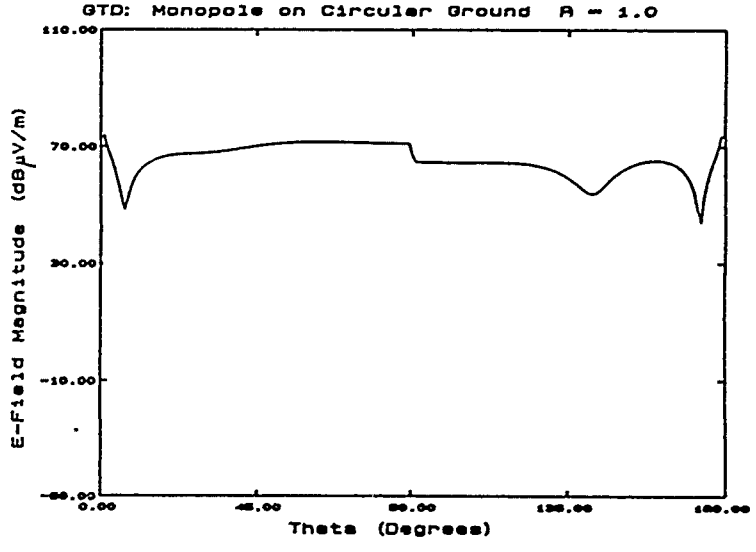


Figure 1

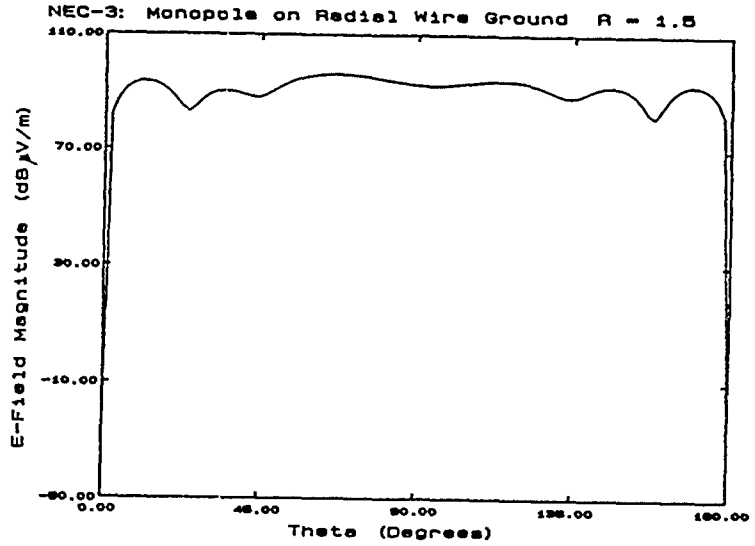


(a)

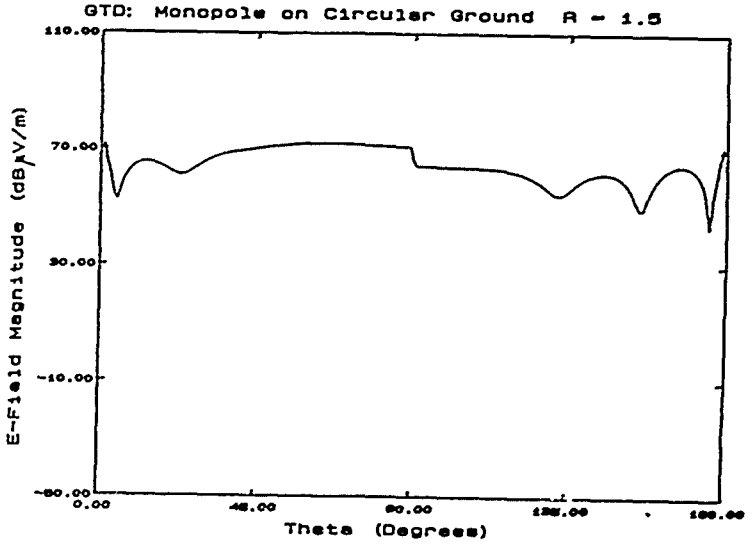


(b)

Figure 2

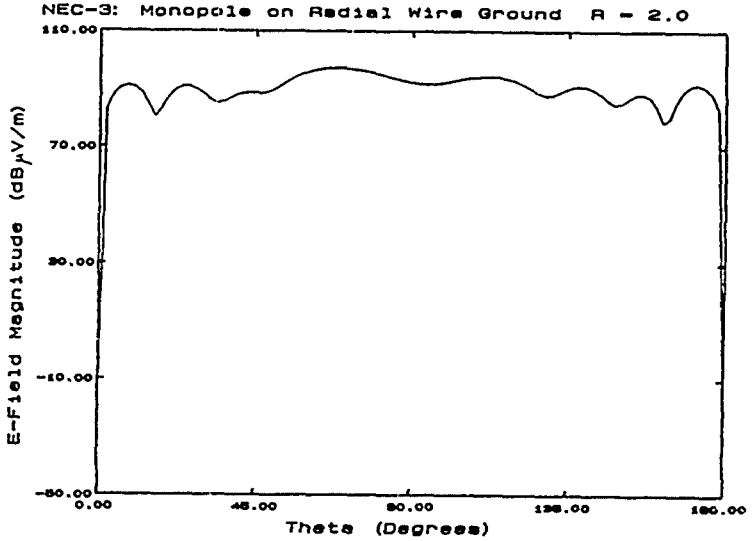


(a)

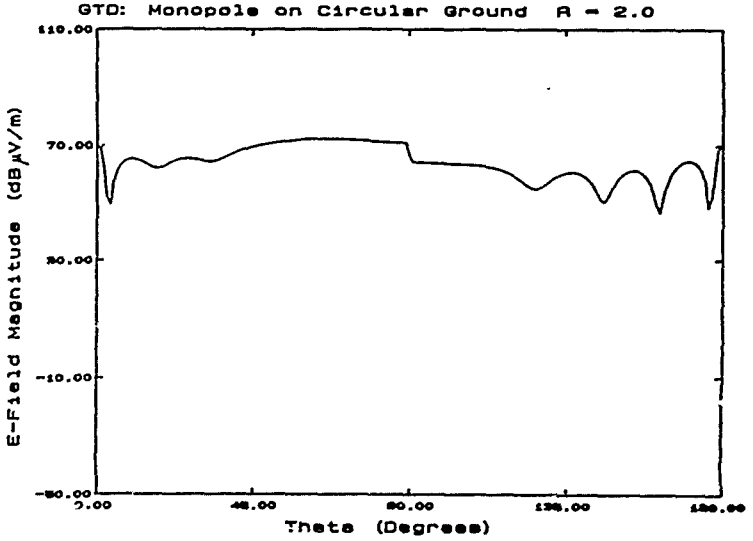


(b)

Figure 3

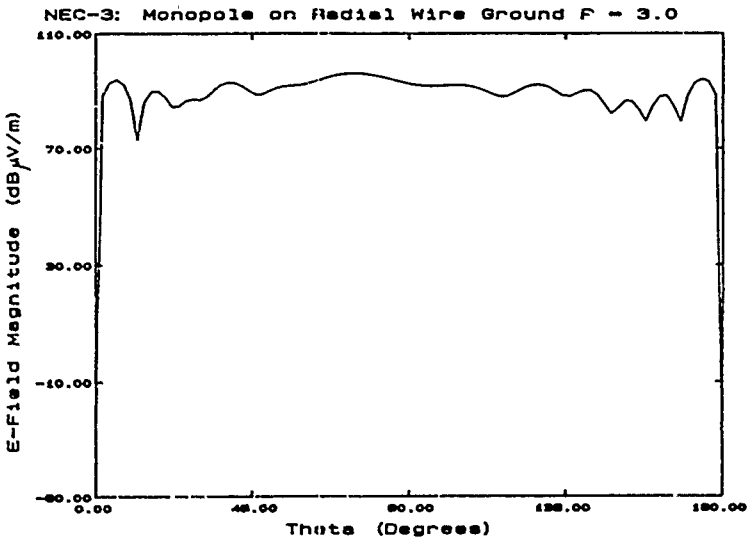


(a)

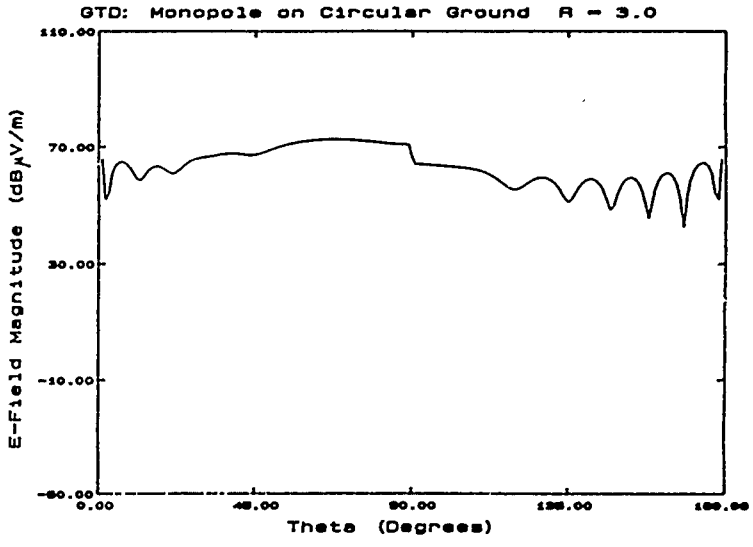


(b)

Figure 4



(a)



(b)

Figure 5

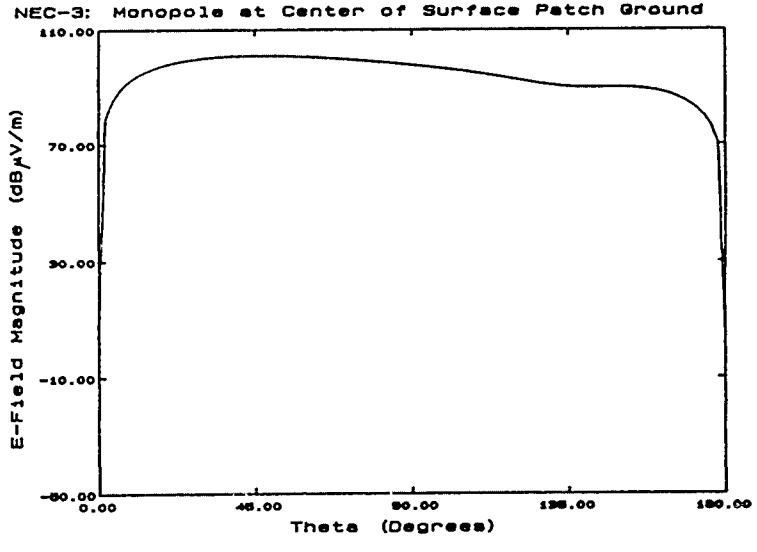
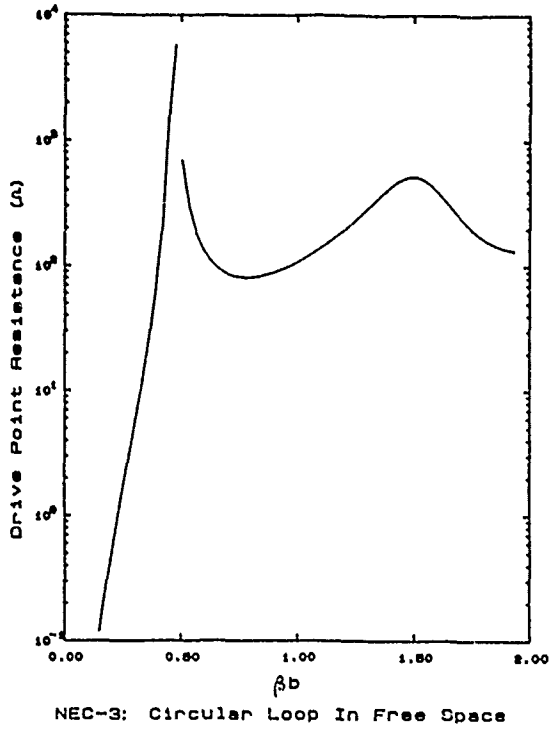
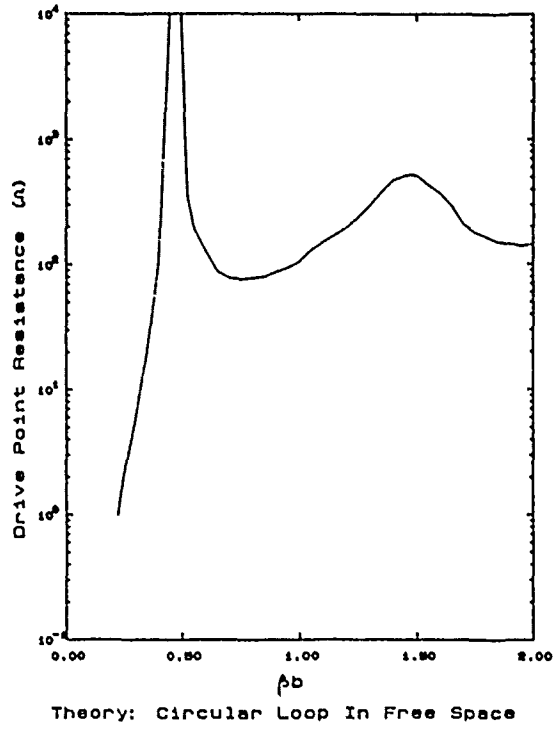


Figure 6

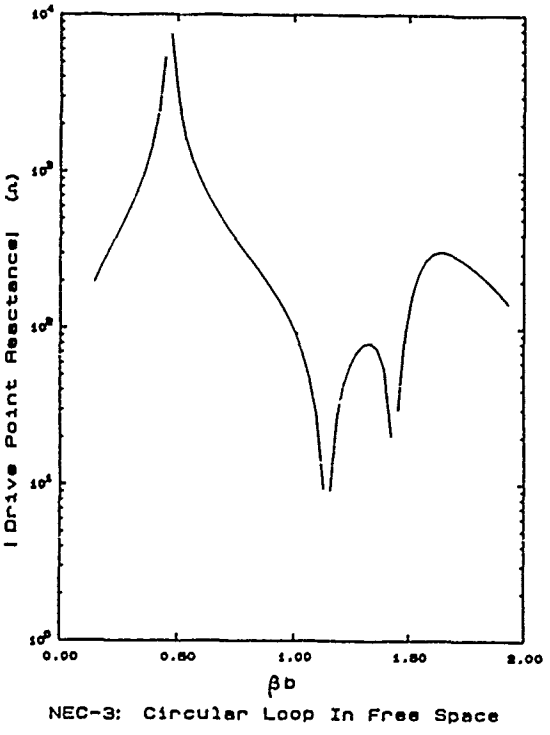


(a)

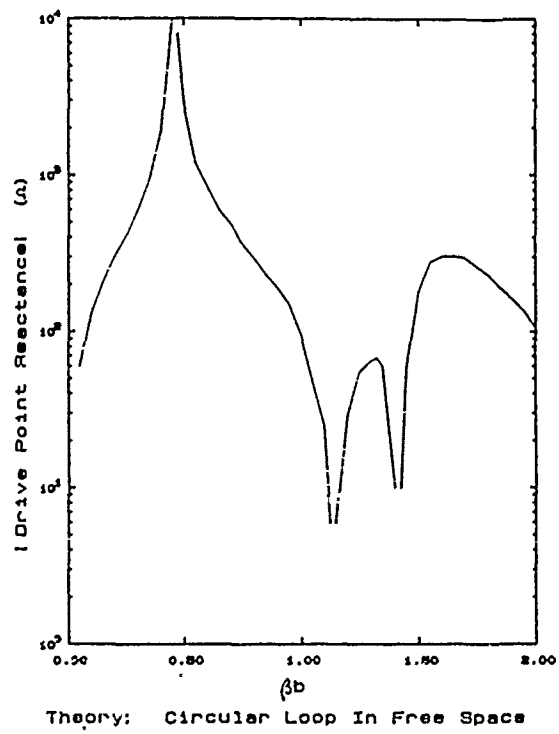


(b)

Figure 7

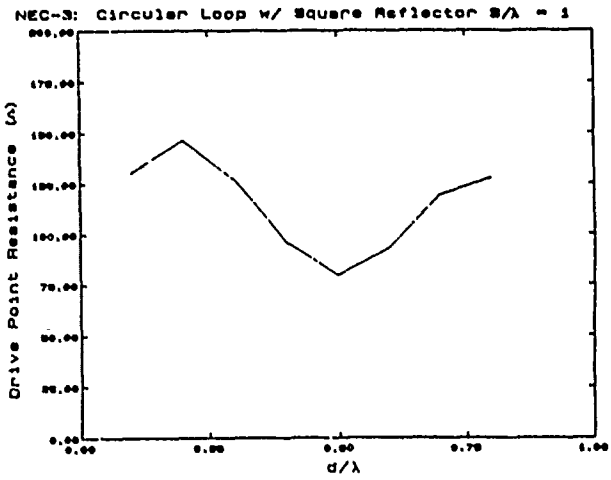


(a)

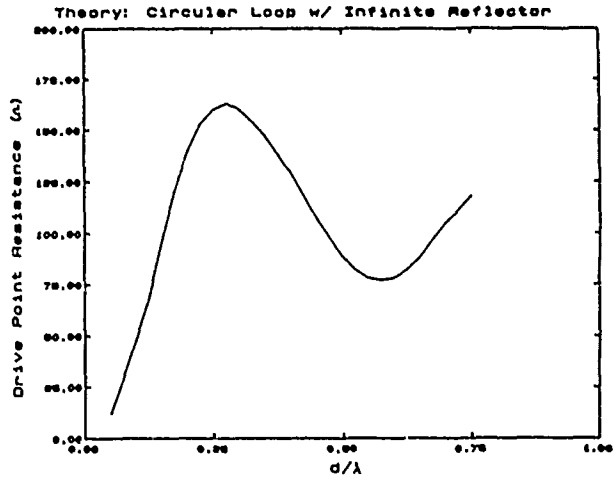


(b)

Figure 8

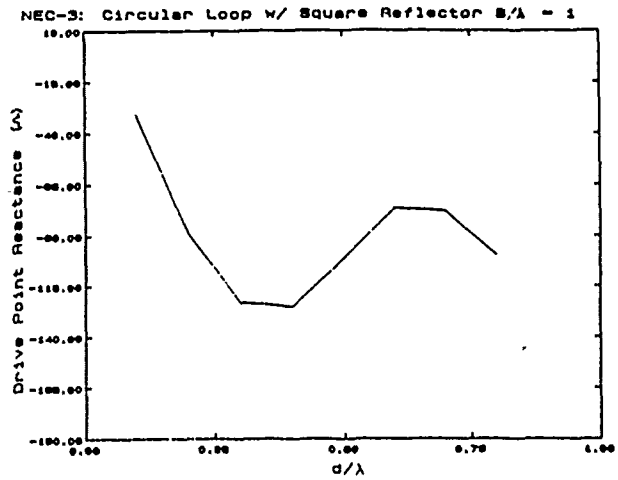


(a)

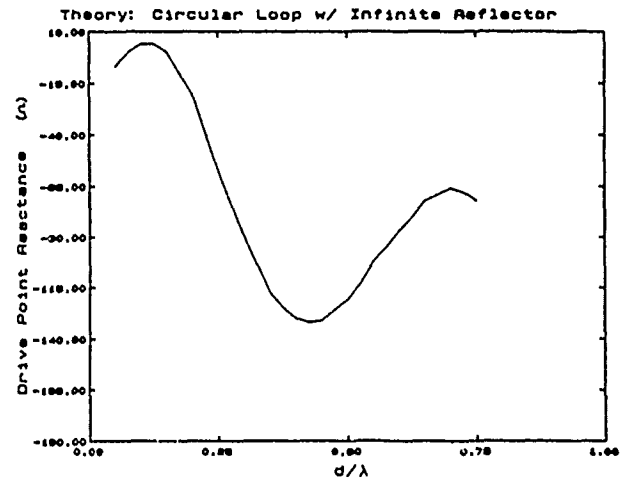


(b)

Figure 9

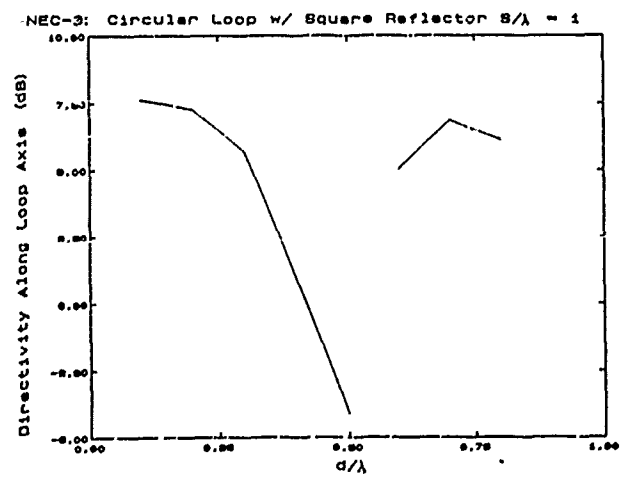


(a)

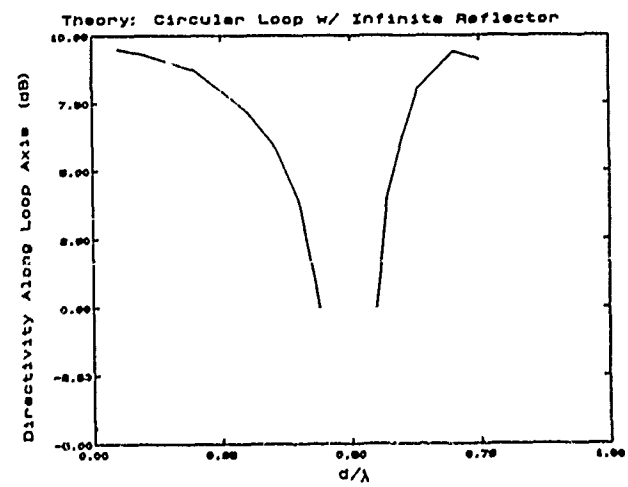


(b)

Figure 10



(a)



(b)

Figure 11

COMPARISON OF PATTERN MEASUREMENTS AND CALCULATIONS FOR A VHF DIPOLE ON THE EMPENNAGE OF AN AIRCRAFT

C. H. Vandament and S. K. Buchmeyer
Advanced Technology Engineering Department
Rockwell International, Dallas, Texas

The purpose of this paper is to illustrate a case history of the operational use of computational electromagnetics. A common class of problems is to determine the radiation properties of antennas on a vehicle such as a ship or an aircraft. The two most generally available and accepted tools for this job are the NEC method-of-moments (NEC-MOM),[1] code and the NEC Basic-Scattering-Code (NEC-BSC),[2].

One chooses an analysis code based primarily on the size of the vehicle relative to the wavelength. If the maximum dimensions of the vehicle are less than a few wavelengths at the radio frequency of interest, then the method-of-moments code is used. If the vehicle is very large in terms of wavelengths, the basic scattering code is used. However, at in-between frequencies, neither code is attractive. Using the method-of-moments code requires a large number of wire-segments to create the skeletal model of the vehicle and thus becomes very expensive to run in project dollars, calendar time, or both. It is possible to create the vehicle model without disobeying the established guidelines for convergence and the accuracy of the results would probably be acceptable. Using the basic scattering code forces one to break or bend the modeling guidelines on that code. The results may be acceptable, but some sort of independent.check is necessary.

This case study is within the in-between region of the two codes as described above. It is necessary to place a 67.5 MHz dipole on the tail of a moderately large four-engine aircraft. It is to be a side-looking antenna having a wide azimuthal beam pointed generally broadside, and the vertical beam of interest is from five-degrees above the horizon to fifteen degrees below the horizon. However, it is necessary to know the gain within a few dB's accuracy over the whole sphere of radiation. It is also necessary to be able to predict the impedance of the antenna over a ten-percent bandwidth so the design of terminal equipment can proceed. The "gotcha" is that proof-of-performance inflight testing of the real, full scale aircraft will be conducted and discrepancies between predicted and actual performance will be exposed.

Further realities put various costs into perspective. The fixed cost of a flight test is about $10,000, which includes preparation of the aircraft, take-off and landing, and stowage after landing. Flight time costs about $3,000 per hour including crew and fuel. If tests extend over several days then the per diem of the crew must be added on. Hence, one day of flight testing can approach $40,000. It becomes quickly apparent that a cheaper alternative to flight testing is desirable.

The method-of-moments approach is somewhat cheaper. A safely sparse skeletal model of the aircraft would use about 10,000 wire segments. Calculating the patterns over the whole sphere at 10-degree increments would cost about $4,000 per frequency at the lowest priority on our CYBER-990. At least five frequencies would be required. We have no basis for estimating the calendar time for such a run on our "free" Hewlett-Packard 9000. The NEC-BSC would run for less than $1,000 per frequency on the CYBER, but as mentioned earlier, low confidence levels would be attributed to the results because of all the broken and bent rules of the model.

The reasoning above drove us to the old technology of scale model pattern measurement (no offense to vendors of modern pattern range equipment). A full scale mock-up was built for impedance measurement. An accurate 1/15-th scale model of the aircraft was constructed of dense polyurethane foam and flame-sprayed with metallic copper. The pattern range used was an outdoor range. The full swept area of the model was probed for amplitude and phase variations. The gain was calibrated by manual pattern integration.

After the patterns were measured, it was decided that we would use NEC-MOM and NEC-BSC over the area of primary pattern interest for a cross check on the gain and pattern shape in that region. To conserve costs, we ran only one frequency and abbreviated the aircraft model rather severely, such that only one side of the empennage remained. The model is displayed in figure-1 with dimensions as used in the Basic Scattering Code.

The wire model is shown in several views with the dipole in figure-2. The polarization of interest is horizontal, so only horizontal wires were used in the model. The segment currents were visually scanned to make sure there were no anomalies due to the lack of cross connections. The wires of the model were 0.075 wavelengths apart and that was also the approximate length of each segment of those wires. The dipole antenna element was just under a half-wavelength long (2.09 meters long at .02 meters radius). The length to radius (l/a) ratio was about 35:1 for the skeletal model and about 9:1 for the dipole segments. The extended thin wire kernel was not used in the calculations shown here.

The NEC-BSC model was made to the exact dimensions of the NEC-MOM model, with the empennage being defined as two flat plates. The source information, segment currents and phases, and the normalizing value of the input power were taken directly from the NEC-MOM run. The User's Guide for NEC-BSC states that no plate-edge should be less than a wavelength long and that no antenna element should be less than a wavelength from an edge. A parenthetical statement relaxes the wavelength dimension to a quarter-wavelength for "engineering purposes". It can be seen from the dimensions in figure-1 that liberties have been taken with those rules. The size of the aircraft and the antenna are fixed; we must model them as they are and apply a critical eye to the results.

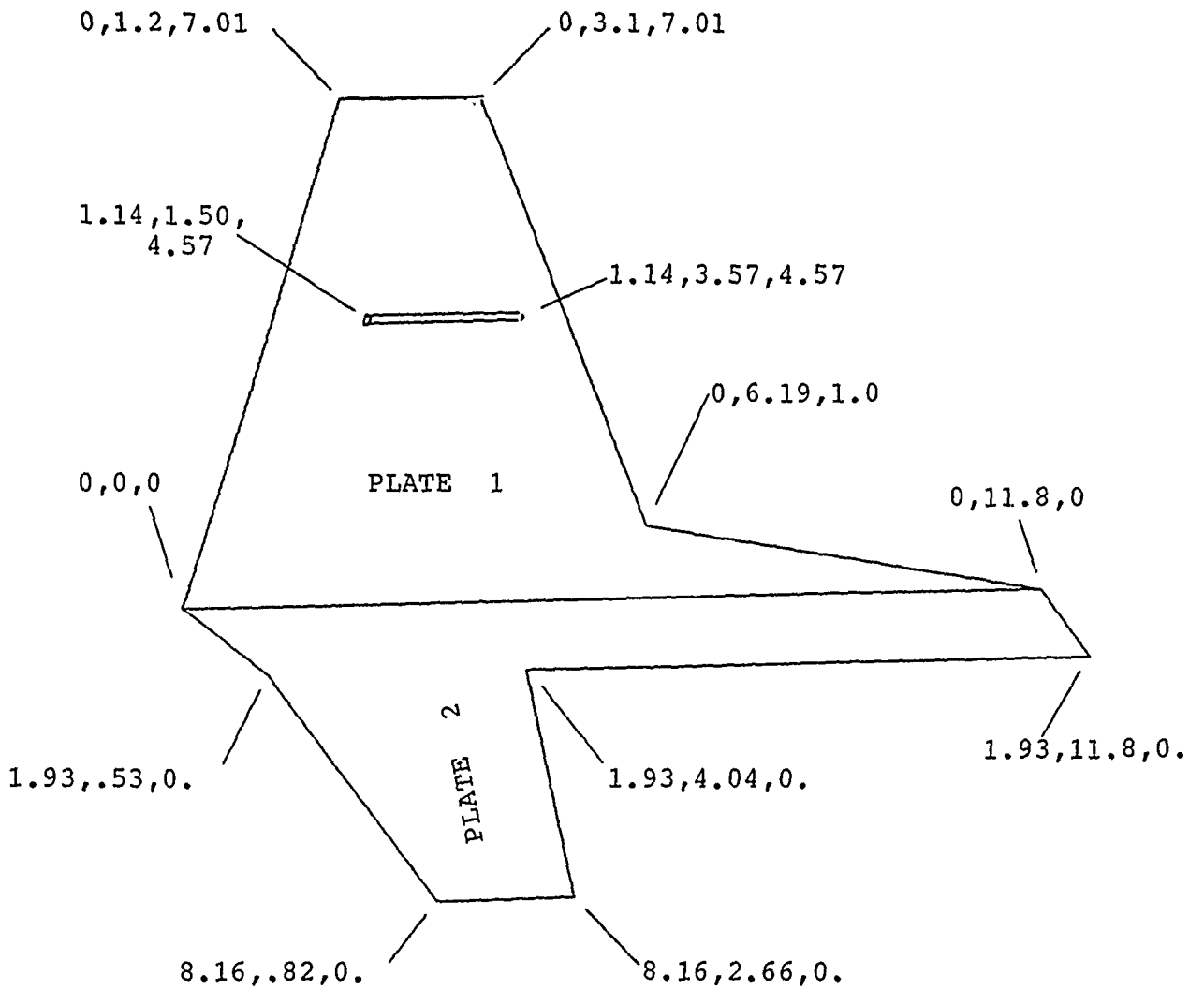


FIGURE 1. NEC-BSC MODEL OF THE EMPENNAGE AND ANTENNA WITH COORDINATES (METERS)

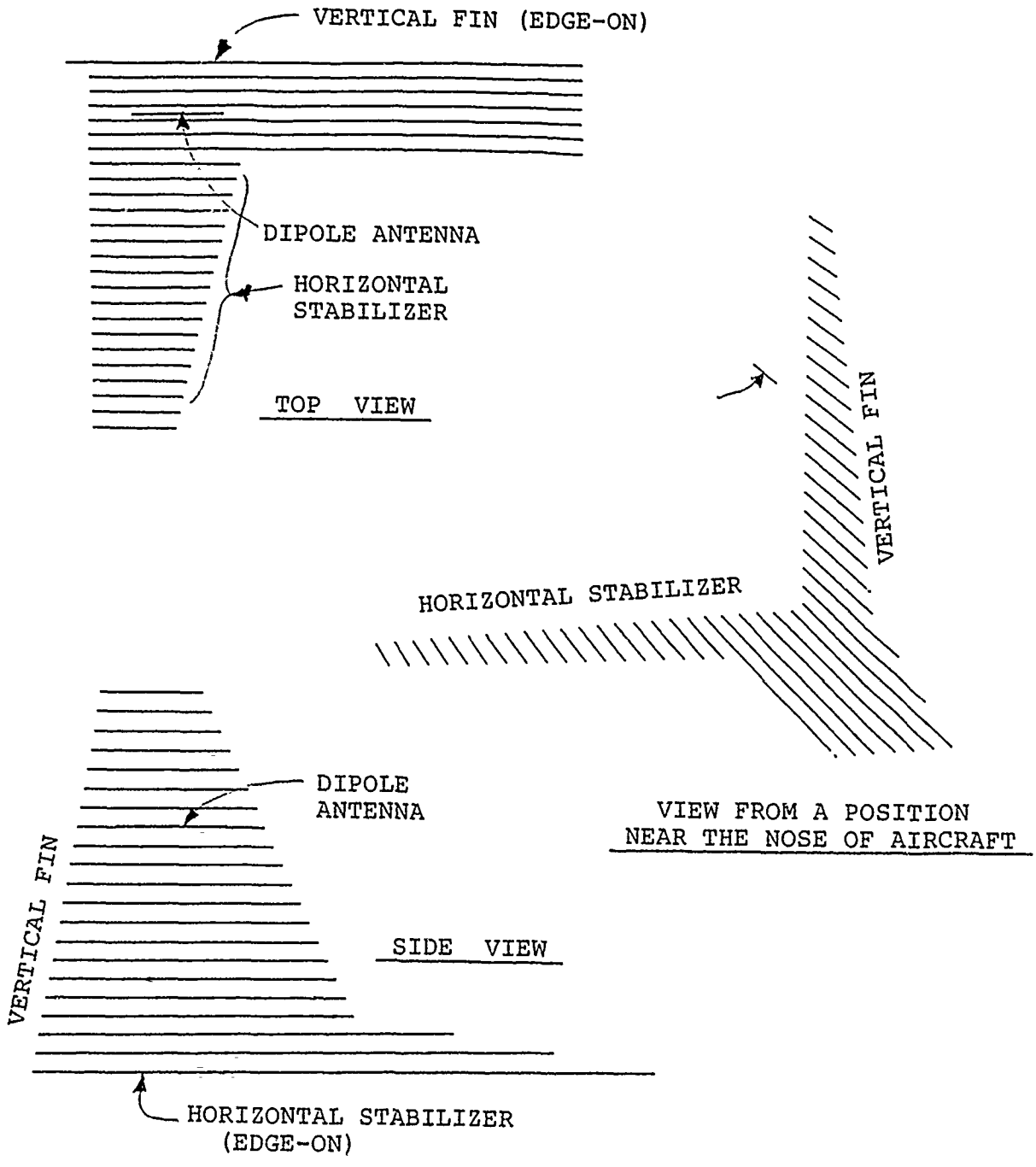


FIGURE 2. WIRE SKELETAL MODEL OF EMPENNAGE USED IN NEC-MOM PROGRAM.

The pattern results are shown in figures 3 thru 5. The differences between the measured, NEC-MOM and NEC-BSC patterns are acceptably small over the narrow bounds of the region of primary interest. The MOM results seem to provide the best fit to the measured data in the upper-half, or the direct/reflected region of the pattern, while the BSC results are a better fit in the lower, or diffracted region of the pattern. It is significant to the engineering user that the major discrepancies occur in the regions where the radiation is some 20-dB down from the beam-maximum and are therefore of little interest.

It has been gratifying and confidence building to make this limited comparison. If time and budget permit, we might get a run on a more complete NEC-BSC model and compare it to the measured data.

References:

[1] Burke, G.J. and A.J. Poggio, "Numerical Electromagnetics Code (NEC) - Method of Moments", Technical Docoment 116 (User's Guide), Jan 1980, Naval Ocean Systems Center, San Diego, CA 92152.

[2] Marhefka, R.J., and W.D. Burnside, "Numerical Electromagnetic Code - Basic Scattering Code", Technical Report 712242-14 (713742), Dec 1982, Ohio State University Electro Science Laboratory, dist. by Chief of Naval Operations (Op-62), Long Beach, CA 90822.

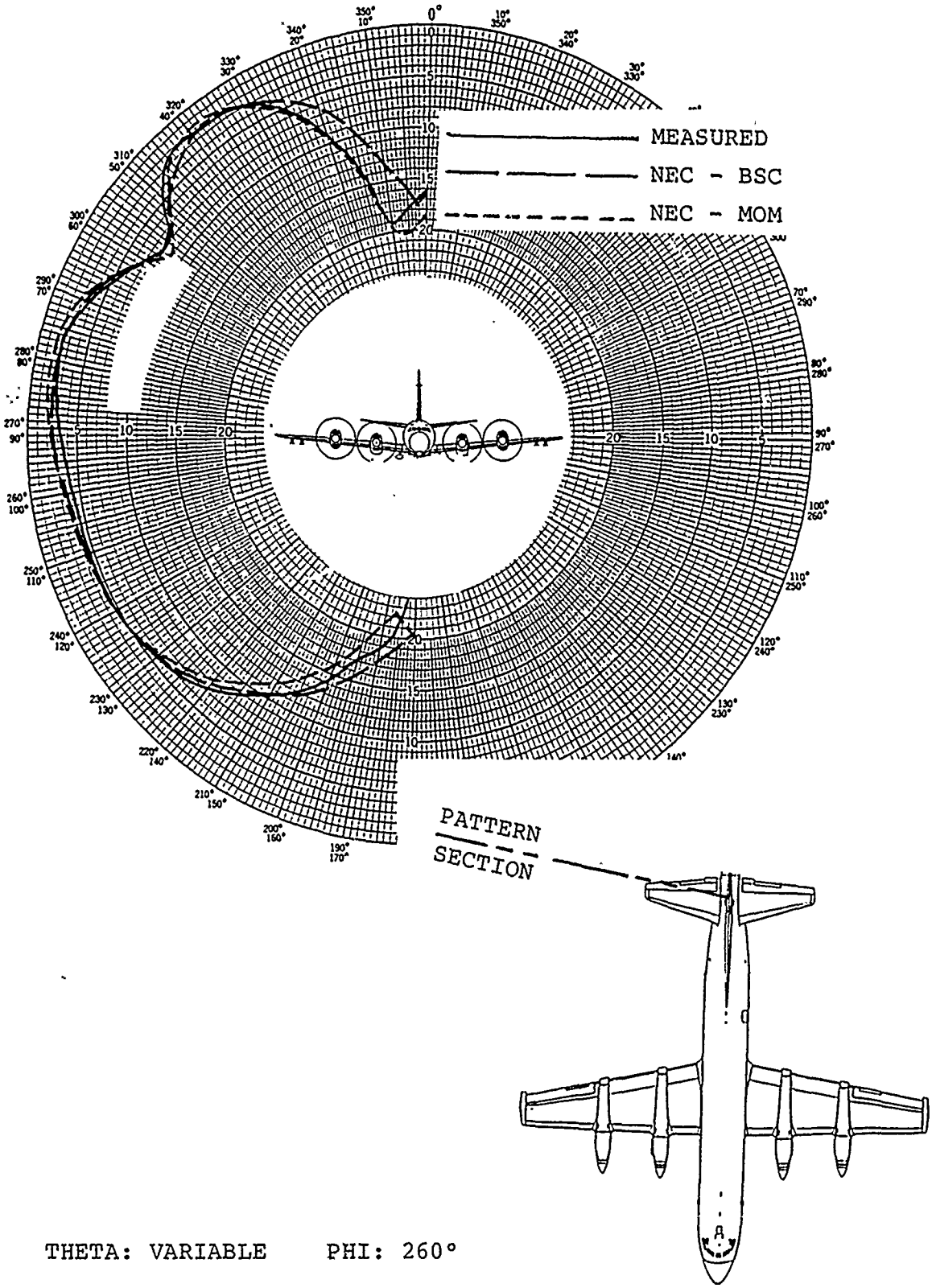


FIGURE 3. MEASURED AND CALCULATED PATTERNS OF A VHF DIPOLE ANTENNA MOUNTED ON THE SIDE OF THE VERTICAL FIN.

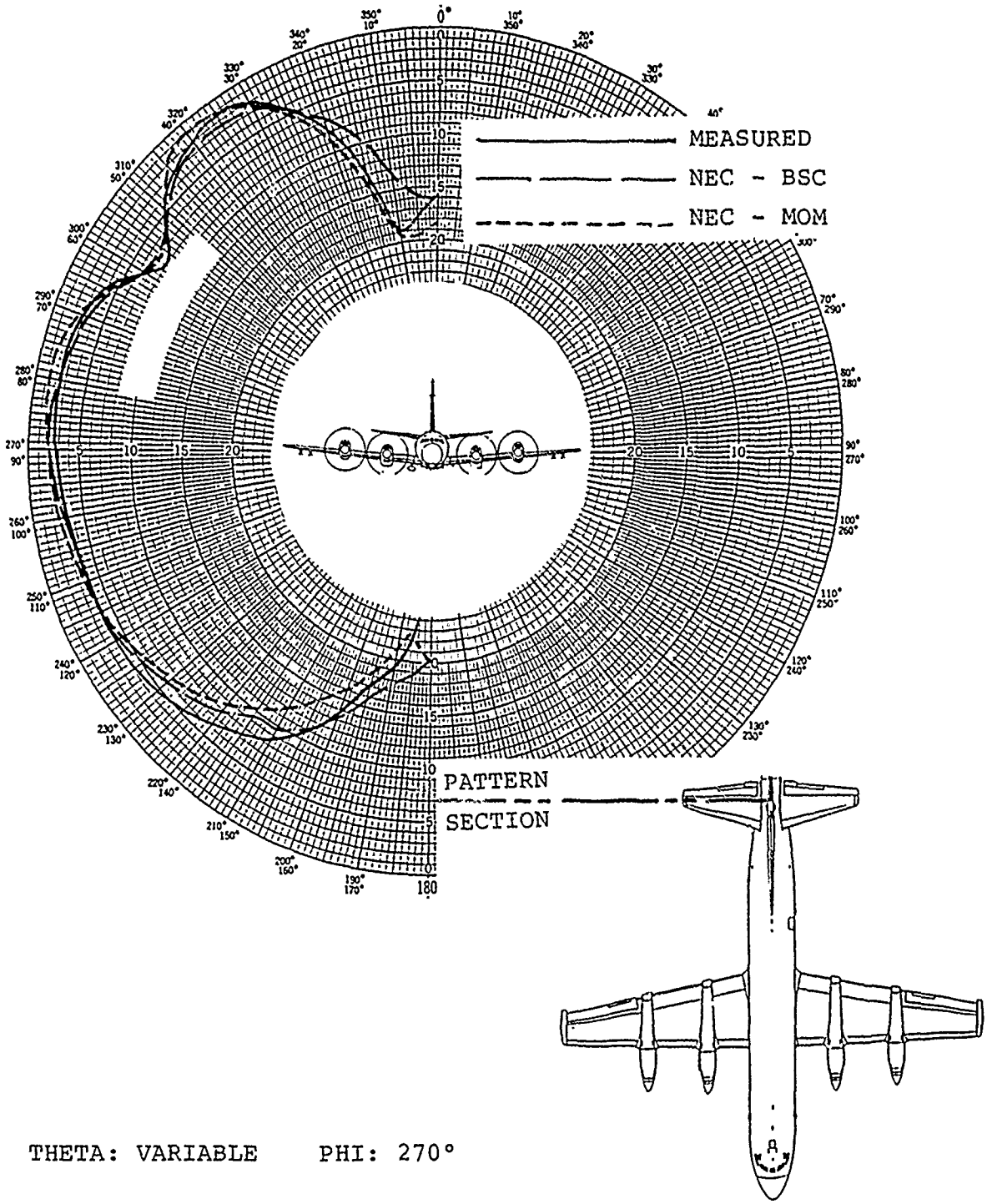


FIGURE 4. MEASURED AND CALCULATED PATTERNS OF A VHF DIPOLE ANTENNA MOUNTED ON THE SIDE OF THE VERTICAL FIN.

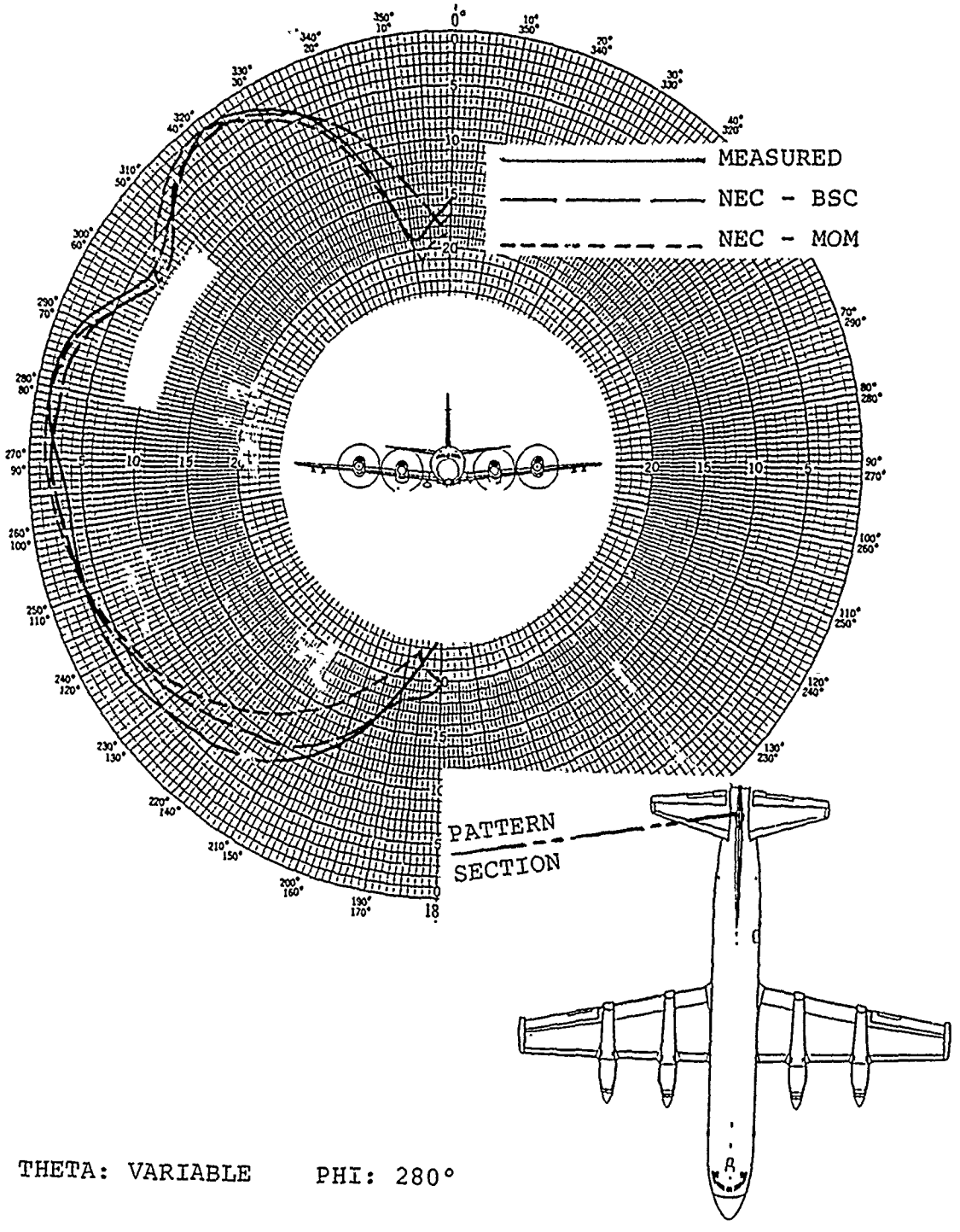


FIGURE 5. MEASURED AND CALCULATED PATTERNS OF A VHF DIPOLE ANTENNA MOUNTED ON THE SIDE OF THE VERTICAL FIN.

A COMPARISON OF THE FIELDS OF A MEDIUM WAVE DIRECTIONAL ANTENNA AS CALCULATED BY THE FCC METHOD AND THE NUMERICAL ELECTROMAGNETIC CODE

James B. Hatfield
Paul W. Leonard

Hatfield & Dawson Consulting Engineers, Inc.
4226 6th Ave. NW
Seattle, WA 98107

ABSTRACT

In the U.S.A. standard AM medium wave broadcast stations frequently use directional antenna arrays of monopoles over radial wire ground screens to meet the allocation and interference criteria of the Federal Communications Commission. The method that is used for calculating the horizontal plane pattern of AM directional antennas for FCC purposes uses far field approximations. The assumptions are also made that the antennas are thin wire radiators with sinusoidal current distributions along their lengths and that the phase of the radiation from each element is the same as that of the current at the current maximum.

A more accurate current distribution (amplitude and phase) for the type of antenna used in AM directional arrays is developed by the NEC III computer program. An accurate depiction of the array near field is also provided by NEC III since both the geometry of the array and the geometry of the observation point in relation the the array is developed in the use of the program. Calculations using NEC III have been made to show the discrepancies between the fields calculated by the traditional FCC method and the fields one would actually expect to find.

INTRODUCTION

In the U.S.A. standard AM medium wave broadcast stations frequently use directional antenna arrays of monopoles over radial wire ground screens to meet the allocation and interference criteria of the Federal Communications Commission. These arrays typically use two to six towers that are most often a quarter wave length in physical height. These towers are

usually in a line or at the vertices of a regular geometrical figure such as a parallelogram. The determination of whether the criteria of the Commission are met is based on the radiation pattern submitted when an application is made for an AM facility using a directional antenna. This pattern is a plot of the unattenuated, inverse distance (1/R), field intensity at one kilometer.

Verification that the installed array has been adjusted so that the actual field pattern is acceptably similar to the pattern shown in the original application is made by taking radial field intensity measurements in various directions from the antenna. These measurements are made in the horizontal plane at ground level, generally in radial directions related to pattern features. Ground level (horizontal plane) measurements are the only practical means of experimental verification of pattern shape. Therefore it is in the horizontal plane where discrepancies in the calculation methodology may be observed.

The expression used for calculating the horizontal plane pattern for FCC purposes (Equation One, Figure One) gives the per unit field at a given azimuth. The per unit pattern is then multiplied by a constant which is determined by the antenna input power and the array parameters. The result is the unattenuated inverse distance field at one kilometer in millivolts per meter. The expression for calculating the field has a term for each element in the array. This term is a polar number whose magnitude is determined by the relative contribution of the element to the field at the observation point. The angle of this polar number is determined by the phase shift of the field from the element at the observation point relative to an arbitrary reference point.

The derivation of the expression used for directional antenna field calculations (See Figure One, Equation One) relies upon far-field assumptions. These assumptions are, (1) that at a great distance from the array the lines drawn from the elements to the observation point are parallel and, (2) that the magnitudes of the field contributions from the various elements at the observation point are not affected by the different distances to the observation point from the various elements. A further assumption made in the use of this expression is that the relative phase at the maximum current point (at the tower base for a 90 degree radiator) in identical radiators is the same as the relative phase of the fields as they leave the towers. Sinusoidal current distribution on all radiators in an array is also assumed for this calculation. These geometric and current

distribution assumptions, implicit in the calculation of fields from AM arrays for FCC purposes, result in inaccurate predictions of fields in the null regions of AM directional antenna patterns. When far-field assumptions are used for AM pattern calculations (Figure One, Equation One) the fact that the shape of the pattern in the null region varies with distance from the array is ignored. The problems associated with the far-field geometry assumptions, called the proximity effect, of the standard FCC calculation of AM patterns are well known (Equation Two, Figure One is used for proximity effect). They have been recently discussed in papers by Ogden Presthold (unpublished) and Frank S. Colligan (page 21, "Radio World", Jan. 15, 1987). The geometric assumptions used in the traditional pattern calculation for near and far fields are illustrated in Figure One.

AM PATTERN ANALYSIS USING NEC

Appendix A of CRC Report No.1379 of the Canadian Department of Communications by G. M. Royer presents pattern calculations on a Canadian AM station using the Numerical Electromagnetic Code. It demonstrates that calculations using more realistic current distributions on the elements of the array result in a far field pattern with a null that is displaced in azimuth from the location of the null shown in the pattern that is calculated by the FCC method (Equation One, Figure One). Figure Two, which is extracted from that report, demonstrates this effect for an actual array.

NEC and traditional FCC type calculations (Equation One, Figure One) have been made on a three tower array with quarter wave spacing and quarter wave height towers located on a North-South line. The end towers are phased plus and minus 90 electrical degrees from the center tower and have equal base currents. The center tower is the reference tower and has twice the base current as the end towers. The tower parameters and FCC pattern are shown in Figure Three.

Calculations according to the FCC method (Equation One, Figure One) show zero field due north of the tower. Figure Four shows the pattern calculated by NEC using parallel ray geometry and calculated current distribution on the towers. This calculation shows a minor maximum to the North and symmetrical minima about 26 degrees off of the line of the towers.

Figures Five, Six and Seven show the current distributions calculated for the three towers (the towers are numbered sequentially starting at the South tower). Figure Eight shows a sinusoidal current distribution scaled to the same maximum as the

other figures. The magnitudes of these currents do not differ greatly along the lengths of the towers when scaled to the same reference point. There is a greater difference in the way the phases of the currents vary along the lengths of the towers (each relative to its own base current) as shown in Figure Nine. The relative phase between the currents in the end towers vary by more than three degrees over more than half of the tower length. This variation in the relative phase between the current distributions of towers results in the shifting of the pattern minima seen between Figures Three and Four.

When both near (actual geometry) and far (parallel ray geometry) fields, as calculated by NEC, are compared as one travels outward from the array along a pattern minima (determined by NEC) the field values do not converge at distances as great as thirty or forty kilometers. Measurements on AM directional antennas are only made out to thirty kilometers for FCC purposes. This demonstrates the necessity of using near field NEC calculations for accurate determination of field intensities in radial directions from the minima of AM patterns with "zero" nulls.

The FCC specified minima (Using Equation One, Figure One) in patterns are of special concern when arrays are adjusted. For the case at hand the patern minimum for FCC purposes is at zero degrees (in line with the towers). The variation in field intensity with distance North of the towers is shown in Figure Ten. The NEC near and far field calculations converge at two kilometers.

The third curve shown in Figure Ten results when a traditional near field analysis (Equation Two, Figure One) is made. It shows the inverse field variation with distance. These "Proximity Analysis" values are within a factor of two of the NEC near field analysis values for distances less than 0.9 kilometer from the center of the array. As shown, however, they diverge sharply at greater distances. At distances greater than a kilometer the traditional near field analysis technique shows field intensities much less than those computed by NEC for this particular "zero null" array. This disagreement results from the fact that the traditional "Proximity Analysis" near field technique uses oversimplified current distributions for the array elements.

Because it solves both the current distribution and geometry problems NEC is a valuable tool in determining AM directional antenna behavior in the vicinity of pattern minima. The authors would like to thank R. Adler for his help with the NEC program.

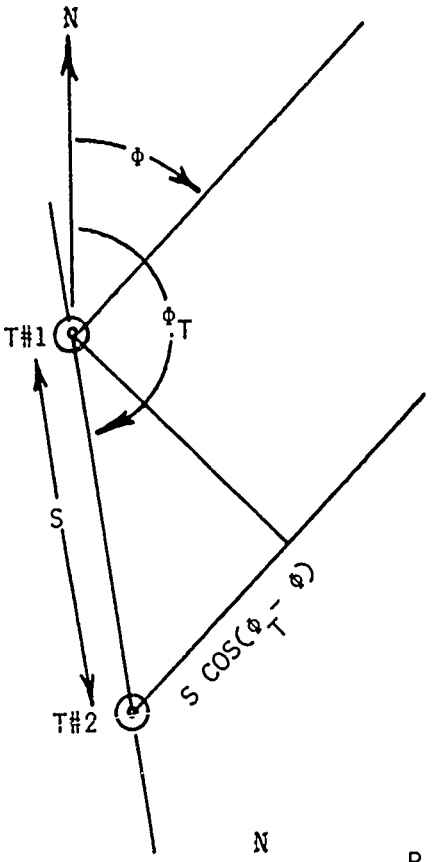
FIGURE ONE

EQUATION ONE

$$E = F_1 + F_2 \angle S \cos(\Phi_T - \Phi) + \Psi_2$$ FAR FIELD

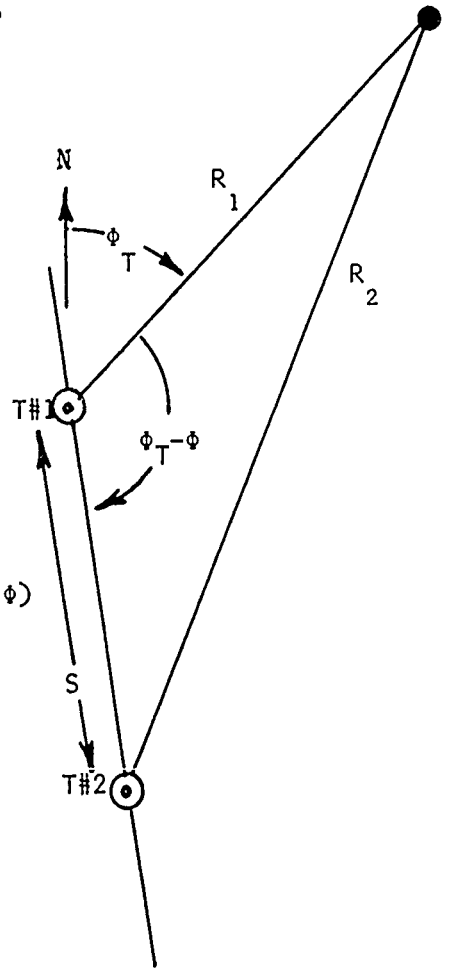
Ψ_2 = PHASE OF TWR#2 RELATIVE TO TWR#1

F_1, F_2, RELATIVE FIELD RATIOS OF TOWERS



EQUATION TWO

$$E = F_1 \angle -R_1 + \frac{R_1}{R_2} F_2 \angle -R_2 + \Psi_2$$ NEAR FIELD



$$(R_2)^2 = (S)^2 + (R_1)^2 - 2(S)(R_1)\cos(\Phi_T - \Phi)$$

PER UNIT FIELDS

FIGURE TWO

(MODIFIED FROM CRC RPT. NO. 1379)

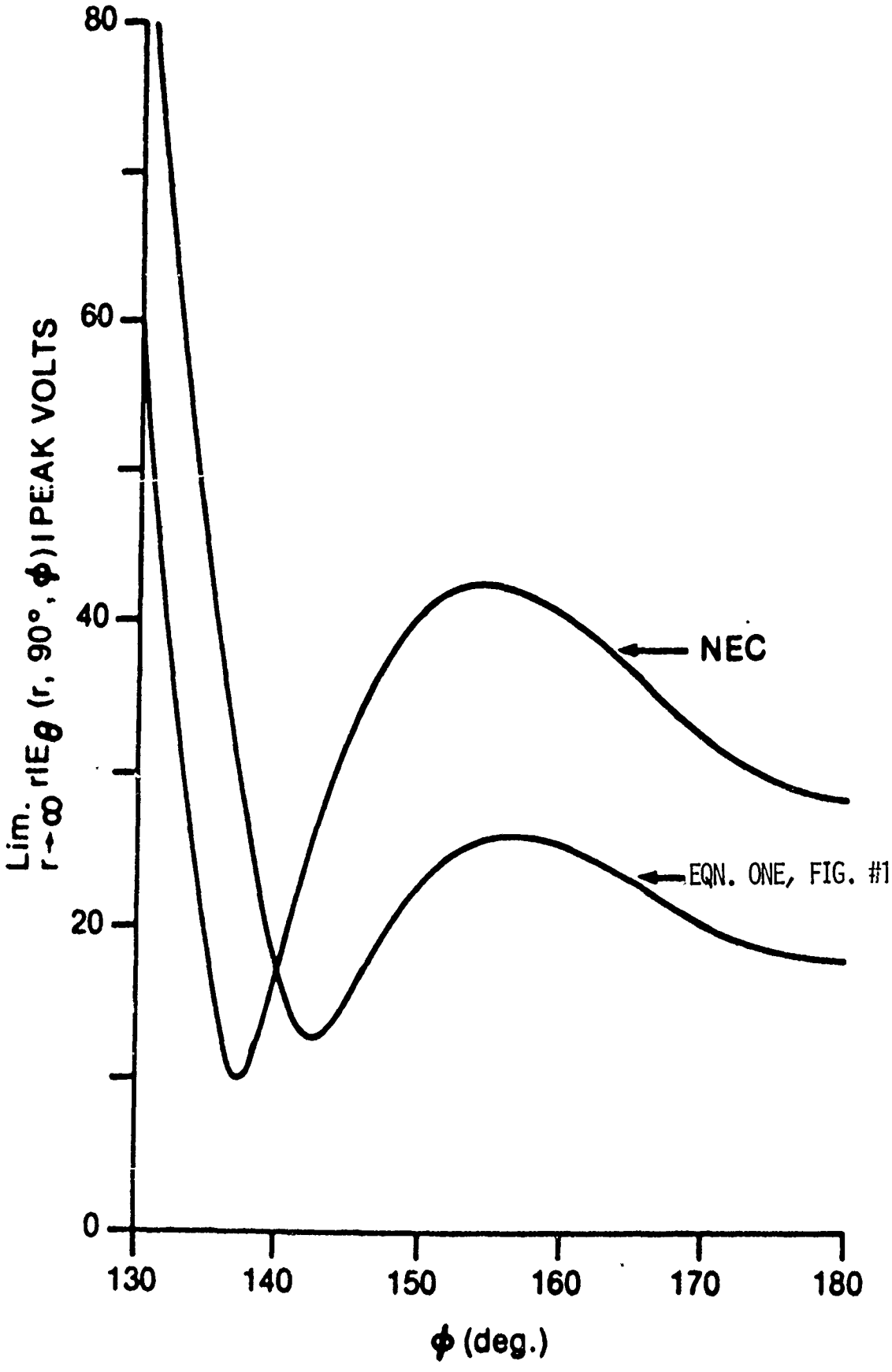
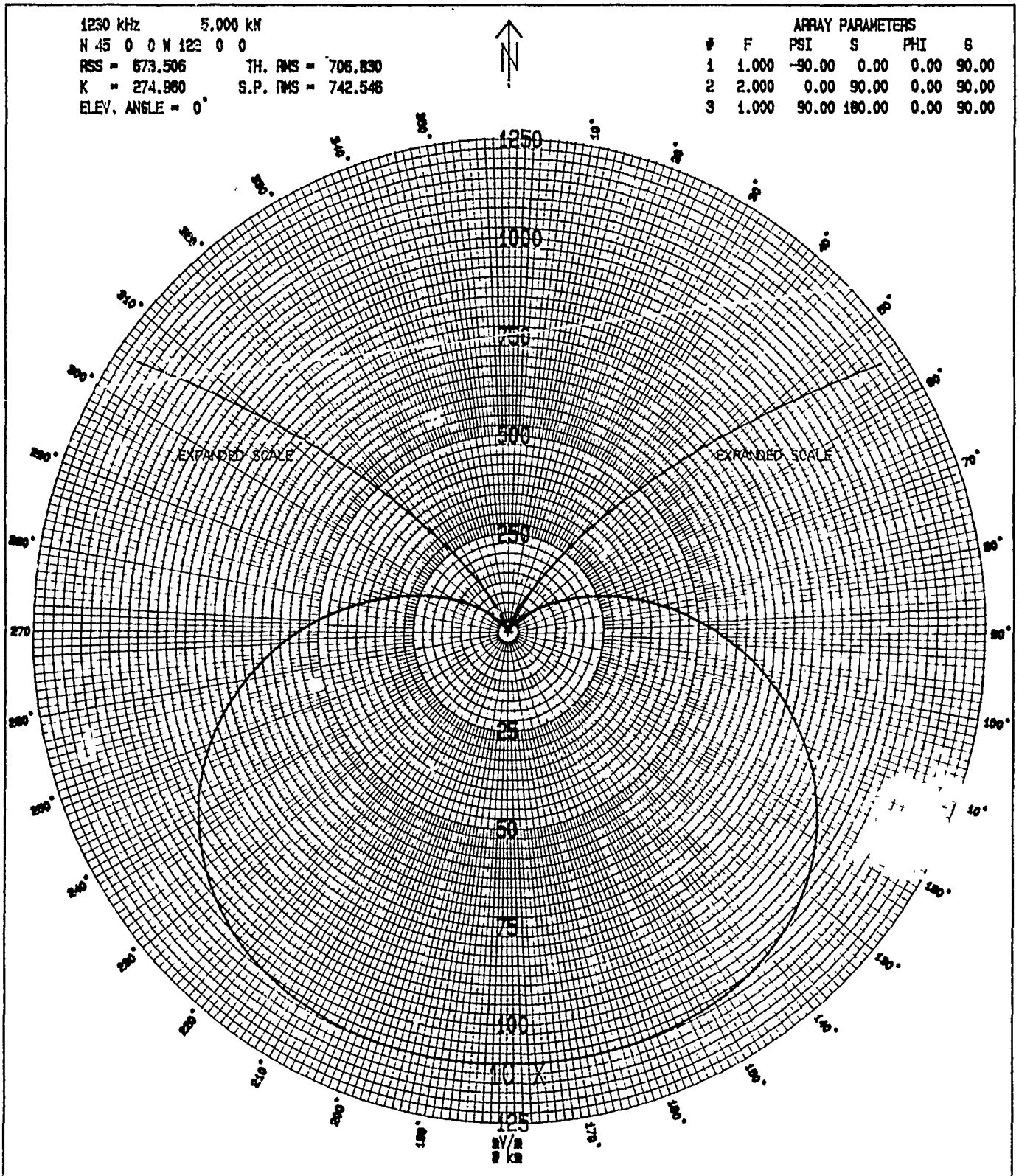


FIGURE THREE



HATFIELD & DAWSON CONSULTING ENGINEERS	EXHIBIT FCC FCC THEORETICAL PATTERN FCC NOWHERE, WASH. 3/87

FIGURE FOUR

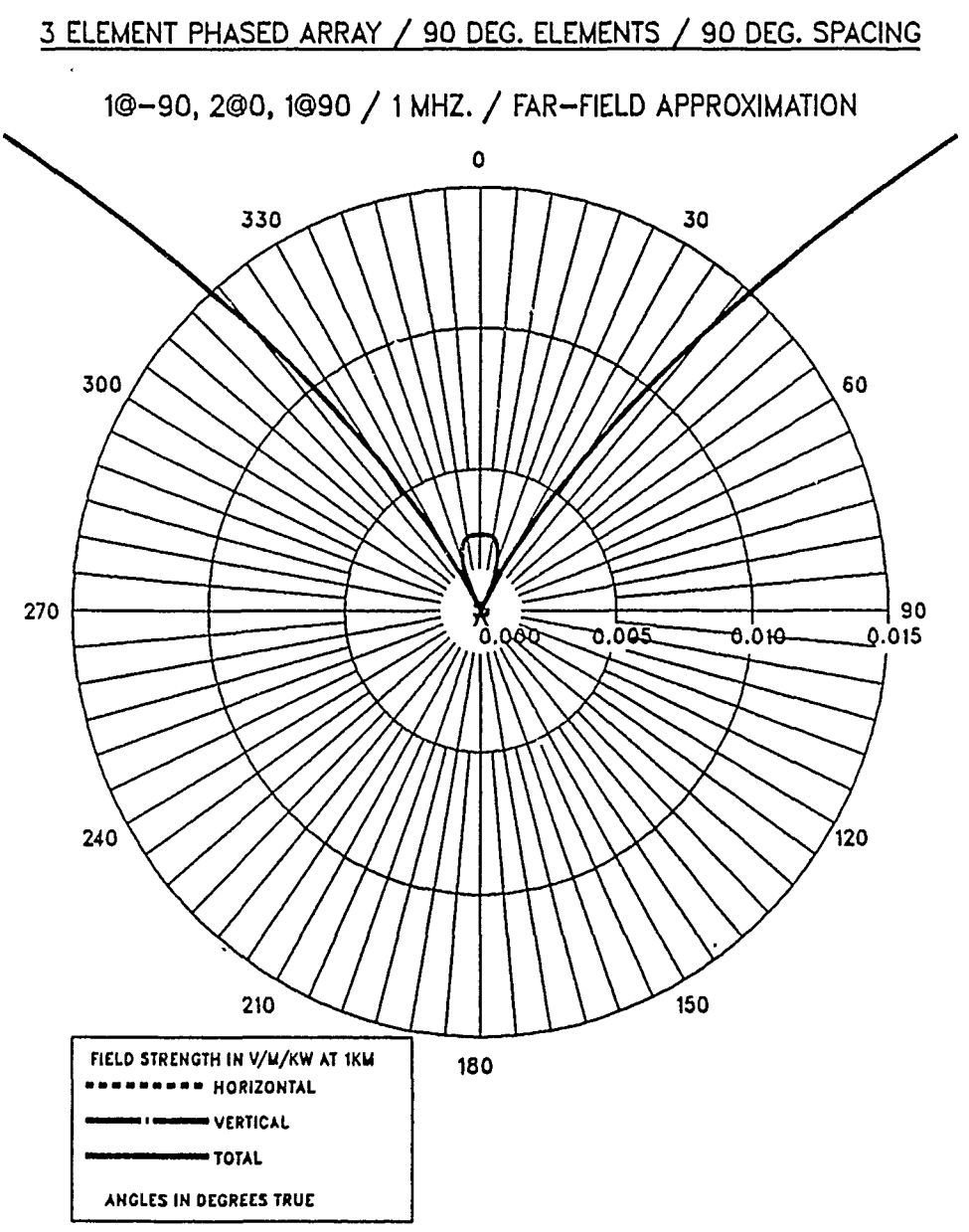

3 ELEMENT PHASED ARRAY / 90 DEG. ELEMENTS / 90 DEG. SPACING
1@-90, 2@0, 1@90 / 1 MHZ. / FAR-FIELD APPROXIMATION
0
30
60
90
120
150
180
210
240
270
300
330
0.000
0.005
0.010
0.015
FIELD STRENGTH IN V/M/KW AT 1KM
HORIZONTAL
VERTICAL
TOTAL
ANGLES IN DEGREES TRUE

FIGURE FIVE

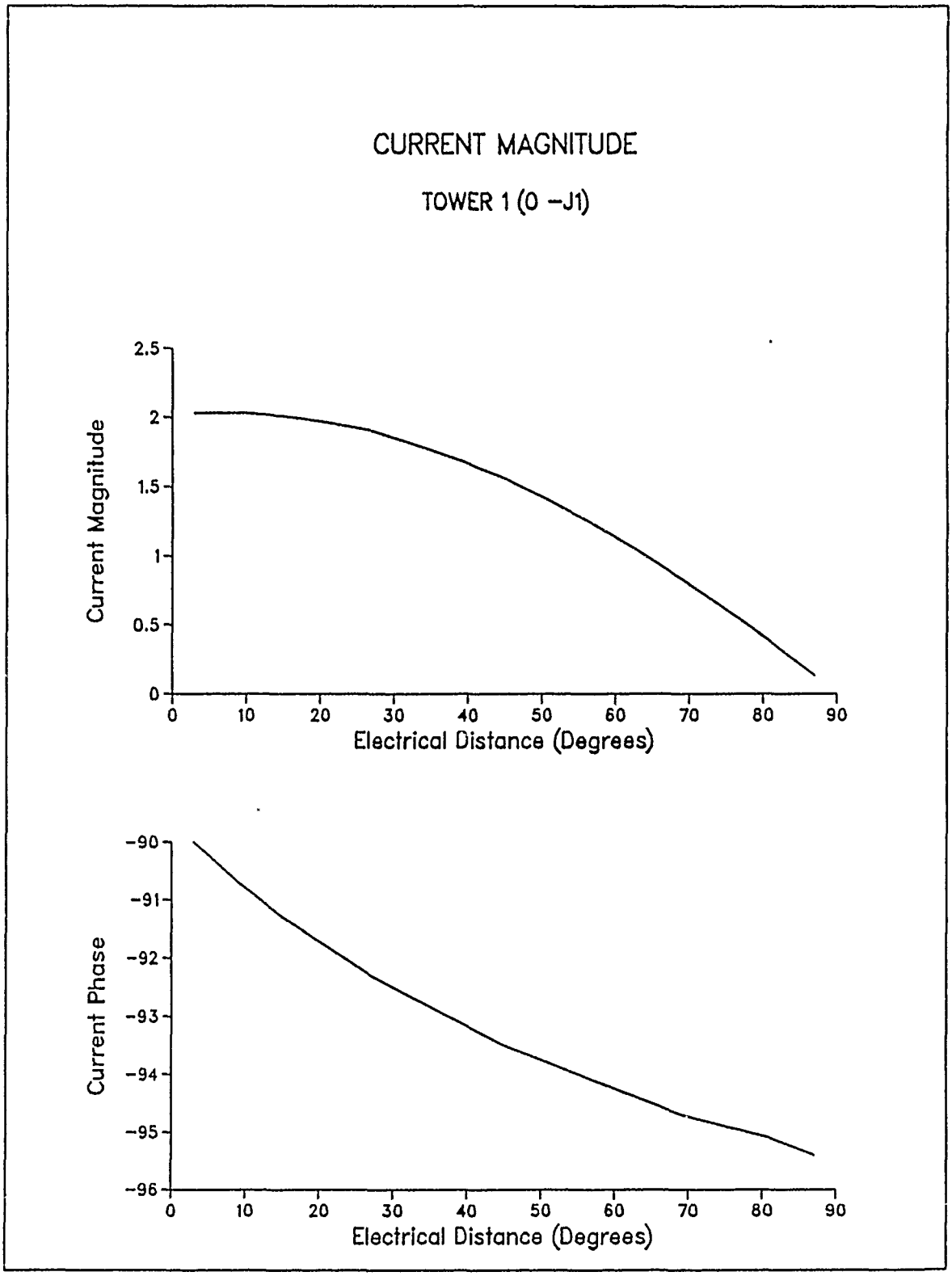

CURRENT MAGNITUDE
TOWER 1 (0 -J1)
Current Magnitude
2.5
2
1.5
1
0.5
0
0
10
20
30
40
50
60
70
80
90
Electrical Distance (Degrees)
Current Phase
-90
-91
-92
-93
-94
-95
-96
0
10
20
30
40
50
60
70
80
90
Electrical Distance (Degrees)

FIGURE SIX

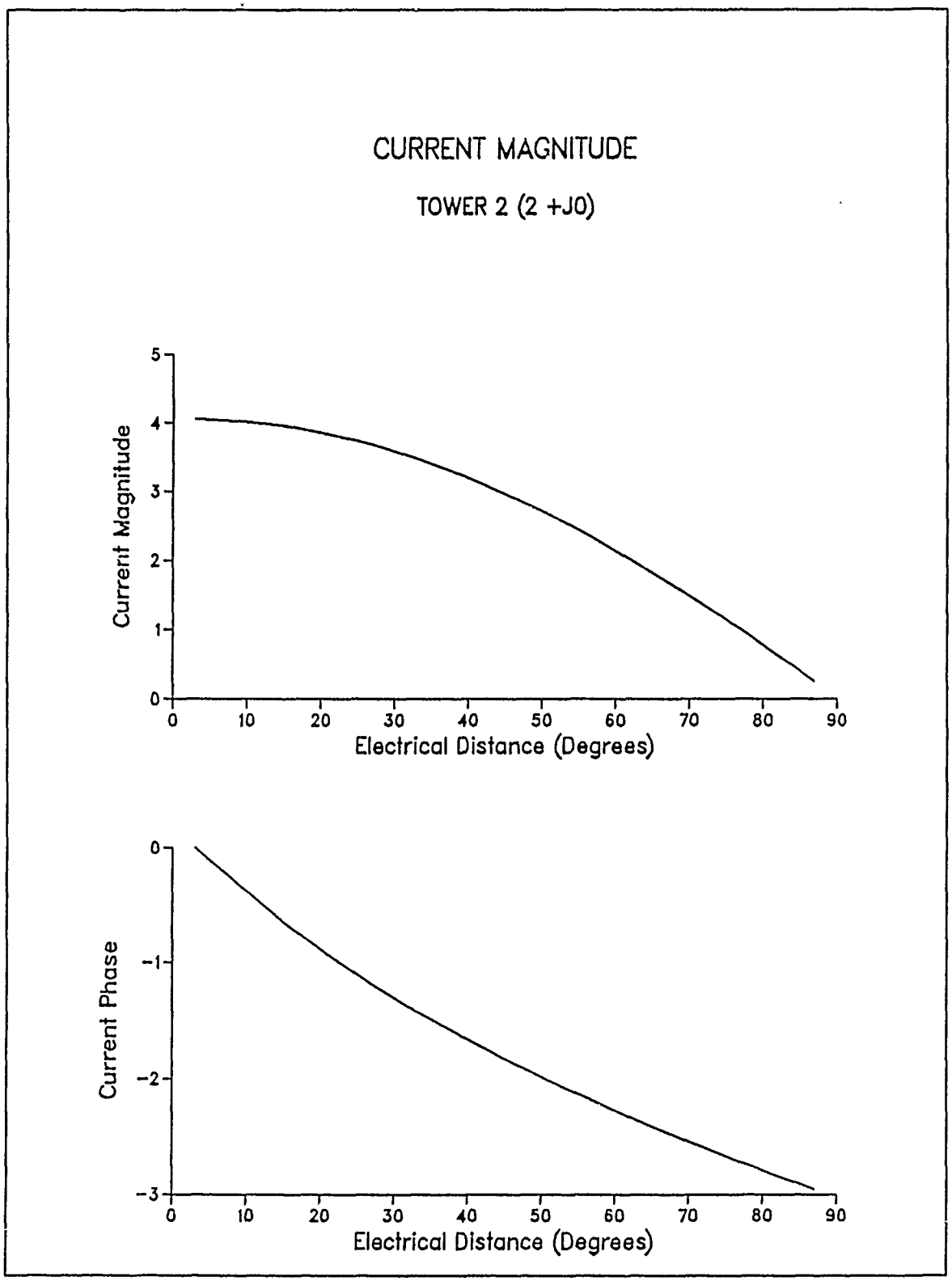

CURRENT MAGNITUDE
TOWER 2 (2 +J0)
Current Magnitude
5
4
3
2
1
0
0
10
20
30
40
50
60
70
80
90
Electrical Distance (Degrees)
Current Phase
0
-1
-2
-3
0
10
20
30
40
50
60
70
80
90
Electrical Distance (Degrees)

FIGURE SEVEN

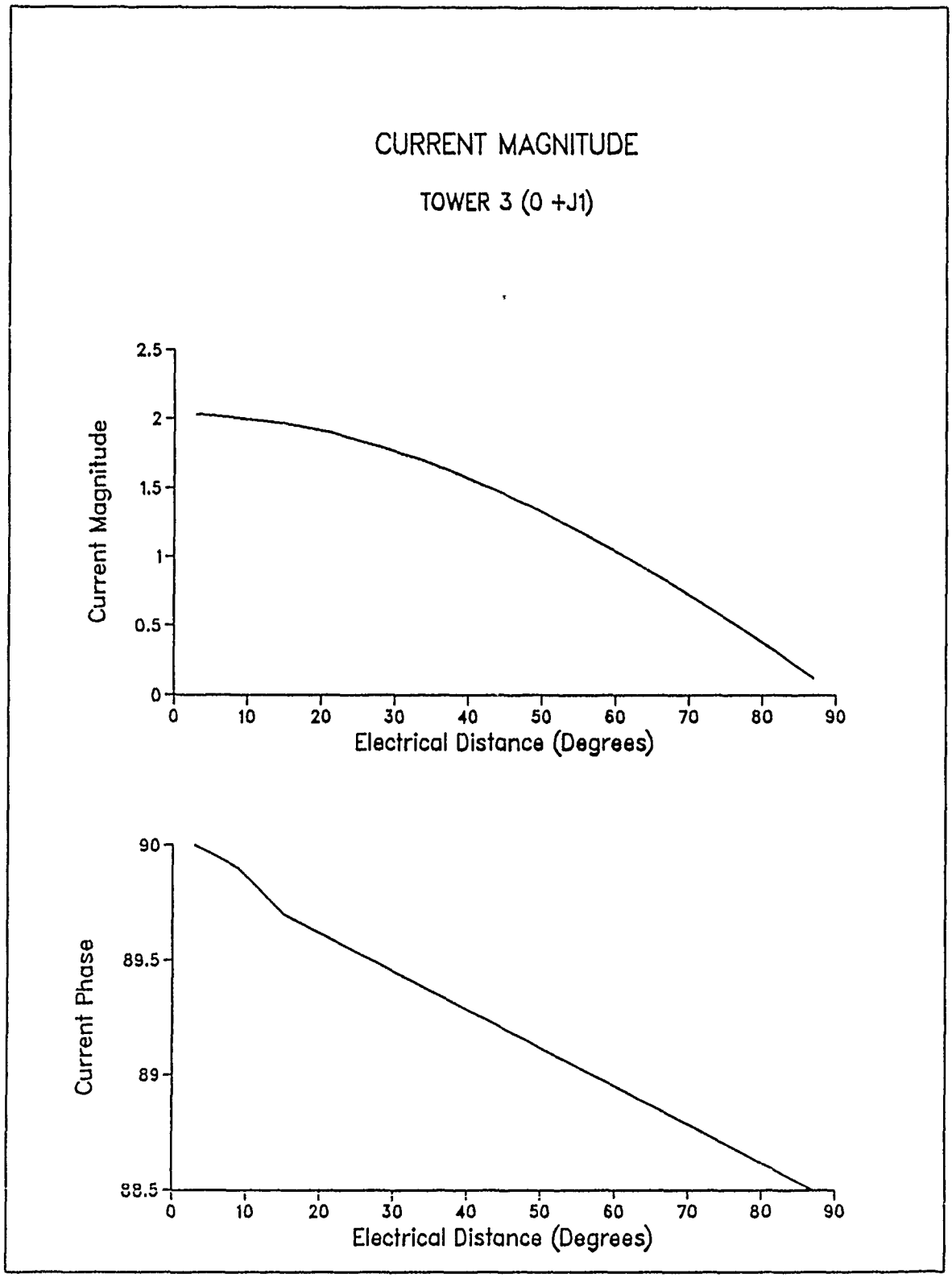


FIGURE EIGHT

CURRENT MAGNITUDE

SINUSOIDAL CURRENT DISTRIBUTION

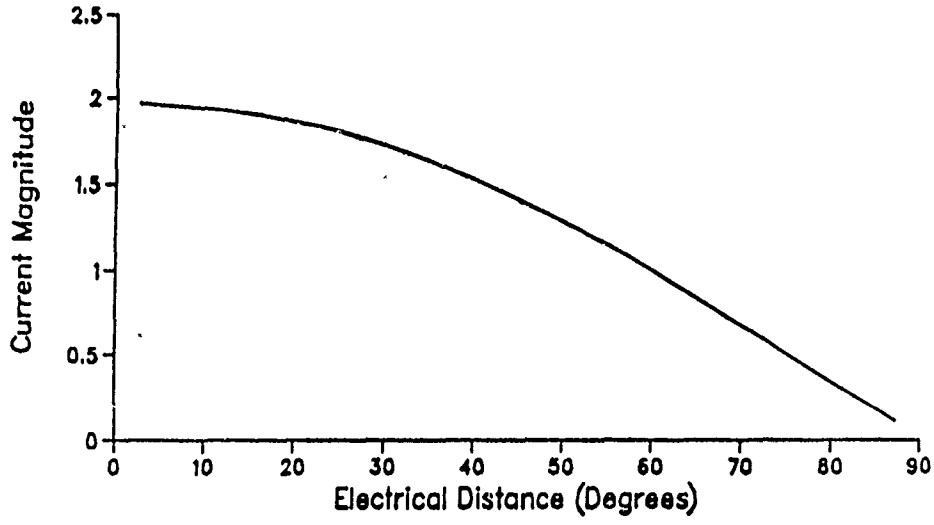
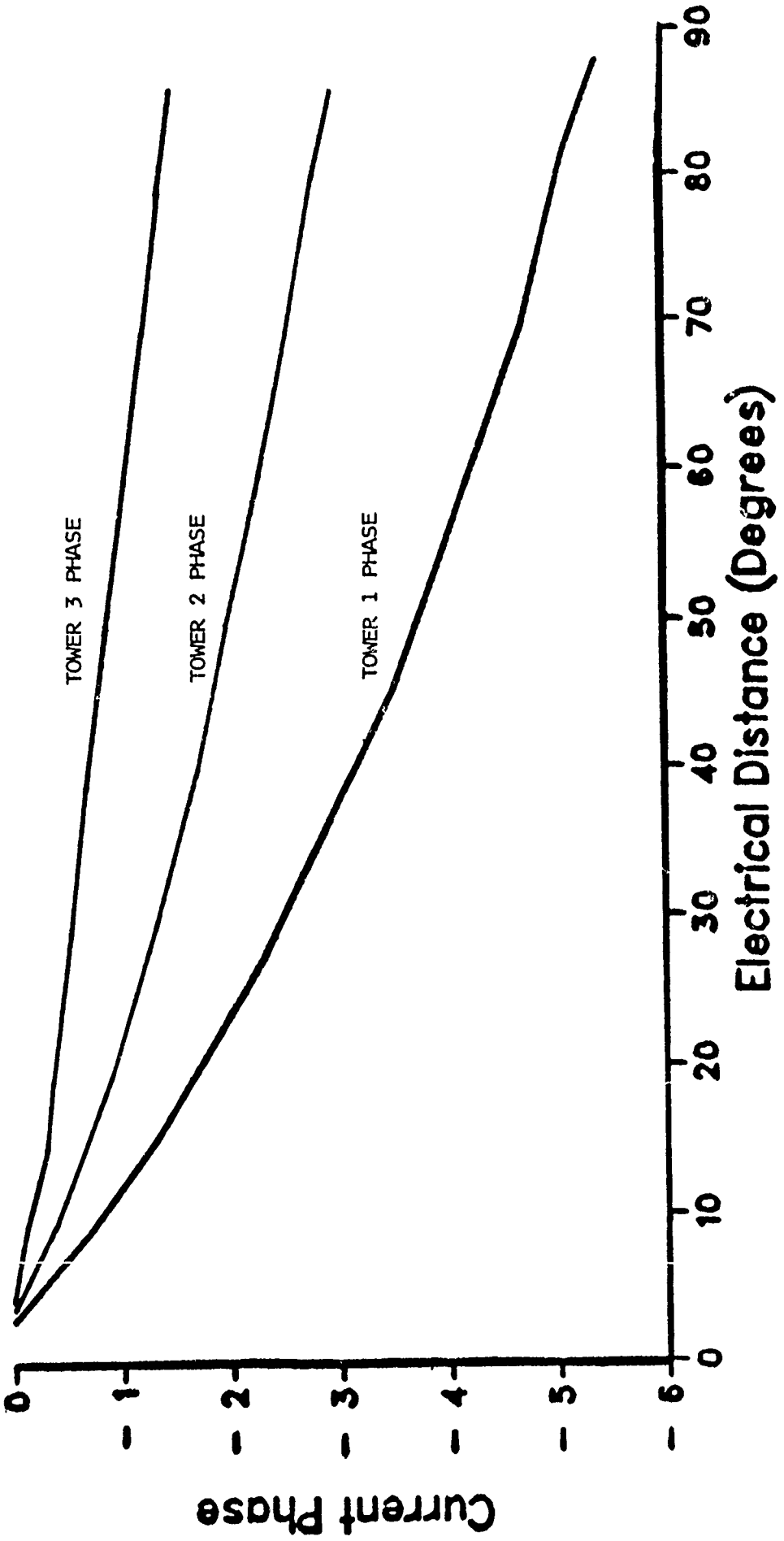
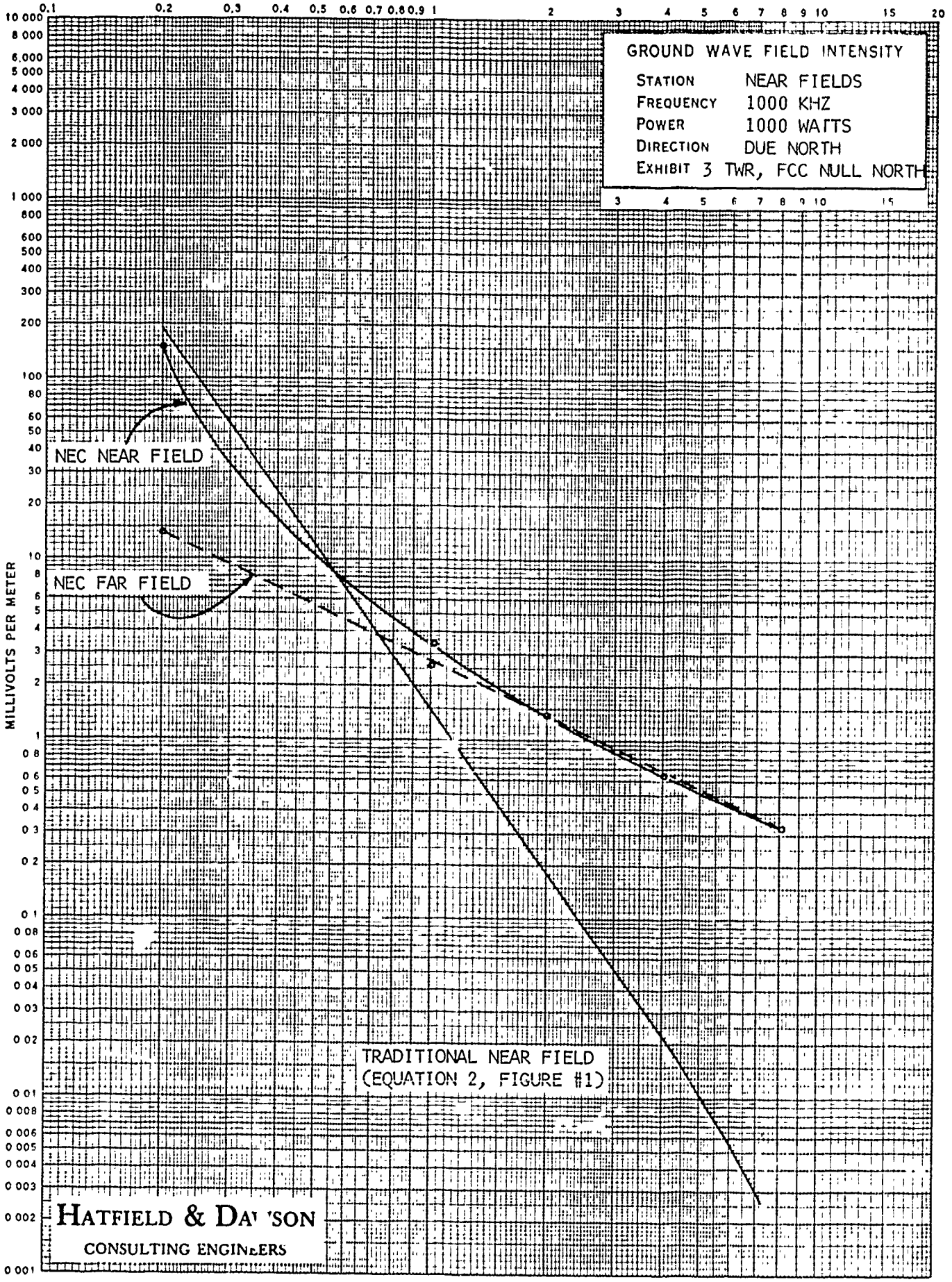


FIGURE NINE


TOWER 3 PHASE
TOWER 2 PHASE
TOWER 1 PHASE
Current Phase
0
-1
-2
-3
-4
-5
-6
0
10
20
30
40
50
60
70
80
90
Electrical Distance (Degrees)

KILOMETERS FROM ANTENNA

FIGURE TEN



HATFIELD & DAWSON

CONSULTING ENGINEERS

Numerical Computation and Experimental Verification of Near Fields from Horns

Don W. Metzger

Kaman Sciences Corporation

Colorado Springs, Colorado

Motivation

The testing of system response and vulnerability to high power microwaves necessarily involves the creation of high power densities. In the generation of these signals, certain factors limit the output capability of the generating system. One of the primary factors is dielectric breakdown or arcing in the waveguide which transmits the wave from the source to the experimental area. Therefore, it is necessary to use the output power available in the most efficient manner.

In order to simulate actual threat pulses, testing should be performed in the far-field region where the propagating waves most closely approximate plane waves. However, in order to best utilize the output capabilities of the microwave source, it is also desirable to have the system under investigation in the near-field region where the power density is maximum. When the system under investigation is in the near-field region a method of predicting the field structure is useful.

Approach

When calculating the fields from an antenna typically the far-fields are of interest. Some assumptions appropriate to the far-field region are applied to the integral forms of Maxwell's equations. These assumptions are generally that the distance from all parts of the antenna to the observation point can be considered constant in magnitude terms. The phase terms however are left as functions of the antenna geometry. With this simple assumption it is sometimes possible to evaluate the integrals analytically and find expressions for the fields at a general observation point.

When calculating the near fields from antennas it is not possible to make the constant distance approximation as in the far-field case and hence the equations are more complex and often impossible to evaluate analytically. Thus, numerical evaluation of these equations is often necessary. Since integral equations lend more readily toward numerical evaluation, Maxwell's equations in integral generally form the basis of the numerical solution.

A classical solution for the fields scattered by an assortment of currents was developed by Silver[1]. This solution starts with the fully symmetric forms of Maxwell's equations in which both electric and magnetic charges and currents are considered. The solution for the scattered fields from electric and magnetic currents are

$$\bar{E}_s = \frac{-j\eta}{4\pi k}\int_A \left[k^2\bar{J}\psi + (\bar{J}\cdot\nabla)\nabla\psi - \frac{jk}{\eta}(\bar{M}\times\nabla\psi)\right]dA$$

and

$$\bar{H}_s = \frac{-j}{4\pi k\eta}\int_A \left[k^2\bar{M}\psi + (\bar{M}\cdot\nabla)\nabla\psi + jk\eta(\bar{J}\times\nabla\psi)\right]dA.$$

where :

$\bar{J}$ is the electric current density,

$\bar{M}$ is the magnetic current density,

ψ is the point source Green's function.

With some effort these equations can be reduced to forms more useful for numerical solution:

$$\bar{E}_s = \frac{-j\eta k}{4\pi}\int_A \left[(1+\alpha)\bar{J} + \beta(\bar{J}\cdot\hat{r}_1)\hat{r}_1 + \frac{1}{\eta}\left(1-\frac{j}{kr_1}\right)(\bar{M}\times\hat{r}_1)\right]\psi\ dA$$

and

$$\bar{H}_s = \frac{-jk}{4\pi\eta}\int_A \left[(1+\alpha)\bar{M} + \beta(\bar{M}\cdot\hat{r}_1)\hat{r}_1 - \eta\left(1-\frac{j}{kr_1}\right)(\bar{J}\times\hat{r}_1)\right]\psi\ dA$$

where:

$$\alpha = -\frac{j}{kr_1} - \frac{1}{k^2 r_1^2},$$

$$\beta = -1 + \frac{3j}{kr_1} + \frac{3}{k^2 r_1^2} \text{ and}$$

r_1 is the distance from source to observation.

Typically a single mode is propagating in the waveguide and its composition is known. If it is assumed that no mode conversion occurs in the horn then the distribution of fields at the mouth of the horn is also known. With knowledge of the horn mouth fields equivalent currents can be calculated and Silver's solution applied.

The assumption of no modal conversion permits knowledge of the fields which exist in the plane of the horn mouth. If an imaginary surface S is placed over the mouth of the horn, then equivalent currents can be found for each point on S which correspond to the E and H fields which exist there. Call the normal to S the unit vector n. The current J and M on S are then related to the modal fields E and H by

$$J = n \times H \text{ and}$$

$$M = -n \times E.$$

Effects of Horn Flare

The assumption that the fields exist on a planar surface S is an approximation to reality. There must be some distortion of a planar constant phase surface in the waveguide as it passes out through the horn in order to meet the boundary conditions of the horn surfaces.

There have been various approaches to the calculation of the shape of this surface. The most general case of a horn that flares in both planes will be considred. Consider one plane of the horn. The sides of the horn converge to a center point C. The distance from C to any point on the assumed surface at the horn mouth is r. The functional dependence of r as a function of the angle θ can be found which satisfies the boundary conditions at the horn surface. This condition is that the surface must be normal to the horn edge in order to agree with the relation between the planar

wave and the waveguide. First consider the general form of an equation for ellipses, parabolas and hyperbolas:

$$r = \frac{p}{1-\epsilon\cos\theta}$$

where:

p is an arbitrary constant,
$\epsilon < 1$ for an ellipse,
$\epsilon = 1$ for a parabola, and
$\epsilon > 1$ for an hyperbola.

The boundary conditions dictate that $\frac{\partial r}{\partial \theta} = 0$ at the horn surface. Evaluation of this quantity yields

$$0 = \frac{-p\epsilon\sin\theta}{(1-\epsilon\cos\theta)^2}$$

$$0 = -p\epsilon\sin\theta$$

$$0 = \theta.$$

Thus it is apparent that ellipses, parabolas and hyperbolas will not match the boundary conditions for any real horn geometry.

A circle it may be observed, has a constant r and therefore will meet the boundary conditions of $\frac{\partial r}{\partial \theta} = 0$. Thus it is seen that the surface may be approximated by a circle in the cross-section of each horn plane.

It would appear that a good approximation for the actual shape of the constant phase surface at the mouth of the horn would be a sphere. This is true if both planes of the horn converge to a single point as with a pyramid. However, in general, the E and H planes of a horn do not converge at the same point due to differences in the flare angles and throat and mouth dimensions. However, for this work the constant phase surface was assumed to be spherical with its center at the average of E and H plane centers. It should be noted that the careful choice of a sphere for the constant phase surface is invalidated somewhat by this approximation since this averaged surface will not explicitly meet the boundary conditions in either plane. However for horns whose phase centers in each plane do not vary greatly, this is a good approximation. For the specific cases of E or H plane sectoral horns, a cylindrical surface will meet the boundary conditions imposed by the horn.

In summary, the horn is treated as a distribution of source currents which can be determined from a known modal distribution of E and H fields. The effect of the horn is to curve a constant phase plane into a spherical surface. Thus, the currents exist on a planar surface from which the wave is launched; a phase correction is added to account for the spherical phase front due to the horn flare.

Results

Several examples of the results of this code for the geometry shown in figure 1 are given in figures 2-5. The horn geometry is for a standard W band horn being driven in-band at 2.5 GHz. Figures 2-5 show equal-valued contours plotted in a specified plane.

Figure 2 shows the pattern in the E plane of the horn. For this case the magnitude of the y and z components were combined to give the magnitude of the E field lying in the E plane. These components were chosen in order to facilitate comparison with experimental data. The pattern shows the development of main and side lobes as expected. However, in the very near-field region there is a local minimum on axis. This feature has been verified using an infrared field mapping technique.

Figure 3 shows the pattern in the H plane of the horn for the x and z components of the E field. The H plane has been shifted from y=0 to the edge of the horn mouth since both theory and experiment show that the x and z components are approximately 0 in the y=0 H plane. As in figure 1, the structure in the very near-field region is quite different from that in the far-field. This structure has also been verified using the infrared mapping technique.

Figures 3 and 4 show the x and z components of the H field in the y=0 H plane. By comparing the plots it can be seen that the radial components tend to attenuate quickly while the radiating components attenuate much more slowly, as expected. Thus, it can be observed that the H_z component nulls on boresight but has value in the plane of the horn, while the opposite holds true for the H_x component.

Features of the Computer Implementation

The code written for this analysis first calculates the equivalent currents which exist on the horn mouth. This is accomplished by breaking the horn mouth down into small

patches, the number of which is controlled by the user. The currents are found by cross products of the normal to the mouth surface and the assumed modal distribution of E and H fields. It is possible to mix modes in the computer solution and not significantly alter the execution time. For example, a solution could be found for a horn radiating 90% TE_{10} and 10% TE_{11}.

The code then numerically calculates the result of each patch at the point of observation. The superposition sum of these contributions is the resulting field at the point of interest. All three components of E and H as complex numbers can be determined at each point of interest. The code can repeatedly call this routine to determine the fields in a region of space.

Typical execution times are approximately 2 seconds to determine the equivalent current distribution on the horn mouth and about 2 seconds to determine the field values at each point of interest. These times are for a 30x30 array of patches, e.g. 900 total patches. The computer used was a VAX 11/750 running single precision FORTRAN.

Conclusions

Use of this code over a period of 2 years has shown that patterns calculated in the far-field region using this near-field approach, tend to agree quite well with typical far-field calculations. At present there is some work being done to determine the validity of results in the plane of the horn but external to the horn mouth.

References

1) Silver, Samuel; *Microwave Antenna Theory and Design*; M.I.T. Radiation Laboratory Series; Boston Technical Lithographers, Inc.; Lexington Mass.; 1963

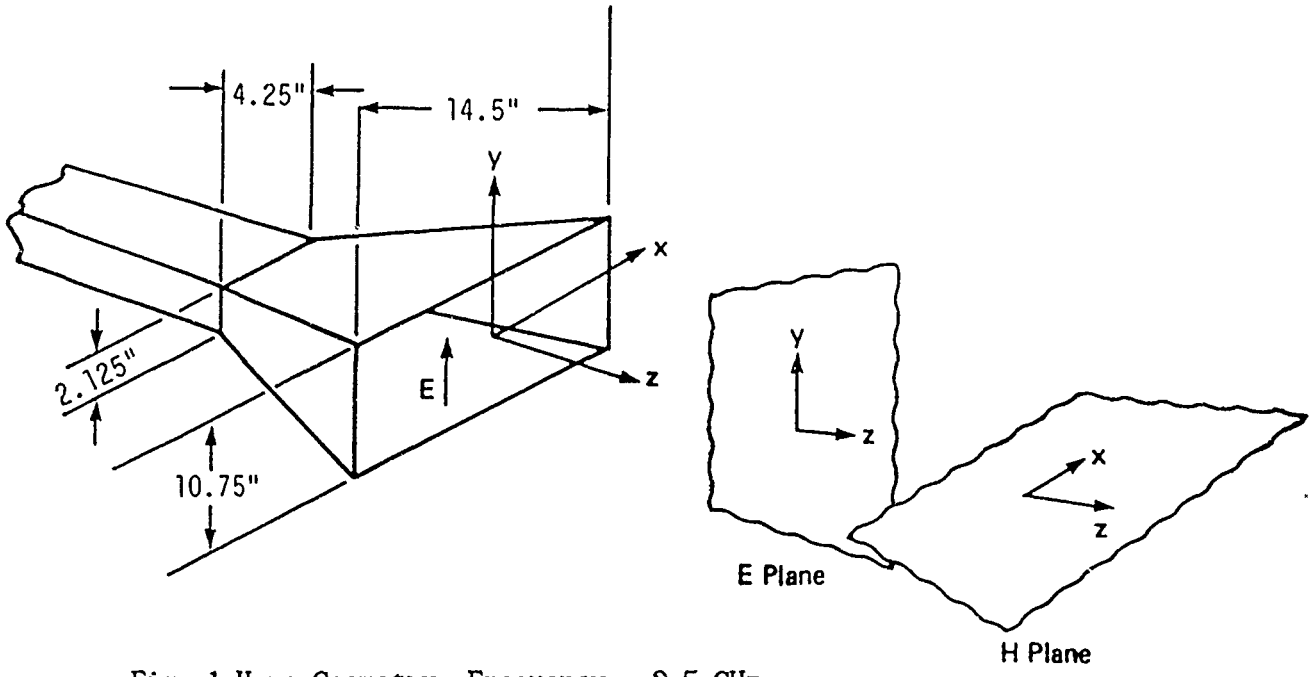


Fig. 1 Horn Geometry, Frequency = 2.5 GHz

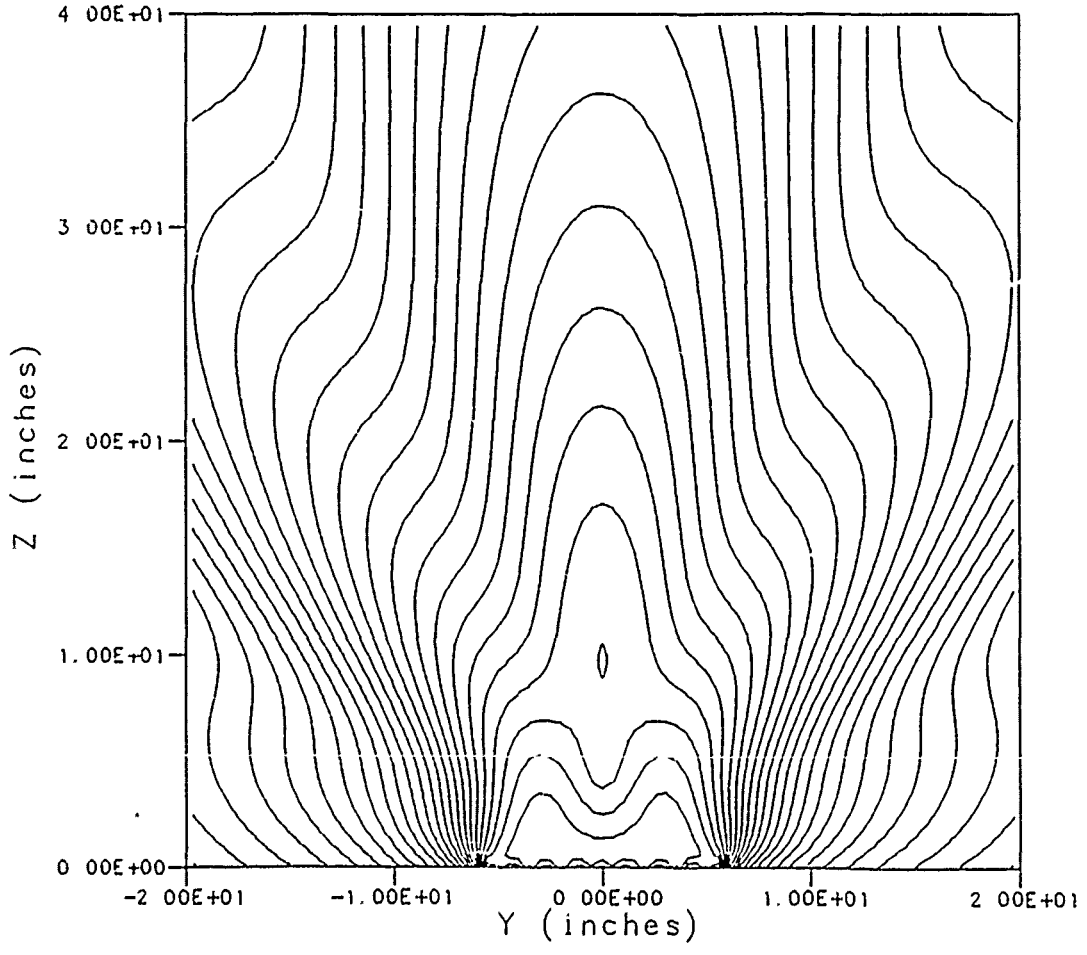


Fig. 2 Magnitude of E_{yz} in the E plane with x=0

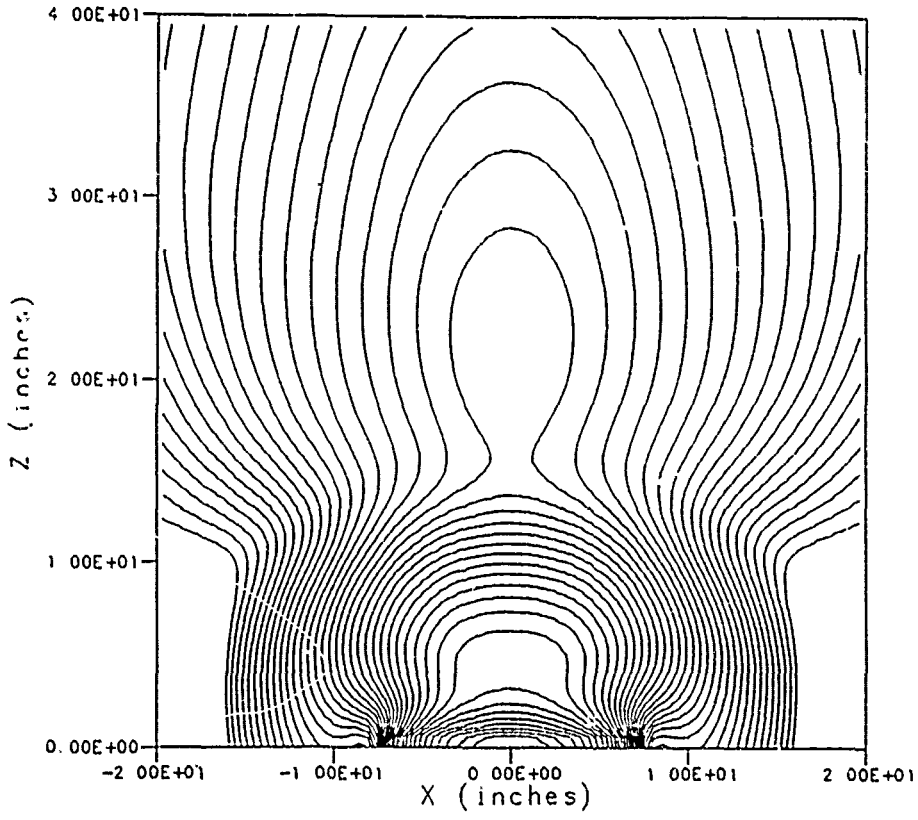


Fig. 3 Magnitude of E_{xz} in the H plane with y set at the edge of the horn mouth.

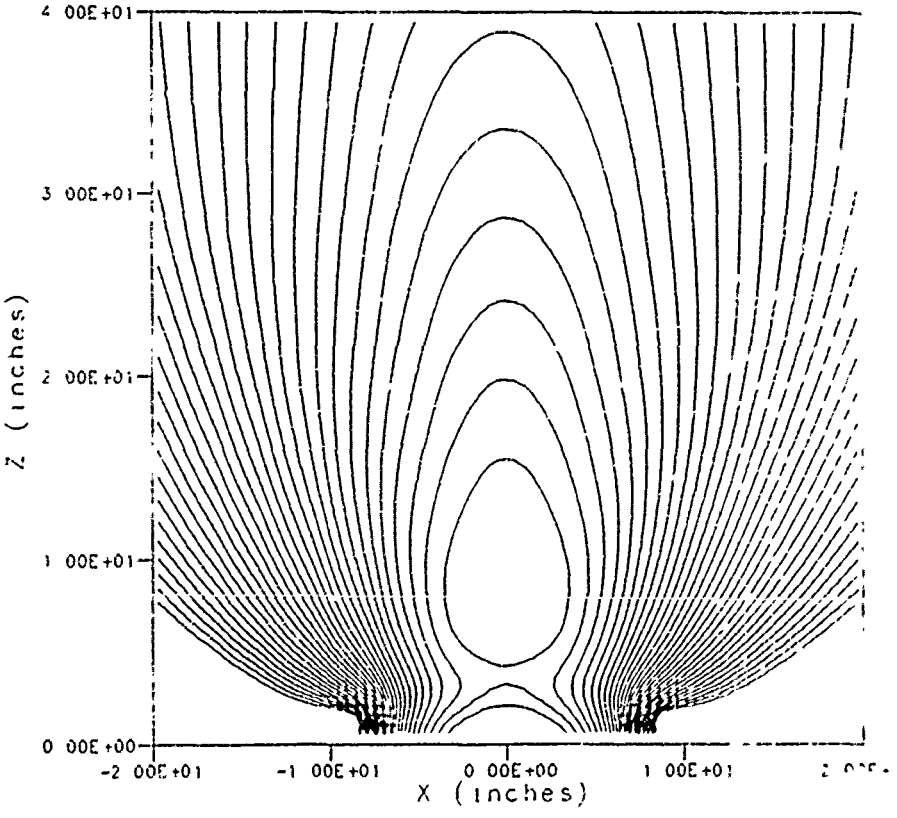


Fig. 4 Magnitude of H_x in the H plane with y=0

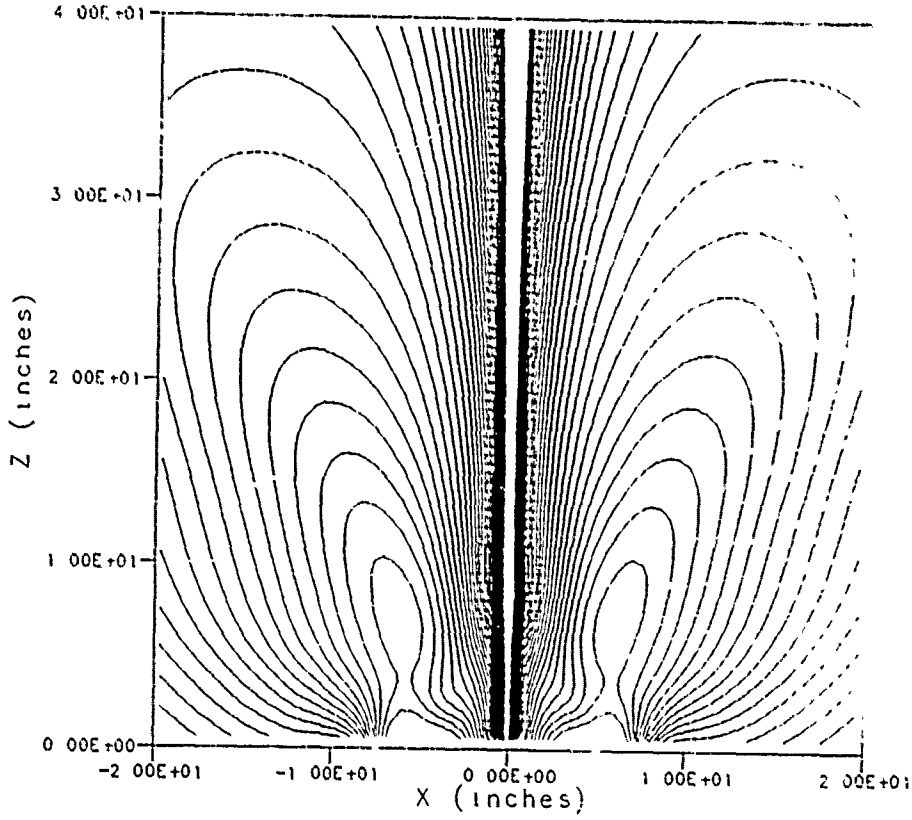


Fig. 5 Magnitude of H_z in the H plane with y=0

HELICOPTERS, HF ANTENNAS: MODELS, MEASUREMENTS AND ALL THAT

Stanley J. Kubina
EMC Laboratory
Concordia University
Montreal, Que., Canada

Introduction

Information on the comparative evaluation of HF antennas on aircraft and helicopters is somewhat scattered in the literature and incomplete. The systematic evaluation of aircraft HF antennas was first carried out at the Stanford Research Institute [1]. A very compact evaluation of notch, wire and cap antennas is to be found in the Transactions on Aeronautical and Navigational Electronics[2]. Valid Method of Moments modelling via NEC offers the possibility of re-examining the performance of these antennas.

In recent ACES Review Meetings, the modelling of HF antennas on helicopters was discussed in terms of the model creation process using DIDEC (Digitize, Display, Edit and Convert)model design software and an integrated system of interactive graphics for the display and manipulation of input/output files. The present paper presents some of the results that have been obtained in the modelling of shorted transmission line(STL) and 'Zig-Zag' antennas on the CH-135/TWIN-HUEY helicopter. Figure 1 shows the wire-grid models and the antennas. The name of the "Zig-Zag' antenna is evident from the nature of its path around the helicopter body in order to achieve the required length for matching over the HF 2-30MHz band by commercially-available couplers.

The results of the wire-grid model analysis are presented over the entire 2-30MHz frequency range. These pattern results are also compared to initial 1/24-scale model measurements. Some serious discrepancies between measured and computed results are examined and reconciled. The process demonstrates the utility and power of a combined computation/measurement approach for complex applications.

The computer model analysis is then extended to utilize the ground imaging features within NEC to examine the radiation pattern variations with altitude. Such information is most useful in analyzing antenna pattern contributions to both short and long range communication scenarios.

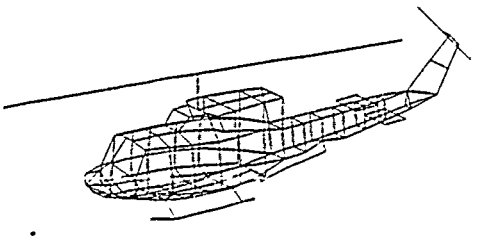
Radiation Pattern Comparisons

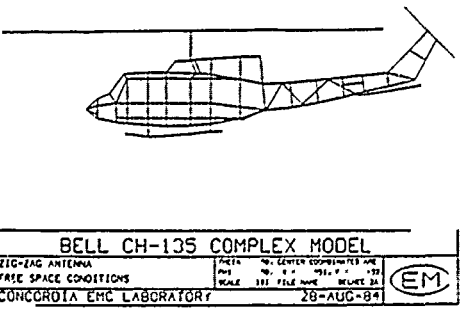
The wire-grid model that is being used in these comparisons was developed using the considerations that had been used for aircraft antennas[3]. Model segment lengths were selected to be approx. 0.1λ in the middle of the band(15MHz). The models of Figure 1 have 302 and 305 segments respectively. The STL antenna is approximately 1 ft. from the fuselage and is 10 feet long. The ZIG-ZAG antenna uses the same feed point and loops around the fuselage for a total length of 46.3 feet.

Figure 2 shows the principal plane results for the two antennas at 2 MHz. Note that these patterns are plotted with reference to the isotropic reference level. This latter level is derived from an integration of the radiation pattern data, a procedure which is exactly the same as that used with the experimental data. Although the results are similar, there is some significant difference in the level of the E-phi component. The nature of the two antennas accounts for this but the analyst can examine the current distributions computed by NEC in order to appreciate the exact reasons for the pattern differences.

It can be seen that communication at this frequency would be very much dependent on helicopter attitude. For a full operational analysis it is necessary to examine the volumetric radiation pattern characteristics. It is the practice at Concordia to compute a set of 21 standard conical cuts. These are presented as a hidden line display in Figure 3. Note the differences in the E-phi polarization are more evident in this display.

Computations such as the above are carried out at 2 MHz increments over the entire frequency band. Figure 4 shows the volumetric pattern plots at 8MHz. The pattern structure is more complex because more of the airframe is excited at these higher frequencies. A sizeable difference is noted in the E-phi polarization.





a) Wire-Grid Model - Shorted Transmission Line Antenna (STL)

b) Wire-Grid Model - "Zig-Zag" Antenna

Figure 1 - Wire-Grid Models and HF Antennas

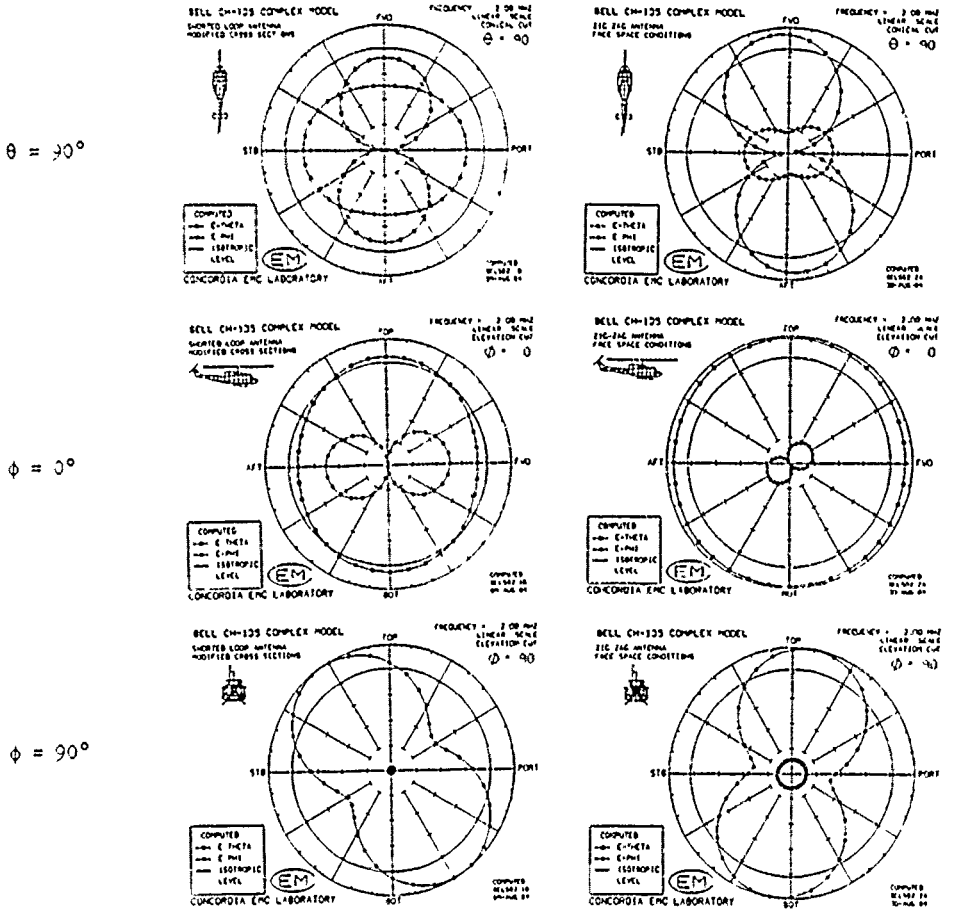
The detailed examination of patterns at fine frequency increments is important but such an extensive data base is difficult to condense when decisions are to be made about different antenna types. For this purpose, it is instructive to derive and examine single-value pattern-based parameters at each frequency that can be related to operational performance[3]. The terms, radiation pattern efficiency, np, %E-Theta, and %E-Theta* or SUB-E-Theta, have been used for this purpose as well as others. These terms are defined in terms of the power ratios in a 'useful' sector, thus,

$$\eta_p = \frac{\int_0^{2\pi}\int_{60}^{120}(|E_\theta|^2 + |E_\phi|^2)\sin\theta\, d\theta d\phi}{\int_0^{2\pi}\int_0^{\pi}(|E_\theta|^2 + |E_\phi|^2)\sin\theta\, d\theta d\phi}$$

$$\%E_\theta = \frac{\int_0^{2\pi}\int_0^{\pi}|E_\theta|^2\sin\theta\, d\theta d\phi}{\int_0^{2\pi}\int_0^{\pi}(|E_\theta|^2 + |E_\phi|^2)\sin\theta\, d\theta d\phi}$$

$$\%E^* = \frac{\int_0^{2\pi}\int_{60}^{120}|E_\theta|^2\sin\theta\, d\theta d\phi}{\int_0^{2\pi}\int_0^{\pi}(|E_\theta|^2 + |E_\phi|^2)\sin\theta d\theta d\phi}$$

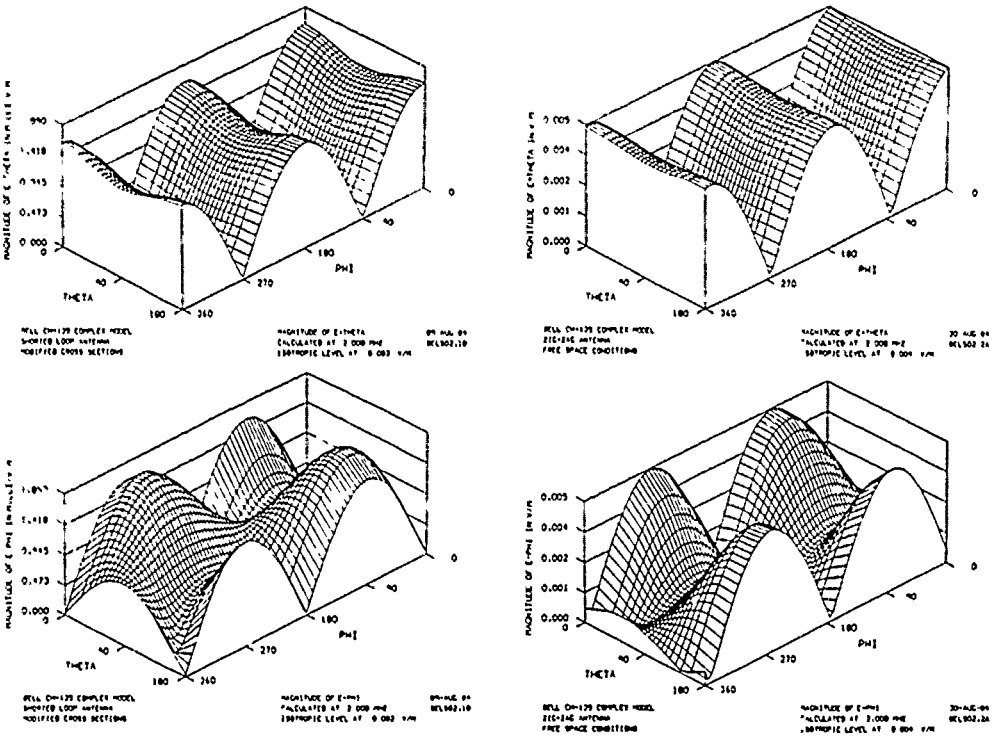
where the angles have the conventional definition.



a) STL Antenna

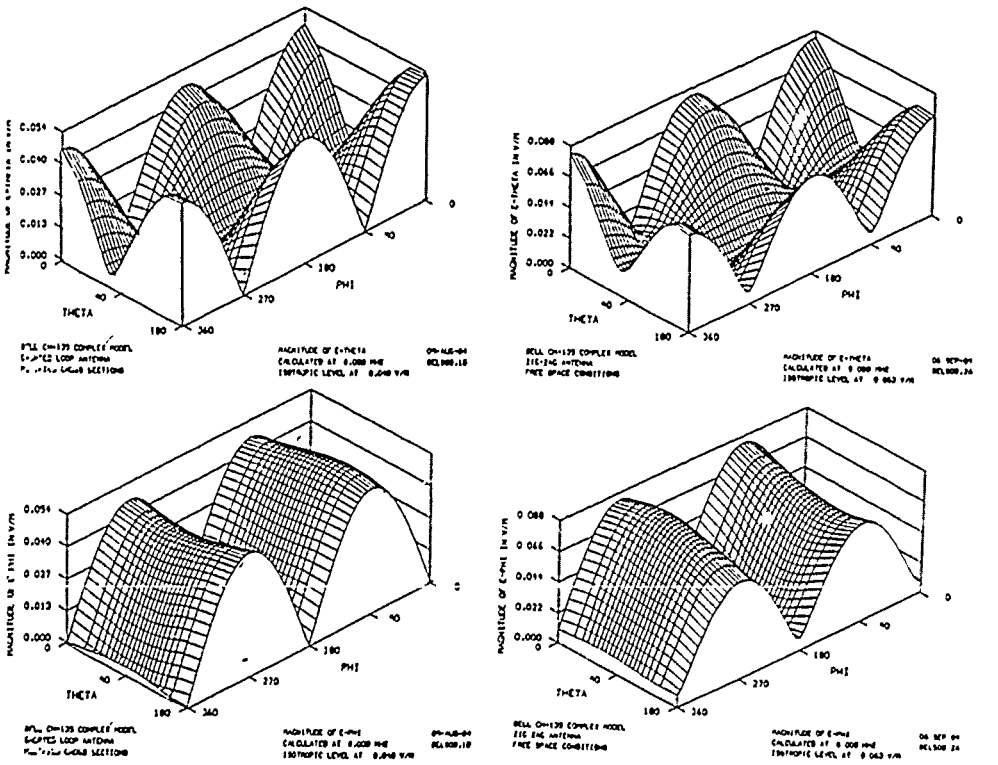
b) Zig-Zag Antenna

Figure 2 - Principal Plane Patterns - 2 MHz



a) STL Antenna b) Zig-Zag Antenna

Figure 3 - Volumetric Patterns - 2 MHz



a) STL Antenna b) Zig-Zag Antenna

Figure 4 - Volumetric Patterns - 8 MHz

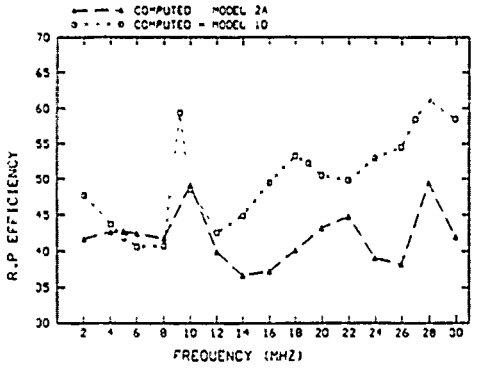
The radiation pattern efficiency for the two antennas versus frequency is shown in Figure 5. Note the closeness of the values at 8MHz confirms the pattern examination but that substantial differences exist at other frequencies.

For ground wave propagation, %E-theta is important. Figure 5 b) plots this parameter versus frequency. Note the ZIG-ZAG antenna has higher values at 2 MHz. Should differences such as this be considered operationally significant, the coupler efficiency must be examined in order to establish that coupler efficiency differences will not cancel any pattern distribution advantages. The third parameter %E-theta*, is the power in the +or-30° sector around the horizon and might correspond to the probability of communication in a ground wave communication mode when nominal helicopter attitude changes are taken into account.

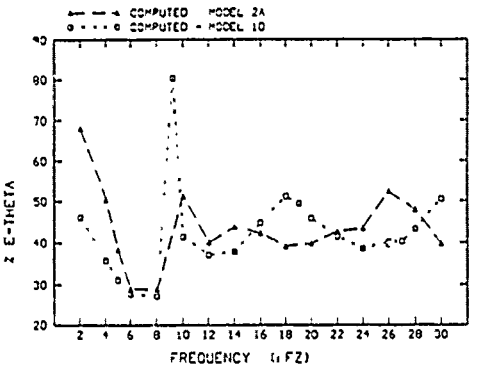
Having concentrated on the parameter values, it is always important to refer back to the actual pattern shapes for an appreciation of heading and attitude differences. For example, examining the plots of Figure 6 for the two antennas at 26MHz, produces immediately the appreciation as to why the parameter values are so different. Thus for any special mission applications, the parameters can be weighted based on the pattern detail that is of consequence.

The ease with which the complete pattern data can be generated from valid NEC models makes this procedure a valuable adjunct to HF system performance analysis. In this paper, it remains to establish that the computed patterns are valid.

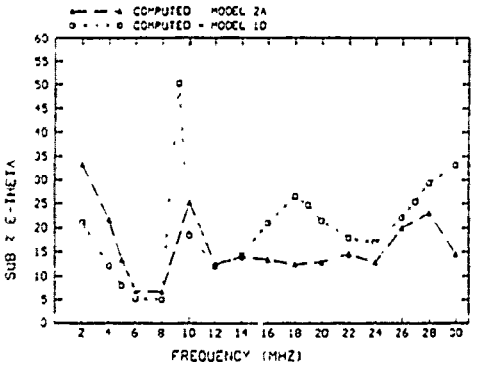
Scale-model radiation pattern measurements were undertaken at the Canadian National Research Council aircraft roof range for comparison and validation purposes[4] and the initial results are summarized.



a) η_p vs Frequency



b) $\%E_\theta$ vs Frequency



c) $\%E_\theta$* vs Frequency

Figure 5 - Parametric Plots vs Frequency - STL and Zig-Zag Antennas

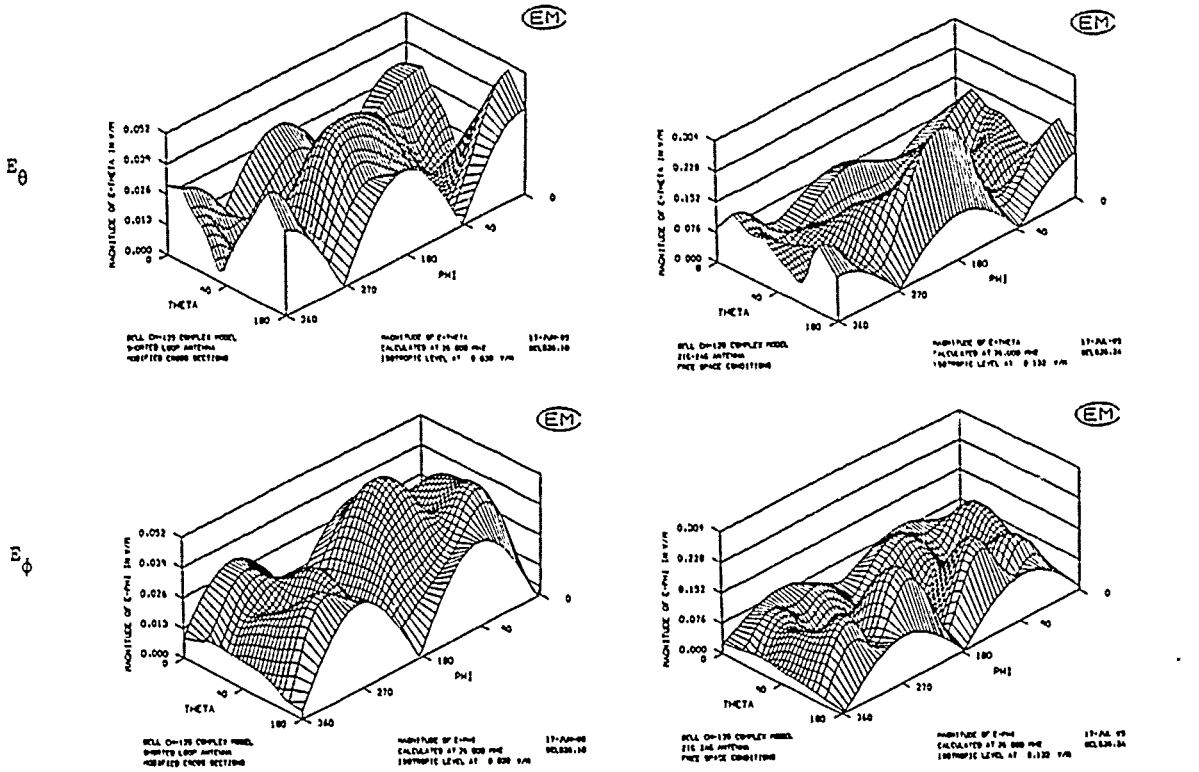


Figure 6 - Volumetric Patterns - 26 MHz

Comparison with Measured Results

A copper-plated aluminum 1/24-scale model of the CH-135/TWIN-HUEY helicopter was constructed by the National Research Council workshops. It is shown in Figure 7 mounted on the model support tower.

A comparison of measured and computed results for 2 MHz is shown in Figure 8. These plots are on a linear scale. Figure 9 shows the volumetric pattern plots. The agreement is fair. Figures 10 and 11 show the results at 8 MHz. Here the results are in very poor agreement. Disagreement of this type poses a most serious dilemna for computer modelling and gives rise to the plethora of doubts about model parameters, segmentation, band-width, interior body resonances, etc. The extent of the disagreement must be methodically identified.

Figure 12 plots the radiation pattern efficiency versus frequency for computed and measured results. It can be seen that there is wide disagreement over extensive frequency ranges. In addition it appeared that the disagreement was more pronounced in the E-theta polarization. Several model stability tests were undertaken by increasing the density of segmentation in selected regions of the helicopter. None produced meaningful results. The field at several point in the interior of the helicopter was computed and found to be very close to zero. In addition the extended boundary condition was incorporated by introducing an interior wire across the fuselage. No significant change was computed.

Measurements at low frequencies(here 48MHz and up) usually give rise to a number of range problems involving ground and site reflections. Self-consistency tests are often an indication of this. This involves verifying that the principal plane cross-over points which involve measurements for different orientations of the measurement antenna,i.e. horizontal or vertical, agree for each of the polarizations. In this case, although some discrepancies were identified, they were insufficient to account for the extent of the disagreement. Rotor modulation studies had shown that the rotor position would have a pronounced effect on radiation patterns at frequencies near 8 MHz., however verification of rotor position during the measurement established that this was not a factor in this disagreement.

After exhausting all other possibilities and examining current distributions on the model, a vertical wire was added to the model at the model support point on the assumption that the model support rod might have been metallic. Metallic rods are often used for heavy at higher frequencies where antennas on the opposite side of the aircraft model are being measured and the rods are not likely to perturb the measurement conditions.

Figure 13 shows the principal plane pattern results. The agreement is very much improved. Figure 14 shows that the corresponding volumetric plots demonstrate the extent of the close agreement. Verification of the measurement conditions confirmed that the rod was metallic. It is believed that using an exact length in the computer model would have improved the agreement further. An examination of the current distributions has indicated that had the rod been used on the bottom of the model, the difference would have been smaller and the consequent more subtle differences would have been extremely difficult to diagnose.

This special example of difficulties has underlined the importance of simultaneous computational and measurement modelling in exploring details of complex body behaviour. In this project, for the sake of completenesss, the radiation pattern measurements are being repeated with a phenolic shaft.

Having established the validity of the model, it is possible to compute other operationally-significant configurations such as the variation of patterns with helicopter altitude.

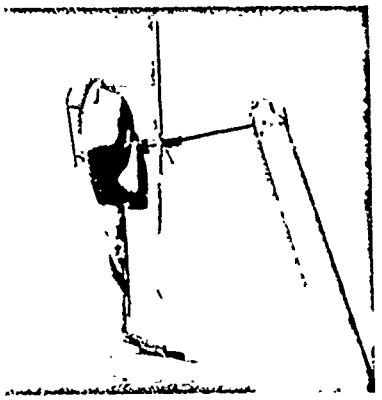
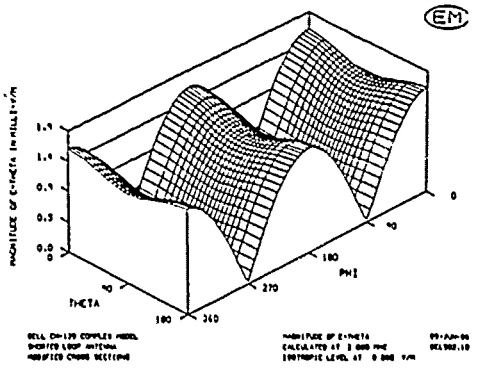


Figure 7 - 1/24 CH-135 Scale Model on Support Tower



Computed

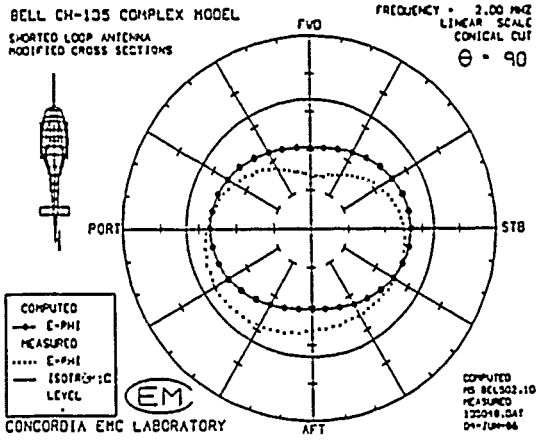
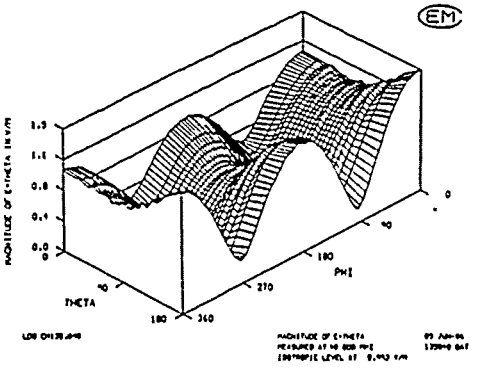


Figure 8 - Computed vs Measured Results
2 MHz, E_θ



Measured

Figure 9 - Computed vs Measured Results
E_θ, 2 MHz, Volumetric Pattern Plots

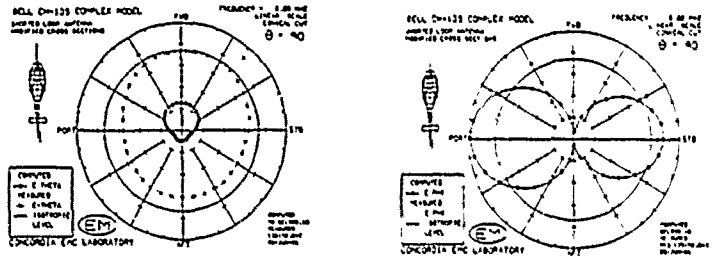


Figure 10 - Computed vs Measured Results - 8 MHz, E_θ,E_ϕ (θ=90°)

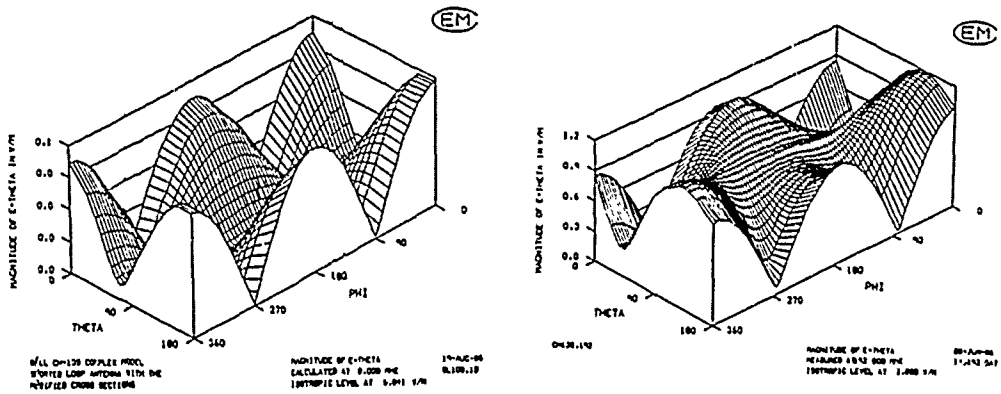


Figure 11 - Computed vs Measured Results, E_θ, 8 MHz Volumetric Pattern Plots

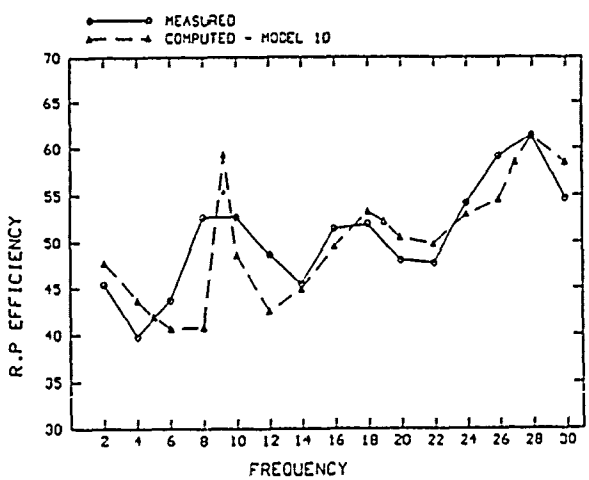


Figure 12 - Measured and Computed η_p vs Frequency STL Antenna

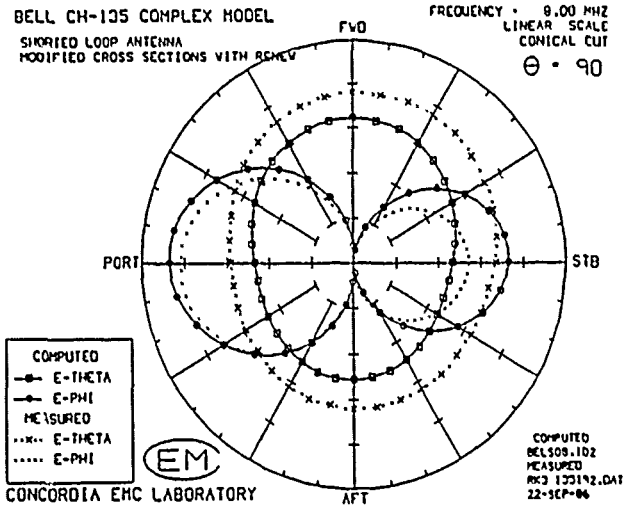


Figure 13 - Computed vs Measured Results - 8 MHz, θ=90°, Adjusted Model

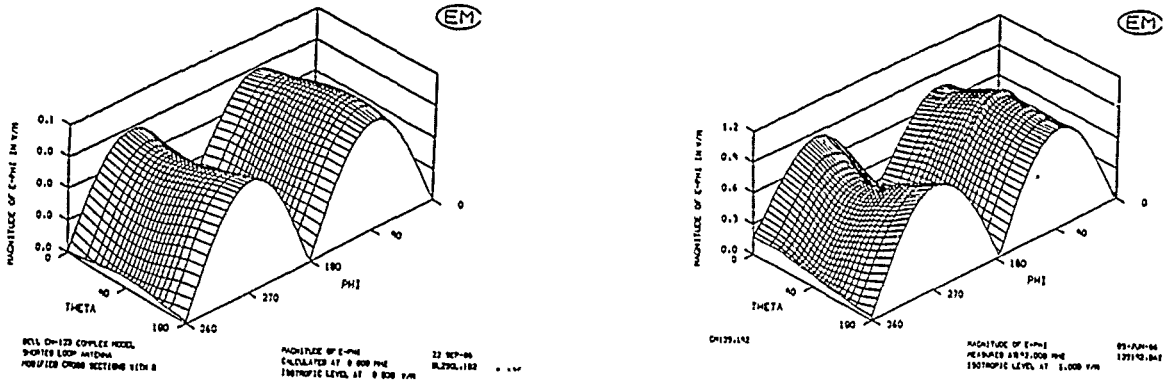
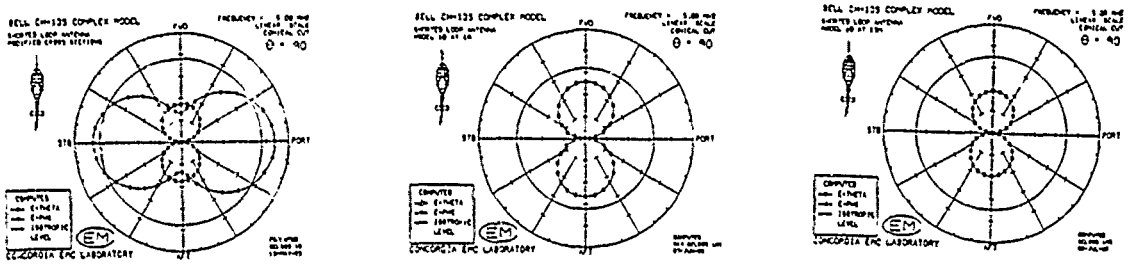
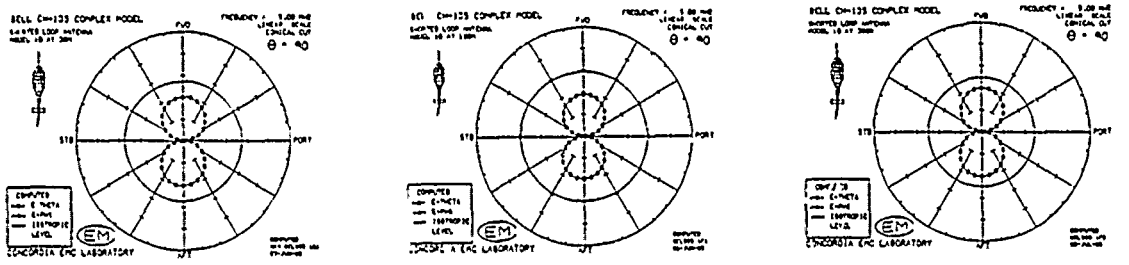


Figure 14 - Computed (Adjusted Model) vs Measured Results, 8 MHz - Volumetric Patterns

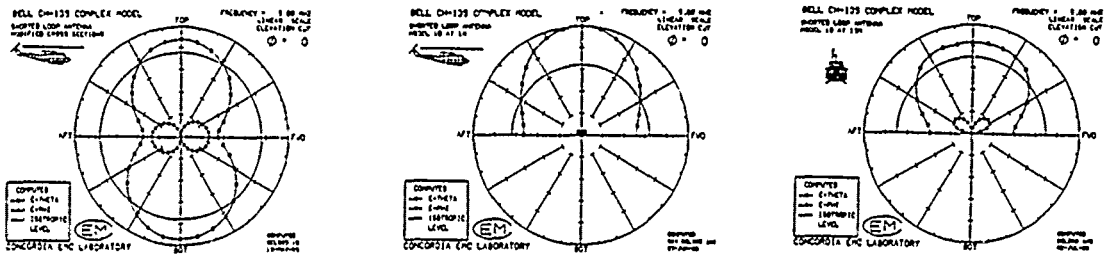


free space 1 m 15 m

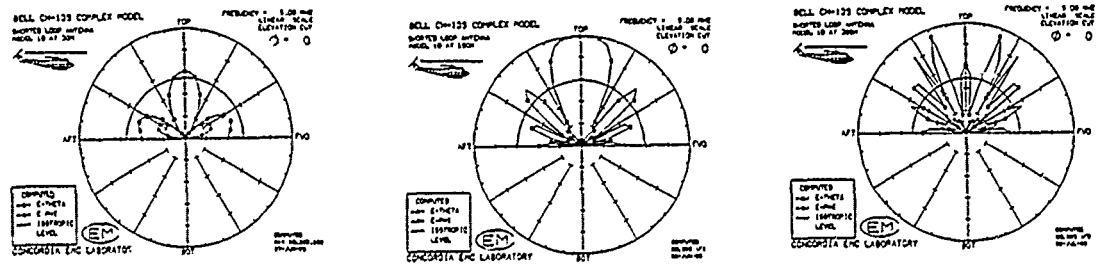


30 m 100 m 300 m

Figure 15 - Pattern Variation with Altitude, $\theta = 90°$, 5 MHz



free space 1 m 15 m



30 m 100 m 300 m

Figure 16 - Pattern Variation with Altitude, $\phi = 0$, 5 MHz

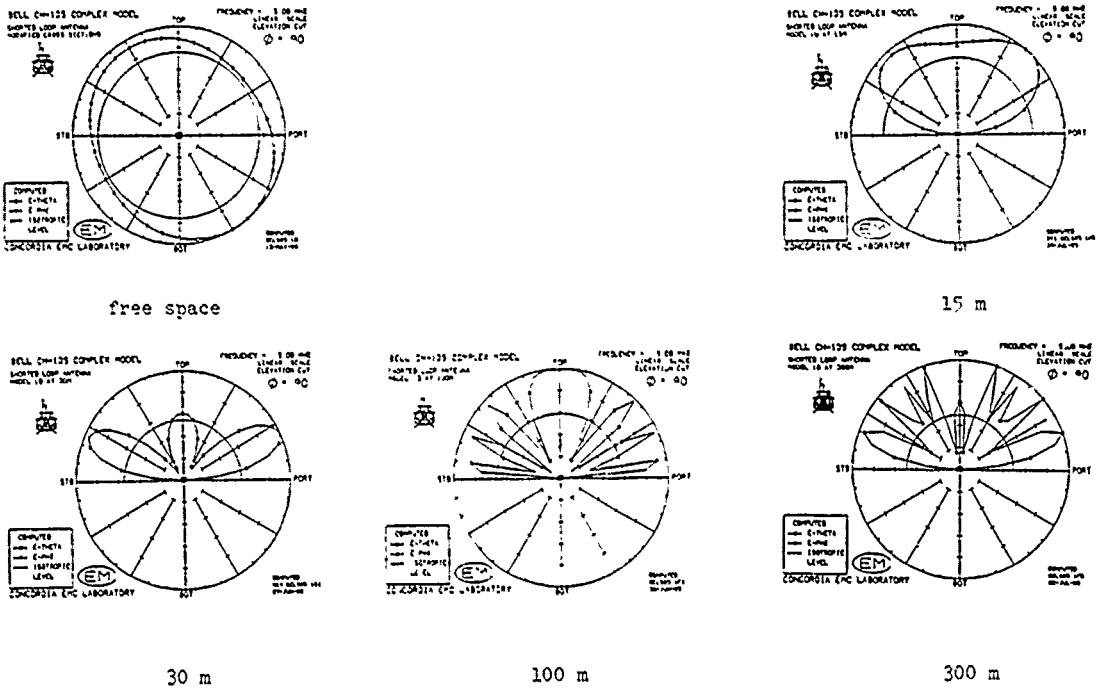


Figure 17 - Pattern Variation with Altitude, $\phi = 90°$, 5 MHz

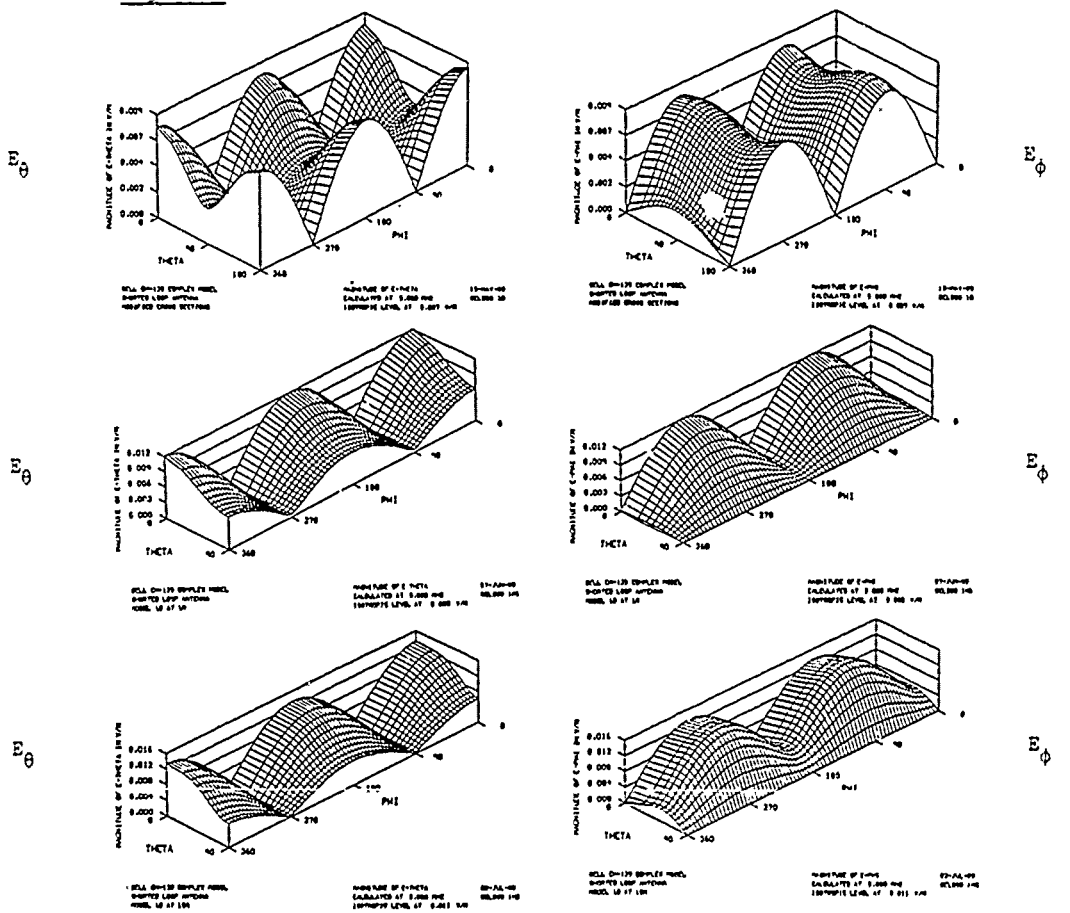


Figure 18 - Pattern Variations with Altitude - Volumetric Patterns, 5 MHz

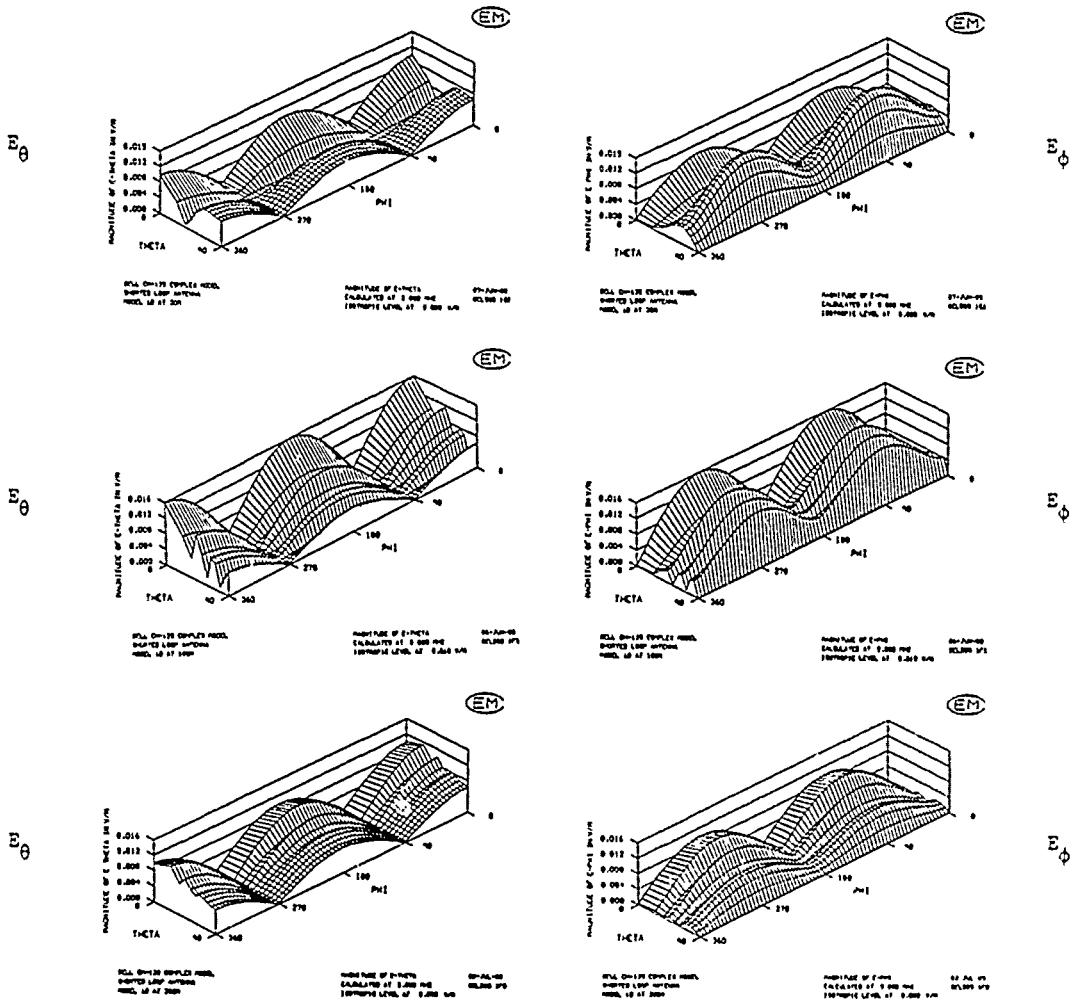


Figure 18 - continued

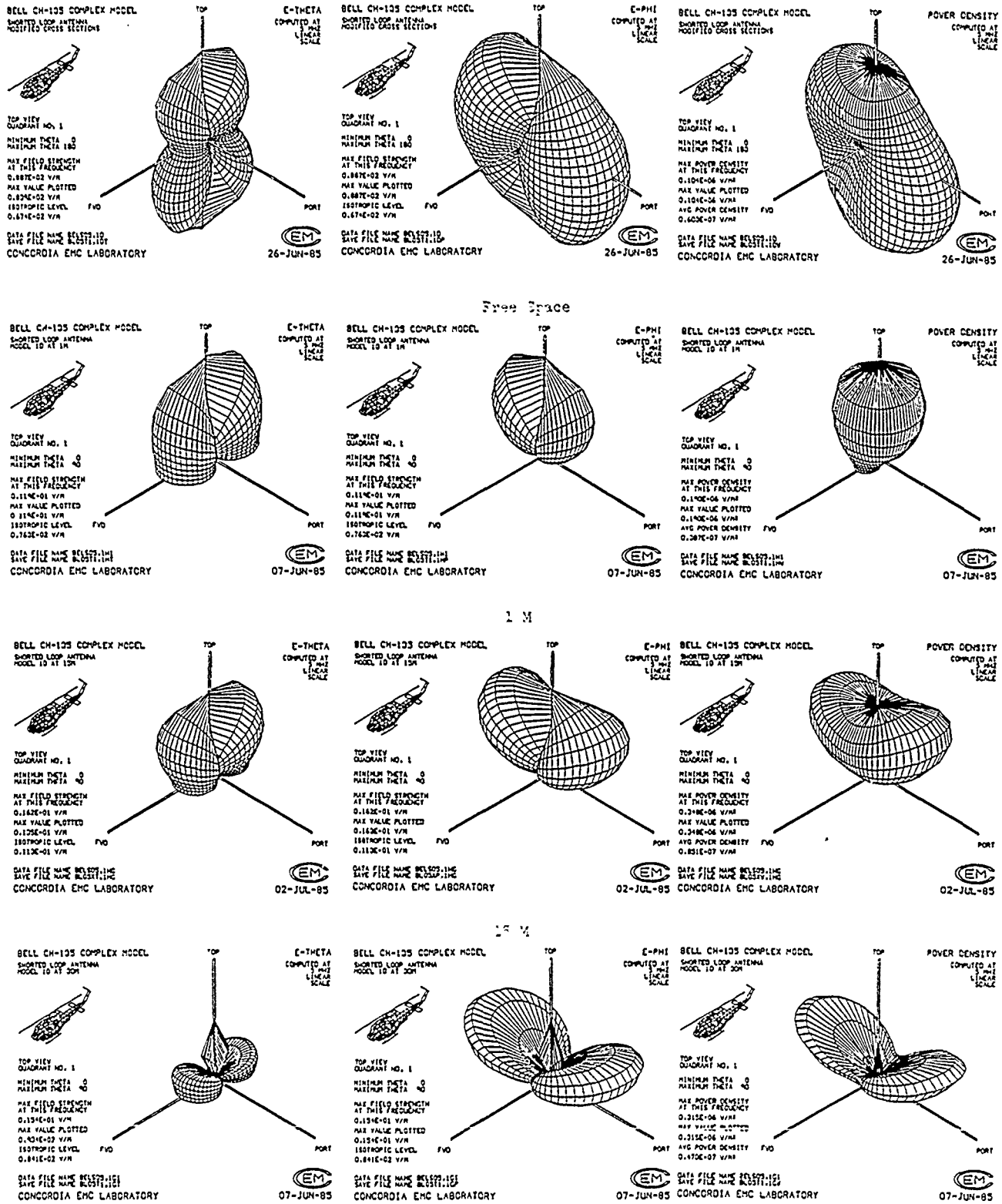
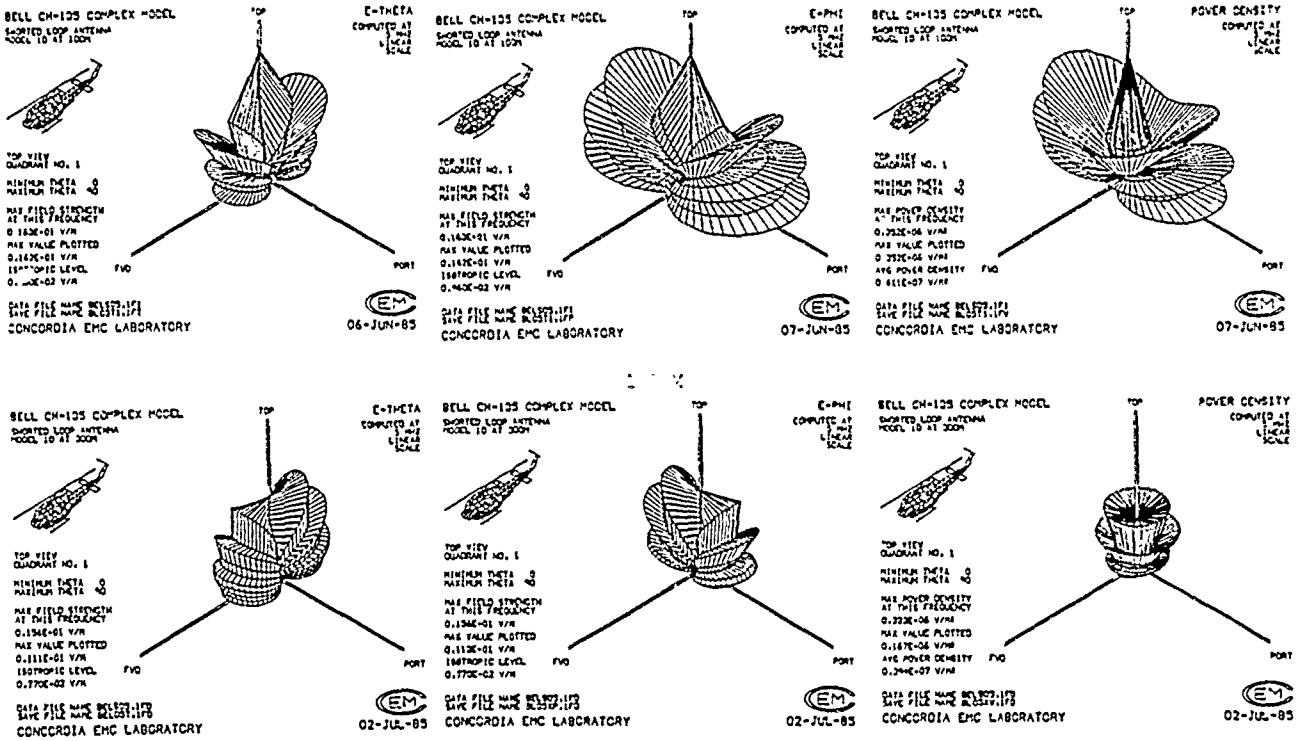


Figure 19 - Three-Dimensional Patterns (TDPAT), 5 MHz



300 M

Figure 19 - continued

Radiation Patterns versus Altitude

Helicopters such as the CH-135 are used on many missions where the use of the HF communications system ranges from line-of-sight, ground wave, sky-wave including high vertical incidence ionospheric propagation. These modes can be exercised while the aircraft is on the ground, hovering at low altitude, in transit altitudes or manoevring at specific nominal altitudes. To identify the antenna contributions to these communications modes, it is necessary to know the radiation patterns under these conditions.

It has been normal practice to measure and compute radiation patterns under free-space conditions alone. Although limited full scale measurements have been carried out, they seldom include the vertical plane distribution. It would be possible to carry out such a measurement with scale models on a ship-range where booms allow vertical plane probing. However there is a limitation to the range of altitudes that can be modelled.

The modelling of the ground plane in NEC and MININEC and GEMACS allows the examination of the radiation patterns versus aircraft altitude. Such computations were carried for the STL antenna at 5 MHz with NEC for heigths, 1,15,30,100 and 300 metres. The results are presented in three different formats, each of which brings out specific features of the resultant patterns.

Figure 15 present the azimuth plane patterns for free space and the various heigths. It can be seen that the E-theta pattern remains unchanged but the levels of E-phi vary as would be expected. The vertical plane principal plane patterns are shown in Figures 16 and 17. Here the formation of the lobe structure is clearly evident and instructive. It now allows the immediate identification of signal level at various elevation angles for ionospheric propagation purposes.

The volumetric patterns, shown in Figure 18 allow the complete conical set to be viewed and provide the missing information with regard to elevation angle disuribution at various azimuth angles.

The three dimensional plots of Figures 19 make the volumetric display more directly comprehensible. The displays of power density are presented for the first time and might be useful for system performance analysis where Faraday rotation effects of the ionosphere cause difficulty in an analysis based on the linear components alone. The nature of the pattern displays make the results easy to interpret by communications operators.

Conclusions

The NEC computer models allow a complete evaluation to be made of the performance of two different antenna types on the CH-135 helicopter. These models have been compared to initial measurements with 1/24-scale model measurements and the discrepancies have been reconciled in terms of the specific measurement conditions. The use of the models to examine the change in radiation patterns with altitude permits a realistic analysis of HF system performance under a variety of flight profiles. Corresponding patterns under conditions of different ground conductivities can be readily computed.

Acknowledgements

This work was supported by the Canadian Defence Research Establishment Ottawa(DREO) under contract No.OST84-00375. The assistance of the technical officers, Dr. David Liang, Mr. Mark Dion and Dr. Prakash Bhartia is gratefully acknowledged. Mr. Colin Larose, Vito Salvaggio and David Gaudine and Victor Phan of the EMC Laboratory participated and contributed significantly to this work. Dr. S. Mishra, and Messrs. R. Balaberda and J. Hazell of the National Research Council of Canada made the scale model measurements possible.

References

[1] Granger, J. V. N. and Bolljohn, J. T. "Aircraft Antennas", Proc. of the I.R.E., Vol.43, No.5, pp.533-550; May 1955.

[2] Wong, J. Y. "Radiation Pattern Efficiencies of Some Suppressed HF Antennas", I.R.E. Transactions on Aeronautical and Navigational Electronics, Vol.ANE-5, No.1; March 1958.

[3] Kubina, Stanley J., Numerical Modelling Methods for Predicting Antenna Performance on Aircraft, AGARD-LS-131, 'Performance of Antennas in their Operating Environment', AGARD October 1983.

[4] Balaberda, R. and Hazell, J., " Radiation Pattern Measurements of a TRANLINE Antenna on a Scale Model of the CH-135 Bell Helicopter" National Research Council of Canada Report ERB-991, July 1986.

NEC2 ANALYSIS OF ARCHEMEDEAN SPIRAL ANTENNA

THOMAS H.B. CRANOR

MCDONNELL DOUGLAS ASTRONAUTICS COMPANY

ST. LOUIS, MO 63166

ABSTRACT

A two-arm, four-turn Archemedean spiral antenna is analyzed by the Method of Moments in the Numerical Electromagnetics Code version two (NEC2). It has been generally accepted that most of the radiation from such antennas occurs from an annular region where the circumference equals the wavelength. Using NEC2 as a soft laboratory, the reliability of this concept as a design tool is tested by an examination of the current distribution along the arms of the spiral and by mapping the near fields in different planes in front of the antenna face. It is found that the current magnitude tapers off well inside the expected radius. The radiation from the inner turns of the spiral contributes to a predicted circularly polarized far field component in the reverse sense from that expected. Measured far-field patterns corroborate this finding. Predicted near-field data does, however show a dominant annular active region but, only in a plane approximately one tenth wavelength from the antenna. Closer range near-field magntiudes follow the tapering current distribution. As a necessary step in the analysis, various forms of graphical presentation are considered in relation to improving ease of interpretation and usefulness of output data.

INTRODUCTION

Since their inception in the 1950's, spiral antennas have become popular for their wide impedance and pattern bandwidth. A number of commercial firms produce planar and non-planar versions of equangular and Archemedean spiral antennas in various forms. In its purest form, the frequency-independent spiral is infinite in extent (fed at the center) and describable in terms of

angles alone [Ref 1]: $r = r_o \exp[a(\phi + \delta_n)]$, where "$r_o$" and "a" determine the wrapping characteristics and the δ_n are offsets giving the angular separation between the edges of the arms. In practice, however, the currents taper off with radius in such a way that the circumference of the spiral need not be much larger than the longest wavelength in the desired bandwidth of operation. The Archemedean spiral has similar performance characteristics, but is described by: $r = a(\phi + \delta_n)$. The conductors therefore, have a constant width and separation. Several authors [Ref 2, 3 and 4] have refered to an annular "active region" of spirals, where the radiated fields emanate. It has been said [Ref 3] that in the active region, the incremental current dipole at one point on a given arm is correctly aligned and in phase with the corresponding current element on the opposite side (Figure 1). The phase of the inverted dipole is accounted for by the half wave arc length along the spiral arm. At a physical angle of 90° away from this pair is a second pair also 90° different in phase. This plus the continuum of infintesimal elements rotated and phase shifted along the arm accounts for the circular polarization known to radiate from such antennas. The existance of this active region and its implied radiating current distribution were inferred from near-field measurements. To the author's knowledge, no current distribution for Archemedean spiral antennas has been published. The object of this work is to examine the current distribution using NEC2 in relation to the current distribution associated with the active region concept.

NEC2 MODEL OF SPIRAL ANTENNA

The Numerical Electromagnetics Code version 2 (NEC2) is a software package developed by Lawrence Livermore National Laboratories [Ref 5] wherein closed surfaces and wire segment structures are modeled with or without the presence of a ground plane in a variety of user-defined configurations. The analysis utilizes the Method of Moments (MoM) [Ref 6] and is accurate, in principal, to the extent which the input data follows the physical structure. The fundamental building blocks for the model are short straight wire segments and flat surface patches.

Since surfaces in NEC2 must be closed (due to the MFIE formulation used for calculating surface currents [Ref 5, & 6], a wire segment model is used to model the spiral. The particular spiral modeled has two-arms and four-turns on each given by

$$r = \begin{cases} a\phi + r_o, \; 0 \leq \phi \leq 8\pi, \text{ arm 1} \\ a(\phi-\pi) + r_o, \; \pi \leq \phi \leq, \; 9\pi \text{ arm 2} \end{cases}$$

with $a = 1.262\text{mm/rad}$

$r_o = 2.54\text{mm}$

maximum radius, $r_{max} = 8a\pi + r_o = 34.25\text{mm}$

The physical dimensions have no special significance other than that they were chosen to coincide with a specimen available in the laboratory and time has not yet permitted fabrication using other parameters, though such work is planned in the future. The nominal operating bandwidth predicted by the active region criterion is from about 1.4 GHz to 18.8 GHz or a wavelength range of about 215mm to 16mm respectively. The segments used to represent wire structures in MoM should be on the order of a tenth of a wavelength long or less in order to adequately account for variations in the current distribution along the structure. Figure 2 shows the spiral as it is segmented for input into NEC2. In order to conform to the sharper curvature of the spiral arms near the center, somewhat shorter segments are used there than towards the edge. Thus, the model segment lengths range from 3.40mm to 4.96mm and the expected frequency bandwidth of validity for the model is from 90 MHz to 6 GHz, the lower cutoff frequency being due to numerical precision problems [Ref 5]. This provides sufficient bandwidth for our purposes here, yet keeps the number of segments (197) at a manageable level. The feed is modeled as a segment connecting the two arms together with a voltage source at the center. The antenna is assumed to operate in a free space enviornment and should radiate with right-hand circular polarization in the forward (+z) direction.

RESULTS

The NEC2 output consists of printed tables of data. To make it more digestable, graphical forms are used for observation and presentation. Figures 3 and 4 give a current distribution as calculated by NEC2 typical of those in the operating band. The expected radiation zone is at $r = "r_c" = 18.5mm$ for the frequency of 2.585 GHz. Note that the current magnitude begins to roll off almost immediately beyond the feed point. This is a departure from what one would expect from the active region concept; that the current would hold a fairly constant amplitude along the inner turns and then roll off in the vicinity of $r = r_c = \frac{\lambda}{2\pi}$ where it should radiate. The fact that the current decays along the arm from nearly the beginning suggests that the inner portion of the spiral contributes significantly to the radiated energy. That this is, indeed the case is also suggested by the presence of opposite sense circularly polarized energy in the far field shown in Figure 5. Apparently, the cross-pol component is substantially due to the lack of 360° phase continuity around the shorter inner turns since the residual current in the outer turns beyond the $r = r_c$ point is so much weaker than the current on the inner terms. A far-field pattern from a spiral with an assumed linearly decreasing current approximating the distribution predicted by NEC2 on the inner turns, but with no reflection is given in Figure 6 for comparison. The assumed current distribution is shown in Figure 7. A measured far-field pattern is shown in Figure 8. The antenna was mounted in front of (but not on) a block of graded absorber to hide the feed. For aspect angles near the plane of the antenna, the absorber attenuates and diffracts the pattern, but within 60° or so of boresight, the measured data supports the predictions made by NEC2. The similarity of all three patterns lends credence to the idea that most of the current radiates before reaching the $r = r_c$ point and the reflected current is not a dominant factor in the far field.

Figures 9, 10, and 11 give the near field real radiated power, $\frac{1}{2}\mathrm{Re}[\overline{E} \times \overline{H}^* \cdot \hat{z}]$, at a distance of ten millimeters (roughly one tenth wavelength) in front of the antenna. Note the annular region at about $r = 12mm$. One millimeter in front of the antenna, Figures 12, 13 and 14 show that the

tangent RHCP E-fields, $.707\mathrm{Re}[E_x + jE_y]$, follow the current distribution. Farther away from the antenna, a quarter wavelength for example, the near fields merge into a smooth taper with a maximum at the center (Figures 15, 16, and 17).

DISCUSSION

It is interesting to note that, although the current distribution tapers along the spiral arm, there is still an apparent annular active region when the fields are sampled at close, but not too close range. Another point to note is that the radius of the annulus is smaller than would be expected. The phase shift along the spiral arm is fairly linear inside $r = r_c$ but the propagation constant implied by its slope is about 2.88 deg/mm whereas the expected value is 3.10 deg/mm. This discrepancy in phase velocity might be expected to increase the radius of the annular region; instead, it is decreased. The reasons for these anomalies are not clear at present but will be the subject of future work.

CONCLUSION

The study of the Archemedean spiral antenna has been an interesting and educational way to become acquainted with the NEC2 software package. Graphical processing of the output data has proven indispensible in interpreting results. It has been shown to a fair degree of realiability that the annular active near field region mentioned in the literature is not incompatible with a current distribution that tapers away from the feed point. From the practical point of view, the value of understanding the current distribution lies in development work such as changing the geometry of the inner region to facilitate alternative feed techniques, mitigating cross-pole contamination or making the structure more compact.

REFERENCES

1. Stutzman, W. L. and Theile, G. A. Antenna Theory and Design pp 281-287 John Wiley and Sons 1981

2. Dyson, J. D., "The Characteristics and Design of the Conical Log-Spiral Antenna," IEEE Transaction on Antennas and Propagation: pp 488-499 1965

3. Milligan, T. A. Modern Antenna Design, p 374 McGraw Hill 1985

4. Skinner, P. and Terzwoli, A. J. "A Moment Method Solution to Spiral Antenna Radiation" Proceeding of the 1984 Antenna Applications Symposium (pages not numbered w.r.t. book: article appears at about middle)

5. Burke, G. J. and Poggio, A. J. Numerical Electromagnetic Code (NEC) - Method of Moments Naval Ocean Systems Center 1977

6. Harrington, R. F. Field Computation by Moment Methods Robert E. Krieger Publishing Co. 1985.

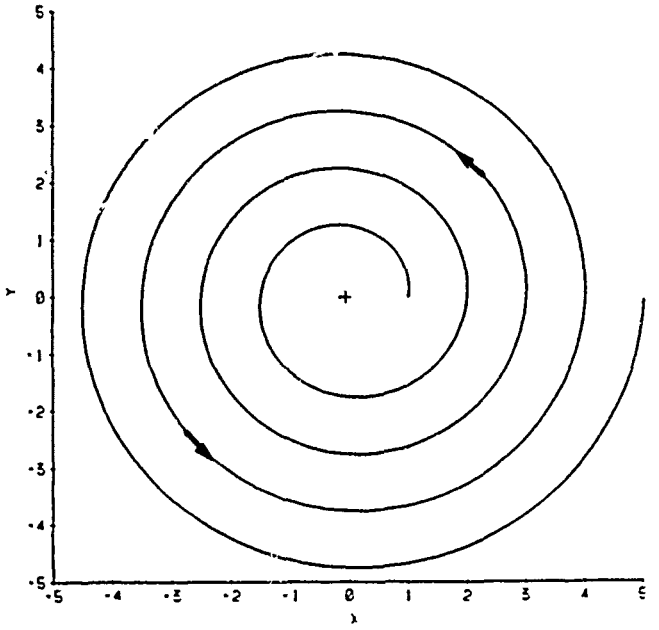


FIGURE 1. INCREMENTAL DIPOLE CURRENT ELEMENT LOCATED ON OPPOSITE SIDES OF SPIRAL ARM

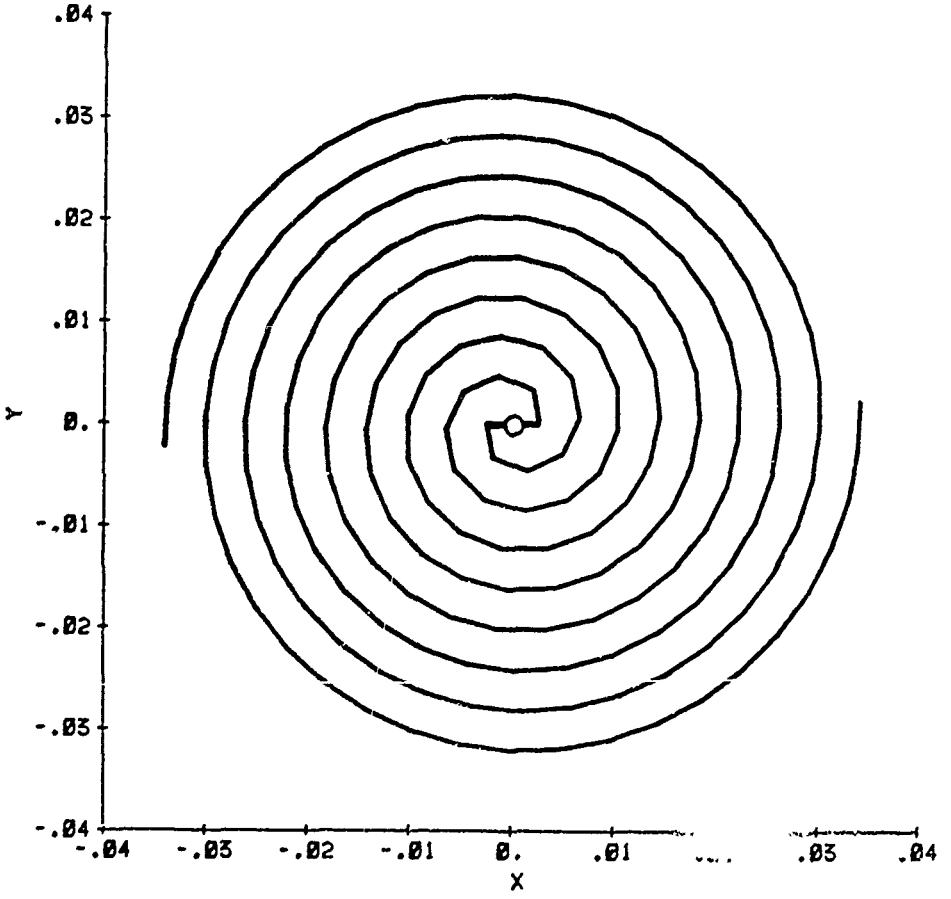
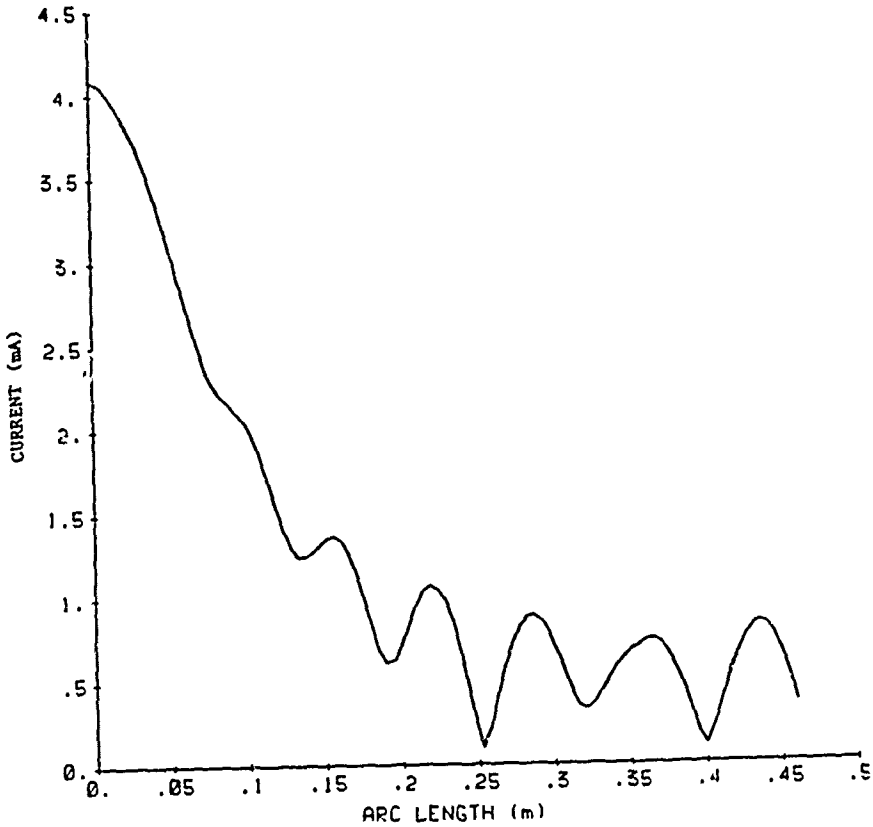


FIGURE 2. SEGMENTATION OF 4-TURN ARCHEMEDEAN SPIRAL FOR INPUT INTO NEC2



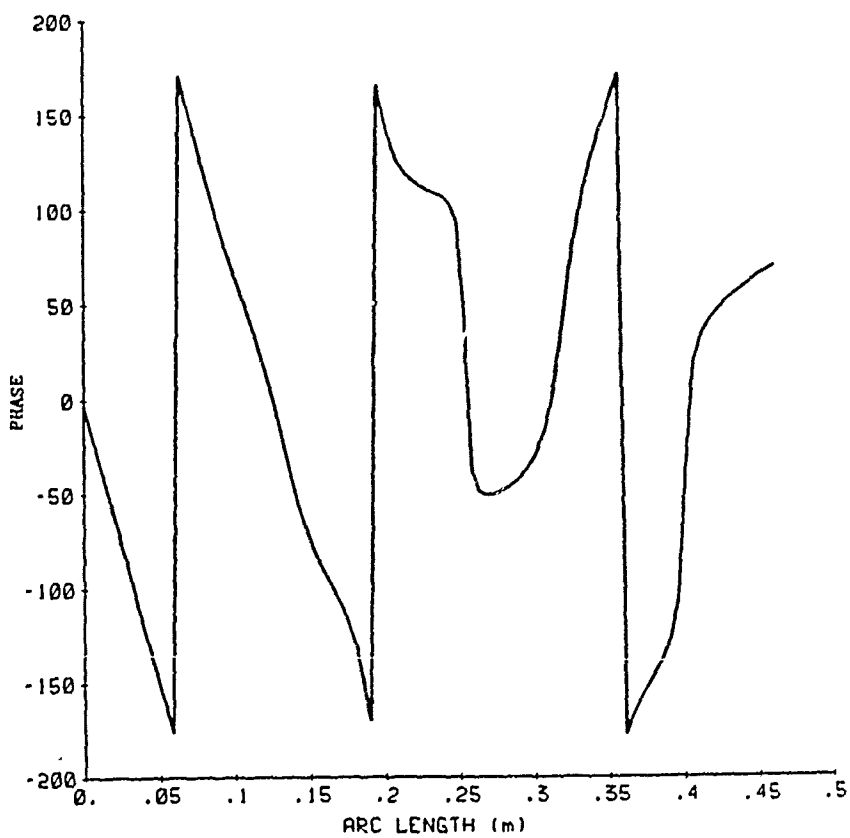
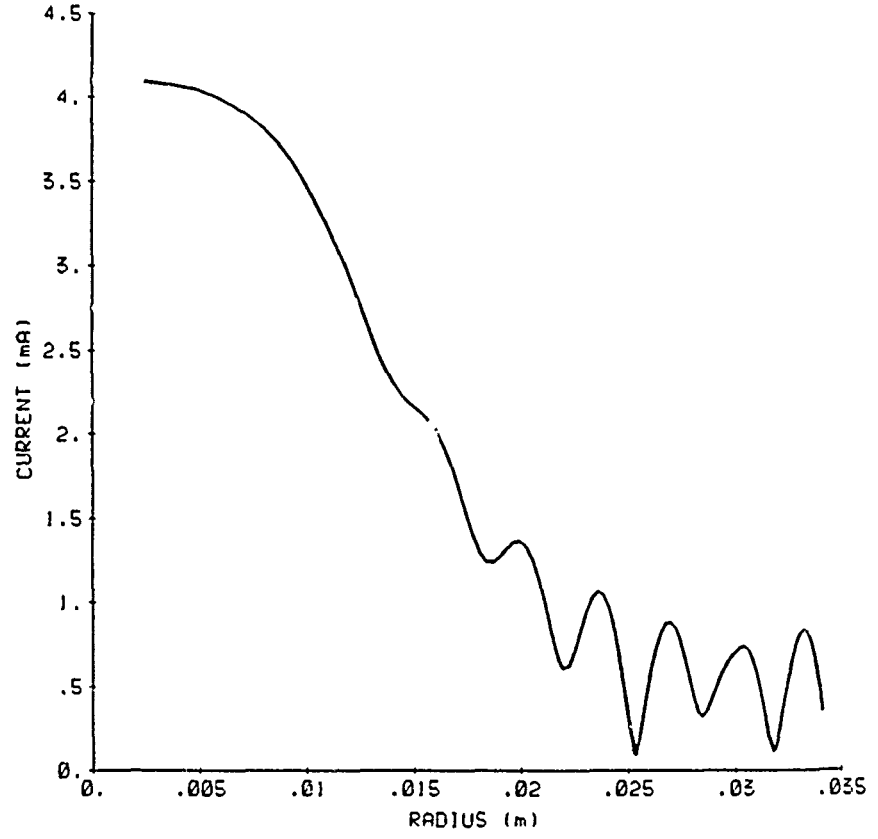


FIGURE 3. CURRENT DISTRIBUTION (a) MAGNITUDE AND (b) PHASE AS A FUNCTION OF ARC LENGTH ALONG SPIRAL ARM



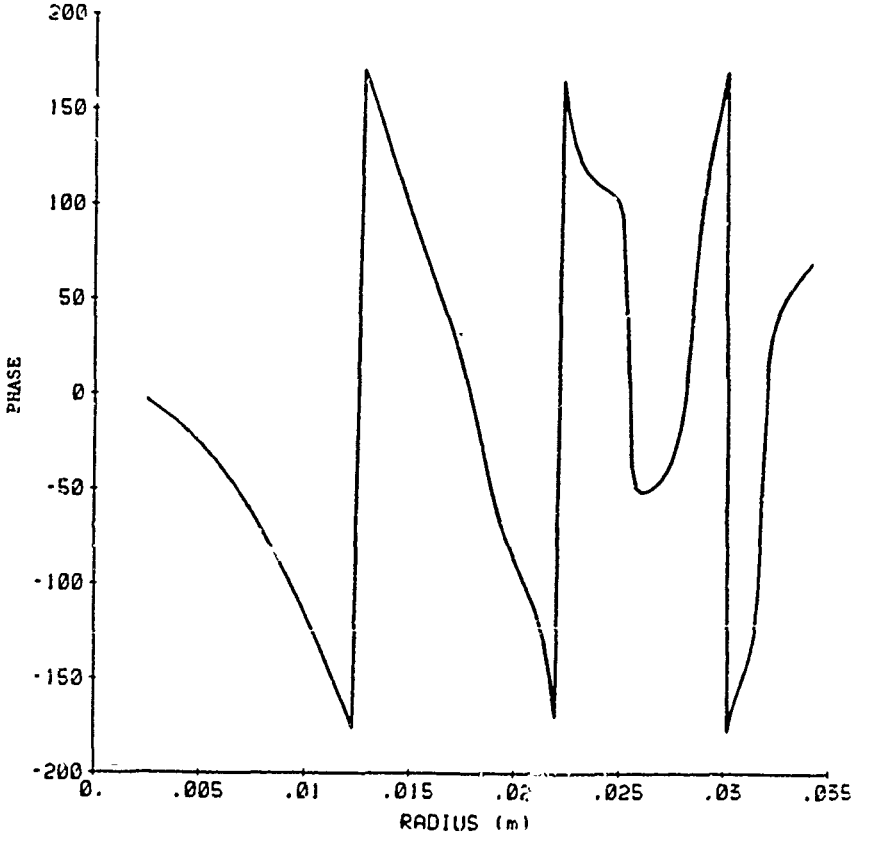


FIGURE 4. CURRENT DISTRIBUTION (a) MAGNITUDE AND (b) PHASE A FUNCTION OF RADIUS FROM THE CENTER OF THE SPIRAL

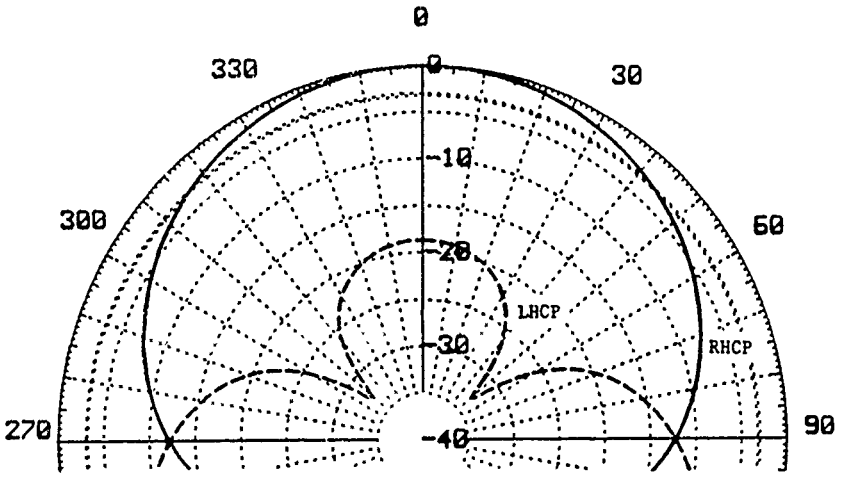


FIGURE 5. RADIATION PATTERN OF SPIRAL AS PREDICTED BY NEC2

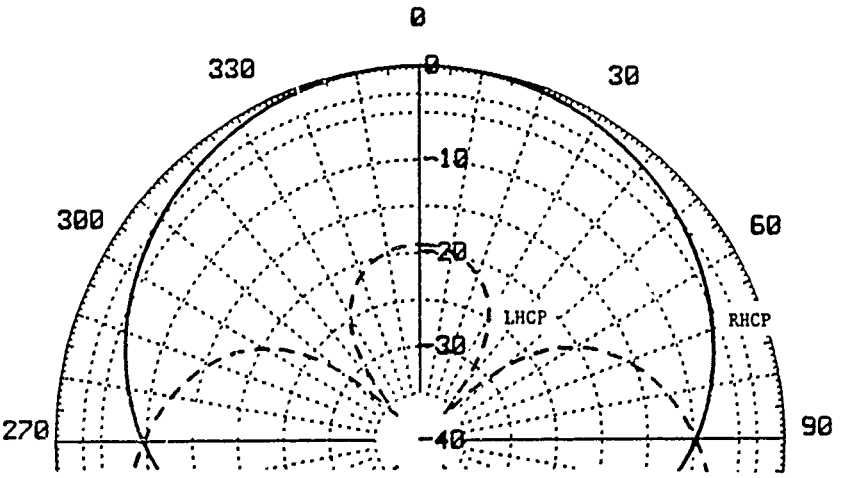


FIGURE 6. RADIATION PATTERN OF SPIRAL USING LINEAR APPROXIMATION TO NEC2 CURRENT PREDICTION WITH NO REFLECTED CURRENT

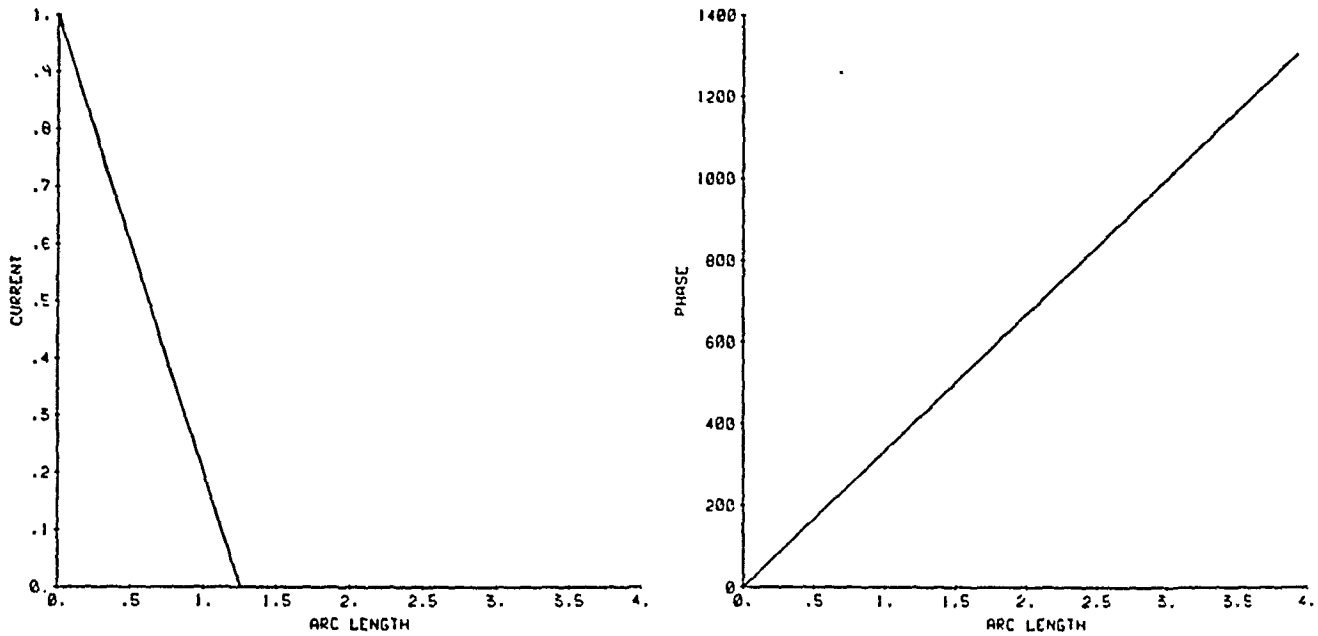


FIGURE 7. LINEAR APPROXIMATION CURRENT DISTRIBUTION USED IN FIGURE 6

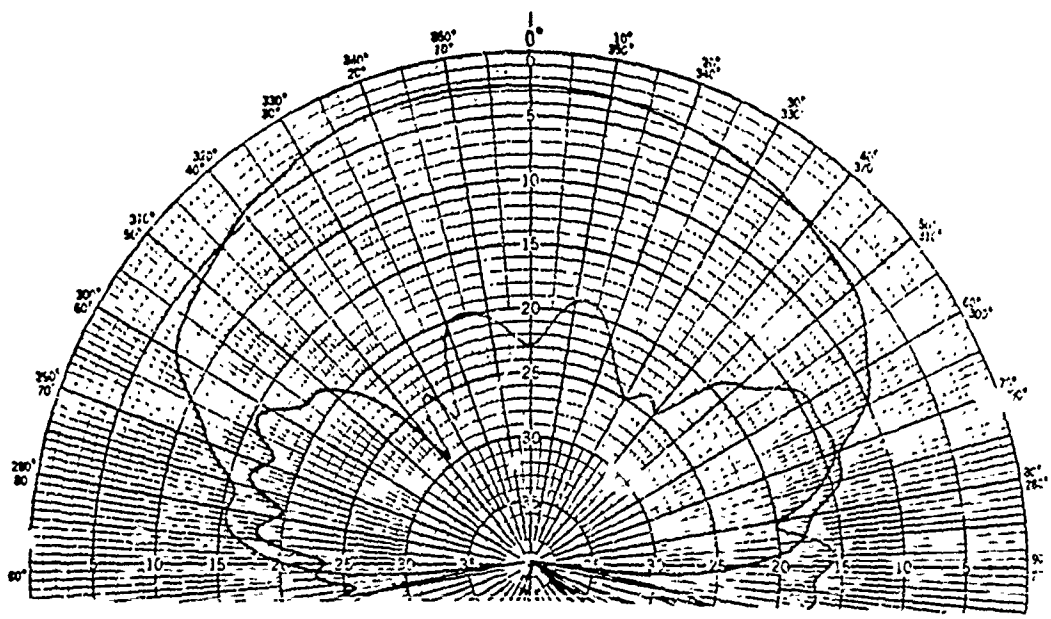


FIGURE 8. MEASURED RADIATION PATTERN OF SPIRAL MOUNTED OVER ABSORBER TO HIDE FEED NETWORK

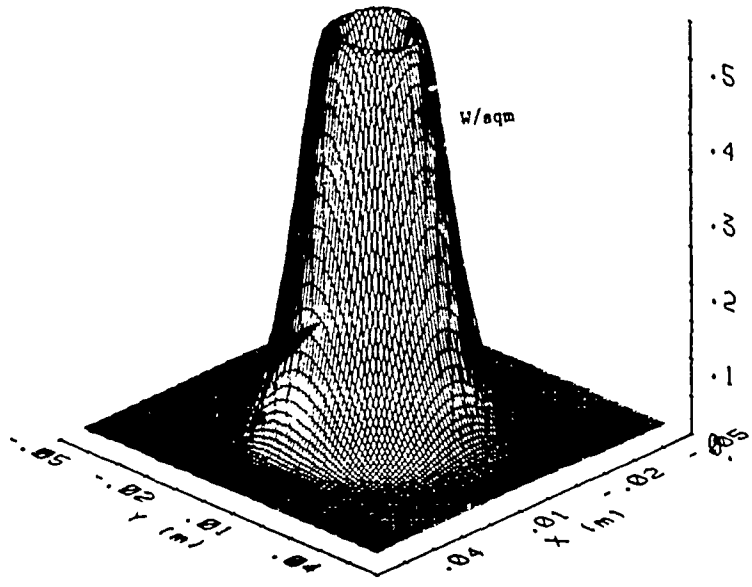


FIGURE 9. REAL RADIATED POWER 10mm (ROUGHLY ONE TENTH WAVELENGTH) IN FRONT OF ANTENNA; 3-D SURFACE PLOT

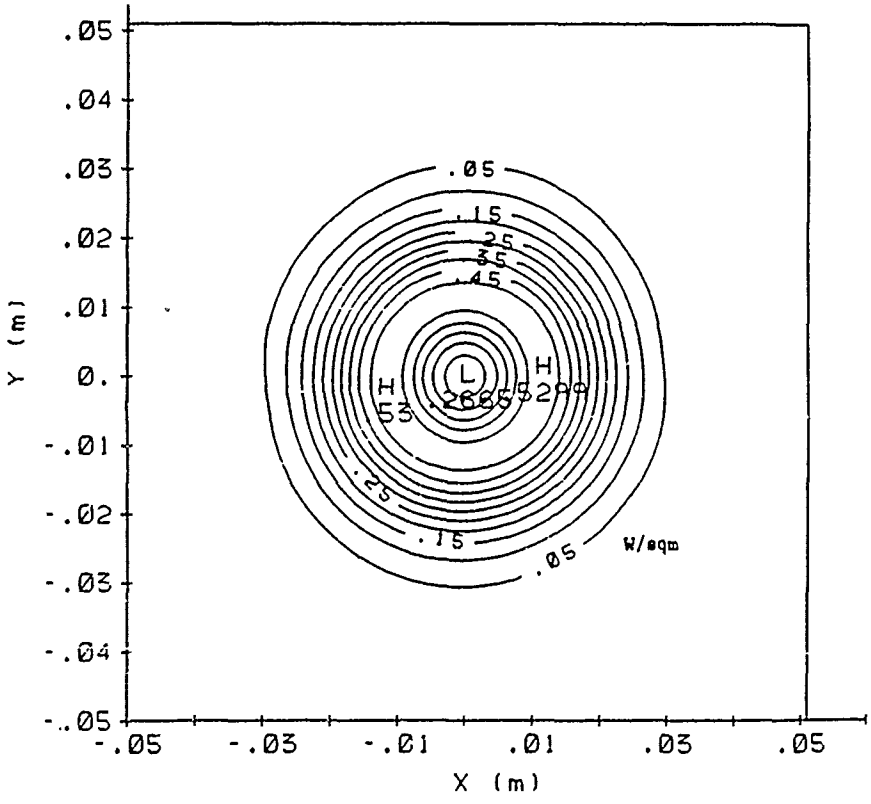


FIGURE 10. REAL RADIATED POWER 10mm (ROUGHLY ONE TENTH WAVELENGTH) IN FRONT OF ANTENNA; CONTOUR PLOT

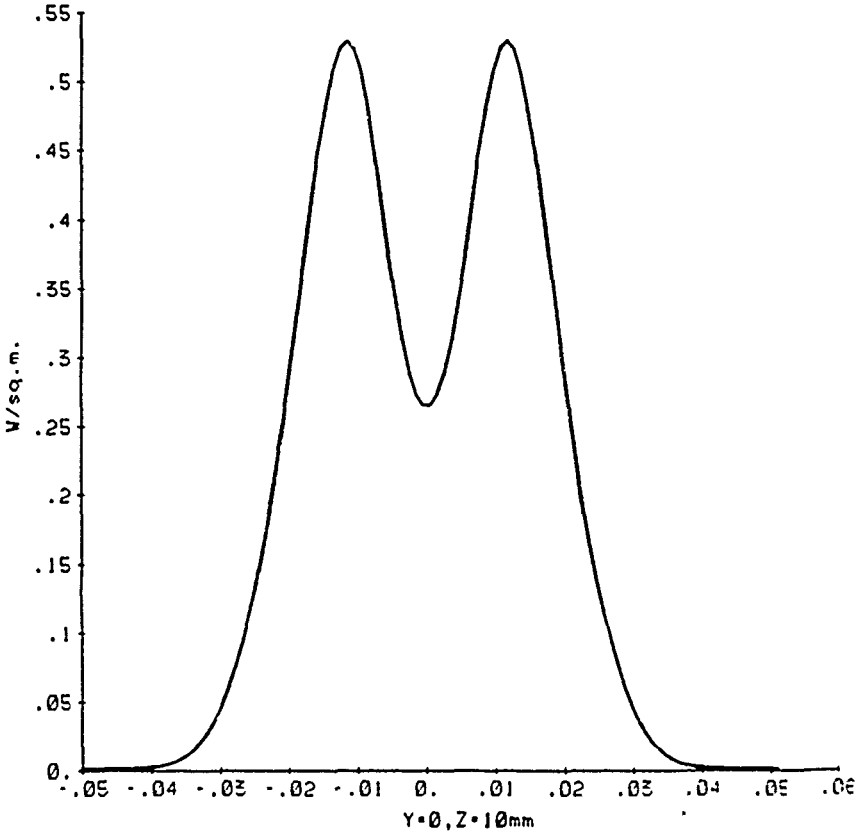


FIGURE 11. REAL RADIATED POWER 10mm (ROUGHLY ONE TENTH WAVELENGTH) IN FRONT OF ANTENNA; CROSS SECTION SLICE ALONG X-AXIS

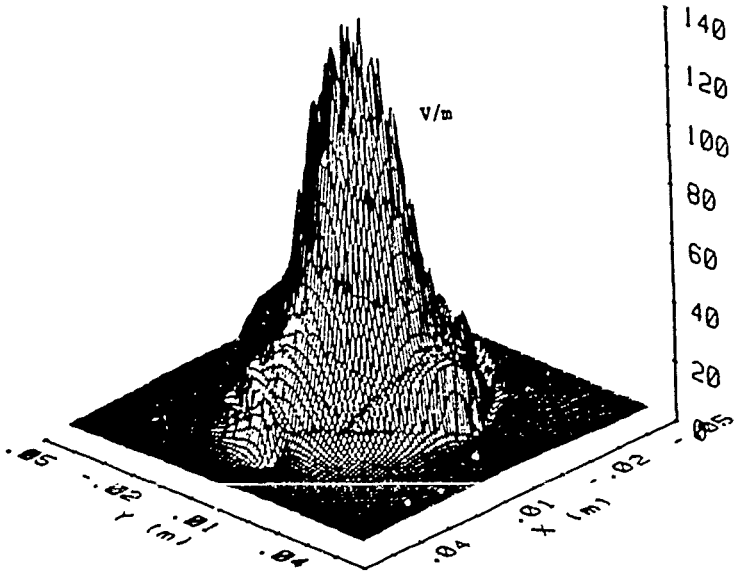


FIGURE 12. RIGH-HAND CIRCULAR E-FIELD 1mm IN FRONT OF ANTENNA; 3-D SURFACE PLOT

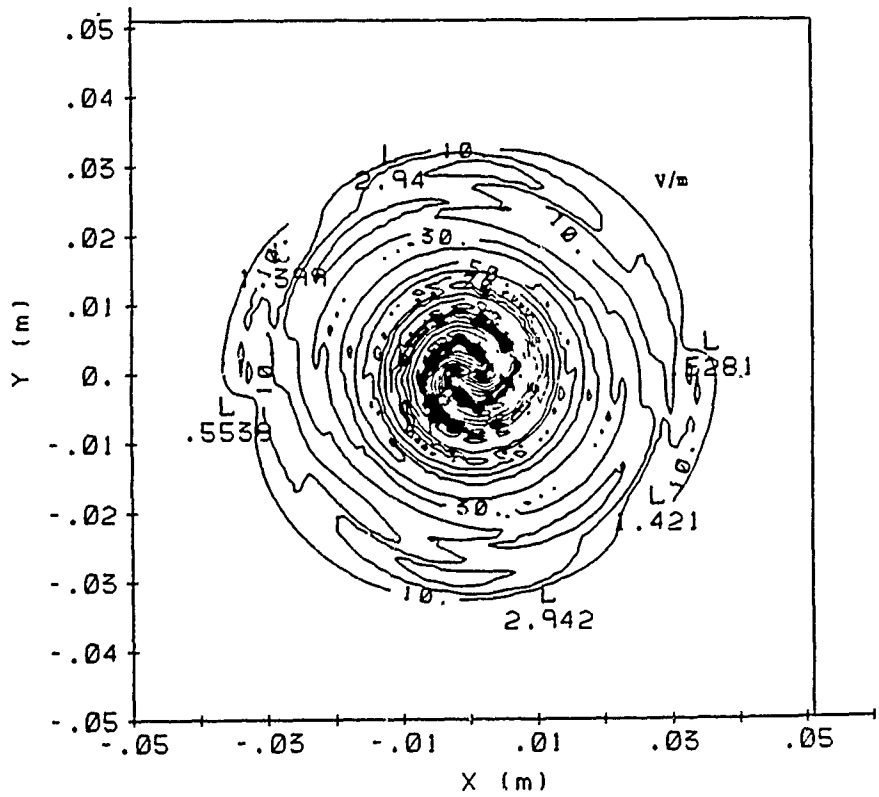


FIGURE 13. RIGHT-HAND CIRCULAR E-FIELD 1mm IN FRONT OF ANTENNA; CONTOUR PLOT

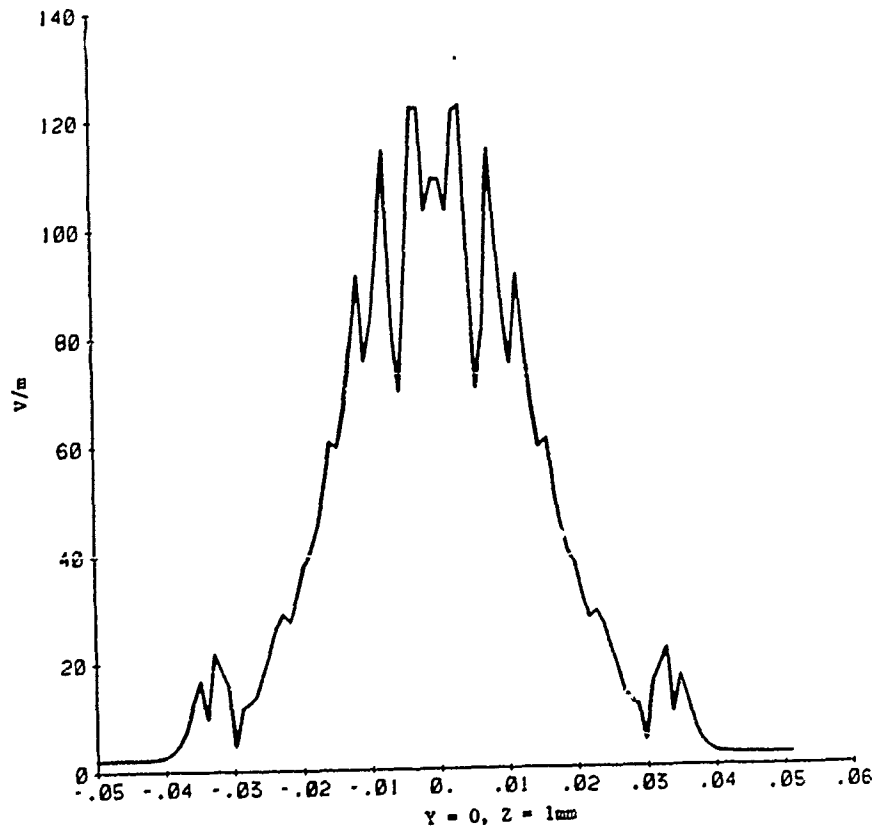


FIGURE 14. RIGHT-HAND CIRCULAR E-FIELD 1mm IN FRONT OF ANTENNA; CROSS SECTIONAL SLICE ALONG X-AXIS

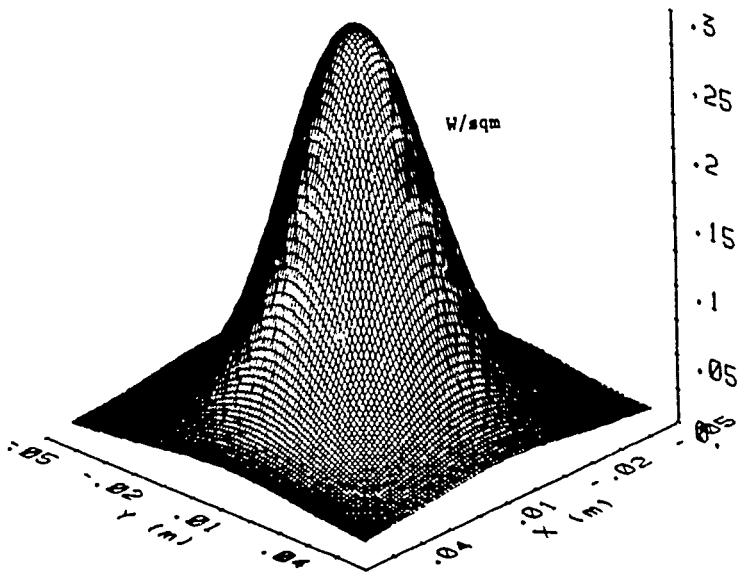


FIGURE 15. REAL RADIATED POWER 29mm (ROUGHLY ONE QUARTER WAVELENGTH) IN FRONT OF ANTENNA; 3-D SURFACE PLOT

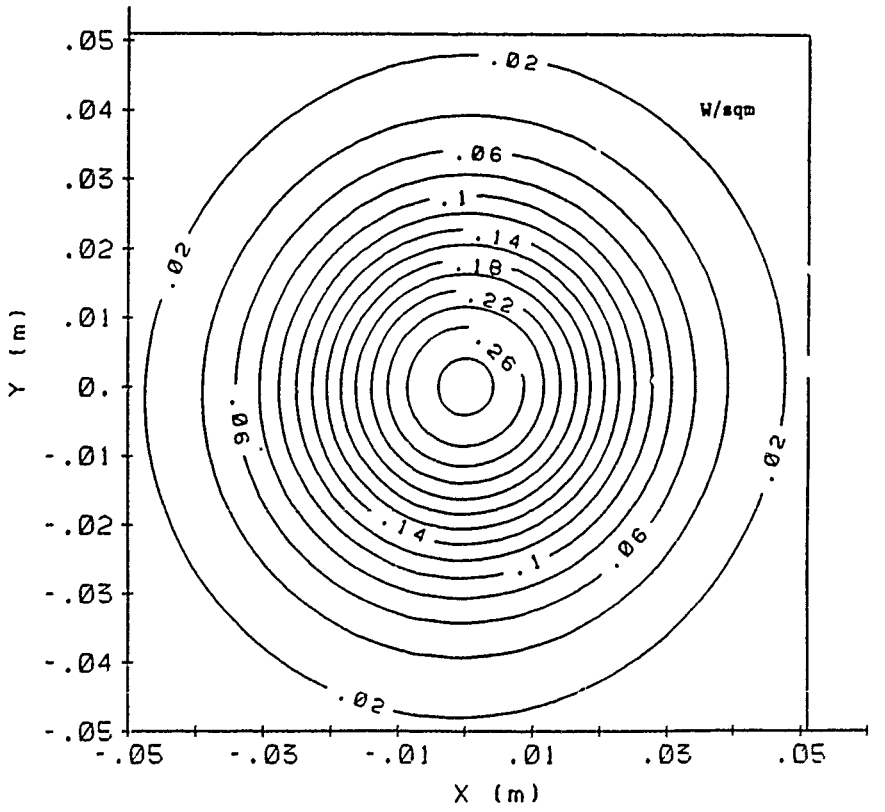


FIGURE 16. REAL RADIATED POWER 29mm (ROUGHLY ONE QUARTER WAVELENGTH) IN FRONT OF ANTENNA; CONTOUR PLOT

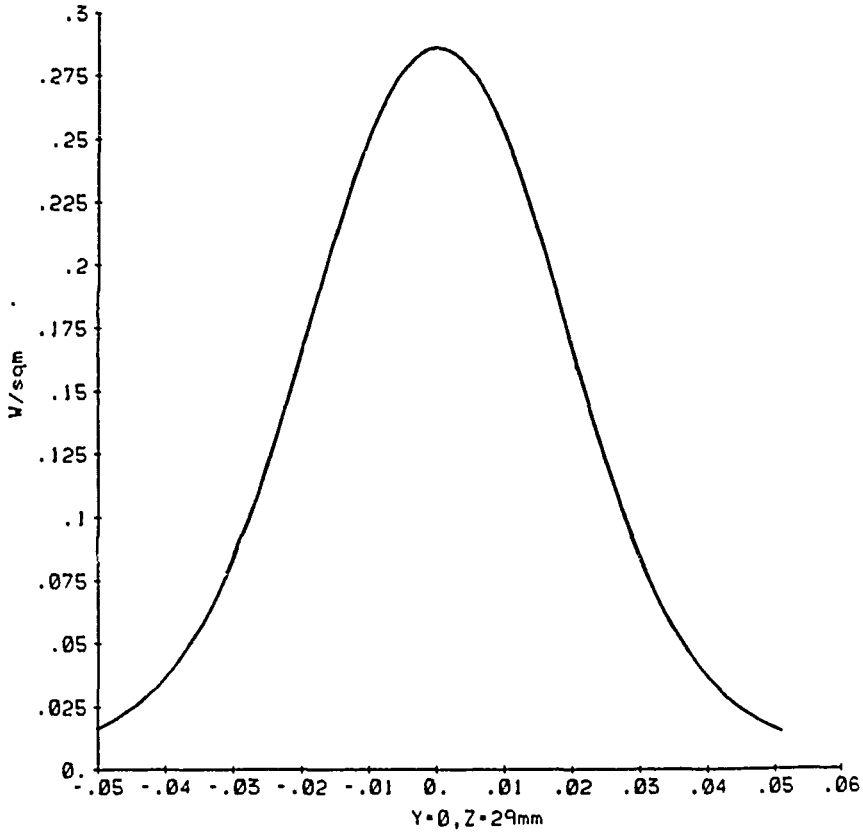


FIGURE 17. REAL RADIATED POWER 29mm (ROUGHLY ONE QUARTER WAVELENGTH) IN FRONT OF ANTENNA; CROSS SECTIONAL SLICE ALONG X-AXIS

FINITE AND INFINITE BROADSIDE SCAN DIPOLE ARRAYS*

H.K. Schuman and T.J. Cleary
Atlantic Research Services Corporation
1721 Black River Blvd.
Rome, NY 13440

Abstract

A recent analysis with the NEC moment method computer program has shown that the mutual coupling inherent in a small planar dipole array can, even for broadside scan excitation, result in a negative real part for the active impedance of the center element over a significant bandwidth [1]. This result is confirmed. Also it is shown with a plane wave expansion moment method computer program that the corresponding infinite array does not exhibit unusual broadside scan active impedance behavior such as the zero resistance indicative of array 'blindness'. An approximation to the very large, but finite, array case is developed as well and applied in a study of active impedance as a function of array size. As an aside, a possible deficiency with NEC in modeling very short dipoles is uncovered.

1. Introduction

Phased array antennas often are under consideration for use in radar systems, especially those calling for rapid beam steering and stringent pattern control. Space-based radar (SBR) surveillance and tracking applications, in particular, call for such attributes.

Key technologies in realizing SBR phased array antennas are associated with the development of lightweight, inexpensive, phase shifters (usually one per array radiating element) that can be adjusted to effect feed focusing, beam steering, membrane surface distortion compensation, and pattern nulling in directions of strong interference. Satisfactory performance of such phase shifters depends, in part, on the RF load (impedance) that the radiating elements impart on the phase shifters.

The impedance of an element in an array usually is quite different from that of an isolated element because of the mutual coupling contributions from other elements in the array. A recent presentation [1] has shown that small arrays of near resonant dipoles of typical interelement spacings can result in

*This work was supported by USAF Contract F30602-85-C-0295.

the active impedance (impedance with all elements excited) of the center element to have a negative real part over a band of frequencies even for the elements phased for broadside radiation. The negative active resistance is indicative of strong mutual coupling phased to cause net power to flow into the center element source rather than out of it. The results were obtained with the Numerical Electromagnetic Code (NEC) computer program [2]. The NEC program has been widely used and proven to be accurate and reliable for many problems of interest. The program is based on a moment method technique that, in the array case, accounts for all mutual coupling between the radiators.

The NEC program, in practice, is limited to relatively small arrays because of the rapid increase in computer run time with increase in array size. Thus large arrays were not included in the study reported in [1]. It was speculated at the presentation of [1], however, that the negative center element input resistance would, as the array were increased in size to approach an infinite array by continually adding identical elements at the same lattice spacings, approach zero which is indicative of large array 'blindness' reported elsewhere [3]. Large (or infinite) array blindness for broadside excitation was never experienced before.

This paper describes an investigation into the possibility of such a result. The investigation was performed by applying a technique for accurately computing the active impedance of infinite, planar arrays to the dipoles and lattices of the finite arrays discussed above. The technique was based on a plane wave expansion moment method described in [3].

Following this, a method for approximating the center element impedance of large finite arrays is described. Although only an approximation, the method is very efficient. It can be applied reasonably to arrays of millions of elements as well as smaller arrays. It is shown to yield reasonable results. The method is applied here to a study of the center element impedance as the array is made progressively larger.

2. Finite and Infinite Broadside Scan Arrays

A 9 element dipole array is shown in Figure 2-1. A 5 element array is indicated as those elements within the dashed contour. All elements are center excited with identical voltage sources. The active impedance of the center element as computed with NEC for the 5 element array (other four elements absent) is shown in Figure 2-2. These computations were obtained with nine

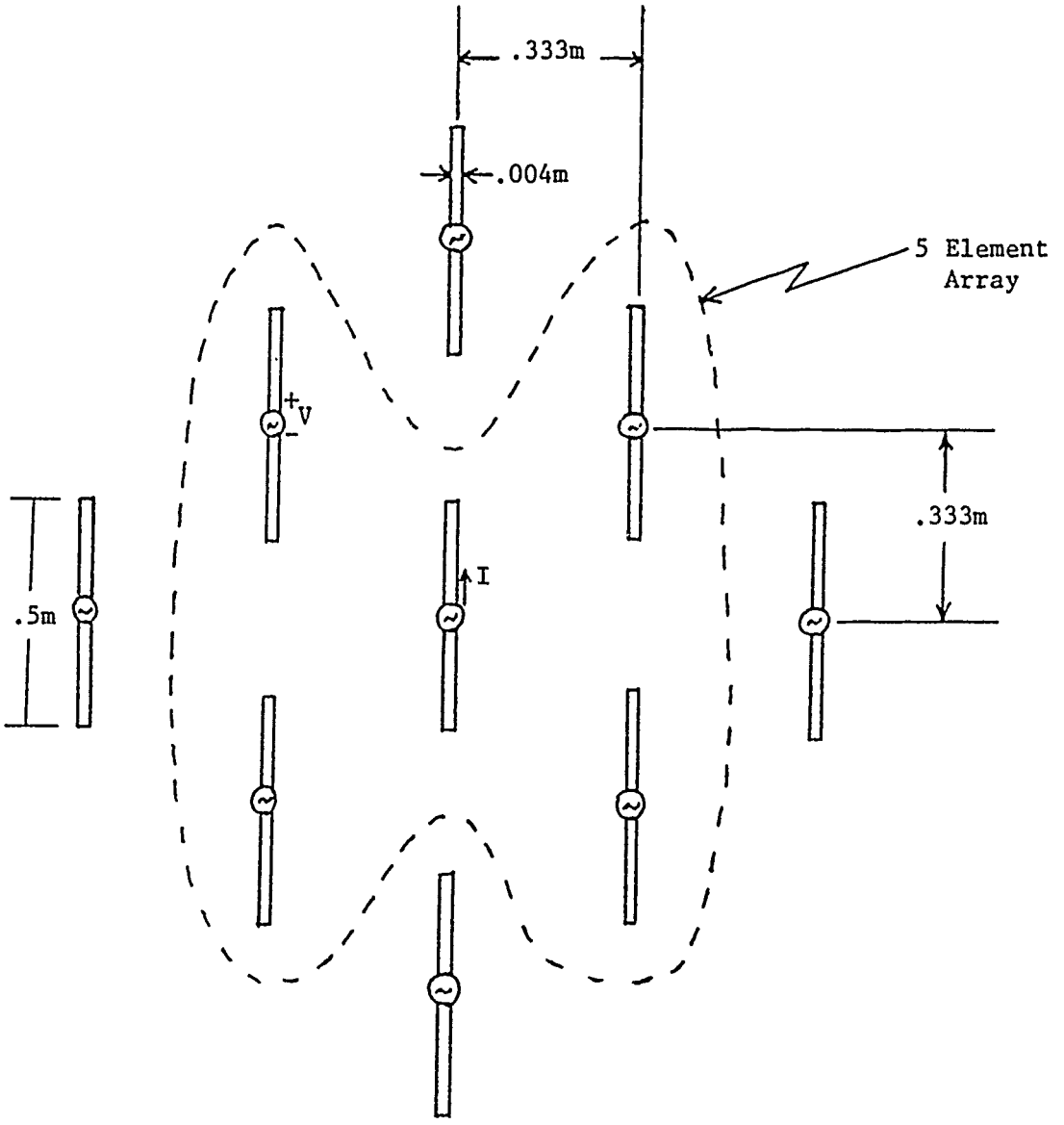


Figure 2-1. Nine Element Voltage Source Excited Dipole Array

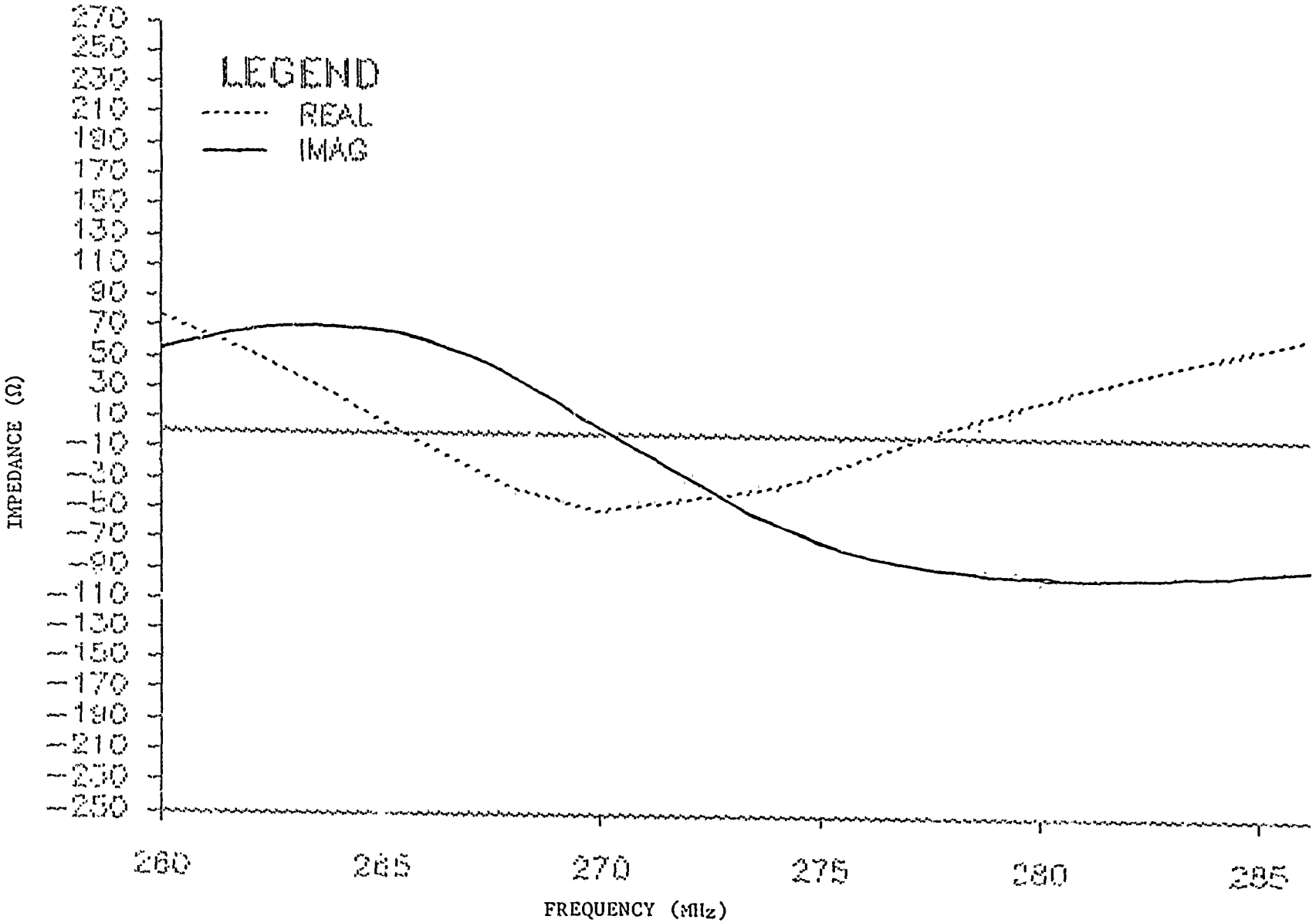


Figure 2-2. Center Element Active impedance of Five Element Array Above a Ground Screen (Nine Segments per Dipole)

segments per dipole and assuming a perfect ground screen located 0.25 m behind each array. Close agreement between these results and others obtained with different numbers of segments per dipole provided confidence in the use of nine segments per dipole in the NEC moment method procedure. Clearly a negative resistance is apparent over a 10 MHz bandwidth. The central element active impedance of the 9 element array as computed with NEC is shown in Figure 2-3. The negative resistance over a 10 MHz bandwidth is even more pronounced for the 9 element array.

These results confirm those presented in [1]. The results are not surprising if one approximates the open circuit mutual impedance between two halfwave dipoles in an array by that with all other elements absent. The real part of the mutual impedance as a function of the separation between the elements alternates between positive and negative values as illustrated by the NEC result for parallel dipoles shown in Figure 2-4. Between 0.6λ and 1.1λ the resistance is negative prompting the conclusion that many of the elements in an array within a wavelength radius of the center element might be expected to contribute components to the center element active resistance that are of opposite sense of that of the self resistance. This would drive the active resistance to a very low or even negative value. Actually this simple summation relationship between pairwise mutual impedance and active impedance applies only to the current source excited finite array (Figure 2-5) and not the voltage source excited array under consideration. In the latter case, pairwise mutual admittances must be superimposed. In that case, the contribution of mutual admittance real part between an array element and the center element can be expected also to alternate positively and negatively with increasing element distance from the center of the array. An assumption of neglecting short circuited element scattering in relating the superimposed mutual admittance to active admittance, however, is considerably less accurate than is the open circuited assumption applicable to the current source case, but the qualitative nature of the agreement is still pertinent.

The results in Section 4 will show that the current source excited array appears to not exhibit the negative active resistance even for small arrays. Since the infinite array active impedance is the same, however, whether the array is current source excited or voltage source excited, the current source excited case then lends doubt to the supposition that if the center element of a broadside scan voltage source excited finite array experiences a negative active resistance, the corresponding infinite array would experience array

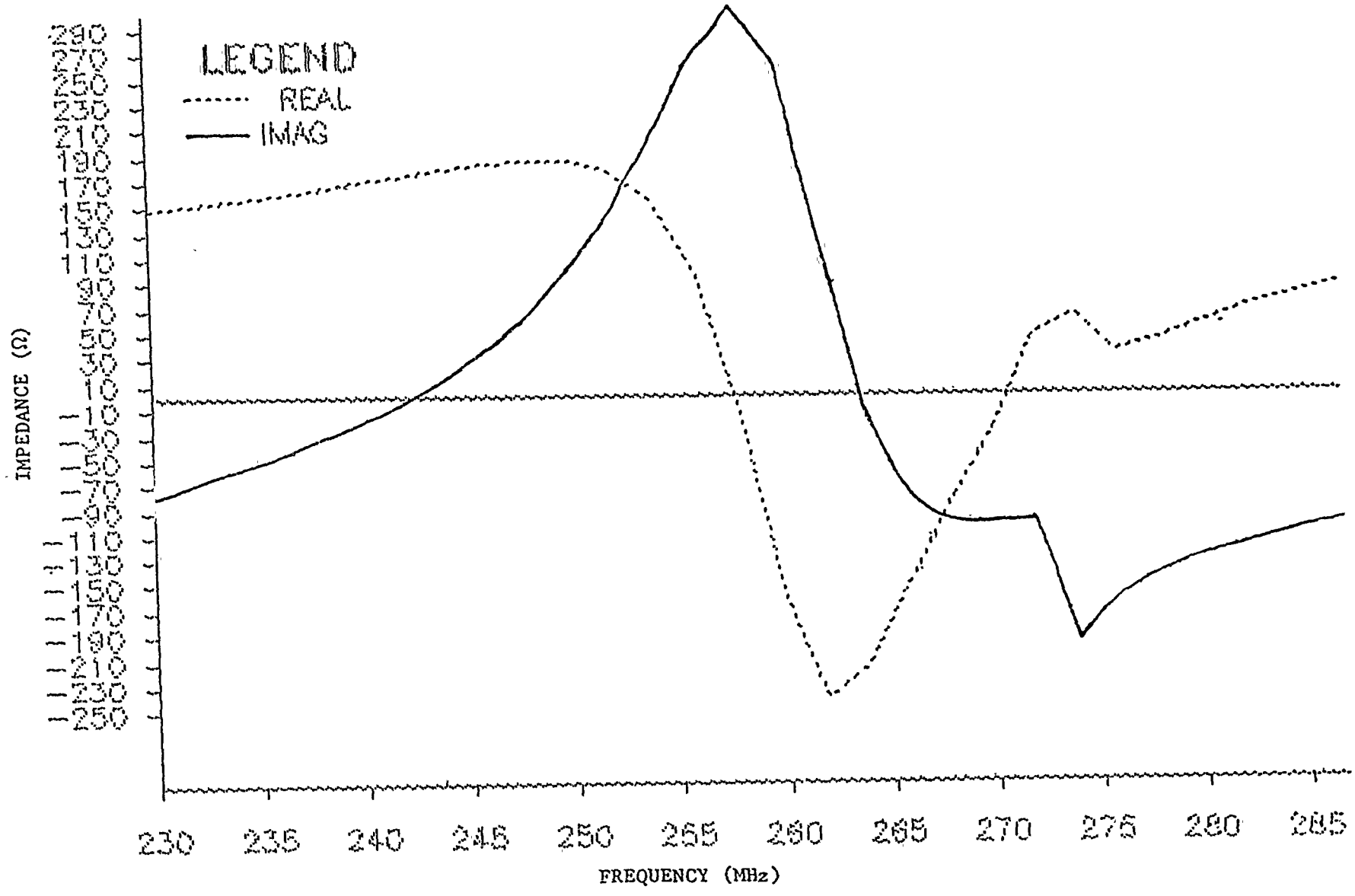


Figure 2-3. Center Element Active Impedance of Nine Element Array Above a Ground Screen (Nine Segments per Dipole)

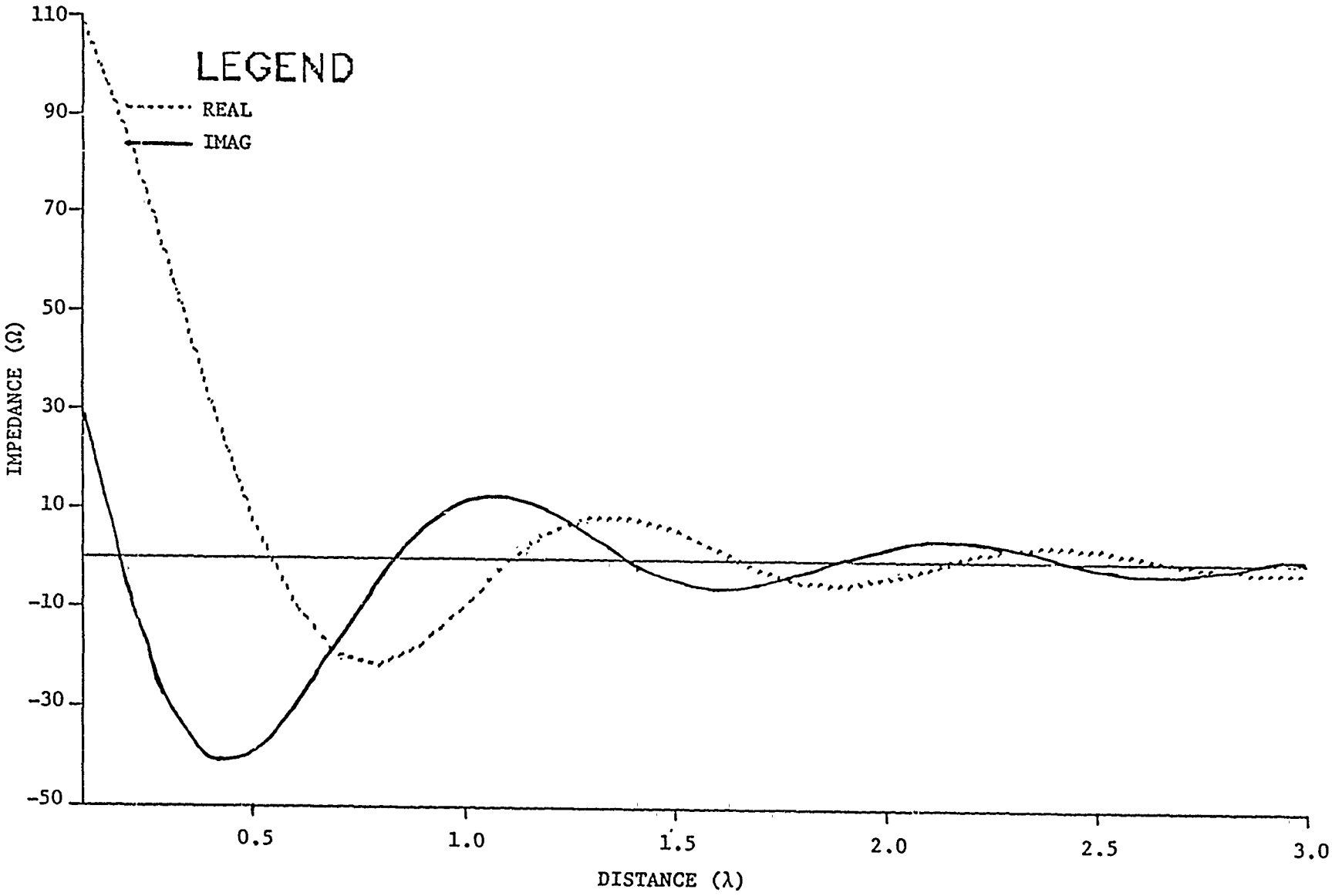


Figure 2-4. Mutual Impedance Between Two Halfwave Parallel Dipoles Above a Ground Screen

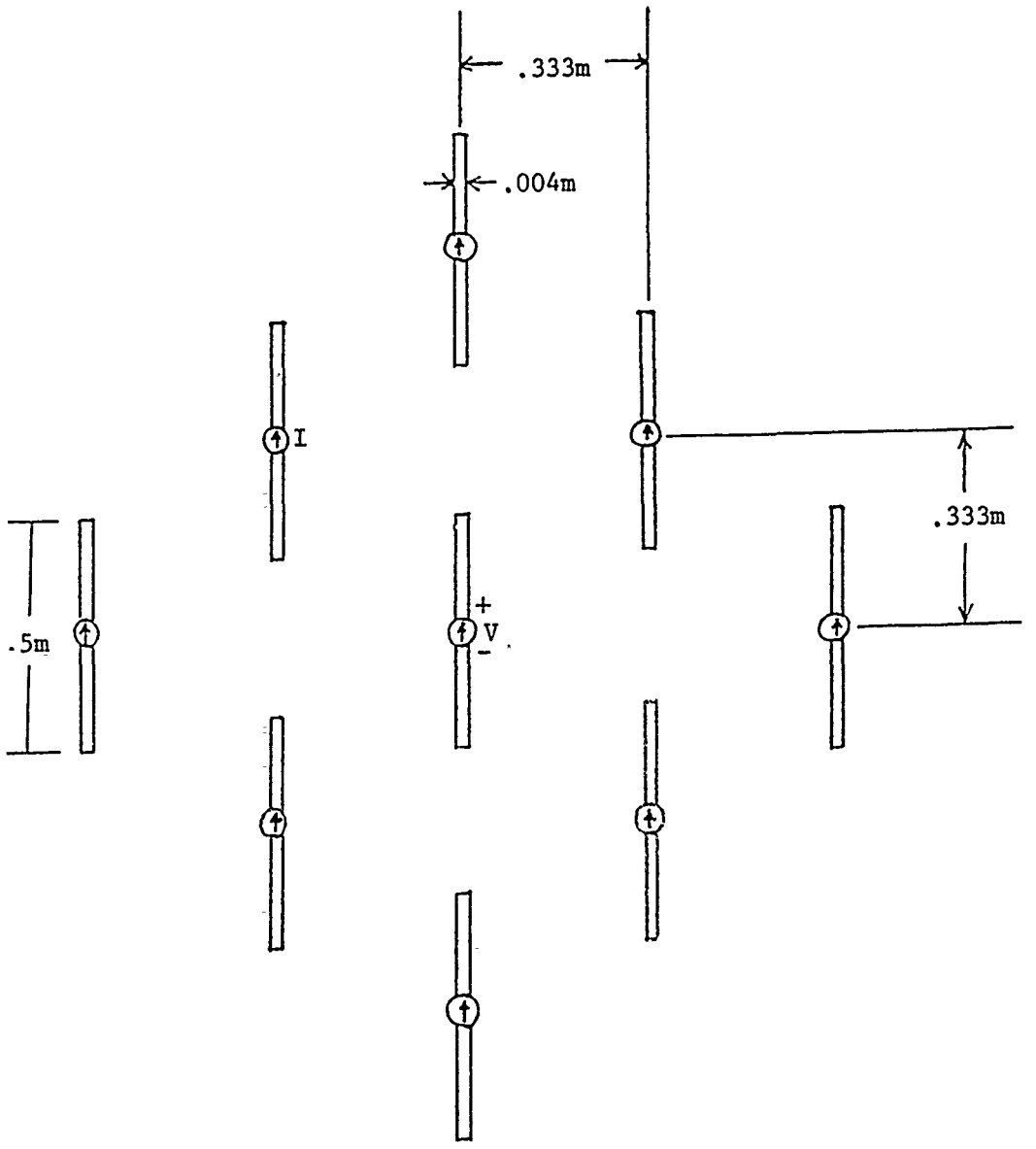


Figure 2-5. Nine Element Current Source Excited Dipole Array

blindness. In fact, the active impedance of the infinite array corresponding to the Figure 2-1 elements and lattice does not exhibit severe impedance values as shown in Figure 2-6. These results were obtained using the plane wave expansion moment method described in [3].

The remainder of this paper addresses the behavior of broadside arrays as they transition from the finite to the infinite. For simplicity, the arrays considered do not include ground screens. The center element active impedance of the voltage source excited 9 element array without a ground screen is shown in Figure 2-7. The corresponding infinite array active impedance is shown in Section 4 (Figures 4-4 and 4-5). As in the ground screen present case, a negative resistance is apparent in the finite array case whereas the infinite array case exhibits no unusual impedance behavior.

3. Comparison of Point Source Approximation with Moment Method

The transition of broadside scan active impedance from finite to infinite arrays is considered here for the ground screen absent current source excited triangular lattice dipole array of the previous section. The element dimensions and lattice are as shown in Figure 2-5. As indicated in Section 2, with current sources, the center element active impedance is given by the sum of the center element self impedance and the mutual impedances between each element and the center element. The self and mutual impedances refer to the two port open circuit impedance parameters obtained under the condition of all other elements present but open circuited (current sources removed). The scattering from open circuited half wave dipoles is of considerably less amplitude than that from short circuited dipoles so that, for the current source excited case, it is reasonable to approximate the impedance parameter computations with those obtained with all array elements except the two under consideration absent rather than open circuited. This approximation leads to an expression for the center element active impedance of a finite array that is computationally efficient even for arrays of millions of elements.

Within this approximation, elements distant from the center element contribute a mutual impedance that can be well approximated by that arising from an equivalent point source. The point source contributions are particularly simple to compute. The active impedance, then, is approximated by

$$z = z_o + \sum_i z_i^{nec} + \sum_i z_i^{pt} \qquad (3\text{-}1)$$

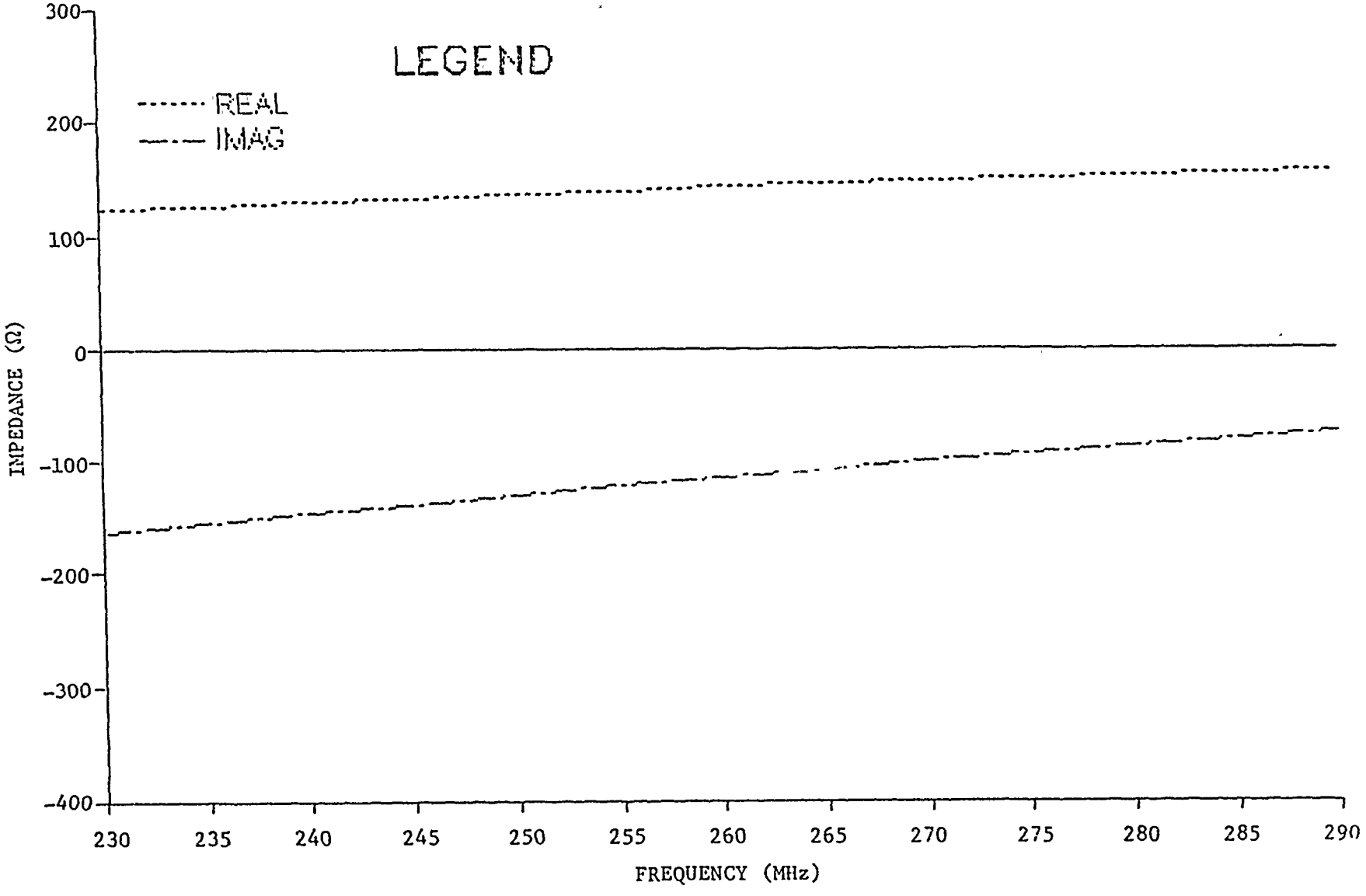


Figure 2-6. Active Impedance of Infinite Array of Dipoles Over Ground Screen

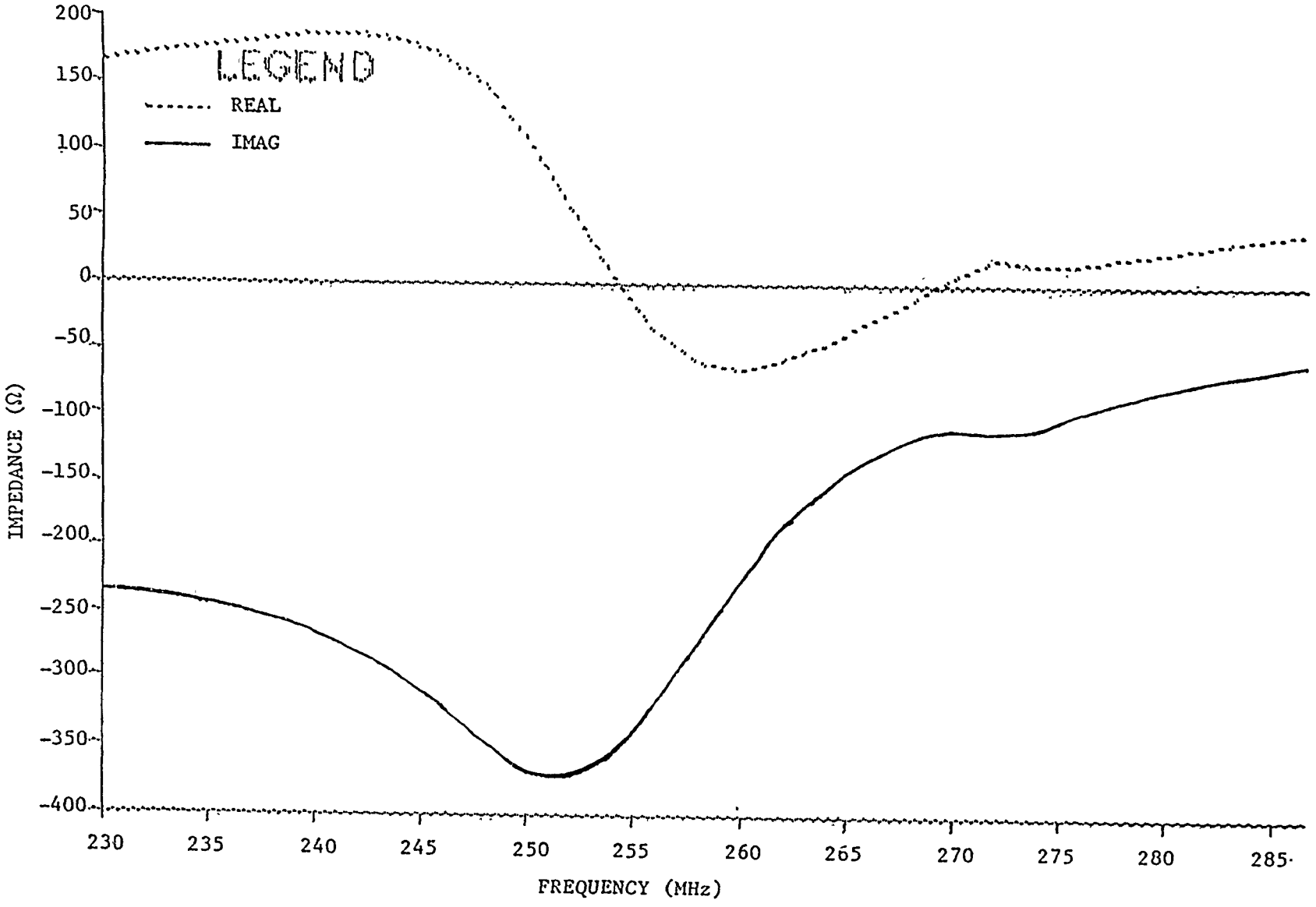


Figure 2-7. Center Element Active Impedances of Nine Element Array without Ground Screen (Nine Segments per Dipole)

where z_o is the input impedance of an isolated dipole as with NEC, z_i^{nec} is the open circuit mutual impedance between the center element and the i^{th} element in the neighborhood of the center element with all other elements absent as computed with NEC, and z_i^{pt} is the open circuit mutual impedance between the i^{th} remaining element and the center element in the absence of all other elements as given by the point source approximation derived below.

The point source approximation to the mutual impedance between two dipoles is determined by exciting one and open circuiting the other and assuming that the coupling is that which occurs when the distance between excited and open circuited dipoles is much greater than the dipole lengths and that the excited dipole current is not affected by the presence of the open circuited dipole. The resulting expression for the mutual impedance between parallel dipoles can be shown to be

$$z_{mut} = - \frac{2\lambda^3 (z_o F)^2}{\eta k} \left(\frac{jk}{R} + \frac{1}{R^2} + \frac{1}{jkR^3} \right) \exp(-jkR) \qquad (3\text{-}2)$$

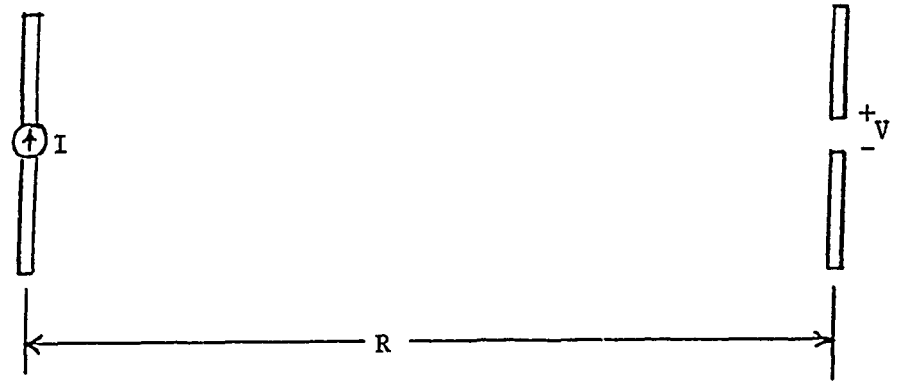
where λ is the wavelength, k is the wavenumber ($2\pi/\lambda$), η is the free space wave impedance ($\approx 376.7\ \Omega$), R is the distance between dipole centers, and F is the dipole pattern function. The latter is given by

$$F = \frac{\lambda \vec{E} \hat{\ell}}{R} \exp(jkR)$$

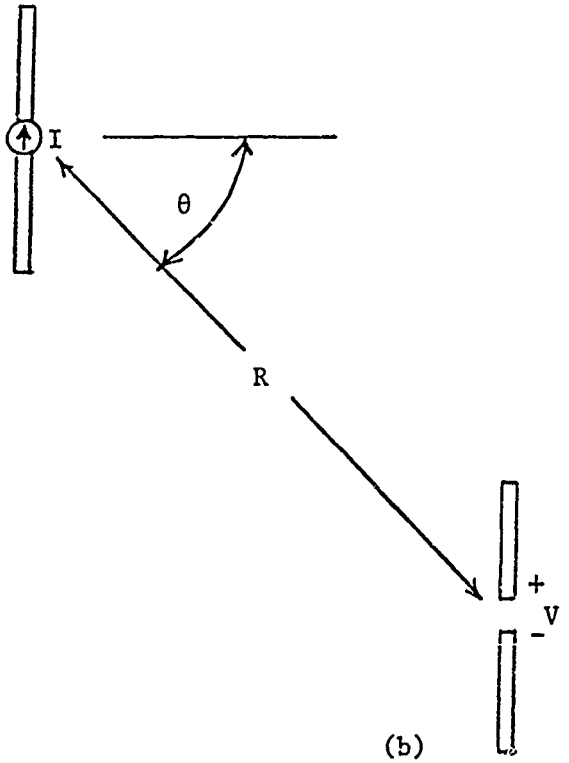
where $\hat{\ell}$ is the dipole orientation unit vector and $\vec{E}$ is the dipole radiation zone $\vec{E}$-field due to a unit voltage source exciting the dipole. The quantities z_o and F are normal NEC outputs. The pattern function is dependent on the "skew" angle, θ, between the dipoles as defined in Figure 3-1.

Equation (3-2) can be derived by solving via reciprocity for the dipole open circuit voltage induced by an incident plane wave and combining the result with the expression for the far radiated field of a dipole excited by a voltage source equal to z_o. This result in turn is augmented to include the point source R^{-2} and R^{-3} field variations corresponding to dominant terms in the induction and quasistatic regions respectively [4].

The R^{-2} and R^{-3} terms were not expected to be significant when applying (3-2) to near resonant dipoles because the 'far field' requirement imposed by the point source approximation then, by itself, limits the useful ranges



(a)



(b)

Figure 3-1. Parallel Dipole Configurations for Mutual Impedance Computations

(values of R) to values exceeding the extent of the induction field. This in fact was found to be the case, and the reduced version (3-2) given by

$$z_{mut} = - \frac{2\lambda^3 (z_o F)^2}{j\eta R} \exp(-jkR) \qquad (3\text{-}3)$$

was used in the computations applied to the near resonant dipole array.

It was instructive to retain the R^{-2} and R^{-3} terms of (3-2), however, during an investigation into the accuracy of the point source approximation. The investigation was conducted by applying (3-2) to the dipole configurations of Figure 3-1 and comparing the results with those obtained by using NEC. NEC yielded two port short circuit admittance parameters directly and from these the mutual open circuit impedance parameters were readily computed.

Two skew angles were considered, $\theta = 0°$ (Figure 3-1a) and $\theta = 45°$. The mutual impedance for the broadside separation ($\theta = 0°$) case for 0.1λ dipoles is shown in Figures 3-2 and 3-3. The results of three point source approximations are shown along with those from NEC. The results denoted "R R2 R3" refer to (3-2) and those denoted "R" refer to (3-3). Those denoted "R R2" refer to (3-2) with the R^{-3} term omitted. As was to be expected from point source theory (3-2) yielded a good approximation for $R \leq 0 \leq 7\lambda$. For $0.2 \leq R \leq 0.7\lambda$ the successive addition of the R^{-2} and R^{-3} terms yielded successively better approximations. For smaller separations the finite length of the dipole may have been the primary cause of discrepancy between the results of NEC and (3-2).

Figures 3-4 and 3-5 show the corresponding results for the $\theta = 45°$ skew case (Figure 3-1b). The agreement between NEC and (3-2) appears to have been somewhat worse than in the nonskewed ($\theta = 0°$) case. It is particularly disturbing that for $R \leq .4\lambda$ NEC compared better with (3-3) than with (3-2).

Figures 3-6 and 3-7 show the corresponding results for an order of magnitude shorter dipole, and also where the dipole radii were decreased to avoid NEC computational problems. Surprisingly, the minimum dipole separation for agreement between NEC and (3-2) were not noticeably less for the shorter dipole case. The same analysis applied to dipoles shortened further by 50% did not yield any appreciable improvement.

The NEC computations were carried out with 3 segments per dipole for the 0.005λ dipoles and with 5 segments per dipole for the 0.01λ and 0.1λ dipoles. The 0.1λ dipole results of Figures 3-4 and 3-5 were recomputed with 3 segments

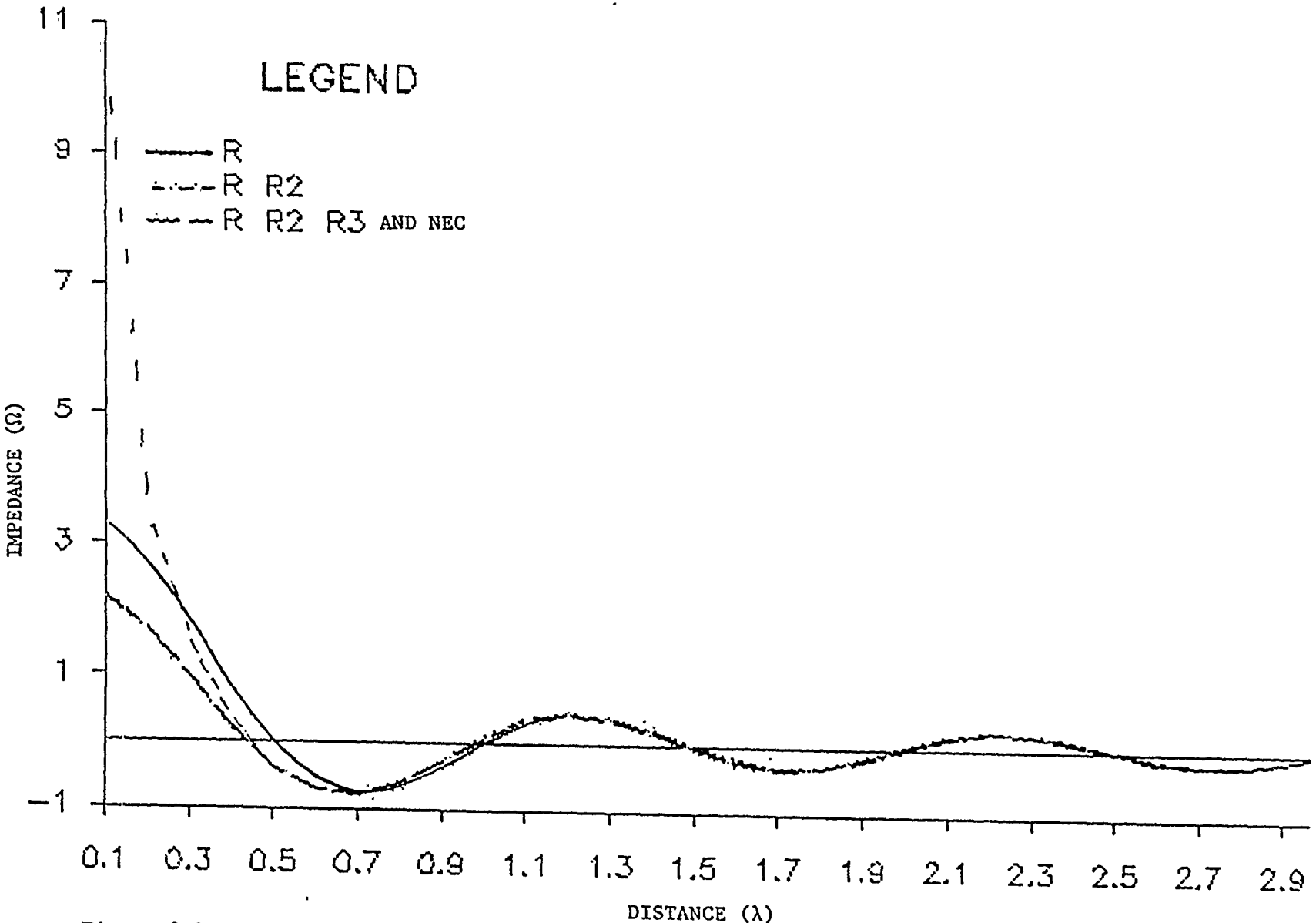


Figure 3-2. Real Part of Mutual Impedance Between Parallel 0.1λ Dipoles of 0.0004λ Radii Spaced in Broadside Direction (NEC Computations Used 5 Segments Per Dipole)

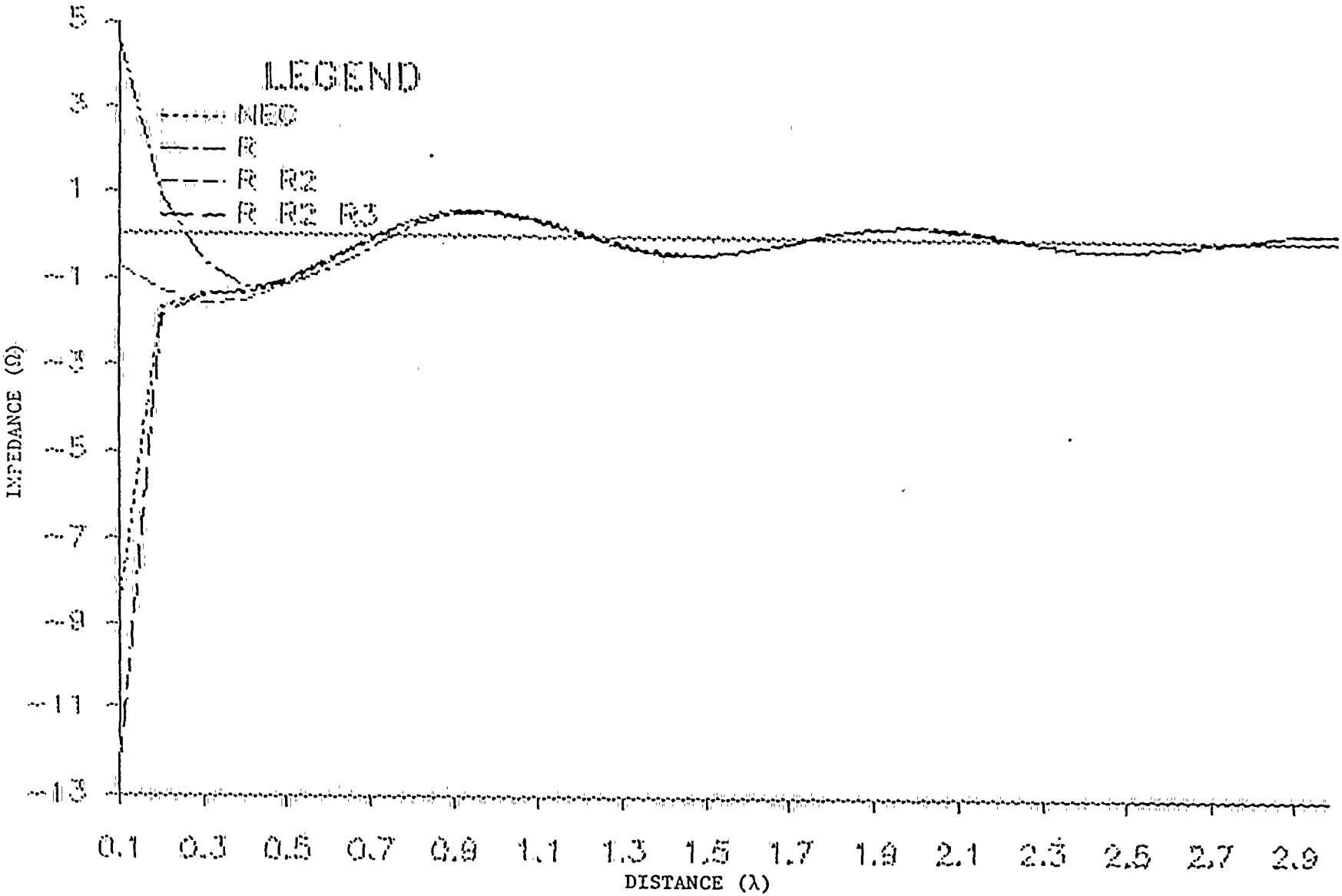


Figure 3-3. Imaginary Part of Mutual Impedance Between Parallel 0.1λ Dipoles of 0.0004λ Radii Spaced in Broadside Direction (NEC Computations Used 5 Segments Per Dipole)

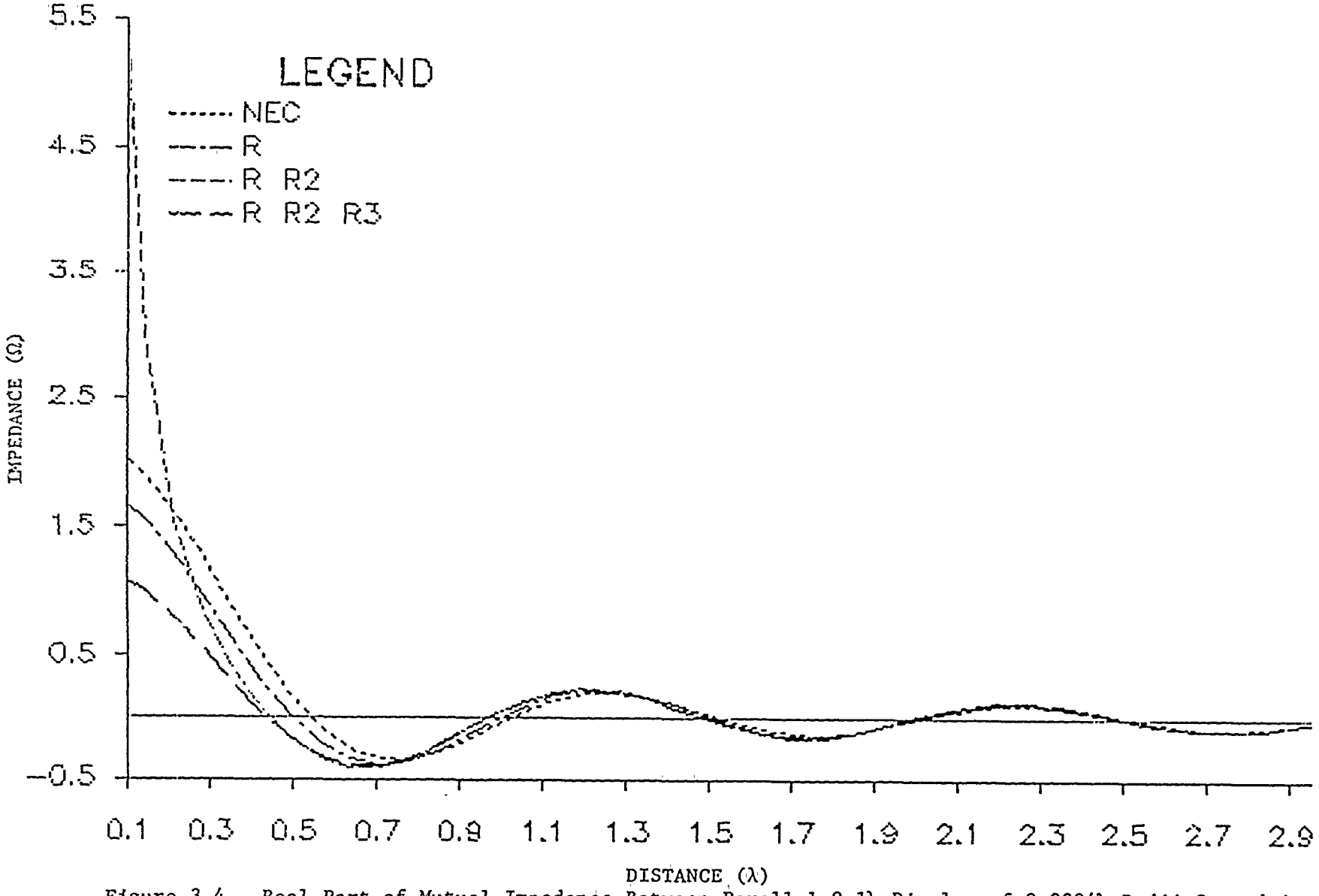


Figure 3-4. Real Part of Mutual Impedance Between Parallel 0.1λ Dipoles of 0.0004λ Radii Spaced in 45° Slew Direction (NEC Computations Used 5 Segments Per Dipole)

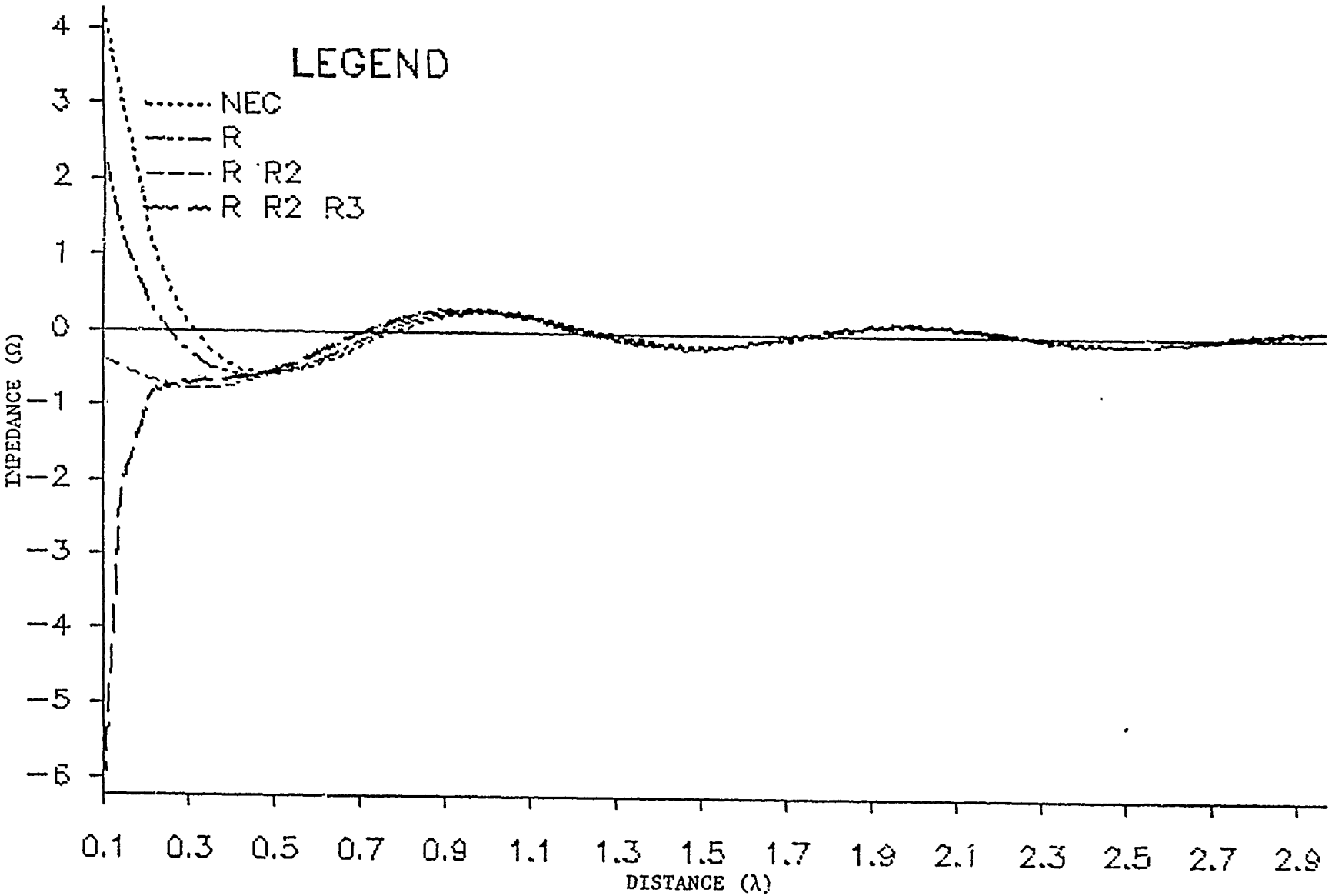


Figure 3-5. Imaginary Part of Mutual Impedance Between Parallel 0.1λ Dipoles of 0.0004λ Radii Spaced in 45° Slew Direction (NEC Computations Used 5 Segments Per Dipole)

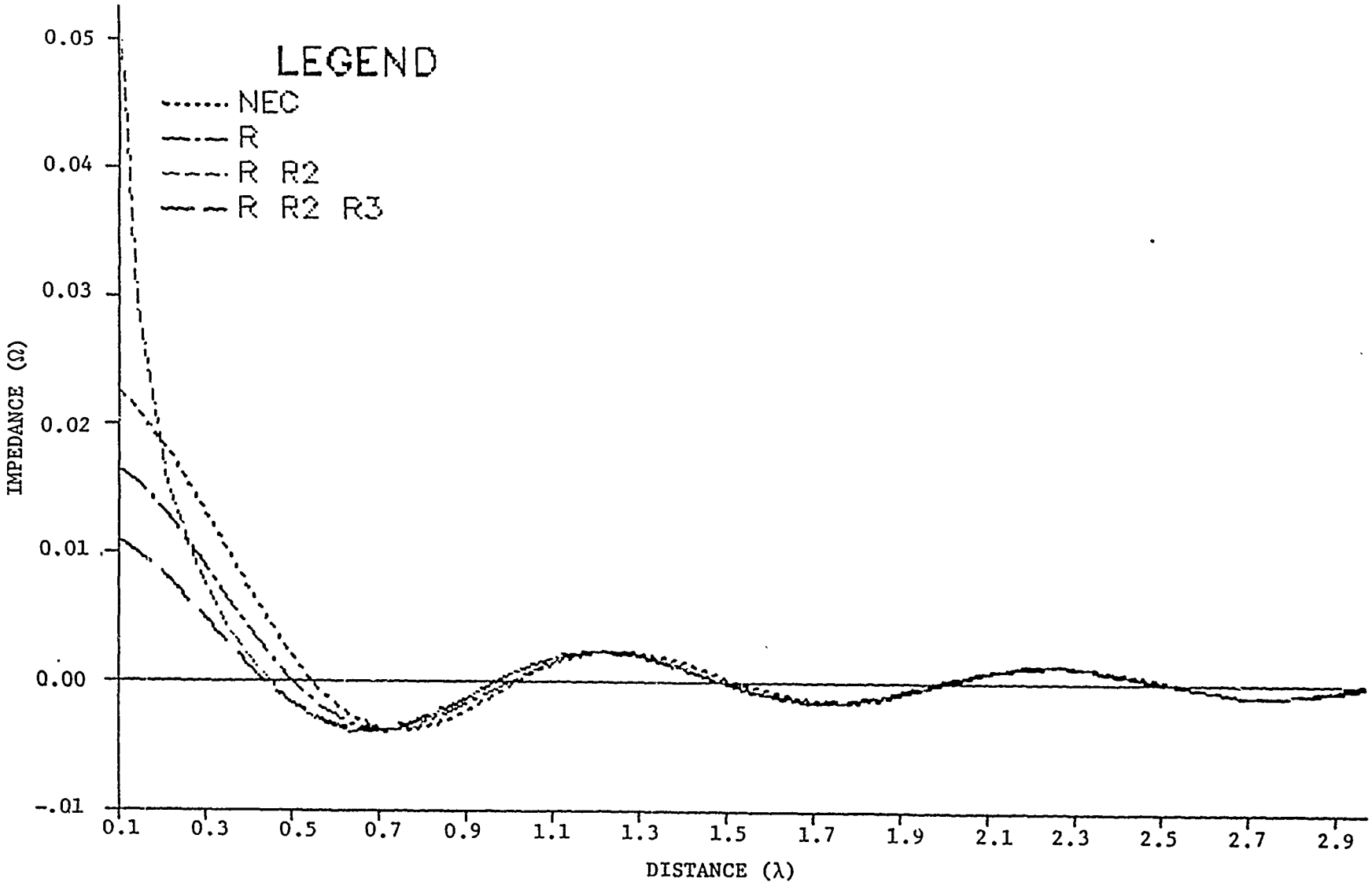


Figure 3-6. Real Part of Mutual Impedance Between Parallel 0.01λ Dipoles of 0.00004λ Radii Spaced in 45° Slew Direction (NEC Computations Used 5 Segments Per Dipole)

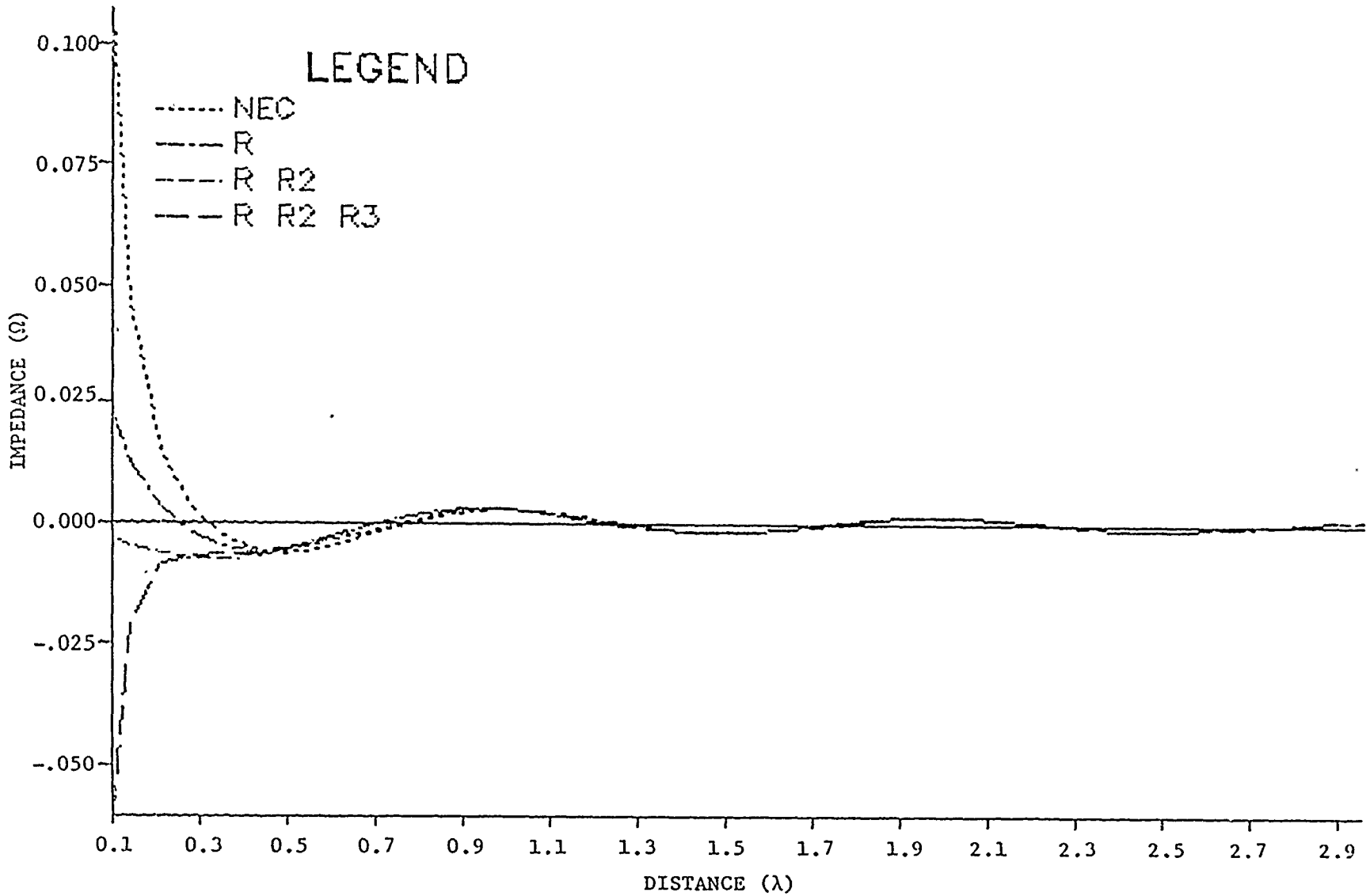


Figure 3-7. Imaginary Part of Mutual Impedance Between Parallel 0.01λ Dipoles of 0.00004λ Radii Spaced in 45° Slew Direction (NEC Computations Used 5 Segments Per Dipole)

per dipole. The mutual reactance tracked well for the different number of segments. There was some lowering of mutual resistance, however, for the 3 segment case although the relative values between the curves in each case were about the same. The point source approximation results varied with number of segments because z_o in (3-2) and (3-3) is computed with NEC. As a result of these numerical exercises, an error in the NEC program, or a modeling deficiency, was suspected that can affect the accuracy when analyzing short dipoles. The matter has not been investigated further.

Of particular interest were the mutual impedances between near resonant dipoles separated by a quarter wavelength or more. Figures 3-8 and 3-9 show the results of applying NEC and of applying (3-3) to computing the mutual impedance of 0.5 m dipoles at 260 MHz. The agreement was not excellent but was satisfactory for purposes of approximating array behavior in progressing from the finite to the infinite. As a result, it was determined that the point source approximation mutual impedance contribution to approximating the active impedance, i.e., the z_i^{pt} of (3-1), would apply for all elements beyond 1 m of the center element. The results of computing the active impedance via (3-1) in this manner and comparison with the corresponding infinite array result are given in Section 4.

4. Transition from Finite to Infinite Arrays

Approximations to the active impedances of the current source excited dipole array (ground screen absent) of elements and lattice defined in Figure 2-5 were computed via (3-1) for successively larger arrays. All elements were excited equally. Figure 4-1 shows the element tagging and array boundary schemes. The m = n = 0 element was the "center element" at which the active impedance was computed. Mutual impedance contributions from elements within the NEC Boundary contour were computed using NEC. Contributions from those beyond the contour were computed using the point source approximation of (3-3). Each array was assumed to be that containing all elements bounded by the parallelogram defined by a specified maximum $|n| = |m| = M$. The M = 4 array boundary is indicated in Figure 4-1. There were $(2M+1)^2$ elements within each M array. Thus M = 2 implied 25 elements, M = 3 implied 49 and so forth.

Some results are shown in Figures 4-2 and 4-3. The convergence with respect to number of array elements appears very slow considering that the M = 100 array contained 40,401 elements and M = 800 contained 2,563,201 elements. The very slow convergence is not necessarily inconsistent with the

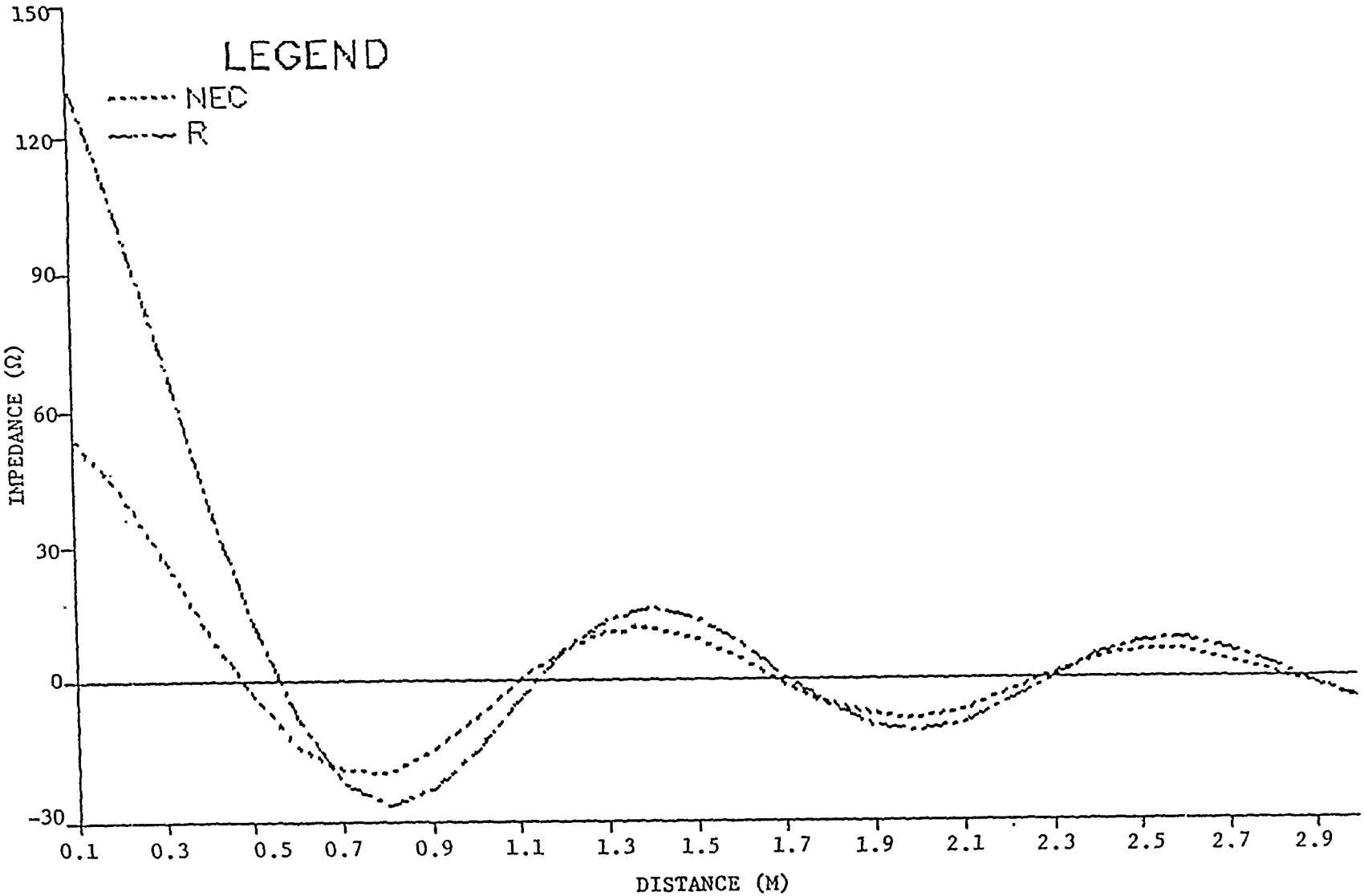


Figure 3-8. Real Part of Mutual Impedance Between Parallel 0.5 m Dipoles of 0.002 m Radii at 260 MHz Spaced in Broadside Direction (NEC Computations Used 9 Segments Per Dipole)

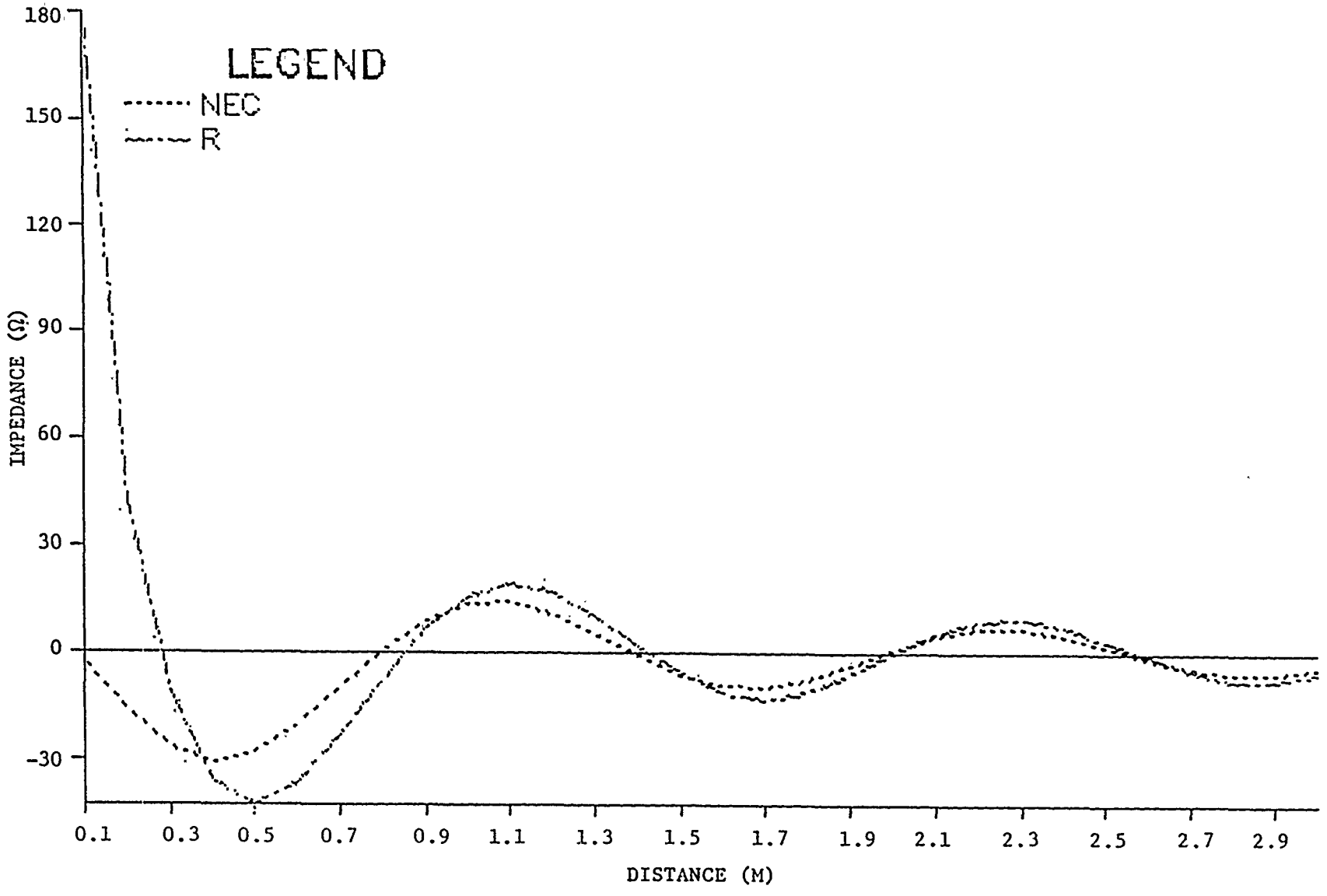


Figure 3-9. Imaginary Part of Mutual Impedance Between Parallel 0.5 m Dipoles of 0.002 m Radii at 260 MHz Spaced in Broadside Direction (NEC Computations Used 9 Segments Per Dipole)

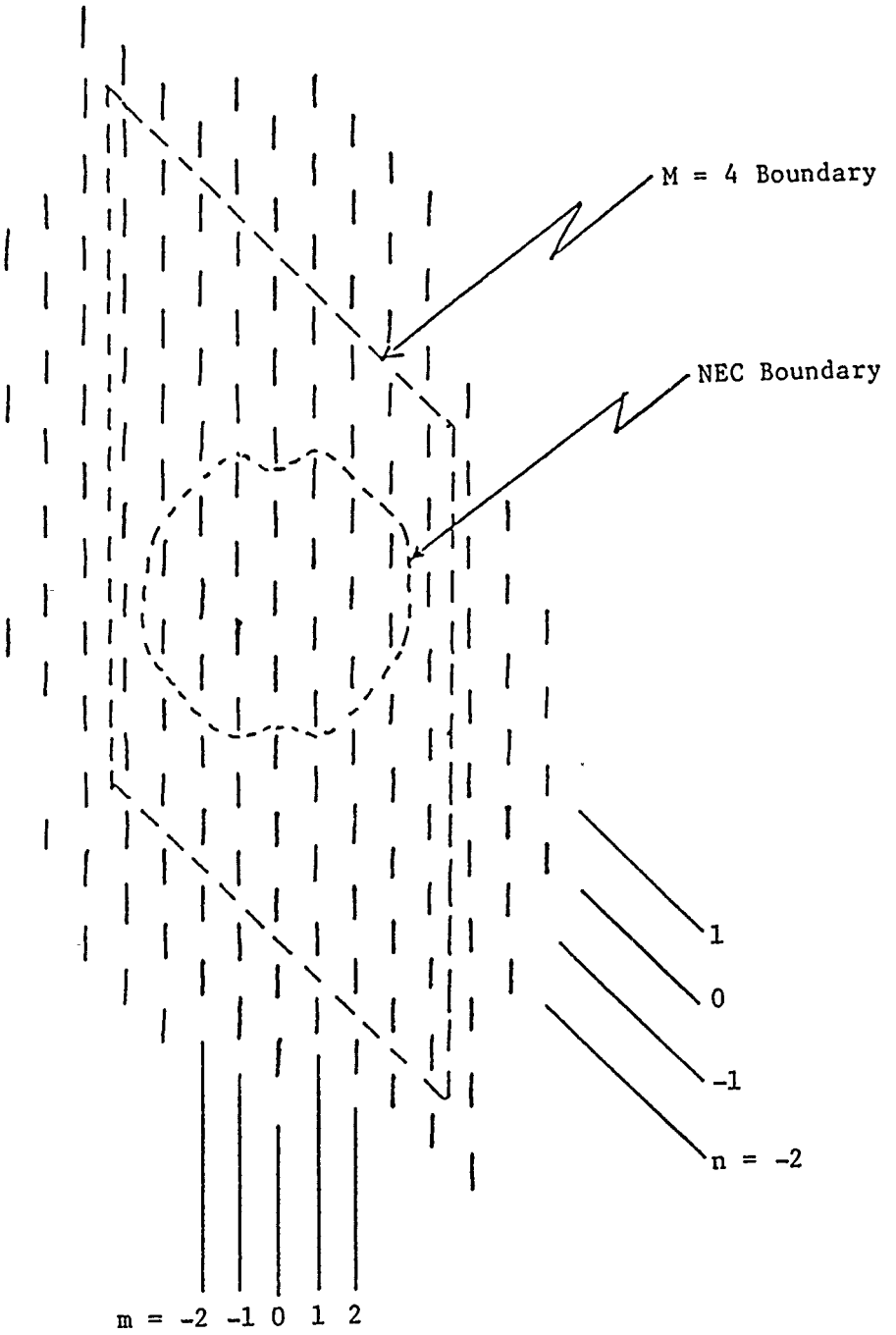


Figure 4-1. Array Tagging and Boundary Schemes

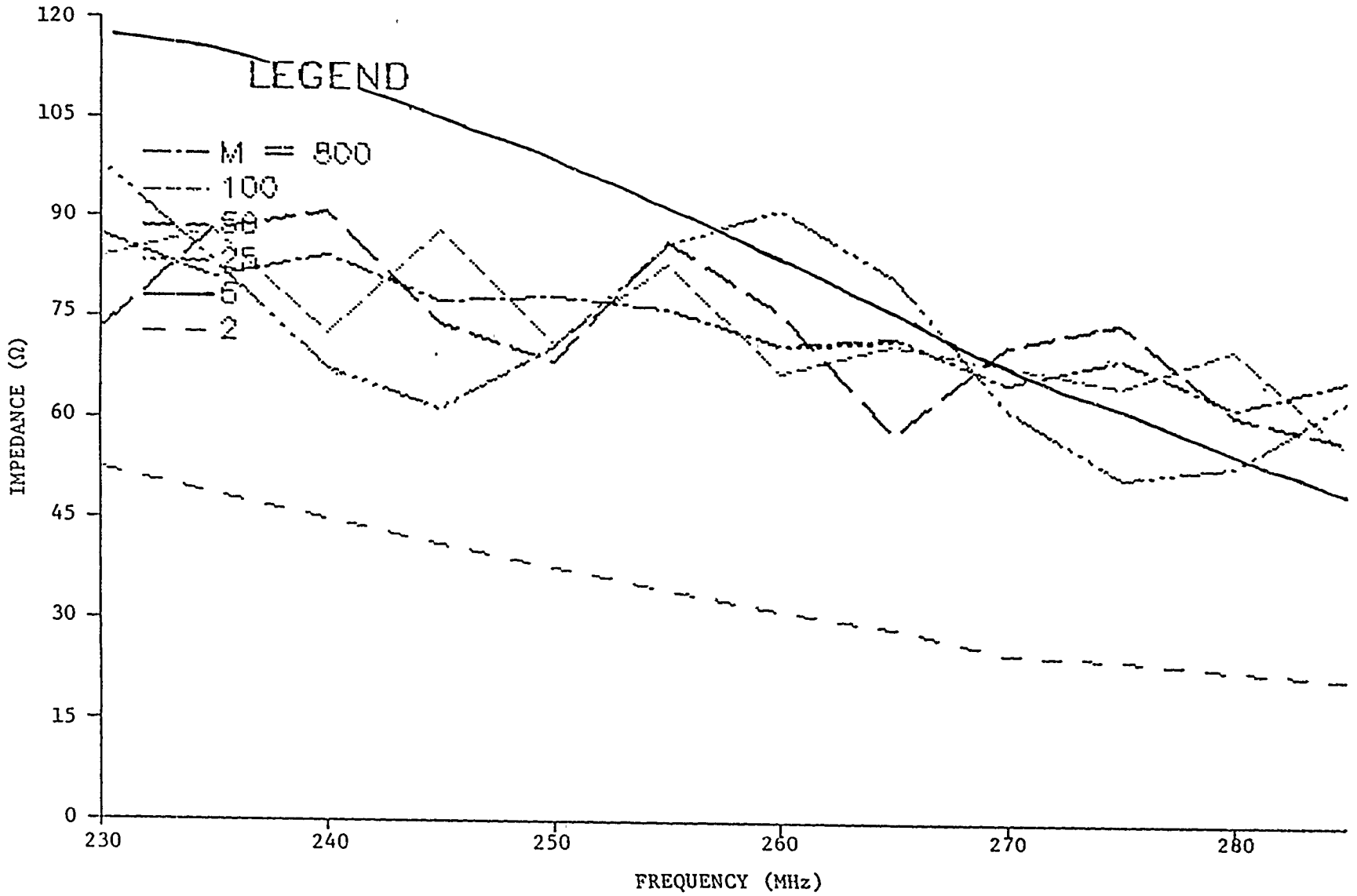


Figure 4-2. Real Part of Active Impedance via NEC/Point Source Approximation

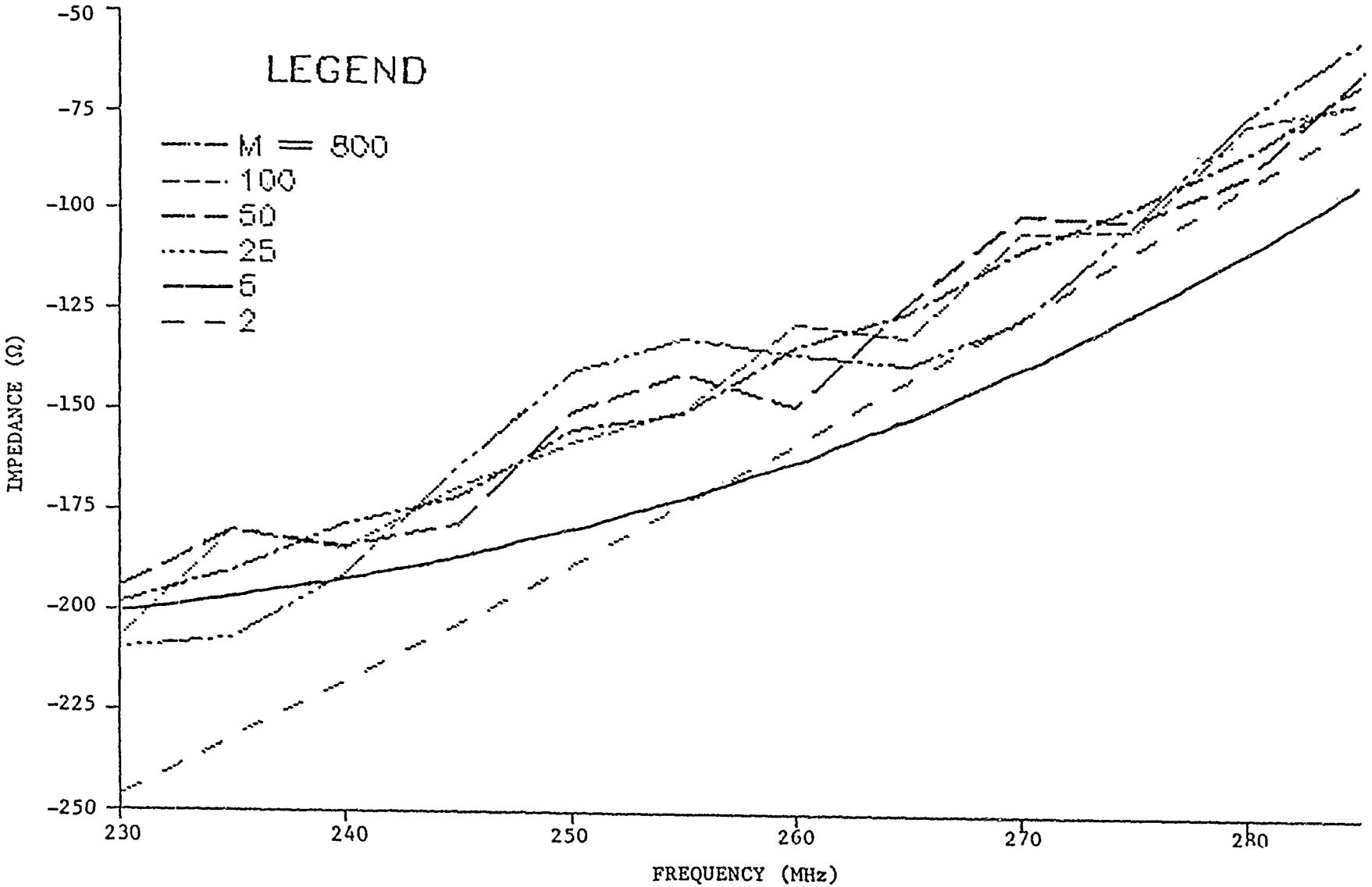


Figure 4-3. Imaginary Part of Active Impedance via NEC/Point Source Approximation

fact that the contribution to the active impedance from a distant element falls off as R^{-1}. One must consider also that the number of elements on a ring of radius R increases with R, thus potentially negating the R^{-1} fall off.

The corresponding infinite array active impedances were computed as per [3]. These are shown in Figures 4-4 and 4-5 along with the M = 800 finite array approximate results of the previous two figures. In view of the approximations employed in computing with (3-1) as described in Section 3, the agreement between the two sets of results appears reasonably good.

5. Conclusions

The NEC moment method computer program was applied to the computation of the center element active impedances of finite broadside scan dipole arrays. For near resonant dipole lengths and a typical lattice spacing a band of frequencies were found at which the real part of the impedance was negative. This result was in agreement with that reported in [1]. A plane wave expansion moment method infinite array analysis computer program then was applied to the infinite array comprised of the same dipoles and lattice. The severe variation in active impedance experienced in the finite array case was seen to vanish in the corresponding infinite array case. In particular, no array blindness phenomena (very small or zero active resistance) was observed in the infinite array case.

An approximation to the center element active impedance of finite arrays of current source excited dipoles was developed. (It was noted that the infinite array active impedance is independent of whether the array is excited with current sources or with voltage sources.) The approximation basically combined moment method and equivalent point source modeling of the open circuit mutual impedance between parallel dipoles. The approximation was applied to very large arrays, in excess of millions of elements, and exhibited reasonable computation time. The approximation was shown to yield good agreement with the infinite array active impedance for a corresponding finite array of a very large number of elements.

The approximation was applied to progressively larger arrays beginning with a 25 element array. The center element active impedance was found to be poorly convergent as the array size was increased, at least in the case of broadside excitation with current sources.

As an aside, a possible modeling deficiency with NEC was observed when modeling short dipoles. No extensive investigation as to the cause of the unusual observations was undertaken.

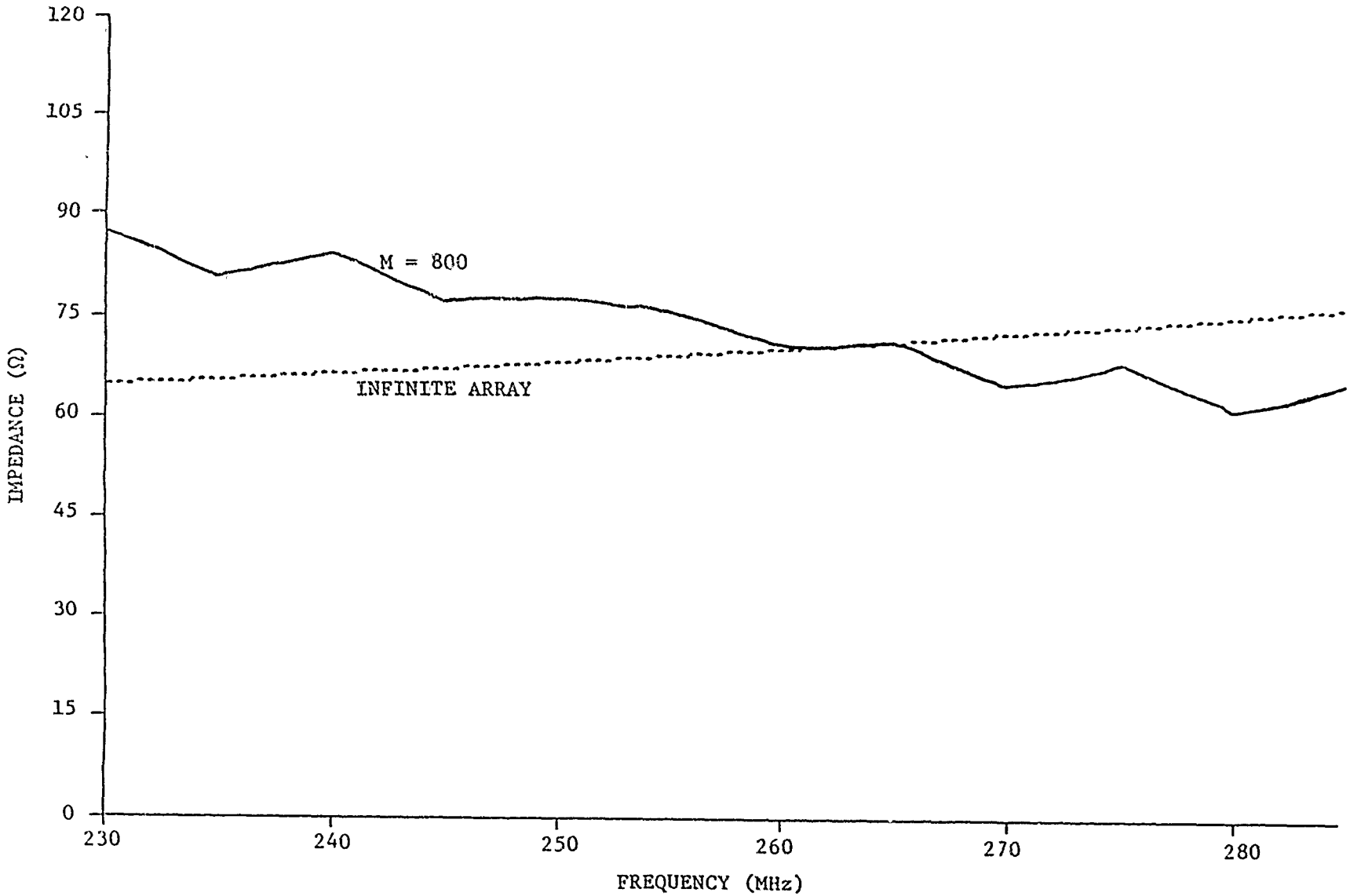


Figure 4-4. Real Part of Active Impedance of Infinite Array and Approximated Large Finite Array

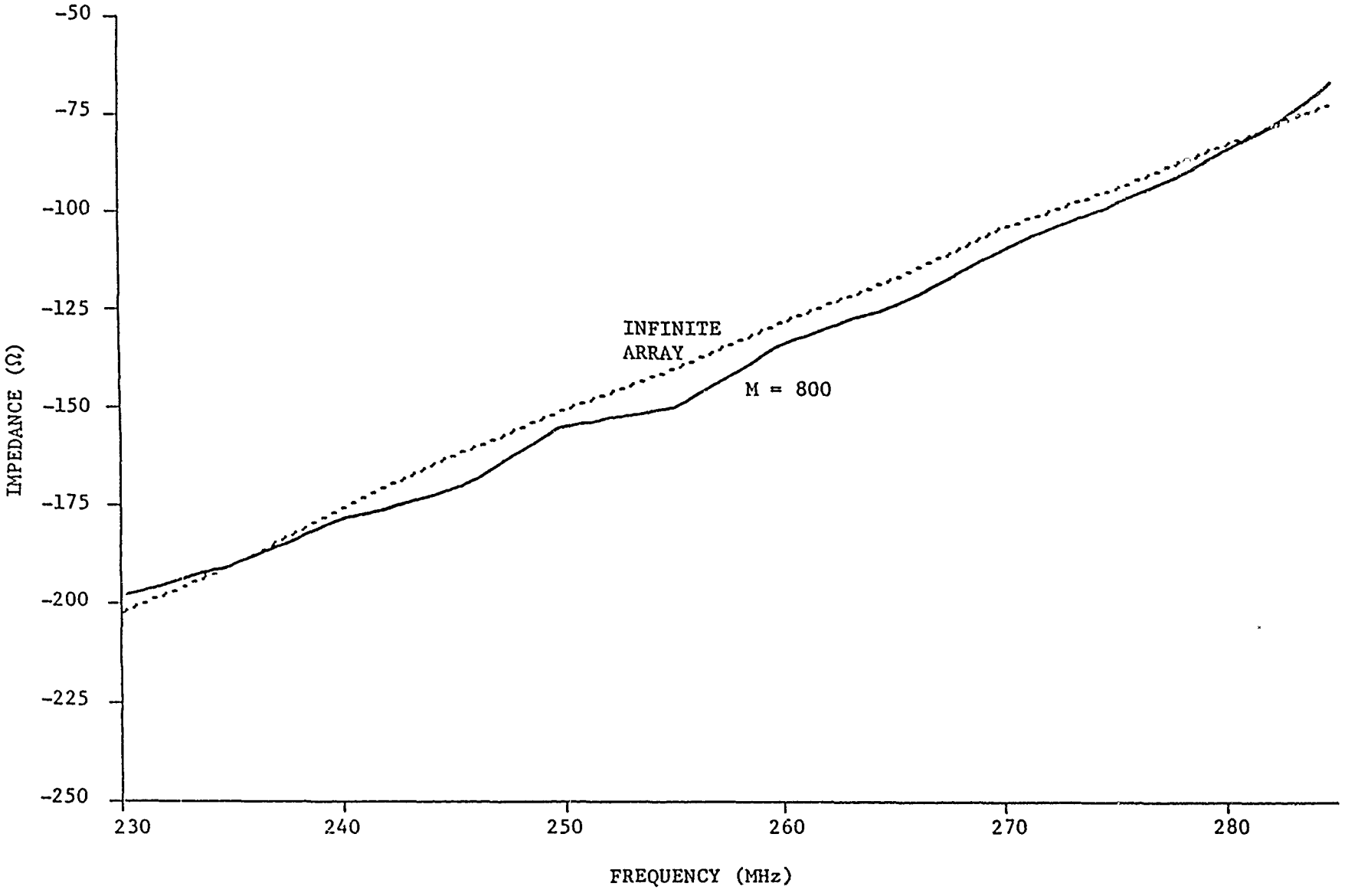


Figure 4-5. Imaginary Part of Active Impedance of Infinite Array and Approximated Large Finite Array

6. References

1. P. Elliot and D. Lamensdorf, "Negative Input Resistance Calculated for the Center Element of a Broadside Array," International Union of Radio Science (U.R.S.I.) Meeting, Philadelphia, PA, pg. 218, June 1986.
2. G.J. Burke and A.J. Poggio, "Numerical Electromagnetics Code (NEC) - Method of Moments," NOSC TD 116, Naval Ocean Systems Center, San Diego, CA, Vols. 1 and 2, January 1981.
3. H.K. Schuman, D.R. Pflug, and L.D. Thompson, "Infinite Planar Arrays of Arbitrarily Bent Thin Wire Radiators," IEEE Trans. Ants. Propg., Vol. AP-32, No. 4, pp 364-377, April 1984.
4. R.F. Harrington, Time Harmonic Electromagnetic Fields, McGraw-Hill, pg. 79, 1961.

ABSTRACT

INCONSISTENCIES ENCOUNTERED WHILE MODELING
BROADBAND DIPOLE USING NEC-3

Lee W. Corrington
US ARMY INFORMATION SYSTEMS
ENGINEERING AND INTEGRATION CENTER
(USAISEIC ATTN: ASBI-STS)
Ft. Huachuca, AZ 85613-7300
(602)-538-7682

The NEC-3 code contains an option which enables the user to request the computation of the average power gain, G(ave), of the antenna. G(ave) is found by integrating the far field radiation pattern over an appropriate region of space. For an antenna with no ohmic losses present, the value of G(ave) can be used as a check on the accuracy of the user's solution procedure.

When this integration is performed over perfect ground or in free space, the value of G(ave) should be either 2 or 1, respectively. Since the code's implementation of the integration is actually a summation of discrete far-field gain values at points identified by the user, one can expect slight deviations from the above values if the number of points selected for evaluation is too small to permit incorporation of valid radiation field strength variations in space.

Recently, a complex broadband dipole antenna structure was modeled and the values of G(ave) were computed. However, whenever a multiple wire junction was present in the geometry, these values were significantly higher or lower than predicted theoretically and seemed independent of the number of field points in the summation, the segmentation lengths, etc. This paper is being presented both to promulgate the discrepancies encountered in this modeling effort and to solicit solution or mitigation strategies from the Applied Computational Electromagnetic community.

INCONSISTENCIES ENCOUNTERED WHILE MODELING A BROADBAND DIPOLE USING NEC-3

Lee W. Corrington
US ARMY INFORMATION SYSTEMS
ENGINEERING AND INTEGRATION CENTER
(USAISEIC ATTN: ASBI-STS)
Ft. Huachuca, AZ 85613-7300
(602)-538-7682

Recently, communications engineers for one of our customers developed a large, broadband dipole antenna for use at HF frequencies. While they have constructed a prototype of the antenna and conducted some limited real-time tests on various communications circuits, they presently don't have the resources to determine the far-field radiation pattern of the antenna. Consequently, the customer has requested that the Engineering Integration Center perform a NEC(1) analysis of the antenna and report our results to their engineers.

After the geometry data input for the broadband dipole had been verified as accurate using the model-maker capability of the IGUANA(2) code, a preliminary step in the modeling effort was to execute an analysis over perfect earth and obtain a value for the average gain G(ave) of the antenna. G(ave) is obtained by integrating the far-field radiation pattern contained in a volume of space and dividing by the volume of space in which the integration takes place. The NEC code performs this integration by computing a summation of gain values at discrete points in space. The volume of space and the number of points summed over in that space are user-defined parameters which involve a trade-off between the finer resolution and higher accuracy of a large number of points versus the restrictions in computer time available to the user. Once an acceptable compromise between the above conflicting requirements has been achieved, the value of G(ave) obtained can then be used both as a check on the validity of the antenna model's composition and in the calculation of an adjustment factor for the input impedance and discrete far-field gain values computed in subsequent analyses of the antenna. The theoretically predicted value of G(ave) over perfect earth is 2.0; however, the values of G(ave) from various analyses with the broadband

antenna ranged from 1.4 to 3.1. Initially it was thcught that the complexity of the broadband antenna model geometry violated one or more of the constraints or assumptions inherent in the NEC code. The model was reduced in complexity by removing successive wires and values of G(ave) were computed for the new geometries; eventually, the models were reduced to the simple wire structures shown in Figure 1. It became apparent that excessively high values of G(ave) were computed whenever a two-wire ("Y") junction was present in the structure geometry. A number of NEC analyses were examined using these two simple model geometries and varying different parameters, such as segment length, segment to wavelength ratio, number of segments in the feed, and types of feed (current-slope-discontinuity (CSD) versus applied-E-field voltage sources). The results of these analyses are presented in the following figures and tables.

In all of the examinations of both models, the segment-length to wavelength ratio was varied by running the NEC code at 6 frequencies--5 to 30 MHz in 5 MHz increments. Values of G(ave) were computed by integrating over solid angles of 0.5 and 2 pi steradians with a constant elevation cut increment of 1 degree and a variable azimuthal cut increment of from 1 to 30 degrees.

To produce the results depicted in Figures 2 and 3, the models were examined using a segment length of 1.4 meters (length/radius ratio of 2333; length/lambda ratio range of 0.0233 to 0.1400), which matched that used in the original complete broadband antenna model. For both the two-wire and the four-wire models, it is evident that the values of G(ave) are essentially identical for azimuth cut increments of 1, 5, 10, and 15 degrees. For the two-wire model, G(ave) values obtained by integrating over 2 pi steradians are much closer to the predicted G(ave) value of 2.0 than by integrating over 0.5 pi steradians. The four-wire (2 "Y" junctions) model indicate no discernible dependence on the volume of space encompassed in the integration--identical values of G(ave) were observed for both 0.5 or 2 pi steradian solid angle volumes. Since integrating over 2 pi steradians in 10 and 15 degree azimuthal cut increments was 2.4 and 3.5 times as fast, respectively, as integrating over 0.5 steradians in 1 degree increments, a significant savings in

computer resources may be realized by integrating over 2 pi steradians in 10 or 15 degree azimuth cut increments. Similar observations apply to Figures 4 and 5, where the segment length has been halved to 0.7 meters (length/radius ratio of 1166; length /lambda ratio range of 0.0117 to 0.0700), and to Figures 6 and 7, which display results using a segment length of 0.35 meters (length/radius ratio of 583; length/lambda ratio range of 0.0058 to 0.035). In Figure 8, the number of segments in the feed region was increased, thereby shortening the feed segment and increasing the wire-segment to feed-segment ratio. For the two-wire model, there is a very gradual monotonic increase in G(ave) values for increasing feed region segmentation, whereas the four-wire model exhibits a relatively rapid decrease in G(ave) values as the number of segments in the feed region increases. The final analysis performed employed a CSD voltage source to excite the two simple models. The results, shown in Table 1, are inconclusive beyond the observation that the CSD excitation gave a lower value of G(ave) for all cases except the four-wire model at 30 MHz.

The actual data used to generate Figures 2 through 8 are contained in Tables 2 through 9, as follows:

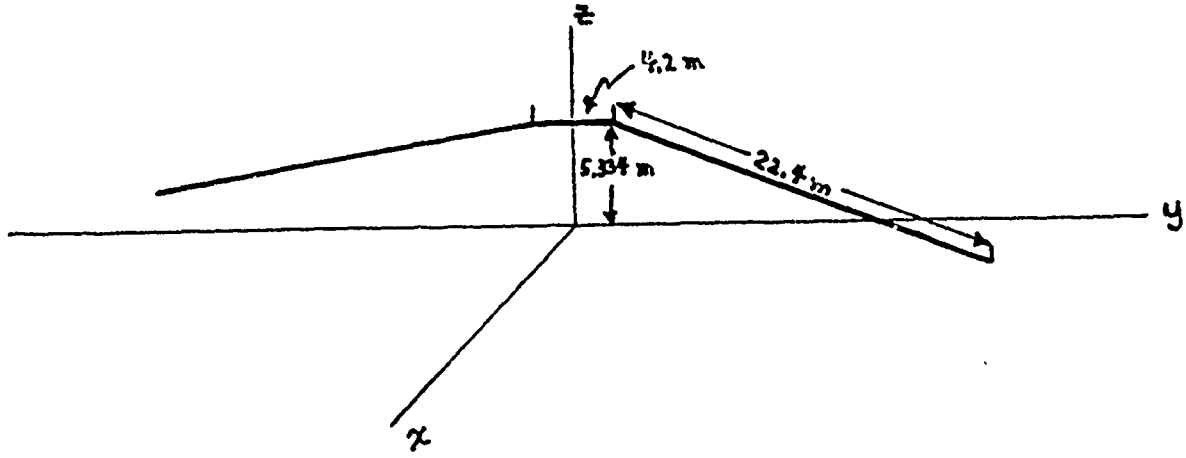
Figures 2 & 3 ..... Tables 2 & 3
Figures 4 & 5 ..... Tables 4 & 5
Figures 6 & 7 ..... Tables 6 & 7
Figure 8 ..... Tables 8 & 9

Additionally, sample NEC data sets for some of the analyses are given in Table 10.

(1) G.J. Burke, A.J. Pogio; Numerical Electromagnetics Code (NEC)--Method of Moments; Naval Ocean Systems Center (NOSC) Technical Document 116, January 1981.
(2) J. Strauch, S. Thompson; Interactive Graphics Utility for Army NEC Automation (IGUANA); NOSC Contractor Report 308, September 1985.

INTEGRATED GAIN MODELS

2 WIRE MODEL



4 WIRE MODEL

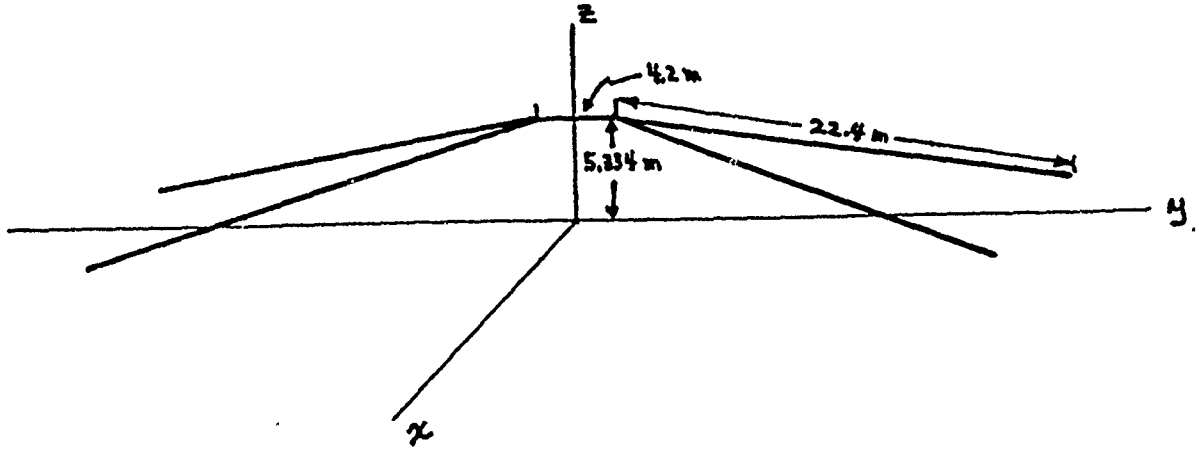
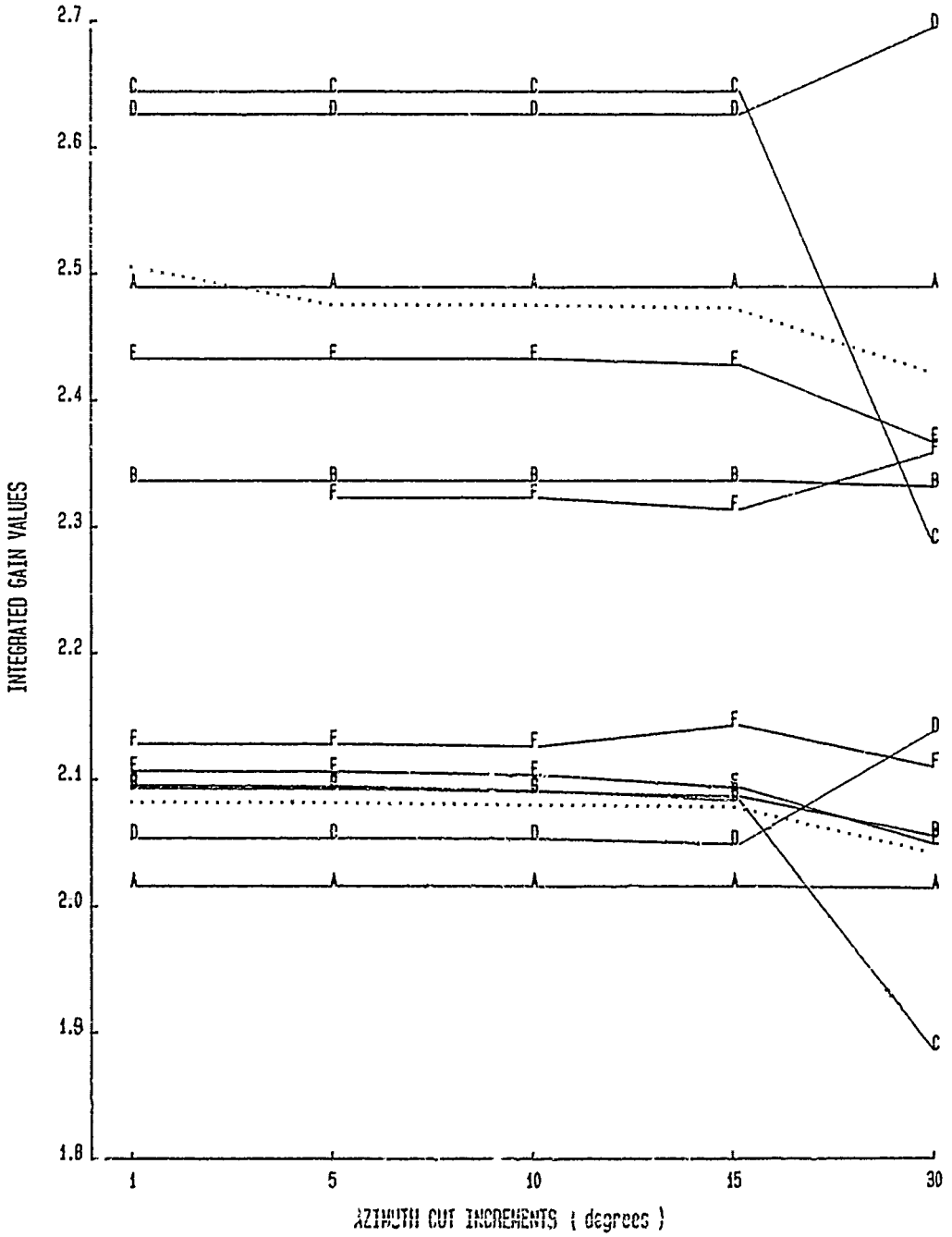


FIGURE 1

GAIN INTEGRATED OVER PERFECT EARTH (0.5 π STERADIANS)

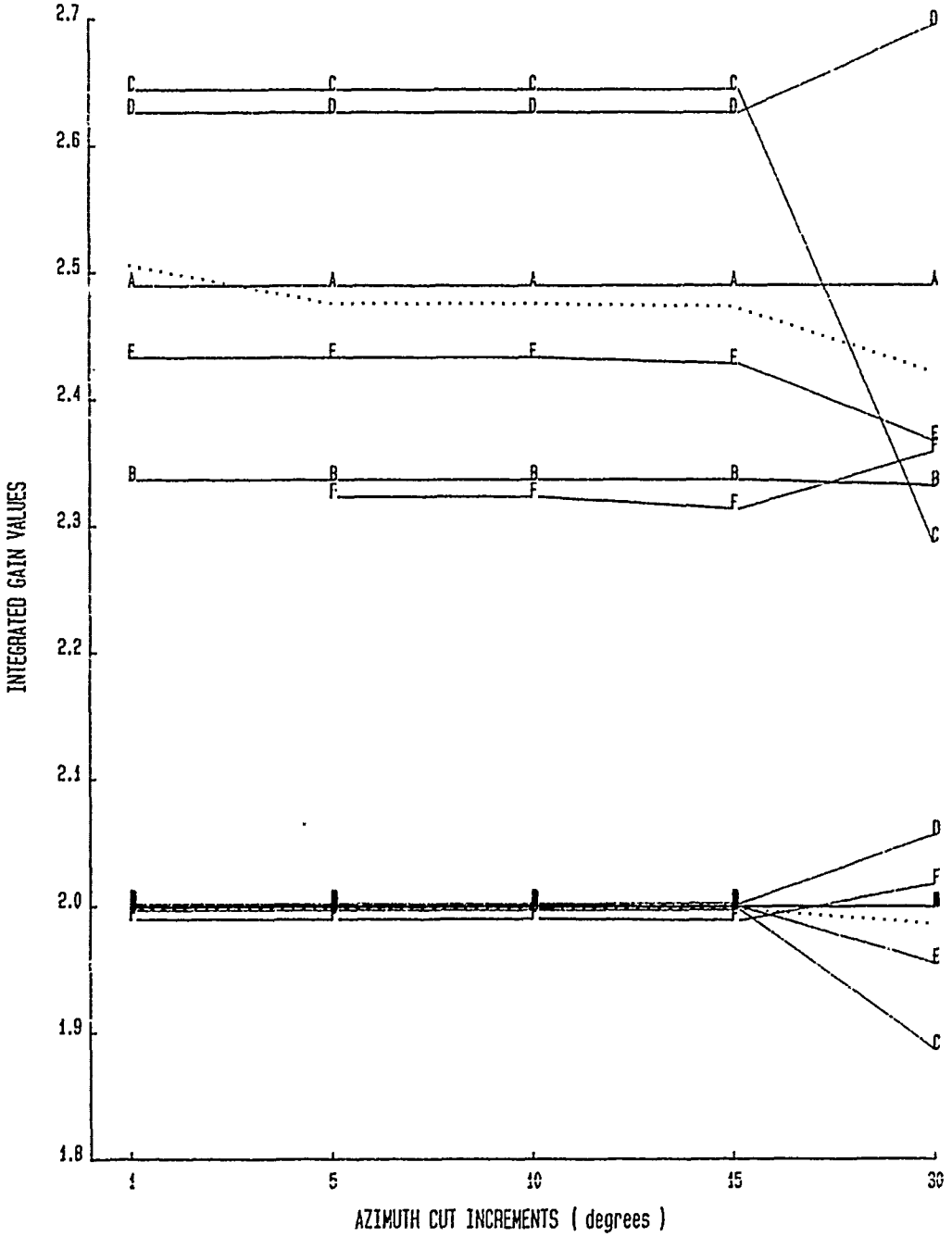


Upper lines = 4 wires
Lower lines = 2 wires
3 Segments in Feed
Segment Length = 1.40 m

A = 5 MHz D = 20 MHz
B = 10 MHz E = 25 MHz
C = 15 MHz F = 30 MHz
..... = Mean Value

FIGURE 2

GAIN INTEGRATED OVER PERFECT EARTH (2.0 π STERADIANS)

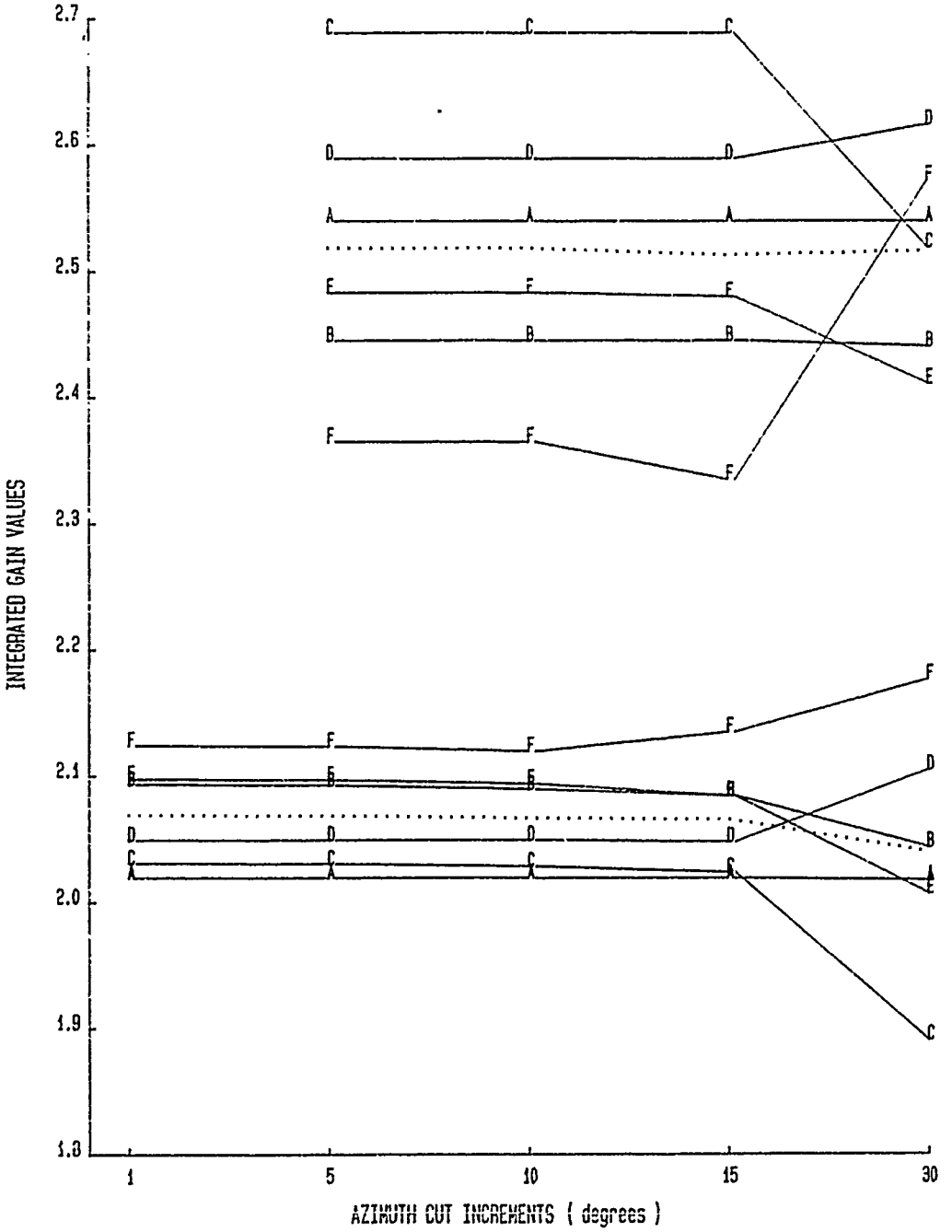


Upper lines = 4 wires
Lower lines = 2 wires
3 Segments in Feed
Segment Length = 1.40 m

A = 5 MHz D = 20 MHz
B = 10 MHz E = 25 MHz
C = 15 MHz F = 30 MHz
..... = Mean Value

FIGURE 3

GAIN INTEGRATED OVER PERFECT EARTH (0.5 π STERADIANS)

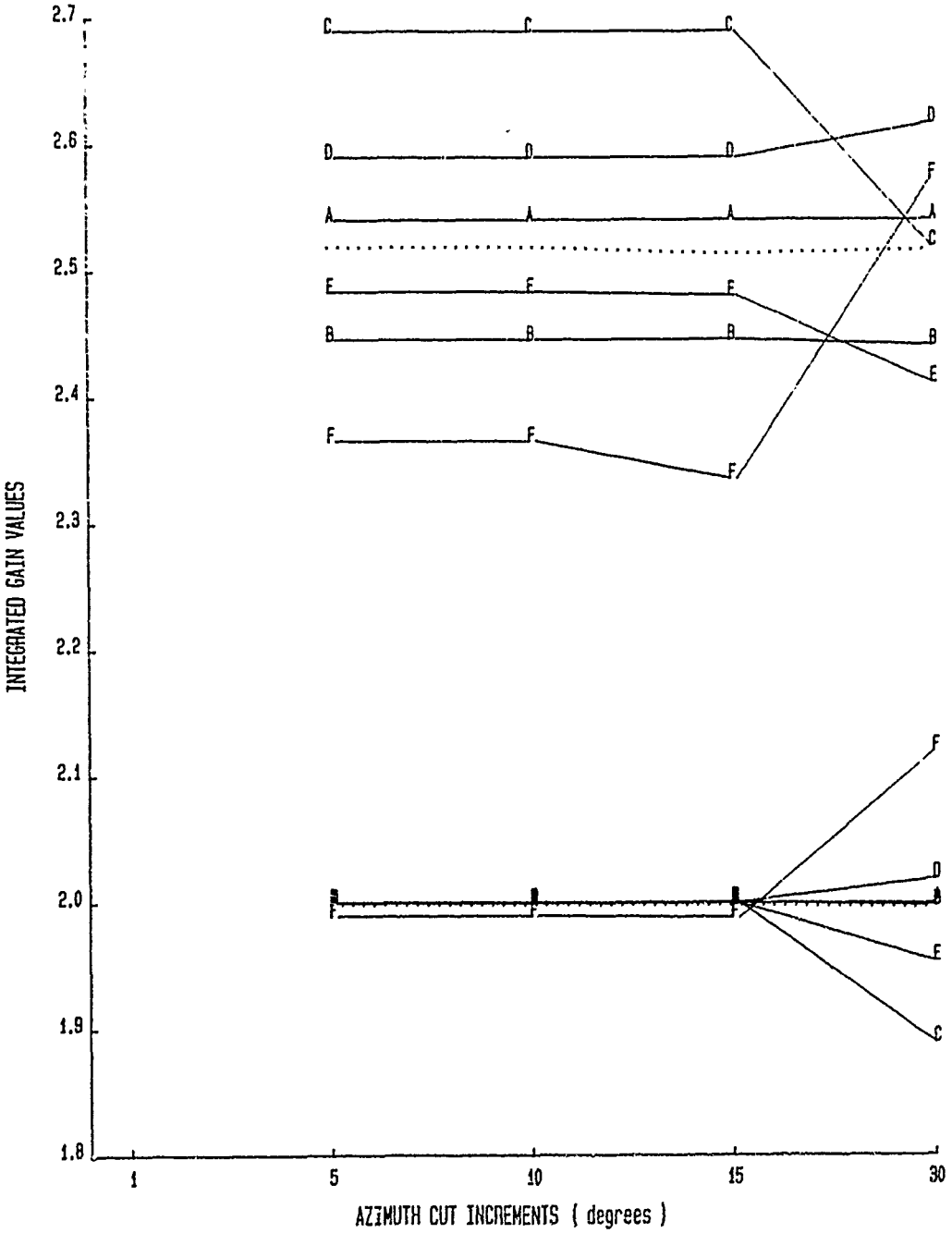


Upper lines = 4 wires
Lower lines = 2 wires
3 Segments in Feed
Segment Length = 0.70 m

A = 5 MHz D = 20 MHz
B = 10 MHz E = 25 MHz
C = 15 MHz F = 30 MHz
..... = Mean Value

FIGURE 4

GAIN INTEGRATED OVER PERFECT EARTH (2.0 π STERADIANS)

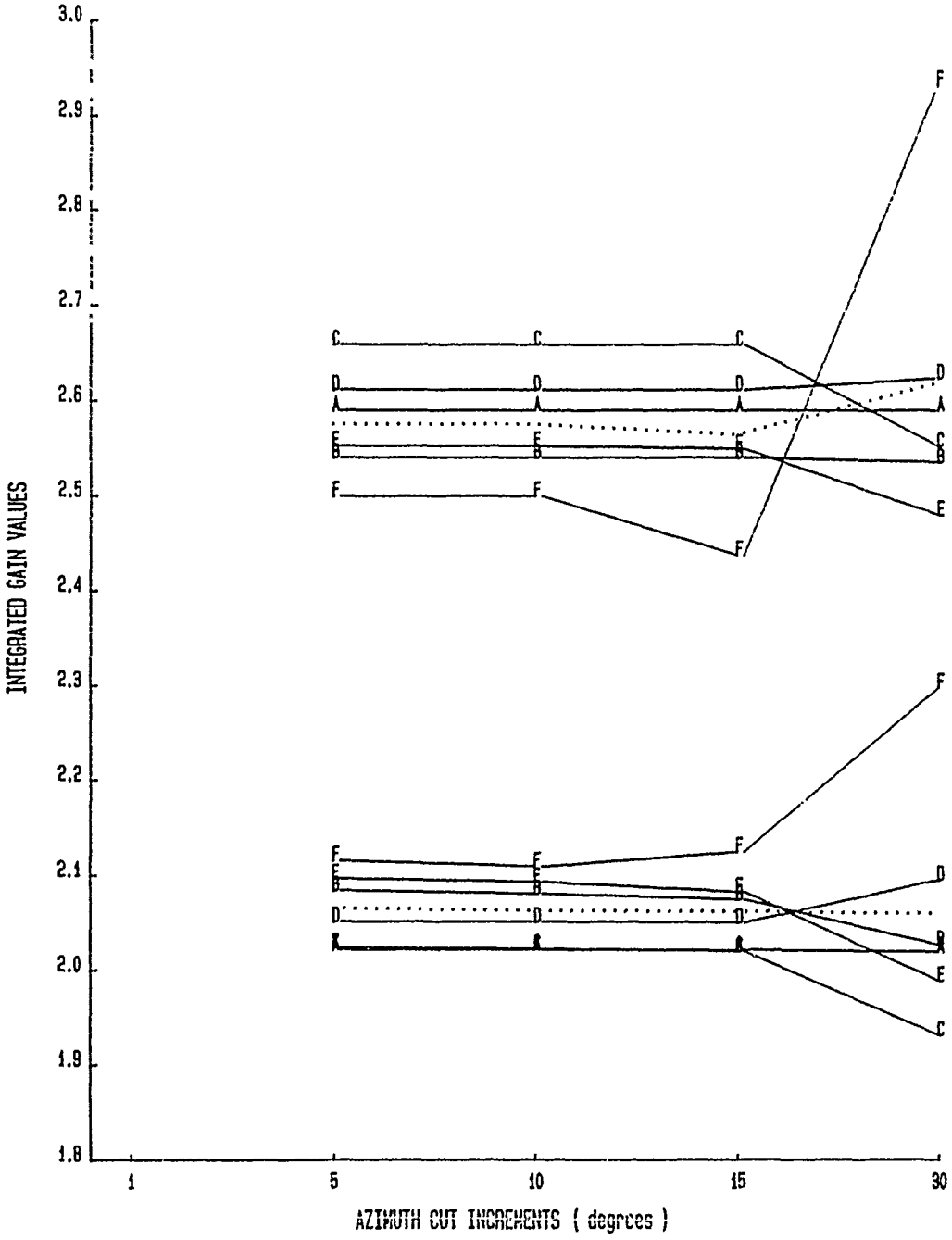


Upper lines = 4 wires
Lower lines = 2 wires
3 Segments in Feed
Segment Length = 0.70 m

A = 5 MHz D = 20 MHz
B = 10 MHz E = 25 MHz
C = 15 MHz F = 30 MHz
..... = Mean Value

FIGURE 5

GAIN INTEGRATED OVER PERFECT EARTH (0.5 π STERADIANS)

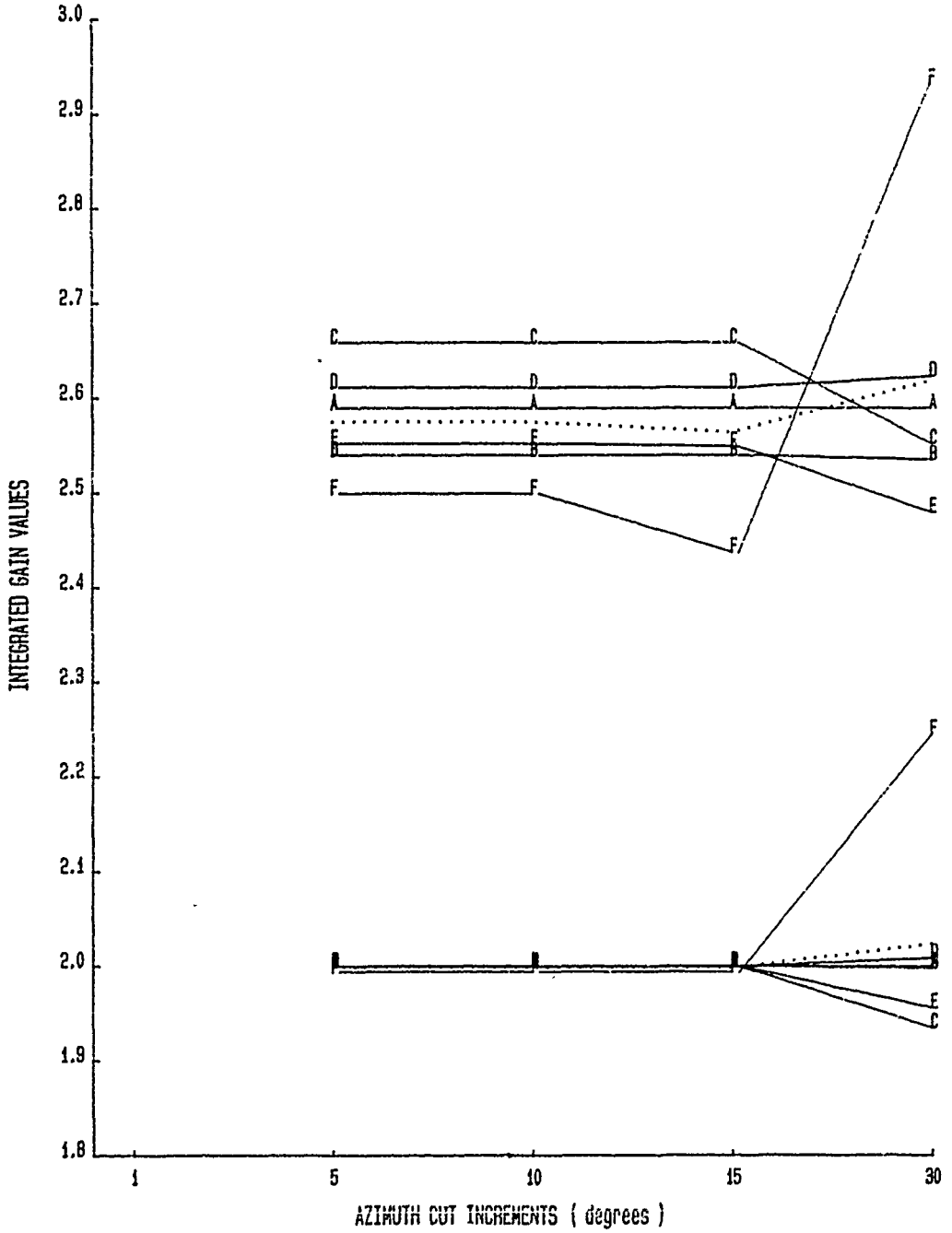


Upper lines = 4 wires
Lower lines = 2 wires
3 Segments in Feed
Segment Length = 0.35 m

A = 5 MHz D = 20 MHz
B = 10 MHz E = 25 MHz
C = 15 MHz F = 30 MHz
..... = Mean Value

FIGURE 6

GAIN INTEGRATED OVER PERFECT EARTH (2.0 π STERADIANS)



Upper lines = 4 wires
Lower lines = 2 wires
3 Segments in Feed
Segment Length = 0.35 m

A = 5 MHz D = 20 MHz
B = 10 MHz E = 25 MHz
C = 15 MHz F = 30 MHz
..... = Mean Value

FIGURE 7

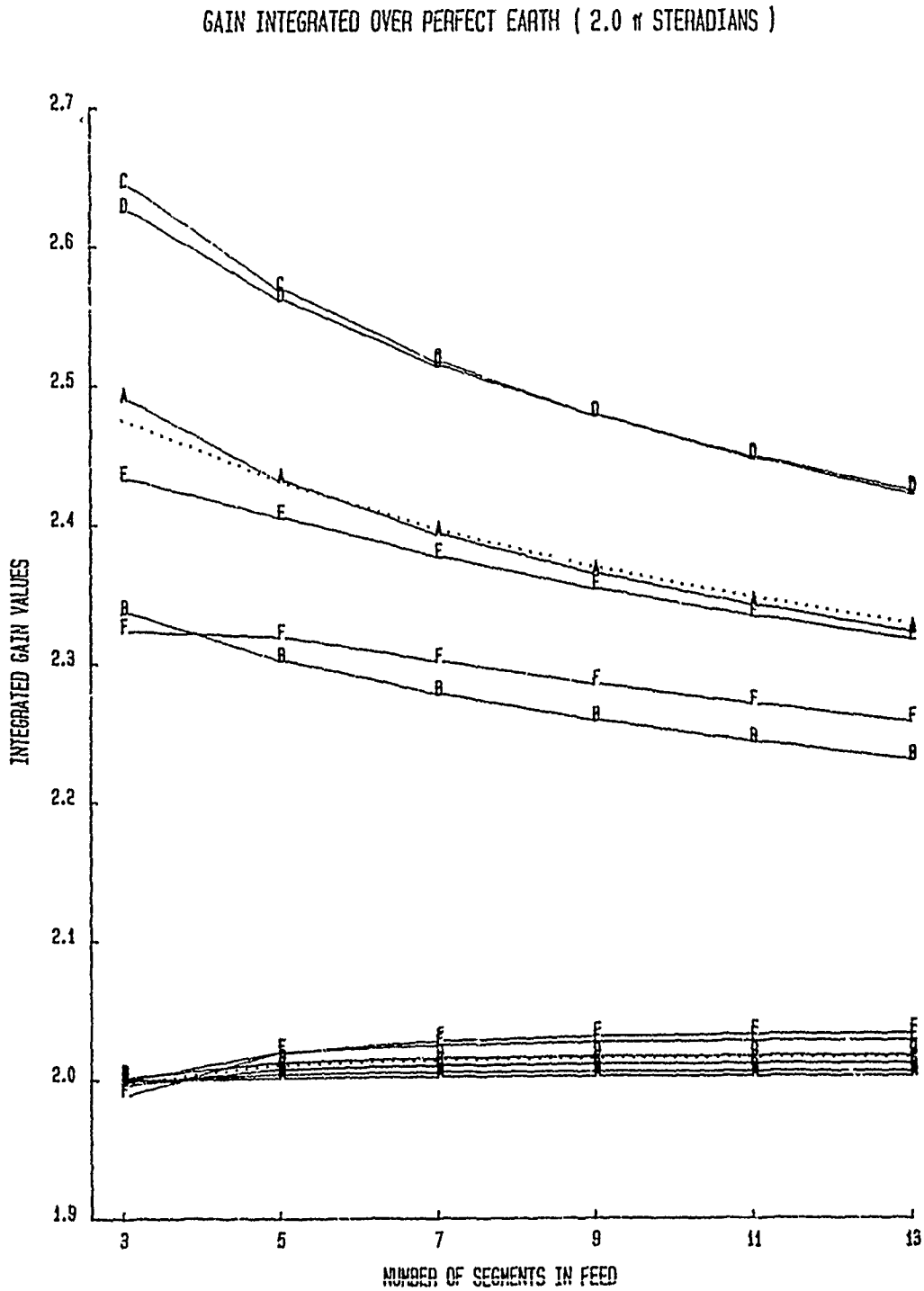

GAIN INTEGRATED OVER PERFECT EARTH (2.0 π STERADIANS)
INTEGRATED GAIN VALUES
2.7
2.6
2.5
2.4
2.3
2.2
2.1
2.0
1.9
3
5
7
9
11
13
NUMBER OF SEGMENTS IN FEED
Upper lines = 4 wires
Lower lines = 2 wires
Azimuth Cut = 10 deg
Total Feed Length = 4.2 m
A = 5 MHz
B = 10 MHz
C = 15 MHz
D = 20 MHz
E = 25 MHz
F = 30 MHz
..... = Mean Value

FIGURE 8

TABLE 1

INTEGRATED GAIN G(ave) VALUES

INTEGRATION VOLUME = 2 PI STERADIANS

MHZ	2 WIRE (S = 1.4 m)		4 WIRE (S = 1.4 m)	
	AEF	CSD	AEF	CSD
5	1.9993	1.9189	2.4896	2.3918
10	1.9997	1.9235	2.3364	2.2481
15	1.9968	1.9395	2.6444	2.5606
20	2.0019	1.9380	2.6263	2.5436
25	2.0002	1.9375	2.4327	2.3993
30	1.9895	1.9155	2.3230	2.3923

AEF = Applied-E-Field Voltage Source
CSD = Current-Slope-Discontinuity Voltage Source

TABLE 2

INTEGRATED GAIN G(ave) VALUES

2 WIRE MODEL (S = 1.40 m)

	AZIMUTHAL CUT INCREMENT (degrees)				
	1	5	10	15	30
.5 pi 5 MHz	2.0158	2.0158	2.0156	2.0154	2.0138
2 pi	1.9993	1.9993	1.9993	1.9993	1.9993
.5 pi 10 MHz	2.0931	2.0923	2.0901	2.0862	2.0550
2 pi	1.9997	1.9997	1.9997	1.9997	1.9997
.5 pi 15 MHz	2.0953	2.0944	2.0911	2.0831	1.8859
2 pi	1.9969	1.9969	1.9969	1.9969	1.8767
.5 pi 20 MHz	2.0536	2.0536	2.0531	2.0487	2.1376
2 pi	2.0019	2.0019	2.0019	2.0018	2.0560
.5 pi 25 MHz	2.1067	2.1060	2.1033	2.0933	2.0490
2 pi	2.0002	2.0002	2.0002	1.9992	1.9547
.5 pi 30 MHz	2.1282	2.1279	2.1261	2.1425	2.1093
2 pi	1.9895	1.9895	1.9895	1.9884	2.0174

TABLE 3

INTEGRATED GAIN G(ave) VALUES

4 WIRE MODEL (S = 1.40 m)

	AZIMUTHAL CUT INCREMENT (degrees)				
	1	5	10	15	30
.5 pi 5 MHz	2.4896	2.4896	2.4896	2.4896	2.4896
2 pi	2.4896	2.4896	2.4896	2.4896	2.4896
.5 pi 10 MHz	2.3364	2.3364	2.3364	2.3364	2.3315
2 pi	2.3364	2.3364	2.3364	2.3364	2.3315
.5 pi 15 MHz	2.6444	2.6444	2.6444	2.6444	2.2873
2 pi	2.6444	2.6444	2.6444	2.6444	2.2873
.5 pi 20 MHz	2.6263	2.6263	2.6263	2.6259	2.6943
2 pi		2.6263	2.6263	2.6259	2.6943
.5 pi 25 MHz	2.4327	2.4327	2.4327	2.4276	2.3670
2 pi		2.4327	2.4327	2.4276	2.3670
.5 pi 30 MHz		2.3230	2.3230	2.3134	2.3583
2 pi		2.3230	2.3230	2.2134	2.3583

TABLE 4

INTEGRATED GAIN G(ave) VALUES

2 WIRE MODEL (S = 0.70 m)

	AZIMUTHAL CUT INCREMENT (degrees)				
	1	5	10	15	30
.5 pi 5 MHz	2.0196	2.0196	2.0194	2.0191	2.0174
2 pi		1.9997	1.9997	1.9997	1.9997
.5 pi 10 MHz	2.0935	2.0925	2.0895	2.0841	2.0436
2 pi		2.0000	2.0000	2.0000	1.9976
.5 pi 15 MHz	2.0311	2.0305	2.0285	2.0238	1.8906
2 pi		2.0001	2.0001	2.0001	1.8893
.5 pi 20 MHz	2.0494	2.0494	2.0493	2.0478	2.1046
2 pi		2.0004	2.0004	2.0004	2.0189
.5 pi 25 MHz	2.0975	2.0967	2.0937	2.0840	2.0070
2 pi		1.9998	1.9998	1.9996	1.9536
.5 pi 30 MHz	2.1241	2.1234	2.1196	2.1348	2.1766
2 pi		1.9897	1.9897	1.9882	2.1193

TABLE 5

INTEGRATED GAIN G(ave) VALUES

4 WIRE MODEL (S = 0.70 m)

	AZIMUTHAL CUT INCREMENT (degrees)			
	1	5	10	15	30
.5 pi 5 MHz		2.5400	2.5400	2.5400	2.5400
2 pi			2.5400	2.5400	2.5400
.5 pi 10 MHz		2.4452	2.4452	2.4452	2.4405
2 pi			2.4452	2.4452	2.4405
.5 pi 15 MHz		2.6890	2.6890	2.6890	2.5190
2 pi			2.6890	2.6890	2.5190
.5 pi 20 MHz		2.5893	2.5893	2.5892	2.6165
2 pi			2.5893	2.5892	2.6165
.5 pi 25 MHz		2.4832	2.4832	2.4800	2.4111
2 pi			2.4832	2.4800	2.4111
.5 pi 30 MHz		2.3651	2.3650	2.3352	2.5721
2 pi			2.3650	2.3352	2.5721

TABLE 6

INTEGRATED GAIN G(ave) VALUES

2 WIRE MODEL (S = 0.35 m)

	AZIMUTHAL CUT INCREMENT (degrees)			
1	5	10	15	30
.5 pi 5 MHz	2.0215	2.0213	2.0210	2.0192
2 pi	1.9998	1.9998	1.9998	1.9998
.5 pi 10 MHz	2.0842	2.0805	2.0742	2.0265
2 pi	1.9999	1.9999	1.9999	1.9975
.5 pi 15 MHz	2.0242	2.0227	2.0195	1.9311
2 pi	1.9997	1.9997	1.9997	1.9346
.5 pi 20 MHz	2.0513	2.0511	2.0499	2.0951
2 pi	1.9999	1.9999	1.9999	2.0085
.5 pi 25 MHz	2.0965	2.0930	2.0821	1.9885
2 pi	1.9995	1.9995	1.9995	1.9556
.5 pi 30 MHz	2.1154	2.1090	2.1243	2.2974
2 pi	1.9943	1.9944	1.9936	2.2445

TABLE 7

INTEGRATED GAIN G(ave) VALUES

4 WIRE MODEL (S = 0.35 m)

	AZIMUTHAL CUT INCREMENT (degrees)			
	1	5	10	15	30
.5 pi 5 MHz 2 pi		2.5893	2.5893	2.5893	2.5893
.5 pi 10 MHz 2 pi		2.5398	2.5398	2.5398	2.5350
.5 pi 15 MHz 2 pi		2.6584	2.6584	2.6584	2.5517
.5 pi 20 MHz 2 pi		2.6110	2.6110	2.6109	2.6230
.5 pi 25 MHz 2 pi		2.5519	2.5519	2.5489	2.4796
.5 pi 30 MHz 2 pi		2.4994	2.4994	2.4372	2.9322

TABLE 8

INTEGRATED GAIN G(ave) VALUES

2 WIRE MODEL (S = 1.4 m)

FEED SEGS	MHz					
	5	10	15	20	25	30
3	1.9993	1.9997	1.9969	2.0019	2.0002	1.9895
5	2.0017	2.0043	2.0079	2.0128	2.0201	2.0201
7	2.0024	2.0055	2.0104	2.0157	2.0252	2.0280
9	2.0026	2.0059	2.0114	2.0168	2.0271	2.0312
11	2.0027	2.0061	2.0117	2.0173	2.0281	2.0328
13	2.0028	2.0062	2.0120	2.0176	2.0286	2.0335

TABLE 9

INTEGRATED GAIN G(ave) VALUES

4 WIRE MODEL (S = 1.4 m)

FEED SEGS	MHz					
	5	10	15	20	25	30
3	2.4896	2.3364	2.6444	2.6263	2.4327	2.3230
5	2.4312	2.3021	2.5689	2.5615	2.4047	2.3188
7	2.3926	2.2774	2.5165	2.5138	2.3763	2.3010
9	2.3640	2.2584	2.4777	2.4777	2.3530	2.2845
11	2.3413	2.2431	2.4469	2.4482	2.3336	2.2702
13	2.3225	2.2303	2.4216	2.4240	2.3171	2.2576

TABLE 10

EXAMPLES OF NEC DATA SETS

A. DATA SET -- 2 WIRE (NO "Y" JUNCTIONS)
5-30 BY 5 MHz INTEGRATE .5 PI 1 DEG AZ INC

```
GW,01,16,0.0,2.1,5.1816,1.4496,23.8442,0.0,0.0006
GW,02,16,0.0,-2.1,5.1816,-1.4496,-23.8442,0.0,0.0006
GW,03,03,0.0,-2.1,5.1816,0.0,2.1,5.1816,0.0006
GM,0,0,0.0,0.0,0.0,0.0,0.0,0.0,0.1524,0.0
GE,-1
EX,0,03,02,00,100.0,0.0,,600.0
FR,0,6,,,5.0,5.0
GN,1
RP,0,91,91,1002,0.0,0.0,1.0,1.0
EN
```

B. DATA SET -- 4 WIRE (TWO "Y" JUNCTIONS)
5-30 BY 5 MHz INTEGRATE 2 PI 5 DEG AZ INC

```
GW,01,16,0.0,2.1,5.1816,1.4496,23.8442,0.0,0.0006
GX,10,110
GW,02,03,0.0,-2.1,5.1816,0.0,2.1,5.1816,0.0006
GM,0,0,0.0,0.0,0.0,0.0,0.0,0.0,0.1524,0.0
GE,-1
EX,0,02,02,00,100.0,0.0,,600.0
FR,0,6,,,5.0,5.0
GN,1
RP,0,91,73,1002,0.0,0.0,1.0,5.0
EN
```

C. DATA SET -- 5-SEG FEED (NO "Y" JUNCTIONS)
5-30 BY 5 MHz INTEGRATE 2 PI 5 DEG AZ INC

```
GW,01,16,0.0,2.1,5.1816,1.4496,23.8442,0.0,0.0006
GW,02,16,0.0,-2.1,5.1816,-1.4496,-23.8442,0.0,0.0006
GW,03,05,0.0,-2.1,5.1816,0.0,2.1,5.1816,0.0006
GM,0,0,0.0,0.0,0.0,0.0,0.0,0.0,0.1524,0.0
GE,-1
EX,0,03,03,00,100.0,0.0,,600.0
FR,0,6,,,5.0,5.0
GN,1
RP,0,91,73,1002,0.0,0.0,1.0,5.0
EN
```

A MININEC MODEL OF

THE MINILOOP ANTENNA

James C. Logan

Naval Ocean Systems Center
Code 822
271 Catalina Blvd.
San Diego, CA 92152-5000

ABSTRACT

The Miniloop is an HF loop antenna which has found use on U.S. Coast Guard vessels. The antenna is a large diameter loop mounted on a pedestal. It is tuned with a variable capacitor mounted in series at the top of the loop. Inductive coupling from a much smaller loop on the lower rim is used as a feed.

MININEC (NOSC TD 938, "The New MININEC "ersion 3); a Mini-Numerical Electromagnetics Code", by J. W. Rockway and J. C. Logan, September 1986, is used to represent the Miniloop antenna mounted over a perfectly conducting ground plane. The development and validation of the MININEC model of the Miniloop will be discussed. A sample method for determining radiation efficiency will also be presented.

INTRODUCTION

In general, HF antennas mounted on ships will couple into metallic parts of the ship. This means that strong RF currents can be excited on closely coupled conducting surfaces, which in turn re-radiate. The total near field is the (vector) sum of the fields radiated by the antenna, the deliberate antenna, and the non-deliberate antennas. Re-radiation is enhanced whenever the non-deliberate antennas are similar in size to the deliberate antennas, or whenever resonant length conducting paths and spacings occur.

A computer model can be used to include the deliberate and non-deliberate interactions to accurately predict the near fields on exposed weather decks. This usually involves creating a wire grid model of all conducting surfaces. A wire grid model consists of a mesh of closely spaced, connected wires, which are close enough together to approximate a solid conducting surface. Building a wire grid model of a ship is a time consuming, tedius process, requiring detailed blue prints and considerable experience. The resulting computer model requires the resources of a large main frame computer system.

In some cases, a simplified antenna model may be used to avoid the expense of wire grid models. This requires good judgement and usually some additional information, such as measurements of the antennas in similar shipboard environments. The simplified model provides an upper bounds on the fields and the measurements are used tc determine a suitable safety margin.

The first step is to develop and validate, if possible, a model of the antenna. This is a process of deciding how many wires and segments are required to achieve acceptable accuracy. This process will be described for the development of a MININEC model of the Miniloop antenna.

BACKGROUND

The "Mini" Numerical Electromagnetics Code, or MININEC (reference 1), is a method of Moments computer program for analysis of thin wire antennas . A Galerkin procedure is applied to an electric field integral equation to solve for the wire currents. This formulation results in an unusually short computer program suitable for implementation on a microcomputer. Hence, MININEC is written in a BASIC language compatible with many popular microcomputers.

MININEC solves for impedance and currents on arbitrarily oriented wires, including configurations with multiple wire junctions, in free space and over a perfectly conducting ground plane. Options include lumped parameter impedance loading of wires and calculation of near zone and far zone fields. Both near electric fields and near magnetic fields can be determined for free space and over a perfectly conducting ground. The far zone electric fields and radiation pattern (power pattern) can also be determined for free space and perfectly conducting ground.

The miniloop is a single turn, HF loop antenna which has been used for communications by the U. S. Coast Guard for both transmit and receive. It features capacitive remote tuning and inductive feed.

The are two versions of the Miniloop antenna (see reference 2). Version MLA-1/E is for use in the band from 1.8 MHz to 14.5 MHz. Version MLA-2/D is for use from 3 MHz to 24.5 MHz. Both consist of a large loop mounted on a pedestal. The loop is excited from a much smaller feel loop and turned via a variable capacitor at the top of the large loop. Figure 1 illustrates the basic configuration.

THE MININEC MODELS

For MININEC, the main loop of the Miniloop antenna is represented by a series of one segment wires connected end to end to form the main loop. A convergence test is performed to determine the number of wires or segments required for reasonable accuracy.

The impedance of the Miniloop is not known. Referring to the open literature, a loop whose characteristics are well established is chosen. Figure 2 shows the convergence test for a one wavelength circumference loop in free space. The admittance given by R.W.P. King (from reference 3) is used to measure convergence. Based on this data, a 22 segment or 22 sided polygon model of the loop is selected. Figure 3 shows the performance of this model over a wide band of frequencies. Figure 3 is a comparison of the MININEC model to the published data by R.W.P. King. The Miniloops are used in the region below the first self resonance. It is seen in Figure 3 that the MININEC model tracks the theory very well below resonance.

Using the MININEC loop model, the Miniloop configuration of Figure 1 was explored further. It has been determined that the currents on the mast support are two orders of magnitude lower than the loop currents. The mast can therefore be removed from the model without loss of accuracy. Likewise, the feed loop can also be removed from the model. The feed loop serves the purpose of impedance matching and does not contribute significantly to the properties of the RF fields. Hence, the loop model is simplified to a circular loop over a perfectly conducting ground plane. For each version of the Miniloop, the diameter of the loop model is adjusted to give the same area as the Miniloop version, i.e., the loop model has the same self resonance as the Miniloop version

Both versions of the Miniloop use a vacuum capactor located at the top of the large loop to tune the antenna to resonance at the operating frequency. The MININEC model must be exercised once at each desired frequency to determine the value of reactance required for tuning. The model is excited or fed at the load point. The negative of the reactance of the antenna input impedance is the required load value. A second run with this reactance at the load point, but fed at the bottom of the loop, is generally done to verify the tuned condition.

MINILOOP EFFICIENCY

One way to determine the radiation efficiency of an antenna system is as follows:

The system efficiency is:

$$n = \frac{BW_o}{BW_m}$$

where BW_o is the ideal bandwidth from the MININEC model and BW_m actual bandwidth achieved or measured. The bandwidth of the Miniloops on a ground plane has been previously measured by NAVOCEANSYSCEN. The results from references 2 and 4 are given in figure 4.

The ideal bandwidth is determined from the MININEC model and the Q as follows:

$$BW_o = \frac{f_o}{Q_o}$$

Where the f_o is the operating frequency and Q_o is the ideal Q determined by the slope-reactance technique given in Jasik (reference 8). To apply this technique, the change in reactance of the tuned antenna is determined for a small change in frequency, and the Q is determined from

$$Q_o = \frac{! X_a ! + f_o ! \frac{dX_a}{df} !}{2R}$$

Where X_a is the antenna reactance and R is the radiation resistance at the frequency f_o. Figure 5 shows the efficiency versus frequency for the two Miniloop antennas as determined by this procedure.

SUMMARY

The process for development and validation of a MININEC model has been illustrated. In this case the Miniloop model has been used to determine antenna efficiency, which in turn can be used to set power levels for RF near field predictions.

REFERENCES

1. NOSC TD 938, "The New MININEC (Version 3): a Mini-Numerical Electromagnetic Code", J. C. Logan and J. W. Rockway, Sep. 1986

2. Department of Transportation/U. S. Coast Guard, "Instruction Booklet for MLA-1/E and MLA-2/D Miniloop Antenna Systems", Electronics Engineering Division, U.S. Coast Guard Station, Alexandria, Va., 1 Mar. 1982.

3. R. W. P. King, "Tables of Antenna Characteristics", IFI/Plenum Data Corporation, New York 1971

4. NELC TD 317, "MLA-1 Miniloop Antenna: A Technical Evaluation", by J. L. Lievens and D. W. DuBrul, 10 May 1974.

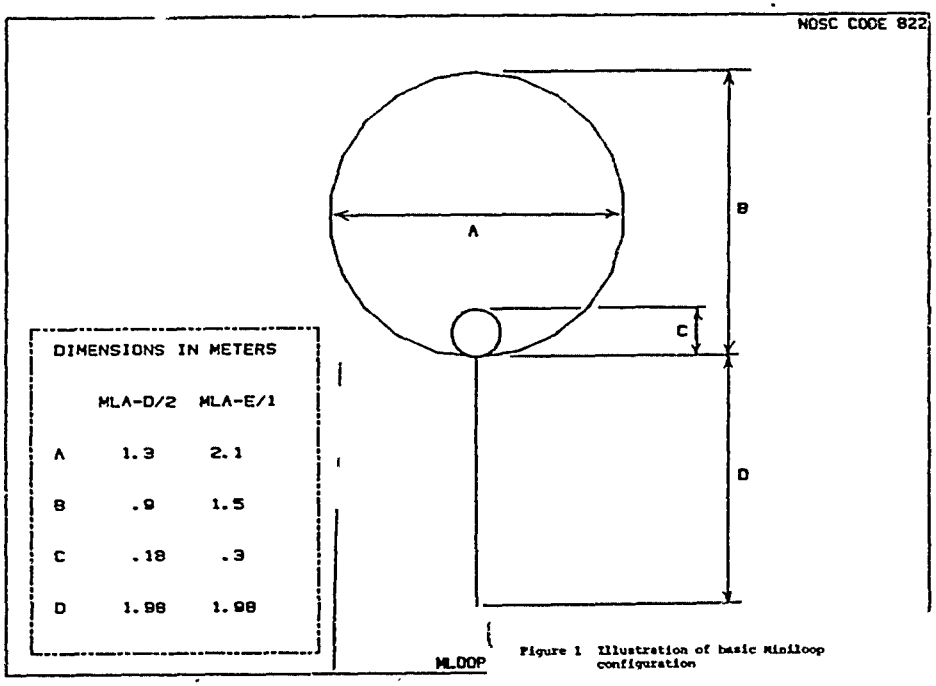


Figure 1 Illustration of basic Miniloop configuration

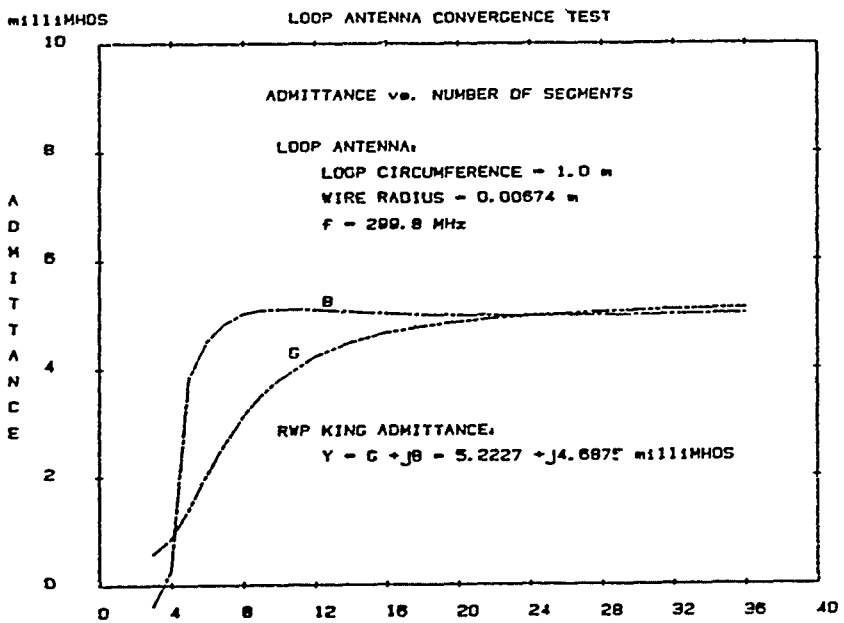


Figure 2 Convergence Test of MINIMOC for a loop in free space

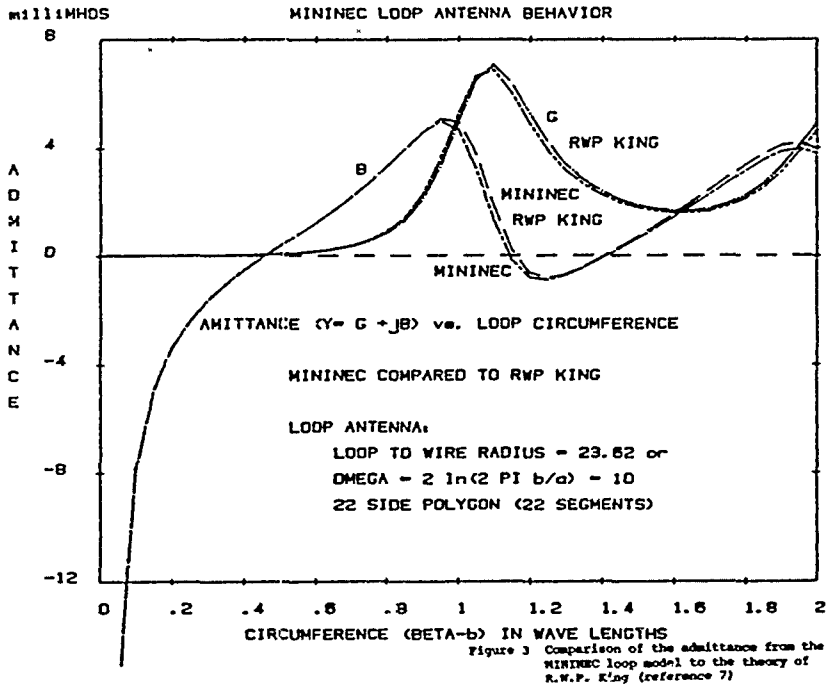


Figure 3 Comparison of the admittance from the MININEC loop model to the theory of R.W.P. King (reference 7)

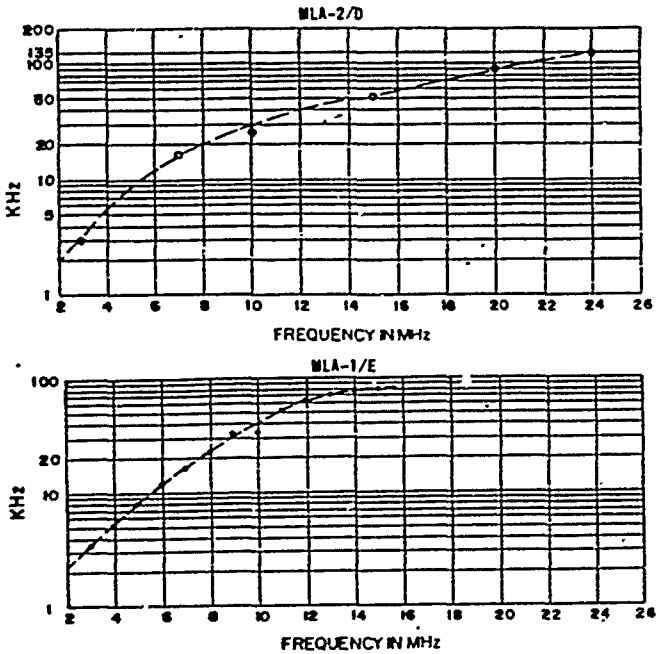


Figure 4 Half-power bandwidth measured on a ground plane

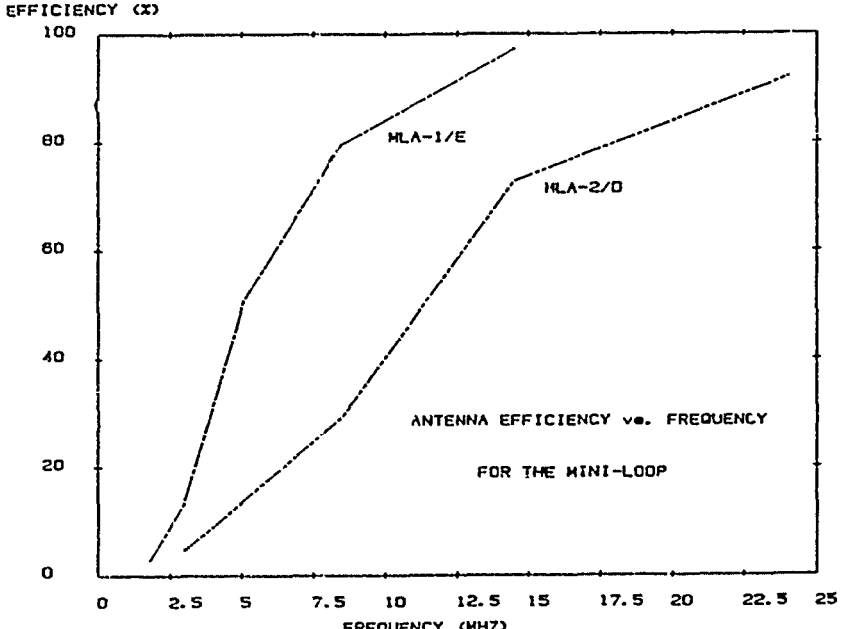


Figure 5 Miniloop efficiency based on the measured bandwidth and the MINIMMC Model

Antenna Handbook

Edward E. Domning, James K. Breakall
Alan M. Christman and Stuart J. Hayden
University of California
Lawrence Livermore National Laboratory

Introduction:

We were tasked to study parameter variations of certain HF antennas that the Army and the Marines could use in field scenarios. We looked at variations in geometry, over five ground constants and two frequencies. Our objective was to come up with performance criteria comparing one antenna to another, which we solved by creating a table of selected sky and ground wave data. This table can only give a limited comparison; field operators would need more complete data to construct efficient antennas. So we supplemented the tabular data with ground and sky wave plots that give more detail. Gathering this data for all the antenna variations we had turned into a very large task. The problem and its solution is given in this report.

Problem Encountered:

We want to give the field radio operators a very accurate description of the fields radiated by these antennas, so we decided that for the sky wave we want to gather data in one degree increments in azimuth for each degree in elevation. When trying to store this data on a practical computer system (a VAX cluster for us) we calculate the storage requirement to be approximately 506 blocks or .25 Mbytes per antenna. With all of our variations, we would model 500 different antennas consuming 125 Mbytes of storage. While this is possible, we came up with a more compact way to store the data which doesn't stress the storage facilities of our computer system.

Solution:

Marvin Barth pointed out that given the geometry of the wire segments and the current along those segments, we could calculate any field patterns we wished. This solution was applicable to our problem because we only needed elevation plots at selected azimuthal angles. We then modified a version of NEC3 double precision operating on the VAX to write the common blocks needed in the NEC3 routine RDPAT (routine to calculate field data) to binary files. With the size of these files 24 to 70 blocks in length the worst case for storage need is 17.1 Mbytes. Not only have we reduced our storage size but we have increased our flexibility. Unfortunately we had to develop a code to take advantage of this flexibility.

NEC3 Modifications:

We inserted a new instruction in NEC3 called the CO (current output) card. The instruction must be inserted after a GE instruction but before any instruction that solves for currents (e.g. XQ, RP). After NEC3 calls the routine NETWK a subroutine is called to output the binary data. The files are named after the text output file with the postscript of .CUR added. If no text output file is specified then the output file name of TEMP.CUR is used.

Program Development:

To be able to use this data we created a program that calculates the data we need for our plots and tables. We made it menu driven so that it is easy to use. We also included a file handler so the user has easy access to the binary files created in NEC3. It has a quick look facility to view radiation patterns of a selected antenna to see if the model gives reasonable results. It also submits batch jobs to our VAX 8600 for creating ground and sky wave patterns for reference. The batch job also pulls out table information that gives the field operator quick information before referring to the in-depth field information. This program can also sort the tabular information by different priorities.

Conclusions:

We have run our large set of antennas through our program and have obtained plots and tables. We are now forming this data into an engineering handbook. We are also working on a version of this program to operate on the IBM PC.

Acknowledgements:

Work done under contract for USAESEIA (Fort Hauchuca) Arizona and USACECOM (Fort Monmouth) New Jersey.

Work done under auspices of the U. S. Department of Energy by Lawrence Livermore National Laboratory under contract W-7405-Eng-48.

HF ANTENNA HANDBOOK

J.K. Breakall

E.E. Domning

A.M. Christman

S.J. Hayden

Lawrence Livermore National Laboratory

Third Annual Review of Progress in Applied Computational Electromagnetics

Naval Postgraduate School, Monterey California

March 24,25 and 26, 1987

Introduction

We investigated the effect of varying different antenna parameters on the ground and sky wave radiation patterns of chosen HF antennas. To do this we developed a program that uses data from common blocks in NEC3 to calculate the field data for analysis.

Parameters Varied :

- Geometry
- Ground Parameters
- Frequency

Data Needed

To give a good description of each antenna, we need data in one degree increments over the whole hemisphere.

Storage requirements on a VAX system :

8 bytes (double Precision)

360 (points/elevation)

x 90 (elevations)

= 259200 bytes = 506.25 VAX blocks

Total Storage for Project

5 sets of antennas

10 variations

5 Ground Constants

2 Frequencies

= 500 Different antennas

= 253125 VAX blocks for storage

or

123.6 Mbytes storage

Solution

Have NEC3 write out the current and geometry data to a binary file and calculate the field data when needed.

- Results :
- 24 - 70 blocks/antenna

35000 VAX blocks = 17.1 mbytes

- Increased flexibility

Has Geometry data

can calculate whatever you want

- Harder to program

NEC3 Modifications

We added a new instruction in NEC3D to write geometry and current data (plus more) for field calculations.

Model listing :

```
CM GEOMETRY : BASIC WHIP WITH 8 1/4 WAVELENGTH GROUND RADIALS
CM RADIO : NONE
CM FREQUENCY : 17 MEGAHERTZ
CM GROUND : EPSILON = 34 , SIGMA = 0.15
CE
GW 1 7 0 0 .008 0 0 33.008 .05
GW 21 4 0 0 .008 14.47 0 .008 .05
GM 1 7 0 0 45 0 0 0 21
GS 0 0 .3048
GE
FR 0 0 0 0 17
GN 2 0 0 0 34 .15
EX 0 1 1 0 1
CO
XQ
EN
```

Program Development

Included NEC3 routine RDPAT in a menu driven program to get the data we need in the necessary format.

- File handling via numbers (includes title)
- Interactive pattern plotting (quick look)
- Submits calculation intensive part to batch queues
- VAX/VMS specific

Main Menu from Program

```
Main Menu

1) List Data Base
2) Add File to Data Base
3) Delete File from Data Base
4) Change Title of Data Store
5) Do Pattern Plots
6) Print Out Sorted Table
7) Submit Job for Plots and Table
8) Exit from Program
```

Basic Whip with 8 1/4 Wave Ground Radials

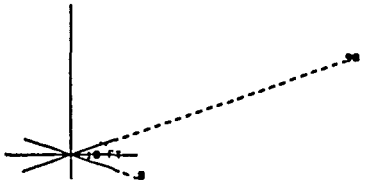
FREQUENCY(MHZ) : 17.00

GROUND CONDUCTIVITY (MHOS): 0.15000

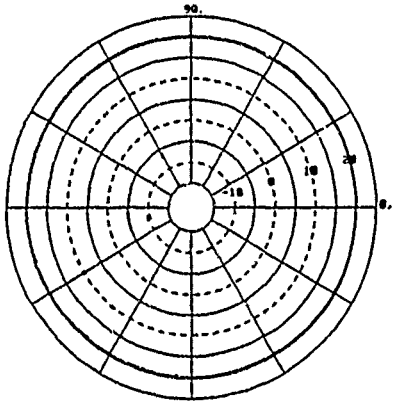
GROUND DIELECTRIC CONSTANT (REL) : 34.00

INPUT IMPEDANCE : 557.15 -j 663.60

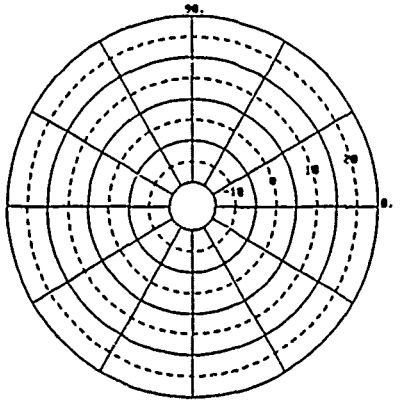
VSWR (FOR 50 OHMS) : 27.007



3-D PLOT

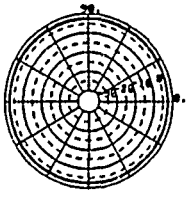


VERTICAL GROUND WAVE IN dB(1mV/m)

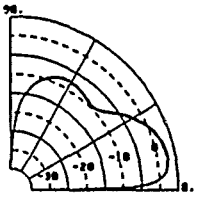


HORIZONTAL GROUND WAVE IN dB(1mV/m)

TOTAL GAIN IN dBi

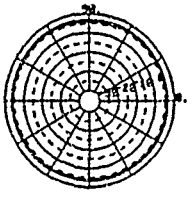


AZIMUTH PLOT AT
10 DEGS
IN ELEVATION

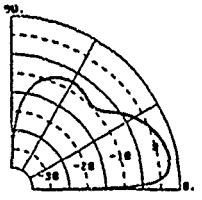


ELEVATION PLOT AT
14 DEGS
IN AZIMUTH

TOTAL GAIN IN dBi

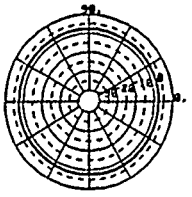


AZIMUTH PLOT AT
20 DEGS
IN ELEVATION

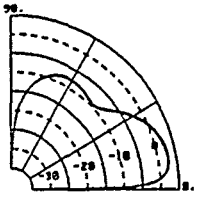


ELEVATION PLOT AT
20 DEGS
IN AZIMUTH

TOTAL GAIN IN dBi

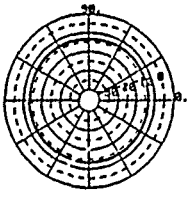


AZIMUTH PLOT AT
30 DEGS
IN ELEVATION

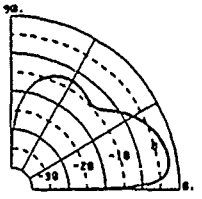


ELEVATION PLOT AT
14 DEGS
IN AZIMUTH

TOTAL GAIN IN dBi

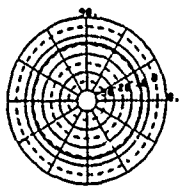


AZIMUTH PLOT AT
40 DEGS
IN ELEVATION

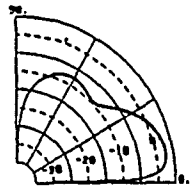


ELEVATION PLOT AT
0 DEGS
IN AZIMUTH

TOTAL GAIN IN dBi

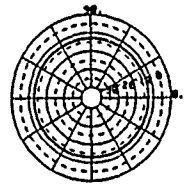


AZIMUTH PLOT AT
50 DEGS
IN ELEVATION

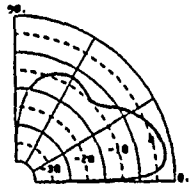


ELEVATION PLOT AT
0 DEGS
IN AZIMUTH

TOTAL GAIN IN dBi

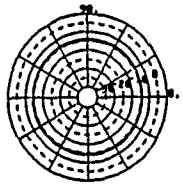


AZIMUTH PLOT AT
60 DEGS
IN ELEVATION

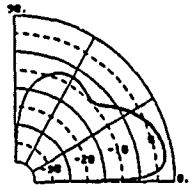


ELEVATION PLOT AT
0 DEGS
IN AZIMUTH

TOTAL GAIN IN dBi

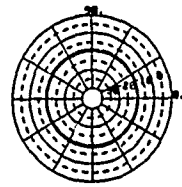


AZIMUTH PLOT AT
70 DEGS
IN ELEVATION

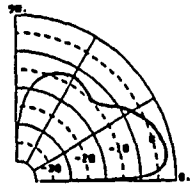


ELEVATION PLOT AT
0 DEGS
IN AZIMUTH

TOTAL GAIN IN dBi



AZIMUTH PLOT AT
80 DEGS
IN ELEVATION



ELEVATION PLOT AT
0 DEGS
IN AZIMUTH

ANTENNA TYPE	DIFF OF CONSTR	MAX SURFACE WAVE VERT mV/m	VERT db	HORZ mV/m	HORZ db	MAXIMUM dbi AT THE ELEVATION ANGLE (Angles in Degrees) 10	20	30	40	50	60	70	80	90
Basic Whip with 8 foot Ground Stake	--	10.52	20.44	0.00	******	3.2	2.0	-2.1	-7.8	-8.5	-7.4	-8.7	-13.6	******
		Epsilon: 34.00		Sigma: 0.15000		Frequency (MHz): 17.00								
Basic Whip with 8 1/16 Wave Ground Radials	--	10.44	20.37	0.00	******	3.2	1.9	-2.2	-7.9	-8.6	-7.4	-8.8	-13.7	******
		Epsilon: 34.00		Sigma: 0.15000		Frequency (MHz): 17.00								
Basic Whip w/ 8 1/2 Wave Ground Radials & Radio	--	10.34	20.29	0.00	-72.37	3.1	1.8	-2.4	-8.1	-8.3	-7.1	-8.5	-13.4	-49.7
		Epsilon: 34.00		Sigma: 0.15000		Frequency (MHz): 17.00								
Basic Whip w/ 8 1/4 Wave Ground Radials & Radio	--	10.27	20.23	0.00	-60.92	3.0	1.7	-2.4	-8.0	-8.3	-7.0	-8.4	-13.1	-37.5
		Epsilon: 34.00		Sigma: 0.15000		Frequency (MHz): 17.00								
Basic Whip with 8 1/2 Wave Ground Radials	--	10.22	20.19	0.00	******	3.0	1.8	-2.3	-8.0	-8.9	-7.8	-9.1	-14.8	******
		Epsilon: 34.00		Sigma: 0.15000		Frequency (MHz): 17.00								
Basic Whip with 8 1/4 Wave Ground Radials	--	10.21	20.18	0.00	******	3.0	1.7	-2.4	-8.1	-8.8	-7.7	-9.0	-13.9	******
		Epsilon: 34.00		Sigma: 0.15000		Frequency (MHz): 17.00								
Basic Whip with Radio	--	10.13	20.11	0.00	-69.53	2.9	1.6	-2.6	-8.2	-8.5	-7.3	-8.7	-13.6	-46.4
		Epsilon: 34.00		Sigma: 0.15000		Frequency (MHz): 17.00								
Basic Whip w/ 8 1/16 Wave Ground Radials & Radio	--	10.11	20.10	0.00	-56.17	2.9	1.6	-2.5	-8.3	-8.1	-6.9	-8.2	-12.8	-32.9
		Epsilon: 34.00		Sigma: 0.15000		Frequency (MHz): 17.00								
Basic Whip w/ 8' Ground Stake & Radio	--	9.63	19.67	0.00	-60.24	2.4	1.2	-3.0	-8.6	-8.6	-7.4	-8.8	-13.5	-37.1
		Epsilon: 34.00		Sigma: 0.15000		Frequency (MHz): 17.00								

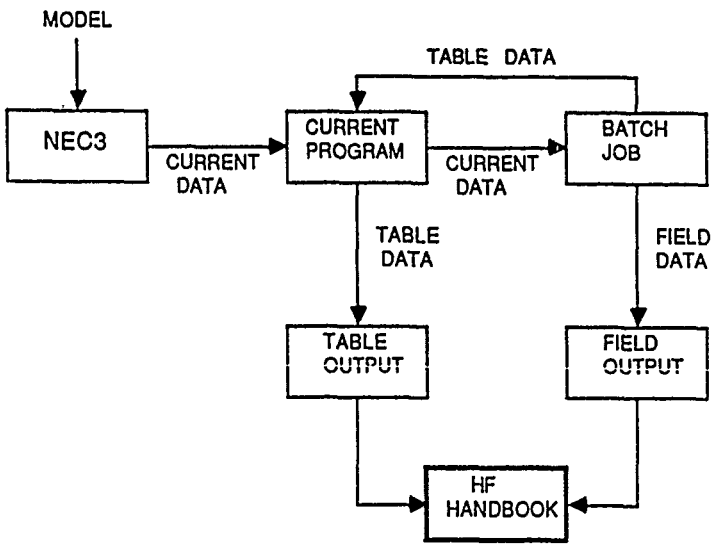
DATA SORTED BY: MAX VERTICAL SURFACE WAVE

Table Sorting

One can sort the tabular data by :

```
1=DIFFICULTY OF CONSTRUCTION
2=MAXIMUM VERTICALLY POLARIZED SURFACE WAVE
3=MAXIMUM HORIZONTALLY POLARIZED SURFACE WAVE
4=MAXIMUM POWER AT VARIOUS ELEVATION ANGLES
5=LIST ORIGINAL FILE
```

Calculation Process



Conclusions

When we completed the program we ran our host of HF antennas through our process.

- We are still in the process of forming the data into a handbook.

- We are also working on a version of this program for the IBM PC.

GEMACS

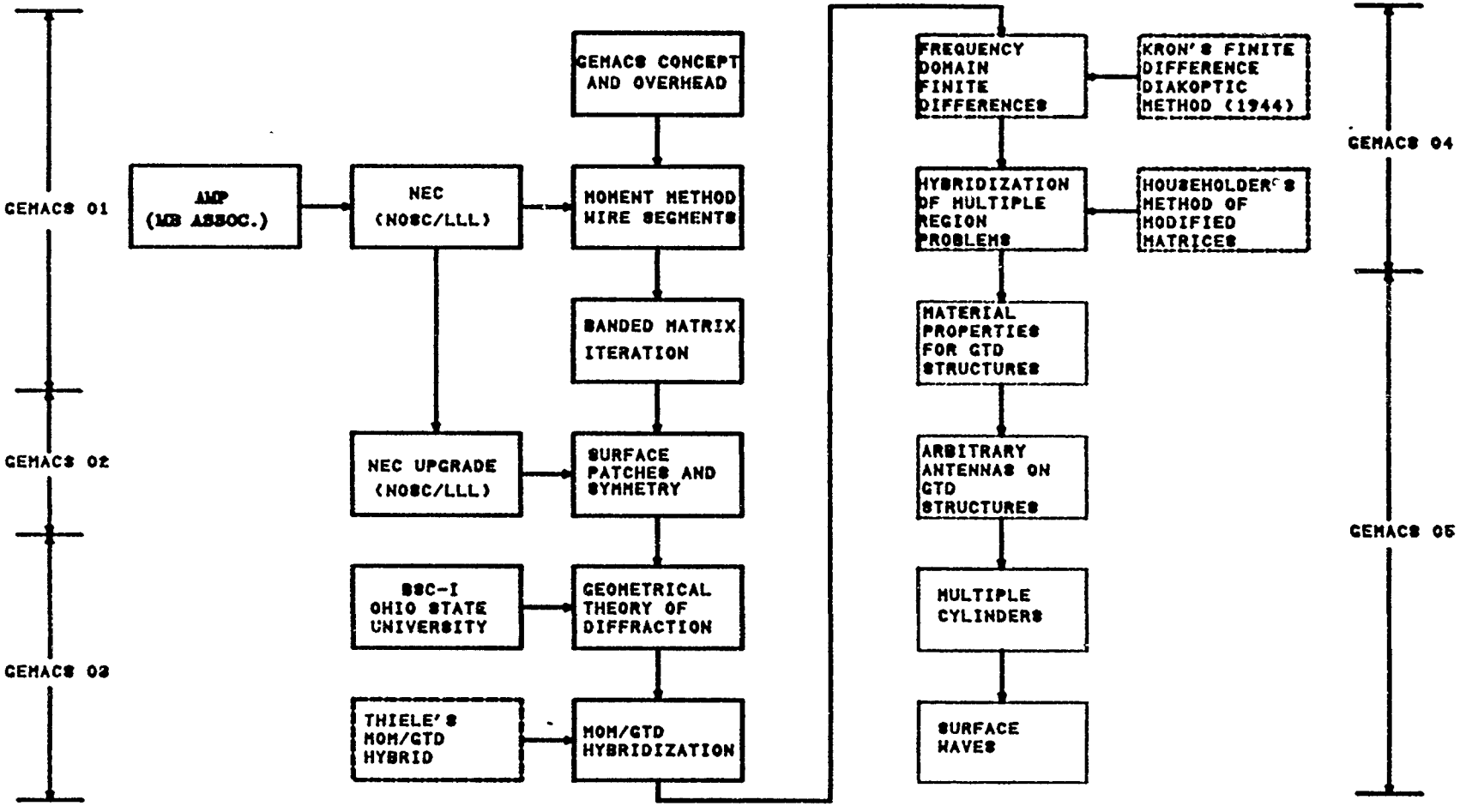
The General Electromagnetic Model for the Analysis of Complex Systems

KENNETH R. SIARKIEWICZ
(315)330-2466 (AV)587-2466
ROME AIR DEVELOPMENT CENTER
COMPATIBILITY TECHNIQUES & APPLICATIONS BRANCH
GRIFFISS AFB, NY 13441-5700

ROME AIR DEVELOPMENT CENTER

Air Force Systems Command
Griffiss Air Force Base, NY 13441

DEVELOPMENT OF THE GEMACS COMPUTER PROGRAM



SUMMARY

Veritable Tool Box of Techniques Range of Applicability is Growing Central Agency for Distribution and Support

RADC/RBCT
Attn. Kenneth R. Siarkiewicz
Griffiss AFB, NY 13441-5700
(315)330-2465 (AV)587-2465

ANALYSIS TECHNIQUES

Method of Moments (MOM)

- Loaded Wire Scatterers } V1
- Imperfect Ground } V1
- Surface Patches } V2

Geometrical Theory of Diffraction (GTD)

- MOM/GTD Hybridization } V3

Finite Difference (FD)

- MOM/GTD/FD Hybridization } V4

FINITE DIFFERENCE

Electrically Moderate Size
Fine Resolution
Cell Gridding
Wires Within Cells
Electric Fields

HYBRIDIZATION METHODOLOGY

Exterior Problem Interaction
Matrix Is Calculated Using MOM/GTD

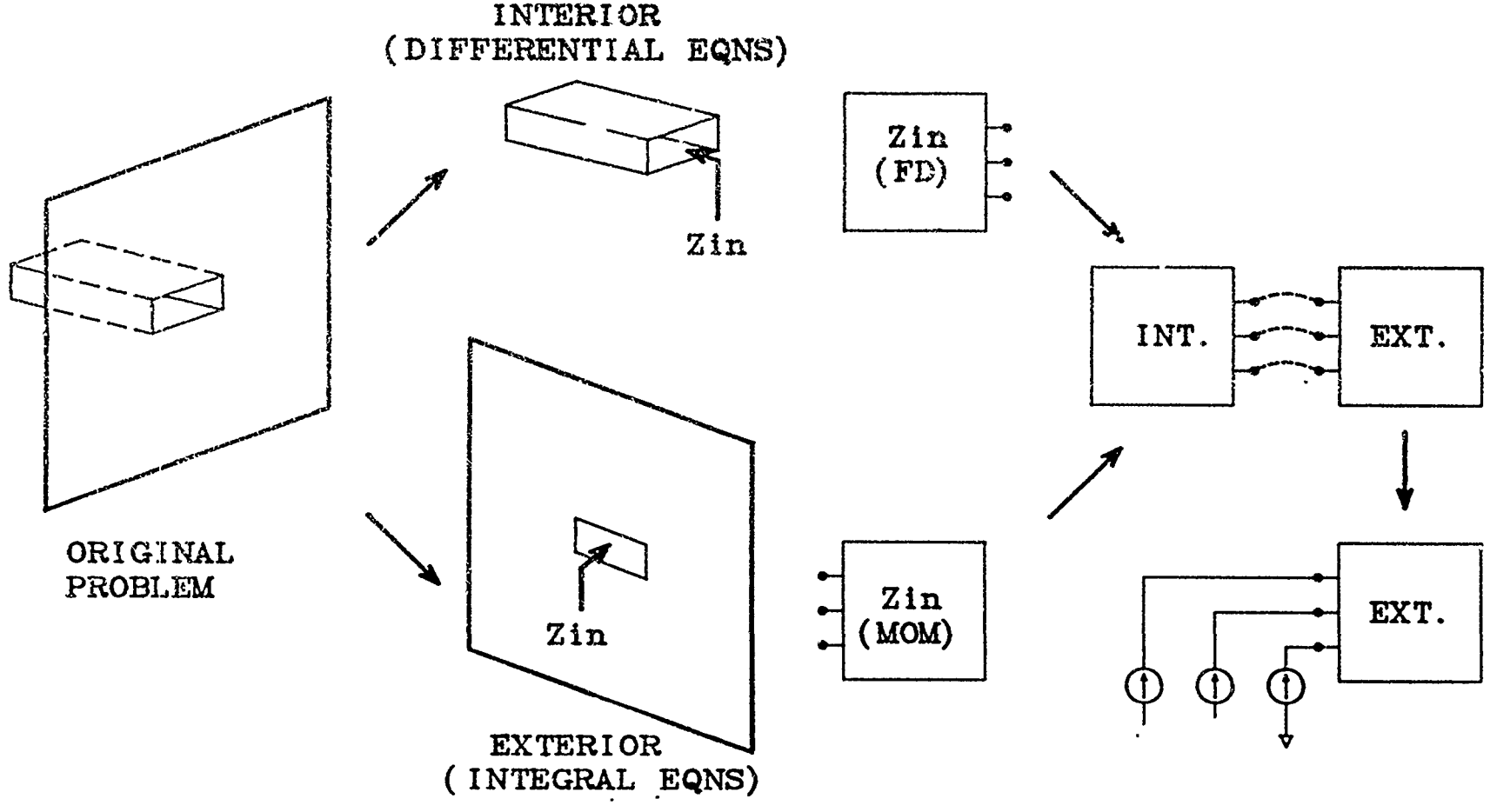
Interior Problem Interaction Matrix
Is Calculated Using FD

Total Problem Solution Is Found by
Using Householder Method of Modified
Matrices to Link the Separate
Solutions at Their Common Interfaces

GEMACS techniques / APPLICATIONS	MOM	GTD	MOM/GTD	FD	$MOM/GTD/FD$	Potential GEMACS Examples
1. Antenna Analysis	●					Spiral, log periodic
2. In-Place Antenna Patterns		●	●			Spiral, slot, blade on F-16, B-52
3. EMC/EMI Antenna-to-Antenna Coupling			●			F-16, B-52 plus two or more antennas
4. Radiation Hazards		●		●		F-16 on ground
5. Vulnerability of Weapons Systems to EM Threats	●	●		●	●	External field on missle with seams, radome, multiple shielding levels, int. cables
6. EMC/EMI Aperture/Cavity Coupling	●	●		●	●	Similar to #5, with on board radiator
7. EM Emissions	●	●		●	●	Inside-out version of #5
8. EM Properties of Materials	●	●		●	●	Dielectric cylinder scattering RAM materials
9. RCS	●	●	●	●	●	Canonical objects: aircraft from #2; missle from #5
10. Characterization of Measurement setup	●	●	●			Canonical objects from #9; other examples from #2

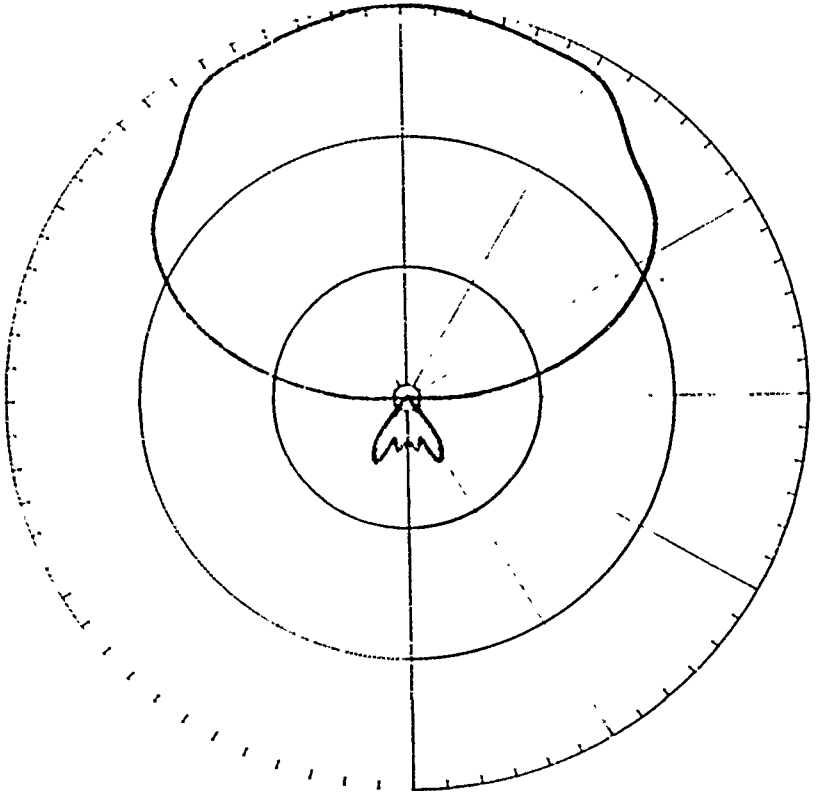
ROME AIR DEVELOPMENT CENTER
Air Force Systems Command
Griffiss Air Force Base, NY 13441

SOLUTION OF OPEN-ENDED WAVEGUIDE PROBLEM

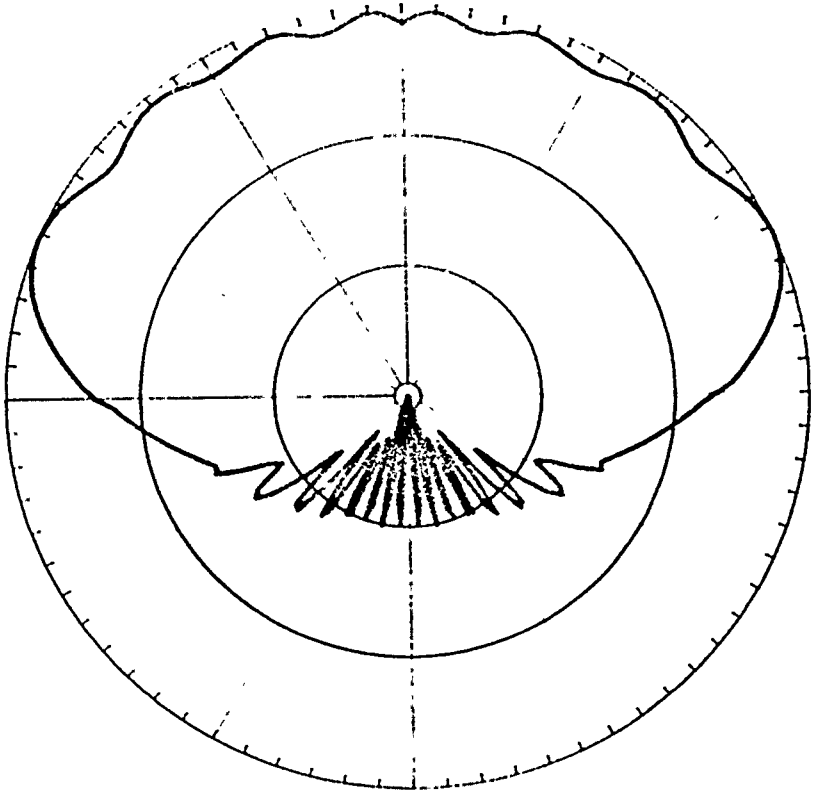


ROME AIR DEVELOPMENT CENTER
Air Force Systems Command
Griffiss Air Force Base, NY 13441

FIELD PATTERNS FROM OPEN-ENDED WAVEGUIDE



H-PLANE CUT



E-PLANE CUT

OPEN SESSION/LATE PAPERS/FINAL DEMOS

RELATIVE COMMUNICATION EFFICIENCY OF SHORT HF MONOPOLE ANTENNAS WITH SPARSE, ABBREVIATED, RADIAL-WIRE GROUND SYSTEMS

Ric Thowless, Code 822
Naval Ocean Systems Center
San Diego, CA 92052

Abbreviated radial-wire ground systems are commonly used with field-expedient, high-frequency, electrically-short, whip-type antennas. Little is known about the technical quality of such antenna/ground systems for ground-wave propagation. This study compares the Relative Communication Efficiencies (RCE) of combinations of monopole length, radial length, numbers of radials, soil type, and location of the radials above ground or buried.

Eight-foot and 32-foot monopoles are combined with all combinations of the listed parameters below, from which RCE is determined. Admittedly, buried radials are not appropriate for field-expedient antennas, but are included in the study for completeness. All calculations are at 4 MHz.

Monopole length:	8 ft (.033 wavelength; 2.44 m)	
	32 ft (.130 wavelength; 9.75 m)	
Radial lengths:	.05 wavelength (12.3 ft; 3.75 m)	
	.10 wavelength (24.6 ft; 7.50 m)	
	.15 wavelength (36.9 ft; 11.2 m)	
	.20 wavelength (49.2 ft; 15.0 m)	
	.25 wavelength (61.5 ft; 18.4 m)	
Radial wire density:	1 radial	
	2 radials, symetrically positioned	
	4 " "	"
	8 " "	"
	16 " "	"
	32 " "	"
	64 " "	"
	120 " "	"
Radial location:	Above ground:	1 cm above surface
	Below ground:	buried 5 cm below surface
Soil type:	Good ground:	conductivity = .01 mhos/m dielectric constant = 10
	Poor ground:	conductivity = .001 mhos/m dielectric constant = 4

RCE, the basis of comparison, is the ratio (expressed in dB) of the ground wave field intensity at a given distance from (1) the antenna/ground system under study to that from (2) a reference antenna at the same location, for the same ground constants, and equal rf power into each antenna. RCE is similar to gain. It is essentially independent of distance and only the effects of losses attributed to the antenna, its ground system, and soil type are apparent in the comparative results. (The concept of RCE was first used by Fenwick and Weeks (1968), and recently used by Burke et al (1984)). The reference antenna for RCE evaluation is the quasi-standard quarter-wave vertical monopole with 120 buried radials, each a half-wavelength long.

A variant of the NEC program, NEC-GS, was used for the computations of radiated fields near ground at 250 wavelengths distance. The NEC-GS code takes advantage of the symmetry of the radial ground wires to greatly shorten computer run time. Except for manually extracting some values from the NEC output files, the numbers were processed and plotted using spreadsheet software.

An awkward aspect of this task was determining reasonable segmentation, because of the unknown wavelength of current in the radials, either buried or above ground, due to proximity to the air/ground interface; and maybe due to the feed-point being at the junction of sometimes many wires, and of the proximity of the feed-point to the ground.

BURIED RADIALS

RCE curves for buried radials are reasonably well behaved. (See figures 1 to 4.) The ordinate value of 0 dB on all the graphs represents the reference level field strength of the reference antenna for the soil type.

The 32-foot monopole on good ground (fig. 1) has RCE behavior that is surprisingly independent of radial length. There is little benefit from more than about 32 radials.

The 8-foot monopole on good ground (fig. 2) has, for sparse numbers of radials, very low RCE values. Radial numbers above about 32 are not overly beneficial.

Poor ground with the 32-foot monopole (fig. 3) lowers the general RCE values relative to RCE from good ground from 1 to 7 dB; especially noticeable for short radials.

Poor ground with the 8-foot monopole (fig. 4) shows markedly poorer RCE than with the 32-foot whip over the same poor ground, by 4 to 10 dB.

RADIALS ABOVE GROUND

The 32-foot monopole over good ground (fig. 5) exhibits roll-off of RCE at the longer radial lengths for sparse numbers of radials. Note the little increase in RCE with increasing numbers of radials from 8 to 120.

The 8-foot monopole over good ground (fig. 6) produces much lower RCE than the 32-foot monopole - up to 10 dB decrease. Note the negative slopes with increasing radial length. The benefit of many radials is evident, even for very short radials.

Poor ground with the 32-foot monopole (fig. 7) does not show the roll-off of RCE with increasing radial length that's evident with good ground. Adding radials improves RCE more than lengthening them will, though little improvement occurs for more than about 32 radials.

Poor ground with the 8-foot whip (fig.8) results in a 15 to 20 dB spread in RCE between 120 radials and very sparse numbers; many radials are needed for good efficiency.

AZIMUTHAL VARIATION WITH FEW RADIALS

The greater positive slope for RCE for 1 and 2 radials especially for poor soil, which is noticable in some of the graphs, seems to be the result of the 1 or 2 radials functioning in a manner that directs/guides rf energy in the direction of the radial. Figure 9 shows the inhanced azimuthal directivity of a single radial and an 8-foot whip. The null depth is 17 dB, and the front-to-back ratio is 9 dB.

RCE VS RADIAL LENGTH (Radials above ground)

The variable RCE vs radial length for 4 radials is explored for radial lengths out to one-half wavelength, and with the four combinations of ground type and monopole length (fig 10). First, note the much greater efficiencies for the longer monopole, which is typical. The greatest variability of RCE occurs with good soil. A poorly chosen radial length with sparse radials could be very detr.mental to ones radio communications capability.

CONCLUDING COMMENTS

The longer monopole is the universally better way to go to increase RCE.

The rate of improvement in efficiency is generally greatest with increasing numbers of radials instead of increasing radial length.

Very sparse numbers of radials should not be used with 8-foot monopoles nor with a 32-foot monopole over poor ground.

RCE can be very variable for radials above ground -- even decreasing as radial length increases. Very poor antenna performance is possible with some seemingly adequate ground systems.

These results should be verified, at least in part, by measurements in the field before proceeding with additional extensive NEC analyses of some of the interesting behavior and questions raised by the results.

REFERENCES:

Fenwick, R.C. and W.L. Weeks. 1963. Submerged antenna characteristics. IEEE Trans Ant Prop. May, pp296-305.

Burke, G.J., R.J. King and E.K. Miller. 1984. Surface wave excitation study. Lawrence Livermore National Laboratory, UCID-20214.

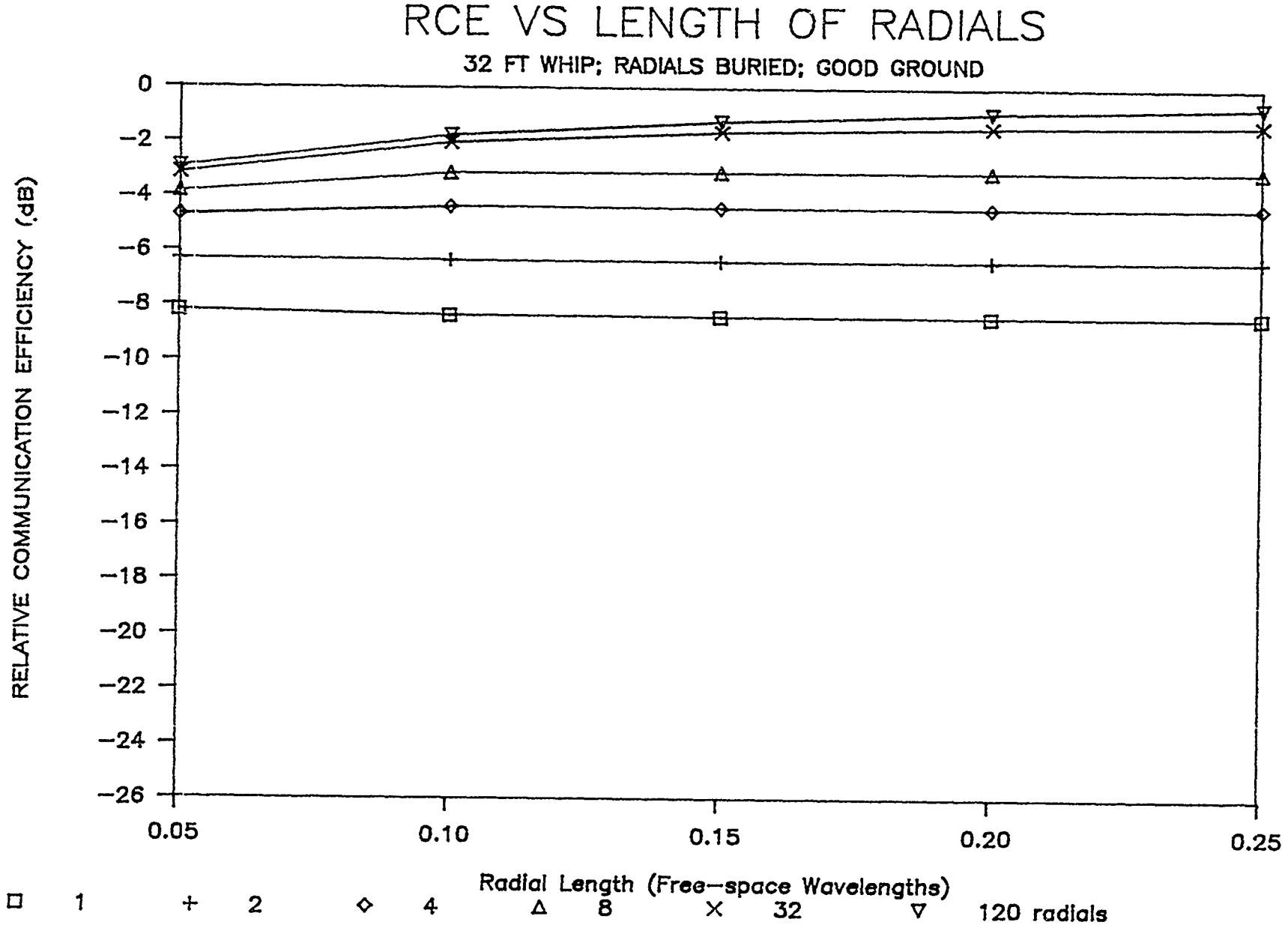


Figure 1. RCE vs Length of Radials; 32 ft monopole; radials buried in good ground

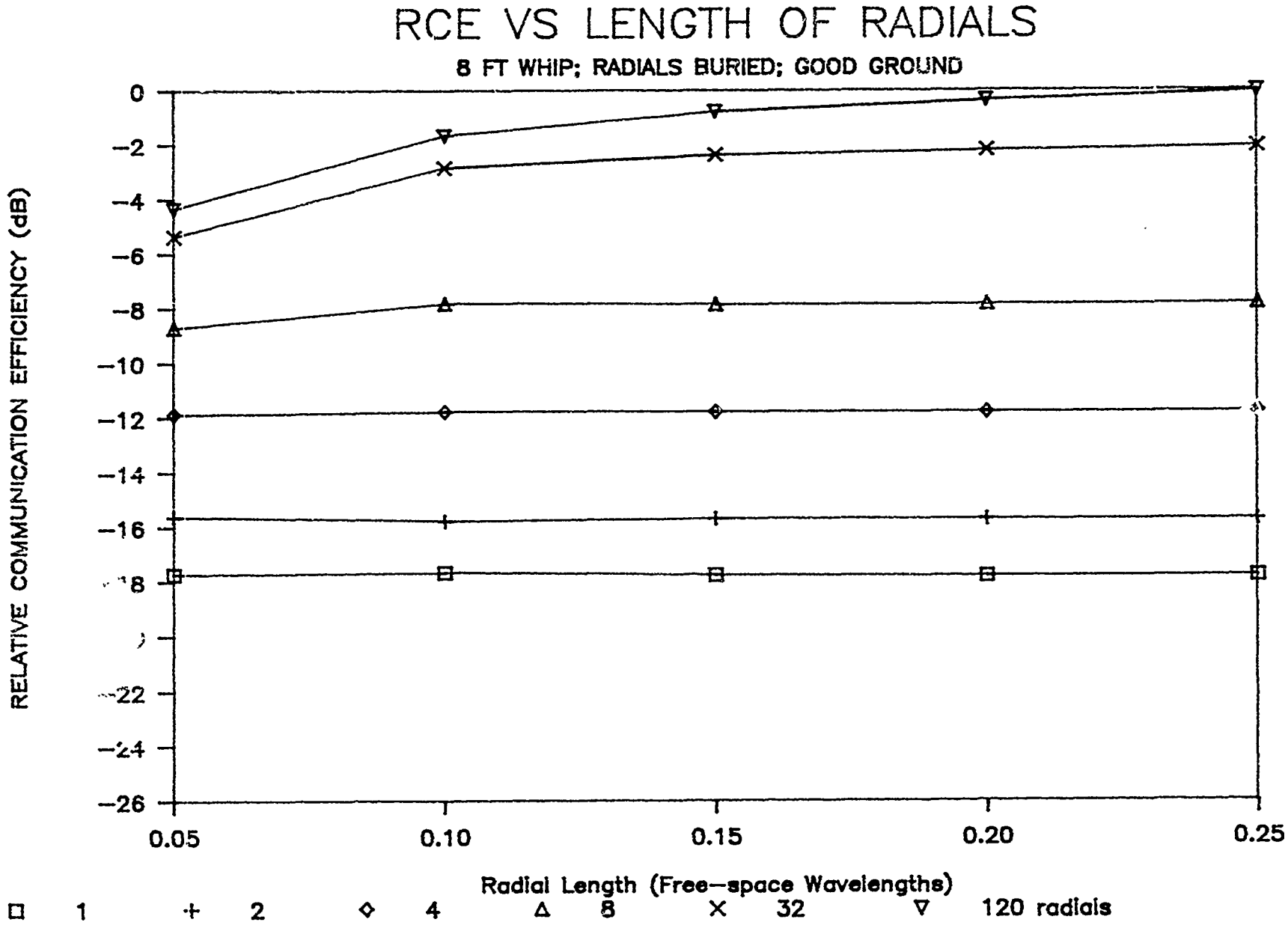


Figure 2. RCE vs Length of Radials; 8 ft monopole; radials buried in good ground

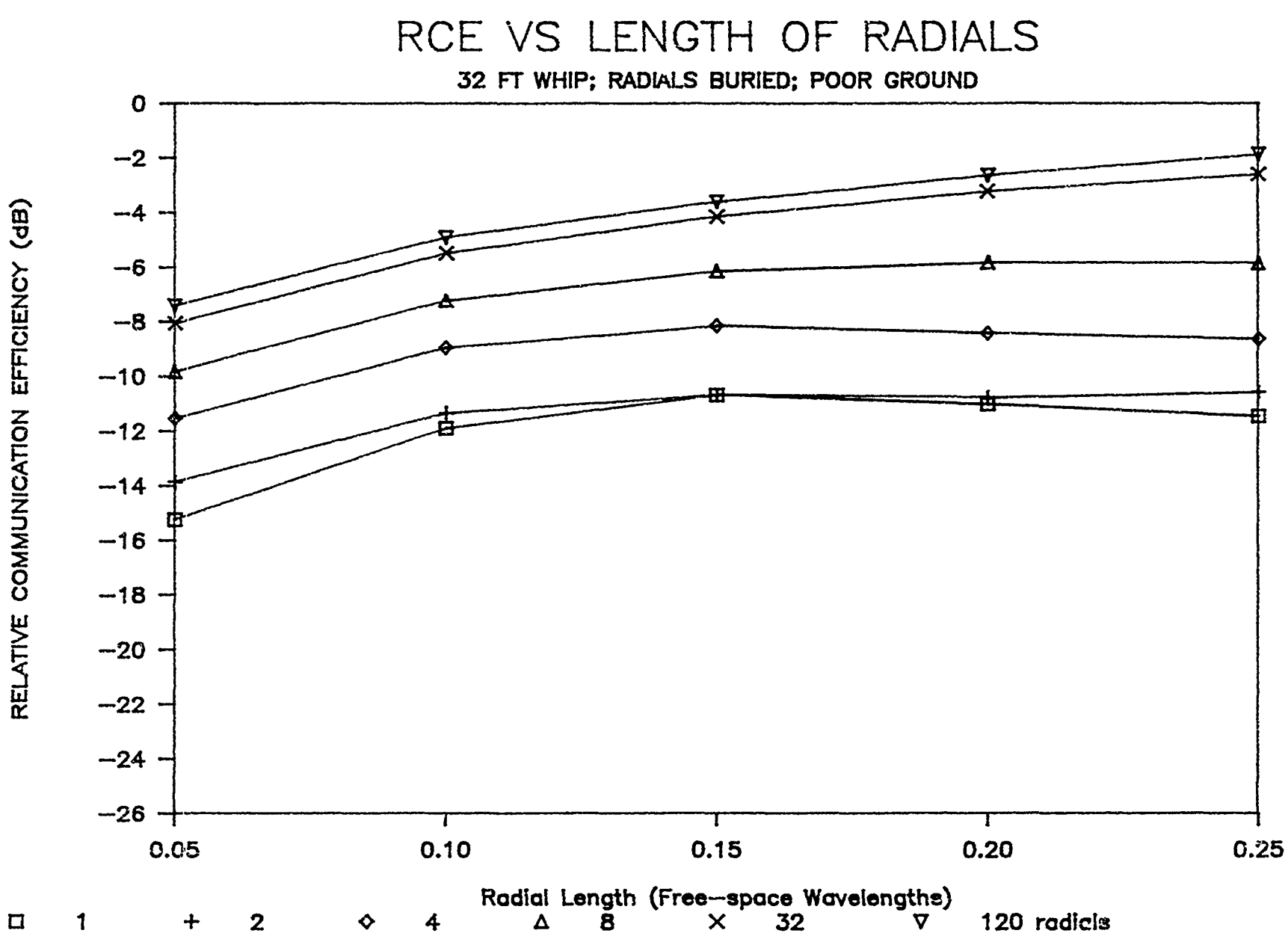


Figure 3. RCE vs Length of Radials; 32 ft monopole; radials buried in poor ground

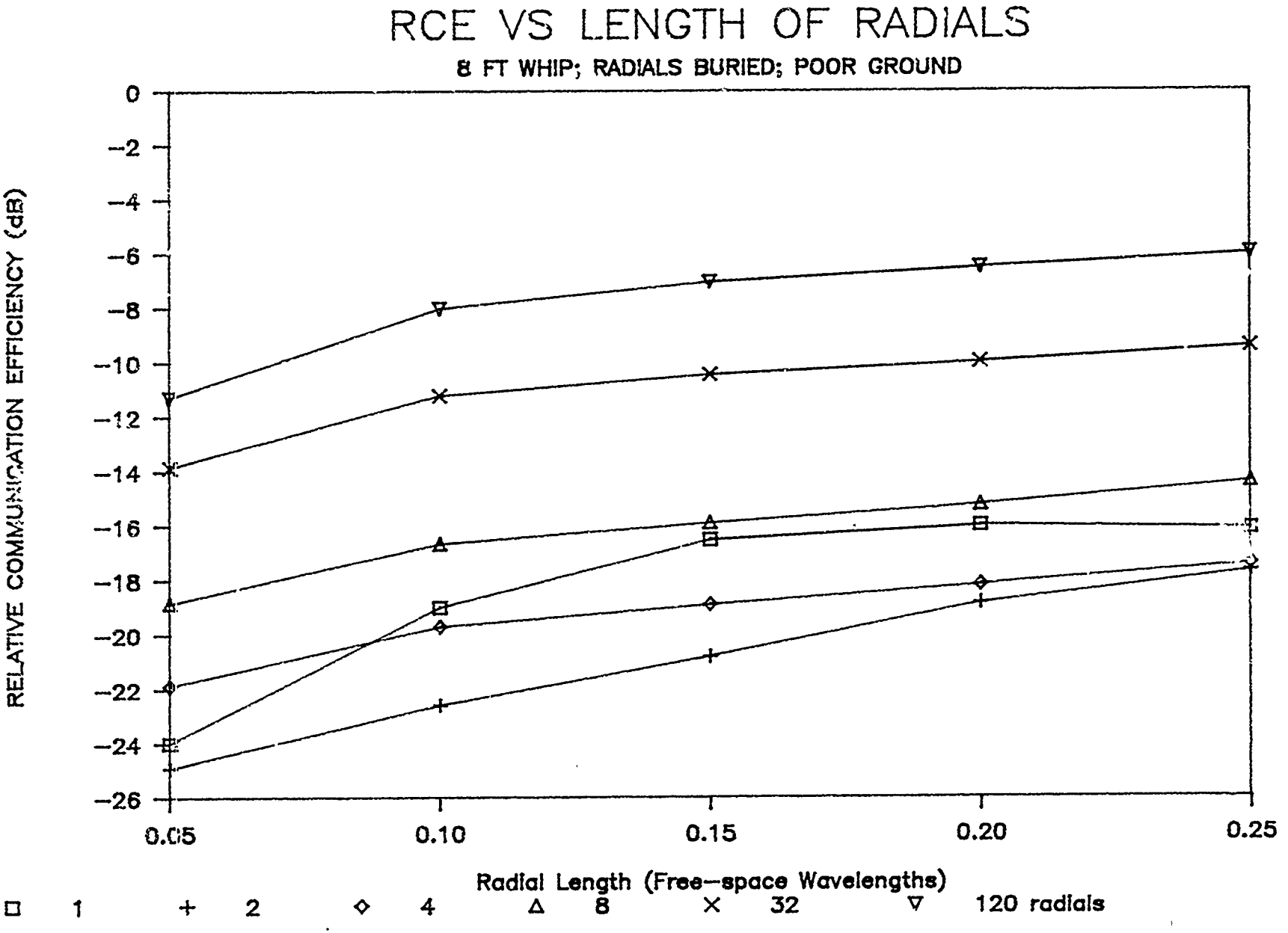


Figure 4. RCE vs Length of radials; 8 ft monopole; radials buried in poor ground

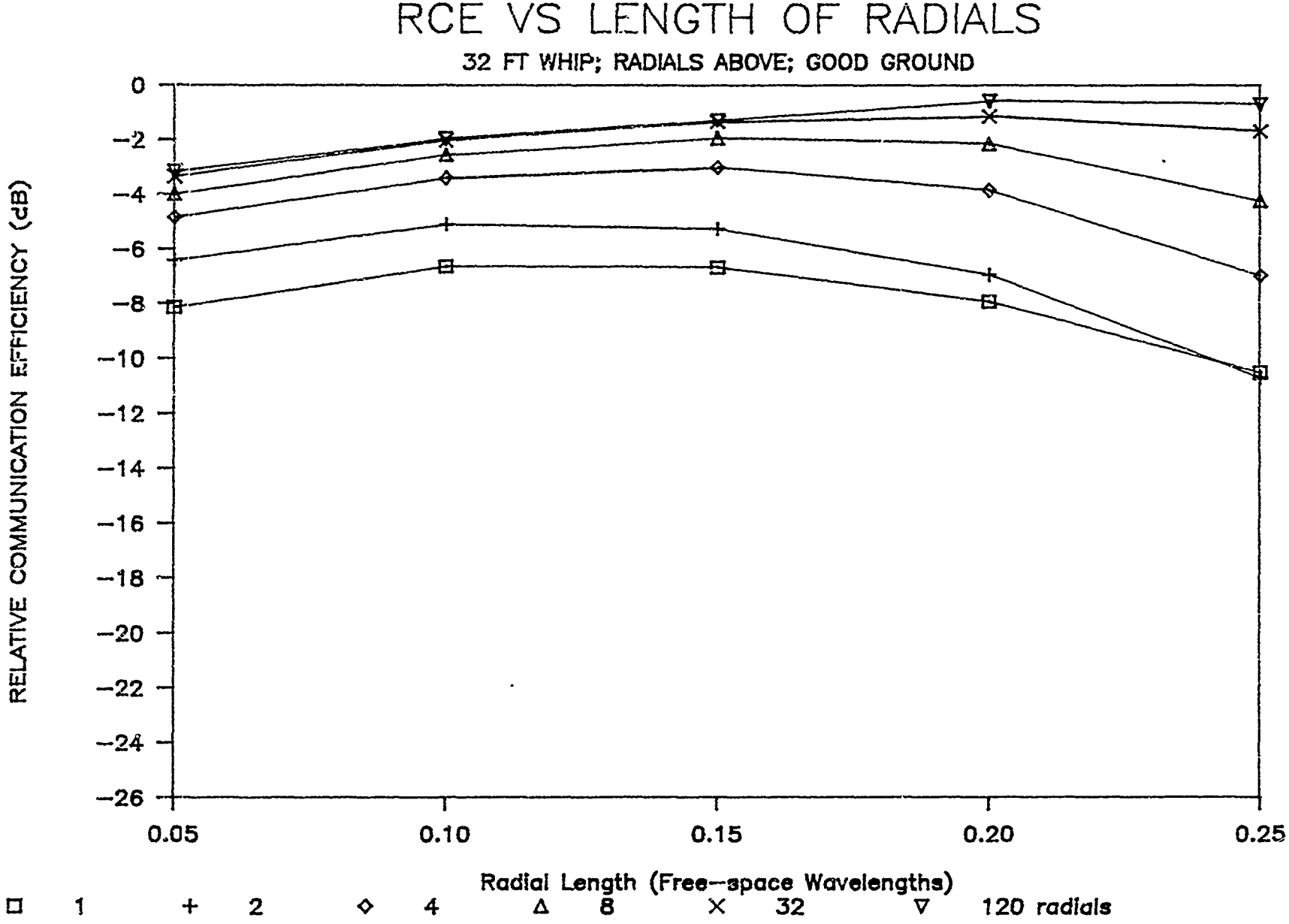


Figure 5. RCE vs Length of Radials; 32 ft monopole; radials above good ground

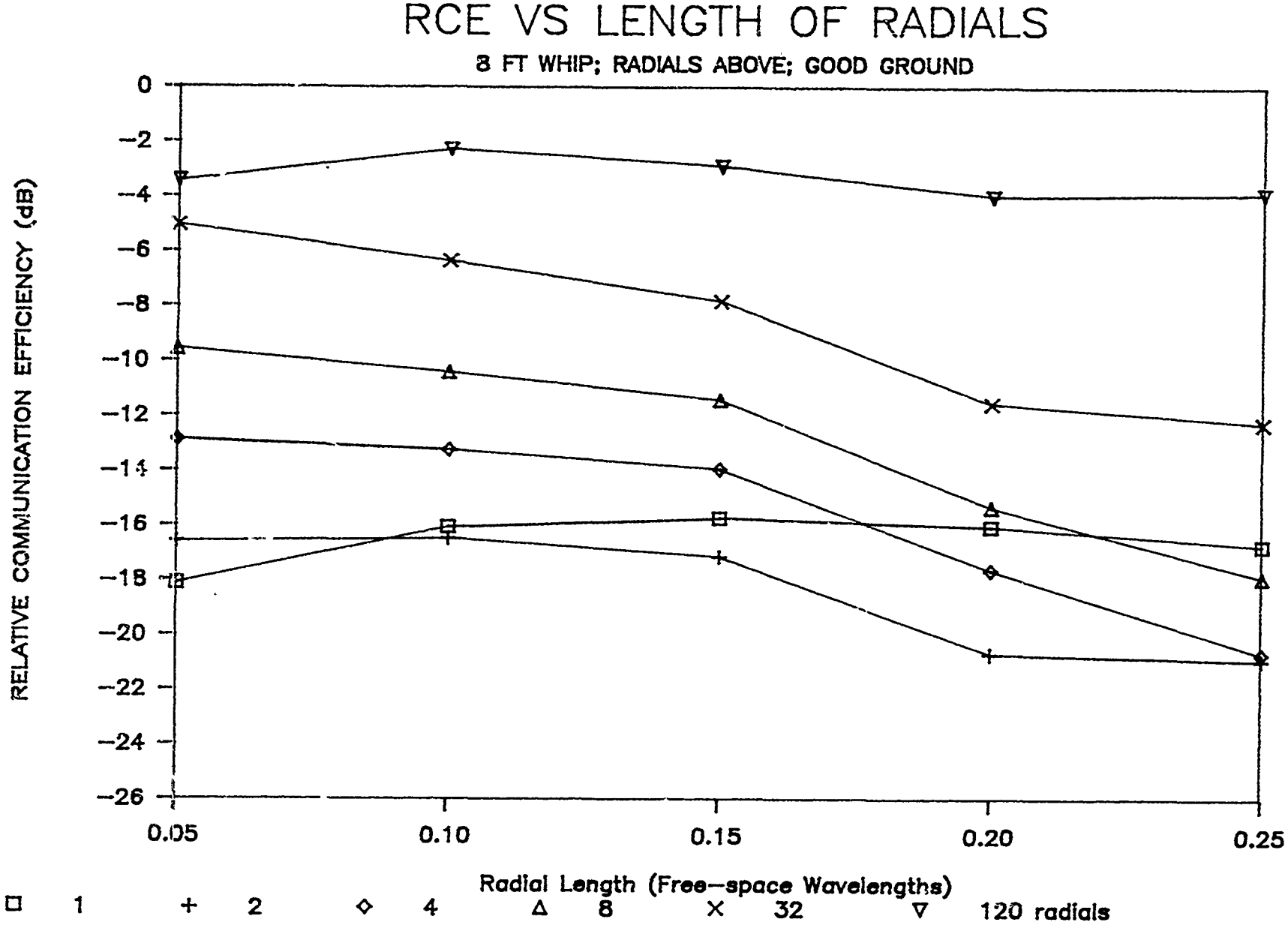


Figure 6. RCE vs Length of Radials; 8 ft monopole; radials above good ground

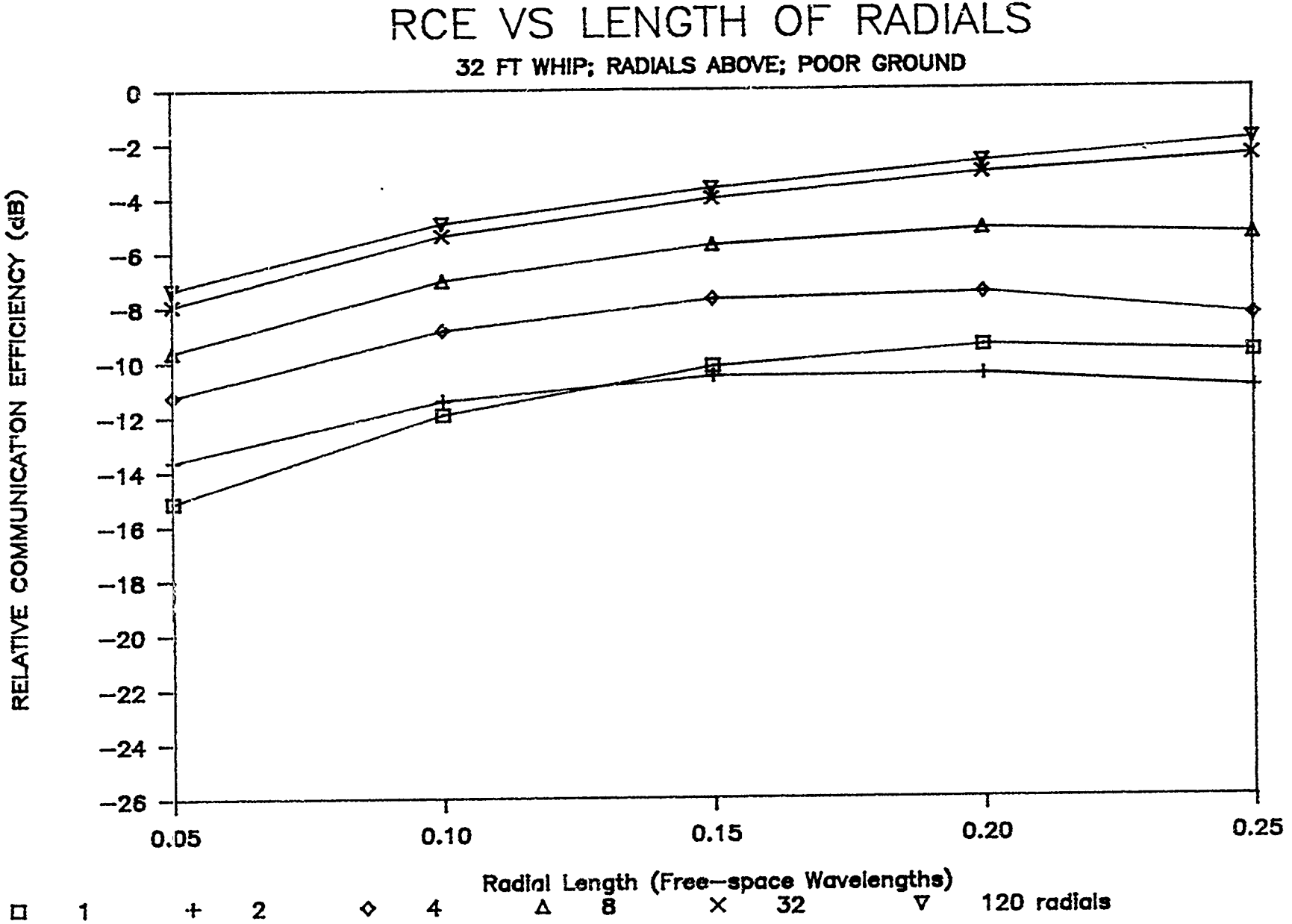


Figure 7. RCE vs Length of Radials; 32 ft monopole; radials above poor ground

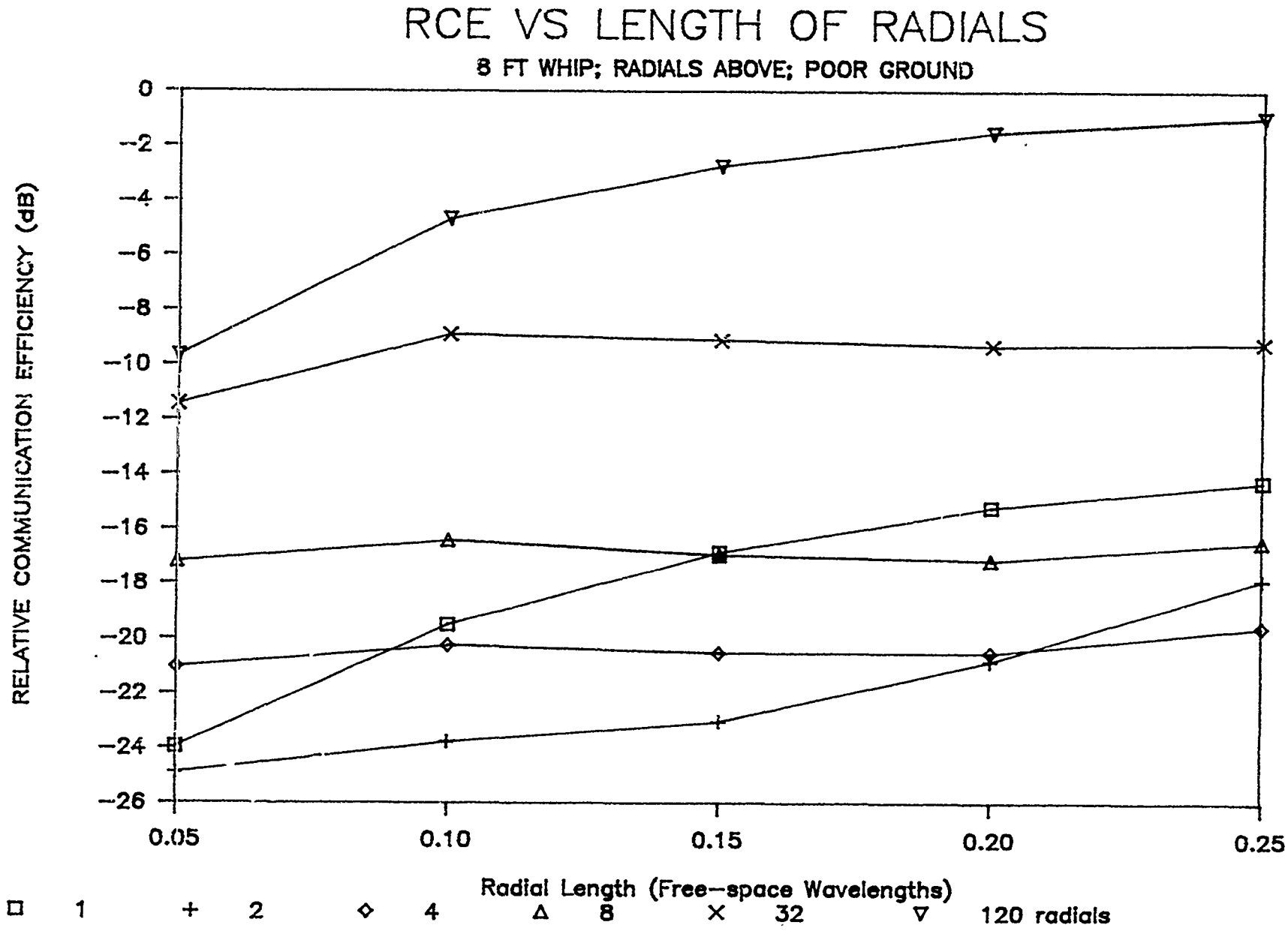


Figure 8. RCE vs Length of Radials; 8 ft monopole; radials above poor ground

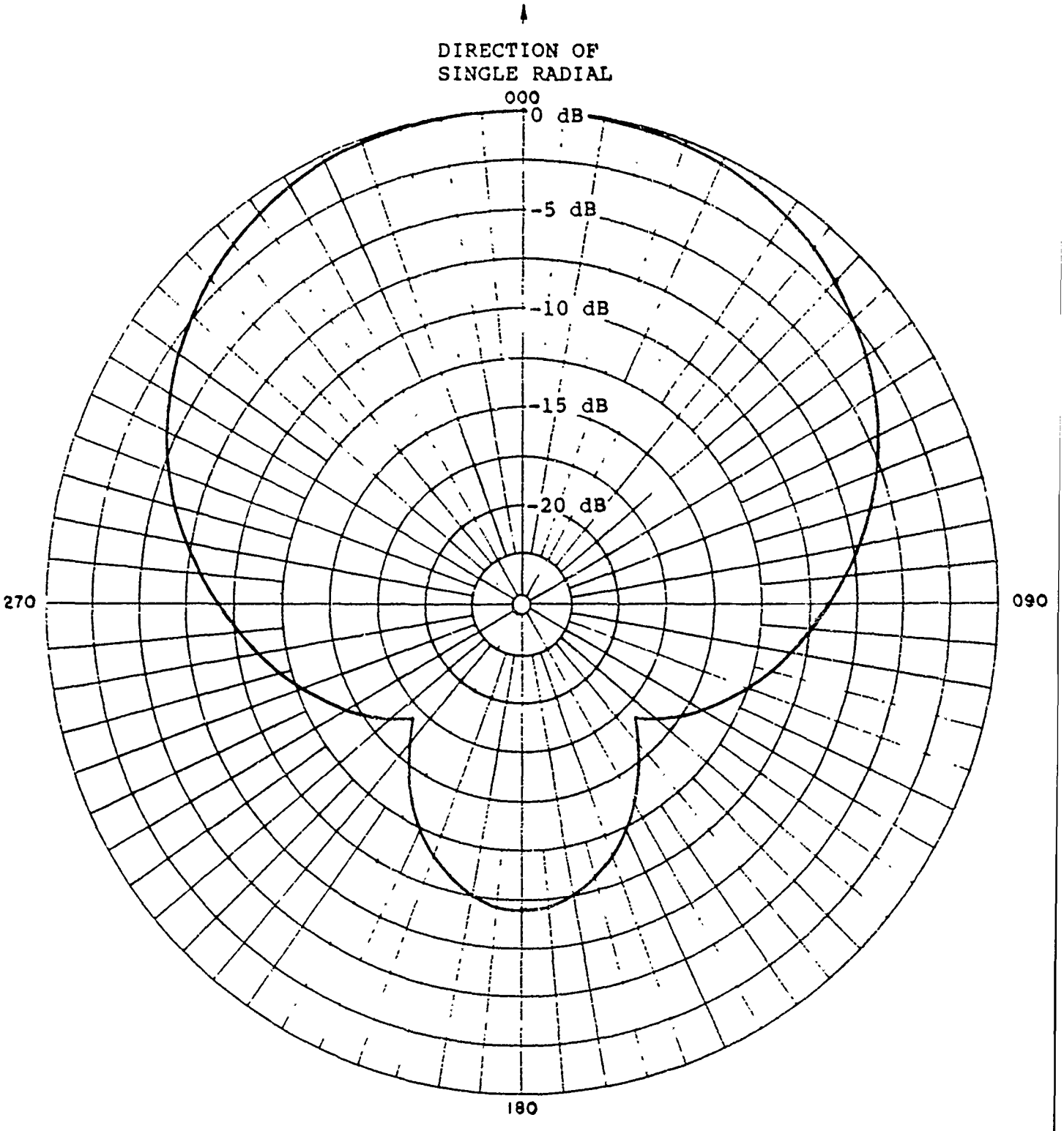


Figure 9. Azimuthal radiation pattern for 8 ft monopole with single radial above poor ground; an example of considerable pattern distortion caused by a single radial.

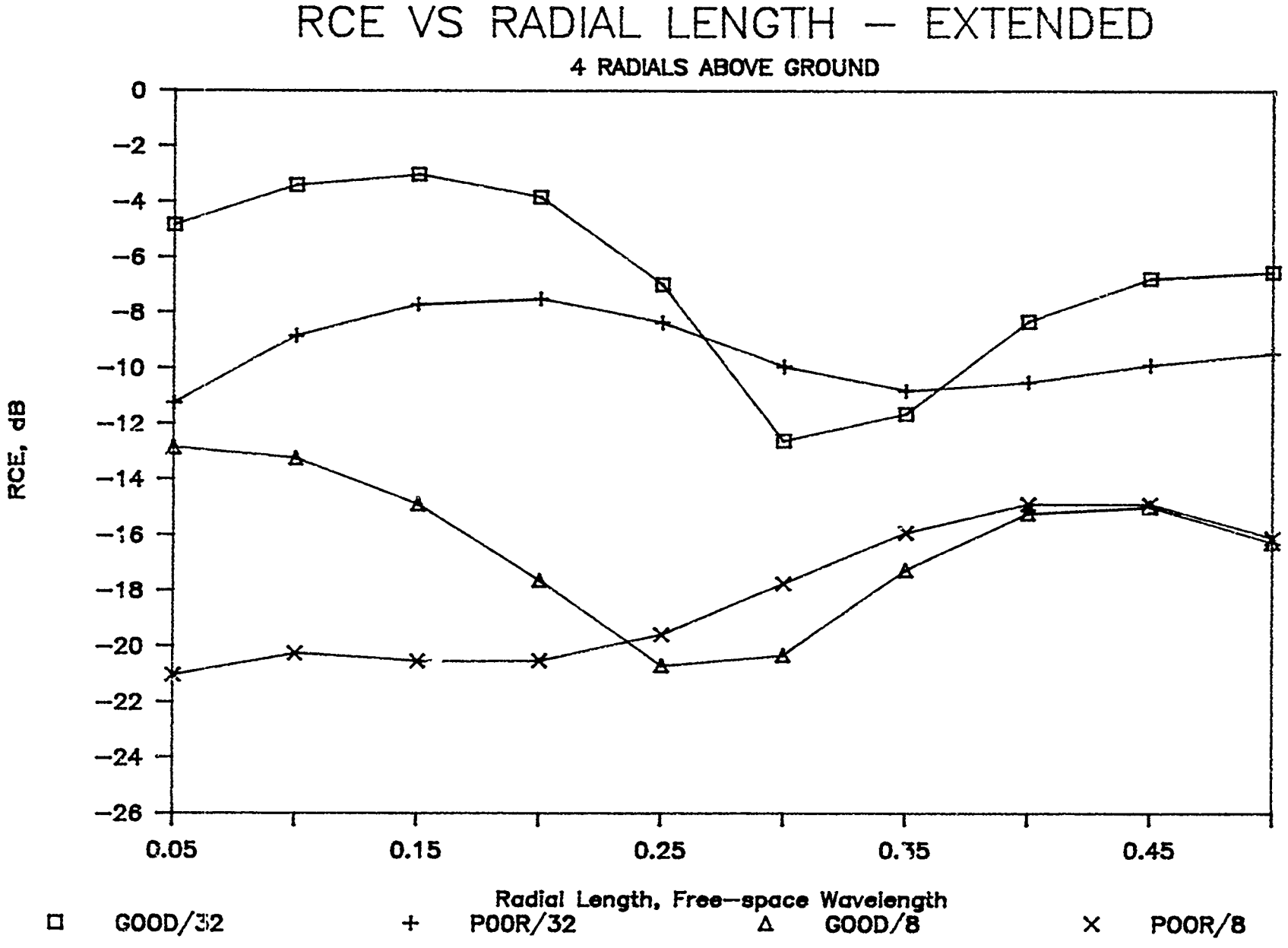


Figure 10. RCE vs Radial Length for four radials above ground, with 32 ft and 8 ft monopoles over good and poor grounds

RADIATION HAZARD EVALUATION USING NEC-BSC

W. J. Koh and R. W. Adler
Naval Postgraduate School

ABSTRACT

The Numerical Electromagnetic Code - Basic Scattering Code (NEC-BSC) is a user oriented computer code for the analysis of electromagnetic radiation from antennas in the presence of complex structures at UHF and above. This code was used to assist in the design of a large planar array to be placed on top of a tracked vehicle. The whole system is also modeled by the same code and the near field radiation patterns are obtained to determine the radiation hazard level near the vehicle.

The purpose of this paper is to discuss the problems encountered in evaluating the radiation hazard using the NEC-BSC code. These include the types of supporting routines used to assist the modeling and evaluation, the types of simplified array models needed to simulate the large array and the flipping of the mainlobe of the slotted array with different array configurations.

INTRODUCTION

The Flyswatter System is a short range electronic countermeasure (ECM) device used to counter active missile attacks. It consists of a high power large planar array mounted on an tracked vehicle with a reflector plate placed directly above the array as shown in Fig. 1. The array and the reflector plate are rotatable in azimuth and elevation angles respectively. This ECM system is required to produce a very high peak power density at close range. With this amount of energy radiating toward an incoming active missile, it will degrade or damage the highly sensitive seeker head sensors and cause the missile to lose its tracking capability. The other specifications of the Flyswatter System are listed below :

Frequency	10 GHz
Maximum output peak power	5 GW
Maximum aperture E-field	10.6 KV/cm
Duty cycle	10^{-6}
Maximum array area	2.5m x 2m

Array type	endfeed broadside array
Full gain elevation coverage	0° to 45°
Azimuth coverage	180°

A project is initiated to use software simulation to design a large planar array that will meet the system specifications and evaluate the near field radiation hazard level. The Numerical Electromagnetic Code - Basic Scattering Code (NEC-BSC) is used in this project to model both the planar array and the vehicular structures and to compute the near field and far field radiation patterns. The purpose of this paper is to present the problems encountered in the project evaluation. These include the types of supporting routines needed to assist the modeling and analysis, the types of simplified array models used to simulate the large planar array and the flipping of the mainlobe of the slot array with different array configurations.

SOFTWARE SUPPORT

The NEC-BSC code is chosen for this project for its capabilities in modeling complex structures and slot arrays and computing near and far field radiation patterns. However there are two problems associated with this code. The first one is the accuracy of the radiation patterns produced by the code. The present code, version 2.5, is capable of handling up to second order diffracted and reflected fields excluding the doubly diffracted terms. When complex structures are modeled, the contributions from higher order terms may be significant. Hence the code manual recommends an accuracy range of 30 dB from the peak value. This accuracy is certainly not enough for radiation hazard evaluations. Fortunately, the main beam of the array is very narrow. Most of the energy is concentrated toward the reflector plate and is reflected back without interacting with other structures. By designing the array such that the sidelobe and backlobe levels are very low, we can improve the effective accuracy range of the computed results.

The second problem is that the NEC-BSC code does not have any supporting routines. The input data can be very tedious to generate when complex structures and large arrays are involve. The output data listing is also not easy to interpret. Hence, several software programs were written to assist in the project evaluation. These programs are listed below :

1. **Output Plotting Programs :**

Two programs were written to select and plot the amplitude radiation patterns using DISSPLA plotting subroutines. The NEC-BSC code is first modified to output all amplitude related data in a specific format. An interfacing program GTDRWSEL is then used to read in this data and display the various options for selection. Finally, the selected plot data is plotted using the GTDPLOT program.

2. **Geometry Plotting Program :**

The GTDGEOMP code was written to read the input data for NEC-BSC code and plot the three dimensional geometries of the structures using DISSPLA plotting subroutines. Fig. 2 shows the geometry plot of the Flyswatter System model plotted by the GTDGEOMP code. The wheels are not included since they do not have a significant effect on the radiation patterns.

3. **Source Array Card Generating Program :**

The GTDSA code is written to compute the input data of the SA card of the NEC-BSC code. It reads in the geometry of the array and computes the center locations of each element. It then computes the E-field excitation of each element based on the following selections :

Element distribution : TE_{10} mode or Uniform.
Tapering type : Uniform, Cosine, Cosine-Square, Triangular or Binomial.

Due to the limited amount of code development time available, these supporting routines have limited capabilities. Further improvements are needed in the following areas :

- Output Plotting Programs :
  - * Include phase and antenna coupling pattern plots.
- Geometry Plotting Program :
  - * Perfect the cylinder plotting algorithm.
  - * Include a subroutine to remove hidden objects.
- SA Card Generating Program :
  - * Include a phase variation subroutine.

LARGE PLANAR ARRAY MODELING

The computation time of the NEC-BSC code is very much dependent on the number of array elements. Hence, simplified models may be needed to simulate large arrays. Fig. 3(a) shows an array with 13 x 20 elements arranged in a rectangular grid with no gap between elements. All elements are assumed to be in-phase. If the amplitude tapering along the X_t axis is Uniform, then we can use only 13 elements each with width equal to 20 times the original element's width to model the array as shown in Fig. 3(b), while the tapering along the Z_t direction remains the same as the original array. Such a simplified model will yield exactly the same radiation patterns as the original array. Alternatively, if we have Uniform or Cosine tapering along Z_t direction, we can use the second simplified model shown in Fig. 3(c) to simulate the large array. This second simplification technique allows the modeling of any tapering type along the X_t direction. The NEC-BSC code is capable of modeling either TE_{10} mode or uniformly distributed slot antenna elements. Combining with either Uniform or Cosine tapering type along the Z_t direction, we thus have four different modeling configurations for the second simplified model; namely,

a) Uniformly tapered TE_{10} linear array simulated by a single uniformly distributed element.
b) Cosine tapered TE_{10} linear array simulated by a single TE_{10} element.
c) Cosine tapered uniformly distributed linear array simulated by a single TE_{10} element.
d) Uniformly tapered uniformly distributed linear array simulated by a single Uniformly distributed element.

The aperture E-field distribution of these configurations are shown in Fig. 4. These simplified models do not yield exact solutions except for configuration (d). Fortunately, the near and far field radiation patterns generated by NEC-BSC code for both the simplified and actual models are very similar, and the relationship of the gain and maximum aperture E-field between the two models are predictable as listed in Table 1.

Both of these simplification techniques were used to model a large planar array consisting of 96 x 133 elements.

TABLE 1

THE PERFORMANCE RELATIONSHIP BETWEEN THE ACTUAL AND SIMPLIFIED MODELS USING THE SECOND SIMPLIFICATION TECHNIQUE

Config.	Element Length Ratio (Actual/Simpl.)	Max. Aperture E-field Ratio (Actual/Simpl.)	Boresight E-field Ratio (Actual/Simpl.)
(a)	$\frac{1}{N}$	2	$\frac{4}{\pi}$
(b)	$\frac{1}{N+1}$	$\sqrt{2}$	$\frac{\sqrt{2}}{N+1}\cot\frac{\pi}{2(N+1)}$
(c)	$\frac{1}{N+1}$	$\frac{1}{\sqrt{2}}$	$\frac{\pi}{2\sqrt{[2(N+1)]}}\cot\frac{\pi}{2(N+1)}$

MAINLOBE FLIPPING OF SLOTTED ARRAY

The mainlobe of a plate mounted slot antenna modeled by the NEC-BSC code should point in the same direction as the normal of the mounting plate defined by the user. However, there are several occasions whereby this rule is not followed. Below are three examples chosen to show this "mainlobe flipping" problem.

Example 1

A 10 x 10 half wavelength slot array with Cosine-Square tapering in both directions, operating at 10 GHz, is placed directly on the center of a conducting plate of size 4.5m x 3.0m. The plate normal is chosen to point toward +Z direction, but the radiation pattern in Fig. 5 shows that the mainlobe points toward -Z direction.

Example 2

A 5 x 5 half wavelength slot array with Uniform tapering in both directions is mounted directly on the same plate as in Example 1. Fig. 6(a) shows that the mainlobe is pointing in the correct direction. When 2 cylinders are attached to the mounting plate as shown in Fig. 7, the mainlobe flipped toward the opposite direction as shown in Fig. 6(b).

Example 3

Fig. 8(a) shows a large element of size 83.391λ x 66.7128λ with uniformly distributed aperture E-field mounted directly on the same plate. Fig. 9(a) shows that the mainlobe is pointing in the +Z direction. When the 2 cylinders are again attached to the plate as shown in Fig. 8(b), the radiation pattern of Fig. 9(b) shows two mainlobes of equal amplitude point toward the +Z and -Z directions. The peak E-field of each lobe is equal to one half of that shown in Fig. 9(a).

For the cases where the mainbeam points toward the wrong direction as in example 2 and 3, one can always elevate the array elements slightly above the plate (~ 0.003λ) in the direction of the normal and bring the mainlobe back to the correct angle. However, if the mainlobe is split evenly into two lobes as in example 3, lifting the elements may not work. Instead, one can increase the length of the cylinders so that they protrude slightly beyond the plate or reduce them so that they do not touch the plate, and the original radiation patterns may be restored.

ANALYSIS RESULTS

The analysis of the Flywatter System resulted in a Uniform - Cosine tapered array with the following configuration :

Element size	0.8687λ x 0.5λ
No. of elements	96 x 133
Element spacing	Nil
Element excitation	TE_{10} mode
Tapering type along Z_t direction	Uniform
Tapering type along X_t direction	Cosine

The overall system performance is listed below :

Output peak power	1.88GW
Maximum Aperture E-field	10.6 KV/cm

The near field radiation patterns measured at 5m distance from the center of the reflector plate are shown in Fig. 10. The array is facing φ = 90° and the reflector plate is tilted at 45°. The plots show that most of the radiated energy is concentrated in

the main beam and the radiation levels drop to below 50 dB W/m^2 at elevation angles greater than 120°. The center of the reflector plate is about 5m above the ground, hence, the radiation level near the ground plane will not exceed 50 dB W/m^2. The ANSI C95.1-1982 Protection Guide suggested a radiation hazard limit of 5 mW/cm^2 of average radiated power density at X band. Converting this limit to peak power density yields 77 dB W/m^2. Hence, we have 27 dB of safety margin.

CONCLUSIONS

The NEC-BSC code is a powerful software tool for the analysis of electromagnetic radiation in the presence of complex structures. However, the code alone without any supporting software is not very useful. Four software programs were then written to support data input and output for the code. These programs were written mainly for the project and need to be improved for general usage.

Although there is no limit on the number of source elements used in the code, except the computer storage limitation, computing time increases proportionaly with number of sources. Hence, for large arrays simplified models are needed to reduce computation time. In this report, two simplification techniques for in-phase planar arrays that are applicable to the NEC-BSC code are mentioned. The first one is restricted to Uniformly tapered elements along X_t direction while the second technique is applicable to either Uniform or Cosine tapering along Z_t direction. The first technique yielded the same solution as the original source model while the second technique required some simple compensation in magnitude to restore the radiation patterns to the original levels.

The present NEC-BSC code used at NPS is version 2.5. This version has two main disadvantages. The first one is the limited computation capability in handling multiple reflected and diffracted rays, thereby, reducing the accuracy range of the radiation patterns when complex structures are present. The second disadvantage is the flipping of the mainlobe between the correct and opposite pointing position when a plate mounted slot array is used. Until this problem is fixed, one should always check the radiation patterns of any slot array before proceeding with additional structure computations.

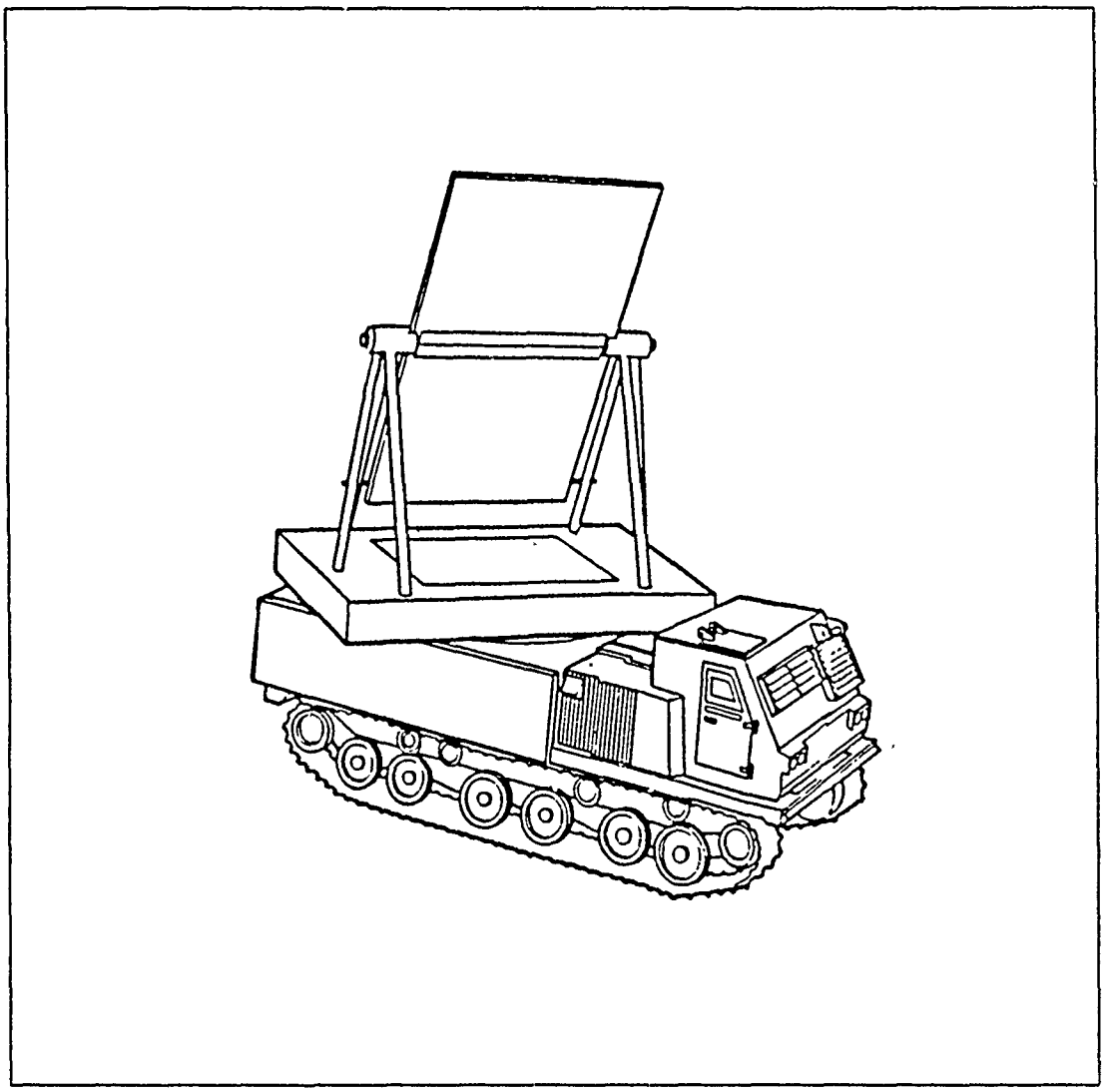


Figure 1 Flyswatter System.

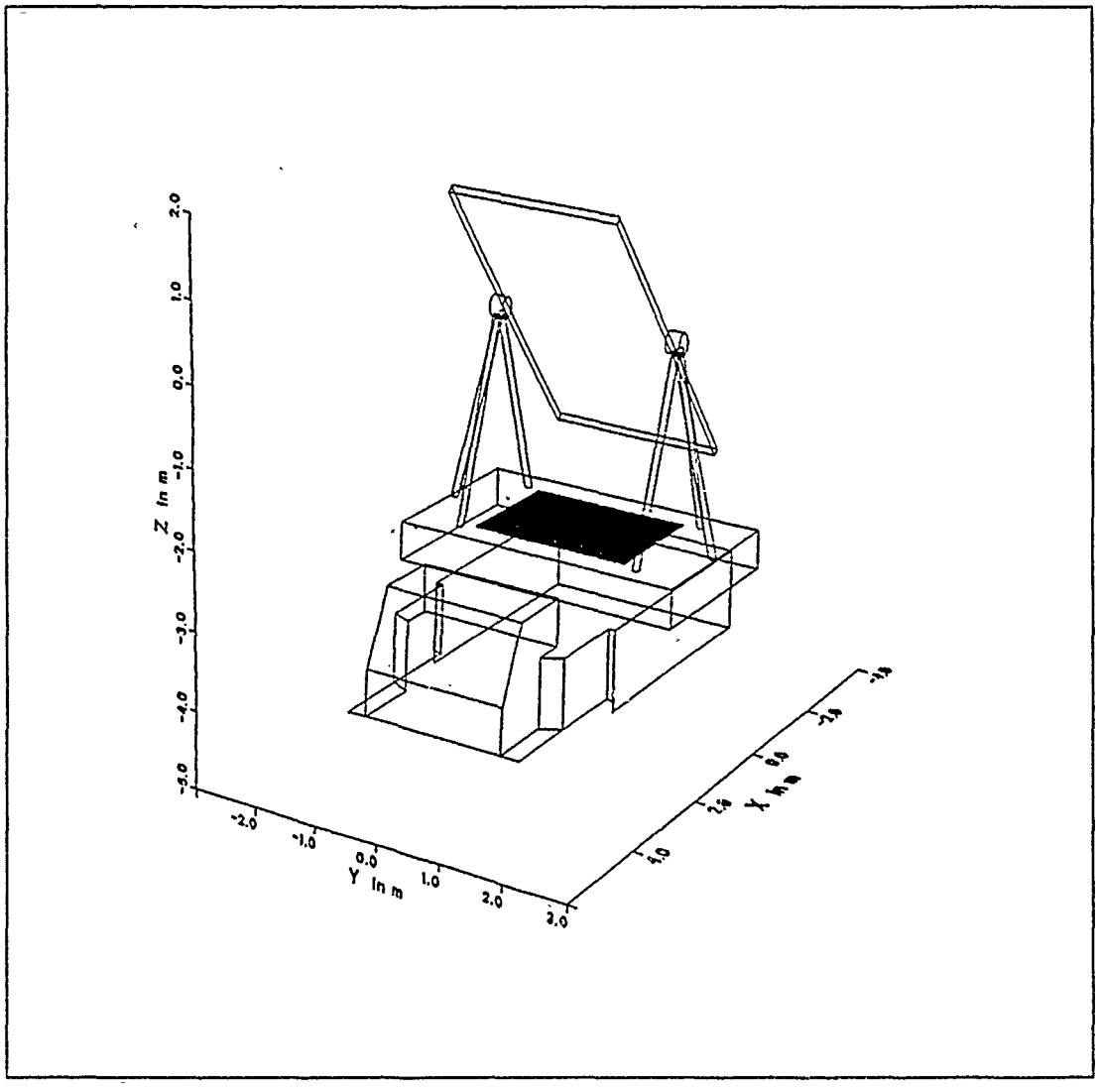


Figure 2 Computer Model of Flyswatter System Plotted by GTDGEOMP.

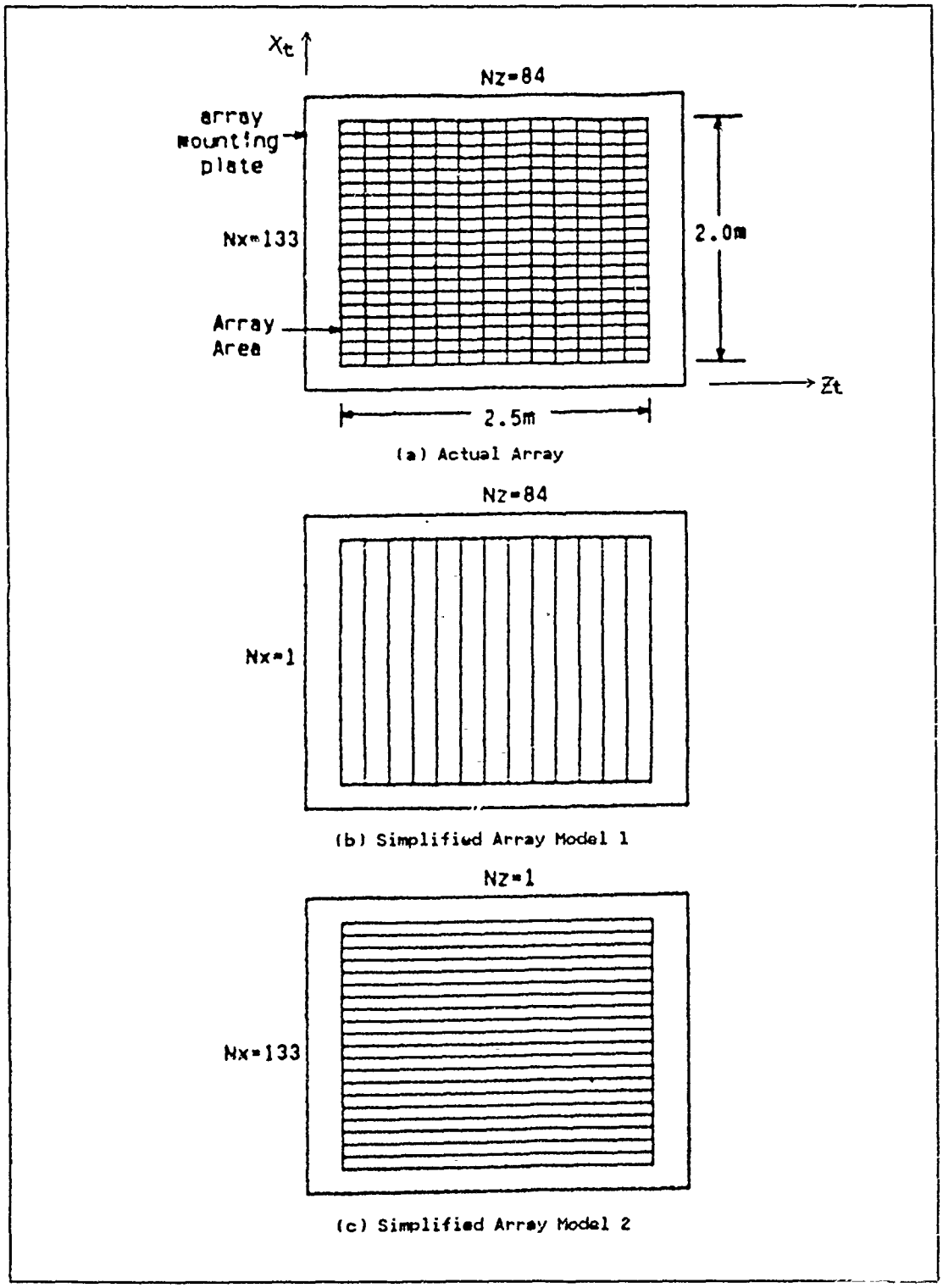


Figure 3 Array Model Simplifications.

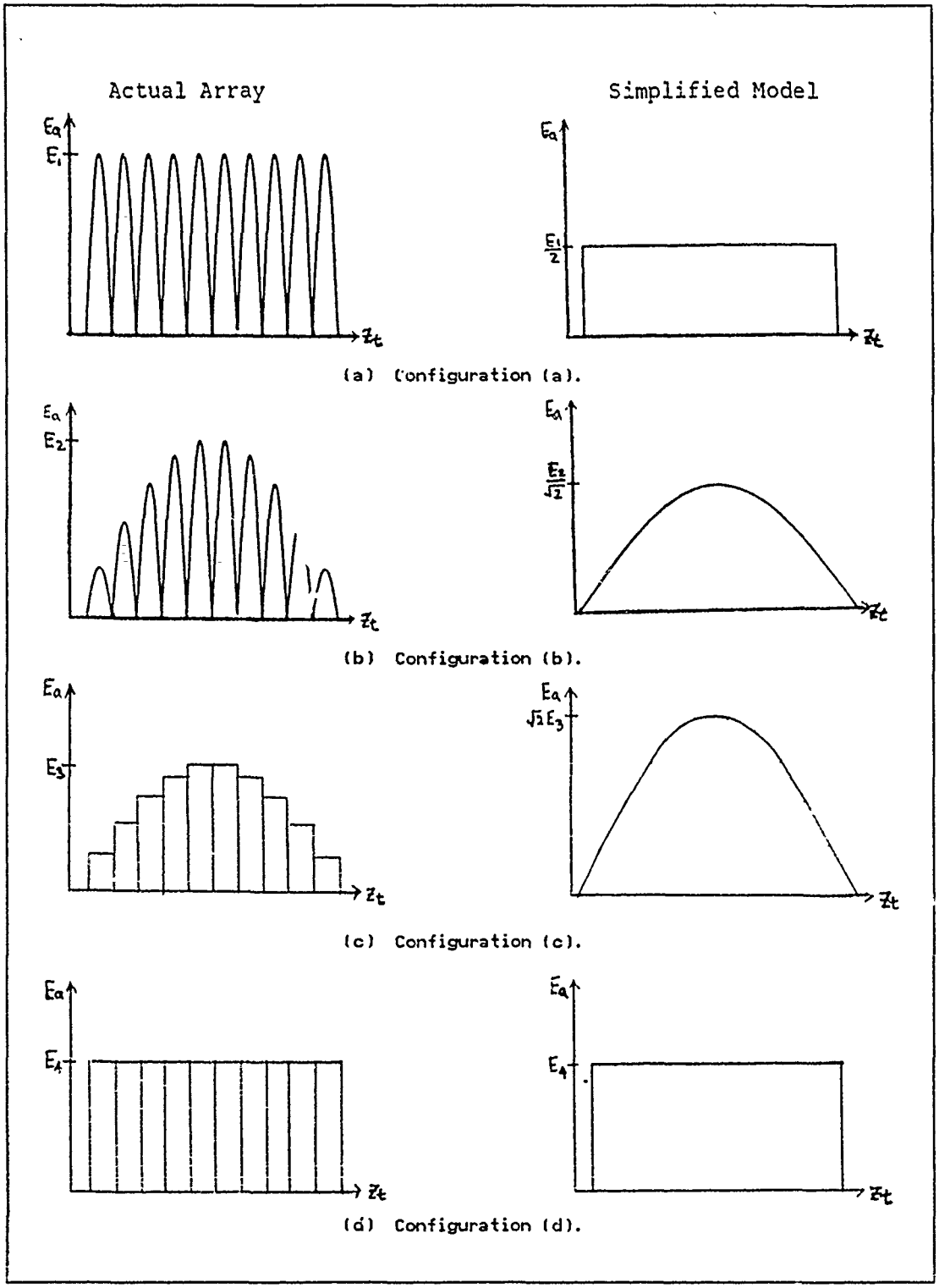


Figure 4 Aperture E-field Distributions for Both the Actual and Simplified Model.

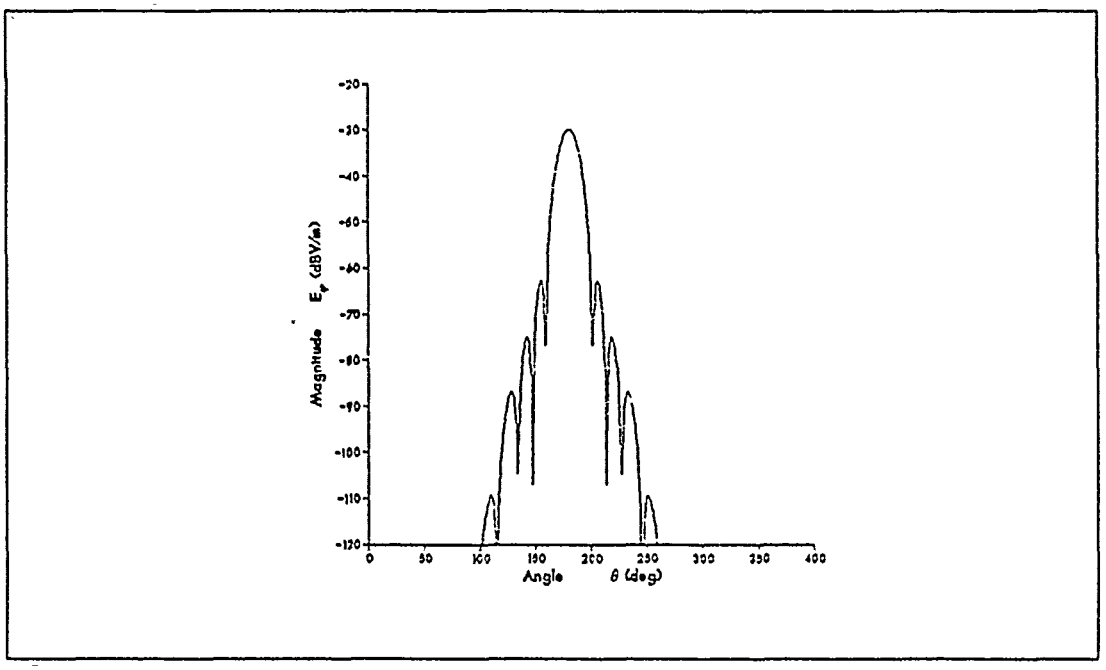


Figure 5 Far field Radiation Pattern of Example 1.

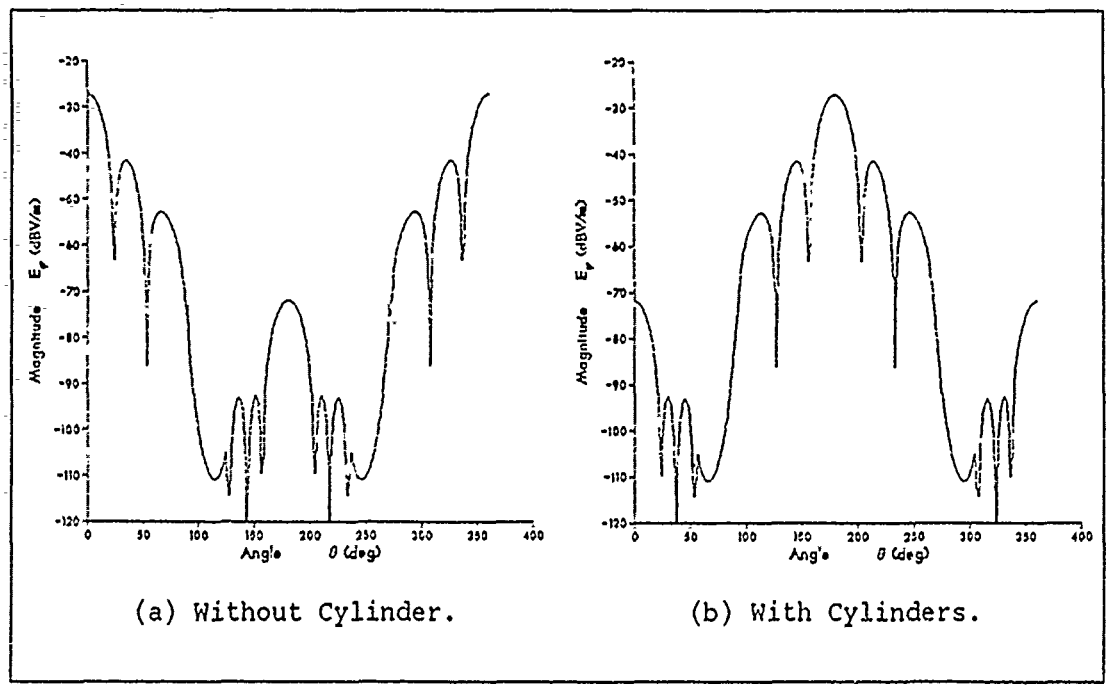


Figure 6 Far Field Radiation Patterns of Example 2.

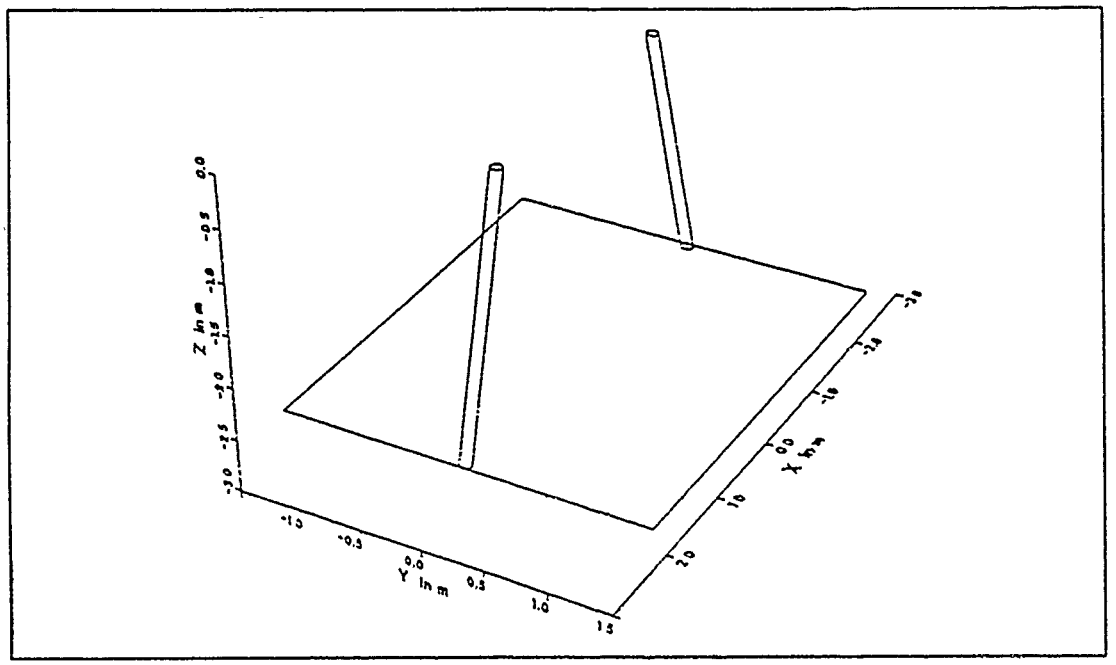


Figure 7 Geometry Plot of Example 2.

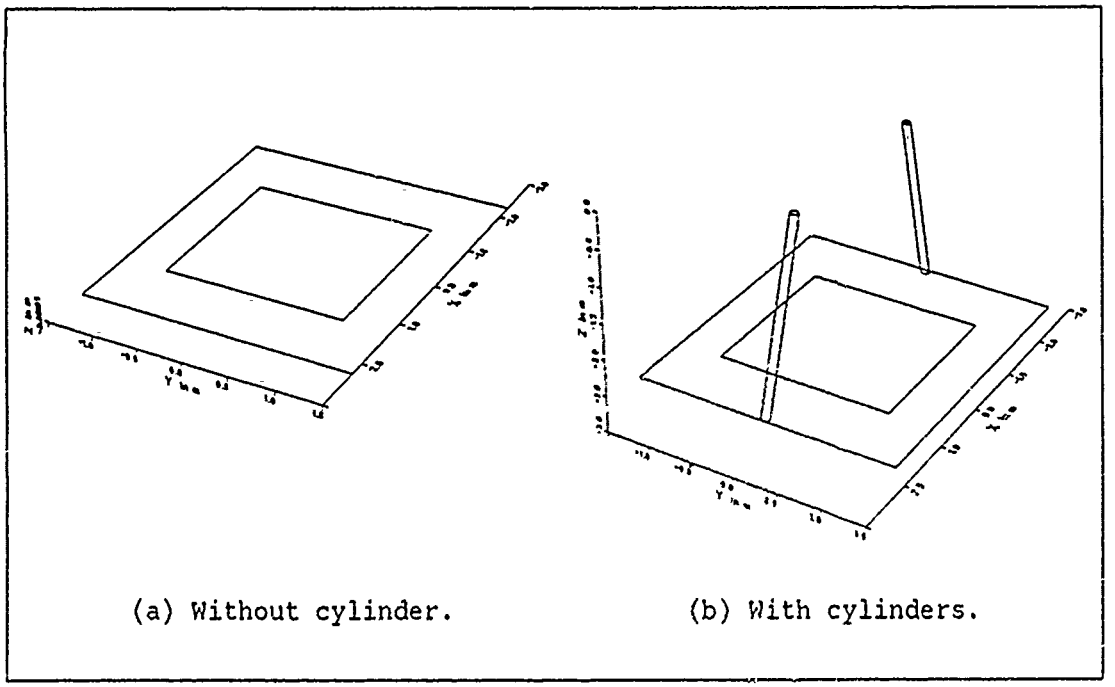


Figure 8 Geometry Plots of Example 3.

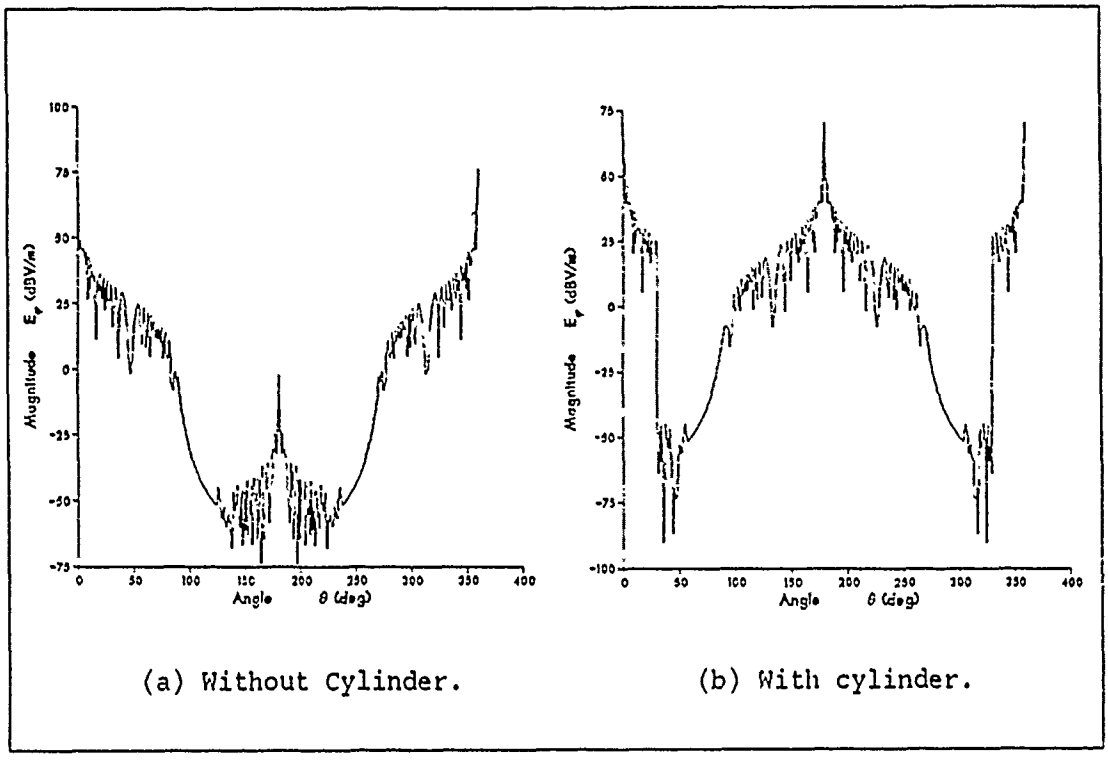


Figure 9.1 Far Field Radiation Patterns of Example 3.

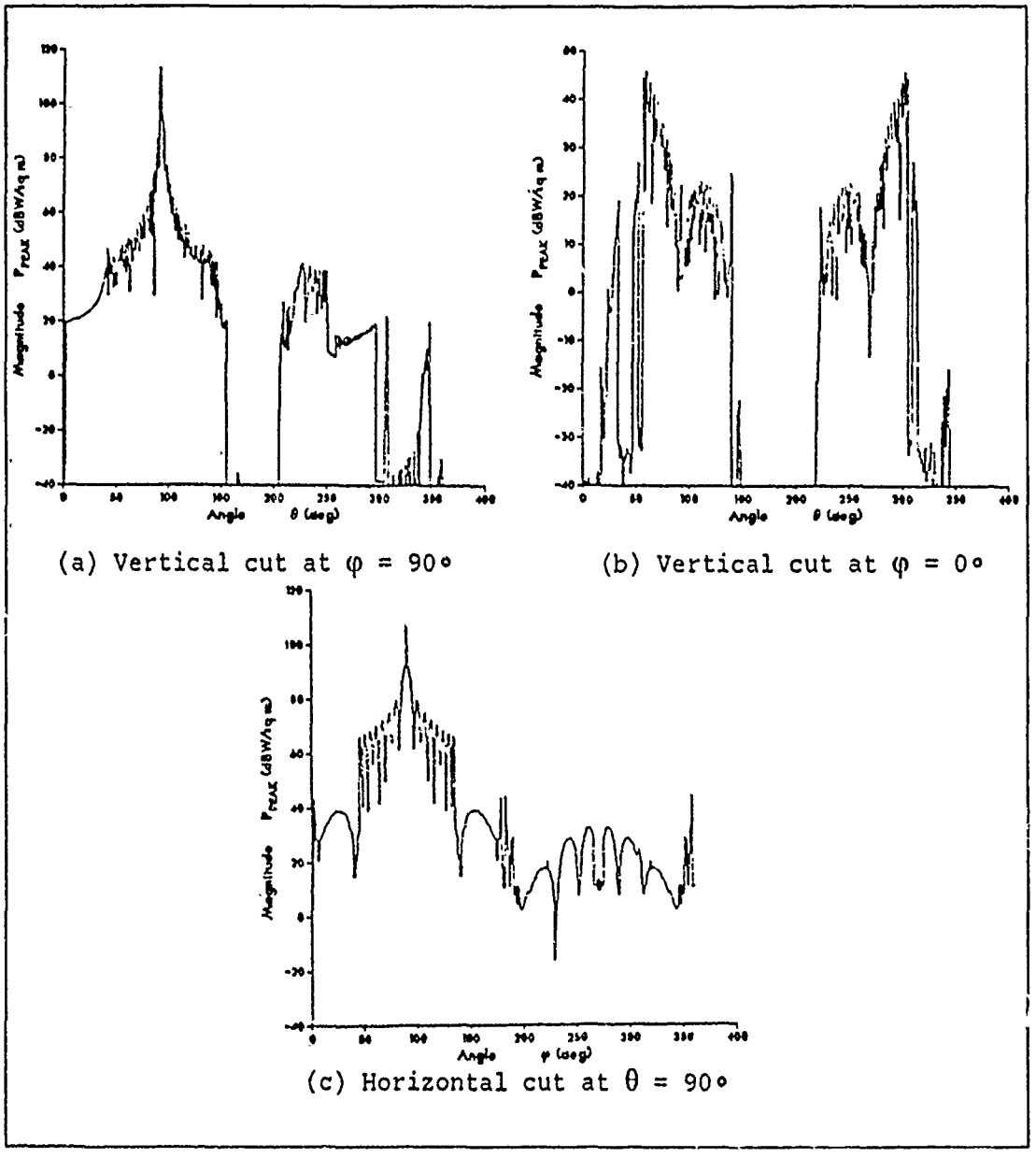


Figure 10 Near Field Plots of Flyswatter System.

TWO COMPUTER GRAPHICS SIMULATIONS OF THE ELECTRIC FIELD RADIATED BY A DIPOLE ANTENNA

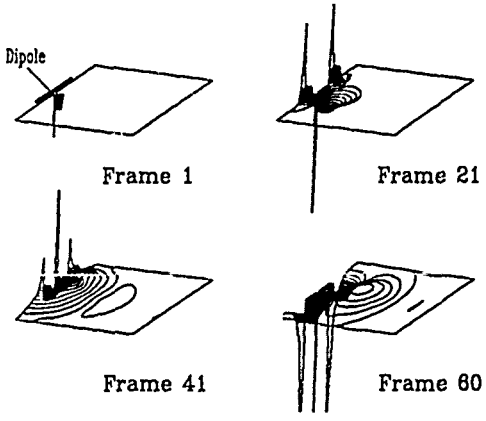
Dennis E. Fessenden
Naval Underwater Systems Center
New London, CT. 06320

Steven G. Satterfield
Computer Aided Design/Interactive Graphics
U. S. Naval Academy
Annapolis, MD. 21402

Two types of dynamic graphics simulations were produced for the time varying electric field data about an axi-symetric dipole antenna. The field data was generated by an axi-symetric finite difference - time domain (FD-TD) computer program applied to a center fed half-wave dipole excited by a sinusoidal source running for three cycles. Only the vertical component of the electric field is shown in the simulation.

For each simulation, the FD-TD program produces a series of data files. The data files represent the field strength for a two dimensional array of discrete points for each time step calculated. This data can be considered as a surface description of x,y,z triplets where the x,y coordinate is the field location and the corresponding z value is the field strength. Since each data file represents the field at a discrete point in time, it can be used to produce a single frame of a graphics animation sequence. These frames were then combined on two different graphics systems to produce two animation sequences.

The first animation sequence illustrates the field propagation as three dimensional contour lines. Each data file was converted to a polygonal surface description. A contouring program was applied to each surface description to produce contours of equal field strength. The appropriate field strength (z component) was added to the x,y contour values producing a set of three dimensional contours. The result was a series of files containing three dimensional contours for each time step of the simulation. Utilizing an Evans & Sutherland PS300 graphics display, a three dimensional display program was used to display the contours. The PS300 has control dials which allows the user to dynamically rotate, scale and translate the data being displayed. For a typical simulation, sixty frames were generated and displayed in sequence to simulate the motion of the electric field. Shown below are frames 1, 21, 41, and 60 of the sequence. During the animation, the user has full three dimensional viewing control via the PS300 dials.



The second animation sequence illustrates the field propagation as a two dimensional color shaded image with field strength color coded. The polygonal surface description corresponding to each time step was used. A display program for an Ikonas RDS-3000 color frame buffer was used to create a two dimensional display of each polygon file. The z (field strength) component was applied to a color scale for each of the calculated points. Each polygon was filled by linearly interpolating between the color values of the polygon points. The resultant image was displayed at a resolution of 512 scan lines by 512 pixels per scan line with 24 bits of color per pixel. Real time animation of this sequence was not possible since the image creation time for each frame was excessive. However, a Lyon-Lamb VAS-IV was used to record the images frame by frame onto video tape. Since the VAS-IV allows single video tape frames to be recorded, a dynamic animation sequence is produced.

The three dimensional contour lines animation should provide insight into wave propogation from an antenna through radome enclosures of various shapes and material properties. Both animations are useful for educational purposes.